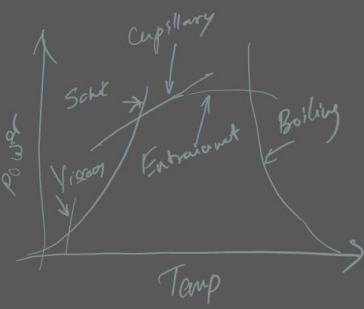
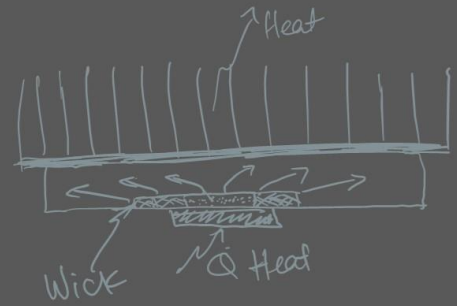


Limits



$$(\Delta P_c)_m \geq \int \frac{\partial P_v}{\partial x} dx + \left(\frac{\partial P_c}{\partial x} dz + \Delta P_{\text{inlet}} + \Delta P_{\text{pump}} + \Delta P_n + \Delta P_{\text{out}} \right)$$



$$q_{be} = \left(\frac{2\pi L e k_{eff} T_v}{\lambda R \ln(r_i/r_o)} \right) \left(\frac{2S}{r_n} - \Delta P_{cm} \right)$$

$$P_{cap} = \left(\frac{1}{R_I} + \frac{1}{R_{II}} \right)$$

capillary pressure

Effective Thermal Conductivity
Wick and liquid

$$k_e = \frac{k_l k_w}{\epsilon k_w + k_l (1 - \epsilon)}$$

Joint 21st International Heat Pipe Conference and 15th International Heat Pipe Symposium

Melbourne, Australia 5th to 9th February 2023

Proceedings



<https://heatpipeaus.com/>

Advanced Hot Reservoir Variable Conductance Heat Pipe for Space Applications

Kuan-Lin Lee^{1*}, Calin Tarau¹, William G. Anderson¹, Cho-Ning Huang², Chirag Kharangate² and Yasuhiro Kamotani²

¹ *Advanced Cooling Technologies Inc., Pennsylvania, USA*

² *Case Western Reserve University, Ohio, USA*

**Corresponding author email address: kuan-lin.lee@1-act.com*

Abstract

The lunar landers and rovers are exposed to harsh extreme temperature conditions such as those during the lunar day and night. Therefore, a reliable passive tight thermal control link between the payload and the radiator is needed. A Hot Reservoir Variable Conductance Heat Pipe (HR-VCHP) is an ideal thermal link since it can provide a much tighter and passive thermal control when compared to the cold reservoir variable conductance heat pipes. However, previous International Space Station (ISS) test results concluded that multiphase flow management is the key to improve the reliability of HR-VCHP for long-term lunar surface missions. In NASA funded Small Business Technology Transfer (STTR) programs, Advanced Cooling Technologies Inc. (ACT) and Case Western Reserve University (CWRU) worked together to perform fundamental studies and develop advanced fluid features that can better handle multiphase flow within the device. An aluminum HR-VCHP prototype with improved reliability was developed. A detailed experimental analysis of the HR-VCHP prototype, that includes startup testing, purging testing, and thermal control testing, is presented. The effect of using different working fluid was investigated. Moreover, the purging rate, for different working fluids, was numerically predicted.

Keywords: Variable conductance heat pipe; Thermal control; Lunar landers; Multiphase flow management

1. Introduction

NASA's plans to further expand human and robotic presence in space automatically involve significant challenges. Spacecraft architectures will need to handle unprecedented thermal environments in deep space. In addition, there is a need to extend the duration of the missions in both cold and hot environments, including cis-lunar and planetary surface excursions. The heat rejection turn-down ratio of the increased thermal loads in the above-mentioned conditions is critical for minimizing vehicle resources (e.g., power). Therefore, future exploration activities will have the need of thermal management systems that can provide higher reliability and performance, and, at the same time, with reduced power and mass.

To meet these requirements passive thermal management concepts that offer large turn-down ratios are encouraged. As an example, the anchor node network (which is a lander that includes a seismometer, a laser reflector, and a probe for measuring heat flow from the Moon's interior) has a Warm Electronics Box (WEB) and a battery, both of which must be maintained in a fairly narrow temperature range. A variable thermal link between the WEB and radiator is required. During the day, the thermal link must transfer heat from the WEB electronics to the radiator as efficiently

as possible, with minimum thermal resistance, to minimize the radiator size. On the other hand, the thermal link must be as ineffective as possible (provide as high thermal resistance as possible) during the Lunar night. This will keep the electronics and battery warm with minimal power, even with the very low temperature (100 K) heat sink. At this time, heat must be shared between the electronics and battery, to keep the battery warm. Moreover, since the cold lunar night is very long (14 days) minimizing or even eliminating the survival power is highly desired. This can be done with a passive variable thermal link between the WEB and the Radiator, variable thermal link that can be a hot reservoir VCHP (HR-VCHP).

A HR-VCHP as Figure 1 shows, has a Non-condensable Gas (NCG) reservoir located near the evaporator and the reservoir temperature follows the evaporator. This will significantly improve the tightness of thermal control capability compared to a conventional cold-biased reservoir VCHP and it is fully passive (i.e., reservoir is heated by the payload waste heat). The HR-VCHP was tested on ISS in 2017 as part of the Advanced Passive Thermal eXperiment (APT_x) project [1]. The pipe showed higher than admissible temperatures that tripped the safety thermostats. The description of the failure mechanism is as follows: during

startup, the absence of natural convection in microgravity delayed the NCG heating compared to vapor heating that was much more effective because of metallic (copper) path of the incoming heat. The consequence was that vapor pressure increased faster than NCG pressure (because of poor heating) and the resulted pressure wave put vapor into the colder NCG from reservoir where part of it condensed. As a result, the NCG was pushed out in the condenser increasing vapor temperature considerably. Next step was the attempt to remove vapor from the reservoir by applying heat to the reservoir, which is referred as “purging process”. It was found that the rate of purging was very low as it was dominated by diffusion.

Based on the ISS test experience, it was concluded that fluid management within the reservoir and the NCG tube (typically non-wicked) of VCHPs is the key area to be improved. More specific, advanced features/solutions that can (1) prevent working fluid condensing inside a reservoir and (2) remove working fluid from the reservoir efficiently. Under this STTR program, ACT in collaboration with CWRU developed an aluminum HR-VCHP with improved reliability in both ground and microgravity operations. The concept is shown in Figure 2. The configuration consists of a hot reservoir, heat pipe sections, and two NCG links. One link is internal, coming out from the reservoir and going through the heat pipe section from the evaporator side. The second NCG link is external, connecting the end of the condenser with the reservoir. This advanced loop configuration would allow a secondary (NCG) fluid flow to be induced by the momentum of the primary vapor flow through the annular region of the heat pipe section. The secondary flow will travel along the loop in the favorable direction (reservoir-internal tube – condenser) and purge excessive vapor from the reservoir if exists. The continue momentum induced flow will maintain the moisture level of reservoir as long as the heat pipe is operating. This will significantly improve the reliability of the device for future space missions.

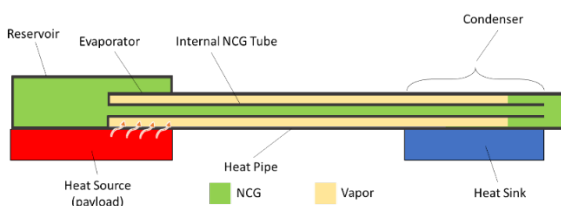


Figure 1. HR-VCHP with internal NCG tube and reservoir integrated with heat pipe evaporator

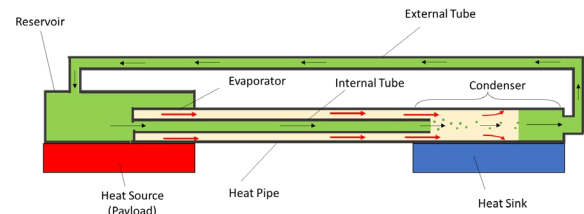


Figure 2. HR-VCHP with improved fluid management (red arrows: primary vapor flow; black arrows: secondary NCG flow)

2. Prototype Development

A great deal of effort has been spent under STTR program on improving the prototype to optimize multiphase flow. Most of the design modifications were applied on the internal and external NCG tubes. More details on the original and improved HR-VCHP prototypes can be found in [2-4]. The improved prototype design, used in this study, is shown in Figure 3. The whole prototype is made from aluminum. The heat pipe wick structure consists of axial grooves along the whole heat pipe. The evaporator integrated reservoir is 10.2 cm (4 inches) long. The length of the condenser is 15.2 cm (6 inches), and the adiabatic section is 14.6 cm (5.75 inches).

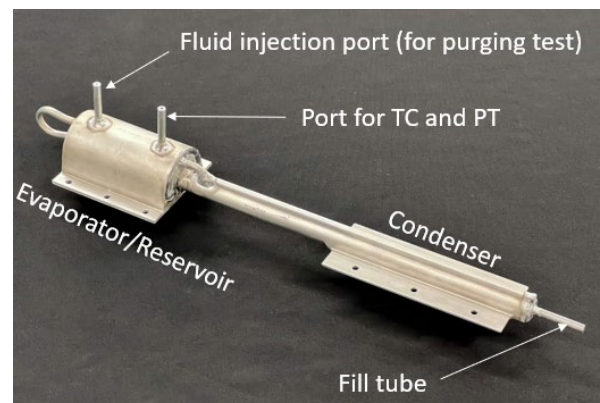


Figure 3. The advanced HR-VCHP prototype.

The grooves and reservoir profiles were fabricated through electrical discharge machining (EDM). Figure 4 shows cross-sectional views at the evaporator/reservoir and condenser sections.

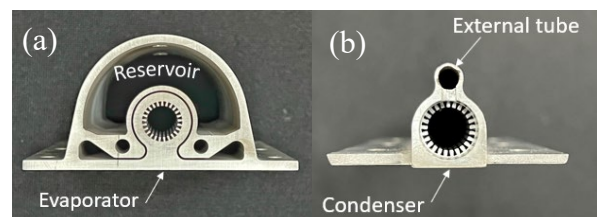


Figure 4. Cross-sectional views at: (a) the evaporator/reservoir and (b) condenser sections.

3. Test Apparatus

An experimental setup was built for HR-VCHP

prototype testing. As Figure 5 shows, the test apparatus consists of an 80/20 frame with adjustable tilted angle, heater block, cold plate, and instrumentation. A heater block was made of aluminum block with two inserted cartilage heaters. The cold plate was also made of aluminum block with embedded copper tubing for LN cooling. Figure 5 shows the thermocouples map. A total number of 23 TCs were used for temperature measurements. In addition to temperature measurement, a pressure transducer (PT) was attached to the reservoir to measure the system pressure. Thermal control and reliability testing were performed. The reliability test includes the baseline test (i.e., demonstrates the HR-VCHP functions as a heat pipe), purging test, and extreme start-up test.

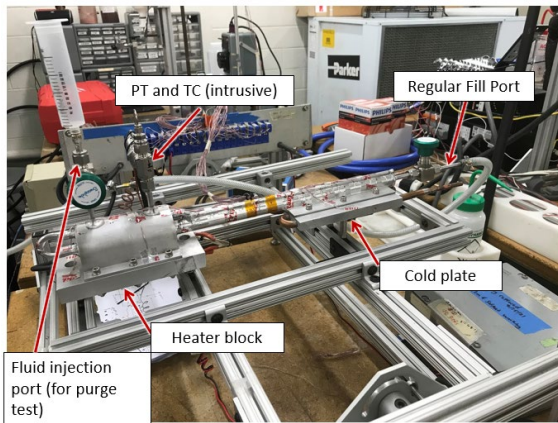


Figure 5. The test apparatus.

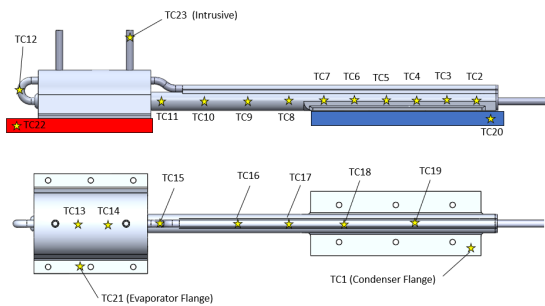


Figure 6. The thermocouples map.

4. Thermal Control Testing

The experiment was performed in two stages. In the first stage, the sink temperature was decreased from a nominal condition (40°C) to a survival temperature of -80°C while keeping the heat input a constant. In the second stage the sink temperature was maintained at a constant of -80°C and the input power was gradually reduced until the evaporator temperature (TC21) dropped below the minimal survival temperature (-40°C). Toluene was used as the working fluid and helium was the NCG. The pipe was tested in horizontal

orientation. Temperature variation was shown in Figure 7 and the instantaneous temperature profile along the heat pipe (from evaporator flange to the condenser flange) at nominal mode ($t = 2900$ seconds) and the survival model ($t = 32400$ seconds) were shown in Figure 8. At $t = 2920$ seconds, the sink temperature was reduced from 40°C to -80°C . The evaporator flange temperature (representing the payload temperature) dropped by 27°C . At $t = 8200$ seconds, heat input was scaled down from 75W all the way to 2.5W . The test ended at 32400 seconds. The final evaporator temperature before shutting off the test was -15°C . The thermal conductance during ON and OFF conditions can be calculated based on the ΔT between evaporator and condenser flanges and the heating power, which is around 80:1. It can be seen from the instantaneous temperature profile (Figure 8) that during the nominal mode, the condenser is not fully opened and during survival mode, the evaporator did not reach -40°C (survival temperature of the payload). By further lowering the sink temperature and survival power, a lower OFF thermal conductance can be obtained. Thus, a higher turn-down ratio could be achieved.

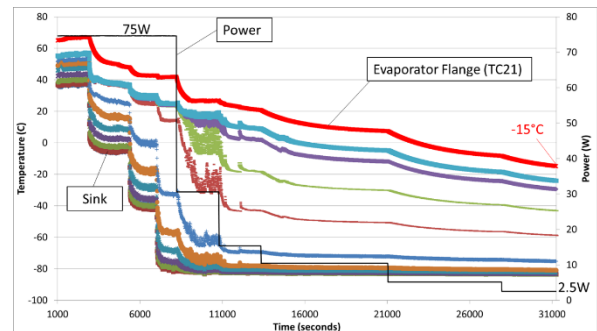


Figure 7. Thermal control testing result of HR-VCHP with toluene as working fluid and helium as NCG.

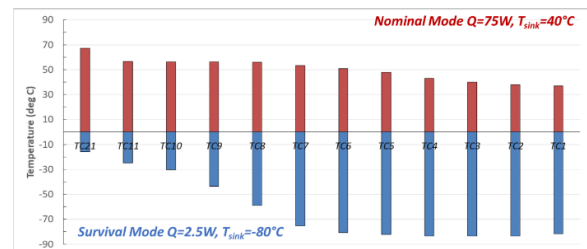


Figure 8. Instantaneous temperature profile along the VCHP in nominal and survival modes

5. Reliability Testing

The reliability test is an important test since this is the major focus and motivation of this STTR program. The objective of the reliability test is to demonstrate that the HR-VCHP prototype can

recover from critical situations to normal operation quickly. Two critical situations investigated are: (a) Some liquid working fluid presents in the hot reservoir while the heat pipe is operating; and (b) Startup heat pipe with all working fluid in the reservoir

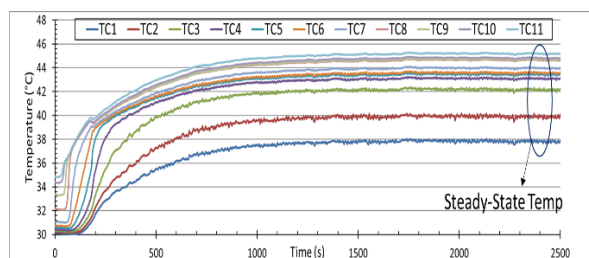
Situation (b) is most likely not going to occur during the actual mission and is considered to be the worst-case scenario.

The reliability test consists of three testing performed in series:

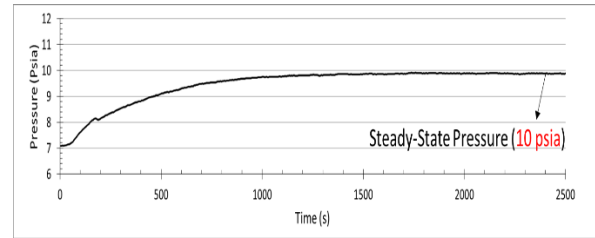
- (1) Baseline – Charge working fluid and NCG to the heat pipe section. Start up the pipe with 75W of heat input until the pipe reaches a steady state.
- (2) Purge test – After the heat pipe reaches a steady-state, add 0.5 cc of working fluid into the hot reservoir. Record the response of HR-VCHP.
- (3) Extreme startup – Charge NCG and all working fluid to the reservoir. Start up the pipe with 75W of heat input until the pipe reaches a steady state. Two working fluids were tested: acetone and toluene. Helium was the NCG. Both temperature and pressure variations during the test were recorded. The heat pipe was tested in horizontal orientation.

5.1. Baseline Testing

In this test, $5.8E-4$ moles of helium and 10 cc of acetone were charged to the heat pipe section via the regular fill tube (i.e., the fill tube at the end of condenser) at room temperature. The sink temperature was set at 30°C . Figure 9a shows the startup process of the HR-VCHP with all the fluid originally in the heat pipe section. The upper figure shows the temperature data from the adiabatic section to the end of the condenser. Figure 9b shows the pressure data. The steady-state heat pipe pressure was 10 psia, which corresponds to the saturation vapor pressure of TC11. The duration to reach the steady state was around 2000 seconds.



(a)



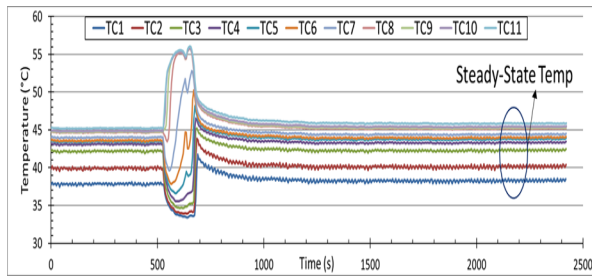
(b)

Figure 9. HR-VCHP baseline startup test results using acetone as working fluid (a) temperature (b) pressure

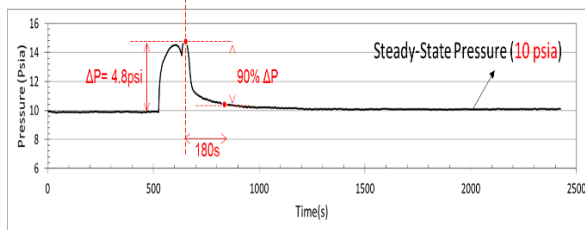
5.2. Purging Testing

Once the heat pipe reached the steady state, we started a new data collection sheet to perform purge test. The purge test result is shown in Figure 10. At $t = 530$ seconds, 0.5 cc of acetone was injected into the hot reservoir. As shown in Figure 10a, the adiabatic section temperature increased, and the condenser temperature dropped. This was caused by the effect that NCG originally in the reservoir was pushed out by the acetone vapor that was added into the reservoir. The condenser was fully blocked by the NCG so the heat pipe temperature elevated. Based on the momentum-induced flow theory of HR-VCHP discussed in the previous quarterly reports, the flow generated within the VCHP can purge the vapor out from the reservoir and deliver NCG back to the reservoir. It can be seen from the figure that the vapor/NCG front quickly recovered from an abnormal location to the original position. The pressure dropped from a peak value of 14.8 psia to 10 psia quickly, indicating efficient purging (see Figure 10b). ACT defined the purge time as the duration for the system pressure dropping from a peak value to 90% ΔP . Afterward, the heat pipe was in the normal operation mode. The purge time was 180 seconds.

With the given added fluid volume, pipe geometry and measured purge time, the bulk purge mass rate, volumetric flow rate via the NCG tubing and purge velocity can be estimated. It was estimated that the bulk purge flow velocity in this test was 1.2 cm/s. It is worth noting that the estimation was conservative since we only considered that the gas phase in the reservoir was 100% vapor. The heat pipe was then evacuated for the next test – the extreme startup.



(a)



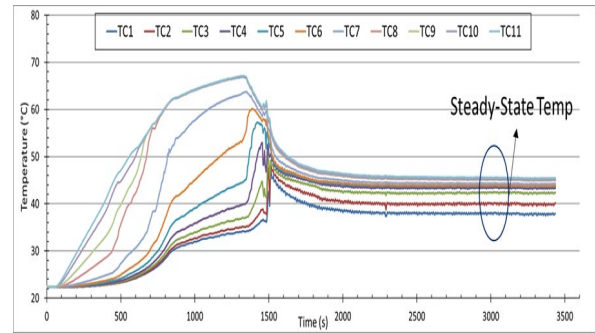
(b)

Figure 10. HR-VCHP purging test using acetone as working fluid (a) temperature (b) pressure

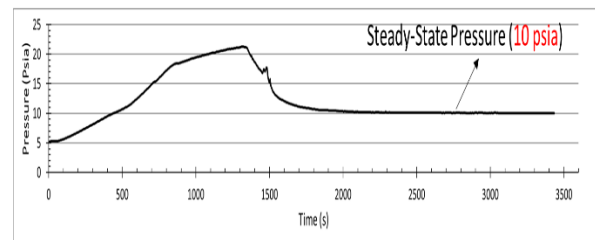
5.3. Extreme Startup Testing

In this test, 5.8×10^{-4} moles of helium were first charged to the heat pipe from the regular fill tube. 10 cc of acetone was charged to the reservoir and no working fluid was charged to the heat pipe. 75W of heat was applied to the evaporator and the sink temperature was set at 30°C . Temperature and pressure data during the startup process is shown in Figure 11. In the beginning of startup, the heat pipe was not operating. Since that the reservoir is thermally integrated with the evaporator, heat conducting to the reservoir will vaporize the working fluid over there and the vapor will migrate via two NCG tubing to the condenser. Some vapor will turn into liquid and capillary driven by the grooves to the heat pipe evaporator. Once the liquid is present in the evaporator, the heat pipe can startup.

This process can be seen from the temperature plot that at 700 seconds, TC 8 (last TC in the adiabatic section) merges with other adiabatic section TCs. This indicates vapor is being generated in the heat pipe section and is marching toward the condenser. The heat pipe temperature reached a peak value at $t = 1350$ seconds when the set point was reached, and LN started cooling the condenser. The heat pipe temperature started decaying. It was anticipated that the momentum-induced flow was continuously working to dehumidify the reservoir and organize the vapor/NCG distribution during the startup process. The pipe successfully started up and reached the steady state with the pressure value of 10 psia, same as the baseline test. It only took around 2200 seconds to startup.



(a)

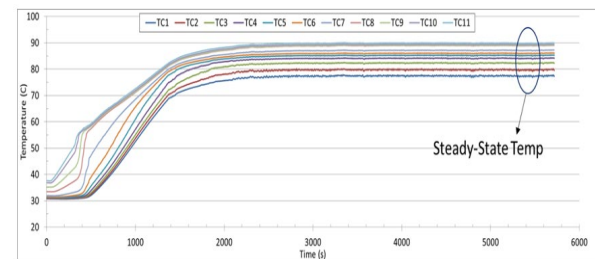


(b)

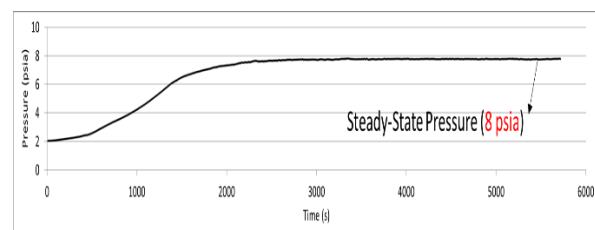
Figure 11. HR-VCHP startup with all working fluid initially in the reservoir (acetone as working fluid)

5.4. Effect of Using Different Working Fluid

The reliability test was repeated with toluene as working fluid and helium as NCG and the corresponding baseline, purge and extreme start up test results are shown in Figures 12-14. Similar performance was observed. The pipe was able to recover quickly from an abnormal situation (0.5 cc liquid in the hot reservoir) and was able to start up from the extreme condition with all working in the reservoir. The estimated purge velocity for toluene was 2.1 cm/s.

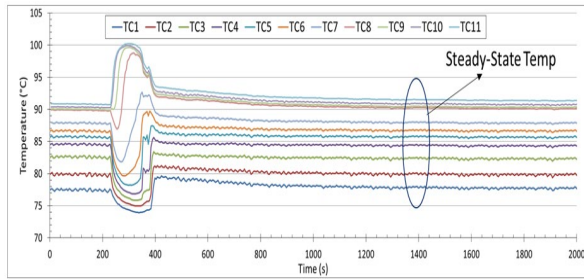


(a)

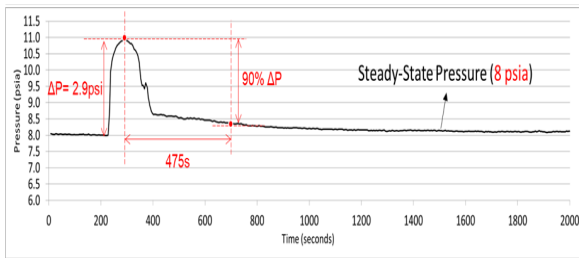


(b)

Figure 12. HR-VCHP baseline startup test (toluene as working fluid)

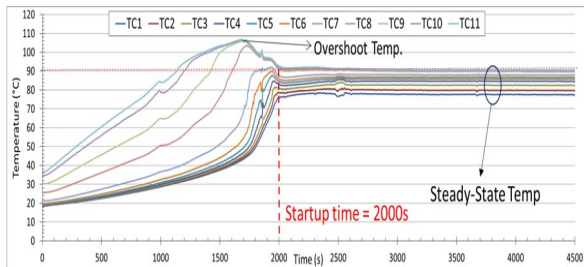


(a)

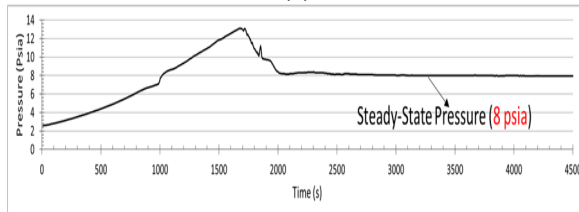


(b)

Figure 13. HR-VCHP purging test (toluene as working fluid)



(a)



(b)

Figure 14. HR-VCHP startup with all working fluid in the reservoir (toluene as working fluid)

6. Numerical Modeling

Case Western Reserve University (CWRU) developed a purge model that can predict how fast a HR-VCHP can complete the purging with known momentum-induced flow velocity. Test data of the previous HR-VCHP prototype was used to validate their numerical model. As the external reservoir and the external loop domains are not axisymmetric, a CFD model is set up in ANSYS Fluent to accurately estimate the time of

purging in the reservoir. The 3D model is transient and incompressible. The flow field domain contains acetone and helium mixture. Figure 15a shows the reservoir and the external tube of the VCHP. To reduce computation time, the domain was simplified to only concentrate on the reservoir section, as shown in Figure 15b. The tube sections are removed because the estimated purging time is not significantly impacted by them.

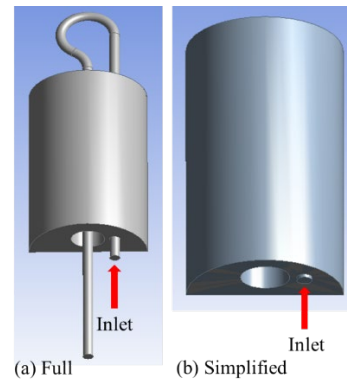


Figure 15. (a) Full geometry provided by ACT; and (b) simplified domain for simulation

Based on the experimental data as shown in Figure 16, two extreme states of the working fluid can be observed in the figure. One is at steady-state and the other one is at the peak pressure state which happens just after the addition of the extra liquid into the reservoir. Based on the experimental test information, the purging pressure and purging velocity for toluene at the two states can be calculated utilizing the in-house CFD code. The results for toluene are listed in Table 1.

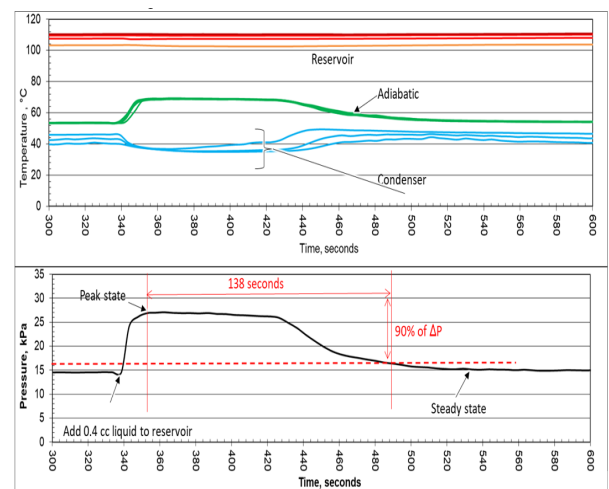


Figure 15. Experimental data of the toluene purging test

Table 1. Purging pressure and velocity of toluene/helium mixture in the condenser at steady-state, peak state, and mean state

	Steady state	Peak state	Mean state
Density (kg/m ³)	0.4908	0.8865	0.6887
Viscosity (Pa-s)	7.79*10 ⁻⁶	8.17*10 ⁻⁶	7.98*10 ⁻⁶
Toluene concentration (condenser region)	62.6%	28.8%	45.7%
Purging pressure (Pa)	0.6575	0.5188	0.58815
Purging velocity (cm/s)	4.4	2.6	3.5

Since purging is a transient process, the properties of toluene keep changing during the whole process as well as the corresponding purging pressure and velocity. Therefore, the properties implemented into the ANSYS Fluent model were the average value between these two extreme states (Mean state in 1). The inlet flow velocity is 3.5 cm/s and concentration of toluene is 45.7%. The initial concentration in the reservoir was set to 100% of toluene at the beginning of purging. The CFD result of the concentration of toluene is shown in Figure 16. The x-axis is flow time and the y-axis is the average concentration of toluene vapor in the reservoir. In this calculation, the purging process was considered completed when the concentration drops below 110% of the mean concentration. It can be seen that the total purging process is about 235 seconds. The experimental purging time shown in 15 is around 134 seconds.

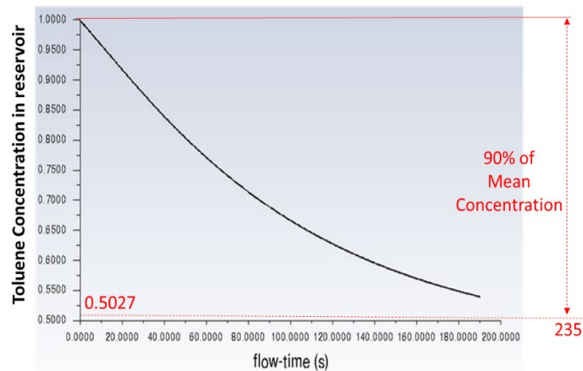


Figure 16. Concentration drop of toluene in the reservoir during purging (CFD)

Similar to the toluene case, average properties of acetone from both states were used in the CFD

model. Table 2 lists the properties, purging pressures, and purging velocities at two extreme states.

Table 2. Purging pressure and velocity of acetone/helium mixture in the condenser at steady-state, peak state, and mean state

	Steady state	Peak state	Mean state
Density (kg/m ³)	0.7722	1.132	0.9521
Viscosity (Pa-s)	7.52*10 ⁻⁶	7.79*10 ⁻⁶	7.6*10 ⁻⁶
Acetone concentration (condenser region)	53.2%	29.1%	41.2%
Purging pressure (Pa)	0.7934	0.4155	0.6045
Purging velocity (cm/s)	4.9	2.1	3.5

Inlet velocity is 3.5 cm/s and inlet concentration is 0.412. Same as toluene's case, the purging process was considered completed when the average concentration of reservoir drops below 110% of the mean concentration (110%×41.2%). Figure 17 shows the CFD prediction of the concentration change in the reservoir. It takes about 260 seconds for the purging process to complete 90% change in concentration difference. Meanwhile, in the experiment, the measured time of acetone case is 340 seconds. It should be noted that the CFD simulation can only predict the part after the peak state.

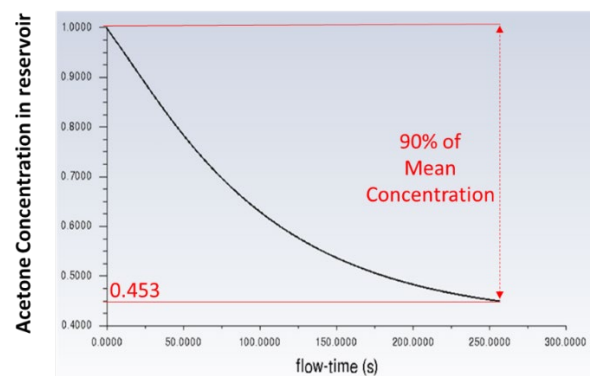


Figure 17. Concentration drop of acetone in the reservoir during purging (CFD)

7. Conclusions

In this paper, ACT and CWRU developed an improved HR-VCHP prototype design to optimize the multiphase flow management inside it. A detailed experimental analysis of an advanced

HR-VCHP, that includes startup testing, purging testing, and thermal control testing, is presented. The effect of different using different working fluids was investigated. Moreover, the purging rate, for different working fluids, was numerically predicted. The conclusions can be summarized as follows:

- The modified HR-VCHP prototype did not compromise the thermal control capability of the original HR-VCHP prototype.
- For the two different working fluids, the modified HR-VCHP prototype showed a successful baseline test results where it functions as a heat pipe when no NCG is charged.
- For the two different working fluids, the modified HR-VCHP prototype provided a much faster purging process when compared to the conventional diffusion purging process.
- For the two different working fluids, the modified HR-VCHP was able to successfully overcome an extreme startup scenario (i.e., starts from a highly humidified reservoir) in less than 30 minutes.
- The developed numerical model provided an acceptable predicted purging rate when compared to the experimental one.

Acknowledgement

This project is sponsored by NASA Marshall Space Flight Center (MSFC) under an STTR Phase II program (Contract# 80NSSC20C0023) and Phase I program (Contract# 80NSSC18P2155). We would like to thank the program manager, Dr. Jeff Farmer for support and valuable discussions during the program. In addition, special appreciation goes to Philip Texter, Ramy Abdelmaksoud, Larry Waltman, and Jonathan Murray and who have provided significant technical contributions to this project.

References

- [1] C. Tarau, M. T. Ababneh, W. G. Anderson, A. R. Alvarez-Hernandez, J. T. Farmer and R. Hawkins, "Advanced Passive Thermal eXperiment (APT_x) for Warm-Reservoir Hybrid-Wick Variable Conductance Heat Pipes on the International Space Station (ISS)," in 48th International Conference on Environmental System (ICES), 2018.
- [2] Lee K-L., Tarau C., Lutz A., Anderson W.G., Huang C-N., Kharangate C. and Kamotani Y.,

"Advanced Hot Reservoir Variable Conductance Heat Pipes for Planetary Landers", in 49th International Conference on Environmental Systems (ICES), 2020

[3] Lee K-L., Tarau C., Adhikari S., Anderson W.G., Kharangate C., Huang C-H., Kamotani Y., "Hot Reservoir Variable Conductance Heat Pipe with Advanced Fluid Management," in 50th International Conference on Environmental Systems (ICES), 2021

[4] Lee K-L., Tarau C., Anderson W.G., Huang C-H., Kharangate C., Kamotani Y., "Integrated Hot Reservoir Variable Conductance Heat Pipes with Improved Reliability," in 51st International Conference on Environmental Systems (ICES), 2022

Computational simulation of a vapor jet into a subcooled flow inside a capillary jet loop system operating in direct condensation mode

Camila Braga Vieira^{1*}, Thomas Nicolle², Flavio Accorinti³, Olivier de Ghelin⁴, Cecile Goffaux⁵ and Vincent Dupont⁶

^{1,4,5}*Cenaero, Gosselies, Belgium*

^{2,3,6}*CALYOS, Jumet, Belgium*

*Corresponding author email address: camila.vieira@cenaero.be

Abstract

This work approaches numerical simulations applied for the investigation of vapor injection into a Capillary Jet Loop (CJL) system, aimed at the improvement of the injector design by investigating several parameters influencing its performance. Therefore, this paper will cover the influence of the entrainment ratio γ (ratio of the mass flow rate of the low-pressure flow – secondary flow - to the mass flow rate of the high-pressure flow - primary flow), the working fluid and the geometry on the pressure rise in the mixing region, the criterion chosen here for the injector efficiency. Considering that a full condensation is expected to occur, part of the simulation will also cover the numerical aspects related to phase-change. From Computational Fluid Dynamics (CFD) simulations, performed using the commercial software ANSYS-FLUENT 19.4, the parametric study showed a negative impact of the increasing injection angle on the pressure rise. The same negative impact was observed for the increase of the entrainment ratio. In terms of the working fluid, methanol and acetone proved to increase the pressure rise in the vapor injection region, inducing faster condensation, and consequently, affecting positively the injector efficiency.

Keywords: Two-phase flow; Direct Contact Condensation; Injector; Ejector; Capillary Thermosyphon; Capillary Jet Loop.

1. Introduction

Much is known about the efficiency of vapor injectors in heat transfer systems, which acts to boost the pressure and temperature to very useful levels [1]. Its simple construction, low cost, and easy installation, make the application of vapor injectors possible in combination with a capillary driven-system to create a Capillary Jet Loop (CJL) or a two-phase loop thermosyphon [2]. An extensive literature review on injector functionality and applications can be found in [3, 4].

In the present study only two-phase injectors are considered where fully or partial condensing condition might take place inside the subcooled flow (secondary stream) at vapor injection level (primary flow). This direct contact condensation (DCC) mode, coupled with the jet pump effect (momentum exchange), allows the development of two-phase systems to be less sensitive to acceleration forces or inclination, very practical for aeronautical applications [2] and simplify the distribution of the heat around complex surface at subcooling element.

In the present paper, such a condensing injector has been studied. The device, depicted in Figure 1, is similar to the concept presented by Dupont et al. [2] and the one here investigated.

The aim of this work is to provide further understanding of the parameters affecting the

efficiency of the vapor injector by the pressure rise in the mixing region. Higher pressure rise leads to a larger pumping capability, which is expected to occur in the circuit, so for each parameter investigated here (entrainment ratio γ , working fluid and geometry), the pressure profile along the axial direction has been obtained.

Having in mind the complexity involved in modelling the complete physics in a condensation process, this paper also aims to provide an explanation of the significant aspects required for a converged simulation of phase change, in terms of turbulence model, numerical schemes and heat/mass transfer parameters.

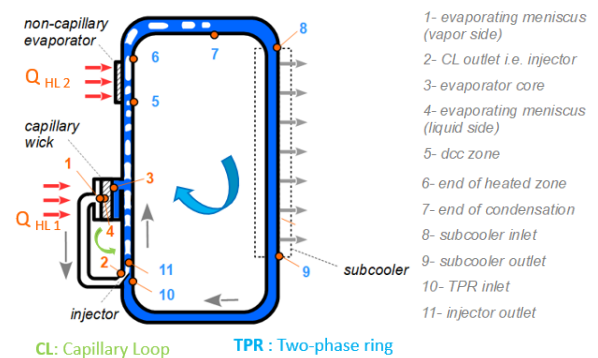


Figure 1. Location of the injector inside a CJL-DCC [2].

2. Physical problem

The simulation domains considered in the present work are shown in Figure 2. Table 1 lists all the test-cases investigated in this paper, including the respective parameters studied.

In terms of boundary conditions, the mass flow rate was specified in the inlet of the primary and secondary flow domains, while a pressure-outlet (saturation pressure) condition was imposed at the outlet. All the walls were adiabatic, and the inlet temperature was varied for each case (from 35 °C to 50 °C for the secondary flow, and 65 °C to 104 °C for the primary flow).

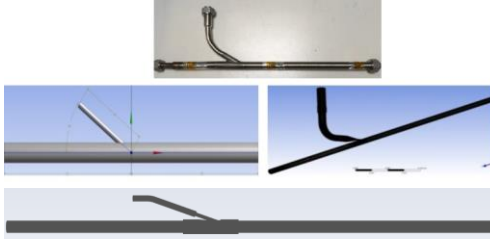


Figure 2. Calyos baseline injector (top), #1 - simplified geometry (middle left) and #2 - complete geometry (middle right), similar to the geometry on the top, both used in the parametric studies, and #3 - geometry used in the mesh-sensitivity and validation studies (bottom).

Table 1. Simulation cases studied in this work

Geometry	Parameters studied
#1 baseline	injector angle (15°, 35°, 40°, 60°, 90°) working fluid (methanol and R1233zd(E))
#2 (injector angle equal to 20°, acetone as working fluid)	γ (3, 5, 7.5 and 10) time discretization
#3 (injector angle equal to 20°, acetone as working fluid)	γ (18.6 to 23.07) mesh phase-change

3. Governing Equations

The solution for the two-phase problem here studied was obtained using the Eulerian model for the two separate, yet interacting, phases. Therefore, the volume fraction concept is introduced, and is assumed to be a continuous function of space and time, with the sum of all the volume fractions being equal to unity [5]. The conservation equations have a similar structure for all phases, and the coupling between them is

achieved through the pressure and interphase exchange coefficients [5].

In terms of conservation of mass, the continuity equation for phase i is:

$$\frac{\partial}{\partial t}(\alpha_i \rho_i) + \nabla \cdot (\alpha_i \rho_i \vec{v}_i) = \sum_j^1 (\dot{m}_{ji} - \dot{m}_{ij}) + S_p, \quad (1)$$

where α_i refers to the volume fraction of phase i , ρ_i is the density of phase i , \vec{v}_i the velocity of that phase, \dot{m}_{ji} and \dot{m}_{ij} characterize, respectively the mass transfer from phase j to i , and the other way around. The source term S_p is zero in our case.

The momentum balance for phase i may be expressed:

$$\frac{\partial}{\partial t}(\alpha_i \rho_i \vec{v}_i) + \nabla \cdot (\alpha_i \rho_i \vec{v}_i \vec{v}_i) = -\alpha_i \nabla p + \nabla \cdot \bar{\tau}_i + \alpha_i \rho_i \vec{g} + \sum_j^n (\vec{R}_{ji} + \dot{m}_{ji} \vec{v}_{ji} - \dot{m}_{ij} \vec{v}_{ij}) + (\vec{F}_i + \vec{F}_{l,i} + \vec{F}_{wl,i} + \vec{F}_{vm,i} + \vec{F}_{td,i}), \quad (2)$$

where p is the pressure, shared by all phases, $\bar{\tau}_i$ is the phase i stress-strain tensor, \vec{F}_i is an external body force (here neglected), $\vec{F}_{l,i}$ is the lift force, $\vec{F}_{wl,i}$ the wall lubrication force, $\vec{F}_{vm,i}$ the virtual mass force, $\vec{F}_{td,i}$ the turbulent dispersed force and \vec{v}_{ji} is the interphase velocity, defined according to the mass-transfer between the phases:

- if $\dot{m}_{ji} > 0$: phase j is being transferred to phase i , so $\vec{v}_{ji} = \vec{v}_j$,
- if $\dot{m}_{ji} < 0$: phase i is being transferred to phase j , so $\vec{v}_{ji} = \vec{v}_i$,
- similarly, if $\dot{m}_{ij} > 0$: $\vec{v}_{ij} = \vec{v}_i$, and if $\dot{m}_{ij} < 0$: $\vec{v}_{ij} = \vec{v}_j$.

All the details of the stress-strain tensor and the phase interaction forces between the phases can be found in the theory guide of Ansys Fluent [5]. In the present study, a virtual mass coefficient equal to 0.5 has been adopted, and no lift, wall-lubrication and turbulent dispersion term were considered.

Equation (2) must be closed with an appropriate formulation for \vec{R}_{ji} , which is an interaction force between the phases that depends on the interfacial area concentration (i.e., the interfacial area between two phases per unit of mixture volume), and the drag function. Here, the interfacial area

density was obtained by a model that treats both phases i and j symmetrically [5], while the drag function is based on Schiller and Naumann model [6].

Finally, the energy conservation equation is expressed in terms of a separate enthalpy equation for the i^{th} phase as written below:

$$\frac{\partial}{\partial t} \left(\alpha_i \rho_i \left(e_i + \frac{\vec{v}_i^2}{2} \right) \right) + \nabla \cdot \left(\alpha_i \rho_i \vec{v}_i \left(h_i + \frac{\vec{v}_i^2}{2} \right) \right) = \nabla \cdot \left(\alpha_i k_{eff,i} \nabla T_i - \sum_s h_{s,i} \vec{J}_{s,i} + \bar{\tau}_{eff,i} \cdot \vec{v}_i \right) + \sum_i^n (Q_{ij} + \dot{m}_{ij} h_{ij} - \dot{m}_{ji} h_{ji}) + p \frac{\partial \alpha_i}{\partial t} + S_i, \quad (3)$$

where $k_{eff,i}$ and $\bar{\tau}_{eff,i}$ are the effective thermal conductivity and stress-strain tensors, respectively, Q_{ij} is the heat exchange between the phases, h_{ij} is the interphase enthalpy (for instance the enthalpy of the vapor at the saturation temperature, in case of condensation). If species are present in any phase, s refers to the species, $h_{s,i}$ is the enthalpy of the species, and $\vec{J}_{s,i}$ is the diffusive flux of species s in i phase. In this work, no species transport is considered, so that term of the equation is negligible. Since no source term S_i is present in our problem, this term is also neglected.

Both in the momentum and energy equations, the mass transfer term (\dot{m}_{ij}) and heat transfer (Q_{ij}) have been introduced. These two terms are essential for the correct prediction of condensation.

For the interphase mass transfer, the Lee model [7] has been adopted. In this model, the liquid-vapor mass transfer (evaporation and condensation) is governed by the vapor equation, as written below:

$$\frac{\partial}{\partial t} (\alpha_v \rho_v) + \nabla \cdot (\alpha_v \rho_v \vec{V}_v) = \dot{m}_{lv} + \dot{m}_{vl}, \quad (4)$$

in which v refers to the vapor phase and l to the liquid phase, and \dot{m}_{lv} and \dot{m}_{vl} are the rates of mass transfer due to evaporation and condensation, respectively.

These mass transfers are obtained based on the temperature conditions, as explained below:

- If $T_l > T_{sat}$ (this means evaporation takes place):

$$\dot{m}_{lv} = C_{ev} \alpha_l \rho_l \frac{(T_l - T_{sat})}{T_{sat}}. \quad (5)$$

- If $T_v < T_{sat}$ (which means condensation takes place):

$$\dot{m}_{vl} = C_{cond} \alpha_v \rho_v \frac{(T_{sat} - T_v)}{T_{sat}}, \quad (6)$$

where, C_{ev} and C_{cond} means, respectively, the coefficients of evaporation and condensation, α and ρ are the phase volume fraction and density, respectively, and the subscript sat refers to the saturation condition.

It is important to mention that these two coefficients must be well tuned for the correct prediction of the desired phase change (in our case, condensation).

Since, the densities of the vapor and liquid phases may differ greatly, such as the case of the working fluid here studied for condensation, acetone ($\rho_l = 755 \text{ kg/m}^3$, while $\rho_v = 2.53 \text{ kg/m}^3$, at their respective inlet temperatures), it was necessary to manipulate the coefficients in order to avoid any mass imbalance. Therefore, the condensation coefficient was obtained according to the following correlation:

$$C_{cond} = C_{ev} \frac{\rho_l}{\rho_v}. \quad (7)$$

In Subsection 5.5, the effect of the values chosen for these coefficients will be discussed.

Regarding the interphase heat exchange, Ranz-Marshall model [8] was used to compute the heat transfer coefficient, more specifically, the Nusselt number, as shown below:

$$h_{ij} = \frac{\lambda_j Nu_i}{d_i}, \quad (8)$$

$$Nu_i = 2 + 0.6 Re_i^{1/2} Pr_j^{1/3}, \quad (9)$$

in which, λ_j is the thermal conductivity of j^{th} phase, d_i the diameter of the i^{th} phase, Re_i is the relative Reynolds number based on the i^{th} phase, and on the relative velocity, and Pr_j is the Prandtl number of the j^{th} phase.

One important point to mention here is that, since in the present injector problem, the two phases are not thoroughly mixed (meaning that

there is a significant separation of the liquid and vapor phases), it is necessary to work with a low value of d_i , so that the heat released during the condensation process can be uniformly spread over the phases. The value here used for d_i was 10^{-6} m, which was enough to guarantee a uniform heat-transfer between the phases.

Finally, turbulence was simulated using the mixture version of the $k-\omega$ SST model. This choice was based on literature studies [9-11], and from the fact that two-phase turbulence models are generally less stable than the mixture version [5].

4. Numerical modelling

All the simulations were performed in the commercial CFD software ANSYS-FLUENT (version 19.4). Calculation convergence was determined (residuals less than the mass conservation criteria of 10^{-4}) using a first-order schemes for both space and time discretization. This choice was made due to stability issues, since first-order schemes are more stable than second-order ones, but less accurate.

Relaxation factors on convergence ($f_r = 0.5$) were necessary to all the equations, to avoid numerical instabilities.

In order to avoid any backflow, each case was initialized with an initial pressure consistent with the stagnant condition (hydrostatic pressure), as shown in Figure 3.

The mesh used in each geometry had at least 4 cells per mm in the transverse direction in the mixing region, as suggested by Ariaifar et al. [1]. More information about the mesh can be found in subsection 5.1. The time-step had to be carefully chosen to avoid any heat and mass imbalances, and violation of the CFL condition. A time-step equal to 10^{-4} s was adopted following a time-discretization study, which is discussed further in subsection 5.2.

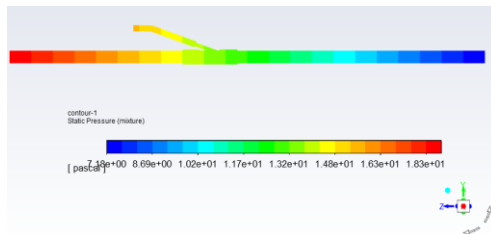


Figure 3. Initial pressure field (hydrostatic pressure) used in the initialization step to avoid backflow issue.

5. Results and Discussion

5.1. Mesh Sensitivity study

To check that the solution is mesh independent, three hexahedral dominant meshes were investigated. The geometry in which this study was carried out was the same as that used in the validation simulations (see bottom picture of Figure 2).

All the meshes were generated by ANSYS-Fluent-Meshing program [12] and quantified according the Roache method for grid convergence studies [13-14], which is based on the use of Richardson extrapolation [15].

The variable used for this study was the pressure rise in the cross-sectional area in the middle of the mixing region whose values for each mesh can be found on Table 2. That choice was taken since pressure rise was here used as criterium for the injector efficiency, as explained in the introduction section. The mesh size indicated on Table 2 refers to the cell size in the bulk region and the normalized values were obtained by dividing the bulk cell size by the minimum mesh size (0.25 mm).

The normalized-mesh #1, depicted in Figure 4 (3'377'636 elements) was then chosen to be used in all the cases, since it proved to be already in the asymptotic range of convergence (as shown in Figure 5), and provided a lower grid refinement ratio [13] in comparison to the coarser and medium meshes. Also, it contains four cells per mm in the transverse direction, as suggested by Ariaifar et al. [1], for a better prediction of the mixing between the two phases.

It is important to notice that, even though the geometries were slighted modified, the parameters used for the mesh generation in this mesh sensitivity study have been applied for each geometry here studied.

Table 2. Mesh sensitivity study

Mesh size [mm]	Normalized mesh size	ΔP [bar]
0.25	1	0.01786
0.4	1.6	0.01794
0.5	2	0.01852

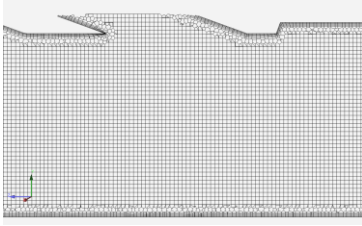


Figure 4. Mesh chosen for the simulation cases investigated in this work.

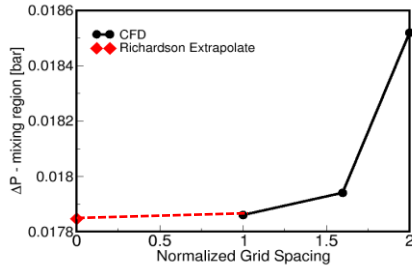


Figure 5. Mesh sensitivity study using the Richardson extrapolation.

5.2. Time-discretization study

Apart from the space discretization, the time discretization is also expected to play an important role in the correct prediction of the results.

Notwithstanding vastly different velocity scales of the mixing region (see Figure 6), the timescale must be small enough to obtain a satisfactory mass balance.

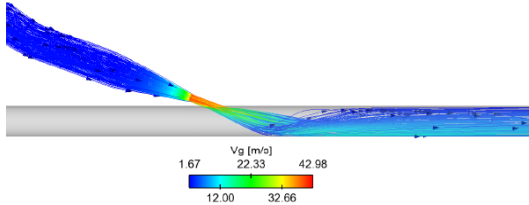


Figure 6. Velocity streamlines of the case with entrainment ratio $\gamma = 5$ with acetone as the working fluid.

The effects of the time-step for different values of γ , with acetone as the working fluid can be seen in Figure 7. For $\gamma = 3$, a good mass balance could be attained for $\Delta t = 10^{-3}$ s (Figure 7a), while increasing γ to 7.5 (Figure 7c) a smaller time-step was needed for a more stable mass balance to be obtained. In Figure 7a, we can see that at 6s, a decrease in the time-step to 0.01s drastically affected the mass balance.

Increasing γ , which also means increasing the velocity scales, necessitates reduction of the time-step, as we can see from Figures 7a and 7b.

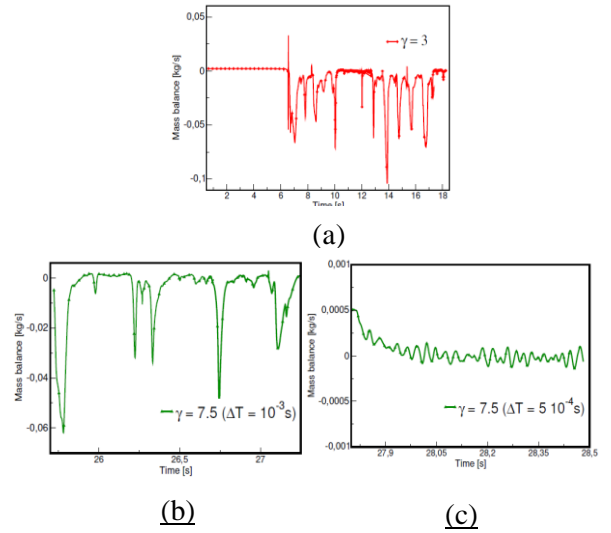


Figure 7. Time-history of mass balance for two simulation cases with acetone as working fluid: (a) $\gamma = 3$, $\Delta t = 10^{-3}$ s up to 6s and $\Delta t = 10^{-2}$ s from 6s on; (b) $\gamma = 7.5$, $\Delta t = 10^{-3}$ s; and (c) $\gamma = 7.5$, $\Delta t = 5 \cdot 10^{-4}$ s.

The choice of time-step can, consequently, affect the prediction of the pressure jump in the mixing region, as shown in Figure 8.

Since having to incorporate a very small time-step can lead to drastic slowing down of the computational simulations, the simulations can be first run as steady-state with a large time-factor (in pseudo-transient mode) for a few hundred iterations, then be switched to transient mode, in order to reduce the overall run time. It is important to note that due to Kelvin-Helmholtz instabilities generated by the shear at the liquid-vapor interface, a true steady-state solution cannot be obtained.

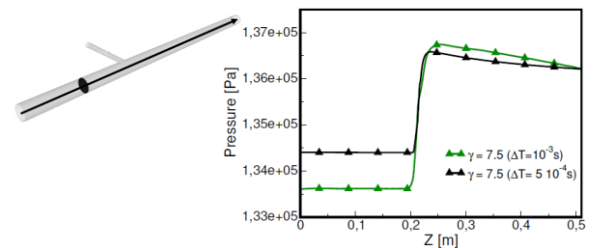


Figure 8. Pressure profiles (average pressure on the cross-sectional area, along the arrow indicated on the left picture) for acetone and $\gamma = 7.5$ for different time-steps.

5.3. Injector angle analysis

Once mesh and time discretization had been evaluated, the first part of the investigation of the injector efficiency (measure in terms of the pressure rise in the mixing region) was the study of the effect of different injector angles.

In total 5 injector angles were studied (as showed in Figure 9), considering methanol as the working fluid, and no phase-change, meaning that condensation was not considered by the simulations.

As it can be seen from Figure 10, increasing the injector angle leads to an increase of fluid recirculation in the mixing zone. This recirculation can affect the pressure in the liquid region (the first 10 cm of height indicated in the graph depicted in Figure 9), by slightly increasing the angle. As shown in Figure 9, the lower the angle the higher the pressure jump, which means a positive effect on the injector efficiency. Due to a strong impinging jet caused by angle 90°, the pressure oscillation in the mixing of the two-phases is higher (see the red profile in the graph in Figure 9).

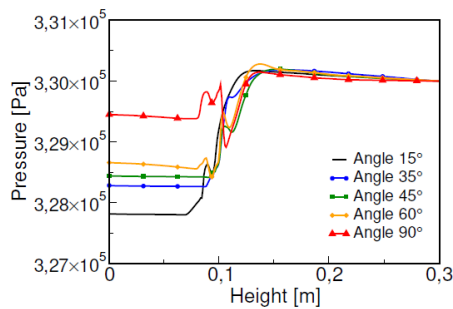


Figure 9. Pressure profiles along the height of the main pipe for different injector angles, methanol as working fluid and $\gamma = 20$.

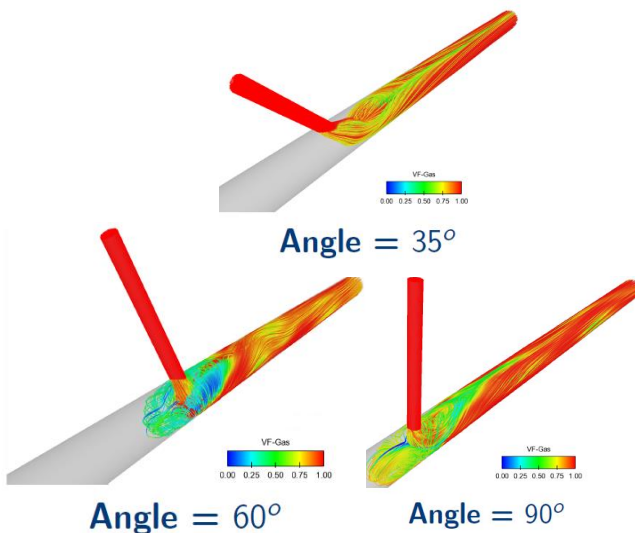


Figure 10. Streamlines coloured according to vapor volume-fraction for different injector angles, methanol as working fluid and $\gamma = 20$.

5.4. Working fluid and γ analysis

After checking the effect of the injector angle on the pressure rise in the mixing region, two further parameters were investigated: the working fluid and the entrainment ratio γ .

For the standard CJL working fluid, methanol (close characteristics to acetone) and R1233zd(E) were chosen for the study.

As shown in the graphs depicted in Figure 11, methanol presented a better performance, since it provided a higher pressure jump in comparison to R1233zd(E). Due to the physical characteristics of the two fluids - R1233zd(E) is much heavier and has a higher viscosity in the vapor-phase than methanol – it observed that methanol is more susceptible to oscillations during mixing for larger injector angles than R1233zd(E), which has a higher influence of the viscous force than methanol.

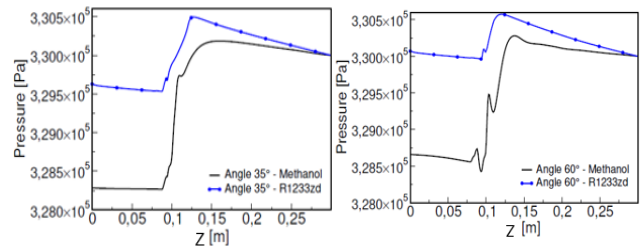


Figure 11. Pressure profiles along z coordinate (height) for different working fluids and injector angles, with $\gamma = 20$.

In terms of the entrainment ratio γ , i.e., the ratio of the mass flow of the liquid phase to the mass flow rate of the vapor phase, it can be seen from Figure 12 that an increase of γ led to an increase of the pressure in the system, but a decrease of the pressure jump in the mixing region, thereby affecting negatively the injector efficiency.

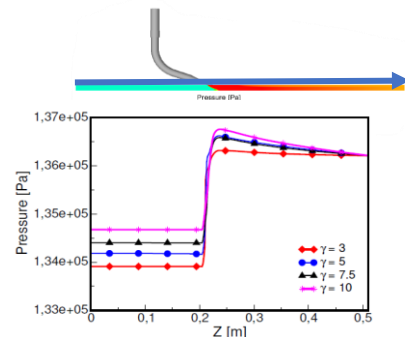


Figure 12. Pressure profiles along the z coordinate (height) for different values of γ , with acetone as working fluid.

5.5. Comparison with test data

After some initial parametric studies of the geometry, i.e., injector angle, physical properties and γ , on the injector efficiency, a suitable validation test performed in the Calyos S.A manufacturer laboratory was selected.

For this analysis, the geometry depicted by Figure 13 was used, which was the same geometry used in the mesh sensitivity study. With acetone as working fluid, and an applied power of 373 W, the inlet temperature of the liquid and vapor phases were 50 °C and 64 °C, respectively, the injector angle was 20°, and γ varied from 18 to 23.

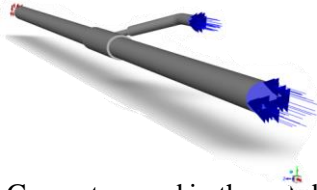


Figure 13. Geometry used in the validation study, in which the blue arrows indicate the inlets of the vapor and liquid phases (top and bottom, respectively), and the red arrows the outlet.

Since phase change was here included in the model, some parameters of the mass interphase transfer model needed to be investigated (more specifically the evaporation C_{ev} and condensation C_{cond} coefficients in the equations [5] and [6], respectively).

From Figure 14, it can be seen the effects of the choice of these coefficients on condensation prediction. Using the correlation described in equation [7], three different cases were investigated, all with the same ratio of 253, based on the liquid to vapor densities (better explained in Subsection 3).

As can be observed from Figure 14, to achieve a full condensation before the outlet, it is necessary to work with the following coefficients: $C_{ev} = 20$, $C_{cond} = 5060$.

It is important to note that these coefficients act as relaxation factors for the mass transfer model, so the values should be well chosen to avoid any convergence issue on mass balance.

Once the mass-transfer coefficients have been chosen, a comparison of the outlet temperature with the experimental measurement was done for different entrainment ratios γ .

As can be observed from Figure 15, an overall good agreement with the outlet temperature could be obtained (with a maximum error of 6.44 % for $\gamma = 18.6$).

The discrepancies between the simulations and experiment for smaller values of γ (18.6 and 19.77) can be explained by the fact that these two γ , experimentally speaking, are very close to a non-DCC (direct contact condensation) condition, which is not the case for the numerical model.

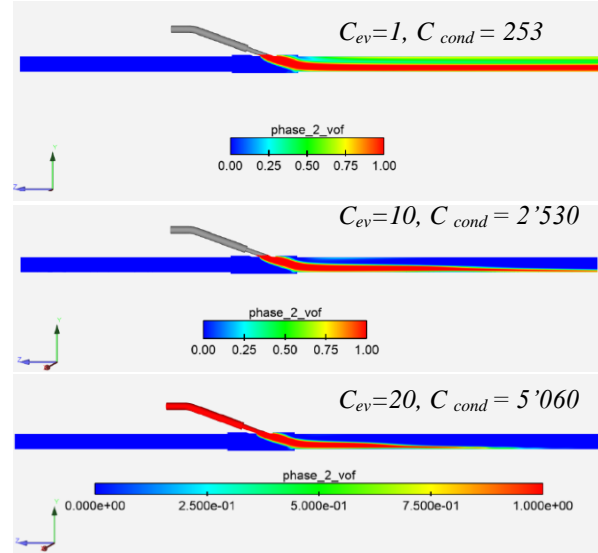


Figure 14. Vapor-phase fields for $\gamma = 23$ and different values of the evaporation and condensation coefficients of the mass-transfer model (equations [5] and [6]).

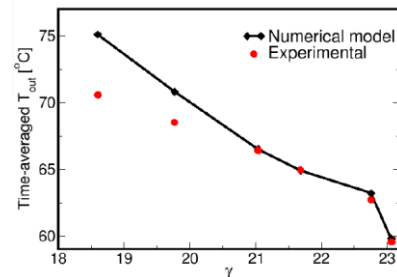


Figure 15. Comparison of outlet temperature from the numerical simulation with experimental measurement for different values of γ .

6. Conclusions

This paper had as its objective to validate a numerical method and to examine several parameters that can affect the efficiency of an injector in a Capillary Jet Loop (CJL).

Since, the two-phase heat transfer device here studied operates in a DCC mode, meaning that a full condensation of the vapor phase should occur after the injector and before the cold source, the parameter used for estimating the injector

efficiency is the pressure rise in the region where the two-phases mix.

It could be observed that the mesh with four cells per mm was the one providing a solution in an asymptotic region of mesh convergence, and, was thus chosen for the simulations. The time-step for all the cases studied here had to be in order of 10^{-4} s, to better capture all the velocity scales in the mixing zone. In terms of mass-transfer, it was proven here that the values of the evaporation (even though does not occur in any case investigated here) and condensation rates should be well chosen to correctly predict the phase change occurring and to avoid convergence issues.

Considering the injector parameters here investigated, it could be concluded that an increase in either the injector angle or γ negatively affects the efficiency of the injector, since they decrease the pressure-rise in the mixing region. The use of methanol (similar to acetone in terms of physical properties) proved to be the better choice than R1233zd(E), since it resulted in a higher pressure-jump in the mixing zone.

The validation study done, undertaken for the case $\gamma = 23$ showed that the model can correctly predict the outlet temperature, though with some discrepancies for values of γ lower than 19.77.

The good agreement with the temperature measurements, together with observations from the other numerical investigations provide evidence of the trustworthiness of the numerical model, and its application for the study of CJL devices with phase-change.

As a next step, more standard injector configurations including axial injection and convergence-divergence section will be optimized thanks to the present validated set of numerical parameters and a simplified design tool proposed.

Acknowledgement

This project has received funding from the Walloon Region under CWALity DE (DGO6) convention n°1810169, and Skywin SW_ELOISE convention n°8524.

References

- [1] K. Ariafar, D. Buttsworth, G. Al-Doori and N.Sharifi, Mixing layer effects on the entrainment ratio in steam injectors through ideal gas computational simulations. *Energy*, 2016. 95: p. 380-392.
- [2] Dupont V., Paran, B., Van Oost, S. and Billet, C., Capillary Jet Loop, Proc. of 19th International Heat Pipe Conference, Pisa, June 10-14, Italy (2018).

- [3] M. Atmaca and C. Ezgi, Three-dimensional CFD modelling of a steam injector. *Energy Sources, part A: recovery, utilization and environmental effects*, 2019, p. 1-12.
- [4] G. Besagni, R/. Mereu and F. Inzoli, Injector refrigeration: A comprehensive review. *Renewable and Sustainable Energy Reviews*. 2016. 53: pp. 373-407.
- [5] Ansys@Fluent, Release 2019 R2, Theory Guide, ANSYS, Inc, pp. 569-751.
- [6] L. Schiller and Z. Naumann, A drag coefficient correlation. *Z. Vereins Deutsch Ing.*, 1935. 77: pp 318-320.
- [7] W.H. Lee, A pressure iteration scheme for two-phase modeling. Technical Report LA-UR 79-975. Los Alamos Scientific Laboratory, Los Alamos, New Mexico, 1979.
- [8] W.E. Ranz and W.R. Marshall, Vaporation from Drops, Part I. *Chemical Engineering Progress*, 1952, 48(3): pp 141-146.
- [9] H. Lee, C.R. Kharangate, N. Mascarenhas, I. Park and I. Mudawar, Experimental and computational investigation of steam upward flow in a vertical pipe. *Advances in Mechanical Engineering*, 2015, 85: pp 865-879.
- [10] C.R. Kharangate, H. Lee, I. Park and I. Mudawar, Experimental and computational investigation of vertical upflow condensation in a circular tube. *International Journal of Heat and Mass Transfer*, 2016, 95: 249-263.
- [11] G. Grazzini, A. Milazzo and F. Mazzelli, Ejectors for Efficient Refrigeration - Design, Applications and Computational Fluid Dynamics. Springer, Gewerbestrasse, Switzerland, 2018.
- [12] Ansys@Fluent, Release 2022 R2, User Guide, Part II: Meshing Mode, ANSYS, Inc, pp. 197-791.
- [13] P.J., Roache, K. Ghia and F. White, Editorial Policy Statement on the Control of Numerical Accuracy. *ASME Journal of Fluids Engineering*, 1986, 108: pp 2.
- [14] P.J. Roache, Verification and Validation in Computational Science and Engineering. Hermosa Publishers, Albuquerque, 1998.
- [15] L.F. Richardson, The approximate arithmetical solution by finite differences of physical problems involving differential equations with an application to the stresses in a masonry dam. *Trans. Roy. Soc. London, Ser. A.*, 1910, 210: pp. 307-357.

Advanced Structurally Embedded Thermal Spreader II (ASETS-II) Oscillating Heat Pipe Flight Experiment and Database

Corey A. Wilson^{1*}, Bruce Drolen², Brent Taft³, Jon Allison³

¹ThermAvant Technologies, Columbia, Missouri, USA

²Consultant to ThermAvant, Columbia, Missouri, USA

³U.S. Air Force Research Laboratory, Kirtland Air Force Base, New Mexico, USA

*Corresponding author email address: Corey.Wilson@ThermAvant.com

Abstract

The U.S. Air Force Research Laboratory evaluated six oscillating heat pipes (OHPs) for 780 days through a series of experiments on ground and in microgravity for the second Advanced Structurally Embedded Thermal Spreader (ASETS-II) flight experiment. The three primary scientific objectives of the experiment were to measure the on-orbit thermal performance including operational limits, long duration operation, and assess lifetime operational degradation. All OHPs were constructed from aluminum in a flat plate, 34-channel, single-layer, closed-loop design. The six OHPs were split into two matching groups to enable concurrent ground and microgravity testing. In each group, two were charged with butane and one was charged with R-134a and each had a different thermal configuration to evaluate different operational characteristics. One group was launched on-orbit on September 7, 2017 and the other remained on ground. Throughout the 780 days on orbit, all tests conducted on the flight units were mirrored on the ground units. At the end of the experiment, the OHPs were returned to ground for further analysis. The compiled experimental results from this experiment were made available on the PSI NASA Database for future analysis and model development.

Keywords: Oscillating Heat Pipe; Pulsating Heat Pipe; Space Flight Experiment; ASETS-II; Microgravity; Database

1. Introduction

A flat plate oscillating heat pipe (OHP) is a type of heat pipe where a capillary channel passes multiple times between evaporators and condensers inside a monolithic structure. This type of heat pipe has been shown to transfer high heat loads and fluxes in a thin, structural formfactor. Because of these advantages, the OHP is a compelling passive thermal management solution for satellite applications.

In 2012, the U.S. Air Force Research Laboratory (AFRL) Space Vehicles Directorate set out to validate OHP microgravity performance with the first Advanced Structurally Embedded Thermal Spreader (ASETS) experiment onboard a Space Test Program funded, and NASA managed, parabolic flight experiment [1]. The experiment demonstrated that an OHPs' behavior was consistent for terrestrial horizontal testing and microgravity operation during the short duration tests.

The second ASETS experiment (ASETS-II) was developed to conduct long duration on-orbit testing of OHPs. The experiment was designed, developed, assembled, and integrated from 2015 to 2016. In 2016, on ground testing of six OHPs began to establish a performance baseline. On September 7, 2017, AFRL launched three OHPs on the second ASETS experiment (ASETS-II) on-board the X-37B Orbital Test Vehicle 5 (OTV-5) for a 780-day mission. The OHPs were evaluated to

determine functionality, characterize behavior, and explore the predicted limits of operation [2] in a long-term microgravity environment. The X-37B landed on October 27, 2019 and the OHPs were subsequently analyzed to determine if fluidic or structural degradation occurred via radiation and/or corrosion.

The ASETS-II flight hardware consisted of three flat plate aluminum OHPs, heaters, heat rejection surfaces, and an experiment control unit (Figure 1). The three geometrically identical flight OHPs were setup to validate a range of operational and performance conditions in microgravity conditions. This was achieved by varying the working fluid (butane and R-134a) and heat imposition (large and small centered heaters with single- and double-ended cooling).

The OHPs underwent periodic checkout tests, a series of short duration thermal cycling, and six-week long duration tests. In addition, a mirrored experiment was conducted on ground to investigate microgravity versus terrestrial performance variations. Pre-launch ground truth results were published by Taft et al. [3], the first six months on orbit by Taft et al. [4], and the 780 day orbital results by Drolen et al. [5].

The dataset for the more than 2.2 million data points of OHP terrestrial and on-orbit testing hours was made available to the public via the NASA Physical Sciences Informatics (PSI) website [6]. The intention of this resource is to provide the

researchers of OHPs a high quality dataset for analysis and model development.

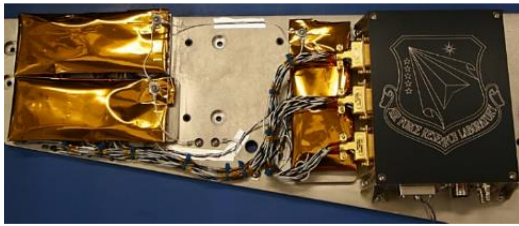


Figure 1. ASETS-II Flight Hardware

2. Experimental Method

The ASETS-II experiment was designed to investigate OHP performance in a long-term microgravity environment across a range of test conditions including transient, steady-state and intersecting with operational limits. These tests included repeat check-out testing in a ramp up and down profile and long duration tests. The operational limits shutdown, heating and cooling configuration, and operational variation due to hysteresis and repetition of the standard set of tests during the two years on orbit. The heating configurations are center heating with large low flux heaters and a small high flux heater, and cooling configurations include two end cooling, one end cooling, and large low flux heaters.

Figure 2 shows the OHP design used in this experiment. It consisted of a single layer array of 34 channels arranged in a closed-loop configuration. The channels had a square cross-section with dimensions of 1 mm x 1 mm with 0.38 mm walls between each channel. Figure 3 shows a detailed view of the channel turn. The channels were embedded in a 2 mm thick flat aluminum 3003 plate. All designs due to manufacturing tolerances had a measured internal volume relative to designed volume of 93% \pm 4%. Mounting holes were integrated into the flanges at each end of the OHP outside of the channel field to fixture to the testbed.

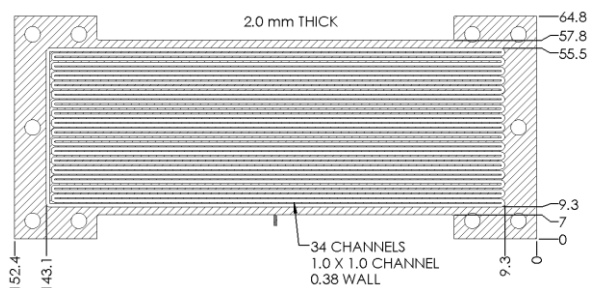


Figure 2. Schematic of ASETS-II OHP (dimensions in mm)

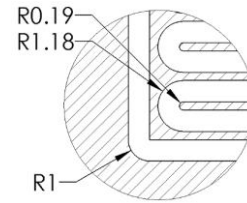


Figure 3. Schematic detail view of bottom left corner of channel field (dimensions in mm)

Table 1 shows the six test configurations for the ASETS-II OHPs. These OHPs had a designation of OHP #1, OHP #2, and OHP #3. Three OHPs were tested on-orbit in microgravity (Flight or F) and three matching OHPs were tested on ground (Flight Spare or FS). All OHPs were center heated with two large low flux heaters and a small high flux heater. OHP #1 was cooled on two ends. OHP #2 and #3 were cooled on one end. OHP #1 and OHP #2 were charged with Butane, and OHP #3 was charged with R-134a. All units had fill ratios of 45-47% with an uncertainty of \pm 2%.

Table 1. Configurations of the ASETS-II OHPs

OHP #	Category	Heating	Cooling	Fluid	FR [%]
1	FS	Center	Two End	Butane	47
1	F	Center	Two End	Butane	47
2	FS	Center	One End	Butane	46
2	F	Center	One End	Butane	45
3	FS	Center	One End	R-134a	46
3	F	Center	One End	R-134a	47

These testing configurations were selected to provide stable operation in some testing conditions and unstable or non-operation at other testing conditions. OHPs #1 and #2 were designed to be stable across the test parameters, and OHPs #3 was designed to explore the Bond number limit, swept length limit, and vapor inertia limit [2].

Figures 4 and 5 depict the instrumentation and heater and cold plate contact zones. Each OHP had a small area 12.7 mm x 12.7 mm ceramic heater printed at the middle of one side of the OHP, two large polyimide 25.4 mm x 50.8 mm patch heaters positioned on the opposite side of the OHP in the center. The ceramic heater had a maximum rated heat load of 40 W and each polyimide heater had a maximum rated heat load of 20 W resulting in a combined heat load of 40 W. These heat loads were set by varying the duty cycle of the a relatively constant supply voltage. In addition, each OHP had start-up heaters

positioned on the surface opposite the cold plate contact surface to initiate fluid motion in the OHP if necessary. Throughout the flight experiment, the OHPs started-up without the assistance of the start-up heaters, therefore they were never activated.

OHP 1 was instrumented with 8 resistance temperature detectors (RTDs) numbered 1 through 8. OHP 2 & 3 were instrumented with 7 RTDs numbered 1, and 3 through 8. For these OHPs RTD 2 was attached to the adapter plate to measure the heat rejection plate temperature. The operational control system for the test monitored all sensors and if any exceeded 110 °C, the heater power was set to zero.

In addition to power and temperature, the flight electronics box included a three-axis accelerometer to measure the gravitational environment.

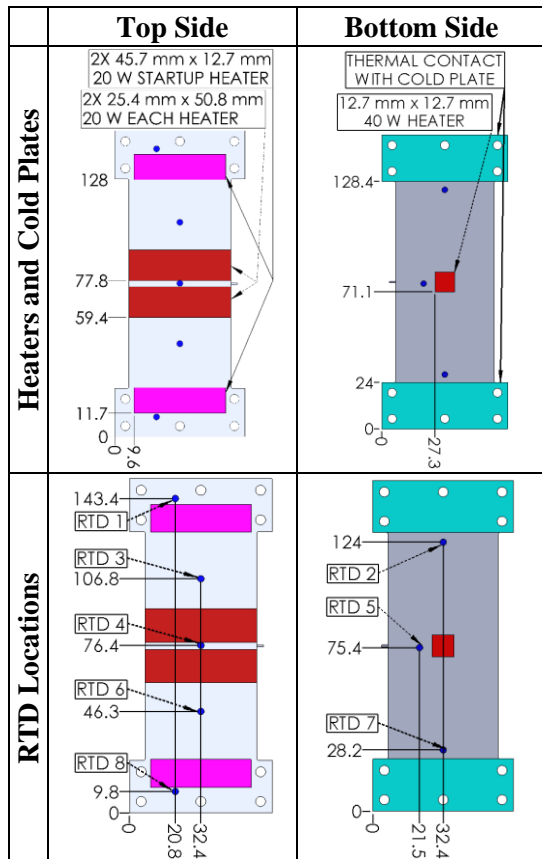


Figure 4. Configuration and Instrumentation of OHP #1 (dimensions in mm)

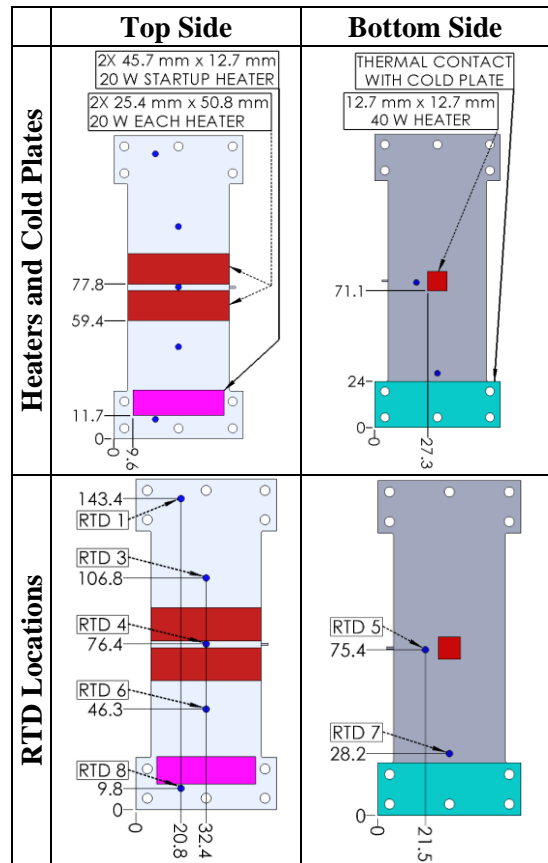


Figure 5. Configuration and Instrumentation of OHPs #2 and #3 (dimensions in mm)

3. Experiment States

A set of experiments were established and repeated throughout the duration of the program for both on-ground and in-orbit testing. These experiment cases are shown in Table 2. Additionally, the experiment states are defined in the Appendix.

Table 2. Experiment Case Definitions and Color Coding

Test Mode I: Initial Checkout
Test Mode II: Periodic Checkout (Repeat Initial)
Test Mode III: Hysteresis Testing
Test Mode IV: Long-Duration Testing
Buffer State (heaters turned off)

The Initial Checkout test mode was used to establish the baseline performance by starting at an off-state equilibrium temperature, stepping to a power for 30 minutes, then back to an off-state to return to equilibrium. The power steps were 10 W, 20 W, 30 W, and 40 W. The Initial Checkout tests were repeated quarterly to evaluate performance change over time.

The Hysteresis Test mode evaluated the performance variance as power increases and decreases. The test started out at an off-state equilibrium temperature then iterated stepwise through 10 W, 20 W, 30 W, 40 W, 30 W, 20 W, 10 W and then back to an equilibrium off-state.

The Long Duration test was used to determine performance variance with time of the OHP and instability risk. These tests were conducted at 20 W for 42 days.

4. Results and Analysis

Prior to launch the Flight Hardware and Flight Spare Hardware went through a series of tests in a horizontal orientation including thermal vacuum chamber (TVAC) testing, ground truth testing, hysteresis test, and Bond limit tests. Figures 6 to 8 depict the initial TVAC test results for Flight Hardware with the small-area heater at 10 W. The vertical green line depicts the start of the data analysis period and the vertical red line depicts the end of the analysis period and end of the power step. This region is a predefined duration and is intended to capture the steady-state performance of the OHP.

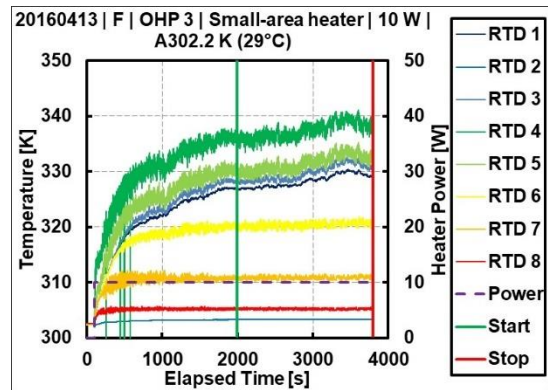


Figure 8. On-ground initial TVAC testing of OHP 3

Figure 9 shows the on-orbit performance of OHP 2 with the small area heater at 10 W. The sink temperature was a little over 10 °C colder than initial on-ground testing resulting in slightly different performance and in some instances intersection with operational limits. Figure 10 shows the long duration stability of OHP 2 on-orbit. During the 42 day test the OHP fluctuated significantly, however this was due to the orbital variation in the sink temperature as can be seen in Figure 11 by observing RTD 2 which was attached to the adapter plate.

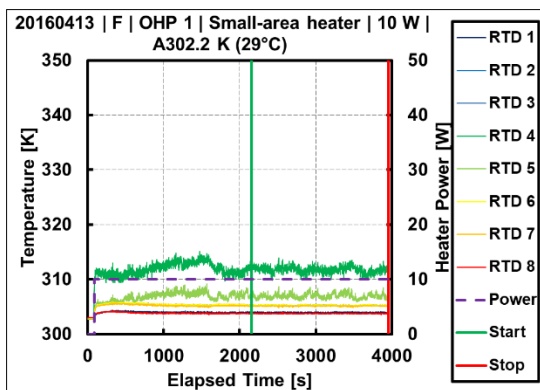


Figure 6. On-ground initial TVAC testing of OHP 1

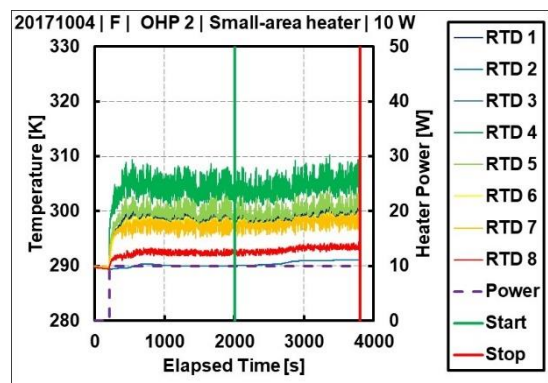


Figure 9. On-orbit testing of OHP 2

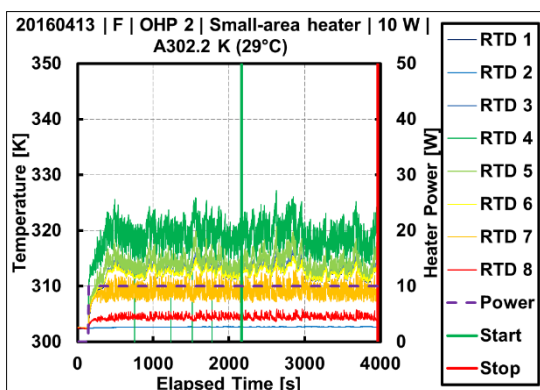


Figure 7. On-ground initial TVAC testing of OHP 2

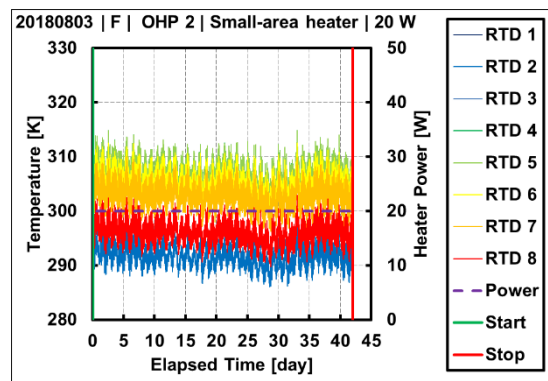


Figure 10. On-orbit long duration testing of OHP 2

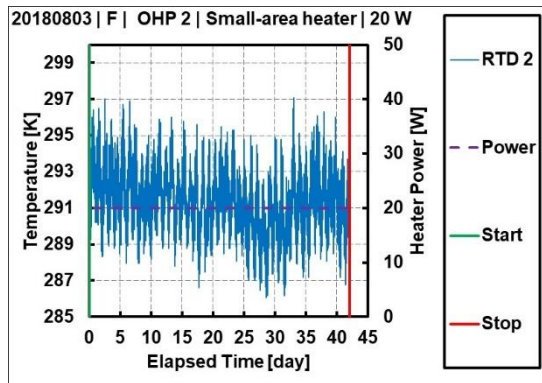


Figure 11. On-orbit long duration sink temperature for OHP 2

Throughout the experiment the OHPs showed consistent and repeatable operation and non-operation across the power vs adiabatic temperature space. In addition, the OHP performance did not degrade with time.

5. Experiment Database

The full set of experimental data for both the ground and the flight experiments has been released as a dataset on the NASA PSI website, <https://www.nasa.gov/PSI> [7]. It includes 2.2 million data points for the more than 6,600 hours of on-ground and on-orbit testing. This dataset has been released to provide high quality real-world performance information to guide OHP model development.

Acknowledgments

This work was funded by multiple U.S. Air Force Research Laboratory Space Vehicles Directorate contracts including FA9453-18-F-0002 and FA9453-19-C-0002 and a Small Business Innovation Research Phase IIe Sequential Program (FA9453-17C-0423).

References

- [1] B.S. Taft, F.F. Laun, S.M. Smith, D.W. Hengeveld, Microgravity Performance of a Structurally Embedded Oscillating Heat Pipe, *Journal of Thermophysics and Heat Transfer*. 29 (2015) 329–337. <https://doi.org/10.2514/1.T4151>.
- [2] B.L. Drolen, C.D. Smoot, Performance Limits of Oscillating Heat Pipes: Theory and Validation, *Journal of Thermophysics and Heat Transfer*. 31 (2017) 920–936. <https://doi.org/10.2514/1.T5105>.
- [3] B.S. Taft, S.M. Smith, ASETS-II Oscillating Heat Pipe Space Flight Experiment: Ground Truth Results, in: *American Society of Mechanical Engineers Digital Collection*, 2017. <https://doi.org/10.1115/HT2017-4706>.

- [4] B. Taft, K. Irick, ASETS-II OSCILLATING HEAT PIPE SPACE FLIGHT EXPERIMENT: THE FIRST SIX MONTHS ON ORBIT, *Frontiers in Heat and Mass Transfer (FHMT)*. 12 (2018).
- [5] B.L. Drolen, C.A. Wilson, B.S. Taft, J. Allison, K.W. Irick, Advanced Structurally Embedded Thermal Spreader Oscillating Heat Pipe Micro-Gravity Flight Experiment, *Journal of Thermophysics and Heat Transfer*. 36 (2022) 314–327. <https://doi.org/10.2514/1.T6363>.
- [6] AFRL's Oscillating Heat Pipes are even cooler in space, ONE AFRL / TWO SERVICES. (n.d.). <https://www.afrl.af.mil/News/Article-Display/Article/3136877/afrls-oscillating-heat-pipes-are-even-cooler-in-space/http%3A%2F%2Fwww.afrl.af.mil%2FNews%2FArticle-Display%2FArticle%2F3136877%2Fafrls-oscillating-heat-pipes-are-even-cooler-in-space%2F>.
- [7] Physical Sciences Informatics (PSI), NASA. <https://www.nasa.gov/PSI>.

Appendix

Table 3. Experiment State Definition

State #	Case #	OHP Select	Heater Select	Heater Power [W]	Dwell Time	Record Period [sec]
1	0	None	None	0	2 min	1
2		1	Large	10	2 min	1
3		1	Small	10	2 min	1
4		1	Startup	10	2 min	1
5		2	Large	10	2 min	1
6		2	Small	10	2 min	1
7		2	Startup	10	2 min	1
8		3	Large	10	2 min	1
9		3	Small	10	2 min	1
10		3	Startup	10	2 min	1
11	100	None	None	0	10 min	1
12		1	Large	20	30 min	1
13		2	Large	20	30 min	1
14		3	Large	20	30 min	1
15	1	None	None	0	1 hour	1
16		1	Large	10	1 hour	1
17	5	None	None	0	1 hour	1
18		2	Large	10	1 hour	1
19	9	None	None	0	1 hour	1
20		3	Large	10	1 hour	1
21	2	None	None	0	1 hour	1
22		1	Large	20	1 hour	1
23	6	None	None	0	1 hour	1
24		2	Large	20	1 hour	1
25	10	None	None	0	1 hour	1
26		3	Large	20	1 hour	1
27	3	None	None	0	1 hour	1
28		1	Large	30	1 hour	1
29	7	None	None	0	1 hour	1
30		2	Large	30	1 hour	1
31	11	None	None	0	1 hour	1
32		3	Large	30	1 hour	1
33	4	None	None	0	1 hour	1
34		1	Large	40	1 hour	1
35	8	None	None	0	1 hour	1
36		2	Large	40	1 hour	1
37	12	None	None	0	1 hour	1
38		3	Large	40	1 hour	1
39	13	None	None	0	1 hour	1
40		1	Small	10	1 hour	1
41	17	None	None	0	1 hour	1
42		2	Small	10	1 hour	1
43	21	None	None	0	1 hour	1
44		3	Small	10	1 hour	1
45	14	None	None	0	1 hour	1
46		1	Small	20	1 hour	1
47	18	None	None	0	1 hour	1
48		2	Small	20	1 hour	1
49	22	None	None	0	1 hour	1
50		3	Small	20	1 hour	1
51	15	None	None	0	1 hour	1
52		1	Small	30	1 hour	1
53	19	None	None	0	1 hour	1
54		2	Small	30	1 hour	1
55	23	None	None	0	1 hour	1
56		3	Small	30	1 hour	1
57	16	None	None	0	1 hour	1
58		1	Small	40	1 hour	1

Table 3. Experiment State Definition (cont.)

State #	Case #	OHP Select	Heater Select	Heater Power [W]	Dwell Time	Record Period [sec]	
59	20	None	None	0	1 hour	1	
60		2	Small	40	1 hour	1	
61	24	None	None	0	1 hour	1	
62		3	Small	40	1 hour	1	
63	25	None	None	0	1 hour	1	
64		1	Large	10	1 hour	1	
65		1	Large	20	1 hour	1	
66		1	Large	30	1 hour	1	
67		1	Large	40	2 hours	1	
68		1	Large	30	1 hour	1	
69		1	Large	20	1 hour	1	
70		1	Large	10	1 hour	1	
71		26	None	None	0	1 hour	1
72			1	Small	10	1 hour	1
73	1		Small	20	1 hour	1	
74	1		Small	30	1 hour	1	
75	1		Small	40	2 hours	1	
76	1		Small	30	1 hour	1	
77	1		Small	20	1 hour	1	
78	1		Small	10	1 hour	1	
79	27	None	None	0	1 hour	1	
80		2	Large	10	1 hour	1	
81		2	Large	20	1 hour	1	
82		2	Large	30	1 hour	1	
83		2	Large	40	2 hours	1	
84		2	Large	30	1 hour	1	
85		2	Large	20	1 hour	1	
86		2	Large	10	1 hour	1	
87		28	None	None	0	1 hour	1
88			2	Small	10	1 hour	1
89	2		Small	20	1 hour	1	
90	2		Small	30	1 hour	1	
91	2		Small	40	2 hours	1	
92	2		Small	30	1 hour	1	
93	2		Small	20	1 hour	1	
94	2		Small	10	1 hour	1	
95	29		None	None	0	1 hour	1
96			3	Large	10	1 hour	1
97		3	Large	20	1 hour	1	
98		3	Large	30	1 hour	1	
99		3	Large	40	2 hours	1	
100		3	Large	30	1 hour	1	
101		3	Large	20	1 hour	1	
102		3	Large	10	1 hour	1	
103	30	None	None	0	1 hour	1	
104		3	Small	10	1 hour	1	
105		3	Small	20	1 hour	1	
106		3	Small	30	1 hour	1	
107		3	Small	40	2 hours	1	
108		3	Small	30	1 hour	1	
109		3	Small	20	1 hour	1	
110	3	Small	10	1 hour	1		
111	31	None	None	0	1 hour	1	
112		1	Large	20	42 days	60	
113	32	None	None	0	1 hour	1	
114		1	Small	20	42 days	60	
115	33	None	None	0	1 hour	1	
116		2	Large	20	42 days	60	

Table 3. Experiment State Definition (cont.)

State #	Case #	OHP Select	Heater Select	Heater Power [W]	Dwell Time	Record Period [sec]
117	34	None	None	0	1 hour	1
118		2	Small	20	42 days	60
119	35	None	None	0	1 hour	1
120		3	Large	20	42 days	60
121	36	None	None	0	1 hour	1
122		3	Small	20	42 days	60
123	N/A	None	None	0	90 days	1
124	N/A	None	None	0	90 days	1

Thermal performance evaluation of a novel vapor chamber with multi-artery vapor spreading channels

Guohui Zhou^{1,2*}, Jingzhi Zhou^{1,2}, Xiulan Huai^{1,2,3}

¹ *Institute of Engineering Thermophysics, Chinese Academy of Sciences, Beijing, China*

² *Nanjing Institute of Future Energy System, Nanjing, China*

³ *University of Chinese Academy of Sciences, Beijing, China*

*Corresponding author email address: zhouguohui@iet.cn

Abstract

With the rapid development of electronic technology industry, the push to reduce the size and ever-increasing power density of electronics have driven the thermal management to be a significant challenge for their continuing progress. As passive heat transfer devices, vapor chambers are widely used in the thermal management systems of electronic devices due to the high thermal conductivity and temperature uniformity, which could effectively transfer heat utilizing the phase-change latent heat of the working fluid inside it. Herein, we present a 2.5 mm novel vapor chamber for cooling high-power electronics, in which multi-artery vapor spreading channels were employed in the capillary wick structure. Experimental investigations were conducted under forced air cooling condition to carefully evaluate the thermal performance, and the effects of the air flow rate on the heat transfer performance were also analyzed systematically. The results indicated that the proposed vapor chamber could stably operate at a low heat load of 20 W, and effectively dissipate a maximum heat load of 280 W. In addition, with the increase of the air flow rate, the heat removal capacity of the vapor chamber gradually increased, and meanwhile the total thermal resistance decreased, attaining a minimum total thermal resistance of 0.28 °C/W.

Keywords: Vapor chamber; Multi-artery; Forced air cooling; Heat transfer performance; Thermal resistance

1. Introduction

The rapid development of semiconductor technology has led to the high operational performance and miniaturization of electronic devices. In general, most of the power consumed by electronic components will be converted into waste heat needed to be dissipated in time to ensure the operating reliability and lifetime of electronics. It is clearly stated that the operational reliability and stability of electronics decreased by 10% for every 2 °C rise above the maximum allowable operating temperature [1]. Therefore, thermal management has been a crucial factor for the continuing progress of electronic industry, and to develop highly efficient cooling techniques is urgently in demand [2]. As a highly efficient heat transfer device, a vapor chamber could spread heat passively from a concentrated heat source to a sufficiently extended condensation surface by utilizing the latent heat of the working fluid inside it. Due to the crucial hallmarks of high thermal conductivity and temperature uniformity, vapor chambers have been widely used in thermal management of electronics, such as mobile phones, laptops, computer, and data center servers [3-6].

As the main component of vapor chambers, capillary wicks play a significant role in determining the heat transfer performance of vapor chambers [7]. In the past decades, various wick

structures have been developed by researchers at home and abroad in order to improve the thermal performance of vapor chambers [8-15]. Peng et al. [8,9] presented a novel leaf-vein-like fractal structure as the condenser wick of vapor chambers, and found that the fractal structure demonstrated a good performance in heat and mass transfer, and the vapor chamber thermal resistance was less than 0.3 °C/W. Subsequently, they also examined the effects of the fractal angle on the thermal performance of vapor chambers [10]. It was shown that when the fractal angle was between 40° and 50°, the vapor chamber exhibited the best heat transfer performance and surface temperature uniformity. Wong et al. [11] designed and fabricated a novel vapor chamber, where the conventional condenser wick was replaced with parallel grooves in order to facilitate the liquid reflow and improve the heat transport capacity. It is noted that the peaks of the grooves were directly connected with the evaporator wick of the vapor chamber, where the parallel grooves served as the vapor removal channels, extended condensation surface, and supporting structure simultaneously. Chen et al. [5] developed a novel ultra-thin vapor chamber for cooling portable electronic devices. Due to the combination of the sintered wire mesh wick and the etched micropillar arrays, the separation of the vapor and liquid removal channels was achieved, in which the space between

the micropillar arrays functioned as the vapor removal channels, and the condensate flowed through the sintered mesh wick. Results showed that the effective thermal conductivity of the ultra-thin vapor chamber was founded to be 12000 W/(m·K), nearly 30 times higher than that of pure copper. Chen et al. [12] designed and fabricated a novel vapor chamber for cooling high-power LEDs, in which multi-artery Ω -shaped reentrant microchannels inside porous wicks was employed to separate the passages for liquid and vapor flow. Experimental results indicated that compared to plain copper plate, the vapor chamber demonstrated a faster startup process, and the time required for the temperatures reaching the equilibrium state was shorter. In addition, the vapor chamber reduced the substrate surface temperature and thermal resistance of the LED module by up to 27% and the 48%, respectively.

Through the rigorous literature review, it can be concluded that vapor chambers with multi-artery radial microchannels in porous wicks could effectively achieve the separated flow passages for liquid and vapor, improving the heat transfer performance of vapor chambers. In this study, a novel vapor chamber with multi-artery vapor spreading channels in the wick structure was developed, which could separate the liquid and vapor flow passages to reduce the viscous force. Systematic experimental investigations were conducted using forced air cooling as the cooling mechanism in order to fully evaluate the heat transfer performance. Additionally, effects of the air flow rate on the thermal performance of the vapor chamber were also examined. The results indicated that the proposed vapor chamber could effectively tolerate a wide heat load range from 20 W to 280 W, and a minimum total thermal resistance of 0.28 °C/W was attained at an air flow rate of 68.1 CFM.

2. Design and fabrication of the vapor chamber

Fig. 1 presents the schematic diagram of the vapor chamber in the study. It is clearly showed that the vapor chamber is mainly comprised of a bottom plate, a capillary wick structure, a top plate, and a charging tube. The overall dimension of the vapor chamber was 85 mm × 85 mm × 2.5 mm. Both the bottom and top plates were made of a 0.5-mm-thick pure copper plate via a stamping process. The capillary wick had the overall dimension of 75 mm in length, 75 mm in width, and 1.5 mm in thickness, which was fabricated from 100 mesh copper wire mesh. Firstly, a nine-layer 100 in-1

copper wire mesh was sintered at a sintering temperature of 850 °C for 50 min in a vacuum further guarded by a mixture gas of 95% nitrogen and 5% hydrogen. Subsequently, the sintered multi-layer copper mesh was machined through the entire thickness by using the wire-electrode cutting method, thereby forming the proposed capillary wick structure with stripped wick structures, as shown in Fig. 2. The machined grooves functioned as the vapor removal channels, and the striped wick structures were employed as the flow passages for condensate, which could effectively separate the vapor and liquid flow, and significantly reduce the entrainment resistance. Additionally, it should also be noted that the square region at the center of the capillary wick with the dimension of 15 mm × 15 mm served as a liquid reservoir in order to possibly delay the dry-out in the evaporation section. Fig. 3 gives the SEM photograph and the wettability of the capillary wick. From Fig. 3(a), it is demonstrated that the wire diameter and pore size of the sintered copper mesh wick were 96.2 μm and 150.8 μm, respectively. In addition, as shown in Fig. 5(b), a 5 μl water droplet could absolutely penetrate into the wick within 26 ms, demonstrating a good hydrophilic property.

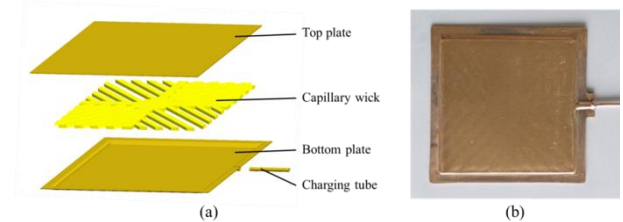


Fig. 1. The proposed vapor chamber: (a) exploded view; (b) a photo after bonding.

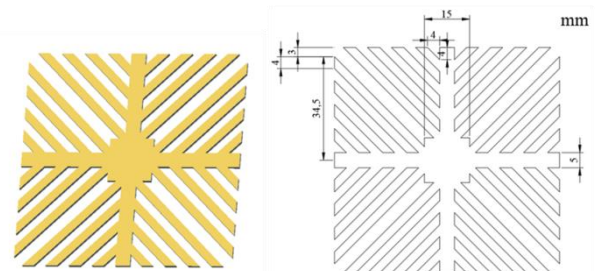


Fig. 2. The structure and geometrical parameter of the capillary wick.

The wick structure was enveloped with the top and bottom plates, and integrated together through another sintering process. And then, the top and bottom plates were thoroughly welded together by diffusion welding under a protective atmosphere.

Finally, a copper tube with the outer diameter/inner diameter of 2/1.5 mm was placed into the charging opening as a charging tube, which was welded together using high-frequency welding equipment. A photo after the bonding of the vapor chamber was clearly shown in Fig. 1(b). Subsequently, for the charging process, the air inside the vapor chamber was first pumped out using a high vacuum pump system including mechanical pump and molecular pump until the inner pressure was 10⁻³ Pa, and then a certain amount of DI water was charged into the vapor chamber as the working fluid. In this work, nearly 2.88 ml DI water was filled into the vapor chamber, and the filling ratio was calculated to be approximately 40%, where the filling ratio is defined as the ratio of the volume of the working fluid to the total inner space volume including the porosity of the capillary wick. After charging, the charging tube was flattened and welded by cold pressure welding and argon arc welding, thus forming the vapor chamber presented in this study. The main parameters of the proposed vapor chamber are listed in Table 1.

(L × W × H)	mm × 1.5 mm
Porosity	65.2%
Material	Copper mesh
Wire diameter	96.2 μm
Pore size	150.8 μm
Permeability	1.736 × 10 ⁻¹⁰ m ²
Working fluid	DI water
Filling ratio	40%

3. Experimental setup

Fig. 4 indicates the schematic of the experimental system. As shown in Fig. 4, a ceramic heater was employed as the simulated heat source, which had an active heating area of 20 mm × 20 mm. During the experiments, the ceramic heater was mounted onto the evaporator of the vapor chamber, and a very thin layer of thermal grease with the thermal conductivity of 2.5 W/(m K) was filled into the air gap between the heater and vapor chamber to minimize the contact thermal resistance. In addition, in order to reduce the heat loss, the ceramic heater was fully wrapped by a layer of 10-mm-thick adiabatic foam made of NBR/PVC, whose effective thermal conductivity was about 0.034 W/(m K). For the cooling system, an aluminum finned heat sink with the overall dimension of 80×80×60 mm³ was placed on the condenser of the vapor chamber, which were fixed by four stainless steel screws. Aiming at reducing the contact thermal resistance between the vapor chamber and aluminum heat sink, a layer of thermal grease with a thickness of about 0.5 mm was inserted into the gap. Additionally, an axial fan was mounted onto the aluminum finned heat sink, which was powered by a DC power supply. It can be seen that a fan speed governor was used to adjust the air flow rate. In the data acquisition system, an Agilent 34970A data acquisition was employed to monitor and record the temperature data obtained from the T-type thermocouples including those located on the vapor chambers. Fig. 5 shows the locations of the thermocouples mounted onto the vapor chamber. It is demonstrated that four thermocouples (T1-T4) was placed onto the evaporator surface of the vapor chamber to measure the evaporator temperature, and five thermocouples (T5-T9) was mounted onto the condenser surface of the vapor chamber to determine the condenser temperature. It should be pointed out that there was another thermocouple was used to measure the ambient temperature.

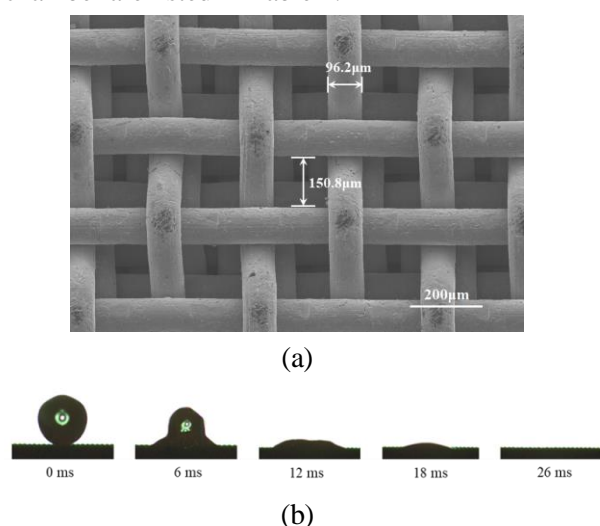


Fig. 3. (a) SEM photograph of the capillary wick; (b) wettability of a 5 μl water droplet on the capillary wick.

Table 1

The main parameters of the vapor chamber presented in this study.

Component	Specification	
Vapor chamber	Outer dimension	85 mm × 85
	(L × W × H)	mm × 2.5 mm
Bottom plate	Thickness	0.5 mm
Top plate	Thickness	0.5 mm
Charging tube	OD/ID	2/1.5 mm
Capillary wick	Outer dimension	75 mm × 75

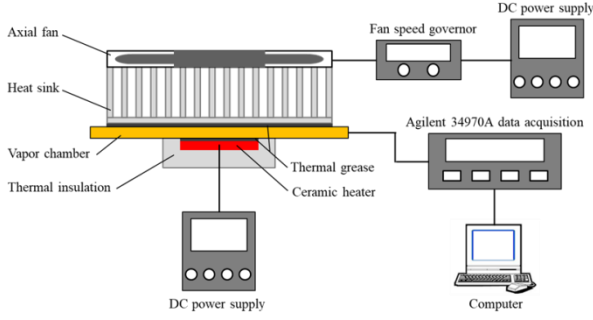


Fig. 4. Schematic of the experimental setup.

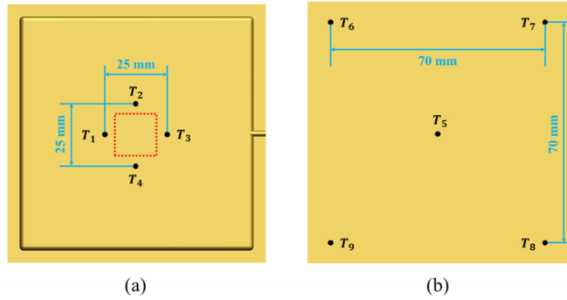


Fig. 5. Locations of the thermocouples attached onto the vapor chamber surface: (a) thermocouples mounted onto the bottom evaporator surface (the red dash-line rectangle represented the distribution of the heater); (b) thermocouples mounted onto the top condenser surface.

In the study, in order to assess the effects of air flow rate on the heat transfer performance, the proposed vapor chamber was tested at four different air flow rates by manipulating the fan speed governor, namely 16.2 CFM (nearly the minimum air flow rate), 27.6 CFM, 46.8 CFM, and 68.1 CFM (rated air flow rate). During all the tests, the ambient temperature was maintained at 25 ± 1 °C.

The evaporator and condenser temperatures of the vapor chamber were defined as the average temperatures of the thermocouples closely mounted onto evaporator and condenser surface of the vapor chamber. Thus, the evaporator temperature and condenser temperature can be calculated by the following equations, respectively.

$$T_e = \frac{T_1 + T_2 + T_3 + T_4}{4} \quad (1)$$

$$T_c = \frac{T_5 + T_6 + T_7 + T_8 + T_9}{5} \quad (2)$$

As the critical parameters to examine the thermal performance of vapor chambers, the vapor chamber thermal resistance R_{vc} and total thermal resistance of the cooling system R_t were approximately defined as follows:

$$R_{vc} = \frac{T_e - T_c}{Q} \quad (3)$$

$$R_t = \frac{T_e - T_{air}}{Q} \quad (4)$$

where T_{air} is the ambient temperature, and Q is the applied heat load.

The uncertainty of the total thermal resistance can be calculated by

$$\frac{\Delta R_t}{R_t} = \sqrt{\left(\frac{\Delta T_e}{T_e}\right)^2 + \left(\frac{\Delta T_a}{T_a}\right)^2 + \left(\frac{\Delta Q}{Q}\right)^2} \quad (5)$$

where ΔT_e and ΔT_a are the measurement errors of heat source temperature, ambient temperature, respectively, and ΔQ is measurement error of the heat load.

Under forced air cooling, it is calculated that the uncertainty of the total thermal resistance was estimated to be less than 6.52%.

4. Results and discussion

Fig. 6 plots the startup characteristics of the vapor chamber at a heat load of 100 W. It is clearly shown that with the increase of the air flow rate from 16.2 CFM to 68.1 CFM, the startup time required for the vapor chamber to attain the steady state, where the maximum temperature fluctuations for all the temperatures obtained by the thermocouples were within 0.2 °C for 3 min, gradually decreased. When the heat load was 100 W, the startup times were nearly 1600 s and 1000 s at the air flow rates of 16.2 CFM and 68.1 CFM, respectively. In addition, it is obvious that the steady-state temperatures at the air flow rate of 68.1 CFM were lower than those at the air flow rate of 16.2 CFM, and the steady-state evaporator temperatures were 54.2 °C and 67.1 °C, respectively.

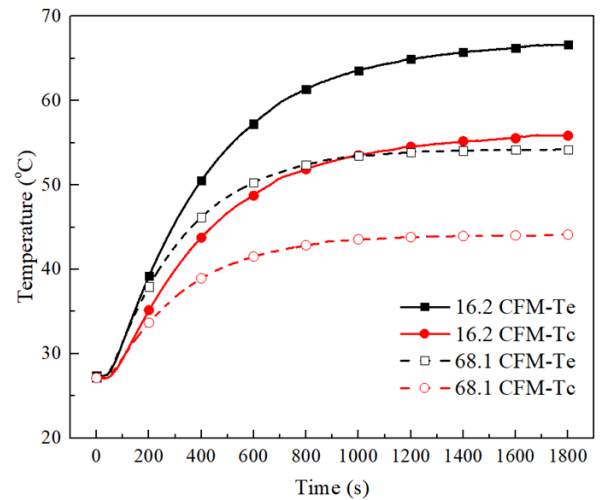


Fig. 7. Startup characteristics of the proposed vapor chamber.

Fig. 8 presents the steady-state evaporator temperatures at different heat loads and air flow rates. It is demonstrated that for all air flow rates, the steady-state evaporator temperatures nearly linearly increased with increasing heat load. Moreover, at the same heat load, the steady evaporator temperature decreased with the increase of the air flow rate. Correspondingly, the maximum heat transfer capacity increased. For example, when the air flow rate was 16.2 CFM, the vapor chamber could transport a maximum heat load of 200 W with the steady-state evaporator temperature of 110.7 °C, while 280 W for the air flow rate of 68.1 CFM with the evaporator temperature of 119.2 °C.

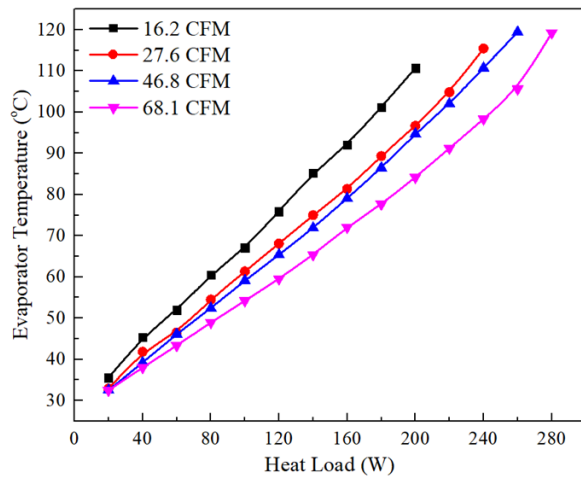


Fig. 8. Steady-state evaporator temperatures at different heat loads and air flow rates.

Fig. 9 shows the heat load dependence of the total thermal resistance at different air flow rates. It can be seen that at a same heat load, with the increase of the air flow rate, the total thermal resistance of the system gradually decreases. When the air flow rates were 16.2 CFM, 27.6 CFM, 46.8 CFM, and 68.1 CFM, the minimum total thermal resistances of the cooling system were 0.41 °C/W, 0.35 °C/W, 0.33 °C/W and 0.28 °C/W, respectively. When the air flow rate was 68.1 CFM, a minimum total thermal resistance of 0.28 °C/W was attained at 120 W. In addition, it should be noted at the air flow rate of 68.1 CFM, the total thermal resistance of the system sharply increased at 280 W. A possible explanation may be that the heat transfer limit of the vapor chamber may be achieved at 280 W, and the evaporator temperature sharply increased due to the partial dryout of capillary wick.

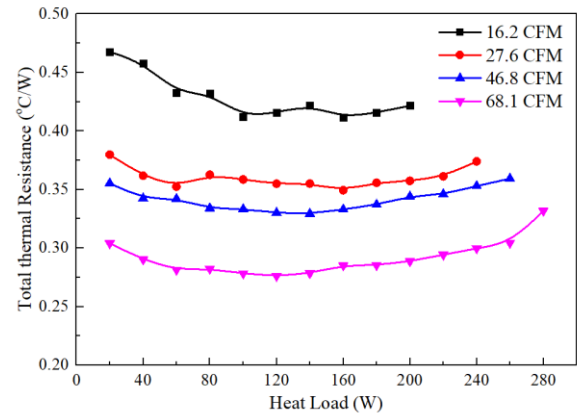


Fig. 9. The total thermal resistance at different heat loads and air flow rates.

5. Conclusions

In this study, a novel vapor chamber with multi-artery vapor spreading channels was developed and investigated. Systematic experimental investigations were conducted under forced air cooling in order to examine the heat transfer performance and fully evaluate the effects of the air flow rate on the thermal performance. The results demonstrated that the proposed vapor chamber could effectively tolerate a wide heat load range from 20 W to 280 W. Moreover, at a same heat load, the startup time required for the vapor chamber and evaporator temperature gradually decreased with increasing air flow rate. When the air flow rate was 68.1 CFM, the vapor chamber could transfer a maximum heat load of 280 W, at which a minimum total thermal resistance of 0.28 °C/W was obtained.

References

- [1] G. Zhou, J. Li, and Z. Jia, Power-saving exploration for high-end ultra-slim laptop computers with miniature loop heat pipe cooling module. *Applied Energy*, 2019. 239: p. 859.
- [2] R. van Erp, R. Soleimanzadeh, L. Nela, G. Kampitsis, and E. Matioli, Co-designing electronics with microfluidics for more sustainable cooling. *Nature*, 2020. 585(7824): p. 211.
- [3] M. Wang, W. Cui, and Y. Hou, Thermal spreading resistance of grooved vapor chamber heat spreader. *Applied Thermal Engineering*, 2019. 153: p. 361.
- [4] G. Huang, W. Liu, Y. Luo, and Y. Li, A novel ultra-thin vapor chamber for heat dissipation in ultra-thin portable electronic devices. *Applied Thermal Engineering*, 2020. 167.
- [5] Z. Chen, Y. Li, W. Zhou, L. Deng, and Y. Yan, Design, fabrication and thermal performance of a novel

ultra-thin vapour chamber for cooling electronic devices. *Energy Conversion and Management*, 2019. 187: p. 221.

[6] C. Liu, D. Hu, Q. li, X. Chen, Z. Zhang, and F. Zhou, Vapor chamber with two-layer liquid supply evaporator wick for high-heat-flux devices. *Applied Thermal Engineering*, 2021. 190.

[7] D. Xie, Y. Sun, G. Wang, S. Chen, and G. Ding, Significant factors affecting heat transfer performance of vapor chamber and strategies to promote it: A critical review. *International Journal of Heat and Mass Transfer*, 2021. 175.

[8] Y. Peng, W. Liu, N. Wang, Y. Tian, and X. Chen, A novel wick structure of vapor chamber based on the fractal architecture of leaf vein. *International Journal of Heat and Mass Transfer*, 2013. 63: p. 120.

[9] Y. Peng, W. Liu, B. Liu, J. Liu, K. Huang, L. Wang, and W. Chen, The performance of the novel vapor chamber based on the leaf vein system. *International Journal of Heat and Mass Transfer*, 2015. 86: p. 656.

[10] W. Liu, Y. Peng, T. Luo, Y. Luo, and K. Huang, The performance of the vapor chamber based on the plant leaf. *International Journal of Heat and Mass Transfer*, 2016. 98: p. 746.

[11] S.-C. Wong, K.-C. Hsieh, J.-D. Wu, and W.-L. Han, A novel vapor chamber and its performance. *International Journal of Heat and Mass Transfer*, 2010. 53(11-12): p. 2377.

[12] L. Chen, D. Deng, Q. Huang, X. Xu, and Y. Xie, Development and thermal performance of a vapor chamber with multi-artery reentrant microchannels for high-power LED. *Applied Thermal Engineering*, 2020. 166.

[13] D. Deng, Q. Huang, Y. Xie, X. Huang, and X. Chu, Thermal performance of composite porous vapor chambers with uniform radial grooves. *Applied Thermal Engineering*, 2017. 125: p. 1334.

[14] Y. Li, Z. Li, W. Zhou, Z. Zeng, Y. Yan, and B. Li, Experimental investigation of vapor chambers with different wick structures at various parameters. *Experimental Thermal and Fluid Science*, 2016. 77: p. 132.

[15] Y. Luo, W. Liu, and G. Huang, Fabrication and experimental investigation of the bionic vapor chamber. *Applied Thermal Engineering*, 2020. 168.

Traction System Cooling Options for Electric Vehicles

Randeep SINGH^{1*}, Tomoki ORIDATE¹, Takeshi KOSHIO, Harutoshi HAGINO¹, Phan Thanh LONG¹, Masahiro MATSUDA¹, Yoji KAWAHARA¹, Tsuyoshi OGAWA¹, Yuji SAITO¹, Tien NGUYEN¹, Thang NGUYEN¹, Masataka MOCHIZUKI², Thomas Van RAAY³

¹Fujikura Ltd, 1-5-1 Kiba, Koto-Ku, Tokyo 135-8512, Japan

²The Heat Pipes, 1-4-33-1022 Shiohama, Koto-ku, Tokyo, 135-0043 Japan

³Fujikura Technology Europe GmbH The Squire 12, 60549 Frankfurt am Main, Flughafen

* E-mail: randeep.singh@jp.fujikura.com

Abstract

Electrification of vehicles intensify their cooling demands due to requirements of maintaining electronics/electrical system below their maximum temperature threshold. In this paper, passive cooling approaches based on heat pipes has been considered for the thermal management of electric vehicle (EV) traction system including battery, inverter and motor. For battery, heat pipe base plate is used to provide high heat removal (180 W per module) and better thermal uniformity (< 5 C) to battery module in a pack while downsizing liquid cold plate system. In the case of Inverter, two phase cooling system based on heat pipes were designed to handle hot spots arising from high flux (~100 W/cm²) – for liquid cooling, and provide location independence and dedicated cooling approach - for air cooling. For EV motor, heat pipe based system are explored for stator and rotor cooling. The paper also provide glimpse of development on high performance microchannel based cold plate technologies based on parallel fins and multi-layer 3D stacked structures. Specifically, this work extends the concept of hybridization of two-phase technology based on heat pipes with single-phase technology, predominately based on liquid cooling, to extend performance, functionalities and operational regime of cooling solutions for components of EV drive train. In summary, heat pipes will help to improve overall reliability, performance and safety of air and liquid cooling systems in electric vehicles.

Keywords: Li-ion battery, Inverter, motor, Electric vehicle, Heat pipe, Two-phase cooling, High performance cold plate.

1. Introduction

Electric vehicles have electric propulsion system that includes battery system, traction inverter and electric motor as the main components for automotive traction. These power systems are supported by auxiliary components for power transmission (cabling), power conversion (Inverter, DC/DC converter) and battery charging (onboard/induction charger, charging port). Figure 1 presents that simplified form of vehicle electric power train with charging system from inlet port to battery, and discharging system (or traction system) from battery to motor [1, 2]. In Figure 2, heat output from different components of traction system is presented, along with automotive electronics (e.g. display, headlamp, ECU) for comparison purpose. It can be seen that power systems covers wide range of load-distance spectrum with general trend towards high power and longer heat transfer distances. In other words, thermal solution for electric vehicles will need to be develop to handle high flux and transfer high power over significant distances while satisfying robust structural quality. Such requirements are unique for two-phase and single-phase systems originally developed for consumer and high performance stationary electronics. Thus, necessitate focus on development of high performance, modular and dedicated thermal systems for electric vehicles.

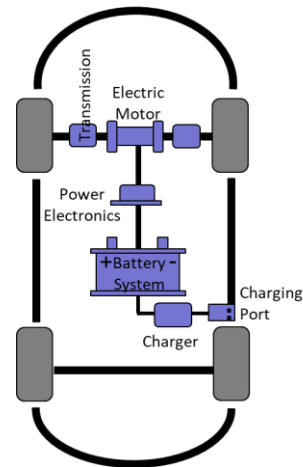


Figure 1. Electrified propulsion system in electric vehicle showing battery system and motor along with control electronics

Electric vehicle, in contrast to engine vehicle, have more specific and specialized cooling needs. Specific needs because of high sensitivity of electronics and electrical systems to temperature. Engine vehicle generally uses materials, which have high tolerance to wider temperature ranges. Specialized needs because of exclusive requirements and design customization needed per

system functionalities and specifications. For example, EVs typically require cooling solutions for high voltage systems with isolation needs to prevent short-circuiting. New generation optical systems in headlamp and display have low temperature requirements to maintain good optical performance from such devices. Although, EVs are predominately built out of electronic/electric systems that are made of materials which are thermally sensitive to temperature for performance and structural integrity. However, there is general trend in automotive, including engine vehicles, towards higher electrification arising from autonomy and computerization of vehicular functions. Therefore, overall cooling requirements in automotive are on the rise.

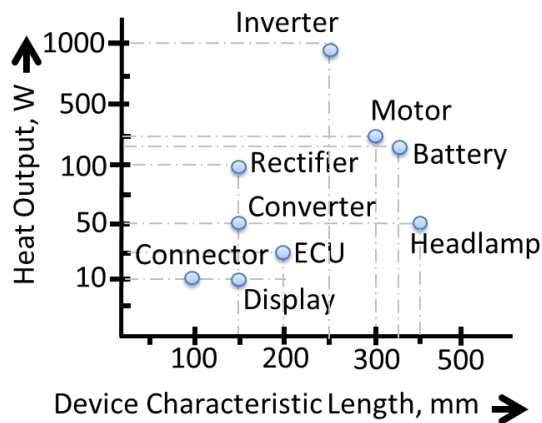


Figure 2. Waste heat output from different electronic/electric system in car

As stated earlier, overall electric propulsion system consists of electric system (like cables, connector, fuse, motor), electronic system (like inverter, converter, OBC) and electrochemical system (like Li-ion batteries). Each of these categories have very specific cooling requirements due to different materials and functions of these systems. Additionally, each system even in similar categories have diverse thermal challenges owing to their electrical architecture (or simply design), location in car (front, back, in-cabin, under-cabin) and cooling method (air-base, liquid-base, conduction to chassis). Cooling requirements of these devices could be dictated by material temperature limits (SiC chip have higher temperature limits than Si chip), criticality of system (autonomous drive system need higher redundancies than infotainment system) and sometime mere system cost (to avoid replacement costs).

For simplicity, in this paper, we have chosen three major systems from electric drive train to provide an overall overview on types of cooling requirements, thermal solutions development at component and overall device level that are needed in area of traction systems.

Most components of electric drive train requires thermal management for performance and longevity. Electrical (e.g. e-motors) and electronic systems (e.g. IGBTs – inverter, converters) can sustain higher operating temperatures (~ 100 to 150°C) than electrochemical systems like battery cells (~ 40 °C) [3]. Lithium-Ion cells, in either prismatic or pouch form, are invariably used for automotive batteries owing to their high energy density and better charging-discharging efficiency. For good calendar life and performance of Li-ion battery, temperatures should be maintained within narrow temperature range ~ 25 to 40 °C. For the battery electric vehicle (BEV), the range can reduce by 18% when driving on hot summer day (+35 °C, 40% RH) and by 36% when driving on cold winter day (~ -10 °C, 90% RH), due to cabin and battery thermal management. Based on aforesaid facts, it can be safely asserted that thermal management of automotive batteries is very critical for vehicle range (economy), performance and lifetime cost.

Traction inverters, also commonly referred as power electronics, provides a controlling and switching link between battery and motor. Development in inverter have provided variable challenges for cooling system to handle high heat fluxes (35-100 W/cm²), large heat loads (1-2kW) while keeping working temperatures within limits of semiconductor materials used in inverter built.

Motors have main heat source as bearing and electrical coils. Both components can sustain temperature level 100-150 °C range. Motor could be cooled at stator or rotor area depending on motor type, design and main areas of thermal generation. For rotor cooling, main challenges comes from the fact that heat source is in rotational motion so cooling system will be required to give thermal and structural performance while in high RPM motion.

Figure 3 present thermal roadmap for electric vehicles that help to identify applicable cooling technology w.r.t heat ranges. In light of above discussion, it is important to understand that existing state of cooling technology in vehicle has been mainly developed to manage engines and other mechanical systems, and therefore could not provide an efficient migration to vehicles with significant electric built (plug in hybrids - PHEVs,

battery electric vehicles - BEVs). Electronic/electric systems in EVs gives out concentrated heat fluxes, which need to be managed by highly developed cooling system (single phase as well as two phase). Per Figure 3, there is an opportunity to improve operational regime for air cooling, two-phase solutions as well as liquid cooling within capability index of respective technology. Particularly, hybridization or optimum mixing of technologies would help to provide cooling design breakthroughs in area of traction drive train.

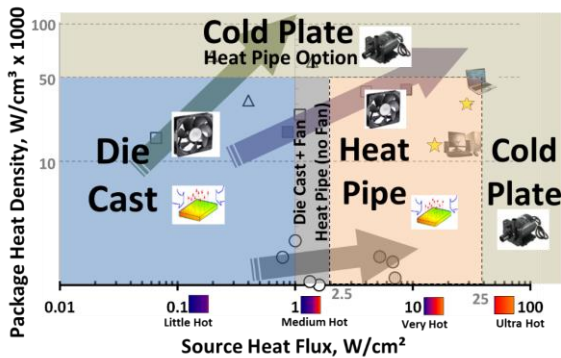


Figure 3. Thermal Roadmap for Automotive

In this paper, cooling challenges for components of EV drive train has been outlined for relevance of current work. Technological improvements in area of two phase and single phase have been outlined, followed by enhanced cooling systems built and characterization as outcomes of present research undertaking.

2. Cooling Device Requirements

As discussed in previous section, different components in electric power train have different permissible temperatures (owing to material, reliability needs), structural (owing to component location, built), electrical (owing to voltage class – low, high) and operational (owing to functional modes – sudden surge, steady, transient) requirements.

The cooling device is designed to achieve required thermal resistance, $-R_t$, as determined by its source permissible temperature (T_h) and output heat load (Q^*) for given sink temperature (generally ambient air $-T_c$). it can be represented mathematical as:

$$R_t = \frac{(T_h - T_c)}{Q^*} \quad (1)$$

Other requirements are more component specific and targeted to achieve maximum performance and lifetime for the device while operating reliably and safely. Cooling device should be able to maintain temperature uniformity within $\pm 5^\circ\text{C}$ over active heat source to reduce thermal stress on semiconductor surface or Li-ion cell. For high voltage devices, cooling device need to maintain isolation gap of 1-2 kV/mm (depending on voltage and proximity of other power sources). In traction invertors, cooling device need to possess 2 to 3 times higher cooling capacity or thermal mass to overcome and absorb sudden power surges of waste heat during vehicle acceleration/deceleration. Similarly, charging line components and battery system need to have adequate cooling means to keep temperature within allowable ranges during normal/fast-charging cycles. In addition to these, thermal solution are require to satisfy lifetime requirements regarding freeze sustainability, cyclic temperature operation, high temperature endurances and alike. Geometrical tolerances and structure of device should keep intact during designed lifetime.

3. Technology Enhancements

In this section, cooling technologies of interest in thermal management of traction system of EVs has been identified with key developments that has been in effect to make these technologies more application in terms of performance, reliability and cost. Figure 4 present length versus capacity for different cooling technologies with solid conduction at lower bands, two phase solution covering most of low to medium band and liquid phase towards long distances and high heat load bands.

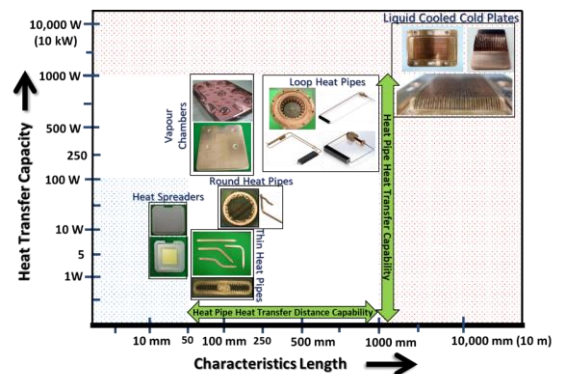


Figure 4. Heat transfer performance of different cooling technologies

3.1 Heat Pipes

In EV thermal management, heat pipes have significant scope to apply as high conductive heat transfer devices in air as well as liquid cooled system. Heat pipes could complement cooling solution in following different ways:

- ① Enhance temperature uniformity or reduce hot spots
- ② Reduce liquid leakage hazard in proximity of high voltage area (due to limited liquid in heat pipe. No drip leak)
- ③ Improve thermal response of cooling solution for sudden power surges
- ④ Increase thermal capacity of overall cooling system

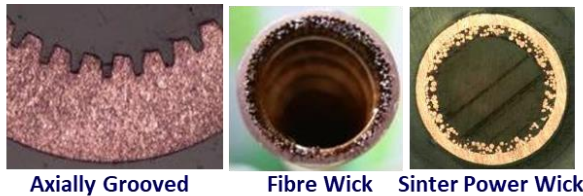


Figure 5. Types of heat pipe wick structure

Typically, heat pipe constitutes of axial, fibre or sinter power wick as shown in Figure 5. In order to enhance effective thermal conductivity of heat pipe and overall heat load, wick design could be enhanced in different ways. Fibre wick is beneficial to achieve smaller thicknesses for heat pipe while keeping high heat capacity whereas power wick helps to achieve high evaporative/condensation heat transfer coefficients along with high capillary pressure for heat transfer against gravity. Figure 6 present heat transfer capacity of diameter 9.4 mm heat pipe with 0.5 and 1 mm thick copper powder wick. As evident, thermal capacity of heat pipe could be almost double by choosing appropriate size and thickness of wick.

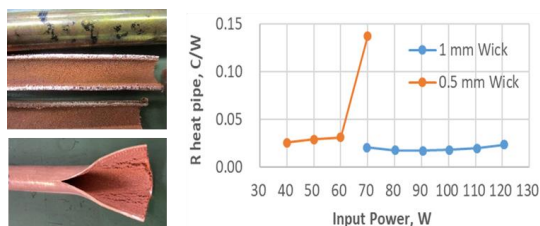


Figure 6. Thermal performance of powder wick with different thicknesses

In Figure 7, heat transport capacity and thermal resistance of 570 mm long heat pipe have shown to improve by using combination of fibre and powder wick. Maximum heat load of 50 W was achieved while thermal resistance was improved from 0.5 to 0.09 °C/W. Such enhancements are possible due to best mix of permeability (possible from linear flow passages in fibre wick), and capillary pressure/phase heat transfer coefficients (possible from fine pore size of powder wick). In this case, relative placement and geometrical design of two wick types is important to achieve best mix of thermal capacity and thermal resistance (or thermal conductivity) of heat pipe.

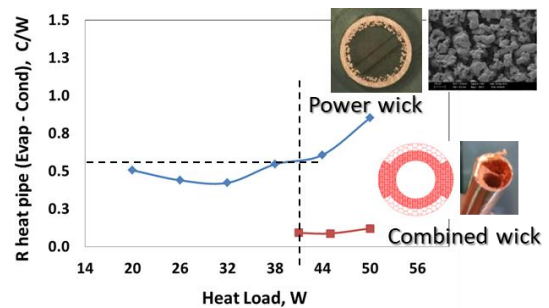


Figure 7. Power versus combined wick thermal performance

Further approaches based on surface texturing of wick by micro powder deposition on fibre/powder to improve wettability, mixing high conductive carbon fibre with copper fibre to enhance wick thermal conductivity, gradation of wick along heat pipe length to achieve best mix of flow properties, and variable thickness of wick around heat pipe cross section to achieve best thermal hydraulic performance from wick has been attempted to improve workability of heat pipe for electric vehicles cooling.

Structural enhancements of heat pipe in terms of improvement in container strength using different alloy of copper, 3D bending/shaping by altering wick alignment, corrosion protection by painting/Ni-plating, and high voltage isolation by polyimide/ceramic coating has been attempted, to apply this technology successfully for automotive. Figure 7 presents heat pipe coated with polyimide to achieve >5V/mm voltage isolation for traction inverter application.



Polyimide Coated Heat Pipe

Figure 7. Heat pipe with electrical isolation

3.2 Cold Plates

Liquid cooling is one of main mode of heat removal from components of traction system owing to high heat load per component, and necessity to cool multiple component by single cooling infrastructure. Battery systems are generally very low flux ($< 1 \text{ W/cm}^2$) and thus can be cooled by low performance macro channel cooling plates. For power electronics, including traction inverter, DC-DC converter and on-board charger, highly developed cold plates based on microchannel technology are needed to achieve cooling performance expected by devices. In Figure 8, two different version of cold plates based on; 1) Parallel micro channel technology and 2) Multi-stacked layer technology are presented.

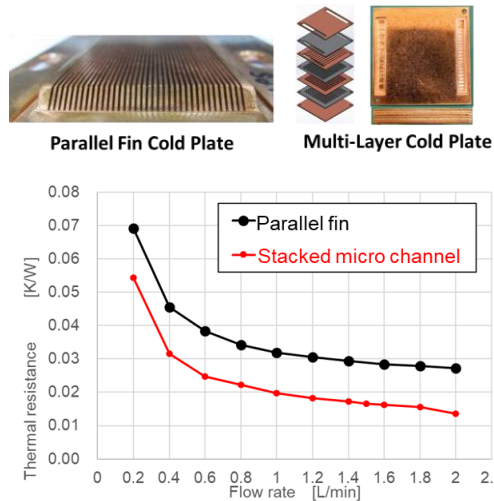


Figure 8. Cold plates based on microchannel technology: Design and expected thermal performance

Parallel channel based design provide simpler and cheaper option whereas multi-layer design offers more performance (~ 40% higher) achieved through 3D stacked structure (5 to 7 stacked layers). Stacked layer structure provide lower pressure drop (due to shorter flow path), lower thermal resistance (due to 3D heat and fluid interaction) and smaller form factors (due to possibility to fabricate such

structures through micro etching techniques) but at higher costs. In Figure 8, thermal performance of two types of cold plate structure is presented with respect to flow rate.

Based on aforesaid discussion on applicable cooling technologies, in next section, cooling architectures for thermal management of different components based on two phase and single phase (predominately liquid cooled) hybridized system has been presented.

4. Traction Systems Cooling

In this section, cooling system based on combination of two phase and single phase for three main components of traction system namely battery, inverter and motor are presented, with an aim to provide current state of applicability and improvements needed in order to make such system more viable for electric drive train cooling in EVs.

4.1 Battery Cooling

Most of cabin base in EVs are occupied by battery modules arranged in packs, and customarily cooled by low-end cold plates positioned under the modules. Such cooling system poses safety issues from liquid leakage in high voltage areas, presents temperature gradient within/amongst modules, have heavy weight due to extend of liquid coolant and cold plate volume, and have high system complexity (cold plate integration and connectivity).

In this case, two-phase systems based on heat pipes can extend significant advantages to improve temperature uniformity, reliability and safety [4, 5]. Figure 9 present cooling approach for battery pack with heat collection using heat pipe carrier plates and heat transfer to radiator area using significant downsized cold plate.

Each heat pipe carrier plate was more than 600 mm long with condenser area ~ 50 mm, and was required to transfer 240 W heat load from 1.5 share of battery modules per heat pipe carrier plate. Heat pipe plate provide temperature uniformity within $\pm 5 \text{ C}$ and significant temperature reduction (~ 40 °C) compared to metal Aluminum plate design. Pack level cooling approach as presented in Figure 9 is readily easy to apply and integrate in the vehicle without any major mechanical changes. However, benefits from such methodology approaches limits as extent of heat load increases from next generation high voltage batteries, and even low voltage batteries during fast charging sequences.

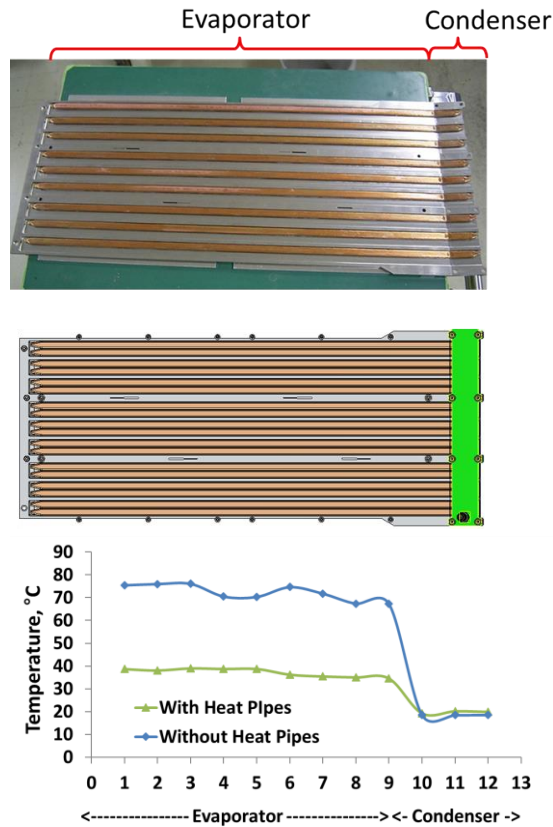


Figure 9. Heat pipe carrier plate for cooling battery pack

Figure 10 shows the breakdown thermal resistance from cell terminal to battery radiator that clearly shows that bulk of thermal flow obstruction lies close to generation areas inside cell. This means targeting efficient heat flow elements (like heat pipes) closer to cell generation areas, although difficult to implement, would provide best cooling benefits in the form of temperature drops. Two such approaches based on module and cell level cooling are shown in Figure 10 (bottom). Cell level cooling approaches has been investigated in details by integrating heat pipes externally or internally in Li-ion cells [6, 7].

It should be noted that mix of two phase and single-phase system, as outlined above, would provide most performance and cost optimum approach for battery cooling [4]. Fully two-phase system are high performance but integration and cost intensive. Similarly, fully single-phase system are bulky, complex and low performance (particularly thermal non-uniformity close to battery cells). The innovative aspect of using heat pipes in battery cooling is hybridization of two-phase and single-phase systems to improve performance and simplify design.

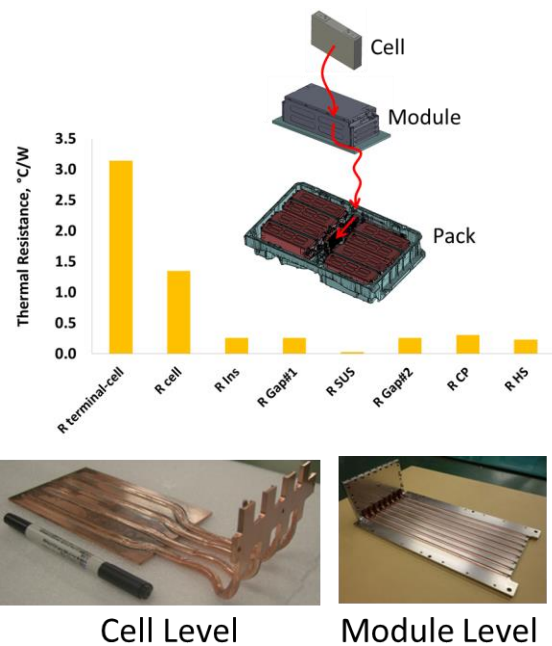


Figure 10. Battery system breakdown thermal resistance (top), Cell and module level cooling approaches with heat pipes (bottom)

4.2 Inverter Cooling

Power or traction inverters are located between battery and motor, and perform power controlling and switching functions. Typical EV inverter consists of multiple chips with control electronics, and heat load ranging from 0.5-2 kW. Hot spots and thermal uniformity are typical cooling challenges for inverters [8]. Traction inverter in EVs are generally liquid cooled, except in very specific circumstances when inverter is located far from liquid cooling loop these could be air cooled. In either case, air or liquid cooling, limited thermal conductivity of metal spreader between inverter chips and liquid flow possess limit on maximum heat transfer, system response time and hot spot issues.

Figure 11 presents dedicated air-cooled system for traction inverter based on heat pipe heat sink [9, 10]. The system was designed to handle more than 35 W/cm² flux from 3x chips, with total heat load exceeding 1kW in continuous operation, and 2kW during power surges imposed at acceleration/deceleration cycles. Advantages from such systems include design simplicity, allow independent placement of inverter remote from liquid cooling loop, better thermal uniformity than single phase cooling and operational reliability.

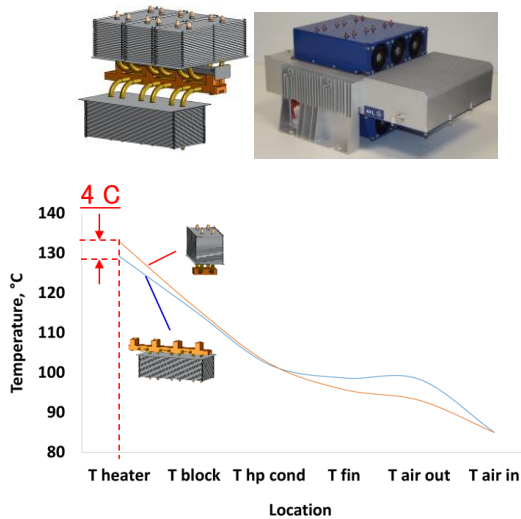


Figure 11. Air-cooled traction inverter for EV with heat pipe spreading and transport: Design and performance characteristics [10]

Temperature uniformity of inverter chips with heat pipe based spreading is represented to be within 4 °C, in Figure 11, which is difficult to achieve, by purely metal spreaders. Nonetheless, liquid cooling of traction inverter provide more compact and high performance system, however single phase does poses limitation to handle hot spots on chips, which has dual heated faces in many cases.

Local spreading enhancement with heat pipes from die to coolant flow face could provide dual benefits of improving cooling response time as well as cooling performance as shown in Figure 12. In this case, heat pipes tend to diffuse hot spots and increase dissipation area from heat sink to coolant by increasing fin efficiency.

Further, passive two-phase system based on heat pipe and vapour chamber are under development to handle fluxes higher than 100 W/cm² from next generation of SiC (Silicon Carbide) inverters. In this case, heat pipes with non-homogenous structured wick structure, as discussed in Section 3.1, have been developed to handle high heat load and thermal fluxes. Vapour chamber have higher potential to reduce temperature of dense hot spots as compare to heat pipes, however the form factor and cost of these devices will need to be reduce to make them viable for application in automotive. Additionally, single phase liquid cold plate technologies based on impingement and 3D heat transfer concept, as discussed in Section 3.2, have been developed to improve heat transfer coefficients on liquid side of cooling solution.

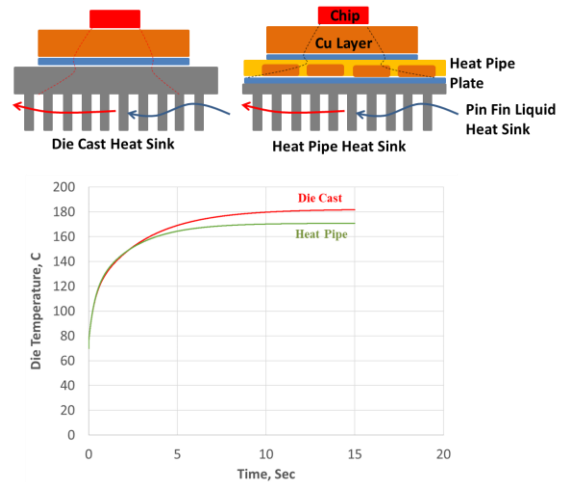


Figure 12. Liquid cooled traction inverter for EV with heat pipe spreading: Design and performance characteristics

4.3 Motor Cooling

Cooling of electric vehicle motor is important for overall performance and longevity of electromagnetic system and associated control electronics. There are different method for cooling motor including stator cooling and rotor cooling (as shown in Figure 13). Thermal management at stator provide limited cooling due to presence of high thermal resistance path from heat source (coil) to heat sink (circulating air or water). In this case, direct cooling of rotor provide superior cooling option however there are different implementation and operation challenges due to high speed rotation of rotor during operation.

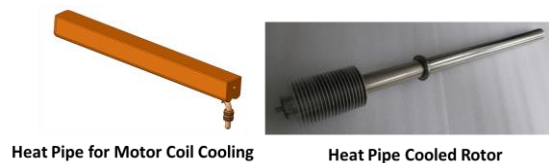


Figure 13. Heat pipe options for electric motor cooling

Components in motor that need thermal management include bearing and coils. In this case, heat sources need to have thermal coupling with cooling solution while maintaining electrical isolation to avoid internal short-circuiting and external current leaks via cooling elements. Reliable integration of heat pipe(s) to coil and motor parts to avoid bending of parts during rotation, balancing of parts in rotation (to avoid any residual unbalance forces on rotating parts) and sealing of coolant fluid

around rotating parts need to be given due consideration in the design and implementation of two phase cooling system for motors. Still, rotational heat pipes have undergone limited investigation and applications due to their complex thermal fluids behavior and mechanical interactions. Further work on these devices will need to be done to apply them in cooling high-speed motors in EVs.

5. Conclusions

The paper have provided mix of two-phase and single phase cooling approaches for components of electric drive train of vehicle with cooling performance in range of 0.5 to 2 kW, ~ 35-100 W/cm² heat fluxes. In summary, heat pipe based passive system will provide system with high runtime reliability, better thermal uniformity and more safety, for battery, inverter and motor cooling in electric vehicles.

References

- [1] R. Singh, Electric Vehicle Cooling with Heat Pipes: Challenges and Scope, Invited Keynote, 20th IHPC & 14th IHPS, 7 – 10th September 2021, Gelendzhik, Russia
- [2] R. Singh, Vehicle Thermal Management Using Heat Pipes, Proc. of the IEEE CPMT Symposium Japan 2019, November 18 – 20, 2019, Kyoto, Japan
- [3] A. Jeckel, Battery Thermal Management: Key to Performance, Durability and Safety, Proc. of the 7th International Conference on Thermal Management for EV/HEV, 13 – 15 Feb, 2018, Berlin, Germany
- [4] R. Singh, Gero Lapp, Jason Velardo, Phan Thanh Long, Masataka Mochizuki, Aliakbar Akbarzadeh, Abhijit Date, Karsten Mausolf, Kristin Busse, Battery Cooling Options In Electric Vehicles With Heat Pipes, *Frontiers in Heat and Mass Transfer (FHMT)*, 16 (2), 2021, DOI: 10.5098/hmt.16.2, ISSN: 2151-8629
- [5] J. Smith, R. Singh, M. Hinterberger, M. Mochizuki, Battery thermal management system for electric vehicle using heat pipes, *International Journal of Thermal Sciences*, 134, December 2018, pp. 517-529
- [6] J. Kleiner, R. Singh, M. Schmidt, L. Komsysiaka, G. Elger; C. Endisch, Influence of Heat Pipe Assisted Terminal Cooling on the Thermal Behavior of a Large Prismatic Lithium-Ion Cell during Fast Charging in Electric Vehicles, *Applied Thermal Engineering* 188, 2021, 116328
- [7] J. Kleiner, F. Lambauer, R. Singh, L. Komsysiaka, M. Hinterberger, C. Endisch, Experimental study of cell integrated heat pipe cooling with a lithium-ion cell emulator, *Journal of Energy Storage*, 56, Part A, 2022, 105808, ISSN 2352-152X, <https://doi.org/10.1016/j.est.2022.105808>
- [8] B. Orr, R. Singh, T.L. Phan, Thermal management of an IGBT inverter, Proc. of the 55th National Heat Transfer Symposium, June, 2018, Sapporo, Japan
- [9] M. Tiesler, Konzeptionierung einer Luftkühlung für Automotive-Wechselrichter mit Siliziumkarbid-Halbleitertechnologie, Master Thesis, Technische Universität Braunschweig, September 2018
- [10] J., Zachariae, C., Schweikert, T.A., Benning, R., Singh, AirSiC – A Silicon-Carbide based air-cooled cooled traction inverter is the enabler for a simplified, distributed powertrain system in a passenger vehicle, Proc. of PCIM Europe Konferenz 2021, 04-05 May, 2021, Nuernberg, Germany

Preliminary Multi-Variable Experimental Analysis To Determine The Startup Criteria of Pulsating Heat Pipes

Mauro Abela^{1*}, Mauro Mameli¹, Mattia Capuani¹, Sauro Filippeschi¹, Brent S. Taft²

¹Department of Energy, Systems Land and Construction Engineering, University of Pisa, Largo L. Lazzarino, Pisa, Italy.

²U.S. Air Force Research Laboratory, Kirtland Air Force Base, NM 87117, USA

* mauro.abela@phd.unipi.it

Abstract

Pulsating Heat Pipes (PHP) are passive two-phase heat transfer devices characterized by a simple structure and high heat transfer capabilities. Despite this, their large-scale application is still hindered by the actual unpredictability of their dynamic behavior during the start-up and the thermal crisis. An innovative experimental apparatus is designed to systematically investigate the above phenomena. It consists in a square loop made of four borosilicate transparent glass tubes joined at corners by means of brass connectors. The external tube surface is coated with several transparent Indium Tin Oxide heaters. The device is used to topologically reproduce 5, 7, and 11 turns (i.e., heated sections in the evaporator) PHPs with an 2 mm inner diameter tube, filled with pure ethanol and tested in horizontal position. The condenser temperature is varied from 10°C to 40°C; the input power goes from 10 W to 40W. It is observed that the startup occurrence does not depend only on the number of heating sections but also on the condenser temperature. Increasing condenser temperature lowers the critical number of heated sections. At the same time, with the increase of the condenser temperature the startup time increases. Moreover, thanks to the direct fluid visualization, the increase of condenser temperature is linked to the formation of long liquid plugs that are found to be detrimental in terms of startup time.

Keywords: Pulsating heat pipes; Number of turns; Number of heated sections; Start-up; Operational Limits; Indium Tin Oxide.

1. Introduction

The need of efficient and reliable heat transfer devices channeled the researchers' attention towards a relatively new technology: the Pulsating Heat Pipe (PHP) [1]. It consists in a capillary tube bent in several turns, vacuumed, and partially filled with a working fluid. Despite its advantages with respect to the standard Heat Pipes (simple structure, ability to cover complex and wide geometries, foldability and so on), the PHP is still facing the hesitation of the industry since its operational boundaries are not clearly defined in terms of optimal start-up conditions. The attempts done so far in the literature to define quantitative criteria for the PHP start-up do not consider the interplay of all the variables affecting the PHP operation bringing to different outcomes by different authors. Indeed, the PHP start up is affected by several parameters such as: the number of heating sections (often ambiguously called "number of turns" in the literature; in the present work it is indeed replaced with "number of heated sections"), the orientation with respect to gravity, the filling ratio, the condenser temperature, the wall to fluid heat flux at the evaporator, the initial fluid distribution, and so on. For example, if on one hand it is generally accepted there exists a critical number of heated

sections that ensures the startup occurrence, different authors find different critical numbers and generally the analysis lacks of a clear physical explanation.

Khandekar et al. [2] conducted experiments on a PHP made of copper using water, ethanol and R-123 as working fluids. The device is tested in various orientation and results show that it does not operate in horizontal mode because of the small number of heated sections and low operating pressures. Charoensawan et al. [3] studied the effect of orientation on PHP filled with different working fluids (ethanol, R123a, water) for various number of heated sections (from 5 to 23). They report critical values of around 16, needed for the full activation of PHP with an inner diameter of 2mm. The same authors [4] report that the critical number of heated sections depends on evaporators temperature and the inner diameter of the tube; the higher the number of heated sections the lower the evaporators temperature needed for the startup. Lee et al. [5] perform a similar study on a PHP filled with FC72 showing that performance becomes independent from orientation when the number of heated sections is 20. The main reason behind the apparent incoherency of results reported by different authors is related to the fact that results are obtained from different test cells with different features and results

are often difficult to scale or compare; therefore, results lack of general validity.

Many other authors deal with the study of the relationship between different parameters and the startup occurrence and performance both experimentally and numerically. Xu et al.[6] tested a copper PHP and filled with FC72. They observed the existence of two rather different startup processes: the first is dominated by latent heat exchange and characterized by sudden temperature overshoot in the evaporator; the second, where sensible heat exchange is predominant, is characterized by a smooth oscillations period. Similar observations are reported by Khandekar et al. [7] who built a branch PHP and tested it for long durations. Absolute pressure measurements along with temperature measurements are taken along the tube. They observed two types of startup: a sudden startup and a gradual one. The occurrence of a specific type is likely linked to the local void fraction distribution and the special two-phase distribution of working fluid. Liu et al. [8] performed a comprehensive experimental study of PHP startup and used the control theory to make a quantitative estimation of startup performance; effects of filling ratio, fluid thermophysical properties and inclination angle are reported. The optimal filling ratio for water, ethanol and methanol is reported to be respectively 41%, 52% and from 35% to 41%. Moreover, a working fluid with small dynamic viscosity, small specific heat and large saturation pressure gradient versus temperature can improve the start-up performance. Daimaru et al. [9] present a methodology for the numerical modeling of pulsating heat pipe with check valves. Authors perform the model validation by comparing simulations with on orbit data of a flat plate PHP. Main objective is to understand the influence of the initial phase distribution on the startup since experimentally *“reproducing and specifying initial vapor-liquid distribution in OHPs is virtually impossible”*. Results suggested that difficult startup are due to concentration of liquid plugs in the condenser zone as result of cooling during the eclipse. In accordance, Nikolayev [10] performed a theoretical study of a single branch PHP startup considering as primary cause the meniscus/film evaporation rather than boiling. Among other parameters, he identified the temperature gradient along the tube as the most important. The following year Nekrashevych and Nikolayev [11] extended the previous study to a multibranch PHP. One of the main results is that there is no startup without bubble generation. They report that without this effect, after initial oscillation the liquid gathers in a single plug and the motion

declines quickly. The same model is then used [12] to simulate the startup of a PHP tested in microgravity conditions. It is pointed out that the initial phase distribution has a major impact on the startup performance. For this reason authors report that the initial distribution is one of the parameters to be known to perform a complete validation of the PHP model. This is one of the most difficult initial condition to obtain from experiments, since most of the tested PHPs in literature are not fully transparent.

The objective the present work is contribute to the definition of the Pulsating heat pipe operational limits by showing the results of the analysis of 1) the effect of the number of heated sections on the start of fluid motion and on the steady state performance; 2) the relationship between various parameters (condenser temperature, liquid plugs length, phase distribution) and the startup performance. In order to obtain results that are independent from the specific PHP, an innovative approach is adopted. A modular test cell is designed and built; it allows to perform a multi-variable analysis and to quantitatively investigate the effects of various parameters on the PHP performance in a well-defined framework of initial and boundary conditions. Moreover, transparent tubes and innovative transparent evaporators open to new analysis possibilities in terms of phase distribution tracking and visualization of the thermofluidic phenomena.

Within such system, three different configurations are studied; each configuration is tested at various input powers and condenser temperatures. Results suggest that the startup occurrence is not only function of the number of heated sections but also a function of the condenser temperature and therefore a function of the temperature gradient between evaporator and condenser. The study is the focused on the startup performance analysis in terms of startup time, trying also to define it more rigorously with respect to previous literature. A relationship between startup time and thermal gradient between evaporator and condenser is observed. Moreover, visual analysis reveals a relationship between startup time and the length of liquid plugs before the startup.

2. Experimental Apparatus

The experimental apparatus is designed in a modular way to reproduce different PHP layouts. The PHP is ideally unbent and reconfigured as single loop (Fig. 1 a) where it is possible to play with the number/position/length of heating and cooling

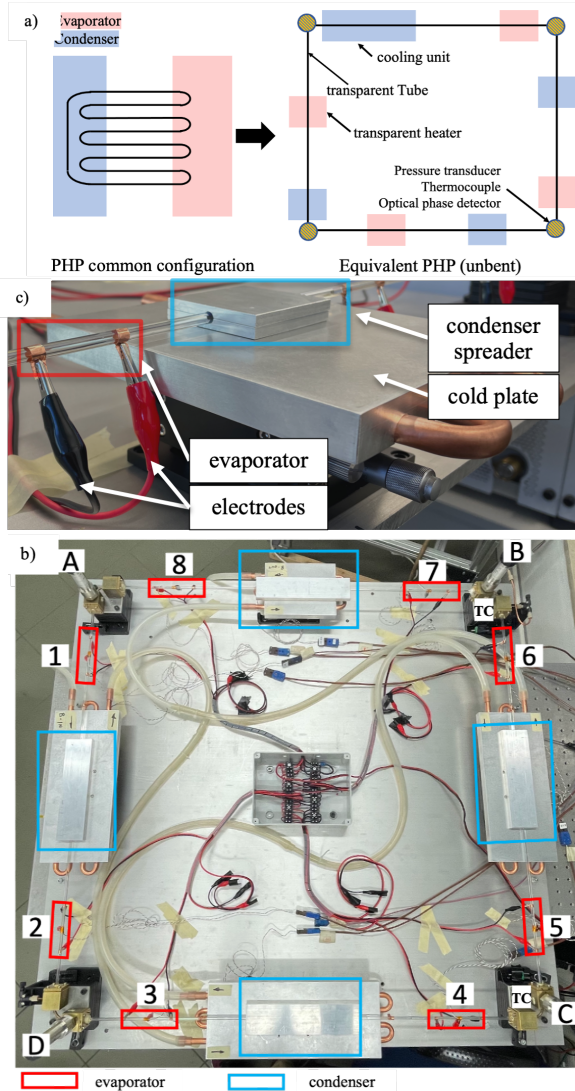


Figure 1. a) Schematic representation of a PHP (left) and its unbent configuration (right). b) Picture of the experimental apparatus. c) Detail of the evaporator and condenser.

zones. A similar approach is used by Okazaki et al. [13] who compared a similar unbent configuration with an equivalent PHP with meanderings and demonstrated that both show a similar behavior characterized by an almost identical thermal resistance and very close temperatures and pressures. Therefore, the number of turns in the evaporator section of a standard meandering PHP, correspond here to the number of heating sections. The experimental test cell (Fig. 1 b) is a planar closed loop consisting of four transparent borosilicate tubes (I.D. 2mm, O.D. 5mm, tube

length 765 mm, total channel length 3460 mm) joined at the corners by four brass joints, designed without any flow section discontinuity. Each tube is equipped with a series of 16 transparent Indium Tin Oxide (ITO) heaters (length: 40mm) vacuum deposited on the external surface by Diamond Coatings[®], UK. The heaters (labelled “1-8” in Figure 1 b) are connected to a programmable power supply (ELC[®] ALR3206D) by means of custom-tailored copper-foil electrodes (Figure 1 c); when voltage is applied, heat is generated by Joule effect. The temperature of each evaporator is measured by a T-type thermocouple (RS[®] pro 363-0266, bead diameter 1 mm) clamped by means of kapton tape on its external surface. The heat dissipation system in the condenser zones is shown in Figure 1c and consists in a series of aluminum spreaders sandwiched on the borosilicate tubes and coupled with aluminum cold plates connected in a loop to a thermal bath (HAAKE[®] 0024276). Each brass joint hosts a custom-made pressure transducer for the fluid pressure measurement (Keller[®] PAA-33X, 3 bar abs, 0,2%FSO accuracy; denoted with “A-D” labels in Figure 1b); in the same position, joints B and C host a micro-thermocouple for the fluid temperature measurement (TC Direct[®] 406-590, bead diameter 0.25 mm, response time 0.1s; denoted with “TC” label in Figure 1b). Joints B and D are also equipped with a vacuum/filling micro-metering valve (IDEX[®] Upchurch Sc. P-447). The data acquisition system is composed of an FPGA chassis (National Instruments[®] NI-cRIO-9074) + modules (National Instruments[®] NI-9213, NI-9472, NI-9205). A labVIEW[™] software is used to acquire temperature signals at 50 Hz; pressure and power are acquired at 100 Hz. A 12 MP camera is used to capture the fluid position. Measured quantities and their maximum uncertainties are summarized in Table 1.

Table 1. Measured quantities and uncertainties.

Quantity	Maximum uncertainty
Evaporator temperature	± 0.1 K
Fluid Temperature	± 0.5 K
Fluid Pressure	± 150 Pa
Liquid Plug length	± 1 mm

3. Experimental Procedure

Main objective of the present work is to investigate the effects of various parameters on the PHP performance during the startup operation. To obtain results with a general validity, it is necessary to cover a large number of possible combinations of

the governing variables. The experimental matrix with the varying parameters is summarized in Table 2.

Table 2. Experimental Matrix.

Working Fluid	Filling ratio (%)	Number of Heated sections	Condenser Temperature (°C)	Input Power (W)	Initial phase dist.
Ethanol	50	5, 7, 11,	10, 20, 30, 40	10, 20, 30, 40	various

The working fluid is ethanol and the PHP is charged at 50% volumetric filling ratio; three different geometrical configurations are tested at different condenser temperatures and input powers.

The heat load is supplied to the evaporators by 10 W steps up to 40 W and then decreased by 10 W steps every 20 min. If the temperature of an evaporator Before each refill, the device is emptied and vacuum-tested using a helium leak detector (Agilent® G8610A); moreover, before each test, the internal pressure is checked to make sure it is equal to the saturation pressure corresponding to the measured fluid temperature. All wired ITO heaters resistances are checked making sure they correspond to the expected values. Finally, the device is closed into a box to account only for free convection losses.

Two kinds of test are performed. The first (Figures from 2 to 7) investigates the effect of the number of heated sections and of the condenser temperature on the device activation (partial or full startup) and on the steady state performance. The typical power profile is plotted on the bottom of Figure 4; if an evaporator temperature exceeds 110°C, the power level is decreased to prevent degradation of ITO heaters. The objective of the second test (Figures from 7 to 14) is to study the effect of the condenser temperature and phase distribution on the full startup time. In this case the power is kept at its lowest value (10W) for 10 minutes.

4. Results

This section describes the results of the two kinds of tests described in the previous section.

For each configuration (number of heated sections 5, 7, 11) the device is tested at different input power (from 10W to 40W) and different condenser temperatures (10-40°C). From now on each configuration (n5, n7, n11) coupled with a condenser temperature will be shortened for the sake of brevity; for instance, n5@20°C stands for 5 heated sections configuration 20°C condenser. The

size of evaporators and condenser is scaled in such a way that the heat flux per evaporator is constant regardless the number of heated sections.

Figure 2 shows the temporal evolution of the evaporators temperatures (on top), fluid temperatures (second subplot from top), pressures (third subplot from top) and input power (subplot

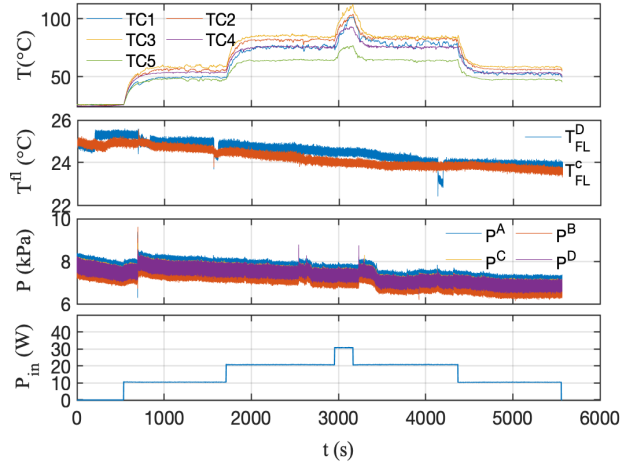


Figure 2. 5 Turns, 10°C condenser temperature test.

on the bottom) of the n5@10°C PHP tested at 10°C condenser temperature. As soon as the power supply is switched on, the evaporators temperature rises and reaches a steady-state temperature; when input power is increased the temperature increases accordingly and reaches a new steady-state temperature. The flow motion is negligible: the PHP does not start up and works mainly as conductive medium. An almost identical behavior is shown by the n5 configuration and 20°C condenser temperature test. In the case of n5@30°C, initially the device does not startup. In fact, for $t < 2000$ s the temporal evolution of temperature and

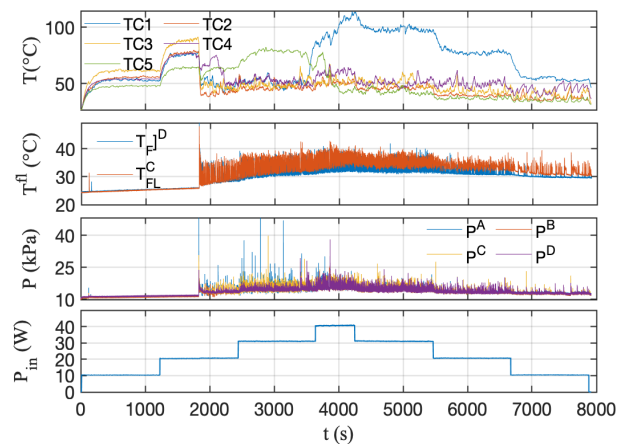


Figure 3. 5 Turns, 30°C condenser temperature test.

pressures is similar to the case n5@10. At $t \cong 2000$ s there is a quick pressure rise. Pressures and fluid

temperatures rise and start to oscillate; evaporators temperature exhibits a steep drop (also known as “overshoot” phenomena in the literature) which is a sign of the wall to fluid heat exchange; in fact, when oscillations start, cold fluid coming from the

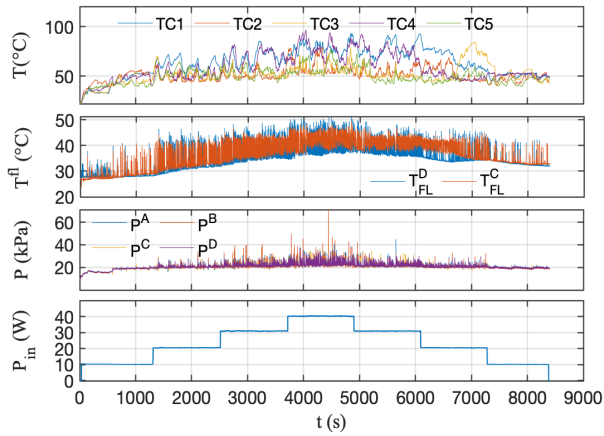


Figure 4. 5 Turns, 40°C condenser temperature test.

condenser sections wet hot evaporators wall and lower their temperature. In this case the operation is intermittent; pressures signals are characterized by sudden absence of oscillations (also known as

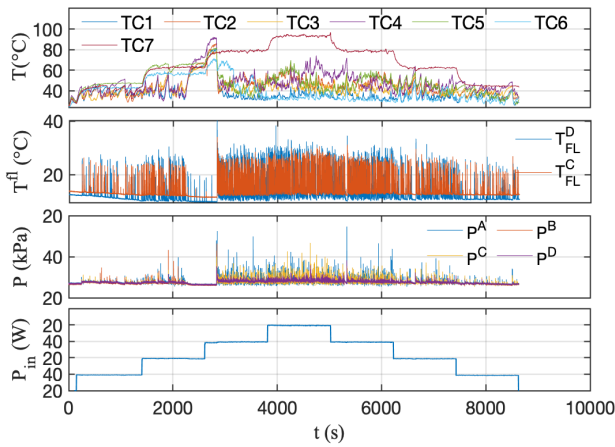


Figure 5. 7 Turns, 10°C condenser temperature test.

“stopovers” in the literature) and some evaporators dry out during the operation. In fact, initially ($t > 2000$ s) evaporator 5 (see T_5 in Figure 3) exhibits a higher temperature with respect to the others; for $t \cong 3500$ s, T_5 drops and adjacent evaporator temperature T_1 rises. Direct visualization allows to find the reason behind this behavior: for $t < 3500$ s a long bubble occupies the evaporator 5 region; then at $t \cong 3500$ s the bubble is pushed in the evaporator 1 region. The presence of a bubble in the same region throughout the entire test indicates that no circulation is present. In the case $n5@40^\circ\text{C}$ (Fig. 4), the device starts up at a lower heat load (10W)

with respect to the previous case; pressures oscillation frequency is higher than $n5@30^\circ\text{C}$ even if stopovers are still observed for lower heat load

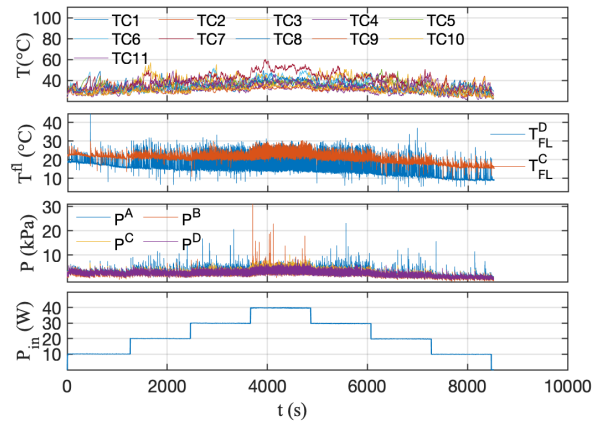


Figure 6. 11 Turns, 10°C condenser temperature test.

(10W). The 7 heated sections PHP exhibits the startup for all the condenser temperatures. The $n7@10^\circ\text{C}$ condenser temperature test (Fig. 5) follows the trend observed in $n5@30^\circ\text{C}$ (Fig.3); presence of stopovers and partial dry-out is

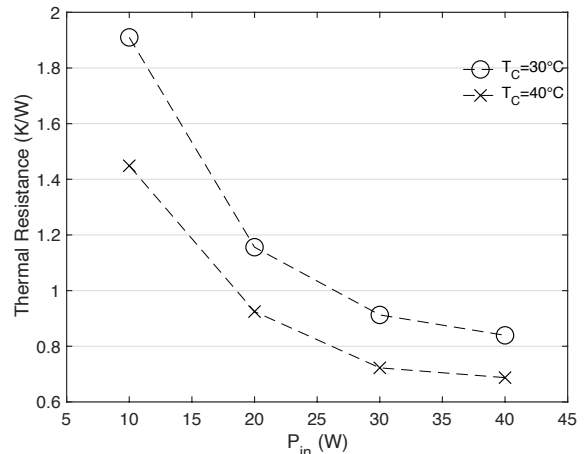


Figure 7. Thermal Resistance for 7 turns configuration

observed. With increasing condenser temperature, stopovers disappear, and the device is able to reach a full startup, the mean evaporators temperature during the pseudo steady state decreases. The $n11$ configuration exhibits the best performance even at the lowest condenser temperature 10°C (Fig. 6). The full startup takes place at the lowest input power for all the condenser temperatures. In this configuration the device performance appears to be less influenced by the condenser temperature with respect to the previous cases.

To quantify the performance enhancement due to the increase of number of heated sections and condenser temperature, the equivalent thermal

resistance is evaluated as $R = \langle \Delta T_{ec}^{P_{in}} \rangle / P_{in}$ where $\langle \Delta T_{ec}^{P_{in}} \rangle$ is the average temperature

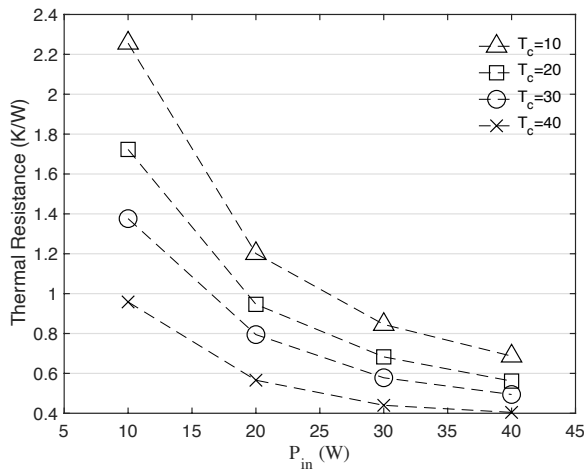


Figure 8. Thermal Resistance for 11 turns configuration

difference between evaporator and condenser for an input power P_{in} . The resistance is plotted (see Fig.7 and Fig. 8) for the n7 and n11 configurations; the n7@10°C and n7@20°C thermal resistances, as well as the n5 thermal resistances are not evaluated since the device operation is not stable. From the figures 7 and 8, it is clear that increasing the number of heated sections is beneficial in terms of global

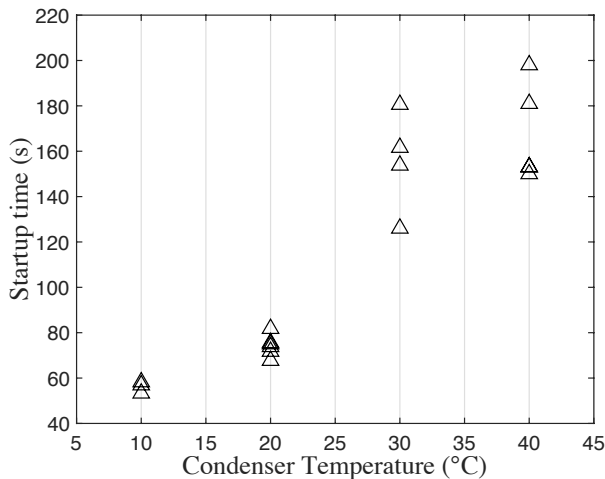


Figure 9. Startup time vs condenser temperature for 11 turns configuration.

performance (as expected from the literature). In fact, for constant condenser temperature and input power the overall thermal resistance on n11 is lower of 0.3 – 0.4 W/K than the on of n7. Moreover, the increase of condenser temperature lowers the thermal resistance. This effect is presumably related to the change of the fluid physical properties and in particular viscosity and density that decrease when temperature increases. As already observed by Cai et al. [14], lower density liquid has smaller inertia

and reduces the temperature gradient between evaporator and condenser needed to sustain oscillations; lower viscosity contributes to the reduction of temperature gradient because the decrease of viscous drag reduces the driving pressure difference between evaporator and

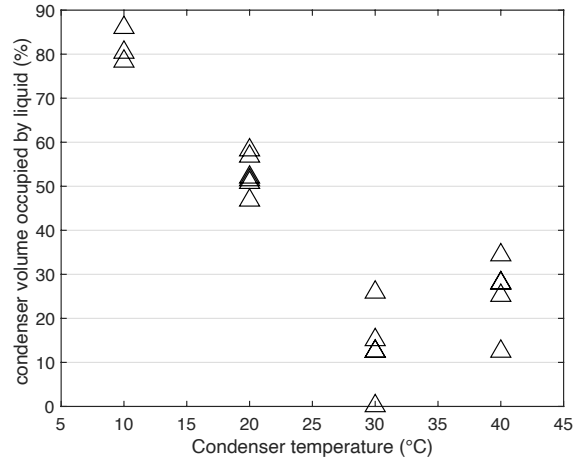


Figure 10. Condenser volume occupied by liquid phase vs condenser temperature

condenser.

If on one hand the increase of the condenser temperature is beneficial in terms of global performance, on the other hand it has an opposite effect in terms of startup performance. To the authors' knowledge literature does not provide a unified definition of startup time therefore here a definition is proposed. The full startup occurs when two conditions are true at the same time: 1) when pressure peaks take place in all measuring points within 2 seconds from one to another; 2) pressure do not go below the 95% of the pseudo steady state average pressure reached after the transient. In this way, the first condition ensures that fluid motion takes place in all branches; the second condition ensures that partial stopovers are not taken into account. the above criteria is also able to include the two different kind of startup observed by Xu et al.[6] and Khandekar [7]

The most suitable configuration to perform the startup analysis is the n11 since it exhibits full startup from low input powers; for these tests the input power is 10W. Figure 9 shows the startup times of the n11 configuration plotted against the condenser temperature. The trend shows that for lower condenser temperatures the startup time tends to be lower; with increasing condenser temperature the startup time increases. This is reasonably due to the fact that for low condenser temperature the thermal gradient between evaporator and condenser is higher. This could validate Nikolayev's [10] numerical outcomes.

It is observed that the condenser temperature affects the initial phase distribution. Figure 10 and 11 show the percentage of condenser and evaporator section occupied by liquid phase before the startup plotted against the condenser temperature. The analysis of the two trends suggests that liquid phase tends to gather in the condenser

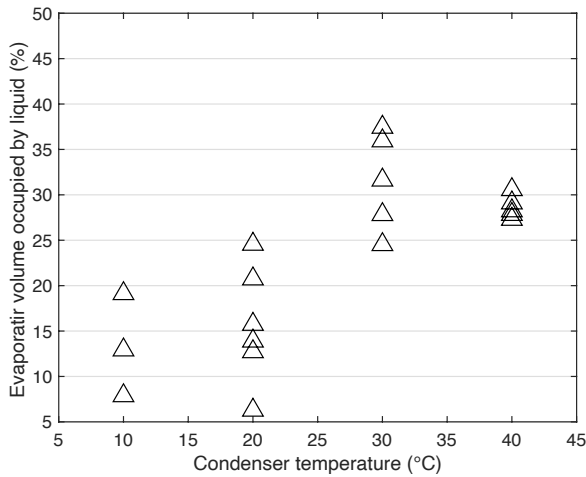


Figure 11. Evaporator volume occupied by liquid phase vs condenser temperature

sections for 10°C and 20°C condenser temperature which are lower than the ambient temperature ($\cong 25^\circ\text{C}$) while it tends to randomly occupy evaporator (which is an adiabatic zone before the startup) and adiabatic zones for condenser temperatures higher than the ambient temperature. However, no evidence of a relationship between the liquid distribution in evaporator and condenser before the startup and the startup performance emerges. In

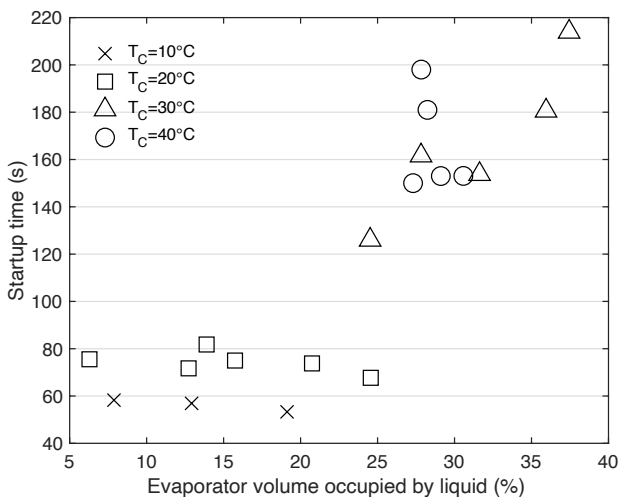


Figure 12. Evaporator volume occupied by liquid phase vs startup time.

Figure 12 the startup time is plotted against the evaporator volume occupied by liquid phase. For 10°C and 20°C condenser temperature

the startup time is almost constant for various value of evaporator volume occupied by liquid. For 30°C and 40°C the distribution shows a different trend. The 40°C startup times appear to be higher with increasing evaporator volume occupied by liquid phase. However, this trend is rather related to the effect of condenser temperature on liquid plugs length. Figure 13 shows the maximum liquid plug length and condenser temperature. It emerges a tendency of the liquid phase to gather in longer liquid plug with increasing temperature. This effect is observed to be more emphasized for 40°C condenser temperature. The presence of long liquid plugs is linked to longer startup time.

Figure 14 shows the startup time against length of the longest liquid plug visible before the

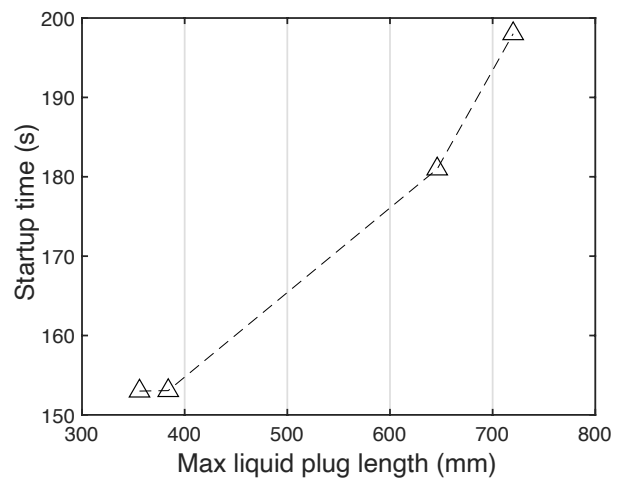


Figure 14. Startup time vs Maximum liquid plug length

startup. A clear tendency emerges: the startup time increases with the increase of liquid plug length. In some cases, extremely long liquid plugs (> 700 mm) impeded the startup for low input power. This is presumably due to 1) the higher inertia of long liquid plugs and 2) the high bubble nucleation overshoot (i.e., higher thermal energy needed to activate nucleate boiling in the liquid slug, with respect to the energy needed to evaporate liquid/vapor interfaces). In fact, the fluid motion induced by menisci or liquid film evaporation and bubble expansion is less energetically demanding than bubble generation in the liquid bulk.

5. Conclusions

An innovative modular experimental apparatus is used to perform a systematic investigation of the influence of number of heated sections, condenser temperature and phase initial distribution on the startup and the steady state performance of three

PHP configurations. Tests are performed on 5 – 7 – 11 heated sections PHP; the working fluid is ethanol at 50% volumetric filling ratio. Main outcomes can be summarized as follows:

- 1) A rigorous definition of full startup is proposed; adopting this definition ensures that fluid motion takes place in all PHP branches and ensures that the full startup is not confused with the partial one.
- 2) The PHP activation depends not only on the number of heated sections but also on the condenser temperature. By increasing the condenser temperature, the startup (partial or full) takes place for lower number of heated sections and lower input powers. The pseudo steady-state performance of the PHP is increased both by increasing the number of heated sections and increasing the condenser temperature. To quantify this effect, the overall thermal resistance is evaluated for the n7 and the n11 configurations. The n11 configuration shows a thermal resistance of 0.3-0.4 W/K less than the n7 configuration for the same input power and condenser temperature. Moreover, the increase of condenser temperature lowers the average evaporator temperature and the overall thermal resistance at constant number of heated sections.
- 3) The full startup time is influenced by the condenser temperature. The increase of the condenser temperature lowers the thermal gradient between evaporator and condenser; as result, the full startup time increases.
- 4) Fluid visualization reveals the influence of the condenser temperature on the initial phase distribution. For condenser temperatures lower than the ambient temperature, the liquid phase tends to gather in the condenser section. For condenser temperatures higher than the ambient one, the liquid is distributed randomly in evaporator section and condenser section. However, the initial phase distribution in evaporator and condenser has no clear effect on startup time.
- 4) Condenser temperature is also related to the liquid plug length. A tendency of the liquid to gather in longer liquid plugs for higher condenser temperature is observed. Moreover, a link between the liquid plug length and the full startup time is found: the increase of liquid plug length causes an increase of startup time.

References

- [1] M. Mameli, G. Besagni, P. K. Bansal, and C. N. Markides, “Innovations in pulsating heat pipes: From origins to future perspectives,” *Appl Therm Eng*, vol. 203,

- Feb. 2022, doi: 10.1016/j.applthermaleng.2021.117921.
- [2] S. Khandekar, N. Dollinger, and M. Groll, “Understanding operational regimes of closed loop pulsating heat pipes: An experimental study,” *Appl Therm Eng*, vol. 23, no. 6, pp. 707–719, 2003, doi: 10.1016/S1359-4311(02)00237-5.
- [3] P. Charoensawan, S. Khandekar, M. Groll, and P. Terdtoon, “Closed loop pulsating heat pipes - Part A: Parametric experimental investigations,” *Appl Therm Eng*, vol. 23, no. 16, pp. 2009–2020, Nov. 2003, doi: 10.1016/S1359-4311(03)00159-5.
- [4] P. Charoensawan and P. Terdtoon, “Thermal performance of horizontal closed-loop oscillating heat pipes,” *Appl Therm Eng*, vol. 28, no. 5–6, pp. 460–466, Apr. 2008, doi: 10.1016/j.applthermaleng.2007.05.007.
- [5] J. Lee, Y. Joo, and S. J. Kim, “Effects of the number of turns and the inclination angle on the operating limit of micro pulsating heat pipes,” *Int J Heat Mass Transf*, vol. 124, pp. 1172–1180, 2018, doi: 10.1016/j.ijheatmasstransfer.2018.04.054.
- [6] J. L. Xu and X. M. Zhang, “Start-up and steady thermal oscillation of a pulsating heat pipe,” *Heat and Mass Transfer/Waerme- und Stoffuebertragung*, vol. 41, no. 8, pp. 685–694, Jun. 2005, doi: 10.1007/s00231-004-0535-3.
- [7] S. Khandekar, A. P. Gautam, and P. K. Sharma, “Multiple quasi-steady states in a closed loop pulsating heat pipe,” *International Journal of Thermal Sciences*, vol. 48, no. 3, pp. 535–546, Mar. 2009, doi: 10.1016/j.ijthermalsci.2008.04.004.
- [8] X. Liu, Y. Chen, and M. Shi, “Dynamic performance analysis on start-up of closed-loop pulsating heat pipes (CLPHPs),” *International Journal of Thermal Sciences*, vol. 65, pp. 224–233, Mar. 2013, doi: 10.1016/j.ijthermalsci.2012.10.012.
- [9] T. Daimaru, H. Nagai, M. Ando, K. Tanaka, A. Okamoto, and H. Sugita, “Comparison between numerical simulation and on-orbit experiment of oscillating heat pipes,” *Int J Heat Mass Transf*, vol. 109, pp. 791–806, 2017, doi: 10.1016/j.ijheatmasstransfer.2017.01.078.
- [10] V. S. Nikolayev, “Effect of tube heat conduction on the single branch pulsating

- heat pipe start-up,” *Int J Heat Mass Transf*, vol. 95, pp. 477–487, Apr. 2016, doi: 10.1016/j.ijheatmasstransfer.2015.12.016.
- [11] I. Nekrashevych and V. S. Nikolayev, “Effect of tube heat conduction on the pulsating heat pipe start-up,” *Appl Therm Eng*, vol. 117, pp. 24–29, 2017, doi: 10.1016/j.applthermaleng.2017.02.013.
- [12] M. Abela, M. Mamei, V. Nikolayev, and S. Filippeschi, “Experimental analysis and transient numerical simulation of a large diameter pulsating heat pipe in microgravity conditions,” *Int J Heat Mass Transf*, vol. 187, May 2022, doi: 10.1016/j.ijheatmasstransfer.2022.122532
- [13] S. Okazaki, H. Fuke, and H. Ogawa, “Performance of circular Oscillating Heat Pipe for highly adaptable heat transfer layout,” *Appl Therm Eng*, vol. 198, Nov. 2021, doi: 10.1016/j.applthermaleng.2021.117497.
- [14] Q. Cai, R.-L. Chen, and C.-L. Chen, “IMECE2002-33334 AN INVESTIGATION OF EVAPORATION, BOILING, AND HEAT TRANSPORT PERFORMANCE IN PULSATING HEAT PIPE.” [Online]. Available: <http://www.asme.org/about-asme/terms-of-use>

Study of operating characteristics of a gravity-assisted cryogenic loop heat pipe with different charging pressures

Xinyu Chang^{1*}, Takeshi Yokouchi¹, Kimihide Odagiri², Hiroyuki Ogawa², Hosei Nagano³ and Hiroki Nagai¹

¹Tohoku University, Sendai, Japan

²Japan Aerospace Exploration Agency, Sagami, Japan

³Nagoya University, Nagoya, Japan

*Corresponding author email address: xinyu.chang.c3@tohoku.ac.jp

Abstract

Cryogenic loop heat pipe (CLHP) is a robust two-phase heat transfer device for cooling cryogenic heat sources. Compared to connecting an electronic component directly to a cryocooler, CLHP results in a higher flexible arrangement of the heat sources/the cryocooler and less disturbance from the cryocooler's vibration. In this research, a gravity-assisted CLHP was experimentally investigated. Nitrogen was selected as the working fluid. The CLHP was covered by insulation and tested in a vacuum chamber to reduce the heat leak to the ambient. The CLHP's temperature and gas reservoir's pressure were measured to investigate the operating characteristics. Tests were conducted to confirm the CLHP's operating behavior under the insufficiently charged working fluid condition with the charging pressure 2.5 MPa, under the moderately charged working fluid condition with the charging pressure 2.8 MPa, 3.0 MPa and 3.2 MPa, under the overcharged working fluid condition with the charging pressure 3.4 MPa. As a result, the CLHP can transfer 30 W heat at the most for more than 2 m heat transport distance at a charging pressure of 3.4 MPa. The hysteresis phenomena at the charging pressures 3.0 MPa, 3.2 MPa and 3.4 MPa were also studied.

Keywords: Cryogenic loop heat pipe; gravity-assisted attitude; nitrogen; charging pressure, hysteresis phenomena

1. Introduction

Loop heat pipe (LHP) is a robust capillary pumped two-phase heat transfer device [1]. The cryogenic loop heat pipe (CLHP) is proposed for cooling future cryogenic temperature applications such as passive optical bench, space-based infrared sensor and detector, small particle detectors, an optic, detector arrays, cryogenic propellant tanks and unmanned aerial vehicles [2-6]. CLHP's operating temperature ranges from 2 K-220 K, depending on the working fluids: ethane, propane, methane, krypton, nitrogen, argon, neon, hydrogen and helium [2,4-9]. Compared to the cooling method that directly connects heat sources to a cryocooler, CLHP is free of vibration as well as enables a flexible layout of heat sources and cryocoolers, resulting that the CLHP can transfer a large amount of heat over a long distance. Besides the zero-gravity application, the CLHP is also a potential heat transfer device under the gravitational environment on the earth, moon or other planets, such as cooling the superconducting electromagnet, the liquid hydrogen tank or the liquid nitrogen tank.

Currently, few research conducted to research the gravity-assisted CLHP. To the best of the author's knowledge, only one research discussed the gravity-assisted CLHP [4]. However, that research focused on confirming the CLHP's operating performance, without enough deep insights into the experimental

results.

This research aims to investigate the CLHP's operating characteristics under the gravitational environment. Therefore, a gravity-assisted CLHP was designed, fabricated and tested. Compared to the prevalent CLHP designed for the zero-gravity environment, the gravity-assisted used gravitational head to realize the preconditioning process without the secondary evaporator and compensation chamber (CC), resulting in more simple configurations and more predictable operating behaviors [10].

The design, fabrication methods and demonstration tests of the CLHP were presented in our previous conference papers [11-12]. In this paper, the influence of the charging pressure on the CLHP's operating characteristics was illustrated. Different from the previous research that confirmed the CLHP's optimal charging pressure through conducting the experiments under all the possible charging pressures [13-14], in this research, the charging pressure's influence was firstly studied based on the vapor-liquid distribution in the gravity-assisted CLHP's evaporator core and CC under each heat load condition. The CLHP's operating characteristics, such as the heat transport capability and the temperature hysteresis phenomena were elucidated under the insufficiently charged working fluid condition, moderately charged working fluid

condition and overcharged working fluid condition.

2. Operating principle of CLHP

Figure 1 shows a schematic of CLHP. The operating principle of CLHP is almost the same as LHP except for the startup process. A porous structure called a primary wick is installed in an evaporator. When the evaporator starts to absorb waste heat from a heat source, vapor generates at a primary wick's vapor-liquid interface. The generated vapor flows through a vapor line to a condenser where the condensation occurs, and the heat is rejected from the condenser to the cryocooler. The subcooled liquid flows back through the liquid line and the bayonet tube to the inner part of the evaporator (evaporator core) which is connected to the compensation chamber (CC). Capillary force drives the liquid from the evaporator core and CC to the vapor-liquid interface, replenishing the evaporation. Thus, with the circulation of a working fluid, waste heat is continuously transported from

the heat source to the remote cold cryocooler.

The CLHP is able to cool a heat source without consuming electric power. Since the working fluid in CLHP is in a supercritical state in the room temperature range, the main problem for the CLHP startup is that the working fluid is in an extremely high pressure supercritical state in the room temperature range. A gas reservoir is installed to reduce the pressure in the room temperature range and mitigate the design requirement of the CLHP components. In addition, the working fluid has to be subcritical before the startup. The condenser has to be cooled sufficiently to liquefy the working fluid. The CLHP startup will occur when the liquid flows into the evaporator and enough liquid exists in the evaporator core and CC followed by the evaporator heating. To assist the condensate flow into the evaporator, the CLHP requires a different configuration from LHP. In this research, the gravity-assisted CLHP was proposed and studied.

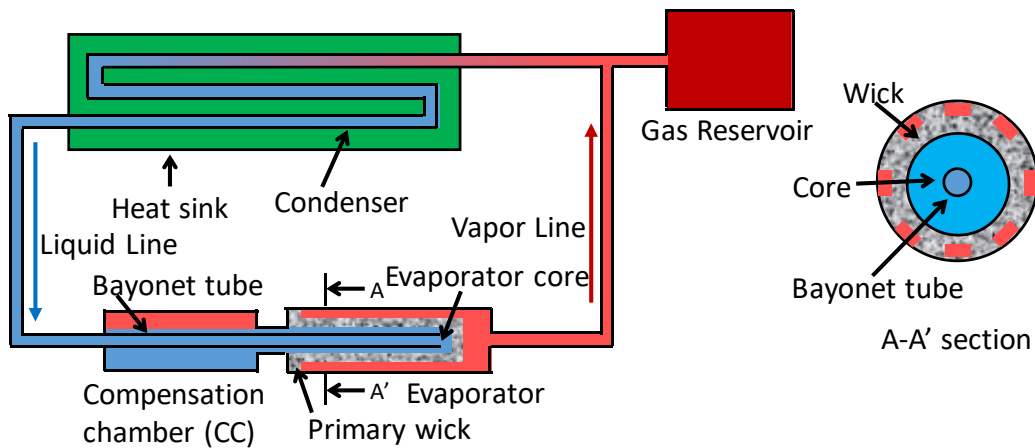


Figure 1. Schematic of cryogenic loop heat pipe

3. CLHP's configurations and test conditions

Table 1 shows the present configurations of CLHP. The heat transport distance was 2.05 m. The vapor line, liquid line, condenser was made of a 1/8-inch tube. The primary wick was made of stainless steel 316L with 1.56 μm porous radii. The volume of the gas reservoir was 300 ml. The working fluid was nitrogen.

Figure 2 presents the image of the gravity-assisted CLHP and the experimental system (not to scale). The condenser is located at a higher position than that of the evaporator and CC. A liquid nitrogen tank is employed to cool the working fluid in the condenser. In a pre-conditioning period before the evaporator heating, condensate in the condenser flows to the CC and the evaporator core by gravity. In this

experimental system, the gravitational head was 0.1 m. After the CC and the evaporator core are filled with the condensate, the startup of CLHP will succeed with the evaporator heating.

Table 1. CLHP's configurations (I.D.: inner diameter, L.: length, O.D. outer diameter)

Evaporator/CC		Primary wick	
I.D. [mm]	10	O.D. [mm]	10
L. [mm]	50/54	I.D. [mm]	4
Vapor/liquid line		L. [mm]	40
I.D. [mm]	1.75	r_p [μm]	1.56
L. [m]	2.05/2.05	Working fluid: Nitrogen	
Condenser		Charged pressure:	
I.D. [mm]	1.75	2.5, 2.8, 3.0, 3.2, 3.4 MPa	
L. [m]	1.66	Gas reservoir: 300 ml	

In the test, the gas reservoir was arranged in the atmospheric temperature (i.e. T_{amb}) about 298 K, while the other component of CLHP was arranged in the vacuum chamber. During the test period, a rotary pump was kept operating to evacuate the vacuum chamber, and the pressure of the vacuum chamber was about 5 Pa pressure. Both the vacuum chamber and the CLHP were wrapped with multi-layer insulations to reduce the heat leak from the environment. The average temperature of the

condenser was about 82 K. The temperature of the shroud (i.e. T_{shroud}) was about 288 K. The gas reservoir's pressure, the evaporator case's temperature (i.e. T_{evap}), the vapor line inlet's temperature (i.e. T_{vl}), the condenser inlet's temperature (i.e. T_{in}) and the condenser outlet's temperature (i.e. T_{out}) the CC's temperature (i.e. T_{cc}) and the liquid line's temperatures (i.e. T_{ll1} , T_{ll2} , T_{ll3}) were measured by local T-type thermocouples and pressure gauge shown in figure 2.

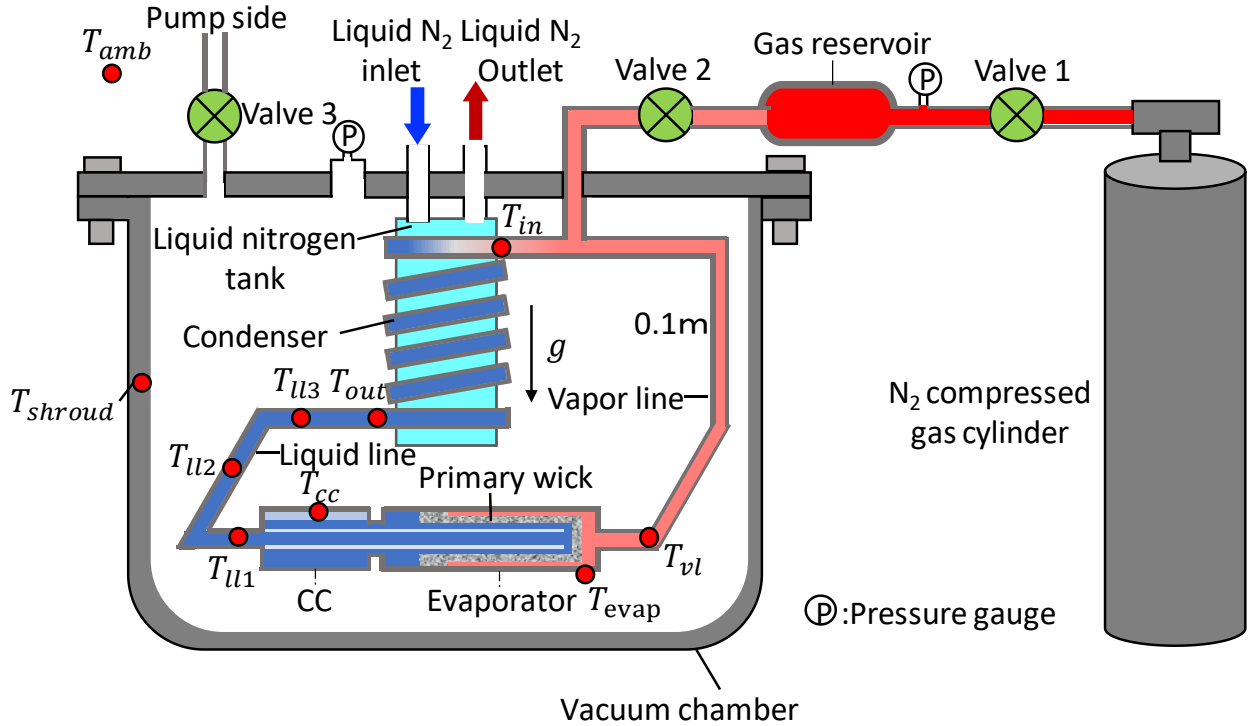


Figure 2. Gravity-assisted CLHP and the experimental system (not to scale)

The charging pressures were 2.5 MPa, 2.8 MPa, 3.0 MPa, 3.2 MPa, 3.4 MPa at a room pressure of 298 K. The variation process of charging pressures was conducted without waiting for the whole CLHP to recover to the room temperature of 298 K for saving the liquid nitrogen. The variation process of charging pressures was illustrated as follows: at first, opened valve 1 and valve 2, and charged the MLHP with 2.5 MPa pressure. Then closed valve 1. After the pre-conditioning process, heated the evaporator and conducted the heat load cycle test. When the test with 2.5 MPa charging pressure was finished, closed valve 2 and opened valve 1, increasing the gas reservoir's charging amount, which was equal to the charging amount increment from 2.5 MPa to 2.8 MPa. Then closed valve 1, opened valve 2 and continued to conduct the test with 2.8 MPa charging pressure. In this method, with the variation of the

charging amount in the gas reservoir, the variation of charging pressure can be realized.

The vapor-liquid distribution in CLHP is explained as follows: equation (1) is the equation for the charge amount m_h under high-temperature condition, while equation (2) is that for the charge amount m_l under low-temperature condition. Under high-temperature condition, the whole CLHP is assumed to operate at 110 K except the gas reservoir operates at a room temperature of 298 K. Under low-temperature condition, the whole CLHP is assumed to operate at 95 K except the gas reservoir operates at room temperature of 298 K. $\rho_{h,v}$, $\rho_{h,l}$, $\rho_{h,r}$ are the density of vapor, liquid and the gas reservoir under high-temperature condition, respectively, whereas $\rho_{l,v}$, $\rho_{l,l}$, $\rho_{l,r}$ are the density of vapor, liquid and gas reservoir under low-temperature condition, respectively. $V_{h,v}$, $V_{h,l}$ are the volume of the vapor

region in the whole loop except CC and the gas reservoir, and the volume of the liquid region in the whole loop except CC and the gas reservoir, under high-temperature condition, respectively, whereas $V_{l,v}$, $V_{l,l}$ are the volume of the vapor region in the whole loop except CC and the gas reservoir, and the volume of the liquid region in the whole loop except

$$m_h = \rho_{h,v}V_{h,v} + \rho_{h,l}V_{h,l} + \rho_{h,r}V_{res} + \rho_{h,v}\alpha V_{cc} + \rho_{h,l}(1 - \alpha)V_{cc} \quad (1)$$

$$m_l = \rho_{l,v}V_{l,v} + \rho_{l,l}V_{l,l} + \rho_{l,r}V_{res} + \rho_{l,v}\beta V_{cc} + \rho_{l,l}(1 - \beta)V_{cc} \quad (2)$$

Figure 3 presents the vapor fraction in CC and evaporator core under the high-temperature condition (i.e. α) and the vapor fraction in CC and evaporator core under the low-temperature condition (i.e. β) with the different charging pressures. When the vapor fraction in the CC and evaporator core was smaller than 0, the CC and evaporator core was flooded and the CLHP operated under the overcharged working fluid condition. When the vapor fraction in the CC and evaporator core was larger than 1, no liquid existed in the CC and evaporator core, and the CLHP operated under the insufficiently charged working fluid condition. When the working fluid was smaller than 1 and larger than 0, vapor and liquid existed in the CC and evaporator core, and the CLHP operated under the moderately charged working fluid condition. Therefore, according to figure 3, the CLHP operated under the overcharged working fluid condition when the charging pressure was 3.4 MPa, the moderately charged working fluid condition when the charging pressures were 2.8 MPa, 3.0 MPa and 3.2 MPa, the insufficiently charged working fluid condition when the charging pressure was 2.5 MPa.

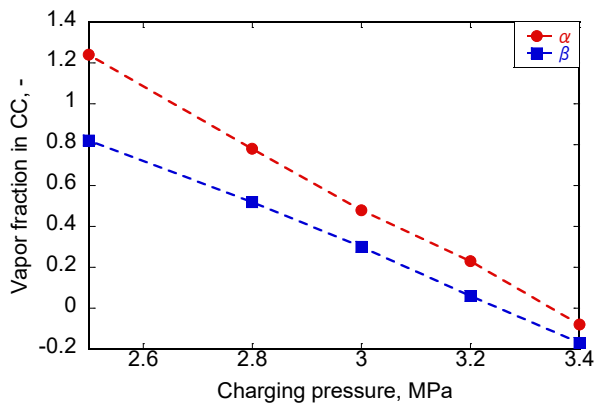


Figure 3. Vapor fraction (i.e. α) in CC and evaporator core under high-temperature condition (i.e. 110 K) and vapor fraction (i.e. β) in CC and evaporator core under low-temperature condition (i.e. 95 K).

CC and the gas reservoir, under low-temperature condition, respectively. V_{cc} is the volume of CC, and V_{res} is the volume of the gas reservoir. α is the vapor fraction in CC and evaporator core under the high-temperature condition, whereas β is the vapor fraction in CC and evaporator core under the low-temperature condition.

4. Test results

Figure 4 shows the CLHP's temperature and gas reservoir's pressure profile in the preconditioning process at the charging pressure of 3.4 MPa. The temperatures of the condenser outlet (i.e. T_{out}), condenser inlet (i.e. T_{in}), liquid line (i.e. T_{l1} , T_{l2} , T_{l3}), CC (i.e. T_{cc}), evaporator case (i.e. T_{evap}) and vapor line (i.e. T_{vl}) decreased in sequential order. The refilling of the liquid nitrogen tank was conducted when the temperature of the condenser inlet started to increase. Because of the small thermal resistance, the temperatures of the condenser inlet and outlet were close to the liquid nitrogen tank's temperature. Given the temperature difference among the CLHP and the heat input from the environment, the CLHP's startup was realized at the heat load of 0 W from the supercritical state. Therefore, operating characteristics at 0 W were also investigated in this paper.

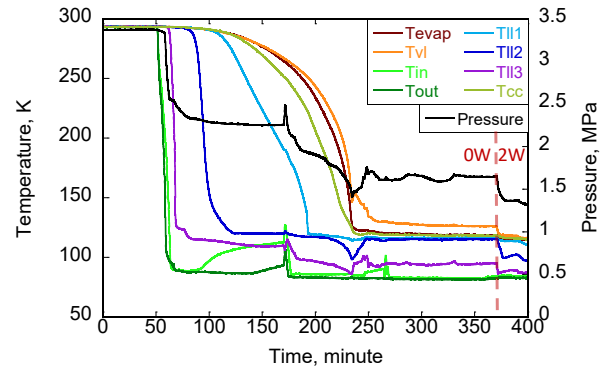


Figure 4. CLHP's temperature and gas reservoir pressure profile in the preconditioning process at the charging pressure of 3.4 MPa.

Figure 5 shows the evaporator case's temperatures (i.e. T_{evap}) under the heat load cycle experiment with the different charging pressures at 2.5 MPa, 2.8 MPa, 3.0 MPa, 3.2 MPa, 3.4 MPa and figure 6 presents the gas reservoir's pressures under the corresponding conditions. According to figure 5 and figure 6, the

temperature and pressure differences generated among all the charging pressures at 0 W due to the influence of charging pressure on the CLHP's saturated state. The CLHP under the insufficiently charged working fluid condition 2.5 MPa operated at the lowest evaporator case's temperature because the lowest gas reservoir's pressure can facilitate the decrease in the evaporating surface's temperature in the primary wick. As the result, the evaporator case's temperature decreased, increasing the heat input amount from the environment. The increasing heat input amount from the environment increased the amount of subcooled liquid returned to the evaporator core and CC, which promoted the temperature decrease at the evaporator case and evaporating surface. The temperature and pressure differences were also generated among all the charging pressures at 2W, indicating that the effect of heat input from the environment remained. That heat input effect will be mitigated if the vacuum chamber can operate at lower pressure.

When the heat loads were at 5 W, 6 W and 10 W, the temperature and the pressure differences among all the charging pressures became smaller, indicating that the heat input amount from the environment was much smaller than the heat loads and its effect can be neglected. At that time, all the evaporator cores and CCs operated in the saturated state, and the influence of charging pressure was small. The CLHP's heat transport capability was 6 W under insufficiently charged working fluid condition at 2.5 MPa charging pressure because the amount of the working fluid in the CC and evaporator core was insufficient to replenish the evaporation amount when the heat load was increased from 6 W to 10 W. At that time, the dryout occurred in the evaporator core, failing the operation.

When the heat loads were 15 W, 20 W, the temperature and pressure differences under the moderately charged working fluid condition at 2.8 MPa, 3.0 MPa and 3.2 MPa were small, indicating that the vapor-liquid saturated state existed in the evaporator core and CC. The pressure and temperature under the overcharged working fluid condition at 3.4 MPa were the highest among all the charging pressure conditions, indicating that the CC and evaporator core were flooded. At that time, the gas reservoir's pressure was influenced by the evaporating surface's temperature in the primary wick. With the increase in the heat load, the two-phase flow region in the condenser cannot be extended due to the flooded evaporator core and CC. On the contrary, the temperature of the evaporating surface increased to form a more subcooled region

for the excess working fluid, decreasing the two-phase flow region. Simultaneously, the gas reservoir's pressure increased, containing part of the excess working fluid. Thus both the temperature and the pressure were the highest under the overcharged working fluid condition 3.4 MPa at 15 W, 20 W. Considering the pressure gradient of the working fluid nitrogen and the 300 ml gas reservoir volume, only slight pressure variation on the gas reservoir side can re-distribute the working fluid under the flooded CC and evaporator core condition. As the result, in the flooded CC and evaporator core condition, with the increase in heat loads, the gas reservoir's pressure variation was small. The evaporator case's temperature increased due to the increase in the thermal resistance between the evaporator case and the evaporating surface.

When the heat loads were increased to 25 W, the temperature difference was generated and the pressure difference was small among the moderately charged working fluid condition at 2.8 MPa, 3.0 MPa, 3.2 MPa. At that time, a large heat leak amount from the evaporating surface to the evaporator core and CC was generated. Simultaneously, the liquid supply from the evaporator core and CC to evaporating surface decreased, resulting in the increase of the thermal resistance between the evaporator case and the evaporating surface. The CLHP with 2.8 MPa charging pressure operated at the largest heat leak amount due to the smallest liquid fraction in the evaporator core and CC. Thus the evaporator case's temperature at the charging pressure of 2.8 MPa was the highest at 25 W. Given that the overcharged CC and evaporator core increased evaporating surface's temperature and also decreased the thermal resistance between the evaporator case and the evaporating surface, the evaporator case's temperature under the overcharged working fluid condition 3.4 MPa was not the highest among all the charging pressures.

Figure 7 presents the temperature profile at the charging pressure 2.8 MPa, 3.0 MPa, 3.2 MPa and 3.4 MPa when the heat load increased from 25 W to 30 W. According to figure 7, under the moderately charged working fluid conditions, the evaporator case's temperature increased rapidly at 2.8 MPa and 3.0 MPa, indicating that the insufficient liquid supply from evaporator core and CC to the evaporating surface. The temperature increased slowly and the temperature excursion occurred about 13 minutes after the heat load was increased to 30 W due to the larger liquid fraction in the evaporator core and CC at 3.2 MPa than that at the 2.8 MPa and 3.0 MPa. Under the overcharged working fluid condition of

3.4 MPa, the sufficient liquid supply from the evaporator core and CC to the evaporating surface in the primary wick enabled the operation of CLHP at 30 W. Thus the heat transport capability at the overcharged working fluid condition of 3.4 MPa was the largest among all the charging pressure conditions.

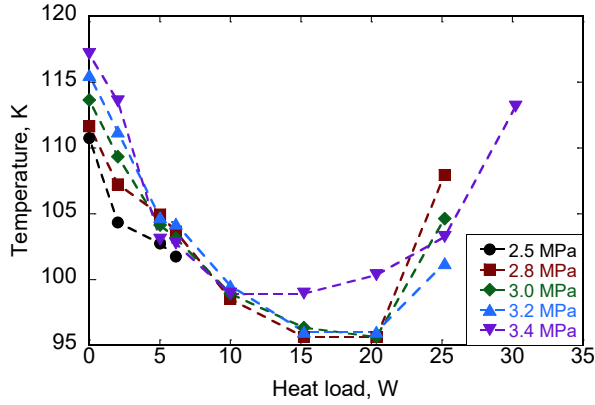


Figure 5. Evaporator case's temperatures (i.e. T_{evap}) under the heat load cycle experiment when the heat load profile was 2 W→5 W→6 W→10 W→15 W→20 W→25 W (→30 W) with the different charging pressures at 2.5 MPa, 2.8 MPa, 3.0 MPa, 3.2 MPa, 3.4 MPa.

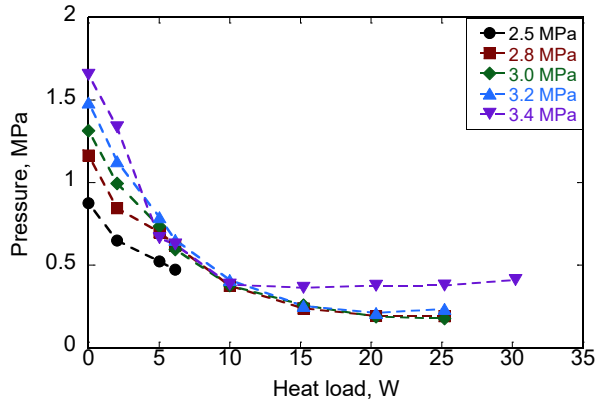


Figure 6. Gas reservoir's pressures under the heat load cycle experiment when the heat load profile was 2 W→5 W→6 W→10 W→15 W→20 W→25 W (→30 W) with the different charging pressures at 2.5 MPa, 2.8 MPa, 3.0 MPa, 3.2 MPa, 3.4 MPa.

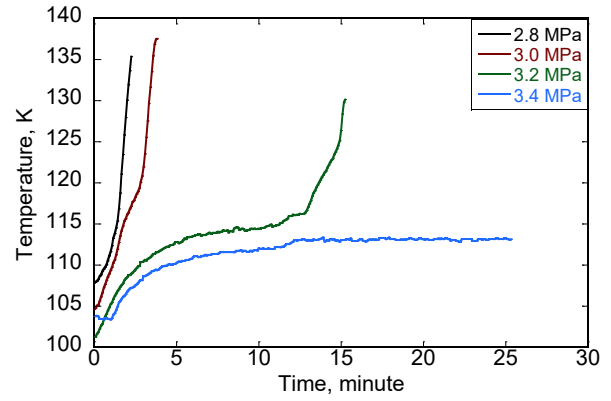


Figure 7. Evaporator case's temperature (i.e. T_{evap}) profiles at 30 W with different charging pressures at 2.8 MPa, 3.0 MPa, 3.2 MPa, 3.4 MPa.

Figure 8 presents the evaporator case's temperature under the heat load cycle experiment with the different charging pressures at 3.0 MPa, 3.2 MPa, 3.4 MPa. Figure 9 presents the corresponding gas reservoir pressures. The up cycle means the heat load increased from 2 W to 25 W (30 W), the down cycle means the heat load decreased from 25 W (30 W) to 2 W.

Under the moderately charged working fluid condition 3.0 MPa and 3.2 MPa at 20 W heat load, the pressure difference between the up cycle and the down cycle was small according to figure 8, indicating that the temperature difference at the evaporating surface between the up cycle and the down cycle was small. The temperature difference at the evaporator case between the up cycle and the down cycle was generated according to figure 8. When the heat load was increased from 20 W to 25 W, a large heat leak amount was generated from the evaporating surface to the evaporator core and CC, resulting in a small liquid supply from the evaporator core and CC to the evaporating surface in the primary wick and increasing the thermal resistance between the evaporating surface in the primary wick and evaporator case. When the heat load was decreased from 25 W to 20 W, the heat leak influence at 25 W remained, resulting in the unrecovered thermal resistance between the evaporating surface in the primary wick and evaporator case. Thus the thermal resistance between the evaporating surface and evaporator case was larger in the down cycle than that in the up cycle. The evaporator case's temperature in the down cycle was larger than that in the up cycle. The evaporator case's temperature difference between the up cycle and the down cycle at 3.2 MPa was smaller than that at 3.0 MPa because more liquid existed in the CC and evaporator core at 25 W, mitigating the heat leak effect and the

increased thermal resistance between the evaporating surface and evaporator case. The evaporator case's temperature difference between the up cycle and down cycle became small when the heat load was not larger than 15 W, indicating that the heat leak effect at 15 W can be neglected. At that time, the liquid supply from the evaporator core, CC to the evaporating surface and the thermal resistance between the evaporating surface and evaporator case were recovered.

Under the overcharged working fluid condition 3.4 MPa at 20 W and 25 W heat loads, according to figure 8, the evaporator case's temperature difference was larger than that at 3.0 MPa and 3.2 MPa due to the larger heat leak generated at 30 W, which exacerbated the increasing of thermal resistance between the evaporating surface and evaporator case. According to figure 8, different from the 3.0 MPa and 3.2 MPa, the gas reservoir's pressure in the down cycle was larger than that in the up cycle at 25 W, indicating the large evaporating temperature difference at 25 W between the up cycle and the down cycle. The large evaporating temperature difference at 25 W also resulted in the larger temperature difference of CC between the up cycle and down cycle at 25 W compared to that at 3.0 MPa and 3.2 MPa. The CC's temperature in the heat load range 10 W~25 W (30 W) at 3.0 MPa, 3.2 MPa, 3.4 MPa was shown in figures 10-12.

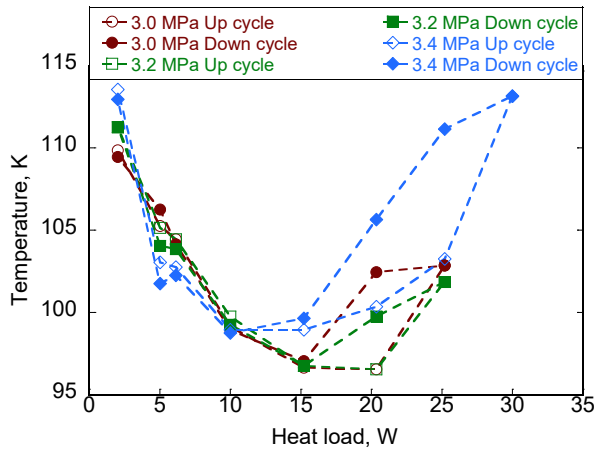


Figure 8. Evaporator case's temperature (i.e. T_{evap}) under the heat load cycle experiment with the different charging pressures at 3.0 MPa, 3.2 MPa, 3.4 MPa. The heat load profile of the "up cycle" was 2 W~25 W (30 W), whereas the heat load profile of the "down cycle" was 25 W (30 W) ~2 W.

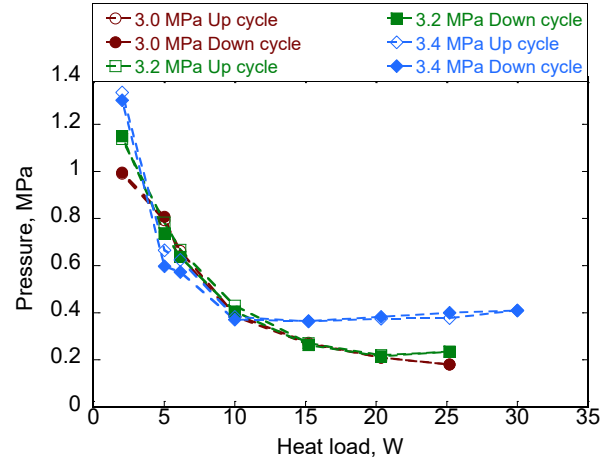


Figure 9. Gas reservoir pressure under the heat load cycle experiments with the different charging pressures at 3.0 MPa, 3.2 MPa, 3.4 MPa. The heat load profile of the "up cycle" was 2 W~25 W (30 W), whereas the heat load profile of the "down cycle" was 25 W (30 W) ~2 W.

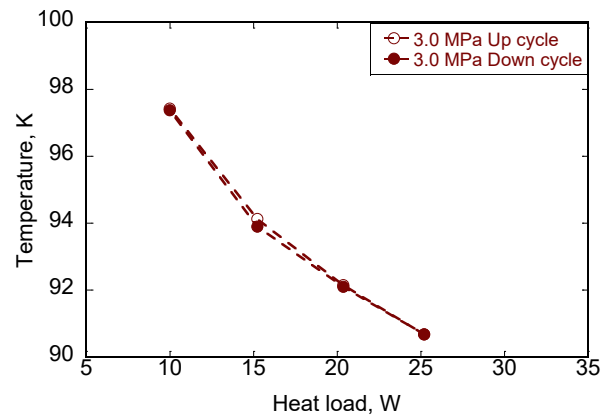


Figure 10. CC's temperature (i.e. T_{cc}) under the heat load cycle experiment at charging pressures 3.0 MPa in the heat load range 10~25 W.

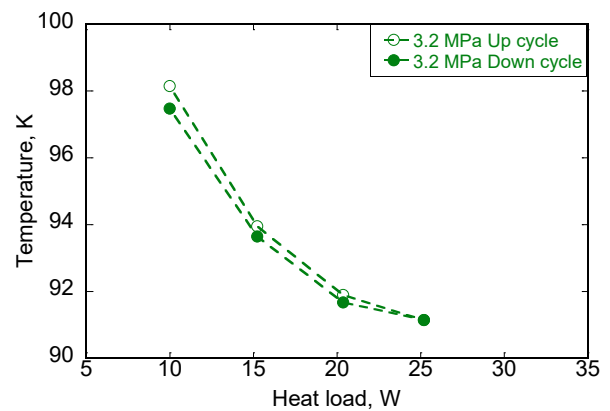


Figure 11. CC's temperature (i.e. T_{cc}) under the heat load cycle experiment at charging pressures 3.2 MPa in the heat load range 10~25 W.

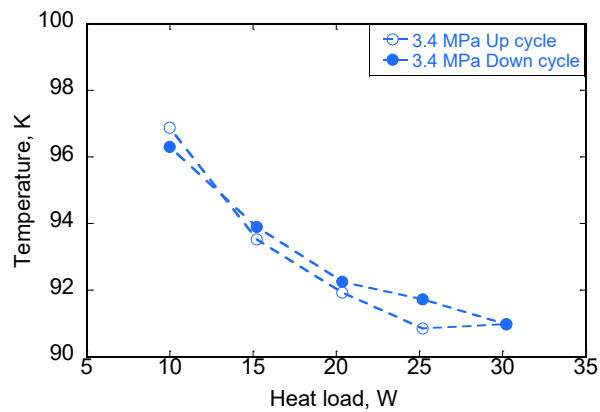


Figure 12. CC's temperature (i.e. T_{CC}) under the heat load cycle experiment at charging pressures 3.4 MPa in the heat load range 10~30 W.

5. Conclusion

In this research, the operating behavior of CLHP was investigated with different charging pressures through vacuum tests. Under the insufficient charged working fluid condition at 2.5 MPa, the evaporator case's temperature was the lowest at the same heat load, however, the heat transport capability was the smallest. Under the moderately charged working fluid condition at 2.8 MPa, 3.0 MPa and 3.2 MPa, the evaporator case's temperature was almost the same until the increasing heat leak at 25 W, where the receding of evaporating surface occurred. Under the overcharged working fluid condition at 3.4 MPa, the evaporator case's temperature was higher than other charging pressures when the evaporator was flooded. The heat transport capability of 30 W was the largest. In the temperature hysteresis tests, under the moderately charged working fluid condition at 3.0 MPa and 3.2 MPa, the evaporator case's temperature difference between the up cycle and down cycle generated due to the remained heat leak influence from 25 W and the unrecovered thermal resistance between the evaporating surface and the evaporator case in the down cycle at 20 W. According to the corresponding gas reservoir's pressures, the temperature difference of evaporating surface between the up cycle and the down cycle was small. Under the overcharged working fluid condition at 3.4 MPa, the evaporator case's temperature difference between the up cycle and the down cycle was larger than that at 3.0 MPa and 3.2 MPa and the gas reservoir's pressure difference generated at 25 W, indicating that the larger heat leak amount generated at 25 W in the down cycle. The large heat leak amount also increased the temperature of evaporating surface and CC. Those findings in the charging pressure effect will contribute to the future application of the gravity-assisted CLHP.

References

- [1] J. Ku, Operating Characteristics of Loop Heat Pipes. SAE Technical Paper, 1999. Series No. 1999-01-2007.
- [2] J. Yun, E. D. Krolczek, and L. Crawford, Development of a Cryogenic Loop Heat Pipe (CLHP) for Passive Optical Bench Cooling Applications. SAE Technical Paper, 2000. Series No.2002-01-2507.
- [3] T. T. Hoang, T. A. O'Connell, J. Ku, C. D. Butler, T. D. Swanson and D. K. Khrustalev, Design Optimization of a Hydrogen Advanced Loop Heat Pipe for Space-Based IR Sensor and Detector Cryocooling. in Optical Science and Technology, SPIE's 48th Annual Meeting. 2003. San Diego, USA.
- [4] H. Pereira, F. Haug, P. Silva, J. Wu and T. Koettig, Cryogenic Loop Heat Pipes for the Cooling of Small Particle Detectors at Cern. 2010. CERN-ATS-2010-017.
- [5] J. Ku and F. Robinson, Thermal Vacuum Testing of a Helium Loop Heat Pipe for Large Area Cryocooling. in 46th International Conference on Environmental System. 2016. Vienna, Austria.
- [6] D. R. Zakar, R. W. Baldauff and T. T. Hoang, Zero-Boil-Off Cryogen Storage Cryogenic Loop Heat Pipe for use in Unmanned Air Vehicles. 2017. AIAA Paper, No. 2017-4696.
- [7] Y. Guo, G. Lin, H. Zhang, and J. Miao, Investigation on thermal behaviours of a methane charged cryogenic loop heat pipe. Energy, 2018. 157: p. 516-525.
- [8] L. Bai, G. Lin, H. Zhang, J. Miao and D. Wen Experimental study of a nitrogen-charged cryogenic loop heat pipe. Cryogenics, 2012. 52: p. 557-563.
- [9] J. He, Y. Guo, H. Zhang, J. Miao, L. Wang, and G. Lin, Design and experimental investigation of a neon cryogenic loop heat pipe. in Joint 18th IHPC and 12th IHPS. 2016. Jeju, Korea.
- [10] L. Bai, L. Zhang, G. Lin, J. He and D. Wen, Development of cryogenic loop heat pipes: A review and comparative analysis. Applied Thermal Engineering, 2015. 89: p. 180-191.
- [11] X. Chang, T. Adachi, K. Odagiri, H. Ogawa and H. Nagai, Development of cryogenic loop heat pipe for deep space mission. in 50th International Conference on Environmental Systems. 2021. Online.
- [12] T. Yokouchi, X. Chang, K. Odagiri, H. Ogawa, H. Nagano and H. Nagai, Supercritical Startup Experiment of Cryogenic Loop Heat Pipe for Deep Space Mission. in 51st International Conference on Environmental Systems. 2022. Saint Paul, USA.
- [13] C. Du, L. Bai, G. Lin, H. Zhang, J. Miao, D. Wen, Determination of charged pressure of working fluid and its effect on the operation of a miniature CLHP. International Journal of Heat and Mass Transfer, 2013. 63: p. 454-462.
- [14] T. Yan, Y. Zhao, J. Liang, F. Liu, Investigation on optimal working fluid inventory of a cryogenic loop heat pipe. International Journal of Heat and Mass Transfer, 2013. 66: p. 334-337.

Study of Nonlinear Effects in a Pulsating Heat Pipe

Alok Kumar*, Suneet Singh

Indian Institute of Technology Bombay, Mumbai, 400076, India

Corresponding authors; email: 17i170013@iitb.ac.in

Abstract

Miniaturization being a prime characteristic of today's electronic industry requires a high amount of heat to be dissipated from small areas. This heat usually deteriorates the efficiency of the surrounding components resulting in the further degradation of the overall efficiency of the device. Among many cooling solutions to these modern-day problems, Pulsating Heat Pipe is one of the most promising solutions. Pulsating Heat Pipe is a multi-turn pipe device with heating at one end and cooling at the other. The temperature gradient between both ends creates a pressure difference in the pipe which leads to the startup of the oscillations in the flow field. Many advantages like simple design, and lightweight put them at the peak of utility. Further, their utility rises because of the independence of the orientation in many applications (both space and terrestrial). Despite their simple geometry, Pulsating Heat Pipes exhibit complex dynamical characteristics due to the multi-physics processes involved during the transient operation. Although an understanding of the complex operation has been developed using numerical modeling and experimental analysis, the mathematical interpretation of the interplay between the multi-physics processes and the nonlinearity remains unaddressed. Research attention is widely centered on the start-up process and design parameter optimization. However, to understand the functioning at the micro-level, it is necessary to analyze the system with nonlinear models. The analysis of the available nonlinear models is mostly limited to linearisation. Therefore, a state-of-the-art model consisting of the phenomena like two-phase flow, capillary actions, thermo-hydrodynamics, and phase change is employed. The model is a coupled system of ordinary differential equations that contain the conservation equations for the liquid slug and vapor plug separately. The time series analysis for the state variables provides an enriching insight into the start-up conditions and the impact on the initial position and the velocity of the liquid slug. Further, the effect of plug length on the position and velocity of the liquid plug has been studied. This parametric analysis provides dynamical characteristics of the PHP for a discrete set of parameters. Therefore, both codimension one and codimension two bifurcation analysis may provide a rich insight into the sudden variability in the position of slug, mass flow rate, and temperature profiles.

Keywords: Pulsating Heat Pipe; Nonlinear stability analysis; Parametric analysis; Thermal management;

1. Introduction

Pulsating Heat Pipe (PHP) is a meandering tube partially filled with a working fluid. Two ends of the tube are exposed to two different temperature fields consisting of the heat-dissipating (condenser at low temperature) section and heat-generating (evaporator at high temperature) section, respectively [1]. The PHP is evacuated before getting filled in a certain filling ratio called filling ratio and thus it plays an important role in the overall dynamics of the PHP [2-3]. The tube has a slug-plug-type flow structure due to its capillary size diameter. The vapor plugs start expanding as heat is applied to the wall. As this applied heat increases, the temperature difference also increases resulting in an increased pressure difference. As the applied heat crosses a certain threshold value, the liquid slugs start oscillating. This process of beginning the oscillations is called the start-up process [4]. Identifying the threshold value of the applied heat for the startup process and minimizing it to enhance the applicability of the system has been a major part of the research in the field of PHP.

The simple design and wickless structure are important attributes of the practical applications of PHP. Though most of the aspects involved in the system operation have been explored using theoretical and experimental studies, a generalized description of the operating dynamics could not be established. The reason behind this is the failure in the coupling of the results which has been established till now. Most of the studies are based on a particular aspect of the system, whereas to identify the real dynamics, it is needed to follow an integrated approach. Also, the linearization of the mathematical models limits their reliability for the application [5-6]. Therefore, there is a need of considering a nonlinear model which may provide realistic operating dynamical characteristics. A single branch pulsating pipe (SBPHP) is a conceptualized prototype of a PHP for modeling purposes. SBPHP is a tube open at the cooling end and closed at the heated end. Initially it was conceptualized to understand the PHP dynamics, but, now, it has its own applications. Therefore, most of the preliminary studies of the PHP

consist of the SBPHP models. In current work also the control volume is selected from a SBPHP.

2. Mathematical modeling

Basic modeling consists of conservation equations which are primarily nonlinear partial differential equations and two-phase flow correlations of pressure drop and other entities which further enhance the nonlinearity of the system. Therefore, analysis of the system with these models is a cumbersome task to perform. Therefore, it is imperative to have a simplified model comprising ODEs and correlations.

A control volume shown in Figure 1 has been taken for the mathematical modeling of the system. As shown in the schematic, different modes of heat transfer constitute the conservation equation for the liquid slug and the vapor plug. While writing the conservation equation, the nonlinearity has not been removed by linearization and thus, the final system is a second-order nonlinear system of ordinary differential equations. The nonlinearity has also been provided by the term corresponding to the interfacial heat transfer between the two phases. The contraction and expansion of the bubble play a major role in the pulsating phenomenon. Therefore, an explicit analysis of the volume change has been done in terms of the interfacial phase change.

2.1. Assumptions

The following assumptions have been incorporated into the mathematical modeling.

1. Liquid and gas properties have been taken as constant throughout the process.
2. Vapour has been considered an ideal gas.
3. The heat transfer coefficient for the liquid-to-vapor and wall-to-liquid heat transfer is constant.

2.2. Energy Conservation

The complex dynamical characteristics of a PHP occur due to the simultaneous cooling and heating of the two ends. The thermal interaction of the two phases makes the system more desirable to various types of instabilities. Several two-phase flow patterns are initially visible following a mix of many of these patterns which further complicate the characteristics to analyze. Therefore, chaotic flow and pulsating flow have been mainly analyzed. A quantitative analysis of each of these flow patterns is present in the literature in the context of other applications. The

transition from one to the other is also well-defined. But a configuration with simultaneous heating and cooling has not been analyzed in that detail except for some preliminary studies. [7].

Since the pulsating nature is desirable in the current system to harvest the maximum heat possible. The system should operate in the unstable regime of the parameter space, but it should not exceed the maximum values to occur mechanical vibrations. Therefore, it is required to optimize the parameter values to study the tradeoff between the pulsating phenomena and the mechanical vibrations in order to operate the system with maximum efficiency. A state-of-the-art model is considered to study this tradeoff and the operating characteristics have been obtained. The heat balance of the schematic shown in Figure 1 formulates the energy conservation equation for the system.

2.2.1 Critical Diameter

Diameter, being a key parameter to establish the capillary process, needs to be quantified thoroughly. Other design parameters also are decided based on the value of the diameter. Therefore, critical diameter analysis provides the appropriate design parameters to identify the initial conditions to operate from a steady-state condition. The mathematical modeling is based on [8] and the system has been solved without linearization or without neglecting the higher-order terms, which makes it very sensitive to the initial conditions and the parameter values.

The schematic (Figure 1) shows that a vapor bubble is squeezed by two liquid slugs and enclosed by a thin liquid boundary of thickness δ . The heat flux has been provided on the walls and is transferred from the wall to liquid slug and liquid film, and from liquid slug and liquid film to vapor bubble. The walls are extended to the evaporator and condenser region. Red arrows show the direction of heat transfer from wall to liquid film, liquid to vapor, etc. Wall temperature has been kept constant, T_w .

The capillary force should balance with the surface tension of the fluid to sustain the capillary process in a tube. The Bond Number is the ratio of the gravitational to the surface tension force.

$$B_o = \frac{g(\rho_l - \rho_v)D^2}{\sigma} \quad (1)$$

The maximum diameter to sustain the capillary process can be calculated by re-arranging Eq.1.

$$D = \sqrt{\frac{B_o \cdot \sigma}{g(\rho_l - \rho_v)}} \quad (2)$$

In terrestrial use of a PHP, the Bond number is in the range of (3.39 to 4) which correspond to the maximum diameter as the following (taking $B_o = 3.39$ for safe operation) [9].

$$D_{max} \approx 1.84 \sqrt{\frac{\sigma}{g(\rho_l - \rho_v)}} \quad (3)$$

Similarly, the minimum diameter needed to maintain the slug–bubble flow in the stable region ranges from 0.36 to 0.49. Thus (for $B_o = 0.49$)

$$D_{min} \approx 0.7 \sqrt{\frac{\sigma}{g(\rho_l - \rho_v)}} \quad (4)$$

2.2.2 Interfacial mass transfer

Electronic cooling applications require a very high heat flux to be handled without a significant change in the temperature. It is essential to study the liquid-vapor interface at the molecular level to identify the limits of the high heat flux for a given condition of evaporation and condensation. Maxwell's velocity distribution of kinetic theory of gases is used for a fraction of molecules. The molecular flux passing through a surface is calculated using the integral in the fractional volume. Similarly, a surface of the vapor phase, which is immediately adjacent to the liquid phase, has been taken and expression for the flux through it in the direction of motion has been established. The basic concept of derivation is based on the fact that due to a dynamic equilibrium, the flux hitting the vapor region should be balanced by escaping from liquid to vapor. The molecular flux of both phases is characterized by their corresponding temperature and their saturation pressures [10]. In the transient condition, the interfacial mass transfer can be calculated by finding the difference of both the mass fluxes [11].

$$r_m = \left(\frac{2\bar{\sigma}}{2 - \bar{\sigma}} \right) \left(\frac{1}{\sqrt{2\pi R}} \right) \left(\frac{p_v}{\sqrt{T_v}} - \frac{p_l}{\sqrt{T_l}} \right) \quad (5)$$

p_v and p_l the saturation pressure corresponding to the given temperatures of the vapor and liquid respectively. $\bar{\sigma}$ is the accommodation coefficient. Different values have been reported in the literature for the accommodation

coefficient. For a non-contaminated interfacial wet surface, it has been taken one. Other approaches to finding the interfacial mass transfer have also been attempted [8].

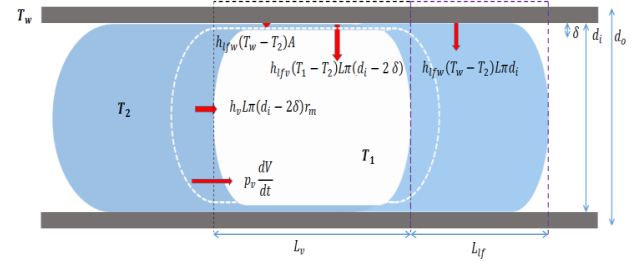


Figure 1. A control volume schematic for the modeling of the system consisting of a liquid slug squeezed between two consecutive vapor bubbles

The temperature variation of the vapor bubble constitutes three heat transfer mechanisms, (1) from the liquid film to the vapor bubble, (2) energy transfer due to mass transfer, and (3) work done by the vapor bubble to expand. Thus, the energy balance equation is presented in Eq. (1) and (2). The expansion of the liquid film is negligible in comparison to that of the vapor bubble. Therefore, it has not been presented in the heat balance equation. Figure 1 shows that the liquid film is involved in the (1) heat transfer from wall to liquid film, (2) from a liquid film to vapor bubble, and (3) mass transfer due to evaporation. Thus, the energy balance equation for the liquid film is given in Eq. 1 and Eq. 2.

$$m_v C_{vv} \frac{dT_1}{dt} = -h_{lfv}(T_1 - T_2)L\pi(d_i - 2\delta) - h_v L\pi(d_i - 2\delta)r_m - p_v \frac{dV}{dt} \quad (6)$$

$$m_f C_{vl} \frac{dT_2}{dt} = h_{lfw}(T_w - T_2)L\pi d_i + h_{lfv}(T_1 - T_2)L\pi(d_i - 2\delta) + h_v L\pi(d_i - 2\delta)r_m \quad (7)$$

2.3 Mass Conservation

The vapor flow rate depends on the interfacial mass transfer between both phases. During the process of condensation, the net flow is from vapor to liquid and is in opposite direction during evaporation. A mass balance for the vapor bubble is shown in Eq. 3.

$$\frac{dm_v}{dt} = -\pi(d - 2\delta)r_m, \quad \text{where, } m_v = \rho_v V \quad (8)$$

$$\frac{dm_v}{dt} = \rho_v \frac{dV}{dt} + V \frac{d\rho_v}{dt} \quad (9)$$

$$\text{or, } \rho_v \frac{dV}{dt} = -\pi(d_i - 2\delta)r_m - r_v\pi d_i L_v$$

2.4 Momentum Conservation

The vapor which is squeezed between two liquid slugs experiences different forces. The force acting on it has three components, (1) gravitational, (2) shear stress, and (3) pressure drop.

2.4.1 Gravitational force

The gravitational force on a plug is equivalent to its weight force. In varying or microgravity also the same expression is valid with different values of the gravitational constant.

$$F_g = m_p g \quad (10)$$

2.4.2 Wall shear stress

$$s_w = \frac{1}{2} C_f \rho_l v_p^2, \quad C_f = \left\{ \frac{16}{Re}, Re < 1180 \right. \quad (11)$$

Where, C_f is the friction factor, and has been correlated using the Moody diagram.

2.4.3 Pressure drop across the plug

The force exerted on the plug due to the pressure difference is simply the product of the surface area and the pressure drop.

$$F_p = \frac{\pi}{4} d_i^2 (P_{v1} - P_{v2}) \quad (12)$$

The momentum conservation equation is presented in Eq. 8.

$$m_p \frac{d^2 x_p}{dt^2} = \frac{\pi}{4} d_i^2 (P_{v1} - P_{v2}) - \pi d_i L_p s_w + m_p g \quad (8)$$

Where $(P_{v1} - P_{v2})$ is the pressure difference between the trail and the front of a vapor bubble. The mass of the liquid slug can be written as: $m_p = \frac{\pi}{4} (d_i - 2\delta)^2 (L_o - x_p) \rho_l$, where $L_o \approx 25 d_i$ and $\rho_l = 1000 \text{ kg m}^{-3}$.

3. Result and discussion

Eq. 1, Eq. 2, Eq. 3, and Eq. 8 collectively form the final system of equations. The momentum conservation equation, Eq. 8 is a second-order ODE and, thus, is converted into two first-order ODEs. The final system of the equation is a five-dimensional nonlinear model. It can be solved using various numerical methods. Parametric optimization using the firefly algorithm shows a range of the parametric value with some degree

of variation, which matches that of the analytical values obtained from the simulations [12]. A similar model has been employed with the dynamic liquid film thickness with the brute force simulation to identify the temporal characteristics [13].

The phase change coefficient expression provides a term for the temperature with negative power. Also, the momentum balance equation consists of a nonlinear term with negative power (m_p^{-1} , and x_p^{-1}). The numerical methods often fail at such negative nonlinearities because they work as singularities in the variable space. Asymptotic failure of a system leads to a limit in the analysis of actual dynamics. As value of x_p approaches close to L_o , acceleration of the slug tends to infinity, which can be regarded as a limitation of the model. Therefore, finding exact equilibrium is crucial for any solver at varying values of the parameters.

The above system of equations can be represented by

$$\frac{d\vec{X}(t)}{dt} = f(\vec{X}(t), \vec{r}) \quad (9)$$

Where $\vec{X}(t)$ and \vec{r} are the vectors of variables and the design parameters respectively, and can be represented as follows,

$$\vec{X}(t) = (T_1, T_2, m_v, x_p, x_p') \quad (10)$$

$$\vec{r} = (h_{lfv}, L, L_p, r_m, \delta, d_i)$$

3.1 Initial Conditions

The initial conditions are given as:

Initial temperature $T_1 = T_2 = 20^\circ C$, wall temperature $T_w = 40^\circ C$, vapor flow rate (using the ideal gas equation) $m_v = 3.95 \times 10^{-5} \text{ kg s}^{-1}$, the initial displacement of the liquid-slug

$x_p = 0.001 \text{ m}$ and initial velocity $v_p =$

0 ms^{-1} , $R = 8.31$, $C_{vv} = 1800 \frac{J}{kg} C$, $C_{vl} =$

$1900 \frac{J}{kg} C$, $L = 0.18 \text{ m}$, $d_i = 3.3 \times 10^{-3} \text{ m}$,

$\delta = 2.5 \times 10^{-5} \text{ m}$, $L_p = 0.01 \text{ m}$, $h_{lfw} = 1000 \text{ W/m}^2 C$, $h_v = 10 \text{ W/m}^2$.

3.2 Time series

The Jacobian matrix of the final system is obtained at the given equilibrium points. The entries of the Jacobian matrix are the function of the parameters and variables. Therefore, the eigenvalues are highly dependent on the initial conditions. The temporal evolution shown in

Figure 2 shows the influence of the purely complex conjugate eigenvalues. The pair of complex eigenvalues characterizes the oscillatory dynamics for several perturbations in liquid plug temperature. As can be seen from Figure 2 the liquid temperature is approaching the wall temperature asymptotically in a pulsating manner. This can be understood with the help of the corresponding position of the liquid slug. Therefore while oscillating in the flow regime; there is a vibrating factor in the temperature also.

On the other hand, the vapor temperature steadily approaches the wall temperature without any type of pulsation. It can also be explained using the position analog. When the liquid slug starts oscillating, the vapor bubble did not follow the same position, but it starts contracting and expanding accordingly. Therefore vapor temperature does not show any such phenomena. These sustained oscillations along with the contracting and expanding nature of the vapor bubble are desired in such heat transfer devices to achieve greater heat transfer capacity. For a set of parameter values, this oscillatory behavior may convert into chaotic nature also. The study of chaotic dynamics has been planned as future work. To identify the strength of the attractor (wall temperature), two perturbations of totally different sizes have been considered. The system response to these perturbations has been given below. Both the temperatures of the slug and that of the plug, converge to the wall temperature. Therefore, The wall temperature ($T_w = 40^\circ C$) is a stable attractor for the thermal profiles. The system is perturbed from the first IC ($T_1 = 293.15 K$, $T_2 = 293.15 K$) to the other ($T_1 = 373.15 K$, $T_2 = 293.15 K$). In the second IC, the vapor temperature is very high compared to that of the liquid. The heat transfer from the plug to the slug is very high initially from the vapor to liquid; therefore a spike in the slug temperature can be seen.

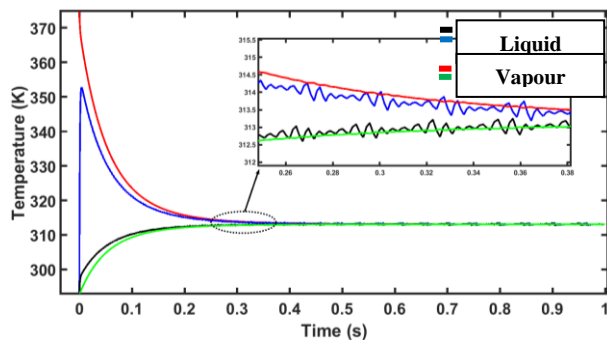


Figure 2. Temperature evolution with time at different initial conditions

The temporal evolution of the position and velocity to support the arguments discussed in the previous section is shown in Figure 3. It can be seen from the figure that initially the liquid slug moves fast in the axial length and once reached the adiabatic section, starts oscillating there. When the bunch of such slugs forming the bulk of the flow travels in the oscillatory motion, the process of heat transfer enhances by multiple folds. Similarly, the velocity associated with these liquid slugs is also higher at the initial stage and then fluctuated around zero for the oscillating position of the plug. The large amplitude jump in the velocity is due to the sudden exposure of the liquid slug to the heat at the evaporator section. Further over time, these oscillations progress with high frequency and low amplitude. Both the magnifying parts show the smooth progression of the liquid slug in oscillatory motion. The amplitude for both the position and velocity are gradually decaying.

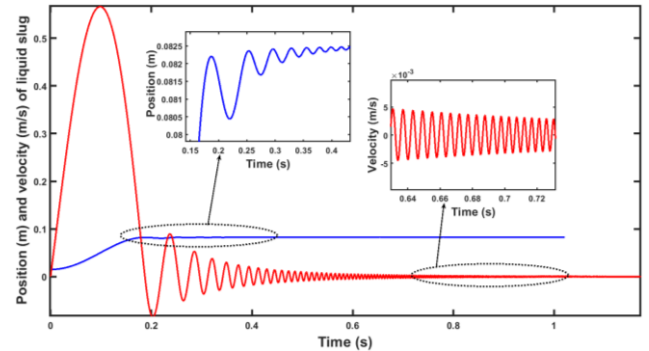


Figure 3. Position and velocity of the liquid slug

3.3 Plug Length

The slug length depends on the working fluid properties. The position and velocity characteristics are shown in Figure 4 and Figure 5, corresponding to the slug length of 0.01 mm (red), 0.02 mm (black), and 0.05 mm (blue) respectively. The longer liquid slugs occupy more volume of the tube and thus are less likely to move with faster velocity covering broader displacement. As observed by the analysis, with an increase in the length of the slug, the amplitude of the corresponding position and velocity oscillations decays. It is interesting to notice that in all three cases despite having different amplitude, phase and frequency, the oscillations are converging towards the same point, i.e., 0.0825 mm ($L_0 \approx 25 d_i$).

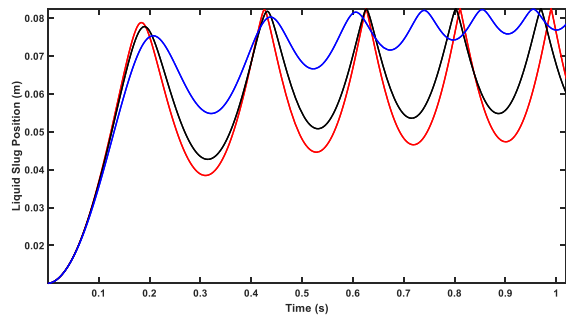


Figure 4: Position of the liquid slug for different slug lengths

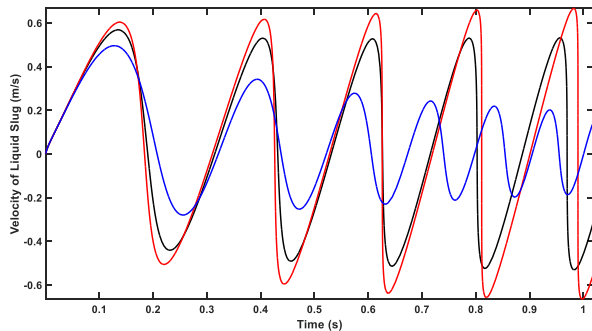


Figure 5: Velocity of the liquid slug for different slug lengths

The prompt growth shown in Figure 4 is due to the initial dominance of the largest eigenvalue among the combined contribution of all the eigenvalues. But in the longer period, the complex conjugate pair plays a significant role and converts the dynamics into an oscillatory one. Similarly in Figure 5, the continuous increment in the amplitude with the reduction in the plug length indicates its motion on the path back and forth to the center. Since the center is not fixed in the transient and the system is damped, the oscillations are not symmetric. The analysis has been done using the same frame of the center for each slug of different lengths.

It can be observed over time that the center is also varying for these different slug lengths.

Moreover, further explicit eigenvalue analysis may provide insight into the change in the dynamical behavior of the system. Also, phase portraits are of elliptic shape representing the oscillatory character.

4. Conclusion

The analysis of a state-of-the-art model gives a rich insight into the dynamics of a PHP. The consideration of the interfacial phase-change along with other multiphysics phenomena makes the model adaptive to realistic characteristics. The temporal evolution of the temperature of the

liquid slug and the vapor bubble shows that the temperature approaches the wall temperature. Similarly, the position and velocity show a sudden increase due to the initial exposure to heat flux. Also, the impact of the plug length has been studied and it has been concluded that a higher plug length limits the space in the control volume to move resulting in a decrease in the amplitude of the oscillations. Similarly, the velocity also decreases with an increase in the plug length. Further, the parametric analysis can be carried forward with a continuous variation of the parameter which is called codimension one bifurcation analysis. Also, a stability boundary depicting the stable and unstable region may provide a feasible region of operation.

Nomenclature

T	Temperature	[K]
h	Overall heat transfer coefficient	[W/m ² K]
\dot{r}_m	Interfacial mass transfer rate	[Kg/s]
p_v	Saturated pressure with respect to T_v	[bar]
p_l	Saturated pressure with respect to T_l	[bar]
$\bar{\sigma}$	Accommodation coefficient	
R	Gas constant	[JK ⁻¹ mol ⁻¹]
L	Mean length of the liquid slug	[m]
L_v	Length of vapor bubble	[m]
F_p	Force due to pressure drop	[N]
s_w	Wall shear stress	[bar]
V	The volume of the vapor bubble	[m ³]
d_i	The inner diameter of the tube	[m]
δ	Film thickness	[m]
ρ_v	Vapour density	[Kg m ⁻³]
ρ_l	Liquid density	[Kg m ⁻³]
m_p	Mass of liquid slug	[Kg]
m_v	Vapor flow rate	[Kg/s]
v_p	The velocity of the liquid slug	[m/s]
x_p	Displacement of the liquid slug	[m]
Re	Reynolds number	

References

- [1] L. L. Vasiliev, "Heat pipes in modern heat exchangers," *Appl. Therm. Eng.*, vol. 25, no. 1, pp. 1–19, 2005, doi: 10.1016/j.applthermaleng.2003.12.004.
- [2] H. Barua, M. Ali, M. Nuruzzaman, M. Q. Islam, and C. M. Feroz, "Effect of Filling Ratio on Heat Transfer Characteristics and Performance of a Closed Loop Pulsating Heat Pipe," *Procedia Eng.*, vol. 56, pp. 88–95, 2013, doi: 10.1016/j.proeng.2013.03.093.

- [3] M. L. Rahman, M. Chowdhury, N. A. Islam, S. M. Mufti, and M. Ali, "Effect of filling ratio and orientation on the thermal performance of closed loop pulsating heat pipe using ethanol," 2016, p. 050011, doi: 10.1063/1.4958402.
- [4] W. Qu and H. B. Ma, "Theoretical analysis of startup of a pulsating heat pipe," *Int. J. Heat Mass Transf.*, vol. 50, no. 11–12, pp. 2309–2316, 2007, doi: 10.1016/j.ijheatmasstransfer.2006.10.043.
- [5] A. Kumar and S. Singh, "Parametric Analysis of Pulsating Heat Pipes for Space Applications," in *Proceeding of the 26th National and 4th International ISHMT-ASTFE Heat and Mass Transfer Conference December 17-20, 2021, IIT Madras, Chennai-600036, Tamil Nadu, India, 2022*, pp. 1003–1007, doi: 10.1615/IHMTC-2021.1520.
- [6] Alok Kumar, Govind Maurya, Nadeem Ahmed, Suneet Singh, "Insights from a nonlinear and corresponding linear model of a Pulsating Heat Pipe," in *Proceedings of 9th International and 49th National Conference on Fluid Mechanics and Fluid Power (FMFP), IIT Roorkee, India, 2022*, pp. 963–967.
- [7] S. Khandekar and M. Groll, "On the Definition of Pulsating Heat Pipes: An overview," *Proc. 5th Minsk Int. Semin. (Heat Pipes, Heat Pumps Refrig.*, vol. 3, p. 12, 2003.
- [8] G. Swanepoel and R. T. Dobson, "Thermal Management of Hybrid Electrical Vehicles," no. November, 2001, [Online]. Available: <https://core.ac.uk/download/pdf/37375037.pdf>.
- [9] J. Gu, M. Kawaji, and R. Futamata, "Microgravity performance of micro pulsating heat pipes," *Microgravity Sci. Technol.*, vol. 16, no. 1, pp. 181–185, 2005, doi: 10.1007/bf02945972.
- [10] Y. Zhang and A. Faghri, "Advances and unsolved issues in pulsating heat pipes," *Heat Transf. Eng.*, vol. 29, no. 1, pp. 20–44, 2008, doi: 10.1080/01457630701677114.
- [11] V. P. Carey, *Liquid-Vapor Phase-Change Phenomena*, (3rd ed.). Boca Raton: CRC Press., 2020.
- [12] X. S. Yang, M. Karamanoglu, T. Luan, and S. Koziel, "Mathematical modelling and parameter optimization of pulsating heat pipes," *J. Comput. Sci.*, vol. 5, no. 2, pp. 119–125, 2014, doi: 10.1016/j.jocs.2013.12.003.
- [13] Y. Zhang and A. Faghri, "Heat transfer in a pulsating heat pipe with open end," *Int. J. Heat Mass Transf.*, vol. 45, no. 4, pp. 755–764, 2001, doi: 10.1016/S0017-9310(01)00203-4.

Simultaneous Measurement of Temperature Distribution and Flow Inside a Pulsating Heat Pipe Using Temperature Sensitive Paint with *in-situ* Calibration

Keiko Ishii^{1*}, Yuya Otaka¹, and Koji Fumoto¹

¹*Aoyama Gakuin University, Sagamihara, Japan*

**Corresponding author email address: ishii@me.aoyama.ac.jp*

Abstract

A Pulsating Heat Pipe (PHP) is attracting attention as one of the efficient heat transfer devices. However, a thermal fluid property inside the PHP is complicated and still unclear. In this study, temperature distribution and flow inside the PHP were visualized simultaneously by using Temperature-sensitive Paint (TSP) and dissolved fluorescence dye. The TSP was painted on a glass plate in stripe shape to cover a half of a channel. The TSP was excited by LED light and the intensity of luminescence was captured by a high-speed camera in heating and cooling area of the PHP. The inner wall temperature of the PHP changed corresponding to passages of liquid and vapor. The temperature decreased when liquid slag flowed into heating area. In addition, it increased when liquid slag flowed into cooling area directly from the heating area. These experimental results have possibility that determine boundary temperature corresponding to flow condition.

Keywords: Pulsating Heat Pipe; Temperature-sensitive Paint; Visualization; Temperature Distribution

1. Introduction

Pulsating Heat Pipes (PHP) are attracting attention because they are easier to miniaturize and have higher heat transport performance than conventional heat pipes. On the other hand, since the internal heat flow phenomenon is complicated, there are many unclear points about the operating principle.

Various computational models have been proposed for the internal flow of HP, but most of them are based on assumptions about the gas-liquid temperature, and there are no reliable experimental data. Charoensawan et al. reported that the heat transport performance varies greatly depending on the flow configuration, and understanding the relationship between the temperature distribution and internal flow of HP would contribute to clarifying the phenomenon [1]. Mangini et al. used an infrared-transmitting sapphire glass as a flow channel to simultaneously measure the temperature distribution of the internal liquid and the liquid film. However, it is difficult to focus only on the temperature of the inner liquid because the infrared radiation emitted by the heating/cooling equipment causes measurement noise [2].

Therefore, the authors have tried to measure the gas-liquid contact wall temperature inside PHP using a temperature-sensitive paint (TSP) that has temperature sensitivity and the emission intensity changes with temperature [3]. By bringing the TSP into contact with the inside of PHP and observing it through the visualization glass, the temperature distribution can be continuously measured without interfering with the internal flow. In addition, a

fluorescent dye was mixed with the working fluid to perform simultaneous measurement with the fluid flow. Francom et al. placed cameras in front of and behind an acrylic PHP to simultaneously measure the temperature distribution and visualize the flow using TSP [4]. The heat flux and flow were compared, and it was shown that latent heat transport was significant on the vapor plug with liquid film. However, whether latent or sensible heat is the dominant form of heat transport in PHP is still under debate, and phase change phenomena inside PHP are thought to occur on a thin liquid film. The measurement of the boundary temperature between the channel wall and the fluid using TSP is expected to provide important findings for further clarification of the phenomenon [5].

In this report, to improve the measurement accuracy, the temperature is calibrated for each pixel and a more detailed temperature field is discussed.

2. Methodology

Figure 1 shows the experimental setup. The equipment includes a PHP body, a glass plate coated with TSP, a PHP system consisting of a heat insulating holder, a bolt slider, a constant temperature bath, and a temperature control system consisting of water cooling blocks Blocks A to C, a thermocouple and a data logger. PHP processed a rectangular flow path with a width of 2 mm and a depth of 2 mm on a 15 mm thick aluminum alloy plate (A5052P) with an NC milling machine, and applied black alumite treatment to the surface. The shape of the flow path is a 24-channel loop type.

As shown in Figure. 2, TSP was applied in stripes so that only half of the flow path was in contact with TSP. The flow path is sealed with a glass plate so that the coating surface of the TSP is in contact with the flow path, and the temperature distribution is measured at the part where the TSP is applied by irradiating the flow path with excitation light from above the glass plate and observing it. The flow can be observed in the uncoated part.

Water at a constant temperature was passed through Blocks A to C using a constant temperature bath, the temperature of the entire PHP was controlled, and the emission intensity for each temperature was obtained. Since the temperature sensitivity of the phosphor differs slightly depending on the pixel position in the captured image, a temperature calibration function was obtained for each pixel. The spatial measurement accuracy was ± 0.922 °C in the heating section and 0.308 °C in the cooling section.

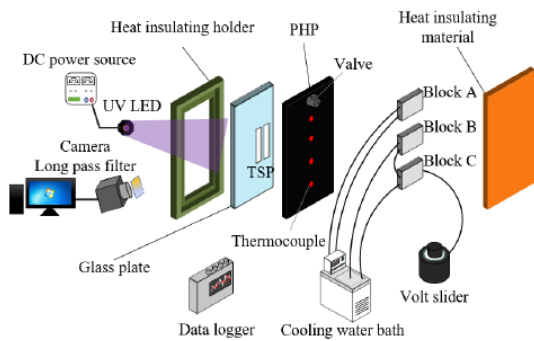


Figure 1. Experimental setup.

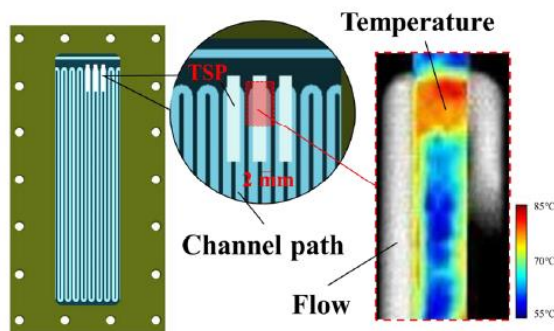


Figure 2. The geometry of TSP and channel .

3. Results and Discussions

Figure 3 shows the flow and temperature distribution focused on the moment when the liquid slag flows into the heating section. Figure 4 shows the time-series temperature changes at the measurement points shown in Figure 1. From Fig. 3, the temperature of the droplet adhesion part is relatively low from 2.800s to 2.825s. This is because the droplets evaporate. In addition to this, the temperature of the working fluid in the heating part

is lower than the wall surface temperature, so it is possible that the difference in the heat transfer coefficient of the gas and liquid has an effect. Focusing on 2.860s ~ 2.885s, the visualization results confirm that the liquid slag is flowing into the visualization region. The wall surface temperature decreased in response to the inflow of liquid slag. Since the temperature of the working fluid flowing from the cooling section was lower than the wall surface temperature in the heating section and the heat transfer coefficient of the liquid phase was higher than that of steam, heat was easily absorbed from the wall surface and the temperature was lowered.

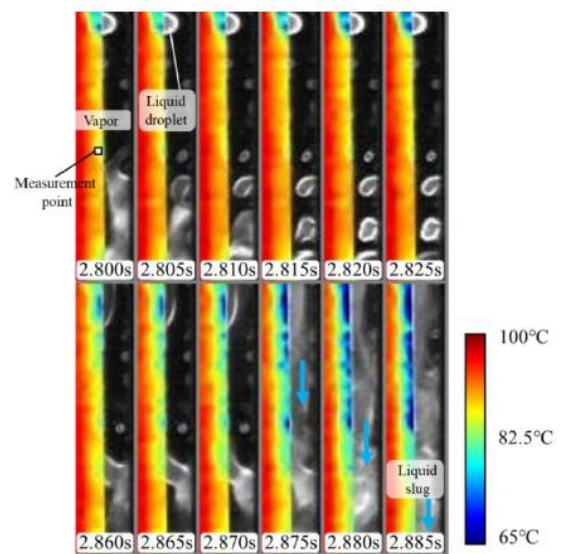


Figure 3. Fluid flow and temperature distribution when liquid slag flowed into heating area.

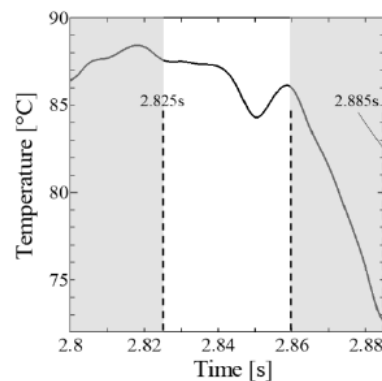


Figure 4. Time variation of temperature at the measurement point focusing on the moment

Figure 5 shows the flow and temperature distribution focusing on the moment when the liquid slag flows into the cooling section. Figure 6 shows the time-series temperature variation at measurement points 1 and 2 shown in Figure 5. Liquid slag begins to flow into the visualization area

at 0.505s, and the visualization area is filled with liquid slag at 0.540s. The temperature at measurement point 1 increased between 0.520s and 0.540s as the liquid slag passed through. This is due to the high temperature of the working fluid flowing directly from the heating section. Compared to vapor, the liquid phase has a higher heat transfer coefficient and transfers heat more easily to the wall surface, so the wall surface temperature increased when the liquid slag passed through the channel compared to when vapor passed through. Thereafter, the temperature slightly decreased, and the temperature change was small from 0.545s to 0.560s. This is because the inner wall of the channel was sufficiently warmed up to approach the temperature of the working fluid. On the other hand, the time-series temperature change at measurement point 2 shows that the temperature decreases after 0.530s, when the liquid slag passes through. This is because the liquid slag dissipates heat by the time it flows into measurement point 2. The liquid slag flowed from the left side channel across the turn to the measurement point 2, and since it stayed in the cooling section for a long time, it had already dissipated enough heat to reach a temperature lower than the temperature of the channel wall at the measurement point 2. The temperature of the channel wall at measurement point 2 increased with the progress of the liquid slag. The time when the temperature at measurement point 2 started to increase and the time when the change in the channel wall temperature at measurement point 1 started to decrease were almost the same. The temperature rose at measurement point 2 is considered to be caused by the fact that the liquid slag does not release enough heat from the wall of the cooling section by the time it flows into measurement point 2. The heat released by the fluid to the wall surface is small compared to that when the wall surface temperature is rising. It is conceivable that the temperature rose because the liquid slag, which did not release heat, flowed into Measurement Point 2. When the wall surface is sufficiently warmed up at measurement point 2, the change in the wall surface temperature in the channel becomes small after 0.555 s. The temperature of the wall surface at measurement point 2 is also small after 0.555 s.

Figure 7 shows the flow and temperature distribution focusing on the moment when vapor flows into the cooling section. Figure 8 shows the time-series temperature variation at the measurement points shown in Figure 7, where the steam inflow can be seen in the visible area after 3.015s. The temperature continued to increase after

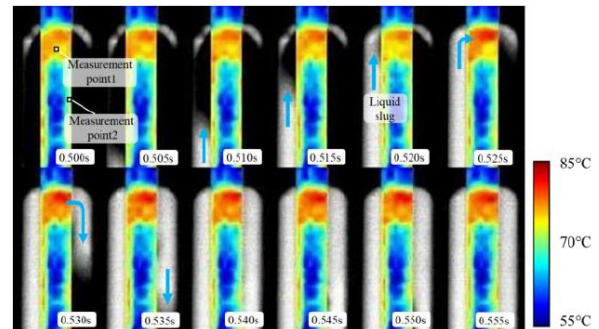


Figure 5. Fluid flow and temperature distribution when liquid slag flowed into cooling area

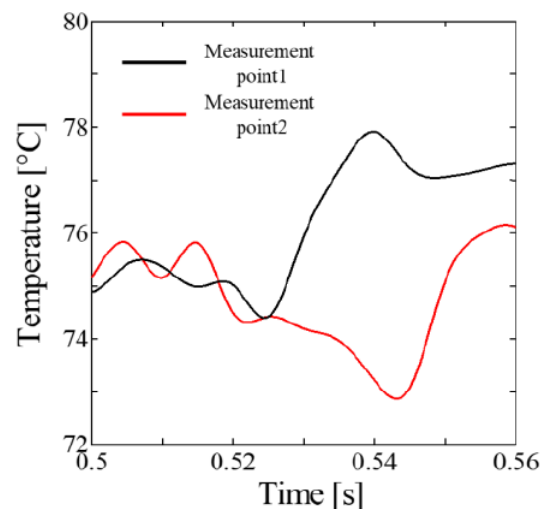


Figure 6. Time variation of temperature at the measurement point 1 and 2 focusing on the moment when the liquid slag flowed into the cooling area

the vapor inflow. This is because a liquid film covers the vapor area. If the liquid film does not cover the TSP surface, the temperature of the channel wall is expected to decrease. In the cooling section, the temperature of the fluid is higher than the temperature of the channel wall, so the temperature of the channel wall rises when the fluid flows in from the heating section. However, because the heat transfer coefficient of vapor is lower than that of the liquid phase, heat is not transferred to the wall when the same working fluid passes through the vapor, and the temperature of the channel wall decreases in the cooling section because the heat is released to the heat sink. On the other hand, if the vapor area is covered by a liquid film, the temperature drop is less likely to occur because the heat transfer is between the liquid phase and the channel wall. At 3.045s, visually confirms the formation of the liquid film. This liquid film covers the surface of the TSP, this is the reason why the temperature continues to rise. The temperature rise is also considered to occur when condensation

occurs in this vapor region. It is conceivable that condensation of vapor releases latent heat to the wall surface, which raises the temperature of the wall surface in the channel. However, it is difficult to visually evaluate the presence or absence of condensation, and a quantitative evaluation of the degree of influence of latent heat has not yet been completed.

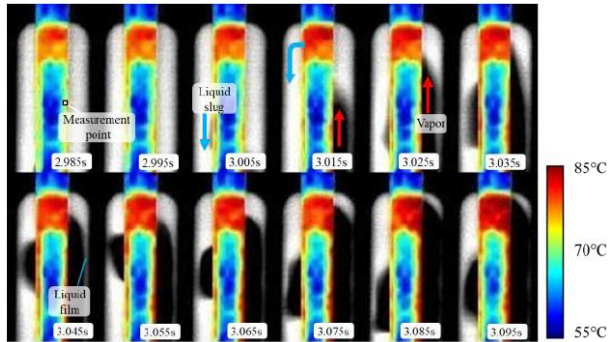


Figure 7. Fluid flow and temperature distribution when vapor flowed into the cooling area

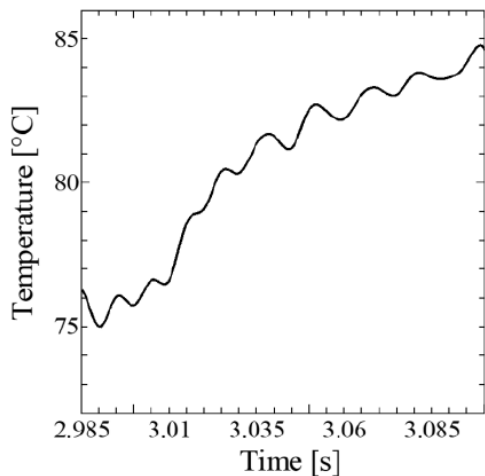


Figure 8. Time variation of temperature at the measurement point focusing on the moment when the vapor flowed into the cooling area

4. Conclusion

The TSP internal temperature was measured with higher accuracy using in-situ calibration. When the liquid slug flowed into the heated part, the temperature of the wall surface inside the flow path dropped. When liquid slug flowed into the heating section, the temperature of the channel wall surface decreased. When liquid slug flows directly from the heating section in the cooling section, the temperature of the channel wall rose. When the sufficiently cooled liquid slug passes through the cooling section, the temperature of the channel wall surface decreased.

References

- [1] Mangini, D., Marengo, M. and Araneo, L., Infrared analysis of the two phase flow in a single closed loop pulsating heat pipe, *Exp. Therm. and Flu. Sci.*, Vol.97, (2018), pp.304-312.
- [2] Charoensawan, P., Groll, M., Khandekar, S. and Terdtoon, P., Closed loop pulsating heat pipes Part B: visualization and semi-empirical modeling, *Appl. Therm. Eng.*, Vol.23,(2003), pp.2021-2033.
- [3] K. Ishii, K. Fumoto, Temperature Visualization and Investigation Inside Evaporator of Pulsating Heat Pipe Using Temperature-sensitive Paint, *Applied Thermal Engineering*, 2019, 155: p.575-583
- [4] Francom, M. and Kim, J., Experimental Investigation into the Heat Transfer Mechanism of Oscillating Heat Pipes Using Temperature Sensitive Paint, *J. Heat Transfer*, Vol.143, (2021), pp.1-11.
- [5] Jo, J., Kim, J. and Kim, S.J., Experimental investigations of heat transfer mechanisms of a pulsating heat pipe, *Energy Convers. Manag.*, Vol.181, (2019), pp.331-341.

Operating characteristics of a pressure-controlled loop heat pipe with a mechanically-driven gas pressure controller

Cheongyong Park¹, Bomi Nam², Wukchul Joung^{1, 2*}

¹ Department of Intelligent Robot Engineering, Pukyong National University, Busan, Republic of Korea

² Department of Mechanical Engineering, Pukyong National University, Busan, Republic of Korea

*Corresponding author email address: wukchuljoung@pknu.ac.kr

Abstract

In this work, a closed-type pneumatic temperature control of a pressure-controlled loop heat pipe (PCLHP) was realized with a mechanically-driven gas pressure controller (MDGPC) which consisted of a variable-volume bellows chamber and linear actuator. A linear actuator was employed to change the axial dimension of the variable-volume bellows chamber to control the internal gas pressure of the bellows chamber. The control characteristics of the MDGPC were tested in the context of stability and precision of the controlled gas pressure and ability to recover from external pressure disturbances. The pressure control stability and resolution of the MDGPC were approximately 1 Pa and 10 Pa, respectively, and a rapid and stable recovery from external pressure disturbances was achieved with a stability of approximately 1 Pa. The operating temperature of the PCLHP was actively controlled by changing the compensation chamber pressure with the MDGPC. Stability of the pneumatically-controlled temperature of the PCLHP with the MDGPC was approximately 0.01 °C. Temperature steps of approximately 0.8 °C were generated from pressure steps of ± 2.5 kPa, and the changed temperatures were accurately predicted by the thermodynamic relation (i.e., Clapeyron-Clausius approximation). Overall, pneumatic temperature control of the PCLHP was attained in a closed manner using the MDGPC.

Keywords: Pneumatic temperature control; Pressure-controlled loop heat pipe; Mechanically-driven pressure controller; Pressure stability; Temperature stability;

1. Introduction

Recently, a novel pneumatic temperature control method based on the unique thermohydraulic linkage of a pressure-controlled loop heat pipe (PCLHP) was suggested and proved successful active pneumatic control of the operating temperature of the PCLHP [1]. In this method, the saturated vapor temperature in the evaporator was actively controlled by changing the pressure of the compensation chamber with an external gas pressure controller (GPC). Stepwise temperature changes with a temperature stability of approximately 0.01 °C without overshooting or undershooting were realized, and the controlled temperatures were accurately matched by the thermodynamic predictions based on the Clapeyron-Clausius approximation [1, 2].

However, the pneumatic temperature control of the conventional PCLHP with a commercial GPC is inherently open in nature as the commercial GPC requires a pressure source and sink (e.g., a high-pressure control gas (helium) and vacuum pump, respectively), resulting in complicated operating procedures to prevent working fluid leakage to the GPC. In particular, when a toxic or highly reactive fluid (e.g., Hg or alkali metals) is used as the working fluid for operation at higher temperatures,

numerous safety measures should be made to prevent leakage of the working fluid into the atmosphere. Therefore, for simplicity and safety in the pneumatic temperature control method, it is of prime importance to operate the PCLHP in a closed manner, replacing the open-type commercial GPC with a closed-type GPC, yet retaining a similar control stability and speed to the commercial GPCs.

To resolve this problem, in this work, a closed-type pneumatic temperature control of the PCLHP was attempted using a mechanically-driven gas pressure controller (MDGPC). The MDGPC consisted of a variable-volume bellows chamber and linear actuator, and the gas pressure inside the bellows chamber was controlled by changing the axial dimension of the bellows chamber, thus attaining the gas pressure control in a closed manner. With the MDGPC, the pneumatic temperature control of the PCLHP was realized in a closed manner, and its temperature control characteristics were systematically examined in terms of the stability, precision, and rate of temperature change.

2. Test setup and method

The structure of the PCLHP employed in this work is provide in Figure 1. The evaporator of the PCLHP was constructed with a sintered stainless-

steel cylindrical wick, and the compensation chamber was designed to have approximately 50 % volume of the total PCLHP volume. A part of the vapor line was configured to have an annular vapor flow passage to generate a cylindrical isothermal working space (isothermal region), and the temperature of this isothermal region was actively controlled by controlling the pressure of the compensation chamber with the MDGPC.

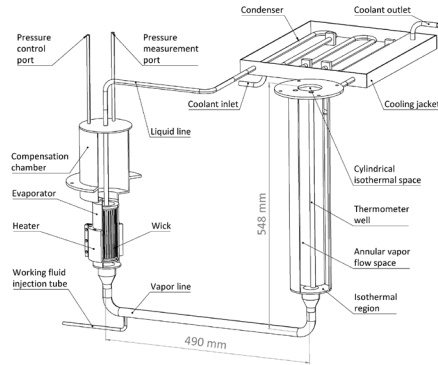


Figure 1. Schematic of the PCLHP.

As to the MDGPC, which comprised a variable-volume bellows chamber and linear actuator, Figure 2 shows the structure of the MDGPC and its operation during expansion and compression processes. The nominal diameter of the bellows chamber was 110 mm and its axial dimension ranged from 70 mm to 170 mm. The axial dimension of the bellows chamber was precisely controlled using a feedback-controlled linear actuator and its displacement resolution was 0.01 mm within a range of 250 mm.

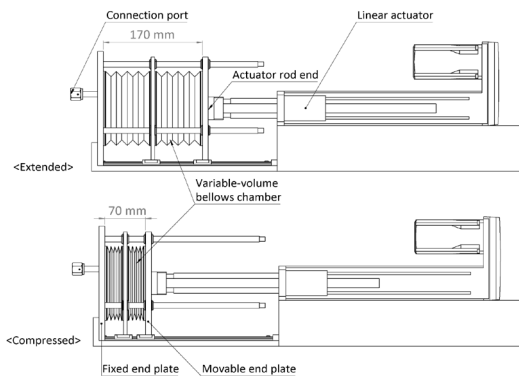


Figure 2. Structure and operation of the MDGPC during expansion and compression.

The rod end position of the linear actuator was controlled with a stepped proportional control method. The axial dimension change (Δl) of the

bellows chamber was controlled in three steps (i.e., 0.01 mm, 0.1 mm, and 1 mm) depending on the difference between the pressure set-point and measured values ($|\Delta p|$), and the current rod end position of the actuator (l_i) was determined by correcting the previous rod end position (l_{i-1}) with the determined axial dimension change (Δl). Equation (1) shows a mathematical expression for the rod end position of the actuator (l_i).

$$l_i = l_{i-1} + \Delta l \times \frac{\Delta p}{|\Delta p|},$$

$$\Delta l = \begin{cases} 1 \text{ mm} & (1 \text{ kPa} < |\Delta p|) \\ 0.1 \text{ mm} & (0.1 \text{ kPa} < |\Delta p| \leq 1 \text{ kPa}) \\ 0.01 \text{ mm} & (0.01 \text{ kPa} < |\Delta p| \leq 0.1 \text{ kPa}) \end{cases} \quad (1)$$

In this work, the MDGPC was connected to the compensation chamber of the PCLHP to realize closed-type pneumatic temperature control. Helium (He) was used as the control gas, and pneumatic temperature control was performed by pressurizing or depressurizing the control gas in the compensation chamber using the MDGPC. A cold trap maintained at approximately -5°C was located between the MDGPC and PCLHP to prevent vapor inflow into the MDGPC. A Ni-Cr heater was employed to supply a fixed heat load of 800 W to the evaporator with a feedback-controlled DC power supply. As to the coolant supply to the cooling jacket of the condenser, water at approximately 55°C was circulated at approximately 5 L/min. Figure 3 shows a schematic of the test setup.

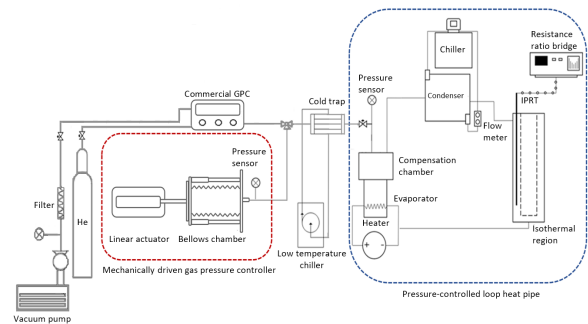


Figure 3. Schematic of the test setup.

3. Result and discussion

3.1. Gas pressure control characteristics of the MDGPC

Figure 4 shows the change in the control gas pressure in terms of the difference between the

pressure readings and 12 h mean value before and after pressure control with the MDGPC. Before the pressure control, the axial dimension of the bellows chamber was fixed to be 120 mm (i.e., fixed-volume mode), and when MDGPC operation was started, the volume of the bellows chamber became variable (i.e., variable volume mode). During the test, the room temperature changed by ± 5 °C. As shown in the figure, the gas pressure during the fixed-volume mode varied significantly due to the room temperature change, whereas under the pressure control with the MDGPC (i.e., in the variable-volume mode), the gas pressure in the variable-volume bellows chamber remained nearly unchanged within a much narrower range. The pressure stability, which was defined as the standard deviation of the pressure readings for each mode (i.e., for each 12 h), the pressure stability was apparently reduced from approximately 130 Pa to approximately 1 Pa due to active pressure control by the MDGPC, thus demonstrating the effectiveness of gas pressure control with the MDGPC.

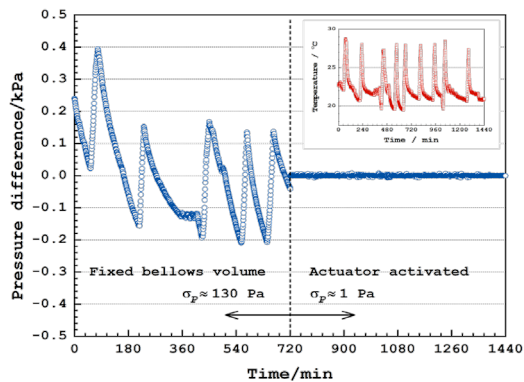


Figure 4. Change in the control gas pressure in the variable-volume bellows chamber before and after the gas pressure control with the MDGPC. The inset shows the variation in the room temperature.

Figure 5 shows the pressure recovery characteristics of the MDGPC when the variable-volume bellows chamber, which was originally maintained at 80 kPa, was exposed to sudden external pressure disturbances of 5 kPa and -5 kPa for 10 s. As shown in the figure, the gas pressure in the bellows chamber was temporarily affected due to the imposed pressure disturbances, but within 30 s, the MDGPC recovered the gas pressure to the original set-point value and attained a stability of approximately 1 Pa without overshooting or undershooting. Thus, the recoverability of the MDGPC from external pressure disturbances was proved satisfactory.

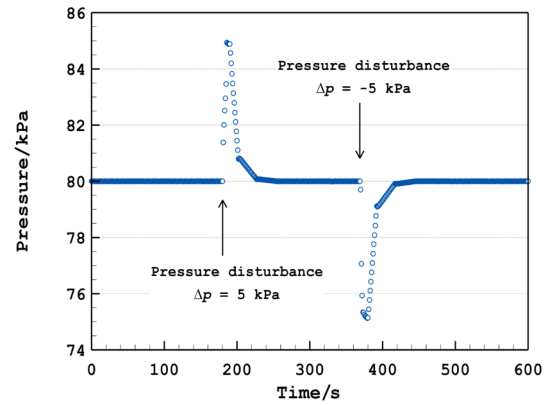


Figure 5. Response of the MDGPC to external pressure disturbances.

The MDGPC was then tested in terms of its ability to generate rapid pressure changes without overshooting or undershooting. Figure 6 shows the response of the control gas pressure (p_{measured}) to step changes in the set-point pressure ($p_{\text{set value}}$) and the corresponding rod end position of the actuator ($l_{\text{rod end}}$). The set-point pressure was changed by ± 5 kPa in a tested pressure range from 70 kPa to 90 kPa. As shown in the figure, the gas pressure in the bellows chamber showed stepwise pressure increases or decreases, accurately following the change in the set-point pressure without any overshooting or undershooting; the pressure stability at each pressure step was approximately 1 Pa. Therefore, it was concluded that the MDGPC satisfactorily realized closed-type pressure control in terms of the stability, precision, and speed of pressure control, which could be used as a gas pressure controller of the PCLHP.

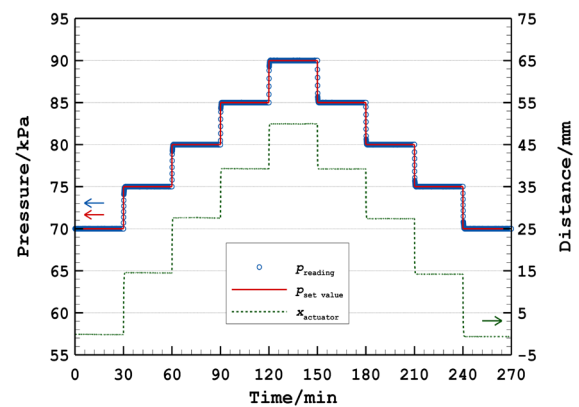


Figure 6. Stepwise pressure changes of the MDGPC with modified proportional control.

3.2. Temperature control characteristics of the PCLHP with the MDGPC

Figure 7 shows the change in the temperature variation in the isothermal region when pneumatic temperature control with the MDGPC was started in terms of the temperature difference between the temperature readings and 12 h mean value. As shown in the figure, when the MDGPC controlled the control gas pressure in the compensation chamber, the stability of the isothermal region temperature was notably improved due to precise pressure control of the compensation chamber with the MDGPC. The temperature stability, which is defined as the standard deviation of the measured temperature readings over 12 h, was enhanced from approximately 0.23 °C to approximately 0.01 °C, indicating that the closed-type pneumatic temperature control of the PCLHP was successfully attained with the MDGPC.

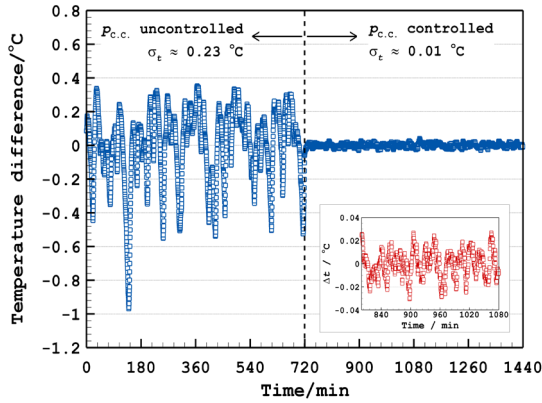


Figure 7. Change in the stability of the pneumatically-controlled temperature of the isothermal region. The inset shows the magnified view of the variation in the isothermal region temperature during the pneumatic temperature control with the MDGPC.

Completing the evaluation of the temperature stability, the response of the isothermal region temperature to stepwise increases and decreases in the control gas pressure, generated by the MDGPC, was examined to determine whether rapid and stable temperature control characteristics of pneumatic temperature control could be realized with the MDGPC. Figure 8 shows the response of the isothermal region temperature to stepwise changes in the control gas pressure in the MDGPC. The control gas pressure was increased from 80 kPa to 90 kPa and then decreased to 80 kPa with ± 2.5 kPa pressure steps. As shown in the figure, the isothermal region temperature (black square

symbol) stably followed the stepwise pressure changes (blue dotted line) without any instabilities (i.e., overshooting or undershooting); temperature steps of approximately 0.8 °C were generated from the stepwise pressure changes of ± 2.5 kPa; at each temperature step, a temperature stability of approximately 0.01 °C was attained. In addition, the pneumatically-controlled temperature was accurately matched by the thermodynamic predictions (red solid line) based on the Clapeyron-Clausius approximation (Equation (2)), demonstrating that the thermodynamic characteristics of the pneumatic temperature control method were retained with the use of the MDGPC.

$$T_{\text{sat, evap } 2} = \frac{T_{\text{sat, evap } 1}}{1 - T_{\text{sat, evap } 1} \frac{R_s}{h_{fg}} \left(1 + \frac{\Delta p_{\text{control gas}}}{p_{\text{sat, evap } 1}} \right)} \quad (2)$$

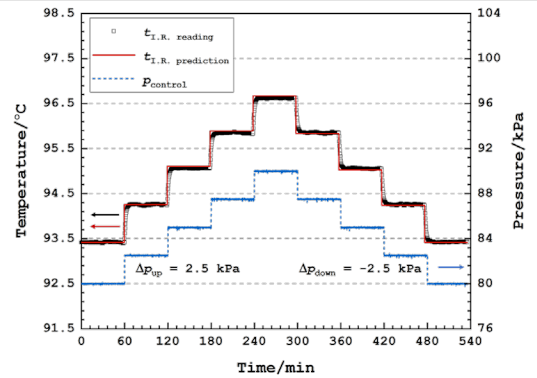


Figure 8. Response of the pneumatically-controlled temperature to the stepwise pressure changes.

4. Conclusion

In this work, a closed-type pneumatic temperature control of a pressure-controlled loop heat pipe (PCLHP) was realized with a mechanically-driven gas pressure controller (MDGPC). The MDGPC comprised a variable-volume bellows chamber and linear actuator, and the gas pressure inside the bellow chamber was controlled by changing the axial dimension of the bellow chamber using the linear actuator. The PCLHP was operated with the MDGPC to realize pneumatic temperature control in a closed manner. The following conclusions were obtained in this study:

1. The MDGPC controlled the pressure of the control gas in the variable-volume bellows chamber

by varying the axial dimension of the bellows chamber. The attained pressure control stability was approximately 1 Pa under severe room temperature changes of approximately ± 5 °C. The MDGPC showed rapid and stable recovery characteristics from sudden external pressure disturbances of ± 5 kPa. In addition, stepwise pressure changes of ± 5 kPa were successfully achieved with the MDGPC, and the controlled pressure accurately followed the set-point pressure changes with a pressure stability of approximately 1 Pa.

2. The isothermal region temperature of the PCLHP was pneumatically controlled by adjusting the control gas pressure in the compensation chamber with the MDGPC. Pneumatic temperature control was realized in a closed manner, and the stability of the controlled temperature was approximately 0.01 °C. Temperature steps of approximately 0.8 °C were stably generated under pressure steps of ± 2.5 kPa, and the temperature stability at each step was approximately 0.01 °C. The controlled temperatures were accurately predicted with a thermodynamic relationship, thus retaining the distinctive features of the pneumatic temperature control method. Overall, closed-type pneumatic temperature control of the PCLHP was successfully accomplished with the comparatively simple and low-cost pressure control with the MDGPC.

References

- [1] W. Joung, K. S. Gam, Y. Kim, I. Yang, Hydraulic operating temperature control of a loop heat pipe, *International Journal of Heat and Mass Transfer*, 2015. 86: p. 796-808.
- [2] C. Park, W. Joung, Effect of heat load on pneumatic temperature control characteristics of a pressure-controlled loop heat pipe, *International Journal of Heat and Mass Transfer*, 2022. 186: 122472.

Acknowledgements

This research was supported by the Basic Science Research Program of the National Research Foundation of Korea (NRF) funded by the Ministry of Education (NRF-2020R111A3072736).

Thermographic investigation of heat spreading characteristics of a vapor chamber-type heat spreader

Jaehyuk Jeong¹, Wukchul Joung^{1, 2*}

¹Department of Intelligent Robot Engineering, Pukyong Natl'Univ, Busan, Republic of Korea

²Department of Mechanical Engineering, Pukyong Natl'Univ, Busan, Republic of Korea

*Corresponding author email address: wukchuljoung@pknu.ac.kr

Abstract

Recent advances in modern electric systems have led to a strong motivation toward extensive use of the highly conductive heat spreaders such as vapor chambers to effectively reduce the heat flux of the heat generating devices to an acceptable level. For practical application of these heat spreaders, quantification of the heat spreading characteristics is of prime importance, and the effective thermal conductivity based on the temperature distribution on the heat spreader has been widely used to characterize the temperature homogeneity of the heat spreaders. In this work, a noncontact thermographic method was employed to characterize the temperature distribution and corresponding distribution of the effective thermal conductivity of the vapor chamber-type heat spreader. A copper vapor chamber-type heat spreader with dimensions of 102 mm × 102 mm × 3 mm (length × width × thickness) was fabricated with a 1 mm thick patterned porous wick for realization of inward liquid replenishment and outward vapor flow. Water was used as the working fluid, and the vapor chamber was charged at various working fluid charge ratios. The effect of change in the operational parameters such as the heat flux, inclination, and working fluid charge ratio was systematically investigated.

Keywords: Vapor chamber, Heat spreader, Thermographic thermometry, Temperature distribution, Effective thermal conductivity

1. Introduction

Recent advances in modern electric systems have led to miniaturization of high-power electronic devices such as RF power amplifiers and IGBTs. However, due to their small physical size, these devices possessed unacceptably high level of heat flux amounting up to a few hundred watts per square centimeters. Operation of these high heat flux devices with conventional diffusion-based heat sink results in local hot spots due to finite thermal conductivity of traditional heat conducting materials (e.g., aluminum or copper), thus causing malfunctions or premature failures of these devices. In this circumstance, highly conductive heat spreaders such as vapor chambers have extensively been employed to effectively reduce the heat flux of the concentrated heat source by spreading heat very fast over an extended surface area.

Vapor chambers passively spread heat based on (radially) outward vapor flow and inward liquid replenishment due to saturation pressure difference across the heat spreader and capillary pressure difference generated by the porous wick [1-3]. For practical application of the vapor chambers as highly conductive heat spreaders, quantification of their heat spreading characteristics is of prime importance, and the effective thermal conductivity based on the temperature difference over the heat spreading surface of the heat spreader has been widely used to characterize the temperature

homogeneity of the heat spreaders, which facilitates a direct comparison with traditionally used heat spreading materials. However, due to the thin yet wide nature of the vapor chamber-type heat spreaders, measurement of the temperature distribution over the heat spreading surface with contact thermometers, which do not affect operation of the vapor chamber, is becoming increasingly challenging, thus necessitating a thermometry technique measuring temperature distribution in a noncontact manner.

In this circumstance, a thermographic camera, which measures a two-dimensional thermal image of a target surface, has been widely used to characterize the temperature homogeneity of the heat spreader, replacing the traditional contact thermometers. As large uncertainty in a measured temperature value, which is the major drawback of the noncontact thermometry method, can be significantly reduced when measuring temperature difference with a single thermographic camera due to the correlation in the systematic uncertainties, it is possible to measure temperature differences over various heat spreading distances to a high precision amounting down to a few tens of millikelvins [6]. For these reasons, noncontact thermographic method was considered suitable for measurement of the temperature differences over the heat spreading surface of the heat spreader [3-5].

In this work, a noncontact thermographic method

was employed to characterize the temperature distribution and corresponding distribution of the effective thermal conductivity of the vapor chamber-type heat spreader. A copper vapor chamber having dimensions of 102 mm × 102 mm × 3 mm (length × width × thickness) was fabricated, and water was used as a working fluid. The effect of change in the operational parameters such as the heat flux, inclination and working fluid charge volume was systematically investigated.

2. Test setup and method

Figure 1 shows the structure and dimensions of the tested vapor chamber-type heat spreader. A copper vapor chamber, having external dimensions of 102 mm × 102 mm × 3 mm (length × width × thickness), was fabricated with a 1 mm thick patterned porous wick for realization of inward liquid replenishment through the porous channels and outward vapor flow through empty space between the porous channels. Distilled water was used as the working fluid, and the vapor chamber was charged at various working fluid charge volumes. For one-dimensional (radial) heat spreading, a copper block accommodating a cartridge heater having thermo-contact area 1 cm² was attached to the center of the bottom surface of the heat spreader. A copper coolant channel, through which water at 20 °C flowed at approximately 1.5 l/min, was attached to the outer edge of the heat spreader, providing a condensing area for the vapor phase working fluid.

Based on the one-dimensional conduction equation in the cylindrical coordinate, the measurement model for the effective thermal conductivity (k_{eff}) of the heat spreader was constructed as shown in Equation (1) [7]. Figure 2 shows the radial locations (r_o and r_i) for measurement of the temperature difference (Δt_{HS}). The spread heat through the heat spreader was

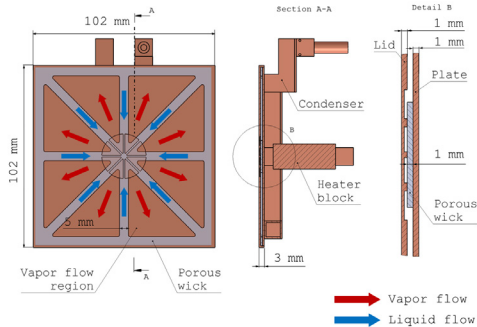


Figure 1. Structure and dimensions of the tested vapor chamber-type heat spreader.

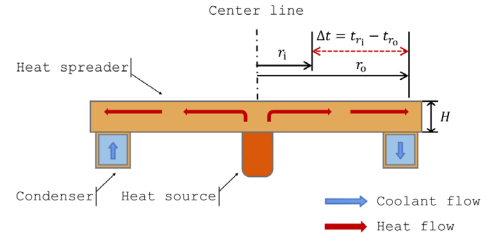


Figure 2. Dimensional parameters necessary for the determination of the effective thermal conductivity.

assessed with the dissipated heat (\dot{Q}_{diss}) to the coolant flowing through the coolant channel.

$$k_{\text{eff}} = \frac{\dot{Q}_{\text{diss}} \ln(r_i/r_o)}{2\pi H \Delta t_{\text{HS}}} \quad (1)$$

(1)

With the measured temperature change (Δt_{clnt}) and volumetric flow-rate (\dot{V}_{clnt}) of the coolant, the dissipated heat to the coolant (\dot{Q}_{diss}) was assessed based on Equation (2).

$$\dot{Q}_{\text{diss}} = (\rho c_p)_{\text{clnt}} \dot{V}_{\text{clnt}} \Delta t_{\text{clnt}} \quad (2)$$

(2)

For measurement of the temperature difference over the heat spreading surface from the heated center, a thermographic camera having a temperature sensitivity of 40 mK and calibration uncertainty of approximately 1 K ($k = 2$) was used; a high-emissivity paint having a spectral emissivity of approximately 0.95 was painted on the heat spreading surface of the heat spreader. For calorimetry of a spread heat, the volumetric flow-rate (\dot{V}_{clnt}) and temperature change (Δt_{clnt}) of the coolant were measured using a calibrated positive displacement-type flowmeter, having a calibration uncertainty of approximately 0.26 % ($k = 2$) and two calibrated IPRTs (industrial platinum resistance thermometers), having calibration uncertainties of approximately 0.06 K ($k = 2$), respectively.

In this work, the effect of the influential parameters, such as the heat flux, working fluid charge volume, and inclination to the ground, was systematically investigated; the heat flux ranged from 50 W/cm² to 200 W/cm² (with an increment of 25 W/cm²); the tested inclination to the ground included 0°, 45°, and 90°; the working fluid was injected approximately 5 ml, 6 ml, and 7 ml, which corresponded to the working fluid charge ratios of approximately 60 %, 70 %, and 80 %, respectively.

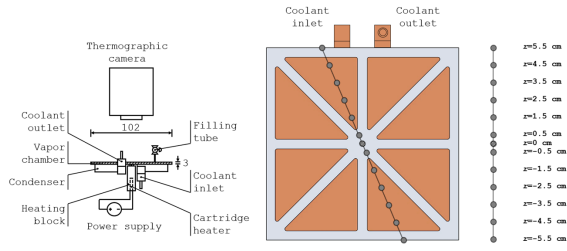


Figure 3. Schematic of the test setup (left) and the radial locations of temperature measurement over the heat spreading surface of the heat spreader (right).

As to the test procedure, the heat spreader was started up at a startup heat flux; when steady-state operation was reached, radial temperature distribution and radial temperature differences across specific radial distances from the center of the heat spreader (Δt_{radial}), volumetric flow-rate of coolant (\dot{V}_{coolant}) and temperature change of coolant ($\Delta t_{\text{coolant}}$) were measured. In order to estimate the uncertainty due to repeatability, the test was repeated 5 times. Based on the obtained results, the cumulative effective thermal conductivities over the heat spreading surface of the heat spreader were determined with measurement uncertainties at approximately 95 % level of confidence. Figure 3 shows the schematic of the test setup and the radial locations of temperature measurement over the heat spreading surface of the heat spreader; the radial distance was ranged from -5.5 cm to 5.5 cm with an 1 cm interval and 0 cm refers to the center of the heat spreader.

3. Results and discussion

Prior to the evaluation of the effective thermal conductivity of the heat spreader, in this work, an effective thermal conductivity of a copper plate having the same external dimensions as those of the tested heat spreader was evaluated to validate the

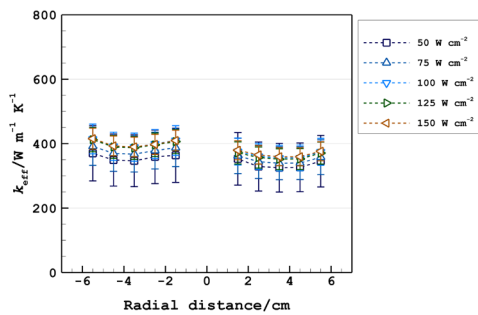


Figure 4. Cumulative effective thermal conductivity distributions at different heat fluxes (heat flux: 50 W cm^{-2} – 150 W cm^{-2}).

proposed thermographic method. Figure 4 shows cumulative effective thermal conductivity distribution measured on the copper plate at different heat fluxes. As shown in the figure, the measured cumulative effective thermal conductivity of the copper plate matched the known thermal conductivity value of copper ($k_{\text{Cu}} \approx 386 \text{ W/(m K)}$) [9] within the measurement uncertainties. Therefore, it was found that the effectiveness of the proposed thermographic method of determining an effective thermal conductivity of a heat spreader was valid.

The vapor chamber-type heat spreader was operated at different influential parameters (i.e., heat flux, inclination angle, and working fluid charge volume). Figures 5 and 6 show the two-dimensional temperature distributions measured on the heat spreading surface of the copper plate and heat spreader at a heat flux of 150 W cm^{-2} and for the case of the heat spreader, at different inclinations and working fluid charge volumes. Compared to the results obtained with the copper plate, the vapor chamber-type heat spreader demonstrated more uniform temperature distribution, indicating more effective heat spreading due to the radially outward vapor flow through the vapor flow space. Based on the obtained thermographic images, radial temperature distributions were obtained, and then cumulative effective thermal conductivity distributions of the heat spreader were evaluated using the measurement model (Equation (1)). Figures 7 (a) and (b) show examples of the distributions of the radial temperature and cumulative effective thermal conductivity on the heat spreading surface of the heat spreader inclined parallel to the ground (i.e., inclination angle: 0°) and at different heat fluxes.

In this work, to characterize the heat spreading performance of the tested heat spreader in the context of the effect of the influential parameters, the cumulative effective thermal conductivities at

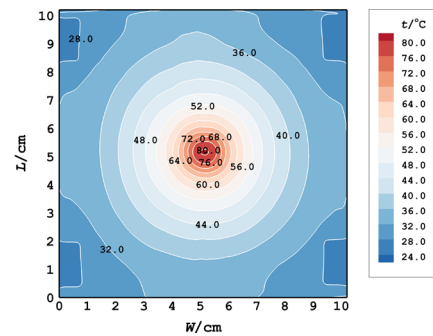


Figure 5. Two-dimensional temperature distribution measured on a copper plate at a heat flux of 150 W cm^{-2} .

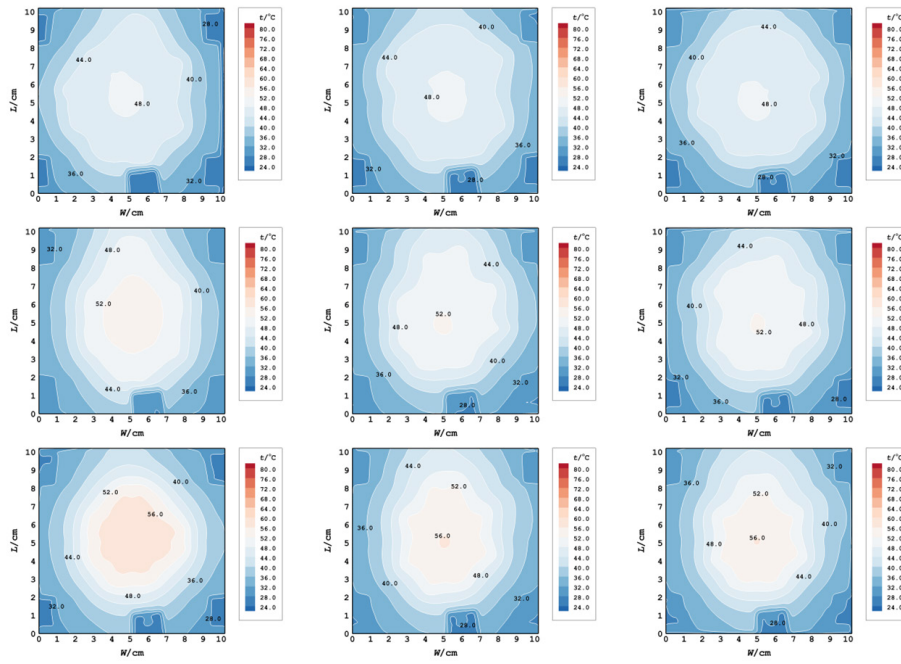


Figure 6. Two-dimensional temperature distributions measured on the heat spreader at a heat flux of 150 W/cm^2 . Inclination angle: 0° , 45° , 90° (from left to right). Working fluid charge volume: 5 ml, 6 ml, 7 ml (from top to bottom).

the outermost radial locations for the vapor flow (i.e., $\pm 3.5 \text{ cm}$ from the center), obtained at different

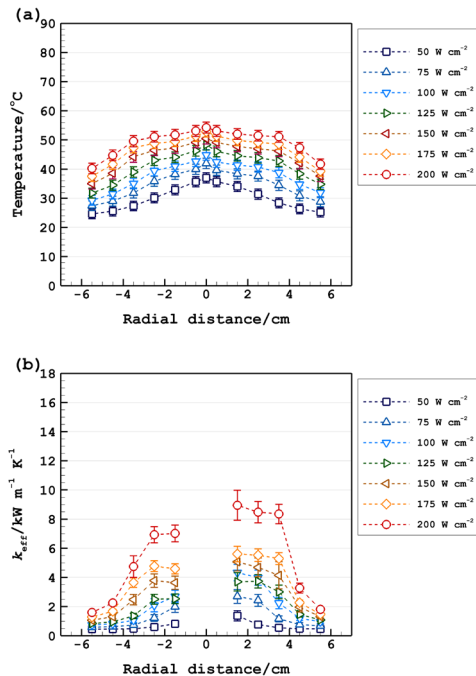


Figure 7. Distributions of (a) the radial temperature and (b) the cumulative effective thermal conductivity of the heat spreader with increasing heat flux (inclination angle: 0° , working fluid charge volume: 5 ml).

operating conditions, were compared. Figures 8 (a), (b), and (c) show variations of the cumulative effective thermal conductivities at the outer edge of the vapor flow region with increasing heat flux at different working fluid charge volumes and at specific inclinations. As shown in the figures, in all the tested conditions, the effective thermal conductivity increased with increasing heat flux due to the increased mass flow rate of the working fluid with increasing heat flux.

As shown in Figure 8, the cumulative effective thermal conductivity at the outer edge of the vapor flow region decreased with increasing working fluid charge volume. It was caused by the selective accumulation of the excess liquid near the condensing region [7], hindering the vapor phase working fluid from accessing the condensing region; due to this, as the working fluid charge volume increased, the temperature difference between the center and outer region increased, reducing the cumulative effective thermal conductivity at the outer edge of the vapor flow region.

The effective thermal conductivity of the heat spreader shows the highest value at a working fluid charge volume of 5 ml in all the tested heat fluxes and inclinations. However, at this working fluid charge volume, a local dryout in the center region was observed at heat flux of 200 W/cm^2 and at inclination angles of 45° and 90° . Figures 9 (a), (b),

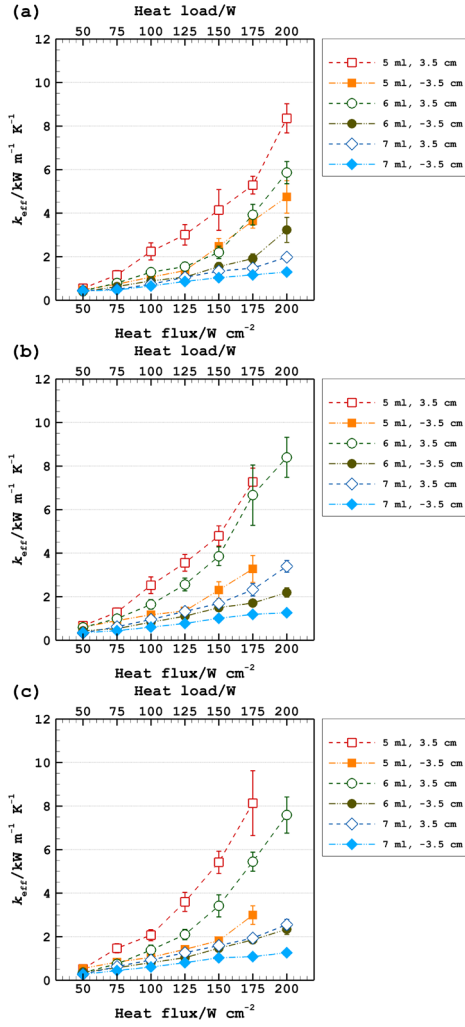


Figure 8. Variations of the cumulative effective thermal conductivities at the outer edge of the vapor flow region ($r = \pm 3.5$ cm) with increasing heat flux at different working fluid charge volumes and at specific inclinations. (a) Inclination angle: 0° . (b) Inclination angle: 45° . (c) Inclination angle: 90° .

and (c) show the transient variations in the radial temperatures at various radial locations of the heat spreader having a working fluid charge volume of 5 ml; the tested heat flux was 200 W/cm^2 and the inclination changed from 0° to 90° . As shown in the figures 9 (b) and (c), at the inclination angles of 45° and 90° , the center region temperatures (within ± 0.5 cm) showed continuous rises whereas the radial temperatures at the other radial locations reached steady-state values, implying that local dryout was caused by insufficient liquid supply to the center region at this high heat flux and inclinations. At inclination angle of 0° the local dryout was not observed. Based on these results, it was found that the local dryout was produced due to the reduced liquid supply to the center at high heat flux and inclinations other than 0° , which caused a shortage

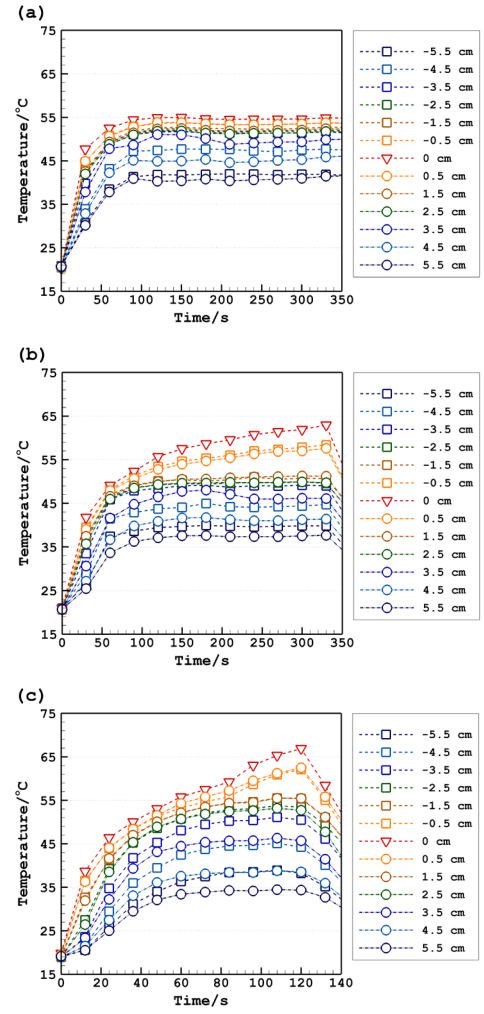


Figure 9. Transient variations in the radial temperatures at various radial locations of the heat spreader operating at 200 W/cm^2 with a working fluid charge volume of 5 ml. (a) Inclination angle: 0° . (b) Inclination angle: 45° . (c) Inclination angle: 90° .

of the liquid phase to fill the entire void volume of the wick and increased liquid hydrostatic head loss for the liquid replenishment, thus drying out the center region. On the other hand, at working fluid charge volumes of 6 ml and 7 ml, the local dryout was not observed, and this was due to the sufficient amount of the liquid phase working fluid to fill the entire void volume of the wick, guaranteeing sufficient liquid replenishment to the center region of the heat spreader.

In addition, for the tested heat spreader, asymmetric distributions of the effective thermal conductivity in different directions were observed. As the inclination angle of 0° , it was caused by the change in the coolant temperature as it flowed through the coolant channel attached to the outer edge of the heat spreader [7]. At inclination angles

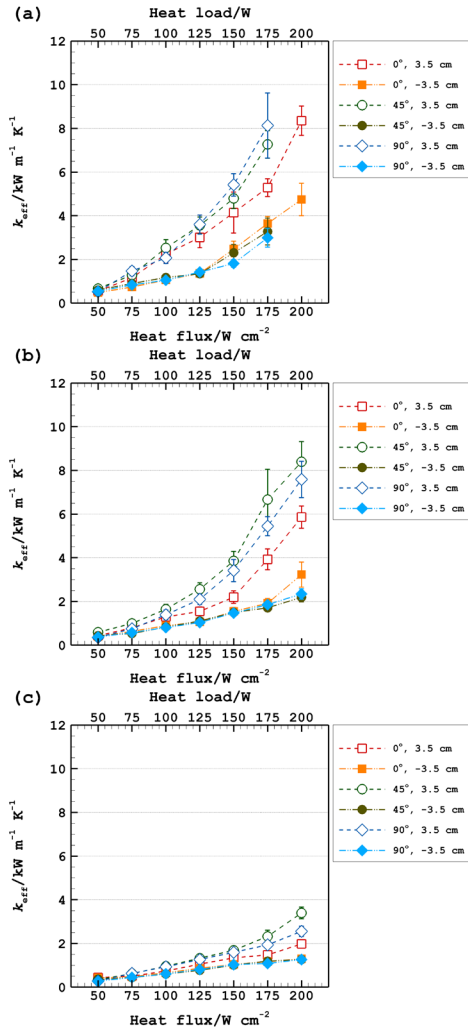


Figure 10. Variations of the cumulative effective thermal conductivity at the outer edge of the vapor flow region ($r = \pm 3.5$ cm) with increasing heat flux at different inclinations and at specific working fluid charge volumes. (a) Working fluid charge volume: 5 ml. (b) Working fluid charge volume: 6 ml. (c) Working fluid charge volume: 7 ml.

other than 0° , the asymmetric distribution became more pronounced, and it was supposed to be due to the effect of buoyancy of the vapor phase and hydrostatic head change of liquid phase.

Figures 10 (a), (b), and (c) show variations of the cumulative effective thermal conductivity at the outer edge of the vapor flow region with increasing heat flux at different inclinations and at specific working fluid charge volumes. As shown in the figures, the effect of the inclination angle on the asymmetric distributions of the cumulative effective thermal conductivity were clearly seen. In figure 10 (a), in the upper region (i.e., $r = 3.5$ cm) of the heat spreader, the highest effective thermal conductivity was observed at the inclination angle of 90° , whereas in the lower part (i.e., $r = -3.5$ cm), the

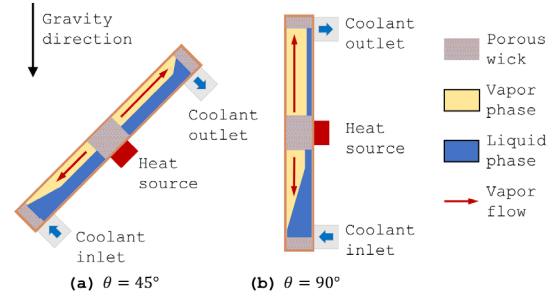


Figure 11. Distributions of excess liquid and range of vapor flow in the vapor chamber at different inclination angles. (a) Inclination angle: 45° . (b) Inclination angle: 90° .

highest value was observed at the inclination angle of 0° . This was caused by the combined effect of the increased effect of buoyancy in the upper region of the heat spreader and the enlarged liquid flooded portion in the lower part of the heat spreader at inclination angles other than 0° [8].

For the cases of the working fluid charge volumes of 6 ml and 7 ml, in the upper region, the highest values were observed at inclination angle of 45° . The reason for this was due to the change in the thickness of the liquid film in the vapor flow region with increasing inclination angle. Figure 11 schematically shows the distributions of excess liquid in the heat spreader at the inclination angles of 45° and 90° . As shown in the figure, at the inclination angle of 45° , the thickness of the liquid film in the upper region of the heat spreader was thicker than the case at the inclination angle of 90° . With the reduced thickness of vapor flow region (due to the thicker liquid film), the vapor speed in this region was higher than the case at higher inclination angles, resulting in a more uniform temperature distribution and higher effective thermal conductivities.

4. Conclusions

In this work, a thermographic method was employed to investigate heat spreading characteristics of the vapor chamber-type heat spreader. A vapor chamber-type heat spreader having external dimensions $102 \text{ mm} \times 102 \text{ mm} \times 3 \text{ mm}$ (length \times width \times thickness) was constructed with a patterned porous wick having thickness of 1 mm; copper was used as a material for the heat spreader and wick, and water was used as the working fluid. The proposed thermographic method was validated by measuring an effective thermal conductivity of a copper plate having the same dimensions as those of the heat spreader, and the

measured effective thermal conductivity of the copper plate matched the known value of the thermal conductivity of copper within the measurement uncertainty.

Effect of the influential parameters such as the heat flux, working fluid charge volume, and inclination angle to the ground, was examined by comparing the cumulative effective thermal conductivities at the outer edge of the vapor flow region. With increasing heat flux, the effective thermal conductivity increased in all the tested conditions. The effective thermal conductivity at the outer edge of the vapor flow region decreased with increasing working fluid charge volume due to the accumulation of the excess liquid near the condensing region at outer edge of the heat spreader, hindering the vapor flow from reaching the condensing region. As the inclination angle to the ground increased, asymmetric distribution of the effective thermal conductivity became more pronounced.

References

- [1] D. Deng, Q. Huang, Y. Xie, X. Huang, and X. Chu, Thermal performance of composite porous vapor chambers with uniform radial grooves, *Applied Thermal Engineering*, 2017. 125: P. 1334
- [2] Y. Sungtaek Ju, M. Kaviyani, Y. Nam, S. Sharratt, G.S. Hwang, I. Catton, E. Fleming, and P. Dussinger, Planar vapor chamber with hybrid evaporator wicks for the thermal management of high-heat-flux and high-power optoelectronic devices, *International Journal of Heat and Mass Transfer*, 2013. 60: p. 163
- [3] K. Mizuta, R. Fukunaga, K. Fukuda, S. Nii, and T. Asano, Development and characterization of a flat laminate vapor chamber, *Applied Thermal Engineering*, 2016. 104: p. 461.
- [4] R. Boukhanouf, A. Haddad, M.T. North, and C. Buffone, Experimental investigation of a flat plate heat pipe performance using IR thermal imaging camera, *Applied Thermal Engineering*, 2006. 26: p. 2148.
- [5] C. Chen, C. Chen, G. Wu, and S. Chen, A High Thermal Dissipation Performance Polyethylene Terephthalate Heat Pipe, *International Scholarly and Scientific Research & Innovation*, 2013. 7(10): p. 1967.
- [6] Joint Committee for Guides in Metrology (JCGM), Evaluation of measurement data - Guide to the expression of uncertainty in measurement, JCGM 100:2008 (BIPM, Paris, 2008) pp. 18-23.
- [7] J. Han, H. Bae, and W. Joung, Effect of the Working Fluid Charge Ratio and Heat Flux on the Temperature Homogenization Characteristics of a Vapor Chamber-Type Heat Spreader, *International Journal of Thermophysics*, 2022. 43: p. 168
- [8] J. Li and L. Lv, Experimental studies on a novel thin flat heat pipe heat spreader, *Applied Thermal Engineering*, 2016. 93: p. 139
- [9] J. Carvill, *Mechanical Engineer's Data Handbook*, (Butterworth-Heinemann, 1993) pp. 102-145

Acknowledgements

This work was supported by the National Research Foundation (NRF), South Korea, under project BK21 FOUR (Smart Robot Convergence and Application Education Research Center).

Experimental study on gravity-effect for startup performance of high-temperature sodium heat pipe

Zhi-Hu XUE, Bang-Cheng AI*, Rong-Xu NIE, Chao LIU, Wei LI, and Wei QU*

China Academy of Aerospace Aerodynamics, Beijing, China

**Corresponding author email address: xuezhihu9@hotmail.com, aimen011@163.com, weiqucaaa@163.com*

Abstract

The gravity-effect plays important factor on the startup and thermal performance of high-temperature heat pipes (HTHPs). But the results of past studies are quite different and confusing our perception. In this paper, a sodium HTHP is fabricated and experimented to study the gravity-assisted, horizontal and anti-gravity three modes on the startup behaviors and quasi-steady thermal performance. The HTHP is designed to $\Phi 25 \times 410$ mm, two wraps of 100 mesh screen, and filling mass of 15 g sodium. The HTHP is tested at the inclination angle of 0° , 90° , -30° and -90° . The results show that no startup failures are found during all the three operating modes and the startup time for HTHP fully starting at different inclination angle is the same as 10 min. However, the gravity-effect cannot be ignored and plays important influence on the HTHP startup. Compared with the horizontal mode, the gravity-assisted mode (90°) is beneficial for the starting more favorably and decreasing the temperature difference between the evaporator and condenser after the startup. The anti-gravity working mode has a significant adverse effect on the temperature rise-rate of the HTHP condenser and increase the temperature difference after the startup in a large step as the inclination angle changed from 0° , -30° to -90° .

Keywords: High temperature heat pipe; Sodium; Startup performance; Gravity effect; Inclination angle

1. Introduction

High-temperature heat pipes (HTHPs) are considered as an effective way to transfer high heat flux and maintain small temperature drop in the operating temperature over 500°C . HTHPs are now mainly applied in aerospace [1-4], nuclear reactor [5,6], concentrated solar power plant [7,8], and high-temperature waste heat recovery [9,10]. The working fluids of HTHPs are usually selected as one kind of liquid metals whose melting point temperature is low and boiling point temperature is acceptable and latent heat is high. For example, cesium, potassium, sodium and lithium are used. Unlike low or normal temperature heat pipes, HTHPs are not easy to start up or thawing of liquid-metal heat pipes is a unique problem [11]. Therefore, several groups study the factors that affect the startup of HTHPs and the methods to shorten the startup time. Cao [12] indicated how to determine the transient vapor temperature for analysis of thawing front. Zhang [13] found the faster breaking of the sonic limitation and faster startup rate as the higher initial input temperature at evaporator. Lu [14] showed that insufficient and excessive amounts of sodium might cause the startup failures. Faghri [15] experimented that the startup behavior was dependent upon the heat rejection rate at condenser. Ponnappan [16] demonstrated that the startup time of a 2-m-long sodium heat pipe was shortened with the gas-loaded methodology.

In addition, the gravity or inclination angle plays

important influence on the startup and thermal performance of HTHPs [17]. This effect should be taken into consideration for some terrestrial applications and will affect the normal operation and implementation feasibility of HTHP design schemes. For example, in the areas of hypersonic vehicle thermal protection [18-19], aero-engine cooling [20], concentrating solar receiver [21], the inclination angle needs to change as the variations of working state, and sometimes even in the anti-gravity working conditions (the evaporator is placed above the condenser). Tolubinsky [22] had earlier studied the start-up characteristics of HTHP under gravity, found that the temperature fluctuation amplitude and frequency of heat pipe increased as the tilt angle increased from 0° to 15° due to forming a puddle in evaporator. But in Guo [17] studies, they showed that the start-up behaviors were dramatically improved and the temperature difference significantly decreased as the inclination angle increased from 0° to 50° , but slightly decreased when it exceeds 60° . Yang [23] studied an experiment of potassium heat pipe, and concluded that the gravity was beneficial to the improvement of startup and heat transfer performance at angle of 45° and 90° with a suitable filling ratio. Niu [24] conducted a test of sodium heat pipe with length 320 mm, and showed that the evaporator of the HTHP dried out under the anti-gravity condition of -45° and -90° . Wang [25] also found the HTHP's startup failure with a small negative inclined angle of -

15° and the heat transfer performance of inclined heat pipe worse than horizontal condition. However, in the anti-gravity experiment by Zhao [26], their results presented that the working inclination angle including gravity-assisted and anti-gravity both had minimal effects on the frozen startup of a concentric annular HTHP, maybe due to the short total length of 112 mm and large cross-section area of wick for heat pipe. Therefore, determining the influence of the gravity-assisted and anti-gravity on the startup performance is necessary and useful, from the perspectives of the startup time, the temperature fluctuation at evaporator and the temperature difference at steady-state. Unfortunately, some of previous studies showed that gravity assistance was beneficial, while others gave opposite opinions; under anti-gravity operating, some studies found startup failure, while other believed that the HTHP could work normally.

In this paper, an experimental investigation of the startup characteristics of a sodium HTHP at different inclination angle is conducted at China Academy of Aerospace Aerodynamics (CAAA). Firstly, the HTHP is tested at horizontal mode with a fixed heat load to obtain its basic startup behaviors and quasi-steady performance. For a study on the effect of gravity assistance, the HTHP is then experimented at vertical mode (evaporator is lower than condenser) under the same heating condition. In order to study the influence of anti-gravity working mode, two states of inclination angle as -30° and -90° (evaporator is higher than condenser) are carried out. The experiment results of gravity-assisted and anti-gravity mode are compared with the results of horizontal mode, to assess the gravity effect on the startup performance.

2. Experimental

2.1. Design and Fabrication

The stainless steel 316L is used as the raw material of heat pipe shell and two endcaps due to its low cost, good machinability, and high strength. The heat pipe shell is designed to 410 mm in length, with an outside diameter of 25 mm and a wall thickness of 2 mm. The thickness of two endcaps is 5 mm. The two wraps of 100 mesh type 304 stainless steel screen are used as the wicks, providing a liquid return path from the condenser to the evaporators. The screen wick is alternatively spot-welded on inner wall surface of the shell. Sodium with a purity of 99.9% is selected as the working fluid. The filling amount mass of sodium is $15 \text{ g} \pm 0.5 \text{ g}$. Table 1 displays the detailed

information of the designed heat pipe.

The fabrication of heat pipe involves metal structure forming, preparation processes, welding, thermal treatment and charging. The preparation process, welding and thermal treatment are referenced as the works [14]. The sodium charging equipment and processes are detailed in Ref. [27].

Table 1. Detailed information of the heat pipe.

Shell material	stainless steel 316L		
Wick material	stainless steel 304 screen of 100 mesh		
Working fluid	Sodium	Filling mass	$15 \pm 0.5 \text{ g}$
O.D.	25 mm	I.D.	21 mm
Total length	410 mm	Evaporator	220 mm
Adiabatic	90 mm	Condenser	100 mm

2.2. Experiment setup and procedure

Heat pipe wall temperatures are measured with Type K thermocouples, which have the range up to 1300 °C and are calibrated with an accuracy of $\pm 5 \text{ }^\circ\text{C}$. There are three or five wall thermocouples, which are both spot-welded to the heat pipe wall (as shown in Fig. 1). Two thermocouples T1 to T2 are located in evaporator section. One thermocouples T3 is placed near the exit of adiabatic section. Two thermocouples T4 to T5 are located at different circumference positions of the end side-wall in condenser section. In test, since the temperatures of T1 and T2, T4 and T5 are close to each other in horizontal mode, in order to simplify the experimental process, the thermocouples of T2 and T4 measurement points will be not arranged and data collection is not carried out.

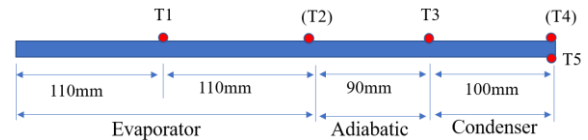


Figure 1. Schematic of temperature test points.

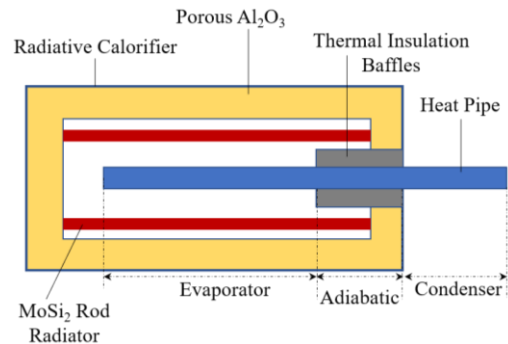


Figure 2. Schematic of the calorifier and HTHP layout for startup experiment.

Startup tests of the sodium HTHP are carried out in a 30 kW calorifier, seen in Fig. 2. The working

principle of the calorifier is radiation heating. During startup tests, heat is supplied to the initial 220 mm-long from the left endcap in Fig.1 as the evaporator of heat pipe. The next 90 mm-long region is around by a concentric annular baffle for thermal insulation, which is made of porous Al_2O_3 , providing an adiabatic condition. Another function of the annular baffle is used as a support structure to fix the heat pipe tightly. The condenser was 100 mm long, exposed directly to air surroundings. The heat is removed from the condenser section by heat radiation and natural heat convection.

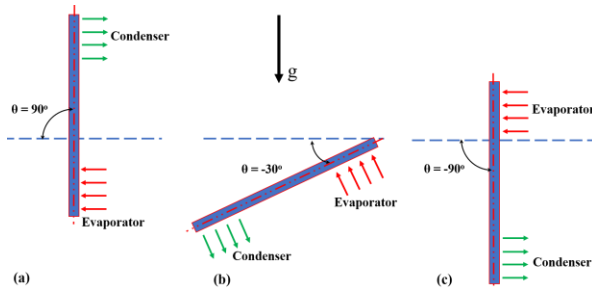


Figure 3. Schematic of the inclination angle, (a) vertical 90° ; (b) anti-gravity -30° ; (c) anti-gravity -90° .

In the startup experiments, the calorifier is set to 900°C . The inclination/tilt angle (θ) in this paper is defined as the angle from the horizontal orientation to its axial direction of the heat pipe, as shown in Fig. 3. The experiment procedure is processed as follows: 1) worked at horizontal mode as tilt angle of 0° , turning on the calorifier for heating evaporator, and beginning the data collector to record the temperature response. When the temperature T1 grows slowly, which means to going a quasi-steady state, the calorifier and data collector will be turned off. 2) worked at vertical mode as tilt angle of 90° , turning on the calorifier and the data collector, and turning off after the quasi-steady state. 3) worked and data-acquired at anti-gravity mode as tilt angle of -30° and -90° , respectively.

3. Results and Discussion

3.1. Startup Results at Horizontal Mode

Fig. 4 shows the temperature increase curves of the measurement points of T1, T3 and T5 as the variation of time to represent the temperature response for the startup behaviors of sodium heat pipe at horizontal mode. The thermocouples T1, T3 and T5 are located at the outside-wall of middle position of evaporator section, the exit of adiabatic section and the top place in condenser section, respectively.

After the heat is inputted into the evaporator, the sodium working mediums in evaporator are thawed and then evaporates from liquid phase to vapor phase, thus the evaporator temperature begins to accelerate and rise, as shown in the curve of T1. The steam flows from the evaporator to the adiabatic, and the sodium mediums in adiabatic are gradually thawed and evaporated to form the free-molecular flow and transition flow. Under the combined action of convection heat transfer in the vapor space and conduction heat transfer in the wall, the wall temperature of the adiabatic section will first rise rapidly and then become to grow slowly following the evaporation section, as shown in the curve of T3. However, at this period (e.g., before the time of 6.5 min) the end of condenser still remains frozen state and its temperature has no change, as shown in the curve of T5. When the adiabatic section starts up, that is, from transition flow to continuous flow regime, the corresponding time period is 6.5 min to 8.5 min in Fig. 4. The temperature of T3 in the adiabatic section has a steep increase of a large slope (greater than $300^\circ\text{C}/\text{min}$), while the temperature of T1 in the evaporation section has a small decrease, forming a sharp peak. Because at this time the sodium working mediums in the adiabatic section evaporate a lot, the heat ratio taken away by the adiabatic from the total heat input is increased. The temperature callback in the evaporation section is a sign of the local start-up of the heat pipe, which also seen in the Ref. [3,28].

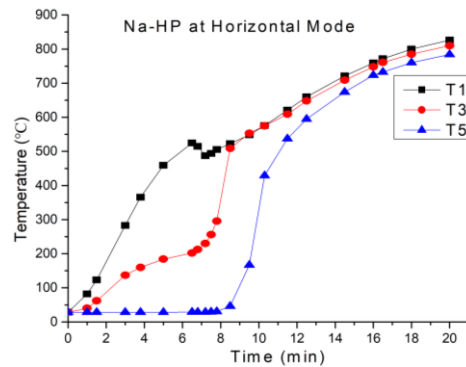


Figure 4. Temperature response curves versus time during startup at horizontal mode.

After the time of 8.5 min, the temperature of T3 is close to T1. And during the time of 6.5 min to 8.5 min, the temperature of T5 appears small fluctuations and increase as $5\text{--}20^\circ\text{C}$, indicating that the condenser works at the free-molecular flow now and the vapor comes into the end of the condenser. After the adiabatic section starts up completely at 8.5 min, the working status of condenser will change from the free-molecular

flow to transition flow analogously, and the temperature of T5 also behaves a steep increase of a large slope (greater than 300 °C/min). Then at the moment of the 10.3 min, the saturated vapor in the condenser will become a continuous flow, and the condensing section will start up, indicating that the heat pipe has also been fully started.

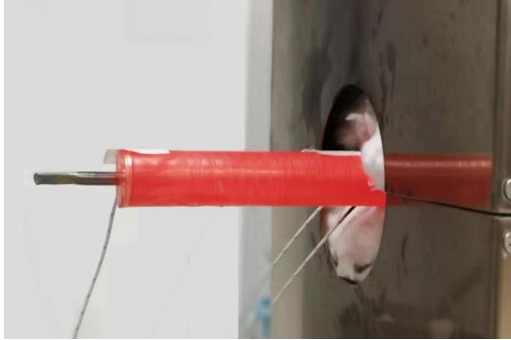


Figure 5. Optical images of the HTHP startup at horizontal mode.

Therefore, the startup time of sodium heat pipe in the horizontal state is about 10-10.3 min in this experiment. The starting temperature of saturated steam in the tube can be taken as about 500 °C, obtained from the average temperature between the measuring points in the evaporator and the condenser. After the heat pipe is started, the temperature of the three measuring points as T1 to T3 will gradually approach to each other and then warm up slowly and synchronously. The Fig. 5 shows the optical image of the HTHP startup at horizontal mode. It can be seen that the sodium HTHP displays a bright red in the whole condenser including its endcap. Therefore, the heat pipe behaves a quasi-uniform temperature distribution and keeps its structure integrity.

3.2. Startup Results at Vertical Mode

Fig. 6 shows the temperature increasement curves of the measurement points of T1 to T5 versus the variation of time at vertical mode. Some previous studies [17,25] found that if the HTHP operated at the gravity-assistance conditions, that is $0^\circ < \theta \leq 90^\circ$, there would be an optimum tilt angle (e.g., 40° or 15°) for obtaining the optimal startup performance. They both indicated that the startup performance at vertical mode ($\theta = 90^\circ$) was worse than horizontal mode ($\theta = 0^\circ$). However, in this paper, we will discover that, compared with the horizontal working mode, the HTHP can start up more favorably and the temperature curve can be smoother in the vertical working state. The possible explanation is related to the amount of working medium charged in the HTHP. The filling

amount of sodium in this paper is relatively moderate, not excessively charged. And the reason for the performance decline in above Ref. [17,25] is that the amount of sodium charged may be too large. Thereby, when the heat pipe works at a large tilt angle, the excess sodium liquid will form a liquid pool at the bottom of the evaporator [25] or partially flooding of evaporator or some puddles arisen near the core holes of the screen [22].

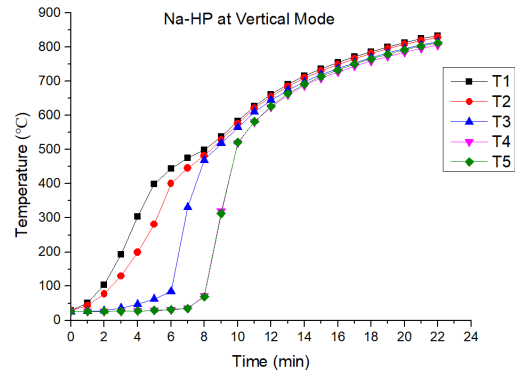


Figure 6. Temperature response curves versus time during startup at vertical mode ($\theta = 90^\circ$).

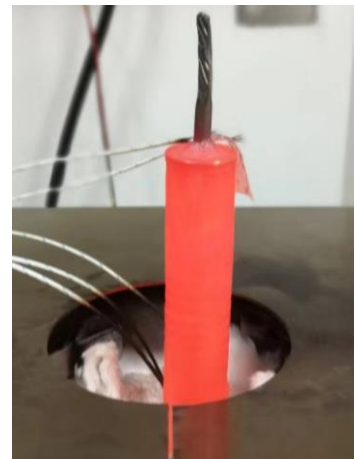


Figure 7. Optical images of the HTHP startup at vertical mode ($\theta = 90^\circ$).

As shown in Fig. 6, when the adiabatic begins to start, the vapor in its exit will change from transition flow to continuous flow, and the temperature increase with a steep slope of 250 °C/min, indicated as the T3 curve during the time from 6 min to 8 min. Simultaneously, the temperature growing speed of T1 curve is slowed, but not presenting a sharp peak or temperature callback, due to that the liquid sodium can flow back to evaporator more easily under the assistance of gravity compared to the horizontal working state. After the time of 8 min, the tail end of condenser also begins to start and its temperature behaves a rapid increasement with a steep slope larger than 245 °C/min, shown as the T4 and T5 curves. At the

time of 10 min, the temperature of T4 and T5 reaches 520 °C and 521.5 °C, respectively, which is close to the temperature of the evaporator and adiabatic section. Therefore, the sodium HTHP at vertical mode can be start up successfully and perfectly, as shown in Fig. 7. Its optical image of the whole condenser appears bright red and keeps its structure integrity.

3.3. Startup Results at Anti-gravity Mode

Fig. 8 is the temperature increase curves of the measurement points of T1 to T5 versus the variation of time at anti-gravity mode with an angle of $\theta = -30^\circ$. From the global temperature response curves of the whole heat pipe shown in Fig. 8, the fabricated HTHP can successfully start up under the adverse gravity condition with a not large anti-tilt angle, and the temperature difference between the evaporator and condenser is relatively small as 68 °C, indicating its excellent startup and heat transfer performance. Compared with the startup failure at tilt angle of -15° in literature [25], this conclusion is completely different, which is of great significance for guiding the terrestrial using of high temperature heat pipes in the anti-gravity working environment. The Fig. 9 shows an optical image of the HTHP startup at anti-gravity mode ($\theta = -30^\circ$). The condenser of the heat pipe behaves bright red and works normally.

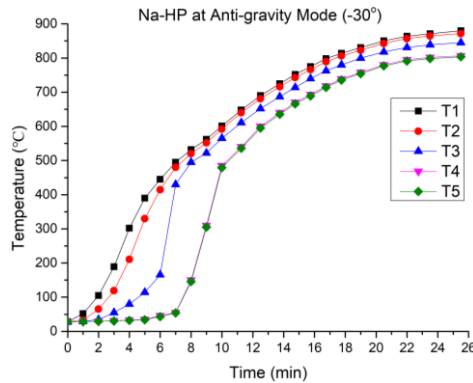


Figure 8. Temperature response curves versus time during startup at anti-gravity mode ($\theta = -30^\circ$).



Figure 9. Optical image of the HTHP startup at anti-gravity mode ($\theta = -30^\circ$).

Compared to the startup processes of the HTHP at horizontal mode and vertical mode, the startup

behaviors in temperature curves of the adiabatic and condenser at anti-gravity mode ($\theta = -30^\circ$) behave three variations. Firstly, before the start of the adiabatic and the condenser section, that is, before the sodium vapor changes from the free-molecular flow to the transition flow, the wall temperature of the measuring points as T3 at the adiabatic and T5 at the end of condensing section both begin to rise significantly, seen in Fig. 8. However, while the HTHPs working at horizontal and vertical modes, the wall temperature of the measuring point at the end of the condensing section barely changes before their start, shown in Fig. 4 and Fig. 6. Because there are three factors contributing to the rise of the wall temperature of the condensing section under adverse gravity condition, including combined action of convection heat transfer in the vapor space, convection heat transfer by liquid sodium flow-down in the capillary core and conduction heat transfer in the wall. The second variation is the reduction in the rising slope of the startup temperature as T3 and T5 denoted in Fig. 8. In the adiabatic section, the maximum temperature rise rate from transition flow to continuous flow is about 260 °C/min, and in the condenser section, the startup maximum temperature rise rate from transition flow to continuous flow is about 185 °C/min, both of which are lower than the temperature rise rate in horizontal and vertical modes. The third variation has an increment of the temperature difference between the evaporator and condenser after entering a quasi-steady state under the condition of anti-gravity. Therefore, although the HTHP is successfully started under the anti-gravity condition of -30° , the gravity factor still has a negative effect on its startup performance and behaviors, slightly weakening its heat transfer performance.

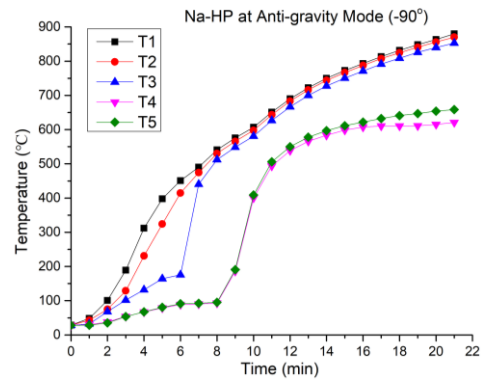


Figure 10. Temperature response curves versus time during startup at anti-gravity mode ($\theta = -90^\circ$).

Fig. 10 is the temperature increase curves of the measurement points of T1 to T5 versus the

variation of time at anti-gravity mode with an angle of $\theta = -90^\circ$. From the Fig. 10, it is also seen that the three differences mentioned previously are more obvious and enlarged. This phenomenon indicates that with the increase of the tilt angle against gravity, the heat pipe startup behaviors and heat transfer performance will deteriorate further. Because in the anti-gravity mode, the direction of gravity is the opposite of the direction of capillary force by wick pore for priming fluid back to evaporator. The stronger the anti-gravity effect is, the weaker the back-suction capacity of the capillary core is, and the more difficult it is for the liquid cooled in the condenser section to return to the evaporator section for replenishment of liquid evaporating. Nevertheless, the HTHP working at anti-gravity mode with $\theta = -90^\circ$ in this paper is still started up successfully, on account of the temperature of condenser-end growing over 490°C with a rapid startup increase slope of $205^\circ\text{C}/\text{min}$, shown as T4 and T5 curves in Fig. 10. The starting temperature of 490°C is far higher than the transition temperature about 420°C for sodium provided in the study of Faghri [15]. Fig. 11 shows the optical image of the HTHP startup at anti-gravity mode of -90° angle. The condenser presents the three colors as orange-red, bright red, and gray-red in the end section but not dark black. Because in the condition of -90° angle, there may be occurred some liquid flooding and accumulation in the end of condenser. Therefore, if we need to improve the performance of HTHPs under anti-gravity working, especially under the condition of -90° , a feasible strategy is to improve the capillary suction capacity of heat pipes by optimizing the capillary core structure, e.g., multi-scale composite wick, which has also been indicated in literature [29], so as to reduce the influence of gravity, improve the start-up performance of heat pipes and improve the temperature uniformity under steady state.

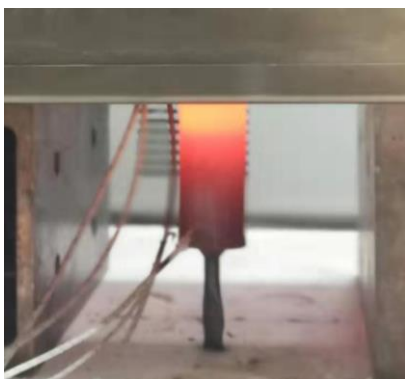


Figure 11. Optical image of the HTHP startup at anti-gravity mode ($\theta = -90^\circ$).

3.4. Comparative Analysis and Discussion

The frozen start-up of HTHPs is a very complicated thermodynamic process. Since no startup failures are found in this paper during the three working modes: vertical mode, horizontal mode and anti-gravity mode, the startup behaviors and quasi-steady thermal performance of the HTHPs are characterized by the following indicators for comparison: start-up time, startup temperature rise-rate, temperature difference between the evaporator and condenser after quasi-steady state, etc.

Fig. 12 is the comparative plot of the startup time of the HTHP at different inclination angle. It can be seen that the inclination angle has a small effect on the startup time for the fully-started in the condenser end of the HTHP, shown as the straight black curve in the figure. The explanation of this phenomenon is described in the contents of Sec. 3.1-3.3. However, the inclination angle has a great effect on the maximum temperature rise-rate in the condenser end of the HTHP during the startup process, as shown in Fig. 13. When the HTHP works at the inclination angle of 90° and 0° , the rise-rate of T3 and T5 is close. When the HTHP works at the inclination angle of -30° and -90° , the rise-rate of T5 will decrease about 25% compared to T3, shown as the blue dotted curve in Fig. 13. This means that the gravity plays an important role in the startup behaviors and final steady-state performance, especially for the condenser startup at anti-gravity mode. The reason is that although the gravity has the minor influence on the thawing of working mediums associated with the startup time, it has the major influence on the starting speed of the condenser. The starting speed of the condenser is greatly dependent upon the heat rejection ability and the back-filling or priming capacity of the liquid fluids from the condenser to the evaporator.

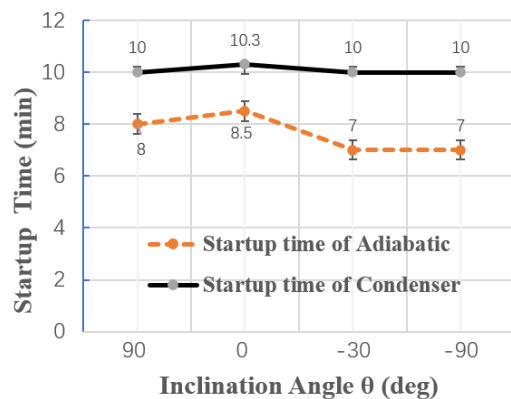


Figure 12. Startup time of the HTHP at different inclination angle

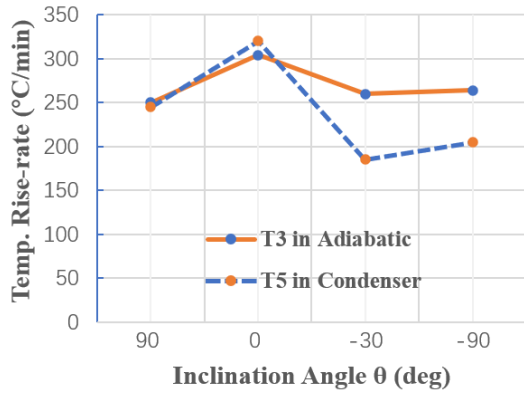


Figure 13. Maximum temperature rise-rate of the HTHP during startup process at different inclination angle

Fig. 14 is the temperature difference between the evaporator and condenser after the HTHP entering quasi-steady state at different inclination angle. It shows that when the HTHP works at the inclination angle of 90° , the temperature difference is only 22°C , which is smaller than the temperature difference of 40°C with the angle of 0° . This demonstrates that the steady-state heat transfer performance of the HTHP operating in gravity-assisted state, such as vertical mode, is better than that in horizontal mode. The precondition is that the heat pipe working medium is charged in a moderate amount. When the HTHP works at the inclination angle of -30° and -90° , the temperature difference behaves 68°C and 225°C , respectively. This means that the anti-gravity working mode has a significant adverse effect on the quasi-steady heat transfer performance of the HTHP, compared with the horizontal mode. The quasi-steady heat transfer performance of the heat pipe will decrease with the increase of the tilt angle under the condition of anti-gravity.

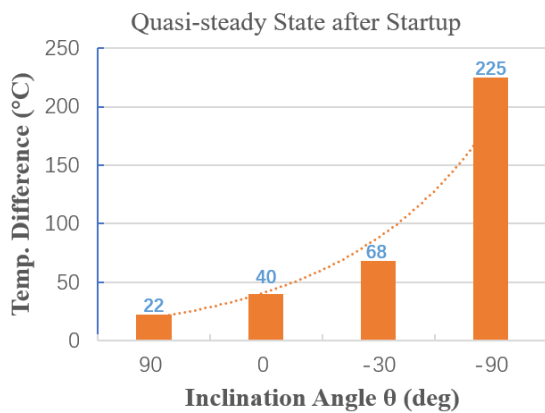


Figure 14. The temperature difference between the evaporator and condenser after the HTHP entering quasi-steady state at different inclination angle

4. Conclusions

This work experiments the startup performance of a sodium heat pipe at different inclination angle, including the three operating modes: horizontal mode (0°), gravity-assisted mode (90°) and anti-gravity mode (-30° and -90°). The following conclusions are obtained:

(1) The startup results show that no startup failures are found during all the three operating modes, even at the anti-gravity condition of -30° and -90° .

(2) The startup time of the HTHP for fully starting at different inclination angle is same, which equals to about 10 min.

(3) Compared with the horizontal mode, the HTHP can start up more favorably in gravity-assisted mode (90°), and all the temperature increasement curve can be smoother. When the HTHP enters quasi-steady state after startup, the temperature difference between the evaporator and condenser is 22°C at the angle of 90° , smaller than the temperature difference of 40°C at the angle of 0° .

(4) The anti-gravity working mode has a significant adverse effect on the temperature rise-rate of the HTHP condenser and the quasi-steady temperature difference between the evaporator and condenser. The temperature difference will increase rapidly from 68°C to 225°C , when the inclination angle varies from -30° to -90° .

References

- [1] C. C. Silverstein, A feasibility study of heat pipe cooled leading edges for hypersonic cruise aircraft, NASA CR-1857, 1971.
- [2] W. Qu, Progress works of high and super high temperature heat pipes, Developments in Heat Transfer, Chapter 25, 2011, ISBN: 978-953-307-569-3, InTech, pp. 503-522.
- [3] B. Ai, S. Chen, J. Yu, Q. Lu, H. Han, L. Hu, Fabrication of lithium/C-103 alloy heat pipes for sharp leading edge cooling, Heat and Mass Transfer (2018) 54: 1359-1366.
- [4] S. Chen, H. Han, J. Shi, Q. Lu, L. Hu, B. Ai, Applications of sodium/GH4099 heat pipes for nose cap cooling, Microgravity Science and Technology (2019) 31: 417-424.
- [5] D. I. Poston, The heatpipe-operated mars exploration reactor (HOMER), AIP Conference Proc. 552, 797 (2001) 797-804.
- [6] Y. Guo, Z. Su, Z. Li, and K. Wang, The super thermal conductivity model for high-temperature heat pipe applied to heat pipe cooled reactor, Frontiers in Energy Research, 2022 (10) 819033.

- [7] G. F. Matthews, R. E. Nygren, T. W. Morganc, et al., Testing of a high temperature radiatively cooled Li/Ta heat pipe in Magnum-PSI, *Fusion Engineering and Design* 146 (2019) 482–485.
- [8] J. H. Booa, S. M. Kimb, Y. H. Kangc, An experimental study on a sodium loop-type heat pipe for thermal transport from a high-temp solar receiver, *Energy Procedia*, 2015, 69: 608-617.
- [9] R. Laubscher and R. T. Dobson, Theoretical and experimental modelling of a heat pipe heat exchanger for high temperature nuclear reactor technology, *Applied Thermal Engineering* 61 (2013) 259-267.
- [10] E. G. Jung, and J. H. Boo, Thermal numerical model of a high temp. heat pipe heat exchanger under radiation, *Applied Energy* 135 (2014) 586–596.
- [11] J. H. Jang, A study of start-up characteristics of a potassium heat pipe from the frozen state, NASA Contractor Report 189173, 1992.
- [12] Y. Cao, and A. Faghri, A numerical analysis of high temperature heat pipe startup from the frozen state, *ASME J. Heat Transfer*, 1993, 115 (1): 247-254.
- [13] Z. Zhang, X. Chai, C. Wang, H. Sun, D. Zhang, W. Tian, S. Qiu, G. H. Su, Numerical investigation on startup characteristics of high temperature heat pipe for nuclear reactor, *Nuclear Engineering and Design* 378 (2021) 111180.
- [14] Q. Lu, H. Han, L. Hu, S. Chen, J. Yu, B. Ai, Preparation and testing of nickel-based superalloy/sodium heat pipe, *Heat Mass Transfer* (2017) 53: 3391-3397.
- [15] A. Faghri, M. Buchko, Y. Cao, A study of high-temperature heat pipes with multiple heat sources and sinks: part I-Experimental methodology and frozen startup profiles, *Journal of Heat Transfer*, 1991, 113: 1003-1009.
- [16] R. Ponnappan, L. I. Boehman, E. T. Mahefkey, Diffusion-controlled startup of a gas-loaded liquid-metal heat pipe, *J. Thermophysics*, 1990, 4(): 332-340.
- [17] Q. Guo, H. Guo, X. K. Yan, F. Ye, and C. F. Ma, Influence of inclination angle on the start-up performance of a sodium-potassium alloy heat pipe, *Heat Transfer Engineering*, 2017, pp. 1-9.
- [18] D. E. Glass, M. A. Merrigan, J. T. Sena and R. S. Reid, Fabrication and testing of a leading-edge-shaped heat pipe, NASA CR-98-208720, 1998.
- [19] H. Liu, W. Liu, Thermal-structural analysis of the platelet heat-pipe-cooled leading edge of hypersonic vehicle, *Acta Astronautica* 127 (2016) 13-19.
- [20] J. Townsend, J. Kerrebrock and D. Stickler, Experimental evaluation of a turbine blade with potassium evaporative cooling, *Journal of Propulsion and Power*, 2008, 24(3): 410-415.
- [21] L. Yang, R. Zhou, X. Jin, X. Ling, H. Peng, Experimental investigate on thermal properties of a novel high temperature flat heat pipe receiver in solar power tower plant, *Applied Thermal Engineering* 109 (2016) 610-618.
- [22] V. I. Tolubinsky, E. N. Shevchuk, V. D. Stambrovsky, Study of liquid-metal heat pipes characteristics at start-up and operation under gravitation, Proc. of 3rd International Heat Pipe Conference, May1978, Palo Alto, CA, USA, pp. 274-282.
- [23] H. Yang, C. Wang, D. Zhang, J. Zhang, W. Tian, S. Qiu, G. H. Su, Parameter sensitivity study on startup characteristics of high temperature potassium heat pipe, *Nuclear Engineering and Design* 392 (2022) 111754.
- [24] T. Niu, Y. Zhang, H. Hou, Y. Wang, D. He, Properties of high-temperature heat pipe and its experiment, *Acta Aeronautica et Astronautica Sinica* (in Chinese), 2016, 37(S1): 59-65.
- [25] C. Wang, L. Zhang, X. Liu, S. Tang, S. Qiu, G. H. Su, Experimental study on startup performance of high temperature potassium heat pipe at different inclination angles and input powers for nuclear reactor application, *Annals of Nuclear Energy* 136 (2020) 107051.
- [26] J. Zhao, D. Z. Yuan, D. W. Tang, Y. Y. Jiang, Heat transfer characteristics of a concentric annular high temperature heat pipe under anti-gravity conditions, *Applied Thermal Engineering* 148 (2019) 817-824.
- [27] W. Qu, B. Ai, J. Yu, Precise differential mechanism, sodium charging equipment and heat pipe performance, *Heat Pipe Science and Technology, An International Journal*, 2014, 5 (1-4): 253-259.
- [28] Z. H. Xue, W. Qu, M. H. Xie, High performance loop heat pipe with flat evaporator for energy-saving cooling system of supercomputers, *ASME Journal of Heat Transfer*, 2020 (142) 031901.
- [29] P. Yu, H. Zhang, H. Xu, Y. Shen, Restart characteristics of high-temperature sodium heat pipe, *Proceedings of the CSEE*, 2015, 35(2): 404-410.

Experimental Investigation on the influence of ambient temperature in a Loop Heat Pipe Battery Thermal Management System

Marco Bernagozzi^{1*}, Anastasios Georgoulas¹, Nicolas Miché¹, Marco Marengo¹

¹Advanced Engineering Centre, University of Brighton, Brighton, UK

*Corresponding author email address: m.bernagozzi3@brighton.ac.uk

Abstract

The authors previously proposed and successfully studied the feasibility of an innovative Battery Thermal Management System (BTMS) relying on Loop Heat Pipes (LHPs) and graphite sheets. LHPs act as thermal vector connecting the bottom of the battery pack and a remote chiller, whilst the graphite sheets allow to achieve satisfactory temperature homogenization of the cells surface, containing the added system weight. This design was developed aiming to improve on fast charge timings, all-electric range and reduce costs and complexity. Preliminary studies revealed the potential of this innovative passive BTMS of providing better performance of an active BTMS using a liquid cold plate. Moreover, a novel low-pollutant, non-toxic and non-flammable heat transfer fluid (Novec[®] 649) was tested as working fluid for the LHP. Taking another step in the direction of practical applications, the present work investigates how the proposed BTMS performs in different ambient temperatures by showing the results of several fast charge and heating tests inside an environmental thermal chamber, with temperatures ranging between -20°C to 50°C. The results showed that the LHP worked in all the tested conditions, and that, compared to without the LHP, the detrimental undesired cooling (i.e., 1.2°C) during heating phase is surpassed by the temperature reduction during cooling phases (i.e., 3.2°C).

Keywords: Battery Thermal Management; Electric Vehicle; Loop Heat Pipe; Thermal Chamber.

1. Introduction

To solve the great challenge of limiting Earth's global warming, the reduction of Green House Gases (GHG) emissions is of vital importance. This needs to be tackled from various angles, from energy production, sustainable agricultural practices, to improved remanufacturing and recycling of goods. One of the biggest strategies sought to tackle global warming, already in place nowadays, is vehicle electrification.

Electric Vehicles (EVs) bring along several challenges, one of them being the thermal management of the batteries. Temperature is in fact a critical aspect for the performance and operative life of the battery pack. It has been reported that the optimum temperature range for a Li-ion battery (being these the present standard on commercial EVs) is between 25°C and 40°C, with heavy power and capacity losses reported both at higher and lower temperatures. Therefore current EVs need a properly designed Battery Thermal Management System (BTMS), and to achieve this, different cooling technologies are employed [1]. The maximum temperature targets are 40°C for optimum performance, 50°C for acceptable performances [2] and 60°C is set as a safety threshold to prevent the occurrence of disruptive

phenomena [3] (e.g., thermal runaway).

In a previous work, the Authors developed [4] a novel BTMS based on Loop Heat Pipes (LHPs) and graphite sheets, aimed at increasing all-electric range of the vehicle and reducing cost and charging time. Moreover, the Authors employed for the first time an innovative heat transfer fluid, 3M[®] Novec[®] 649, which features extremely low ODP and GWP values, on top of not being toxic nor flammable, in this way reducing the risk posed to human safety as well as pollution [5].

The aim of this work is to investigate how the proposed BTMS performs in different ambient temperatures, taking a step further in the direction of practical application. The goal of this investigation is to understand if the LHP, being a passive device capable of only cooling, can be used also in situation where heating is necessary without being a burden to the performances. To do so, two different layouts, one with LHP and one without, are repeatedly tested inside an environmental chamber, with temperatures ranging from -20°C to 50°C. This work investigates the BTMS performance over different fast charge and heating conditions and over a bespoke driving cycle including motorway driving and fast charge.

2. Battery Thermal Management System and Design and Experimental Setup

The proposed BTMS design, illustrated in Figure 1, foresees to place an array of LHPs at the bottom of the modules forming the battery pack, acting as thermal vector transferring the excess heat from the cells to a remote chiller (part of the built-in HVAC circuit of the vehicle). Finally, graphite sheets are sandwiched in between the cells to promote cell isothermalization and prevent heat spreading from one cell to another.

This BTMS, thanks to the use of LHPs, provides very effective heat removal and allows to reduce the parasitic power consumption, compared to an active BTMS. The Authors already proved that this passive LHP-based BTMS can reduce the cells temperature by more than 3°C than a standard active liquid cold plate BTMS, during aggressive drive cycles and fast charge rates [4].

In the experimental set up, for which a schematic diagram is provided in Figure 2, the battery module is composed of dummy cells, made from 5083-O aluminium plates having the same dimensions as the considered cell type (presented in Table 1 together with the graphite sheets dimensions).

Table 1. Dimension and physical properties of aluminum plates and graphite sheets (RS PRO) used for cell dummy model.

Parameter	Aluminum	Graphite	Units
Thickness	10	0.8	mm
Height	96	96	mm
Width	280	240	mm
λ_{\parallel}	109	350	W/m·K
λ_{\perp}	109	10	W/m·K
ρ	2670	1300-1500	kg/m ³
c_p	900	810	J/kg·K

The use of dummy cells is a proven practice already used in literature that allows to minimize the risk of generating excessive thermal stress to a real battery cell, while still evaluating the efficiency of the cooling methods. The LHP was made by Professor Yury Maydanik's company THERCON, Yekaterinburg, Russia. The chosen working fluid for the copper LHP was ethanol, due to its low vapour pressure, as pressures greater than 1 bar would have posed mechanical issues to the LHP evaporator, being that made by thin copper sheets. Further details of the equipment used in the set up shown below are given in previous publications by the Authors [4].

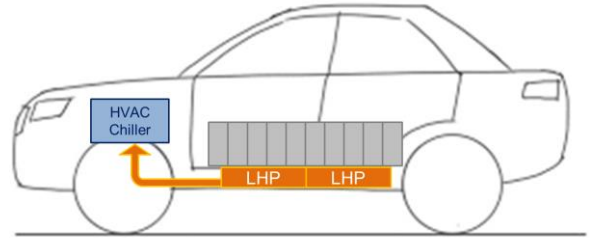


Figure 1. Illustration on the proposed BTMS design idea based on LHPs [4].

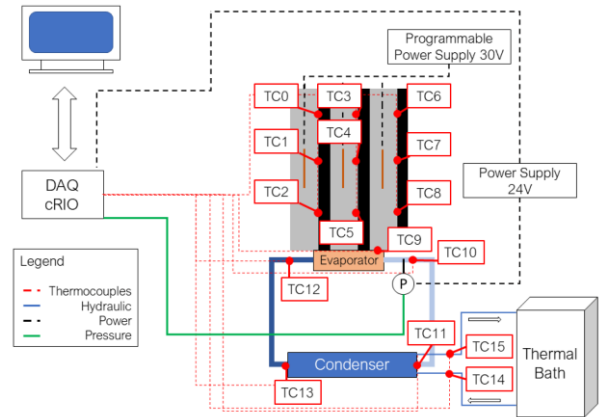


Figure 2. Experimental set up schematic [5].

The experiments are performed in a climatic chamber (TAS Ltd¹, www.tasltd.co.uk, 4.5m x 4m x 3.5m, Figure 3) capable of maintain temperatures from -40°C to 60°C with 4kW of internal load. The tests are performed in a temperature range from -20°C to 50°C, to respect the operative temperature range limitations set by some of the data acquisition instrumentation.



Figure 3. TAS Environmental Chamber at University of Brighton used for the tests presented in this work.

¹ www.tasltd.co.uk

3. Experimental Tests

This work is divided in two experimental campaigns, the first one at temperatures lower than the standard temperature reference of 20°C and the second one at higher temperatures. In the first part, the effect of the presence of the LHP during heating from lower temperatures is investigated, with a particular interest on establishing and quantifying if the LHP has a detrimental effect on the heating speed and power required to bring the battery module up to 20°C. To do so, tests are repeated heating up the battery module with and without the presence of the LHP at its bottom. The second part investigates the cooling effect of the LHP-based BTMS at high ambient temperatures, to investigate how much its performances are affected by environmental conditions. In Table 2 the proposed test sequence is presented.

Table 2. Experimental test sequence.

#	T_{amb} [°C]	LHP
1	-20	w/ LHP
2		no LHP
3	-10	w/ LHP
4		no LHP
5	0	w/ LHP
6		no LHP
7	10	w/ LHP
8		no LHP
10	20	w/ LHP
11		no LHP
12	30	w/ LHP
13		no LHP
14	40	w/ LHP
15		no LHP
16	50	w/ LHP
17		no LHP

The setting up procedure for every test was the same: the thermal chamber was set at the selected ambient temperature and the system was monitored until both the 3-cell module and the LHP reached equilibrium conditions with the ambient. Only then, the heaters were switched on and the data recording started. In other words, in every test the starting temperature of the system was equal to the set ambient temperature.

4. Heating Tests Results

Figure 4 shows the set up equipped with a heater posed on top of the cell. The heater was composed by an aluminium block with two cartridges inserts (Rotfil² heating cartridge 36 V, 120 W, 6.5x100

mm). The decision of placing the heating element at the top of the 3-cell module was taken to keep the LHP at the bottom of the module, as the central part of the investigation was not to evaluate the efficiency of this specific heating configuration with respect to others (such as a THM), but to evaluate whether the LHP would have an effect on thermal management, and ultimately quantify it. Moreover, this leaves the door open to evaluate this thermal design by performing numerical simulations in which the bottom surface of the cell module will be covered by more LHPs [6].

It was chosen to supply 100 W heating power to the cells, for a duration of 15 minutes, as this would make the module average temperature reach optimum temperature from 0°C (i.e., >25°C).

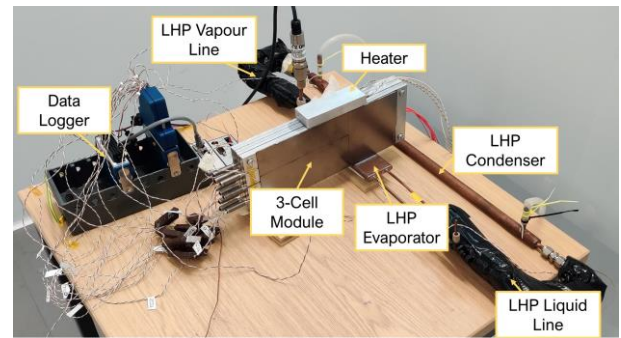


Figure 4. Set up prepared for the heating tests. The aluminum heater with embedded cartridges placed on top of the 3-cell module.

The results in Table 3 show that the presence of the LHP brings about a reduction of the temperature during the heating phase, ranging from 1 to 1.6°C, averaging 1.2°C. This is because the LHP underwent a successful start-up even at low temperatures.

The heat power released by the cells are mimicked by flexible heaters inserted in between the aluminium plates, which in turn are controlled by a programmable power supply that can replicate the trends of the heat released by the cells (as shown in Figure 2).

Figure 5 shows the results of the highest temperature test and it is evident from the trends of the evaporator and vapour lines temperatures (TC9, TC10 and TC11, respectively), that start-up took place, even with an ambient temperature of 50°C.

Table 3. Results summary of heating tests at low ambient and starting temperatures [°C]. \bar{T} stands for the average temperature of the 3 thermocouples in each cell. "Yes" is for the case with LHP, while "No" is for the case without LHP.

LHP	T_{amb}	T_{cell1}	T_{cell2}	T_{cell3}	\bar{T}
yes	-20	5.5	-2.2	-1.1	0.7
no		6.1	-0.8	0.1	1.8
Δ		0.6	1.4	1.2	1.1
yes	-10	15.0	7.4	9.0	10.5
no		15.9	9.0	9.9	11.6
Δ		0.8	1.6	1.0	1.1
yes	0	25.0	17.4	19.0	20.5
no		25.6	18.9	19.9	21.5
Δ		0.6	1.5	0.9	1.0
yes	10	35.5	27.4	28.1	30.3
no		36.1	29.5	30.3	32.0
Δ		0.6	2.1	2.2	1.6

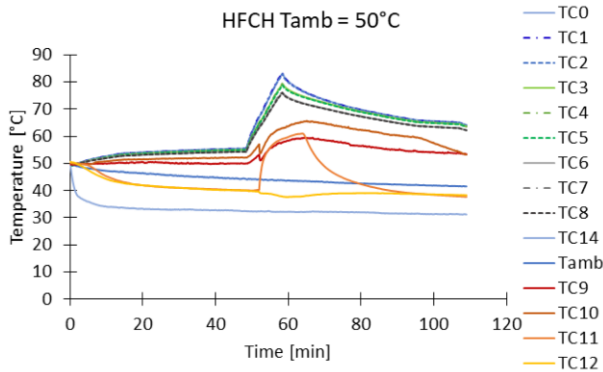


Figure 5. HFCH test results with ambient temperature of 50°C.

In fact, the sudden increase in temperature that the thermocouples see is due to the hot vapour passing through, to signify that the boiling process and fluid circulation takes place. Regarding the start-up process and how this is influenced by the ambient and starting temperature, the graph in Figure 6 shows that there is a trend between the time needed for the start up to take place and the ambient temperature, when subjecting to the same power.

It is interesting to note that the system is more reactive at higher temperatures, which is to be expected from looking at the graphs of dP/dT presented in Figure 7. Having high values of dP/dT at saturation conditions means that a small change in temperature generates a larger change in fluid pressure, augmenting the pumping capability

of the generated bubbles [9,10]. Hence, the graphs in Figure 7 explains the results in Figure 6.

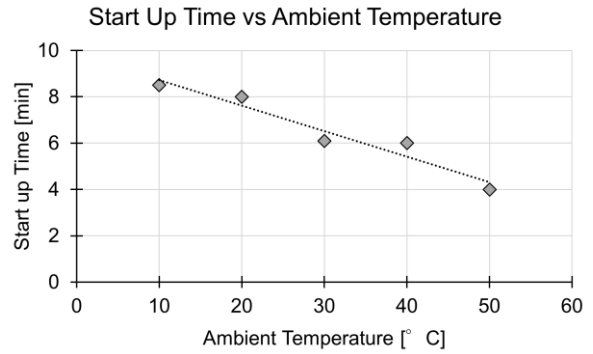


Figure 6. LHP start-up time at different ambient temperatures.

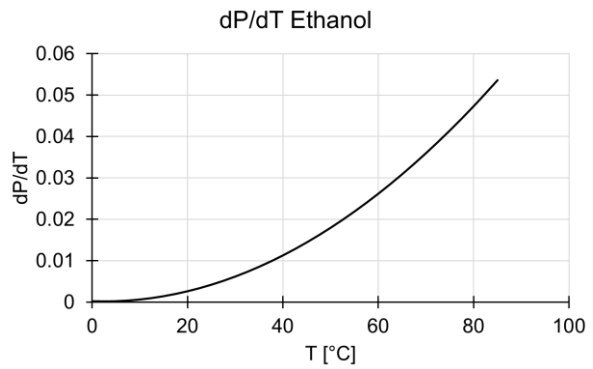


Figure 7. Trend of the derivative of the pressure over temperature (dP/dT) at saturation conditions for ethanol.

Table 4 shows the results of the HFCH tests at different ambient temperatures. Last column also shows that the difference between the maximum temperature and the ambient temperature decreases with the increase of the ambient temperature.

Table 4. HFCH driving cycle tests at different ambient temperatures. All temperatures are expressed in °C. \bar{T} is the average module temperature and ΔT is the difference between the \bar{T} and T_{amb} .

T_{amb}	T_{cell1}	T_{cell2}	T_{cell2}	\bar{T}	ΔT
10	51.2	47.6	44.6	47.8	37.8
20	59.4	55.5	52.7	55.9	35.9
30	67.4	63.5	60.7	63.9	33.9
40	75.8	71.8	69.1	72.3	32.3
50	83.2	79.2	76.3	79.6	29.6

In all cases it is evident from Table 4 that one LHP is not enough to maintain the cells

temperature below the optimum values of 40°C. However, it is enough to keep them below the acceptable and safety thresholds of 50°C and 60°C in the two first cases, respectively.

5.1. Fast Charge at 3C Tests

To appreciate the effect of the single LHP on the battery module temperature evolution during a 3C test, 8 tests were performed at 4 different temperatures (20 °C, 30 °C, 40 °C, 50 °C) with and without the LHP presence. A 3C fast charge will bring the battery SOC from 20% to 80% in 12 minutes. Results are shown in Table 5 and visually in Figure 8.

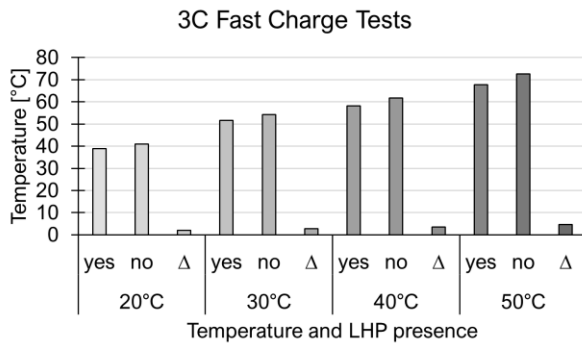


Figure 8. Results of the 3C Fast Charge Tests, in which the battery module' average temperature is compared between cases with or without the LHP, and the relative difference is highlighted. "Yes" is for the case with LHP, while "No" is for the case without LHP.

Table 5. Results from the 3C fast charge tests at high temperatures. The table shows the cells maximum temperatures [°C] after fast charge. \bar{T} stands for average temperature. "Yes" is for the case with LHP, while "No" is for the case without LHP.

LHP	T_{amb}	T_{cell1}	T_{cell2}	T_{cell3}	\bar{T}
yes	20	40.7	39.2	37.1	39.0
no		42.9	41.2	39.0	41.0
Δ		2.2	2.1	1.9	2.0
yes	30	53.6	51.7	49.3	51.5
no		56.6	54.2	52.1	54.3
Δ		3.0	2.5	2.8	2.7
yes	40	60.0	58.3	56.2	58.2
no		63.7	61.8	59.5	61.7
Δ		3.7	3.6	3.2	3.5
yes	50	69.7	67.9	65.8	67.8
no		74.7	72.6	70.2	72.5
Δ		4.9	4.8	4.4	4.7

Especially looking at the temperature reduction that the LHP brings compared to the free convection, this Δ value increases with the increase of the ambient temperature.

The potential effect of the LHP presence will be fully evaluated only via numerical simulations, in which the coverage of the module footprint will be increased as in the practical applications. In fact, in the design/configuration utilised in this work, only the 17% of the bottom of the module is in contact with the active zone of the LHP evaporator, hence representing an important limitation to the maximum transmissible heat (as a function of the heat exchange surface).

5. Discussion

The LHP demonstrated to be able to work in all conditions, vouching for its applications flexibility. It was already known from previous works by the Authors that this specific evaporator design is not the best suited for the considered battery module geometry. However, it was proven that increasing the size of the evaporator [4] or the number of the evaporators [6] allowed for exceptional thermal performances (i.e. temperature in optimum range even at high fast charge cycles). Despite the non-optimal temperatures reached by the cells during the different experiments at high ambient temperatures, this works therefore extends the premise of the LHP application to BTMS, suggesting that this technology can produce good results in a wide range of temperatures, effectively encouraging its adoption in the automotive world.

Figure 9 compares the temperature difference between cases with and without the LHP, during both heating and cooling tests. Since the extra unwanted cooling provided by the LHP is not beneficial during the heating phase, for clarity purposes it is reported with a negative sign on the graph. In this way, the y axis in Figure 9 represents the beneficial effect of the single LHP applied to the 3-cell battery module, compared to free convection only. It shows that during heating phases ΔT is not dependant on the ambient temperature, and that the LHP presence delays the heating process by 1°C. On other hand, during the cooling phase, the LHP does affect the module's temperature, incrementally with the ambient temperature, reaching almost 5°C of difference during the tests at 50°C. It is also intuitive looking at the red and blue areas in the graph in Figure 9 that the advantages provided by the LHP-based

BTMS during cooling largely outweighs the decrease in performance during heating.

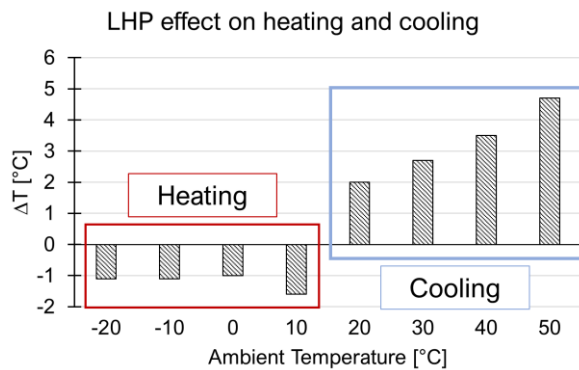


Figure 9. Effect of the LHP presence on the heating and cooling processes. The ΔT value for the heating is represented with a negative sign to signify it is not a positive outcome.

6. Conclusions

In this work, the operation of a LHP-based BTMS was investigated at different ambient temperatures, from -20°C to 50°C , by means of an environmental chamber. The main purpose of this study was to evaluate the effect of the LHP presence during heating and cooling scenarios. Particularly, to understand how much the heating phase would be delayed by the presence of the LHP, and if so, how would this handicap compare to the advantages provided by the device during cooling operations at high temperatures. Several tests were repeated with and without the LHP at the bottom of a 3-cell dummy battery module.

During the heating tests, 100 W were supplied to the module for 15 minutes. For the cooling tests, firstly the conditions of a thermally demanding driving cycle with highway driving and fast charge (HFCH) were replicated, and secondly a 3C fast charge cycle was tested. Each condition was tested at different ambient temperatures: -20°C to 10°C for heating, 20°C to 50°C for cooling. The chosen fluid for the LHP was ethanol.

The main conclusions that can be drawn from the results are:

1. LHP start-up took place at each ambient temperature case; this result advocates for the operational adaptability of this device.
2. During heating, the battery module presents a temperature 1.2°C lower when heated up with the LHP at its bottom, compared to being heated without the LHP; however, this effect seems to be insensitive to the ambient temperature.

3. During the HFCH driving cycle tests, module temperatures were above the safety threshold of 60°C when ambient temperature exceeded 301°C , due to the low heat transfer areas between the two bodies.
4. A qualitative trend emerged between start-up time and ambient temperature, indicating that start-up takes place quicker at higher temperatures; this suggests that a LHP-based BTMS would be naturally quicker to react at higher temperatures, which is a desirable feature.
5. Despite the small dimensions of the LHP active zone, it still provided considerable reduction to the maximum average temperature of the module, from 2°C to 4.7°C lower temperatures than free convection only.
6. Comparing the effect on heating and cooling, the advantage provided by the LHP-based BTMS during cooling clearly outweighs the decrease in performance during heating.

Finally, the results presented herein aim to be foundation to further work in evaluating the feasibility of this LHP-based BTMS idea, in order to go in the direction of an industrial application. Further developments of this study are the investigation of how a design with more LHPs or a larger active LHP evaporator zone affects the module temperature both at heating and cooling phases. In fact, next steps foresee a further validation of the numerical model already developed by the Authors, obtained by matching the results at different ambient temperatures. Following, alternative geometries increasing the heat transfer area between the LHP and the bottom of the battery module will be used in simulations with the same boundary conditions of the tests presented in this work.

Acknowledgments

The Authors would like to thank the Advanced Engineering Centre at the University of Brighton for the access to the environmental chamber and for the economic support obtained to participate to the IHPC conference. The Authors would also like Professor Maydanik for the LHP evaporator and support.

References

- [1] X. Zhang, Z. Li, L. Luo, Y. Fan, Z. Du, A review on thermal management of lithium-ion batteries for electric vehicles, *Energy*. 238 (2022) 121652. doi:10.1016/j.energy.2021.121652.
- [2] P. Qin, M. Liao, D. Zhang, Y. Liu, J. Sun, Q.

Wang, Experimental and numerical study on a novel hybrid battery thermal management system integrated forced-air convection and phase change material, *Energy Convers. Manag.* 195 (2019) 1371–1381. doi:10.1016/j.enconman.2019.05.084.

[3] P.R. Tete, M.M. Gupta, S.S. Joshi, Developments in battery thermal management systems for electric vehicles: A technical review, *J. Energy Storage.* 35 (2021) 102255. doi:10.1016/j.est.2021.102255.

[4] M. Bernagozzi, A. Georgoulas, N. Miché, C. Rouaud, M. Marengo, Novel battery thermal management system for electric vehicles with a loop heat pipe and graphite sheet inserts, *Appl. Therm. Eng.* 194 (2021). doi:10.1016/j.applthermaleng.2021.117061.

[5] M. Bernagozzi, N. Miché, A. Georgoulas, C. Rouaud, M. Marengo, Performance of an Environmentally Friendly Alternative Fluid in a Loop Heat Pipe-Based Battery Thermal Management System, *Energies.* 14 (2021) 7738. doi:https://doi.org/10.3390/en14227738.

[6] M. Bernagozzi, A. Georgoulas, N. Miché, C. Rouaud, M. Marengo, Comparison Between Different Battery Thermal Management Systems During Fast Charge Cycles, in: *17th UK Heat Transf. Conf.*, Manchester, UK, 2021: pp. 4–6.

[7] A. Tomaszewska, Z. Chu, X. Feng, S. O’Kane, X. Liu, J. Chen, C. Ji, E. Endler, R. Li, L. Liu, Y. Li, S. Zheng, S. Vetterlein, M. Gao, J. Du, M. Parkes, M. Ouyang, M. Marinescu, G. Offer, B. Wu, Lithium-ion battery fast charging: A review, *ETransportation.* 1 (2019) 100011. doi:10.1016/j.etrans.2019.100011.

[8] S. Kim, T.R. Tanim, E.J. Dufek, D. Scofield, T.D. Pennington, K.L. Gering, A.M. Colclasure, W. Mai, A. Meintz, J. Bennett, Projecting Recent Advancements in Battery Technology to Next-Generation Electric Vehicles, *Energy Technol.* 10 (2022). doi:10.1002/ente.202200303.

[9] S. Khandekar, N. Dollinger, M. Groll, Understanding operational regimes of closed loop pulsating heat pipes: an experimental study, *Appl. Therm. Eng.* 23 (2003) 707–719. doi:10.1016/S1359-4311(02)00237-5.

[10] Y.F. Maydanik, Loop heat pipes, *Appl. Therm. Eng.* 25 (2005) 635–657. doi:10.1016/j.applthermaleng.2004.07.010.

Capillary Jet Loop in direct contact condensation mode used to perform ice protection function of a turboprop composite nacelle intake.

Vincent Dupont^{1*}, Flavio Accorinti¹, Maxime Henno², Patricia Susana Serrano Perez³, and Francisco Redondo Carracedo³.

¹ Calyos, Charleroi, Belgium

² SONACA, Gosselie, Belgium

³ Airbus Defence and Space, Getafe, Madrid

*Corresponding author email address: vincent.dupont@calyos-tm.com

Abstract

In this experimental study a Capillary Jet Loop architecture (CJL-dcc) is proposed to transport the heat from a hot liquid (oil) as heat source to a composite material as coolant surface that is part of the nacelle in a turboprop transport aircraft (as used for Regional and Business Aviation). The application has dual usage, firstly ice protection in cold conditions and cooling of the oil in all conditions. The reduced scale demonstrator tested is a combination of a single capillary loop with a two-phase transport ring (TPR). The ring provides the liquid to the capillary structure and the capillary evaporator induces vapor jets thanks to four injector elements in parallel. The momentum exchange between the high velocity acetone vapor flows and the low velocity of the subcooled liquid ensures both transport and condensation functions before the connecting lines. This paper discusses the design, material and experimental performances of this demonstrator able to transfer 1.24 kW from a 90 x 90 mm² footprint heater. Two different cold sources are investigated with the same injector system and the results are discussed; a tube-in-tube ethylene-glycol water cooled (RS-0/1 demonstrator) and a carbon fiber composite panel (CFRP) with direct melting of an ice volume (RS-2C demonstrator).

Keywords: Anti-icing; Ice protection; Direct Contact Condensation; Injector; Capillary Thermosyphon; Capillary Jet Loop.

1. Introduction

Today, there are numerous heat sources in the nacelles needing to evacuate heat by using heat exchangers typically cooled by external air, inducing additional drag, and making the energy management inefficient. More complexity and weight are added by actuators necessary to control the external air flow.

reduced, resulting in an increased efficiency compared to traditional designs [1].

Two-phase capillary heat transport technologies can be used to recover waste energy from aircraft (sub) systems and/or components. Loop Heat Pipe Ice Protection System have been proposed and successfully tested on several projects [2] but suffer two main limitations. The first one is due to the presence of vapor and liquid in the transport line that makes the system sensitive to the acceleration forces and limits the transport distance and/or the use of ammonia as a working fluid (large latent heat and surface tension). Moreover, if for any reason the design acceleration is exceeded, the capillary evaporator deprimed and the hot source must be cut off before any new heat application, therefore limiting the operability of the aircraft. The second key point is to ensure uniform heat distribution regardless the combination of aircraft attitude, available power, and local acceleration. With parallel connections (embedded tubes inside the CFRP) additional pressure drops are introduced to successfully distribute the flow. But the two-phase pressure gradient is strongly dependent on the vapor quality and the hydrostatic head between channels that make condenser sizing difficult. To overcome these difficulties, the CJL-dcc, patented by Euro Heat Pipes S.A. in Belgium [3], transforms a two-phase flow into a single-phase system [4] to [7].

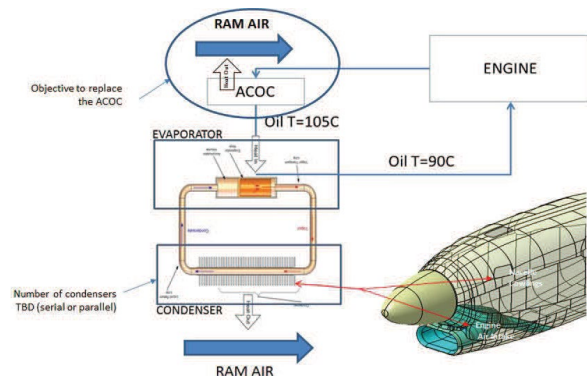


Figure 1. Passive heat recovery concept [1].

For example, the size of traditional heat exchangers could be reduced by extracting part (or all) the heat from the oil used to cool down the engine or the electrical generator and driving it to the nacelle cowlings and/or surfaces where heating is required i.e., ice protected surfaces like engine air intake. In consequence, the nacelle weight and the ram-air required for cooling purposes will also be

2. Direct contact condensation with a Capillary Jet Loop (CJL-dcc)

The working principle of the CJL-dcc is presented in the Figure 2 and is described in detail in [3]. This system is a jet pump driven by the vapor flow generated by one or more capillary evaporator. This architecture creates a convenient “thermal bus” and each injector point (10) creates a two-phase flow that can be used to cool or to heat an additional payload (Q_{HL2}). The momentum exchange between the vapor and the TPR flow induces the fluid motion inside the TPR thanks to the injector elements. The key point of the design in the direct condensation mode is to ensure the complete condensation before reaching the transport line to avoid the presence of vapor at the subcooler inlet and its effects when the TPR is subjected to accelerations.

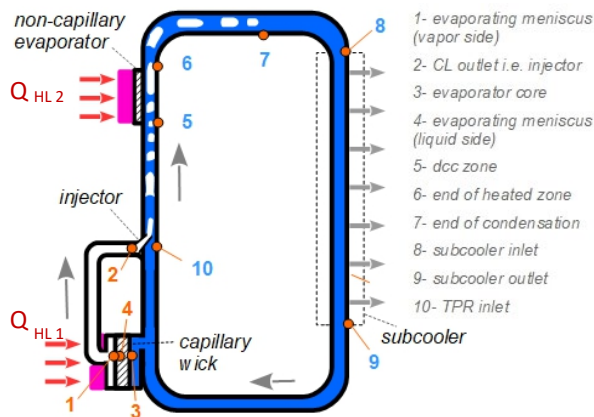


Figure 2. working principle of the CJL-dcc architecture.

3. BISANCE « reduced scale » demonstrator

Due to the advantages mentioned above, the CJL-dcc has been chosen during the preliminary design phase of the BISANCE Cleansky2 project [1] despite a low TRL risk. Based on the Airbus Defence & Space specifications, Calyos and SONACA worked on a collaborative way to propose a full-scale demonstrator design that will be tested in real environment simulator representative of flight dry and icing conditions (RTA Icing Wind Tunnel).

The physics of both hydrodynamics of injection efficiency and in-tube direct condensation heat transfer are poorly documented in the literature, a reduced scale model (TRL-4) is tested to mitigate the design risk and validate the carbon fiber panel manufacturing by SONACA, Belgium. Figure 3 to 5 presents two designs of subcooler tested with acetone as working fluid. The capillary evaporator is a standard Calyos component developed for SiC

power electronic cooling. All the parts of the CJL were made with stainless steel except one copper evaporator wall and the aluminum “-dcc box”.

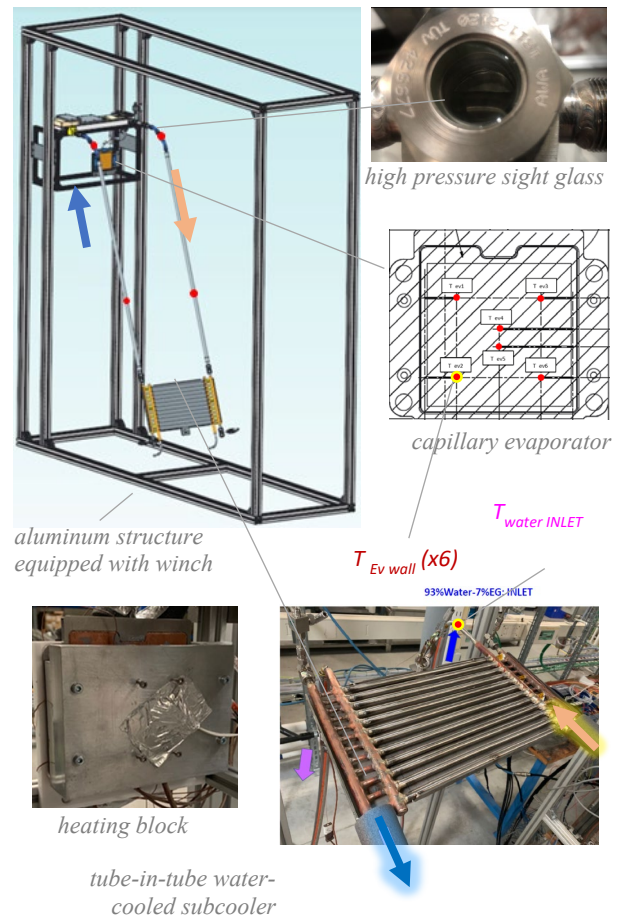


Figure 3. RS-0/1 – overview of the demonstrator equipped with 12 tubes water cooled subcooler.

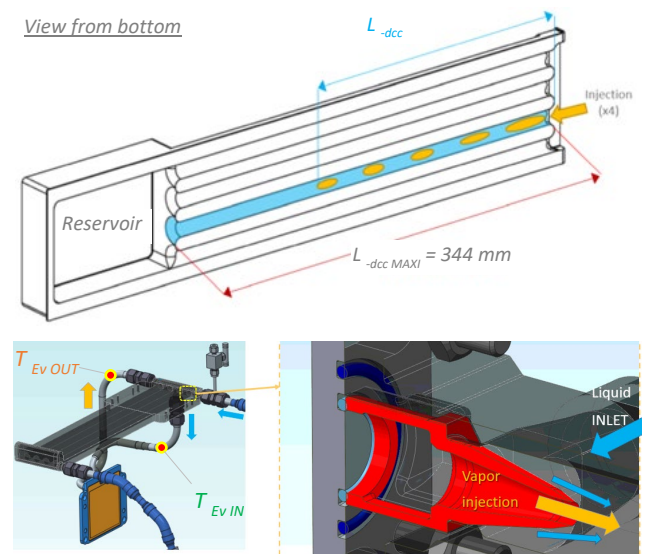


Figure 4. the 3 mm “in-line injector” of the CJL “-dcc box” equipped with four 12mm “-dcc tube”.

The capillary loop and the “-dcc box” are the same for RS-0/1 and RS-2C. Thanks to Swagelok connectors, the sight glass, the lines and the subcoolers can be changed to switch from a version to another. Flexibles part are located on the lines to allow relative movement (cf. Figure 14) and to facilitate integration.

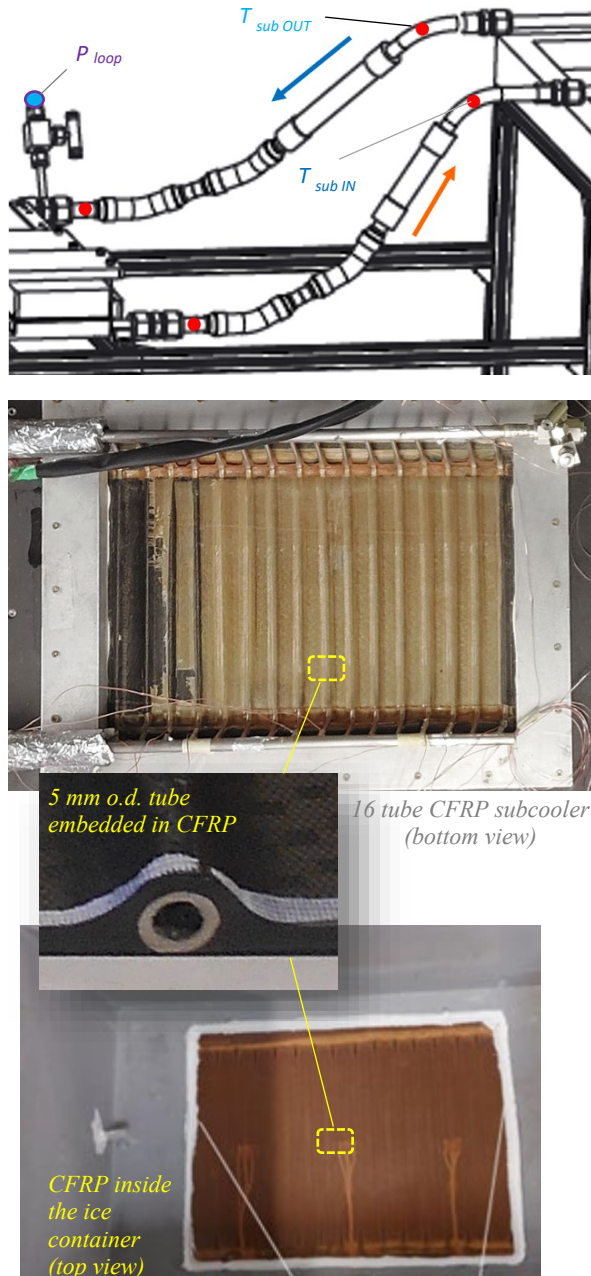


Figure 5. RS-2C – overview of the demonstrator equipped with the 16-tubes CFRP subcooler.

The evaporator performances are evaluated from the temperatures measured, inside the 5 mm thickness wall. The temperature of the 6 thermocouples (TC1 to 6) - bonded inside a 1.2 mm width groove - are averaged to determine T_{Ev}

with an uncertainty of $\pm 0.3K$. The other thermocouples are located outside the tube of the system. The absolute system pressure is measured at the inlet of the “-dcc box” (cf Figure 5) with an absolute pressure transducer Keller PAA-33X, 0-10 bars pressure transducer with an accuracy of 0.10% EM i.e. ± 10 mbar, on the measurement range. This pressure is used to determine the saturation temperature $T_{sat}(P_{loop})$ from the NIST Refprop data for acetone. The heating element is an aluminum block equipped with two heating cartridges that replace the oil heat transfer box (OHTB) used on the full-scale demonstrator. The contact area (thermal grease) is $90 \times 90 \text{ mm}^2$ i.e. $1'460 \text{ W}$ gives 18 W/cm^2 . The energy balance is much easier with an electrical power supply unit but, at contrary there is no decrease of the power with the increase of the saturation condition inside the CJL. The data acquisition device is a standard Agilent 3472A connected to a PC via an Ethernet connection and a LabVIEW interface.

4. RS-0/1 temperature evolution

The RS-0/1 subcooler is based on twelve $7 \times 0.25 \text{ mm}$ copper inner grooved tube (IGT) with a pitch of 22mm. The IGT active length is 360mm and the 14.0mm internal diameter stainless steel manifold (distributor or collector) include a 19.0mm extra length before Swagelok union. A 0.5mm thick annular counterflow is created around each IGT with massflow of 29.2L/min (Water93%-EG7%) and the maximum coolant temperature difference is lower than 0.7K. Figure 6 gives the typical evolutions of the system for 12 hours test with a 143mm favorable tilt identical to the RS-2C setup.

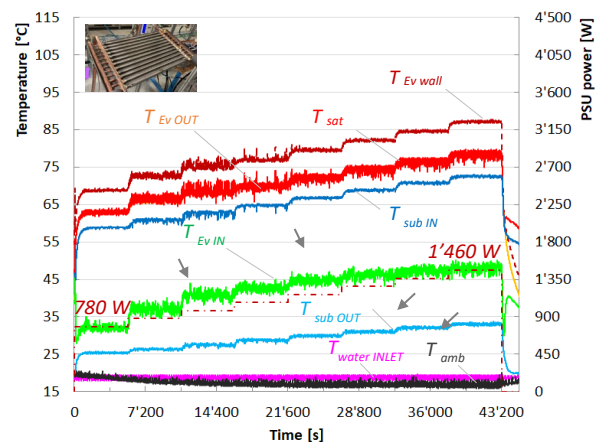


Figure 6. RS-0/1, evolution of the CJL with a favourable tilt $h = +143 \text{ mm}$.

Some instabilities can be observed around 1kW probably linked to the condensation regime inside

the “-dcc tubes” (cf. Figure 4). The corresponding thermal resistances are analysed in §6.3.

5. Test results for RS-2C demonstrator

The RS-2C subcooler is based on 16 stainless-steel smooth tubes (5x0.5 mm) with a pitch of 25 mm. The active length is 230 mm and the 10.0mm internal diameter stainless steel manifold (distributor or collector) includes a 78.0 mm extra length before Swagelok union. Half part of the external tubes #1 and #16 are under the silicone sealant (cf. Figure 5) i.e. only 15 tubes are active.

5.1. Molten ice-based energy balance

The ice container is equipped with a water drain located a few centimeters above the level of the composite panel. After a certain time, the water flows by gravity inside a large container located on a Kern DS 30K0.1 industrial scale with an uncertainty of +/- 0.1 gram. Figure 7 shows the measured liquid water mass versus time with the origin corresponding to the first mass measurement. Two phenomena disturb the measurement. First the large ice cubes stick together, and the operator must separate these ice bridges at regular intervals which gives the irregularities on the temperature evolutions on Figures 8). Second, the inlet of the drain is often closed by a floating ice block.

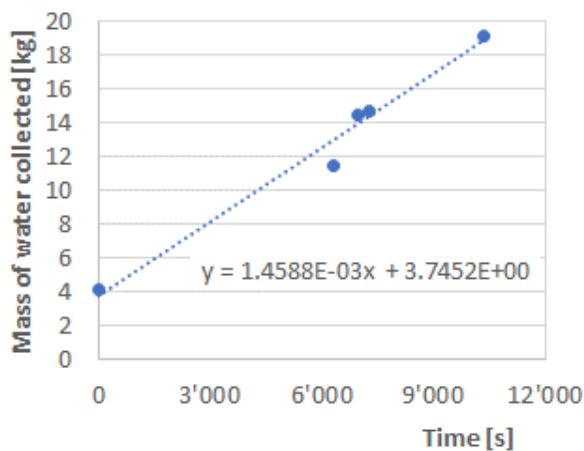


Figure 7. Top: ice grade used during the RS-2C tests. Left: “small” crushed, right: “large” cubes. Bottom: water weight measurement for RUN #2.

The evolution is quasilinear with a melting rate of 1,456 g/s which gives, through an enthalpy balance, a sensible heat power of 52.3W to heat up the ice cubes from -18°C to 0°C (average specific heat of 1'992 J/kg.K) and a fusion power of 486.6W (latent heat of fusion of 333'550J/kg). In total the power estimated from the weight of water is 539W while the average electrical power calculated based on the recordings gives 544W. Thus, the energy balance is respected to within 1% and allows to consider the use of this method at full scale demonstrator level when the heat is extracted from the oil with OHTB's. In this case, the energy balance is more complex in particular because of the variable hydraulic power from the oil pump.

5.2 RS-2C temperature evolution

The ice used can be flakes (ice small) or cylinders of diameter 25 mm and 50 mm in length (ice large). The ice is stored during several days at -18°C before testing and 24kg per run are necessary.

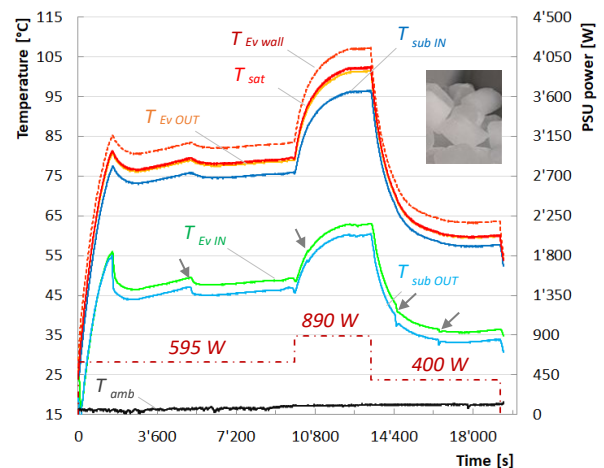


Figure 8. RS-2C, evolution of the CJL temperature during RUN#2 (maximum power).

5.3 Subcooler misdistribution analysis

Figure 9a shows the evolution of the temperature at the outlet of the 16 subcooler tubes (between the CFRP and the collector manifold) as a function of tube position. Tube #0 is T sub IN, tube #17 is T sub OUT and tube #18 is the average value over the 16 outlets. It is demonstrated in §6.3 that for the higher value of massflow the flow remains laminar in the subcooler tubes. In laminar flow, the heat transfer is constant and the measurement of the temperature gradient from inlet to outlet is an indirect measurement of the massflow distribution among the parallel tubes. Figure 9b shows that mass flow varies between -17% and +52% among the 16 subcooler tubes of

the CFRP panel. Better sharing can be obtained with an increase of pressure losses and manufacturing cost of the subcooler with a variable section of the manifolds. Despite a 52% “over massflow” on #2 the corresponding extracted power is only 7.5% above the average. The average value is few degrees below the measured temperature after the collector manifold. This can be explained by the measurement outside the wall (is not exactly the average liquid value). The constant heat transfer coefficient is a too simple assumption and entrance effect and Dean vortices induced by the bends should be considered.

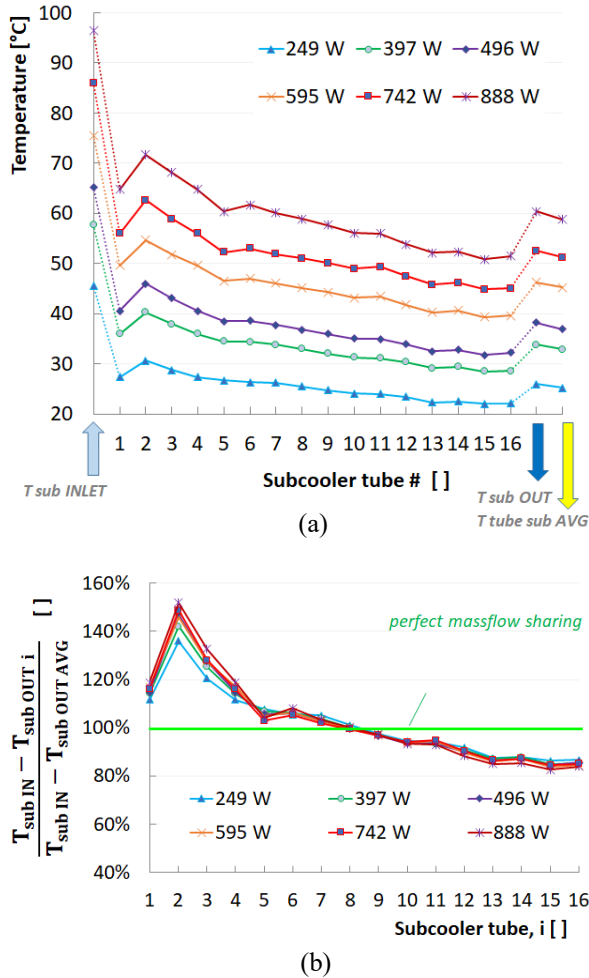


Figure 9. Massflow misdistribution estimation inside the RS-2 composite subcooler: (a) temperature along the manifold for various heat load, (b) deviation from the mean based on the temperature variation of each tube.

6. Performances analysis

6.1. Entrainment ratio γ evaluation

Figure 10 defines the various massflow inside the architecture. One can notice that for a standard LHP

(or CPL) there is no additional massflow i.e. $\gamma = 1$ (cf. equation 1) inside the TPR.

The relation proposed in [4] for standard in tube condensation is completed and adapted to -dcc mode where the fluid is subcooled at $T_{sub\ IN}$. Considering the subcooling before vaporization, the capillary evaporator enthalpy balance is:

$$Q_{HL} - Q_{losses} = \dot{m}_{vap} (\Delta h_{LV} + C_{pL}(T_{sat} - T_{sub\ OUT})) \quad (1)$$

where Δh_{LV} refers to the latent heat of vaporization evaluated at saturation, C_{pL} the specific heat of the liquid evaluated at subcooler outlet temperature, $T_{sub\ OUT}$. The entrainment ratio γ is the total massflow inside the TPR divided by the vaporized one:

$$\dot{m}_{TPR} = \gamma \dot{m}_{vap} = \dot{m}_{vap} + \dot{m}_{add} \quad (2)$$

The subcooler reject the transferred power by sensible heat variation:

$$Q_{HL} - Q_{losses} = \gamma \dot{m}_{vap} (C_{pL}(T_{sub\ IN} - T_{sub\ OUT})) \quad (3)$$

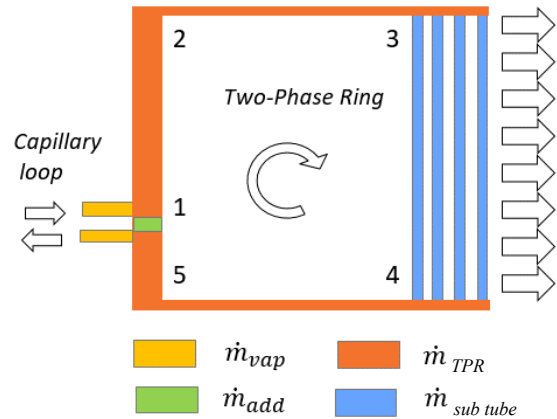


Figure 10. definition of the massflow inside the main hydraulic zones of the CJL-dcc architecture.

Dividing equation 1 by equation 3 gives the relation to evaluate the minimum entrainment ratio (necessary to achieve the -dcc mode) from the measurement of the liquid temperature at inlet (i) and at outlet of a subcooler (ii) and the saturation temperature (iii).

$$\gamma_{-dcc\ min} = \frac{\Delta h_{LV} + C_{pL}(T_{sat} - T_{sub\ OUT})}{C_{pL} \Delta T_{sub\ coller}} \quad (4)$$

This value is a thermal constraint mandatory to achieve the complete condensation within the subcooled 344 mm length tubes located before the reservoir, but a higher value can be reached inside

the TPR depending on the hydraulic performances of the TPR. It is possible to simplify equation 4 by considering an ideal system where the subcooler inlet is at saturation:

$$\gamma_{-dcc\ min} \approx \frac{\Delta h_{LV}}{C_{pL} \Delta T_{subcooler}} + 1 \quad (5)$$

Equation 4 is used to plot γ versus the power in Figure 11 where the heat losses are estimated to 15% and 1% respectively for the water and the ice container tests. Due to the presence of liquid water in contact with the CFRP, no impact of the type of ice (large or small) has been noticed. The TPR massflow results from the balance between pressure drops and motor terms i.e. injectors momentum and buoyancy forces. Despite a significant difference in the hydraulic network of the RS-0/1 and RS-2C it seems that the two curves overlap perfectly. In subsection 6.3, one can see that the thermal performances of the two types of subcooler, with IGT or smooth tubes, are close. Thus, the overlap of the two curves is more induced by design effect than a general trend but γ seems more driven by the thermal performances than the hydraulic ones. A non-intrusive flowmeter should be used to confirm this analysis.

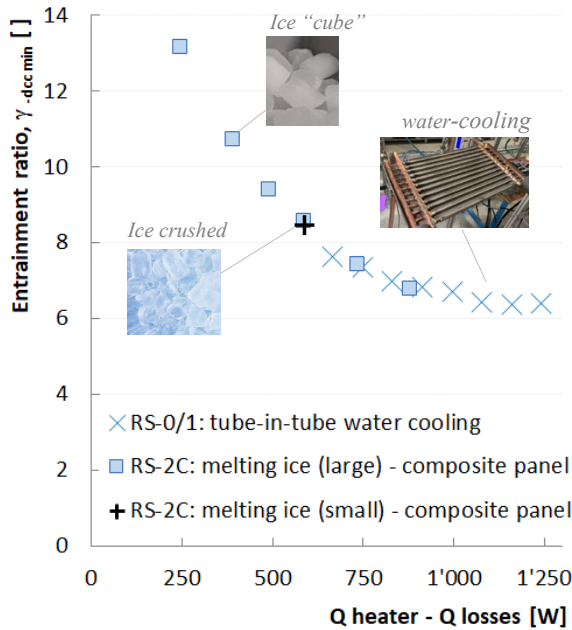


Figure 11. minimum entrainment ratio $\gamma_{-dcc\ min}$ versus power for the two version of the RS-demonstrator. γ is determined from equation 4.

Based on the evaluation of the entrainment ratio γ and the flow distribution over the 16 tubes presented respectively §6.1. and §5.3 it is possible to calculate the liquid velocity of each tube. In our subcooler configuration the maximum mass flow reaches

0.83g/s at tube #2 i.e. the maximum Reynolds number of the inlet of the subcooler tube remains very low, below 15.1, over the entire dataset with melting ice condition which confirms the laminar flow assumption inside the tube 4.0 mm internal diameter smooth tube. In established laminar condition the heat transfer coefficient is independent of the internal massflow ($Nu=3.66$ for constant temperature boundary condition). Thus, it is a simple justification of the massflow distribution presented in §5.3. In fact, the situation is more complex and entrance effect and Dean vortices induced by the bend should be considered.

6.2. Thermal resistance of the CFRP

The initial goal of the Clean Sky 2 call [1] was to investigate the feasibility and the thermal performance of the carbon fiber panel equipped with embedded hydraulic network. SONACA has developed the Bisance subcooler in collaboration with Calyos to magnify the thermal performances at reasonable cost and weight. In particular, the manufacturing constraint impose limitations in terms of tube diameter, material and pitch.

Calyos performed 2D simulations of the SONACA CFRP stacking. The thermal conductivity of the CFRP is 0.4 W/m.K transverse and 15 W/m.K in-plane. The stainless-steel tube, the adhesive and the bronze mesh are at, respectively, 16, 0.2 and 42 W/m.K. The number and the thicknesses of the various layers are SONACA proprietary information's and cannot be disclosed in the present communication. Figure 12 gives a view of the complex conductivity field due to the specific shape of the CFRP fabric.

The freeFEM++ open-source software has been used with a structured mesh approach with a typical cell size of 0.1 mm. The main result of these calculations is that the transmittance value of the CFRP including the 5x0.5mm stainless steel tube is estimated to 162 W/m²K (with respect to the external panel area) and is not sensitive to the value of internal heat transfer coefficient.

This transmittance can be used to determine the local heat transferred to the ice along each subcooler tube. Due to the fin efficiency effect of the stacking, the heat flux is 67% higher in front of the tube in comparison to the center of the pitch (Figure 12). Considering an area of 900 cm² in contact with the ice (15 tubes) the conductive thermal resistance is 68.6 K/kW. It is a rough approximation because it does not consider the variation of the liquid temperature inside the subcooler (a log min temperature approach should be used for example).

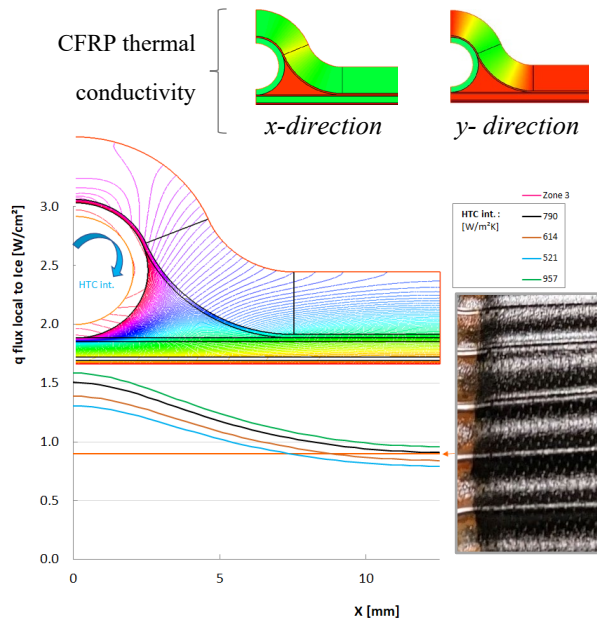


Figure 12. 2D simulations of the elementary section for the composite stacking. The heat flux versus position is given for various internal heat transfer coefficient with $T_{\text{fluid}} = 100^{\circ}\text{C}$ and $T_{\text{ext. panel}} = 0^{\circ}\text{C}$ (melting ice condition).

6.3. Thermal resistance synthesis

Figure 13 shows the evolution of the various thermal resistances inside the system from the evaporation copper wall to the coolant inlet flow.

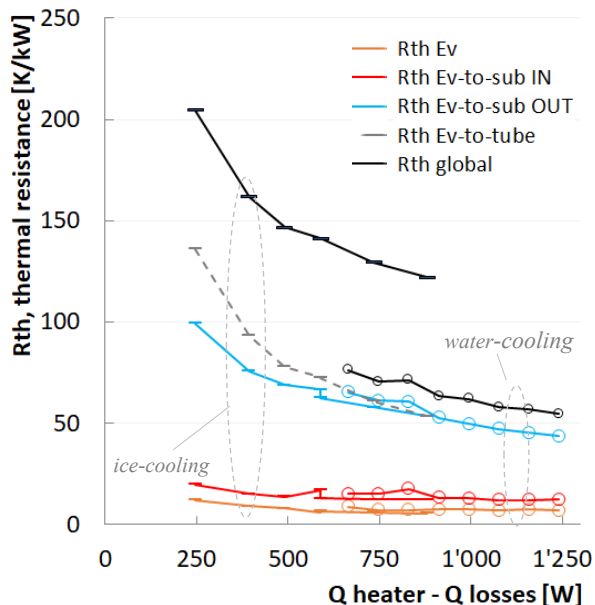


Figure 13. Thermal resistance sharing during the tube-in-tube water cooling and ice container tests.

The sum of the vaporization and the direct contact condensation thermal resistances is lower than 17 K/kW i.e. from 20 to 25% of the total

thermal resistance for the tube-in-tube water cooling and from 9 to 12% for the melting ice on CFRP. The condensation takes place inside 344 mm long 12mm i.d. “-dcc tubes” located directly after the 4 injectors. By design the vapor is not allowed to flow to the subcooler. This type of condensation is efficient, and the number of injectors in parallel can be scaled up to address higher heat load values.

The efficiency of the subcooler tubes is the bottle neck of the RS-2C water-cooled version and because the flow remains laminar multiport approach must be privileged.

The transmittance of the CFRP induces an additional thermal resistance of the same order than the liquid heat transfer coefficient and clearly limits the transferred power in the RS-0/1 configuration.

Thus, it is not yet possible to use the tested panel for anti-icing purpose. Improvements are necessary to decrease the necessary minimum oil temperature. It is possible to gain 15% of exchange surface by reducing the thickness of stainless-steel tubes and / or by splitting the flow with a multiport approach

6.4. Tilt impact

Figure 14 shows the impact of the tilt on the TPR entrainment ratio evaluated from equation 4 and also the buoyancy pressure induced by the liquid density difference between the “hot” riser and the “cold” downcomer at 1'271 W.

The entrainment ratio γ inside the TPR decreases with the heat load and ranges from 6.4 to 13.1 in the present conditions. Increasing the heat load induces an increase of the saturation condition (cf. Figure 6 and 8) that leads to lower velocity at injector outlet. Thus, the contribution of the injector is too low at high temperature with respect to the buoyancy forces and it is necessary to operate lower saturation condition and/or to adapt the section of the injector.

CFD simulation work is underway to increase γ parameter value through an optimization of the injector zone and is presented in a sister paper [8].

4. Conclusions and perspectives

The tests carried out on this demonstrator made prove that it is possible to functionalize carbon fiber panels (CFRP) by including metal tubes to evacuate heat from a passive two-phase loop and to perform anti-icing function.

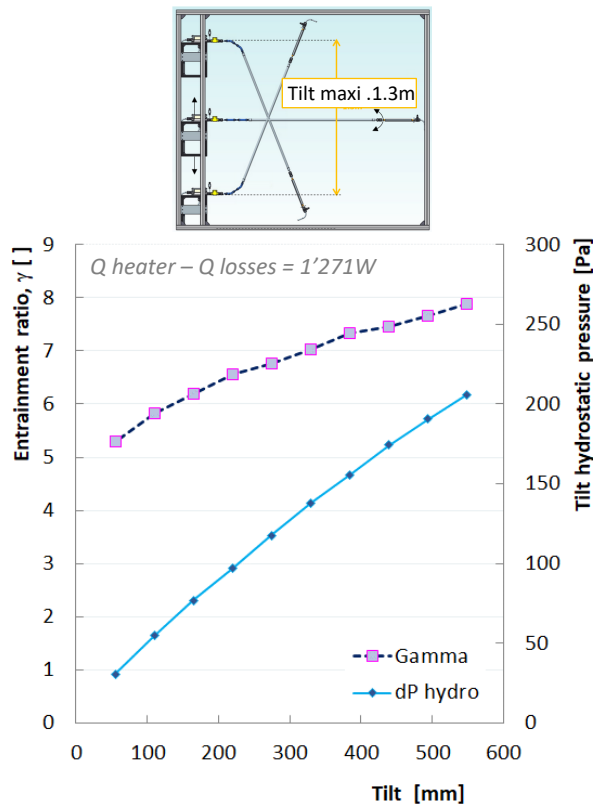


Figure 14. Influence of the location of the subcooler position with respect to the injectors.

During the trade-off phase the direct condensation Capillary Jet Loop appear to be the most promising technology. The main advantages are a better resistance to accelerations and ease of distribution of the liquid flow on a complex volumetric heat exchanger like a turbomachine air intake.

The system was tested by melting a volume of ice to mimic the final demonstrator configuration and its operating range has been extended thanks to a tube-in-tube water exchanger but keeping the thermal performance equivalent to that of the CFRP subcooler.

It has been shown that the Capillary evaporator equipped with 4 injectors can transport 1.46 kW in the full-size demonstrator conditions. The condensation takes place inside 344 mm long “-dcc tubes” located directly after the 4 injectors. By design of the “-dcc box” the vapor cannot flow to the subcooler. The part of vaporization and condensation contribution to thermal resistance ranges from 20 to 25% for the tube-in-tube water cooling and from 9 to 12% for the melting ice on CFRP.

The constraints of the CFRP manufacturing process as well as the thermomechanical limits

dictated the diameter, the material and the pitch of the integrated tubes limiting the transmittance to 160 W/m.K.

TRL 4 level is reached with this reduced scale demonstrator and TRL-5 tests on the full size prototype are scheduled in the RTA main Icing Wind Tunnel in Vienna (Austria) for the second week of February 2023.

Acknowledgement

The Bisance project has received funding from the Clean Sky 2 Joint Undertaking under the European Union’s Horizon 2020 research and innovation programme under grant agreement No 865113. This publication reflects only the author’s views, and the JU is not responsible for any use that may be made of the information it contains.

References

- [1] Biphasic Heat Transport Integration for Efficient Heat Exchange within Composite materials Nacelle. JTI-CS2-2018-CFP09-AIR-02-69. Cleansky Call for proposal.
- [2] Q. Su, S. Chang, Y. Zhao, H. Zheng and C. Dang, A review of loop heat pipes for aircraft anti-icing applications. Applied Thermal Engineering, 2018. 130: pp. 528-540.
- [3] Patent FR3032027. 2015.
- [4] V. Dupont., B. Paran, S. Van Oost, and C. Billet. Capillary Jet Loop in 19th International Heat Pipe Conference. 2018. Pisa, Italy.
- [5] V. Dupont and O. de Laet. Two-phase thermal bus for multiple heat sources passive cooling. 2019. 1st joint International Forum Automotive Aerodynamics & Thermal Management. Manchester, UK.
- [6] L. Araneo, R. Clavenna, R. Boubaker, V. Dupont. Performance analysis and simplified modelling of a capillary jet loop heat pipe. 2021. Applied Thermal Engineering. Volume 197, 117407.
- [7] R. Clavenna, L. Araneo, V. Dupont, R. Boubaker. Capillary Jet Loop performance in parabolic flight. Applied Thermal Engineering, 2022. 217: 119221.
- [8] C. Braga Vieira, T. Nicolle, F. Accorinti, O. de Ghelin, C. Goffaux and V. Dupont. Computational simulation of a vapor jet into a subcooled flow inside a capillary jet loop system operating in direct condensation mode in Joint 21st IHPC and 15th IHPS. 2023. Melbourne, Australia.

An ultra-thin stainless steel vapor chamber with biomimetic copper forest wick and ultra-high thermal conductivity

Jiali Luo^{1,2}, Mou Xu^{1,2}, Dongchuan Mo^{*1,2} and Shushen Lyu^{*1,2}

¹ School of Materials, Sun Yat-Sen University, Shenzhen, P. R. China

² Guangdong Engineering Technology Research Centre for Advanced Thermal Control Material and System Integration (ATCMSI), Guangzhou, P. R. China

* Corresponding author email address: lvshsh@mail.sysu.edu.cn, modongch@mail.sysu.edu.cn

Abstract

Ultra-thin vapor chamber (UTVC) becomes the preferred solution for the rapid heat dissipation of portable electronic devices because its high heat transfer efficiency. Limit space and high-power consumption require vapor chambers with thinner thickness and higher thermal conductivity. We prepared an UTVC with a thickness of 0.27 mm and high equivalent thermal conductivity, which using stainless steel foil as shell material. The self-supporting channels wick structure can provide the capillarity and the space for vapor flow. The wick is made by biomimetic copper forest structure through electrodeposition, which has abundant micro/nano dendrites and natural channels to provide larger capillarity and lower flow resistance. The results show that the maximum heat transfer power of this UTVC can be 4 W, the thermal resistance is 0.17 °C/W when it is placed in horizontal. The effect of gravity is also been studied. When gravity is resistance, the thermal resistance is 0.64°C/W at 4.5 W; when gravity is driving force, the occurrence of drying out can be delayed, the thermal resistance is as low as 0.08°C/W at 4 W, and the effective heat transfer coefficient reaches 1.04×10^5 W/m²·K, which is 2 times higher than that when it is placed horizontally.

Keywords: Ultra-thin vapor chamber; Ultra-high equivalent thermal conductivity; Copper-forest structure wick; Heat transfer limit;

1. Introduction

Ultra-thin vapor chambers are now an effective solution to address the thermal management of portable electronic devices because their advantages like high heat transfer efficiency, lighter weight, thinner thickness and wider cooling area[1,2].

For UTVC, the decrease of thickness causing the space for vapor flow and wick thickness greatly reduced at same time, thence the vapor flow resistance increasing and capillarity decreasing[3]. Designing for ultra-thin space to ensure adequate capillarity and vapor flow become is the key to preparing UTVC. In particular, a wick with high capillarity and high permeability is required for UTVC[4]. In the previous study, we made a copper forest structure with micro/nano dendrites and abundant Ω -like grooves as wick, then prepared an UTVC (0.6 mm), which showed excellent heat transfer performance[5].

In this study, on the basis of the previous study, we made a new type of UTVC with self-supporting structure wick was developed which has thinner thickness. The structure of wick has also been optimized. Stainless steel was used as shell material in order to enhance the strength of UTVC.

2. Experiments and characteristics

The dimension of the UTVC is 90 mm(L)×30 mm(W)×0.27 mm(T). The structure schematic diagram of UTVC is shown in Figure 1(a). The UTVC is a two-layer structure, the upper layer is

channels consisting of wick structure, which provide supporting and vapor flow space, the lower layer is a 50 μ m thick wick structure. The 30 μ m stainless-steel foil is used as shell material. A copper layer with good adhesion to the stainless-steel foil is then electrodeposited in order to isolate the substrate from the working fluid to avoid the problem of corrosion. The natural copper forest wick structure is electrodeposited on the dense copper layer by one step. The micro-morphology of wick structure is shown in Figure 1(b).

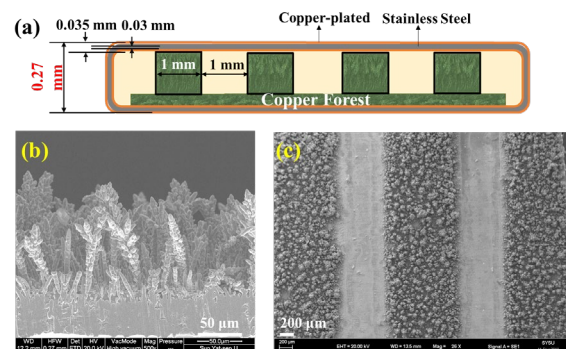


Figure 1. (a) Schematic diagram of the cross-section of UTVC; (b) SEM image of the bottom plate wick; (c) SEM image of the upper layer channel structure.

The above two prepared plates were spliced, welded, vacuumed, and filled with water as working fluid. The UTVC is tested in natural convection without additional condensation. The thermocouples

and infrared radiation camera were used to test the temperature distribution of UTVC, and a ceramic heater with 15 mm×15 mm is used as heating source.

3. Results and discussion

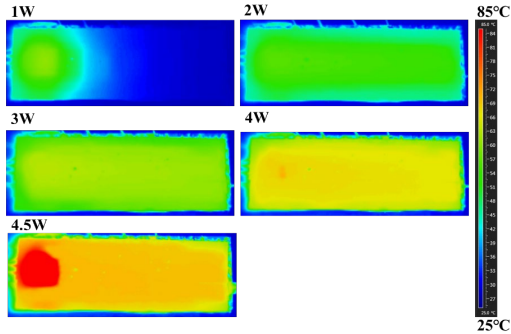


Figure 2. Photographs taken by infrared cameras at different power when UTVC placed horizontally.

The thermal performance of the UTVC under optimum filling rate is tested. Figure 2 shows the temperature distribution captured by the infrared camera under different heating power. It can be clearly seen that the UTVC has not started at 1 W, the heat accumulates at the evaporation end. The UTVC has good temperature uniformity at 2-4 W, there are no obvious hot spots on the upper surface of UTVC. When the heating power up to 4.5 W, there are obvious drying phenomenon occurs at the evaporation end. To sum up, the UTVC starts at 2 W when the temperature is 52 °C, and its maximum heat transfer capacity is 4 W.

The effect of gravity for the UTVC is also tested. The UTVC is placed vertical, the heater is putted on the top and bottom to differentiate the role of gravity. Figure 3(a) shows that when the gravity is propulsion, the UTVC exhibit better temperature uniformity, and the maximum cooling power is also increase to 5 W. In addition, the UTVC also has anti-gravity performance (Figure 3(b)), the thermal resistance is 0.64 °C/W at 4.5W when the gravity is resistance.

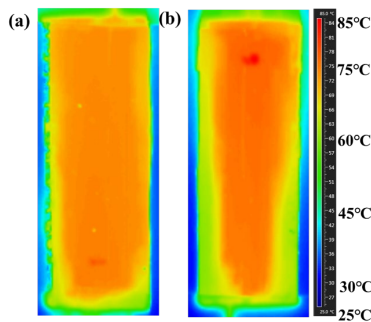


Figure 3. IR images at 4 W when UTVC placed vertically; (a) when the heater is on the bottom and gravity is the propulsion, (b) when the heater is on

top the gravity is the resistance.

The equivalent thermal conductivity λ_{eff} of the UTVC varies with different placement methods is shown in Figure 4. The UTVC shows great heat transfer performance at these three conditions. When the gravity is propulsion, the λ_{eff} is up to 1.04×10^5 W/m·K at 4 W, which is 2 times of higher than that the UTVC when placed horizontally, much higher than other thermally conductive materials.

In conclusion, we prepared biomimetic copper forest structure and used it as wick to fabricated a UTVC whose thickness is only 0.27 mm. The UTVC showed excellent heat transfer performance, and maximum cooling power is 4 W under natural convection. Besides, the UTVC shows antigravity ability, and has almost uniform temperature in all orientations, the equivalent thermal conductivity can up to 1.04×10^5 W/m·K at 4 W when the UTVC is vertical placement, gravity is the propulsion.

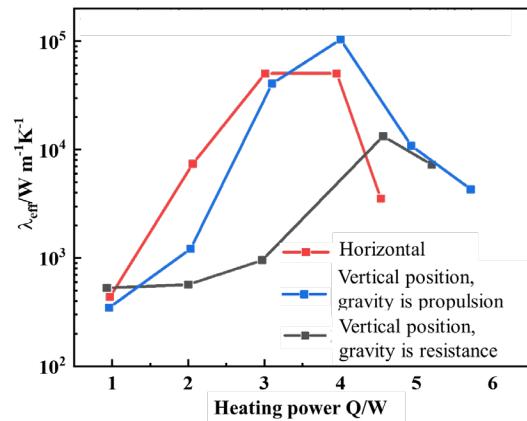


Figure 4. Effects of different placement on equivalent thermal conductivity at different heating powers.

References

- [1] M. Egbo, A review of the thermal performance of vapor chambers and heat sinks: Critical heat flux, thermal resistances, and surface temperatures. *Int. J. Heat Mass Transfer*, 2022. 183: p. 122108.
- [2] M. J. Gibbons, M. Marengo, and T. Persoons, A review of heat pipe technology for foldable electronic devices. *Appl. Therm. Eng.*, 2021. 194: p. 117087.
- [3] H. Tang, Y. Tang, Z. P. Wan, J. Li, W. Yuan, L. S. Lu, Y. Li, and K. R. Tang, Review of applications and developments of ultra-thin micro heat pipes for electronic cooling. *Appl. Energy*, 2018. 223: p. 383.
- [4] G. Chen, D. Q. Fan, S. W. Zhang, Y. L. Sun, G. S. Zhong, Z. W. Wang, Z. P. Wan, and Y. Tang, Wicking capability evaluation of multilayer composite micromesh wicks for ultrathin two-phase heat transfer devices. *Renewable Energy*, 2021. 163: p. 921.
- [5] J. L. Luo, D. C. Mo, Y. Q. Wang, and S. S. Lyu, Biomimetic Copper Forest Wick Enables High Thermal Conductivity Ultrathin Heat Pipe. *Acs Nano*, 2021. 15(4): p. 6614.

Heat transport characteristics of a 2 m long flat-evaporator flexible loop heat pipe for thermal control of power electronics of electric vehicles

Bomi Nam¹, Jaeyeon Kim², Manhee Park², Wukchul Joung^{1, 3*}

¹Department of Mechanical Engineering, Pukyong National University, Busan, Republic of Korea

²Thermal Energy System Research Lab., R&D Division, Hyundai Motor Group, Hwaseong, Republic of Korea

³Department of Intelligent Robot Engineering, Pukyong National University, Busan, Republic of Korea

*Corresponding author email address: wukchuljoung@pknu.ac.kr

Abstract

In this work, heat transport characteristics of a flat-evaporator flexible loop heat pipe (FEFLHP) were systematically investigated, which was devised for thermal control of a power electronics module of electric vehicles. The tested FEFLHP was fabricated to have a 100 cm² flat heat absorbing surface with a rectangular sintered stainless-steel wick, and the overall distance between the evaporator and condenser was designed to be approximately 2 m. In particular, the evaporator and condenser were connected using 1.5 m long flexible tubes (metal bellows type) for incorporation into a thermal management circuit of the electric vehicles. The FEFLHP was operated at different elevations, heat sink temperatures, and with different working fluids in a heat load range from 100 W to 700 W. The elevation between the evaporator and condenser was changed from -0.2 m to 0.2 m, and the tested heat sink temperatures included 10 °C, 20 °C, and 40 °C. Regarding the working fluid, water was used as a reference fluid, and ethanol and water-ethanol mixtures of different mixing ratios were also tested. Details on the test results are provided with in depth discussion of the heat transport characteristics of the tested FEFLHP.

Keywords: Flat evaporator loop heat pipe; Flexible working fluid transport lines; Electric vehicle thermal control; Elevation change; Heat sink temperature; Working fluids

1. Introduction

With increasing demand on an extended range and power, thermal control of electric vehicles (EVs) is currently becoming a limiting factor on the overall performance of the EVs. In particular, due to limited volume and restricted access of the modulated power electronics in the inverter, the thermal control of power electronics modules (e.g., IGBTs modules) is considered highly challenging, which requires effective and efficient heat transport from the heat generating power electronics to a remote heat dissipating element [1, 2]. In this circumstance, loop heat pipes (LHPs), which are highly recognized passive two-phase heat transfer devices, are

gathering ever-increasing interest as a key element in a thermal control system of the EVs.

For successful application of the LHPs to the thermal control system of the EVs, the LHPs are required to have a flat thermo-contact surface and long flexible heat transport path to reduce thermal resistance from the power electronics and be in a reliable operation in a geometrically complicated and vibration-exposed environment. To meet these requirements, in this work, a flat-evaporator flexible loop heat pipe (FEFLHP) was devised; the evaporator of the FEFLHP was fabricated to have a 100 cm² flat heat absorbing surface with a sintered stepped flat wick; flexible working fluid transport

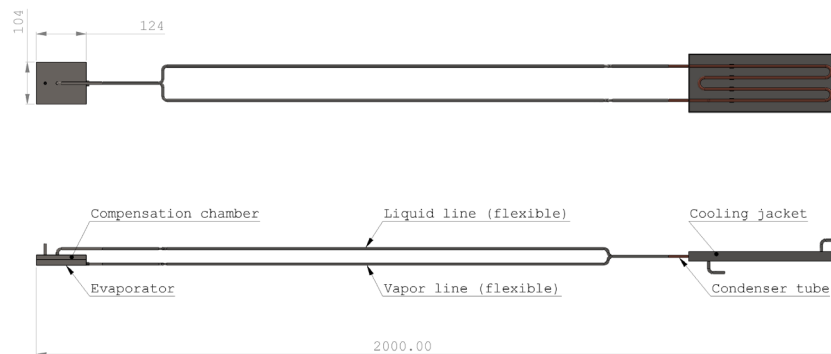


Figure 1. Exterior view and dimensions of the flat-evaporator flexible loop heat pipe (FEFLHP). Dimensions are in millimeters.

lines were employed; the overall length of the FEFLHP was approximately 2 m. Figure 1 shows the overall dimensions and shape of the FEFLHP.

In this work, heat transport characteristics of the FEFLHP were systematically investigated in the context of the effect of the influential parameters, such as the heat load, elevation (i.e., relative height differences between the evaporator and condenser), heat sink temperature, and working fluid. Test results were analyzed in terms of the operating temperature and various thermal resistances of the FEFLHP as well as the amount of actual heat transport rate and heat leak of the FEFLHP at different operating conditions. Detailed design of the FEFLHP and test setup are presented in Section 2, test results are provided and discussed in Section 3, and Conclusions are summarized in Section 4.

2. Flat-evaporator flexible loop heat pipe and test setup

The evaporator of the FEFLHP was designed to have a simple cuboid shape with a 100 cm^2 flat heat absorbing surface. To this end, a stainless-steel flat wick having a stepped structure (patent pending) was sintered with projection dimensions of $100 \text{ mm} \times 120 \text{ mm}$ (width \times length). The stepped flat wick possessed a 7 mm thick portion over a heated area (i.e., $100 \text{ mm} \times 100 \text{ mm}$ portion) and 3 mm portion over the vapor collector near the vapor exit of the evaporator (i.e., $100 \text{ mm} \times 20 \text{ mm}$ portion). By employing this structure, it was possible to construct a simple cuboidal evaporator without a complicated phase-separation structure or having a vapor exit on the bottom surface of the evaporator, thus enabling the use of the evaporator of the FEFLHP without interfering the form factor of the power electronics module [3]. Figure 2 shows the structure of the evaporator of the FEFLHP.

The compensation chamber of the FEFLHP was designed to have an approximately half of the total

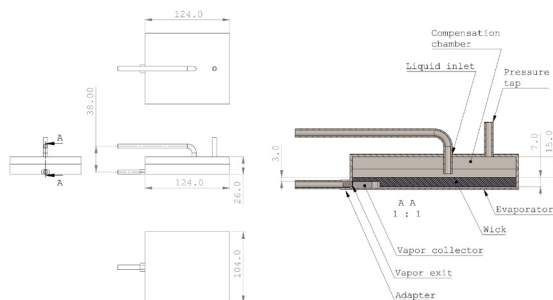


Figure 2. Exterior and section views of the flat-cuboidal evaporator (dimensions in mm).

FEFLHP internal volume, and with the projection dimensions identical to the evaporator, its thickness was determined to be 15 mm. With 26 vapor removal channels of $2 \text{ mm} \times 1 \text{ mm} \times 100 \text{ mm}$ (width \times depth \times length), located below the heated portion of the wick, the evaporator of the FEFLHP was designed to have overall dimensions of $104 \text{ mm} \times 124 \text{ mm} \times 26 \text{ mm}$ (width \times length \times thickness).

A cooling jacket-type condenser was constructed with a copper tube of $6.4 \text{ mm} \times 1500 \text{ mm}$ (nominal diameter \times length) and stainless-steel housing, emulating a shell-and-tube-type heat exchanger. The evaporator and condenser were connected using 1.5 m long metal bellows tubes, which provided a flexible heat transport path to the FEFLHP. The overall length of the assembled FEFLHP was approximately 2 m. Figure 1 shows the overall dimensions and shape of the FEFLHP.

Figure 3 shows the schematic of the test setup constructed for the parametric study of the influential factors on the heat transport characteristics of the FEFLHP (e.g., heat load, elevation, heat sink temperature, etc.). Heat load was supplied to the evaporator from 100 W to 700 W using a feedback-controlled DC power supply, and an aluminum block containing four cartridge heaters was used to emulate the power electronics module. Tested relative elevations between the evaporator and the condenser included -0.2 m (favorable), 0.0 m (horizontal), and 0.2 m (adverse), which emulated an actual working environment of the FEFLHP as a heat transport device in an electric vehicle. To investigate the effect of heat sink temperature, which the condenser of the FEFLHP may experience during operation on road (except for extreme cold weather), a coolant (water) at different temperatures (e.g., $10 \text{ }^\circ\text{C}$, $20 \text{ }^\circ\text{C}$, and $40 \text{ }^\circ\text{C}$) was supplied to the cooling jacket at approximately 2.0 l/min. As to the effect of the working fluids, water was used as a reference fluid, and ethanol and water-ethanol mixtures at different ethanol contents (e.g., 30 % and 60 % of the mixture volume) were also tested for use of the FEFLHP operating outdoor

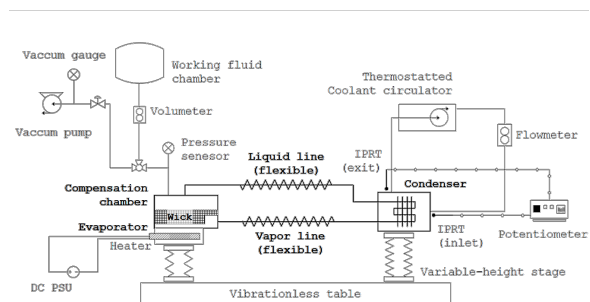


Figure 3. Schematic of the test setup.

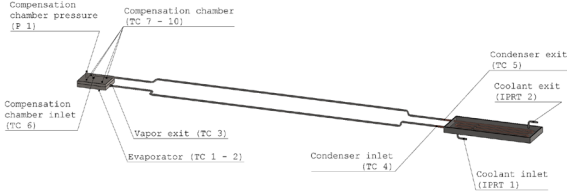


Figure 4. Locations of the temperature and pressure measurements.

where temperature drops below the ice point. The FEFLHP was charged with the tested working fluid to fill approximately 54 % of its internal volume.

Ten type T thermocouples were attached to the FEFLHP to monitor its operating temperatures at different operating conditions. To assess the actual heat transport rate, calibrated positive displacement flowmeter was used to measure the flowrate of the coolant (\dot{V}_{clnt}) and two calibrated IPRTs (industrial platinum resistance thermometers) were used to measure temperature changes of the coolant (Δt_{clnt}) at the inlet and exit of the cooling jacket, respectively. The actual heat transport rate was evaluated by measuring the heat dissipation rate in the condenser with the measured volume flowrate and temperature change of the coolant (Equation (1)). In addition, one calibrated pressure transducer was also used to monitor internal pressure of the compensation chamber. Figure 4 shows the locations of the temperature measurement.

$$\dot{Q}_{dis} = (\rho c_p)_{clnt} \dot{V}_{clnt} \Delta t_{clnt} \quad (1)$$

3. Result and discussion

Figure 5 shows the start-up response of the FEFLHP at 100 W heat load; the FEFLHP was filled with water at approximately 54 % of the FEFLHP internal volume, and the evaporator and

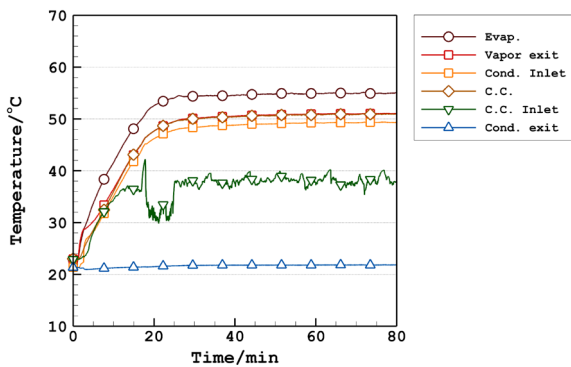


Figure 5. Start-up response of the FEFLHP (working fluid: water, elevation: horizontal, heat load: 100 W).

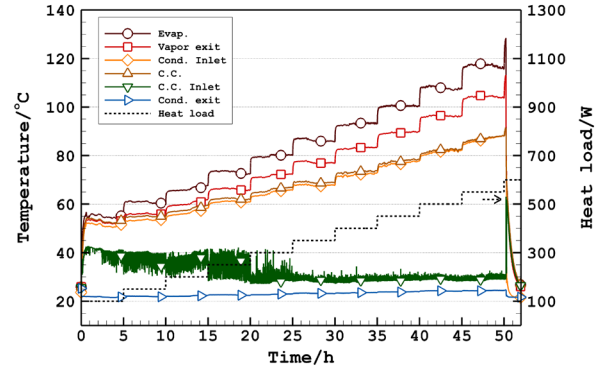


Figure 6. Response of the FEFLHP to increasing heat load (working fluid: water, elevation: horizontal).

condenser were configured to be at the same height (i.e., at the horizontal elevation). As shown in the figure, when a heat load of 100 W was supplied to the evaporator, vaporized working fluid was discharged from the evaporator and flowed into the condenser, which manifested themselves as the sequentially increasing temperatures at the evaporator (i.e., the interface between the evaporator housing and heater), vapor exit, and condenser inlet. During this stage of vapor discharge, the liquid-phase working fluid, originally existed in the working fluid transport lines, surged into the compensation chamber (through the condenser), which was indicated by the initial fall in the compensation chamber inlet temperature at approximately 15 min from the heat input. When the liquefied condensate reached the compensation chamber, the FEFLHP attained a steady-state operation at approximately 25 min from the heat input.

Figure 6 shows the response of the FEFLHP to increasing heat load from 100 W to 600 W with a 50 W increment and 5 hours stay at each step. As shown in the figure, the operating temperatures at the evaporator, vapor exit, condenser inlet, and compensation chamber monotonically increased with increasing heat load up to 550 W; the compensation chamber inlet temperature firstly decreased with increasing heat load due to the increased mass flow rate of the returning condensate, and then reached a nearly unchanging value at 350 W. At 600 W, due to the upper temperature limit, which was set to be 120 °C at the interface between the evaporator and heater, the FEFLHP was forced to stop the operation. From the obtained result, it was found that the FEFLHP successfully transported heat in the heat load range from 100 W to 550 W at the horizontal elevation and with water.

Figure 7 shows the steady-state response of the

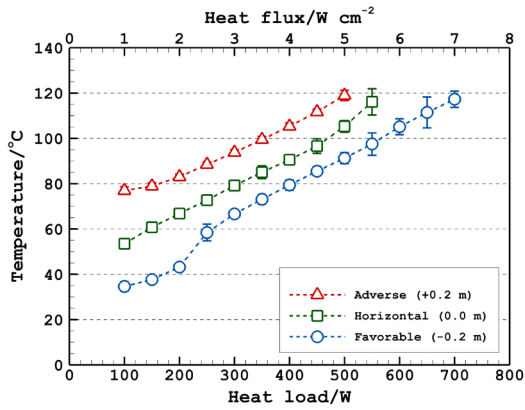


Figure 7. Steady-state response of the evaporator temperature to increasing heat load at different elevations (working fluid: water). The error bars indicate the measurement uncertainties at approximately 95 % level of confidence.

evaporator temperature, which was measured at the heated bottom surface of the evaporator, with increasing heat load at tested elevations. As shown in the figure, the evaporator temperature monotonically increased with increasing heat load in distinct groups from the operations at other elevations over the entire heat load range, indicating

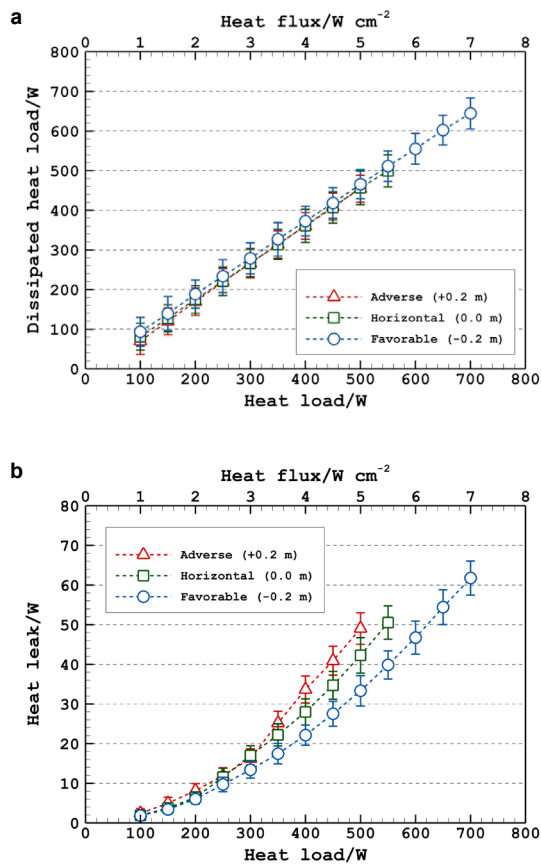


Figure 8. Variations in the heat dissipation rate and heat leak at different elevations. The error bars indicate the measurement uncertainties at approximately 95 % level of confidence. (a) Heat dissipation rate. (b) Heat leak.

significant effect of the hydrostatic head loss of the liquid phase working fluid. The steady-state operating temperatures decreased with decreasing elevation (i.e., from the adverse elevation to favorable elevation), thus extending the operation range of the FEFLHP.

Figures 8 (a) and (b) show the variations in the actual heat transport rate, which was assessed by the dissipated heat load in the condenser (i.e., heat dissipation rate), and heat leak from the evaporator to the compensation chamber. As shown in Figure 8 (a), the heat transport rates of the FEFLHP at different elevation coincided within the claimed uncertainty, indicating that the effect of the elevation was insignificant on the heat transport rate. The heat leak from the evaporator to the compensation chamber increased with increasing heat load yet at different rates depending on the elevation; as the elevation increased from the favorable to adverse elevation, the rate of increase in the heat leak was augmented due to the increased hydrostatic head loss of the liquid phase.

Based on the measured temperatures and dissipated heat load, total thermal resistances of the FEFLHP at difference elevations were evaluated using Equation (2). Figure 9 shows the variation in the total thermal resistance with increasing heat load at tested elevations. As shown in the figure, the total thermal resistance monotonically decreased as the heat load increased, with decreasing significance for the adverse and horizontal elevations, but when the evaporator of the FEFLHP was favorably elevated, the total thermal resistance first slightly decreased, followed by slight increase at 250 W, and then decreased again monotonically yet at more reduced rate.

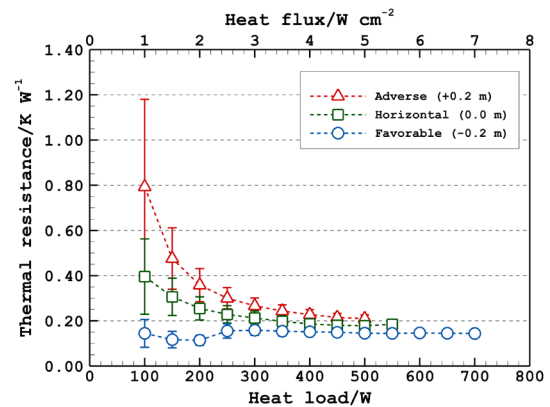


Figure 9. Variations in the total thermal resistance of the FEFLHP at different elevations. The error bars indicate the measurement uncertainties at approximately 95 % level of confidence.

$$R_{th,tot} = \frac{t_{evap} - t_{cond,exit}}{\dot{Q}_{dis}} = \frac{t_{evap} - t_{cond,exit}}{(\rho c_p \dot{V})_{clnt} \Delta t_{clnt}} \quad (2)$$

The early decreases in the thermal resistance at all of the tested elevations (i.e., the variable-conductance mode operation) were caused by the increased mass flow rate of the working fluid with increasing heat load, which led to augmented liquid subcooling in the compensation chamber, resulting in the limited increase in the operating temperatures. In addition, the total thermal resistances at different elevations at low heat loads were clearly deviated from each other, demonstrating the significant effect of the liquid hydrostatic head loss in the low heat load range. As the heat load increased, due to the reduced sensible cooling of the condenser, the variation in the total thermal resistance became nearly constant (i.e., the fixed-conductance mode operation). In particular, with increasing heat load, the difference in the total thermal resistance between the operations at other elevations became insignificant due to the increased effect of the frictional pressure loss compared to the liquid hydrostatic head loss.

Figure 10 shows the change in the steady-state evaporator temperature with increasing heat load at different heat sink temperatures (i.e., temperatures of the coolant supplied to the condenser). In this case, the evaporator temperature remained nearly unchanged when the sink temperature changed from 10 °C to 40 °C. Figure 11 shows the changes in the compensation chamber inlet temperature with increasing heat load and at different heat sink temperatures. As shown in the figure, the

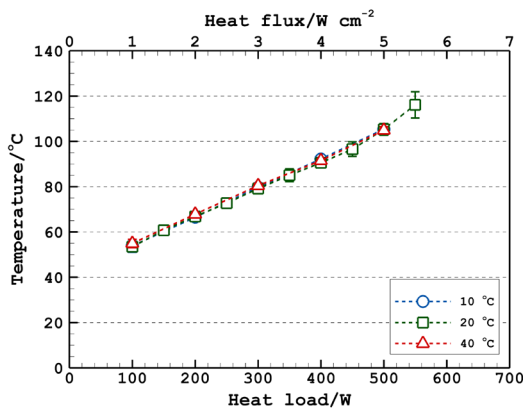


Figure 10. Steady-state response of the evaporator temperature to increasing heat load at different heat sink temperatures (working fluid: water). The error bars indicate the measurement uncertainties at approximately 95 % level of confidence.

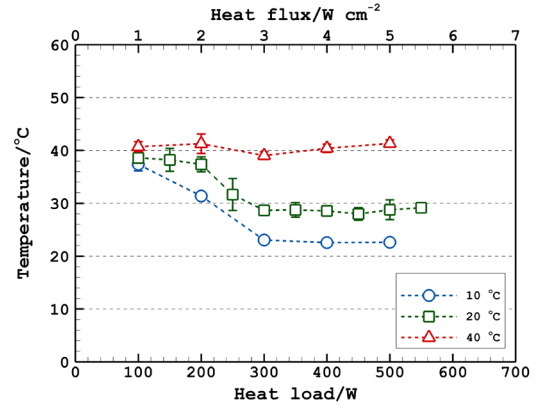


Figure 11. Steady-state variation in the compensation chamber inlet temperature with increasing heat load at different heat sink temperatures (working fluid: water). The error bars indicate the measurement uncertainties at approximately 95 % level of confidence.

compensation chamber inlet temperature, which manifested itself as an indication of the amount of liquid subcooling in the compensation chamber, decreased with increasing heat load at the heat sink temperatures of 10 °C and 20 °C, indicating that the liquid subcooling in the compensation chamber increased with increasing heat load due to the increased mass flow rate of the liquid condensate at low temperatures; this was due to the fact that the liquid condensate returning to the compensation chamber at lower temperatures provided higher liquid subcooling to the compensation chamber, which must be balanced with the heat leak from the evaporator to the compensation chamber. On the other hand, at the heat sink temperature of 40 °C, the compensation chamber inlet temperature remained nearly unchanged with increasing heat load, implying that the liquid subcooling provided by the liquid condensate produced at this high heat sink temperature (40 °C) was less than those produced at the lower heat sink temperatures despite the increased mass flow rate of the working fluid. As the liquid subcooling to the compensation chamber must be balanced with the heat leak from the evaporator, the heat leak at the heat sink temperature of 40 °C was expected to be lower than the heat leaks at other tested heat sink temperatures.

Figure 12 shows the change in the heat dissipation rate and heat leak with increasing heat load at different heat sink temperatures. As shown in Figure 12 (b), the heat leak from the evaporator to the compensation chamber decreased with increasing heat sink temperature due to the reduced liquid subcooling provided by the warmer liquid condensate produced at elevated heat sink temperatures. This variable heat leak to the compensation chamber was supposed to be

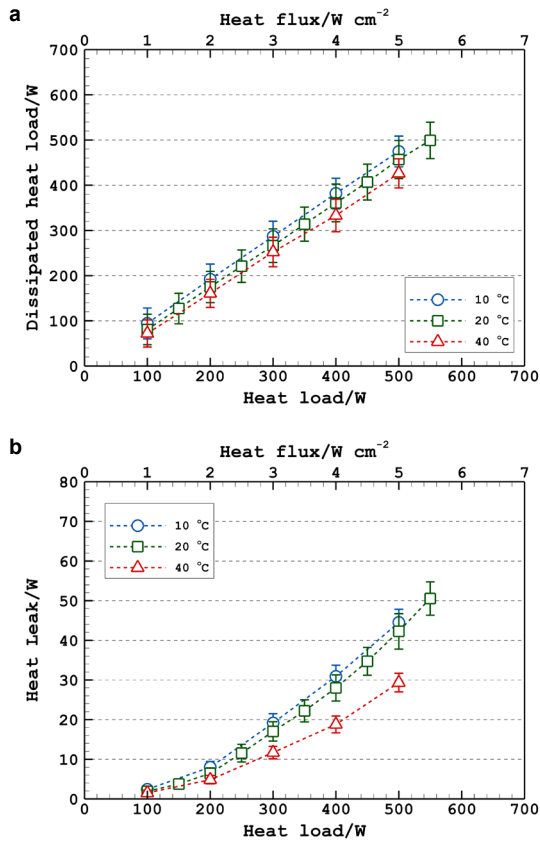


Figure 12. Variations in the heat dissipation rate and heat leak at different heat sink temperatures. The error bars indicate the measurement uncertainties at approximately 95 % level of confidence. (a) Heat dissipation rate. (b) Heat leak.

responsible for the nearly unchanging evaporator temperature with increasing heat load, changing the amount of heating of the compensation chamber.

Based on the energy balance in the evaporator, this reduced heat leak at an elevated heat sink temperature should result in an increase in the evaporative heat rate, which is responsible for the working fluid evaporation in the evaporator and

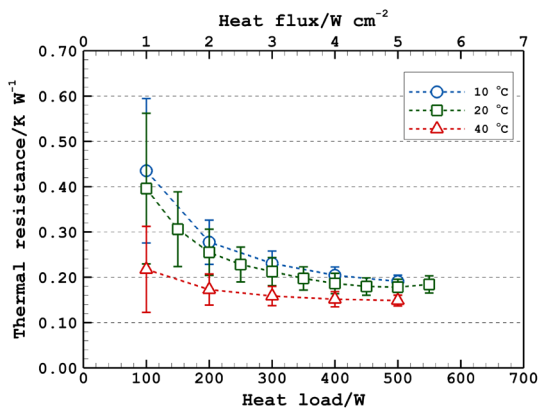


Figure 13. Variations in the total thermal resistance of the FEFLHP at different heat sink temperatures. The error bars indicate the measurement uncertainties at approximately 95 % level of confidence.

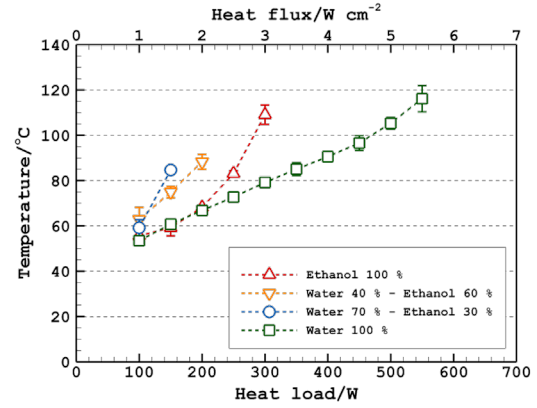


Figure 14. Variations in the heat dissipation rate and heat leak at different heat sink temperatures. The error bars indicate the measurement uncertainties at approximately 95 % level of confidence. (a) Heat dissipation rate. (b) Heat leak.

mass flow rate of the vapor phase working fluid transported to the condenser, thus leading to increased heat dissipation rate in the condenser. However, as shown in Figure 12 (a), the heat dissipation rate in the condenser increased with decreasing heat sink temperature. This was due to the fact the heat dissipation rate in the condenser comprises latent and sensible portions of the heat dissipation rate; that is, further sensible cooling of the liquid condensate is provided by the condenser after completion of the condensation of the vapor phase working fluid. Thus, the observed increased heat dissipation rate in the condenser with decreasing heat sink temperature was caused by the higher sensible cooling provided by the condenser at lower heat sink temperatures.

Figure 13 shows the variation in the total thermal resistance with increasing heat load at different heat sink temperatures. As shown in the figure, the total thermal resistance decreased with increasing heat sink temperature; this was simply due to the elevated condenser outlet temperature at higher heat sink temperatures and the nearly unchanging evaporator temperature regardless of the heat sink temperatures. Therefore, the obtained results should be carefully interpreted such that the smaller thermal resistance at higher heat sink temperature does not necessarily represent better heat transport characteristics.

The variation in the evaporator temperature of the FEFLHP, filled with different working fluids at the same charge volume, with increasing heat load was illustrated in Figure 14. As shown in the figure, when a mixture of water and ethanol was used, the operating temperature was higher than the operating temperatures obtained with pure working fluids (i.e., water and ethanol). In particular, with the use of the

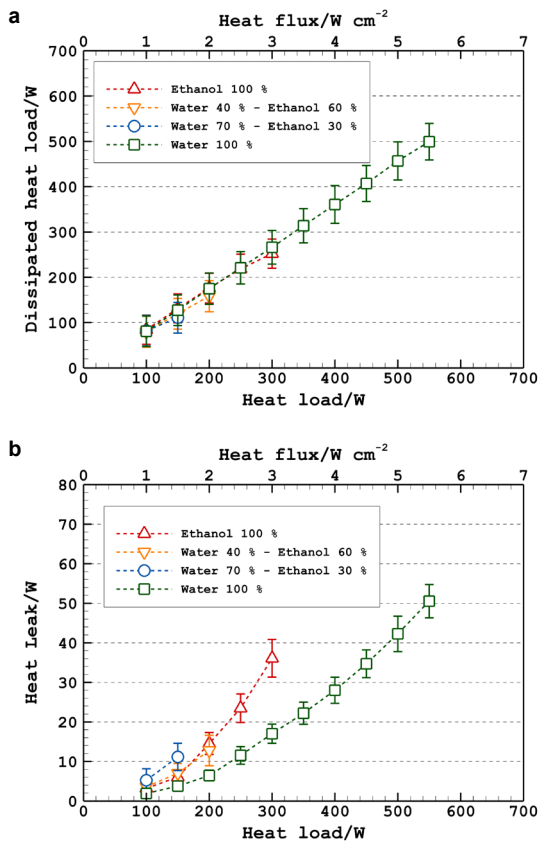


Figure 15. Variations in the heat dissipation rate and heat leak at different heat sink temperatures. The error bars indicate the measurement uncertainties at approximately 95 % level of confidence. (a) Heat dissipation rate. (b) Heat leak.

mixture, a large amount of noncondensable gases was generated, leading to shortened operating heat load range compared to the cases with pure fluids; the generation of noncondensable gases was supposed to be caused by thermal decomposition of ethanol in the mixture at elevated operating temperatures, exceeding the boiling point of ethanol. The reason for the higher operating temperatures and large noncondensable gas generation for the mixtures was not certain, and further study is required.

Figure 15 shows the variation in the heat dissipation rate and heat leak with increasing heat load for different working fluids. As shown in Figure 15 (a), there were insignificant differences between the heat dissipation rates obtained with different working fluids. However, the heat leak significantly deviated from each other, implying that the liquid subcooling to the compensation chamber differed with different working fluids; water showed the smallest heat leak due to its large heat capacity; with decreasing ethanol content, the heat leak increased beyond the values for the tested pure fluids.

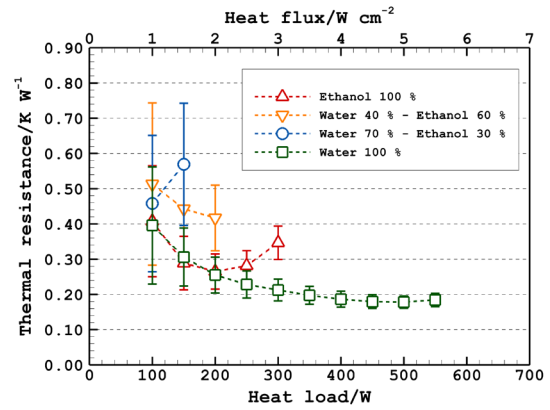


Figure 16. Variations in the heat dissipation rate and heat leak for different working fluids. The error bars indicate the measurement uncertainties at approximately 95 % level of confidence. (a) Heat dissipation rate. (b) Heat leak.

Figure 16 shows the variation in the total thermal resistance of the FEFLHP, operated with different working fluids, with increasing heat load. As shown in the figure, water demonstrated the lowest total thermal resistance over almost entire operating heat load range, followed by the total thermal resistance obtained with ethanol. When the mixtures were used, the total thermal resistance was elevated beyond the values for the pure fluids. In particular, when the mixture of 70 % water and 30 % ethanol was used, the thermal resistance monotonically increased with increasing heat load, due to the generation of the noncondensable gases which increased the operating temperature considerably.

4. Conclusions

In this work, a flat-evaporator loop heat pipe with a 2 m long flexible heat transport path was developed. A simple cuboid shape evaporator of the FEFLHP was constructed with the use of the stepped flat wick which was designed to provide a thicker vapor collector near the exit of the evaporator and thinner vapor removal channels on the heated portion of the evaporator, thus enabling the connection of a conventional standard sized tubes without use of a complicated phase separation structure at a minimal conduction thermal resistance through the vapor removal channels. The operating characteristics of the FEFLHP were investigated in terms of the operating temperature, heat dissipation rate, heat leak, and total thermal resistances at different elevations, heat sink temperatures, and for different working fluids.

As to the effect of elevation, a clear deviation due to the changed hydrostatic head loss of the liquid phase working fluid was observed, implying that for extended operation range of the FEFLHP (i.e.,

increased heat transport rate), the evaporator of the FEFLHP should be favorably elevated. The effect of heat sink temperature manifested itself as an insignificant factor due to the increased heat leak with decreasing heat sink temperature, yet the increased sensible cooling at lower heat sink temperature resulted in larger heat dissipation rate at lower heat sink temperatures. With the use of different working fluids other than water, especially when a mixture of water and ethanol was used, the FEFLHP showed shortened operating heat load range due to the excessive generation of noncondensable gases. The reason for the generation of large amount of noncondensable gases for water and ethanol mixtures was not certain, but the elevated operating temperature with the use of mixtures was supposed to result in decomposition of ethanol in the mixture. To clarify this, further study is required.

References

- [1] L. Vasiliev, et al., Loop heat pipe for cooling of high-power electronic components, *International Journal of Heat and Mass Transfer*, 2009. 52(1-2): p. 301.
- [2] R. Singh, T. Nguyen, Loop heat pipes for thermal management of electric vehicles, *Journal of Thermal Science and Engineering Applications*, 2022. 14: p. 061010.
- [3] J. Lee, W. Joung, Operating characteristics of a flat-evaporator loop heat pipe having a flexible heat transport path, *Journal of Mechanical Science and Technology*, 2022. 36(7): p. 3735-3751.

Acknowledgements

This research was supported by the Basic Science Research Program of the National Research Foundation of Korea (NRF) funded by the Ministry of Education (NRF-2020R111A3072736).

Effect of Fabric Parameters on Rate of Evaporation and Salt Accumulation for Thermosyphon Based Interfacial Solar Vapor Generation Systems

Debartha Chatterjee¹, Sameer Khandekar^{1*}

¹Indian Institute of Technology Kanpur, India

*Corresponding author email address: samkhan@iitk.ac.in

Abstract

Advent in interfacial vapor generation systems has enabled solar-thermal based desalination technologies to remain technologically and commercially relevant. However, salt accumulation and drastic reduction in vapor generation efficiency due to that remains the most challenging hurdle, which prevents such technologies from being adopted commercially. Novel salt mitigation strategies involving design of new pathways, to either enhance the rate of mitigation, or spatially isolate the accumulated salt, and blocking salt directly, have received tremendous attention lately. However, very few investigations have focused to understand the role of geometric parameters of wicking structures on evaporation dynamics and salt diffusion time scales. Although, such parameters are known to significantly influence heat and mass transport in high heat flux applications and have been widely studied in heat pipe literature, very few investigations exist which focus primarily on low heat flux applications. Additionally, the role of such parameters on salt precipitation effecting the heat and mass transport and their mitigation have been studied traditionally in geological domains, which primarily consider natural evaporation based systems. In this study, we investigate the role of such geometric parameters on evaporation dynamics and salt mitigation especially for low heat flux ranges, primarily addressing systems dedicated for solar thermal based desalination applications. The performance of three different 100% cotton fabric samples with varying fabric parameters were evaluated on the basis of average evaporation rate and heat-to-vapor conversion efficiency for two input heat flux cases viz., 1-Sun and 2.5 Sun. The non-woven fabric performed much better in generating vapor efficiently as it provided the least resistance to water transport as well as salt diffusion back flow to the bulk reservoir.

Keywords: Solar-thermal desalination; Interfacial solar evaporation; Salt-mitigation; Weave pattern; Fabric parameters.

1. Introduction

Small-scale decentralized solar-thermal-desalination (STD) portable technologies were identified as the ideal choice for countries like India, which face the problem of water stress in addition to an acute shortage of resources. STD systems are recognized as the ideal choice in this regard and hence have received renewed interest from the global research community [1]. The concept of heat localization was proposed for the first time to mitigate this associated parasitic heat loss and achieve a thermal to vapor conversion efficiency of around ~ 65% [2]. Initially, most studies focused on developing new material combinations that could absorb the complete solar spectrum and localize the input irradiation along the interface [3,4]. Several methodologies adopted by researchers, mainly involve tuning nano-material-based structures to achieve solar absorptivity (α) values as high as ~ 0.98 were reported. The other aspects which have received significant attention are the design of the water pathway and the choice of insulating material, which plays a critical role in influencing the solar to vapor conversion efficiency (η_t).

The performance parameter for such STD systems (as shown in Eq. 1) and the key performance metrics that would play the dominant role to further improve the SWP.

$$SWP = \frac{E}{h_{lv}} \times \alpha \eta_t GOR \quad (1)$$

Gain Output Ratio (GOR) was identified to be the key parameter that needs attention; however, practical limitations of implementing latent heat

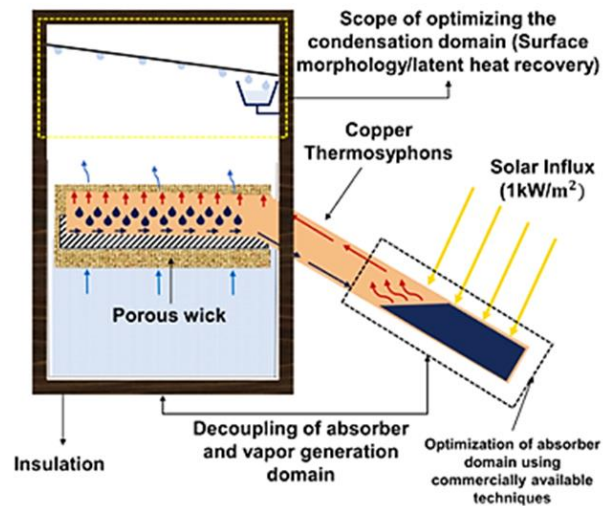


Figure 1. The working principle of the proposed TPCT based heat localization strategy, which decouples the absorbing and vapor generating surface as well as provides provision for latent heat recovery in a forward evaporation-based system [6].

recovery in these STD systems remain a key challenge that needs to be addressed. In addition, salt accumulation drastically reduces system performance; hence, several researchers have shifted their focus in designing novel salt mitigation strategies [5]. Recently, Chatterjee et al. proposed a TPCT based heat localization strategy which not only decouples the vapor generating surface from the solar absorbing surface see Figure 1, but also provides scope of harnessing the latent heat of condensation (Enhanced values of GOR) which generally gets dissipated into the ambient. However, in spite of decoupling, it was observed that although at low input heat flux ranges ~ 1 Sun the proposed strategy performed fairly well, at higher heat fluxes $\geq \sim 2$ Sun accumulation of salt on the vapor generating surface reduced the heat to vapor conversion efficiency drastically [6].

Effect of parameters like pore radius, fiber or particle radius, thickness of material, and thermal conductivity of wicking structures play a significant role in heat and mass transport and has been widely under scrutiny in literature dedicated towards understanding operation of heat pipes [7]. Several experimental investigations as well as modelling studies have helped in designing appropriate wick structures for heat pipes used for dissipating high to very high heat fluxes. Interestingly, majority of such studies are focused in understanding the role of such geometric and material parameters of wick structures that either enhance CHF (Critical Heat Flux) or help in developing a better understanding of the dominant parameters that effect the CHF more. Moreover, such investigations are carried out in pure vapor environment and also involve pure working fluids such as DI water. Other working fluids like ethanol, methanol, pentane, and liquid sodium are also investigated based on their application and operation ranges. Very few of these investigations focused on understanding evaporation dynamics from porous structures which consider waste water or seawater (which are generally contaminated and are prone to fouling) [8].

Effect of fouling due to salt precipitation is an area of interest to researchers studying evaporation from soil related to geology or investigating the effect of salt fouling on building structures. However, such investigations involve developing an understanding primarily of the dry out phenomena (naturally driven without external heat inputs) on porous structures which mostly comprise of particle/granular particle based porous structures like soil and sand [9,10].

In this background, the prime objective of this study is to identify the dominant geometric and material properties of wicking structures that significantly influence the heat and mass transport involving low input heat flux. Based on which a suitable range of wicking materials can be identified that will be able to generate vapor continuously, avoiding fouling due to salt accumulation for a TPCT based heat localization strategy with low to medium input heat fluxes. Three different fabric samples with different weave types, porosity, permeability, and tortuosity are investigated here for 1 Sun and 2.5 Sun input heat flux using 3.5% simulated seawater as the testing fluid. The role of permeability to maintain a sustained wicking rate such that the vapor generating structure remains always saturated with the testing fluid is investigated. The role of porosity and tortuosity in affecting rate of salt diffusion back flow to the bulk reservoir avoiding accumulation of salt on the vapor generating surface is also analyzed.

2. Experimental section

Three different fabric samples were tested in order to understand their suitability to be used as a wicking material, for the proposed TPCT based heat localization strategy proposed earlier. Spatial temperature distribution, average evaporation rate, heat to vapor conversion efficiency, and digital microscopy are considered as evaluating parameters, to understand the effect of several fabric parameters to achieve a sustained vapor generation rate by avoiding fouling due to salt accumulation.

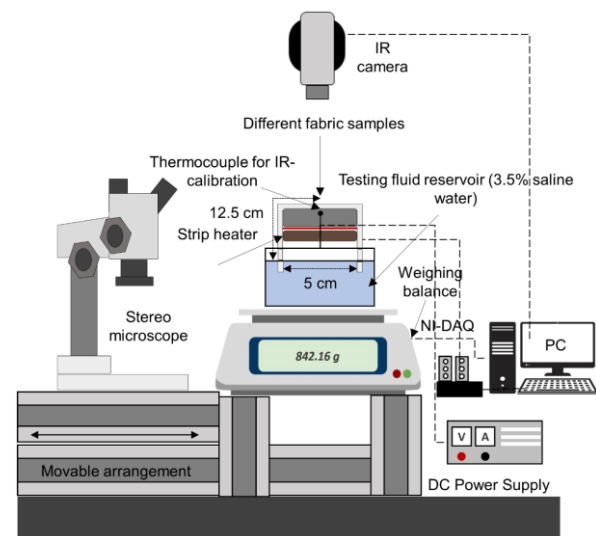


Figure 2. Experimental setup to investigate the effect of geometric fabric parameters on evaporation dynamics and the rate of salt mitigation for generating vapor efficiently.

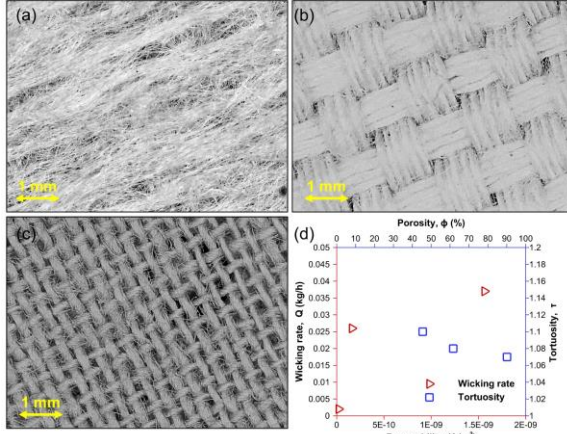


Figure 3. Microscopic images of three different cotton fabrics with different weave type (a) non-woven, (b and c), and (d) showing the wicking rate, porosity, permeability, and tortuosity of the three fabric samples.

2.1. Experimental setup

Figure 2 shows the schematic of the experimental setup used for evaluating the performance of the three fabric samples as an ideal choice to be used as a wicking material for the TPCT based heat localization strategy. The fabric samples are made of 100% cotton having different weave type, porosity, permeability and tortuosity. Table 1 presents the detail characteristics of these three fabric samples used in the present study. An aluminum block (50 mm \times 50 mm) attached with a strip mica heater of similar dimension (Minco[®] mica thermfoilTM heater, model HM6955, with a resistance of 23.2 ohms) and insulated on all sides appropriately using teflon slabs except the top surface, is used to mimic the TPCT as a heat source. A DC power supply (Elnova[®] DC power supply 0-60 V, 0-50 A) is used to power the mica heater (simulating the solar flux) in a manner similar as described in [1]. The fabric samples (250 mm \times 50 mm) are hanged over the aluminum block and placed in a floating condition over a testing fluid reservoir (3.5% simulated sea water, ASTM D1141-52), as shown in Figure 1. The wicking length is fixed at 12.5 cm from both the ends letting the samples remain in completely saturated condition during the start of the experiment on all cases. The testing fluid reservoir is placed on a digital weighing balance (Sartorius Quintix[®] 2102-1x, least count = 10 mg, and repeatability = \pm 5%), which is used to digitally record the evaporative mass loss rate. A K-type thermocouple (Omega[®] 5TC-TT-K-24-36) is placed, as shown in Figure 1, such that it is just in contact with the fabric sample surface underneath.

A NI-DAQ (National Instruments[®] NI-PCI-9213) is used for the purpose of temperature signal datalogging. An infrared (IR) thermography camera (FLIR[®] A655sc, with a temporal resolution of 3.13 fps, and a spatial resolution of \sim 417 μ m/pixel) is placed vertically above the vapor generating surface at a distance of 1 m. A digital microscope (OLYMPUS[®] SZX2-ILLTS) is placed on a movable fixture in order to capture the microscopic images of the vapor generating surface periodically in between the testing duration.

2.2. Data reduction

The solar to vapor conversion efficiency is calculated [11] as:

$$\eta = \frac{\Delta m \times h_{lv}}{V \times I} \quad (2)$$

The total enthalpy gained is estimated in (kJ/kg) [11] as:

$$h_{total} = h_{fg} + h_L \quad (3)$$

where, the latent heat of evaporation is given in (kJ/kg) by:

$$h_{fg} = 1.92 \times 10^6 \left[\frac{T_{Eavg} + 273.15}{(T_{Eavg} + 273.15) - 33.91} \right]^2 \quad (4)$$

and the sensible heat component is calculated as:

$$h_L = C_p (T_{Savg} - T_W) \quad (5)$$

here, Δm is the evaporation rate (kg/m²h), C_p (kJ/(kg.K)) is the specific heat of water, T_{Savg} ($^{\circ}$ C) is the average temperature of the cotton cloth, T_W ($^{\circ}$ C) is the bulk water temperature at the time of experiment.

$$\phi = \frac{V_{water}}{V_{sample}} \quad (6)$$

where, $V_{water} = \frac{M_{fabric+testing\ fluid} - M_{sample}}{\rho_{testing\ fluid}}$ and

$$V_{sample} = Area \times Fabric\ thickness \quad [13].$$

$$K = 0.129 \frac{\phi}{1-\phi} \ln \frac{0.64}{(1-\phi)^2} \quad (7)$$

$$\tau = 1 + a \frac{(1-\phi)}{(\phi - \phi_m)^m} \quad (8)$$

where, $a = 0.65$, $m = 0.19$, are constants and $\phi_m = 0.33$ is the percolation coefficient [14].

Table 1. The characteristics of the fabrics used for generating vapor.

GSM (g/m ²)	Fiber diameter (μm)	Thickness (mm)	Weave type
97 (S-1)	18	0.19	Non-woven
197 (S-2)	23	0.41	Plain
78 (S-3)	16	0.16	Plain

3. Results and Discussion

Figure 4 shows the average temperature at the vapor generating surface during the test duration of 1 hr. for the three different fabric samples for two input heat flux cases 1 Sun and 2.5 Sun. At 1 Sun input heat flux all the three samples remain completely saturated with the testing fluid as evident from the steady temperature readings, and no possible hot spot is visible due to partial dry-out or blockage of fabric pores due to accumulation of salt. However, at 2.5 Sun input heat flux the average temperature of the vapor generating surface is not able to reach a steady state for S-2 and S-3 fabric samples, see Figure 4. The possible reason for which is discussed below.

Figure 5 shows the mass loss rate from the vapor generating surface for the three fabric samples as recorded by the digital weighing balance for the

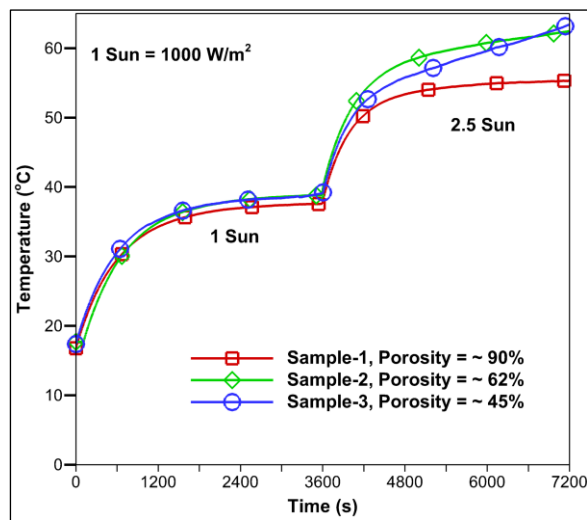


Figure 4. Average temperature distribution at the vapor generating surface for the three different fabric samples for input heat flux of 1 Sun and 2.5 Sun, for a testing duration of 1 hr each.

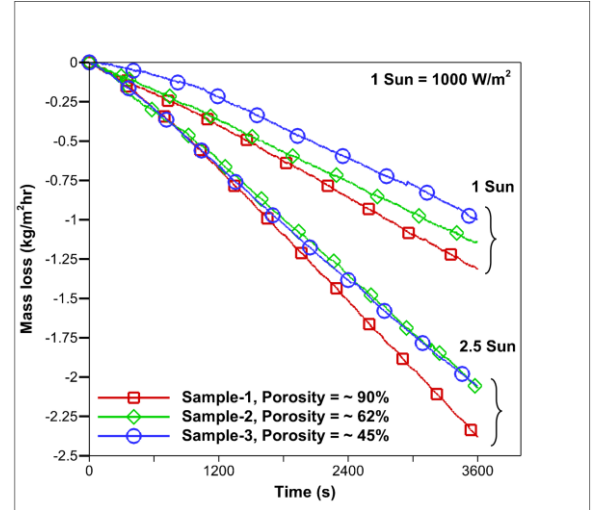


Figure 5. Mass loss rate from the vapor generating surface for the three different fabric samples for input heat flux of 1 Sun and 2.5 Sun case, for a test duration of 1 hr. each.

two input heat flux cases. S-1 (non-woven) reported the maximum mass loss rate for both the input heat flux cases whereas, S-2 performed better for 1 Sun case than the S-3, but reported similar mass loss for 2.5 Sun case. The average evaporation rate and heat to vapor conversion efficiency for the three fabric samples, for the two input heat flux cases, are plotted against their permeability values. This establishes the fact that S-1 having the maximum permeability leading to higher wicking rate is able to maintain the supply of testing fluid to keep the vapor generating surface saturated throughout the test duration, for both the input heat flux case reporting better evaporation rate and heat to vapor conversion efficiency among the three fabric samples considered in this study, see Figure 6.

$$J = \frac{\phi D \Delta C}{\tau} \quad (9)$$

where, J is the salt diffusion rate and D is the diffusion coefficient of NaCl in water ($1.99 \times 10^{-9} \text{ m}^2 \text{ s}^{-1}$).

$$J^\# = \frac{\Delta m C_\infty}{3600} \quad (10)$$

where, $J^\#$ is the rate of salt accumulation and C_∞ is the salt concentration of the testing fluid.

For S-2 and S-3 in addition to their lower wicking rate because of lower permeability (S-2 one order of magnitude less, and S-3 two orders of magnitude less than S-1) tortuosity played an important role which is shown in Figure 7 and also evident from Equations 9 and 10.

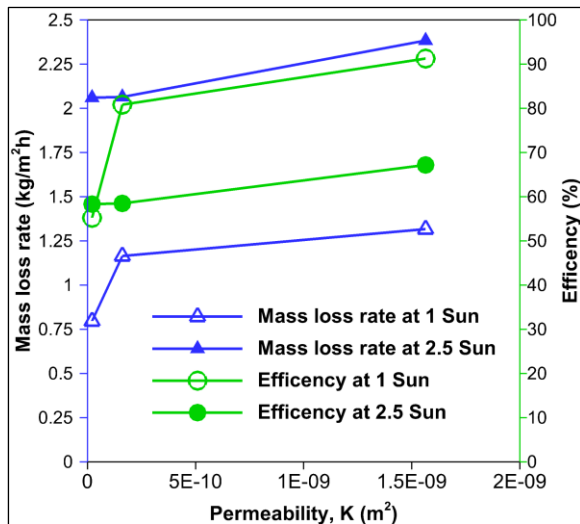


Figure 6. Average evaporation rate and heat-to-vapor conversion efficiency at the end of 1 hr. of testing duration, for the three fabric samples with different values of permeability.

In case of generating vapor continuously for a long time scale it is important that the wicking material is able to dissolve back the accumulated salt on the vapor generating surface into the bulk reservoir through diffusion. Tortuosity in this case becomes a deciding factor, viz., how easily the accumulated salt is allowed to diffuse back to the bulk reservoir experiencing least resistance.

In Figure 7 it is evident as highlighted that the tortuosity values for S-1 and S-2 are such that the salt diffusion time scale is able to overcome significant accumulation of salt on the vapor generating surface within the test duration for all cases. On the other hand, S-3 had comparatively more resistance in diffusing back the salt due to its comparatively higher tortuosity. This leads to accumulation of salt on the vapor generating surface for the 2.5 Sun input heat flux case which

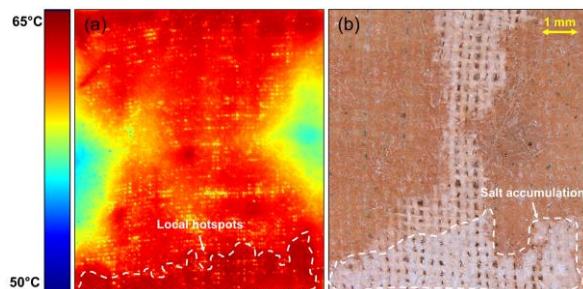


Figure 8. (a) Infrared image showing the spatial distribution of temperature at the vapor generating surface, (b) microscopic image showing local partial dry out and salt accumulation for Sample-3 for a given input heat flux of 2.5 Sun, at the end of test duration of 1 hr.

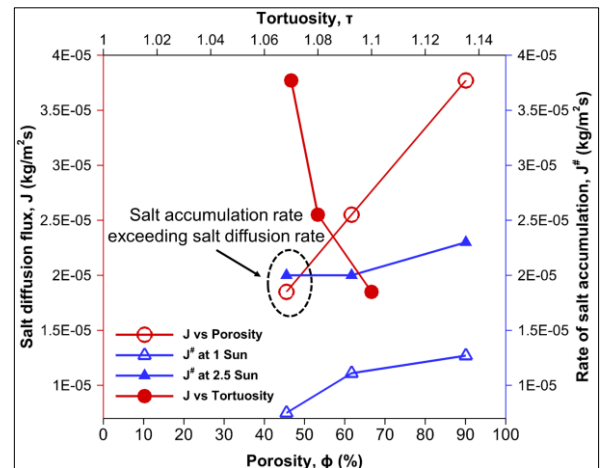


Figure 7. Variation of salt diffusion flux back to the reservoir with porosity and tortuosity, and salt accumulation rate on the vapor generating surface with two different input heat flux cases, for the three different fabric samples.

is visible in the microscopic images of the vapor generating surface, as shown in Figure 8 (b). The Infrared image of the vapor generating surface for S-3 also revealed local hot spots due to partial dry out in the same location of the vapor generating surface, see Figure 8 (a).

Although, in spite of visible salt accumulation and local hot spots emerging on the vapor generating surface at the end of test duration for S-3 and 2.5 Sun input heat flux case, the average evaporation rate for S-2 and S-3 comes out to be almost equal. This can be explained as follows: although inter fiber pores get clogged by accumulation of salt, inter yarn pores for S-3 were still available which contributed in vapor generation. The inter fiber pores and inter yarn pores for S-2 and S-3 are largely different because of their different weave type and it is necessary to understand the role of these pore dimensions on the local evaporation rate to develop a complete understanding of evaporation dynamics on such fabric structures.

4. Summary and Conclusions

The existing literature in interfacial vapor generation for solar thermal desalination applications are majorly devoted to developing new wicking materials and pathway designs, which enables either mitigation of salt or completely blocking salt accumulation on the vapor generating surface, in order to achieve sustained rate of vapor generation. However, the effect of fabric parameters like porosity, permeability, tortuosity, fiber diameter, fabric thickness,

and pore radius on the evaporation dynamics for such applications, a have received minimal or practically no attention in the existing literature. This study for the first time, tries to incorporate a holistic understanding of the role of all such fabric parameters in evaporation dynamics and the resulting salt diffusion time scale.

In this study we show that non-woven fabric weave types have inherently higher permeability leading to high wicking rate and offer low transport resistance to salt diffusion back flow to the bulk reservoir. Hence, non-woven weave type fabrics will have better advantage in maintaining sustained evaporation rate by preventing salt accumulation on the vapor generating surface. Thus, TPCT based heat localization strategies in future must consider non-woven weave type fabric structures as an ideal choice for its wicking and vapor generating surface. It is also important to highlight that fabric thickness remains an important parameter; on one hand it effects the tortuosity of the sample which plays an important role in salt diffusion time scale, and on the other hand increase in fabric thickness would inherently increase the thermal resistance between the vapor generating surface and the heat source for a TPCT based heat localization system. Effect of inter fiber pore and inter yarn pore on the evaporation dynamics also remain unexplored, as gross average temperature and mass loss rate measurements fail to take their effect into consideration. Modern Infrared thermography enabled with microscopic optical accessories can prove handy in future to understand the evaporation and salt precipitation dynamics locally on such fabric structures.

References

- [1] C. Chen, Y. Kuang and L. Hu, Challenges and opportunities for solar evaporation. *Joule*, 2019. 3(3): pp.683-718.
- [2] Z. Wang, T. Horseman, A.P. Straub, N.Y. Yip, D. Li, M. Elimelech and S. Lin, Pathways and challenges for efficient solar-thermal desalination. *Science Advances*, 2019. 5(7): p.eaax0763.
- [3] G. Vaartstra, L. Zhang, Z. Lu, C.D. Díaz-Marín, J.C. Grossman and E.N. Wang, Capillary-fed, thin film evaporation devices. *Journal of Applied Physics*, 2020. 128(13): p.130901.
- [4] L. Zhang, Z. Xu, L. Zhao, B. Bhatia, Y. Zhong, S. Gong and E.N. Wang, Passive, high-efficiency thermally-localized solar desalination. *Energy & Environmental Science*, 2021. 14(4): p.1771-93.
- [5] K. Xu, C. Wang, Z. Li, S. Wu and J. Wang, Salt mitigation strategies of solar-driven interfacial desalination. *Advanced Functional Materials*, 2021. 31(8): p.2007855.
- [6] D. Chatterjee, T. Kulshrestha and S. Khandekar, Continuous Vapor Generation for Thermal-Desalination Applications Using a Thermo-siphon Based Heat Localization Strategy, <https://dx.doi.org/10.2139/ssrn.4302832>.
- [7] M. A. Halon and H. B. Ma, Evaporation Heat Transfer in Sintered Porous Media, *Journal of Heat Transfer*, 2003. 125(4): p.644-52.
- [8] X. Chen, C. Qi, W. Wang, J. Miao and H. Zhang. Investigation of interface profiles in meshed wicks and related evaporation characteristics, *International Journal of Thermal Sciences*, 2022. 1;177: p.107522.
- [9] U. Nachshon, N. Weisbrod, R. Katzir, and A. Nasser. NaCl crust architecture and its impact on evaporation: Three-dimensional insights. *Geophysical Research Letters*, 2018. 28;45(12): p.6100-8.
- [10] S.M. Shokri-Kuehni, T. Vetter, C. Webb, and N. Shokri, New insights into saline water evaporation from porous media: Complex interaction between evaporation rates, precipitation, and surface temperature. *Geophysical Research Letters*, 2017. 44(11), pp.5504-5510.
- [11] H. Ghasemi, G. Ni, A.M. Marconnet, J. Loomis, S. Yerci, N. Miljkovic and G. Chen, Solar steam generation by heat localization. *Nature Communications*, 2014, 5(1): p.1-7.
- [12] G. Ni, S.H. Zandavi, S.M. Javid, S.V. Boriskina, T.A. Cooper and G. Chen, A salt-rejecting floating solar still for low-cost desalination. *Energy & Environmental Science*, 2018. 11(6): p.1510-9.
- [13] G. Peng, S. Deng, S.W. Sharshir, D. Ma, A.E. Kabeel and N. Yang, High efficient solar evaporation by airing multifunctional textile. *International Journal of Heat and Mass Transfer*, 2020. 147: p.118866.
- [14] R. Vallabh, P. Banks-Lee, and A.F. Seyam, New approach for determining tortuosity in fibrous porous media. *Journal of Engineered Fibers and Fabrics*, 2010. 5(3):155892501000500302.

Simultaneous measurement of two-dimensional temperature distribution and flow inside a single channel simulating pulsating heat pipe

Rikuto Shimoda^{1*}, Keiko Ishii¹, and Koji Fumoto¹

¹*Aoyama gakuin univ., Kanagawa, Japan*

* *Corresponding author email address: c5621150@aoyama.jp*

Abstract

The mechanism of Pulsating Heat Pipe (PHP) is still unclear because of its complex thermal fluid property. This study executed the temperature distribution and flow and Pressure inside a single channel simulating PHP. Temperature Sensitive Paint (TSP) painted on the optical window covered half of the channel. The TSP was excited by UV LED light and the luminescence intensity was captured by a high-speed camera. Boiling of the liquid film was observed on the hydrophilic channel wall, resulting in a decrease in the wall temperature. On the hydrophobic channel wall, boiling of the liquid column and evaporation of droplets were observed. A decrease in wall surface temperature occurred during droplet evaporation. It was found that the heat transport performance was higher in the hydrophobic channel than in the hydrophilic channel in the single channel.

Keywords: Pulsating heat pipe; TSP; Visualization; Pressure distribution; Single channel

1. Introduction

In recent years, as the amount of heat generated by electronic devices increases due to miniaturization and high integration, the development of heat transport devices that are smaller and have higher heat transport performance is desired. Pulsating heat pipes (PHPs) are attracting attention because they are more compact than conventional heat pipes and have very high heat transport performance. On the other hand, its operation mechanism and heat transport phenomena have not yet been fully understood due to the complexity of the internal heat flow phenomena. The heat transport mechanism of PHP is complicated by many parameters. It is difficult to investigate the effect of a single parameter on the heat transport in a real PHP. Miura et al. mechanically oscillated a working fluid in a single straight channel with heating and cooling sections to simulate the flow in a PHP. They varied the oscillation frequency and amplitude investigated the temperature distribution on the outer wall and effective thermal conductivity by thermocouples [1]. Nagasaki et al. also cut off one turn of multiple channels to form a straight channel and investigated the liquid column oscillation frequency, oscillation amplitude, and gas pressure waveforms at various heating rates [2]. However, temperature measurement using thermocouples is a point measurement and cannot measure detailed and localized temperature distribution.

In this study, we attempted to measure temperature distribution using Temperature

Sensitive Paint (TSP) of which the emission intensity that changes with temperature. The TSP painted surface was in contact with the inside of a single channel to observe the temperature through a visualization glass. At the same time, the internal flow was visualized using fluorescent dyes and the internal pressure was measured using a pressure sensor. The internal flow, temperature distribution, and pressure were measured simultaneously by mechanically oscillating the working fluid back and forth inside a single channel device that simulates the flow in PHP. The objective of this study is to clarify the relationship between the fluid column oscillation and the temperature field, and the phase change behavior of the fluid due to differences in wettability.

2. Experimental apparatus and methods

Figure 1 shows a schematic diagram of the experimental apparatus. The apparatus consists of a test section with a visualization window and a rectangular flow channel, an excitation system consisting of a syringe and a piston-crank mechanism, a heating system connecting a cartridge heater and a transformer, a cooling system connecting a thermostatic bath and a water-cooled heat sink, a vacuum pump system including a digital vacuum gauge and a vacuum pump, a measurement system including a thermocouple and a pressure sensor, and an optical system including a camera and an excitation light. The crank mechanism consists of a motor and a linear guide rail connected by a connecting rod

and converts rotation into reciprocating motion. A cross joint and valves are used for vacuuming, fluid injection, and forced oscillation of the working fluid, respectively. A K-type sheath thermocouple was used and attached to the heating section as shown in Figure 1 to measure the temperature of the outer wall of the channel at a distance of 1 mm from the inner wall of the channel. The pressure sensor was connected to a valve at the top of the back of the copper plate and measured the pressure in the channel at the uppermost point of the channel.

Figure 2 shows the details of the test section used in this experiment. A rectangular channel 2 mm wide, 2 mm deep, and 180 mm long was fabricated on a 15-mm-thick brass plate. The channel was sealed by a 5-mm-thick glass plate and a 15-mm-thick insulating plate with a groove to fit the glass plate and a window for visualization. Only half of the channel was in contact with TSP, and excitation light was irradiated from above the glass plate. In this experiment, hydrophilic paint (GA-150, Hosho Corporation) and hydrophobic paint (Glaco, 04169) were applied to a glass plate coated with TSP and a brass plate, respectively, in order to change the wettability of the entire inner surface of the channel. The system consists of a cartridge heater heated by applying voltage and cooled by passing water from a thermostatic bath to a water-cooled heat sink. The working fluid was a solution of luminescent Rhodamine 6G in distilled water to facilitate observation of the flow. A high-speed camera was used to capture images, and a power LED ($\lambda=365\text{nm}$) was used as a light source for TSP excitation. The camera was equipped with a single focal length lens and a long-pass filter to cut ultraviolet rays from the LED excitation light source. The camera and pressure sensor can be simultaneously measured by a function generator. In this experiment, the liquid was heated at a constant power of 80 W. At this input power, boiling of liquid columns and films could be observed.

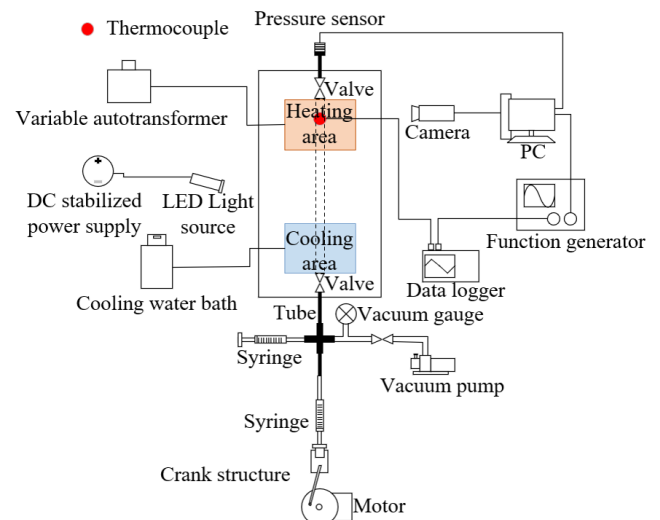


Figure 1. Schematic diagram of the experimental setup.

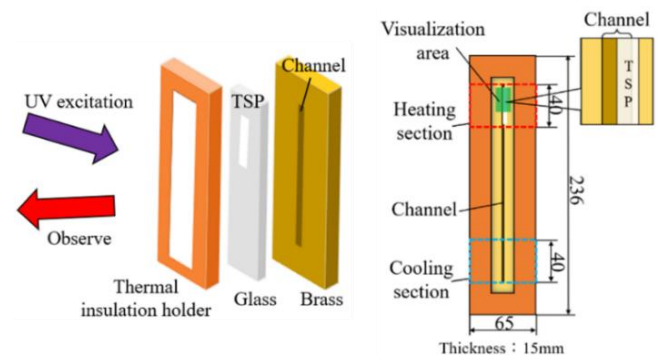


Figure 2. Schematic diagram of the test section.

3. Results

3.1. Relationship between flow and temperature

Figures 3(a) and (b) show the flow and temperature distribution for the hydrophilic inner wall of the channel, and the time-series graphs of the temperature extracted from the measurement area, respectively. The vertical and horizontal axes of the graphs represent TSP temperature and time, respectively. The heat input is 80W and the oscillation frequency of the liquid column is 0.5 Hz. In Figure 3(a), the liquid exists in the white area and the vapor exists in the black area. The temperature measurement area is the black area indicated by the yellow arrow, and the black arrow indicates the direction of movement of the liquid. The blue area in Figure 3(b) indicates the presence of a liquid column in the temperature measurement area, and the red area indicates the presence of vapor. The data shown by the solid line indicates the temperature of TSP. The data

indicated by the dashed line shows the time-series variation of the saturation temperature corresponding to the measured pressure. Figure 3(a) shows that after the liquid column descends, the remaining liquid film boils and disappears. Figure 3(b) shows that the wall temperature decreases as the liquid film boiling. This is due to the absorption of heat from the wall surface as the liquid film boiling. Thereafter, the temperature rises at about 1.0~1.6s. This is due to the disappearance of the liquid film and the addition of heat from the heater. Since the wall temperature is higher than the saturation temperature for the pressure in the channel from 0.2s to 1.7s, it means that the liquid film formed in the heating section boils or evaporates during that time. Figures 4(a) and (b) show the flow and temperature distributions for the case where the inner wall of the channel is coated with hydrophobic paint to make it hydrophobic, and the time-series variations of the temperature extracted from the measurement area, respectively. Figure 4(a) shows that after the liquid column descends, the liquid film turns into droplets. Figure 4(b) shows that the temperature drops slightly during the period of about 2.0~2.4s when the droplets exist. This is due to the evaporation of the droplet. After that, the temperature rises at about 2.4~3.3 s. This is due to the disappearance of the droplets. Since the wall temperature is higher than the saturation temperature for the pressure in the channel from 2.0s~3.3s, it means that the droplets formed in the heating section boil or evaporate during that time.

Figure 5 shows the dimensionless temperature variation normalized to one oscillation cycle for different hydrophilicity, hydrophobicity, and oscillation frequency. The solid line indicates the hydrophilic case, and the dashed line indicates the hydrophobic case. The vertical axis shows the dimensionless temperature and the horizontal axis is one oscillation cycle of the liquid column. The dimensionless temperature is normalized by the maximum and minimum values of temperature in one oscillation cycle as defined in Equation (1). where T_{dl} is the dimensionless temperature of the wall surface, T_{max} and T_{min} are the maximum and minimum values of the wall surface temperature in one oscillation cycle of the liquid column. The figure shows that for the hydrophilic case, a temperature drop occurred at a frequency of 0.5 Hz, while no temperature drop occurred at frequencies of 1.5 Hz, and 2.0 Hz. This is because an increased frequency keeps the liquid film thick, thereby suppressing evaporation of the film [4]. Furthermore, this is because the time between the

formation of the liquid film on the wall and its recovering by the liquid column is short when the frequency is increased. On the other hand, in the case of hydrophobic, there was no significant difference in the dimensionless temperature waveforms at any frequency. This is because the hydrophobic of the wall causes the formation of droplets on the wall surface and evaporation at all frequencies.

$$T_{dl} = \frac{T(t) - T_{min}}{T_{max} - T_{min}} \quad (1)$$

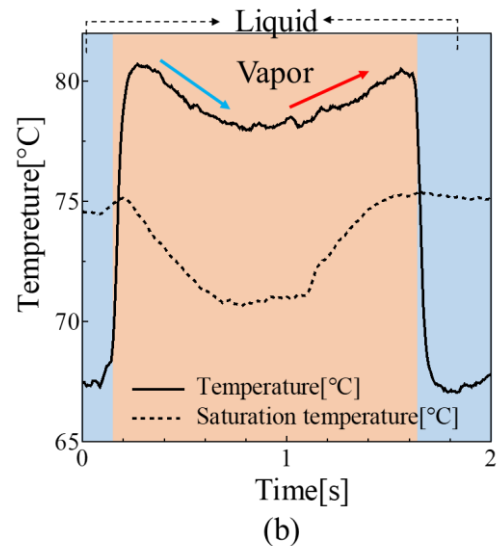
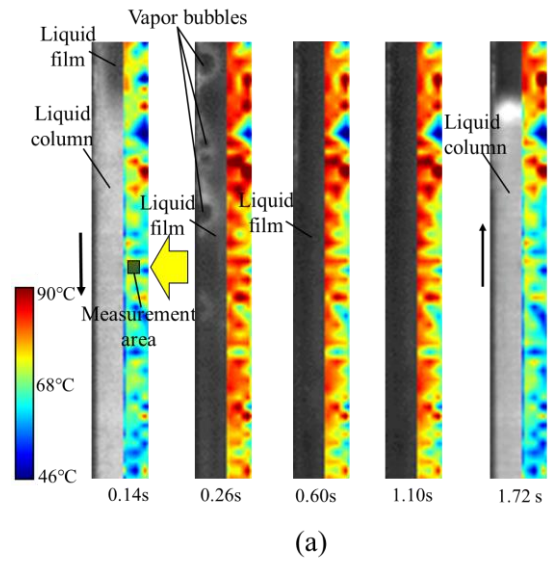


Figure 3. The fluid flow and temperature distribution at heating section with hydrophilic (80W): (a) fluid flow and temperature distribution, (b) time variation of temperature and saturation temperature.

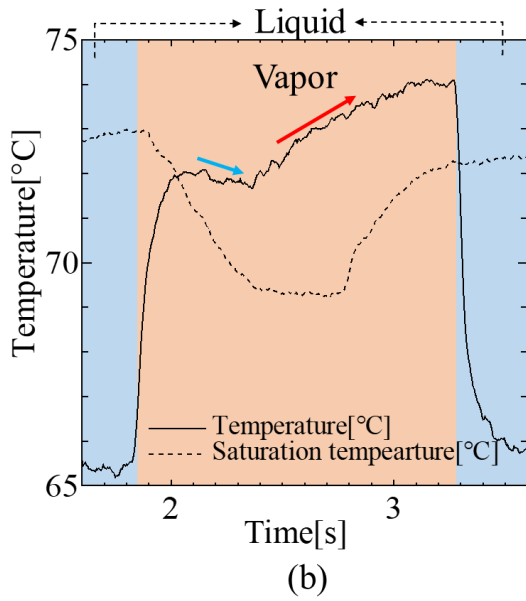
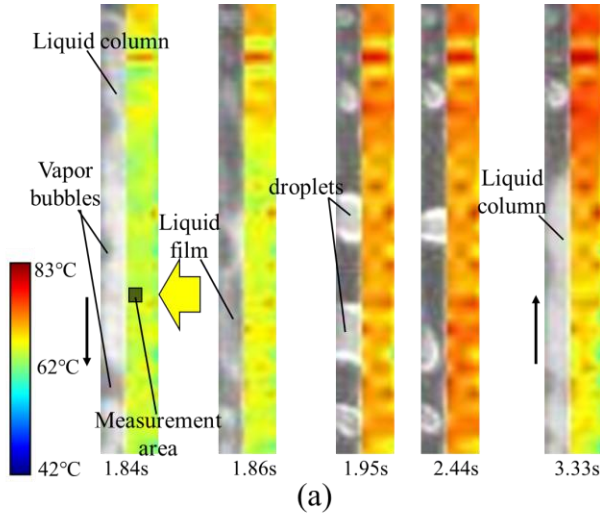


Figure 4. The fluid flow and temperature distribution at heating section with hydrophobic (80W): (a) fluid flow and temperature distribution, (b) time variation of temperature and saturation temperature.

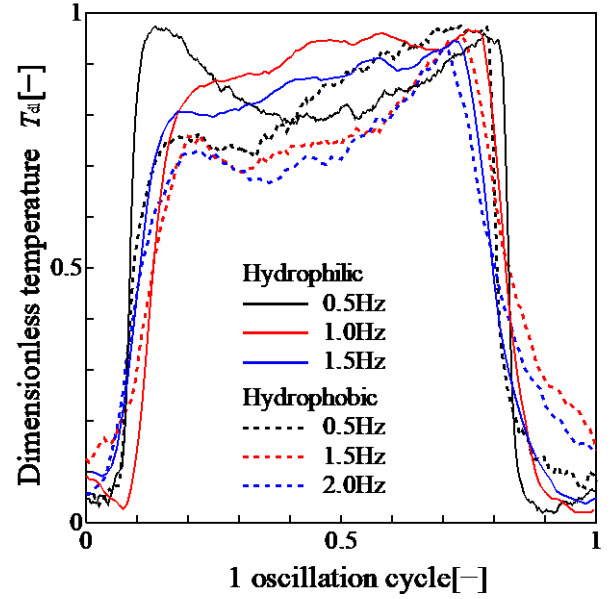


Figure 5. Dimensionless wall temperature in one oscillation cycle of liquid column. Comparison of hydrophilic and hydrophobic and various oscillation frequencies.

3.2. pressure variation

Figure 6 shows the amount of pressure change for one vibration cycle at each frequency for the hydrophilic and hydrophobic properties. The figure shows that the amount of pressure change was larger for hydrophilic than hydrophobic at all frequencies. This is because differences in vapor volume and vapor temperature depend on whether the wall nature is hydrophilic or hydrophobic. When adiabatic compressive expansion due to liquid column oscillation is considered, the larger the density of water molecules in the gas phase, the larger the amount of pressure change in one oscillation cycle of the liquid column. Also, the higher the vapor temperature, the larger the amount of pressure change. However, the actual vapor volume has not been calculated and the vapor temperature has not been measured. It is necessary to consider this hereafter.

$$P_{dl} = \frac{P(t) - P_{min}}{P_{max} - P_{min}} \quad (2)$$

Figure 7 shows the dimensionless pressure change normalized by the minimum and maximum pressure values as defined in Equation (2) for one vibration cycle at each frequency. The comparison was made under three conditions: hydrophilic, hydrophobic, and no phase change in the original glass plate, in which wettability was not changed. In the no-phase-change condition,

the liquid column oscillated with a working fluid sealed in it without vacuuming. In addition, the temperature of the entire channel wall was controlled to approximately 8°C to prevent the phase change of the liquid. P_{max} is the maximum pressure value during one oscillation cycle of the liquid column and P_{min} was the minimum pressure value. The input power was 80 W and the oscillation frequency was 0.5 Hz, 1.5 Hz, and 2.0 Hz. The solid black data is hydrophilic, the solid red data is hydrophobic, and the solid blue data is case of no phase change occurs. The figure shows that the pressure increase was greater for hydrophobic than hydrophilic conditions at all frequencies during the time when the liquid column penetrated the heating section, compared to the no-phase-change condition. This is because that the hydrophobic condition enhanced evaporation of the liquid column compared to the hydrophilic condition. The visualization results shown in Figures 3 and 4 also indicated that only hydrophobic conditions cause evaporation of the liquid column. In the hydrophobic case, water molecules have less energy to adsorb on the wall, resulting in decrease of the evaporation temperature, while in the hydrophilic case, water molecules have more energy to adsorb on the wall, resulting in increase of the evaporation temperature [3]. As a result, boiling of the liquid column occurred only in hydrophobic at that time the amount of vapor increased and caused the pressure to rise.

3.3. Heat transport rate

Figure 8 shows the relationship between the oscillation frequency of the liquid column and heat transport rate in hydrophilic and hydrophobic. The heat input is 80 W. The red plot is hydrophilic and the blue plot is hydrophobic. As shown in the figure, the heat transport performance of the hydrophobic was larger than that of all conditions of the hydrophilic. This is because of the contribution of the boiling of the liquid column and the evaporation of the droplets in the hydrophobic. In the case of hydrophilic, boiling of the liquid film occurred, but boiling of the liquid column did not occur. this caused the difference in the heat transport rate between the hydrophilic and the hydrophobic.

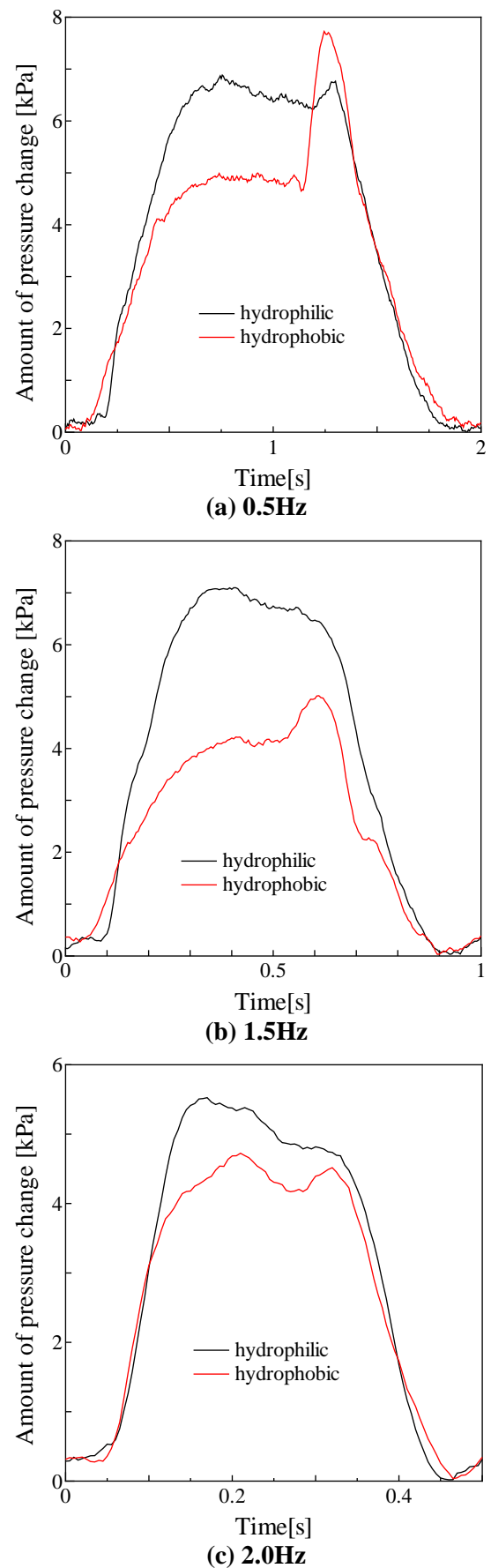


Figure 6. Pressure variation for one liquid column oscillation cycle at various frequencies (80W).

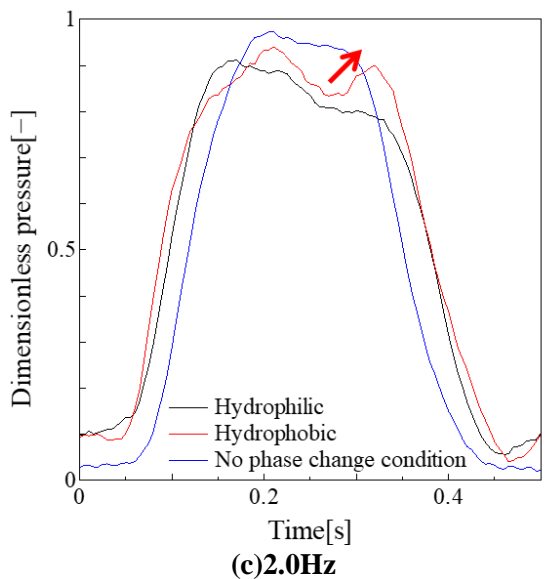
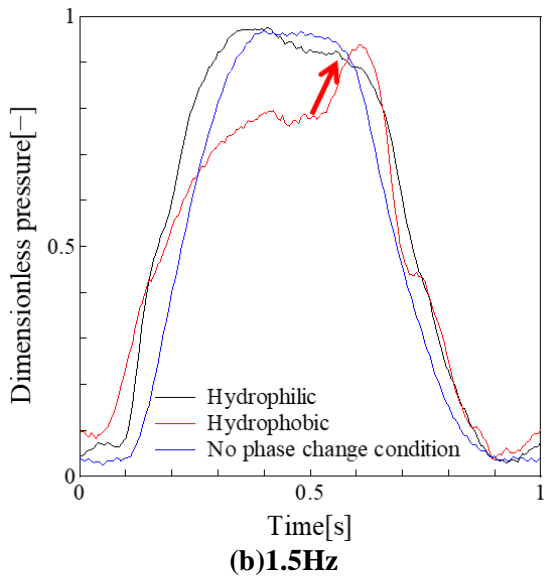
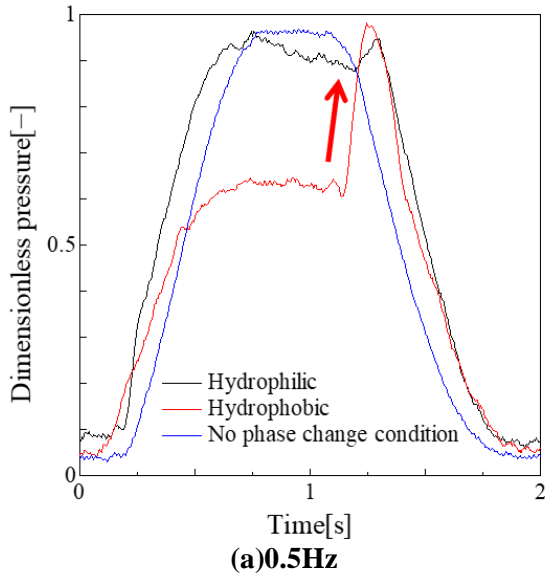


Figure 7. Dimensionless pressure variation for one liquid column oscillation cycle at various frequencies (80 W).

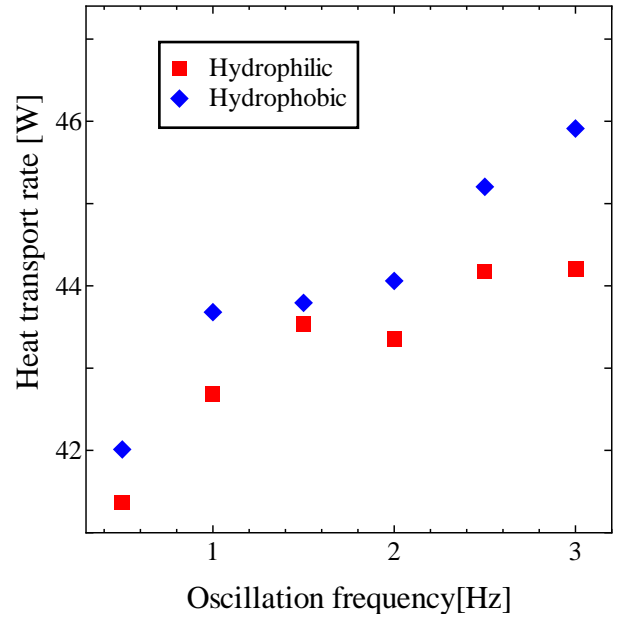


Figure 8. Relationship between the frequency of oscillation of the liquid column and the heat transport rate (80W).

4. Conclusion

The flow and temperature distribution in the heating section were measured for hydrophilic and hydrophobic inner walls of the channel. The relationship between the flow and temperature and the heat transfer performance due to the difference in wettability were investigated. In addition, the pressure inside the channel was measured, and the pressure changes were compared between hydrophilic and hydrophobic.

In the Hydrophilic case, the wall surface temperature decreased with the boiling of the liquid film. This indicates that the latent heat from the boiling of the liquid film was absorbed from the wall. On the other hand, in the hydrophobic condition, the wall surface temperature decreased with evaporation of the droplet. This indicates that the wall absorbed the latent heat from the evaporation of the droplet. The dimensionless temperature variation of the liquid column during one oscillation cycle showed a difference in the temperature waveform between hydrophilic and hydrophobic conditions. This is attributed to the difference in the hydrophilic and hydrophobic flow phases.

The pressure change was larger for hydrophilic than hydrophobic. This is because the difference in vapor volume and vapor temperature in the channel depending on whether the hydrophilic or hydrophobic occurs. In the dimensionless pressure of a liquid column during one oscillation cycle, the pressure increase was greater in the hydrophobic

than in the hydrophilic during the time when the liquid column covered the heating section, compared to the condition in which no phase change occurred. This is because the enhanced evaporation of the liquid column in the hydrophobic than in the hydrophilic.

Heat transport rate was greater for hydrophobic than hydrophilic at all frequencies. This difference is due to the difference in the flow pattern between hydrophilic and hydrophobic. It means that the boiling of the liquid column contributes to the increase in heat transport rate.

References

[1] Miura, M., Nagasaki, T. and Ito, M. A fundamental study on heat transport characteristics in a pulsating heat pipe by using a forced oscillation system (Measurement of effective thermal conductivity) (in Japanese), Transactions of the JSME, 2015. 81(827), pp.14-27.

[2] Nagasaki, T., Miura, M., and Ito, M. Study on self-oscillation heat pipe with a horizontal straight channel (in Japanese), Proceedings of 50th National Heat Transfer Symposium of Japan, 2013. Vol.50, pp.422-423.

[3] Ogaswara, M., Ito, T., Tamaki, M., and Tsuji Y. Study on the heat transfer enhancement in a heat pipe (in Japanese), Proceedings of the Yamanashi Lecture Meeting, 2013. 253, pp.52-53.

[4] Han, Y., Shikazono, N., Measurement of liquid film thickness in micro square channel, International Journal of Multiple flow, 2009. 35(10), pp.896-903.

[5] Mangini, D., Marengo, M., Araneo, L., Mamei, M., Fioriti, D., Filippeschi, S. Infrared analysis of the two phase flow in a single closed loop pulsating heat pipe, Experimental Thermal and Fluid Science, 2018. 97, pp.304-312.

Experimental studies on sintered bi-porous wicks for loop heat pipe

Chandan Nashine¹, Nadaf Arman Mohaddin¹, Sandip Kumar Sarma¹ and Manmohan Pandey^{1*}

¹Department of Mechanical Engineering, Indian Institute of Technology Guwahati, Guwahati, India

*Corresponding author: manmohan@iitg.ac.in

Abstract

The current work deals with the development and characterization of bi-porous copper wicks with different sizes and porosities for loop heat pipes. It involves the measurement of maximum pore radius, effective thermal conductivity, surface wettability, and surface morphology. The surface wettability of the wick is tested by contact angle measurement for different working fluids and it is found that acetone poses a better wetting behavior. The effective thermal conductivity of the wick, determined using infrared thermography, is found to be 8.72 W/m-K. The liquid movement in the porous wick during the capillary rise phenomena is also studied by infrared thermography. The maximum pore radius of the wick is calculated using bubble point method and is found to be 0.9 μm . SEM imaging of pore structures shows the presence of large pores, which leads to enhanced porosity and interconnects fine pore network responsible for the generation of the capillary pumping pressure required.

Keywords: Loop heat pipes; Bi-porous wick; Porosity, Effective thermal conductivity

1. Introduction

Thermal management of high heat dissipating miniaturized electronic equipment are the need of the hour. Heat loads are unevenly concentrated in specific areas of the electronic components, requiring site-specific cooling that cannot be achieved with traditional cooling techniques such as air cooling. Therefore, the compact loop heat pipe, with its high heat removal capacity, is one of the leading technologies for thermal management in passive cooling of electronic components.

Figure 1 shows a schematic of the loop heat pipe (LHP). Capillary wick is the heart of the LHP, as it helps in the circulation of the working fluid around the loop [1]. The wick is also the key to the heat dissipation process as it provides the required area for evaporation. Because the function of the wick is critical to the overall performance of the system, its design parameters, the material used and the working fluids, must be carefully assessed to ensure the desired performance [2]. The capillary rise developed in the sintered porous wick should be adequately high enough to overcome the total pressure drop inside the loop. The high capillary pumping force also ensures sufficient liquid feedback to prevent the dry-out condition in the evaporator. The porous capillary wick for LHP is generally fabricated using cold press sintering, additive manufacturing, metal injection moulding and 3-D printing. The key parameter of sintered porous wick includes the low hydraulic resistance to ensure a high flow rate and minimized effective pore radius to ensure high capillary pressure [3,4]. Singh et al. [5] compared copper and nickel wicks and found copper wick has higher heat leak due

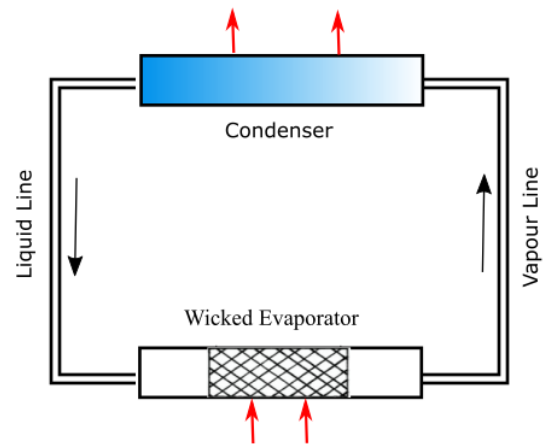


Figure 1. Schematic of Loop heat pipe

to higher effective thermal conductivity. Prasad et al. [6] studied the experimental characterization of pore size, porosity, and thermal conductivity for a flat disk-shaped porous nickel wick. Wu et al. [7] presented the application of sintered polytetrafluoroethylene (PTFE) wick for LHP and found that the pore size of the PTFE wick was about 300-500 μm . Deng et al. [8] studied the characterization of 4 categories of sintered wicks and compared the results and found that the porous copper wicks had higher capillary rise and permeability than nickel wicks. Seidel [9] studied the values of permeability as a function of pore radius. Choi et al. [10] investigated the low-temperature sintering of wicks and found that porous copper wicks possess improved capillary pressure and porosity. Samanta et al. [11] studied the physical characteristics of porous wick fabricated using metal injection moulding. They found that the ideal temperature for sintering was

about 60 minutes at 900 °C. Choi et al. [12] performed an experimental study on sintered porous wick for mLHP. They developed experimental setup to measure maximum capillary pressure and used the laser flash method for thermal conductivity measurement. Anvesh et al. [13] fabricated the porous nickel wick and performed the experimental characterization. They drew the details of the experimental module used to characterize porous wick for use in LHP.

Although wicks are vital in LHP, manufacturing them is complicated and requires an optimum balance of critical characteristics like: porosity, permeability, pore diameter, and pore structure. In a wick, small pores should be employed for high capillary suction, but on the other hand, small pores will trap vapor and prevent rewetting. It indicates that the wicks with single pore characterization exhibit poor compromise between high capillary force and high vapor permeability [14]. Therefore, to improve the performance of LHPs, it is important to implement and better understand the characteristics of bi-porous wicks.

2. Fabrication Methodology

Copper powder (average particle size < 10 microns) is mixed well with polyvinyl alcohol (PVA) solution, which acts as a pore former and binding agent for bi-porous metallic wicks. The prepared sample is then sintered at three different temperatures and durations. Based on the porosity achieved, the best sintering condition is identified as 650°C and 90 minutes. Figure 2 shows the fabricated test samples of cylindrical and flat wicks. The cylindrical wicks are 10 mm dia and 15–50 mm long. The flat wick is 49 mm dia and 4 mm thick.

3. Characterization of wick

3.1 Surface Wettability

The contact angle (CA) is the angle between the solid-liquid and liquid-vapor interfaces which can

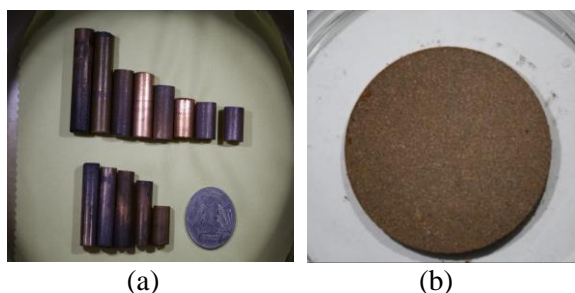


Figure 2. Bi-porous wicks fabricated for loop heat pipes (a) Cylindrical shaped wicks (b) A flat disk-shaped

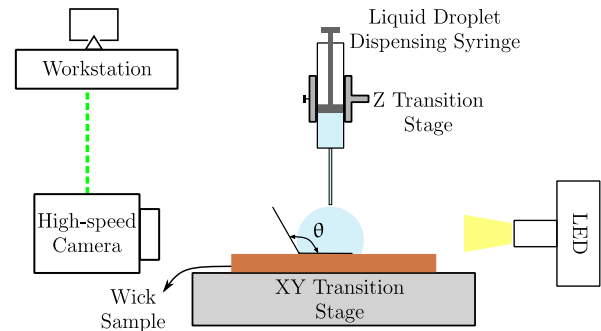


Figure 3. Schematic of experimental setup for contact angle measurement of wick surface

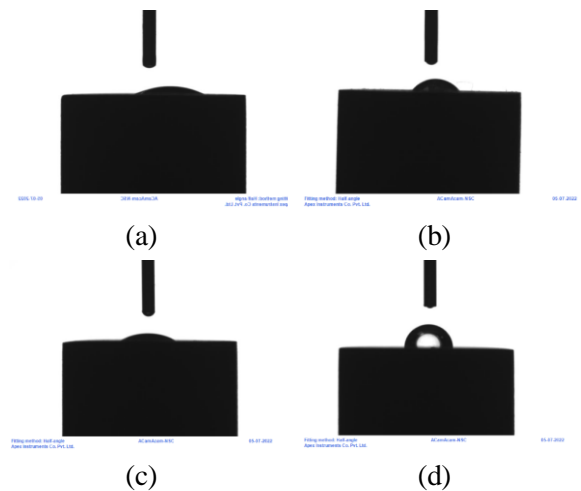


Figure 4. Contact angle measurement of wick surface with (a) Acetone (b) Methanol (c) Propanol and (d) Water

indicate the wettability and capillary strength of the surface. Two methods which are commonly used to estimate the static contact angle are the sessile drop method and the pendant drop method.

Figure 3 shows the experimental setup used for the measurement of static contact angle of porous wick surface. In the current work, the contact angle is measured by a three-point tangent method using the sessile drop technique with a volume of 5 μL . Surface wettability of the copper wick is tested with four working fluids. The measured contact angles for acetone, methanol, propanol and water, are found to be 18.84°, 51.23°, 29.23°, and 96° respectively (Figure 4). The result shows that acetone has the better surface wettability against copper wicks as compared to the other fluids.

3.2 Effective Thermal Conductivity

To calculate the effective thermal conductivity of porous wick, the wick and heater system is considered as an extended surface, and the estimated temperature gradient through the fin (equation 1) is compared with the temperature data

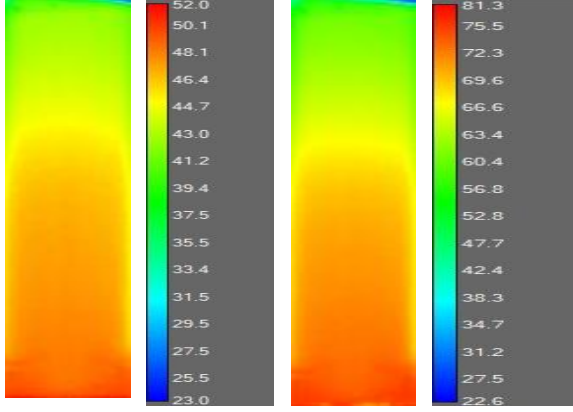


Figure 5. Steady-state temperature contours of wick at 1 W and 2 W using IR thermography

extracted from the infrared thermography (FLIR A655SC). Figure 5 shows the temperature profile of the porous copper wick in steady state condition. The fin is considered of finite length and loses heat by convection from its end. The measured effective thermal conductivity of the wick is found to be 8.72 W/m-K.

$$\frac{T - T_{amb}}{T_b - T_{amb}} = \frac{\cosh m(L - x) + \frac{h}{mk} \sinh m(L - x)}{\cosh mL + \frac{h}{mk} \sinh mL} \quad (1)$$

Here L, P, and A are the length, perimeter and cross-sectional area of the porous wick. h is the ambient heat transfer coefficient.

3.3 Pore Radius Measurement

The maximum pore radius of the porous wick is experimentally measured using the bubble point method (Figure 4). The minimum pressure difference across the wick required to create a bubble gives a measure of the largest pore radius.

$$\Delta P = P_{gauge} - P_{atm} = \frac{2\sigma}{r_{pore,max}} \quad (2)$$

The air pressure is slowly increased and the pressure at which the first bubble appears is noted. The maximum pore radius is calculated using Young- Laplace relation. The pore radius of the bi-porous wicks is found to be 0.9 μm . Figure 6 shows the experimental setup for pore radius measurement using bubble point method.

3.4 Surface Morphology

SEM imaging (Figure 7) shows the presence of large pores, which leads to enhanced porosity and interconnects fine pore network responsible for

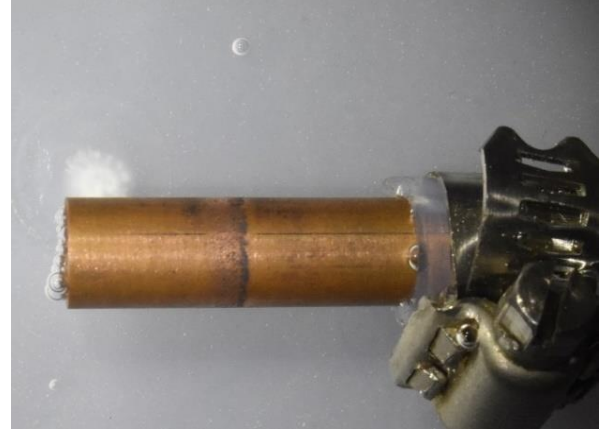


Figure 6. Pore radius measurement using bubble point method

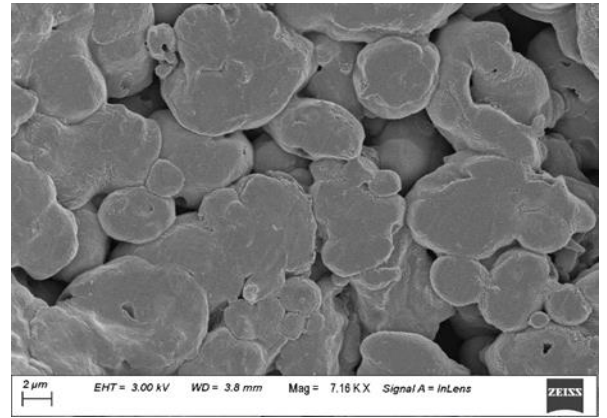


Figure 7. SEM image of sintered wick

the generation of the capillary pumping pressure required.

3.5 Porosity & Permeability

The porosity of the sintered wicks is measured by the Archimedes method. In Archimedes' method, three independent weights are required: a) dry weight (m_d), b) weight of the saturated wick in the air (m_a), and c) weight of the saturated wick in the liquid (m_w). First, the dry weight of the wick is measured using an electronic weighing machine after preheating of the sample to remove the moisture content in the wick. Then the sample is soaked in liquid deionized water at 65 °C for about 12 hours, till it gets fully saturated. The porosity of the sample is estimated by the following relation:

$$\varepsilon = \frac{V_{void}}{V_{total}} = \frac{m_a - m_d}{m_a - m_w} \quad (3)$$

Where V_{void} is the volume of the void and V_{total} is the total volume of the wick sample. The porosity is found to be 46%. It is found that the porosity of the wick depends upon sintering parameters such as sintering temperature and

sintering time. It is found that by increasing either sintering temperature or time while keeping other parameters fixed, the porosity of the wicks decreases. The permeability of the wick is determined by the Carman-Kozeny formula [15]. The permeability of the wick is found to be $0.036 \mu\text{m}^2$.

$$k = \frac{d^2 \varepsilon^3}{180(1 - \varepsilon)^2} \quad (4)$$

4. Conclusion

The present work involves the fabrication and detailed characterization of bi-porous copper wicks with different shapes and sizes for loop heat pipes. Cylindrical and flat biporous copper wicks are fabricated by compaction and sintering. The wicks are characterized and the properties like surface wettability, porosity, permeability, pore radius, surface morphology and effective thermal conductivity are calculated. The measured contact angles for acetone, methanol, propanol and water, are found to be 18.84° , 51.23° , 29.23° , and 96° respectively using sessile drop method. It can be concluded that acetone has the better surface wettability against copper wicks as compared to the other fluids. The measured effective thermal conductivity of the wick is found to be 8.72 W/m-K using IR thermography. The pore radius of the bi-porous wicks is calculated using the Young–Laplace relation and is around $0.9 \mu\text{m}$. SEM examination of the wick surface shows the existence of large pores, which leads to increased porosity and interconnects the fine pore network responsible for generating the required capillary pumping pressure. The porosity of the prepared sample is found to be 46 % using the Archimedes' method. The permeability of the fabricated bi-porous samples is found to be $0.036 \mu\text{m}^2$.

Acknowledgements

This work was partially funded through Grant No. CRG/2020/006333 of SERB, DST, Govt. of India. The SEM imaging was conducted at the Central Instruments Facility of IIT Guwahati.

References

[1] Maydanik, Y.F., 2005. Loop heat pipes. *Applied thermal engineering*, 25(5-6), pp.635-657.
 [2] Kumar, P., Gachake, M. and Khandekar, S., 2022. Effect of wick oxidation on the thermal performance of a copper-acetone loop heat pipe. *Applied Thermal Engineering*, 200, p.117627.
 [3] Xu, J., Zou, Y., Yang, D. and Fan, M., 2013. Development of biporous Ti_3AlC_2 ceramic wicks for loop heat pipe. *Materials Letters*, 91, pp.121-124.

[4] Samanta, S.K., Das, P. and Lohar, A.K., 2013. Study of physical characteristics of nickel wicks developed by metal injection moulding. *Powder metallurgy*, 56(3), pp.221-230.
 [5] Singh, R., Akbarzadeh, A., and Mochizuki, M. (2009). Effect of wick characteristics on the thermal performance of the miniature loop heat pipe. *Journal of Heat Transfer*, 131(8).
 [6] Prasad, Arpana, A. R. Anand, D. Raghavendra Kumar, V. Ramakrishnan, Amrit Ambirajan, Dinesh Kumar, and Pradip Dutta. Measurement of thermal conductivity, pore size, permeability and coefficient of thermal expansion of porous nickel wick for lhps. *Heat Pipe Science and Technology, An International Journal* 5, no. 1-4 (2014).
 [7] Wu, Shen-Chun, Tzu-Wei Gu, Dawn Wang, and Yau-Ming Chen. Study of PTFE wick structure applied to loop heat pipe. *Applied Thermal Engineering* 81 (2015): 51-57.
 [8] Deng, Daxiang, Dejie Liang, Yong Tang, Jiemin Peng, Xiaodong Han, and Minqiang Pan. Evaluation of capillary performance of sintered porous wicks for loop heat pipe. *Experimental Thermal and Fluid Science* 50 (2013): 1-9.
 [9] Siedel, Benjamin. Analysis of heat transfer and flow patterns in a loop heat pipe: Modelling by analytical and numerical approaches and experimental observations. PhD diss., INSA de Lyon, 2014.
 [10] Choi, Jeehoon, Yuan Yuan, Wataru Sano, and Diana-Andra Borca-Tasciuc. Low temperature sintering of copper biporous wicks with improved maximum capillary pressure. *Materials Letters* 132 (2014): 349-352.
 [11] Samanta, S. K., P. Das, and A. K. Lohar. Study of physical characteristics of nickel wicks developed by metal injection moulding. *Powder Metallurgy* 56, no. 3 (2013): 221-230.
 [12] Choi, Jeehoon, Wataru Sano, Weijie Zhang, Yuan Yuan, Yunkeun Lee, and Diana-Andra Borca-Tasciuc. Experimental investigation on sintered porous wicks for miniature loop heat pipe applications. *Experimental Thermal and Fluid Science* 51 (2013): 271-278.
 [13] Anvesh, Chintala, T. Srikanth, and V. S. Jasvanth. Characterization of Sintered Porous Wick for use in Loop Heat Pipe. In *Proceedings of the 26th National and 4th International ISHMT-ASTFE Heat and Mass Transfer Conference December 17-20, 2021, IIT Madras, Chennai-600036, Tamil Nadu, India*. Begel House Inc., 2021.
 [14] Kumar, P., Wangaskar, B., Khandekar, S. and Balani, K., 2018. Thermal-fluidic transport characteristics of bi-porous wicks for potential loop heat pipe systems. *Experimental Thermal and Fluid Science*, 94, pp.355-367.
 [15] Yeh, C. C., Chen, C. N., and Chen, Y. M. (2009). Heat transfer analysis of a loop heat pipe with biporous wicks. *International Journal of Heat and Mass Transfer*, 52(19-20), 4426-4434.

Numerical Investigation of Heat Transfer Augmentation in Miniature Channels with Microfins having Axially Varying Fin Pitch

Rohit Kumar¹, and Manmohan Pandey^{1*}

¹ *Department of Mechanical Engineering, Indian Institute of Technology, Guwahati, India*

**Corresponding author: manmohan@iitg.ac.in*

Abstract

The microchannel heat exchanger (MCHX) is very efficient in providing a cooling solution to many applications where high heat flux dissipation is required. Many heat transfer enhancement techniques are explored to improve the cooling capacity and thermal performance of these MCHX devices. This work numerically investigates the effect of variable microfin pitch along the flow axis on the heat transfer and fluid flow in rectangular miniature channels. The augmentation in heat transfer and thermal performance is analyzed for three different arrangements of varying fin pitch along the flow axis. The fin pitch kept constant in the channel along the flow is termed a case of uniform pitch (UP), fin pitch increases along the flow axis is increasing pitch (IP), and the fins arranged as decreasing pitch along the flow axis is named as decreasing pitch (DP). The simulation results show that the heat transfer is enhanced by more than 200% in the finned miniature channel compared to the plain channel albeit at the expense of a significant pressure drop. The hydraulic loss in the case of UP was maximum and that in IP was minimum. The Nusselt number for IP was maximum while that for DP was minimum. The thermal performance of IP was the best and that of DP was inferior to the other two arrangements.

Keywords: Heat Transfer Augmentation; Microfins; Miniature Channels; Conjugate Heat Transfer; Numerical Simulation

1. Introduction

The demand for high heat flux dissipation is increasing rapidly with the development and advancement of technology in many applications like high computing electronic devices, defense, laser cooling, solar and energy, medical components, etc. [1]. An efficient cooling system is necessary for the optimal operation of these devices. Many techniques are adopted as high heat removal methods like phase-change cooling, piezoelectric cooling, jet spray, heat pipes and loop heat pipe, microchannel heat exchanger, and microchannel cooling [2]. The microchannel heat exchanger and microchannel cooling are very promising and efficient among all heat dissipation techniques for high heat flux. The large surface area to volume ratio facilitates maximum heat transfer in microchannels. The MCHX cooling and methods of heat transfer augmentation of these devices have been extensively explored in the last four decades [3]. In the current work, the design of miniature channels with a different arrangement of microfins is proposed, and their thermal performance is evaluated. The three different cases of variable fin pitch along the flow are investigated, and an optimized design is proposed, which gives better heat transfer performance.

2. Channel Design and Numerical Model

The miniature channels having a rectangular cross-section with microfins are designed in the Design modeler of ANSYS Fluent. The width,

height, and length of the channel ($w \times h \times L$) is 0.4 mm x 1 mm x 10 mm. The specification of channel configuration is shown in Figure 1. The width and height of the substrate ($W \times H$) are 0.55 mm x 1.5 mm. The cross-section of microfins is circular, having a diameter of 0.2 mm, and a height is 0.75 mm. The three different configurations of channel arrangement with microfins having fin pitch varying axially are proposed. The fin pitch is kept constant along the flow axis and denoted as uniform pitch (UP), shown in Figure 1 (d). In the second case, the pitch axially increasing denoted as increasing pitch (IP), represented in Figure 1 (e). The fin pitch gradually decreases along with the flow in the third case and is termed decreasing pitch (DP).

The simulation is performed for the three-dimensional conjugate heat transfer and fluid flow through the proposed design of miniature channels with microfin. The finite volume method is adopted, and commercial software ANSYS Fluent is used for the numerical investigation. The SIMPLE method is used, and the governing equation is solved by pressure velocity coupling. The second-order upwind scheme is selected for the discretization of these equations. Fine meshing is done in the fluid region near the wall and the fins and the mesh for the solid domain is kept coarse except for the region near the interface. The simulation is conducted at an optimized mesh for all the proposed geometries. The conservation equation solved by solver for numerical analysis of three-dimensional conjugate

heat transfer and fluid flow are mentioned below [5]:

Mass conservation (continuity equation):

$$\nabla \cdot (\rho_l \vec{V}) = 0 \quad (1)$$

Momentum conservation (Navier-Stokes equation):

$$\rho_l \vec{V} \cdot \nabla \vec{V} = -\nabla p + \nabla \cdot \mu_l \left[(\nabla \vec{V} + \nabla \vec{V}^T) - 2/3 \nabla \cdot \vec{V} \right] + \rho_l \vec{g} \quad (2)$$

Equation of energy for fluid:

$$\rho_l c_{p,l} \vec{V} \cdot \nabla T = \nabla \cdot (k_l \nabla T) \quad (3)$$

Energy equation for solid:

$$k_s \nabla^2 T = 0 \quad (4)$$

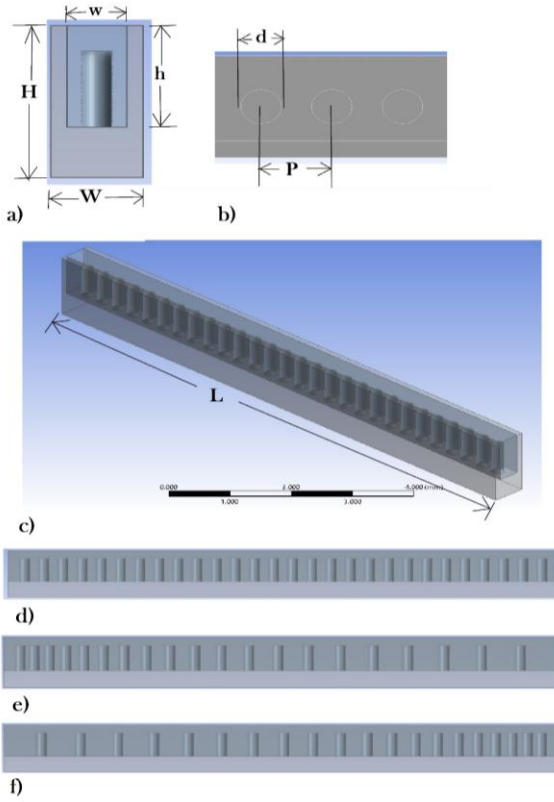


Figure 1 (a) Cross-sectional view and detail of channel geometry, (b) Top view, (c) isometric view, (d) Uniform pitch, (e) Increasing pitch, (f) Decreasing pitch

The thermophysical properties of fluid varied with temperature is implemented in the solver for simulation of conjugate heat transfer [4]. The equations of thermophysical properties used are given as:

$$\rho(T) = 765.33 + 1.8142T - 0.0035T^2 \quad (5)$$

$$c_p(T) = 28070 - 281.7T + 1.25T^2 - (2.48 \times 10^{-3})T^3 + (1.857 \times 10^{-6})T^4 \quad (6)$$

$$k(T) = -0.5752 + (6.397 \times 10^{-3})T - (8.151 \times 10^{-6})T^2 \quad (7)$$

$$\mu(T) = (9.67 \times 10^{-2}) - (8.207 \times 10^{-4})T + (2.344 \times 10^{-6})T^2 - (2.244 \times 10^{-9})T^3 \quad (8)$$

3. Model Validation and Data Reduction

3.1 Grid Independence Test

The design of proposed miniature channels is discretized for the simulation. The unstructured tetrahedral grid elements are used for the computational domain. The mesh size of fluid and solid interface, and microfins is kept fine for accuracy. This meshing style will help in determining the very small changes in the temperature and velocity near the wall. The size of grid elements of computational domain is gradually increasing away from the wall. The mesh size of solid domain is kept coarse. The grid independence test is performed for all the geometry and analysis is done for optimized mesh. The simulation is performed for each geometry starting from coarse mesh and then mesh size is gradually reduced to fine mesh. The results of each case are compared to optimize the grid size and further analysis is performed at the optimized mesh. The optimized meshing of uniform-pitch (UP) is shown in figure 2. The least mesh size is taken as 0.05 mm and largest is 0.08 mm. The details of optimized grid elements which is selected for the study is presented in table 1. The error in pressure drop is observed large for coarse mesh which reduces on reducing the mesh size as shown in table 2 and figure 3.

3.2 Validation of Numerical Model

The model selected for the numerical analysis is validated with the experimental data of Qu and Mudawar [6]. The simulation results of selected model are in acceptable range of experimental data with 8% of MAE (mean absolute error). The numerical results of selected model compared with the experimental pressure drop data is shown in figure 4. The validation of model is done for laminar flow of Reynolds number varied from 200 to 800.

3.3 Data Reduction

The analysis of numerical data is performed to determine the heat transfer and fluid flow behavior. The value of convective heat transfer is determined as

$$q = h(T_w - T_m) \quad (9)$$

Channel wall temperature is defined as T_w , and mean bulk fluid temperature is denoted by T_m .

$$h = \frac{q}{(T_w - T_m)} \quad (10)$$

$$T_m = \frac{\iint u.TdA}{\iint u.dA} \quad (11)$$

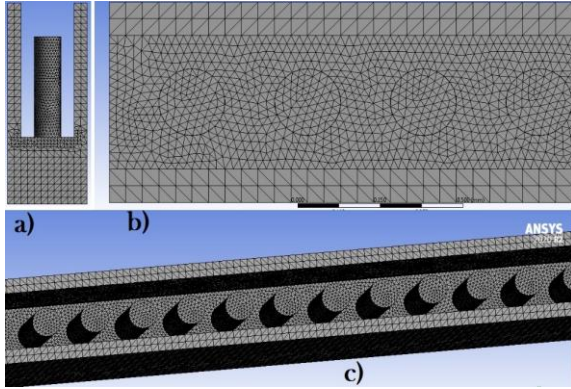


Figure 2. Meshing of computational domain of Case-1 channel; a) side view, b) Top view, and c) isometric view.

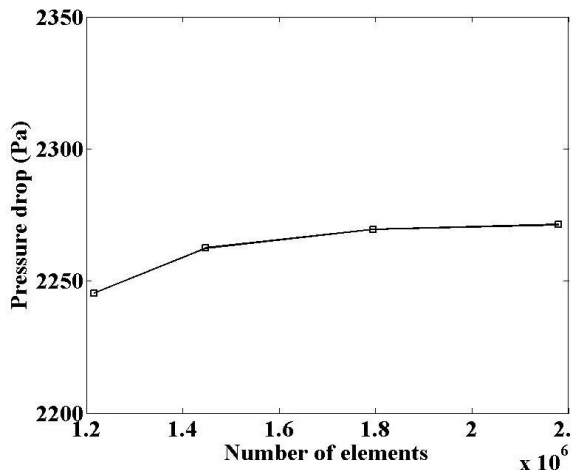


Figure 3. Variation of pressure drop with number of elements

Table 1. Detail of selected mesh for designed channels

Sl no.	Channel design	Minimum mesh size (mm)	Number of elements	Number of nodes
1	UP	0.05	1785204	355873
2	IP	0.05	1357021	234871
3	DP	0.05	1350313	235896

Table 2. Mesh details of UP for test of grid independence

Sl no.	Minimum element size (mm)	Number of elements	Number of nodes	Pressure drop (Pa)	Error (%)
1	0.06	1216836	211876	2245.4	1.41

2	0.055	1446817	251864	2262.5	0.387
3	0.05	1795244	357135	2269.53	0.0779
4	0.045	2180050	378773	2271.3	0

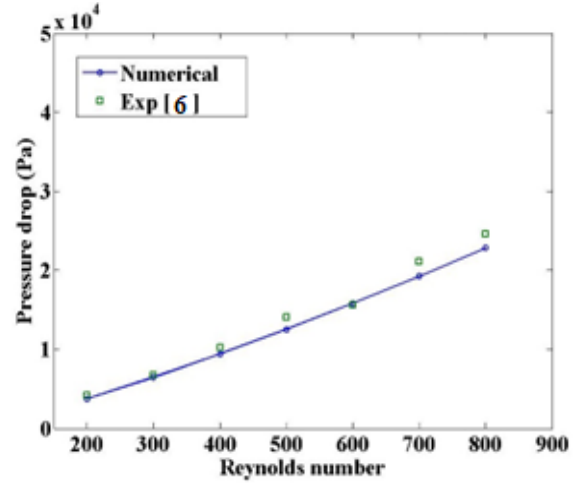


Figure 4. Validation of numerical model with experimental data

4. Results and Discussion

The numerical analysis is done at a constant heat flux of 250 W/cm^2 provided from the bottom wall of the substrate for all three proposed designs. Figure 5 shows the cross-sectional velocity contour of flow along the length of channel at the position of 0.75 mm of channel height. The channel with uniform fin pitch (UP) has larger number of flow obstructions in comparison to increasing pitch (IP) and decreasing pitch (DP) miniature channels. The IP and DP has same number of microfins. The average velocity of fluid at the inlet of IP is minimum and maximum in DP. The fluid velocity is maximum at the outlet of IP. The velocity contour of longitudinal section at the center of channel along the axis of flow is shown in figure 6. The velocity vector of fluid flow in all three cases is shown in figure 7. The mixing of fluid is enhanced in the downstream of IP in comparison to other two cases while the fluid mixing is better in the upstream of DP. The temperature contour of longitudinal plane at the center of channel along the flow is shown in figure 8. The heater wall temperature of IP is highest among all the three cases at the upstream location.

It is observed that fins are acting as flow-resistant elements, so the pressure drop is dependent on the number of fins, and hence UP has a larger pressure drop compared to the other two cases because of the number of fins, in this case, is the largest as shown in Figure 9. IP and DP have an equal number of fins, and the difference in pressure drop between these two cases is

similar. The flow resistance is more at the inlet of IP than DP and vice-versa at the outlet. The average fluid and wall temperature near the outlet is more significant in IP, which results in a decrement in the viscous effect of fluid compared to DP. Hence IP has a marginal lower pressure drop penalty at a high flow rate than DP. The effect of varying fluid velocity on Nusselt number of fluid flows in all three configurations is shown

in Figure 10. The Nusselt number for increasing fin pitch design is highest, while the decreasing fin pitch arrangement is lowest. The thermal performance of IP is superior, and DP is the lowest, as represented in Figure 11. The thermal performance in all cases decreases with Reynolds number due to an increase in pressure drop penalty.

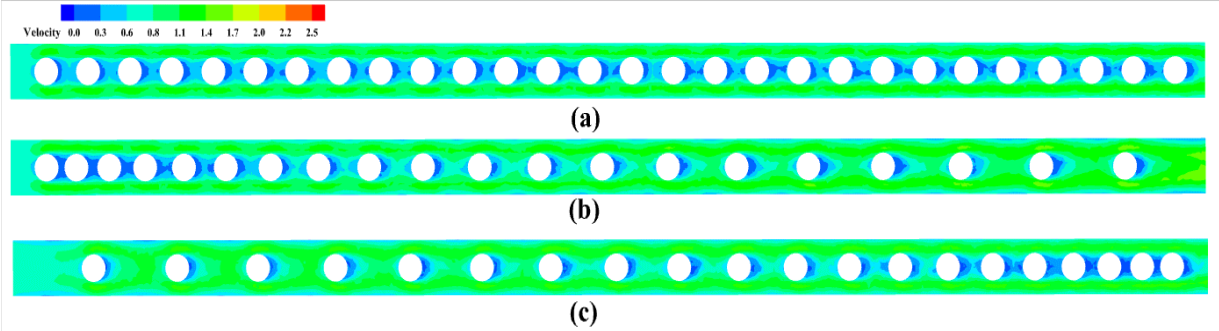


Figure 5. Velocity contour of fluid flow at horizontal plane of channel cross-section at height 0.75 mm in case of a) UP, b) IP, and c) DP

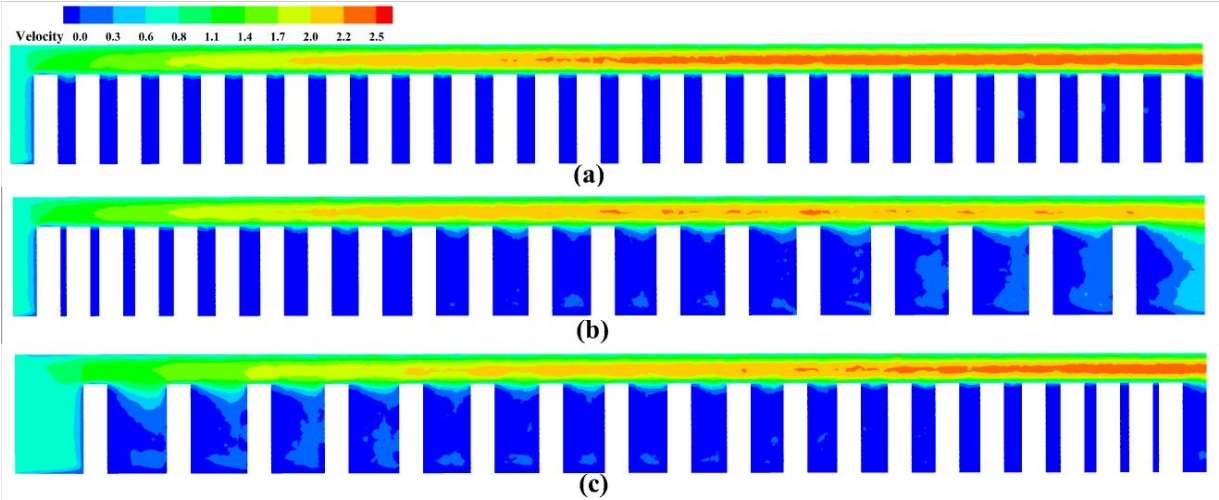


Figure 6. Velocity contour of fluid flow along the flow axis at the vertical mid-plane of channel cross-section in case of a) UP, b) IP, and c) DP

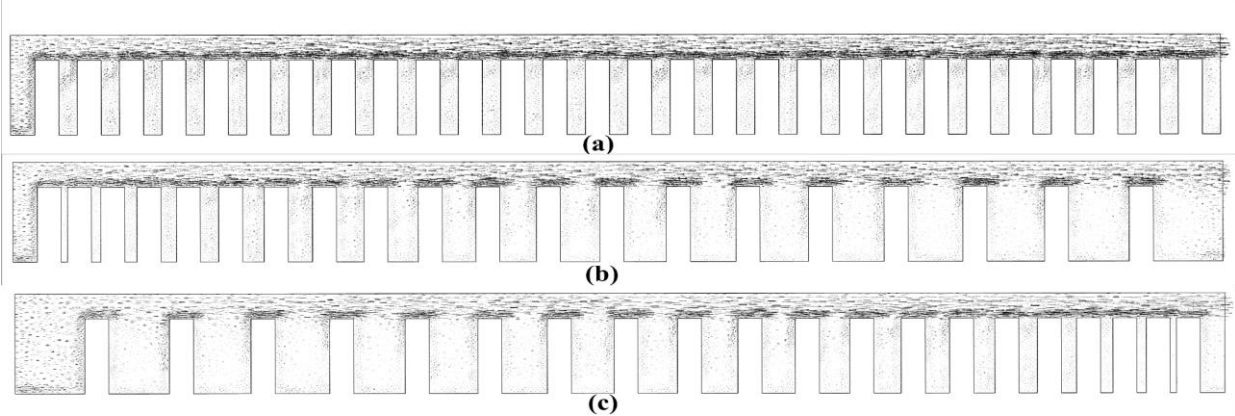


Figure 7. Velocity vector of fluid flow along the flow axis at the vertical mid-plane in case of a) UP, b) IP, and c) DP

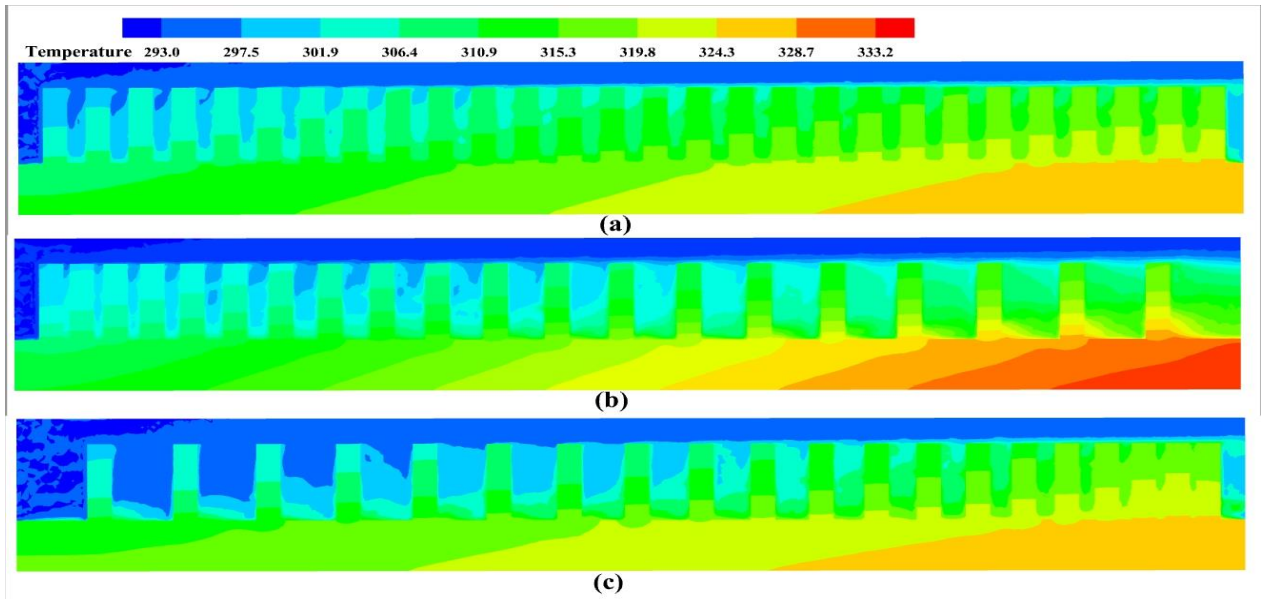


Figure 8. Velocity contour of fluid flow along the flow axis at the vertical mid-plane of the channel in case of a) UP, b) IP, and c) DP

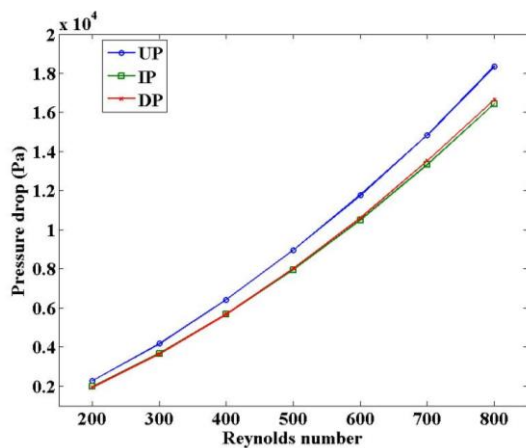


Figure 9. Effect of Reynolds number on pressure drop

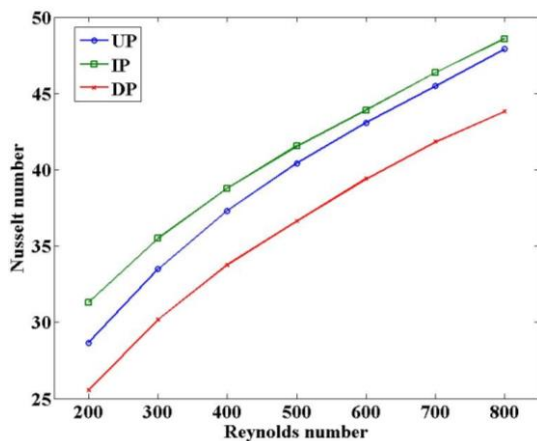


Figure 10. Effect of Reynolds number on Nusselt number

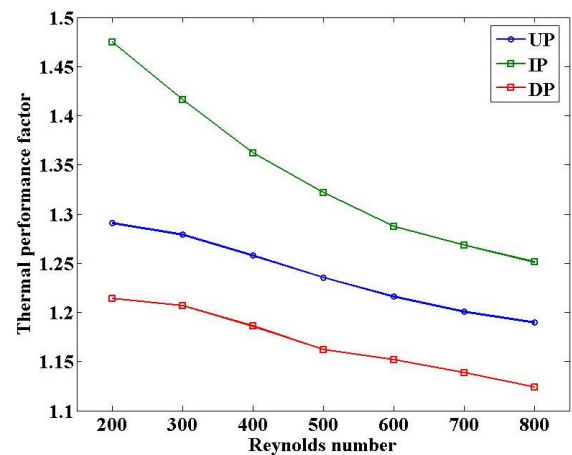


Figure 11. Effect of Reynolds number on Thermal performance factor

Conclusions

The simulation is performed for the three-dimensional conjugate heat transfer and fluid flow in miniature channel with microfins. The three different designs of variable fin pitch are uniform pitch (UP), increasing pitch (IP), and decreasing pitch (DP). The heat transfer and fluid flow analysis of proposed design is summarized as follows:

1. The Nusselt number and heat transfer in all three cases increases on increase in Reynolds number. Nusselt number is maximum in IP while it is superior in UP than DP.
2. The UP has better thermal performance than DP while IP is the best of the three.

3. The hydraulic loss is maximum in UP because of the greater number of flow restriction element as microfins in comparison to other two cases. The pressure drop is approximately same in IP and DP configuration.
4. The pressure drop increases in all three design on increasing the Reynolds number of flow.
5. The average velocity of fluid flow, mixing of fluid and heater wall temperature is maximum in upstream of IP.

References

- [1] Deng D, Zeng L, Sun W. A review on flow boiling enhancement and fabrication of enhanced microchannels of microchannel heat sinks. *International Journal of Heat and Mass Transfer*. 2021.
- [2] Ebadian MA, Lin CX. A review of high-heat-flux heat removal technologies. *Journal of heat transfer*. 2011 Nov 1;133(11).
- [3] Garimella SV, Singhal V. Single-phase flow and heat transport and pumping considerations in microchannel heat sinks. *Heat transfer engineering*. 2004 Jan 1;25(1):15-25.
- [4] Bhandari, Prabhakar, and Yogesh K. Prajapati. "Thermal performance of open microchannel heat sink with variable pin fin height." *International journal of thermal sciences* 159 (2021): 106609.
- [5] R. Kumar and M. Pandey, Effect of Geometry in Conjugate Heat Transfer and Fluid Flow through Triangular Copper Miniature Channels, Proceedings of 26th National and 4th International ISHMT-ASTFE Heat and Mass Transfer Conference, Madras, India, 2021.
- [6] Qu, Weilin, and Issam Mudawar. "Experimental and numerical study of pressure drop and heat transfer in a single-phase micro-channel heat sink." *International journal of heat and mass transfer* 45, no. 12 (2002): 2549-2565.

Effect of Far-field Ambient Conditions on Interfacial Solar Vapor Generation using a Two-Phased Closed Thermosyphon

Tarun Kulshrestha¹, Sameer Khandekar^{2*}

^{1,2}Indian Institute of Technology Kanpur, Kanpur, India

*E-mail: samkhan@iitk.ac.in

Abstract

Interfacial solar vapor generation has been the preferred state-of-the-art for driving various applications. Novel photothermal materials have been proposed for maximizing vapor generation, but only few studies have focused on the fundamental heat and mass transport of the solar vapor generating system. A thorough is required for commercialization of solar driven, continuous and efficient interfacial vapor generating systems. We perform a parametric study on the effect of far-field ambient conditions, on evaporative mass flux generated by a solar driven thermosyphon-based heat localization strategy. A controlled environmental chamber is used to investigate the principal mode of mass transport at various heat fluxes, and to identify the threshold heat flux responsible for the transition from diffusive to advective mass transport. The mass loss rate of test fluid and heat-to-vapor conversion efficiency decrease with the increasing ambient relative humidity (RH) at 25°C and 0.5 Sun heat flux. Further, the effect of RH on the evaporation rate and efficiency diminishes with the increase in heat flux. Experimentally obtained mass flux is in good agreement with natural convection-based evaporation.

Keywords: Interfacial vapor generation; Thermosyphon; Environmental chamber; Mass transport

1. Introduction

Steam and vapor generated through fundamental solar heating of water has numerous applications, such as desalination, steam sterilization, fuel production and electricity generation. However, traditional techniques of vapor generation through solar energy have been far from commercialization due to major parasitic heat losses to the bulk water and ambient, thus leading to poor photothermal efficiency [1]. Interfacial solar vapor generation through heat localization has been the preferred state-of-the-art to curb the heat losses and enhance the photothermal efficiency [2]. Though a large number of studies have focused on fabricating innovative materials with high solar absorptivity and enhanced wickability of the evaporating surface, only a few have emphasized on the fundamental transport phenomenon of solar-to-vapor conversion [3,4]. Further, continuous saline water evaporation leads to fouling on the evaporator surface, which significantly reduces the evaporation rate. Thus, numerous salt mitigation strategies have been proposed to ensure continuous and efficient vapor generation [5]. Here, a heat localization strategy by incorporating a two-phase closed thermosyphon, with continuous and efficient vapor generation has been proposed (Figure 1), to mitigate the parasitic heat losses and also, to tackle salt accumulation [6]. Decoupling of sunlight absorbing surface and vapor generating surface not only allows us to optimize each surface independently through available materials, but also provides a scope of latent heat recovery for enhancing the freshwater productivity.

Evaporation systems with porous media have been classified as open system and closed system based on their configuration, see Figure 2. In open configuration-based systems the vapor generated diffuses into the far-field ambient, whereas the vapors condense at a finite distance from the evaporator surface in closed configuration-based systems [3,4]. A thorough understanding of the fundamental heat and mass transport is necessary to develop a continuous and efficient interfacial solar vapor generating system. Evaporation is governed by the mode of mass transport i.e., diffusion, where Fick's Law is valid or, advection, where advection-diffusion equation is valid.

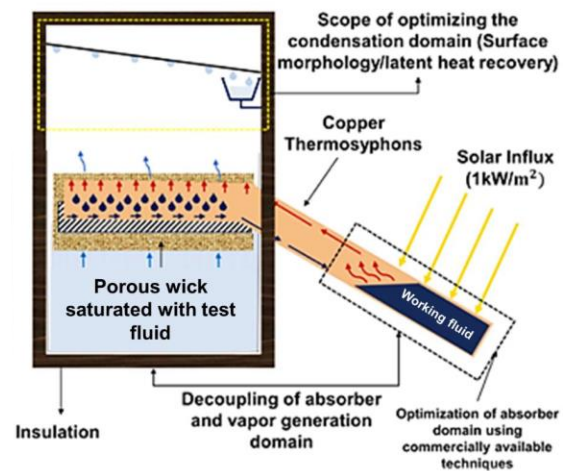


Figure 1. Thermosyphon based heat localization strategy for continuous and efficient interfacial solar vapor generation [6].

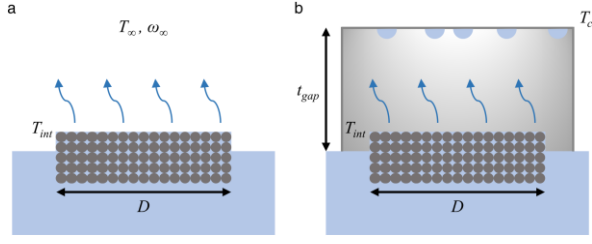


Figure 2. Evaporation configurations with porous media (a) open and (b) closed systems [3].

Peclet number (Pe), see Equation 1, is used to determine the dominant mode of mass transport,

$$Pe = \frac{u_{int}\delta}{D_V}, \quad (1)$$

where u_{int} is the air-vapor mixture velocity at the interface (m/s), δ is the diffusive boundary layer thickness (m), that depends on the geometry and boundary conditions of the system, and D_V is the diffusivity of vapor in air (m^2/s). For high heat fluxes ($\sim 100 \text{ W}/\text{cm}^2$), the measurement of interface temperature is crucial to predict the mass flux accurately, which has been addressed by Lu et al., by fabricating an ultrathin nano porous membrane [7]. Moreover, for solar driven processes that involve low heat fluxes ($< 1500 \text{ W}/\text{m}^2$), the evaporative mass flux has generally been modelled by assuming diffusive vapor transport [8]. However, the experimentally obtained mass flux suggests that the diffusive model underpredicts the evaporation rate beyond a certain heat flux. In this regard, a theoretical model to predict the threshold heat flux for the transition from diffusive to advective mass transport is required to address the research gaps.

Evaporation under advection is further classified into two categories viz. natural convection and forced convection respectively. The evaporative flux is determined according to the dominant mode of convective heat transfer. In this regard, a non-dimensional, has been defined, see Equation 2, known as the Richardson number (Ri),

$$Ri = \frac{g\beta\Delta TL}{U_o^2} = \frac{Gr}{Re^2}, \quad (2)$$

where g is the gravitational acceleration (m/s^2), β is the coefficient of thermal expansion ($1/\text{K}$), ΔT is the temperature difference (K), L is the characteristic length (m) and U_o is the bulk velocity (m/s). Table 1 shows the classification of various modes of convective heat transfer based on the Ri, for determining the dominant force among the inertia force (Re) and gravitational force (Gr), that drives the evaporation phenomenon. Previous studies in

the literature have parameterized the natural convection dominated evaporation of inland water bodies like lakes, ponds etc. as a function of wind speed, vapor pressure, and the size of the corresponding water body [9]. However, the applicability of such equations is reduced due to variation of factors like climate, solar insolation, season, geographical location etc. To characterize evaporation under natural convection, a power law relationship between the Sherwood (Sh), Rayleigh (Ra) and Schmidt (Sc) numbers, see Equation 3, has been suggested [10],

$$Sh = ARa^m Sc^n, \quad (3)$$

where A , m and n are constants. Though numerous correlations have been proposed in the literature to determine the evaporative flux from the water surface of inland water bodies under natural convection, the literature still lacks a standard correlation with a wider range of utility [11].

In this background, the present work aims to study the effect of far-field ambient conditions (temperature and relative humidity) on the evaporative mass flux for a two-phased closed thermosyphon based open configuration strategy, as proposed in Figure 1, through controlled experiments under various heat fluxes. The aim is to identify the parameters that dictate the transition from diffusive evaporation to advective evaporation under low heat fluxes by comparing experimental results with the theoretical models available. To perform these experiments indoors under different far-field ambient conditions, a controlled environmental chamber was fabricated to mimic the conditions of water evaporation through a saturated wick at various heat fluxes. The air velocity inside the chamber has been kept of the order of 0.15 m/s or less, to limit the evaporation between diffusion and natural convection [11]. Here, we show the parametric effect of RH at an ambient temperature of 25°C on the evaporation rate of water by exposing the evaporator of the thermosyphon with the heat flux ranging between $500 \text{ W}/\text{m}^2$ to $1500 \text{ W}/\text{m}^2$, and also compare experimental results with theoretical models.

Table 1. Ri based convective heat transfer modes.

Ri	Dominant mode of convection
< 0.1	Forced convection
$0.1 < Ri < 10$	Mixed (both forced and natural)
> 10	Natural convection

2. Experimental Setup

The decoupling strategy shown in Figure 1 involves a copper-based closed loop thermosyphon, whose fabrication details are available in our previous work [6]. The evaporator section of the thermosyphon absorbs the solar irradiation, which is transferred to the working fluid in the form of heat. The working fluid transfers its heat to the impure test fluid (brackish/saline water) at the condenser section of the thermosyphon. Heat localization on the vapor generating surface is ensured by placing a 100% pure cotton porous wick over the condenser surface of the thermosyphon. The test fluid wicks through the cotton fabric and evaporates into the ambient from the condenser surface. The thermosyphon is charged with the predetermined optimum working fluid (degassed water) at an optimal filling ratio (40%), obtained at low heat fluxes ($\sim 1000 \text{ W/m}^2$). The design and construction details of the aforementioned controlled environmental chamber are described here, followed by the experimental procedures required to maintain different far-field ambient conditions.

2.1. Design of Environmental Chamber

The environmental chamber is designed to mimic different ambient conditions (30-90% RH and 25-45 °C temperature range) experienced inside a room throughout the year. Figure 3(a) shows flowchart of processes required to achieve different combinations of temperature and RH. First, air is blown into a bubble column humidifier for cooling and humidification. Further, the cool saturated air is sensibly heated by passing it through a cross flow heat exchanger, see process 1-4 in Figure 3(b). The dry air at the outlet of the heat exchanger is further divided equally into two streams. The first stream of air enters the mixing chamber in a dry state, whereas the second stream is further saturated by passing it through a bubble column humidifier, represented as state 5 in Figure 3(c). The required RH is achieved by mixing the aforementioned streams at various flow rates through valves. Finally, the mixed air, denoted by 6 in Figure 3(d), is passed to the test section at a specified temperature and RH. The mass flow rates of the two streams can be obtained through Equations 4-6 of mass, moisture and energy conservation,

$$\dot{m}_{a4} + \dot{m}_{a5} = \dot{m}_{a6}, \quad (4)$$

$$\dot{m}_{a4}\omega_4 + \dot{m}_{a5}\omega_5 = \dot{m}_{a6}\omega_6, \quad (5)$$

$$\dot{m}_{a4}h_4 + \dot{m}_{a5}h_5 = \dot{m}_{a6}h_6, \quad (6)$$

where \dot{m} is the mass flow rate (kg/s), ω is the specific humidity (kg/kg of dry air) and h is the enthalpy (kJ/kg) of moist air respectively. The subscripts 4, 5 and 6 in the equations represent dry, saturated and mixed air, respectively.

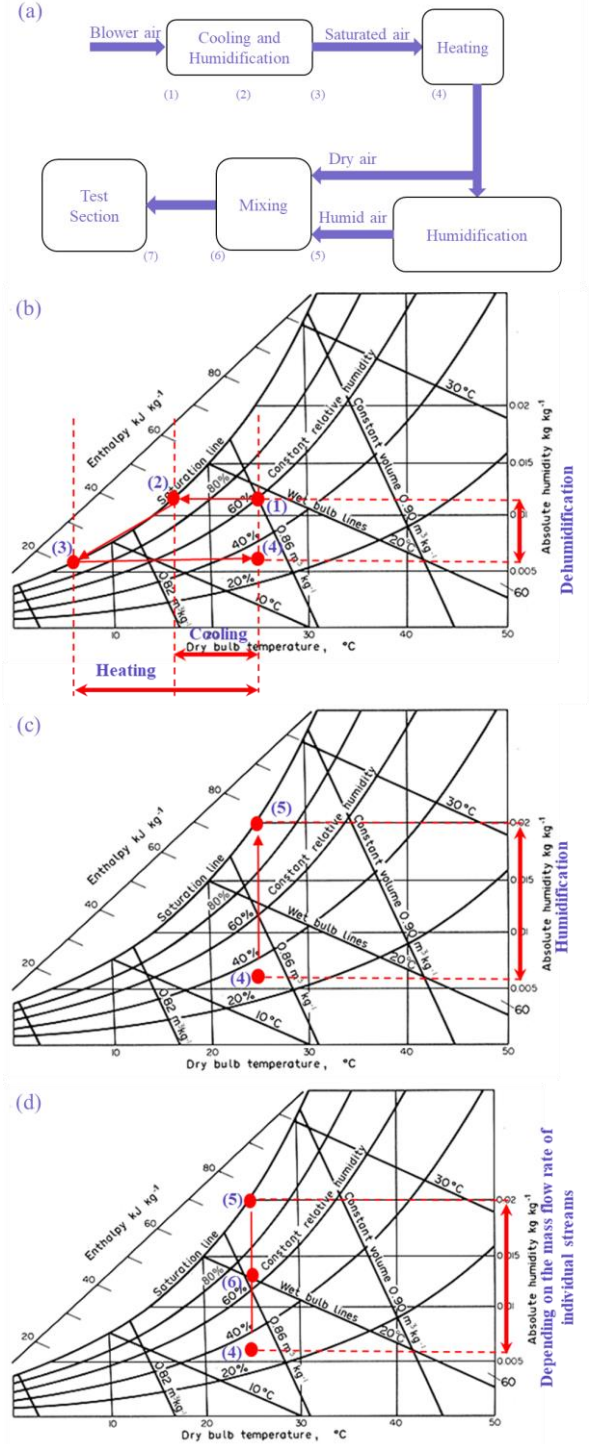


Figure 3. Representation of various psychrometric processes required to attain different far-field ambient conditions (temperature and RH) inside the environmental chamber on (a) a flowchart and, (b-d) on a psychrometric chart.

2.2. Methodology

To measure the ambient temperature and RH inside the environmental chamber, a sensor probe (Vaisala® HMP3, with RH accuracy = $\pm 0.8\%$ and temperature accuracy = $\pm 0.1^\circ\text{C}$) is placed at the top corner, see Figures 4 (a-b), of the chamber. The thermosyphon is placed inside the chamber such that its evaporator section protrudes just outside the chamber at angle of 30° with the horizontal. The cotton cloth hangs over the condenser surface of the thermosyphon with its ends dipped in the test fluid reservoir (distilled water). The test fluid reservoir rests on a weighing balance (Sartorius Quintix® 2102-1x, least count = 10 mg, and repeatability = $\pm 5\%$) with a USB enabled datalogging. Temperature of the evaporator and condenser section is recorded by embedding two pairs of K-type thermocouples (Omega® 5TC-TT-K-24-36) at their backend and three at the frontend of the adiabatic section. A mica heater (Minco® mica thermofoil heater, model HM6955, resistance of 23.2Ω , $50 \text{ mm} \times 50 \text{ mm}$) powered by a DC supply (Elnova® DC power supply 0-60 V, 0-50 A) is placed on the top of evaporator surface by the support of Teflon plates, to simulate the solar flux. The complete thermosyphon is sufficiently insulated excluding the vapor generating surface. NI-DAQ (National Instruments® NI-PCI-9213) is used for the purpose of temperature signal datalogging. Figure 4 (c) shows the isometric view of the experimental setup along with the components required to maintain the desired far-field ambient conditions.

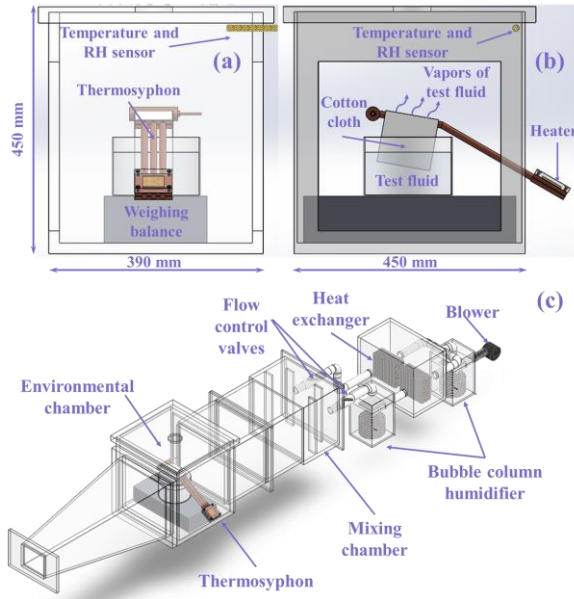


Figure 4. Schematic showing the assembly of the thermosyphon based strategy inside the environmental chamber in (a) front view and (b) side view respectively, and (c) isometric view of the setup.

The parametric effect of RH at 25°C ambient temperature on the mass loss of the test fluid is studied by operating the thermosyphon at 40% filling ratio, with degassed water as the working fluid by ranging the heat flux between 0.5 Sun ($\sim 500 \text{ W/m}^2$) to 1.5 Sun ($\sim 1500 \text{ W/m}^2$). The air velocity inside the environmental chamber is maintained below 0.15 m/s by adjusting the power supplied to the blower. An air velocity transducer (TSI®, model 8455, repeatability $< \pm 1\%$ of the reading) measures the velocity of air at the exit of the diffuser section, as shown in Figure 4 (c). Mass loss rate of the test fluid is recorded throughout the experiment. and the solar-to-vapor conversion efficiency evaluated for each case has been discussed later.

2.3. Data Reduction

The thermal resistance of the thermosyphon is obtained from Equation 7,

$$R_{th} = \frac{T_{Eavg} - T_{Cavg}}{V \times I}, \quad (7)$$

where T_{Eavg} and T_{Cavg} is the average temperature of the evaporator and the condenser section of the thermosyphon ($^\circ\text{C}$), V is the input voltage (V) and I is the input current (A) [12].

The heat-to-vapor conversion efficiency is calculated [13] from Equations (8-11),

$$\eta = \frac{\Delta m \times h_{lv}}{V \times I}, \quad (8)$$

$$h_{lv} = h_{fg} + h_L, \quad (9)$$

$$h_{fg} = 1.92 \times 10^6 \left[\frac{T_{Savg} + 273.15}{T_{Savg} + 239.24} \right]^2, \quad (10)$$

$$h_L = c_p \times (T_{Savg} - T_w), \quad (11)$$

where Δm is the evaporation rate (kg/s), h_{lv} is the total enthalpy change (J/kg), h_{fg} is the latent heat of evaporation [9], h_L is the sensible enthalpy change, c_p is the specific heat of water (J/kg.K), T_{Savg} & T_w is the average temperature of the cotton cloth and bulk water temperature at the time of experiment ($^\circ\text{C}$).

Theoretical evaporative mass flux for diffusive transport and advective transport is calculated from Equations 12 [3] and 13 [9], respectively,

$$\dot{m} = \rho D_V S (\omega_{sat}(T_s) - \phi_\infty \omega_{sat}(T_\infty)), \quad (12)$$

$$\dot{m} = h_m (\rho_{w,s} - \rho_{w,\infty}), \quad (13)$$

where ρ is the density of air (kg/m^3), D_V is the diffusivity of air (m^2/s), S is the geometric shape factor (m), $\omega_{sat}(T_s)$ & $\omega_{sat}(T_\infty)$ is the vapor mass fraction at the evaporating surface and ambient respectively, ϕ_∞ is the RH of the ambient, h_m is the mass transfer coefficient (m/s) and, $\rho_{w,s}$ & $\rho_{w,\infty}$ is the density of water vapor at the evaporation surface and ambient air, respectively.

3. Results and Discussion

Figure 5 shows the temperature distribution for the evaporator (T_{Eavg}), condenser (T_{Cavg}), adiabatic (T_{Aavg}), and vapor generating surface (T_{Savg}) for a period of 2-h each, for input heat fluxes ranging between 0.5-1.5 Sun, using distilled water as the test fluid which evaporates on the cotton wick, for 50-60% ambient RH range with 25°C as the average ambient temperature. The corresponding thermal resistance of the thermosyphon is also shown in Figure 5. During steady-state operation, the thermal resistance of the thermosyphon is minimum for 1.5 Sun case i.e., 0.18 K/W. The thermal resistance shows a decreasing trend with increase in heat flux due to transition from natural convection heat transfer to boiling of the working fluid.

The parametric effect of far-field ambient conditions on the mass loss rate and heat-to-vapor conversion efficiency is studied for 30-40%, 50-60% and 70-80% RH ranges with 25°C as the average ambient temperature. The RH and temperature data recorded (see Figure 4 (a-b) for the position of the corresponding sensor inside the chamber) throughout the course of the experiment is shown in Figure 6. Similar trends for the performance of the thermosyphon subjected to different input heat fluxes viz. 0.5 Sun - 1.5 Sun have been observed for each RH range at 25°C average ambient temperature.

Table 2 shows the variation of vapor generating surface temperature for each RH range at different input heat fluxes viz. 0.5 - 1.5 Sun. It can be seen that the T_{Savg} increases with increasing RH. Such effect is seen because the mass loss rate of the test fluid is coupled with the RH of the environmental chamber. The vapor content required for moist air to reach its saturation state at a particular temperature and pressure, decreases with increase in the relative humidity. Moreover, the rate of heat rejection from the condenser section of the thermosyphon also decreases. Since the heat supplied at the evaporator section is constant, the thermosyphon adjusts itself by increasing the temperature at its critical locations.

Table 2. T_{Savg} variation with RH at 25°C ambient.

Heat Flux (kW/m^2)	T_{Savg} ($^\circ\text{C}$)		
	30-40% RH	50-60% RH	70-80% RH
0.5	33.5	34.8	35.5
1	44.0	45.4	46.0
1.5	52.4	52.7	53.9

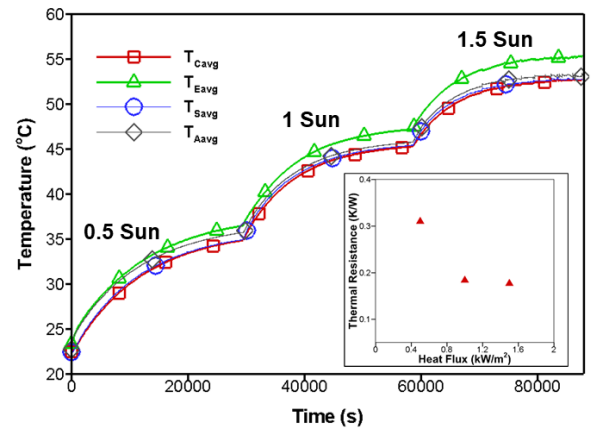


Figure 5. Temperature distribution at various critical locations of the thermosyphon system during vapor generation using the testing fluid (distilled water) for 50-60% ambient RH range with 25°C as the average ambient temperature and the corresponding resistance of thermosyphon at different input heat fluxes viz. 0.5 - 1.5 Sun.

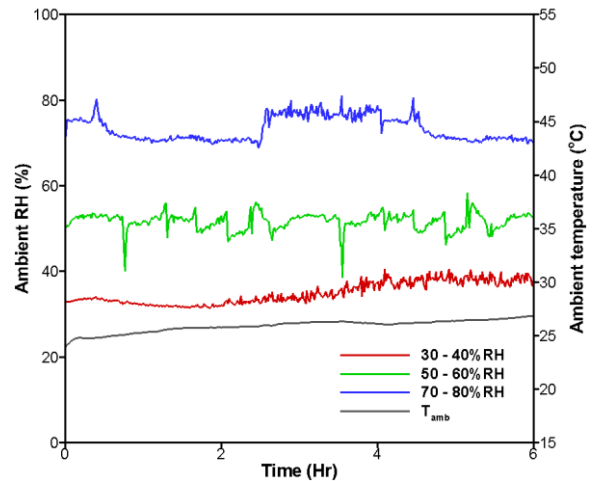


Figure 6. The recorded temperature and RH of the controlled environmental chamber for each case during the thermosyphon operating at different input heat fluxes viz. 0.5 Sun - 1.5 Sun.

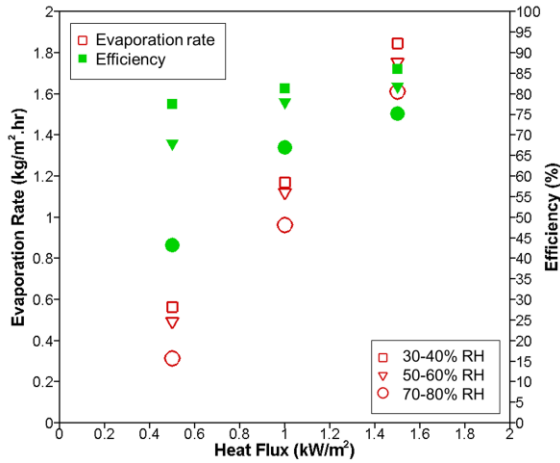


Figure 7. Comparison of mass loss rate of the test fluid and the heat-to-vapor conversion efficiency for three different ambient relative humidity ranges with 25°C average ambient temperature with thermosyphon operating at different heat fluxes viz. 0.5 - 1.5 Sun.

Figure 7 shows the mass loss rate and heat-to-vapor conversion efficiency values for 30-40%, 50-60% and 70-80% ambient RH ranges with 25°C as the average ambient temperature at different input heat fluxes viz. 0.5 - 1.5 Sun. Both the evaporation rate and efficiency have maximum values for 30-40% RH range for each heat flux case. As mentioned earlier, such effect is evident that the mass loss of the test fluid is more, due to less vapor content present in the ambient at a lower RH range as compared to a higher range at a particular temperature and pressure. Moreover, the gap between the heat-to-vapor conversion efficiency diminishes with the increase in heat flux. This is due to the fact that the contribution of dark evaporation (evaporation of water from the liquid-vapor interface due to concentration gradient without any external heat source) is reduced as the heat flux increases [3,4].

The mass loss rate of the test fluid obtained from Equation 12, assuming purely diffusive transport did not match well with our experimental mass loss rates obtained from the average temperature of the evaporating surface, as shown in Table 2. The effective boundary layer thickness δ (dependent on the system geometry and boundary conditions) used in Equation 1 for Pe calculation, also plays an important factor to determine the dominant mode of mass transport. Thus, even at low heat fluxes, the theoretical mass loss is not ensured to be purely diffusive, i.e., advective effects may play a role. The Ri obtained from our experimental data using Equation 2 was of the order of 10^3 for each case, indicating that the mass transport is dominated by

natural convection. Finally, the experimental mass loss rate is compared with the theoretical mass loss rate calculated using Equation 13, as shown in Figures 8 (a-b). An opposite trend is observed for the theoretical mass loss rate in comparison to the experimental mass loss of the test fluid, see Figure 8 (a), calculated from the average temperatures of the evaporating surface (see Table 2) obtained in each case. Though the mass loss in Equation 13 is a function of both the temperature of the evaporating surface and the relative humidity of the ambient, the mass loss is more sensitive toward the change in evaporating surface temperature (increasing with RH) in comparison to the change in RH. To study the effect of RH on Equation 13, the average temperature of the vapor generating surface is kept constant and the mass loss is evaluated. It can be seen from Figure 8 (b), that the theoretical trend obtained in Figure 8 (a) gets diminished. However, the mass loss obtained from Equation 13 is barely sensitive to the change in RH.

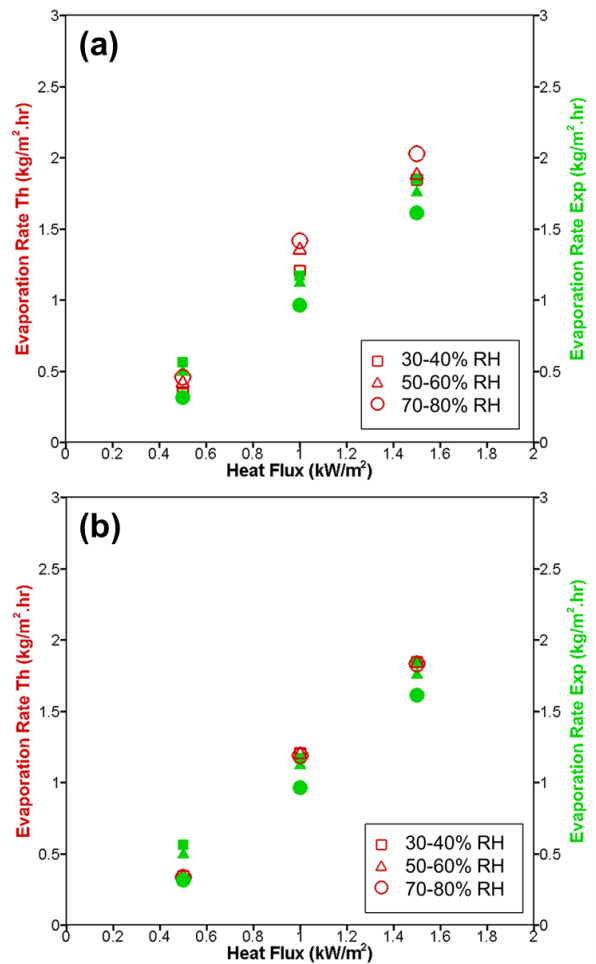


Figure 8. Comparison between theoretical and experimental mass loss (a) at different surface temperatures (see Table 2) and, (b) at same surface temperatures with three different RH ranges thermosyphon operating at different heat fluxes.

4. Summary and Conclusions

To study the parametric effect of far-field ambient conditions (temperature and relative humidity) on the mass loss rate and, heat-to-vapor conversion efficiency of the thermosyphon based strategy, an environmental control chamber is designed and fabricated. The thermosyphon is operated at optimum filling ratio (40%) and working fluid (degassed water) obtained from our previous work for different input heat flux ranges viz. 0.5 Sun - 1.5 Sun [6]. The following conclusions can be drawn from the controlled experiments conducted for three different RH ranges viz. 30-40%, 50-60% and 70-80% at an average ambient temperature of 25°C:

- The assumption of the mode of mass transport (diffusive or advective) for calculation of theoretical mass loss, should be based on the Peclet number calculated from Equation 1. Moreover, the Richardson number should be calculated to determine the dominant mode of convection in case of advective mass transport.
- The thermosyphon adjusts the temperature at its critical locations with the change in the ambient RH at a particular ambient temperature and heat flux.
- The effect of dark evaporation on the heat-to-vapor conversion efficiency diminishes with the increase in heat flux.
- The comparison of the experimental mass loss of the test fluid with the theoretical available evaporation model requires constant boundary conditions (constant temperature of vapor generating surface), which is difficult to maintain in the current proposed strategy.

In order to make the thermosyphon based strategy perform better, the parametric effect of ambient temperature on the mass loss of test fluid and heat-to-vapor conversion efficiency will be further studied experimentally. Moreover, the effect of heat flux (0.5 Sun - 10 Sun) at a particular far-field ambient condition will also be conducted to determine the threshold heat flux, beyond which the contribution of dark evaporation completely diminishes, as suggested by the different theoretical models in the literature [3,4].

References

- [1] C. Chen, Y. Kuang and L. Hu, Challenges and opportunities for solar evaporation. *Joule*, 2019. 3(3): pp.683-718.
- [2] Z. Wang, T. Horseman, A.P. Straub, N.Y. Yip, D. Li, M. Elimelech and S. Lin, Pathways and

challenges for efficient solar-thermal desalination. *Science Advances*, 2019. 5(7): p.eaax0763.

- [3] G. Vaartstra, L. Zhang, Z. Lu, C.D. Díaz-Marín, J.C. Grossman and E.N. Wang, Capillary-fed, thin film evaporation devices. *Journal of Applied Physics*, 2020. 128(13): p.130901.
- [4] L. Zhang, Z. Xu, L. Zhao, B. Bhatia, Y. Zhong, S. Gong and E.N. Wang, Passive, high-efficiency thermally-localized solar desalination. *Energy & Environmental Science*, 2021. 14(4): p.1771-93.
- [5] K. Xu, C. Wang, Z. Li, S. Wu and J. Wang, Salt mitigation strategies of solar-driven interfacial desalination. *Advanced Functional Materials*, 2021. 31(8): p.2007855.
- [6] D. Chatterjee, T. Kulshrestha and S. Khandekar, Continuous Vapor Generation for Thermal-Desalination Applications Using a Thermosyphon Based Heat Localization Strategy. DOI: 10.2139/ssrn.4302832.
- [7] Z. Lu, K.L. Wilke, D.J. Preston, I. Kinofuchi, E. Chang-Davidson and E.N. Wang, An ultrathin nanoporous membrane evaporator. *Nano Letters*, 2017. 17(10): p.6217-20.
- [8] G. Ni, S.H. Zandavi, S.M. Javid, S.V. Boriskina, T.A. Cooper and G. Chen, A salt-rejecting floating solar still for low-cost desalination. *Energy & Environmental Science*, 2018. 11(6): p.1510-9.
- [9] G. Peng, S. Deng, S.W. Sharshir, D. Ma, A.E. Kabeel and N. Yang, High efficient solar evaporation by airing multifunctional textile. *International Journal of Heat and Mass Transfer*, 2020. 147: p.118866.
- [10] T. Poós and E. Varju, Review for prediction of evaporation rate at natural convection. *Heat and Mass Transfer*, 2019. 55(6): p.1651-60.
- [11] S.M. Bower and J.R. Saylor, A study of the Sherwood-Rayleigh relation for water undergoing natural convection-driven evaporation. *International Journal of Heat and Mass Transfer*, 2009. 52(13-14): p.3055-63.
- [12] M. Groll and S. Rösler, Operation principles and performance of heat pipes and closed two-phase thermosyphons. *Journal of Non-Equilibrium Thermodynamics*, 1992. 17(2): p.91-151.
- [13] H. Ghasemi, G. Ni, A.M. Marconnet, J. Loomis, S. Yerci, N. Miljkovic and G. Chen, Solar steam generation by heat localization. *Nature Communications*, 2014. 5(1): p.1-7.

Multi-Condenser Variable Conductance Heat Pipes for Electric Aircraft

Jeff Diebold^{1*}, Brett Leitherer¹, Calin Tarau¹ and Kuan-Lin Lee¹

¹Advanced Cooling Technologies, Inc., Lancaster, PA, USA

*Corresponding author email address: jeffrey.diebold@1-act.com

Abstract

Advanced Cooling Technologies, Inc. (ACT) is collaborating with NASA Glenn Research Center (GRC) to develop a heat pipe-based thermal delivery system to efficiently manage the waste heat generated onboard an electric aircraft. The heat pipe system will interface with NASA GRC’s thermoacoustic heat pump in order to recycle waste heat by transporting thermal energy to various end users onboard the aircraft, such as icing protection or cabin air heating. The heat pipe network utilizes a multi-condenser variable conductance heat pipe (MCVCHP) concept developed by ACT to actively control the heat delivered to the various end users without the use of moving parts. Each condenser contains a reservoir of non-condensable gas. By actively heating or cooling the gas within the reservoir it is possible to control heat transfer to individual condensers. This paper will discuss the design and operation of a multi-condenser VCHP proof-of-concept system, followed by a reduced-scale prototype of the heat pipe network for an electric aircraft.

Keywords: Variable Conductance Heat Pipe; Electric Aircraft; Thermal Management

1. Introduction

Advanced Cooling Technologies (ACT) is working with NASA Glenn Research Center (GRC) to develop an innovative solid-state thermal management system (TMS) for MW-scale hybrid-electric aircraft. Thermal management of electric aircraft is challenging due to the large amount of relatively low-grade waste heat. In order to overcome this challenge NASA GRC is developing a thermoacoustic heat pump that will actively cool electronics, such as the solid-state DC fault management system, and elevate the temperature of the waste heat [1].

An innovative heat pipe network, developed by ACT, will acquire heat at the hot end of the thermoacoustic heat pump and then distribute this heat throughout the aircraft. This heat can be recycled onboard the aircraft by delivering it to various end users benefiting from thermal energy such as anti-icing and cabin air heating.

The heat pipe network developed by ACT utilizes variable conductance heat pipe technology (VCHP). A single evaporator is connected to multiple variable conductance condensers, each with a dedicated reservoir of non-condensable gas (NCG). Each condenser delivers heat to a separate end user on the aircraft and by heating/cooling the reservoirs it is possible to control the amount of thermal energy delivered to the various end users.

2. Multi-Condenser VCHP Concept

ACT’s multi-condenser VCHP (MCVCHP) concept is illustrated in Figure 1. In Figure 1a, a single evaporator delivers heat to multiple condensers (end users requiring thermal energy). In Figure 1b, heat transfer to Condensers 1-2 is

blocked by heating NCG reservoirs 1-2. The NCG/vapor front in Condenser 4 passively adjusts accepting the heat previously delivered to Condensers 1-2.

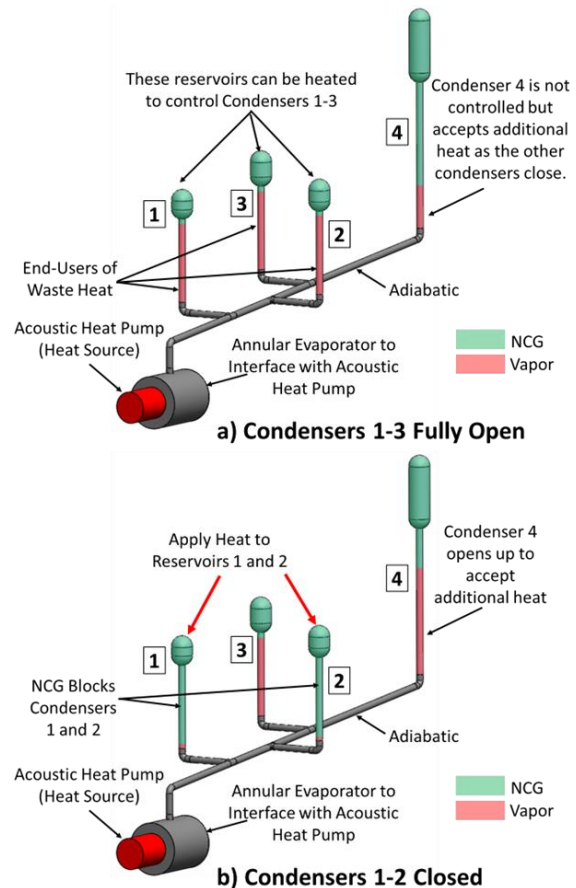


Figure 1. Multi-condenser VCHP concept. a) One evaporator delivers heat to multiple condensers. b) Heating of individual reservoirs controls heat transfer to respective condensers.

In the context of a hybrid-electric aircraft, the passive Condenser/Reservoir 4 can represent the ultimate heat sink to atmosphere or turbofan bypass exhaust. By passively accepting heat from other end users, Condenser/Reservoir 4 allows the system to operate at a nearly steady temperature as heat transfer to the other condensers is altered.

Modeling of the MCVCHP concept was done using the “Flat-Front Theory” described by Marcus [2]. It was assumed that vapor and NCG were separated by a discontinuous boundary. The total pressure in the system is the vapor pressure of the working fluid and the NCG was modeled as a perfect gas.

The NCG reservoirs must be properly sized to ensure the proper distribution of NCG during startup. Prior to startup, the entire system is at ambient temperature and no power is applied to the evaporator. In this state, the working fluid will be nearly all condensed liquid or may even be frozen in the evaporator region, and as a result most of the system will be occupied by NCG at a relatively low pressure. As power is applied to the evaporator, the working fluid will begin to evaporate, and the pressure will begin to increase pushing the NCG front towards the condensers.

Certain aspects of the system geometry are set by the application, such as the evaporator size, heat pipe diameter, and length of adiabatic and condenser sections. This leaves the reservoir volumes as design parameters that can be selected to achieve the desired NCG distribution at the design operating temperature. For example, the reservoirs can be sized such that all NCG is contained only within the reservoirs at the design operating temperature.

To demonstrate the proper startup of the MCVCHP concept, ACT designed the prototype shown in an IR image in Figure 2a. The prototype had three condensers/reservoirs connected to a single evaporator, was fabricated from stainless steel, and used toluene as the working fluid [3]. In Figure 2a, the system was at ambient temperature and all working fluid was condensed in the evaporator. In Figure 2b, heater power was applied, and the vapor temperature began to increase. The approximate location of the NCG front can be seen in the IR image just before the first condenser. By Figure 2d, there were three separate NCG fronts located in each condenser. Figure 2f corresponds to the design operating temperature and the NCG fronts were located at the entrance to each reservoir. Note that the reservoirs were all different sizes in order to

control the rate at which the NCG front advanced through each condenser.

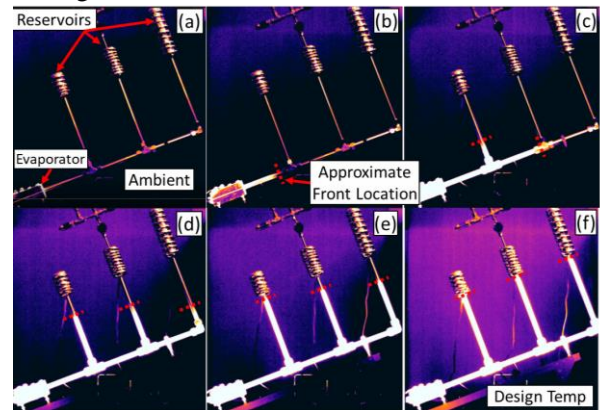


Figure 2. IR imaging of startup of MCVCHP proof-of-concept with three variable conductance condensers. Time progresses from (a) to (f) showing the vapor/NCG reaching the reservoirs at the design operating temperature.

After successfully demonstrating the control of NCG during startup, ACT fabricated the prototype MCVCHP shown above in Figure 1 [4]. This was a four condenser MVCHP designed with the intention of controlling heat to Condensers 1-3 via heating/cooling of Reservoirs 1-3.

Figure 3a shows the temperature distribution of the system near its nominal design operating condition, or the “Fully-On” condition, Condensers 1-3 were fully open. Note that the different sections of the pipe are color coded, and the size of the plot is not to scale. Each branch in Figure 3 is numbered and corresponds to the branches shown in Figure 1. The power to the system was 160W. At this power the average temperature of the adiabatic TCs was approximately 92°C, slightly above the design temperature of 90°C. The temperatures of Reservoirs 1-3 were slightly above ambient due to their proximity to the hot vapor. Most of the length of Condenser 4 and all of Reservoir 4 were at ambient temperature. By design, approximately 10% of Condenser 4 was utilized in this condition. This temperature distribution corresponds to the illustration of Figure 1a.

Figure 3b shows the temperature distribution of the system after heating Reservoirs 1 and 2 in order to block heat transfer to Condensers 1 and 2, corresponding to the illustration of Figure 1b. The MCVCHP prototype was operated at a constant power applied to the evaporator. As Condenser 1 and 2 were shut down, the area available for heat transfer was reduced resulting in an increase in vapor temperature that pushed the NCG fronts in Condensers 3 and 4 towards their respective

reservoirs. Reservoir 4 had the largest volume and therefore the NCG front in Condenser 4 was most sensitive to vapor temperature and the front rapidly moved towards Reservoir 4. This increased the surface area available for heat transfer in condenser 4 thus minimizing the vapor temperature rise. After blocking vapor from reaching Condensers 1 and 2, the average vapor

temperature of the adiabatic section increased to 93.9°C. Note that Reservoir 1 required a higher temperature than Reservoir 2 to shut down the respective condenser. This was due to smaller size of Reservoir 1 and the corresponding reduced sensitivity of the NCG front to reservoir temperature. The different reservoir sizes were a

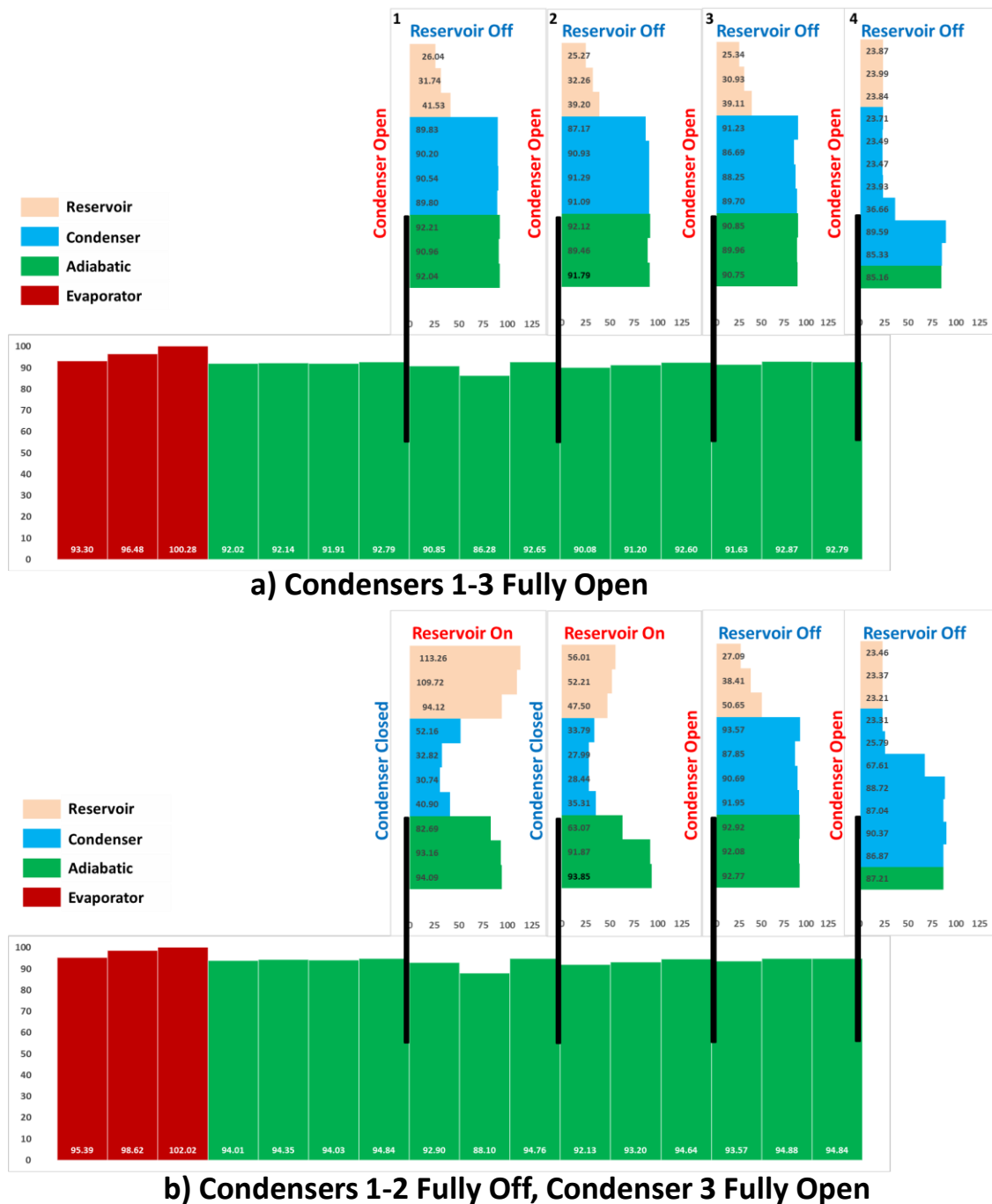


Figure 3. Comparison of temperature distributions of the 4 Condenser MVCHP prototype shown in Figure 1. The design operating temperature was 90°C. a) Design operating point, Condensers 1-3 fully open and Condenser 4 10% utilized. b) Heat applied to Reservoirs 1 and 2 to shut down Condensers 1 and 2. Heat previously dissipated by Condensers 1 and 2 was now dissipated at Condenser 4.

consequence of controlling the NCG distribution during startup.

3. Thermosyphon for Electric Aircraft

ACT developed and tested a prototype thermosyphon, with multi-condenser VCHP capability, to cool the DC fault management system onboard a hybrid-electric aircraft. The thermal management system is being designed for an electric aircraft with a nominal size similar to a Boeing 737. An approximate layout of the heat pipe network on the aircraft is illustrated in Figure 4. Due to the long lengths involved it is necessary to utilize a thermosyphon to transport the heat.

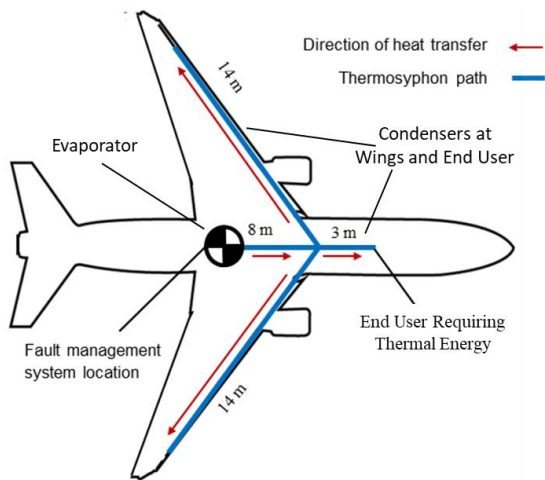


Figure 4. Illustration of aircraft and potential thermosyphon routing for cooling the fault management system.

In this design, one evaporator, connected to the thermoacoustic heat pump, delivers heat to three condensers. One condenser in each wing and a third located towards the front of the aircraft that represents an end user requiring thermal energy such as cabin warming. The heat delivered to the wings is dissipated to the atmosphere through the aircraft skin and can protect the wings from ice. Each condenser has a reservoir of NCG. The reservoir of the central condenser can be heated/cooled to control heat transfer to the end user. If heat transfer to the end user is not required, the condensers in the wings can take the additional heat load with minimal impact on thermosyphon operating temperature.

ACT has designed and fabricated a reduced-scale prototype of the proposed thermosyphon network. Figure 5 shows a CAD model of the prototype. An annular evaporator was designed to interface with the thermoacoustic heat pump. The thermosyphon prototype was placed on a large support structure that was capable of tilting about

two axes to simulate aircraft pitch and roll. The thermosyphon evaporator was designed to store excess working fluid to compensate for the reduced liquid return when the aircraft is banked, and one wing is oriented against gravity.

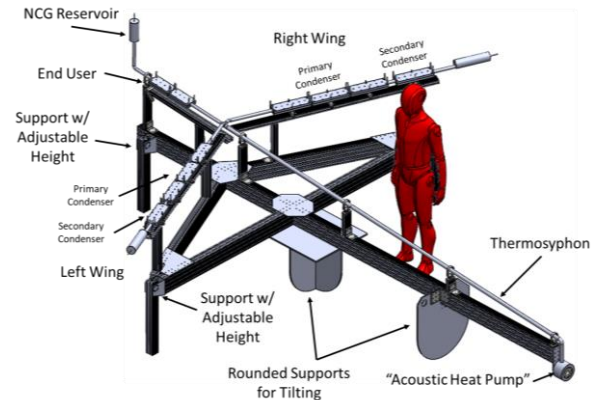


Figure 5. CAD model of reduced-scale thermosyphon network for electric aircraft currently being tested at ACT.

Figure 6 shows a time sequence of temperature distributions, during startup, along the two wings and the central end user of the prototype thermosyphon shown in Figure 5. The prototype began at a uniform ambient temperature and 2kW were applied at the evaporator until the system reached the target operating temperature of 100°C.

The initial plot, $t = 0s$, was an arbitrarily selected time shortly after the NCG front had passed the intersection of the three branches resulting in three separate fronts. Figure 6 shows a progression of the NCG front towards each reservoir as the vapor temperature increased. The temperature distribution in the two wings were nearly identical and the NCG front within the wings advanced at a faster rate than the NCG front within the central end user branch. The rate of NCG front advancement with vapor temperature is controlled by the sizes of the NCG reservoirs and the wings were designed with larger reservoirs due to the longer condenser lengths. Figure 6f indicates the theoretical predictions of the NCG front locations at the design operating point, calculated using Flat-Front Theory. The predicted front locations matched very well with the temperature gradient on the prototype.

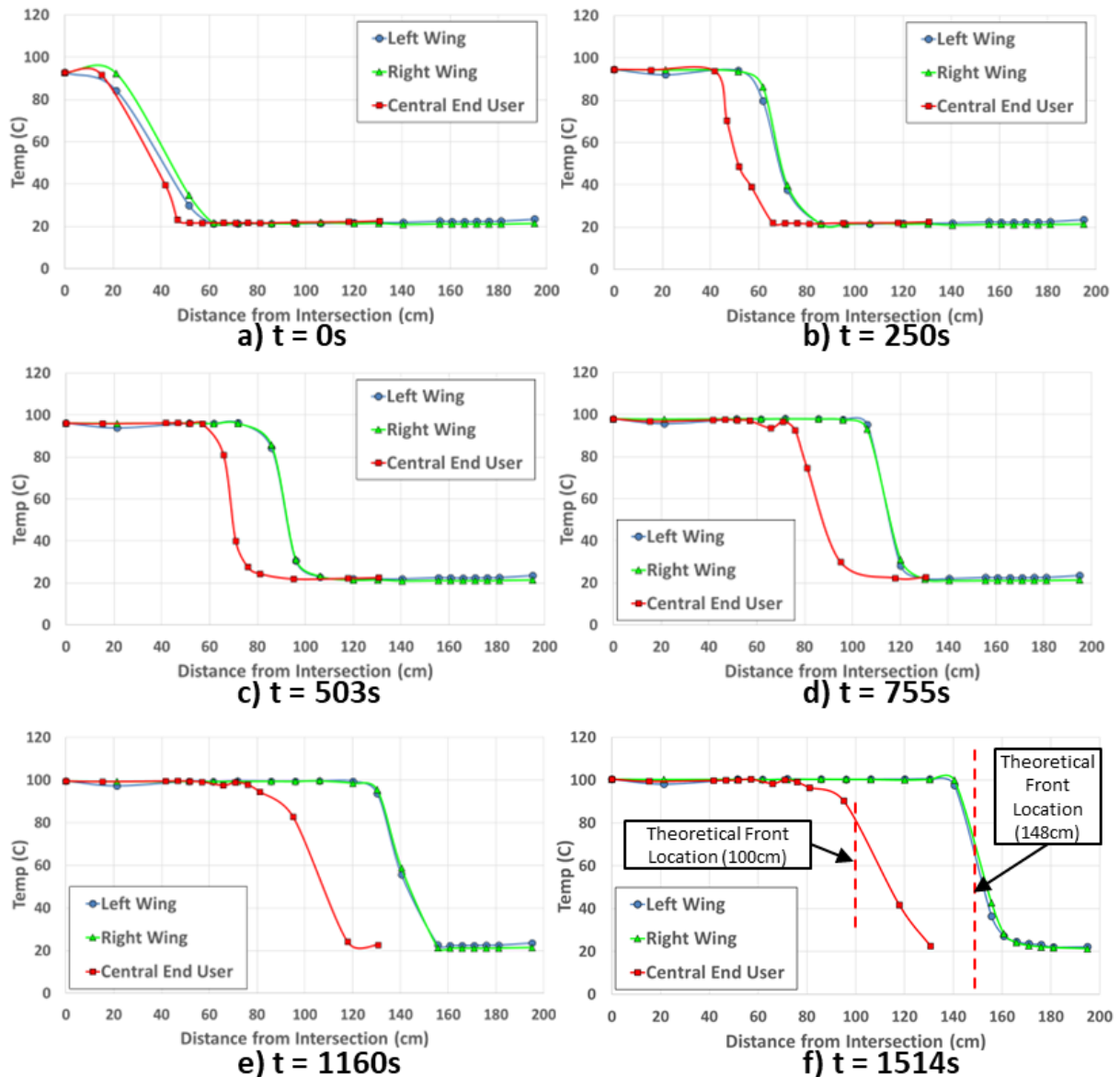


Figure 6. Time sequence of temperature distributions along the wings and central end user branches during startup of the reduced-scale thermosyphon prototype for electric aircraft shown in Figure 5. The x-axis is referenced to the intersection of the three branches. $t = 0$ was an arbitrarily selected time during the startup process.

Figure 7 shows the temperature distributions along the wings and the central end user branch during a test in which heat was applied to the central NCG reservoir. In Figure 7a, the system was at the design operating point with all three condensers fully open and 2kW were applied to the evaporator. The central reservoir temperature, also indicated in Figure 7a, was at the ambient temperature. Initially, the NCG front within the central branch was located beyond the condenser region approximately 85cm from the start of the branch. The central condenser spanned from approximately 40cm to 80cm.

In Figure 7b, the central reservoir temperature had increased to 40°C pushing the NCG front to 60cm blocking approximately half of the central end user condenser. Figure 7c and Figure 7d show the reservoir temperature continuing to rise and the NCG moving beyond the condenser region. In Figure 7d, the central condenser was fully occupied by NCG and the heat transfer to the region was blocked.

As the central condenser was blocked, the area available for heat transfer was decreased but the power to the system and the cooling remained constant. In order to compensate, the system temperature increased slightly and the NCG fronts within the wings moved towards the respective

reservoirs. Though difficult to see on the plot, the average temperature along the isothermal section of the wings increased by approximately 1°C. The temperature change along the wings between approximately 130cm and 150cm was more noticeable as the front moved outward. The wing condensers play a similar role as condenser 4 in the prototype illustrated in Figure 1. The heat that was rejected at the central end user condenser was redirected to the wing condensers with minimal increase in overall system temperature.

Figure 8 shows a time series of temperature corresponding to the experimental data of Figure 7. The plot includes the temperatures of the central NCG reservoir, both ends of the central condenser, and the vapor temperature. Reservoir heating began at approximately 7,300s and was quickly followed by a decrease in temperature of the far end of the central condenser (80cm). Figure 8 more clearly shows the slight rise in the vapor temperature as the area for heat transfer was reduced.

The power applied to the central reservoir during heating was not measured but was estimated based on thermal mass and the data of Figure 8 to be approximately 3-5W. A higher heating rate could be used to block heat transfer more rapidly to the central end user. Slightly beyond 10,000s heating to the reservoir was stopped and cooling was applied to the reservoir. The system rapidly adjusted back to the design operating condition.

The thermal control method demonstrated here is dependent only on the temperature of the vapor and NCG. As a result, a small amount of heater power applied to a reservoir can be used to control an arbitrary amount of power carried by the vapor. As shown in Figure 8, the system was maintained at a relatively steady state between 9,000s and 10,000s. During this time, heater power to the reservoir is only necessary to compensate for heat leaks from the reservoir.

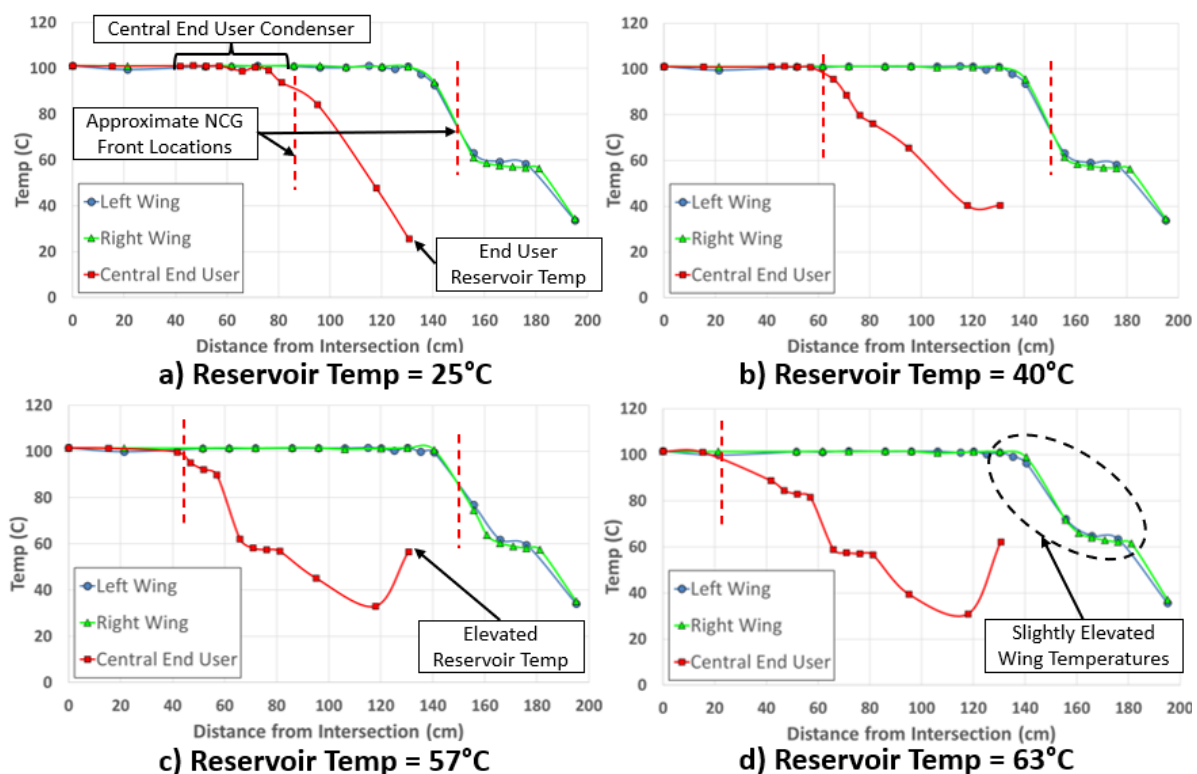


Figure 7. Temperature distributions along the wings and the central branch of the thermosyphon during a VCHP control test. The heater on the central NCG reservoir was used to increase the temperature of the NCG in order to block vapor from reaching the central end user. Reservoir temperature is indicated below each subfigure. The approximate location of the NCG front in the central end user branch is indicated in each plot. 2kW were applied to the evaporator.

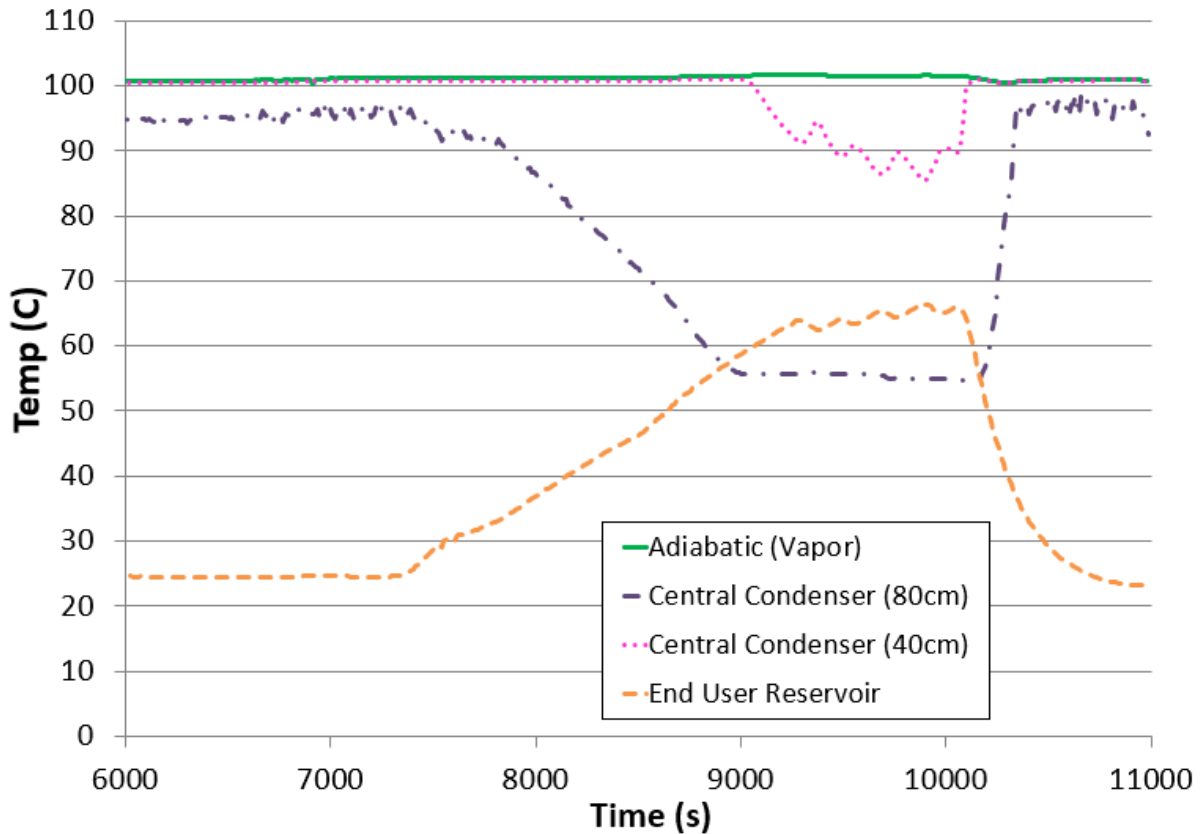


Figure 8. Temperature measurements at various locations on the thermosyphon during the VCHP control test (Corresponding to data shown above in Figure 7). At approximately 7,300s heater power to the central reservoir was turned on. A constant 2kW was applied to the evaporator. The Central Condenser temperature measurements were at 40cm and 80cm from the beginning of the central branch, see Figure 7.

4. Summary

Advanced Cooling Technologies has developed a multi-condenser VCHP heat pipe concept for an electric aircraft thermal management application. Heat is collected at a single evaporator and transported to multiple condensers each with a reservoir of NCG. The system can act as a variable conductance heat pipe and heat transfer to arbitrary condensers can be controlled via heating/cooling of individual reservoirs.

The design, startup and operation of the concept has been successfully demonstrated in three unique prototypes. The thermal control feature is entirely temperature dependent and small amounts of heater power can be used to control an arbitrary amount of power transferred by the heat pipe network.

References

- [1] R.W. Dyson, L. Rodriguez, M.E. Roth and P. Raitano, "Solid-State Exergy Optimized Electric Aircraft Thermal and Fault Management," *AIAA Propulsion and Energy Forum*, AIAA 2020-3576.
- [2] B.D. Marcus, "Theory and Design of Variable Conductance Heat Pipes," NASA CR-2018, 1972.
- [3] J. Diebold, K-L. Lee, C. Tarau and W. Anderson, "Development of Solid-State Waste Heat Delivery System for Electric Aircraft," 20th IEEE ITherm Conference, 2021.
- [4] J. Diebold, C. Tarau, K-L. Lee, W. Anderson, and R.W. Dyson, "Electric Aircraft Thermal Management using a Two-Phase Heat Transfer System with Solid-State Thermal Switching Capability," *AIAA Propulsion and Energy Forum 2021*, AIAA 2021-3334

A model of flat heat pipes leading to the classical fin equation for the pipe temperature

Salar Saadatian, Harris Wong*

Louisiana State University, Baton Rouge, Louisiana

**Corresponding author email address:hwong@lsu.edu*

Abstract

A flat heat pipe is a thin rectangular sealed duct with the inner wall typically covered by a porous structure. The pores are filled with a liquid and its vapor occupies the rest of the pipe. As one end of the pipe is heated, the liquid evaporates and increases the local vapor pressure that pushes the vapor to the cooler end, where the vapor condenses into liquid. Finally, capillary forces drive the liquid back to the hot end. Since heat is transferred by evaporation, vapor flow, and condensation, flat heat pipes are highly efficient and have been used in cooling computer chips. However, previous models impose heat rate through the pipe as an input parameter, preventing optimization of heat transfer. We incorporate evaporation kinetics into our model and obtain analytic solutions for the heat rate, pipe temperature, and liquid and vapor flow along the pipe for a given imposed temperature difference. Our model shows that the pipe behaves like a fin with evaporative cooling instead of convective cooling.

Keywords: Flat heat pipe; Evaporation kinetics; Classical fin equation; Porous wicks

1. Introduction

A heat pipe is a sealed container with the inner wall typically covered by a wick structure. The wick is filled with a working liquid and its vapor occupies the rest of the container. Various types of heat pipes have been developed, including rotating heat pipes, capillary pumped loop heat pipes, micro heat pipes, and flat heat pipes. They have been extensively used for thermal management in many areas, such as in microelectronic components, nuclear reactors, and spacecraft structures [1-4]. Heat transfer in a heat pipe is initiated by a temperature difference imposed between the two ends of the pipe. The temperature difference creates a vapor pressure difference that drives a vapor flow. This driving mechanism was analyzed by Zhang et al. [5] in their modeling of heat and mass transfer in a dual-wet micro heat pipe. They obtained the dimensionless heat rate through the pipe in terms of three dimensionless groups. Later, Rao and Wong [6] applied this model to micro heat pipes and reduced the dimensionless groups from three to two. Here, we apply the model to flat heat pipes and show that the evaporation rate depends only on the pipe temperature which further reduces the dimensionless groups from two to one.

Our model flat heat pipe (Figure 1) is described in section 2; it consists of a rectangular vapor-filled cavity with a wick on either one or both walls. Liquid filled circular capillaries run along and across the wick. In section 3, we derive analytically the evaporation rate in a single pore opening on the wick surface and show that the evaporation occurs chiefly near the pore edge. This pore-level mass evaporation rate is incorporated in section 4 into

pipe-level mass, momentum, and energy balances to yield a governing equation for the pipe temperature. In section 5, the governing equation is simplified with only one dimensionless number left (the length ratio S). The simplified equation is exactly the same as the classical fin equation. This equation is then solved analytically, which yields analytic solutions of the pipe temperature (Figure 2), the mass evaporation rate, the vapor pressure and flow rate, and the heat rate through the pipe. We discuss the results in section 6 and conclude in section 7.

2. A flat heat pipe

Our model heat pipe is shown in Figure 1 and Figure 2. The pipe is a closed thin rectangular duct of length $2L$, width W , and height h . The top part of the duct is occupied by a vapor and the bottom part by a solid wick. The height of the vapor region is G and that of the wick is D . There are N_x , N_y , and $2N_z$ straight capillaries evenly distributed in the x , y , and z directions, respectively, as shown in Figure 1. The capillaries are circular with uniform radius R_p and are filled with a liquid. The capillaries along the y direction are open to the vapor region at the top and closed at the bottom duct surface. Hence, there are $2N_x N_z$ circular pores on the wick surface that connect the vapor to the liquid in the wick. Results derived for our heat pipe can also be applied to a flat heat pipe with two identical wicks, one attached to the top wall and the other to the bottom wall. If we take the combined thickness of the two wicks to be the same as the thickness D of our single wick, then the analyses for our heat pipe will also hold for the

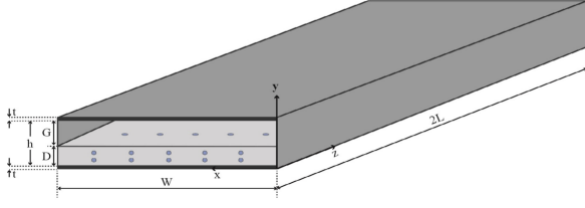


Figure 1. Isometric view of the model flat heat pipe.

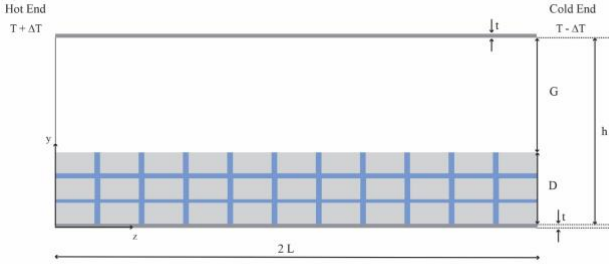


Figure 2. A longitudinal cross section of the flat heat pipe

two-wick heat pipe, except that the top wick presents another set of pores for evaporation. This difference is handled by using $2nN_xN_z$ as the number of pores with $n = 1$ or 2 , indicating either one or two wicks. Initially, the temperature of the heat pipe is kept at T_0 (absolute). The capillaries are filled with the working liquid to the extent that the liquid-vapor interface in each pore is planar. At first, the liquid temperature is at T_0 , and the vapor is saturated at the corresponding equilibrium pressure P_0 . The outer surface of the pipe is insulated. The temperature at one end of the pipe is increased to $T_0 + \Delta T$ and the temperature at the other end is decreased to $T_0 - \Delta T$. These end temperatures are maintained, and the heat-pipe temperature reaches a steady profile. The equilibrium vapor pressure at the hot end is higher than that at the cold end. This pressure gradient drives a vapor flow from the hot end towards the cold end. As the vapor leaves the hot end, the vapor pressure at the hot end drops below the equilibrium vapor pressure which leads to continuous evaporation from the pores. At the cold end, the vapor pressure is higher than the local equilibrium vapor pressure, leading to continuous condensation. Thus, the liquid volume at the cold end is increased which raises the liquid-vapor interface. At the hot end, however, the interface curves towards the liquid side owing to evaporation. This interfacial curvature difference generates a pressure gradient in the liquid that drives the liquid from the cold end towards the hot end to complete a fluid-flow cycle in the heat pipe.

Heat transfer is assumed to be one-dimensional

along the pipe. Generally, $\Delta T \ll T_0$, and the temperature distribution along the pipe is skew-symmetric. Thus, we will study only the heated half of the pipe.

3. Evaporation at a pore

3.1. Evaporation kinetics

A typical pore cross section is shown in Figure 3. Due to the small size of the pore, surface tension dominates, and the liquid-vapor interface can be taken as flat [7]. The local pore-wall temperature is T_p , and the local vapor pressure outside the pore is P_g . These pipe-level variables can be treated as constant around the pore because they vary over a length scale that is much larger than the pore size. The liquid temperature at the interface is denoted by T_i which varies along the interface owing to non-uniform evaporation along the interface. At each point on the interface, the liquid temperature T_i has a corresponding saturation pressure P_i . Over the heated half of the pipe, $P_i > P_g$, because the vapor moves away from the hot end and therefore cannot sustain the equilibrium vapor pressure. The pressure difference leads to continuous evaporation at that point on the interface [5-10]:

$$m = c(P_i - P_g), \quad (1)$$

$$c = \frac{\alpha}{\sqrt{2\pi R_s T_g}}, \quad (2)$$

where m is the evaporative mass flux, c is inversely proportional to the speed of sound in the vapor, α is the accommodation coefficient ($\alpha=1$), R_s is the specific gas constant, and T_g is the saturation temperature at vapor pressure P_g . The saturation pressure P_i depends only on the interfacial temperature T_i . Therefore, the pressure difference in Eq.1 is converted into a temperature difference using Taylor's expansion of P_i about P_g :

$$P_i = P_g + \frac{dP_i}{dT_i}(T_i - T_g) + \dots \quad (3)$$

We find dP_i/dT_i using the Clapeyron equation [11]:

$$\frac{dP_i}{dT_i} = \frac{\rho_g h_{fg}}{T_g}, \quad (4)$$

where h_{fg} is the latent heat of vaporization of the liquid and ρ_g is the saturated vapor density, both evaluated at T_g . Thus, the evaporative mass flux becomes

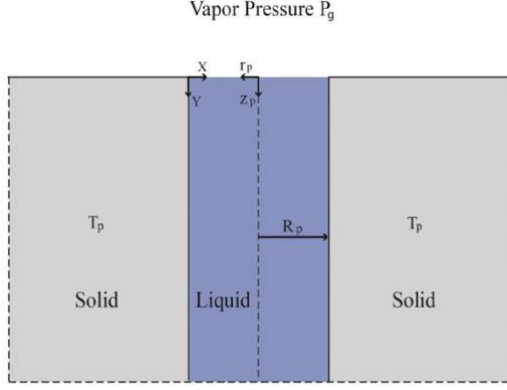


Figure 3. A cross section of a liquid-filled circular pore of radius R_p

$$m = \frac{c\rho_g h_{fg}(T_i - T_g)}{T_g} \quad (5)$$

Hence, m is found in terms of the interfacial temperature T_i and the saturation temperature T_g corresponding to the vapor pressure P_g . To find T_i , we need to solve for the liquid temperature in the pore.

3.2. Liquid temperature in the pore

Due to the small size of the pore, convective heat transfer is negligible, and the liquid temperature obeys

$$\nabla^2 T = 0, \quad (6)$$

where ∇^2 is the axisymmetric cylindrical Laplacian operator, and a cylindrical coordinate system (r_p, z_p) is defined at the center of the pore (Figure 2). The Laplace equation is subject to the following boundary conditions. At the capillary wall $r_p = R_p$, the liquid temperature is equal to the wall temperature T_p . At the liquid-vapor interface $z_p = 0$, the heat flux needed to convert liquid into vapor is supplied by the conductive heat flux through the liquid:

$$mh_{fg} = k_f \frac{\partial T}{\partial z_p}, \quad (7)$$

where k_f is the liquid thermal conductivity. Since $m = m(T_i)$ as shown in Eq.5, it imposes a mixed boundary condition on T . Because the pore radius is small compared with the height of the capillary, the capillary can be taken as infinitely long [12]. Therefore, the liquid temperature far from the interface as $z_p \rightarrow \infty$ approaches the wall temperature T_p . We solve Eq.6 with the boundary conditions to find the liquid temperature inside the

pore and consequently the interfacial temperature T_i . The evaporative mass flux m can then be found from Eq. 5 which, when integrated over the interfacial area, gives the mass evaporative rate at the pore:

$$M_p = \int_0^{R_p} 2\pi r_p m dr_p \quad (8)$$

3.3. Solution of the evaporation rate at the pore

A set of pore-level dimensionless variables is defined:

$$r_p^* = \frac{r_p}{R_p}, z_p^* = \frac{z_p}{R_p}, T^* = \frac{T - T_g}{T_p - T_g},$$

$$M_p^* = \frac{M_p}{c\rho_g h_{fg} R_p^2 (T_p - T_g) / T_g}. \quad (9)$$

The Laplace equation becomes

$$\nabla^{*2} T^* = 0, \quad (10)$$

where ∇^{*2} is the dimensionless Laplacian and $T^* = T^*(r_p^*, z_p^*)$. The boundary condition at the capillary wall located at $r_p^* = 1$ becomes $T^* = 1$. At the interface $z_p^* = 0$, m in Eq. 5 is substituted into Eq. 7 to give

$$T^* = \frac{1}{E} \frac{\partial T^*}{\partial z_p^*}, E = \frac{cR_p \rho_g h_{fg}^2}{k_f T_g}. \quad (11)$$

Here, E is the Evaporation number that represents the ratio of the evaporative heat flux to the conductive heat flux in the liquid, assuming both are driven by the same temperature difference. For common liquids and capillary sizes, $E \gg 1$. Far away from the interface, as $z_p^* \rightarrow \infty$, $T^* \rightarrow 1$. Thus, we have sufficient boundary conditions to determine the liquid temperature $T^* = T^*(r_p^*, z_p^*)$, and subsequently the interfacial temperature $T^*(r_p^*, 0)$ yields the evaporative mass flux m at the interface according to Eq. 5. Thus, the non-dimensionalized mass evaporation rate at the pore can be found following Eq. 8:

$$M_p^* = 2\pi \int_0^1 T^*(r_p^*, 0) r_p^* dr_p^*. \quad (12)$$

The liquid in the pore evaporates chiefly near the pore edge. In the limit $E \rightarrow \infty$, Eq. 11 gives $T^* = 0$ at the interface. However, the interfacial temperature must jump to $T^* = 1$ at the pore wall. Thus, an inner region of size $O(E^{-1})$ exists near

the pore edge in which the interfacial temperature varies smoothly from 1 to 0 [13]. Owing to the rapid temperature variation within the small inner region, high temperature gradients exist that drive high evaporation rates. Therefore, the pore liquid evaporates mainly in the inner region near the pore edge. The Laplace equation in the inner region has been solved in the limit $E \rightarrow \infty$ [13], and the non-dimensionalized mass evaporation rate is found at leading order as [13]

$$M_p^*(E) = \frac{4}{E} \ln(E) \quad (13)$$

Thus, the dimensional mass evaporation rate is

$$M_p = c \rho_g h_{fg} R_p^2 \frac{(T_p - T_g)}{T_g} M_p^*(E) \quad (14)$$

This mass evaporation rate M_p at the pore will be connected to pipe-level variables in the following sections.

4. Pipe-level mass, momentum, and energy balances

The capillaries in the wick are arranged regularly. Thus, the pipe can be divided into rectangular cells, each containing a single pore. This base unit cell is shown in Figure 4. Mass, momentum, and energy balances on the unit cell relates the evaporation rate at the pore derived in the last section to pipe-level variables. A mass balance on the vapor region of the unit cell shown in Figure 4 gives that the rate of vapor mass entering the vapor region plus the rate of mass evaporated at the pore is equal to the rate of vapor mass leaving the vapor region:

$$\rho_g [V_g(z + \Delta z) - V_g(z)] = n M_p, \quad (15)$$

where V_g is the vapor volume flow rate through the unit cell, z is the axial coordinate of the front side of the cell, $\Delta z = L/N_z$ is the length of the cell, ρ_g is the saturated vapor density at vapor pressure P_g , n ($=1$ or 2) is the number of wicks in the pipe, and M_p is the mass evaporation rate at the pore given in Eq. 14. Applying Taylor's expansion and substituting $\Delta z = L/N_z$ yield

$$\frac{dV_g}{dz} = \frac{n N_z M_p}{\rho_0 L}, \quad (16)$$

where ρ_g has been replaced by the equilibrium vapor density ρ_0 evaluated at T_0 . This equation

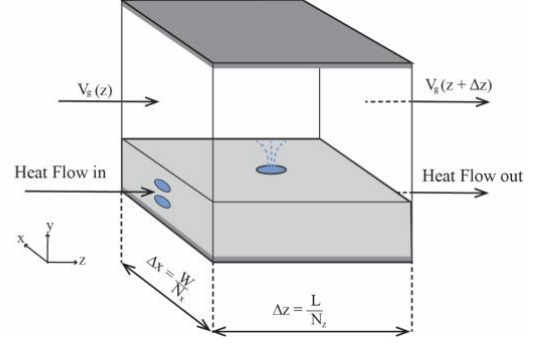


Figure 4. A base unit cell

relates the variation of vapor volume flow rate along the pipe to the pore evaporation rate. Thus, we have brought a pore-level result up to the pipe level.

Since the vapor flow in the thin pipe is laminar, the classical channel-flow results apply [14] and the vapor pressure gradient is related to the local volume flow rate V_g by a momentum balance:

$$\frac{dP_g}{dz} = -\frac{12\mu_g V_g}{G^3 \Delta x}, \quad (17)$$

where μ_g is the vapor viscosity and $\Delta x = W/N_x$ is the width of the unit cell (Figure 4). Differentiating Eq. 17 and substituting dV_g/dz from Eq. 16 lead to:

$$\frac{d^2 P_g}{dz^2} = -\frac{12n N_x N_z \mu_g}{G^3 W L \rho_0} M_p. \quad (18)$$

An energy balance on the non-vapor region of the unit cell shown in Figure 4 specifies that the conductive heat rate entering the non-vapor region supplies the evaporative heat rate at the pore, and the remaining heat rate then exits the non-vapor region:

$$n h_{fg} M_p = (k_f A_f + k_w A_w + k_s A_s) \left[\frac{dT_p}{dz} (z + \Delta z) - \frac{dT_p}{dz} (z) \right], \quad (19)$$

where k is the thermal conductivity and A is the cross-sectional area with subscripts f , w , and s denoting the liquid, wall, and wick solid, respectively. The pipe is assumed insulated outside, so that heat cannot escape through the top and bottom walls. By applying Taylor's expansion with $\Delta z = L/N_z$, we get

$$(k_f A_f + k_w A_w + k_s A_s) \frac{d^2 T_p}{dz^2} - \frac{n N_z h_{fg}}{L} M_p = 0. \quad (20)$$

This is a one-dimensional heat diffusion equation with a sink. It connects the pore-level evaporation rate M_p to the pipe-level variable T_p . We show in [13] that liquid flow in the wick and heat conduction in the vapor have negligible contributions to the energy balance in Eq. 20.

5. Analytic solutions of heat and mass transfer along the pipe

5.1. Pipe temperature

To solve for the pipe temperature T_p in Eq. 20, we need to express M_p in terms of T_p . The mass evaporation rate M_p in Eq. 14 depends explicitly on pipe temperature T_p , and implicitly on vapor pressure P_g through its dependence on temperature T_g . This implicit dependence can be made explicit by expanding T_g about the initial temperature T_0 and Eq. 14 can be written as [13]

$$M_p = cM_p^*(E)R_p^2 \left[(T_p - T_0) \frac{\rho_0 h_{fg}}{T_0} - (P_g - P_0) \right]. \quad (21)$$

The initial pipe temperature T_0 and vapor pressure P_0 are also the pipe temperature and vapor pressure at the midpoint of the pipe during steady heat transfer owing to symmetry. Therefore, M_p varies linearly with pipe-temperature and vapor-pressure deviations from the mid-pipe values ($M_p = 0$ at midpipe). We have shown in [13] that the vapor-pressure difference term in Eq. 21 is negligible compared with the pipe-temperature difference term and can be dropped. Thus, M_p becomes

$$M_p = \frac{c\rho_0 h_{fg} M_p^*(E) R_p^2}{T_0} (T_p - T_0). \quad (22)$$

When this is substituted into Eq. 20, we get

$$\frac{d^2 T_p}{dz^2} - \frac{ncN_z \rho_0 h_{fg}^2 M_p^*(E) R_p^2}{T_0 L (k_f A_f + k_w A_w + k_s A_s)} (T_p - T_0) = 0. \quad (23)$$

Equation 23 is the classical fin equation when the cross-sectional area of the fin is constant [15]. In the classical fin equation, the fin is cooled convectively by a flow with specified far-field temperature T_∞ . Here, T_∞ is replaced by T_0 , and the pipe is cooled by evaporation. The evaporative mass rate in Eq. 22 depends on the temperature difference ($T_p - T_0$), similar to the convective cooling of a fin.

We define a set of pipe-level dimensionless variables:

$$z^* = \frac{z}{L}, T_p^* = \frac{T_p - T_0}{\Delta T} \quad (24)$$

The governing equation becomes

$$\frac{d^2 T_p^*}{dz^{*2}} - S^2 T_p^* = 0, \quad (25)$$

where S is a dimensionless group defined as

$$S = \left[\frac{ncN\rho_0 h_{fg}^2 M_p^*(E) R_p^2}{T_0 (k_f A_f + k_w A_w + k_s A_s)} \right]^{1/2} L, \quad (26)$$

where we have replaced N_z/L by N , which is the one-dimensional pore density in the z -direction. Equation 25 reveals that S^2 is the ratio of evaporative to conductive heat transfer through the whole pipe. The pipe temperature obeys the following boundary conditions: at $z^* = 0, T_p^* = 1$, and at $z^* = 1, T_p^* = 0$. Thus, we find

$$T_p^* = \frac{\sinh[S(1-z^*)]}{\sinh S}. \quad (27)$$

This is plotted in Figure 5 for $S=1, 2, 5, 10, 20, 50$. For heat pipes, $S \gg 1$ and Figure 5 shows that there is a boundary layer of thickness $O(S^{-1})$ at $z^* = 0$. Since M_p is linearly proportional to T_p , as shown in Eq. 22, the dimensionless evaporation mass flow rate is simply the dimensionless pipe temperature.

5.2. Vapor flow

The vapor volume flow rate V_g is related to M_p by Eq. 16 and to the vapor pressure P_g by Eq. 17. Using a scale for M_p invoked by Eq. 22, we find a scale for V_g and one for P_g , which yield the following dimensionless variables:

$$V_g^* = \frac{V_g}{ncN_z h_{fg} R_p^2 M_p^*(E) \Delta T / T_0}, \quad (28)$$

$$P_g^* = \frac{P_g - P_0}{12nc(N_x N_z L / G^3 W) \mu_g h_{fg} R_p^2 M_p^*(E) \Delta T / T_0} \quad (29)$$

Equations 16 and 17 become

$$\frac{dV_g^*}{dz^*} = M^*, \quad (30)$$

$$\frac{dP_g^*}{dz^*} = -V_g^*, \quad (31)$$

where M^* is the dimensionless evaporation mass flow rate. At the end of the pipe, there is no flow and $V_g^* = 0$ at $z^* = 0$. Thus, by integrating Eq.

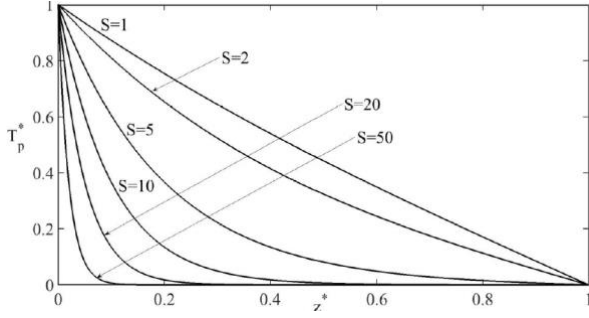


Figure 5. Dimensionless temperature T_p^*

30 once, we get

$$V_g^* = \frac{\coth S}{S} - \frac{\cosh[S(1-z^*)]}{S \sinh S}. \quad (32)$$

At the middle of the pipe, $P_g = P_0$ by symmetry, which means $P_g^* = 0$ at $z^* = 1$. Thus, Eq. 31 is integrated once subject to this boundary condition to give

$$P_g^* = \frac{\coth S}{S} (1 - z^*) - \frac{\sinh[S(1-z^*)]}{S^2 \sinh S}. \quad (33)$$

Dimensionless vapor volume flow rate V_g^* is plotted in Figure 6 for various S . It reveals that for $S \gg 1$ there is a thermal boundary layer of thickness $O(S^{-1})$ near the hot end, and V_g^* increases from 0 to a constant level within this boundary layer.

Dimensionless vapor pressure P_g^* is plotted in Figure 7 for various S . It shows that P_g^* starts uniformly at the end and then decreases almost linearly along the pipe. The evaporated vapor flows along the pipe with constant volume flow rate, as confirmed by the results of V_g^* in Figure 6. This constant volume flow rate is driven by a constant pressure gradient (Figure 7). Therefore, the results are consistent and physical. Even

though the vapor-pressure difference has a negligible effect on evaporation, it is the driving force behind vapor flow and must be retained here.

5.3. Heat rate through the unit cell

The energy equation in Eq. 20 can be integrated after M_p from Eq. 16 has been substituted:

$$-(k_f A_f + k_w A_w + k_s A_s) \frac{dT_p}{dz} + \rho_0 h_{fg} V_g = q, \quad (34)$$

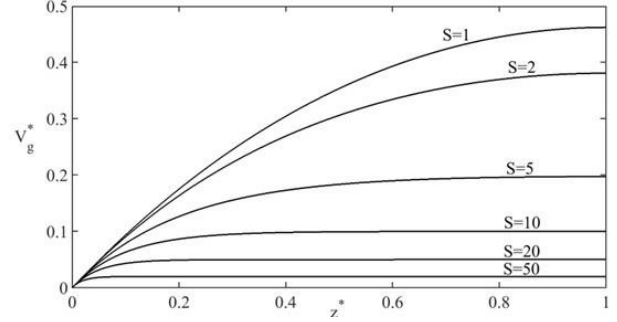


Figure 6. Dimensionless vapor flow rate V_g^*

here the integration constant q is recognized as the total heat rate through the unit cell which is the sum of the conductive heat rate through the non-vapor region of the unit cell (Figure 4) and the vapor flow heat rate. Because the pipe is insulated outside, q is constant along the pipe. Equation 34 is made dimensionless to give

$$-\frac{dT_p^*}{dz^*} + S^2 V_g^* = \frac{q}{q_c} = Nu, \quad (35)$$

$$q_c = (k_f A_f + k_w A_w + k_s A_s) \frac{\Delta T}{L}, \quad (36)$$

where q_c is the conductive heat rate along the pipe in the absence of vapor flow, and Nu is the Nusselt number. The first term in Eq. 35 is the conductive heat rate, the second term is the evaporative heat rate, and the sum is the constant heat rate through the pipe. When the solutions of T_p^* in Eq. 27 and V_g^* in Eq. 32 are substituted into Eq. 35, we obtain the Nusselt number as

$$Nu = S \coth S. \quad (37)$$

For heat pipes, typically $S \gg 1$, and Eq. 37 gives $Nu \rightarrow S$.

6. Discussion

Our model heat pipe is driven by fixed temperatures imposed at the two ends of the pipe. We assume that the liquid-vapor interface in the pore deviates infinitesimally from the flat position, which yields an analytic solution for the liquid temperature in the pore. Our model assumes that the heat transfer and fluid flow along the pipe are one-dimensional. We have shown in [13] that the vapor-pressure difference has negligible influence on the mass evaporation rate along the pipe. This enables us to build our model based on only one dimensionless number S . An interesting result revealed by our model is that the differential equation that governs the pipe temperature (Eq.

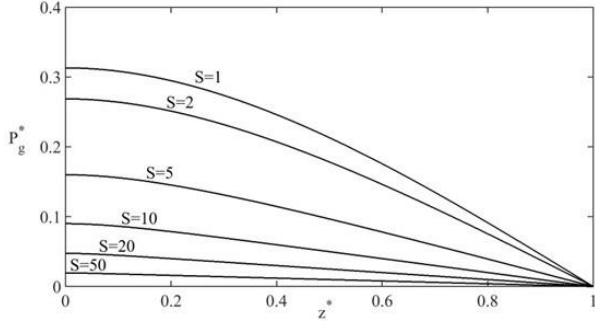


Figure 7. Dimensionless vapor pressure P_g^*

23) is the same as that of a classical fin, cooled by evaporation instead of convection. This analogy, which is presented here for the first time, helps us better understand the working mechanisms of flat heat pipes and improve their future designs.

An effective thermal conductivity is defined as

$$k_{eff} = \frac{N_x q L}{A_t \Delta T} = \frac{N_x (k_f A_f + k_s A_s + k_w A_w) q}{A_t q_c}, \quad (38)$$

where N_x is the total heat rate through the pipe, and $A_t = W(h + 2t)$ is the total cross-sectional area of the heat pipe. Since $q/q_c = Nu \gg 1$ and $N_x A_f \sim N_x A_s \sim N_x A_w \sim A_t$, k_{eff} is much larger than k_s , k_w , and k_f . Therefore, the flat heat pipe operates more efficiently than any of the components alone. We can also define an effective heat-transfer coefficient as

$$h_{eff} = \frac{N_x q}{2 \Delta T A_t} = \frac{k_{eff}}{2L}. \quad (39)$$

The pores in our wick are assumed to be straight circular capillaries. This idealized porous wick yields analytic solutions for heat and mass transfer along the pipe. However, typical flat heat pipes have wicks made of sintered metal spheres [1-3]. We have shown that our wick parameters (N_x , N_s , N_w , and R_p) can be converted to porous-medium parameters (porosity and permeability) [13]. This allows our model to be applied to real porous wicks [13]. We apply our model, which has no fitting parameters, to two flat heat-pipe experiments [16, 17] and obtain reasonable agreements for the heat rate through the pipe.

Unlike most models in the literature, the heat rate q through the pipe is solved here as a part of the solutions instead of being imposed as a boundary condition. Therefore, it is possible to optimize q by varying the pipe length or the wick thickness. We have analyzed the effects of pipe length and wick thickness on the heat rate through the pipe. For a fixed wick thickness, to fully utilize

the evaporative heat transfer, we need $S > 10$, which provides a criterion for the optimum pipe length. For a fixed pipe length, our model results show that thicker wicks enhance the total heat transfer through the pipe. It should be noted that the maximum capillary pressure at the hot end sets a lower and an upper bound on the wick thickness [13]. Our optimization results provide guides for future design of flat heat pipes.

7. Conclusions

The heat and mass transfer in a flat heat pipe with an idealized porous wick is studied. We assume that the heat transfer is one-dimensional, and the pore size is extremely small compared with the pipe length. Hence, pore-level events can be studied separately from those at the pipe level. An analytical solution for the mass evaporative rate in a single pore is found and incorporated into the mass, momentum, and energy balances along the pipe. We find that the mass evaporative rate depends on the pipe temperature and is essentially independent of the vapor-pressure difference. Thus, the pipe behaves like a fin with evaporative cooling instead of convective cooling. Henceforth, analytic solutions are obtained for the pipe temperature T_p , mass evaporative rate M_p , vapor volume flow rate V_g , vapor pressure P_g , and Nusselt number Nu . We found that the heat rate through the pipe depends on only one dimensionless number S , which is defined in Eq. 26. We observe that for normal operation of heat pipe $S \gg 1$, and heat is transferred predominantly by vapor flow, leading to $Nu \approx S$.

References

- [1] H. Tang, Y. Tang, Z. Wan, J. Li, W. Yuan, L. Lu, Y. Li, and K. Tang, Review of applications and developments of ultra-thin micro heat pipes for electronic cooling, *Applied energy*, 2018. 223: p. 383.
- [2] Y. Yu, G. An, and L. Wang, Major applications of heat pipe and its advances coupled with sorption system: a review. *Frontiers in Energy*, 2019. 13 (1): p. 172.
- [3] X. Chen, H. Ye, X. Fan, T. Ren, and G. Zhang, A review of small heat pipes for electronics, *Applied Thermal Engineering*, 2016. 96: p. 1.
- [4] H. Jouhara, A. Chauhan, T. Nannou, S. Almahmoud, B. Delpech, and L. Wrobel, Heat pipe based systems-advances and applications, *Energy*, 2017. 128: p. 729.

- [5] J. Zhang, S. Watson, and H. Wong, Fluid flow and heat transfer in a dual-wet micro heat pipe. *Journal of Fluid Mechanics*, 2007. 589: p. 1.
- [6] S. S. Rao and H. Wong, Heat and mass transfer in polygonal micro heat pipes under small imposed temperature differences. *International Journal of Heat and Mass Transfer*, 2015. 89: p. 1369.
- [7] Z. Lu, I. Kinefuchi, K. Wilke, G. Vaartstra, and E. Wang, A unified relationship for evaporation kinetics at low Mach numbers, *Nature Communications*, 2019. 10: <https://doi.org/10.1038/s41467-019-10209-w>.
- [8] M. S. Plesset and A. Prosperetti, Flow of vapour in a liquid enclosure, *Journal of Fluid Mechanics*, 1976. 78 (3): p. 433.
- [9] P. C. Wayner Jr, Spreading of a liquid film with a finite contact angle by the evaporation/condensation process, *Langmuir* 1993. 9 (1): p. 294.
- [10] V. S. Ajaev and G. Homsy, Modeling shapes and dynamics of confined bubbles, *Annual Review of Fluid Mechanics*, 2006. 38: p. 277.
- [11] V. P. Carey, *Liquid-vapor phase-change phenomena: an introduction to the thermophysics of vaporization and condensation processes in heat transfer equipment* (CRC Press, 2020).
- [12] P. Regmi and H. Wong, Heat and mass transfer in a cylindrical heat pipe with a circular-capillary wick under small imposed temperature differences, *International Journal of Heat and Mass Transfer*, 2018. 120: p. 228.
- [13] S. Saadatian and H. Wong, Analytic solutions of heat and mass transfer in flat heat pipes with porous wicks, *International Journal of Heat and Mass Transfer* (accepted).
- [14] F. M. White, *Viscous Fluid Flow* (McGraw-Hill, New York, 2006).
- [15] T. Bergman, A. Lavine, F. Incropera, and D. DeWitt, *Fundamentals of Heat and Mass Transfer* (Wiley, New York, 2018).
- [16] S. Wong, H. Tseng, and S. Chen, Visualization experiments on the condensation process in heat pipe wicks, *International Journal of Heat and Mass Transfer*, 2014. 68: p. 625.
- [17] D. Jafari, W. Wits, and B. Geurts, Phase change heat transfer characteristics of an additively manufactured wick for heat pipe applications, *Applied thermal engineering*, 2020. 168: <https://doi.org/10.1016/j.applthermaleng.2019.114890>.

Investigation of the Thermal Performance of Rod-Plate Heat Pipes

Elvis Falcão de Araújo^{1*}, Márcia Barbosa Henriques Mantelli¹, Juan Pablo Flórez Mera¹, and Luis Hernán Rodríguez Cisterna²

¹Heat Pipe Laboratory, Federal University of Santa Catarina, Florianópolis, Brazil

²Universidad de Tarapacá, Arica, Chile

*Corresponding author email address:
elvis.araujo@labtucal.ufsc.br

Abstract

Inspired in wire-plate mini heat pipes developed for electronics, this work proposes a novel type of heat pipe of larger dimensions aiming nuclear applications. The proposed device, named rod-plate heat pipe, is manufactured from the diffusion bonding of rods and plates. A hydraulic model was implemented, based on fluid motion equations, with the objective of predicting the capillary heat transfer limit and the optimal working fluid charging volume. A 0.5 m long water-stainless steel prototype with 23 ml of fill charge is fabricated and tested at a horizontal orientation. Up to 191.4 W, delivered by a cartridge electrical heater, is applied at the evaporator, while natural convection is used to cool the condenser. The device is also tested in only conduction mode, without working fluid. The heat pipe presented thermal resistances of 0.11 °C/W and 0.09 °C/W at heat inputs of 25.6 W and 88.5 W, respectively, while the empty heat pipe (pure conduction) resistance is 4.61 °C/W for 25.6 W heat input. The steady-state temperatures are respectively 99.5 °C, 92.8 °C and 207.1 °C. So far, the theoretical analysis and data have shown that the relatively large rod-plate technology is promising.

Keywords: Diffusing Welding; Heat pipe; Capillarity; Thermal Performance.

1. Introduction

Grooved heat pipes are heat transfer devices widely used in several applications such as for electronics cooling and in space. Actually, the sharp corners along the devices provided by the grooves allow the working fluid displacement from condenser to evaporator. Usually, this technology has been applied for small heat pipes, as the presence of corners inside the device showed to be enough for pumping the liquid, with no need for wicks [1]. Wire-plate mini heat pipes is one of the grooved technologies that has deserved the attention of many researchers, with several theoretical models and experimental data for small-scale devices available [2].

Inspired by the mini wire-plate heat pipes, this work proposes a macro scale device based on the same concept, named as Rod-Plate Heat Pipe. As for the wire-plate device, this new heat pipe is manufactured from sandwiches of flat plates filled with massive bars (or rods). The set is bonded by diffusion welding. This fabrication method ensures high tensile resistance, reliable external sealing, and high groove quality at the edges formed between the rods and the sheets, which is responsible for providing the capillary pressure. Figure 1 shows an inside schematic view of the heat pipe under investigation. Figure 2 displays the cross-section of the heat pipe.

This technology is aimed for the space nuclear field of application in the future, where sodium will

used as working fluid, for around 1 kW heat transfer rate. The supposed involucre and rods will be made of stainless steel 316 L. This paper shows the first steps in this direction.

In the present work, the working fluid is water. The evaporator contains a liquid chamber with screen meshes welded at the superior and inferior inner faces. This feature assists the even fluid distribution among the channels. The geometry details of the tested devices are shown in Table 1.

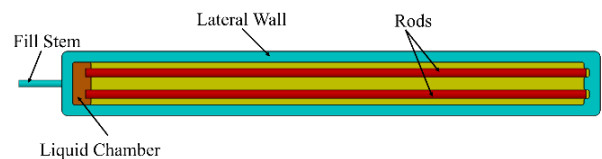


Figure 1. Schematic inside view of the studied heat pipe.



Figure 2. Cross-section of the studied heat pipe.

Table 1. Heat pipe geometry.

Heat Pipe Length [mm]	500
Heat Pipe Width [mm]	59.7
Liquid Chamber Length [mm]	10
Lateral Wall Width [mm]	10
Rod Diameter [mm]	7.93
Rod Pitch [mm]	19.83
Plate Thickness [mm]	2

2. Mathematical Model

2.1. Governing Equations

The liquid inside the heat pipe is contained within the sharp corners formed between the rod and the plate. Evaporation in the heating section and condensation in the cooling section makes the working fluid recede into the corner of the evaporator and flood the condenser, which yields a liquid meniscus variation along the heat pipe, as shown in Figure 3.

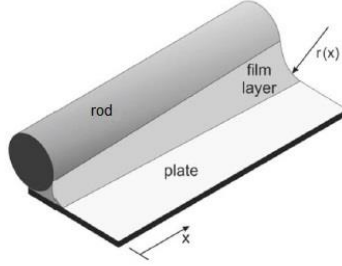


Figure 3. Axial liquid meniscus variation [1].

Capillary pressure drawn from the variation of the meniscus radius pushes the liquid toward the evaporator, allowing the continuous operation of the device. However, this mechanism is restricted by the capillary limit, above which the capillary pumping is insufficient to compensate for the evaporation in the heating section, leading the evaporator to dry out and overheat.

A one-dimensional model inspired by the works of Wang & Peterson [2] and Paiva *et al.* [3] is used to predict the capillary limit. The model considers isothermal and steady-state conditions. Furthermore, the liquid and vapor flows are considered incompressible and laminar. The conservation equations are applied to the working fluid, considering the variation of the meniscus geometry (and so of the vapor and liquid masses) along the heat pipe.

The meniscus radius varies along the heat pipe according to the Young-Laplace equation:

$$\frac{dP_v}{dx} - \frac{dP_l}{dx} = -\frac{\sigma_l}{r^2} \frac{dr}{dx} \quad (1)$$

where P is pressure, r is meniscus radius and σ_l is liquid surface tension (sub index l for liquid and v for vapor). The thermal resistance associated with the phase change is very small when compared with the conduction resistance of the liquid phase and of the container material along the length of the heat pipe. Thus, mass conservation considers that heat input or output through the upper and lower walls of the channel is mostly used to evaporate or condensate fluid. The mass and energy balance of the vapor phase is expressed by:

$$\frac{d\dot{m}_v}{dx} = \frac{2q_e''w}{h_{lv}} \quad \text{Evaporator} \quad (2)$$

$$\frac{d\dot{m}_v}{dx} = 0 \quad \text{Adiabatic Section} \quad (3)$$

$$\frac{d\dot{m}_v}{dx} = -\frac{2q_c''w}{h_{lv}} \quad \text{Condenser} \quad (4)$$

Analogously, for the liquid phase:

$$\frac{d\dot{m}_l}{dx} = -\frac{2q_e''w}{h_{lv}} \quad \text{Evaporator} \quad (5)$$

$$\frac{d\dot{m}_l}{dx} = 0 \quad \text{Adiabatic Section} \quad (6)$$

$$\frac{d\dot{m}_l}{dx} = -\frac{2q_c''w}{h_{lv}} \quad \text{Condenser} \quad (7)$$

where $\dot{m} = \rho uA$ is mass flow rate, ρ is density, u is velocity, A is cross section area, q'' is heat flux, w is the rod pitch (center-to-center distance) and h_{lv} is the latent heat of vaporization. To maintain the energy balance in the heat pipe, the evaporator and condenser heat transfer rates must be equal, with opposite signs, thus:

$$q_e''wl_e = -q_c''wl_c \quad (8)$$

The variation of linear momentum in a differential fluid control volume is influenced by surface forces (normal and tangential components) and body forces, that is, gravity. Hence, the liquid and vapor momentum conservation equations are:

$$\frac{d(\dot{m}_l u_l)}{dx} = -A_l \frac{dP_l}{dx} + p_l \tau_l - g\rho_l \sin \theta \quad (9)$$

$$\frac{d(\dot{m}_v u_v)}{dx} = -A_v \frac{dP_v}{dx} - p_v \tau_v - g\rho_v \sin \theta \quad (10)$$

where p is cross section perimeter, τ is shear stress, g is gravity and θ is angle of inclination.

2.2. Geometrical Correlations

As shown in Figure 4, the liquid distribution profile formed between the rod and the plate depends on the diameter of the bar and the properties of the working fluid. For capillary flow at very low Reynolds numbers, the liquid-vapor interface will have a nearly constant radius of curvature at a fixed longitudinal position. Thus, the liquid-vapor interface profile can be assumed to be a section of a circle. Considering the four liquid menisci within a channel, the following equations can be deduced from the geometry of the flow passage [2]:

$$\beta_1 = \text{atan} \left(\frac{\beta}{2} \left\{ -r \sin \alpha + \left[(r \sin \alpha)^2 + 4Rr \cos \alpha \right]^{\frac{1}{2}} \right\} \right) \quad (11)$$

$$\beta_2 = \frac{\pi}{2} - \alpha - \beta_1 \quad (12)$$

$$p_{wl} = 2R(\beta_1 + \tan \beta_1) \quad (13)$$

$$p_l = p_{wl} + 2r\beta_2 \quad (14)$$

$$p_v = 2(w + \pi R) + 8(r\beta_2 - R \tan \beta_1 - R\beta_1) \quad (15)$$

$$A_l = 2Rr \sin \beta_1 \sin \beta_2 - R^2(\beta_1 \quad (16)$$

$$- \sin \beta_1 \cos \beta_1) - r^2(\beta_2 - \sin \beta_2 \cos \beta_2) \\ A_v = R(2w - \pi R) - 4A_l \quad (17)$$

The hydraulic diameters of the liquid and the vapor phases are:

$$D_l = 4A_l/p_{wl} \quad (18)$$

$$D_v = 4A_v/p_{wv} \quad (19)$$

where p_w stands for wetted perimeter. From the vapor perspective, the liquid can be considered stopped and treated as a wall [4], so $p_v = p_{wv}$.

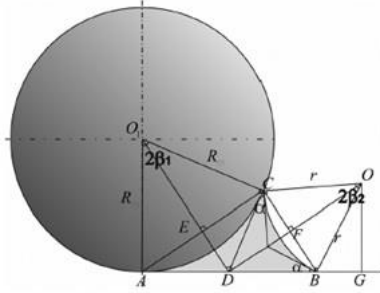


Figure 4. Liquid meniscus geometry [3].

2.3. Shear stresses

The liquid and vapor shear stresses are obtained from the friction factors as

$$\tau_l = f_l \frac{1}{2} \rho_l u_l^2 \quad (20)$$

$$\tau_v = f_v \frac{1}{2} \rho_v u_v^2 \quad (21)$$

Liquid shear stress arises from its interactions with the vapor and the wall. The counterflow between the liquid and the vapor is addressed with a dimensionless flow number to correct the friction factor [5]:

$$f_l Re_l = (f_l Re_l)_0 \left(1 + 0.0002 Re_v \left(\frac{1}{2} + \xi \right) \right) \quad (22)$$

where $(f_l Re_l)_0$ is the friction factor of the liquid phase with no vapor flow effect, which is estimated with a correlation from the data provided by Shah and Bhatti [6]:

$$(f_l Re_l)_0 = 12.0(1 + 0.5162\xi - 0.8018\xi^2 \\ + 0.4177\xi^3) \quad (23)$$

where the shape factor ξ is defined as

$$\xi = W/2H \quad (24)$$

with W and H the width and the height of the triangle ABC in Figure 4, respectively. Furthermore, a technique proposed by Bejan [7]

is used to consider the irregularity of the triangle formed by the sharp corner:

$$(f_l Re_l)_r = \frac{8[1 + \sin(\beta_1/2)]^2 A_l}{\sin \beta_1 p_{wl}} \quad (25)$$

where r is a sub-index for rod. The vapor friction factor is calculated using the approach devised by Bejan [7], where the friction factor depends on the shape of the cross-section. As shown in Figure 5, the vapor cross section changes its shape along the heat pipe due to evaporation and condensation.

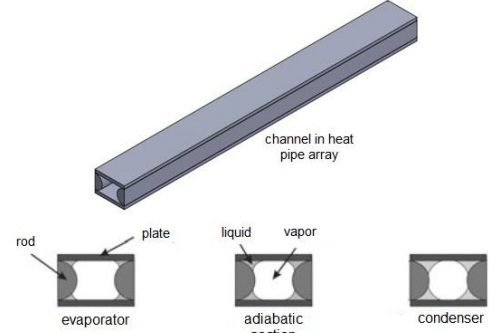


Figure 5. Variation of liquid and vapor cross sections along heat pipe [1].

In this model, the vapor cross-section is considered a rectangle in the evaporator, a square in the adiabatic section, and a circle in the condenser. The friction factors for each section are [6,8]:

$$f_v Re_v = 16 \quad \text{Condenser} \quad (26)$$

$$f_v Re_v = 14.2 \quad \text{Adiabatic Section} \quad (27)$$

$$f_v Re_v = 24(1 - 1.3553\alpha^* \quad (28)$$

$$+ 1.9467\alpha^{*2} - 17012\alpha^{*3} \\ + 0.9564\alpha^{*4} - 0.2537\alpha^{*5} \quad \text{Evaporator}$$

where $\alpha^* = 2R/W < 1$ is the channel aspect ratio.

2.4. Numerical Treatment

A numerical approach, namely the fourth-order Runge Kutta method, was used to solve the set of nonlinear ordinary equations in r , u_l , u_v , P_l and P_v . The algorithm was programmed employing a MATLAB® routine. The solution starts at the end of the condenser and proceeds toward the beginning of the evaporator. The boundary conditions at the end of the condenser are:

$$u_v = 0 \quad (29)$$

$$u_l = 0 \quad (30)$$

$$r = r_{max} = \frac{R}{\cos \alpha - \sin \alpha} \quad (31)$$

$$P_v = P_{sat}(T_{op}) \quad (32)$$

$$P_l = P_v - \sigma_l/r \quad (33)$$

2.5. Contact Angle

The contact angle is particular to each case of study and must be measured before the application of the mathematical model. For that, a piece of a heat pipe containing the bar-plate junction was machined with a water-cut tool. A few drops of water were introduced into the sharp corner. The contact angle of the formed meniscus was then measured, with a 20 deg value obtained, as shown in Figure 6.

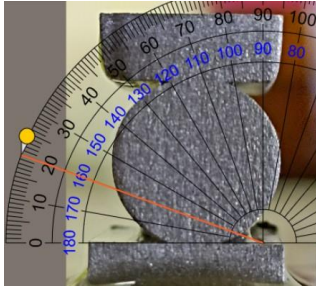


Figure 6. Contact angle measurement.

3. Experimental Setup

3.1. Heat Pipe Manufacturing

The rod-plate heat pipe is formed by an arrangement of intermediate plates and bars sandwiched between cap plates. The set is diffusion-bonded under high pressure and high temperature in a special furnace. Figure 7 shows the heat pipe, which has a liquid chamber with screen meshes next to the umbilical, to help distributing the entering working fluid among the channels.

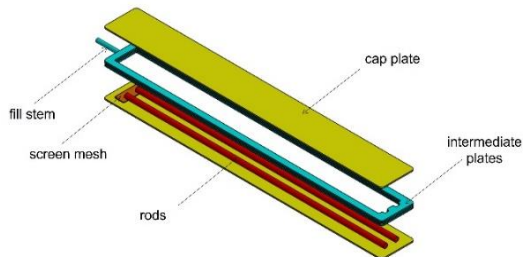


Figure 7. Rod-plate heat pipe assembly layout.

The rods and plates are 7.93 mm diameter and 2 mm thick, respectively, and both are made of stainless steel 316 L. Initially, the plates are machined through a water-cut process. The bars are then cut with a saw and their edges are polished by a power emery. Since the quality of the diffusion welding relies strongly on the roughness of the bonded surfaces [9], the parts are polished with #500 and #600 sandpapers. After that, 3 layers of stainless steel 304 screen mesh are spot welded on the surface of each cap plate. The parts are then cleaned in an ultrasonic bath. They

are also cleaned manually with isopropyl alcohol. Finally, the outer surfaces of the cap plates are covered in boron nitride to avoid its bonding with the plates of the press oven.

The heat pipes are diffusion bonded in a PVA TePla MOV 635 HP high vacuum press furnace. The temperature, pressure and time of welding are respectively 1005 °C, 20 MPa and 1 hour [10]. Figure 8 shows two heat pipes just before the diffusion bonding process. After the diffusion bonding, the devices proceed to the installation of the umbilical and to the leak test.

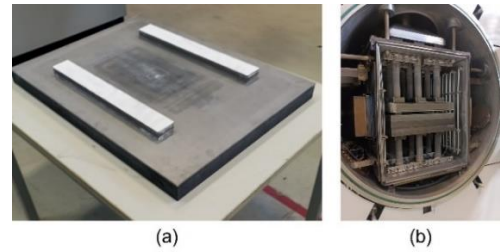


Figure 8. Diffusion bonding. (a) Heat pipes before bonding. (b) Heat pipes in the press oven.

3.2. Experimental System

The device under study is a 0.5 m long Rod-Plate Heat Pipe with lengths of 0.16 m, 0.18 m and 0.16 m for the evaporator, adiabatic and condenser sections, respectively. K-type Omega® thermocouples measure the temperatures along the heat pipe and at the inner and outer insulation surfaces. Figure 9 shows the distribution of the thermocouples along the heat pipe.

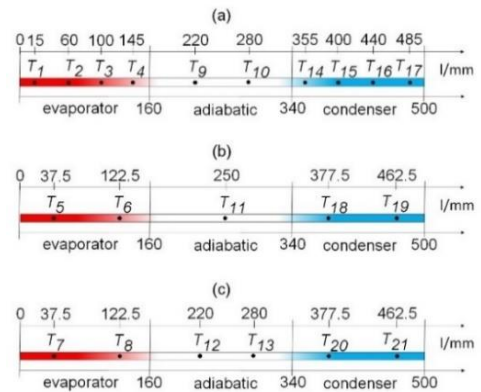


Figure 9. Temperature measurement points. (a) Top face. (b) Lateral face. (c) Bottom face.

The top, lateral and bottom faces of the heat pipe are instrumented to verify cross-section temperature distributions. The thermocouples are connected to a CAMPBELL® data acquisition system (frequency 0.2 Hz).

Heat is transferred from electrical resistances (220 V, 50 W) to the evaporator by conduction through aluminum blocks. For the fabrication of

the heaters, two 50 W electrical resistances are embedded within two aluminum blocks. Grooves are machined on one surface of each block to accommodate thermocouples.

The blocks are attached to the testing device with thermal paste applied at the contact surfaces between the heat pipe and the heaters. The resistances are connected to a TDK Lambda® GEN3300W power source. Figure 10 shows the heating blocks separately and coupled to the heat pipe.



Figure 10. Heating System. (a) Heating block. (b) Heaters attached to the instrumented heat pipe.

The heat power into the evaporator is expressed by:

$$\dot{Q}_e = VI \quad (34)$$

while the transported heat transfer rate is obtained by:

$$\dot{Q} = \dot{Q}_e - \frac{2\pi k_{ins} L_a (T_{22} - T_{23})}{\ln \frac{D_{out}}{D_{in}}} \quad (35)$$

where the second parcel on the right-hand side stands for the heat lost by conduction through the thermal insulation at the adiabatic section. In this equation, V , I , k_{ins} , T_{22} , T_{23} , D_{out} , D_{in} and L_a are respectively voltage, current, thermal conductivity of the insulation (0.04 W/mK), temperatures at the inner and outer walls of the insulation, inner (0.02 m) and outer (0.15 m) diameters of the insulation, and length of the adiabatic section. The experimental test bench can be seen in Figure 11. The heat pipe is kept at a horizontal position by a supporting device. The whole device is thermally insulated, except for the condenser, which remains exposed to ambient temperature to reject heat by natural convection.

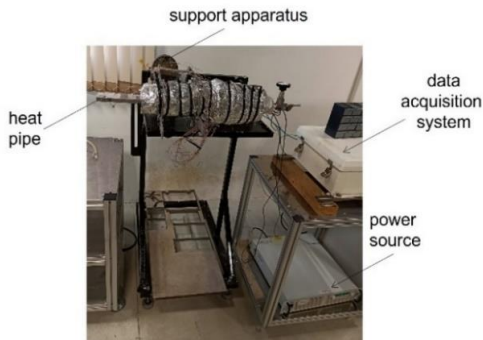


Figure 11. Experimental test bench.

3.3. Experimental Procedure

The experiments are performed according to the following methodology: steady-state conditions are reached (defined by checking whether the temperature variation is less than 1°C within a 10 min period) after applying the power to the evaporator section. Temperature data is collected for 15 min at a frequency of 0.2 Hz. Then, the input power is raised and the process repeats.

Initially, an experiment is carried out using a heat pipe with no working fluid and 25.6 W heating power, to study its thermal behavior for heat being transferred only by conduction. Afterwards, the heat pipe is charged with 23 ml of deionized water. The experiment is then conducted using 25.6 W, 88.5 W and 191.4 W heating powers.

The equivalent thermal resistance R_t is used in the present study as a metric for the heat transfer performance of the device. The total thermal resistance is the sum of the thermal resistances of the evaporator:

$$R_e = \frac{T_e - T_a}{\dot{Q}_e} \quad (36)$$

and that of the condenser:

$$R_c = \frac{T_a - T_c}{\dot{Q}} \quad (37)$$

where T_e , T_a and T_c are the average temperatures of the evaporator, adiabatic and condenser sections, respectively.

3.4. Uncertainty Analysis

In this paper, the measurement errors are assessed through an uncertainty analysis. The temperature uncertainty derives from the accuracy of the thermocouples. According to the manufacturer, the K-type thermocouple produces an uncertainty of ± 1.1 °C until 275 °C and 1% of the measured value until 1425 °C. Following the standard procedure for the B-type evaluation of uncertainty and considering a rectangular distribution of errors, the temperature standard uncertainty $U_{B,T}$ until 275 °C can be obtained by:

$$U_{B,T} = \frac{\Delta}{C} = \frac{1.1}{\sqrt{3}} = 0.63 \text{ °C} \quad (38)$$

where Δ is the quoted uncertainty and C is the confidence coefficient. During the experiments, the temperature range is from 23 to 380 °C, and the temperature uncertainty lies within ± 2.74 %.

The uncertainty of the input heat power $\Delta \dot{Q}_e$ is calculated from the uncertainties produced by the voltmeter and the ammeter, which are both ± 1 %, and is expressed as

$$\frac{\Delta \dot{Q}_e}{\dot{Q}_e} = \sqrt{\left(\frac{\Delta V}{V}\right)^2 + \left(\frac{\Delta I}{I}\right)^2} \quad (39)$$

$$= \sqrt{(1\%)^2 + (1\%)^2} = 1.41\%$$

The uncertainty of the transported heat power $\Delta \dot{Q}$ is influenced by the uncertainties in temperature, voltage and current, and is expressed by:

$$\Delta \dot{Q} = \sqrt{I^2 \Delta V^2 + V^2 \Delta I^2 + 2 \left(\frac{2\pi k_{ins} L_a}{\ln \frac{D_{out}}{D_{in}}} \right)^2 (\Delta T)^2} \quad (40)$$

The voltage and current values used in each input power step are 80 V/0.32 A, 150V/0.59 A and 220V/0.87 A. The maximum value of $\pm 3.15\%$ is obtained at the minimum power step.

The uncertainty of the equivalent thermal resistance ΔR , which is within $\pm 3.15\%$, is obtained from the expression:

$$\frac{\Delta R}{R} = \sqrt{\left(\frac{\Delta \dot{Q}}{\dot{Q}}\right)^2 + \left(\frac{\Delta(\Delta T)}{\Delta T}\right)^2} \quad (41)$$

4. Results and Discussions

4.1. Theoretical Results

The computational routine was benchmarked using theoretical field distributions found in the literature [2]. Computational results were found acceptable for the case of an aluminum-acetone tube with a 1.016 mm wire diameter, 2.1 mm wire pitch, 10° contact angle, 2500 W/m^2 of input heat flux and 20°C operating temperature. A mesh independence check was performed using the input conditions of the experiment and 25.6 W of heat input. The study pointed out that 461 nodes are enough for yielding reliable results. Further refinement only increases computational cost without considerable accuracy gain.

In the present study, the mean temperature of the adiabatic section is considered the operating temperature of the heat pipe. Figure 12 shows the obtained profiles for the liquid meniscus radius, for actual geometry and the operating temperatures obtained experimentally. The radius of meniscus decreases continuously from the condenser to the evaporator. Moreover, the distributions decrease with increasing heat transfer rate.

Because the excessive working fluid in the condenser produces a liquid pool that hinders the capillary effect, the optimum amount of working fluid is an important parameter, which is calculated by integrating the distribution of mass

along the heat pipe. Both distributions of the mass and of the cross-sectional area of the liquid meniscus are proportional to the radius of curvature. Therefore, they also decrease with increasing heat input. For 191.4 W heating power, the optimum charging volume is approximately 23 ml .

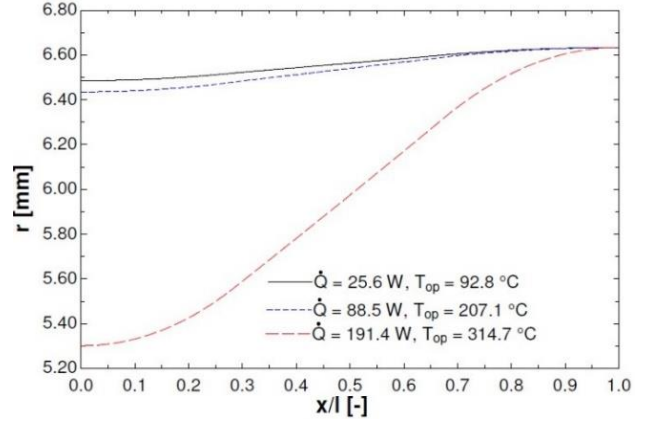


Figure 12. Meniscus radius profiles along channel.

The capillary limitation is achieved when the amount of working fluid in the evaporator section is too low to maintain a steady operation. Physically, it can be interpreted by a condition where the capillary pumping cannot overcome the viscous forces that oppose the liquid return to the evaporator. In the present study, the capillary limit is considered reached when the radius of the meniscus at the beginning of the evaporator is below $100 \mu\text{m}$, which is an estimation for the bar-plate bonding radius [3]. The meniscus can't have a smaller radius than the edge of the groove in which the liquid is contained.

The applied heat inputs and the maximum heat transfer capacities dictated by the capillary limit and the for each operation temperature obtained experimentally are shown in Table 2.

Table 2. Applied heat inputs and maximum heat transfer capacities

$T_{op} [^\circ\text{C}]$	$\dot{Q} [\text{W}]$	$\dot{Q}_{max} [\text{W}]$
92.7	25.6	1593.3
207.1	88.5	2266.4
314.7	191.4	746.4

Both the surface tension and liquid viscosity decrease with increasing temperature. These trends have opposite effects on the capillary limit. The dominant factor depends on the operating temperature. Usually, the capillary limit augments with temperature to a peak value and then decreases. The capillary limit was not reached in any experimental scenario.

4.2. Experimental Results

Figure 13 shows the transient temperatures at the top face of the charged heat pipe. Because of the low convection heat transfer coefficient associated with natural convection, the steady-state operating temperatures are very high: 92.8 °C and 207.1 °C for input heat transfer rates of 25.6 W and 88.5 W, respectively. At both conditions, there is no evidence of dry-out at the evaporator, thus the heat transfer is below the capillary limit, as predicted by the mathematical model. Also due to the low heat rejection rate, the device takes a long time to reach a steady state: approximately 7 hours.

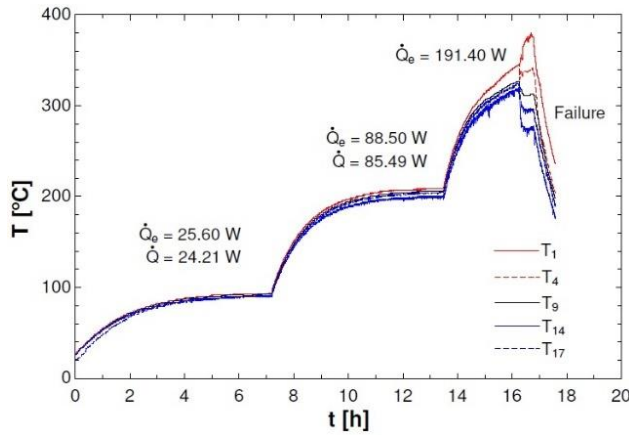


Figure 13. Temperatures on the heat pipe's top face during experiment with charged heat pipe.

Since the saturation pressure of water at 207.12 °C is very high, 17.99 bar, the experiment was able to the maximum internal pressure that the container can withstand. By 16 hours of experiment, at the input heat transfer of 191.4 W, the operating temperature reached 314.72 °C, which means a saturation pressure of 105.12 bar. In this work, the container succumbed to the high internal pressure and swelled. Another evidence of the collapse was that the temperature of the evaporator increased more than that of the condenser. Furthermore, the evaporator temperature (380.0 °C) exceeded the water critical point (374.0 °C), so the fluid in the channel turned into a gas, and the heat pipe failed, which can be seen by the sudden rise in the temperature gradient. Heat pipe operation is feasible in the temperature range between the triple and the critical point of the working fluid, with reduced heat transport capacity near the two extremes [1].

The failed heat pipe was approved in the leak test, validating the fabrication methodology for a future application on sodium heat pipes, where the temperature ranges from 800 °C to 1100 °C and

the saturation pressure lies between 0.47 bar and 5.49 bar.

The steady-state temperature distribution of each heat pipe face is displayed in Figure 14. In both heat transfer rates, the profiles of the top and bottom faces are approximately the same, which indicates that gravity does not exert a considerable influence on the heat pipe operation. Also, in the condenser, the temperature is slightly lower at the beginning, which might be a consequence of vapor pressure recovery due to the loss of linear momentum.

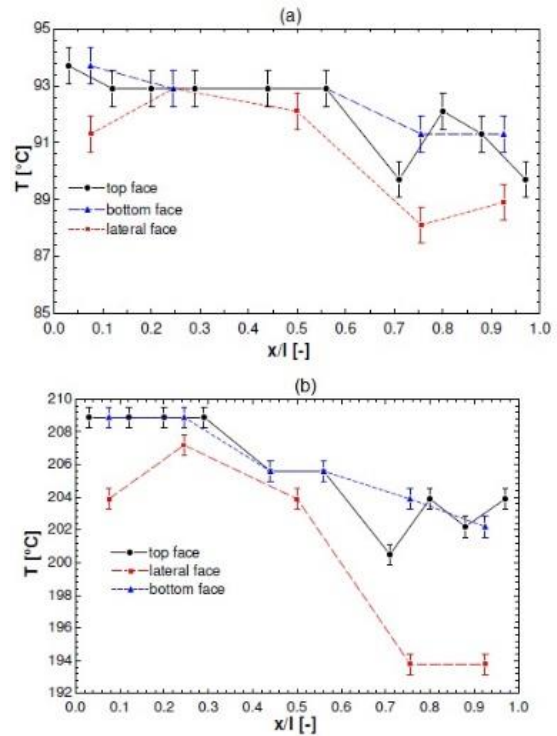


Figure 14. Steady-state temperature distribution. (a) Heating power of 25.6 W. (b) Heating power of 88.5 W.

The temperature gradient of the lateral wall is considerably higher than that of the other faces, especially for 88.5 W heat input. It should be noted that the lateral channels have fewer sharp corners than the central one and, therefore, lower capillary pumping capacity. Due to this unbalance, the central channel is preferred for liquid distribution, augmenting temperature uniformity. Another contributor to the higher lateral gradient is the thicker lateral wall, which increases conduction heat transfer resistance.

Table 2 shows the steady-state thermal resistances for all experiments. For the non-working fluid experiment, the thermal resistances of the evaporator and condenser are similar, which is reasonable since the heat transfer occurs solely by conduction. The total resistance is considerably

lower for the charged heat pipe, which means that the device is a better heat conductor than the pure container material. This proves that rod-plate technology is a valid concept for heat pipe manufacturing. Also, the filled heat pipe showed that the evaporator thermal resistance is significantly lower than that of the condenser at the lower heat input. In the scenario with higher heat input, the condenser resistance decreases because more vapor reaches the condenser. However, the evaporator increases. The total resistance decreases with increasing heat input.

Table 3. Steady-state thermal resistances.

	Dry 25.6 W	Charged 25.6 W	Charged 88.5 W
R_e [°C/W]	2.1827 ± 0.0687	0.0060 ± 0.0002	0.0317 ± 0.0010
R_c [°C/W]	2.4280 ± 0.0765	0.1007 ± 0.0032	0.0554 ± 0.0017
R_t [°C/W]	4.6106 ± 0.1452	0.1070 ± 0.0034	0.0870 ± 0.0027

5. Conclusions

This paper proposes a novel heat pipe technology, namely rod-plate heat pipe, using the concept of capillary pumping through grooves formed by the junction between a curved surface and a flat one. The heat pipe is manufactured from the diffusion bonding of stainless steel 316 L plates and rods and is tested horizontally with heat rejection in the condenser by natural convection.

Experiments are performed using a device without working fluid and with deionized water. The operation temperature attains high values due to the low convection heat transfer coefficient, until it reaches the capillary limit. The container gives in to the internal pressure at 105.12 bar, but the failed heat pipe is approved in the leak test, which validates the fabrication methodology. The thermal resistances show that the device operates successfully as a heat pipe.

In conclusion, the theoretical and experimental results obtained so far show that the grooves formed between the rod and plates are able to pump the liquid along the heat pipe. Thus, the technology originally proposed for mini heat pipes can be successfully used for larger and hotter devices.

References

[1] M. B. H. Mantelli, *Thermosyphons and Heat Pipes: Theory and Applications*. Springer, 2021.

[2] Y. X. Wang and G. P. Peterson, "Analysis

of Wire-Bonded Micro Heat Pipe Arrays," *J. Thermophys. Heat Transf.*, vol. 16, no. 3, 2002.

[3] K. Vieira De Paiva, M. Barbosa Henriques Mantelli, and L. Kessler Slongo, "Thermal behavior analysis of wire mini heat pipe," *J. Heat Transfer*, vol. 133, no. 12, pp. 1–9, 2011, doi: 10.1115/1.4004526.

[4] J. P. Longtin, B. Badran, and F. M. Gerner, "A one-dimensional model of a micro heat pipe during steady-state operation," *J. Heat Transfer*, vol. 116, no. 3, pp. 709–715, 1994, doi: 10.1115/1.2910926.

[5] H. B. Ma, G. P. Peterson, and X. J. Lu, "The influence of vapor-liquid interactions on the liquid pressure drop in triangular microgrooves," *Int. J. Heat Mass Transf.*, vol. 37, no. 15, pp. 2211–2219, 1994, doi: 10.1016/0017-9310(94)90364-6.

[6] R. K. Shah and M. S. Bhatti, "Laminar Convective Heat Transfer in Ducts," in *Handbook of Single-Phase Convective Heat Transfer*, New York: Wiley, 1987, pp. 3.45-3.70.

[7] B. Adrian, *Convection Heat Transfer*. New York: Wiley, 2013.

[8] R. K. Shah and A. L. London, *Laminar Flow Forced Convection in Ducts. A Source Book for Compact Heat Exchanger Analytical Data*. Elsevier Inc., Academic Press, 1978.

[9] J. Ziegelheim, S. Hiraki, and H. Ohsawa, "Diffusion bondability of similar/dissimilar light metal sheets," *J. Mater. Process. Technol.*, vol. 186, no. 1–3, pp. 87–93, 2007, doi: 10.1016/j.jmatprotec.2006.12.020.

[10] M. V. V. Morteau, A. J. de A. Buschinelli, K. V. de Paiva, M. B. H. Mantelli, and J. Rimmel, "Soldagem por difusão de aços inoxidáveis para fabricação de trocadores de calor compactos," *Soldag. e Insp.*, vol. 21, no. 1, pp. 103–114, 2016, doi: 10.1590/0104-9224/SI2101.10.

Design of a new flat plate pulsating heat pipe for battery cooling: Validation of the modeling approach by experimental tests

Thibault Van't Veer^{1,2*}, Baptiste Lepinoy², Vincent Ayel², Mouad Diny¹, Yves Bertin², and Etienne Videcoq²

¹ Stellantis – Site de Carrières-sous-Poissy, 78955 Carrières-sous-Poissy, France

² Prisme Institute CNRS – ENSMA – Université de Poitiers, UPR 3346, 86961 Futuroscope-Chasseneuil, France

*Corresponding author email address: thibault.vantveer@stellantis.com

Abstract

A new Flat Plate Pulsating Heat Pipe (FPPHP) has been designed to integrate the battery cooling system for an automotive application. Due to embedding and battery pack architecture, the FPPHP is oriented in unfavorable vertical orientation, with the condenser at the bottom side of the device. The hydraulic diameter is below 1 mm. An analytical model of a single U-turn, *i.e.* one vapor bubble trapped between two liquid slugs, has been developed and used to select most performing fluids. It has been observed by the model that both latent and vapor sensible heat play a huge part on the vapor expansion and then on the liquid motion. Results show that R1234yf seems to be the most efficient fluid due to a high value of $(dp/dT)_{sat}$, but its motion remains slow, and takes several tens of seconds to reach the condenser with a vapor temperature rise of 0.6 K. Thus, a compromise between lowest temperature rises and fastest meniscus displacement finally shows the R1233zd as the most efficient fluid for such a configuration. An experimental campaign was carried out to test the FPPHP under different operating configurations and working fluids. Experimental results with the working fluid R1233zd at a filling ratio of 30% show the best thermal performances. The thermal resistance was evaluated and found lower than 0.15 K/W for a heat power supply above 40 W for this unfavorable inclination.

Keywords: Flat plate pulsating heat pipe; Slug flow; Thermal performances; Infrared thermography

1. Introduction

Due to their complexity and unsteady operations, designing a new kinds of flat plate pulsating heat pipes (FPPHP) for battery cooling application requires specific attention. Characteristics of this new device are: large evaporator area regarding the condenser section (90% of the overall surface of the FPPHP is covered by the heat source), no adiabatic zone, and unfavorable vertical top heat mode.

Special attention must be given to the working fluid selection: working fluids must respect industrial constraints and give the best thermal performances. For channel hydraulic diameters below 1 mm, previous studies showed that refrigerants like R1234yf or R1233zd give promising results [1-2].

On one hand, Kim *et al.* [1] experimentally studied the fluid flow behavior in a micro flat plate pulsating heat pipe, closed by crystalline glass to enable visualizations (channel cross section of $1 \times 0.5 \text{ mm}^2$). They observed that the flow behavior depends on the condenser temperature and on the working fluid. They associated their findings with a mathematical approach to compare the heat transfer capabilities and the fluid flow behavior, arguing that the vapor phase remains in saturated state, which is not the case in every conditions. Finally, they managed to obtain a figure of merit

that ranks the working fluids according to their thermophysical properties. On the other hand, Nikolayev *et al.* [3] approached the vapor phase thermodynamic state by a theoretical description. They assumed that the vapor is superheated and follows the equation of state ($P = mR_v T_v / V_v$). From this assumption, they obtained one figure of merit related to the startup of the PHP. Then they compared their merit number with numerical simulations that have shown that water or ethanol give better thermal performances than FC-72.

In this paper, an academic modeling approach, reduced to a single vapor plug surrounded by two liquid slugs, is detailed and applied to make a comparison between the working fluids. It simulates the vapor expansion over a given temperature rise, and the resulting motions of surrounding liquid slugs. Then, based on the results obtained, the most promising selected fluids were tested in a flat plate PHP specifically designed for such application, and a test campaign has been carried out focusing on a parametric study on the condenser temperature, the filling ratio and the orientation of the device.

2. Fluid selection by modeling approach

While Kim *et al.* [1] assumed that the working fluid follows the saturation state, Nikolayev *et al.* [3] relate that the vapor can be superheated. From

these both approaches, an analytical model has been developed and is presented in the following.

2.1. Description of the model

Starting from the assumptions that the liquid motion is due to the vapor bubble expansion, one vapor plug has been isolated, and is surrounded by two similar liquid slugs. Their boundary conditions have been fixed at constant pressure at both ends (equilibrium state, $P_{v,0}$, Figure 1). Figure 1 shows the studied system, where the condenser is 10 mm length at the bottom. In the initial state, the vapor plug is in the evaporator section (i.e. above the condenser section). In the initial condition, fluid is supposed at equilibrium state. By imposing a temperature rise of the wall, the vapor plug will be heated, will expand, and then push the liquid/vapor meniscus towards the condenser. During this evolution, a thin liquid film will be deposited on the wall, and will enhance the thermal transfer through high rate of evaporation. Simulation stops when the liquid/vapor interface reaches the condenser. The aim of the model is to perform a relative comparison between fluids based on the lowest wall temperature instability able to trigger the motion of the meniscus towards the condenser.

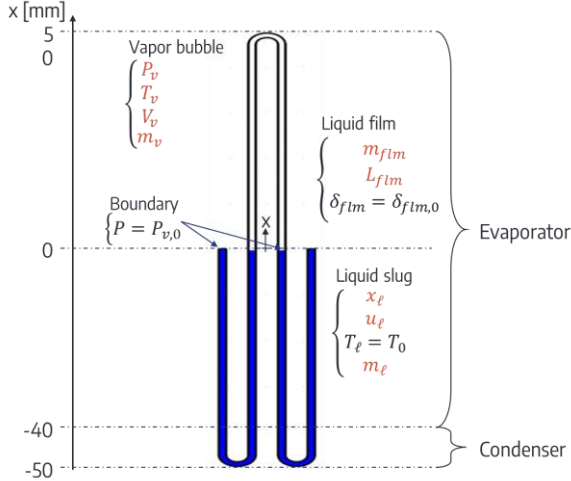


Figure 1. Schematic diagram of the analytical modeling: vapor bubble surrounded by two liquid slugs

2.2. Equations

To develop a modeling method for the liquid slug motion, some mathematical approaches have been studied. Yoon *et al.* [4] linked their experimental data from high-speed camera with a vapor spring-liquid mass model. On the other hand, Ando *et al.* [5] studied the initial liquid-

vapor distribution during the startup of the pulsating heat pipe by modeling.

Nikolayev, in his review paper [6], proposed a state of the art and explained the physical modeling of the pulsating heat pipe: starting from the momentum equation for the liquid plug (1), inertia of the liquid plug depends on the pressure difference force, F_P , between vapor bubbles at both ends of the liquid slug (caused by vapor expansion), the gravity force, F_G , and the frictional forces, F_{fr} , that are assumed to be like pressure drop in a Poiseuille flow. Capillary forces are neglected.

$$\frac{d(m_l u_l)}{dt} = F_P + F_G + F_{fr} \quad (1)$$

Evolution of the vapor phase is given by the energy equation (2), where both sensible and latent heat counterbalance the work of the pressure forces, leading to the temperature rise:

$$m_v c_{v,v} \dot{T}_v = \dot{Q}_{sens} + \dot{Q}_{lat} - P_v \dot{V}_v \quad (2)$$

The sensible heat (3) is evaluated between the wall and the vapor with a constant heat transfer coefficient computed with the assumption of the Nusselt number equal to 4 (laminar flow).

$$\dot{Q}_{sens} = H_v S_{v,w} (T_w - T_v) \quad (3)$$

Concerning latent heat (4), Nikolayev [7] certified that the quantity of heat transferred by mass exchange \dot{m}_v between liquid and vapor phases is described by:

$$\dot{Q}_{lat} = r T_v \dot{m}_v \quad (4)$$

In this case, it has been assumed that the major part of evaporation occurs by the deposited thin liquid film rather than at the triple line or in the meniscus. Consequently, the evaporated mass flow rate (5) depends on the thickness of the liquid film, its thermal properties, the geometry of the channel and the temperature difference between the wall and the saturated temperature of the vapor. The thickness of the liquid film, which is kept constant during the calculation, is analytically computed by the capillary number following the Taylor's law ($\delta_0 \sim C_a^{2/3}$).

$$\dot{m}_v = \frac{k_l}{\delta_{film} h_{lv}} \mathcal{P}_{cr} L_{film} (T_w - T_{sat}) \quad (5)$$

Equations (1) to (5) are solved together with the explicit solver Runge Kutta (of order 4).

2.3. Working fluid ranking

To develop a modeling method for the liquid slug motion, some mathematical approaches have been studied. Yoon *et al.* [4] linked their experimental data from high-speed camera with a vapor spring-liquid mass model. On the other hand, Ando *et al.* [5] studied the initial liquid-vapor distribution during the startup of the pulsating heat pipe by modeling.

Main thermophysical properties of the working fluids which have been pre-selected for this study are listed in Table 1. For each, the Bond number (eq. 6) is lower than 2, defined as the limit above which the gravity forces become higher than the surface tension forces in static conditions:

$$Bo^2 = \frac{D_h^2 g(\rho_l - \rho_v)}{\sigma} \quad (6)$$

Table 1. Properties of working fluid at 20°C

Properties	R1336mzz	HFE700	R1233zd	R1234yf
$dp/dt _{sat}$ [kPa/K]	2.46	2.4	4.03	17.21
Latent heat [kJ/kg]	170.74	139.5	193.7	149.3
Surface tension [mN/m]	16.12	12.85	15.22	6.8
Liquid density [kg/m ³]	1378	1418	1275	1110
Vapor density [kg/m ³]	4.21	5.02	6.07	32.8
Thermal conductivity of the liquid [mW/m/K]	73.18	66.24	84.25	65.08

Following criteria defined to establish the fluid ranking are linked by the thermophysical properties of the working fluids. The properties of the liquid phase (density, viscosity) are nearly close the one to the other. Thus, the motion of the liquid slug will be mainly driven by the vapor bubble expansion. One of the most important properties related to the driving pressure force is the slope of the saturation curve, given by Clapeyron's law, $(dp/dT)_{sat}$. It directly controls the temperature rise needed to provide the pressure forces which will counterbalance the gravity forces in saturated conditions.

To select the most suitable working fluids, two criteria have been defined, corresponding to the operating and geometric conditions of figure 1:

1- The minimum wall temperature rise to let the vapor bubble reach the condenser, ΔT_{min} ;

2- The elapsed time Δt necessary for the vapor bubble to reach the condenser, for a fixed wall temperature rise, $\Delta T = 1$ K.

Figure 2 shows the motion of the meniscus for both criteria with R1233zd as working fluid. Looking for the minimum wall temperature rise ΔT_{min} to let the meniscus reach the condenser without overshoot ($\Delta T_{min} = 0.19$ K, orange curve), imposing a higher value induces an

overshoot below the condenser position ($\Delta T = 1$ K, black curve).

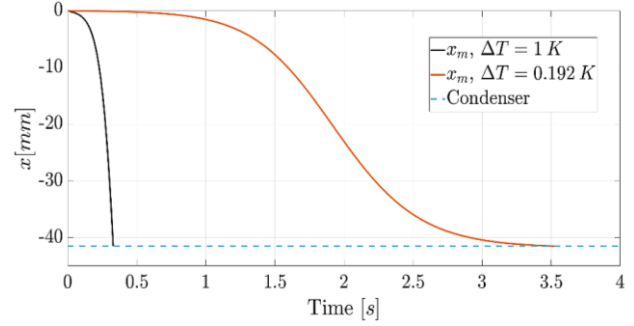


Figure 2. Evolution of the position of the meniscus for two temperature rises: 0.192 K and 1 K (R1233zd, $T_{v,0} = 30^\circ\text{C}$)

- Discussion on the two criteria

Table 2 shows the previous results, displayed on Figure 2, for four different working fluids. Starting from an initial filling ratio of 50%, the temperature of the wall in contact with the vapor plug is set at a temperature higher than the initial equilibrium state ($\Delta T_{wall} = 1$ K). This temperature rise is kept constant during the expansion of the vapor plug. It results the elapsed time (Δt) for the meniscus to reach the condenser area. Although R1234yf presents the highest values of $(dp/dT)_{sat}$, it leads to the slowest motion. Indeed, the fastest motion is given by HFE7000, whose vapor density is the lowest (4.21 g/cm³, see Table 1). Then, the working fluid ranking follows more or less that of the vapor density. It has been assumed that, at constant volume of vapor, for a higher mass, more energy is needed provided by latent and sensible heat (eq. (2)). Therefore, at constant boundary conditions, the elapsed time of the vapor expansion increases.

Table 2. Simulations results: time to reach the condenser for $\Delta T = 1$ K; and minimum temperature rise ΔT_{min} and its corresponding elapsed time Δt for the meniscus to reach the condenser.

Fluid	@ 1 K	To reach condenser	
	Δt [s]	ΔT_{min} [K]	Δt [s]
R1234yf	3.96	0.042	294
R1233zd	0.33	0.192	3.5
R1336mzz	0.38	0.327	1.9
HFE-7000	0.29	0.346	1.9

Comparing working fluids with one another can also be done thanks to the minimum temperature rise (ΔT_{min} , two right hand sides columns of Table 2). The corresponding elapsed time (Δt) necessary for the meniscus to reach the condenser is also indicated. For this second criterion, in terms of temperature difference, the more efficient than

others is the R1234yf, with a temperature rise of 0.042 K, while the values are of 0.192 K for R1233zd, and even more for the others. Although R1234yf requires a lower value of ΔT_{min} , it takes 294 s to reach the condenser, while the other fluids are much faster (less than 3.5 s). The difference comes from the value of $(dP/dT)_{sat}$. The classification follows the increase of this parameter. In fact, due to similar values of liquid density for every fluid, the masses of plugs are very close the one to the other. In steady state, at the end of the motion, only gravity forces counterbalance the pressure forces between menisci. That's why only value of $(dP/dT)_{sat}$ influences the minimum temperature rise ΔT_{min} required for vapor to push the meniscus towards the condenser.

Anyway, the wall temperature gap should not be limited to its minimum value to let vapor reach the condenser: higher values are required to increase pressure forces to drive the liquid out of the condenser.

Concerning the disparity of the results regarding the elapsed time to reach the condenser Δt , the explanations come from the energy equation (2).

2.4. Thermal analysis of the fluid ranking

The thermodynamic state evolution of the vapor phase is presented on the P - T diagram in Figure 3. Two successive steps are observed: An isobaric transformation from the initial state into the temperature of the wall (A-B); and a quasi-isothermal transformation until the vapor reaches the final equilibrium state along the saturation curve (B-C). Figure 4a shows the motion of the meniscus, and figure 4b the corresponding evolutions of the vapor phase pressure and temperature. During the first isobaric phase (A-B), the temperature increases very quickly and reaches the wall temperature: less than 0.1 s is needed for this step for R1233zd. Then, when the meniscus moves forward, evaporation occurs that slowly increases the vapor pressure. Quicker the pressure increases and faster the meniscus moves, that let a longer liquid film which generates more evaporation and more pressure increases. Result is the acceleration of the meniscus which allows it to reach the condenser area. This trend depends on the thermophysical properties of the working fluid, and particularly results of the consequence of the value of $(dP/dT)_{sat}$.

Figure 5 compares the importance of each part of the energy equation. The two phases previously observed are visible on the graphic. The isobaric phase corresponds to the first pic caused by the sensible heat, whereas both latent heat and work of pressure forces correspond to the isothermal transformation. The oscillations of the curves during the first 0.25 s are the compensation of the rapidly increase of the energy rate due to the work of pressure forces and of the inertia of the liquid slug.

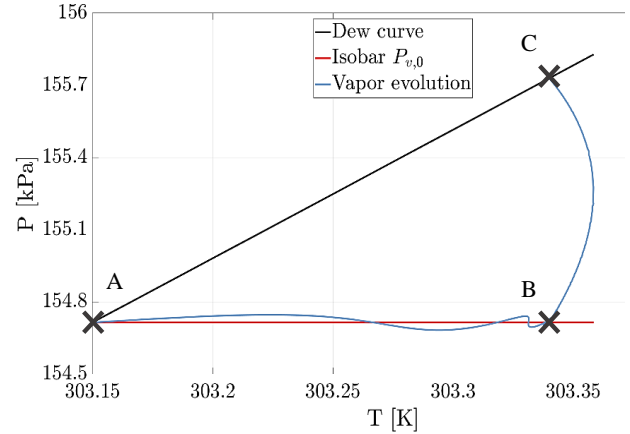


Figure 3. Evolution of the vapor state in a P - T diagram (R1233zd, $\Delta T_{min} = 0.19$ K)

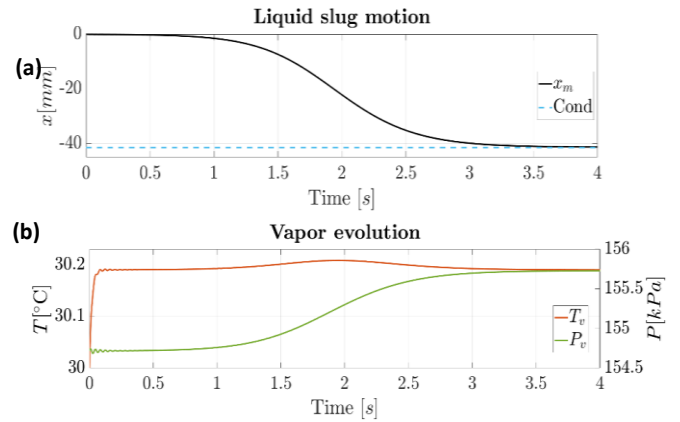


Figure 4. (a) Evolution of the meniscus position; and (b) evolutions of both the temperature and the pressure of the vapor phase (R1233zd, $\Delta T_{min} = 0.19$ K)

During the latent heat exchange, the sensible heat becomes negative. When the pressure increases, the temperature has already reached the temperature of the wall. As vapor compression implies temperature rise, the vapor temperature overshoots the wall temperature, that involves a reverse sensible heat exchange.

Both graphs of Figure 5 present the weight of the different terms of equation (2) for R1233zd (fig. 5a) and R1234yf (fig. 5b). They have been computed with the minimum value ΔT_{min} to reach

the condenser area (*i.e.* 0.19 s for R1233zd and 0.04 s for R1234yf). The order of magnitude of the time scale is significant for these two working fluids. It takes 100 times longer for R1234yf to reach the condenser (400 s), compared to R1233zd (4 s). That may be explain by the value of ΔT_{min} . As $(dP/dT)_{sat}$ is higher for R1234yf, that means that the wall temperature rise may be lower for a similar value of pressure difference (caused by gravity forces between initial and final state). Due to a lower ΔT_{min} for R1234yf, the heat rate from latent heat (defined by eq. (4)) is lower than for R1233zd.

As a result, the value of the latent heat power is lower for R1234yf, around 3.5×10^{-4} W, whereas it is upper than 5×10^{-3} W for R1233zd. Thus, moving an equivalent mass of liquid with such different levels of heat power will necessary highly impact the duration of the motion for these two fluids.

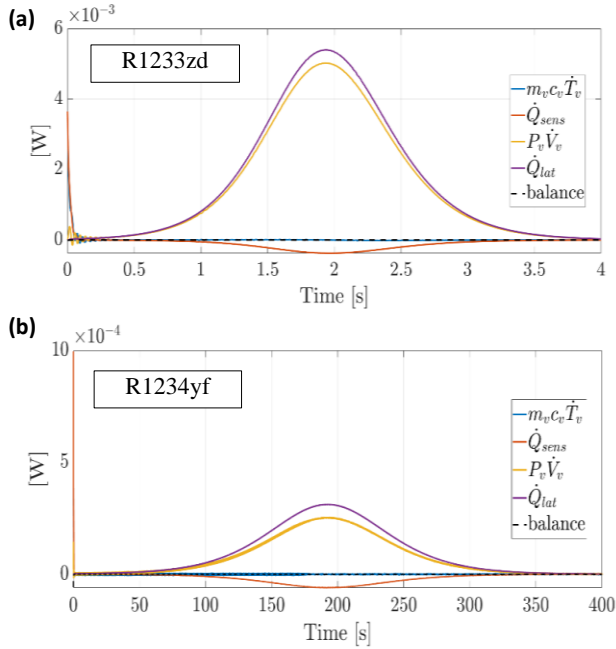


Figure 5. Comparison of the different terms in the energy equation (2) for: (a) R1233zd ($\Delta T = 0.19$ K); and R1234yf ($\Delta T = 0.04$ K)

Finally, in conclusion, both latent and sensible heat are necessary to generate the expansion of the vapor bubble and thus drive the meniscus towards the condenser area. Sensible heat first initiates the motion by quickly increasing the vapor temperature. Then a relative slow evolution of the pressure occurs and slowly pushes the liquid plug. During this displacement, a liquid film is deposited behind the receding meniscus and, regarding the temperature level, highly increases the evaporation rate, and then the driving forces, and soon.

3. Experiments apparatus and procedure

3.1. Experimental set-up

The FPPHP is made of two copper plates (94×110 mm²), one machined with a single rectangular shaped groove forming a closed serpentine (cross section of 0.5×0.8 mm²); both are brazed together to form a closed device (1.5 mm thickness). Heating films were stuck on the evaporator zone (90 cm²) and connected to three independent electrical power supplies. The condenser area (7.5 cm²) is cooled by a brazed cold plate through which flows a coolant fluid circulating in a cooling loop connected to a cryothermostat.

The experimental setup is shown in Figure 6. To evaluate the thermal performances, one side of the FPPHP has been painted black (IR emissivity: 0.95 ± 0.1) for infrared visualizations (IR camera INFRATEC®, ± 1 K spatial resolution and ± 0.03 K temporal resolution). One pressure sensor (GE® ADROIT6222, ± 200 Pa) is connected to the filling tube located in the evaporator area. Two T-type thermocouples (± 0.8 K) measure the inlet and outlet temperatures of the coolant fluid through the condenser.

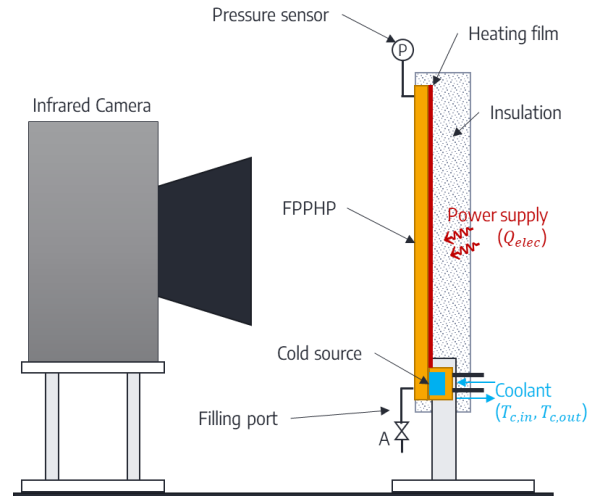


Figure 6. Schematic diagram of the experimental system

3.2. Filling procedure

Two working fluids were tested for the experimental campaign. R1336mzz and FORANE® HTS 1233zd from Arkema have been tested, with filling ratio from 15% to 50%. The device was positioned both in vertical and horizontal orientations. The filling process was established as follow:

- A container was filled with the computed mass of fluid to obtain the targeted value of filling ratio, taking into account the mass of vapor phase and

the volume remaining in the filling system (*i.e.* container, tubes, valves). The container was overcharged to proceed several degassing to remove non-condensable gases (NCG).

- Then, the container was connected to the filling system by a valve. A vacuum pump evacuated most of NCG inside the FPPHP and the filling tubes. After few hours of vacuum process, valves were finally closed.

- The cold source was set at 0°C and the container and its tubes were heated before introducing the fluid in the PHP by opening valve A (Figure 6). The working fluid went towards the device both by gravity and pressure difference.

- Then, valve A was closed, and the pressure signal was controlled to match with the equilibrium saturation state at room temperature.

- Finally, the container was weighed again to ensure that the difference corresponds well to the fluid mass to be introduced in the system.

3.3. Evaluation of the thermal performances

To evaluate its thermal performances, the FPPHP was heated by heat power steps from 15 W to 75 W. After few minutes (3-4 min), the behavior of the PHP remains in a pseudo steady state. From there the thermal performances can be evaluated.

The thermal resistance is usually used to compare relative thermal performances between different cases. It is defined by the ratio of temperature difference between evaporator and condenser zones, over the heat power transmitted towards the condenser (eq. 7). \bar{T}_{ev} and \bar{T}_{cd} are defined as the time and spatial averaged temperatures measured on the black side by the infrared camera during 300 s.

Thermal losses, Q_{lost} , have been experimentally evaluated with empty device: for one cold source spatial average temperature the power supply has been slightly increased to balance temperatures between evaporator and condenser. This gives, for several set points temperatures, an evaluation of the thermal losses.

$$R_{th} = \frac{\bar{T}_{ev} - \bar{T}_{cd}}{Q_{elec} - Q_{lost}} \quad (7)$$

Cooling fluid flowrate has been set at its maximum value to ensure the independence of the results with respect to the cold source. The set point temperature has been slightly adjusted to keep constant the condenser average temperature recorded by the infrared camera.

4. Results and discussions

4.1. Working fluid selection

First, a rough comparison has to be made between working fluids in the FPPHP set in vertical top heat mode orientation (V-THM), regarding the specifications, in order to specifically study the chosen candidates functions of several parameters (filling ratio, section 4.2, and orientation, section 4.3). A comparison between FPPHP filled with two working fluids (R1336mzz and FORANE® HTS 1233zd, filling ratio: 50% at ambient temperature) and empty device is presented in Figure 7 for two cold source temperatures (20°C and 35°C). In this comparative study, in order to simplify the experimental process, only the cooling fluid inlet temperature has been set constant. In the following sections, it is the external surface temperature of the condenser \bar{T}_{cd} which will be kept constant, considerably complicating the control process.

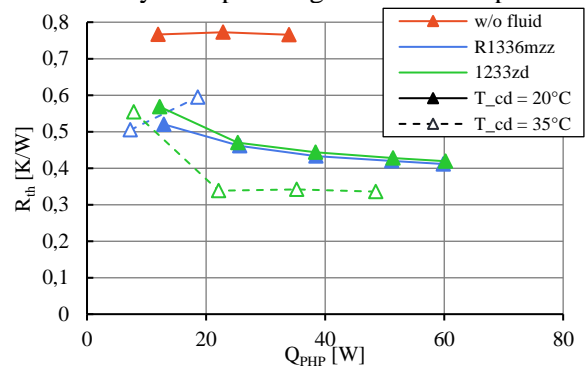


Figure 7. Thermal resistance vs. heat power for the FPPHP filled with two working fluids (V-THM inclination)

At 20°C cold source temperature, Figure 7 shows that the two working fluids have nearly the same behavior (superimposed resistance curves). The thermal resistance, starting from 0.55 K/W at 15 W, then decreases and reaches 0.42 K/W at 60 W for R1233zd. In contrast, at 35°C, R1336mzz shows unstable behaviors. At low heat power supply, oscillations sometime stopped and imply a large rise of the temperatures, thus increasing the thermal resistance. Contrarily, for R1233zd, performances are improved at 35°C compared to 20°C. Beyond 20 W, the thermal resistance quickly decreases and reaches a stable value of around 0.33 K/W, lower than for the test at 20°C cold source temperature.

Thereby, in view of these first results, R1233zd was chosen as the working fluid selected for this FPPHP application, being more stable and more efficient for these specific operating conditions. It

will be the only working fluid that will be tested in the following parametric studies.

4.2. Influence of the Filling Ratio

Figure 8 shows the thermal resistances curves for three filling ratios (15%, 30% and 50%), for the fluid FORANE® HTS 1233zd, tested at two condenser temperatures: 20°C and 35°C. FPPHP is here still oriented in unfavorable vertical top heat mode (V-THM).

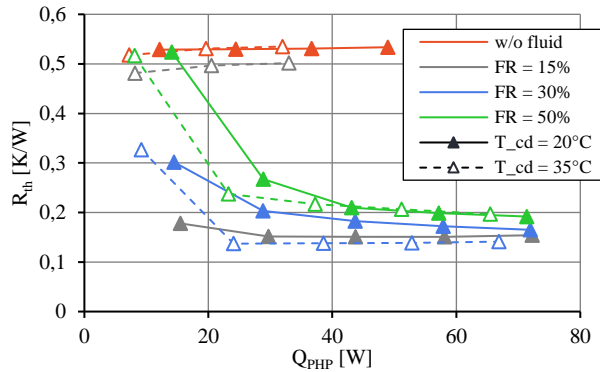


Figure 8. Thermal resistance vs. heat power for the FPPHP tested with three filling ratios (R1233zd, V-THM inclination)

For a filling ratio of 50%, the thermal resistance curves decrease from their maximal value at lowest heat power applied (0.52 K/W, *i.e.* no fluid oscillations, equivalent to the empty PHP) until a steady value at high heat powers supplied (around 0.18 K/W above 40 W). Increasing the condenser temperature from 20°C to 35°C decreases the thermal resistance for low heat power supplied (below 40 W). Now, for a filling ratio of 30%, one can see that the thermal performances of the FPPHP are far better and it works for lowest power supplied with a thermal resistance of around 0.3 K/W, until 0.18 K/W for highest heat powers. For these two filling ratios (30% and 50%), a higher condenser temperature leads to significant improvement of the thermal performances along the heat power charge. Finally, a filling ratio of 15% shows significant improvements at low heat power loads, for the condenser temperature set at 20°C; whereas at 35°C the oscillations are frozen and the device doesn't operate anymore, like for the empty device.

Although decreasing the filling ratio improves the thermal performance of this FPPHP, particularly for the lowest heat loads, it seems to exist a limit in such conditions, between 15% and 30%, where the FPPHP starts to freeze for higher condenser temperatures and operates with only dried evaporator.

4.3. Influence of the orientation

Figure 9 shows the thermal resistance of the FPPHP regarding its orientations. FORANE® HTS 1233zd is used with a filling ratio of 30% and for two cold source temperatures: 20°C and 35°C.

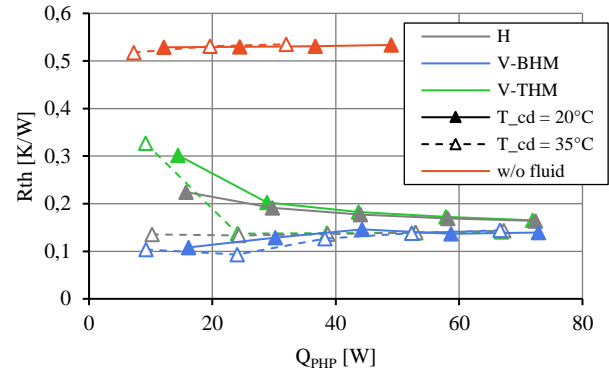


Figure 9. Thermal resistance vs. heat power for three orientations: Top Heat Mode (V-THM, Horizontal (H) and Bottom heat mode (V-BHM) (R1233zd, $FR = 30\%$)

For the favorable vertical bottom heat mode (V-BHM), the thermal resistance slightly increases, especially at low heat power, from 0.1 K/W to around 0.14 K/W at high powers supplied. For this configuration, the condenser temperature does not affect the performances.

In horizontal orientation (H), a higher condenser temperature improves the thermal performances, especially at low heat power supplied. Resistance curve also slightly increases with heat power, whereas at 20°C it decreases from 0.22 K/W down to 0.16 K/W.

Lastly, in unfavorable V-THM, thermal performances are also slightly affected by the condenser temperature, especially at low heat load. At 20°C, the thermal resistance, close to 0.3 K/W and then decrease with increasing heat power down to 0.16 K/W. At 35°C, results are like previous inclination: thermal resistance remains constant at 0.14 K/W for heat loads above 20 W, as it was already observed in Figure 8.

As conclusion, the gravity, through the orientation of the FPPHP, slightly affects the thermal performances, especially at low heat power. At 15 W, values increase from 0.11 K/W, 0.22 K/W to 0.30 K/W respectively for V-THM, H, and B-THM inclinations. At heat power above 40 W, the thermal resistances curves converge towards 0.15 K/W.

5. Back to the model

In section 2.3, it has been shown that the fluids with intermediate values of $(dP/dT)_{sat}$ give the best compromise between vapor temperature

increase -and then the vapor bubble expansion-, and the time for the liquid/vapor interface to reach the condenser. R1233zd requires a lower temperature difference to allow the same displacement. Although it has been computed that the time for the vapor to reach the condenser is higher for R1233zd than for R1336mzz, R1233zd shows better performances.

During the experimental tests, an irregular operating mode has been observed with R1336mzz. In vertical top heat mode, sudden stop over occurred during a pseudo steady state mode. It means that, during few tens of seconds, the condenser was full of liquid and the top of every channel were occupied by dried vapor bubbles. Suddenly, a disequilibrium appeared and FPPHP operated again in a normal mode. This kind of long-time instability is obviously to be avoided when considering a real application.

6. Conclusions

Both modeling and experimental studies have been performed to design a flat plate PHP of small channel dimensions: without adiabatic zone, the evaporator area is more than 90% of the total area. Its current operating mode is unfavorable, vertical top heat mode.

Modeling approach allowed to understand the behavior of vapor plug expansion regarding the working fluid properties:

- Higher is the value of $(dP/dT)_{sat}$, lower the temperature rise is needed for an overall displacement of the menisci from evaporator to condenser. R1234yf, with a value of 17.21 kPa/K at 20°C, only needs a temperature rise of the vapor phase of 0.042 K.

- A higher value of $(dP/dT)_{sat}$ disadvantages the heat rate by evaporation due to the small temperature difference between the wall and the equilibrium temperature of the fluid. Result is an increase of time for the vapor to reach the condenser area.

Modeling approach has been validated by experimental tests. For the two tested fluids, their thermal performances follow the fluid ranking established with the model. Experimental results are the following:

- The working fluid which give the lower thermal resistance is R1233zd with 0.14 K/W
- The FPPHP is able to operate in the three inclinations: horizontal and both vertical top and bottom heat mode.
- The optimal filling ratio has been found around 30%.

- For a heat power supply of 40 W, the FPPHP operates regardless the filling ratio, the inclination, or the cold source temperature. Its thermal resistance decreases down to 0.15 K/W.

7. References

- [1] J. Kim, S. J. Kim, Experimental investigation on working fluid selection in a micro pulsating heat pipe, *Energy Conversion and Management* 205, 2020
- [2] F. Cataldo, J. B. Marcinichen, J. R. Thome, Mini-scale pulsating heat pipe cooling systems for high-heat-flux electronic equipment, *Journal of Physics: conference Series*, 1868, 2021
- [3] V. Nikolayev, Yaroslav Nekrashevych, Vapor thermodynamics and fluid merit for pulsating heat pipe, Congress Joint 19th IHPC and 13th IHPS, Pisa, Italy, June 10-14, 2018
- [4] A. Yoon, S. J. Kim, Characteristics of oscillating flow in a micro pulsating heat pipe: Fundamental-mode oscillation, *International Journal of Heat and Mass Transfer* 109, p242-253, 2017
- [5] M. Ando, K. Tanaka, A. Okamoto, H. Nagai, Comparison between numerical simulation and on-orbit experiment of oscillating heat pipes, 46th International Conference on Environmental Systems, Vienna-Austria, 10-14 July 2016
- [6] V. Nikolayev, Physical principles and state-of-the-art of modeling of the pulsating heat pipe: A review, *Applied Thermal Engineering*, Elsevier, 195, pp117111, 2021
- [7] V. S. Nikolayev, Comment on "Flow and heat transfer of liquid slug and neighboring vapor plugs in a pulsating heat pipe" by Yuan, Qu, & Ma, *International Journal of Heat and Mass Transfer* 54, p2226-2227, 2011

Acknowledgments

This study was carried out by CIFRE convention (ANRT Program) established between Pprime Institute (Poitiers) and Stellantis (Site de Carrières-sous-Poissy) with the OpenLab Fluidics.

Development and performance evaluation of an ultra-thin vapor chamber with gradient capillary wick under natural convection cooling

Feng Zhou^{1,2,3}, Jingzhi Zhou^{1,2,*}, Guohui Zhou^{1,2}, Xiulan Huai^{1,2,*}, Yawen Jiang^{1,2,3}, and Naijia Zhang^{1,2,3}

¹ Institute of Engineering Thermophysics, Chinese Academy of Sciences, Beijing, China

² Nanjing Institute of Future Energy System, Nanjing, China

³ School of Engineering Sciences, University Chinese Academy of Sciences, Beijing, China

*Corresponding author email address: zhoujingzhi@iet.cn, hxl@iet.cn

Abstract

The booming development of portable electronics has imposed continuously severe thermal management challenges, and more efficient cooling technologies are urgently needed to ensure the operational stability of electronic chips. In this research, a novel vapor-liquid passage-separated ultra-thin vapor chamber (UTVC) with a thickness of 0.9 mm was fabricated, and its thermal performance was systematically investigated under natural convection conditions. Guided by the findings of previous scholars, a highly cost-effective gradient copper meshes wick structure was designed to balance the contradiction between capillary pressure and permeability. Additionally, the effect of passage width on the performance of UTVC was studied to optimize the wick structure. Encouragingly, the proposed UTVC presented a 12.2 °C reduction in the maximum temperature and reduced the thermal resistance of 42.6% compared to the copper plate. Results indicating that the UTVC with gradient capillary wick exhibited a favorable thermal performance, and providing a promising cooling solution for the thermal management of portable electronics.

Keywords: Ultra-thin vapor chamber (UTVC); Gradient capillary wick; Vapor-liquid passage-separation; Thermal performance; Natural convection cooling.

1. Introduction

In recent years, electronic information technologies have developed rapidly, and the power demands of portable electronic devices continue to increase substantially. Meanwhile, the ever-increasing miniaturization of portable electronic devices has resulted in continuously severe challenges of efficient thermal management. As an extremely reliable and effective heat dissipation technology, two-phase heat transfer devices, such as heat pipes [1,2], loop heat pipes [3,4], thermosyphons [5,6] and vapor chambers [7,8] have been widely used in high-power electronics cooling. Although the excellent heat dissipation performance of high-power electronic devices can be achieved with heat pipe technologies, traditional heat pipes cannot be sized for portable electronics [9]. In addition, the one-dimensional heat transfer mode of traditional cylindrical and flat heat pipes is not conducive to the elimination of multiple local hot spots in electronic chips [10]. It is urgent to develop an efficient heat transfer element to meet the heat dissipation requirements of miniaturized portable electronics.

The ultra-thin vapor chamber (UTVC) not only realizes two-dimensional heat dissipation and can be used to eliminate multiple hot spots, but also has a flexible size and is more suitable for the miniaturization development of electronic devices.

Therefore, extensive attentions have been paid to the UTVCs for the thermal management of various portable electronics, such as smartphones, laptops and LED modules [11-13]. Chen et al. [14] designed a novel vapor-liquid channel-separated UTVC with a total thickness of 0.4 mm for thermal management of electronic devices, and its thermal performance was studied experimentally. The results showed that the maximum heat transfer power was 4.5 W and the temperature difference was 4.75 °C in the horizontal test state. The effective thermal conductivity of the UTVC was 30 times higher than that of pure copper plate. Huang et al. [15] designed and investigated a cost-effective mesh-type UTVC with a thickness of 1.53 mm for miniaturized electronics cooling. The proposed UTVC could dissipate 50 W in the horizontal orientation with a thermal resistance of 0.197 K/W, about 4.4 times lower than that of 1.5 mm copper sheet. The authors [16] subsequently fabricated a 0.5-mm-thick UTVC with four spiral woven meshes and one bottom mesh composite wick, the effects of filling ratio and gravity on the thermal performance of UTVC were investigated experimentally. The maximum effective thermal conductivity of the UTVC was found to be about 20900 W/(m·K) in horizontal state, which was about 52 times higher than that of pure copper. Obviously, the UTVC as an efficient and reliable heat transfer element can be used to address the increasingly severe cooling requirements of

miniaturized electronics.

However, as the thickness of the vapor chamber continues to decrease, resulting in a reduced heat transfer performance and a significant increase in manufacturing costs. The wick as its core component which has a significant influence on the heat transfer characteristics of the UTVC. Capillary pressure and permeability are two important but contradictory parameters of the wick structure. In order to realize the dual objective of maximizing capillary pressure while achieving a sufficiently high permeability, numerous scholars have improved the thermal performance of the UTVC by designing and optimizing the wick structures, such as composite wicks [17-19], nanostructured wicks [20,21] and two-layer evaporator wicks [22,23]. Li et al. [18] proposed three composite wick structures for 1.0-mm-thick ultra-thin flat heat pipes, experimental results showed that the maximum heat transport capacity was found to be 14 W for mesh-grooved composite wicks. Patankar et al. [19] proposed a biporous condenser-side wick to facilitate a thicker vapor core and reduced the condenser surface peak-to-mean temperature difference by 37% relative to a monolithic wick structure. Aiming at reducing the shear force between the vapor and liquid counterflow and improving the vapor-liquid conversion efficiency, two-layer evaporator wicks were designed by Sudhakar et al. [23] to separate flow passages for vapor and liquid flow. Liquid film evaporation experimental results showed that the two-layer evaporator wick reached a dry-out limit of 512 W/cm² at a heat source area of 1 cm², and the minimum thermal resistance was 0.08 K/W. Furthermore, Chen et al. [10] developed a 3-mm-thick vapor chamber with radial multi-artery Ω -shaped reentrant microchannels inside porous wicks to provide separated flow passages for vapor and liquid flow. Experimental results showed that compared to copper plate, the VC reduced the substrate surface temperature of LED module for 7–27%, and the thermal resistance for 19–48%. Cui et al. [24] presented an ultra-thin flat heat pipe with the striped-channel structure to separate the vapor and liquid flow, and its thermal performance was investigated under natural convection cooling condition. The minimum thermal resistance was 0.26 K/W with a maximum temperature of 74.07 °C at a heat load of 8 W. Likewise, Li et al. [25,26] also experimentally demonstrated the excellent performance of the heat pipes with a vapor-liquid passage-separated wick structure in thermal management of high-power portable electronics. As aforementioned, the vapor-liquid

passage-separated wick structure is an ideal configuration for ultra-thin vapor chambers.

It is worth noting that the extremely complex composite wick structures and nano-fabrication technologies are not suitable for the ultra-thin development and mass industrial production of vapor chambers. In this study, a novel UTVC with an easy-to-manufacture vapor-liquid passage-separated wick structure was designed and investigated for portable electronics cooling. The gradient meshes combination was used to balance the contradiction between capillary pressure and permeability. Aiming at maximizing the use of the limited space inside the UTVC and reducing the vapor spreading thermal resistance, there were gradually expanding vapor diffusion spaces at both ends of the wick. Furthermore, to optimize the designed wick structure, two UTVCs with different vapor-liquid passage sizes were fabricated and tested under the identical experimental conditions.

2. Design and fabrication of the UTVC

Zhang et al. [27] demonstrated experimentally and analytically the gradient porous meshes could effectively promote bubble dynamics and exhibited superior thermal performance in pool boiling, the gradient meshes consists of 3 fine mesh layers at the bottom and 3 coarse mesh layers on the top. Based on previous research, in this study, a novel cost-effective wick structure with gradient porosity was designed to further improve the critical heat flux of the UTVC. Figure 1 shows that the configuration of the proposed UTVC, which is mainly composed of a evaporator plate, a condenser plate and a gradient capillary wick, as shown in Figure 1(a) and 1(b). Additionally, two UTVCs with different vapor-liquid passage sizes were fabricated to optimize the designed wick structure, as shown in Figure 1(c) and 1(d), respectively. The parameters of proposed UTVCs are detailed in Table 1. As shown in Figure 1(d), the proposed capillary wick structure contains an evaporation center and several parallel liquid flow passages, the remaining passages are used for vapor diffusion. Moreover, in order to maximize the use of the limited space inside the UTVC and reducing the vapor spreading thermal resistance, there are gradually expanding vapor diffusion spaces at both ends of the wick. Figure 2 presents the SEM images of the copper meshes used in the upper and lower wicks. As clearly shown in Figure 2(c), the proposed gradient wick consists of 6 fine mesh layers at the bottom and 2 coarse mesh layers on the top. The coarse and fine wire meshes were 150 μm and 300 μm , as shown in Figure 2(a) and

2(b), respectively.

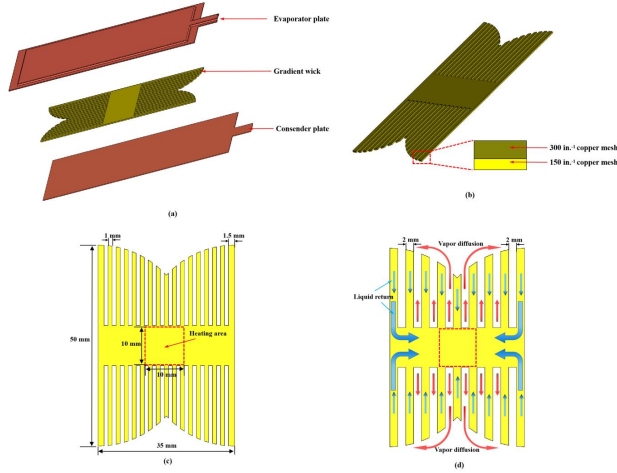


Figure 1. Schematic of the proposed UTVCs: (a) the exploded view of the UTVC; (b) gradient capillary wick; (c) the wick for UTVC-1; (d) the wick for UTVC-2.

Table 1. Geometrical parameters of the UTVCs

Parameters	Material/value	
Overall dimensions of the UTVC	60×40×0.9 mm ³	
Thickness of evaporator plate	0.2 mm	
Thickness of condenser plate	0.2 mm	
Total thickness of gradient wicks	0.5 mm	
Material of sintered wicks	Copper meshes	
Thickness and size of the upper wicks	0.2 mm / 150 in. ⁻¹	
Thickness and size of the lower wicks	0.3 mm / 300 in. ⁻¹	
Working fluid	Deionized water	
Filling ratio	60%	
Vapor-liquid passage widths of the wick	UTVC-1	1mm
	UTVC-2	2mm

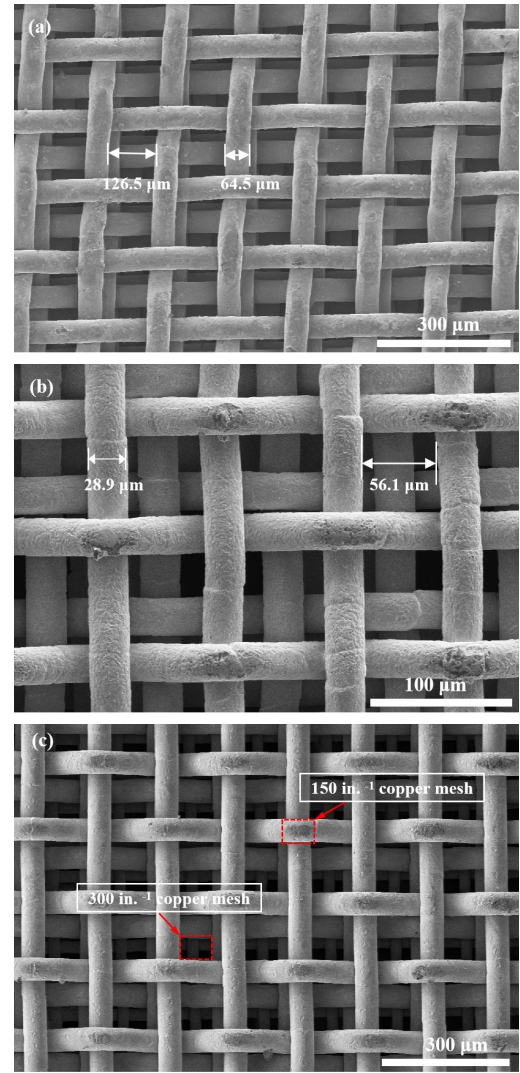


Figure 2. SEM photographs of the copper meshes for the UTVCs: (a) 150 in.⁻¹ copper mesh; (b) 300 in.⁻¹ copper mesh; (c) gradient copper meshes.

The fabrication process of the UTVC mainly consists of six steps: (1) The evaporator plate was formed by stamping, and the condenser plate was cut directly by an electric spark cutting machine. (2) The cleaned copper meshes were sequentially arranged on the graphite mold with a fixed thickness, then sintered under 900 °C for 30 min protected by the reducing gas of 95% N₂ and 5% H₂. (3) The sintered copper meshes were cut into designed shapes by an electric spark cutting machine. (4) Fill the prepared wick into the reserved cavity of the evaporator plate, and the evaporator and condenser plates were fully welded together by diffusion welding under pressure and protecting atmosphere. (5) As the filling pipe for vacuuming and working fluid charging, a copper tube was filled into the charging opening between the evaporator and condenser plates, and then

welded together by high frequency welding. (6) Deionized water was used as the working fluid and filled into the UTVCs. The filling ratios employed in this study was 60%, which can be estimated by the following equation:

$$\eta = \frac{V_l}{V_t} \times 100\% \quad (1)$$

where V_l is the volume of the DI water filled into the UTVCs, and V_t denotes the total inner space volume of the UTVC including the porosity of the wick.

After the charging process, the filling pipe was flatted by cold welding and sealed by argon arc welding. The two UTVCs with gradient capillary wicks were obtained finally, and the photos of the proposed UTVCs were shown in Figure 3.

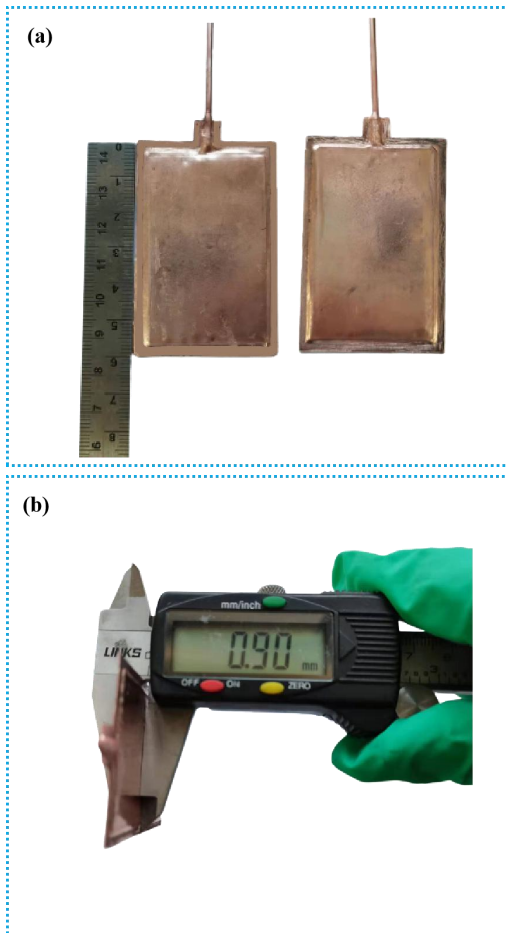


Figure 3. The pictures of the UTVCs: (a) two test samples and the length scale; (b) the thickness of the UTVC.

3. Experimental system and method

3.1. Experimental system

Fig. 4(a) shows the schematic diagram of the experimental system. The test system mainly consists of three parts: a heating system, the proposed UTVCs and a data acquisition system. In the heating system, a copper block with an active area of 10 mm×10 mm served as a simulated heat source, in which a ceramic plate heater (24 V, 120 W) was tightly attached to the copper block, and the plate heater was powered by an adjustable DC power supply (150 V, 20 A). In the experiments, a layer of thermal tape with the thermal conductivity of 1.5 W/(m·K) was used to eliminate the gap between the UTVC and heating surface and hold the UTVC in place. Furthermore, the heating copper block was insulated by fully wrapping adiabatic foam to minimize the heat loss of the heater. The data acquisition system included a temperature acquisition module (Yokogawa GP20) and 10 K-type thermocouples, among them, 9 thermocouples were directly attached to the condenser of the UTVC, one thermocouple was used to monitor the ambient temperature (T_a). And Figure 4(b) illustrates the distribution of 9 thermocouples in the condensation end of the UTVC.

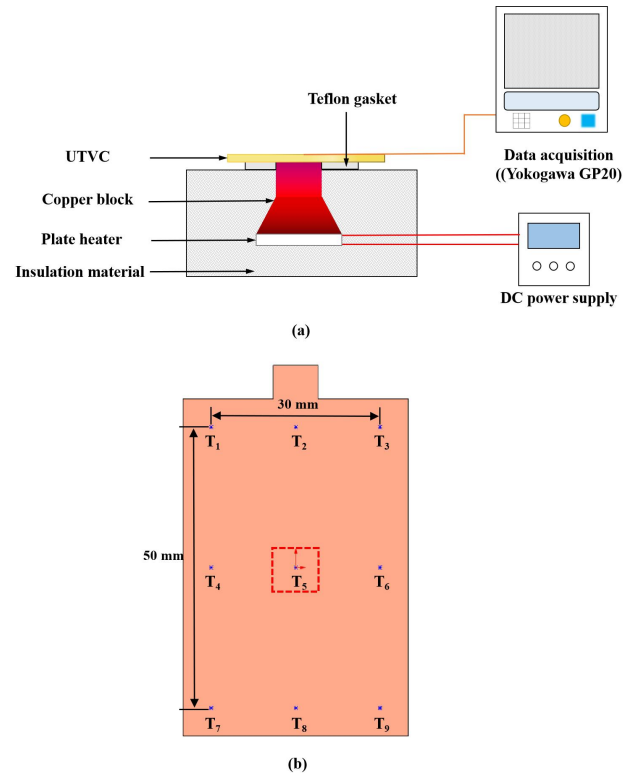


Figure 4. Experimental test system: (a) schematic diagram of experimental system; (b) the distribution of thermocouples.

3.2. Data reduction and uncertainty analysis

In this study, the maximum temperature of the UTVC and spreading thermal resistance are two key parameters for evaluating the performance of UTVC. The spreading thermal resistance refers to the ratio of the maximum temperature difference between two points to the power under thermal equilibrium, which be determined as follows:

$$R = \frac{\Delta T_{max}}{Q} \quad (2)$$

where Q is the heat load applied to the UTVC, ΔT_{max} is the max temperature difference of UTVC, which can be calculated by:

$$\Delta T_{max} = T_{max} - T_{min} \quad (3)$$

where T_{max} and T_{min} are the maximum and minimum temperatures of the condenser surface of the UTVC, respectively.

The uncertainty of the spreading thermal resistance may be calculated by the following equation [28]:

$$\frac{\Delta R}{R} = \sqrt{\left(\frac{\Delta T_{max}}{T_{max}}\right)^2 + \left(\frac{\Delta T_{min}}{T_{min}}\right)^2 + \left(\frac{\Delta Q}{Q}\right)^2} \quad (4)$$

where ΔT_{max} , ΔT_{min} , and ΔQ are the measurement errors of the maximum temperature, minimum temperature and heat load, respectively.

For the individual temperature measurements, the uncertainties were ± 0.2 °C for the measurement accuracy of the K-type thermocouples. The uncertainty of the heat load supplied by the DC power supply was $\pm 0.5\%$. From the error analysis of Equation (4), the uncertainty of the thermal resistance in this study was estimated to be less than 7.08%.

4. Results and discussion

4.1. Thermal performance of the UTVC at different heat loads

In order to further verify the excellent performance of the proposed UTVC, a copper plate with the identical geometrical dimensions was tested under same experimental conditions.

Figure 5 presents the thermal performance of the UTVCs and copper plate under the heat loads ranging from 2 W to 8 W. Obviously, as shown in Figure 5(a), the maximum temperatures of the UTVCs were noticeably lower than that of copper plate under all heat loads, and the difference increased gradually with the increase of heat loads. For example, the maximum temperatures of the UTVC-1 and copper plate in the steady-state were 71.2 °C and 83.4 °C at a heat load of 8 W, respectively. However, when heat load was 2 W, the maximum temperatures for both were 31.1 °C and 35.6 °C, respectively. Similar to UTVC-1, the maximum temperature differences between UTVC-2 and copper plate were 1.8 °C and 8.9 °C at heat loads of 2 W and 8 W, respectively. The reasons for this phenomenon may be as follows: (1) the UTVCs undergone a continuous phase change cycle of evaporation and condensation inside the chamber during operation, which was far superior to the heat transfer mechanism of thermal conductivity than the copper plate. (2) the phase transition strength of the working fluid inside the vapor chamber increased with the increase of heat loads, so that the heat generated by the heat source was dissipated more quickly under higher heat loads. (3) the gradient wick with separated vapor and liquid flow passages effectively improved the comprehensive performance of the capillary structure and the vapor-liquid transport efficiency. Consequently, the surface temperatures of the UTVCs were significantly lower the copper plate at high heat loads.

Similar to the maximum temperature, the thermal resistances of the UTVCs were lower than that of the copper plate at all heat loads. As clearly shown in Figure 5(b), the thermal resistance of the copper plate was almost kept at approximately 0.70 K/W under different heat loads, and there was no obvious change trend due to the heat conduction mechanism. However, the thermal resistances of the UTVCs presented a significant decreasing trend with the increase of heat load. For instance, the thermal resistance of UTVC-1 was 0.60 K/W at a heat load of 2 W and decreased significantly with the increasing heat loads. The minimum thermal resistance was obtained of 0.39 K/W at 8 W, that is, the UTVC-1 presented a notable reduction of 42.6% in thermal resistance than that of copper plate. Generally, when the heat loads was lower, the phase change process in the UTVC was relatively weak, and the accumulation of working fluid in

the evaporation center leads to a large thermal resistance of the UTVC. However, all the working fluid under higher heat loads participated in the vapor-liquid circulation, and the phase change strength was significantly improved, resulting in a continuous decrease in thermal resistance. Additionally, the unique wick structure of the UTVC reduced the vapor spreading thermal resistance considerably. Results indicated that the proposed UTVCs enhanced cooling capacity significantly and yield a favorable performance for passive heat dissipation of portable electronic devices.

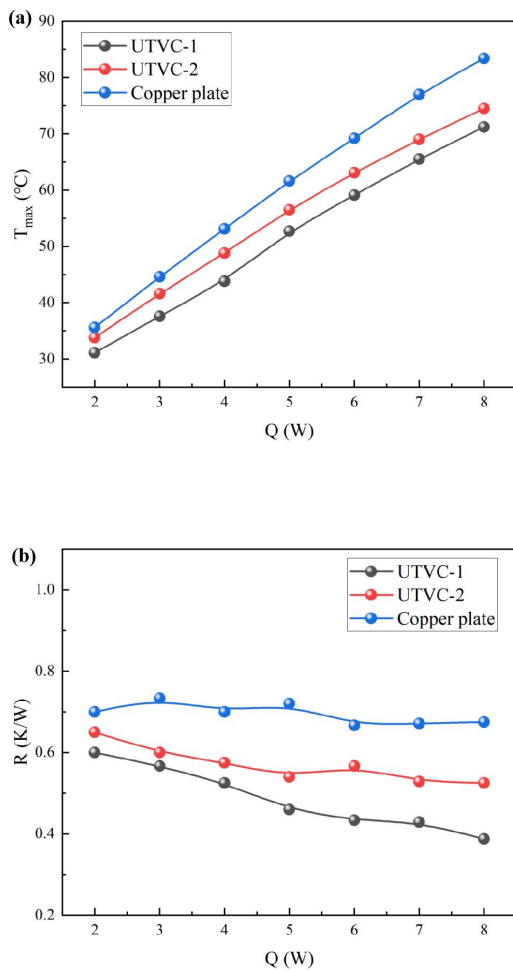
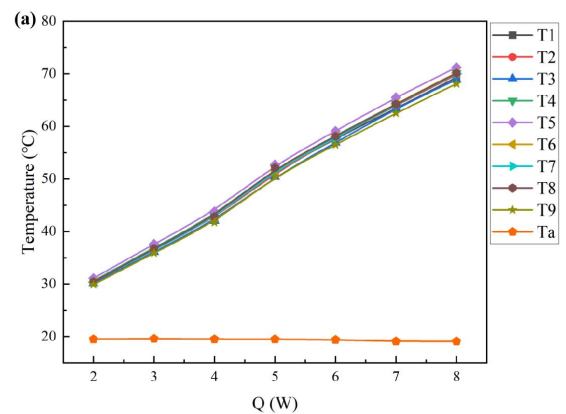


Figure 5. Thermal performance of the UTVCs and copper plate: (a) the maximum temperatures; (b) the thermal resistances.

4.2. Effect of passage width on the performance of UTVCs

In order to further optimize the designed wick structure, two UTVCs with passage widths of 1 mm and 2 mm were fabricated and the heat transfer performance was studied under the

identical experimental conditions. Figure 6(a) and 6(b) show the steady-state temperature distribution at all test points of the UTVC-1 and UTVC-2 under different heat loads, respectively. As illustrated in Figure 6, the temperature of each testing points continuously rose with the heat load increased. Due to the closest distance to the heat source, both UTVC-1 and UTVC-2 have the highest temperature at T_5 . When the heat load was 8 W, the highest temperature were 71.2 °C for the UTVC-1 and 74.5 °C for UTVC-2, respectively. Furthermore, under the lower heat loads, the passage width of the UTVC has little effect on the temperature uniformity performance, but the effect becomes more obvious with the increase of the heat loads. And the UTVC with a passage width of 1 mm exhibited more excellent thermal performance. For example, the maximum temperature difference on the condenser surface of UTVC-1 was 1.2 °C at a heat load of 2 W, and it was 1.3 °C for UTVC-2. However, when the heat load increased to 8 W, the maximum temperature difference between the two were 4.2 °C and 3.1 °C, respectively. Possible causes are as follows: although UTVC-1 and UTVC-2 have almost the same capillary wick area, the liquid passages of UTVC-1 are more evenly distributed so that the condensing working fluid can return to the evaporation center promptly. Additionally, compared with UTVC-2, the vapor channel space of UTVC-1 is more narrower, resulting in a larger vapor flow velocity and a higher vapor-liquid circulation efficiency. And the UTVC-1 with more vapor-liquid transport passages makes the temperature distribution of the vapor chamber more uniform. Therefore, the wick with a passage width of 1 mm presented a superior thermal performance with the increment of heat loads.



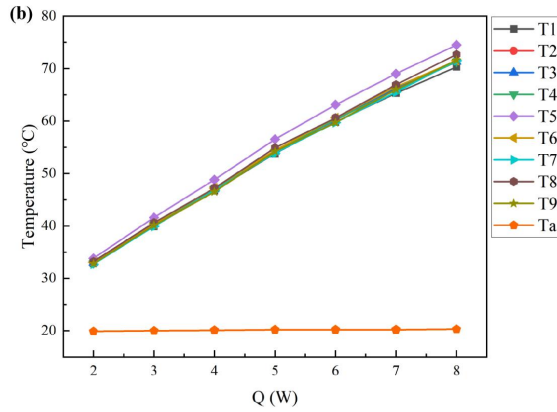


Figure 6. Temperature distribution of UTVCs under different heat loads: (a) UTVC-1; (b) UTVC-2.

4.3. Comparison with others

In order to more comprehensively evaluate the performance of the proposed UTVC, a thermal resistance comparison between this study and other advanced works was summarized in Figure 7. Chen et. al [14] designed a novel vapor-liquid channel-separated UTVC with a total thickness of 0.4 mm for thermal management of electronic devices, results showed that the maximum heat transfer power was 4.5 W with a thermal resistance of about 1.05 K/W. Cui et al. [24] presented a 0.68 mm thick ultra-thin flat heat pipe with the striped-channel wick structure, which could tolerate 8 W with a thermal resistance of about 0.27 K/W. Huang et al. [29] fabricated a novel 0.5 mm thick UTVC with six spiral woven meshes and single-layer mesh acting as the wick, and the minimum thermal resistance was about 0.52 K/W at 10.5 W. Tang et al [30] investigated the thermal performance of 1 mm thick heat pipes with mesh wicks in various mesh structure. Results shown that the 180 in.⁻¹ mesh wick may be a better choice to achieve the optimum performance for the ultra-thin heat pipe, and the thermal resistance was about 1.10 K/W at a heat load of 10 W. Yu et al. [31] designed the UTVC with a thickness of 0.4 mm and experimentally investigated the effect of passage area ratio of wick on its heat transfer performance, the minimum thermal resistance of around 0.8 K/W was obtained at 6 W. From the above comparison, the proposed UTVC with a gradient meshes wick seems to provide a promising and reliable candidate for portable electronics cooling.

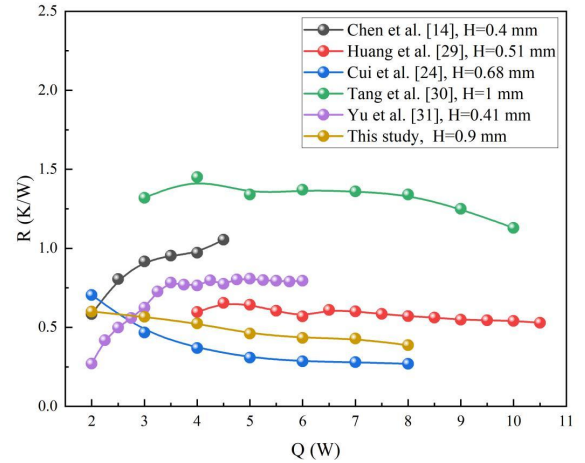


Figure 7. Comparison of thermal resistances between the UTVC-1 and previous works.

5. Conclusion

In this study, a novel vapor-liquid passage-separated UTVC with the thickness of 0.9 mm was developed for portable electronics. Two UTVCs with different vapor-liquid passage widths were fabricated to optimize the designed wick structure, and the thermal characteristics were experimentally investigated under natural air convection. Additionally, in order to further evaluate the heat transfer performance, comparative studies were conducted between the proposed UTVC and other previous advanced works. The main conclusions can be summarized as follows:

- (1) Gradient capillary wick was utilized in the proposed UTVC to improve the vapor-liquid conversion efficiency of the working fluid and enhance the heat transfer capability.
- (2) The thermal performance of UTVCs was affected by the vapor-liquid passage width, the wick with a passage width of 1 mm exhibited more superior thermal performance in this study.
- (3) Compared to the copper plate, the UTVC-1 with gradient capillary wick presented a reduction in maximum surface temperature of 12.2 °C and a 42.6% reduction in the thermal resistance at a heat load of 8 W.

References

- [1] H. Tang, Y. Tang, Z. Wan, J. Li, W. Yuan, L. Lu, Y. Li, and K. Tang, Review of applications and developments of ultra-thin micro heat pipes for electronic cooling. *Applied Energy*, 2018. 223: p. 383-400.
- [2] H. Jouhara, A. Chauhan, T. Nannou, S. Almahmoud, B. Delpech, and L. C. Wrobel, Heat pipe based systems - advances and applications. *Energy*, 2017. 128: p. 729-754.
- [3] Q. Su, S. Chang, and C. Yang, Loop heat pipe-based solar thermal façade water heating system: A review of performance evaluation and enhancement. *Solar Energy*, 2021. 226: p. 319-347.
- [4] J. Li, F. Lin, D. Wang, and W. Tian, A loop-heat-pipe heat sink with parallel condensers for high-power integrated LED chips. *Applied Thermal Engineering*, 2013. 56: p. 18-26.
- [5] H. Ghorabae, M. R. S. Emami, F. Moosakazemi, N. Karimi, G. Cheraghian and M. Afrand, The use of nanofluids in thermosyphon heat pipe: A comprehensive review. *Powder Technology*, 2021. 394: p. 250-269.
- [6] J. Li, W. Tian, and L. Lv, A thermosyphon heat pipe cooler for high power LEDs cooling. *Heat and Mass Transfer*, 2016. 52: p. 1541-1548.
- [7] M. Bulut, S. G. Kandlikar, and N. Sozbir, A review of vapor chambers. *Heat Transfer Engineering*, 2019. 40: p. 1551-1573.
- [8] X. Cheng, G. Yang, and J. Wu, Recent advances in the optimization of evaporator wicks of vapor chambers: From mechanism to fabrication technologies. *Applied Thermal Engineering*, 2021. 188: p. 116611.
- [9] R. Lewis, L. A. Liew, S. Xu, Y. C. Lee, and R. Y. Microfabricated ultra-thin all-polymer thermal ground planes. *Engineering Sciences*, 2015. 60: p. 701-706.
- [10] L. Chen, D. Deng, Q. Huang, X. Xu, and Y. Xie, Development and thermal performance of a vapor chamber with multiartery reentrant microchannels for high-power LED. *Applied Thermal Engineering*, 2020. 166: p. 114686.
- [11] Y. Chen, Q. Jian, Z. Huang, J. Zhao, X. Bai, and D. Li, Improvement of thermal management of proton exchange membrane fuel cell stack used for portable devices by integrating the ultrathin vapor chamber. *International Journal of Hydrogen Energy*, 2021. 46: p. 36995-37006.
- [12] F. Zhou, G. Zhou, J. Zhou, X. Huai, Y. Jiang, and Q. Huang, Thermal performance evaluation of a novel ultra-thin vapor chamber with Laval-like nozzle composite wick under different air cooling conditions. *Case Studies in Thermal Engineering*, 2022. 31: p. 181045.
- [13] Y. Yang, J. Lian, H. Wang, D. Liao, and H. Qiu, Microstructured wettability pattern for enhancing thermal performance in an ultrathin vapor chamber. *Case Studies in Thermal Engineering*, 2021. 25: p. 100906.
- [14] Z. Chen, Y. Li, W. Zhou, L. Deng, and Y. Yan, Design, fabrication and thermal performance of a novel ultra-thin vapour chamber for cooling electronic devices. *Energy Conversion and Management*, 2019. 187: p. 221-231.
- [15] G. Huang, W. Liu, Y. Luo, Y. Li, and H. Chen, Fabrication and thermal performance of mesh-type ultra-thin vapor chambers. *Applied Thermal Engineering*, 2019. 162: p. 119263.
- [16] G. Huang, W. Liu, Y. Luo, and Y. Li, A novel ultra-thin vapor chamber for heat dissipation in ultra-thin portable electronic devices. *Applied Thermal Engineering*, 2020. 167: p. 114726.
- [17] H. Tang, C. Weng, Y. Tang, H. Li, T. Xu, and T. Fu, Thermal performance enhancement of an ultra-thin flattened heat pipe with multiple wick structure. *Applied Thermal Engineering*, 2021. 183: p. 116203.
- [18] Y. Li, W. Zhou, J. He, Y. Yan, B. Li, and Z. Zeng, Thermal performance of ultra-thin flattened heat pipes with composite wick structure. *Applied Thermal Engineering*, 2016. 102: p. 487-499.
- [19] G. Patankar, J. A. Weibel, and S. V. Garimella, Patterning the condenser-side wick in ultra-thin vapor chamber heat spreaders to improve skin temperature uniformity of mobile devices. *International Journal of Heat and Mass Transfer*, 2016. 101: p. 927-936.
- [20] Y. Nam, S. Sharratt, C. Byon, S. Kim, and Y. Ju, Fabrication and characterization of the capillary performance of superhydrophilic Cu micropost arrays. *Journal of Microelectromechanical Systems*, 2010. 19: p. 581-588.
- [21] M. Kim, and M. Kaviany, Multi-artery heat-pipe spreader: monolayer-wick receding meniscus transitions and optimal performance. *International Journal of Heat and Mass Transfer*, 2017. 112: p. 343-353.
- [22] S. Sudhakar, J. A. Weibel, and S. V. Garimella, Design of an area-scalable two-layer evaporator wick for high-heat-flux vapor chambers. *IEEE Transactions on Components, Packaging and Manufacturing Technology*, 2019. 9: p. 458-472.
- [23] S. Sudhakar, J.A. Weibel, F. Zhou, E. Dede, and S. Garimella, The role of vapor venting and liquid feeding on the dryout limit of two-layer evaporator wicks. *International Journal of Heat and Mass Transfer*, 2020. 148: P. 119063.
- [24] Z. Cui, L. Jia, C. Dang, and L. Yin, Thermal performance of an ultra-thin flat heat pipe with striped super-hydrophilic wick structure. *Applied Thermal Engineering*, 2022. 208: p. 118249.
- [25] J. Li, X. Li, G. Zhou, and Y. Liu, Development and evaluation of a supersized aluminum flat plate heat pipe for natural cooling of high power telecommunication equipment. *Applied Thermal Engineering*, 2021. 184: p. 116278.
- [26] G. Zhou, J. Li, and Z. Jia, Power-saving exploration for high-end ultra-slim laptop computers with miniature loop heat pipe cooling module. *Applied Energy*, 2019. 239: p. 859-875.
- [27] S. Zhang, X. Jiang, Y. Li, G. Chen, Y. Sun, Y. Tang, and C. Pan, Extraordinary boiling enhancement through micro-chimney effects in gradient porous micromeshes for high-power applications. *Energy Conversion and Management*, 2020. 209: p. 112665.
- [28] G. Zhou, J. Zhou, X. Huai, F. Zhou, and Y. Jiang, A two-phase liquid immersion cooling strategy utilizing vapor chamber heat spreader for data center servers. *Applied Thermal Engineering*, 2022. 210: p. 118289.
- [29] G. Huang, W. Liu, Y. Luo, Y. Li, and H. Chen, A new ultra-thin vapor chamber with composite wick for thin electronic products. *International Journal of Thermal Sciences*, 2021. 170: p. 107145.
- [30] Y. Tang, S. Hong, S. Wang, and D. Deng, Experimental study on thermal performances of ultra-thin flattened heat pipes. *International Journal of Heat and Mass Transfer*, 2019. 134: p. 884-894.
- [31] J. Yu, Y. Li, Z. Chen, Q. Luo, H. Chen, and X. Tang, Effect of the passage area ratio of wick on an ultra-thin vapour chamber with a spiral woven mesh wick. *Applied Thermal Engineering*, 2021. 196: p. 117282.

Temperature and pressure frequency analyzes of a flat plate pulsating heat pipe: influence of the edge orientation angle

Vincent Ayel^{1*}, Thibault Van't Veer^{1,2}, Luca Pagliarini³, Maksym Slobodeniuk¹,
Fabio Bozzoli³, Cyril Romestant¹, Yves Bertin¹

¹Prime Institute CNRS – ENSMA – Université de Poitiers, UPR 3346, 86961 Futuroscope-Chasseneuil, France

²Stellantis – Site de Carrières sous Poissy, 78955 Carrières sous Poissy, France

³Department of Engineering and Architecture, University of Parma, Parco Area delle Scienze 181/A I-43124 Parma, Italy

*Corresponding author email address: vincent.ayel@ensma.fr

Abstract

A closed loop flat plate pulsating heat pipe (FPPHP), filled with Opteon™ SF33 as working fluid ($FR = 50\%$), has been experimentally studied in different orientations: 0° (horizontal), 22.5° , 45° , 67.5° and 90° (vertical, on the edge) related to the floor surface and with channels positioned perpendicularly to gravity vector. Dried-out was observed in horizontal orientation, but increase of inclination angle (starting from 22.5°) led to regular oscillatory movement due to help of gravity pressure drop between channels. The thermal performance remains very similar for the device inclination angles from 45° to 90° (edge inclination). FFT analysis of the pressure signal and temperatures of the external wall of the device (measured with IR camera) have been done to characterize the dominant oscillatory frequencies depending on the device inclination angle. A comparison between the internal pressure and the temperature signals showed that the dominant frequency increases with applied heat power, but it also spreads and disappears for the highest heat powers applied.

Keywords: Flat plate pulsating heat pipe; Edge orientation; Thermal performances; Infrared; FFT frequency analysis

1. Introduction

Flat plate pulsating heat pipes (FPPHPs), due to their design (material/thermal continuity between channels), are often subjected to unstable operation and low thermal performances in horizontal inclination: intermittently stopover phenomena or even complete stop of operation due to early dry-out of the evaporator are specifically attributed to a lack of pressure perturbations between channels [1-3]. But, starting from a dried-out configuration, when the fluid starts to flow, the ends of a U-shape liquid column oscillate in opposite directions. If the amplitude of oscillations is sufficient, liquid flow into the evaporator and vapor flow into the condenser occur, completing the circulation cycle. As the heat load increases, oscillations become larger, with the liquid occasionally overflowing into neighboring turns. Because the phases of liquid column oscillations are not independent from one another, they vary continuously and the menisci at each end move in a waveform [2-3]; due to the spring effect of the vapor bubbles, the fluid motion is sequentially transmitted from one branch to another along the FPPHPs.

This effect can be enhanced when gravity pressure drop is added to the pressure perturbations between channels. It is obtained when the device is oriented vertically, but with horizontal channels in the so-called “edge” -or “side”- orientation [1,4]. Pressure imbalance in the liquid slugs is occasioned by difference in height at each U-turn, leading to a

particularly high gravity pressure head for the last surrounding bend; this can drive a continuous long-term oscillatory motion between all liquid slugs, even for the lowest heat powers applied, without encountering any dry-out at the evaporator. The liquid slugs oscillate in a waveform from bottom into top, through the vapor phase into the evaporator region, as oscillation velocities and amplitudes increase with heat input augmentation. Pagnoni *et al.* [4] performed visualizations of liquid menisci oscillating in a FPPHP tested with ethanol in edge orientation. They found an oscillation dominant frequency increasing from 2.5 Hz at 80 W to 4 Hz at 200 W heat load applied, as well as menisci velocities, demonstrating the regularity of transfer under such conditions. Chi *et al.* [5] performed FFT analysis of a temperature signal recorded in the evaporator zone of a tubular PHP filled with ethanol and tested with different orientations starting from vertical bottom heated mode (BHM): they found a dominant peak frequency around 0-0.1 Hz in BHM, whereas increasing the filling ratio or the inclination angle both reduce the power spectrum density (PSD) distribution. In contrast, the use of the wavelet scalogram and power spectrum methodology has also shown very promising results considering frequency analysis of oscillating motions detected by non-intrusive infrared thermography [6-7].

Studies on PHPs tested under edge orientation are rather rare, as well as the impact on a dominant

frequency of the oscillations. This will be studied in the present work through the influence of heat input and edge inclination angle on the thermal performances, and through FFT and wavelet frequency analyzes of both pressure and infrared signals for every tested conditions.

2. Experimental apparatus

The FPPHP consists of a copper plate ($80 \times 200 \times 3.5 \text{ mm}^3$) machined with a single square shaped groove ($3 \times 3 \text{ mm}^2$) forming a series of 8 U-turns in the evaporator (see figure 1a). This first plate was covered with a second brazed one (0.5 mm thick). Both were brazed with tin to guarantee perfect sealing. Sealing test and vacuuming were made thanks to a Pfeiffer Vacuum® pump (ASM 142 Adixen) coupled with a helium detector. The evaporator zone is heated by a wire electrical (Thermocoax®, 1 mm), embedded in a copper plate brazed on the back side of the FPPHP ($40 \times 80 \times 2 \text{ mm}^3$), and connected to electrical power supply (ELC® ALR3220, $\pm 10 \text{ mV}$). On the opposite side, the condenser section is cooled by a grooved brazed copper plate ($80 \times 80 \text{ mm}^2$) cooled by water flow from a cryothermostat (Huber® CC240 wl).

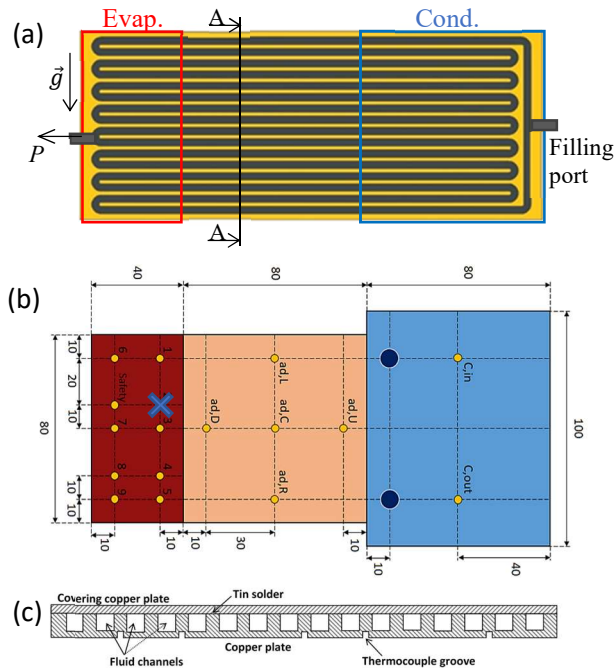


Figure 1. Schematic description of the FPPHP: (a) copper plate with machined grooves (edge orientation); (b) back-side with heater, cold source, and thermocouples positions; (c) A-A cross-section.

Fifteen T-type thermocouples (TCs, $\pm 0.8 \text{ K}$ from internal switch calibration, 0.2 Hz) are used for the temperature measurements between evaporator and

heating plate (8 TCs), adiabatic zone (5 TCs), and two measure the cold plate temperatures (C_{in} and C_{out} , figure 1b). Two connection pipes were brazed on the device (figure 1a): one for the filling; the other, in a central bend of the evaporator zone, leading to a tee, connected to a pressure sensor (GE® PTX5076, $\pm 200 \text{ Pa}$, 100 Hz) and a plug for emptying process. Finally, the device top face has been coated with a highly emissive paint (emissivity: 0.95 , ± 0.1) for infrared visualizations (IR camera INFRADEC®, 10 Hz) in order to detect the impact of internal thermofluidic interactions on the external wall temperature distribution. The camera is always oriented in the direction of the normal to the external black painted face. All other faces of the FPPHP have been thermally insulated using 50 mm of Rockwool ($\lambda \approx 0.04 \text{ W.m}^{-1}\text{K}^{-1}$).

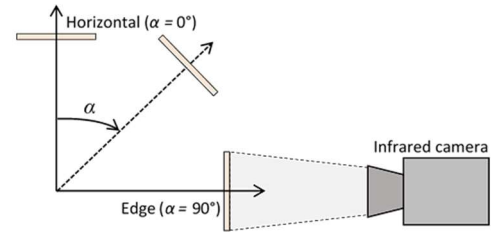


Figure 2. Experimental set-up.

Before filling, the device was cleaned using Finox® and rinsed several times. In the following, Opteon™ SF33 was chosen as the working fluid (appropriate for replacing HCFCs, HFC, etc.). Based on the widely used critical diameter derived from the Bond number criterion ($D_{crit} = 2\sqrt{\sigma/g(\rho_l - \rho_v)}$), this gives approximately 2.2 mm at 20°C and 1.98 mm at 50°C . This means that the channel of the FPPHP is above D_{crit} , leading to a stratification of the liquid/vapor phases, particularly in vertical orientation.

The operating conditions are summarized below:

- Volumetric filling ratio: 50% at 20°C ;
- Cold source: water set at 20°C ;
- Heat power applied: 25–50–100–150–200 W;
- Inclination: from horizontal ($\alpha = 0^\circ$) to vertical edge ($\alpha = 90^\circ$), with 3 intermediate steps: 22.5° , 45° and 67.5° (figure 2).

Finally, let us mention that the gravity pressure head between two adjacent channels ($\Delta P_g = \Delta P_{g,0} \sin(\alpha)$, where $\Delta P_{g,0} = \rho_l g d$, and d the inter-channel distance) can reach, for the edge inclination, values of $\Delta P_{g,0}$ of 64.9 Pa at 20°C , and 61.1 Pa at 50°C , whereas it reaches 973.3 Pa at 20°C , and 916.4 Pa at 50°C , for the last surrounding bend, which is far above the maximum capillary pressure drop of menisci in the transverse section of the

grooves (of 21.5 Pa -and 16.4 Pa- at 20°C -and 50°C-, respectively).

3. Results and discussions

3.1. Thermal performances

Figure 3 presents an example of thermocouples transient temperatures evolution with increasing heat power steps for the FPPHP tested in edge inclination ($\alpha = 90^\circ$). It can be seen that the overall level of temperatures increases with increasing heat power, but remains relatively stable, particularly at lowest heat powers (25 W and 50 W). This shows that the device operates quite well in this position. However, it can be observed that the level of temperature fluctuations increases with increasing heat power, being the result of growing instabilities in the device.

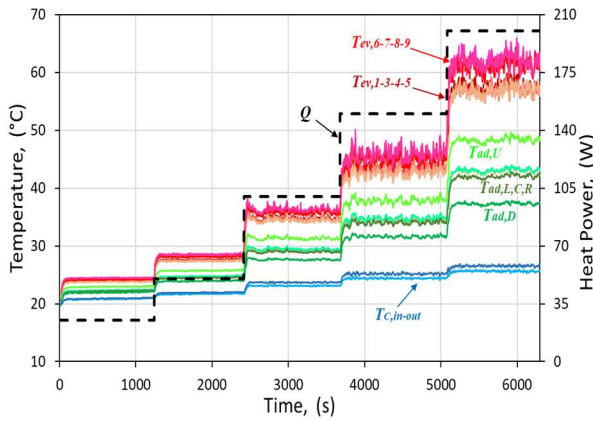


Figure 3. Transient temperature responses of the FPPHP to increasing heat power levels ($\alpha = 90^\circ$).

Figure 4 plots the average temperature differences ΔT_{e-c} between evaporator ($T_{ec,1-9}$) and cooling fluid ($T_{C,in-out}$), as well as the thermal resistance obtained in steady-state conditions, with their corresponding error bars ($R_{th} = \Delta T_{e-c} / \dot{Q}$, \dot{Q} being the electric power from which the thermal losses have been subtracted, taking into account natural convection and radiation heat transfer from the black coated face). It can be seen that the thermal resistance slightly decreases, as is often the case in literature, for low heat powers from 25 W to 100 W (except for $\alpha = 22.5^\circ$ and horizontal positions where it increases), but then increases up to 200 W heat applied, which is less common in literature. This is probably specific to this modus operandi. Furthermore, the thermal performances remain very similar for the inclination angles from 90° down to 45° , slightly decrease for 22.5° , whereas the FPPHP does not activate in horizontal position (0°): the thermal resistance has been found equivalent to empty FPPHP operation. There seems to be an inclination angles range (or gravity pressure head)

for which the performances (heat and fluid flow) remain independent, here between 90° and 45° . This point requires further investigation.

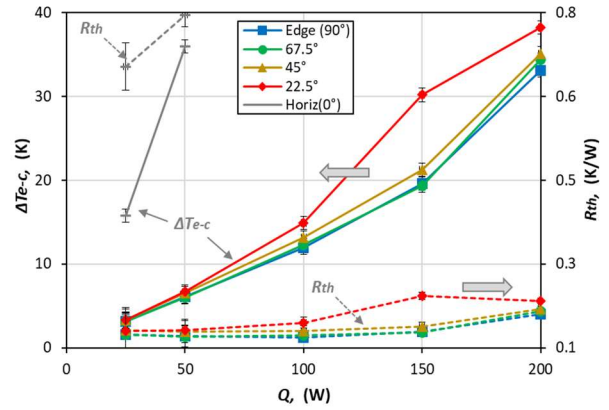


Figure 4. ΔT_{e-c} (-) and R_{th} (-) as functions of heat power applied for the five orientations.

3.2. Frequency analyzes

As stated in the introduction, the edge orientation was one of the only positions in the literature that made it possible to record a dominant frequency of the overall heat and mass transfer. First, to understand the best experimental signal and reduction approach to be used for the estimation of fluid oscillation frequencies in the investigated PHP, the thermographic and fluid pressure data were processed by means of both the FFT and the wavelet methods and will be compared in the following section. Then, a systematic frequency analysis based on only FFT method will be done varying the inclination angle and the heat power applied.

FFT vs wavelet method: IR camera and fluid pressure signals

An oscillatory movement can be observed from the successive infrared images of the end of the evaporator in figure 5 (here in edge orientation at 150 W heat applied). The U-turns can easily be distinguished from one image to another, with an oscillating motion going from bottom to top. It has to be highlighted that, since phase change processes are responsible for pressure increases at the evaporator, they are believed to be inherently linked to the fluid motion towards the condenser, *i.e.*, to the fluid oscillation frequency. Areas used for spectral analysis (4x4 pixels) are delimited by the white squares at the end of each U-turn in the last right-hand side image of figure 5. They are numbered from 1 -for the upper bend- to 8 -for the bottom bend-.

In figure 6, the IR signal related to turn 1 in the evaporator and sampled over 60 seconds is shown

together with the FFT and wavelet outputs (heat load equal to 50 W, edge orientation). The raw temperature signal (figure 6a) exhibits strong fluctuations due to phase-change phenomena, which result in significant wall temperature variations. The power spectrum obtained through the FFT method (figure 6c) presents a peak at about 0.94 Hz, denoting that the oscillatory behavior is characterized by such a dominant frequency.

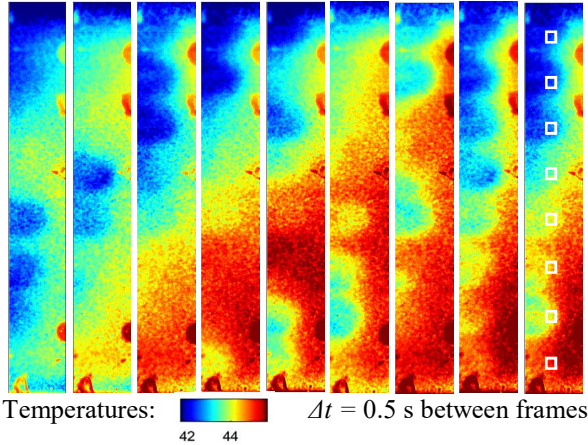


Figure 5. Infrared visualizations in the evaporator zone ($\alpha = 90^\circ$; $\dot{Q} = 150$ W).

Other low-amplitude peaks are here due to both noise in the raw signal and the chaotic motion of the working fluid, which oscillates with non-fixed frequency. In figure 6b, the time representation of the signal's frequency (magnitude scalogram) provided by the wavelet approach confirms the presence of chaotic fluid oscillations. In fact, despite the signal's power is mainly concentrated at around 1 Hz over the observation window, few time instants present high-amplitude peaks at different frequencies, denoting that the fluid oscillation undergoes sudden variations in terms of oscillation frequency. Nonetheless, the power spectrum obtained through the wavelet method exhibits a peak at 0.94 Hz, *i.e.*, the perceived dominant frequency is the same as that given by the FFT analysis (figure 6c). Hence, when IR samples are considered, the frequency analyses carried out by means of different approaches give same results.

The fluid pressure signal is similarly processed for the same working condition of figure 6. In figure 7, the collected fluid pressure is shown together with the FFT and wavelet method outputs. Alike the wall temperature, the pressure signal (figure 7a) exhibits significant fluctuations during the PHP operation, confirming the link between fluid pressure and outer wall temperature. The dominant fluid oscillation frequency is assessed, through the FFT method, equal to 0.95 Hz (figure 7c). The non-fixed feature of fluid oscillations is again perceived in the

magnitude scalogram of Figure 7b, while the power spectrum outputted by the wavelet method presents a peak at 0.94 Hz. Although a slight discrepancy between dominant oscillation frequency estimated through the FFT method and the wavelet method is here perceivable, the two values are reasonably comparable in terms of uncertainty of the approaches, which is affected by the time discretization of the raw samples.

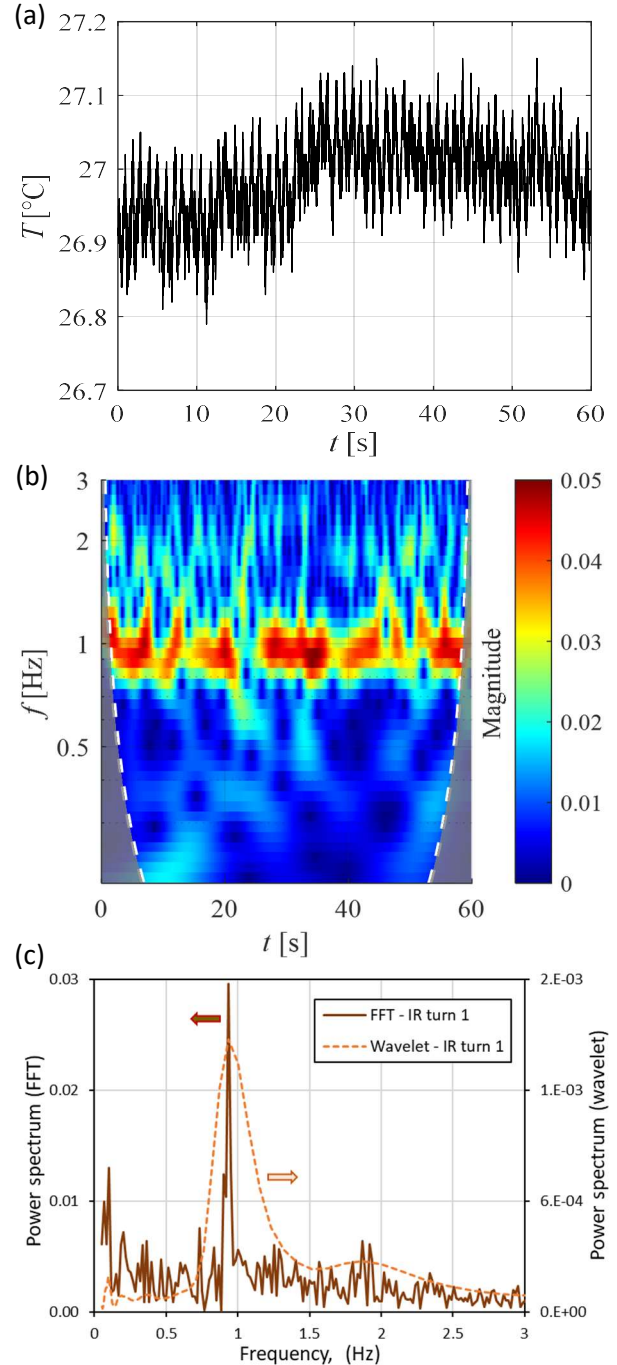


Figure 6. (a) Raw IR thermographic signal of turn 1 (100 Hz); (b) wavelet magnitude scalogram; (c) power spectra for both FFT and wavelet methods ($\alpha = 90^\circ$; $\dot{Q} = 50$ W).

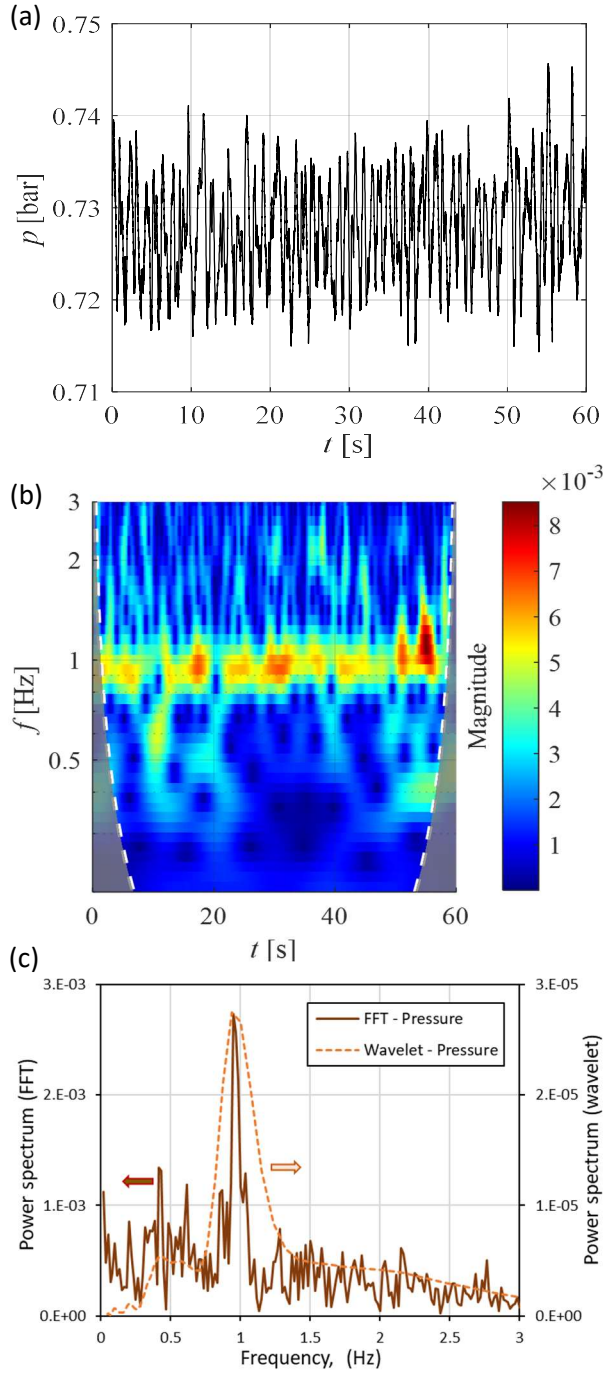


Figure 7. (a) Raw pressure signal corresponding to figure 6 ; (b) wavelet magnitude scalogram; (c) power spectra for both FFT and wavelet methods ($\alpha = 90^\circ$; $\dot{Q} = 50$ W).

In conclusion, the presented analysis highlighted that the wavelet and FFT methods provide similar outcomes. Moreover, the results seem to be independent on the analyzed experimental signal. The agreement in terms of wavelet method between frequency analysis on IR data and fluid pressure signals is in accordance with [6].

Taking into account the FFT approach, the suitability of pressure signals for the dominant fluid

oscillation frequency evaluation in PHPs agrees with the findings of Khandekar *et al.* [8], while it disagrees with the ones provided by Mameli *et al.* [9] and Takawale *et al.* [10]. Further studies on the best signals and reduction techniques to be used for frequency investigations in PHPs must be therefore conducted with the aim of proving the feasibility of different approaches on varying PHP layouts and collected data.

FFT analysis: influence of orientation and heat power applied

On the basis of what was found in the last section, a systematic FFT analysis has been applied to the Gaussian filtered pressure signals (100 Hz, 160 s) and some temperatures signals recorded by the infrared camera (10 Hz, 120 s) during nearly steady-state conditions for every heat power steps and orientations –except the nonfunctional horizontal orientation–.

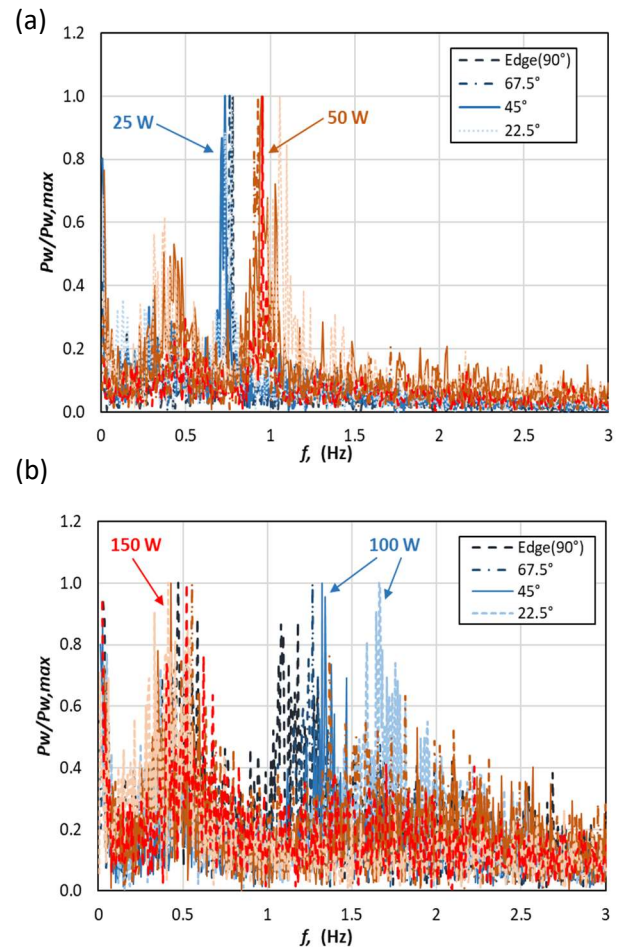


Figure 8. Power spectra from FFT analysis of pressure signals for different inclination angles: (a) at 25 W (blue curves) and 50 W (brown-red curves); (b) at 100 W (blue curves) and 150 W (brown-red curves).

Figure 8 presents the dimensionless power spectra, allowing to plot all curves in the same graphs ($P_w/P_{w,max}$, $P_{w,max}$ being the maximum power spectrum over the frequency range of each series), resulting from the FFT of pressure signals for the four inclination angles (from 22.5° to 90°), and four heat powers applied (25 W and 50 W for figure 8a, and 100 W and 150 W for figure 8b). On the one hand, in the case of figure 8a for the lowest heat loads, the frequency peak is particularly pronounced and almost equal for the four inclinations at 25 W, but it shows a slight divergence for the 22.5° inclination at 50 W. On the other hand, in the case of higher heat loads of figure 8b, the frequency peaks tend to spread and diverge from each other at 100 W, particularly for the 22.5° inclination, and completely fade away for heat loads greater or equal to 150 W: the resulting spectrum becomes close to white noise spectrum, which is more common of classical PHPs operation observed in literature.

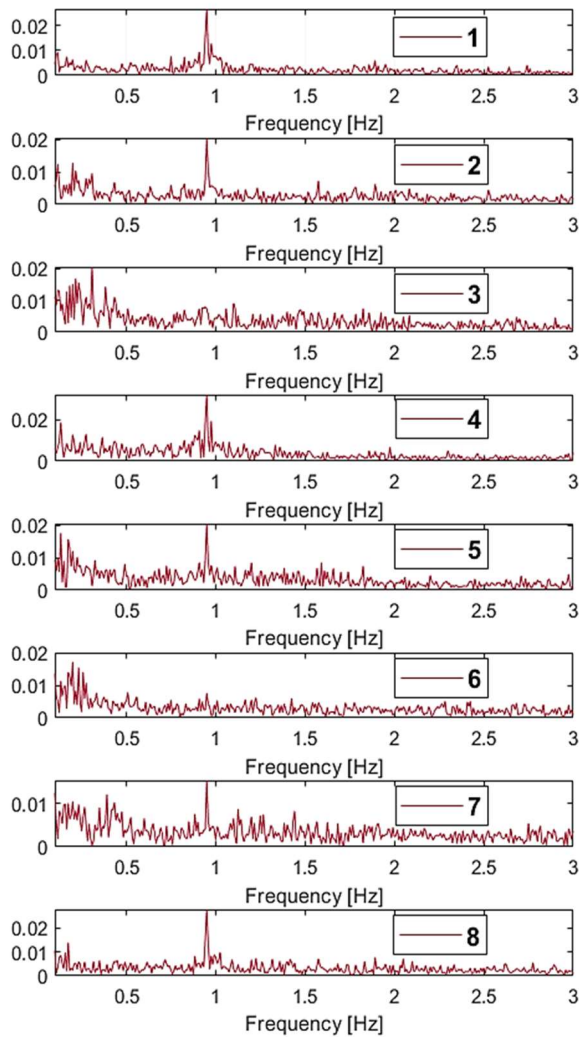


Figure 9. Power spectra from FFT analysis of IR thermographic signals ($\alpha = 90^\circ$; $\dot{Q} = 50$ W).

Note that the power spectrum is also slightly pronounced around 0.5 Hz for both figures. It becomes higher in figure 8b (at 150 W) due to the fact that there is no more dominant frequency, and this ridge, also observed for the lower heat powers, becomes predominant in such dimensionless values. We have no explanation yet on the origin of this frequency peaks (~ 0.5 Hz) at the time of writing this paper.

Figure 9 presents a set of FFT power spectra functions of frequency for the eight IR signals windows recorded in edge inclination at 50 W heat power applied. It can be observed that, as mentioned on figures 6 and 7, the dominant temperature oscillation frequencies peaks are also very pronounced, and are the same for all the U-turns, as well as for the pressure signal (0.95 Hz). Therefore, the oscillations observed for both pressure and resulting temperatures at the outside wall of the FPPHP, fit well together, the first being directly at the origin of the second. There is indeed a transmission of the liquid plugs flow by the spring effect of the vapor bubbles from one turn to another, leading to such detectable periodic behavior of the temperatures signals outside the channels wall (as already observed in [1-4]). Only note that no oscillation dominant frequency was found for U-turns 3 and 6 in the case of figure 9.

Similarly to the pressure signal, the FFT analysis of the IR thermographs signals showed that, for heat powers higher than 100 W, no more dominant frequencies are found whatever the inclination angle. Furthermore, the number of IR windows for which no dominant frequencies are detected increases with increasing heat loads; and the dominant frequencies are also more hardly detectable for IR thermographs signals at 100 W heat power than for pressure signal.

Anyway, increasing heat power implies the vanishing of some dominant frequencies of the pressure signal, leading to some more chaotic flow. It seems that, for low heat flux, the fluid flow is rather governed by gravity forces, triggered by pressure disturbances caused by temperature differences between channels, leading to some periodic oscillating flow as it was observed for heat powers lower than 100 W; whereas the irregular pressure perturbations governed by high heat flux become preponderant above a certain value, although assisted by the gravity pressure head, and leading to some non-periodic oscillating-chaotic flow. Boundary between both –periodic and chaotic- regimes is rather blurry, surely depending on operating conditions (working fluid, filling ratio,

dimensions, temperature, etc.). This point should also be further clarified.

Finally, all the dominant frequencies obtained by FFT analyzes for both pressure (lines) and IR thermographs (markers) signals are plotted in figure 10, together with the error bars corresponding to the peaks flare widths (increasing with heat load). This graph, however, hides the fact that several points from the IR thermographs are nearly perfectly superimposed due to the regularity of the oscillations, as already seen in figure 9. Whatever, values obtained for both signals are very close, those of the IR thermographs being always included in the error bars of the pressure signals.

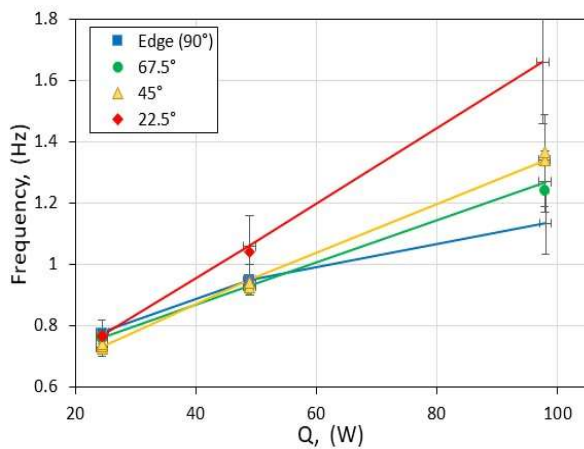


Figure 10. Dominant frequencies of IR thermographic (markers) and pressure (lines) signals as functions of heat power applied for the four orientations ($\alpha = 22.5^\circ:90^\circ$).

Figure 10 confirms that the oscillation frequency peaks increase with increasing heat powers applied and, at a lower level, with decreasing inclination angle. It can be seen that the dominant frequencies differ from each other above 50 W, and seem to follow an increasing trend with decreasing inclination angle (corresponding to a decreasing gravity pressure head). The curve corresponding to an inclination angle of 22.5° (red line and markers) is clearly detached from the others, above 25 W heat power applied. Lastly, for heat loads lower than 25 W, all dominant frequencies converge towards the same value, showing the regularity of the periodic flow regardless of heat flux. From figures 4 and 10, it appears that the edge position is really interesting in that it allows efficient heat transfer even for very low heat flux, with great regularity.

4. Conclusion

In this study, experimental tests were made on a flat plate pulsating heat pipe (FPPHP), filled with SF33 with a filling ratio of 50%, in order to investigate the influence of the inclination angle – from “edge” to horizontal position- and heat power applied on its thermal performances. It was found that the latter increase with increasing angle from horizontal to edge positions, but also decrease with increasing heat power, above 100 W.

A systematic frequency analysis has been performed, using both classical FFT and Wavelet methods, in order to identify the dominant frequencies of heat and fluid flows inside the device, as functions of the operating conditions: inclination angles and heat power applied. The main findings are summarized as follows:

- A comparative study between the two methods showed that both wavelet and FFT analyzes provide similar results, in terms of dominant frequencies.
- The identified dominant frequencies seem independent on the analyzed experimental signal: the agreement between infrared and pressure signals indicates that, at these low levels of frequencies, the fluid flow motions inside the channels of the FPPHP are phased with the resulting thermal response of the wall temperature, even on the external side of the wall.
- The suitability of both signals for estimating the dominant fluid oscillation frequency appears as an opportunity to use either one or the other, depending on instrumentation possibilities.
- The FFT analysis showed that the dominant frequency of the oscillating flow increases with both increasing heat power applied and decreasing inclination angle, from edge (90°) down to horizontal (0°) positions. For heat powers applied below 50 W and inclination angles higher than 45° , the dominant frequencies appear to be independent on the inclination angle.
- Finally, for highest heat power levels and whatever the inclination angle, the dominant frequency tends to fade away: the recorded spectrum becomes closer to white noise spectrum, more typical of classical PHP observations during operation.

Nomenclature

Bo	Bond number	(-)
D	Diameter	(m)
f	Frequency	(Hz)
FR	Feeling ratio	(%)
g	gravity acceleration	(ms^{-2})
P	Pressure	(Pa)
P_w	Power pectrum	(-)
\dot{Q}	Heat power	(W)
R	Thermal resistance	(KW^{-1})
T	Temperature	($^{\circ}C$)
α	Inclination angle	($^{\circ}$)
λ	Thermal conductivity	($Wm^{-1}K^{-2}$)
σ	Surface tension	(Jm^{-2})
ρ	Density	(kgm^{-3})

Acknowledgments

This work has been pursued in the framework of the “Two-phase passive thermal devices for deployable space systems (TOPDESS)” project, financed through the Microgravity Application Program (N. 4000128640) by the European Space Agency. Part of this work was also carried out by CIFRE convention (ANRT program) established between Pprime Institute (Poitiers) and Stellantis (Site de Carrières-sous-Poissy) with the OpenLab Fluidics.

References

- [1] V. Ayel, C. Romestant, Y. Bertin, V. Manno, S. Filippeschi, Visualization of flow patterns in flat plate Pulsating Heat Pipe: influence of hydraulic behavior on thermal performances. *Heat Pipe Science and Technology*, 2014. 5: p. 377.
- [2] Y. Miyazaki, M. Arikawa, Oscillatory flow in the Oscillating Heat Pipe, in: 11th International Heat Pipe Conference, 1999. Tokyo, Japan.
- [3] J.-S. Kim, N.-H. Bui, J.-W. Kim, H. Jung, Flow visualization of oscillation characteristics of liquid and vapor flow in the oscillating capillary tube heat pipe. *KSME International Journal*, 2003. 17: p. 1507.
- [4] F. Pagnoni, V. Ayel, E. Scoletta, Y. Bertin, Effects of the hydrostatic pressure gradient no thermohydraulic behavior of flat plate Pulsating Heat Pipe: experimental and numerical analyses, in 16th International Heat Transfer Conference - IHTC-16, 2018. Beijing, China.

- [5] R-G. Chi, W-S. Chung, S-H. Rhi, Thermal characteristics of an oscillating heat pipe cooling system for electric vehicle Li-Ion batteries. *Energies*, 2018. 11: p.1.
- [6] L. Pagliarini, L. Cattani, F. Bozzoli, M. Mameli, S. Filippeschi, S. Rainieri, M. Marengo, Thermal characterization of a multi-turn pulsating heat pipe in microgravity conditions: Statistical approach to the local wall-to-fluid heat flux. *International Journal of heat and Mass Transfer*, 2021. 169: 120930.
- [7] N. Iwata, F. Bozzoli, L. Pagliarini, L. Cattani, P. Vocale, M. Malavasi, S. Rainieri, Characterization of thermal behavior of a micro pulsating heat pipe by local heat transfer investigation. *International Journal of heat and Mass Transfer*, 2022. 196: 123203.
- [8] S. Khandekar, A. Prasad Gautam, P.K. Sharma, Multiple quasi-steady states in a closed loop pulsating heat pipe. *International Journal of Thermal Sciences*, 2009. 48: p. 535.
- [9] M. Mameli, M. Marengo, S. Khandekar, Local heat transfer measurement and thermos-fluid characterization of a pulsating heat pipe. *International Journal of Thermal Sciences*, 2014. 75: p.140.
- [10] A. Takawale, S. Abraham, S. Sielaff, P.S. Mahapatra, A. Pattamatta, P. Stephan, A comparative study of flow regimes and thermal performances between flat plate pulsating heat pipe and capillary tube pulsating heat pipe. *Applied Thermal Engineering*, 2019. 149: p. 613.

RESULTS OF THE EXPERIMENTAL STUDY ON THE USE OF LOW-TEMPERATURE HEAT PIPES FOR ICE ACCUMULATION

H.Undram¹, Sh.Enkh-Amgalan¹, Doctor (Ph.D)

Mongolia, Ulaanbaatar, Mongolian University of Science and Technology, School of Industrial Technology,
Food Engineering Branch

undram0718@gmail.com; enkhamgalans@yahoo.com

Abstract

Cooling technology is the most important issue in milk and dairy products production. The purpose of this study is to test the possibility of accumulating natural cold using a low-temperature heat pipe and to conduct an experiment on its use in a milk cooling system. The use of the ice that is generated and accumulated with the use of heat pipe in milk cooling equipment does not require additional energy from external sources, has the advantage of reducing operating costs, saving energy, reducing use of refrigerants, and, under possible conditions, eliminates the use of machine cooling. The experiment has shown that a sufficient amount of ice could be formed on the surface of the evaporator when filling 15% of the volume of the heat pipe with refrigerant. For this experiment, a copper heat pipe 1 m long and 22 mm in diameter was used. As a result, an ice cylinder with a mass of 3-4 kg and a diameter of up to 100-120 mm was formed on the surface of its evaporator. We hereby present the results of the experimental study on accumulation of winter cold in ice using low-temperature heat pipe and the use of ice water in milk cooling technology equipment.

Keywords—cold accumulator, heat exchanger, cold capacity, milk cooler,

I. INTRODUCTION

Food refrigeration and storage are still a problem in rural areas where the supply of electricity is limited. On the other hand, one of the many problems facing the world is environmental security and climate change [1]. Climate change continues to negatively affect pastoralism and even the design of engineering structures such as buildings, roads, and bridges. To solve these issues, it is necessary to choose environmentally friendly and efficient models and solutions for refrigeration equipment, as well as to cultivate some technologies in accordance with the specifics of the country.

The cold accumulator method is widely used to balance the daily load of refrigeration equipment. The cold energy stored in the ice reservoir (refrigeration volume) is used to control the level of increasing demand for cold capacity. The use of an ice accumulator reduces the cost of cold capacity and operation of the cooling equipment. Ice is the best accumulator of natural cold, but its production is laborious and costly [4]. The use of heat pipes for the production of ice by accumulating natural cold within refrigeration technology does not require additional energy (other than thermal) and has not only the advantages of reducing operating costs, saving energy and refrigerant use, but also in possible conditions, could eliminate the machine cooling [2].

Cooling and storage of food products, especially milk at small and medium-sized farms, can be carried out by accumulating cold using heat pipes [8]. Since the heat pipe gives off heat to the external cold air in only one direction, when the ambient temperature rises to positive values, the process of cold accumulation i.e. freezing stops, and on the other hand, the heat transfer also stops due to the cessation of the activity of low-temperature boiling refrigerants inside the heat pipe

[2]. This principle will make it possible to use the cold accumulated during the winter to cool food all summer.

The purpose of this research work is to summarize the results of theoretical and experimental studies of the accumulation of natural cold by freezing water using low-temperature heat pipes and using it in the cooling and storage system for dairy products.

II. HEAT PIPE OPERATING PRINCIPLE

The heat pipe is a sealed metal pipe that creates a vacuum system and transfers heat very quickly from the heat source. *Figure 1.*

When the outer surface of the evaporator section of the heat pipe (1) receives heat from the heat source or water in the container (2), the working liquid refrigerant that has impregnated the absorbent material inside the pipe evaporates. At this moment, a pressure difference occurs when the working fluid from a liquid state acquires a gaseous state.

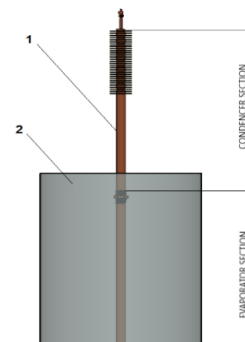


Figure 1. Scheme of ice formation using heat pipe
1- heat pipe; 2-water container

As the pressure increases, the steam flow is directed to the cold zone of the condenser section of the heat pipe.

As the pressure increases, the steam flow is directed to the cold zone of the condenser section of the heat pipe. The condensation zone exchanges heat with the temperature of the surrounding cold air. In the condensation zone, the steam loses heat, liquefies, and leaches into the absorbent material. The condensed and liquefied working fluid returns to the evaporator zone through the capillary channel of the absorbent material. Thus, when the phase flow continues to form a cycle again, the temperature difference between the evaporator and condenser is maintained. As the cooling cycle continues, a layer of ice begins to form on the outer surface of the evaporator. If the evaporator and condenser temperatures get equal, the working fluid in the pipe will become immobile and the heat pipe will stop working. However, as soon as temperature difference occurs, the refrigerant evaporates again and the cold production resumes.

The main advantages of this solution are low operating costs and reduced energy consumption, whereas the disadvantage is a decrease in the boiling point of the refrigerant due to an increase in heat transfer resistance as the ice layer thickens. Also, due to the small heat exchange area, it becomes necessary to intensify the cooling process by forced pumping of chilled water.

Heat pipes have no moving parts, and their robust construction ensures a service life of over 30 years. Due to the very high heat transfer coefficient, the temperature drop in the system is minimal. The maximum thermal conductivity is 10,000–100,000 W/m·K for long heat pipes and about 400 W/m·K for copper [10].

III. RESULTS OF THE WATER FREEZING EXPERIMENT USING A LOW-TEMPERATURE HEAT PIPE

The amount of ice that freezes on the heat exchange surface is important for the process of accumulation of cold and freezing of water. Calculation of the amount of ice that can accumulate and the heat load on the surface of the heat pipe evaporator allows us to determine the time for ice accumulation. Thermal load is determined by the following method [4].

The heat that will be used for freezing the water

$$Q_{ice} = m \cdot (c_{wat} \cdot (t_{wat} - t_{ice.wat}) + \lambda_{ice} + c_{ice} \cdot (t_{ice.wat} - t_{ice})) \quad (1)$$

Here:

c_{wat} – Heat capacity of water, J/(kg · °C);
 $t_{ice.wat}$ – Water temperature at the beginning °C;
 λ_{ice} – Ice heat conductivity, J/kg;
 c_{ice} – Ice heat capacity, J/kg°C;
 t_{ice} – Temperature of frozen ice °C;

Freezing time

$$\tau_{freez} = \left(\frac{Q_{ice} \rho_{ice}}{t_{ice.wat} \cdot t_{ice}} \cdot \left(\frac{\delta_{ice}^2}{2 \cdot \lambda_{ice}} + \frac{\delta_{th}}{\alpha_{ice}} \right) \right) \quad (2)$$

Here:

ρ_{ice} – corresponding density of ice, kg/m³;
 $|t_{ice}|$ – ice temperature, °C;
 δ_{ice} – ice wall thickness, m;
 δ_{th} – thickness of the pipe wall, m;
 α_{ned} – ice thermal conductivity coefficient, Wt/m² · K

The amount of frozen ice on the surface of the heat exchanger

$$m_{ice} = N_{h.p} \cdot \left(\frac{3.14 \cdot (D_{ice}^2 - D_{h.p}^2)}{4} \cdot h_{h.p} + \frac{\pi \cdot D_{ice}^2}{4} \cdot \delta_{ice} \right) \cdot \rho_{ice} \quad (3)$$

Here:

$N_{h.p}$ – heat pipe quantity, ea;
 D_{ice} – outside diameter of frozen ice; m
 $D_{h.p}$ – pipe diameter; m
 h_{ice} – height of the pipe immersed in liquid, m;
 $D_{ice} = D_{h.p} + 2 \cdot \delta_{ice}$

Ice freezing experiment model:

Five experiments were carried out on the accumulation of cold and ice formation of water in a 200-liter cylindrical container using a heat pipe.

Container diameter is 600 mm, and height is 800 mm. Used copper heat pipes numbered 1-12, filled with R134A and R404A refrigerants. The experiment was carried out for 50-60 hours, and during this period the temperature of the outdoor air, heat pipe, water and ice formed on the surface of the pipe was recorded every 2 hours using 4 electronic temperature sensors.

The results of the experiment were processed by graphical, computational, and drawing methods using actual measurement values and calculated values. This includes:

- The geometrical patterns of ice formed on the surface of the heat pipes and the container were consolidated and processed with the actual measured values.

Figure 2

- The correlations of component temperature and air temperature are shown graphically. *Figure 4*
- Based on the results of the experiment, calculations were made for the amount of heat required for freezing ice. *Figure 5*

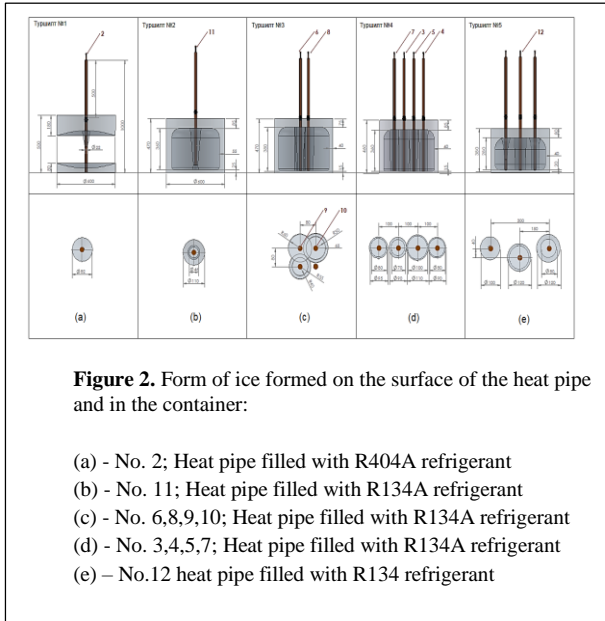
In the experiment, a copper heat pipe was used, the power of which was determined as follows. [2]:

$$N = M_{ref} \cdot (h_1 - h_2) \quad (4)$$

Here:

M_{ref} – weight consumption of refrigerant, kJ/kg
 h_1, h_2 – enthalpies in the vapor and liquid state corresponding to the saturation pressure of the refrigerant, kJ / kg

A. Ice is formed on the surface of the heat pipe and in the container as follows. Figure 2.

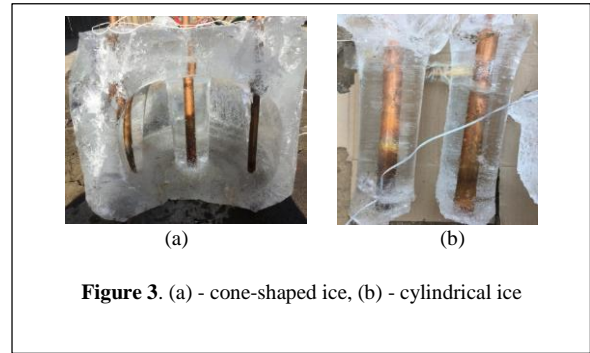


The technical specifications of the heat pipes used in the experiment are shown in Table 1.

TABLE 1. TECHNICAL CHARACTERISTICS OF THE HEAT PIPES

№	Copper heat pipe used in the experiment						
	Pipe diameter, mm	Pipe height, mm	Wall thickness, mm	Charged refrigerant	Pipe weight, g	Weight after filling, g	Heat pipe power, W
1	22	1000	2	R134A	732	832	21
2	22	1000	2	R404A	728	896	31
3	22	1000	2	R404A	722	822	19
4	22	1000	2	R404A	776	876	19
5	22	1000	2	R404A	726	882	29
6	22	1000	2	R134A	742	842	21
7	22	1000	2	R404A	772	886	21
8	22	1000	2	R134A	770	880	23.2
9	22	1000	2	R134A	742	842	21
10	22	1000	2	R134A	730	830	21
11	22	1000	2	R134A	730	830	21
12	22	1000	2	R134A	778	882	22

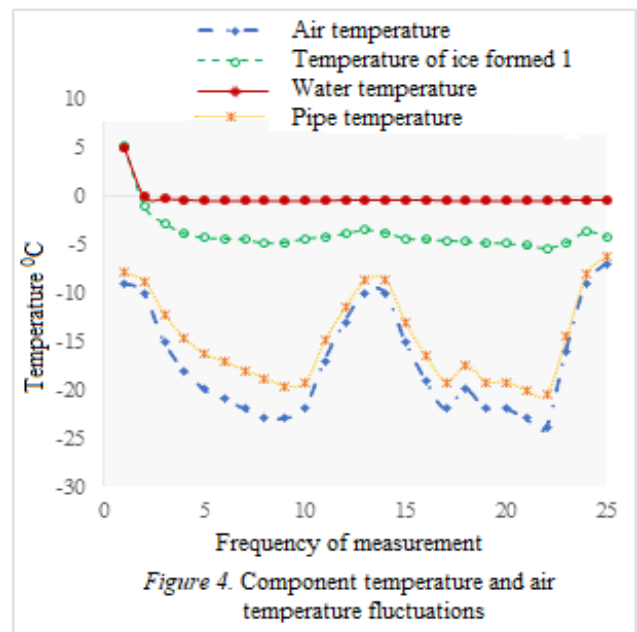
As the temperature of the water near the heat pipe began to decrease due to the evaporation temperature of the refrigerant, crystallization began and ice began to form on the upper surface of the water in the container and around the heat pipe evaporator. The freezing of the surface layer of water inside the container at this time is due to the fact that the freezing point of water in cold air starts from 0°C. During the experiment, the ice formed on the heat pipe evaporator first in a conical shape from top to bottom, and over time, it changed to a symmetrical cylindrical shape. Figure 3.



B. Effect of external air temperature on the efficiency of heat pipes

130 liters of water was poured into a 200-liter cylindrical container, a heat pipe charged with R404A refrigerant was installed, and the temperature was controlled for 46 hours. The air temperature fluctuated in the range of -9 ... -24°C depending on the time of day and night. Within 2 hours after the start of experiment, the ambient temperature reached -10°C, and the surface temperature of the heat pipe evaporator reached -8.8°C. At the same time, a temperature difference occurred in the outward direction from the cylindrical wall of the pipe, which made the water temperature -1.1°C at a distance of 20 mm and -0.1°C at a distance of 120 mm from the heat pipe, and the process of water crystallization and ice formation on the surface of the evaporator began.

The experiment has shown that the increase and decrease in the heat pipe are directly related to air temperature. Although the temperature of the already formed ice will decrease, the temperature of the water remains constant over time. For example, the results of the experiment show that the water temperature is constant in the temperature range from -0.4°C to -0.5°C. (Figure 4).



C. Thermal calculation based on results of experiment

For the calculation of the heat load required for freezing ice, the temperature of the ice formed during the experiment at a distance of 20 mm from the pipe wall was taken as the lowest temperature or -5.4°C .

The calculation results are shown in Fig. 5.

$$\text{Reached the value: } Q_{ice} = 129,766 \cdot \left(4.2 \cdot 10^3 \cdot (5,2 - 0) + 34 \cdot 10^4 + 2.1 \cdot 10^3 \cdot (0 - (-5,4)) \right) = 48426,076 \text{ kJ}$$

It's 2.23 days after the ice formation,

$$\tau_{freez} = \frac{48426,076 \cdot 917,5}{0 + |-5,4|} \cdot \left(\frac{0.044^2}{2 \cdot 34 \cdot 10^4} + \frac{0.002}{0.085} \right) = 2,23 \text{ days}$$

which shows that as the thickness of the ice increases, the amount of heat needed for it increases.

The total amount of ice formed by the heat pipe depends on the number and diameter of the heat pipe, the height submerged in the liquid, and the outside diameter of the cylindrical ice formed on the surface of the pipe:

$$m_{ice} = 1 \cdot \left(\frac{3,14 \cdot (0,11^2 - 0,022^2)}{4} \cdot 0,36 + \frac{3,14 \cdot 0,11^2}{4} \cdot 0,044 \right) \cdot 917,5 = 3,4 \text{ kg.}$$

$$D_{ice} = 0,022 + 2 \cdot 0,044 = 0,11 \text{ m}$$

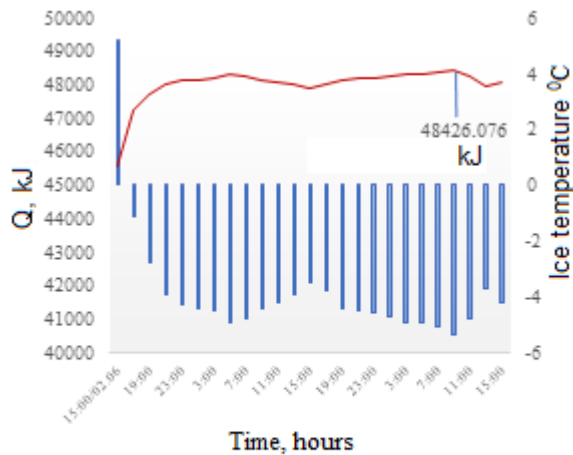


Figure 5. The relationship between the heat and ice temperature used to form ice over time

As the outer diameter of the ice increases, the ice becomes denser and stronger, and there is a decrease in the temperature shift of the ice outward from the pipe wall.

IV. RESULTS OF EXPERIMENT ON MILK COOLING EQUIPMENT

Experiment model of a milk cooling equipment

When milk is cooled to $8...10^{\circ}\text{C}$, the growth of microorganisms in it decreases sharply. Immediately after milking, milk should be cooled to $4...5^{\circ}\text{C}$, and milk stored at this temperature retains its original properties for 1.5-2 days [7]. Therefore, the immediate cooling of milk on the farm is one of the most important and necessary technological processes.

During the summer months, milk yields increase from May to September, but milk quality usually deteriorates due to poor refrigeration and on-site storage and often turns sour [11].

We have developed and tested a scheme of a heat pipe milk cooling equipment to accumulate the cold of Mongolia's winter season and cool the milk to $4...5^{\circ}\text{C}$.

Figure 6 shows a technological equipment for cooling milk using the accumulated cold, i.e. ice water.

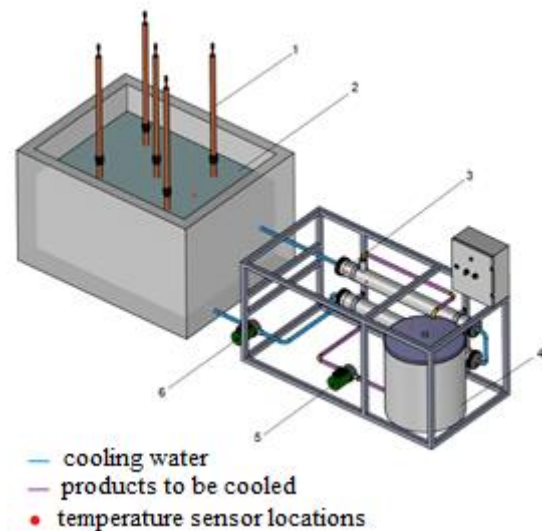


Figure 6. Scheme of equipment for cooling milk with an accumulated cold using the heat pipe.

1-heat pipe; 2-ice water; 3-heat exchanger; 4-container for milk storage; 5-pump for pumping milk; 6-water pump

Modern environmental requirements for refrigeration equipment are more focused on the use of energy-efficient and environmentally friendly refrigerants. In order to comply with the above requirements, we have designed and developed a simple milk cooler consisting of the following components. This device is equipped with a heat pipe filled with R134A, R404A refrigerant (1), thermally insulated ice storage tank (2), a heat exchanger (3), milk storage container (4), pump for liquid (5), (6), electrical automation parts and temperature measuring instruments.

The heat exchanger, which is part of the device, consists of two surfaces with a diameter of Ø100 mm and 7 stainless steel pipes with a diameter of Ø19 mm embedded in a grid. *Figure 7.*

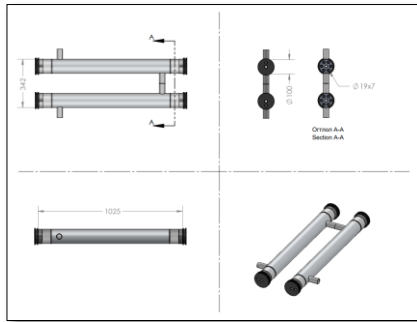


Figure 7. Two-stage heat exchanger with a set of pipes

Automation is set to automatically turn off when the milk cools and reaches a temperature of 5°C and restarts when the milk temperature rises to 7°C.

We have developed and tested a temperature measurement device programmed on the Arduino platform to measure temperature at 5 points and store information in memory.

The ice generated by the heat pipe was used to test the milk cooling equipment, and the container was covered with styrofoam and a special thermal insulation material. A floating rubber tube filled with nitrogen gas was placed above the surface of the container. *Figure 8.*

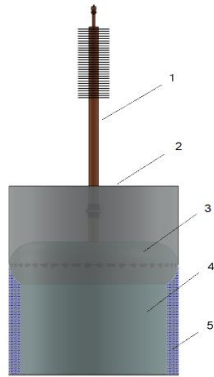


Figure 8. Thermal insulation with a nitrogen-filled tube during freezing ice with the heat pipe.
1-heat pipe; 2-container; 3-nitrogen-filled tube; 4 ice; 5-ice water.

This nitrogen-filled tube insulates the resulting ice cylinder and container wall from cold air, i.e. low atmospheric temperatures. As a result, the ice formed on the heat pipe and in the container is prevented from adhering to the container wall, and the ice water layer is successfully formed (ice height - 0.32 m, ice diameter - 0.52 m, weight - 62.2 kg, ice water volume - 40 liters). The experiment was carried out 4 times during December and January in the following ways.

Prepared 30 liters of milk at 37°C in a cooling pot. At this time, the temperature of the ice water around the ice formed by the heat pipes was 0 ...-1°C. Water consumption is 36 liters/min. Temperatures were

measured at the following 6 points during the experiment. *Figure 7.*

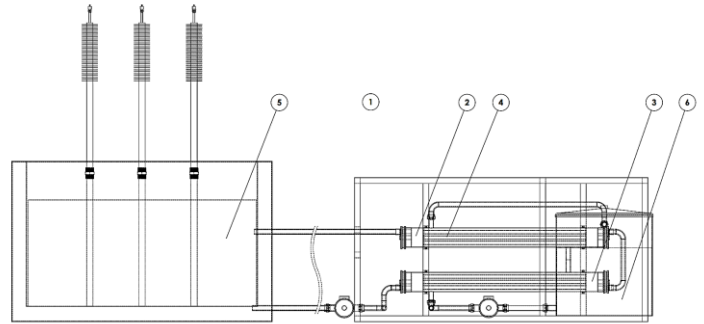


Figure 9. Locations of the temperature measurement points

The locations of the points are indicated in table 2.

Table 2. Locations of the temperature measurement points

№	Measurement points	Temperature at the beginning of the experiment, °C	Temperature at the end of the experiment, °C
Point 1	Air temperature	18°C	15°C
Point 2	Boiling point of ice water	14°C	5°C
Point 3	Temperature of ice water at the supply of the 1st stage of the heat exchanger	13°C	7°C
Point 4	Boiling point of milk	18°C	7°C
Point 5	Temperature of ice water in a container with a heat pipe	1°C	2°C
Point 6	Milk temperature	37°C	5°C

The cooling process lasted an average of 25 minutes at a time until the product was cooled to a predetermined temperature of 5°C and was performed 4 times. At a room temperature of 18°C, the milk maintained the temperature of -5...-6°C for 32 minutes, and when the milk temperature rose to 7°C, the device worked automatically again.

The amount of milk to be cooled by the ice accumulated with the heat pipe and the heat consumption are determined by the following formula. This includes:

$$G_{\text{milk}} = \frac{L \cdot I_{\text{ice}}}{c_{\text{milk}} \cdot (t_1 - t_2)} \quad (5)$$

G_{ice} – ice consumption, kg/s

c_{milk} – heat capacity of milk, J / (kg · °C)

t_1, t_2 – initial and final temperature of the product to be cooled, °C

I_{ice} – latent heat of ice melting, J/kg

Heat consumption for milk cooling,

$$Q = G_{\text{milk}} \cdot c_{\text{milk}} \cdot (t_1 - t_2) \quad (6)$$

From this:

$$G_{\text{milk}} = \frac{62,22 \cdot 333700}{3900 \cdot (37 - 5)} = 166 \text{ litres}$$

$$Q = 166 \cdot 3900 \cdot (37 - 5) = 20716,8 \text{ kJ}$$

From 62.2 kg of ice created during the experiment, it is possible to cool $G = 166$ liters of milk, and to cool this amount of milk $Q = 20716$ kJ of heat would be required. For example, if the milk of a small farm with a capacity of 1 ton per day is cooled with accumulated ice according to the above calculations, then 374.7 kg or 0.4 m³ of ice can be accumulated per day and 58.4 m³ of ice would be required for 365 days of the year.

V. CONCLUSION

We have developed technical solutions for ice accumulation with heat pipes using natural cold and showed the possibilities of their use for cooling milk and liquid products. The heat pipe is a sealed system with no moving parts with an average service life of about 30 years, it is energy efficient and reliable compared to machine cooling, thus reducing operating costs.

The experiment has proved that an adequate amount of ice can be formed in the evaporator zone of the heat pipe. There is a possibility to reduce the use of refrigerant, since the heat pipe is filled with refrigerant only 15% of its volume.

On the surface of the heat pipe evaporator with a diameter of Ø22 mm and a length of 1 m, filled with refrigerants R404A and R134A, it is possible to form 3-4 kg ice cylinders with a diameter of 100 mm. From 62.2 kg of ice generated during the experiment, it is possible to cool $G = 166$ liters of milk and to cool this amount of milk, $Q = 20716$ kJ of heat is required.

Placing a nitrogen-filled rubber float tube during ice formation with a heat pipe insulated the container wall and the resulting ice cylinder from the cold outside air temperature and prevented the ice from adhering and freezing to the container wall and allowed an ice water layer to form.

It was calculated that 58.4 m³ of ice accumulated with heat pipes could meet the annual milk cooling requirement of a small dairy farm with a capacity of 1 ton.

VI. ACKNOWLEDGMENT

We express our sincere gratitude to the Ministry of Nature, Environment and Tourism and the staff of the project "National Capacity Building to Improve the Planning Process for Climate Change Adaptation" (NAP), a joint project of the United Nations Environment Program (UNEP).

REFERENCES

- [1] D.Dulamsuren, "International legal norms for the protection of the ozone layer and Mongolia", thesis for the master's degree. Ulaanbaatar, 2020. p.87
- [2] Sh.Enkh-Amgalan, "Experimental study of soil freezing in food cellars with low-temperature heat pipes", Dissertation for the degree of Doctor (Ph.D). Ulaanbaatar, 2009. p.167
- [3] A.L. Sintsov, "Analysis of cold accumulation," Security in the technosphere, No. 6 (November–December), 2015. DOI: 10.12737/17552
- [4] M.V. Shamarov, "Modeling a cold accumulator based on heat pipes," Izvestiya Universities. Food technology, № 1, 2010
- [5] Bala Abdullahi, Raya K. Al-dadah and Sa'ad Mahmoud, "Thermosyphon Heat Pipe Technology," 1 Department of Mechanical Engineering, Kano University of Science and Technology (KUST), Wudil, Kano, Nigeria 2 School of Mechanical and Manufacturing Engineering, University of Birmingham, United Kingdom, 2019, pp.2-8
- [6] Xiao Ping Wua, Masataka Mochizuki, Koichi Mashiko, Thang Nguyen, Tien Nguyen, Vijit Wuttijumnong, Gerald Cabusao, Randeep Singh, Aliakbar Akbarzadeh, "Cold energy storage systems using heat pipe technology for cooling data centers," R&D Department, Thermal Technology Division, Fujikura Ltd, Tokyo, 1-5-1, Kiba, Koto-Ku, Tokyo 135-8512, Japan, March-2011
- [7] A.P. Petrov, "Guidelines for the implementation of a course project on the mechanization of animal husbandry," Cheboksary, 2014. p.32
- [8] K.G. Sergeevich, "Development and justification of a water-circulating ice accumulator for dairy farms," Abstract of the dissertation for the degree of candidate of technical sciences. Orenburg, 2015. p.21
- [9] Pavel Kuznetsov, "Cold storage in low temperature technology" ITMO University, Thermal storage system project, June-2018.
- [10] "Heat pipes for thermal management" Advanced cooling technologies, The thermal management
- [11] Kh. Giimaa, "Production, supply and processing of milk", Mongolian Association of Food Industry Workers, Dairy Industry Sustainable Development Council. Ulaanbaatar, 2014

Numerical investigation of the influence of size, condensation and evaporation coefficients on the power of the heat pipe

Richard Lenhard^{1*}, Natália Holešová¹, and Katarína Kaduchová¹

¹ *Department of Power Engineering, Faculty of Mechanical Engineering, University of Zilina, Zilina, Slovakia*

**Corresponding author email address: richard.lenhard@fstroj.uniza.sk*

Abstract

Evaporation and condensation are classified among the most important and most used multiphase flows in a wide range of engineering systems for their optimal and safe operation. With the rapid progress in engineering technologies, the requirements for the accuracy of the calculations of these physical phenomena that take place in them have also increased. Multiphase flow is difficult to detect only by experimental measurements, therefore numerical simulations with physical models are also used, which contribute to a better understanding of these complex phenomena of phase transformations. Nowadays, ANSYS Fluent software is most widely used for modelling multiphase flows with heat and mass transfers, in which Lee's model is also used for modelling evaporation and condensation processes. Lee's model contains correlation coefficients – condensation and evaporation coefficient, which are specific to each numerical simulation. The article deals with the analysis, influence, and comparison of these correlation coefficients in the numerical simulations of a heat pipe, where their maximum and minimum values were tested.

Keywords: Evaporation, Condensation, Multiphase flow, CFD, Lee model

1. Introduction

Phase transformations such as evaporation and condensation play an important role in the engineering industry. Water vapor and vapors of other pure substances are often used as working fluids of energy transformation cycles. However, the world is currently developing the use of multicomponent media, especially in high-performance systems. As the condensation of multi-component vapors is inherently much more complex, basic studies are necessary before designing an industrial system, both from the point of view of thermodynamics and from the point of view of heat transfer. Collaboration between basic research and structural engineering is becoming more important. Clearly, with our rapid progress in engineering technology, the demands for progressive and accurate predictions of the systems of interest have also increased. Optimal design, prediction of operating limits and very often safe control of many important systems depends on the availability of realistic and accurate mathematical models of two- or multiphase flows.

A unique characteristic of two-phase or two immiscible mixtures is the presence of one or more interfaces, which are separating the phases or components.

The classification of two-phase flows based on the interface structures and the topographic distribution of each phase is complex because these changes in the interface structure occur continuously. Therefore, a classification based on the standard flow regimes examined by Wallis [1], Hewitt and Hall Taylor [2],

Collier [3], Govier and Aziz [4] are often used and the main classification of two-phase flows according to Ishii [5] and Kocamustafaogullari [6].

Condensation and evaporation phenomena are also included to multiphase flows. It is very important to recognize the correct type of condensation and evaporation occurring in the investigated system. Condensation that occurs in contact with a solid surface can be in two types: droplet or film condensation. The wettability of the solid surface determines which of these two types of condensation takes place in investigated system.

When liquid, which was created by condensation process, wets a solid surface for example wall with continuous condensate, it is a film condensation. Condensate flows down the wall surface due to gravitation force, shear force caused by steam flow or other forces. The rate of heat transfer through film condensation is determined by the thickness of the film of condensate, which in most cases forms the largest part of the thermal resistance.

But this is not applied for the situation when in investigated system occurs the dropwise condensation. It takes place when a continuous condensate does not form after wetting the solid surface, it does not spread, it just forms separated drops. In the work of Hartnett and Irvine [7] is described the cycle of droplet condensation, which consists of four sub-processes and in their work is also described the criterion of wettability and how important it is to take into account the surface tension of liquids during condensation processes.

Film condensation

If film condensation occurs on a solid surface, in most cases the greatest thermal resistance to heat transfer is caused by the condensate film. Nusselt [8] was the first who was focused on film condensation and whose analysis and simplified models are still used till today. For example, formulas for condensation on a vertical flat plate and also for horizontal circular tube were derived by Nusselt:

$$h = \frac{\dot{q}}{T_s - T_w} = \sqrt[4]{\frac{g\rho_l^2 k_l^3 h_{fg}}{4\mu_l(T_s - T_w)z}} \quad (1)$$

where h is the local heat transfer coefficient at a distance z from the top of the plate, \dot{q} is heat flux, T_s and T_w are temperatures of saturation and wall, g is gravitational acceleration, ρ_l is density of liquid, k_l is liquid thermal conductivity, h_{fg} is latent heat of condensation, μ_l is viscosity of liquid and z is coordinate.

Many authors modified the Nusselt analysis, for example Rohsenow et al. [9], who supplemented this analysis by the effect of buoyancy force acting on the same film, significant temperature transfer in the condensate flow, and non-linear temperature distribution in the condensate layer.

Some of the authors used Maxwell's velocity distribution for their research, which is applied when the gas is in a uniform steady state and its macroscopic properties do not change with time or position. The function has the form:

$$f = n \left(\frac{1}{2\pi RT} \right)^{\frac{3}{2}} \exp\left\{ -\frac{1}{2RT} (U - \bar{U})^2 + (V - \bar{V})^2 + (W - \bar{W})^2 \right\} \quad (2)$$

where \bar{U} , \bar{V} , \bar{W} are velocity components due to global mass motion of the total system and R is the gas constant. This theory was used by Schrage [10], whose analysis is easy for understanding and based on a few assumptions for simplification. An overall summary of the individual assumptions of several authors and their complete analysis is provided in the article of Rohsenow [11].

If the Maxwell distribution applies in the system, the net condensation rate \dot{m} per unit area has the following relation:

$$\dot{m} = \sigma_c \Gamma \frac{P_v}{\sqrt{2\pi RT_v}} - \sigma_e \frac{P_i}{\sqrt{2\pi RT_i}} \quad (3)$$

where Γ corresponds to progress of the vapor as a whole toward the surface as long as net condensation takes place. P_i is saturation pressure to T_i and P_v is the vapor pressure at the liquid surface and saturation pressure to T_v .

σ_c and σ_e are the coefficients of condensation and evaporation and they are representing the fraction of molecules captured by the liquid and molecules which actually leaved the surface.

Many authors have tried to modify this relation. For example, Tashiwa [7] described the relation he created under the condition that the condensation and evaporation coefficients are equal and therefore the temperatures $T_v = T_i$ are also equal. Hung [12] concluded that the relation lacks information about molecules hitting the surface at low grazing angles, but his theory has never been verified either theoretically or experimentally. Currently, the relation of Labuntzov and Kryukov [13] is most often used to describe mass transfer at liquid – vapor interface, but it is only valid if the condensation coefficient is close to unity. In their research, the Knudsen layer and the gas-dynamic flow region are mentioned, and the overall relation has the form:

$$\dot{m} = 1.67 \frac{P_v - P_i}{\sqrt{2\pi RT_v}} \left\{ 1 + 0.515 \ln \left[\frac{P_v}{P_i} \left(\frac{T_i}{T_v} \right)^{1/2} \right] \right\} \quad (4)$$

Numerical simulations of multiphase flows

Numerical simulations can contribute to a better physical understanding of the complex phenomena of phase transformations - evaporation and condensation. The ANSYS Fluent program is currently the most widely used software for CFD analysis, which enables the modelling of multiphase flows with heat and mass transfers.

Many methods have been proposed to simulate the problem of phase changes of two- and multiphase flows for vapor – liquid, such as Hirt and Nichols [14], which have used the volume method of fluid (VOF), as well as Huang, Wu and Chen [15] and Youngs [16]. The level adjustment method (LS) has been discussed by Osher and Sethian [17], Osher and Fedkiw [18] and Wang, Sun, Wong, Fukuda, and Ando [19].

The VOF method has the inherent property of preserving mass, it more easily captures the interface with the thermal transfer of phase change [20]. The mass conservation function is particularly important in solving phase change problems [21]. Therefore, it is a good choice to use the VOF method. Currently, the Fluent code uses the VOF method to solve two-phase flows. However, the default VOF method cannot simulate heat and mass transfer through the phase interfaces. To overcome this shortcoming, it is necessary to add a phase change model to the source concepts in the control equations using user-defined functions (UDFs).

There are already many different types of phase change models. The use of empirical expressions to quantify interfacial heat and mass transfer appears to be a common way of modelling phase change phenomena [22,23]. This approach is indeed applicable to certain simple geometries but is limited to any other more complex geometries [24].

The phase change model proposed by Lee [25] is the most commonly used. Mass transfers are given by the following relationships:

If $T_l > T_{sat}$ (evaporation):

$$\dot{m}_{lv} = \lambda_c \alpha_l \rho_l \frac{T_l - T_{sat}}{T_{sat}} \quad (5)$$

if $T_v < T_{sat}$ (condensation):

$$\dot{m}_{vl} = \lambda_c \alpha_v \rho_v \frac{T_{sat} - T_v}{T_{sat}} \quad (6)$$

where T_l , T_v are liquid and vapor temperatures (K), T_{sat} is the saturation temperature (K), \dot{m}_{lv} , \dot{m}_{vl} are the mass flows during evaporation and condensation ($\text{kg}\cdot\text{s}^{-1}$), α_l , α_v are the heat transfer coefficients during evaporation and condensation ($\text{W}\cdot\text{m}^{-2}\cdot\text{K}^{-1}$), ρ_l , ρ_v are the densities of the liquid / vapor ($\text{kg}\cdot\text{m}^{-3}$) and λ_c indicates the mass transfer intensity factor (s^{-1}). It is recommended that the value of λ_c will be such as to keep the interfacial temperature reasonably close to the saturation temperature and to avoid divergence problems.

As an empirical coefficient, λ_c has different values for different situations. In the numerical studies of Wu et al. [26], De Schepper et al. [27] and Alizadehdakhl et al. [28], λ_c was set to 0.1 and 1 to keep the interface temperature numerically close to the saturation temperature. However, in the works of Yang [29] and Fang [30], λ_c was specified at a different value, 100 s^{-1} .

To avoid empirical statements and empirical coefficients, scientists have necessarily developed a purely theoretical and proven formulation that explicitly addresses the problems of phase change. Fourier's law as a theoretical formulation can be used to estimate the jump of the interfacial heat flux and to determine the corresponding latent heat transfer flux.

Many authors have developed their own program codes to simulate phase change problems, such as Welch and Wilson [20] and Guo et al. [31]. The key point of these models is the accuracy of the heat flux calculation on both sides of the interface. These models can accurately simulate evaporation and condensation issues. However, the implementation process is very complicated, which limits the extension of these models to Fluent code.

In the work of Ganapathy [24], Nichita [32] and Mao [33], the phase change model was derived and implemented in Fluent code. However, this model has several shortcomings. For example, the bubble growth rate is not relevant to the thermal conductivity of the λ_v pair in the saturated bubble growth process in the superheated liquid. However, the equation contains information about λ_v that does not correspond to the actual physical phenomena. To overcome the above shortcomings, the current authors proposed in 2012 a phase change model [34] in which mass transfer occurs

at the phase interface. However, in this model, the interfacial mass transfer flows are distributed in the region of the final thickness close to the interface, which reduces the accuracy of the calculation.

In article of Sun, Xun and Wang (2012) [34], a new phase change model based on the Fluent volume method (VOF) in the Fluent code is created to further improve accuracy. Finally, the accuracy of this new phase change model reveals two evaporation problems and one condensation problem.

From what has been mentioned so far, it follows that research focused on the analysis of correlation coefficients, the so-called the condensation coefficient and the evaporation coefficient is still necessary and there is still no sufficiently correct relation, which would include all the necessary variables that affect the resulting value of these phase change coefficients and also the processes of evaporation and condensation itself.

This article describes the theory of condensation and evaporation coefficients and their application to a 2D model of a heat pipe in the ANSYS Fluent program, specifically to the Lee model for multiphase flows, where it is proven how they affect the processes of evaporation and condensation in numerical simulations.

2. Numerical simulation of multiphase flow in an enclosed space

A 2D heat pipe consisting of an evaporative, adiabatic, and condensing section was used as a model, which was necessary for the numerical simulation of multiphase flow in a closed space during evaporation and condensation processes. The heat pipe contained water, steam, and air. The main dimensions and detail of the 2D model are shown in Figure 1. and Table 1.

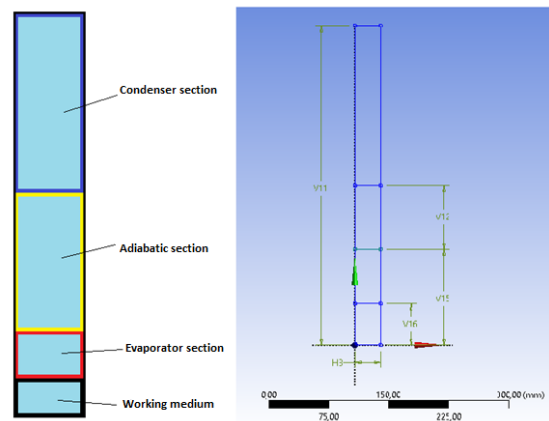


Figure 1. Detail of 2D model of heat pipe

Table 1. Dimensions of heat pipe

V11	400 mm	V15	120 mm
V12	80 mm	V16	52 mm
H8	32 mm		

During condensation and evaporation in closed spaces, it is important to thicken the mesh in places where there are changes of state-interphases, i.e., in the place above the working medium where the process of evaporation and condensation occurs and on the inner walls of the heat pipe.

A square mesh with 57 256 cells was used to create the 2D model of the heat pipe. The Evaporation – Condensation model was used to describe the multiphase heat transport of mass, the settings of which are contained in the following tables with a description of the parameters of boundary, operational, material, and other key conditions. Data are obtained from experimental measurement and used as input values for numerical simulation. The values of the coefficients of evaporation and condensation are set to 0.1 s^{-1} and 10 s^{-1} , which describe in the best our experimental measurements.

In Table 2. are described boundary conditions for walls in sections:

Table 2. Boundary conditions

Name	Set parameters		
	Velocity [m.s ⁻¹]	Temperature [°C]	Temperature flow [W.m ⁻²]
cond_wall	0	10	–
adiab_wall	0	–	0
evap_wall	0	200	–

Table 3. Operational conditions

Pressure [Pa]	Boiling temperature [°C]	Gravitation [m.s ⁻²]
20 000	60	- 9.81

Table 4. Material conditions

Material	Density [kg.m ⁻³]	Thermal capacity [J.kg ⁻¹ .K ⁻¹]	Thermal conductivity [W.m ⁻¹ .K ⁻¹]	Dynamic viscosity [kg.m ⁻¹ .s ⁻¹]
Air	1.225	1 006.43	0.0224	1.7894×10^{-5}
Water	998.2	4182	0.6	1003
Mixture	0.13	*	0.0261	1.34×10^{-5}

$$*c_p(T) = 1563.077 + 1.603755T - 0.002332784T^2 + 3.216101 \times 10^{-6}T^3 - 1.156527 \times 10^{-9}T^4$$

Table 5. Material conditions

Material	Molar mass [kg.kmol ⁻¹]	Enthalpy [J.kmol ⁻¹]	Reference temperature [°C]
Air	28.966	0	25
Water	18.0152	0	25
Mixture	18.01534	4.399×10^7	25

Table 6. General conditions

Space dimension	Precision	Flow	Setting of the model
2D	double	Non-stationary	evaporation - condensation: $T_{\text{sat}} = 60 \text{ °C}$, $\lambda_l = 0.1 \text{ s}^{-1}$, $\lambda_v = 10 \text{ s}^{-1}$
		Non-compressible, laminar	Multiphase model: mixture Liquid phase = water, Gaseous phase (mixture) = water vapor + air

Table 7. Setting of the solution

Type	Coupling	Discretization	Transient formulation
Pressure-based	Simple	1st order upwind	1st order implicit

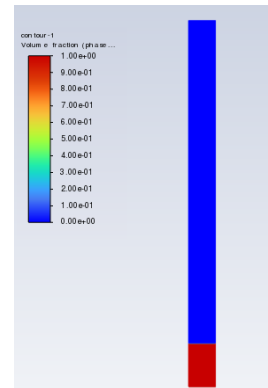
Table 8. Under-relaxation factors

Under-relaxation factors	
Density	0.9
Body Forces	0.9
Pressure	0.3
Momentum	0.7
Species	0.9
Energy	0.7
Volume Fraction	0.5
Slip Velocity	0.1
Vaporization Mass	0.9

Table 9. Setting of the solution

Time stepping method	Time step size	Number of time steps	Max iterations
Fixed	0.001	10 000	20

Initialization belongs to one of the most important parts of the settings, where it was necessary to correctly patch the phases where water and air are situated at the beginning. Figure 2 shows a contour of Volume Fraction of heat pipe and patched areas where the mentioned fluid areas are located.

**Figure 2.** Initial state of Volume Fraction from stationary simulation; phase-1 is water

3. Results of numerical simulation

All numerical simulations were set to 10 000 numbers of time steps and 0.001 time step sizes. The processes that take place in the heat pipe for the first 10s were calculated. In the optimized model, bubbles were formed at the bottom of the tube in the first 10s. The detail of forming bubbles is shown in Figure 3.

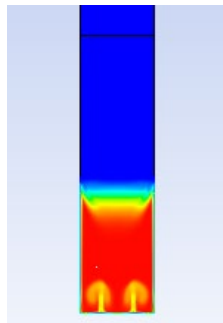


Figure 3. The presence of steam bubble in the bottom of heat pipe

In Figure 4. are shown contours of volume fractions of water at times 1s, 2s, 5s and 10s. At the beginning of the simulation, the water component with a value of 1 was located in the lower part of the heat pipe – in the working medium section (Figure 2). After the start of the simulation, the water was gradually heated and mixed until bubbles began to form in the nucleation cores at the bottom of the vessel, but they disappeared in the liquid volume and did not rise to the surface of the working medium. The value of the condensation coefficient was set to $0.1s^{-1}$ and the evaporation coefficient to $10s^{-1}$.

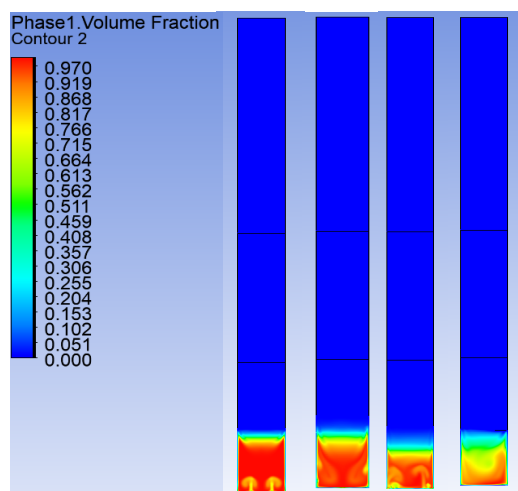


Figure 4. Contours of Volume fraction at the times 1s, 2s, 5s, 10s
Coefficient of condensation: $0.1s^{-1}$
Coefficient of evaporation $10s^{-1}$

Figures 5. and 6. show how the investigated coefficients affect the process of evaporation and condensation. In the first case, when the coefficient of condensation is $10^{-3}s^{-1}$ and the coefficient of

evaporation is 10^2s^{-1} , it is possible to see that the process of evaporation of the working medium is very slow, while in the second case, when the coefficient of condensation has value 10^2s^{-1} and the coefficient of evaporation is $10^{-3}s^{-1}$ all the water was evaporated already after 2s of simulation.

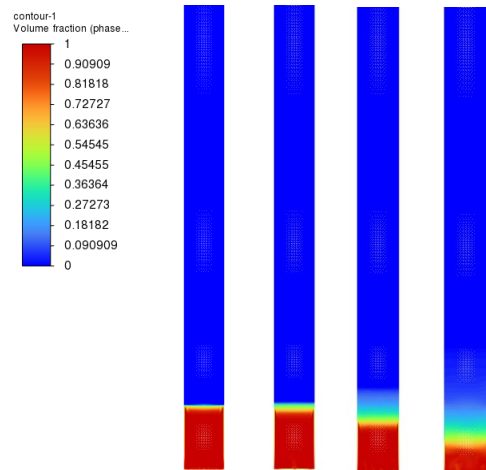


Figure 5. Contours of Volume fraction at the times 1s, 2s, 5s, 10s
Coefficient of condensation: $10^{-3}s^{-1}$
Coefficient of evaporation 10^2s^{-1}

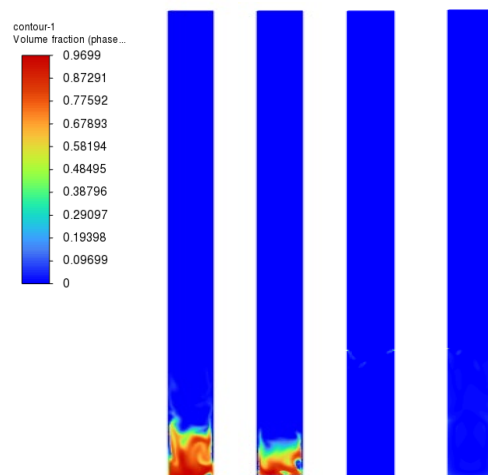


Figure 6. Contours of Volume fraction at the times 1s, 2s, 5s, 10s
Coefficient of condensation: 10^2s^{-1}
Coefficient of evaporation $10^{-3}s^{-1}$

Numerical simulations of the same model with the same external conditions identical to the experimental measurement showed that just by changing the evaporation and condensation coefficients, the phase change processes in the heat pipe either accelerated or slowed down. It follows that it is very important to fine-tune these coefficients so that they correctly represent the real experiment.

4. Conclusion

The article analyses the coefficients of condensation and evaporation in multiphase flows, which influence the processes of condensation and evaporation. Many authors have tried to find an exact definition of these coefficients, but it has not been created till today. They are mostly based only on the assumptions that the authors modify for their researched issue, and the range of values of these coefficients is then determined from them. The environment of ANSYS Fluent contains several models that can be used to set parameters for multiphase flows. One of them is Lee's model, which is able to capture and calculate interphase phenomena in the processes of condensation and evaporation and it is possible to set values for these two coefficients. In Lee's model, the coefficients of evaporation and condensation can reach values in the range from 10^{-3} to 10^2 .

The aim of the article is to show how the selected values of these coefficients influence the simulation in the ANSYS Fluent and the evaporation and condensation processes itself. Simulations were created in which the values of the coefficients reached their maximum and minimum values compared to the optimal values, which were set to represent the experimental measurement as well as possible. It has been proven that the values of the coefficients either speed up or slow down the processes of evaporation and condensation. Since these coefficients depend on many factors, it is necessary to continue their analysis and modifications, and of course, numerical simulations must also be continued with 3D models, from which it will be possible to create correlation graphs, which would show the dependences of condensation and evaporation coefficients on external conditions, and then it will be possible to adapt the CFD simulation to the real experiment as much as possible.

Acknowledge

This research is supported by the project KEGA 047ŽU-4/2022 Innovative approaches to fluid dynamics modelling in energy systems and KEGA 046ŽU-4/2021 Innovative methods of increasing the thermal efficiency of small heat sources using heat recovery through phase transformations.

References

- [1] Wallis G. B. (1969): One-dimensional Two-phase Flow, McGraw-Hill Book Co.
- [2] Hewitt G., Hall Taylor, N. S. (1970): Annular Two-phase Flow, Pergamon Press, Oxford.
- [3] Collier J. (1972): Convective Boiling and Condensation, McGraw Hill, London.
- [4] Govier G. W., Aaziz K. (1972): The Flow of Complex Mixtures in Pipes, Van Nostrand Reinhold Co., New York.
- [5] Ishii M. (1971): Thermally Induced Flow Instabilities in Two-phase Mixture in Thermal Equilibrium, Ph.D. Thesis, Georgia Institute of Technology.
- [6] Kocamustafaogullari G. (1971): Thermo-fluid Dynamics of Separated Two-phase Flow, Ph.D. Thesis, Georgia Institute of Technology.
- [7] Hartnett J. P., Irvine T. F., Jr. (1991): Advances in heat transfer, Academic Press, INC., Volume 21, ISBN 0-12-020021-X
- [8] Nusselt W. (1916): Die Oberllachenkondensation des Wasserdampfes. Z. VDI 60,541,569
- [9] Rohsenow W. M. (1956): Heat transfer and temperature distribution in laminar film condensation. Trans. ASME 78
- [10] Schrage R. W. (1953): A Theoretical Study of Interface Mass Transfer. Columbia Univ. Press, New York
- [11] Rohsenow W. M. (1973): Film condensation of liquid metals. Prog. Heat Mass Transfer 7, 469
- [12] Huang Y. S. (1971): Heat transfer by condensation of low-pressure metal vapors, PhD. Thesis, Case Western Reserve Univ., Cleveland, Ohio
- [13] Labuntzov D. A., Kryukov A. P. (1979): Analysis of intensive evaporation and condensation. Int. J. Heat Mass Transfer 22, 989
- [14] Hirt C. W., Nichols B. D. (1981): Volume of Fluid (VOF) Method for the Dynamics of Free Boundary, J. Comput. Phys., vol. 39, pp. 201–225.
- [15] Huang M., Wu L. L., Chen B. (2012): A Piecewise Linear Interface-Capturing Volume of-Fluid Method Based on Unstructured Grids, Numer. Heat Transfer B, vol. 61, pp. 412–437.
- [16] Youngs D. L. (1982): Time-Dependent Multi-Material Flow with Large Fluid Distortion, in K. W. Morton and M. J. Baines (eds.), Numerical Method for Fluid Dynamics, pp. 273–285, Academic Press, New York.
- [17] Osher S., Sethian J. A. (1988): Fronts Propagating with Curvature Dependent Speed: Algorithms Based on Hamilton-Jacobi Formulations, J. Comput. Phys., vol. 79, pp. 12–49.
- [18] Osher S., Fedkiw R. P. (2001): Level Set Methods: An Overview and Some Recent Results, J. Comput. Phys., vol. 169, pp. 463–502.
- [19] Wang P. T., Sun H. W., Wong P. Y., Fukuda H., Ando T. (2012): Modeling of Droplet-Based Processing for the Production of High-Performance Particulate Materials Using the Level Set Method, Numer. Heat Transfer A, vol. 61, pp. 401–416.
- [20] Welch S. W. J., Wilson J. (2000): A Volume of Fluid Based Method for Fluid Flows with Phase Change, J. Comput. Phys., vol. 160, pp. 662–682.
- [21] Akhtar M. W., Kleis S. J. (2013): Boiling Flow Simulations on Adaptive Octree Grids, Int. J. Multiphase Flow, vol. 53, pp. 88–99.
- [22] Jeon S. S., Kim S. J., Park G. C. (2011): Numerical Study of Condensing Bubble in Subcooled Boiling Flow Using Volume of Fluid Model, Chem. Eng. Sci., vol. 66, pp. 5899–5909.
- [23] Pan L. M., Tan Z. W., Chen D. Q., Xue L. C. (2012): Numerical Investigation of Vapor Bubble

Condensation Characteristics of Subcooled Flow Boiling in Vertical Rectangular Channel, *Nuclear Eng. Des.*, vol. 248, pp. 126–136.

[24] Ganapathy H., Shooshtari A., Choo K., Dessiatoun S., Alshehhi M., Ohadi M. (2013): Volume of Fluid-based Numerical Modeling of Condensation Heat Transfer and Fluid Flow Characteristics in Microchannels, *Int. J. Heat Mass Transfer*, vol. 65, pp. 62–72.

[25] Lee W. H. (1980): A Pressure Iteration Scheme for Two-Phase Flow Modeling, in T. N. Veziroglu (ed.), *Multiphase Transport Fundamentals, Reactor Safety, Applications*, Hemisphere, Washington, DC.

[26] Wu H. L., Peng X. F., Ye P., Eric Gong Y. (2007): Simulation of Refrigerant Flow Boiling in Serpentine Tubes, *Int. J. Heat Mass Transfer*, vol. 50, pp. 1186–1195.

[27] De Scheppers S. C. K., Heynderichx G. J., Marin N. G. B. (2009): Modeling the Evaporation of a Hydrocarbon Feedstock in the Convection Section of a Steam Cracker, *Comput. Chem. Eng.*, vol. 33, pp. 122–132.

[28] Alizadehdakhel A., Rahim M., Alsairafi A. A. (2010): CFD Modeling of Flow and Heat Transfer in a Thermosyphon, *Int. Commun. Heat Mass Transfer*, vol. 37, pp. 312–318.

[29] Yang Z., Peng X. F., Ye P. (2008): Numerical and Experimental Investigation of Two Phase Flow during Boiling in a Coiled Tube, *Int. J. Heat Mass Transfer*, vol. 51, pp. 1003–1016.

[30] Fang C., David M., Rogacs A., Goodson K. (2010): Volume of Fluid Simulation of Boiling Two-Phase Flow in a Vapor-Venting Microchannel, *Frontiers Heat Mass Transfer*, vol. 1, pp. 1–11.

[31] Guo D. Z., Sun D. L., Li Z. Y., Tao W. Q. (2011): Phase Change Heat Transfer Simulation for Boiling Bubbles Arising from a Vapor Film by VOSET Method, *Numer. Heat Transfer A*, vol. 59, pp. 857–881.

[32] Nichita A., Thome J. R. (2010): A Level Set Method and a Heat Transfer Model Implemented into Fluent for Modeling of Microscale Two Phase Flows, *AVT-178 Specialists' Meeting on System Level Thermal Management for Enhanced Platform Efficiency*.

[33] Mao W. B. (2009): Numerical Simulation of Vapor-Liquid Phase Change Heat Transfer and Micromixing in Microfluidic Systems, Master's thesis, Guangzhou Institute of Energy Conversion Chinese Academy of Sciences, China.

[34] Sun D. L., Xu J. L., Wang L. (2012): Development of a Vapor-Liquid Phase Change Model for Volume-of-Fluid Method in FLUENT, *Int. Commun. Heat Mass Transfer*, vol. 39, pp. 1101–1106.

A novel heat pipe with a bypass line for accelerating a working fluid

Eui Guk Jung^{1*}, Cheong Hoon Kwon¹, Won Bok Chung², and Joon Hong Boo³

¹Kangwon National University, Samcheok-city, Korea

²Daehong Enterprise Co., LTD, Siheung-city, Korea

³Korea Aerospace University, Goyang-city, Korea

*Corresponding author email address: egjung@kangwon.ac.kr

Abstract

This study investigates the start-up and steady-state heat transfer performance of a heat pipe with a bypass line for accelerating a working fluid. The interface resistance by the counterflow of vapor and liquid under the operation of a heat pipe has a significant effect on the heat transfer performance. An experimental study was conducted on the thermal performance improvement of a heat pipe, which was induced by a reduction in the flow resistance above the phase interface with a counterflow. A heat pipe was connected to the evaporator start and condenser end with a liquid bypass line. The liquid bypass line was designed to improve the steady-state heat transfer performance of the heat pipe by bypassing a portion of the liquid inside the condenser to the evaporator without passing through the capillary structure. Acetone was used as the working fluid, and the effect of the bypass line on the heat transfer performance of the heat pipe was experimentally investigated. The input thermal load, coolant temperature, and inclination of the heat pipe were selected as the experimental variables. The heat transfer performance of the heat pipe was evaluated by the thermal resistance, and the normal operation mode and bypass operation mode were quantitatively compared. When the bypass line was used, the thermal resistance of the heat pipe decreased by up to a maximum of 61%.

Keywords: Heat pipe, Liquid bypass line, Start-up, Thermal performance, Thermal resistance

1. Introduction

Heat pipes are passive heat transfer devices with an excellent effective heat transfer performance. They are also an evaporation–condensation device that transport thermal energy to long distances with a small temperature difference using the latent heat of vaporization and operates in a two-phase flow area. Since 2010, interest on heat pipes for effective thermal management is rising again owing to thermal constraints and demands due to the inevitably increasing heat levels in many industrial applications including chip-level CPU thermal control [1], refrigeration and air conditioning [2], and aerospace fields [3].

In particular, the heat pipes for the thermal management of batteries applied to electric or hydrogen cars have recently drawn significant attention [4–6]. Since the presentation of the original concept of heat pipes in 1944 by *Gaugler* [7], the research on the concepts of heat pipes has advanced, with primary focus on their suitability for industrial applications such as capillary pumped loops, loop heat pipes, and vapor chambers, and the improvement of heat transfer performance. A typical heat pipe is produced by installing a capillary structure in a cylindrical tube, filling a working fluid under high vacuum, and then sealing the structure. The performance and operation of heat pipes are highly dependent on the container configuration,

working fluid, and capillary structure. However, the fundamental phenomenon that governs the operation of the heat transfer device is dependent on the size of the capillary force through the liquid–vapor interface in the evaporator and condenser inside [8–10]. Many parameters influence the heat transfer performance of heat pipes, including the compatibility of the working fluid and container material, operating temperature range, heat transfer limit, thermal resistance, operating orientation, dimensions, and geometrical constraints.

Previous studies have greatly contributed to the improvement in the heat transfer performance of heat pipes and have extensively investigated the effects of various capillary structures and working fluids, which are essential for the operation of heat pipes. Although a small pore size of the wick structure results in an increase in the capillary pressure that generates the driving force of the heat pipe, it has a negative impact on the heat transfer performance because it increases the pressure drop of liquid that returns from the condenser to the evaporator. Therefore, many studies [11–13] have been conducted on the design of capillary structures to improve the heat pipe performance.

These studies have evaluated the heat transfer performance of working fluids or capillary structures that can be easily selected in the typical design process of heat pipes. *Jung and Boo* [14–17]

improved the start-up performance [14], removed the evaporator temperature overshoot [15, 16], and enhanced the steady-state heat transfer performance [16] using a vapor bypass line for a loop heat pipe.

The present study highlights the need for a more fundamental method to improve the heat transfer performance of heat pipes based on the phase change of the working fluid and the flow patterns of vapor and liquid. The typical structure of a heat pipe was modified with the aim of improving its heat transfer performance. The modified structure of the heat pipe was designed to improve the heat transfer performance by reducing the flow resistance at the liquid–vapor interface inside the heat pipe, thus accelerating the circulation of the working fluid. A heat pipe structure was designed and fabricated such that the liquid condensed and cooled in the condenser would bypass to the evaporator start by interconnecting the evaporator start and condenser end through a liquid bypass line. The experimental results are presented for the comparison of the start-up and steady-state heat transfer performance between the active and inactive liquid bypass lines. In a previous study [17], the effect of the bypass line contributing to the improvement of the maximum heat transfer with dry-out due to the capillary limit was experimentally presented. The purpose of the present study is to investigate the effect of bypass line on the start-up and the steady-state heat transfer performance of the heat pipe.

The liquid bypass line approach can help improve the heat transfer performance of heat pipes.

2. Experimental Setup and Procedure

Fig. 1 shows a photo of a heat pipe with a bypass line designed and manufactured in this experimental study. The bypass line connects the start of the evaporator and the end of the extension, and two needle valves are attached to both ends of the bypass line to control the bypass flow. The heat pipe is fabricated as an aluminum tube with an outer diameter of 15.88 mm and a thickness of 1 mm. The trapezoidal groove processed on the inner wall of the heat pipe supplies capillary pressure. The groove dimensions were as follows: a height of 2 mm,

bottom length of 0.7 mm, and tip length of 0.93 mm.

Acetone with 99% purity was used as the working fluid. The total length of the heat pipe was 750 mm, the condenser and evaporator had the same length of 200 mm, and the adiabatic length was 350 mm. The bypass line was fabricated as an aluminum tube with an outer diameter of 6.35 mm and an inner diameter of 4.35 mm and was connected to the evaporator start and condenser end. The bypass line is a plain tube, and the groove channel is not proceeded on the inner wall. The bypass line was welded in contact with the surface of the heat pipe after drilling a hole at the start of the evaporator and the end of the condenser. As shown in Fig. 1, the position of the bypass line port in the condenser region can be an important experimental variable that can influence the bypass mass flow rate. However, the effect of the attachment position of the bypass line on the heat transfer performance is beyond the scope of this study. As shown in these figures, a bypass line control valve is attached to both ends of the bypass line to control the bypass flow.

This experimental work is to observe the change in the heat transfer performance of the heat pipe when the BOM is applied. Therefore, the filling amount of the working fluid is calculated based on NOM, and the volume of the bypass line was not considered when the fill-charge ratio was determined. The void volume of the groove excluding the vapor space in Fig. 1 was defined as the fill charge ratio of 100%. Fig. 2 shows the thermal resistance of the heat pipe according to the change in the fill charge ratio (Φ) of the working fluid. The input thermal load, coolant temperature and the tilt of heat pipe angle are 500 W, 15°C and 10°, respectively. As shown in Fig. 6, when the fill charge ratio was 120%, the lowest thermal resistance was measured as 0.02793°C/W. Therefore, the amount of working fluid is 17.6 mL, which corresponds to a fill charge ratio Φ of 120% based on the void volume of the trapezoidal groove. An aluminum heater block that enclosed the entire evaporator was fabricated to supply a thermal load to the heat pipe, and four 1 kW-class cartridge heaters were inserted into the heating block. To measure the temperatures at seven positions along



Figure 1. Heat pipe with bypass line manufactured in this study

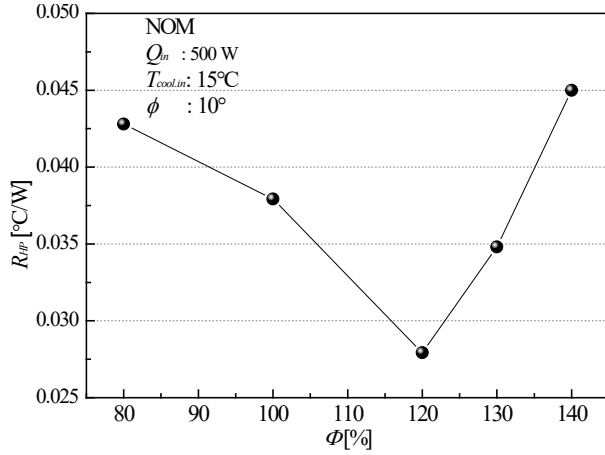


Figure 2. Thermal resistance against fill charge ratio with input thermal load

the axial direction of the heat pipe, K-type AWG 30 (0.25-mm wire diameter) thermocouples were attached, as shown in Fig. 3.

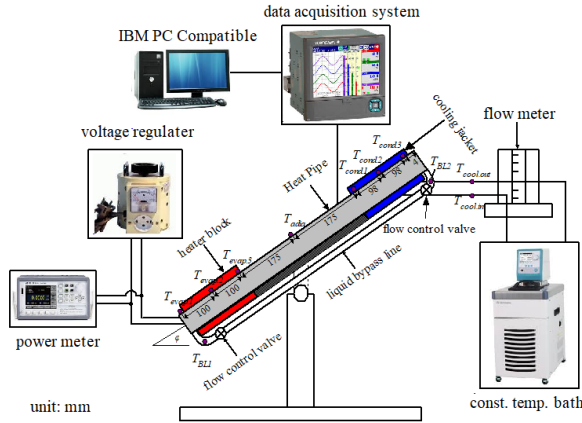


Figure 3. Experimental setup of the heat pipe fabricated in this study and location of thermocouples

Three thermocouples to measure the evaporator temperatures ($T_{evap.1}$, $T_{evap.2}$, and $T_{evap.3}$) and condenser temperatures ($T_{cond.1}$, $T_{cond.2}$, and $T_{cond.3}$) were attached at equal intervals, and the temperature ($T_{adia.}$) of the adiabatic section was measured using a thermocouple attached to the center of the heat pipe. As shown in Fig. 3, thermocouples for measuring the bypass flow of the liquid were attached to the center of the 90° bend at the evaporator start (T_{BL1}) and condenser end (T_{BL2}). To evaluate the thermal energy transferred from the condenser to the cooling source, the temperatures of the inlet and outlet of the cooling jacket were measured using probe thermocouples with a diameter of 3 mm. These thermocouples were calibrated within an error range of 0.1°C.

The coolant temperature was maintained at a

constant value using a thermal bath with distilled water. During the experiment, the volumetric flow of the coolant was maintained at 3 L/min and monitored with a rotameter with a maximum full-scale (4 L/min). The temperature data from the thermocouples were monitored and stored at 1 s intervals using a data acquisition equipment. The thermal load was controlled by a voltage controller and measured using a wattmeter. The components of the heat pipe were washed using an ultrasonic device that used acetone as a cleaning agent. The experiments were performed in a constant-temperature laboratory environment. The heat pipe system was thermally insulated using ceramic wool.

To evaluate the thermal loss, the thermal energy (Q_{out}) recovered by the coolant can be defined as follows:

$$Q_{out} = (\rho \dot{V} c)_{cool} (T_{cool.out} - T_{cool.in}) \quad (1)$$

where $T_{cool,i}$ and $T_{cool,o}$ denote the inlet and outlet temperatures of the coolant, respectively, and \dot{V} and c denote the volumetric flow rate and specific heat of the coolant, respectively. The heat pipe experimental setup was solidly insulated to prevent thermal contact with the surroundings, and the thermal loss from the energy balance between the thermal energy discharged through the coolant from the condenser and the input thermal load was less than 5%. As shown in Fig. 4, the thermal loss increased with the input thermal load (Q_{in}), and the minimum and maximum values of 1.1% (at $Q_{in} = 100$ W) and 5.1% (at $Q_{in} = 500$ W) were measured.

The thermal resistances (R_{HP} and R_{sys}) of the heat pipe and system were used as the evaluation indices for the heat transfer performance.

The heat pipe thermal resistance (R_{HP}) is expressed as follows:

$$R_{HP} = (\bar{T}_{evap.} - \bar{T}_{cond.})/Q_{in} \quad (2)$$

where $\bar{T}_{evap.}$ and $\bar{T}_{cond.}$ denote the average temperatures of the evaporator and condenser, respectively.

The system thermal resistance (R_{HP}) is expressed as follows:

$$R_{Sys.} = (\bar{T}_{evap.} - \bar{T}_{cool.})/Q_{in} \quad (3)$$

where $\bar{T}_{evap.}$ and $\bar{T}_{cool.}$ denote the average temperature of the evaporator wall and the average temperature of the coolant inlet and outlet, respectively. The main objective of this study is to

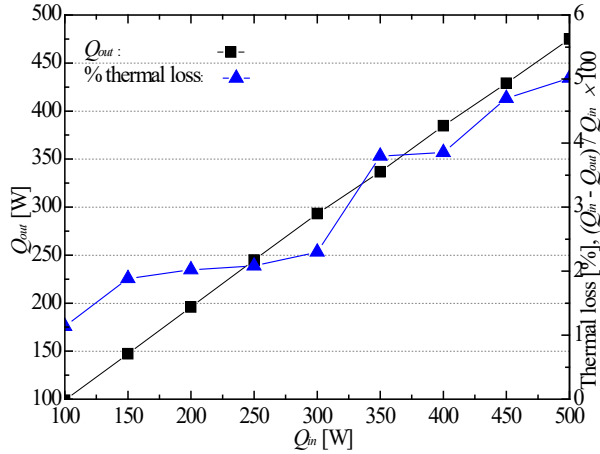


Figure 4. Energy balance between Q_{in} and Q_{out} ($\phi = 20^\circ$).

experimentally determine the effect of a bypass line that contributes to the improvement of the start-up and steady-state heat transfer performance of the heat pipe. Because the steady-state heat transfer performance of the heat pipe is highly sensitive to the inclination, input thermal load, and coolant temperature, which are the condenser cooling conditions, these were defined as the experimental variables. The normal operation mode (NOM) means that the heat pipe is operating under the condition that the two bypass valves presented in Figs. 2 and 4 are fully closed. In the bypass line operating mode (BOM), the bypass flow control valve shown in Figures 1 and 3 is fully opened and the bypass line is activated.

The heat transfer performance was tested and evaluated during the start-up and steady-state operations of the heat pipe under the BOM and NOM.

3. Results and Discussion

A series of experiments were conducted to test the effect of the bypass line on the start-up and steady-state heat transfer performance of the heat pipe in the NOM and BOM. In all the tests, both bypass valves were operated with the heat pipe upright, ensuring that the amount of working fluid trapped in the bypass line was constant.

Fig. 5 shows the test results for the start-up and steady state under the two operating conditions of the NOM and BOM at coolant temperatures of 5 and 15 °C. The input thermal load and tilt angle were 200 W and horizontal, respectively. The overshoot for the evaporator wall temperature was measured in the BOM, unlike in the NOM, as shown in Figs. 5(a) and (b). In the case of the BOM (Fig. 5(a)) with a coolant temperature of

5°C, wall temperature of the bypass tube, T_{BL1} continuously increased because the liquid was not bypassed until 10.7 minutes of the experimental time. As a result, an overshoot of the evaporator wall occurred. Subsequently, the condenser liquid reached the evaporator through the bypass line, and the temperature overshoot for the evaporator wall disappeared as T_{BL1} decreased to 28 °C.

As shown in Fig. 1, in the BOM, the smaller the tilt angle of the heat pipe, the longer the time for the condenser liquid to be bypassed to the evaporator because there is no gravity assistance. It was assumed that this temperature overshoot problem occurred because a part of the input heat load was leaked to the bypass tube due to the delay of liquid bypass at a small tilt angle. In particular, for the case of $\phi = 0^\circ$ and $\phi = 5^\circ$, overshoot on the evaporator wall temperatures was observed during start-up. No overshoot was measured from the evaporator wall temperature ($T_{evap.1}$) during start-up when the tilt angle is increased more than 10° (Fig. 5). As the tilt angle increased, the condensing liquid was rapidly bypassed to the evaporator by gravity assistance, and the temperature overshoot on the evaporator wall disappeared [17]. In order to solve the temperature overshoot problem at a small tilt angle in the future, study on the design of the bypass tube should be actively conducted.

As the liquid was bypassed and reached the evaporator at the experimental time of approximately 17 min, the temperature overshoot disappeared with a reduction in T_{BL1} , and all temperatures reached a steady state. As shown in Fig. 5(b), when the coolant temperature increased to 15 °C, the overshoot for the evaporator wall temperature increased by more than 10 °C compared to that shown in Fig. 5(a). The steady-state arrival time in the BOM was delayed by the effect of temperature overshoot compared to the NOM. Temperature overshoot may overheat the evaporator wall at the beginning of start-up, and it has a disadvantage in that the time to reach a steady-state becomes longer. The steady-state arrival times in the NOM and BOM were approximately 6 and 23.4 min, respectively.

Meanwhile, when all temperatures reached a steady state, the evaporator wall temperatures of the BOM were lower than those of the NOM. At a coolant temperature of 5 °C, the $T_{evap.1}$ and $T_{evap.3}$ of the NOM were measured at 48.8 and 38 °C, respectively, whereas the BOM temperatures were measured at 33 and 35 °C, respectively. At a coolant temperature of 15 °C, the $T_{evap.1}$ and $T_{evap.3}$ of the NOM were measured at 51.4 and 42.2 °C,

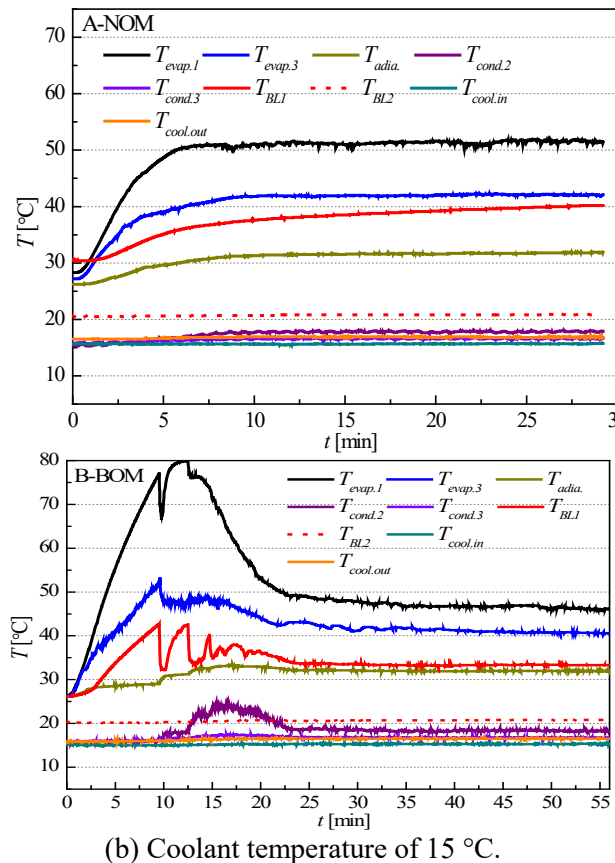
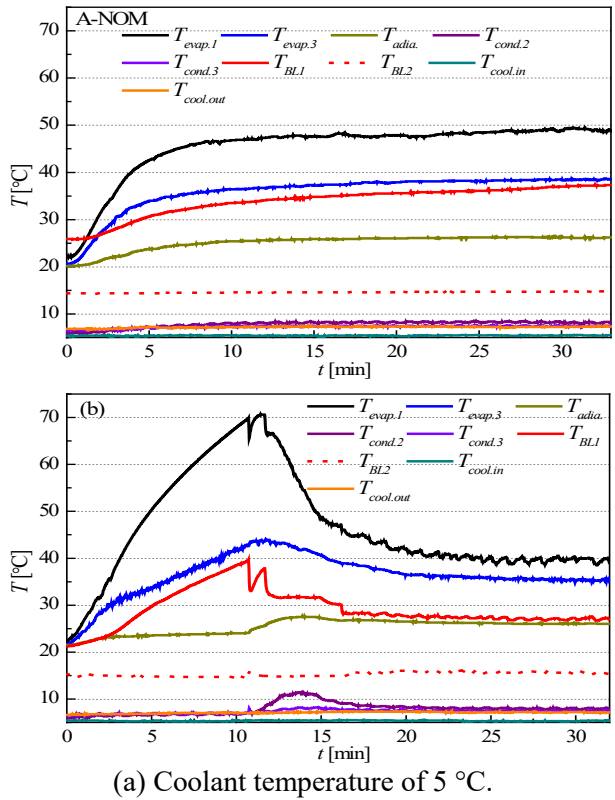


Figure 5. Start-up and steady-state characteristics of the heat pipe under the BOM and NOM for a thermal load of 200 W in the horizontal position with coolant temperatures of (a) 5 °C and (b) 15 °C.

respectively, whereas the BOM temperatures were measured at 46.1 and 40.5 °C, respectively. As shown in Fig. 5, in the steady-state operation condition of the horizontal arrangement, the evaporator wall temperatures of the BOM are lower than those of the NOM. Hence, the thermal resistances in Eqs. (2) and (3) are reduced, and the heat transfer performance is improved. This is because, as mentioned in Section 1.2, in the counterflow of vapor and liquid, the amount of liquid flow in the heat pipe inside space is reduced by the bypass flow, and the flow resistance at the phase interface decreases as a result. Furthermore, the evaporator wall temperature decreased because the liquid condensed and cooled in the condenser was directly bypassed to the evaporator start without passing through the inside of the heat pipe.

Fig. 6 shows the thermal resistance according to the heat pipe tilt angle at coolant temperatures of 5 °C (Fig. 6(a)) and 10 °C (Fig. 6(b)) under an input thermal load of 200 W. As shown in Fig. 14, for every tilt angle, the thermal resistance of the

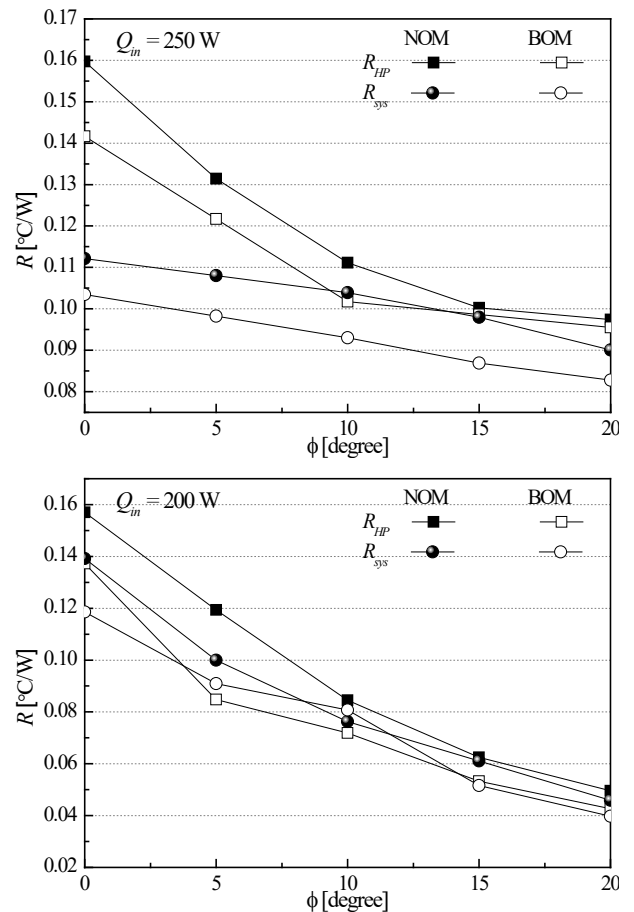


Figure 6. Heat pipe and system thermal resistance against the tilt angle in $Q_{in} = 200$ W with coolant temperatures of (a) 5 °C and (b) 10 °C.

BOM was lower than that of the NOM. At a coolant temperature of 5 °C, the heat transfer performances of R_{HP} and R_{Sys} improved significantly under the horizontal condition and $\phi = 15^\circ$ compared to the other inclination angles. R_{HP} and R_{Sys} decreased by 11.3% and 11.2%, respectively. Furthermore, R_{HP} and R_{Sys} decreased by 1.6% ($\phi = 15^\circ$) and 7.7% (horizontal) at the minimum. At a coolant temperature of 15 °C, the heat transfer performances of R_{HP} and R_{Sys} at $\phi = 5^\circ$ and $\phi = 15^\circ$ improved significantly compared to the other inclination angles. At these inclination angles, R_{HP} and R_{Sys} decreased by up to 29% ($\phi = 5^\circ$) and 15.5% ($\phi = 15^\circ$), respectively. Furthermore, R_{HP} and R_{Sys} decreased by 12.6% (horizontal) and 7.7% ($\phi = 10^\circ$), respectively. Thus, the effect of the BOM on the heat transfer performance was insignificant at these inclination angles compared to the other inclination angles.

Fig. 7 shows the average temperature for the evaporator wall with the coolant temperature as the parameter at horizontal tilt angles of 10°, 15°, and 20°. The test was conducted for each tilt angle at coolant temperatures of 5 and 15 °C. The average temperature ($T_{evap.avg}$) for the evaporator wall was defined as the average of $T_{evap.1}$, $T_{evap.2}$, and $T_{evap.3}$ in Fig. 5. As shown in Fig. 12, for every

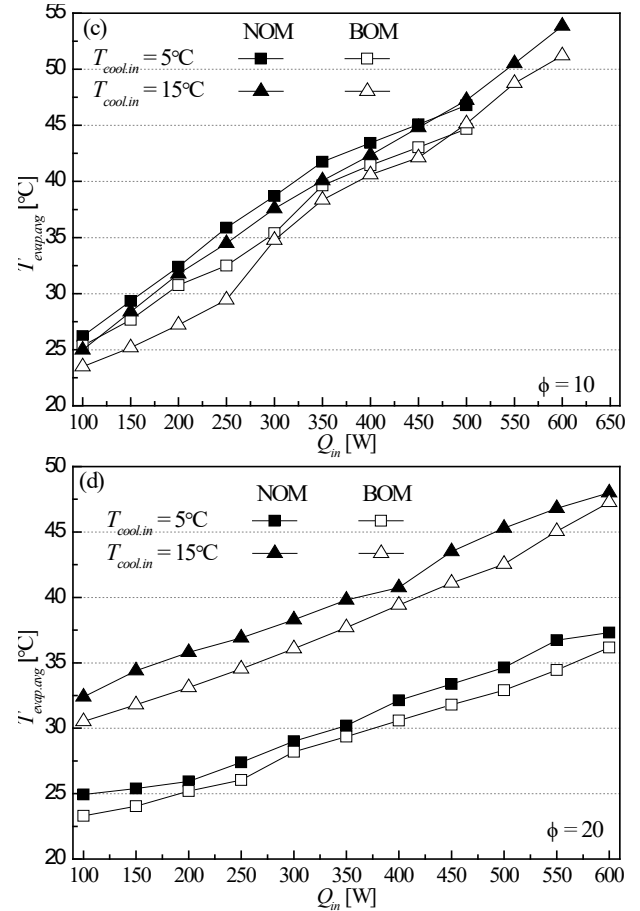
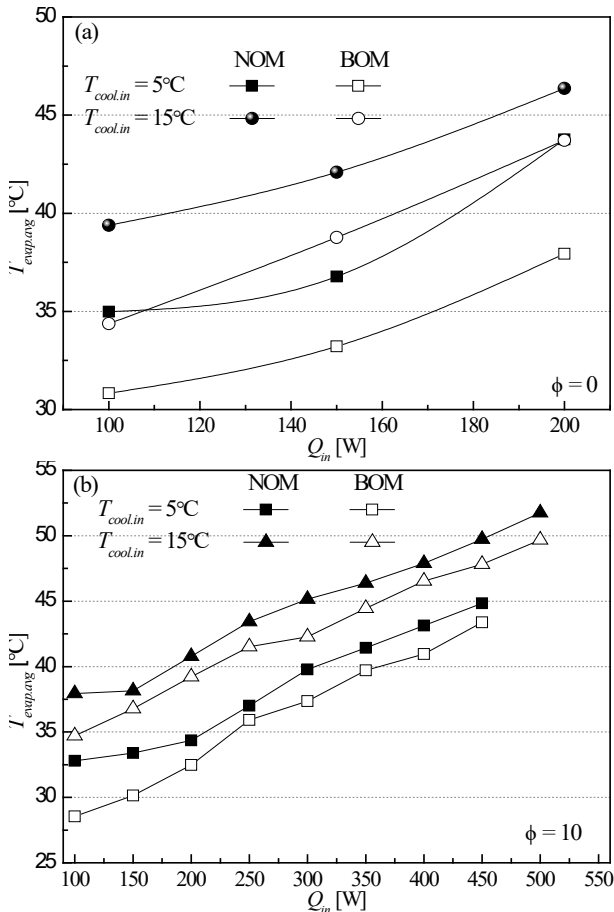


Figure 7. Steady-state evaporator wall average temperature against the thermal load in the horizontal position with a (a) horizontal position and tilt angles of (b) 10°, (c) 15°, and (d) 20°.

coolant temperature and tilt angle, the $T_{evap.avg}$ of the BOM was lower than that of the NOM. In the case of the horizontal arrangement ($\phi = 0$), the $T_{evap.avg}$ of the BOM was lower by up to 5.8 °C ($Q_{in} = 200$ W) at a coolant temperature of 5 °C and by up to 5 °C ($Q_{in} = 100$ W) at a coolant temperature of 15 °C. In the case of $\phi = 10$, the $T_{evap.avg}$ of the BOM was lower by up to 4.5 °C ($Q_{in} = 100$ W) at a coolant temperature of 5 °C and by up to 3.2 °C ($Q_{in} = 100$ W) at a coolant temperature of 15 °C. In the case of $\phi = 15$, the $T_{evap.avg}$ of the BOM was lower by up to 3.4 °C ($Q_{in} = 250$ W) at a coolant temperature of 5 °C and by up to 3.5 °C ($Q_{in} = 200$ W) at a coolant temperature of 15 °C. In the case of $\phi = 20$, the $T_{evap.avg}$ of the BOM was lower by up to 2.3 °C ($Q_{in} = 550$ W) at a coolant temperature of 5 °C and by up to 2.8 °C ($Q_{in} = 500$ W) at a coolant temperature of 15 °C.

4. Conclusions

In this study, a bypass line was theoretically designed and applied to achieve accelerated

circulation of a working fluid by reducing the interface flow resistance generated by the counterflow inside a heat pipe. The bypass line was designed experimentally to reduce the outer wall temperature of the evaporator by bypassing the liquid condensed and cooled by the condenser to the evaporator start.

The bypass line designed in this study was connected to the evaporator start and condenser end. The experimental results demonstrated that the bypass line contributed to the improvement in the steady-state heat transfer performance of the heat pipe. The heat transfer performance was evaluated based on the thermal resistances of the heat pipe and the system. The experimental variables are the input thermal load, heat pipe tilt angle, and coolant temperature. When the bypass line was applied, the heat transfer performance improved under all experimental conditions. However, there was a drawback in measuring the temperature overshoot for the evaporator wall under the operating condition of a tilt angle below 10° . The heat transfer performance improved the most at a tilt angle of 20° with a coolant temperature of 15°C under the BOM. Under these conditions, the thermal resistance of the heat pipe decreased by up to 61%, and the system thermal resistance decreased by up to 59.9%. The overall test results of this study revealed the possibility that the bypass line can contribute to the improvement of the heat transfer performance of heat pipes.

References

- [1] A. Siricharoenpanich, S. Wiriyasart, A. Srichat and P. Naphon, Thermal management system of CPU cooling with a novel short heat pipe cooling system. *Case Studies in Thermal Engineering*: 2019. 15: 100545.
- [2] P. Naphon, On the performance of air conditioner with heat pipe for cooling air in the condenser. *Energy Conversion and Management*: 2010. 51: p. 2362–2366.
- [3] T. Nicolle, F. Kapaun, P. Lasserre, B. Piaud, V. Dupont and L. Ybanez, Using Loop Heat Pipe solutions, and a dielectric fluid, to cool SiC MOSFET power modules for aircraft systems. in *Joint 20th International Heat Pipe Conference and 14th International Heat Pipe Symposium*. 2021. Gelendzhik, Russia, September, 07–10.
- [4] S. Abbas, Z. Ramadan and C. W. Park, Thermal performance analysis of compact-type simulative battery module with paraffin as phase-change material and flat plate heat pipe. *International Journal of Heat and Mass Transfer*: 2021. 173: 121269.
- [5] S. Lei, Y. Shi and G. Chen, Heat-pipe based spray-cooling thermal management system for lithium-ion battery: Experimental study and optimization. *International Journal of Heat and Mass Transfer*: 2020. 163: 120494.
- [6] H. Behi, D. Karimi, M. Behi, M. Ghanbarpour, J. Jaguem, M. A. Sokkeh, F. H. Gandoman, M. Berecibar and J. Mierlo, A new concept of thermal management system in Li-ion battery using air cooling and heat pipe for electric vehicles. *International Journal of Heat and Mass Transfer*: 2020. 174: 115280.
- [7] R. S. Gaugler, Heat transfer device. U.S. Patent, 1944.
- [8] G. P. Peterson, An introduction to heat pipes: Modeling, testing, and applications. John Wiley & Sons, New York, USA, 1994.
- [9] B. Zohuri, Heat pipe design and technology. Springer, Switzerland, 2016.
- [10] S. W. Chi, Heat pipe theory and practice. McGraw-Hill, New York: 33–95, 1976.
- [11] H. Tang, C. Weng, Y. Tang, Y. Lu and T. Fu, Effect of inclination angle on the thermal performance of an ultrathin heat pipe with multi-scale wick structure. *International Communications in Heat and Mass Transfer*: 2020. 118: 104908.
- [12] Y. Li, W. Zhou, J. He, Y. Yan, B. Li and Z. Zeng, Thermal performance of ultra-thin flattened heat pipes with composite wick structure. *Applied Thermal Engineering*: 2016. 102: p. 487–499.
- [13] S. C. Wong and W. S. Liao, Visualization experiments on flat-plate heat pipes with composite mesh-groove wick at different tilt angles. *International Journal of Heat and Mass Transfer*: 2018. p.123: 839–847.
- [14] J. H. Boo and E. G. Jung, Bypass line assisted start-up of a loop heat pipe with a flat evaporator. *Journal of Mechanical Science and Technology*: 2009, 23: p. 1613–1619.
- [15] E. G. Jung and J. H. Boo, Overshoot elimination of the evaporator wall temperature of a loop heat pipe through a bypass line. *Applied Thermal Engineering*: 2020. 165: 114594.
- [16] E. G. Jung and J. H. Boo, Experimental observation of thermal behavior of a loop heat pipe with a bypass line under high heat flux. *Energy*: 2020. 197: 117242.
- [17] E. G. Jung and J. H. Boo, Enhancement of the maximum heat transfer rate of the heat pipe through the bypass line. *Applied Thermal Engineering*: 2021. 198: 117461.
- [18] F. Matsuyama, A. Kawahara, M. Sadatomi, K. Nakashima and Y. Johno, Effects of surface tension on liquid film behavior and interfacial shear stress of two-phase annular flow in a vertical pipe. *Journal of Mechanical Engineering and Automation*: 2017. 7: p. 164–171.

A Novel Pulsing Heat Pipe with a Long, Wickless Serpentine Tube for High-Flux Applications

Abdolmajid Zamanifard¹, M Muneeshwaran^{1,2}, Chi Chuan Wang^{1,*}

¹Department of Mechanical Engineering, National Yang Ming Chiao Tung University, Hsinchu, Taiwan

²Multifunctional Equipment Integration Group, Building Technologies Research and Integration Center (BTRIC), Oak Ridge National Laboratory, Oak Ridge, TN 37830, USA

*Corresponding author email address: ccwang@nycu.edu.tw

Abstract

Due to the fast growth of technology and the improved performance of electronic systems, the demand for devices with high heat dissipation has increased in the electronics cooling industry. This research evaluates a novel 3-D pulsating heat pipe (PHP) with a long, wickless serpentine tube and unique construction for high-flux applications. PHP is equipped with an evaporation section and a fin and tube air-cooled condenser. The experiment used methanol and R134-a as the working fluids. The experiments were performed for different filling ratios and flow rates (CFMs) to determine the optimal operating parameters for the range of heat loads. The thermal resistance of the suggested module changes from 0.14 to 0.095 when the input power increases from 100 W to 600 W, according to the basis of empirical evidence. There is a difference in heat flux between the suggested thermal module and specific previously published research, which can manage 600 W of provided power (52 W.cm^{-2}). Methanol was superior to R134-a, which can be proposed as an alternating working fluid due to its lower GWP.

Keywords: Pulsating heat pipe; High heat flux; Filling ratio; Methanol; R134-a.

1. Introduction

With the rapid expansion of artificial intelligence, internet service, high-speed computers, and data centers that process and store huge amounts of data, it is crucial to employ heat-dispersing devices [1]. One of the most scientific issues that has recently arisen has to do with improving heat transfer and implementing an eco-friendly system with lower energy usage [2].

On the other hand, modern electrical equipment is becoming smaller than in the past. The high heat flux that results from this size reduction is the root of complex heat management issues. Weight, compactness, and energy consumption are three critical requirements the new thermal modules must meet to be used in various applications [3].

In order to solve this problem, researchers have come up with several thermal modules, such as heat pipes, vapor, loop thermosyphons, and pulsating heat pipes. Pulsating heat pipe (PHP) is one of the most efficient components to fulfill the high heat flux dissipation aim investigated in this study. Many researchers and various businesses have praised pulsating heat pipes. Pulsating heat tubes (PHTs) were created in the 1990s as a passive, practical, small, and straightforward future heat management technology. It has attracted much interest and can also address heat flux challenges. [4]. PHPs can be utilized in various applications such as solar cells, fuel cells, space devices, and electronic cooling [5].

The primary distinction between conventional heat pipes and PHPs is that PHPs are wickless. In conventional heat pipes, the liquid returns to the evaporator through the wick structure after evaporation in the evaporation section [6,7].

In contrast to typical heat pipes, PHP requires a more significant amount of working fluid. In the PHP, the heat received in the evaporator generates some elongated bubbles, which then cause an increase in the vapor pressure and form an array of liquid slugs and vapor plugs, as shown in 'Figure 1'.

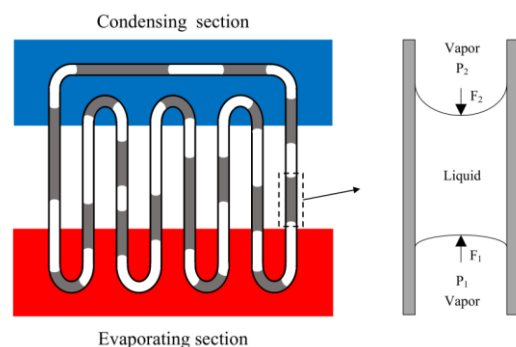


Figure 1. schematic of basic pulsating heat pipe [8].

The bubbles eventually break down due to heat dissipation in the condenser area. The generation of a liquid slug and a vapor plug with the aim of evacuation and capillary force, as shown in 'Figure 1', is the leading PHP transfer mechanism

of fluid between the evaporation and condensation sections and will cause oscillation among PHP. The increased vapor pressure due to the evaporation causes the self-oscillation of vapor and liquid [8]. According to previous studies, sensible heat will be transferred to the condenser from the evaporator by liquid slugs and vapor plugs formed by the internal pressure change caused by the large bubbles in the evaporator. Then vapor plugs undergo a latent heat transfer in the condenser to yield condensate and return to the evaporator [9]. More than 80% of the heat transfer in a liquid slug is termed sensible heat at smaller heat fluxes, as PHP systems tend to be isochoric [10,11].

In contrast, at large heat fluxes, the latent heat transfer mechanism will dominate the sensible heat, resulting in annular flow [10,12,13]. Although the thermal performance of PHPs is lower than that of pure latent heat transfer devices (such as thermosyphons), it is much superior to solid conducting materials [14].

Due to the chaotic behavior and fluctuating motion of the working fluid in PHPs, the thermo-fluidic mechanism has not yet been thoroughly studied and modeled theoretically in very detail. Therefore, most of the research has been carried out experimentally and focused to find the influence of various parameters on the PHP thermal performance, including inner diameter, working fluid properties, heat load, filling ratio, length of the tube, number of turns, and inclination angle [4,15].

Yang et al. [16] investigated the effects of filling ratio, inner diameter, orientation, and heat load on the thermal performance of PHP. They manifested the performance limitation of PHP in terms of dry out. Qian et al. [17] applied a PHP to a rotating grinding wheel and investigated the effect of various diameters of the pipes on thermal performance. They stated that in the acceptable diameter range:

$$(D \leq D_{cr} (= 2[\frac{\sigma}{g(\rho_f - \rho_g)}])) \quad (1)$$

The larger diameter showed better performance in terms of cooling. Furthermore, the effect of inclination angle on the cooling performance of PHP has been investigated by Saha et al. [18].

They concluded that the minimum thermal resistance could be obtained at an optimum filling ratio and inclination angle. Babu et al. [19] found that the thermal resistance could decrease with increasing heat load in a certain filling ratio. For

acetone, a filling ratio of 60 % is optimal for a closed-loop PHP with four turns and a 3 mm inner diameter. They showed that the filling ratio determines the PHP's thermal performance.

Qu et al. [20] investigated the influence of the number of turns. They designed a 3D module and analyzed its behavior under various operating conditions. The results demonstrated that the 3D model showed superior performance and reduced thermal resistance in the horizontal configuration compared to the 2D PHP module. Although many studies have been performed on 2D modules in the past decade, only some studies have been conducted on 3D modules for commercial applications.

Tseng et al. [8] designed a 3D module that handles $15.43 \text{ W}\cdot\text{cm}^{-2}$ for high heat flux applications. The tests indicated that the overall thermal resistance reduces with increasing power. Moreover, they highlighted that the heat transfer occurred due to the oscillating slug flow and the unilateral slug flow with 800 W and greater than 1 kW heat load, respectively. There is an increasing commercial interest in PHPs due to their lightweight, simple construction, and passive operations, and it also offers superior performance at higher heat fluxes [21,22].

The above literature review shows minimal studies concerned with the 3D PHP modules. In particular, $23.7 \text{ (W}\cdot\text{cm}^{-2})$ was obtained as a maximum heat flux value in the open literature, as shown in 'Table 2'. However, these researches are pretty far behind the industry requirement. In this regard, a novel 3D pulsating heat pipe module is suggested for the actual electronic cooling module in the present study.

In this study, a novel pulsating heat pipe was designed and evaluated, suitable for high heat flux applications. Furthermore, the research examined the influence of working fluid and various filling ratios to improve performance.

The proposed module can satisfactorily perform up to a $52 \text{ (W}\cdot\text{cm}^{-2})$ heat flux value, which is approximately two times higher than the one available in the open literature.

2. Experimental set up

'Figure 2' and Figure 3. shows the experimental designs and layouts of the test sections. The experimental setup is made up of a heater component for the evaporator section, a wind tunnel for the air-cooling system, and PHP module. Additionally, the set-up experiment includes a data collection system for analyzing results. The heater is made up of a cooper block

with a cross section of 37 mm × 31 mm. For heat generation, a power supply for providing variable heat load.

Table 1: Review of the previous studies on PHP.

Authors	Heat Flux (W·cm ⁻²)	Working fluid/Filling ratio
Mameli et al. [12]	11.72	FC-72 / 50%
Tseng et al. [8]	15.43	Methanol/ 60%
Yang et al. [16]	23.7	R123 / 50%
Present study	52	Methanol, R134-a.

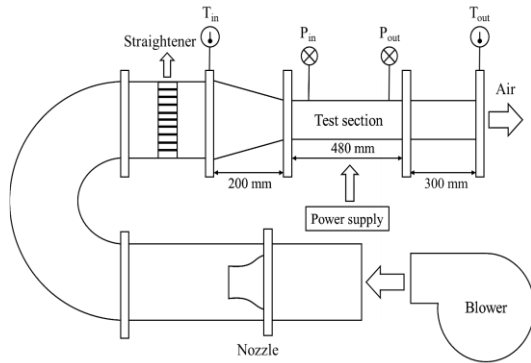


Figure 2. Schematic of the experimental setup.

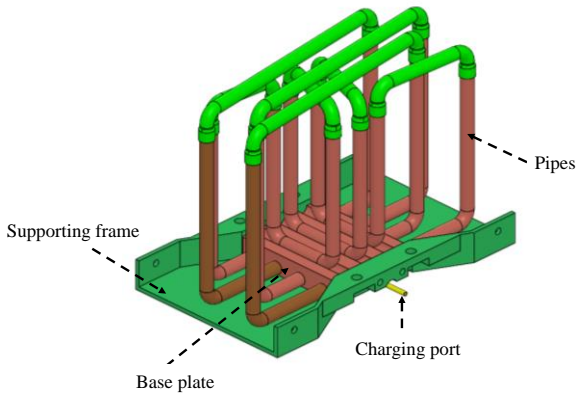


Figure 3. a) Details of the proposed 3D pulsating heat pipe b) The internal view of the proposed 3D pulsating heat pipe (the fins are not shown).

The pulsating heat pipe was constructed using a copper tube, which was bent to produce a continuous loop of pipe (one long pipe). The PHP loop had a total length of 2 meters, and the internal diameter of the copper tube was 5 mm. The methanol and R134-a were utilized as the working fluid with different filling ratios.

The dimensional details of the tube and fins are listed in ‘Table 2’.

Table 2: The dimensional details of the tube and fins.

Tube Side	Outer diameter	6 mm
	Inner diameter	5 mm
	Length of tube	2 m
	Number of turns	16
	Material	Copper
Fins	Face area	75 (W) × 55 (H) mm ²
	Fin pitch	1.2 mm
	Fin thickness	0.1 mm
	Material	Copper

The PHP sample was vacuumed before charging the working fluid to remove air and other non-condensable gases. In this study, two types of working fluid with different filling ratios were used: (1) Methanol (25-40% filling ratio) and R134-a (40 -60%). Furthermore, the experiments were performed at different air flow rates (100-250 CFM) and heating power (100-600 W). For all the experiments, the ambient temperature was maintained at 21±1 °C. The performance of the PHP can be characterized through its thermal resistance, and it was estimated using the below relationship,

$$R = \frac{(T_{\text{Case}} - T_{\text{air,in}})}{Q} \quad (2)$$

where T_{Case} (°C) is the surface temperature of the evaporator, Q (W) is heat input to the PHP, and $T_{\text{air,in}}$ (°C) denotes the inlet temperature of the air.

Accuracy details of different instruments are listed in ‘Table 3’.The method proposed by Kline and McClintock [23] was utilized to calculate the experimental uncertainty. The uncertainty range for the thermal resistance based on below equation is 0.8 – 5.5 %.

$$\frac{\delta R}{R} = \sqrt{\left(\frac{\delta T}{\Delta T}\right)^2 + \left(\frac{\delta Q}{Q}\right)^2} \quad (3)$$

3. Results and discussion

This section analyzes the proposed 3D pulsating heat pipe's performance for different working fluids, including methanol and R 134-a. The PHP's behavior is characterized by thermal resistance and case temperature. Furthermore, the influence of different operating parameters on PHP's thermal

performance, such as heat load, flow rate, and filling ratio.

The experiments were conducted using two distinct fluids, and the key findings are presented in this section. The results indicated that when methanol was used as a working fluid, the test sample could absorb a significant amount of heat from the electronic chip and resulting in superior thermal performance at higher heat flux. Methanol dissipated around 600 W at a 30 % filling ratio, which is greater than R134-a at its optimal filling ratio of 50%, as shown in ‘Figure 4’.

From Figure 5, the thermal resistance of both working fluids will decrease as the heat load increases, but methanol’s thermal resistance exhibits a more rapid decline.

Table 3: Accuracy details of different instruments.

SI. No	Parameter	Instrument	Accuracy
1	Temperature	T-type thermocouple	$\pm 0.1(^{\circ}\text{C})$
2	Pressure	Differential Pressure Transmitter	$\pm 0.04\%$ F.S.
3	Current	Clamp meter	$\pm 1.5\%$
4	Voltage	Clamp meter	$\pm 1.8\%$

3.1. Effect of filling ratio

The filling ratio of the working fluid determines the efficiency of the pulsating heat pipe. Overcharged PHPs only provide a single-phase convective heat transfer, while undercharged ones may experience dry-out concerns. Either way, PHP’s performance can suffer (in the form of increased heat resistance and case temperature). It is crucial to determine the optimal filling ratio for the proposed PHP [3]. Several factors, including working fluid, tube diameter, tube length, and the number of turns, all play a role in determining the ideal filling ratio. Therefore, depending on the specifics of its construction, each module of a pulsing heat pipe may require a different filling ratio. Thus, the filling ratio’s impact on PHP performance is reviewed to establish the optimal filling ratios for

methanol and R 134-a.

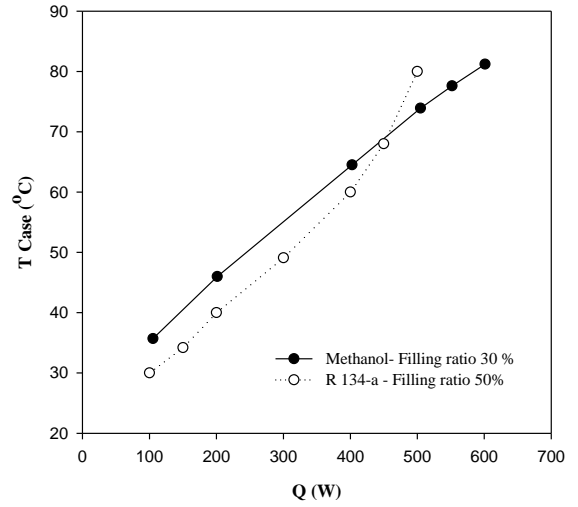


Figure 4. Surface temperature at different heat loads.

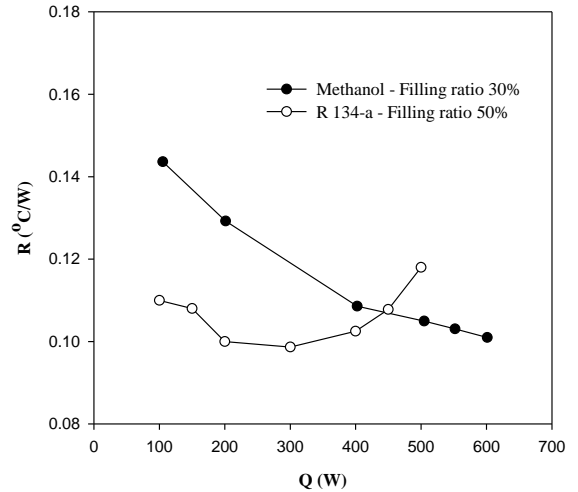


Figure 5. Thermal resistance versus heat load.

The influence of the filling ratio on thermal resistance and case temperature of PHP filled with R 134-a is presented in ‘Figure 6’ and ‘Figure 7’ respectively. According to the results, 50% was obtained as an optimum filling ratio for R134a; the maximum dissipated heat load and lowest thermal resistance will occur at this filling ratio. The PHP could suffer from insufficient liquid levels to facilitate effective latent heat transfer and possible dry-out issues. Whereas, at 60% filling ratios, the overcharging liquid results in a simple single-phase convective heat transfer rather than a two-phase heat transfer mechanism. Consequently, increased thermal resistance in both 40% and 60% filling ratios is encountered. Besides the thermal resistance, the case temperature of 50% is lower than those of 40 % and 60%. For example, at a heat load of 300 W, the case temperature at 50% is

45 °C, which is about 15 °C and 30 °C less than the 60% and 40% filling ratios, respectively. Since the 50% filling ratio provided the minimum thermal resistance and case temperature, it can be considered the optimum filling ratio for R 134-a.

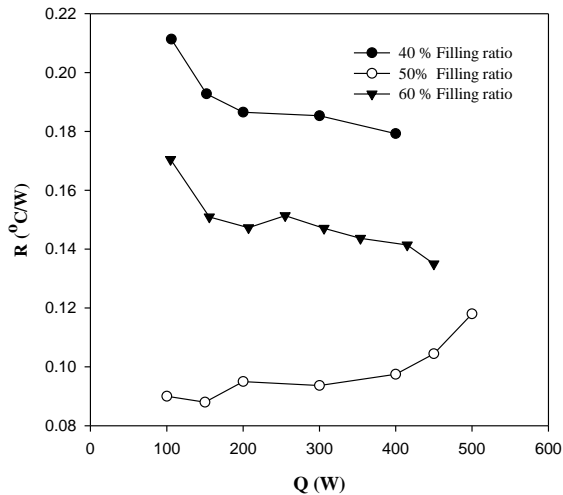


Figure 6. Effect of filling ratio on thermal resistance in different heat loads for R 134-a and 200 CFM.

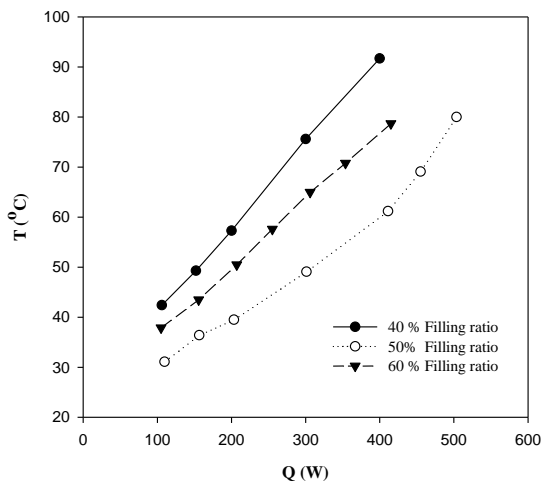


Figure 7. Effect of filling ratio surface temperature in different heat loads for R 134-a and 200 CFM.

‘Figure 8’ demonstrates that, similar to R 134-a, the filling ratio influences the thermal performance of PHP charged with methanol. As anticipated, the thermal resistance reduces as the heat load increases at all filling ratios. Nevertheless, the 30% filling ratio had a lower thermal resistance (0.095) than the 25% and 40% examples. The thermal resistance lowers moderately when the filling ratio increases from 25% to 30%. However, when the filling ratio is

increased to 40%, the performance suffers, and the thermal resistance increases dramatically.

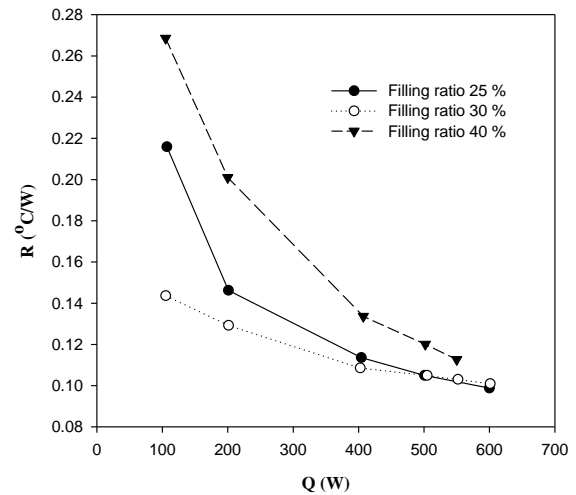


Figure 8. Effect of filling ratio on thermal resistance in different heat loads for Methanol and 200 CFM.

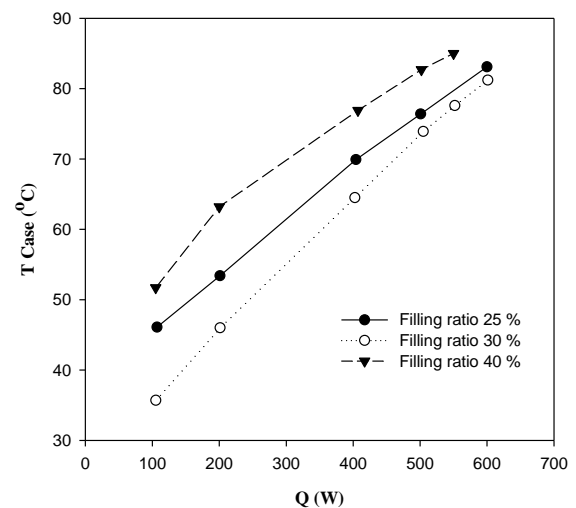


Figure 9. Effect of filling ratio on thermal resistance in different heat loads for Methanol and 200 CFM.

Investigations were also conducted on the surface temperature variation depicted in ‘Figure 9’. The findings reveal that at a heat load of 600 W and a filling ratio of 30%, the surface temperature reaches 80 °C, which is acceptable for electrical cooling. For the remaining filling ratios, the temperature rises to 80 °C with a smaller dissipated heat load, and the surface temperature rises to 81 °C at 550 W for 25% and over 82 °C for 40% at 450 W.

The thermal performance will be impacted by inadequate working fluid supply and

overcharging. A lack of working fluid caused a reduction in latent heat transfer. On the other hand, the overcharging case could be explained by the fact that the single-phase convective heat transfer mode is more important than the latent heat transfer mode and keeps vapor slugs and liquid plugs from growing, which slows down the pulsing motion.

3.2. Effect of flow rate

Due to methanol's superior performance and high heat dissipation rate, the influence of flow rate is examined in this section. Figures 7 and 8 show the impact of air flow rate on the thermal performance of PHP with methanol.

As the flow rate rises, the thermal resistance falls. Condensation and evaporation can be used to understand the cause of this occurrence. The pressure inside the system rises due to the vapor produced at the evaporator. At the condenser, this vapor will condense, lowering the system pressure as a result. Vapor and liquid will pulse due to this alternating rising and falling pressure pattern. The airflow rate will increase with the condensation rate, which can quicken the pulsing motion of liquid plugs and vapor slugs. This might eventually push more liquid to the evaporator and improve two-phase heat transfer. Therefore, the rapid return of liquid to the evaporator caused by the faster pulsing motion and the enhanced condensation rate can work together to lower thermal resistance and case temperature at higher airflow rates. It should be emphasized, though, that a rising flow rate would result in a penalty for pressure drop, and test findings suggested that the pressure loss would get worse as the flow rate rose.

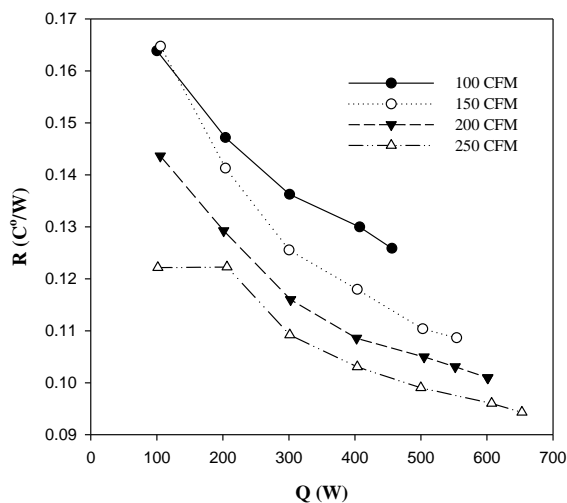


Figure 10. Effect of air flowrate for methanol case temperature vs. heat load at 30% filling ratio.

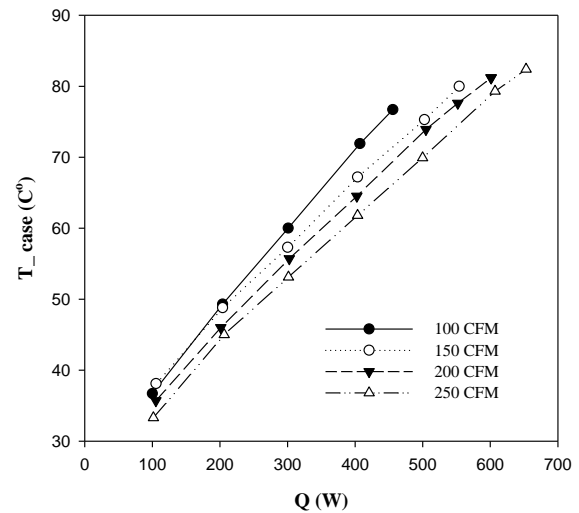


Figure 11. Effect of air flowrate for methanol case temperature vs. heat load at 30% filling ratio.

4. conclusion

The thermal performance of a novel 3D pulsing heat pipe module is examined in this study. Two different filling ratios and working fluids, such as R 134-a and methanol, were used in the studies. These two operating parameters, air flow rate and heat load were looked at to see how they affected the PHP's ability to transfer heat. The findings of the experiment allow for the following inferences:

1. For the proposed 3D PHP, the optimum filling ratio for the methanol and R 134-a is about 30% and 50%, respectively.
2. In a specific filling ratio, the thermal resistance will decrease by increasing the heat load.
3. For methanol, a significant reduction in thermal resistance and case temperature is observed with increasing air flow rate.
4. The proposed 3D PHP is functional satisfactorily (i.e., under 80 °C) up to a maximum heat load of 57 W·cm⁻², which is almost two times higher than the one available in the open literature.

References

- [1] C. Li and J. Li, Passive Cooling Solutions for High Power Server CPUs with Pulsating Heat Pipe Technology. *Frontiers in Energy Research*, 2021: p. 664.
- [2] Y. Xu, Y. Xue, H. Qi, and W. Cai, An updated review on working fluids, operation mechanisms, and applications of pulsating heat pipes. *Renewable and Sustainable Energy Reviews*, 2021. 144: p. 110995.

- [3] V. Ayel, M. Slobodeniuk, R. Bertossi, C. Romestant, and Y. Bertin, Flat plate pulsating heat pipes: a review on the thermohydraulic principles, thermal performances and open issues. *Applied Thermal Engineering*, 2021. 197: p. 117200.
- [4] D. Bastakoti, H. Zhang, D. Li, W. Cai, and F. Li, An overview on the developing trend of pulsating heat pipe and its performance. *Applied Thermal Engineering*, 2018. 141: p. 305.
- [5] F. Polásek and P. Štule. Cooling of electronic elements by miniature and medium-sized heat pipes. in *Proceedings of the European Thermal Science Conference, Roma. 1996.*
- [6] C. Chan, E. Siqueiros, J. Ling-Chin, M. Royapoor, and A. Roskilly, Heat utilisation technologies: A critical review of heat pipes. *Renewable and Sustainable Energy Reviews*, 2015. 50: p. 615.
- [7] X. Chen, H. Ye, X. Fan, T. Ren, and G. Zhang, A review of small heat pipes for electronics. *Applied Thermal Engineering*, 2016. 96: p. 1.
- [8] C.-Y. Tseng, H.-M. Wu, S.-C. Wong, K.-S. Yang, and C.-C. Wang, A novel thermal module with 3-D configuration pulsating heat pipe for high-flux applications. *Energies*, 2018. 11(12): p. 3425.
- [9] B. Tong, T. Wong, and K. Ooi, Closed-loop pulsating heat pipe. *Applied thermal engineering*, 2001. 21(18): p. 1845.
- [10] S. Khandekar, P. Charoensawan, M. Groll, and P. Terdtoon, Closed loop pulsating heat pipes Part B: visualization and semi-empirical modeling. *Applied thermal engineering*, 2003. 23(16): p. 2021.
- [11] D. Yuan, W. Qu, and T. Ma, Flow and heat transfer of liquid plug and neighboring vapor slugs in a pulsating heat pipe. *International Journal of Heat and Mass Transfer*, 2010. 53(7-8): p. 1260.
- [12] M. Mameli, M. Marengo, and S. Khandekar, Local heat transfer measurement and thermo-fluid characterization of a pulsating heat pipe. *International journal of thermal sciences*, 2014. 75: p. 140.
- [13] S. Khandekar and M. Groll, An insight into thermo-hydrodynamic coupling in closed loop pulsating heat pipes. *International Journal of Thermal Sciences*, 2004. 43(1): p. 13.
- [14] S. Khandekar and M. Groll. On the definition of pulsating heat pipes: an overview. in *Proc. 5th Minsk Int. Conf.(Heat Pipes, Heat Pumps and Refrigerators)*, Minsk, Belarus. 2003.
- [15] W.-W. Wang, L. Wang, Y. Cai, G.-B. Yang, F.-Y. Zhao, D. Liu, and Q.-H. Yu, Thermo-hydrodynamic model and parametric optimization of a novel miniature closed oscillating heat pipe with periodic expansion-constriction condensers. *International Journal of Heat and Mass Transfer*, 2020. 152: p. 119460.
- [16] H. Yang, S. Khandekar, and M. Groll, Operational limit of closed loop pulsating heat pipes. *Applied Thermal Engineering*, 2008. 28(1): p. 49.
- [17] N. Qian, Y. Fu, Y. Zhang, J. Chen, and J. Xu, Experimental investigation of thermal performance of the oscillating heat pipe for the grinding wheel. *International Journal of Heat and Mass Transfer*, 2019. 136: p. 911.
- [18] N. Saha, P. Das, and P. Sharma, Influence of process variables on the hydrodynamics and performance of a single loop pulsating heat pipe. *International Journal of Heat and Mass Transfer*, 2014. 74: p. 238.
- [19] E. Babu, H. Reddappa, and G. G. Reddy, Effect of filling ratio on thermal performance of closed loop pulsating heat pipe. *Materials Today: Proceedings*, 2018. 5(10): p. 22229.
- [20] J. Qu, J. Zhao, and Z. Rao, Experimental investigation on thermal performance of multi-layers three-dimensional oscillating heat pipes. *International Journal of Heat and Mass Transfer*, 2017. 115: p. 810.
- [21] H. Jouhara, A. Chauhan, T. Nannou, S. Almahmoud, B. Delpech, and L. C. Wrobel, Heat pipe based systems-Advances and applications. *Energy*, 2017. 128: p. 729.
- [22] M. L. Rahman, R. A. Sultan, T. Islam, N. M. Hasan, and M. Ali, An experimental investigation on the effect of fin in the performance of closed loop pulsating heat pipe (CLPHP). *Procedia Engineering*, 2015. 105: p. 137.
- [23] S. J. Kline, Describing uncertainty in single sample experiments. *Mech. Engineering*, 1953. 75: p. 3.

Improved Modelling of a Heat Recovery System with TEGs and Heat Pipes

Bradley Orr*

*Corresponding author email address: bradley.g.orr@gmail.com

Abstract

An exhaust heat recovery system is a device that converts normally wasted exhaust heat into another usable form of power. For this project, the exhaust heat is converted into electricity. The design utilises heat pipes to transfer heat to and from a TEG (Thermoelectric generator), which converts a small proportion of this heat into electricity. Theoretical modelling and experimentation has already been conducted for this project but in hindsight, the theoretical modelling could have been improved. This paper discusses an improved theoretical model. The new model considers the effect of TEG power output on the thermal resistance network and uses the effective fin resistance rather than just the fin resistance. The Solver tool in Excel was used to solve the many simultaneous equations of the new model. Comparing to previous experimental data shows that the new model is relatively accurate in predicting the temperatures throughout the system and predicting the potential power output of the TEGs.

Keywords: Exhaust gas; Thermoelectric generator; Heat pipe; Counterflow heat exchanger

1. Introduction

Exhaust heat recovery systems are devices that make use of hot exhaust gases that are typically dumped into the atmosphere. This waste heat can be used to power mechanical devices, pre heat air, create electricity, etc. When energy is cheap, these systems are not always viable but as energy prices increase, this will change. The motivation of heat recovery systems is to reduce energy use and therefore reduce energy costs.

The two main technologies used for this project are heat pipes and TEGs (Thermoelectric generators). Heat pipes make use of the evaporation and condensation of a working fluid to transfer heat over relatively long distances with minimal thermal resistance. TEGs make use of the Seebeck effect to convert heat into electricity when there is a temperature gradient over the TEG. The use of these two technologies together allows for the design of a passive and solid state heat recovery system.

In figure 1 is a schematic of a single module of the exhaust heat recovery design. The system consists of two ducts, an exhaust duct and a cool air duct. As exhaust gases pass over the fins in the exhaust duct, heat is transferred from the gas to the fins, to the heat pipe and then to an aluminium heat spreader block. The hot side of the TEG is in contact with the block. The heat transfers through the TEG with a fraction converted into electricity. The remaining heat is transferred to the block on the cold side of the TEG, then to the heat pipe and fins in the cool air duct. Cool air flow over the fins in the cool air duct removes the remaining heat. For this project there are 8 modules in series in a counterflow arrangement.

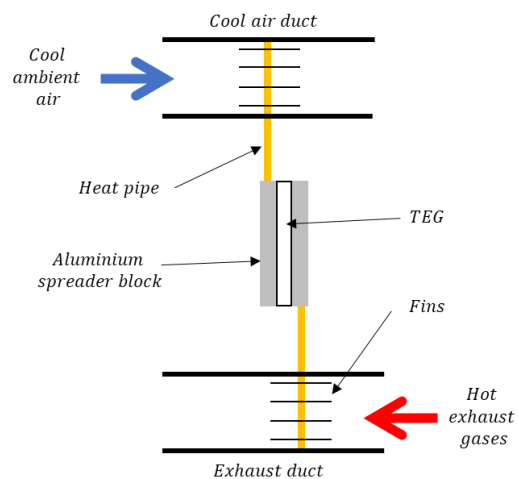


Figure 1. Schematic of a single module of the heat recovery system.

2. Revised thermal model

Previous modelling of this system did not consider the effect of the TEG power output on the thermal resistance network [1]. This new model addresses that issue. The thermal resistance network of an individual module can be seen in figure 2. The heat transfer path is from the hot side inlet, hot side fin base, hot side TEG, cold side TEG, cold side fin base and cold side inlet temperature nodes. The hot side and cold side outlet temperatures are also calculated. Either side of the TEG thermal resistance are the 'other' resistances and effective fin resistances. The 'other' resistance is a sum of thermal paste, aluminium block and heat pipe resistances [1]. These thermal resistances were either hand calculations or data from suppliers. The effective fin resistance is explained in more detail in section 3.

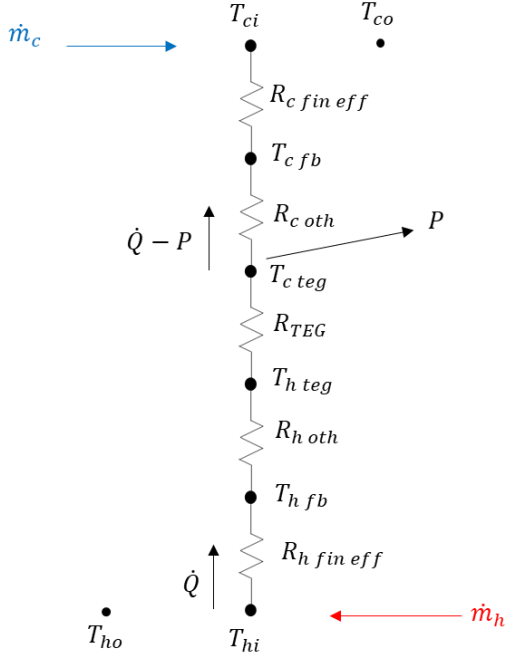


Figure 2. Thermal resistance network of an individual module.

To take into account the power output of the TEG, the rate of heat transfer from the cold side TEG node to the cold side inlet node has the power subtracted. Therefore conservation of energy is upheld. Previously the power output was estimated after the temperatures were calculated [1]. To solve this model the power output and temperatures must be determined simultaneously.

The thermal resistance network in figure 2 has eight unknown variables. Therefore eight equations are required to solve for all unknowns. Equations 1-8 are the governing equations of the model. Equation 4 determines the power output of the TEG which has been derived previously [2].

$$\dot{Q} - P = \dot{m}_c c_{pc} (T_{co} - T_{ci}) \quad (1)$$

$$T_{c fb} - T_{ci} = (\dot{Q} - P) R_{c fin eff} \quad (2)$$

$$T_{c teg} - T_{c fb} = (\dot{Q} - P) R_{c oth} \quad (3)$$

$$P = -\frac{m_2^2 (T_{h teg} - T_{c teg})^2}{4m_1} \quad (4)$$

$$T_{h teg} - T_{c teg} = \dot{Q} R_{TEG} \quad (5)$$

$$T_{h fb} - T_{h teg} = \dot{Q} R_{h oth} \quad (6)$$

$$T_{hi} - T_{h fb} = \dot{Q} R_{h fin eff} \quad (7)$$

$$\dot{Q} = \dot{m}_h c_{ph} (T_{hi} - T_{ho}) \quad (8)$$

For an individual module, equations 1-8 are sufficient. However, for two or more modules in series, equations 9-10 are required. These equations state that the inlet temperatures are equal to the previous outlet temperatures

$$T_{ci} = T_{co prev} \quad (9)$$

$$T_{hi} = T_{ho prev} \quad (10)$$

3. Effective fin thermal resistance

The fin thermal resistance (including fin efficiency) was calculated by hand for the previous model [1]. However, this fin resistance does not consider the change in gas temperature as it moves through the fins. To do this the effective fin thermal resistance needs to be determined. This has been implemented for the new model.

To derive the effective thermal resistance, NTU method theory can be used [3]. For fins with a constant base temperature, equations 11-14 apply.

$$\varepsilon = 1 - e^{-NTU} \quad (11)$$

$$NTU = \frac{hA}{C_{min}} = \frac{1}{\dot{m}_c p R_{fin}} \quad (12)$$

$$\dot{Q}_{max} = \dot{m}_c p (T_{fb} - T_{in}) \quad (13)$$

$$\dot{Q} = \varepsilon \dot{Q}_{max} \quad (14)$$

Substituting equations 11-13 into equation 14 results in equation 15a. This can be simplified down to equation 15b and again down to the final derivation of effective resistance in equation 15c.

$$\dot{Q} = (1 - e^{-\frac{-1}{\dot{m}_c p R_{fin}}}) \dot{m}_c p (T_{fb} - T_{in}) \quad (15a)$$

$$1 = \dot{m}_c p (1 - e^{-\frac{-1}{\dot{m}_c p R_{fin}}}) R_{fin eff} \quad (15b)$$

$$R_{fin eff} = \frac{1}{\dot{m}_c p (1 - e^{-\frac{-1}{\dot{m}_c p R_{fin}}})} \quad (15c)$$

4. Solving the model

For the previous model of this system, a single thermal resistance was used between the hot inlet and cold inlet for each module [1]. This resistance was the sum of all component resistances of the module. This reduced the number of equations required to solve for the duct temperatures. As all the equations were linear and the number of equations were reduced, it was practical to solve

these equations in a matrix form. The power and component temperatures were then determined after the duct temperatures were found.

For this revised model, the effect of the power on the thermal resistance network is considered and must be determined simultaneously. The equation to determine power is not linear and the component temperatures are required to calculate the power. Therefore, it is not practical to solve the new model in a matrix form because of the significant increase in the number of equations and the presence of nonlinear equations. A new solving method was required.

It was decided to use the Microsoft Excel solver add-in for this new model. This tool enables solving of many non-linear equations simultaneously. This solver requires all equations to be in the format as shown in equation 16.

$$0 = f(x, y, z, \dots) \quad (16)$$

For this model, the equations are arranged in an array with 8 columns and 10 rows. A column for each module and a row for each equation (equations 1-10). All equations were put in the format of equation 16. The variables are arranged in a similar 8 column by 10 row array with a column for each module and a row for each variable. The input parameters are referred to in a separate array. In this case there are 80 equations with 80 unknown variables. The solver attempts to make all 80 equations equal zero by changing the 80 variables. If this can be achieved, then all the unknown variables can be determined.

5. Results

The system that was previously tested can be seen in figures 3 and 4 [1]. The final assembly of the system is shown in figure 3 with the ducts and insulation installed. The partially assembled system is shown in figure 4. The fins and heat pipes can be seen in this image.



Figure 3. The full system assembly.

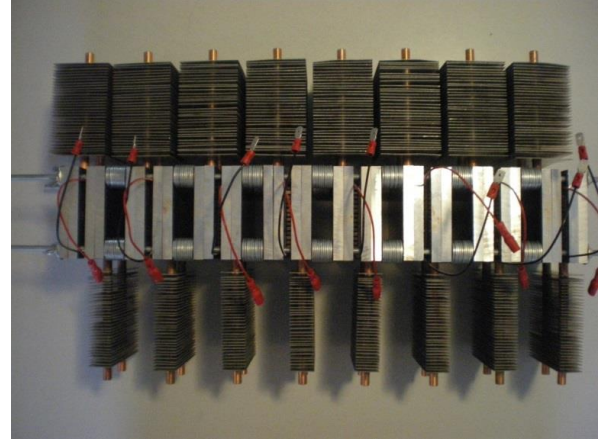


Figure 4. The system without ducts.

The operating conditions [1] of the previous experiment (such as input temperatures, mass flow rates and specific heats) for both ducts are known. These parameters can be used for the new model. Other parameters (such as thermal resistances and TEG properties) are needed as well. Table 1 below shows the input parameters used for the model.

Table 1. Model input parameters.

T_{ci}	31 °C
\dot{m}_c	0.02 kg/s
c_{pc}	1007 J/kg.K
T_{hi}	218 °C
\dot{m}_h	0.0157 kg/s
c_{ph}	1024.5 J/kg.K
R_{TEG}	0.7 °C/W
$R_{c\ oth}$	0.128 °C/W
$R_{h\ oth}$	0.128 °C/W
$R_{c\ fin\ eff}$	0.169 °C/W
$R_{h\ fin\ eff}$	0.228 °C/W
m_1	-1.939 V/A
m_2	0.0479 V/°C

As all the input parameters have been determined, the model can now be solved. The output of the model can be compared to previous experimental data. Duct and TEG temperature comparisons are shown in figure 5. Power, heat transfer rate and efficiency comparisons are shown in table 2.

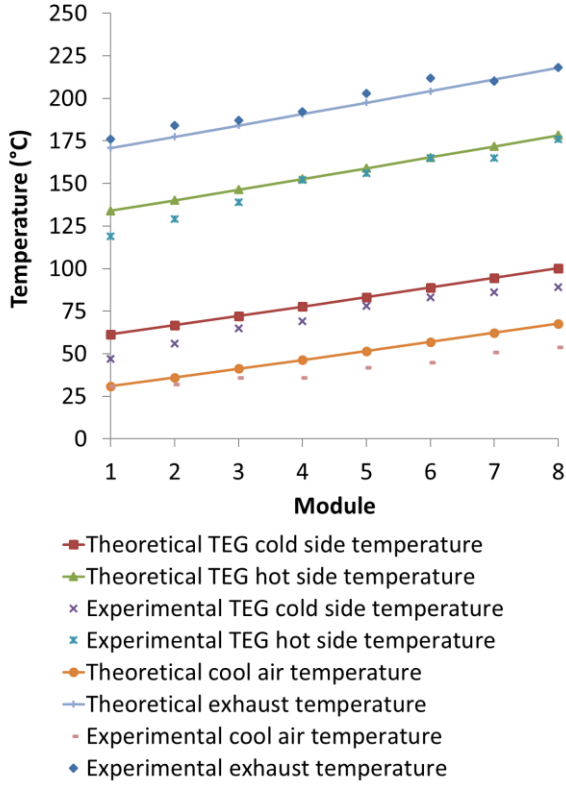


Figure 5. Theoretical vs experimental duct and TEG surface temperatures.

Table 2. Theoretical vs experimental power, heat transfer rate and TEG efficiency.

	Theoretical	Experimental
P_{total}	13.44 W	15.17 W
\dot{Q}_{total}	861 W	897 W
η_{TEG}	1.56%	1.69%

All duct temperatures were measured using thermocouples. TEG surface temperatures were probed with an individual thermocouple. The total heat transfer rate was found using equation 5 with experimental data and summing for all eight modules. The power output was measured indirectly with a multimeter and using equation 17 below [2].

$$P_{total} = \frac{1}{4} V_{oc} I_{sc} \quad (17)$$

It can be seen in figure 5 that the theoretically predicted temperatures by the model match the experimentally determined temperatures quite well. They both match the expected temperature profile of a counterflow heat exchanger. In this case the hot exhaust gas is input at module 8 and gets cooler as it moves along the duct to module 1. The cool air is

input at module 1 and gets warmer as it moves along the duct to module 8. The lower mass flow rate of the exhaust gases results in a higher change in temperature from end to end compared to the cool air duct. Table 2 demonstrates that the theoretical model seems to slightly underpredict the power, heat transfer rate and efficiency but is still relatively accurate. There is an 11.4% discrepancy between the experimental and theoretical power.

Most of the thermal resistance in a module is from the TEG. Therefore, it is expected that most of the temperature drop in the module will be from the hot side to the cold side of the TEG. This is demonstrated in figure 5. By reducing the thermal resistance of the heat pipe heat exchangers on either side of the TEGs, the temperature difference between the duct and TEG surface temperatures would reduce. Consequently, the temperature difference over the TEGs would increase and more power would be produced.

Despite the theoretical improvements to the new model compared to the previous model, the outputs are not significantly different for this particular operating condition [1]. The effect of power on the thermal resistance network is small in this case because of the low 1.56% TEG efficiency. This means that 98.44% of the heat is still transferred to the cool air duct. For this model improvement to make a meaningful difference, the efficiency of the TEG needs to be much higher.

The use of effective thermal resistance did not significantly change the results either. The mass flow rate of both ducts for this operating condition was high enough that the difference between the fin resistance and effective fin resistance is only small. Only situations with low flow rates that result in large temperature change will the outputs of the old and new models start to deviate.

6. Conclusion

A new revised theoretical model was created for an existing heat recovery system with the aim to improve temperature and performance prediction. The model was revised to consider the effect of power generation on the thermal resistance network and to consider the effective resistance of the fins. The output of the new model was compared to previous experimentally determined data and was found to be relatively accurate. However, the outputs of the new and old models are not significantly different for the tested operating conditions. The new model will be more accurate for situations with much higher TEG efficiencies and for situations with low duct mass flow rates.

Nomenclature

A	: Area (m^2)
C_{min}	: Minimum heat capacity (J/K.s)
c_p	: Specific heat (J/kg.K)
h	: Heat transfer coefficient ($W/m^2.K$)
I_{sc}	: Short circuit current (A)
\dot{m}	: Mass flow rate (kg/s)
m_1	: Slope of TEG I-V curve (V/A)
m_2	: Slope of TEG $V_{oc}-\Delta T$ curve ($V/^\circ C$)
NTU	: Number of transfer units
P	: Electrical power (W)
\dot{Q}	: Heat transfer rate (W)
R	: Thermal resistance ($^\circ C/W$)
T	: Temperature ($^\circ C$)
V_{oc}	: Open circuit voltage (V)
ε	: Heat exchanger effectiveness
η_{TEG}	: TEG efficiency

References

- [1] B. Orr and A. Akbarzadeh, Experimental testing of a car exhaust heat recovery system utilising TEGs and heat pipes, SAE-A Vehicle Technology Engineer, 2016, vol. 2, no. 1.
- [2] B. Orr, J. Taglieri, L. C. Ding, and A. Akbarzadeh, Validating an alternative method to predict thermoelectric generator performance, Energy Conversion and Management, 2016, vol. 116, pp. 134-41.
- [3] F. P. Incropera, T. L. Bergman, A. S. Lavine and D. P. Dewitt, Fundamentals of heat and mass transfer (John Wiley & Sons, 2011).

Capillary model of different porous media and experimental verification

Le Liu^{1,2}, Bo Shao^{1,2}, Zhenhua Jiang^{1,2*}, Nanxi Li^{1*}, Deping Dong^{1,2}

¹ Shanghai Institute of Technical Physics of the Chinese Academy of Sciences, Shanghai, China

² University of Chinese Academy of Sciences, Beijing, China

*Corresponding author email address: jiangzhenhua@mail.sitp.ac.cn ; linanxi@mail.sitp.ac.cn

Abstract

The capillary performance of the wick is essential for loop heat pipes. In this paper, a numerical model for the capillary wicking process of porous media was established to simulate the capillary rise of working fluid in the wick. Based on the assumption of flow average, the model assumes that the wick is a homogeneous isotropic porous medium, and the flow of working fluid in the wick follows Darcy's law. The VOF method is used to simulate the two-phase flow in the model, and the position of gas-liquid interface and the direction of capillary force exerted through UDF are determined according to the gradient of phase fraction. The model was verified by wicking experiment using sintered wicks and ethanol as working fluid. The effects of different pore size, porosity and working fluid on wicking were studied by the model. The results show that the larger the pore size and porosity, the smaller the flow resistance and the faster the wicking speed. When water is used as the working fluid, the wicking speed is the fastest, acetone takes the second place, and ethanol is the slowest. This study provides a certain guiding significance in the selection, design and optimization of wicks in terms of thermal control of spacecraft for loop heat pipes.

Keywords: Capillary model; Wicking process; Porous media; Loop heat pipe; CFD;

1. Introduction

The wick provides power for the circulation of working fluid in the loop heat pipe, and is also the main resistance source in the loop heat pipe. The performance parameters of the wick have an important impact on the performance of the loop heat pipe. Ren et al.[1-3] studied the influence of the structural parameters of the capillary core on the heat transfer performance of the loop heat pipe, and pointed out that the permeability and thermal conductivity of the wick were the main influencing factors. Singh et al.[4-6] studied the influence of capillary cores with different materials, structures and physical parameters on the heat transfer performance of loop heat pipes.

In order to obtain good heat transfer performance and capillary limit, the wick must meet the requirements of high capillary force and high permeability. The former requires small aperture, while the latter requires large aperture. Wicking refers to the process of spontaneous wetting of porous media by working medium under capillary force. Wicking performance curve is the comprehensive performance of capillary force and permeability. Capillary force is reflected in the final height when wicking is in balance, and permeability is reflected in the speed of wicking.

The classical L-W equation analyzes the influence of inertial force, viscous force, gravity and other forces in the wick on capillary wicking phenomenon. The change of the height and speed of liquid rising in the wick with time can be obtained by solving the equation. On the one hand, accurate simulation depends on the accurately defined

equivalent radius; on the other hand, it can only simulate one-dimensional capillary suction, and is powerless to simulate the suction of porous media with slightly complex structure.

It is also reasonable to solve the N-S equation of fluid in porous media based on CFD method to simulate the wicking phenomenon. Although the microstructure of different capillary cores is different, there are some similarities in the macro performance. It is considered that wick is regarded as a homogeneous porous media. In model, the flow characteristics of the fluid in the microchannel are no longer considered, but only the average flow parameters such as the velocity and pressure characteristics of the fluid on the macro level are considered. The wicking process of liquid in porous media is mainly affected by two forces: the resistance of liquid due to flow in the microchannel and the capillary force perpendicular to the gas-liquid interface generated by the surface energy of the gas-liquid solid interface in the pores.

In this paper, a numerical model for the capillary wicking process of porous media is established to study the wicking process of working fluid. The model was verified by wicking experiment and analytical solution of momentum equation. Among the parameters describing porous media, porosity, effective pore diameter and permeability are all related to the structure of porous media and affect each other. The capillary parameters are measured in this paper, and the measured capillary parameters are put into the simulation to explore the influence of various parameters on the wicking process.

2. Porous media model

2.1. CFD model

In this paper, ANSYS Fluent software was used for simulation, and the surface phase velocity or mixing velocity was calculated according to the volume flow in the wick region. The momentum equation is as follows:

$$\nabla \cdot (\rho_m V_m V_m) = \nabla \cdot [\mu_m (\nabla V_m + \nabla V_m^T)] + \rho_m g - \nabla p + S \quad (4)$$

Where ρ_m , μ_m and v_m are the mixing density, motion viscosity and mixing velocity of the mixed phase fluid, and S is the additional momentum source term, respectively.

$$S = -\frac{\mu_m}{K} V_m - C_2 \frac{1}{2} \rho_m |V_m| V_m + S_{cap} \quad (5)$$

The first term on the right is Darcy's law term (viscous loss), K is the permeability of the porous medium, d_p is the average pore size of the porous medium, and ε is the porosity of the porous medium. The second term is the inertia loss term and C_2 is the inertia loss drag coefficient. When the fluid is in laminar flow in porous media, the inertia loss can be ignored. The third term on the right is capillary force in porous media.

The model is a two-dimensional rectangle with a length of 70 mm and a width of 14 mm. The lower boundary is the pressure inlet, the phase volume fraction is 1, the upper boundary is the pressure outlet, and the left and right boundary is the wall.

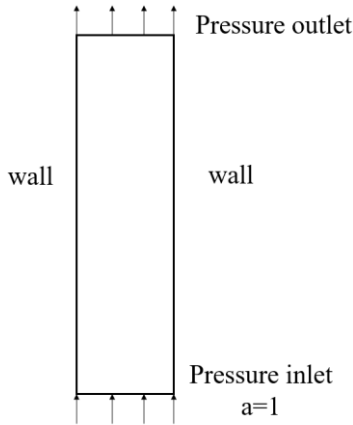


Figure 1. CFD model boundary of wick

The independence of the calculation results from the cells size should be examined to avoid unreliable results. As shown in Figure 2 grids with different size of mesh (0.2mm, 0.5mm, 1mm, 2mm) were applied to a same case. In the case, a higher capillary force and a lower resistance were set up, so the wicking speed was faster. The same courrant

number is selected in the examples with different mesh sizes, so the time step is slightly different.

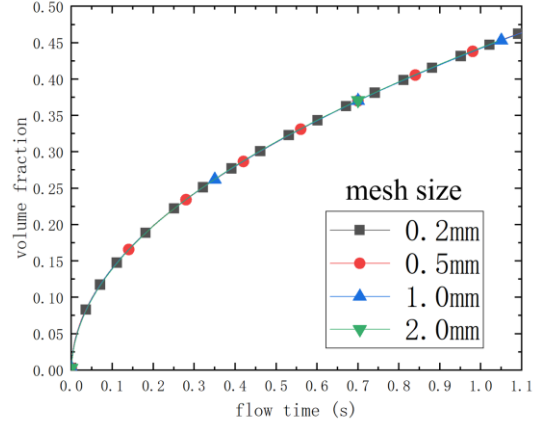


Figure 2. Mesh independence examined

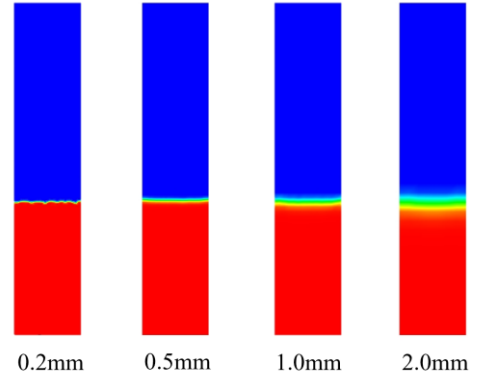


Figure 3. Contours of volume fraction

According to the trend of the volume fraction of the working fluid in the wick over time, it can be found that the selected mesh size has no effect on the wicking process. As shown in Figure 3, the larger the mesh, the less clear the phase interface is, so the 1mm mesh was chosen for the simulations.

2.2. Capillary force model

In capillaries, the capillary force is determined by the Young Laplace equation[7]:

$$p_c = \frac{2\sigma \cos\theta}{R} \quad (6)$$

Here R refers to the capillary radius in the capillary, but for capillary cores in porous media, the effective radius can actually be obtained by the energy equation in the process of capillary wicking. According to the conservation of energy, the work done by capillary force is equal to the change of the surface energy of the solid phase caused by the movement of bending liquid surface[8,9].

$$\delta W_C = (r_{ds} - r_{ws}) dA_{ws,s} = dE_s \quad (7)$$

For the capillary core obtained by particle sintering, the equivalent radius is[10] :

$$R = \frac{2\varepsilon r_{sp}}{3(1 - \varepsilon)} \quad (8)$$

r_{sp} is the effective particle radius, which can be measured by a mercury porosimeter, and ε is the porosity of the entire capillary core, which can be measured by drainage method and a mercury porosimeter. Therefore, for the sintered capillary core, the capillary force can be expressed as:

$$P_c = \frac{3(1 - \varepsilon)\sigma \cos \theta}{\varepsilon r_e} \quad (9)$$

There are two main ways to apply the capillary force to porous media: one is to directly apply the capillary force to the gas-liquid interface of the working medium in the multi-media. Generally, the equivalent surface with a gas phase volume fraction of 0.5 in the vapor-liquid two-phase transition zone of the working medium is used as the vapor-liquid interface. This method is easy to accurately apply the capillary force at the gas-liquid interface, and the operation is relatively simple, but it cannot reflect the difference of the capillary force caused by the different volume fraction of each phase in the two-phase region. At the same time, in the finite element calculation, the gas volume fraction may not be a continuous surface, so it is difficult to define the normal vector of the surface to determine the direction of the capillary force. Another method is to obtain the iso-enthalpy line in the two-phase region according to the enthalpy value, apply the capillary force on the iso-enthalpy line, and take the normal direction of the iso-enthalpy line of the working medium as the direction of applying the capillary force. Because the endothermic enthalpy of the working medium will increase, but the phase transition does not necessarily occur, this method is also different from the real physical process.

In this paper, another method of applying capillary force is proposed, which can not only accurately apply the capillary force to the gas-liquid interface transition region of the working medium, but also distribute the capillary force according to the gradient of the phase fraction of the working medium, which is more consistent with the real physical process. The specific methods are as follows:

$$S_{cap} = \frac{3(1 - \varepsilon)\sigma \cos \theta}{\varepsilon r_e} \nabla \alpha_v \quad (10)$$

$\nabla \alpha_v$ represents the gas phase volume fraction gradient of the working medium in the gas-liquid interface transition zone inside the wick. After the

gas volume fraction distribution field of the working medium in the wick is obtained by the user-defined scalar (UDM), the gas volume fraction gradient of the working medium in the wick is obtained, and then the capillary force is applied to the gas-liquid interface transition zone of the porous medium in the form of gas gradient by the source macro, and finally the capillary wicking process of the porous medium is realized.

The capillary force plays an important role in the LHP circulation. In this work, the wick is assumed as an isotropic porous zone. The capillary force is added as a momentum source term adding to the momentum equation and the momentum source term is only applied to the liquid-vapor interface in the porous zone by UDFs (User Defined Functions). The capillary force, though seems like a body force in the momentum equation, is in fact a surface force perpendicular to the vapor-liquid interface.

3. Experimental setup

An experimental facility is designed and built to study the actual wicking performance of working fluid in different porous media. As shown in the figure 4, the experimental device includes an iron stand, a petri dish, a steel ruler, an electronic balance, a lift and drop platform, a high-speed camera and a computer that collects data in real time. The height of the capillary climbing process and the mass of the working medium pumped are measured in real time by using the weight method and the height method.

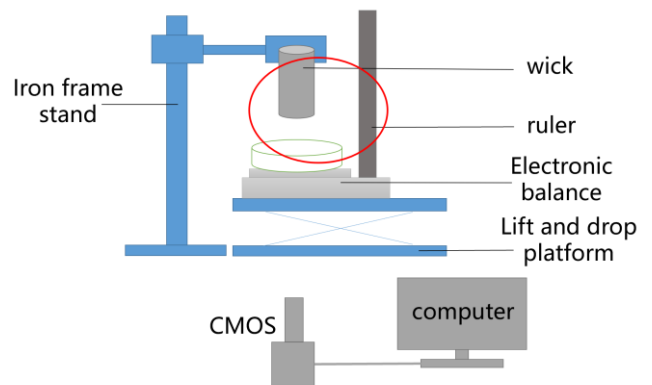


Figure 4. Wicking experimental device

In the preparation stage of the experiment, the wick was fixed on the iron stand, the petri dish was placed on the lift and drop platform, and the working fluid alcohol was poured into the petri dish. At this time, there was a distance between the bottom of the wick and the surface of the alcohol in the petri dish. At the beginning of the experiment, the high-speed camera began sampling, and the lifting platform was adjusted to make the bottom of the wick and liquid

surface just contact, and the wicking process began. The capture time of the high-speed camera is 600 s at a frame rate of 30 fps, and the shot picture is shown in Figure 5. When the collection time was approaching, the lifting platform was used to separate the wick from the liquid level, stopped the collection, and the experiment was over.

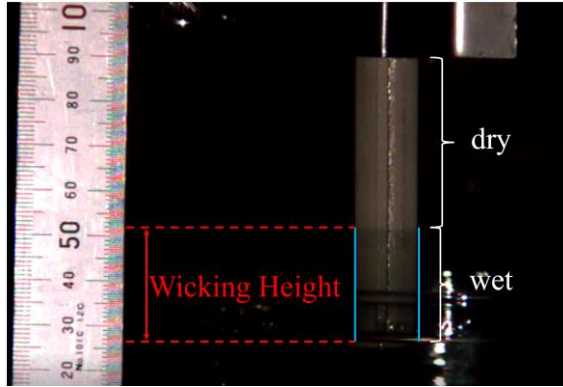


Figure 5. Camera shot of the experiment

In this paper, wicking experiments were carried out on nickel and stainless steel wick. The microscopic parameters of the wicks are measured by mercury porosimeter, as shown in Table 1 and Figure 6 & 7, including the porosity, pore diameter, pore size distribution, etc. The pore size in SEM image and the pore size distribution measured by mercury injection method were considered in the selection of pore diameter size. The permeability was obtained by the formula.

$$K = \frac{d^2 \varepsilon^3}{150(1 - \varepsilon)^2} \quad (11)$$

The morphology of the fracture surface and the outer surface was observed by scanning electron microscopy (SEM), as shown in Figure 8.

Table 1. Parameters of nickel core

Wick	Porosity	Permeability	Pore Diameter
Ni	56.05 %	2.37E-14 m ²	1.975 μm
SS	31.59 %	1.50E-14 m ²	5.786 μm

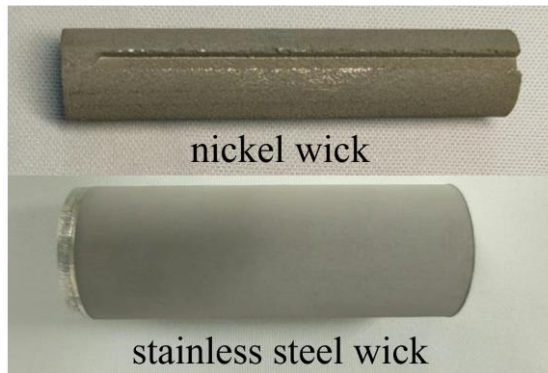


Figure 6. Physical drawing of wick

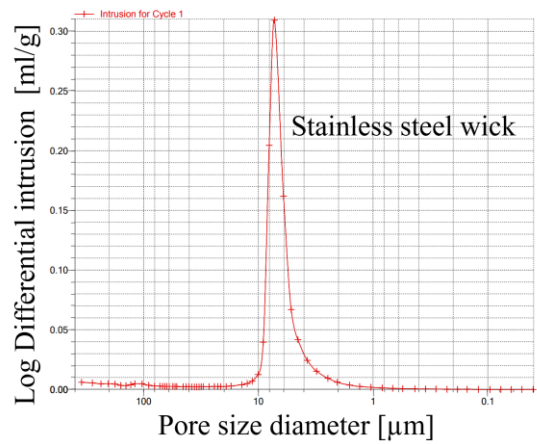
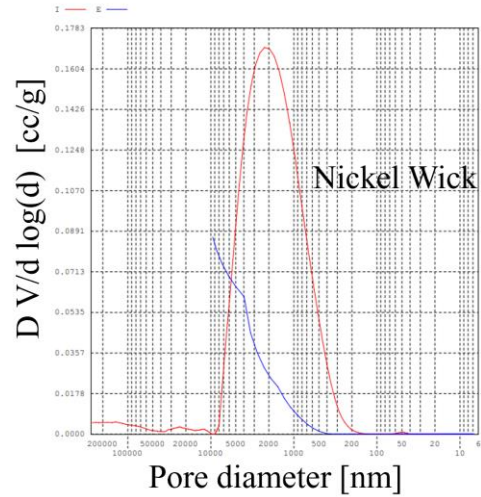


Figure 7. Distribution of pore size

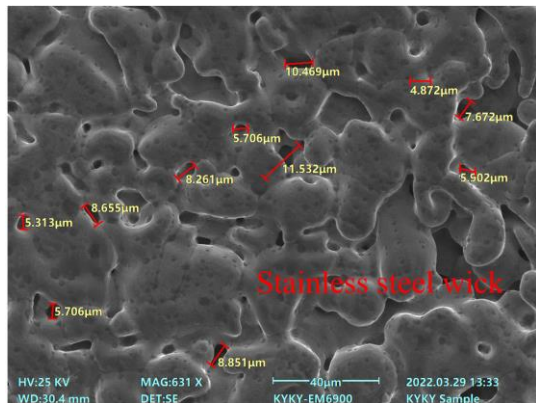
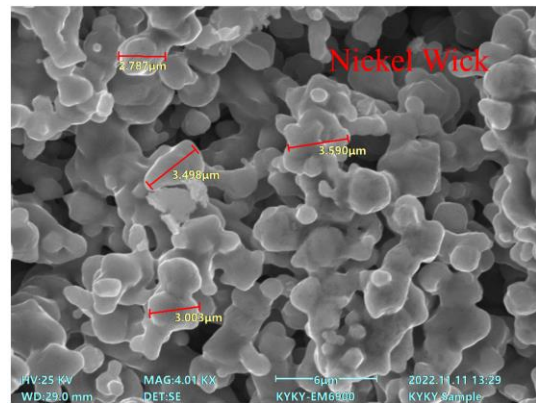


Figure 8. SEM Image

4. Results and discussions

The experimental data obtained by the height method are compared with the simulated solution, as shown in Figure 9. The wicking curves obtained by experiment and numerical solutions do not coincide completely, the error of the stainless steel wick is between -11% and 30%, with an average error of 11%; the error of the nickel wick is between -4% and 21%, with an average error of 7%. At the beginning of wicking, the error is large due to the rapid wicking speed. The possible reason of is that the permeability and capillarity force is calculated theoretically, but the actual permeability is not a constant and may be related to saturation. The error is within a reasonable range, which shows the accuracy of capillary force source term in UDF.

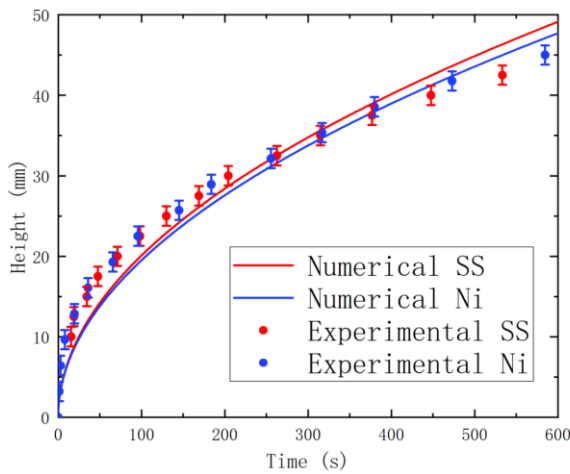


Figure 9. Experimental and numerical solutions

In order to operate the loop heat pipe stably, the wick needs to be kept wet, and the speed of wicking must be greater than or equal to the evaporation rate. The wicking speed is related to the wick parameters and working fluid. Therefore, the effects of different pore size, porosity and working fluid on wicking were studied. As shown in Figure 11, with the same porosity and working fluid, the smaller the pore diameter, the greater the flow resistance and the slower the wicking speed. As shown in Fig. 12, the larger the porosity is, the faster the wicking speed is. As shown in Figure 13, the results show that when water is used as the working fluid, the wicking speed is the fastest, acetone takes the second place, and ethanol is the slowest. Because the density of water is the largest, the density of acetone and ethanol is close, and the viscosity of ethanol is the largest, water takes the second place, and acetone is the smallest, the wicking speed of water and acetone when they are used as the working fluid is significantly greater than that when ethanol is used as the working fluid.

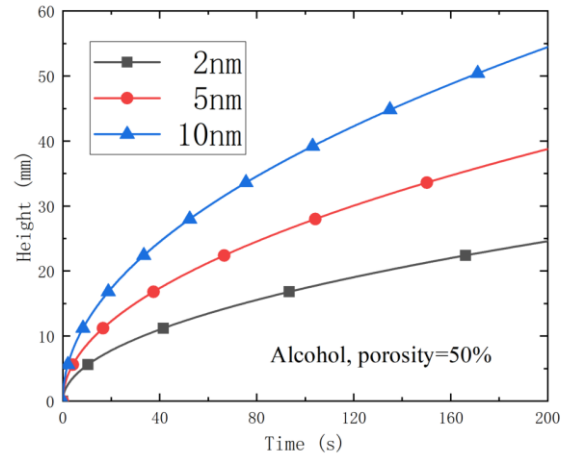


Figure 10. Wicking of different pore diameter

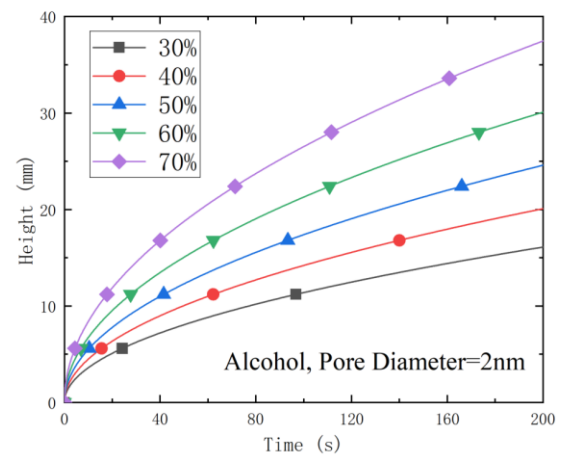


Figure 11. Wicking of different porosity

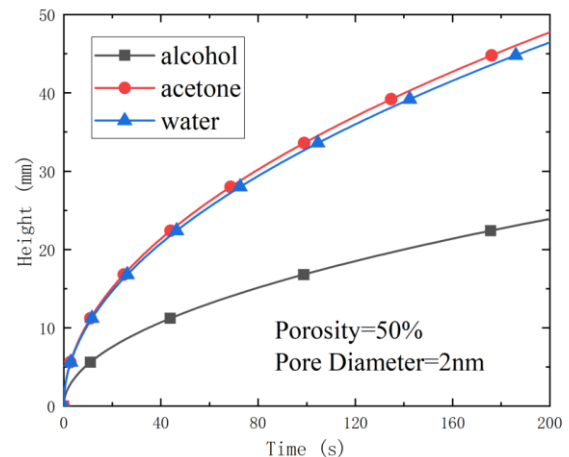


Figure 12. Wicking of different working fluid

5. Conclusions

In order to obtain good heat transfer performance and capillary limit, the wick must meet the requirements of high capillary force and high permeability. The former requires small aperture, while the latter requires large aperture. Wicking refers to the process of spontaneous wetting of porous media by working medium under capillary

force. Wicking performance curve is the comprehensive performance of capillary force and permeability. Capillary force is reflected in the final height when wicking is in balance, and permeability is reflected in the speed of wicking. Therefore, we can obtain some information about capillary force and permeability of wick through wicking experiment and simulation.

The analytical solution can only simulate the one-dimensional capillary wicking phenomenon, and it is unable to simulate the porous media with complex structure. In this paper, based on CFD method, the wicking phenomenon is simulated by applying the capillary force source term in the momentum equation of porous media with UDF. The established model can well predict the wicking phenomenon the porous media, and is of guiding significance for evaporator simulation and future LHP design.

References

- [1] C. Ren, Q. S. Wu, and M. B. Hu, Heat transfer with flow and evaporation in loop heat pipe's wick at low or moderate heat fluxes. *Int J Heat Mass Tran*, 2007. 50(11-12): p. 2296.
- [2] C. Ren, Q. S. Wu, and M. B. Hu, Heat transfer in loop heat pipe's wick: Effect of porous structure parameters. *J Thermophys Heat Tr*, 2007. 21(4): p. 702.
- [3] C. Ren, Parametric effects on heat transfer in loop heat pipe's wick. *Int J Heat Mass Tran*, 2011. 54(17-18): p. 3987.
- [4] R. Singh, A. Akbarzadeh, and M. Mochizuki, Experimental Determination of Wick Properties for Loop Heat Pipe Applications. *J Porous Media*, 2009. 12(8): p. 759.
- [5] R. Singh, A. Akbarzadeh, and M. Mochizuki, Operational characteristics of the miniature loop heat pipe with non-condensable gases. *Int J Heat Mass Tran*, 2010. 53(17-18): p. 3471.
- [6] R. Singh, A. Akbarzadeh, and M. Mochizuki, Operational characteristics of a miniature loop heat pipe with flat evaporator. *Int J Therm Sci*, 2008. 47(11): p. 1504.
- [7] Y. F. Maydanik, Loop heat pipes. *Appl Therm Eng*, 2005. 25(5-6): p. 635.
- [8] R. Masoodi, H. Tan, and K. M. Pillai, Darcy's law-based numerical simulation for modeling 3D liquid absorption into porous wicks. *Aiche J*, 2011. 57(5): p. 1132.
- [9] R. Masoodi, K. M. Pillai, and P. P. Varanasi, Darcy's law-based models for liquid absorption in polymer wicks. *Aiche J*, 2007. 53(11): p. 2769.
- [10] R. M. K. M. Pillai*, A GENERAL FORMULA FOR CAPILLARY SUCTION-PRESSURE IN POROUS MEDIA. *J Porous Media*, 2012. 15: p. 775.

Local heat transfer study of a mini loop heat pipe

Luca Pagliarini¹, Kelvin G. Domiciano^{2*}, Larissa Krambeck², Fabio Bozzoli¹, Marcia B. H. Mantelli²

¹ *Department of Engineering and Architecture, University of Parma, Parco Area delle Scienze 181/A, Parma, Italy*

² *Heat Pipe Laboratory, Department of Mechanical Engineering, Federal University of Santa Catarina, Florianópolis, Brazil*

**Corresponding author email address: kelvin.guessi@labtucal.ufsc.br*

Abstract

Loop heat pipes are promising two-phase heat transfer devices used in many applications, among them for thermal control of electronics. To enhance their modelling and optimization, a better understanding of their working behavior is needed. To this aim, a copper loop heat pipe, whose thin layout was specifically designed for embedment in electronic devices, is tested during start-up to assess differences in terms of local heat transfer behavior between its liquid and vapor lines. The device is filled with ethanol (filling ratio = 40% vol.). The evaporator section is heated by means of an electrical resistance, while the condenser is cooled by free convection. The outer wall temperature along the whole condenser is monitored through a medium-weave infrared camera. The temperature signals, referred to six wall sections, are post-processed by means of the Inverse Heat Conduction Problem resolution approach, resulting in the assessment of the heat fluxes exchanged between the working fluid and the device wall over time. A calibration procedure and uncertainty analysis on the post-processing method are carried out. The provided results set the basis for a deeper and more systematic analysis on the thermo-fluid dynamics underlying the studied device, as well as for future extensions of the adopted approach to similar layouts.

Keywords: Loop Heat Pipes, Thermography, Inverse Heat Conduction Problem, Local Heat Transfer.

1. Introduction

The exponential miniaturization of electronic components has been leading to a dramatic increase in heat flux densities to be effectively dissipated for the long-term operation of electronics. The use of traditional active cooling equipment demands the use of energy [1]. To deal with this issue, different kinds of passive heat transfer systems that do not rely on auxiliary equipment for the cooling fluid motion, which could also cause undesirable vibrations, have been proposed during the last decades. Among these devices, loop heat pipes (LHPs) represent efficient and reliable thermal management solutions. In their standard layout, LHPs are constituted by a heating area (evaporator), a transport area (adiabatic section), a cooling area (condenser) and a compensation chamber, used as liquid storage, close to the evaporator region. In the evaporator regions, a wick structure guarantees high capillary pressures, which, coupled with the phase-change phenomena, promote a unidirectional fluid flow from the evaporator to the condenser. However, this spontaneous behavior is dampened in thin LHPs, (devices lower than 2 mm thick) [2], caused by the larger confinement of working fluid and higher pressure drop along the device. These two combined effects increase the temperature difference between the evaporator

and compensation chamber needed for the successful operation of LHPs. Larger temperature levels raise the heat conduction (leakage) through the casing material [3]. If the area close to the evaporator is too hot, vapor can be formed in the liquid line, jeopardizing the LHP startup. These effects are augmented in very thin LHPs.

The startup of thin LHPs has challenged some researchers, who use visualization methods, temperature measurements and mathematical models in their studies [4–6]. Few works deal with the start-up conditions under low power inputs. Furthermore, no quantitative information referred to the local heat transfer interactions has been provided. The traditional method of measurement provides only a global lumped thermal performance of the devices, suppressing valid knowledge of the liquid and vapor flows inside the channels.

The present work proposes to investigate quantitatively the local thermal interactions occurring between the working fluid and the device wall during the start-up of a mini flat LHP. To this aim, a compact LHP, specifically designed for microelectronics cooling, was tested at different heat loads. During the experiments, the outer wall temperature was recorded by a medium-weave Infra-Red camera (IR). The thermographic acquisitions

were therefore processed by means of the Inverse Heat Conduction Problem (IHCP) resolution approach [7,8] to estimate wall-to-fluid heat fluxes locally exchanged within the condenser of the device, focusing on both liquid and vapor lines.

2. Experimental set-up

The studied device (Figure 1) is a diffusion bonded LHP made of copper with overall dimensions of 76 x 60 x 1.6 mm. Both the vapor and liquid lines have a cross-section of 3 x 1 mm². Two sintered copper powder wicks, one in the evaporator and one in the liquid line, provide the needed capillary pressure to promote the working fluid flow inside the LHP. Both porous media have a porosity of 53.46 ± 3.87% and 1 mm in thickness. For more details about the LHP manufacturing process and wick structure, see [3].

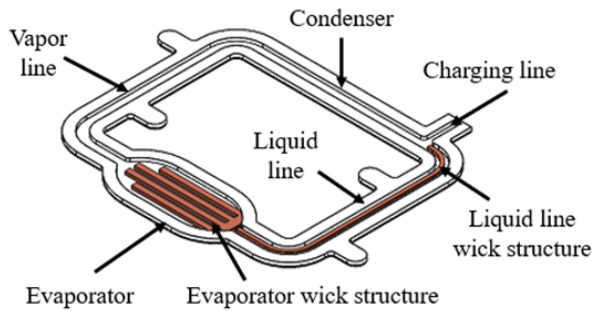


Figure 1. Schematic design of the LHP.

The evaporator is heated by a copper block (heating area of 1 mm²) with one cartridge electrical resistance (3.2 mm of diameter and 25 mm of length) and thermally insulated with a layer of polytetrafluoroethylene, while the condenser dissipates heat to the environment by natural air convection. The external surface of the device is coated with black, high-emissivity paint (emissivity $\epsilon \approx 0.92$) to allow IR measurements of the outer wall temperature by means of a medium-weave IR camera (FLIR[®] ThermaCAM S65) with a pixel resolution of 320 x 240, thermal sensitivity of 0.08 °C in a range from -40 °C to 2000 °C and a sampling frequency of 15 Hz.

The experimental procedure consisted of first calibrating the apparatus. The bottom surface of the LHP (evacuated device - empty) was placed in contact with a machined aluminum block that can circulate water inside it, using a thermal bath. This set-up could provide an isothermal condition of around 60 °C for the LHP. With the IR camera, thirty seconds of measurements were accomplished to calibrate the system.

The second set of tests was to evaluate the local thermal interactions between the working fluid and the LHP walls during its start-up. The LHP was charged with 0.32 ± 0.01 ml of degassed ethanol, representing a filling ratio (ratio between the inserted liquid and the total void volume of the LHP) of 40% vol. The device was positioned in the horizontal orientation. Four different heat inputs, 2 W, 4 W, 6 W and 8 W, were applied by means of a power supply unit.

3. Methods

IR acquisitions were used as inputs for the IHCP to evaluate the heat fluxes locally exchanged between the working fluid and the LHP wall within the condenser section, as shown in Figure 2.

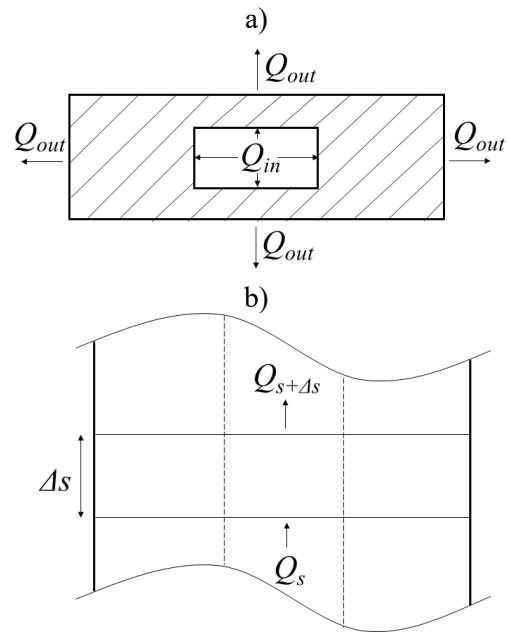


Figure 2. Cross-sectional view (a) and overhead view (b) of the generic wall element.

The energy balance equation in transient conditions (without heat generation) for the generic wall element of length Δs (Fig. 2), whose temperature is assumed uniform in space, given the great device compactness and the high thermal diffusivity of copper, is defined as:

$$\frac{dU}{dt} = Q_s - Q_{s+\Delta s} + Q_{in} - Q_{out} \quad (1)$$

where U is the internal energy, t is time, Q_s and $Q_{s+\Delta s}$ are the power terms referred to the spatial coordinate s , while Q_{in} and Q_{out} are the power terms exchanged at the fluid-to-wall and the wall-

to-environment interfaces, respectively. All the power terms appearing in Equation (1) are expressed as follows:

$$\frac{dU}{dt} = \rho c_p \frac{\partial T}{\partial t} S_{sect} \Delta s \quad (2a)$$

$$Q_s = -k \frac{\partial T}{\partial s} S_{sect} \quad (2b)$$

$$Q_{s+\Delta s} = -k \frac{\partial T}{\partial s} S_{sect} - k \frac{\partial T}{\partial s} S_{sect} \Delta s \quad (2c)$$

$$Q_{in} = q S_{in} \Delta s \quad (2d)$$

$$Q_{out} = h_{env} (T - T_{env}) S_{ext} \Delta s \quad (2e)$$

where S_{sect} , S_{in} and S_{ext} are the cross-sectional area, the inner surface and the outer surface of the wall element, respectively, ρ , c_p and k are the density, specific heat and thermal conductivity of copper, q is the wall-to-fluid heat flux, T_{env} is the environmental temperature and h_{ext} is the overall heat transfer coefficient by both free convection and radiation toward the environment. The ambient temperature was monitored during the tests, and it varied from about 23 to 25 °C. By substituting all the power terms in Equation (1) and rearranging, the wall-to-fluid heat flux reads as:

$$q(s,t) = \frac{\left(\rho c_p \frac{\partial T(s,t)}{\partial t} - k \frac{\partial^2 T(s,t)}{\partial s^2} \right) \cdot S_{sect} + h_{env} (T(s,t) - T_{env}) \cdot S_{out}}{S_{in}} \quad (3)$$

Equation (3) can be solved by means of the finite difference method. However, when raw, noisy temperatures are considered, Equation (3) gives unstable results due to the presence of first and second order derivatives. Among other techniques, the filtering approach [9] was adopted as regularization method to filter out the unwanted noisy components from the raw data, thus allowing a reliable evaluation of q . The optimal cut-off frequency for the filtering technique was chosen by means of the so-called discrepancy principle, whose target function is defined as [10]:

$$\frac{\|T_f - T\|_2^2}{N} \cong \sigma_T \quad (4)$$

where T_f is the filtered temperature, T is the raw temperature, N is the number of samples of T and σ_T is the standard deviation of T .

In the present analysis, six wall sections were considered (dotted lines in Figure 3), and their temperature was assessed by averaging IR acquisitions over 10 x 10 pixels areas (blue squares in Figure 3).

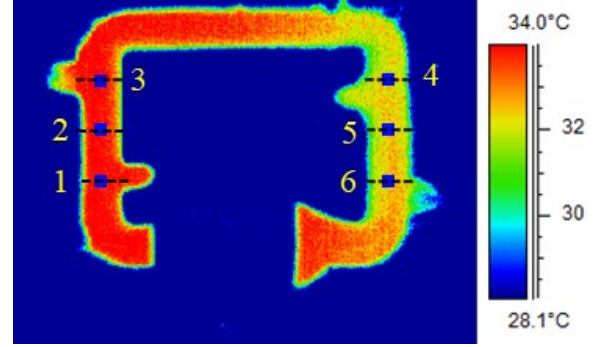


Figure 3. Sample of IR acquisition and sections of interest for the present analysis.

The six resulting temperature distributions were first processed by means of a one-dimensional Gaussian filter, and then used in Equation (3) to estimate the wall-to-fluid heat flux exchanged in sections 2 (vapor line) and 5 (liquid line).

4. Results

The empty LHP (FR = 0%) was first analyzed under steady state conditions to perform both an assessment in terms of energy balance and a calibration procedure for the method provided in Section 3. The device was therefore investigated at different heat loads to the evaporator to give a better insight into the evolution trend of the local wall-to-fluid heat flux exchanged over the vapor and liquid lines.

4.1 Method calibration (empty device, isothermal conditions)

The empty LHP was first placed on a heating plate, in thermal contact with its whole lower surface. By this means, the device was reasonably assumed to be at isothermal conditions, given the low thickness and the high thermal conductivity of copper walls. Four T-type thermocouples were placed on the upper surface to monitor the wall temperature, while 30-second-long IR acquisitions were performed at varying heating powers, i.e., at different isothermal conditions. Under such isothermal test conditions, the standard deviation of the raw thermographic measurements σ_T was assessed equal to 0.04 K. The approach of Section 3 was therefore applied to the thermographic data,

thus estimating the wall-to-fluid heat flux exchanged at the vapor and liquid lines, namely q_{vap} and q_{liq} . In Figure 4, the two estimated heat fluxes are shown for device temperature at 60°C.

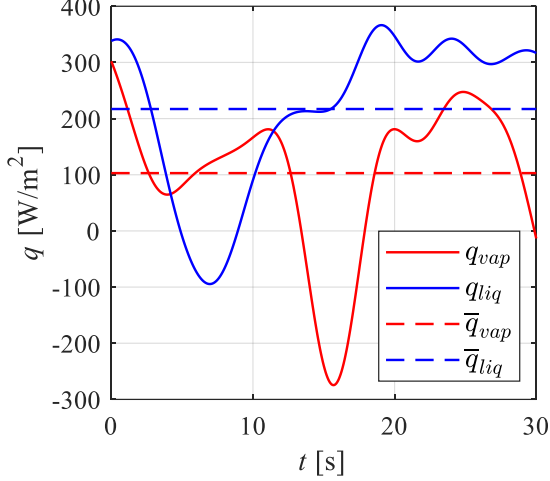


Figure 4. Wall-to-fluid heat fluxes estimated for the empty device in isothermal conditions and average values.

Since the LHP is empty, the wall-to-fluid heat flux is clearly expected to be globally null. Nonetheless, the procedure provides non-null values of heat flux; specifically, the reported trends exhibit fluctuations around a non-null average. On one hand, fluctuations are probably due to uncertainties unavoidably inherent in the inverse approach. The non-null average has instead to be accounted for systematic errors in the experimental data, such as slight non-uniformities in the emissive coating and in the spatial behavior of the IR camera sensors. Such a systematic deviation from zero was confirmed by other heat fluxes computed at different isothermal conditions. To get rid of systematic errors in the estimation procedure, the non-null means $\bar{q}_{vap} = 217.1 \text{ W/m}^2$ and $\bar{q}_{liq} = 102.9 \text{ W/m}^2$ were subtracted from the wall-to-fluid heat fluxes referred to the vapor and liquid lines, respectively. In other words, a preliminary calibration on the heat flux outputs was performed by taking into account the expected physical behavior in known and controlled conditions. On the other hand, the uncertainty introduced by the method of Section 3 was defined as the twice the standard deviation of the computed heat fluxes in isothermal conditions, here evaluated as $\pm 260 \text{ W/m}^2$ for both liquid and vapor lines.

4.2 Overall energy balance (empty device, steady state conditions)

An additional preliminary investigation on the collected data concerned the study of the empty LHP at a power of 6 W to the evaporator was accomplished. IR acquisitions were carried out when the steady state of the system was reached. The outer wall temperature over the whole condenser was hence averaged, resulting in steady state, mean condenser temperature of $T_{cond,ss} = 334.9 \text{ K}$. The outer wall temperature of the insulating block placed over the evaporator was similarly acquired through thermography by assuming, in the medium IR spectrum, a polytetrafluoroethylene emissivity almost equal to that of the black emissive coating (0.92) [11]. The average temperature of the insulation $T_{ins,ss}$ was therefore computed as 328.1 K. Given the outer wall surfaces of the condenser section $S_{cond} = 0.0043 \text{ m}^2$ and the insulation block $S_{ins} = 0.016 \text{ m}^2$, the overall power dissipated to the external environment Q_{ext} by free convection is the sum of the powers dissipated at the condenser and at the evaporator through the insulation, defined as:

$$Q_{ext} = h_{env} [(T_{cond,ss} - T_{env})S_{cond} + (T_{ins,ss} - T_{env})S_{ins}] \quad (5)$$

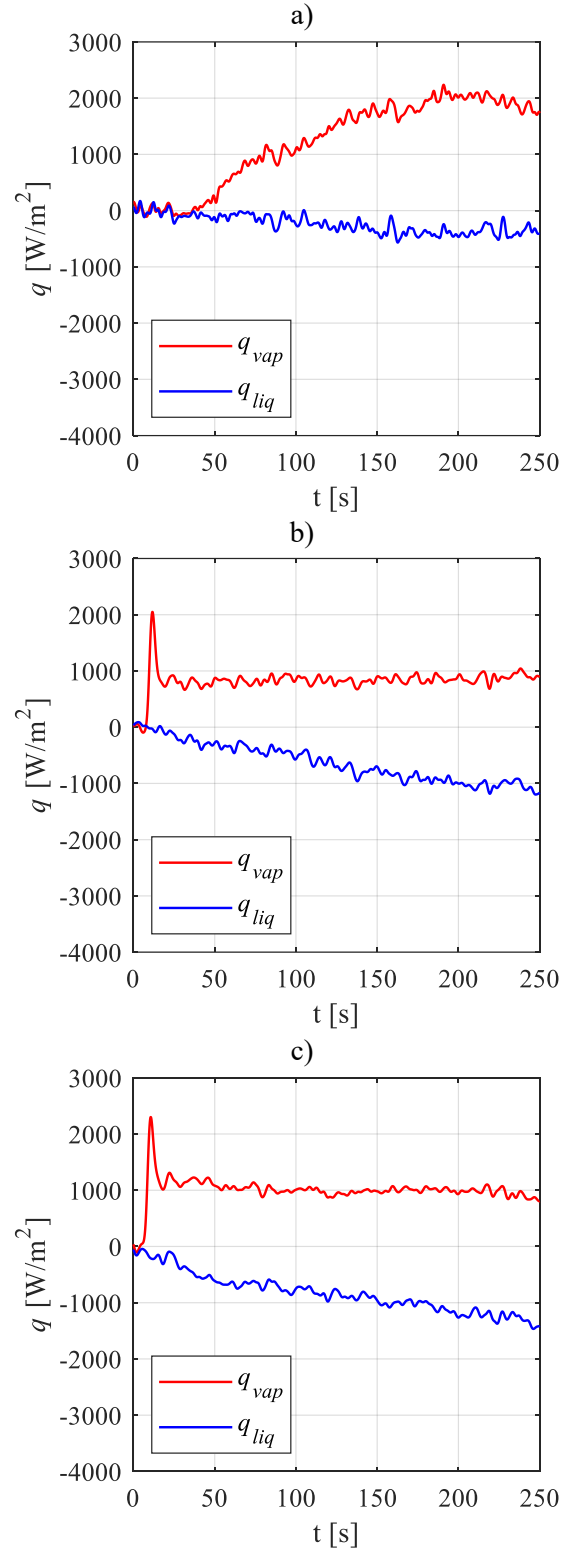
By furtherly considering the condition under which the overall energy balance is satisfied, $Q_{ext} = Q$ (where $Q = 6 \text{ W}$ is the heat load given to the evaporator), and rearranging Equation (5), h_{env} results equal to $27.2 \text{ W/m}^2\text{K}$. Such an estimated heat transfer coefficient is in accordance with that found by adopting the Stefan-Boltzmann law and the available empirical correlations for free convection on horizontal and vertical surfaces [12], confirming the accuracy of the performed IR acquisitions in terms of absolute temperature and the consistency of the overall energy balance. Consequently, heat dissipations at the condenser and at the evaporator were estimated to be equal to about 76% and 24% of Q , respectively.

4.3 Local heat transfer characterization

After conducting a dedicated calibration of the procedure, together with an estimation of the uncertainty of the wall-to-fluid heat fluxes and of the overall heat dissipations to the environment, the charged LHP was tested at varying heat loads to the evaporator. The wall-to-fluid heat fluxes were

estimated for both the vapor and liquid lines during the activation phase of the device. In start-up conditions, the wall temperature was much lower than that measured in Section 4.2; hence, the heat transfer coefficient h_{env} was here reasonably assumed equal to $10 \text{ W/m}^2\text{K}$ [13]. This value is lower than the previous one for natural air convection, which was at higher temperature, because this coefficient also takes into consideration the radiation heat transfer. In Figure 5, the estimated wall-to-fluid heat fluxes are shown over time for heat loads ranging from 2 W to 8 W. According to the reference system of Section 2, the wall-to-fluid heat flux assumes positive values when heat is transferred from the working fluid to the device wall, i.e., when the fluid is warmer than the copper wall. At 2 W (Figure 5a), the poor performance of the LHP, which has been previously highlighted in [3] through equivalent thermal resistance assessment, is confirmed by the local heat flux trends. In fact, q_{vap} slightly increases over the observation window, denoting that the device undergoes a long start-up due to the low heating power, which cannot ensure a strong and sustained vapor generation at the evaporator. Moreover, the heat flux exchanged at the liquid line remains practically null, suggesting that both the fluid and the LHP walls are at almost the same temperature. At 4 W (Figure 5b), q_{vap} exhibits a steep peak of about 2000 W/m^2 at about 10 s, i.e., when the heat load is first supplied to the evaporator. This is due to the fact that the provided heat load promotes phase change at the evaporator, resulting in a fast stream of hot vapor that crosses the vapor line and exchanges heat with the device walls. After the first transient, q_{vap} settles around 1000 W/m^2 , suggesting that the local heat transfer behavior quickly reaches a pseudo-steady condition in terms of heat exchanged at the inner fluid-wall interface. q_{liq} denotes instead a negative increase, probably due to non-negligible conduction (heat leakage) through the LHP walls and wick structures from the evaporator to the liquid line, which enhances the temperature difference between the condensate flowing back to the evaporator and the copper walls. As long as the heat load increases (Figures 5c,d), the heat flux signals exhibit similar trends to those observed in Figure 5b, although the amplitudes of both q_{vap} and q_{liq} tend to increase due to stronger phase-change phenomena and conductive heat transfer. To provide a comprehensive outline of the heat fluxes exchanged in the vapor line during the first transient of the start-up process, the peak values assumed by q_{vap} , $q_{vap,peak}$, are plotted as a

function of the heat load in Figure 6, along with the uncertainty estimated in Section 4.1.



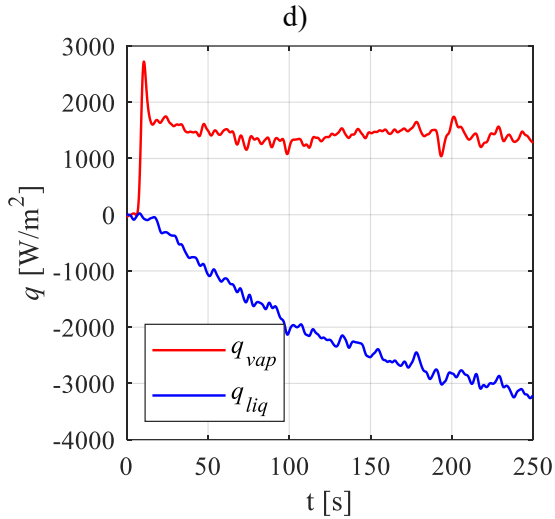


Figure 5. Wall-to-fluid heat fluxes estimated for the charged device during the activation phase; $Q = 2$ W (a), $Q = 4$ W (b), $Q = 6$ W (c), $Q = 8$ W (d).

Specifically, the only heat loads greater than 2 W were considered since they promoted a proper activation of the device.

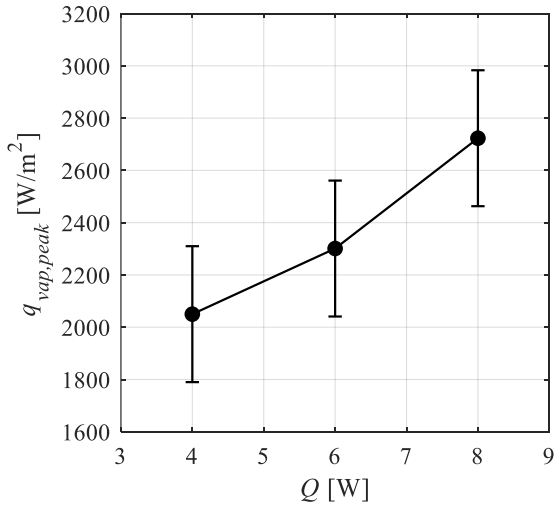


Figure 6. Peak values assumed by q_{vap} during the first transient of the LHP start-up, as a function of the heat load.

Here, q_{vap} denotes peaks which monotonically increase with the power input, suggesting that convective heat transfer becomes more predominant due to a stronger interplay between vapor quality, velocity and temperature. From the present non-intrusive analysis, no additional details concerning the vapor quality and temperature can be drawn. Nonetheless, the vapor velocity can be estimated

by identifying the time delays between wall temperature variations, which sequentially occur as far as the vapor crosses the vapor line during the first start-up transient. This evaluation is based on the assumption that the characteristic velocity of heat diffusion in the highly conductive, thin walls of the device is of the same order of magnitude of the inner fluid dynamics. In Figure 7, the wall temperature referred to sections 1, 2 and 3 of Figure 3, is shown over the first 15 seconds of acquisition, $Q = 8$ W.

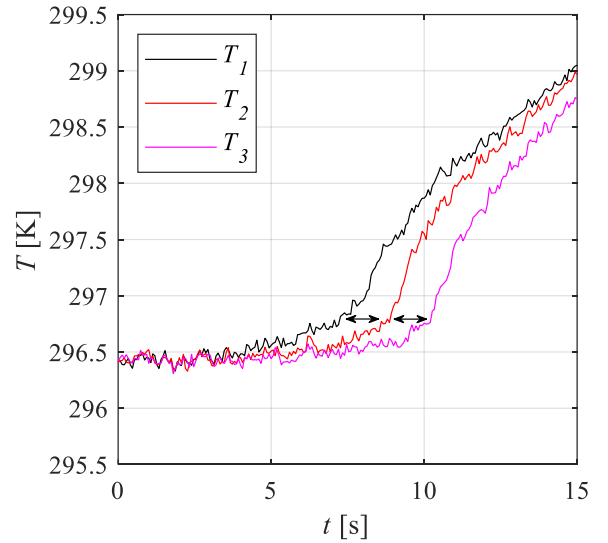


Figure 7. Identification of time delays between temperature profiles referred to sections 1, 2 and 3 of Figure 2 during the first start-up transient.

The black double arrows are here adopted to graphically outline the identified time lags between the three curves. The delays are both assessed equal to 1.33 s, with uncertainty equal to $1/15$ s (reciprocal of the IR camera sampling frequency). By computing the ratio of the distance between the three sections, 0.0138 ± 0.0001 m, to the time lag, the vapor velocity results equal to about 0.01 m/s. Almost the same values were found for $Q = 4$ W and $Q = 6$ W, denoting that the vapor velocity, for the present LHP, is highly independent of the heat load to the evaporator. A reasonable explanation for the equal vapor velocity for all heat loads can be the balancing between vapor pressure and pressure drops along the LHP. In one hand, larger power input rises the vapor mass production and, as the vapor line cross section area is the same, a vapor velocity could be expected to increase. On the other hand, it is known that, in order for the LHP to start operating properly (two-phase phenomenon), an unbalance

temperature between the liquid-vapor interface (in the evaporator wick structure) and the inlet evaporator section, must exist. This temperature difference produces an unbalance pressure between these two regions that promote the working fluid motion through the LHP. Therefore, increasing the heat load, this temperature difference increases and consequently the pressure drop. For this reason, the vapor front velocity does not change significantly with increasing the heat load. This fact can also be visualized by the IR film of the temperature variation along the condenser produced during the start up for all power inputs. Actually, based on the authors knowledge, the assessment of the vapor velocity was never provided before in the literature. This information can be extremely important for the development of new numerical, theoretical or mathematical models for LHPs.

5. Conclusion

Data from a mini loop heat pipe experimentally studied was used with the objective of developing a novel analysis tool for the local heat transfer in LHPs and similar devices. The mini (1.6 mm thick) LHP analyzed was partially filled with ethanol and tested during the start-up in horizontal orientation, for power inputs of 2 W, 4 W, 6 W and 8 W at the evaporator section. The outer wall surface of the condenser was coated with a highly emissive paint and IR temperature measurements were taken through a medium-weave infrared camera. The acquired temperature signals were processed by means of the Inverse Heat Conduction Problem resolution approach, which provided the heat fluxes exchanged between the working fluid and the device wall, in both vapor and liquid lines of the condenser section. The temperature trends confirmed the unidirectional vapor flow along the condenser. In the vapor line, the wall-to-fluid heat flux denoted a vigorous peak of about 2000 W/m² during the first transient with 4 W, i.e., at the moment when the device was activated as a two-phase equipment. After that, in the pseudo steady-state condition, the heat transfer in the vapor line stabilized at 1000 W/cm². On the other hand, the liquid line presented a wall-to-fluid heat flux of 1000 W/m², meaning that the heat leakage from the evaporator to the liquid line is meaningful. During the device operation, the heat fluxes, in both lines, tended to constant values, suggesting quasi-steady working conditions. The IR technique could measure the vapor velocity to be of 0.1 m/s for all applied heat inputs. Actually, the vapor velocity in LHPs is quite an interesting new

information that can be quite useful for the understanding of the vapor flow behavior in a wide range of two-phase flow devices, being the basis for the development of more reliable numerical, theoretical or mathematical models.

Acknowledgments

The Authors would like to acknowledge the European Space Agency (ESA) support through the grant 4000128640/19/NL/PG/pt, ESA MAP project TOPDESS. Also, acknowledgement to FAPESC (Fundação de Amparo à Pesquisa e Inovação do Estado de Santa Catarina) for providing scholarship (grant number 3003/2021).

References

- [1] S.M. Sohel Murshed, C.A. Nieto de Castro, *Renewable and Sustainable Energy Reviews* 78 (2017) 821–833.
- [2] H. Tang, Y. Tang, Z. Wan, J. Li, W. Yuan, L. Lu, Y. Li, K. Tang, *Appl Energy* 223 (2018) 383–400.
- [3] K.G. Domiciano, L. Krambeck, J.P.M. Flórez, M.B.H. Mantelli, *Energy Convers Manag* 255 (2022) 115329.
- [4] M.A. Chernysheva, Y.F. Maydanik, J.M. Ochterbeck, *J Thermophys Heat Trans* 22 (2008) 617–622.
- [5] J. Kizito, M. Hossain, *Frontiers in Heat Pipes (FHP)* 7 (2016).
- [6] L. Bai, Z. Yang, X. Shen, Y. Guo, G. Lin, D. Wen, *Heat and Mass Transfer* 58 (2022) 813–831.
- [7] F. Bozzoli, G. Pagliarini, S. Rainieri, *Exp Therm Fluid Sci* 44 (2013) 858–867.
- [8] L. Pagliarini, L. Cattani, F. Bozzoli, M. Mameli, S. Filippeschi, S. Rainieri, M. Marengo, *Int J Heat Mass Transf* 169 (2021) 120930.
- [9] D.A. Murio, *The Mollification Method and the Numerical Solution of Ill-Posed Problems*, John Wiley & Sons, 1993.
- [10] V.A. Morozov, *Methods for Solving Incorrectly Posed Problems*, Springer-Verlag, 1984.
- [11] T. Wentink, W.G. Planet, *J. Opt. Soc. Am.* 51 (1961) 601–602.
- [12] A.-J.N. Khalifa, *Energy Convers Manag* 42 (2001) 491–504.
- [13] G. Maranzana, S. Didierjean, B. Rémy, D. Maillet, *Int J Heat Mass Transf* 45 (2002) 3413–3427.

Applications of opal techniques in high-efficiency thermal management devices

Qihan Chen^{1,2,3}, Jingzhi Zhou^{1,3*}, Guohui Zhou^{1,3}, Feng Zhou^{1,3,4}, Xiulan Huai^{1,3*}, Gaosheng Wei²

¹ Institute of Engineering Thermophysics, Chinese Academy of Sciences, Beijing, China

² North China Electric Power University, Beijing, China

³ Nanjing Institute of Future Energy System, Nanjing, China

⁴ School of Engineering Sciences, University Chinese Academy of Sciences, Beijing, China

*Corresponding author e-mail address: zhoujingzhi@iet.cn, hxl@iet.cn

Abstract

Vapor Chambers or Heat Pipes are widely used in thermal management devices for electronic products. The porous wick critically influences their heat transfer performance. The opal technique can improve the porous structures' uniformity, capillary force, and permeability, which may be the key to further heat pipe technique. In this paper, the preparation process, structural characterization, permeability analysis, and thin-film phase transformation property of the inverse opal technique in the last decade have been investigated, and some tentative recommendations for future studies are put forward at the end.

Keywords: Porous structure; Inverse opal technique; Heat pipe; Vapor chamber

1. Introduction

With the rapid development of the chip manufacturing process, the microelectronic chips' structural sizes are becoming more and more compact, and the chip power is progressively growing, resulting in increasing heat fluxes year after year. There is no denying that the heat dissipation issue has become one of the critical reasons for restricting chips' development. According to certain studies, the performance of an electronic device will reduce by 5% for every 1 °C rise while the operating temperature is 70~80 °C [1]. So, it is necessary for microelectronic chips to dissipate heat via cooling equipment.

Vapor chambers evenly distribute the heat of mobile devices' high-power chips, and the heat is conducted into the environment through the mobile devices' bodies. Heat pipes are frequently used for high-power servers and data centers, such as pin-fin heat sinks, loop heat pipes, liquid immersion cooling using vapor chambers, etc. The interior wick structures, such as wire meshes, sintered powders, metal fiber felt, grooves, and composite structures, significantly impact the performance of vapor chambers or heat pipes. The properties of various wick structures differ considerably. The sintered wick has the highest capillary limit but lower permeability and porosity. Due to its irregular shape, it is arduous to be studied in theory. In contrast, the grooved wick has the highest permeability but smaller capillary pressure and

poorer anti-gravity capability. The composite wick has the advantages of each component wick. However, it is tough to develop and manufacture. The performance of the wire mesh wick looks close to the optimization, whereas the wire mesh wick lacks integrity. On the whole, it seems impossible to considerably improve the heat pipe's and vapor chamber's performance through conventional wick structures. As a consequence, it may be a better impact on heat pipe and vapor chamber development to introduce novel wick structures.

Inverse opals (IOs) have isotropic and highly regular structures, which are often applied in biology [2], optics [3], and lithium batteries [4], among other fields. Recently, it has been brought into the porous media field by Professor Kenneth Goodson's team at Stanford University [5]. It is demonstrated that the IO wicks have better permeability, greater porosity, and superior heat transfer capability than the common wick. It may be anticipated to play a crucial role in breaking through the limitations of the current vapor chambers and heat pipes. Therefore, this work explains the present IO wick research in preparation processes, structures, and flow and heat transfer performance so that more scholars may join this study.

2. Preparation processes

IOs are manufactured by assembling microspheres into a highly ordered opal template

and then removing the template by heating or dissolution corrosion, as shown in Figure 1. Templates are frequently built with polystyrene (PS), polymethyl methacrylate (PMMA), silicon dioxide (SiO_2), and other microspheres [6]. In the beginning, the microspheres are dissolved in a solvent to make a specific concentration suspension, and the suspension is put on the glass/silicon wafer substrate. When the solvent has evaporated, an opal template will generate. After this, the template is sintered to solidify the structure and then electroplated. Finally, the microsphere templates are etched with a dissolving agent to open the pores. During sintering, many microspheres melt and bond with the increasing temperature, and "necks" will form when copper is electrodeposited here, as shown in Figure 2.

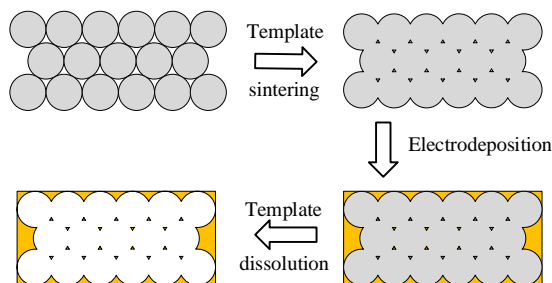


Figure 1. Production processes of IO structure.

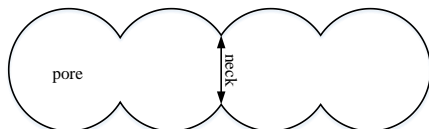


Figure 2. Schematic diagram of pores and necks.

Van der Waals force, Brownian force, steric force, capillary force, hydrogen bonding contact, and hydrophobic interaction are the driving forces of molecular self-assembly in usual [7]. Due to the low cost and ease of operation, capillary force is the most extensively adopted. Drop casting and vertical deposition are based on the capillary force, usually used in self-assembly methods. Besides, electrophoretic assembly and spin coating methods are also commonly utilized [8].

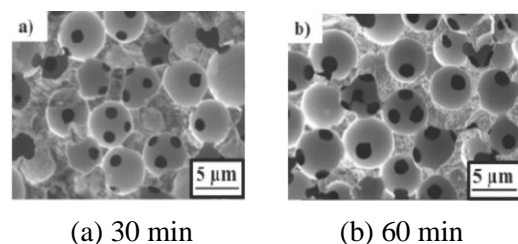
Several IO structure preparation processes will be described below. Won et al. [9] used a drop-casting method to cast 675 nm diameter functionalized SiO_2 spheres into the substrate in 5 μl /drop increments. The solvent was evaporated by heating. A more than 10- μm thick opal structure template was obtained by repeating this operation.

Copper was electrodeposited in the template's gap, and the template was dissolved in a 2~5 % HF aqueous solution, producing 3~7 μm thick copper inverse opals (CIOs). Song et al. [10] dispersed 600 nm diameter functionalized PS spheres in ethanol and added NH_4OH to raise the pH value over 10. The electrophoretic assembly method was used to manufacture a 15-layer PS opal template. After annealing at 95 $^\circ\text{C}$ for 1 h, copper electrodeposition was done. The template was immersed in toluene to remove the PS spheres in the end. Wu et al. [11] made a solution of 340 nm SO_2 microspheres and diffused it on a copper substrate. They used the spin coating method to produce a template and then annealed it for 2 h. After this, $\text{CuSO}_4 \cdot 5\text{H}_2\text{O}$, $(\text{NH}_4)_2\text{SO}_4$, and diethylenetriamine solutions were invested in electrodeposition. Finally, CIOs with a diameter of 300 nm were obtained by placing the template in a 10 wt% HF aqueous solution for 30 min. In addition, CIOs were successfully fabricated by utilizing the Langmuir-Blodgett (L-B) method [5] and using the vertical deposition method [12].

It is feasible to form micron-scale structures at present, thanks to the fast progress of molecular self-assembly. However, the function of self-assembly is considerably reduced when the molecule size is over more than 10 μm . Too small wick pore sizes may lead to many problems, such as a significant pressure drop and arresting bubbles' flowing and growing. It is necessary to find a method to prepare large-scale CIOs in the future.

3. Structural characterization and analysis

Since the scale of IOs is typically in the nanometer and micrometer range, it is more susceptible to external factors, which may cause significant changes in the microstructure even with slight adjustments during preparation. Zhang et al. [13] compared the effect of different sintering time on CIOs' microstructure with 5 μm diameter pore size at a sintering temperature of 103 $^\circ\text{C}$, as shown in Figure 3. The neck diameter grew with increasing sintering time. However, a long sintering time might destroy the formed structure, as shown in Figure 3. (d).



(a) 30 min

(b) 60 min

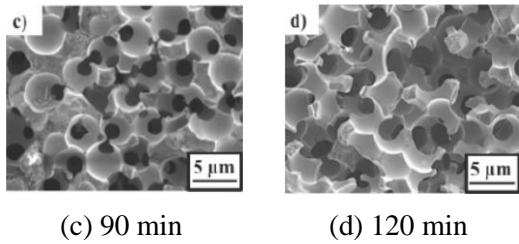


Figure 3. SEM of CIOs at different sintering times [13].

Pham et al. [14] electropolished the CIOs to vary the surface contact angle, and the contact angle increased with the times. When the number of times is 250, the contact angle could reach 150° . After electrochemical oxidation, the porosity and contact angle decreased, and the microstructure was damaged to varying degrees, as shown in Figure 4.

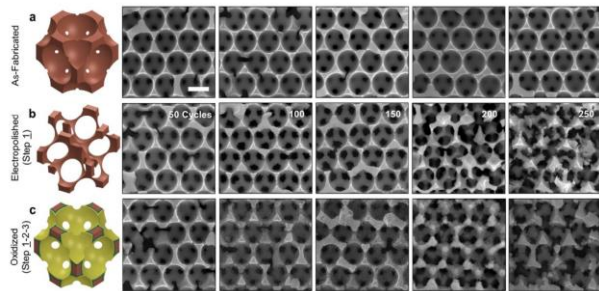


Figure 4. SEM with different cycles of electropolished and oxidized [14].

In addition to the common uniform-pore-size CIOs, Wu et al. [15] prepared gradient CIOs (g-CIOs), as illustrated in Figure 5. It is time-consuming that this structure must be produced in layers, but its CHF might rise 70.5 % more than horizontally oriented CIOs.

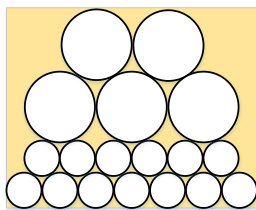


Figure 5. Schematic diagram of g-CIOs.

Sintering and polishing may improve the performance of IOs, but they also have a higher probability of destroying the microstructure and losing the ordering advantage. On the other side,

the rigidity of IOs should also be highlighted. According to certain studies, flow rates greater than 1 ml/min will ruin IO structures [16]. Hence, the robustness of the microstructure has to be improved in the coming years, particularly after repeated cycling.

4. Flow and heat transfer performance research and analysis modeling

4.1. Permeability performance

IOs have a highly ordered microstructure that allows the working liquid to flow smoothly, and their permeabilities may be markedly improved. Dusseault et al. [16] investigated CIO's permeability by preparing CIO with a pore diameter of $4 \mu\text{m}$ and a neck diameter of $1.2 \mu\text{m}$. When the porosity was 0.9, the permeability was about $5 \times 10^{-14} \text{ m}^2$, which might result in damaged CIO owing to the extended sintering time (24 h). Zhang et al. [17] used experiments to compare the permeability of $5\text{-}\mu\text{m}$ diameter CIOs at various sintering time and temperatures. As demonstrated in Figure 6, the permeability could reach $1.3 \times 10^{-12} \text{ m}^2$ when sintered at 110°C for 40 min, but it was only $1.3 \times 10^{-13} \text{ m}^2$ when sintered at 95°C for 2000 min. And, compared to unsintered CIOs, sintered CIOs at 110°C for a longer time had a minor pressure difference between the inlet and outlet of CIOs in the air, and their maximum pressure difference might be decreased by nearly 12 times. This showed that sintering temperature and time have significant effects on permeability.

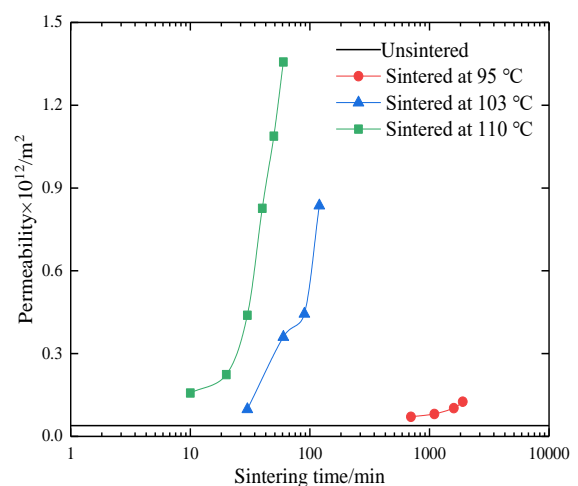


Figure 6. Influence of sintering time and temperature on the permeability.

Zhang et al. [13] evaluated the flow performance of CIOs sintered at 103°C for 30~120 min. They

discovered that the permeability rose by nearly 900 %, the porosity increased by about 16.4%, but the capillary force reduced by about 47.5 % when the sintering time increased. Furthermore, after being sintered for 90 min, the CIO wick could raise ethanol to about 7 mm in 30 s (the meniscus height was 2.4 mm). As shown in Figure 7, Pham et al. [12] summarized the influence of pore size on permeability, capillary force, and flow resistance. It is easy to notice that permeability improved, and capillary force and viscous resistance decreased when pore size grew.

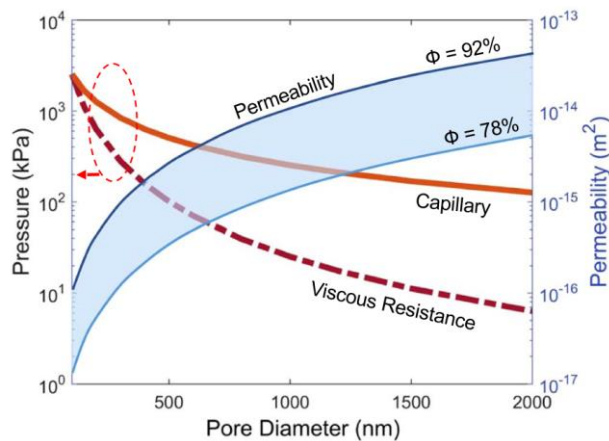


Figure 7. Influence of pore size on flow performance of CIOs [12].

4.2. Strengthening phase transformation performance of the thin liquid film

Heat transfer performance is one of the most significant characteristics in evaluating heat pipes' and vapor chambers' properties. When the IOs are used as their wick structures, it is vital to analyze the heat transfer coefficient (HTC), critical heat flux (CHF), and heat transfer limit. In order to study the impact of CIO's porosity on heat transfer performance, Won et al. [9] investigated the thermal conductivities with varied porosities in the area of $20 \mu\text{m} \times 60 \mu\text{m} \times 400 \mu\text{m}$ through experiments and simulations. The thermal conductivity was $120 \text{ W}/(\text{m} \cdot \text{K})$ when the porosity was 50%. And it might be enhanced to $180 \text{ W}/(\text{m} \cdot \text{K})$ when the porosity was reduced to 40%. Barako et al. [18] compared the performance of CIO with nickel inverse opal (NIO) with thicknesses ranging from $2.76 \mu\text{m}$ to $6.55 \mu\text{m}$ and pore sizes ranging from 100 nm to 1000 nm. The thermal conductivity of CIOs rose with thickness, from $27.1 \text{ W}/(\text{m} \cdot \text{K})$ to $62.7 \text{ W}/(\text{m} \cdot \text{K})$, which might be attributed to increased thickness and pore diameter. CIO's

thermal conductivity could be enhanced by decreasing layers. In contrast, NIO's thermal conductivity was almost independent of the number of layers. Lee et al. [19] contrasted the pool boiling performance of a CIO film with a thickness of approximately $10 \mu\text{m}$ and a pore diameter of $5 \mu\text{m}$ with that of a bare Si surface without the film. Bare Si achieved CHF ($79.1 \text{ W}/\text{cm}^2$) at a superheat of 21.6 K, whereas CIO film achieved CHF ($225.6 \text{ W}/\text{cm}^2$) at a superheat of about 40 K. HTC of Si reached the maximum value when the heat flux became $56.6 \text{ W}/\text{cm}^2$. At this time, the superheat degree was 13.7 K, and HTC was $50 \text{ kW}/(\text{m}^2 \cdot \text{K})$. HTC of CIO achieved its maximum value of $110 \text{ kW}/(\text{m}^2 \cdot \text{K})$ when the heat flux was $148.5 \text{ W}/\text{cm}^2$, and the superheat degree was 12.7 K. In addition, as shown in Figure 8, the author got the pool boiling bubbles flow processes of the CIO under various heat fluxes.

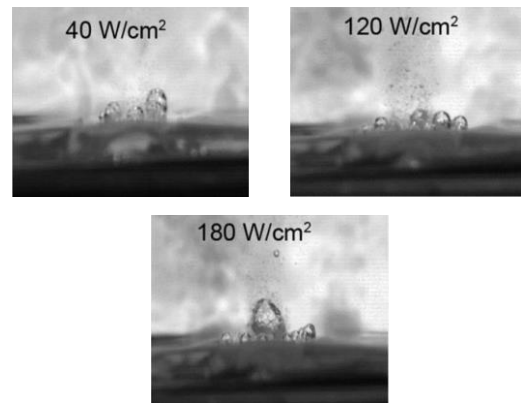


Figure 8. Flow processes of CIOs pool boiling bubbles [19].

The heat transfer performance of IO, as reported by other researchers, is shown in Table 1. The boiling heat transfer limit is also essential. Zhang et al. [20] studied the effects of neck diameter, heating length, and thickness on heat transmission performance on CIOs, as illustrated in Figures 9 and 10. The pore diameters were $3.2 \mu\text{m}$, $5.4 \mu\text{m}$, and $10.2 \mu\text{m}$, respectively. When the heating length and thickness were varied, the transition point between boiling and capillary limits would change accordingly. The boiling limit was negatively related to thickness, but the capillary limit rose as thickness increased and heating time decreased. When the neck diameter increased, both of them improved simultaneously. The authors used this information to fit the data and obtained the correlation formulas for transition length, thickness, capillary limit, and boiling limit, as shown in equations (1) to (4).

Table 1. Heat exchange performance of IOs.

Authors	Sizes	Conditions	Results
Pham et al. [21]	CIO pore diameters (PDs): 0.6~5 μm	Heat flux: 0~110 W/cm ²	HTC _{5μm} , max= 100 kW/(m ² ·K), HTC _{0.6μm} , max= 3.3 kW/(m ² ·K).
Zhang et al. [22]	CIO PD: 5.2 μm	Neck diameter: 0.52~2.08 μm ; superheat: 12 K	With the increase in neck diameter, CHF enhanced from 55 W/cm ² to 1000 W/cm ² .
Montazeri et al. [23]	CIO PDs: 10~20 μm	Contact angles: 20~40°	Changing the contact Angle had little effect on HTC.
Wu et al. [15]	g-CIO PDs: 5 μm and 10 μm ; CIO PD: 5 μm	Same thickness; took the thermal property at 112 °C	G-CIOs could increase CHF by 70.5%.
Soroush et al. [24]	1 layer, 5 layers of 50 μm PD copper wire meshes (CWMs) and a 5 μm PD CIO+5 layers CWMs	The superheat was 8 K, 18 K, and 9 K, respectively.	CHF _{1CWM} =28 W/cm ² , HTC _{1CWM} =3.3×10 ⁴ W/(m ² ·K); CHF _{5CWMs} =150 W/cm ² , HTC _{5CWMs} =8.3×10 ⁴ W/(m ² ·K); CHF _{5CWMs+CIO} =300 W/cm ² , HTC _{5CWMs+CIO} =3.3×10 ⁵ W/(m ² ·K).

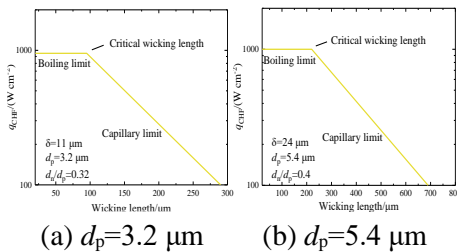
$$l_{\text{cri}} = \frac{\delta}{\rho_v} \left[\frac{8K_{rl}\sigma\mu_v T_s (\rho_l - \rho_v) \cos\theta}{K_{rv} h_{fg} \mu_l d_p \Delta T} \right]^{\frac{1}{2}} \quad (1)$$

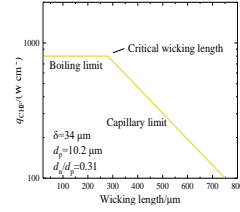
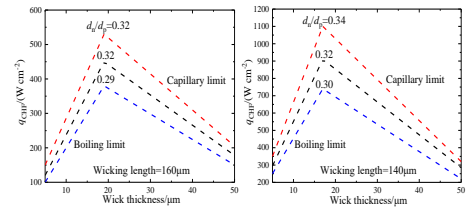
$$\delta_{\text{opt}} = \rho_v l_{\text{eff}} \left[\frac{K_{rv} \mu_l h_{fg} d_p \Delta T}{8K_{rl} \mu_v \sigma T_s (\rho_l - \rho_v) \cos\theta} \right]^{\frac{1}{2}} \quad (2)$$

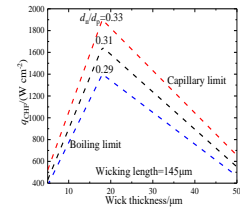
$$q_{\text{cap,CHF}} = \frac{8K_{rl} K h_{fg} \rho_l \delta \cos\theta}{\mu_l d_p l_{\text{eff}}^2} \quad (3)$$

$$q_{\text{boil,CHF}} = \frac{K_{rv} K h_{fg}^2 \rho_l \rho_v^2 \Delta T}{\mu_v T_s (\rho_l - \rho_v) \delta} \quad (4)$$

where δ is the thickness of IOs, m; ρ_v and ρ_l are the vapor and liquid densities, kg/m³; K_{rv} and K_{rl} are the relative permeability of the vapor and liquid phases; σ is the surface tension, N/m; μ_v and μ_l are the vapor phase and liquid phase kinetic viscosity, Pa s; T_s is saturation temperature, K; θ is the contact angle, °; h_{fg} is the latent heat of vaporization, kJ/kg; d_p is the neck diameter, m; ΔT is the temperature difference, K; l_{eff} is the effective length, m, which is half of the total length; K is the permeability, m².


 (a) $d_p=3.2 \mu\text{m}$

 (b) $d_p=5.4 \mu\text{m}$

 (c) $d_p=10.2 \mu\text{m}$
Figure 9. Relationship between heat transfer limits and heating length.

 (a) $d_p=3.2 \mu\text{m}$

 (b) $d_p=5.4 \mu\text{m}$

 (c) $d_p=10.2 \mu\text{m}$
Figure 10. Relationship between heat transfer limits and thickness.

5. Conclusions and prospects

(1) Micron-scale IOs can be manufactured by current technologies, but larger diameters, which are over 10 μm , may be problematic to assemble. Furthermore, some chemicals are toxic, and it is necessary to find a way to replace them in preparation processes for future industrialization.

(2) The microstructure of IOs is greatly influenced by the fabrication process. In addition, the study of g-IOs should be expanded in order to determine the optimum IO structure in future research.

(3) The performance of IO is affected by the sintering temperature and time. The composite wick, made up of conventional wick and IO, already performs well and might be one of the solutions to the problem of high heat flux dissipation. However, there may be gaps at the joints that need to repair immediately.

Acknowledgements

This work was supported by the National Natural Science Foundation of China (52006218).

References

- [1] Z. Guo, The frontier of international heat transfer research —— micro scale heat transfer (in Chinese). *Advances in Mechanics*, 2000(01): p. 1.
- [2] F. Fathi, H. Monirinasab, F. Ranjbary, and K. Nejati-Koshki, Inverse opal photonic crystals: Recent advances in fabrication methods and biological applications. *Journal of Drug Delivery Science and Technology*, 2022. 72: p. 103377.
- [3] J.-Q. Wang, Y.-Y. Wu, S.-S. Yuan, M. Zhang, and X.-B. Chen, Preparation and optical properties of tin dioxide inverse opal film. *Rare Metals*, 2022. 41(3): p. 1032.
- [4] H. Li, Z. Tang, Y. Liu, J. Robichaud, J. Liang, W. Jiang, and Y. Djaoued, Two-Dimensional V2O5 Inverse Opal: Fabrication and Electrochromic Application. *Materials*, 2022. 15(8).
- [5] M. T. Barako, J. M. Weisse, S. Roy, T. Kodama, T. J. Dusseault, M. Motoyama, M. Asheghi, F. B. Prinz, X. Zheng, and K. E. Goodson. Thermal conduction in nanoporous copper inverse opal films. in *Fourteenth Intersociety Conference on Thermal and Thermomechanical Phenomena in Electronic Systems (ITherm)*. 2014. IEEE.
- [6] J. Yu, J. Lei, L. Wang, J. Zhang, and Y. Liu, TiO₂ inverse opal photonic crystals: Synthesis, modification, and applications - A review. *Journal of Alloys and Compounds*, 2018. 769: p. 740.
- [7] A. Jana, A. Meena, S. A. Patil, Y. Jo, S. Cho, Y. Park, V. Gopalan Sree, H. Kim, H. Im, and R. A. Taylor, Self-assembly of perovskite nanocrystals. *Progress in Materials Science*, 2022.
- [8] X. Li, L. Chen, D. Weng, C. Chen, Z. Li, and J. Wang, Tension gradient-driven rapid self-assembly method of large-area colloidal crystal film and its application in multifunctional structural color displays. *Chemical Engineering Journal*, 2022. 427.
- [9] Y. Won, M. T. Barako, D. D. Agonafer, M. Asheghi, and K. E. Goodson. Mechanical and thermal properties of copper inverse opals for two-phase convection enhancement. in *Fourteenth Intersociety Conference on Thermal and Thermomechanical Phenomena in Electronic Systems (ITherm)*. 2014. IEEE.
- [10] H. Song, M. Im, J. T. Song, J.-A. Lim, B.-S. Kim, Y. Kwon, S. Ryu, and J. Oh, Effect of mass transfer and kinetics in ordered Cu-mesostructures for electrochemical CO₂ reduction. *Applied Catalysis B: Environmental*, 2018. 232: p. 391.
- [11] H. Wu, L. Zheng, W. Liu, X. Xia, C. Xiao, J. Xie, L. Su, L. Wang, and N. Du, Three-dimensional porous copper framework supported group IVA element materials as sodium-ion battery anode materials. *Journal of Alloys and Compounds*, 2019. 771: p. 169.
- [12] Q. N. Pham, M. T. Barako, J. Tice, and Y. Won, Microscale Liquid Transport in Polycrystalline Inverse Opals across Grain Boundaries. *Sci Rep*, 2017. 7(1): p. 10465.
- [13] C. Zhang, S. Lingamneni, M. T. Barako, J. W. Palko, M. Asheghi, and K. E. Goodson. Characterization of the capillary performance of copper inverse opals. in *2016 15th IEEE Intersociety Conference on Thermal*

and Thermomechanical Phenomena in Electronic Systems (ITherm). 2016. IEEE.

[14] Q. N. Pham, B. Shao, Y. Kim, and Y. Won, Hierarchical and Well-Ordered Porous Copper for Liquid Transport Properties Control. *ACS Appl Mater Interfaces*, 2018. 10(18): p. 16015.

[15] Q. Wu, C. Zhang, M. Asheghi, and K. Goodson. Design and Fabrication of Graded Copper Inverse Opals (g-CIOs) for Capillary-Fed Boiling in High Heat Flux Cooling Applications. in *International Electronic Packaging Technical Conference and Exhibition*. 2020. American Society of Mechanical Engineers.

[16] T. J. Dusseault, J. Gires, M. T. Barako, Y. Won, D. D. Agonafer, M. Asheghi, J. G. Santiago, and K. E. Goodson. Inverse opals for fluid delivery in electronics cooling systems. in *Fourteenth Intersociety Conference on Thermal and Thermomechanical Phenomena in Electronic Systems (ITherm)*. 2014. IEEE.

[17] C. Zhang, G. Rong, J. W. Palko, T. J. Dusseault, M. Asheghi, J. G. Santiago, and K. E. Goodson. Tailoring of permeability in copper inverse opal for electronic cooling applications. in *International Electronic Packaging Technical Conference and Exhibition*. 2015. American Society of Mechanical Engineers.

[18] M. T. Barako, A. Sood, C. Zhang, J. Wang, T. Kodama, M. Asheghi, X. Zheng, P. V. Braun, and K. E. Goodson, Quasi-ballistic electronic thermal conduction in metal inverse opals. *Nano letters*, 2016. 16(4): p. 2754.

[19] H. Lee, T. Maitra, J. Palko, D. Kong, C. Zhang, M. T. Barako, Y. Won, M. Asheghi, and K. E. Goodson, Enhanced Heat Transfer Using Microporous Copper Inverse Opals. *Journal of Electronic Packaging*, 2018. 140(2).

[20] C. Zhang, J. W. Palko, M. T. Barako, M. Asheghi, and K. E. Goodson, Design and optimization of well-ordered microporous copper structure for high heat flux cooling applications. *International Journal of Heat and Mass Transfer*, 2021. 173.

[21] Q. N. Pham, S. Zhang, L. Cheng-Hui, S. Hao, and Y. Won. Boiling heat transfer performance of three-dimensionally ordered microporous copper with modulated pore diameters. in *2018 17th IEEE Intersociety Conference on Thermal and Thermomechanical Phenomena in Electronic Systems (ITherm)*. 2018. IEEE.

[22] C. Zhang, J. W. Palko, M. T. Barako, M. Asheghi, J. G. Santiago, and K. E. Goodson, Enhanced Capillary - Fed Boiling in Copper Inverse Opals via Template Sintering. *Advanced Functional Materials*, 2018. 28(41).

[23] K. Montazeri, H. Lee, and Y. Won, Microscopic analysis of thin-film evaporation on spherical pore surfaces. *International Journal of Heat and Mass Transfer*, 2018. 122: p. 59.

[24] F. Soroush, T. Liu, Q. Wu, C. Zhang, M. Asheghi, K. E. Goodson, L. Marco, E. Christian, and R. Martin. A Hybrid Microporous Copper Structure for High Performance Capillary-Driven Liquid Film Boiling. in *International Electronic Packaging Technical Conference and Exhibition*. 2021. American Society of Mechanical Engineers.

Experimental investigation on two-phase closed thermosyphons with laser-structured coating in the condenser section

Marc Kirsch^{1*}, Sergio Cáceres², Rudi Kulenovic³ and Jörg Starflinger⁴

^{1,2,3,4}*Institute of Nuclear Technology and Energy Systems, University of Stuttgart, Stuttgart, Germany*
**marc.kirsch@ike.uni-stuttgart.de*

Abstract

A 3 m straight stainless steel two-phase closed thermosyphon (TPCT) with deionized water as working fluid and a superhydrophobic condenser section is experimentally investigated. The TPCT with a 35 mm inner diameter and a wall thickness of 1.5 mm consists of an evaporator, adiabatic and condenser section of equal length. In collaboration with the IFSW of the University of Stuttgart, the surface of the condenser section was modified by applying laser-structuring, and a superhydrophobic contact angle of greater than 150° could be achieved. In this study, the influence of the filling ratios (56 %, 75 % and 100 %) at different evaporator and condenser temperatures (45 – 80 °C in 5 °C steps resp. 10 °C, 20 °C, and 30 °C) on the heat transfer performance of the TPCT have been investigated. The research results show that an improvement of heat transfer between 10-15 % is possible by means of the laser structuring coating. Furthermore, it could be proven that the TPCT start-up temperature could be reduced by more than 5 °C through the laser structuring compared to plain stainless steel TPCTs.

Keywords: thermosyphon; droplet condensation; laser structuring; coating; stainless steel-water

1. Introduction

TPCTs are a widely used system for heat transfer. When considering TPCTs, what stands out is not only their straightforward design but also their low-cost production and high level of reliability in operation. Due to these properties, they have been tested and safely used for years in a wide variety of applications such as de-icing roads, maintaining permafrost soils or turbine blade cooling [1]. In connection with the reactor disaster in Fukushima, the focus of research has been on the development of passive safety systems for cooling nuclear power plants. TPCTs seem to be a suitable system for this purpose due to the above-mentioned properties. Within the PALAWERO research project at Institute of Nuclear Technology and Energy Systems (IKE) at the University of Stuttgart [2; 3], the fundamental suitability of TPCTs for the cooling of spent fuel pools was investigated and confirmed. However, one of the problems discussed was the low heat transfer to the ambient air as the ultimate heat sink. In addition to known approaches to improve the heat transfer such as the application of cooling fins on the outside of the condensation zone of the TPCT, there are coating processes. These are intended to achieve droplet condensation in the condensation section and thus improve the internal heat transfer as well as the overall transfer performance [4–6]. Such tests were successfully carried out with SiO₂ coatings. On copper thermosyphons with water 1-butanol as working fluid, 13 % higher heat transfer coefficients were achieved [7].

Up to now, the works with laser-structured surfaces as coatings were aimed at improving the boiling process in the evaporator by reducing the contact angle. The resulting hydrophilicity made it possible to improve the average heat transfer by 13 % in plate heat exchangers [8]. However, the increase of the contact angle by laser structuring also allows a change of the contact angle into the superhydrophobic range. This is especially of interest on the condensation side to achieve permanent droplet condensation without having to apply further materials as with SiO₂ coating. With droplet condensation it should be possible to achieve a significantly higher heat transfer coefficient compared to film condensation.

Since previous research with laser structured coatings has been more concerned with the possible increase of heat transfer in connection with evaporation, the aim of this work is to show whether laser structuring is a suitable method to increase the heat transfer coefficients during condensation. The effect is considered specifically for thermosyphons.

2. Experimental setup and test procedure

2.1. Experimental setup

The experimental set-up can be seen schematically in Figure 1. The TPCT measured in the test stand consist of 3 zones, a 1 m long evaporation zone, a 1 m long adiabatic zone and a 1 m long condensation zone. For the construction of the TPCT, pipes made of 1.4301 steel with an

inner pipe diameter of 35 mm and a wall thickness of 1.5 mm were used. A cover was welded onto each end of the TPCT, which is equipped with two 1/4-inch connection pieces. This enables evacuation and filling via a connected valve. Furthermore, the pressure and invasive temperature measurement sensors are additionally attached here. Two TPCT are considered for this publication. A reference TPCT, which remained completely untreated, and a TPCT, which has a superhydrophobic laser-structured surface on the inner surface of the condensation zone.

The measurement setup of the two TPCT is identical. At equal distances of 250 mm, 12 PT-100 temperature sensors are located on the outside of the TPCT to determine the TPCT surface temperature. In the evaporation and condensation zones, the tubes were milled to a depth of approx. 1 mm to improve the measuring accuracy. The resulting flat surfaces ensure that the external temperature sensors measure the surface temperature and that there is no undercutting by the fluid of the thermostat circuit. Inside the TPCT there are 4 invasive temperature measuring points, 2 in the condensation zone and 2 in the evaporation zone. These are also PT 100 measuring sensors which are inserted into the TPCT via the 1/4-inch connection described above. The absolute pressure is also measured here by means of a cross piece attached to the connection pieces. A Lauda T 4600 thermostat is used on the heating side and a Huber CC525 on the cooling side. Water was used as the working fluid for heating and cooling. For heating the evaporation zone and cooling the condensation zone, identical semi-circular heat exchangers with an internal diameter of 47 mm are used. The heat exchangers have 11 baffle plates guiding the working fluid of the thermostat circuits along the TPCT in a meandering pattern. A temperature measuring point is located at the outlet and inlet of each heat exchanger for calorimetric heat flow measurement. PT-100 temperature sensors are also used here. The volume flows of the two thermostat circuits are determined with the aid of ultrasonic flow meters. The mass flow rate of the temperature control circuit is adjusted via a bypass. This also ensures that fluctuations greater than 0.2 l/s due to the pump do not occur. The accuracy of the measuring sensors used is as follows. The absolute pressure sensors of type PAA-33x from Omega have an accuracy of $\pm 0.15\%$ FS, where FS stands for full scale. All PT-100 temperature sensors have class A accuracy and thus a measurement uncertainty of $\pm (0.15 + 0.002 T)$. The measurement uncertainty of the volumetric flow meter is $\pm (0.7\% \text{ RD} + 0.7\% \text{ FS})$, where RD stands for

reading. The measurement data acquisition is carried out via a Keysight 34970A data logger, and the measurement software is based on Agilent VEE. The entire measurement setup was insulated with Amaxflex XG with a thermal conductivity of 0.042 W/mK. The ambient and the insulation temperature was also measured with a PT-100 sensor.

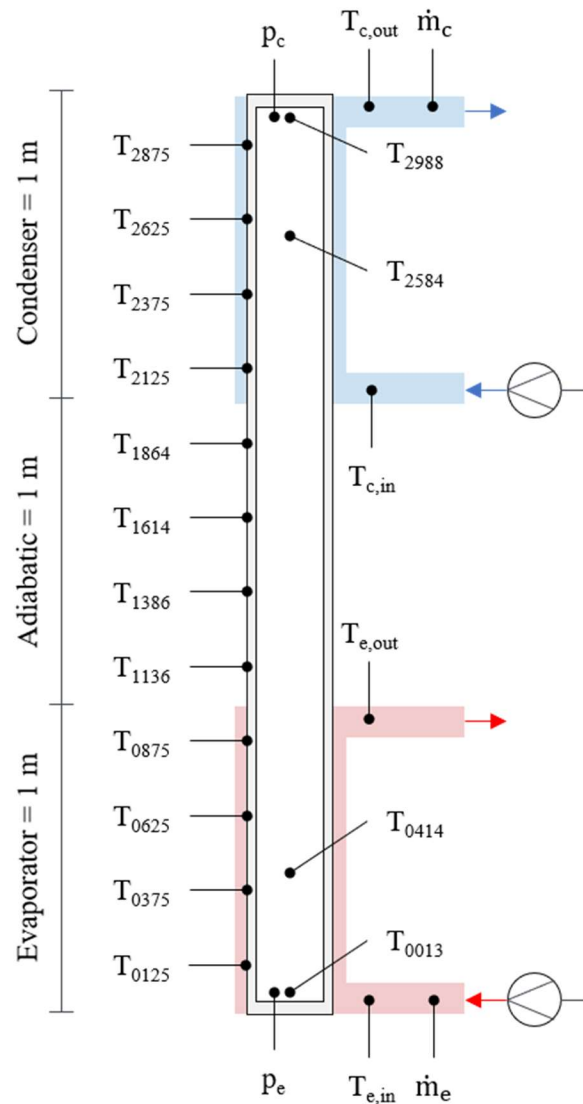


Figure 1 Scheme of the test stand design

2.2. Laser-based surface functionalisation

For the laser-structured TPCT, as described above, the condensation zone was processed by laser functionalisation. This procedure makes it possible to change the contact angle θ with which a fluid touches the surface. This is defined by Young's equation:

$$\theta = \cos^{-1} \frac{\sigma_{SV} - \sigma_{SL}}{\sigma_{LV}} \quad (1)$$

The equation results from the surface tension between solid and gas σ_{SV} , solid and liquid σ_{SL} and liquid and gas σ_{LV} . Figure 2 shows the contact angle of the unprocessed reference TPCT - it is 72° with a measurement accuracy of $\pm 3^\circ$. Figure 3 shows the contact angle of the TPCT with laser functionalisation. The angle there is $153^\circ \pm 3^\circ$. To obtain this surface, it was necessary to cut the tube into two halves by wire erosion. Afterwards, the pipe halves were cleaned and polished. In the next step, the structure was embedded into the half-shells by means of laser surface structuring with ultrashort laser pulses (Figure 4). Then the laser-structured half-shells were stored in a long-chain hydrocarbon for 3 days. The laser-structured half-shell with water droplets can be seen in Figure 5. The two functionalised half-shells were then reassembled into a tube in the next step using electron beam welding and then finally welded to the 2 m-long unprocessed evaporation and adiabatic zone.

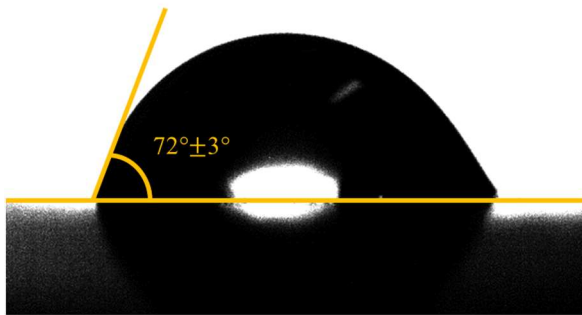


Figure 2 Contact angle of the reference TPCT

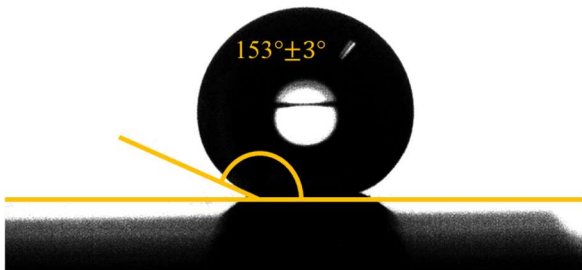


Figure 3 Contact angle of the laser-structured TPCT

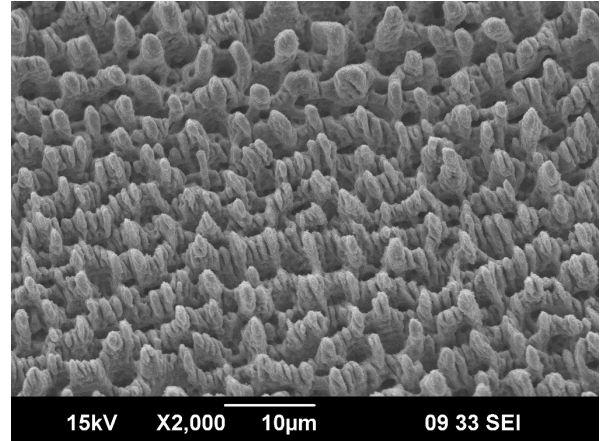


Figure 4 SEM image of the structure in the condensation zone

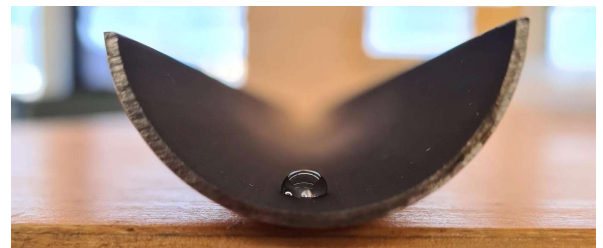


Figure 5 Laser-structured tube half shell

2.3. Test Procedure

Within the scope of measurement campaigns, experimental investigations were performed with filling ratios of 56 %, 75 % and 100 % at varying fluid inlet temperatures of the heat exchanger at the evaporation zone (45°C - 80°C in 5 K steps) and the condensation zone (10°C , 20°C , 30°C). As the first step before the measurement, the TPCT is filled according to a uniform procedure. For this purpose, the TPCT is evacuated before the filling procedure and then possible leakage is searched for with helium. Afterwards, a leak test is carried out with the help of the attached pressure sensors. This ensures that the pressure does not exceed 3 mbar, the maximum error of the pressure sensor. Deionised and degassed water is used for filling and measured according to the degree of filling and weighed before and after degassing. This ensures consistent filling. After the TPCT has been filled, it is degassed. For this purpose, only the temperature control circuit on the evaporation side is brought up to 60°C . In this state, the valve in the upper area of the TPCT is opened and the non-condensable gas that accumulates is released into an attached, vacuumed expansion tank. This process with the expansion tank reliably prevents the ingress of outside air, as it is still a closed system. The non-condensable gas comes from air dissolved in the working medium which cannot be

completely removed during the degassing process before filling. A check is made via the upper of the two invasive temperature sensors mounted in the condensation zone. If degassing is successful, the temperature of the lower sensor adjusts to the temperature of both sensors. The measurements on the filled TPCT were carried out in measurement series with predefined filling levels and predefined temperature at the inlet to the condensation zone. The inlet temperature to the evaporation zone was then raised from 45 °C to 80 °C by 5 °C steps at a time. The measurement was carried out according to the following principle. After reaching the selected inlet temperature in the evaporation zone, 10 min were waited to ensure that the system was completely thermally settled. After that, measurements were taken for 10 min. After completion of this measuring point, the next evaporator temperature is adjusted for subsequent measurement.

2.4. Data reduction

The heat transfer is determined calorimetrically for the condenser \dot{Q}_c . This is done via the difference of the inlet temperature $T_{c,in}$ to the outlet temperature $T_{c,out}$ in relation to the specific heat capacity c_p , the density ρ and the volume flow \dot{V}_c of the coolant water of the thermostat circuits.

$$\dot{Q}_c = \dot{V}_c \cdot \rho \cdot c_p (T_{c,out} - T_{c,in}) \quad (2)$$

Based on this, the average heat transfer coefficient of the condenser h_c can then be calculated.

$$h_c = \frac{Q_c}{2 \cdot \pi \cdot r_o \cdot L_c (T_{Vsat} - T_{cw})} \quad (3)$$

The variables required for this are the TPCT radius r_o of 19 mm, the length of the condenser of 1000 mm, the temperature of the steam in the condenser T_{Vsat} , which in this case is determined by the saturation temperature of the vapour based on the pressure p_c present in the condenser, and the wall temperature of the condenser. For the wall temperature, the average value of the 4 PT-100 temperature sensors T_{2125} , T_{2375} , T_{2625} and T_{2875} , which can be seen in Figure 1, is used. Specific property data for water and steam are determined in this publication using the Industrial Formulation 1997 for the Thermodynamic Properties of Water and Steam IAPWS R7-97.

2.5. Error calculation

The error is calculated using the Gaussian error propagation approach.

$$\Delta y = \sqrt{\sum_{i=0}^n \Delta x_n^2 \left(\frac{\partial y}{\partial x_n}\right)^2} \quad (4)$$

Here Δy is the total error of the parameter y , x_n is the independent measured variable and Δx_n is the measurement error.

3. Results

Figure 7 shows the results of the measurements for both the laser-structured TPCT and the reference TPCT at a filling ratio of 56 % and condensation temperatures of 10 °C, 20 °C and 30 °C. It is noticeable in all measurements that at 45 °C temperature (50 °C for 30 °C condensation temperature) on the evaporator side, the laser-structured TPCT ensures significantly higher heat transfer.

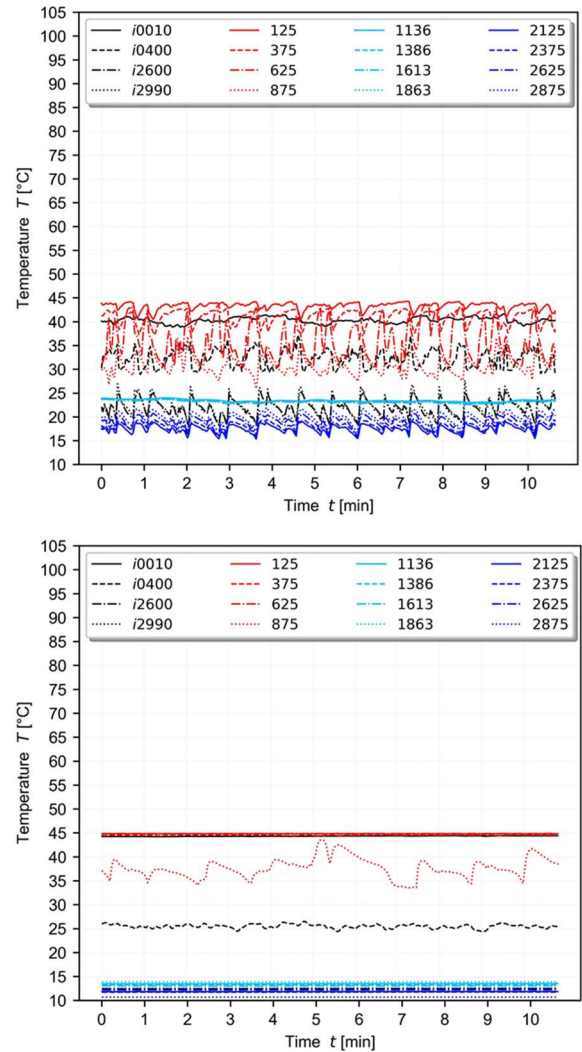


Figure 6 Time-dependent temperature profiles along the TPCT for the laser-structured TPCT (top) and the reference TPCT (bottom) at 10 °C condensation side temperature and 45 °C evaporator temperature

Based on the temperature measurements in and on the TPCT, it can be determined that an oscillating operation occurs during the experiments with the laser-functionalised TPCT, which is exemplarily shown in Figure 6. With this knowledge, a consideration of the results must therefore be divided into two areas, namely the unstable operation of the TPCT at low evaporator side temperature and a stable operation at higher evaporator temperatures. For the unstable operating points, the performance of the laser-structured TPCT are 1.5 kW, 0.92 kW and 0.54 kW for 10 °C, 20 °C and 30 °C condensing side temperature. Compared to the reference TPCT with heat transfer rates of 0.58 kW, 0.31 kW and 0.08 kW this means increases of 158 %, 190 % and 575 %. The relative measurement error here is 20 % for the measurements with the laser-structured TPCT and 60 % for the reference TPCT. The large error for the reference TPCT results from the small change in the absolute measurement error, which results in a large relative error for small transmitted heat outputs i.e. the reference TPCT is not or just beginning to operate at that state. If we look at the individual performance differences for evaporator temperatures at which stable operation also takes place in the reference TPCT, no significant performance difference at 10 °C on the condensation side can be seen. They are around 1 % of each other and thus within the range of the measurement error, which is 7 % on average here and has a maximum value of 10 %. For 20 °C condensation side temperature, the performance difference is somewhat larger, although at 5 % at 80 °C evaporation temperature it is still close to the measurement accuracy. On the other hand, it is striking that at a condensing side temperature of 30 °C a consistently significant improvement can be observed. This is 11.5 to 13.1 % higher than the maximum error of 10 % in the range of 55 to 80 °C evaporator side temperature.

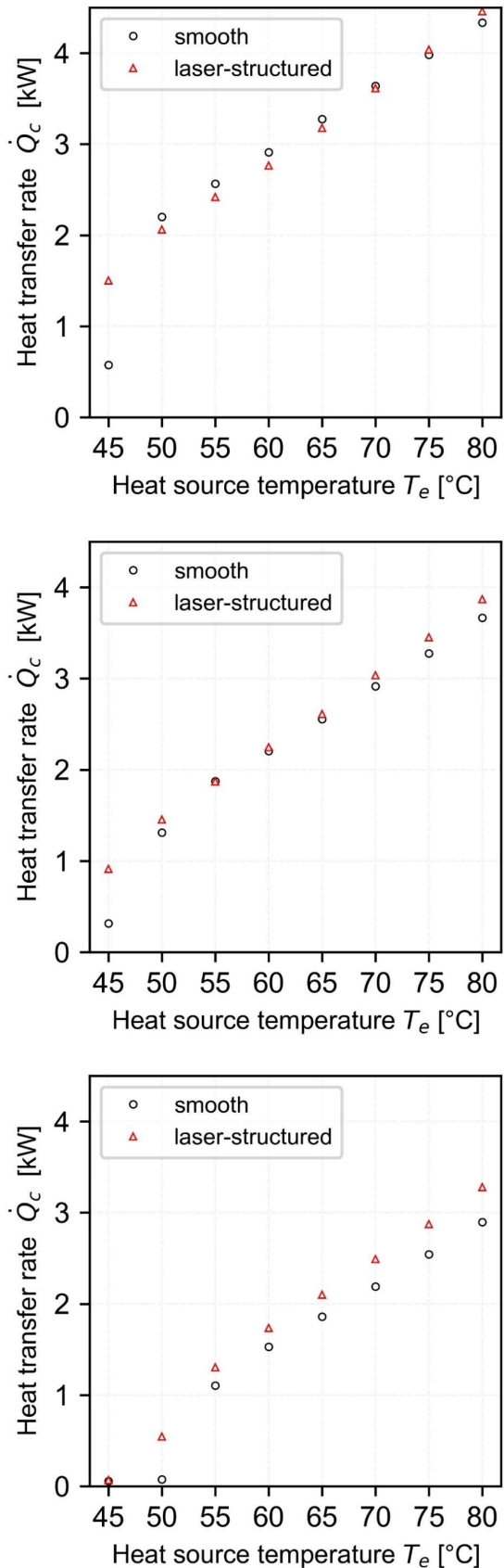


Figure 7 Comparison of the heat transport of laser-structured and reference TPCT at 10 °C(top),20 °C(middle),30 °C(bottom) condenser temperature.

Further on, the influence of the filling ratio on the operational mode of the laser-structured TPCT is also investigated. For this purpose, measurements are carried out with 56 %, 75 % and 100 % filling ratio. As can be seen in Figure 8 for a condensation side temperature of 20 °C, it is shown that the best results are achieved with a filling level of 56 %, with a heat transfer rate of 3.87 kW. At a filling ratio of 75 % the maximum heat transfer is reduced by 2.8 % to 3.76 kW and at a filling ratio of 100 % even by 13.7 % to 3.34 kW. The results show that higher filling levels do not lead to an increase. Observations on lower filling ratios are still pending. New findings with the reference TPCT have shown that lower filling ratios result in a further improvement of the maximum transmittable heat output, so that the tests in this field still have to be extended [9].

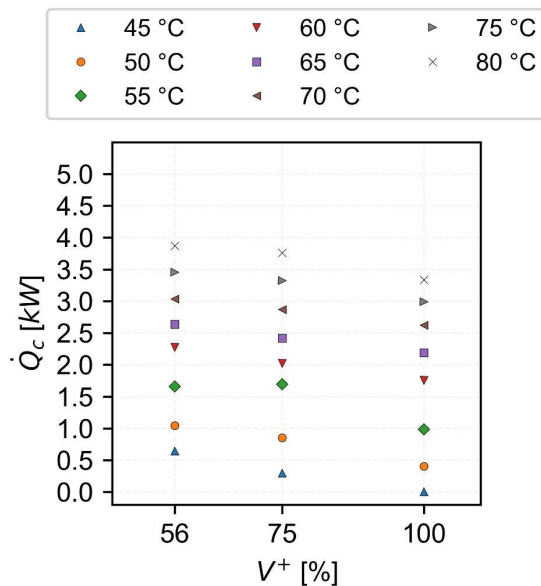


Figure 8 Influence of the filling ratio on the heat transfer performance of the laser-structured TPCT at 20 °C condensing side temperature

The measurements shown in Figure 7 are subject to further investigations. The aim is to determine the heat transfer coefficient in the condenser in order to gain deeper insights into the influence of the laser structuring in the condensation zone. Figures 9 and 10 show the heat transfer coefficients for the laser-structured and the reference TPCT. The measurements at 10 °C are shown in blue, at 20 °C in white and at 30 °C condensation side temperature in red. Here again the influence at low heat transfer rates can be seen. In the range between 0.5 kW and 1.5 kW, the heat transfer coefficients are higher than those of the comparable measurements with the reference TPCT. This also corresponds to the findings in

Figure 7. For heat transfer rates greater than 1.5 kW, this effect levels out in the measurements with 10 °C and 20 °C condensation side temperature. Only in the measurements with 30 °C the heat transfer coefficients are about 5.5 % higher than with the reference TPCT.

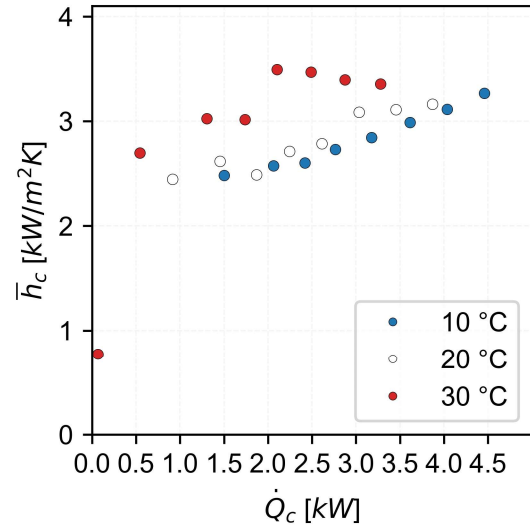


Figure 9 Heat transfer coefficients for the laser-structured TPCT at a 56% filling ratio

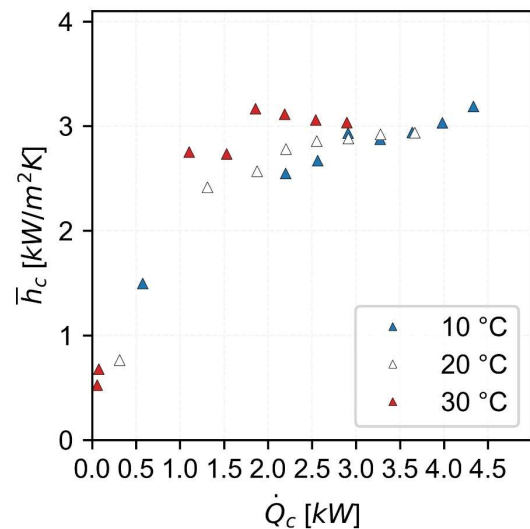


Figure 10 Heat transfer coefficients for the reference TPCT at a 56% filling ratio

4. Conclusion

The influence of laser-structured inner surfaces in the condensation zone of a TPCT is investigated experimentally. Different filling ratios and temperatures on the evaporation and condensation side are considered. The following conclusions from the present work are:

1. Compared to an unprocessed TPCT, operation is found for a 5 °C lower evaporation temperature. As a result, up to 575 % more

heat could be transferred in this operating range.

2. For higher evaporation temperatures, the effect is significantly smaller and in combination with low evaporation temperatures of 10 °C no longer distinguishable from the unprocessed TPCT.
3. For higher condensing side temperatures of 30 °C, a continuous improvement of the transfer efficiency of 11.5 to 13.1 % could be observed.
4. The variation of the filling ratio shows that the highest heat transfer rate is achieved at a filling ratio of 56 %. With higher filling ratios (75 %, 100 %) the transfer efficiency decreases. However, further investigations in this area need to be carried out.
5. The heat transfer coefficients at low heat transfer rates of 0.5 to 1.5 kW are higher for the laser-structured TPCT than for the unprocessed TPCT. For higher heat transfer rates, only a difference of 5 % is observed with a simultaneously high condensation side temperature of 30 °C.

5. Acknowledgements

The presented work is funded by the Federal Ministry for the Environment, Nature Conservation, Nuclear Safety and Consumer Protection (BMUV, project no.1501612A) on basis of a decision of the German Bundestag.

6. References

- [1] A. Faghri. Heat Pipes: Review, Opportunities and Challenges. *Frontiers in Heat Pipes*. 2014. 5(1).
- [2] C. Graß and R. Kulenovic. Abschlussbericht / Final Report Reaktorsicherheitsforschung-Vorhaben-Nr./ Reactor Safety Research Project No.: 1501515. 2020.
- [3]. C. Graß; R. Kulenovic; J. Starflinger. Experimental study on heat transfer characteristics of long two-phase closed thermosiphons related to passive spent fuel pool cooling. in Joint 19th IHPC and 13th IHPS. 2018. Pisa, Italy.
- [4] Pou, P., Del Val, J., Riveiro, A., Comesaña, R., Arias-González, F., Lusquiños, F., Bountinguiza, M., Quintero, F. and Pou, J. Laser texturing of stainless steel under different processing atmospheres: From superhydrophilic to superhydrophobic surfaces. *Applied Surface Science*. 2019. 475: p. 896–905.
- [5] M. Budakli, T. K. Salem, M. Arik, B. Donmez and Y. Menceloglu. Effect of Polymer Coating on Vapor Condensation Heat Transfer. *Journal of Heat Transfer*. 2020. 142(4).
- [6] Y. Kim, J. Sub Kim, D. Hwan Shin, J.Hyeuk Seo, S.M. You and J. Lee. Effects of hydrophobic and superhydrophobic coatings of a condenser on the thermal performance of a two-phase closed thermosyphon. *International Journal of Heat and Mass Transfer*. 2019. 144: p. 118706.
- [7] K. Hosseinzadeh, D. D. Ganji and F. Ommi. Effect of SiO₂ super-hydrophobic coating and self-rewetting fluid on two phase closed thermosyphon heat transfer characteristics: An experimental and numerical study. *Journal of Molecular Liquids*. 2020. 315: p. 113748.
- [8] A.-E. J. Polzin. Evaporation and Condensation in Plate Heat Exchangers with microstructured Surfaces. *Gottfried Wilhelm Leibniz Universität Hannover*. 2020.
- [9]. S. Cáceres, M.Kirsch, R. Kulenovic, J. Starflinger. Heat transfer characteristics of a two-phase closed thermosyphon for passive spent fuel pool cooling. in Joint 21st IHPC and 15th IHPS. 2023. Melbourne.

Numerical simulation of the phase distribution in a loop heat pipe

Nanxi Li¹, Bo Shao^{1,2}, Le Liu^{1,2}, and Zhenhua Jiang^{1,3*}

¹ Shanghai Institute of Technical Physics, Chinese Academy of Sciences, Shanghai, China

² University of Chinese Academy of Sciences, Beijing, China

³ Nantong Academy of Intelligent Sensing, Nantong, China

*Corresponding author email address: zhenhua.jiang@mail.stip.ac.cn

Abstract

The phase distribution of the working fluid in a loop heat pipe is an important indicator of its performance. In this work, a 3D steady-state numerical model was established to simulate the vapor/liquid distribution in the condenser of a loop heat pipe. The model adopts the VOF method capture the vapor front in the condenser. The flow pattern of the condensation process is also captured. The Lee model is used to simulate the condensation process. The model was built based on a prototype LHP developed in the research group. To eliminate the effect of the evaporator, the model only calculates the performance of the condenser when the LHP works under variable conductance mode in which the working temperature of the LHP is the same. The effect of heat load, heat sink temperature and gravity were investigated in this work.

Keywords: Loop heat pipe; Phase distribution; Condensation; CFD

1. Introduction

Due to the high heat transfer efficiency, high stability and long-distance heat transport ability, loop heat pipes (LHPs) have been widely adopted in the thermal management systems of aerospace detectors and many electronic devices, such as optical cameras, semi-conductors, onboard laser systems, LED lights, etc.

The operation characteristics of the loop heat pipe strongly depend on the phase distribution of the working fluid inside. For example, when the compensation chamber of the LHP is filled with liquid, the LHP starts to operate in constant conductance mode where the operation temperature increases linearly with the heat load [1]. Ku et al. concluded that the start-up performance of the LHP are different depending on whether vapor exists in the core and the vapor grooves [2]. Therefore, knowing the phase distribution in the LHP allows researchers and engineers to better predict the operation performance and limits, which can further assist the design of the thermal control systems.

To reveal the phase distribution in an LHP, visualization experiments were commonly adopted at the component level and at the system level. Zhang et al. observed the bubble generation and movement in a half-sectioned cylindrical evaporator-CC coupling structure at different tilt angles, and concluded that the temperature fluctuation of the LHP is caused by the vapor-liquid interface in the evaporation core [3]. Odagiri et al. visualized the thermos-fluid behavior of the wick surface using a microscopic camera and a microscope, and investigated the effect of groove width on the heat transfer performance[4]. Bartuli et

al. visually studied the two-phase flow in a copper-water loop heat pipe condenser and determined its heat transfer coefficient and thermal resistance. Neutron radiography was adopted by Okamoto et al. and Cimbala et al. [5][6][7] Matsuda et al. observed the inside of a wick core and compensation chamber using borescope under microgravity [8]. However, the cost of visualization experiments utilizing neutron radiography can be extremely high. Visualization realized by transparent windows or borescopes are relatively more popular and intuitive, but they also pose other problems such as large thermal resistance, alternation of actual flow, and lower accuracy.

Three-dimensional numerical simulation of the two-phase flow inside the evaporator and the condenser can be very helpful in elucidating the two-phase heat transfer in a loop heat pipe. In the past, much effort has been paid to the detailed simulation of the evaporator. Nishikawara et al. simulated the liquid-vapor liquid distribution and movement in the evaporator of an LHP vapor groove with a 3D CFD model. Phenomena including nucleate boiling, hysteresis and capillary limit were characterized [9]. Zhang et al. simulated the heat and mass transfer in a flat-plate LHP by the Volume of Flume (VOF) method [10]. Zhang et al. established a 3D numerical model for an LHP and found that the heat leakage from the heat source to the compensation chamber is the major reason for the operational failure of the LHP [11]. Although the model is a system-level model, the simulation process of the condenser was simplified, and its effect on the LHP performance was not discussed.

The condenser, as crucial component in the LHP,

also plays a decisive role in the thermal performance of the LHP. However, less attention was paid to the detailed analysis of the condenser. For simplicity of analysis, it was generally assumed that the flow pattern inside the condenser is annular, and the heat transfer performance are often calculated using traditional condensation correlations [12]. However, the visualization result of Yan et al. showed that the flow pattern in a LHP include wavy flow, stratified flow and slug flow [13]. Furthermore, although many flow condensation correlations have been developed [14], it is still not clear how well they fit for the compensation process in LHPs where the low flow rate is extremely small compared to traditional heat exchangers. Therefore, a detailed three-dimensional numerical simulation of the condenser is highly necessary.

In this work, a 3D numerical model is established to simulate the phase distribution of the condenser in a loop heat pipe under different heat loads, heat sink temperatures, and gravity fields. The heat transfer coefficient of the condenser calculated.

2. Model Description

A three-dimensional steady-state CFD model for an LHP condenser was established. The model is based on an LHP prototype developed in our research group. Detailed description can be found in reference [13]. Figure 1 is a cross section surface of the LHP. It consists of the evaporator (including the wick), the compensation chamber (CC), the vapor line, a condenser, and the liquid line. The condenser is made with a copper substrate covered by a sapphire window for visualization. A serpentine square duct was milled on the copper substrate serves as the condenser.

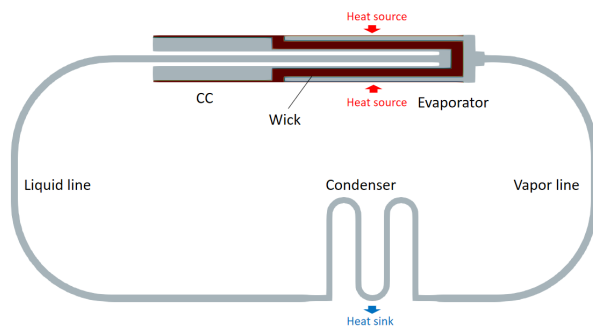


Figure 1. Model geometry

Figure 2 shows the detailed geometry of the condenser modeled in this work. The condenser is 182 mm long. The cross section of the condenser is a square with a side length of 3 mm. The inlet of the vapor is on the right and the liquid outlet is on the left.

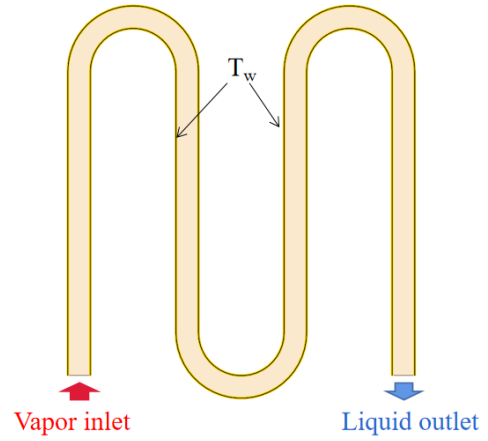


Figure 2. Condenser geometry

Propylene was used as the working fluid, and the physical properties of which were obtained from the REFPROP9.1 database. The boundary conditions of the condenser were determined from the experimental results of Yan et al [13]. The inlet boundary condition is the velocity along the condenser and the outlet boundary condition is pressure. The inlet velocity is extrapolated from experimental results of reference [13]. The condenser boundary condition is constant wall temperature. ANSYS Fluent 18.1 steady-state solver was used for calculation, and PISO algorithm was used for solving pressure and velocity.

2.1. The VOF model

The VOF method was used to simulate the flow condensation process in the condenser of the LHP. The volume fraction α is used to represent the portion of volume of the computational cell filled with either liquid or vapor, therefore it always follows that

$$\alpha_L + \alpha_V = 1 \quad (1)$$

where α_L is the volume fraction of liquid, and α_V is the volume fraction of vapor.

By knowing the volume fraction of a cell and its neighboring cells, an approximate vapor-liquid interface can be roughly reconstructed. After that, the flow field is modeled using an advection algorithm. The two-phase mixture is considered as a single fluid of which the physical properties are calculated as the arithmetic mean of each phase. For example, the density is calculated as follows:

$$\rho = \rho_L \alpha_L + \rho_V (1 - \alpha_L) \quad (2)$$

The following equations are solved:

$$\nabla \cdot (\vec{u} \alpha_L) = \frac{S}{\rho_L} \quad (3)$$

$$\rho \cdot (\vec{u}\alpha_V) = -\frac{S}{\rho_V} \quad (4)$$

$$\begin{aligned} \nabla \cdot (\rho\vec{u}\vec{u}) \\ = -\nabla p + \nabla \cdot [(\mu + \mu_t)(\nabla\vec{u} + \nabla\vec{u}^T)] + \rho\vec{g} + \vec{F}_\sigma \end{aligned} \quad (5)$$

where S is the mass source term of phase change, \vec{F}_σ is the body force at the vapor-liquid interface due to surface tension, which is calculated using the following equation:

$$\vec{F}_\sigma = \sigma_{LV} k_L \nabla_{\alpha L} \frac{\rho}{1/2(\rho_L + \rho_V)} \quad (6)$$

The energy equation is as shown as follows,

$$\nabla \cdot (\vec{u}\rho h) = \nabla \cdot (\lambda_{eff} \nabla T) + h_{LV} S \quad (7)$$

where λ_{eff} is the effective thermal conductivity, h is the specific sensible enthalpy, and $h_{LV} S$ is the energy source due to phase change.

2.2. The flow model

The modeling of the two-phase flow in the condenser used the method of Da Riva et al.[15] The vapor flow in the condenser core is expected to be turbulent, while the liquid flow is considered laminar. The Wilcox's low-Re $k - \omega$ model was used for the laminar flow of liquid in the condenser.

The transport equations are as follows:

$$\nabla \cdot (\rho k \vec{u}) = u_t \bar{S}^2 - \beta f_3 f_4 \rho k \omega + \nabla \cdot [(\mu + \sigma \mu_t) \nabla k] \quad (8)$$

$$\nabla \cdot (\rho \omega \vec{u}) = a f_2 \frac{\omega}{k} \mu_t \bar{S}^2 - \beta f_5 \omega^2 + \nabla \cdot [(\mu + \sigma \mu_t) \nabla \omega] \quad (9)$$

Where \bar{S} is the modulus of the mean rate of the strain tensor, β, σ, a are constants, where f_1 is the damping coefficient of the turbulent viscosity due to a low-Re correction, f_2 and f_3 are damping functions for the low-Re corrections, f_4 and f_5 are empirical closure functions for the round-jet/plane-jet anomaly.

The local turbulent viscosity is obtained as follows:

$$\mu_t = f_1 \frac{\rho k}{\omega} \quad (10)$$

For laminar flow of the liquid phase, the turbulent viscosity is modified to be

$$\mu_t = f_1 \frac{\rho_V k}{\omega} \alpha_V \quad (11)$$

2.3. The phase change model

The classical Lee model is used to simulate the phase change process the condenser. The interfacial temperature is assumed to be the same as the saturation temperature.

$$S = -r \alpha_L \rho_L \frac{T - T_s}{T_s} \quad T \geq T_s \quad (12)$$

$$S = -r \alpha_V \rho_V \frac{T_s - T}{T_s} \quad T < T_s \quad (13)$$

where r is a coefficient, which is positive, and T is the temperature of the cell.

Eq. 13 is used if the cell temperature in the domain is higher than saturation temperature at a certain computational step, otherwise Eq. 14 is used. When the cell is filled with liquid, mass transfer is not calculated, and when the cell is all vapor, mass transfer from the liquid phase to the vapor phase is calculated.

2.4. Meshing

Meshing was done for the calculation domain by sweeping, as shown in Fig 3. Since the model involves wall condensation, a boundary layer grid was added to the tube wall of the condenser, and the thickness of the boundary layer mesh is as small as 20 μm . The grid independence through a single-phase flow test example, was tested and the resulting grids contained 1,288,200 cells.

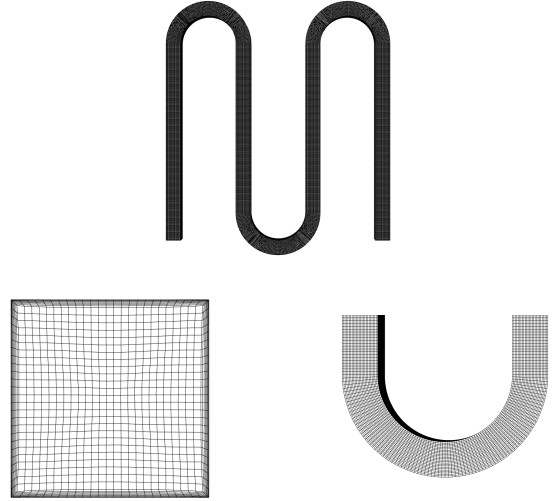


Figure 3. Meshing of the condenser

3. Results and Discussions

The loop heat pipe is a closed two-phase system, therefore both the evaporator and the condenser affect the overall performance. In this work, the charging amount was carefully chosen so that loop heat pipe works under the variable conductance

mode under these working conditions. The experimental results in reference [13] show that when the condenser was fixed at 213 K, the evaporator temperature was almost constant, which is around 236 K, indicating the system pressure was constant.

The phase distribution of a propylene loop heat pipe working with the heat sink temperature of 213–233 K were calculated under the heat load range of 30–50 W. The phase distribution of the condenser without gravity was also investigated numerically.

3.1. Effect of heat loads

The vapor-liquid distribution of the condenser with a heat sink temperature of 213 K under 30 W, 40 W, and 50 W was simulated, and the results are shown in Fig. 4. As the heat load increases, the flow rate increases from 11.26 kg/m²s at 30 W to 18.78 kg/m²s at 50 W. It can be found that with the increase of the heat load, the vapor front gradually moves towards the outlet. The vapor fronts are at 60 mm, 96.5 mm, and 104 mm away from the inlet at 30 W, 40 W, and 50 W, respectively. The length of superheated vapor increases as the heat load increases. However, the two-phase length is the longest at 40 W, while the shortest at 50 W, indicating the two-phase heat transfer coefficient at 50 W is the highest.

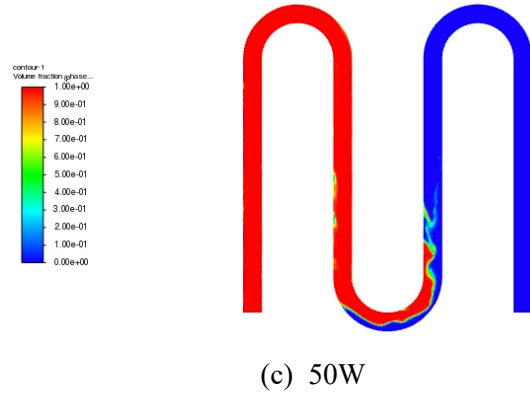
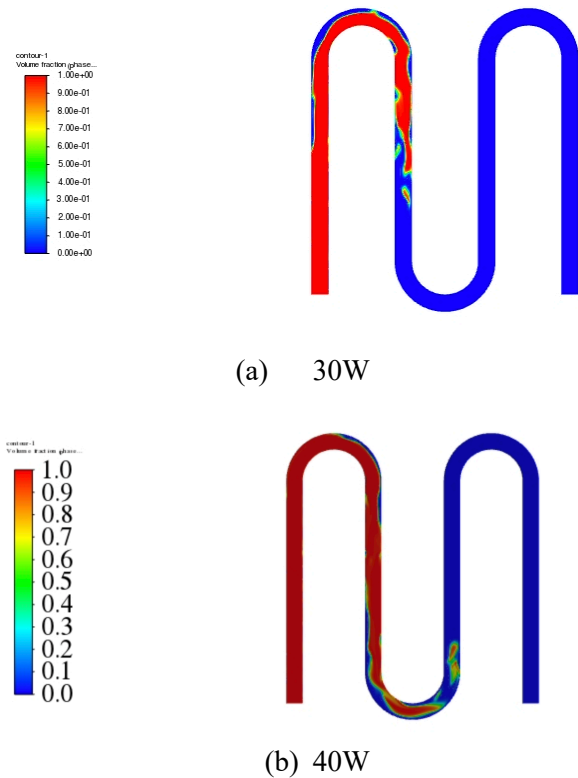


Figure 4. Phase distribution of the condenser under different heat loads at 213 K

Fig. 5 shows the cross section of the condenser at the second turn under 40 W and 50 W. It can be seen that at 40 W, the liquid flow forms an annular inside the condenser duct, but at 50 W, the liquid flow occupied the right side of the duct due to the higher inertia of the flow. More vapor is in direct contact with the cold condenser wall at 50 W, therefore enhancing the condensation heat transfer coefficient, leading to a shorter two-phase length. This indicates that for high heat dissipation requirements with limited condensation area, more turns in the condenser can be beneficial as long as the pressure drop is acceptable.

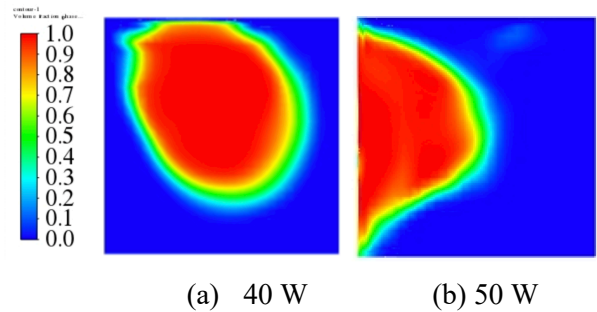


Figure 5. Cross-sectional view of the condenser at the second turn

3.2. Effect of heat sink temperature

The vapor-liquid distribution of the condenser with the heat sink temperature varying from 213 K to 233 K under the heat load of 40 W was numerically calculated. The results are shown in Fig. 6. Since the heat loads at the evaporator are the same under these three cases, the flow rates and velocities at the inlet of the condenser are the same. The distance from the vapor front to the inlet of the condenser is 96.46 mm at 213 K of wall temperature, and 55 mm at 223 K of wall temperature. However, when the wall temperature is 233 K, the condenser is no longer able to dissipate 40 W of heat load,

indicating the probable operational failure of the LHP. As Fig. 6 (c) shows, the entire length of the condenser is filled with vapor. The overall heat transfer coefficient at 213 K is 469.9 W/m²K, and increases to 820.8 W/m²K at 223 K. The overall heat transfer coefficient at 233 K drastically decreased to 181.3 W/m²K due to the absence of condensation process.

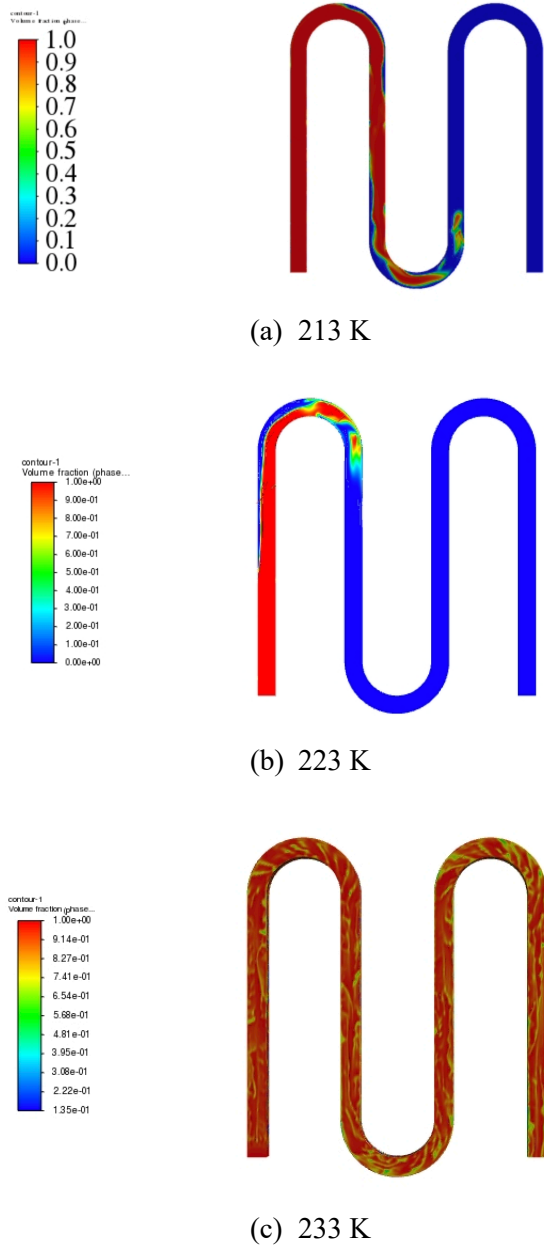


Figure 6. Phase distribution of the condenser at different wall temperature at 40W

Fig. 7 illustrates the vapor-liquid distribution of the two-phase region at 40 W when the wall temperature is 213 K and 223 K. Although both the flow patterns for both cases are annular, the liquid film at 213 K is much thicker than that of 223 K. The thicker liquid film increases the thermal

conductance from the wall to the vapor, lowering the overall heat transfer. The reason for the enhanced heat transfer coefficient is due to the decreased viscosity of liquid. As the wall temperature continues to increase, the temperature difference is no longer able to initiate condensation within the length of the condenser. Therefore, there exists an optimum heat sink temperature for condenser.

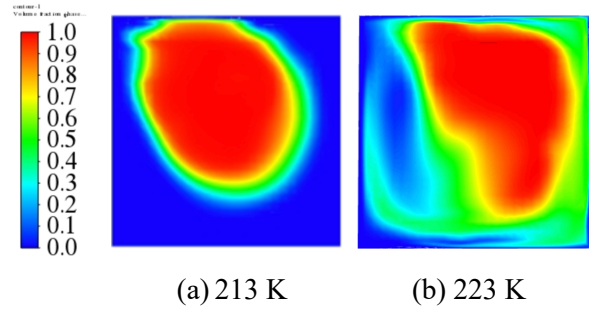
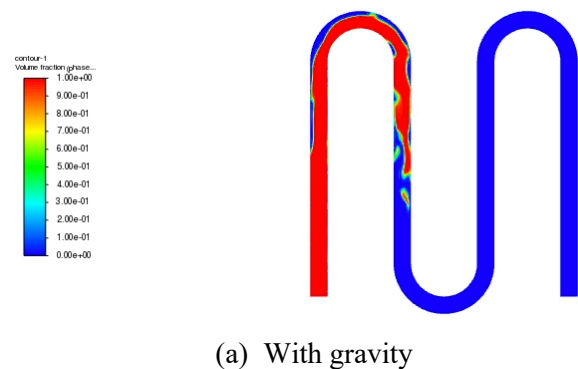


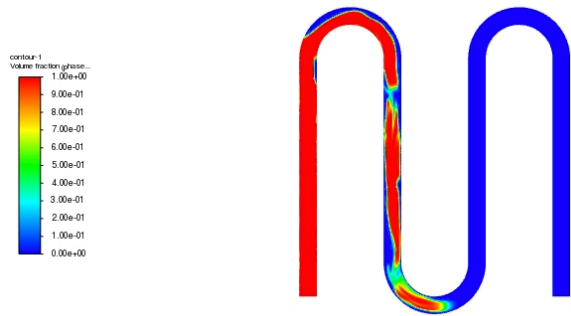
Figure 7. Cross-sectional view of two-phase region of the condenser

3.3. Effect of gravity

Loop heat pipes are generally designed and used for space applications but are tested under terrestrial environment. Therefore, the effect of gravity on the phase distribution and condenser performance was investigated in this work.

Fig. 8 (a) and (b) manifest the vapor-liquid distribution of the condenser at 30 W with the wall temperature of 223 K under 1-g and 0-g, respectively. Calculation results show that although the overall heat transfer coefficients for both cases are the same, the two phase length under 0-g is longer than that at 1-g. The vapor front is 60 mm away from the inlet with gravity, and is 93 mm without gravity.

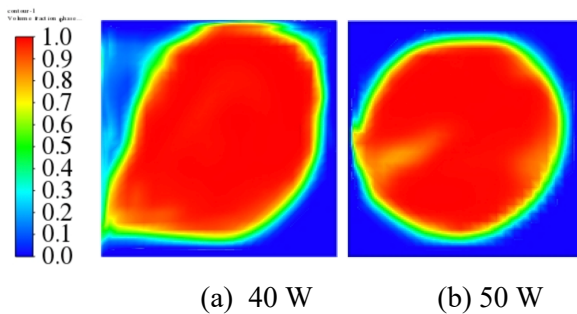




(b) Without gravity

Figure 8. Phase distribution of the condenser at 30 W under different gravity conditions

Fig. 9 shows the cross section of the two-phase region of the condenser for both cases. It can be seen that the although the flow patterns are both annular, the liquid layer at the bottom of the condenser duct is thicker and is thinner at the top under 1-g of gravity. Without gravity, the vapor core is close to a perfect circle, and the liquid layers on all sides of the condenser duct are thicker. Therefore, under gravity conditions, the thinner liquid layer provides a better path for heat flow, thus increasing the heat transfer coefficient.



(a) 40 W

(b) 50 W

Figure 9. Cross-sectional view of two-phase region of the condenser under different gravity conditions

4. Conclusions

A three-dimensional CFD model for a serpentine condenser of a propylene loop heat pipe working under variable conductance mode was established. The boundary conditions were obtained from experiments. The effect of heat load, heat sink temperature and gravity were investigated numerically, and major conclusions are as follows

- 1) The turns in the condenser will enhance condensation heat transfer performance, which is desirable for high heat load applications.
- 2) An optimum heat sink temperature exists for the condenser to work at the highest efficiency.

- 3) The two-phase heat transfer coefficient is larger with gravity than without gravity. It is recommended to increase the length of condenser for space applications under certain application requirements.

References

- [1] Yu.F. Maydanik, Loop heat pipes, *Applied Thermal Engineering*. 25 (2005) 635–657.
- [2] J. Ku, *Operating Characteristics of Loop Heat Pipes*, (n.d.) 16.
- [3] Q. Zhang, G. Lin, X. Shen, L. Bai, D. Wen, Visualization study on the heat and mass transfer in the evaporator-compensation chamber of a loop heat pipe, *Applied Thermal Engineering*. 164 (2020) 114472.
- [4] K. Odagiri, M. Nishikawara, H. Nagano, Microscale infrared observation of liquid–vapor interface behavior on the surface of porous media for loop heat pipes, *Applied Thermal Engineering*. 126 (2017) 1083–1090.
- [5] A. Okamoto, R. Hatakenaka, M. Murakami, Visualization of A Loop Heat Pipe Using Neutron Radiography, 2 (2011) 12.
- [6] J.M. Cimbala, J.S. Brenizer, A.P.-Y. Chuang, S. oHanna, C. Thomas Conroy, A.A. El-Ganayni, D.R. Riley, Study of a loop heat pipe using neutron radiography, *Applied Radiation and Isotopes*. 61 (2004) 701–705. <https://doi.org/10.1016/j.apradiso.2004.03.104>.
- [7] P.-Y.A. Chuang, J.M. Cimbala, J.S. Brenizer, Experimental and analytical study of a loop heat pipe at a positive elevation using neutron radiography, *International Journal of Thermal Sciences*. 77 (2014) 84–95.
- [8] Y. Matsuda, H. Nagano, S. Okazaki, H. Ogawa, H. Nagai, Visualization of Loop Heat Pipe with Multiple Evaporators under Microgravity
- [9] M. Nishikawara, Y. Ueda, H. Yanada, Static and Dynamic Liquid-Vapor Phase Distribution in the Capillary Evaporator of a Loop Heat Pipe, *Microgravity Sci. Technol.* 31 (2019) 61–71.
- [10] Z. Zhang, H. Cui, S. Zhao, R. Zhao, T. Wu, Z. Liu, W. Liu, Simulation of heat and mass transfer process in a flat-plate loop heat pipe and experimental comparison, *Applied Thermal Engineering*. 220 (2023) 119705.
- [11] Y. Zhang, J. Liu, L. Liu, H. Jiang, T. Luan, Numerical simulation and analysis of heat leakage reduction in loop heat pipe with carbon fiber capillary wick, *International Journal of Thermal Sciences*. 146 (2019) 106100.
- [12] S. Launay, V. Platel, S. Dutour, J.-L. Joly, Transient Modeling of Loop Heat Pipes for the Oscillating Behavior Study, *Journal of Thermophysics and Heat Transfer*. 21 (2007) 487–495.

- [13] K. Yan, N. Li, R. Zhao, Y. Wu, R. Xie, Visualization study on the condensation in a propylene loop heat pipe operating at condenser temperatures between 153 and 283 K, *Applied Thermal Engineering*. 185 (2021) 116349.
- [14] A. Cavallini, L. Doretti, M. Matkovic, L. Rossetto, Update on Condensation Heat Transfer and Pressure Drop inside Minichannels, *Heat Transfer Engineering*. 27 (2006) 74–87.
- [15] E. Da Riva, D. Del Col, Numerical Simulation of Laminar Liquid Film Condensation in a Horizontal Circular Minichannel, *Journal of Heat Transfer*. 134 (2012) 051019.

Mathematical modeling and its verification on heat transfer characteristics of ultra-thin heat pipes

Yasushi Koito*, Ryosuke Kakizoe, and Akira Fukushima

Kumamoto University, Kumamoto, Japan

* *koito@gpo.kumamoto-u.ac.jp*

Abstract

A mathematical model was presented for an ultra-thin centered-wick heat pipe. This study was motivated because the ultra-thin centered-wick heat pipe is a recently introduced heat pipe, and few studies have been published on the mathematical modeling. The model consisted of three regions: a vapor channel, liquid-wick, and container wall regions. The heated and cooled sections were on the bottom of the model. The equations of continuity, motion, and energy were solved numerically with boundary conditions. A code was developed for numerical calculations. The numerical results were obtained by varying the vapor channel height, vapor channel width, and container wall thickness, and their effects on the heat transfer characteristics of the heat pipe were discussed. The numerical results were compared with experimental results in literature. A fair agreement was obtained between them. Further comparisons will be made to confirm the validity of the present mathematical modeling.

Keywords: Ultra-thin heat pipe, Centered-wick, Numerical visualization, Thermal design, Electronics cooling

1. Introduction

Ultra-thin heat pipes are a thermal solution for mobile and wearable devices such as notebook, smartphones, and smartwatches [1, 2]. An ultra-thin centered-wick heat pipe is one of them, and is fabricated by using a flattening technique [3]. This type of heat pipe places a wick structure only at the center of the flattened container, which differs from conventional heat pipes with a wick structure on the inner wall. Because of its simplicity in structure, the ultra-thin centered-wick heat pipe is a promising candidate for the thermal management of ultra-thin electronic devices.

Many studies have been conducted for the ultra-thin centered-wick heat pipes [e.g., 4–6]. Most of them are experimental studies; experimental results were presented on the thermal performance of ultra-thin centered-wick heat pipes. However, since the heat pipe container is opaque, fluid flow and heat transfer phenomena occurring in the heat pipe have not been deeply discussed in previous studies. It is needed to understand the phenomena for further improvement of the ultra-thin centered-wick heat pipes.

A numerical analysis is an approach to clarify the phenomena occurring in heat pipes. In addition, the numerical analysis provides parametric studies with reasonable cost. Thus, many papers have been published on the mathematical modeling of heat pipes [e.g., 7–9]. However, regarding the ultra-thin centered-wick heat pipe, because it is a recently introduced heat pipe, few studies have been presented on the mathematical modeling and

numerical analyses.

This paper describes a mathematical model for the ultra-thin centered-wick heat pipe. The model consisted of a vapor channel, wick, and container regions of the heat pipe. Numerical results were presented on the heat transfer characteristics. Comparison was made between the numerical results and experimental results in literature.

2. Mathematical modeling

Figure 1 shows a mathematical model of the ultra-thin centered-wick heat pipe. The heat pipe was modeled in the x - y - z coordinate system. Figure 2 shows the x - z cross-section of the model. Because a wick structure was placed at the center of the heat pipe, calculations were conducted for the half domain. The model consisted of three regions: a vapor channel (width: w_v , height: h_v), liquid-wick (width: w_l , thickness: h_w), and container wall (thickness: δ_w) regions. These three regions were the same length l_t . The heated section (length: l_h , width: w_h) and the cooled section (length: l_c , width: w_c) were on the bottom of the model. Except for these two sections, the outer surface of the model was insulated. Total width, w_t , and total thickness, δ_t , of the mode are expressed respectively by

$$w_t = w_l + w_v + \delta_w \quad (1)$$

$$\delta_t = h_v + 2\delta_w \quad (2)$$

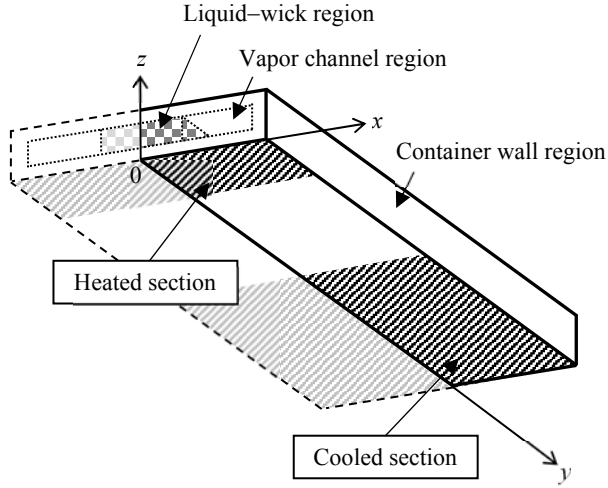


Figure 1. Mathematical model of the ultra-thin centered-wick heat pipe.

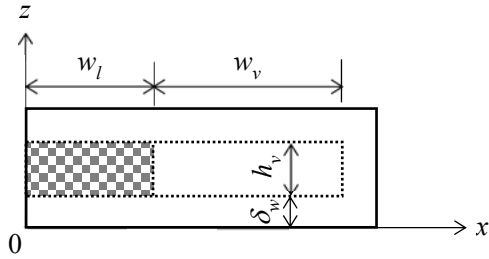


Figure 2. Cross-section of the model.

The governing equations were given as follows for the vapor channel, liquid-wick, and container wall regions, respectively.

For the vapor channel region:

$$\nabla \cdot \mathbf{V}_v = 0 \quad (3)$$

$$\rho_v \mathbf{V}_v \cdot \nabla \mathbf{V}_v = -\nabla p_v + \mu_v \nabla^2 \mathbf{V}_v \quad (4)$$

$$\rho_v c_{p,v} \mathbf{V}_v \cdot \nabla T_v = k_v \nabla^2 T_v \quad (5)$$

For the liquid-wick region:

$$\nabla \cdot \mathbf{V}_l = 0 \quad (6)$$

$$\rho_l \mathbf{V}_l \cdot \nabla \mathbf{V}_l = -\nabla p_l + \mu_l \nabla^2 \mathbf{V}_l - \frac{\varepsilon \mu_l \mathbf{V}_l}{K} \quad (7)$$

$$\rho_l c_{p,l} \mathbf{V}_l \cdot \nabla T_l = \frac{k_{eff}}{\varepsilon} \nabla^2 T_l \quad (8)$$

For the container wall region:

$$\nabla^2 T_w = 0 \quad (9)$$

where \mathbf{V} is the velocity vector ($= (u, v, w)$); u, v, w are the velocities in the x -, y -, z -directions, respectively), p is the pressure, T is the temperature, ρ is the density, μ is the viscosity, c_p is the specific heat at a constant pressure, k is the thermal conductivity, k_{eff} is the effective thermal conductivity, ε is the porosity, and K is the permeability. The subscripts v, l , and w indicate the vapor channel, liquid-wick, and container wall regions, respectively.

The boundary conditions for the heated and cooled sections of the model were given by Eqs. (10) and (11), respectively.

$$-k_w \frac{\partial T_w}{\partial z} = \frac{Q_h}{A_h} \quad (10)$$

$$-k_w \frac{\partial T_w}{\partial z} = h_c (T_w - T_f) \quad (11)$$

where Q_h is the heat input at the heated section, A_h is the area of the heated section ($= l_h \times w_h$), h_c is the heat transfer coefficient at the cooled section, and T_f is the cooling fluid temperature. The following equations were applied to the vapor-liquid interface.

$$u_v = \frac{-k_{eff} (\partial T_l / \partial x)}{\rho_v h_{fg}} \quad (12)$$

$$u_l = \frac{-k_{eff} (\partial T_l / \partial x)}{\rho_l h_{fg}} \quad (13)$$

$$T_v = T_l = \left(\frac{1}{T_{ref}} - \frac{R_g}{h_{fg}} \ln \frac{p_v}{p_{ref}} \right)^{-1} - 273.15 \quad (14)$$

where h_{fg} is the latent heat, R_g is the gas constant, T_{ref} is the reference temperature, and p_{ref} is the reference pressure. Equations (12) and (13) were derived based on the energy balance at the

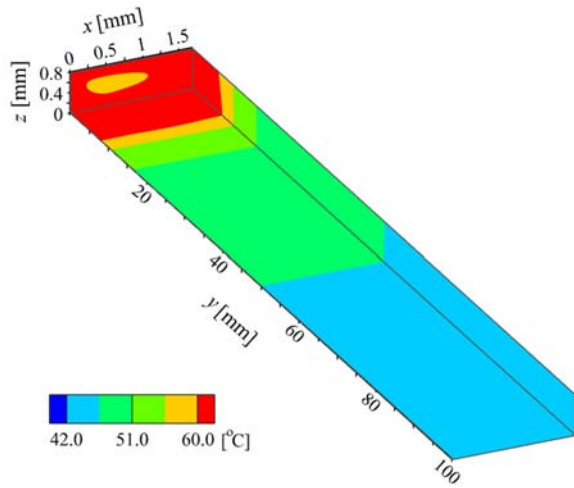


Figure 3. Temperature distribution of the heat pipe ($h_v = 0.4$ mm, $w_v = 1.0$ mm, $\delta_w = 0.2$ mm).

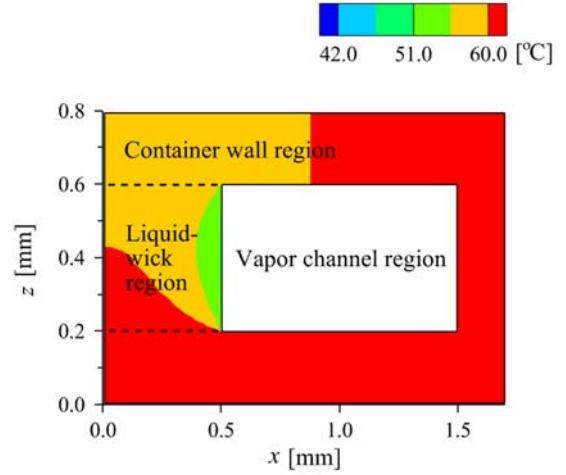
vapor–liquid interface. Except for the heated and cooled sections, an adiabatic condition was employed on the outer surface of the model. A symmetric condition was employed on the surface at $x = 0$. A non-slip condition was used on the vapor–wall and liquid–wall interfaces. Based on the SIMPLE algorithm [10], a calculation code was developed to solve the governing equations with the boundary conditions, and obtain the numerical results. The calculations were conducted with nonuniform grids.

3. Results and discussion

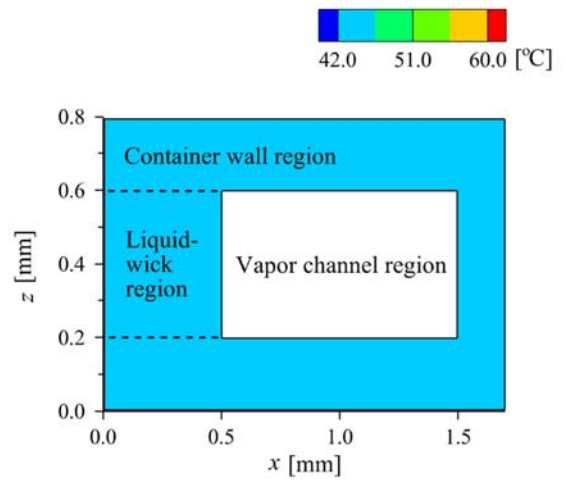
3.1. Characteristics within the heat pipe

In this section, the numerical calculations were conducted by varying h_v , w_v , and δ_w under the conditions of $l_t = 100$ mm and $w_l = 0.5$ mm. The numerical results were obtained under the heating and cooling conditions of $l_h = 10$ mm, $l_c = 50$ mm, $w_h = w_c = w_t$, $Q_h = 3.0$ W, and $T_f = 25^\circ\text{C}$.

Figure 3 shows the numerical results for the temperature distribution of the heat pipe under the conditions of $h_v = 0.4$ mm, $w_v = 1.0$ mm, and $\delta_w = 0.2$ mm. The total thickness, δ_t , of the heat pipe was 0.8 mm. One-dimensional temperature decrease was found in the y -direction with a relatively large temperature drop near the boundary between the evaporator ($0 \text{ mm} \leq y \leq 10$ mm) and adiabatic ($10 \text{ mm} < y < 50$ mm) sections. Figure 4 shows the temperature distributions on the $x - z$ cross-sections at the evaporator and condenser sections under the same conditions as those in Figure 3. The temperature contours at $y = 5$ and 75 mm are shown in Figure 4 (a) and (b),



(a) Evaporator section ($y = 5$ mm)



(b) Condenser section ($y = 75$ mm)

Figure 4. Temperature distributions on the cross-sections of the heat pipe ($h_v = 0.4$ mm, $w_v = 1.0$ mm, $\delta_w = 0.2$ mm).

respectively. Note that the temperature contours in the vapor channel region are not shown. At the evaporator section, the bottom surface of the container wall region was heated by a heat source, and the heat was transferred to the liquid–wick region through the container wall region. Figure 4 (a) indicates that part of the heat was transferred to the upper side of the liquid–wick region, which implies that evaporation of the working fluid occurred not only on the lower side but also on the upper side of the liquid-wick region. Since the effective thermal conductivity, k_{eff} , of the liquid-wick region was small, the temperature drop was larger in the liquid–wick region than in the container wall region. In contrast, at the condenser section, the temperature drop was small as shown

in Figure 4 (b). This is because the heat flux was smaller at the cooled section than at the heated section due to a smaller surface area.

Figure 5 shows the temperature distributions in the y -direction at the bottom of the heat pipe ($x = 0$ mm and $z = 0$ mm). The numerical results are compared for three cases: 1) $h_v = 0.4$ mm, $\delta_w = 0.2$ mm, 2) $h_v = 0.3$ mm, $\delta_w = 0.2$ mm, and 3) $h_v = 0.4$ mm, $\delta_w = 0.1$ mm under the condition of $w_v = 1.0$ mm. δ_t for Case 1), 2), and 3) were 0.8, 0.7, and 0.6 mm, respectively. The vapor velocity increased with decreasing h_v , which increased the vapor pressure drop and the vapor temperature difference over the vapor channel region. Thus, the temperature difference over the bottom of the heat pipe was larger for Case 2) than for Case 1). The difference in h_v between Case 1) and 2) was only 0.1 mm, but their temperature differences over the bottom of the heat pipe differed by 25%. Moreover, the temperature difference was slightly larger for Case 3) than for Case 1). As shown in Figure 4 (a), the heat was transferred in the container wall region not only in the thickness direction but also in the in-plane direction. Thinning the container wall region decreased the heat transfer rate in the in-plane direction, which increased the temperature difference over the bottom of the heat pipe. Note that δ_t for Case 3) was 0.1 mm smaller than that for Case 2), but the former temperature difference was smaller than the latter. Thus, thinning the container wall is more effective than reducing the vapor channel height to decrease the total thickness of ultra-thin heat pipes.

Figure 6 shows the effect of w_v on the temperature distribution of the heat pipe. The temperature distributions in the y -direction at the bottom of the heat pipe ($x = 0$ mm and $z = 0$ mm) are shown for $w_v = 0.5$, 1.0, and 1.5 mm under the conditions of $h_v = 0.4$ mm and $\delta_w = 0.2$ mm. Although Q_h was unchanged, the heat flux at the heated section increased with decreasing w_h , which increased the temperature gradient in the liquid-wick region at the evaporator section. Thus, the temperature difference over the bottom of the heat pipe increased with decreasing w_v . The heat flux as well as the heat rate is a factor dominating the temperature distribution of heat pipes.

3.2. Comparison with experimental results

Figure 7 compares the numerical results with experimental results in literature. The experimental results presented by Zhou et al. [5] were employed, and the numerical calculations

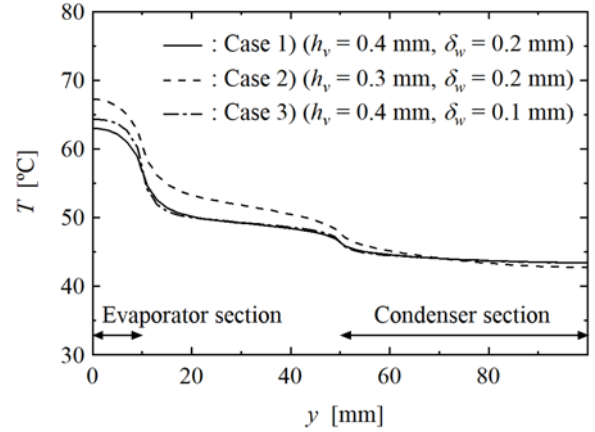


Figure 5. Temperature distributions at the bottom of the heat pipe (Effects of h_v and δ_w under $w_v = 1.0$ mm).

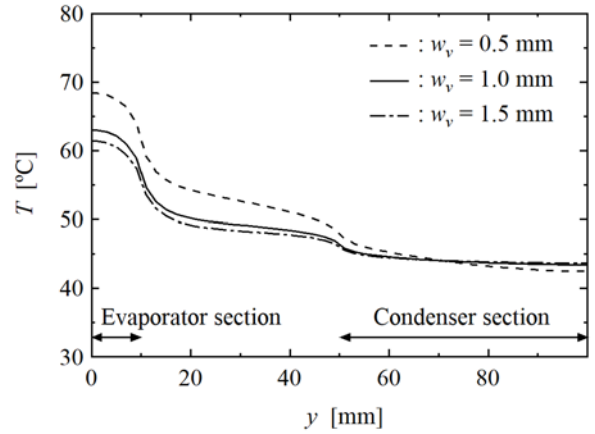


Figure 6. Temperature distributions at the bottom of the heat pipe (Effect of w_v under $h_v = 0.4$ mm and $\delta_w = 0.2$ mm).

were conducted according to the specifications of their ultra-thin centered-wick heat pipe. The comparison was made for two cases of $Q_h = 1.5$ and 2.5 W. Note that $Q_h = 1.5$ and 2.5 W corresponded to 3.0 and 5.0 W, respectively, in Zhou et al. [5] because the half domain of the heat pipe was computed in this study. In Zhou et al. [5], a heat source was wider than the heat pipe, that is, the heating area, A_I , of the heat source was larger than the heated area, A_{II} , of the heat pipe. Because of this difference, the numerical calculations were conducted for two cases of

$$A_h = A_I \quad (15) \quad A_h = A_{II} \quad (16)$$

Since the numerical results were strongly affected by the heat flux at the evaporator section, the temperature distributions obtained with Eq. (15)

and Eq. (16) were very different. However, the experimental results were between these two numerical results for both Q_h , which implies a fair agreement between the experimental and numerical results.

4. Conclusions

A mathematical model was presented for the ultra-thin centered-wick heat pipe. The numerical results for the temperature distribution of the heat pipe were shown, and the effects of the vapor channel height, vapor channel width, and container wall thickness were discussed. A fair agreement was obtained between the numerical results and experimental results in literature. Further comparisons will be made to confirm the validity of the present mathematical modeling.

References

- [1] H. Tang, Y. Tang, Z. Wan, J. Li, W. Yuan, L. Lu, Y. Li, and K. Tang, Review of applications and developments of ultra-thin micro heat pipes for electronic cooling. *Applied Energy*, 2018. 223: p. 383.
- [2] W. Zhou, Y. Li, Z. Chen, Y. Yan, and H. Chen, Design and experimental study on a new heat dissipation method for watch-phones. *Heat and Mass Transfer*, 2021. DOI: 10.1007/s00231-021-03049-2.
- [3] W. Zhou, Y. Li, Z. Chen, L. Deng, and B. Li, Experimental study on the heat transfer performance of ultra-thin flattened heat pipe with hybrid spiral woven mesh wick structure. *Applied Thermal Engineering*, 2020. 170: 115009.
- [4] M. S. Ahamed, Y. Saito, K. Mashiko, and M. Mochizuki, Characterization of a high performance ultra-thin heat pipe cooling module for mobile hand held electronic devices. *Heat and Mass Transfer*, 2017. 53: p. 3241.
- [5] W. Zhou, P. Xie, Y. Li, Y. Yan, and B. Li, Thermal performance of ultra-thin flattened heat pipes. *Applied Thermal Engineering*, 2017. 117: p. 773.
- [6] H. Tang, Y. Xie, Y. Tang, X. Wu, C. Wu, and Y. Sun, Stress analysis and thermal performance of ultra-thin heat pipes for compact electronics. *International Communications in Heat and Mass Transfer*, 2022. 139: 106484.

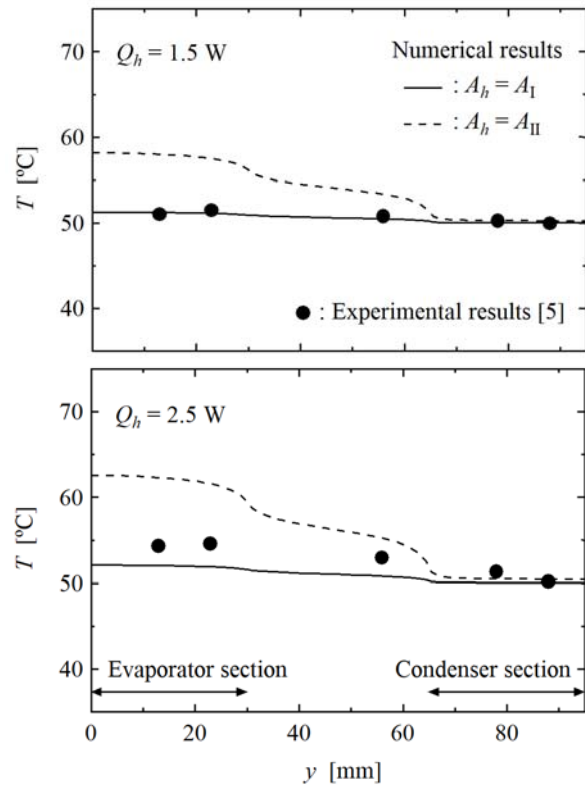


Figure 7. Comparison with the experimental results by Zhou et al. [5].

- [7] A. Faghri and M. Buchko, Experimental and numerical analysis of low-temperature heat pipes with multiple heat sources. *ASME Journal of Heat Transfer*, 1991. 113 (3): p. 728.
- [8] Y. Koito, H. Imura, M. Mochizuki, Y. Saito, and S. Torii, Numerical analysis and experimental verification on thermal fluid phenomena in a vapor chamber. *Applied Thermal Engineering*, 2006. 26: p. 1669.
- [9] R. Ranjan, J. Y. Murthy, S. V. Garimella, and U. Vadakkan, A numerical model for transport in flat heat pipes considering wick microstructure effects. *International Journal of Heat and Mass Transfer*, 2011. 54 (1–3): p. 153.
- [10] S. Patankar, *Numerical Heat Transfer and Fluid Flow*, first ed. (CRC Press, Boca Raton, FL, 1980).

Basic Research on Self-regenerated Bridge Type Heat Pipe

Shunsuke TSUTSUMIUCHI^{1*}, Keiko ISHII¹, and Koji FUMOTO¹

¹*Aoyama Gakuin University, Sagamihara, Japan*

**Corresponding author email address: c5622176@aoyama.jp*

Abstract

In recent years, the heat generation density of electronic components has increased as electronic devices have become smaller and more powerful. Various types of heat pipes have been used as thermal control devices. Pulsating heat pipes (PHP) is a heat transport device that has a structure in which one flow path is arranged in a bellows shape between the heating and cooling parts. However, pulsating oscillation and heat transport in the flow path is not stable. This experiment clarified that the heat transfer was extremely efficient compared with that in the conventional PHPs. Further, the effect of the heat exchange section ratio on the heat transport performance was investigated.

Keywords: PHP, Super Thermal Conducting Device, Self-regenerating Bridge, Aluminum Flat Tube

1. Introduction

Electronic devices such as personal computers and smartphones are becoming smaller and more powerful, and they are indispensable in our daily lives. However, the heat generation density of these central processing units (CPUs) has been increasing, deteriorating the equipment and reducing their processing capacity. Various types of heat pipes have been used as thermal control devices, utilizing the heat transport by the gas-liquid phase change of refrigerants. Among them, pulsating heat pipes (PHP) have attracted attention because of their compact size and high heat transport performance.

A PHP was invented by Akachi around 1990; it comprised a depressurized narrow channel that is reciprocated multiple times and is injected approximately half its volume of working fluid [1]. A PHP typically has a heating section, an adiabatic section, and a cooling section. The gas-liquid phase change occurs in the heating and cooling sections, causing localized pressure fluctuations inside. This produces a self-excited oscillation of the working fluid and heat transport utilizing latent and sensible heat. Because the internal pressure difference leads to a self-excited oscillation, the PHP is less affected by gravity than any other heat pipe. Yasuda et al. investigated the use of HFO refrigerant as the working fluid by comparing the heat transfer performance in the top-heat posture [2]. Suzuki et al. investigated the insertion of a wick to improve the heat transport performance of a PHP in a horizontal position that simulates microgravity conditions [3]. However, design guidelines for a PHP have not yet been established owing to the complexity of its operating phenomena and its slow and unstable initial operation.

This study describes a new heat pipe developed

by the authors, self-regenerating bridge heat pipe (SRBHP, hereinafter called “HP”). The dimensions of a HP are 200 mm length, 48 mm width, and 2 mm thickness. Twenty-eight channels are arranged in parallel in the length direction, with the channels comprising a square cross-section with a side of 1.26 mm. The surface of the flow path is treated to change the wettability. Water is used as the working fluid. The appearance and experimental outline of the HP are almost the same as those of the conventional PHP, but an extremely low filling rate (10 vol.%) is used as the working fluid ratio, which was considered to cause dry-out in the conventional system. HP has an extremely high heat transport efficiency compared with that of the conventional PHP (50 vol.%), and it has excellent values for both effective thermal conductivity and minimum thermal resistance. The low filling ratio (FR) suggests that latent heat is the main factor of heat transport, and the temperature behavior is more stable than that of the conventional type. In this study, we compared the heat transport performance of a HP with that of the conventional type, and evaluated the effect of changes in the heat exchange section ratio on HP.

2. Methods

2.1 Experimental equipment

Figure 1 shows a schematic of the experimental setup. It consists of five systems; the main body of a HP, a heating system connected to a cartridge heater and transformer, vacuum pump system including a digital vacuum gauge, measurement system including a thermocouple attached to the main body of the HP, and syringe for filling the working fluid. The HP is cooled by natural air.

Figure 2 shows a schematic of the main body of the HP. The main material is aluminum, with 200 mm length, 48 mm width, and 2 mm thickness. It has 28 straight channels with a square cross section of 1.26 mm per side. In this experiment, nine thermocouples were installed in the channel located at the center of the HP to evaluate the heat transport performance. The evaporator is heated by applying electric power to a cartridge heater, and the heating mode is vertical bottom heat. Thermal grease is applied between the HP and the heater to reduce contact thermal resistance.

2.2 Experimental methods

Table 1 presents the experimental parameters. In this experiment, the parameters included the size of the evaporator and condenser sections. The evaporator section was fixed at 40 mm (20 area.%) and the condenser section was 40 mm (20 area.%), 100 mm (50 area.%), and 180 mm (80 area.%). The naturally air cooling temperature was 15 to 19 °C.

The HP was evacuated by a vacuum pump to a gauge pressure of -0.099 MPa or less, and the vacuum in the HP was maintained by closing the attached valve. The syringe tube was attached and filled with the working fluid to prevent air from entering. The working fluid was degassed by the vacuum pump in advance because dissolved air in the working fluid could adversely affect the operation of the HP. In this experiment, the FR of the working fluid is defined as follows.

$$FR = \frac{V_{fluid}}{V_{HP}} \times 100 \text{ [vol\%]} \quad (1)$$

Here, V_{HP} [mm³] denotes the volume of all the channels, and V_{fluid} [mm³] denotes the volume of the filled working fluid. A 10 vol.% was adopted as the FR; this was considered to have the best heat transport performance within the experimental parameters. After the fluid was filled, the power was supplied to the HP by the transformer. The temperature of the thermocouple attached to the HP reached a steady state, and this procedure was repeated to increase the applied voltage. The steady state was defined as a temperature fluctuation within 1 °C for 5 min. The experiment was terminated for safety reasons when the temperature of the evaporator reached around 135 °C.

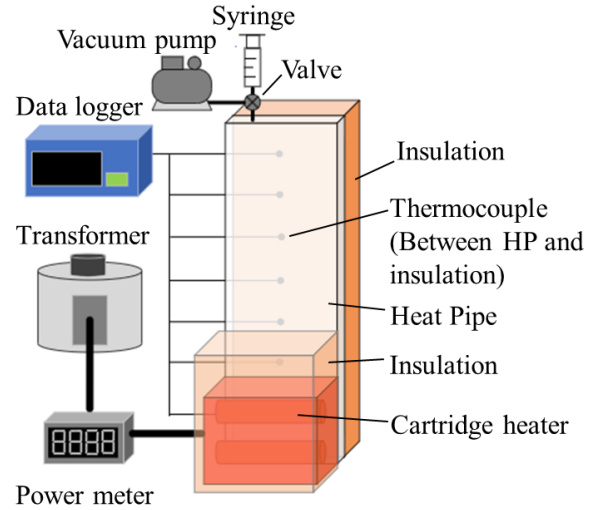


Figure 1. Schematic of the experimental apparatus.

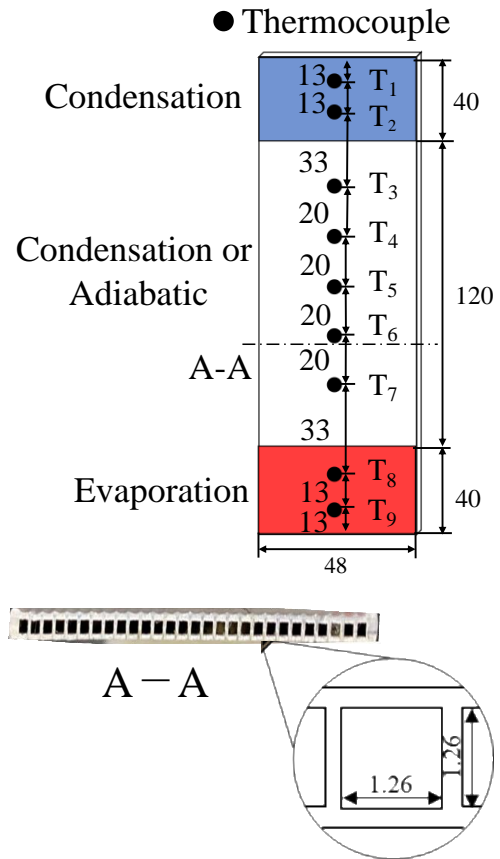


Figure 2. HP sections and thermocouple locations.

Table 1. Experimental parameters.

	Evaporation	Condensation	Adiabatic
Naturally air cooling	20 area.%	20 area.%	60 area.%
		50 area.%	30 area.%
		80 area.%	0 area.%

2.3 Evaluation method

The heat transport performance of the HP was evaluated using thermal resistance. Figure 3 shows the correlation between the heat loss from the heater (Q_L) and the temperature difference between the heating section and ambient air ($T_{evp} - T_a$). The heating section temperature (T_{evp}) is the average value of T_8 and T_9 installed at the positions shown in Figure 2. Net heat input (Q_{net}) is calculated from the difference between the heating value (Q_H) and heat loss (Q_L), as shown in Eq. (2).

$$Q_{net} = Q_H - 0.1012(T_{evp} - T_a) \quad (2)$$

Thermal resistance (R), which indicates heat transfer performance of the HP, is given as

$$R = \frac{T_{evp} - T_{cds}}{Q_{net}} \quad [\text{K/W}] \quad (3)$$

Here, net heat input Q_{net} is calculated from Eq. (2), and T_{cds} is the average value of T_1 and T_2 installed at the positions shown in Figure 2.

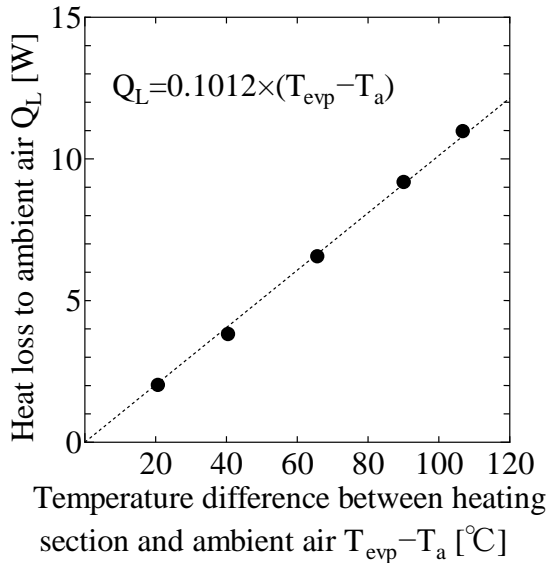


Figure 3. Heat loss to ambient air.

2.4 Primary tests and repeatability

The first several experiments were conducted to check the experimental repeatability. To clearly illustrate the repeatability of the experiment, Figure 4 shows the thermal resistances of the HP with the evaporator section of 20 area.% and the condenser section of 20 area.% in different test runs. This showed that although thermal resistance

varied at the initial heat input, this experiment was considered to have a good repeatability at any other heat input.

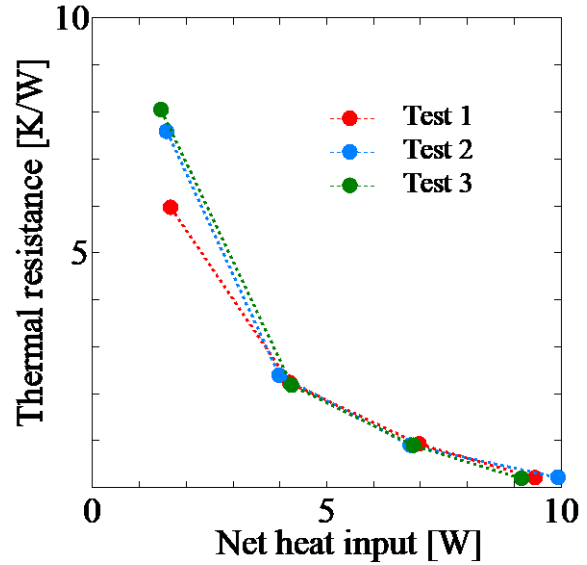


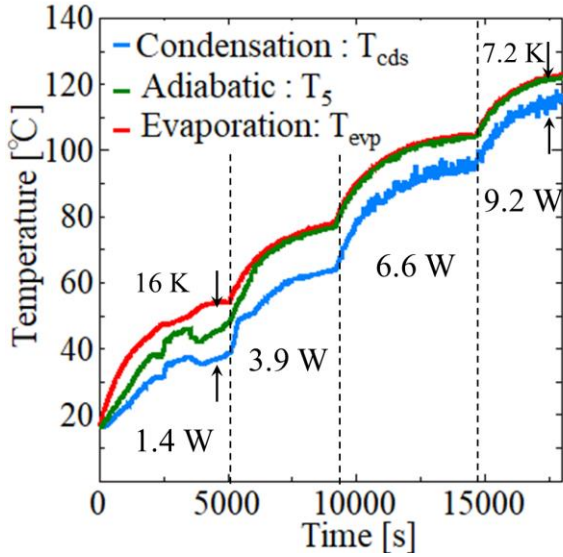
Figure 4. Repeatability tests of the HP.

3. Results and Discussions

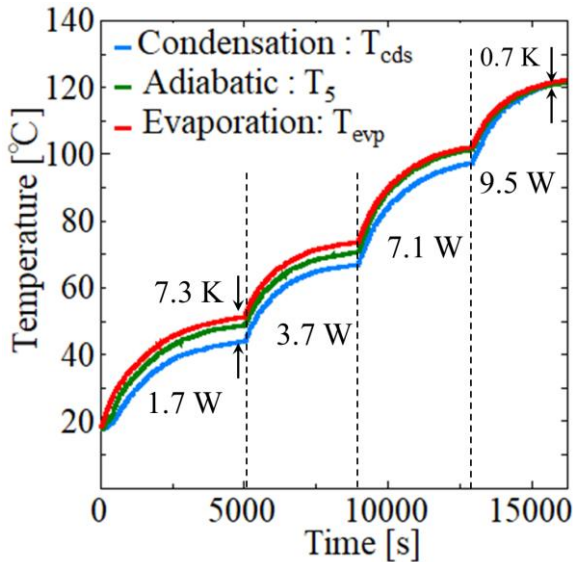
3.1 Comparison with the conventional PHP

Figure 5 shows the temperature–time history for the conventional PHP (50 vol.%) and HP (10 vol.%), and Figure 6 shows their thermal resistance values. The evaporator and condenser sections were both 40 mm (20 area.%), and the cooling method was naturally air cooling with both the PHP and HP. Additionally, Figure 5 shows net heat inputs applied. As shown in Figures 5 and 6, the HP had more stable and efficient heat transport than the conventional PHP with any amount of heat input. The HP was stable in the range of 1.7 to 3.7 W, and the temperature difference between the evaporating and condensing sections was within 7.3 K at 1.7 W, whereas the conventional PHP showed unstable temperature behavior at 1.4 W. Furthermore, the thermal resistance of the HP was lower than that of the conventional PHP at all heat inputs. The minimum thermal resistance of the HP was 0.073 K/W. The high heat transport performance of the HP was achieved by the high-speed self-excited oscillation of the bridged liquid film that blocked the flow path. Additionally, the influence of sensible heat transport on the performance of the HP was small because of its extremely low FR and the difficulty of forming large liquid slugs as well

as those of the conventional PHP. Therefore, latent heat could be considered as the main factor of heat transport, and the bridged liquid film could be predicted to achieve highly efficient heat transport by repeating evaporation and condensation at a high speed. These internal behaviors will be clarified through future visualization experiments.



(a) PHP (50 vol.%).



(b) HP (10 vol.%).

Figure 5. Temperature–time history of the PHP and HP.

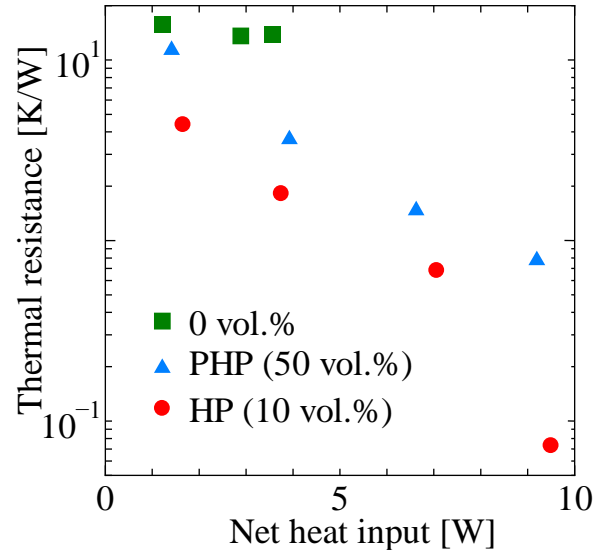
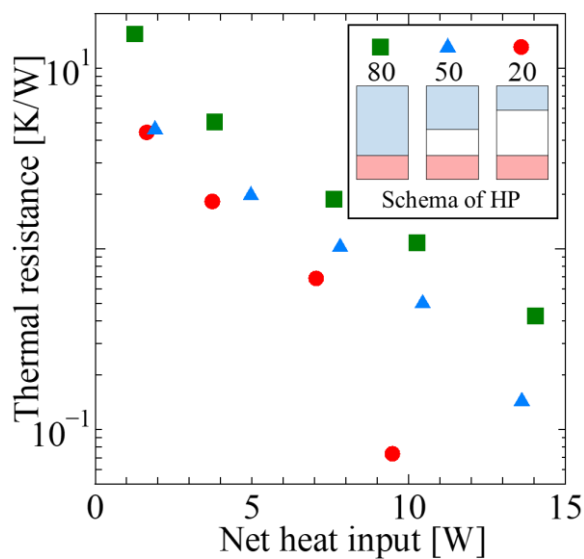


Figure 6. Thermal resistance of the PHP and HP.

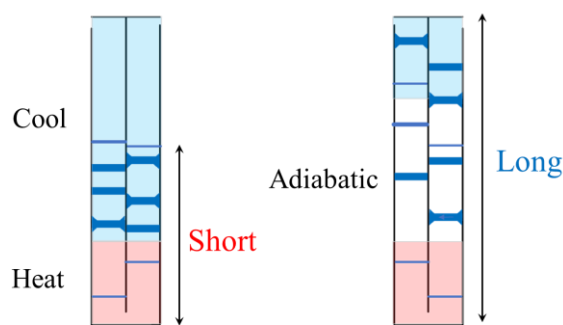
3.2 Effect of heat exchange section ratio on heat transport performance

Figure 7 (a) shows the thermal resistance with different heat exchange section ratios of the HP (10 vol.%). Figure 7 (b) shows the predicted changes in heat transport phenomena caused by changing the condenser area. Experimental parameters are presented in Table 1. The cooling method was natural air cooling. As shown in Figure 7 (a), the thermal resistance of 50 area.% and 20 area.% of the condenser section was lower than that of 80 area.% at the initial heat input range. The thermal resistance was 4.58 K/W at 50 area.% and 4.39 K/W at 20 area.% when net thermal input was approximately 1.8 W, whereas it was 15.4 K/W at 80 area.%. This was because of the increase in the heat transport distance caused by the addition of an adiabatic section between the evaporator and condenser sections. As shown in Figure 7 (b), at 80 area.% of the condenser section, the amplitude of the oscillation of the working fluid was short because the cooling performance of the condenser section was stronger than the driving force associated with the heating rate, particularly at low heat input. However, in the 50 area.% and 20 area.% of the condenser section, shrinking condenser section and weakened cooling performance caused the working fluid to oscillate to the edges, increasing the heat transport distance. Hence, the heat transfer performance improved when the condenser section was reduced.

The minimum thermal resistance in this experiment was 0.073 K/W at 20 area.% of the condenser section.



(a) Thermal resistance.



i) Cool: 80 area.% ii) Cool: 50 or 20 area.%

(b) Changes in heat transport phenomena caused by varying heat exchanging section.

Figure 7. Effects of the heat exchange section ratio on heat transport performance.

4. Conclusion

In this experiment, the heat transport performance of the conventional PHP and HP were compared, and the effects of the heat exchanging section ratio on the HP were investigated. The conclusions obtained within the scope of this experiment are presented below.

- (1) The minimum thermal resistance of the HP at 20 area.% of evaporation and 20 area.% of condensation was 0.073 K/W when the HP was cooled by natural air; this was approximately 1/10 of that of the conventional PHP.
- (2) The heat transport performance was improved by installing an adiabatic section between the evaporator and condenser sections. In particular, within the experimental parameters, the heat transport performance was the best at 20 area.% in the evaporator section and 20 area.% in the condenser section, and it was 0.073 K/W.

References

- [1] H. Akachi, Structure of heat pipe. United States patent, Patent No. 4921041, 1990.
- [2] Y. Yasuda, F. Nabeshima, S. Funakoshi, H. Nagai, Heat transfer performance of pulsating heat pipe with hydrofluoroolefin, *Trans. JSME (in Japanese)* 86 (890) (2020).
- [3] T. Ogushi, Heat Transfer Characteristics of Pulsating Heat Pipe under Top Heating Mode, *Mechanical Engineering Congress. 2012 Japan*, 2012, 1-5

Heat transfer characteristics of a two-phase closed thermosyphon for passive spent fuel pool cooling

Sergio Iván Cáceres Castro^{1*}, Marc Kirsch², Rudi Kulenovic³, Jörg Starflinger⁴

^{1,2,3,4} *Institute of Nuclear Technology and Energy Systems, University of Stuttgart, Stuttgart, Germany*

**sergio.caceres@ike.uni-stuttgart.de*

Abstract

A 3 m prototype model for a large-scale straight two-phase closed thermosyphon related to passive spent fuel pool cooling in nuclear power plants is experimentally investigated. The thermosyphon is made from a stainless steel tube with a 35 mm diameter, which consists of a 1 m evaporator, 1 m adiabatic, and 1 m condenser section, respectively. The evaporator and condenser sections are heated and cooled by water double-pipe heat exchangers. In this work, the objective is to study the effect of the filling ratio (20 %, 30 %, 40 %, 56 %, 75 %, and 100 %, working fluid deionised water) on the thermosyphon's heat transfer performance and the temperature distribution along the thermosyphon under different heat source temperatures (45 °C – 80 °C) and a heat sink temperature of 20 °C. Results show that the best heat transfer performance occurs at a filling ratio of 30 % where the thermosyphon starts to operate at a 45 °C heat source temperature. Furthermore, it was found that the temperature distribution outside as well as inside the thermosyphon is significantly affected by the filling ratio.

Keywords: thermosyphon; temperature distribution; filling ratio; stainless steel-water

1. Introduction

After the accident at Fukushima Daiichi nuclear power plant, passive safety systems are receiving worldwide attention to transport heat from the fuel assemblies to the atmosphere. For so-called spent fuel pools (SFP), in which fuel assemblies are stored in large numbers, active cooling systems are installed, which will stop their operation in case of failure of all (operational and emergency) electricity supply. Alternatively, a passive heat removal system is being developed which is based upon two-phase closed thermosyphons, a highly efficient passive heat transfer device that has been widely used due to its high efficiency, cost-effectiveness, and reliability [1].

Previous experimental work addressed passive cooling applications of SFP and heat transfer characteristics of long thermosyphons. Graß et al. [2; 3] carried out experimental and analytical studies on the heat transfer characteristics of a 10 m thermosyphon related to passive SFP cooling. They concluded that an evaporator section filled with less than 100 % liquid causes an increase of up to 70 % in the heat transfer coefficient at a heat input of 3 kW. For 50 % and 70 % filling ratios, no difference in the heat transfer was noticeable and therefore smaller filling ratios were not investigated.

Kusuma et al. [4] investigated the thermal performance of a prototype model for a large-scale vertical thermosyphon for passive SFP cooling.

The thermosyphon was made from a copper tube 1.5 m long. The results showed that the best thermal performance was achieved at a filling ratio of 60 % and a heat load of 187 W. However, no information of the temperature distribution inside the thermosyphon was given.

Seo and Lee [5] investigated the length effect on entrainment limitation of up to 3 m long vertical wickless heat pipes with inner and outer diameters of 16.5 mm and 19.0 mm, respectively. The results of these experimental investigations were compared with correlations to determine the operation limits of heat pipes. It was found that correlations exhibited an extreme range of prediction errors of a maximum of 49.8 %.

Although the thermal properties of closed two-phase thermosyphons have already been studied in detail in the context of passive SFP cooling, there is a lack of sufficient data on the heat transfer characteristics and temperature distribution outside as well as inside of long thermosyphons. Furthermore, existing correlations are mainly determined and validated for thermosyphons shorter than 3 m. The main objective of this work is to experimentally investigate the effect of the filling ratio and heat source temperature on the heat transfer characteristics and temperature distribution of a prototype model for a large-scale thermosyphon in combination with passive SFP cooling. In addition, the results should contribute to the further development and validation of a

mechanistic ATHLET (Analysis of Thermal-hydraulic of Leaks and Transients) model for 3 m long two-phase closed thermosyphons.

2. Experimental setup and procedure

2.1. Test rig

Figure 1 shows the schematic of the experimental setup and the locations of measuring points for investigating the thermal characteristics of a 3 m-long thermosyphon.

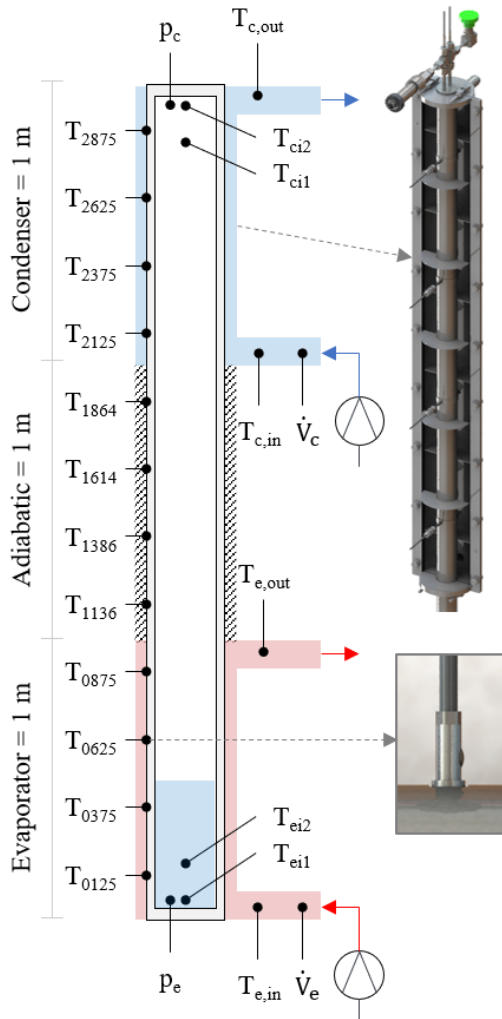


Figure 1. Schematic representation of the experimental setup and the arrangement of the measuring instruments instrumentation.

The smooth pipe is made of 1.4301 stainless steel with an inner and outer diameter of 35 mm and 38 mm respectively. Double-tube heat exchangers are installed in the evaporator and condenser sections as heat source and heat sink, connected to process thermostats operated with water. The adiabatic section is thermally insulated with 19 mm thick Armaflex XG pipe insulation.

On the outer surface of the thermosyphon, 12 resistance thermometers PT100, with a Class A accuracy $\pm (0.15 + 0.002 \cdot T \text{ RD})$, are placed starting at a height of 125 mm in equal intervals of 250 mm. The outer surface of the pipe is milled flat to ensure thermal contact between the pipe surface and the resistance thermometer. Four sheathed resistance thermometers PT100 are placed inside the thermosyphon, allowing the temperature measurement at different heights inside the evaporator and condenser section. The absolute pressure in the evaporator and condenser section is measured with absolute pressure transmitters PAA-33X with an accuracy of $\pm 0.15 \% \text{ FS}$. The inlet and outlet temperatures of both heat exchangers on the heating and cooling side are also measured with sheathed resistance thermometers PT100. The flow rate at the inlet of the evaporator and condenser section is determined with an ultrasonic flow meter with an accuracy of $\pm (0.7 \% \text{ RD} + 0.7 \% \text{ FS})$. The Keysight data logger 34970A and the computer software Agilent VEE are used for the measurement data acquisition.

2.2. Test conditions and data reduction

For the design of fuel pool heat removal systems, the following pool water temperatures according to KTA 3303 [6] are used as a basis for the investigation: 45 °C (normal operation), 60 °C (abnormal or malfunctioning storage tank cooling operation), and 80 °C (accidental operation). For this reason, the experimental investigations in this work are carried out for the heat source temperatures in this range. The heat sink temperature is 20 °C. The filling ratio is varied between 20 % and 100 %. The flow rate of the circulating water through the heat exchangers in the evaporator and condenser section is 10 l/min. Table 1 gives an overview of the experimental parameters. In total, 60 experiments have been carried out in this campaign.

Table 1. Experimental parameters.

Parameter	Unit	Value
Volume flow	l/min	10
Filling ratio	%	20, 30, 40, 56, 75, 100
Heat source temperature	°C	45, 50, 55, 60, 65, 70, 75, 80
Heat sink temperature	°C	20
Measuring frequency	Hz	0.5

The test procedure starts with the evacuation of the thermosyphon with a vacuum pump to a final pressure of 0.2 Pa. Then, the thermosyphon is filled with degassed deionised water. After the filling procedure, the thermosyphon is heated up and the valve at the top is slowly opened to eliminate non-condensable gases in the system. Next, the inlet temperatures ($T_{e,in}, T_{c,in}$) and the volume flows (\dot{V}_e, \dot{V}_c) in the evaporator and condenser sections respectively are determined. The steady state is determined by checking that the fluctuations of inlet temperatures and volume flows are less than ± 0.1 °C and ± 0.2 l/min respectively.

As described above, two sheathed resistance thermometers are placed in both the evaporator (T_{ei1}, T_{ei2}) and condenser (T_{ci1}, T_{ci2}) sections. To determine the temperature distribution inside the evaporator and condenser section, measurements are repeated at the same filling ratio, heat source and sink temperature after displacing the movable resistance thermometers T_{ei2} and T_{ci1} to a new height. The resistance thermometers T_{ei1} and T_{ci2} are left in the same positions and serve as a reference.

A brief overview of the calculations of the most important thermal variables is given below. The fluid properties are derived by the International Association for the Properties of Water and Steam (IAPWS) [7]. The heat transfer rate \dot{Q} of the double-pipe heat exchangers in the evaporator and condenser section is given by

$$\dot{Q} = \rho c_p \dot{V} (T_{out} - T_{in}) \quad (1)$$

where ρ is the fluid density, c_p is the isobaric heat capacity, \dot{V} is the volume flow, and T_{out} and T_{in} are the outlet and inlet temperatures respectively in the double-pipe heat exchanger. The average heat transfer coefficient in the evaporator section $\bar{h}_{e,exp}$ is calculated with the following equation

$$\bar{h}_{e,exp} = \frac{\dot{Q}_e}{A_e (T_{w,e} - T_v)} \quad (2)$$

where \dot{Q}_e is the input heat transfer rate in the evaporator section, A_e is the inner surface area of the thermosyphon evaporation section, $T_{w,e}$ is the mean wall temperature in the evaporator section and T_v is the vapor temperature inside the thermosyphon. To consider the error in the calculations, the Gaussian error propagation is applied,

$$\Delta y = \sqrt{\sum_{i=0}^n \Delta x_n^2 \left(\frac{\partial y}{\partial x_n}\right)^2} \quad (3)$$

where Δy represents the error propagation of the considered equation, x_n is the independent measured variable and Δx_n is the uncertainty of each used measurement device.

3. Results

3.1. Heat transfer performance

Maximum heat transfer rate

Experimental investigations are performed at different filling ratios and heat source temperatures (see Table 1) to determine the maximum heat transfer rate of the thermosyphon. The results are presented in Figure 2, where the heat transfer rate in the condenser section \dot{Q}_c is plotted versus the filling ratio V^+ . Starting with a 45 °C heat source temperature it can be recognized that at 30 % filling ratio a heat transfer rate of 1.40 kW is achieved, showing that the thermosyphon starts to operate at these conditions. On the other hand, for the other filling ratios and at the same heat source temperature no operation of the thermosyphon is noticeable. With increasing the heat source temperature to 50 °C, the results display an increase in the heat transfer rate for all filling ratios, with a maximum heat transfer rate of 1.80 kW at a 30 % filling ratio. If the temperature of the heat source continues to rise, similar behaviour in the heat transfer rate can be observed. In particular, for all heat source temperatures, the highest heat transfer rate is achieved at a 30 % filling ratio. It also should be pointed out that as the filling ratio increases the heat transfer rate decreases. The maximum heat transfer rate of approximately 3.90 kW is achieved at a 30 % filling ratio and 80 °C heat source temperature.

Figure 3 presents the relative error versus the absolute error of heat transfer rates \dot{Q}_e and \dot{Q}_c at different heat source temperatures $T_{e,in}$. Two clusters can be recognized: the values for \dot{Q}_e are indicated with the red dashed line and for \dot{Q}_c with the blue dashed line. Furthermore, it can be differentiated between three groups: steady-state, geyser boiling and no operation. It can be seen that the values for steady-state are within the 6 – 15 % range. Here it is important to point out that the relative error lies on average at approximately ± 8 %. For heat transfer rate \dot{Q}_e , the absolute error lies on average at approximately ± 0.28 kW and for \dot{Q}_c at approximately ± 0.22 kW. The values of

the group geyser boiling show higher values compared to the experiments in steady-state. The main reason for this difference is due to the large filling ratio and low heat source temperature or heat input. This leads to an oscillatory behaviour of the thermosyphon denoted as geyser boiling. And lastly, for the group with no operation, no calculation of the heat transfer is possible since the temperature difference at the inlet and outlet of the heat exchangers are almost equal to zero and these lie within the range of the device's accuracy.

Average heat transfer coefficient at the evaporator section

The average experimental heat transfer coefficient versus the investigated heat source temperatures is shown in Figure 4. Starting from the 100 % filling ratio it can be seen that the experimental heat transfer coefficient increases as the filling ratio decreases to 30 % filling ratio. For 20 % filling ratio, the heat transfer coefficient decreases compared to the 30 % filling ratio. Here, as the filling ratio decreases and the heat input increases, the amount of liquid and wetted area in the evaporator section decrease, resulting in deterioration of the heat transfer coefficient due to partial dryout in the upper part of the evaporator section.

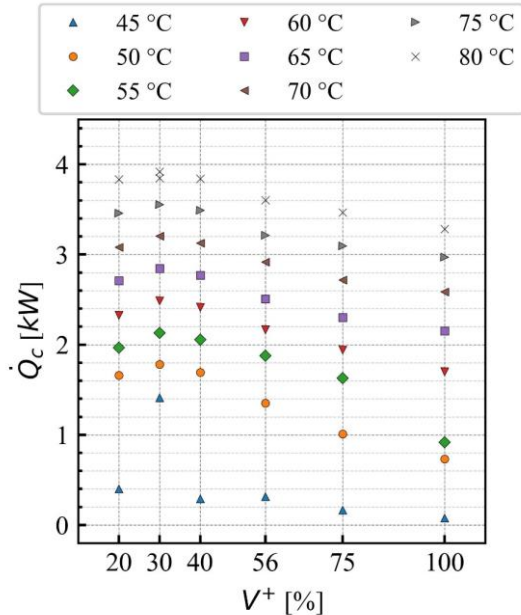


Figure 2. Heat transfer rate \dot{Q}_c vs. filling ratio V^+ at different heat source temperatures $T_{e,in}$.

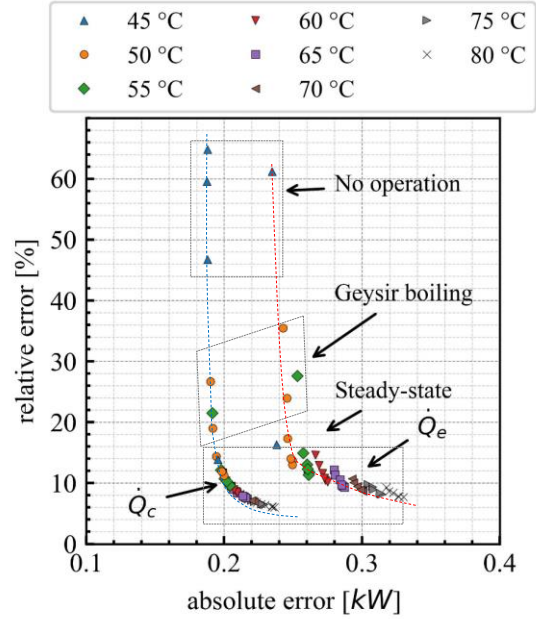


Figure 3. Relative error vs. absolute error of heat transfer rates in the evaporator \dot{Q}_e and condenser section \dot{Q}_c for different heat source temperatures.

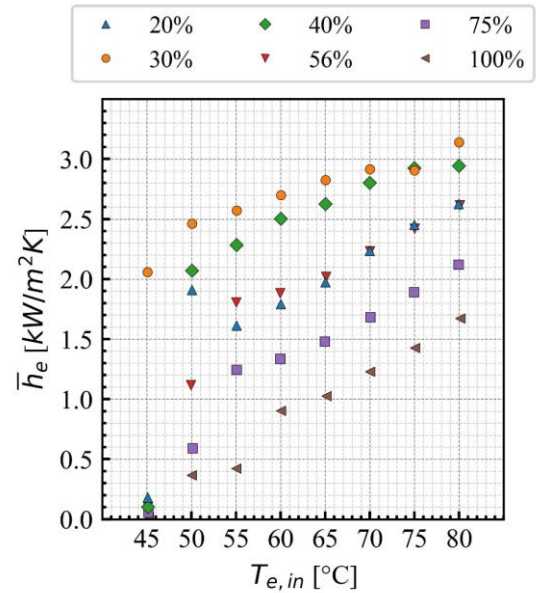


Figure 4. Average experimental heat transfer coefficient in the evaporator section \bar{h}_e vs. heat source temperature $T_{e,in}$.

3.2. Temperature distribution along the outside wall of the thermosyphon

The experiments with heat source temperatures equivalent to the pool water temperatures of 45 °C, 60 °C and 80 °C, and filling ratios equal to 20 %, 30 %, 56 %, and 100 % are chosen for the evaluation of the influence on the temperature

distribution along the outside wall of the thermosyphon. The results are presented in Figures 5 to 7, where the total length of the thermosyphon l_t is plotted versus the outer surface temperature T_s . In the right part of the charts, the temperature measurement points are indicated. In Figure 5 the experiments for a heat source temperature of 45 °C are shown. For filling ratios 20 %, 56 %, and 100 %, the results show a nearly constant temperature distribution of 45 °C in the evaporator section and a temperature of 20 °C in the adiabatic and condenser section. This means that there is no heat transport and thus the thermosyphon does not operate at this heat source temperature. For the 30 % filling ratio, it can be seen that the thermosyphon starts to operate. The maximum temperature difference in the evaporator and condenser section is 10 K resp. 3 K. The adiabatic section shows an isothermal temperature distribution of 30 °C. In Figure 6 the experimental results for the heat source temperature 60 °C are shown. Between the 30 % and 56 % filling ratio no significant difference in the temperature distribution is noticeable. Nevertheless, it can be seen that the temperature distribution is significantly affected at 20 % and 100 % filling ratio. For 20 % filling ratio, the temperature gradient at a height of 625 mm and 875 mm corresponds to 6.5 K and 7.5 K, respectively. This temperature deviation can be caused by partial dryout in the upper part of the evaporator section due to the very small filling ratio. For 100 % filling ratio, the temperature at a height of 2875 mm is slightly lower compared to other condenser surface temperatures. This temperature reduction may be due to the presence of liquid droplets in the upper part of the condenser section. In Figure 7 the experiments for a heat source temperature of 80 °C are shown. For 30 % and 56 % filling ratio, no significant difference in the temperature distribution is noticeable. However, similar to the heat source temperature 60 °C (Figure 6), it can be seen that the temperature distribution is significantly affected in the experiments with 20 % and 100 % filling ratio. For 20 % filling ratio, the temperature gradient at a height of 625 mm and 875 mm corresponds to 3.7 K and 10.9 K, respectively. For 100 % filling ratio, the temperature at a height of 2875 mm is significantly lower compared to the other condenser surface temperatures. Due to the large filling ratio and high heat source temperature, this temperature reduction is caused by a liquid accumulation in the upper part of the condenser section.

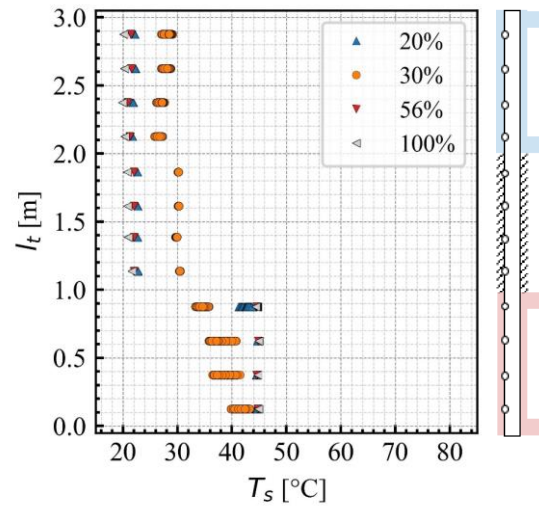


Figure 5. Temperature distribution along the outer wall of the thermosyphon at $T_{e,in} = 45$ °C and different filling ratios.

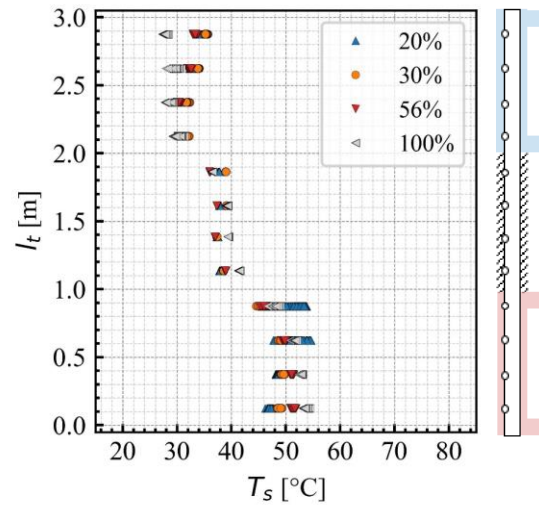


Figure 6. Temperature distribution along the outer wall of the thermosyphon at $T_{e,in} = 60$ °C and different filling ratios.

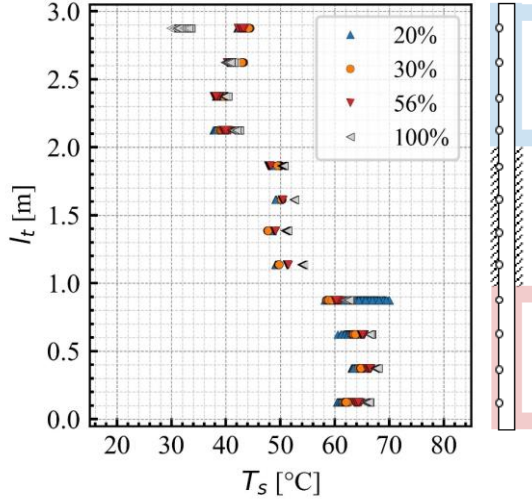


Figure 7. Temperature distribution along the outer wall of the thermosyphon at $T_{e,in} = 80\text{ °C}$ and different filling ratios.

3.3. Temperature distribution inside the evaporator and condenser section of the thermosyphon

As described in section 2.2, the determination of the temperature distribution inside the evaporator and condenser section is carried out by repeated measurements at the same experimental parameters (V^+ , $T_{e,in}$, $T_{c,in}$, \dot{V}_e , \dot{V}_c) after displacing the resistance thermometers T_{ei2} and T_{ci1} to a new height and leaving the resistance thermometers T_{ei1} and T_{ci2} in the same positions as reference. Besides the temperatures T_{ei1} and T_{ci2} , the pressure in the condenser section p_c is used to evaluate the reproducibility of the repeated measurements. Exemplary, in Figure 8 the error bars for p_c and T_{ei1} are plotted for five repeated measurements (011, 021, 031, 041 and 051) at a steady state operation of the thermosyphon with 30 % filling ratio and 80 °C heat source temperature. It can be seen that p_c varies between 122 mbar and 125.5 mbar. The values are in the range of the pressure transmitter accuracy (4.5 mbar) and validate that no condensable gas entrained the system after displacing the resistance thermometers. The temperature range of T_{ei1} is lower than 1 K. Since the thermosyphon shows the best performance at 30 % filling ratio and the temperature distribution is significantly affected at a 100 % filling ratio, the experiments with these two filling ratios are chosen for the evaluation of the influence on the temperature distribution inside the evaporator and condenser section of the thermosyphon.

The results for the 30 % and 100 % filling ratio at 45 °C, 60 °C, 70 °C and 80 °C heat source temperatures are presented in Figure 9 and Figure 10, respectively, where the evaporator length l_e and condenser length l_c is plotted over the inner surface temperature T_i of the thermosyphon. In the right part of the charts, the temperature measurement points are indicated. As can be seen in Figure 9 and also observed in Figure 5, the thermosyphon also shows a slightly oscillatory behaviour of the temperature inside the evaporator section at 45 °C heat source temperature and 30 % filling ratio. Compared to higher filling ratios where the falling liquid film of the condenser persists in the evaporator section, for small filling ratios as 30 %, the liquid film breaks up into rivulets at some points in the evaporator section which leads to the creation of dry patches between the rivulets. However, as described in [8], “this local dryout of the wall is generally not considered to be a heat transport limitation, since the wall will eventually reach a steady temperature”, as seen for 60 °C, 70 °C and 80 °C heat source temperatures. In the condenser section, the temperature distribution is isothermal at different heat source temperatures. It is important to point out that these temperatures correspond to the saturation temperature of the corresponding measured condenser pressure, which confirms the uniform presence of vapour in the centre of the thermosyphon.

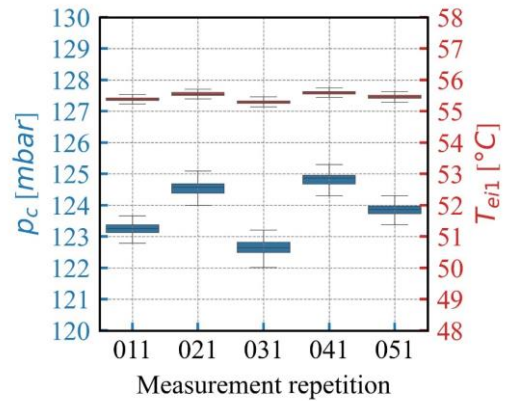


Figure 8. Reproducibility of repeated measurements for $V^+ = 30\%$ and $T_{e,in} = 80\text{ °C}$.

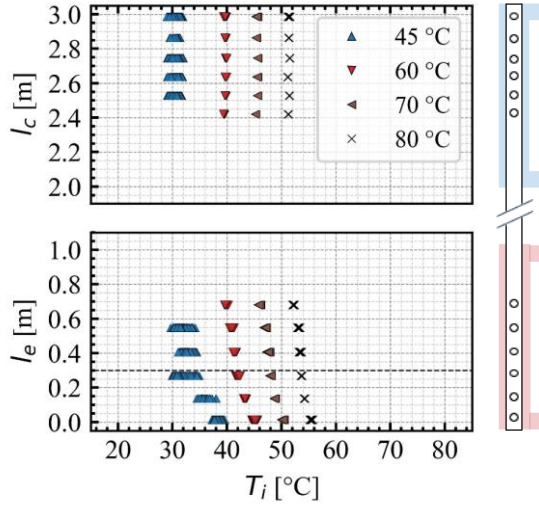


Figure 9. Temperature distribution inside the evaporator and condenser section at $V^+ = 100\%$ and different $T_{e,in}$.

In Figure 10 the thermosyphon also shows an isothermal temperature distribution inside both the evaporator and condenser section at $45\text{ }^\circ\text{C}$ heat source temperature and 100% filling ratio. The temperature in the evaporator and condenser section correspond to $45\text{ }^\circ\text{C}$ and $20\text{ }^\circ\text{C}$, respectively, which confirms that there is no heat transport between the circulating water of the heat exchanger and the thermosyphon. It also can be recognised that with increasing heat source temperatures a significant temperature stratification in the condenser section occurs compared to a 30% filling ratio. For example, at $60\text{ }^\circ\text{C}$ heat source temperature, this stratification or temperature reduction in the upper part of the condenser section is caused by the presence of liquid droplets which are torn from the falling film so they are propelled upwards impinging on the end cap of the condenser section. This behaviour is denoted as the entrainment limit. This is mainly caused by the increase of the relative velocity between the liquid film returning from the condenser and vapour flowing upwards. Compared to the $60\text{ }^\circ\text{C}$ heat source temperature, the relative vapour-liquid velocity at $80\text{ }^\circ\text{C}$ heat source temperature is high enough to prohibit the liquid flow from returning to the evaporator section. In this case, the thermosyphon has reached the flooding limit. Nevertheless, dryout in the evaporator section due to the accumulated liquid in the condenser section could not be detected.

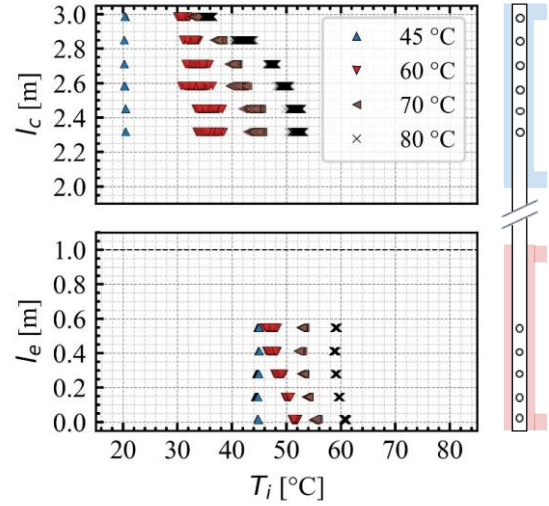


Figure 10. Temperature distribution inside the evaporator and condenser section at $V^+ = 100\%$ and different $T_{e,in}$.

As mentioned above, when the droplets are propelled upwards after being torn from the falling film, they impinge on the end cap of the thermosyphon's condenser section. One way to detect the entrainment is the sound caused by the droplet impingements. However, this can also be seen in the measured pressure in the condenser section. Figure 11 illustrates the time-dependent pressure courses at $45\text{ }^\circ\text{C}$, $60\text{ }^\circ\text{C}$, $70\text{ }^\circ\text{C}$ and $80\text{ }^\circ\text{C}$ heat source temperatures. At $45\text{ }^\circ\text{C}$ heat source temperature, the measured pressure is constant and equivalent to 25 mbar , confirming no thermosyphon operation at these conditions.

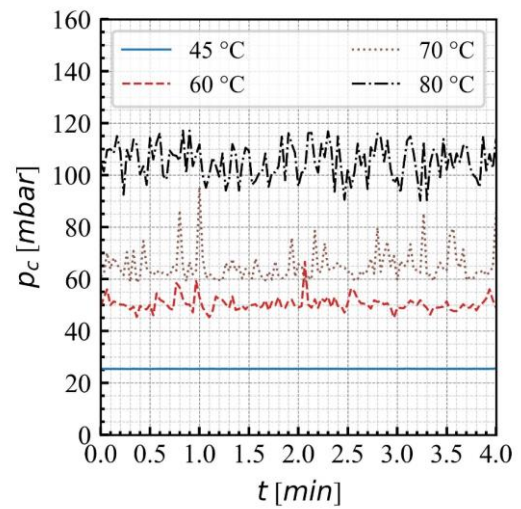


Figure 11. Transient pressure in the condenser section at $T_{e,in} = 45\text{ }^\circ\text{C}$, $60\text{ }^\circ\text{C}$, $70\text{ }^\circ\text{C}$ and $80\text{ }^\circ\text{C}$.

As the heat source temperature increases to 70 °C, higher pressure peaks can be seen compared to the 60 °C heat source temperature. In particular, at 80 °C heat source temperature, strong and frequent droplet impingements are recorded during the measurements. This behaviour can be confirmed and quantified by the frequency and pressure difference observed in the pressure curve at 80 °C heat source temperature.

4. Conclusion

The effect of filling ratio and heat source temperature on thermal behaviour and temperature distribution of a 3 m long two-phase closed thermosyphon was experimentally investigated. The following conclusions from the present work are:

1. The thermosyphon exhibits the maximum thermal performance at a 30 % filling ratio where it starts to operate at a heat source temperature of 45 °C. The maximum heat transfer rate achieved at 80 °C heat source temperature is approximately 3.90 kW.
2. Starting from the 100 % filling ratio, the heat transfer coefficient in the evaporator section increases as the filling ratio decreases to a 30 % filling ratio, where the maximum heat transfer coefficient of 3.30 kW/m²K at a 80 °C heat source temperature is achieved.
3. The deterioration of the heat transfer coefficient in the evaporator section at 20 % may be due to partial dryout in the upper part of the evaporator section.
4. The effect of the filling ratio in the temperature distribution along the outside wall of the thermosyphon is prominent at a filling ratio of 100 %.
5. For 100 % filling ratio, the presence of droplets and liquid accumulation in the condenser section is confirmed by the determined temperature distribution inside the condenser section.
6. Two variables are selected to evaluate the reproducibility of the measurements. The temperature at the bottom of the evaporator shows a maximum variation of less than 1 K. The pressure in the condenser section varies in the range of the device's accuracy.

Acknowledgement

The presented work was funded by the German Federal Ministry for the Environment, Nature Conservation, Nuclear Safety and Consumer Protection (BMUV, project no. 1501612A) on basis of a decision by the German Bundestag.

References

- [1] A. Faghri, Heat Pipes: Review, Opportunities and Challenges. *Frontiers in Heat Pipes*, 2014. 5(1).
- [2] C. Graß; A. Krüssenberg; R. Kulenovic; F. Weyerman; J. Starflinger; A. Schaffrath, Detailed experimental and analytical study on long two-phase closed thermosiphons related to passive spent-fuel pool cooling. in 26th International Conference on Nuclear Engineering - ICONE26, 2018. London, England.
- [3] C. Graß; R. Kulenovic; J. Starflinger, Experimental study on heat transfer characteristics of long two-phase closed thermosiphons related to passive spent fuel pool cooling. in Joint 19th IHPC and 13th IHPS, 2018. Pisa, Italy.
- [4] M. H. Kusuma, N. Putra, A. R. Antariksawan, Susyadi and F. A. Imawan, Investigation of the Thermal Performance of a Vertical Two-Phase Closed Thermosyphon as a Passive Cooling System for a Nuclear Reactor Spent Fuel Storage Pool. *Nuclear Engineering and Technology*, 2017. 49(3): p. 476–483.
- [5] J. Seo and J.-Y. Lee, Length effect on entrainment limitation of vertical wickless heat pipe. *International Journal of Heat and Mass Transfer*, 2016. 101: p. 373–378.
- [6] KTA 3303:2015-11. Heat removal systems for fuel assembly storage pools in nuclear power plants with light water reactors.
- [7] International Association for the Properties of Water and Steam, R7-97(2012): Revised Release on the IAPWS Industrial Formulation 1997 for the Thermodynamic Properties of Water and Steam, 2012).

Improvements of thermal performance by nanoparticle layer coating in heat pipes

Menglei Wang^{1*} and Tomio Okawa¹

¹The University of Electro-Communications, Tokyo, Japan

*Corresponding author email address: wang@eel.mi.uec.ac.jp

Abstract

In this research, nanoparticle-layer was used as the wick in a cylindrical heat pipe to experimentally investigate its effect on the heat transfer performance. The materials of heat pipe and screen mesh were copper and brass, respectively, and the nanoparticle material was silicone-dioxide. When the wall was coated with the nanoparticle layer, the thermal resistance R decreased 53-62% in comparison with the ordinary heat pipe without nanoparticle layer. On the other hand, the critical power CP was reduced up to 35%. It was confirmed that CP increased with an increase in wickability Wi . Similar heat transfer performance was achieved even when the screen mesh was removed. This indicated that the nanoparticle layer coated on the inside wall of heat pipe worked as a high-performance wick. Since the nanoparticle layer is thin, it may effectively be applied particularly to small heat pipes for small electronic devices.

Keywords: Heat pipe; Nanoparticle layer; Heat transfer enhancement; Miniaturization

1. Introduction

Due to a rapid increase in the heat load and the necessity of miniaturization in recent electronic equipment, further improvement of heat transfer performance and downsizing are required for the cooling devices. During nucleate pool boiling in nanofluid, it is known that a thin layer of nanoparticles is formed on the heat transfer surface [1]. Since the nanoparticle layer exhibits strong capillarity, it is expected that it may be used as a high-performance wick in heat pipes [2]. This expectation may be supported by the fact that the capillarity is a particularly important factor in determining the critical heat flux on structured superhydrophilic surfaces [3]. In this work, heat pipes using the nanoparticle layer as the wick are fabricated to measure the two fundamental heat transfer performances: thermal resistance and maximum heat transfer rate. The wickability that is the parameter expressing the capillarity of the nanoparticle layer is also measured to understand the mechanisms to cause the variations in the heat transfer performances.

2. Description of the Experiments

2.1. Nanoparticle layer formation on the inner wall of heat pipe

The outer wall of the copper tube was wrapped with nichrome wire heater for heating and then covered by polyimide tape and fluorine tape for electric and thermal insulations. After immersing it in the SiO_2 -water nanofluid of 0.4 kg/m^3 particle concentration, AC power was applied to the nichrome wire to cause nucleate boiling on the tube inner wall; the heat flux was set to 180 kW/m^2 . During nucleate boiling, a nanoparticle layer was

formed on the inner surface of the copper tube. The microscope images of the tube inner wall are displayed in Fig. 1. The white-colored region on the tube inner wall corresponded to the layer of nanoparticles. The thickness of the deposited nanoparticles was within $4\text{-}30 \mu\text{m}$. The mass of the deposited nanoparticles M was within $0.52\text{-}2.3 \text{ g/m}^2$.

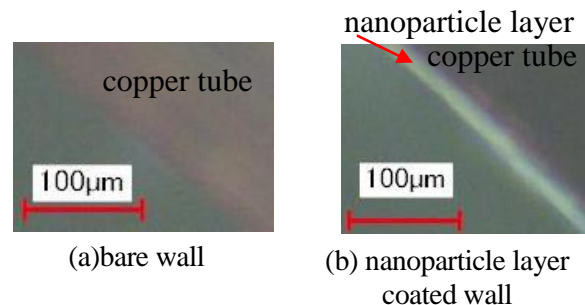


Figure 1. Side views of the nanoparticle layer formed on the copper tube inner wall.

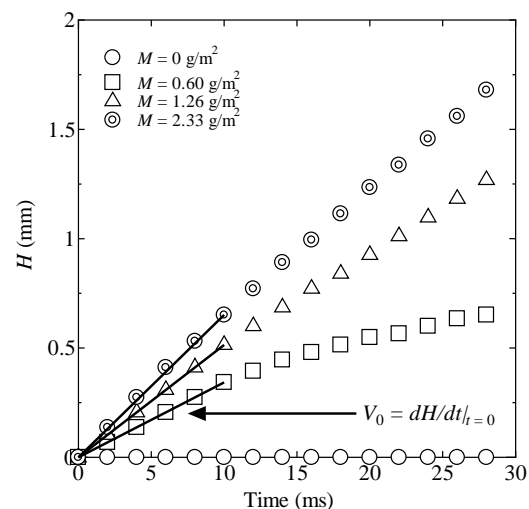


Figure 2. Time variation of the water level.

To measure the wickability Wi , the lower end of distilled water contained in the glass tube of 1.05 mm in inner diameter was touched with the nanoparticle layer. The water was sucked by the capillarity of the nanoparticle layer [3]. The time variation of the water level H in the glass tube was recorded using a high-speed camera, and the value of Wi was calculated by

$$Wi = \frac{V_0 \rho_l}{\rho_v^{1/2} [\sigma g (\rho_l - \rho_v)]^{1/4}} \quad (1)$$

where V_0 is the moving maximum speed of the water level in the glass tube in Fig. 2. The relationship between Wi and M is presented in Fig. 3. It can be seen that Wi tended to increase with an increase in M .

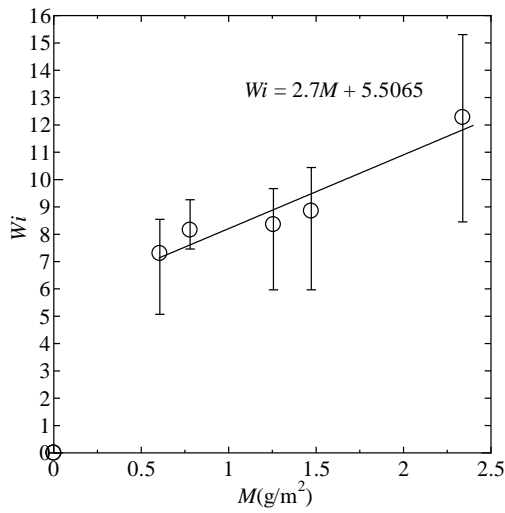


Figure 3. Dependence of the wickability of the nanoparticle layer on the total mass of deposited nanoparticles (symbols and error bars refer the arithmetic mean and range of the values measured at multiple locations).

2.2. Measurement of heat transfer rate

An experimental apparatus used to measure the heat transfer rate is shown schematically in Fig. 4. In measuring the heat transfer performance, the heat pipe was placed horizontally. The one end of the heat pipe of 30 mm in length was heated using a wire heater and the other end of the same length was immersed in the water pool at the saturation temperature for cooling by nucleate boiling. A heater was placed in the vessel to keep the cooling water at the saturation temperature. The middle section of 40 mm in length of the heat pipe was the adiabatic section. Type-K thermocouples were spot welded on the heat pipe outer wall. Temperature measurement was conducted at the 6 horizontal

locations of 5, 15 and 25 mm from both ends of the heat pipe. At each location, thermocouples were placed at the top, side and bottom of the tube. Hence, temperature was measured at 18 points. The heater power Q was increased step by step to measure the temperature difference between the heating and cooling sections ΔT . When Q exceeded a certain value, ΔT and consequently R rose rapidly due to dryout of the inner wall of the heating section. The value of Q at the rapid rise of R was regarded as the maximum heat transfer rate or critical power CP . Using the heater power Q , the average vaporization section temperature T_e and the average condensation section temperature T_c , the thermal resistance of the heat pipe R was calculated by

$$R = \frac{\Delta T}{Q} = \frac{T_e - T_c}{Q} \quad (2)$$

The filling rate of the working fluid in the heat pipe was set to within $15 \pm 1\%$. The heat transfer performance was measured for the four heat pipes listed in Table 1. BBW implies the ordinary heat pipe of bare wall (B), bare mesh (B), and water as the working fluid (W). NXW implies the heat pipe of nanoparticle layer coated wall (N), no mesh (X), and water as the working fluid (W).

Table 1. Specifications of the heat pipes.

No.	Name	Filling rate	M (g/m²)
1	BBW	16.03%	0
2	NXW1	14.89%	0.56
3	NXW2	15.34%	1.13
4	NXW3	15.21%	2.00

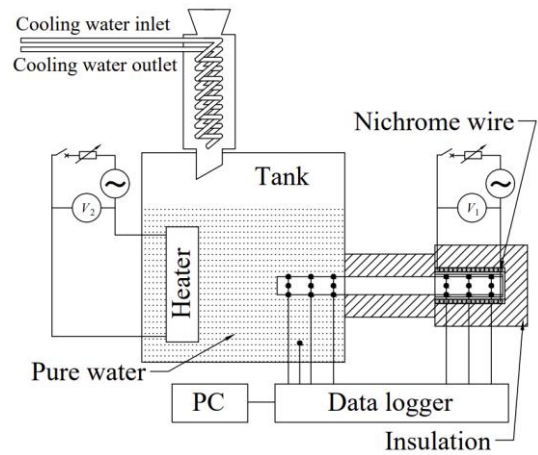


Figure 4. Schematic diagram of the experimental apparatus for measuring the heat transfer performance.

3. Heat Transfer Performance

Experimental results for the nanoparticle-layer coated tube (NXW) are compared with those for the ordinary mesh heat pipe (BBW). The relation between R and Q for the heat pipe is presented in Fig. 5. It can be seen that in the high heat load range of $Q > 20$ W, the R value of BBW distributed within 0.55–0.65 K/W and the R value of NXW is within 0.2–0.35 K/W and much lower than that for the BBW. These results indicate that nanoparticle-layer is effective to reduce R . In the low heat load range of $Q < 20$ W, the value of R varies with the change of Q . This might be attributed to surplus liquid.

As shown in Fig. 6, the experimental data of ΔT within the range of $Q = 0-40$ W were fitted with a straight line to derive the average thermal resistance R_{AVE} .

Figure 7 displays the relation between R_{AVE} and M . It can be seen that although the screen mesh was eliminated, the thermal resistance of NXW1-3 was roughly half of that of BBW. The R_{AVE} did not change significantly with the increase in mass of the deposited nanoparticles.

Figure 8 presents the relation between CP and Wi . It can be seen that the value of CP increases from 40 to 80 W with an increase in Wi . These values are lower than that for BBW of 120 W. The reduction of CP was however only 33% when sufficient amount of nanoparticles was deposited despite the absence of the screen mesh inside of the container.

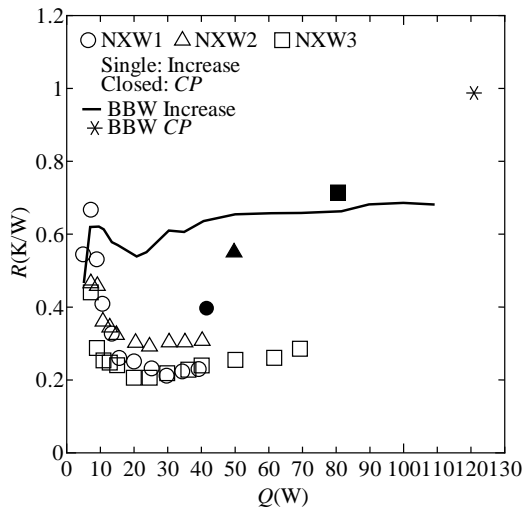


Figure 5. Dependence of R on Q .

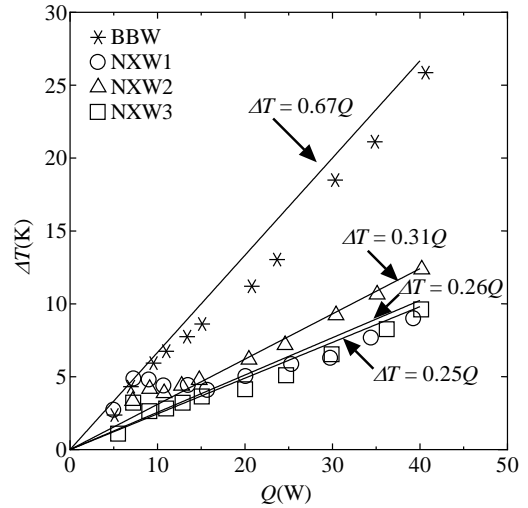


Figure 6. Dependence of ΔT on Q .

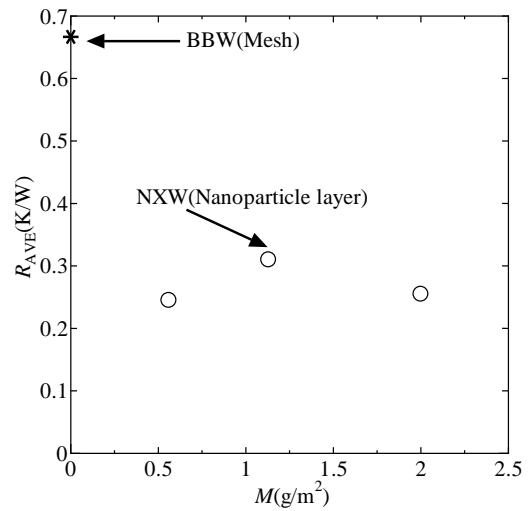


Figure 7. Effect of the M on the R_{AVE} .

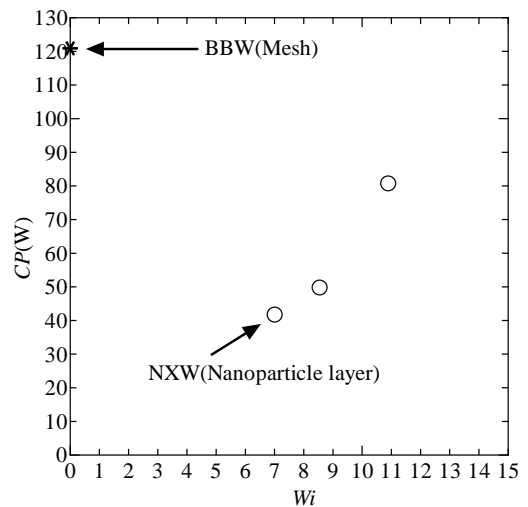


Figure 8. Effect of the wickability Wi on the critical power CP .

4. Conclusion

To save the space within the heat pipe container, the screen mesh used as the wick was eliminated and the tube inner wall was coated with the layer of nanoparticles instead. Although the maximum heat transfer rate was deteriorated to 35-65% but the thermal resistance was improved substantially. In addition, the nanoparticle layer was very thin. It is therefore expected that the proposed technology can be used for cooling of smartphone and space equipment since space-saving is crucial in these applications.

References

- [1] Y. Umehara, T. Okawa, Prediction of extremely high minimum heat flux point during quenching in nanofluid, International Conference on Nuclear Engineering, 2020. ICONE2020-16032.
- [2] M. Wang, T. Okawa, Effect of nanoparticle layer coating on heat transfer performance of heat pipe. Heat Transfer Engineering, 2021. 42(19): p. 1748.
- [3] M. Mahamudur, E. Olceroglu, and M. McCarthy, Role of wickability on the critical heat flux of structured superhydrophilic Surfaces, 2014. 30(37): p. 11225.

Experimental Investigation of Phase and Flow Behavior Trends of Long-Distance Helium Pulsating Heat Pipes

Logan Kossel*, John Pfothenauer, and Franklin Miller

University of Wisconsin – Madison, Madison, US

**Corresponding author email address: lkossel@wisc.edu*

Abstract

Pulsating heat pipes (PHPs) are a promising two-phase heat transfer technology that have shown improvements, such as decreased mass and improved thermal performance, over other thermal links at cryogenics temperatures. This study experimentally investigates the effect of fill ratio and applied heat load on the phase and flow behavior of long-distance helium pulsating heat pipes. An experimental test facility was constructed in which a helium pulsating heat pipe with an adiabatic length of 1.5 m was tested. Using several strategically placed temperature and pressure sensors on two adjacent tubes in the adiabatic section of the PHP, information about the fluid's phase and motion can be inferred. Qualitative arguments are made about the mass distribution, fraction of latent heat transfer, and dominant flow modes using both averaged and time-series data. First, a distinct difference in the thermodynamic behavior between the adjacent tubes was observed, with the fluid in one tube becoming sub-cooled liquid at a specific applied heat load, and the fluid in the adjacent tube becoming superheated vapor at some higher heat load. The data also suggests that the flow is primarily uni-directional at all heat loads tested.

Keywords: Pulsating heat pipe; Cryogenics; Two-phase flow; Helium

1. Introduction

Pulsating heat pipes (PHPs) are an emerging heat pipe variant that have recently gained research interest, especially with cryogenic fluids, due to their ability to transfer heat with very high efficiency. Furthermore, their simple construction makes PHPs inherently lightweight and flexible, giving rise to numerous potential applications. For example, helium pulsating heat pipes, in particular, could aid 4K cryocoolers in cooling superconducting magnets from a sufficient distance such that the magnetic field does not degrade the performance of the cryocooler.

A typical pulsating heat pipe is composed of capillary tubing that traverses a specified length several times and connects at the ends to form a closed loop. Figure 1 shows the general shape of a PHP, although other configurations are possible. Also displayed in Figure 1 are the different sections of a PHP defined by the heat flow direction. The evaporator picks up a heat load, which is transferred through the adiabatic section via the movement of the working fluid to the condenser section, where the heat is expelled to a cooling source. Phase change in the evaporator and condenser sections causes contractions and expansions of the fluid, which subsequently cause the pressure oscillations that drive the fluid from end to end. The complexity of this process, along with the numerous design parameters (number of turns, section lengths, fill ratio), makes predicting the behavior of a PHP difficult.

An essential aspect of a functional pulsating heat pipe is the small inner diameter of the capillary tubes. This diameter should be sized such that the Bond number of the working fluid is less than 2. When this condition is met, the surface tension forces are strong enough to overcome the buoyancy forces, which results in saturated vapor bubbles becoming trapped between distinct sections of saturated liquid.

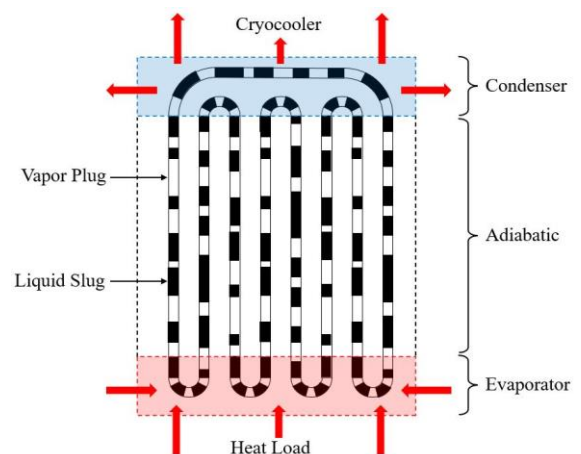


Figure 1. A schematic of a pulsating heat pipe, showing the plug-slug regime as well as the different sections.

This research is motivated by experimental results from Fonseca, Pfothenauer, and Miller [1,2], where helium pulsating heat pipes with significantly different adiabatic lengths (0.3 m and 1 m)

displayed nearly identical thermal resistance over a range of heat loads. In this study, a behavior of helium pulsating heat pipe with an adiabatic length of 1.5 m is experimentally investigated to estimate the phase trends and flow behavior as a function of fill ratio and applied heat load.

2. Experimental Specifications

An experimental facility was constructed to test vertically oriented helium pulsating heat pipes with adiabatic lengths up to 1.75 m. This facility consists of a PHP test rig connected to a large vacuum chamber with a diameter of around 2 m and a depth of around 3 m. Moreover, the test rig is built around a Sumitomo SHI RDK-415D2 cryocooler, with a radiation shield, heat exchanger, and internal valve connected to the first stage, and the PHP thermally anchored to the second stage. The CAD model in Figure 2 shows the internal components of the experiment.

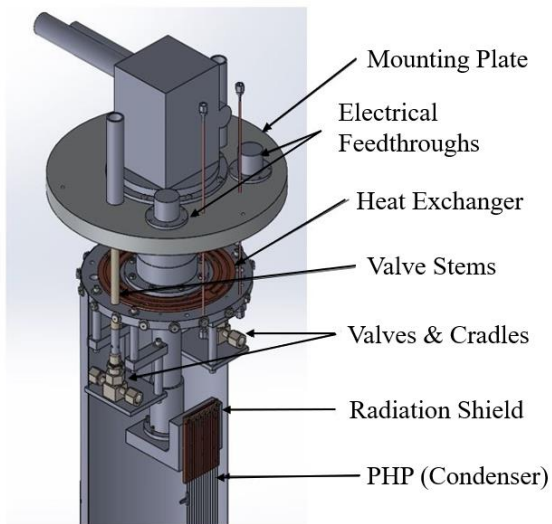


Figure 2. CAD Schematic of the helium PHP test rig, showing the components connected to the cryocooler's first and second stages.

An important operating parameter of a pulsating heat pipe is the fill ratio, defined in Equation (1) as the liquid volume fraction of the working fluid inside the PHP. The fill ratio is varied across these experiments along with the applied heat load.

$$FR = \frac{V_{liquid}}{V_{total}} \quad (1)$$

Temperatures and pressures were measured at several locations in the adiabatic section. The sensors were placed strategically on adiabatic tubes adjacent to one another to extract flow and

phase information during operation. Lakeshore CX-1050-CU-HT thermometers were used to measure temperatures of the following locations: three thermometers each on two adjacent tubes, equally spaced along the span of the adiabatic length. Thermometers were also placed on the evaporator and condenser plates to measure the performance. Furthermore, two Omega PX419-050A5V transducers measured the absolute pressure near the ends of the adiabatic section. Two additional Omega PX2300-1BDI differential transducers were configured to measure the pressure difference across the entire adiabatic length, from the evaporator to the condenser, for a total of four pressure measurements. The schematic in Figure 3 shows all measurement locations on the PHP tested in these experiments.

Since Helium pulsating heat pipes operate at very low temperatures (3 K - 6 K), the temporal resolution of the temperature measurements is excellent owing to the very high thermal diffusivity of metals at these temperatures. Indeed, the thermal diffusion time constant of the sensors is on the order of microseconds. This aspect of the experiment supports the assumption that a given temperature measurement in the adiabatic section is essentially equal to the fluid temperature at the time of measurement.

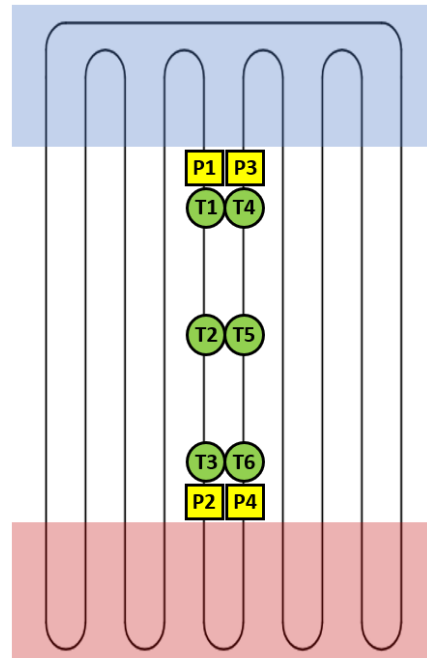


Figure 3. Pressure and temperature measurement locations on the PHP's adiabatic section (PHP is not to scale).

The pulsating heat pipe was tested by incrementally increasing the applied heat load by

20 mW beginning at 30 mW until the PHP's performance, characterized by its effective thermal conductivity, degraded significantly from the peak value. For each heat load tested, data was recorded for 15 minutes over which the temperature and pressure measurements can be averaged. Furthermore, Table 1. outlines the specifications of the PHP tested in these experiments. Most notably, the adiabatic length of the PHP was 1.5 m, which is significantly longer than the Helium PHPs tested in the currently available literature. Previous publications [3,4] present the performance results of this experiment for Helium PHPs with adiabatic lengths of 1.25 m and 1.5 m.

Table 1. PHP Specifications

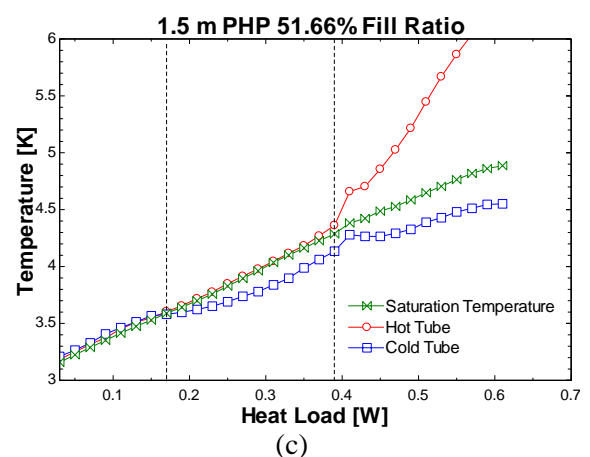
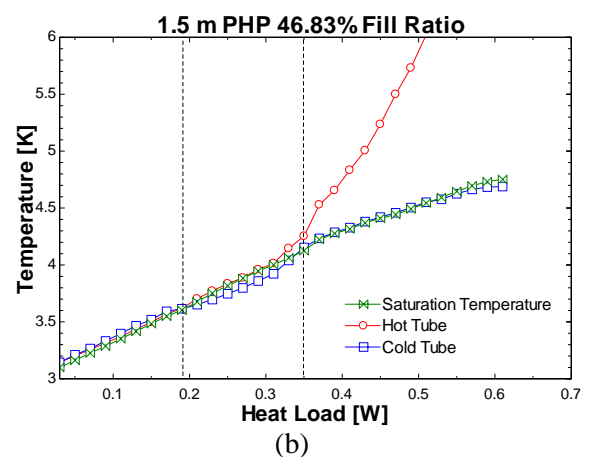
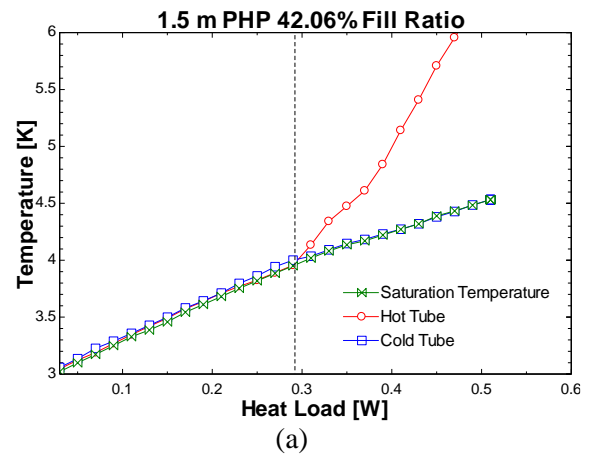
Adiabatic Length	1.5 [m]
Evaporator/Condenser Length	90 [mm]
Fill Ratio	42.06% - 56.42%
Tube Inner Diameter	0.5 [mm]
Number of Turns	7
Orientation	Vertical

3. Phase Trends in the Adiabatic Section

Negating the transient period between heat loads, the average temperatures and pressures measured in the adiabatic section are helpful in analyzing the phases of the fluid contained in each adiabatic tube, with respect to the applied heat load. For multiple fill ratios, the average temperatures are plotted as a function of applied heat load in Figure 4. It was found that for each heat load tested, the time-averaged adiabatic temperature was not strongly dependent on the sensor's location along the tube. Thus, the adiabatic temperature measurements for each tube are also spatially averaged for clarity. Additionally, saturation temperatures can be calculated from the pressure measurements using an equation of state [5]. Since the time-averaged pressures only varied slightly with sensor location (around 1000 Pa), Figure 4 includes the calculated saturation temperature for one of the four pressure measurements.

It is evident from Figure 4 that for all fill ratios, the two adjacent tubes behave differently with increasing heat load. At low heat loads, the tube's temperatures match, but eventually the tubes will diverge in temperature as the applied heat load increases. This divergence occurs at lower heat loads as the fill ratio increases. Moreover, when considering the saturation temperature, it is evident that the fluid in one tube becomes subcooled liquid since the measured temperatures

are less than the saturation temperature. Thus, the tube in which sub-cooling occurs is named the "cold tube," and the tube adjacent the "hot tube." Sub-cooling was not observed in the 42.06% fill ratio case. Additionally, the fluid in the adjacent tube remains two-phase



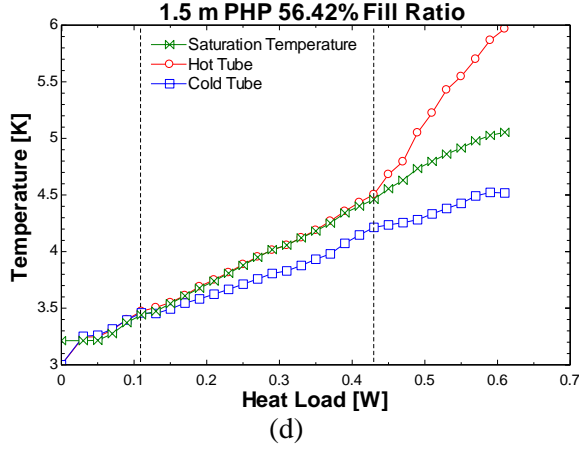


Figure 4. Average temperatures of the hot and cold tubes, and the calculated saturation temperatures as a function of applied heat load for fill ratios (a) 42.06%, (b) 46.83%, (c) 51.66%, and (d) 56.42%.

For heat loads larger than that where sub-cooling is first observed, the PHP continues to operate with good performance on the order of 300 [kW/m-K] for all fill ratios tested. However, as the heat load is increased further, another phase change occurs in the hot tube, where the fluid becomes superheated vapor. This phenomenon results in a significant drop in the PHP's performance. Interestingly, when the hot tube's fluid becomes superheated, the cold tube's fluid remains either liquid or two-phase, depending on the fill ratio. Moreover, the heat load at which superheated vapor is first observed increases with increasing fill ratio. The heat loads at which the phase changes occur are named the "sub-cooling point" and the "superheating," and are listed in Table 2 for the fill ratios tested.

Table 2. Sub-cooling and superheating points.

Fill Ratio	Sub-cooling [mW]	Superheating [mW]
42.06%	N/A	290
46.83%	190	350
51.66%	170	390
56.42%	110	430

Although these measurements indicate that sub-cooled liquid is present in the cold tube during operation, the actual distribution of the fluid's phase in the cold tube is unknown. Saturated vapor could likely coexist between sections of sub-cooled liquid to maintain the plug-slug flow regime. Contrary to metals at cryogenic temperatures, the thermal diffusivity of liquid helium is very low. Equation (2) defines the

diffusion time constant of a thermal wave, where L is the penetration depth of the thermal wave, and α is the thermal diffusivity. For liquid helium at multiple temperatures, the thermal time constant as a function of thermal wave penetration depth is shown in Figure 5.

$$\tau_D = \frac{(2L)^2}{\alpha} \quad (2)$$

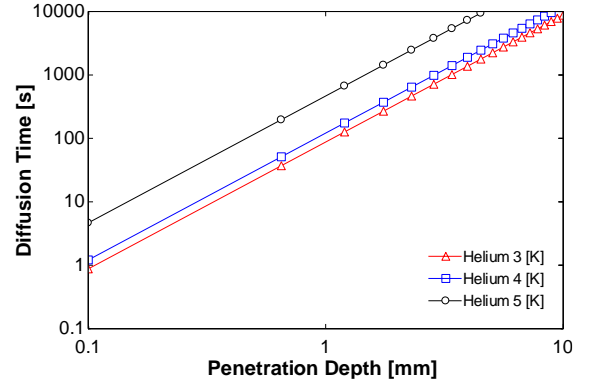


Figure 5. Thermal diffusion time as a function of thermal wave penetration depth of saturated liquid helium at 3 K, 4 K, and 5 K.

Figure 5 shows, for example, that it will take around 50 minutes for a thermal wave to reach the center of a 10 mm liquid slug at 4 K. While the typical length and adiabatic transit time of the liquid slugs are not known, it is unlikely that the sub-cooled liquid slugs in the cold tube would thermally equilibrate with adjacent saturated vapor plugs while traversing the adiabatic section. Thus, sub-cooled liquid slugs and saturated vapor plugs can coexist in the adiabatic section. Furthermore, the ability of a helium pulsating heat pipe to transport the sensible heat stored in liquid slugs via phase change processes in the evaporator and condenser is a potential explanation for their excellent thermal performance, at least at heat loads beyond the sub-cooling point.

4. Flow Behavior Analysis

The fluid motion inside pulsating heat pipes is notoriously complex but can be summarized as the chaotic motion of many distinct vapor and liquid parcels that result in a net uni-directional mass transfer. Despite the complex nature of the flow and the lack of visualization techniques for Helium PHPs, some flow features can be inferred from the adiabatic temperature measurements. From the averaged data presented in Figure 4, it can be reasonably concluded that once the sub-cooling heat load is reached, uni-directional flow modes dominate the oscillatory modes. Once sub-

cooling is observed, the fluid in the cold tube must move from the condenser to the evaporator. By conservation of mass, the fluid in the hot tube must move in the opposite direction, forming a primarily uni-directional flow. This conclusion also follows for heat loads beyond the superheating point. However, the averaged data is not useful for analyzing flow behavior prior to the sub-cooling point.

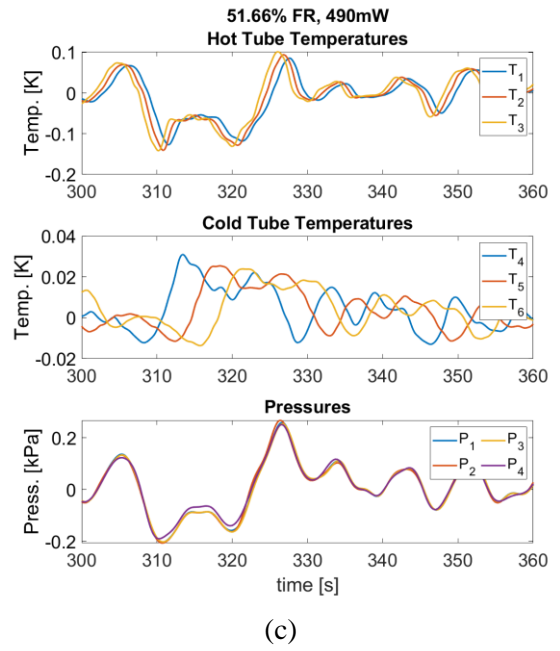
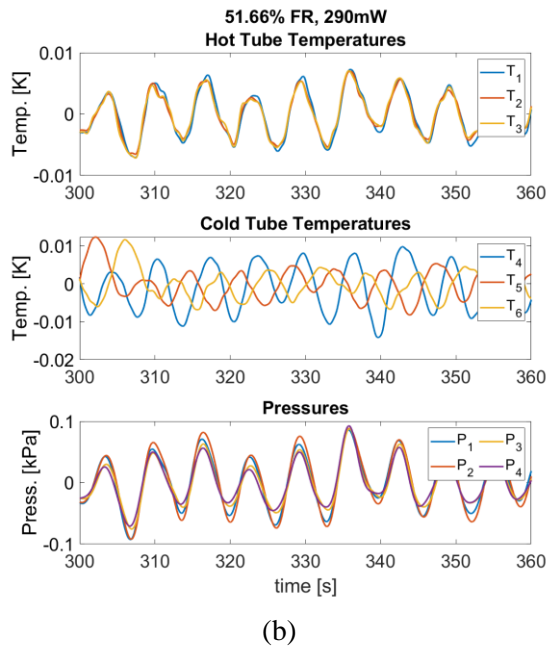
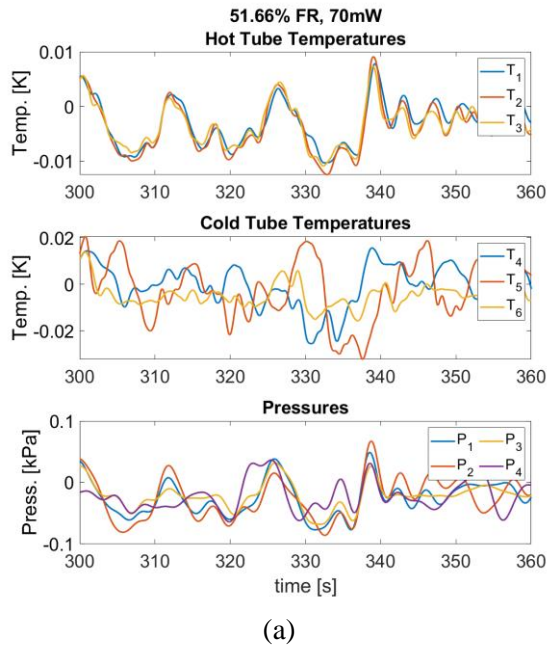


Figure 6. Adiabatic temperature and pressure oscillations of the adjacent adiabatic tubes for heat loads (a) 70 mW, (b) 290 mW, and (c) 490 mW.

Timeseries data from the 51.66% fill ratio test is shown in Figure 6 for heat loads in each distinct region defined by the sub-cooling and superheating points. Here, the temperature measurements are not spatially nor temporally averaged; instead, the oscillations of each temperature with time are shown. While only 60 s of data are shown for clarity, the features of these data are consistent throughout the entirety of the test. Furthermore, the time-averaged value of each temperature measurement is subtracted for clarity of the oscillation amplitudes. As stated in the previous section, the average values of each thermometer are very close to one another for a given tube.

Figure 6 (a) shows data from the 51.66% fill ratio test with an applied heat load of 70 mW, a heat load that is lower than the sub-cooling point for this fill ratio. Unlike the time-averaged data of Figure 4 (c), a significant difference in the behavior of the adjacent tubes is observed at heat loads less than the sub-cooling point. In the hot tube, the temperatures at all locations along the adiabatic length oscillate with nearly the same pattern. This oscillation pattern also matches the pressure oscillations in the hot tube. Conversely, the cold tube temperatures oscillate chaotically with no apparent connection between the measurement locations. These observations likely

indicate an imbalance in the mass distribution of the adjacent tubes.

In the hot tube, it is believed that the fluid is primarily saturated vapor because the temperature oscillations nearly match the pressure oscillations. This behavior is expected since the fluid is two-phase and pressure waves propagate at the speed of sound. Although, the small number of oscillation modes indicates that there are not many vapor-liquid interfaces. Instead, it is possible that very long vapor plugs exist, surrounded by a thin film of liquid at the tube walls. Furthermore, since the inner radius of the tube is only 0.25 mm, thermal equilibration in the radial direction can occur within a reasonable timescale. Table 3 shows the radial thermal time constant for saturated vapor and liquid at several temperatures. Another potential explanation is that the helium vapor in the hot tube can thermally equilibrate radially fast enough so that phase shifting in the temperature signals is not observed.

Table 3. Radial thermal diffusion time constants for saturated helium liquid and vapor

	3 [K]	3.5 [K]	4 [K]	4.5 [K]
Vapor	1.18 [s]	2.01 [s]	3.53 [s]	7.35 [s]
Liquid	5.48 [s]	6.19 [s]	7.58 [s]	10.77 [s]

However, for the cold tube, the chaotic nature of the temperature measurements is evidence of multiple alternating saturated liquid and vapor sections, which behaves much like a multiple mass-spring-damper system. Indeed, several PHP modeling efforts have successfully invoked the mass-spring-damper analogy [2,6]. The data suggest that even at low heat loads, the cold tube contains more liquid and, therefore, more mass than the hot tube. While oscillatory flow modes are clearly present, the mass imbalance and unique thermal behavior of each adiabatic tube suggest that the flow is primarily uni-directional, with superimposed oscillations, at heat loads less than the sub-cooling point.

The time-series trends of the adiabatic temperature measurements change when the applied heat load exceeds the sub-cooling point. Figure 6 (b) shows the time evolution of the temperature measurements of the 51.66% fill ratio test at 290 mW, a heat load that is higher than the sub-cooling point for this fill ratio. Vapor-like behavior is still observed in the hot tube with the 290 mW heat load, although with less frequent deviations than with the 70 mW heat load. The chaotic behavior of the cold tube's temperature measurements ceases at 290 mW. Instead, the

oscillations are nearly sinusoidal with apparent phase shifting and amplitude damping between measurement locations. The amplitude of oscillation is largest for the temperature measured closest to the condenser (T4) and decreases for temperatures measured closer to the evaporator (T5 and T6). This data resembles a second-order frequency response of a low degree of freedom dynamic system. Indeed, fewer oscillation modes exist for heat loads higher than the sub-cooling point, suggesting that the number of distinct liquid slugs has decreased. Furthermore, the deviations of the matching hot tube temperature oscillations at 70 mW may indicate that there is a small amount of saturated liquid present that disrupts the vapor-like behavior, and as the heat load increases past the sub-cooling point, the fraction of liquid in the hot tube decreases, resulting in more uniformity in the temperature oscillations.

After the superheating point is reached, the time-series trends of the adiabatic temperatures change yet again. Figure 6 (c) shows the time-series data for the 51.66% fill ratio test with a 490 mW applied heat load. At this heat load, the hot tube begins to display oscillation phase shifting with respect to measurement location, as well as a larger oscillation magnitude. Thus, for both tubes, the phase shift in the temperature oscillations is only observed when the fluid is single phase, which may suggest that when the cold tube becomes sub-cooled, the plug-slug regime is not present, and instead, the tube is filled with liquid. At 490 mW, the oscillations in the cold tube continue to show phase shifting and amplitude damping, although they are no longer sinusoidal.

Additionally, the direction of the phase shift with respect to the measurement location is more visible at high heat loads. A peak in the cold tube will be observed in T4 first, followed by T5 and T6. In other words, the thermal wave observed in the cold tube travels from the condenser to the evaporator. The order in the hot tube (T3, T2, T1) is opposite to the cold tube, so the wave moves from the evaporator to the condenser. This phenomenon can be observed in the cold tube at heat loads less than the superheating point, but it is not as clear due to sinusoidal oscillations. Although the fluid flow is not directly measured, the directionality of the thermal wave propagation is further evidence that the flow is primarily uni-directional. For all tests, the adjacent tubes were consistent in their behavior, indicating that the flow does not reverse direction.

5. Conclusions

A helium pulsating heat pipe with an adiabatic length of 1.5 m was tested with varying applied heat load and fill ratio resulting in novel insights into their phase and flow behavior. Time-averaged temperature and pressure data show that the phase change occurring in adjacent tubes is different – with one tube eventually becoming sub-cooled liquid and the adjacent tube becoming superheated vapor, with increasing heat load. These phase change phenomena depend on the fill ratio and imply a mass imbalance between alternating tubes.

Timeseries data of multiple heat loads for the 51.66% fill ratio case show how temperature oscillation patterns strongly depend on the applied heat load, with respect to the regimes defined by phase change. A mass imbalance of the adjacent tubes was found to persist at all heat loads, suggesting that the flow is primarily uni-directional with secondary oscillatory modes. Moreover, the relative number of distinct liquid slugs in the flow coming out of the condenser seems to decrease with increasing heat load as evidenced by the decreasing number of temperature oscillation modes as the applied heat load increases. When the fluid is single phase for either tube, a thermal wave will propagate through the adiabatic section, in the direction of the mass flow.

The insights presented could help simplify existing pulsating heat pipe models. Ultimately, further quantitative analysis is needed to validate these findings. Since it is predicted that uni-directional flow is persistent throughout the entire range of heat loads, a study of the effect of gravity on long-distance helium PHPs would help determine the extent to which gravity assists the flow while in the vertical orientation. Future tests with this experimental facility will consist of a vertically-oriented PHP with an adiabatic length of 1.75 m, along with tests of horizontally oriented PHPs.

Acknowledgment

This work was supported by a NASA Space Technology Graduate Research Opportunities Award.

References

- [1] L. D. Fonseca, J. M. Pfothauer, and F. K. Miller, Short communication: thermal performance of a cryogenic helium pulsating heat pipe with three evaporator sections. *International Journal of Heat and Mass Transfer*, 2018. 123: p. 655.
- [2] L. D. Fonseca, Experimental characterization of helium pulsating heat pipes. Ph.D. Dissertation. University of Wisconsin – Madison, 2016.
- [3] L. Kossel, J. M. Pfothauer, and F. K. Miller, Performance comparison of long-distance helium pulsating heat pipes with varying adiabatic lengths. in *Cryocoolers 22: Proceedings of the 22nd International Cryocooler Conference*. 2022. Bethlehem, United States.
- [4] L. Kossel, J. M. Pfothauer, and F. K. Miller, The effect of fill ratio on the performance and flow regime for long-distance helium pulsating heat pipes. in *Proceedings of the 28th International Cryogenic Engineering Conference and International Materials Conference*. 2022. Hangzhou, China, (Virtual Conference).
- [5] D. Ortiz-Vega, A new wide range equation of state for helium-4. Ph.D. Dissertation. Texas A&M University, 2013.
- [6] G. Gursel, A. Frijns, E. Homburg, and A. van Steenhoven, A mass-spring-damper model of a pulsating heat pipe with asymmetric filling. in *5th International Conference on Heat Transfer and Fluid Flow in Microscale*. 2014. Marseille, France.

Pore network simulation of loop heat pipe evaporator with different pore size distribution

Masahito Nishikawara*

Department of Mechanical Engineering, Toyohashi University of Technology, Toyohashi, Japan

**Email address: nishikawara@me.tut.ac.jp*

Abstract

To investigate the relationship between the evaporator heat-transfer coefficient of a loop heat pipe (LHP) and pore size distribution of the wick, this work simulated the two-phase thermal hydraulics in the evaporator by pore network model. The simulation considered liquid-vapor (L-V) two-phase state in the wick, which is induced by nucleate boiling, and local fluid dynamics in pore-scale. Some wick samples were created with different pore size distributions but the same macroscopic porous characteristics such as permeability. Heat transfer and fluid flow of the evaporator were solved. Each wick showed different heat-transfer coefficients and the maximum applied heat flux. Some characteristics with respect to L-V phase distribution in the wick were selected to see the correlation with the heat-transfer coefficients. As a result, it was found that length of three-phase contact line (TPCL) is proportional to the heat-transfer coefficients. The TPCL length had a maximum at moderate dispersion of pore size in some cases. This discovery helps porous structure design of evaporator manufacturing by 3D printing to enhance the thermal performance.

Keywords: Additive manufacturing; Capillary evaporator; Pore network model; Porous media; Three-phase contact line; Two-phase flow

1. Introduction

A thermal control device known as a loop heat pipe (LHP, Figure 1) has recently attracted attention in various fields. The LHP comprises a capillary evaporator, condenser, transport line, and compensation chamber (CC). The condenser and transport line are simple pipes. Unlike conventional heat pipes, the porous medium (wick) is solely located in the evaporator; this facilitates longer transport lengths and larger radiation areas. The capillary pressure develops, and liquid evaporates in the wick. The evaporator configuration is the critical part of the performance design. However, an optimal method for designing this component is yet to be established, because the two-phase thermal hydraulics in the capillary evaporator is complicated.

The evaporator design includes wick and groove shape and porous characteristics. This paper focuses on the latter. Enhancement by microscopic approaches such as biporous void structure [1], a bilayer wick using carbon nanotubes [2], a composite wick [3], a compressed carbon foam wick [4], the unique shape of particles forming the wick [5], and a porous structure with short nano fibers [6] has been reported, however they seem to be heuristic. Rapidly developing 3D printing technology can make the desired microscopic porous structure [7], so it is more valuable to pursue what is the optimized void structure on heat transfer of the capillary evaporator.

The phase state in the wick during an LHP operation is divided into two: liquid saturated and liquid-vapor (L-V) two-phase. The liquid

saturated state appears at a relatively low heat flux applied to the evaporator. Evaporation occurs on the L-V interface between the saturated wick and groove. In addition, because the meniscus is along the three-phase contact line (TPCL) within the casing, wick, and grooves, the applied heat is also transported directly by evaporation through it [8–10]. When high heat flux is applied, vapor phase generates inside the wick due to nucleate boiling at the contact surface between the casing and wick. On the two-phase state, the L-V interface is inside the wick as well as the wick-groove interface. The heat-transfer coefficient and pressure loss through the wick are affected by the L-V interface shape which balances in the flow of the micro-void structure, so microscopic characteristics of the structure can affect thermal performance at a high heat flux.

Therefore, this paper numerically investigates effect of typical pore size distribution of the wick on

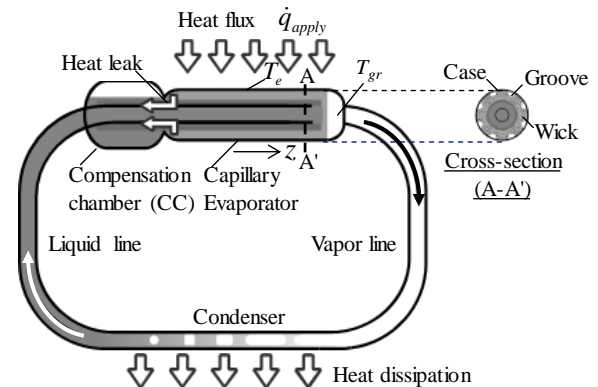


Figure 1. Schematic of a loop heat pipe.

the thermal performance of LHPs. To consider disorder of pore size, pore-network model is employed in the two-phase thermo-fluid simulation of the evaporator. Some wicks with different pore size distributions are created artificially, then are simulated, are discussed on the relationship with the thermal performance.

2. Numerical model

The computational domain corresponding to a portion of the periodic structure of a capillary evaporator is shown in Figure 2. The domain is a cuboid with the size of $4.0 \times 3.5 \times 1.5$ mm ($L_x \times L_y \times L_z$) and consists of a stainless-steel (SS) casing, a wick, and grooves. The groove height is 1.0 mm, the casing thickness is 1.0 mm, and the contact surface between the casing and wick is 50% of the $L_x \times L_z$ area. Actually, the domain can be reproduced in two dimension, however L-V interface shape has distribution in z direction due to disorder of the porous structure, which is considered by only 3D simulation.

2.1. Governing equations

In the simulation, the flow in the capillary structure was represented by a pore network model (PNM) explained later while the energy conservation of the casing and wick were solved,

$$c_p \dot{m} \cdot \nabla T = k_{eff} \nabla^2 T \quad \text{and} \quad (1)$$

$$k_{case} \nabla^2 T = 0 \quad (2)$$

Depending on the heat flux applied to the evaporator, the wick phase state is divided into saturated with a liquid for the low heat flux and L-V two-phase for the high heat flux. In the simulation, the transition condition to the two-phase state is decided based on boiling critical superheat,

$$T - T_{sat}(P) > \Delta T_{nuc} = \frac{2\sigma T_{sat}}{\rho_v r h_{fg}} \quad (3)$$

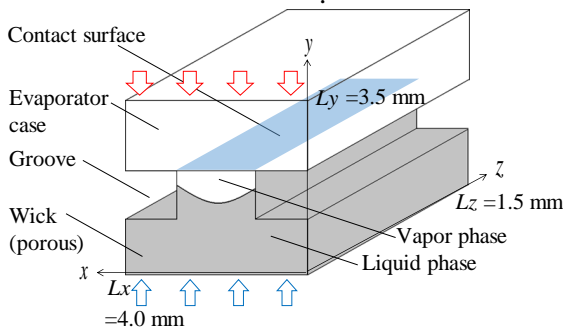


Figure 2. Computational domain.

ΔT_{nuc} is the threshold of nucleation based on boiling critical superheat [11]. In this model, r was set as the peak radius in the pore size distribution of the wick.

The L-V interface in the wick is calculated so that the pressure difference between the vapor and liquid on the interface balances the local capillary pressure. Figure 3 shows a schematic illustration of the PNM for the fluid simulation. The PNM divides the voids of the porous structure into spherical pores and cylindrical throats. Unlike the continuum approach used for solving flows in porous media, the PNM allows a distribution of the pore radius and corresponding local variables. Since local voids are represented as simple shapes associated with throats and pores in the pore network, the present model allows analysis of a greater quantity of pores [12, 13]. The local capillary pressure, P_{cap} is expressed by

$$P_{cap} = \frac{2\sigma \cos\theta}{r_{th}} \quad (4)$$

The mass flow rate in the throat between neighboring pores is proportional to the pressure difference of the pores. Considering mass conservation at a pore i , the following equation with respect to pressure is applied,

$$\sum_{n=1}^6 \frac{g_{i,n}}{V} (P_i - P_n) = 0 \quad (5)$$

$g_{i,n}$ is proportional to the quadruplicate throat radius, and inversely proportional to the throat length. It should be noted that n was six for the three-dimensional lattice, which corresponds to the coordinate number. The pressure was obtained from the solution of Eq. (5). Then, the mass flow rate in the throats was calculated.

2.2. Boundary conditions

A constant saturation temperature and pressure were imposed to the groove and CC. Zero pressure loss through the transport line was given. Constant heat flux was applied to the top of the casing. Insulated walls were imposed on the x - y planes at $L_z = 0$ and 1.5 mm. The simulation used the following values for the heat-transfer coefficient

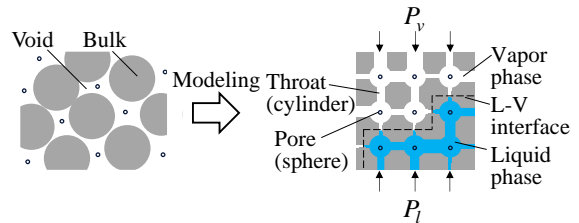


Figure 3. Overview of pore network model.

i.e., 100 W/m²K for the heat-transfer coefficient between the wick and CC, and 1.0×10^5 W/m²K for the contact heat-transfer coefficient between the casing and wick.

2.3. Calculation conditions

Applied heat fluxes were increased up to the operation limitation such as vapor penetration to the CC or upper-temperature limit. Ammonia and R134a as working fluids and stainless-steel and polytetrafluoroethylene (PTFE) porous materials as wicks were chosen. All physical properties of the fluids were obtained from REFPROP [14]. Temperature dependence of surface tension was considered. A contact angle assumed 0°. The mesh size was 0.1 mm.

3. Porous samples

Samples with different pore radius distributions have to be generated while the macroscopic characteristics of permeability, K and mean pore size are kept constant to investigate only the effect of pore radius distribution. To meet the above condition, K was adjusted to fit the same value in all samples. In this work, the peak value was used as representative of r_{th} distribution. r_{th} is allocated on the lattice grid and generated to fit the distribution with the gamma distribution whose probability density function, $f(x)$ is expressed with

$$f(x) = \frac{1}{\Gamma(k)\theta^k} x^{k-1} \exp\left(-\frac{x}{\theta}\right) \quad (6)$$

$\Gamma(k)$ stands for gamma function. Distribution profile is determined by k and θ . θ was set to fit the peak r_{th} with 1.2 μm , which is the real value in [15]. Profile dispersion was adjusted by changing k . Σ^* defined with following equation[16] was introduced to express the dispersion quantitatively,

$$\Sigma^* \equiv (r_{\max} - r_{\min})/\Delta \quad (7)$$

r_{\max} , r_{\min} and Δ stand for the maximum and minimum pore size, and throat length, respectively.

K can be obtained by solving Eq. (5) after sample generation. Porous media disk with cross-section A and thickness t was set in the computer, then Eq. (5) was solved with given ΔP as a boundary condition, finally the flow rate though the porous media was calculated. The computational permeability K_{comp} was calculated with Darcy's law,

$$K_{comp} = \mu \cdot \frac{A}{t} \cdot \frac{\Delta P}{\dot{Q}} \quad (8)$$

K_{comp} was adjusted by multiplying all $g_{i,n}$ by a constant to fit the same value of 2.00×10^{-14} m². Six samples were generated with different Σ^* as shown in Figure 4 and Table 1. Sample no. 5 was fitted to the real porous media in [15]. The above process of porous sample generation was used in the evaporator simulation.

4. Results and discussion

4.1. Validation of the model

The developed model has been validated with two LHP results. One of the comparisons is shown in Figure 5. The evaporator has a PTFE porous wick and ethanol is used as the working fluid. The transport length is 1 m and the cylindrical evaporator is 12 mm diameter. The detailed description is found in [15, 17]. The comparison of measured heat-transfer coefficient, $h_{evap} = q_{apply}/\Delta T_{e-v}$ with simulated one shows rough agreement. The simulation presents two-phase transition at 1.2 W/cm². The experimental results showed hysteresis, which may be caused by difference of the L-V interface positions in the wick due to ink-bottle effect, but the computation doesn't reproduce the characteristics.

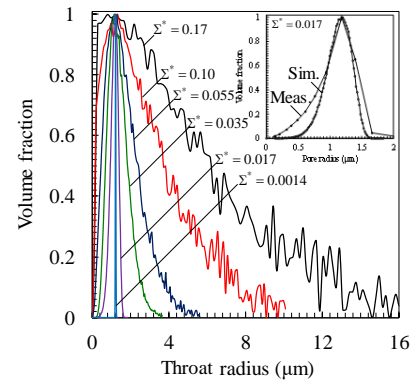


Figure 4. Pore radius distributions of samples.

Table 1. Pore radius characteristics of samples.

Sample No.	Σ^*	r_{\min} (μm)	r_{\max} (μm)
1	0.17	0.014	17
2	0.10	0.024	10
3	0.055	0.063	5.6
4	0.035	0.14	3.6
5 (fitted to real wick)	0.017	0.13	1.8
6	0.0014	1.1	1.3

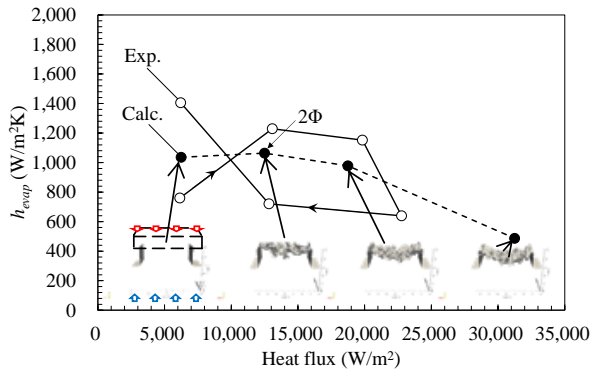


Figure 5. Comparison of an LHP test and PN simulation (PTFE wick – Ethanol¹⁹).

Another validation shown in Table 2 is comparison with the visualization LHP results. The cylindrical evaporator has a quartz porous wick and a quartz transparent casing to observe the L–V phase distribution at the contact surface between the casing and wick. The evaporator diameter is 15 mm and the vapor line length is 0.44 m. Acetone is used as the working fluid. The applied heat flux is at 5.9 W/cm². The detailed description is found in [18]. The evaporator temperature, saturation and phase distribution at the contact surface are compared. The simulated evaporator temperature agrees well with the measured one. Both phase distributions are two–phase state, but the distribution doesn't agree completely. However, liquid phase remains along the TPCL within the casing, wick and grooves in both of experiment and simulation. The simulation showed that the residual liquid is low temperature, therefore, the cooled liquid sites on the contact surface promotes heat–transfer in the evaporator. The simulation could reproduce such a specific characteristic which makes large impact on the heat transfer.

4.2.Characteristic parameters of two–phase state

To find relationship between the heat–transfer coefficient of the evaporator and L–V phase distribution, five characteristic parameters with respect to phase distribution were considered as shown in Figure 6: area of the L–V evaporative interface A_{int} , maximum depth of vapor pocket D_{vp} , length of the TPCL at the contact surface between the casing and wick L_{tri} , Saturation of the wick S , which is liquid content ratio of the wick, and saturation on the contact surface S_{cont} . The correlation coefficients between each parameter and h_{evap} at all applied heat fluxes were calculated and

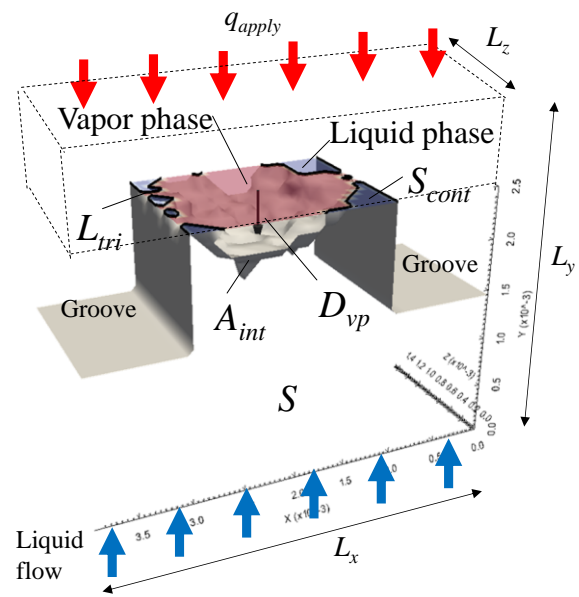
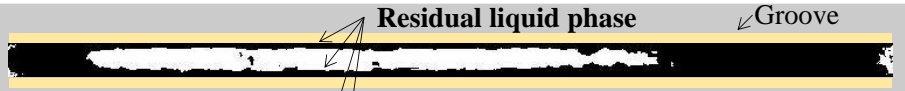



Figure 6. L–V phase distribution example with characteristic parameters with respect to two–phase state in the wick. A_{int} is area of the L–V interface, D_{vp} is depth of vapor pocket, L_{tri} is length of the TPCL at the contact surface, S is saturation of the wick, and S_{cont} is saturation on the contact surface.

Table 2. Comparison of visualization and PN simulation with quartz porous wick and acetone [18]). Black shows liquid phase and white is vapor phase. The applied heat flux is at 5.9 W/cm². Liquid phase remains at the TPCL within the casing, wick and grooves.

	T_e (°C)	S_{cont}	Phase distribution at the contact surface between the casing and wick
Exp.	114	0.63	
Sim.	115	0.58	

listed in Table 3. It is discovered that L_{tri} is positively correlated with h_{evap} for all conditions. Especially, PTFE wicks show strong positive correlation. S is also related for some conditions. For a low thermal conductivity wick, applied heat is difficult to conduct in the depth direction, so L_{tri} that allows evaporation at the contact surface is important. For high thermal conductivity, heat easily conducts in the depth direction, so S is important as well as L_{tri} . The other parameters are not significantly related. It should be noted that D_{vp} is not related even with a PTFE wick of a low thermal conductive material.

Figure 7 shows h_{evap} as a function of L_{tri} at all applied heat fluxes. h_{evap} linearly increases with L_{tri} . As shown in correlation coefficients of Table 3, h_{evap} of the PTFE wick are closer to the linear approximation than that of the SS wick. Comparing slopes of the linear approximations, the slope of the PTFE wick is higher than that of the SS wick. h_{evap} of the PTFE wick are more sensitive to L_{tri} . Enhancement of L_{tri} is effective to enhance h_{evap} , especially for low thermal conductive wicks.

Figure 8 shows h_{evap} as a function of S on the SS–R134a combination which shows a high correlation coefficient in Table 3. The linear approximation shows a high slope. It is important for the wick to be wet sufficiently to keep high h_{evap} on the case of the SS–R134a evaporator.

4.3. Effect of pore size distribution

Figure 9 shows h_{evap} as a function of applied heat flux on each Σ^* . For both wicks, the maximum applied heat flux is increased as Σ^* increases. The PTFE wick reaches the temperature limit at lower applied heat flux than the SS wick. h_{evap} of the SS wick is higher than that of the PTFE wick.

In the simulation, permeability of all simulated wicks was set as a constant. However, it is difficult in reality that only pore distribution changes and permeability keep a constant. Therefore, the simulation shows effect of pore size distribution

Table 3. Correlation coefficients between h_{evap} and each characteristic parameter with respect to L–V phase distribution. L_{tri} shows positive correlation.

	A_{int}	D_{vp}	L_{tri}	S	S_{cont}
SS–R134a	-0.12	-0.59	0.71	0.84	0.37
PTFE– R134a	-0.30	-0.37	0.90	0.69	0.59
SS–Ammonia	0.33	-0.08	0.70	0.49	0.17
PTFE–Ammonia	0.18	0.16	0.91	-0.02	0.01

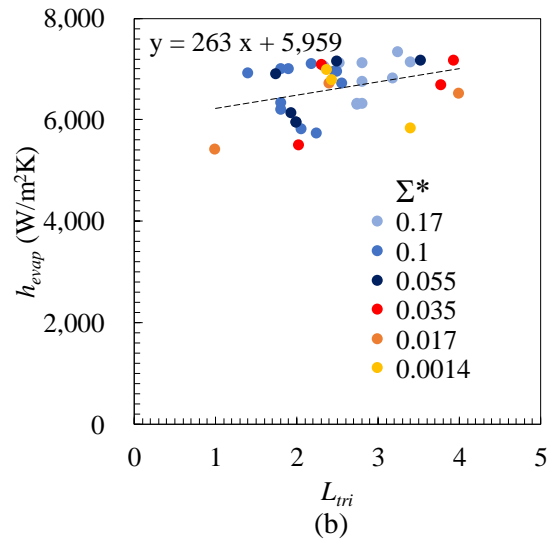
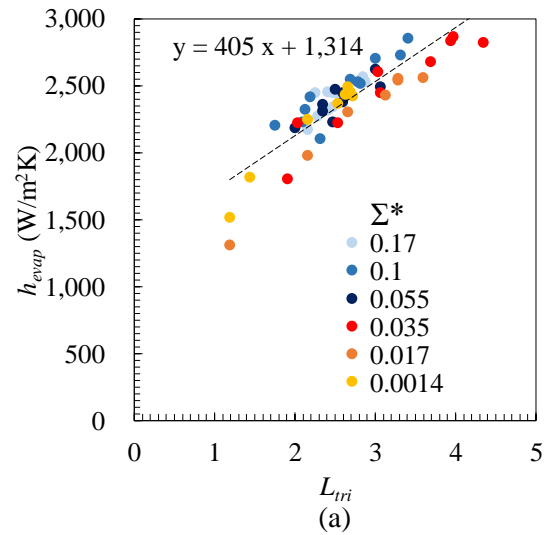


Figure 7. Relationship between the evaporator heat–transfer coefficient, h_{evap} and nondimensional TPCL length, L_{tri} in the (a) PTFE–Ammonia and (b) SS–Ammonia evaporators. L_{tri} is normalized with the TPCL length at the liquid saturated state. Plots at $L_{tri} = 1.0$ or less are excluded.

but doesn't accurately predict the maximum heat flux which is affected by permeability except the case of $\Sigma^* = 0.017$, which was fitted with the measured permeability.

L–V interface shapes in the PTFE–Ammonia evaporator at $q_{apply} = 6.1 \text{ W/cm}^2$ are shown in Figure 10. For $\Sigma^* = 0.0014$, the interface shape is almost symmetric in x direction, which is similar to uniform model. As Σ^* increases, the interface shape become asymmetric and complex. h_{evap} is the highest at $\Sigma^* = 0.035$ in Figure 10. As Σ^* increases more, the shape is still asymmetric but the vapor region is decreased.

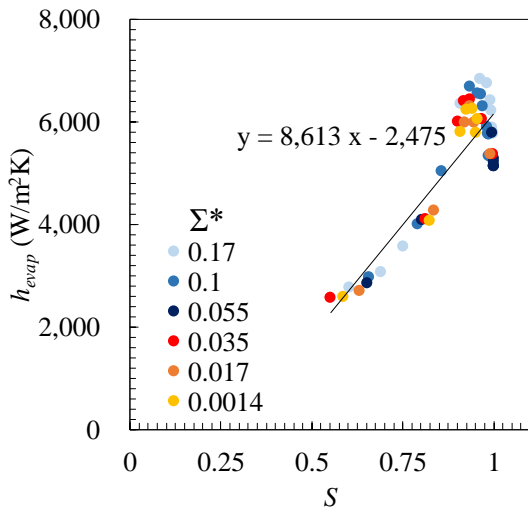


Figure 8. Relationship between the evaporator heat-transfer coefficient, h_{evap} and saturation, S on the SS-R134a evaporators. Plots of the liquid saturated state ($S = 1$) are excluded.

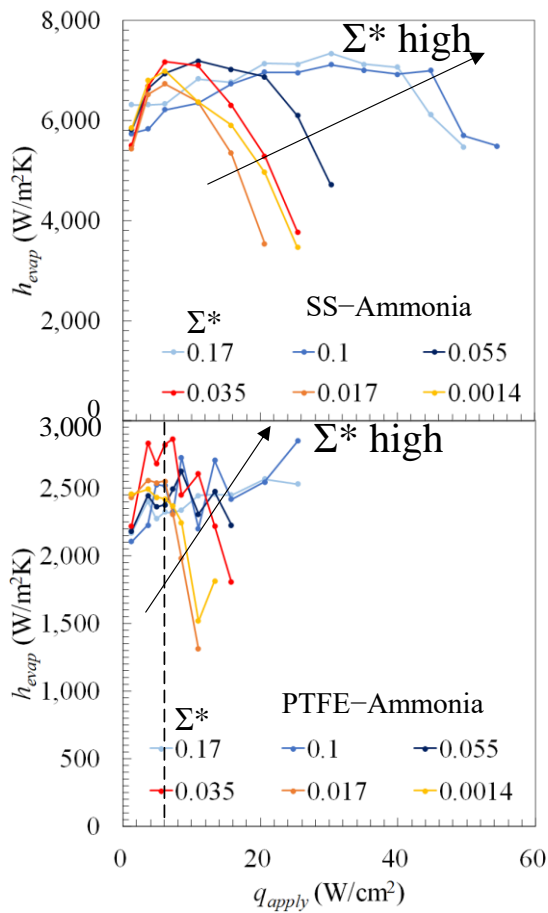


Figure 9. h_{evap} as a function of heat flux on each radius distribution.

Figure 11 shows L_{tri} as a function of heat flux with the PTFE-ammonia evaporator. As discussed in Table 3, L_{tri} is strongly correlated with

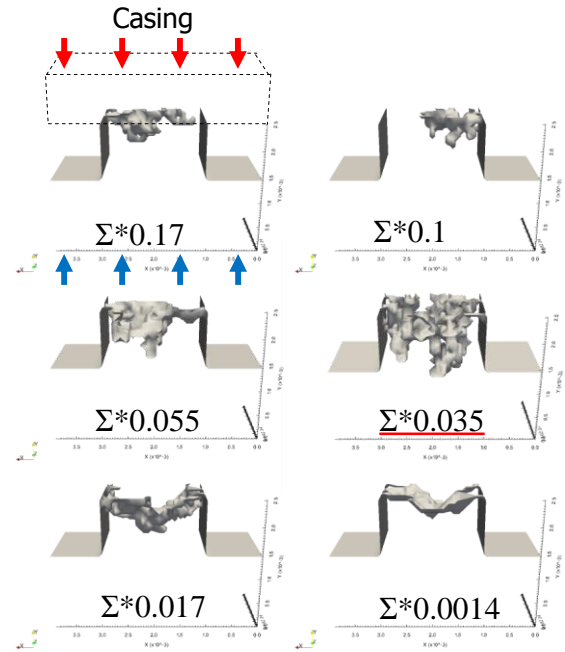


Figure 10. L-V interface shapes in the PTFE-Ammonia evaporator at $q_{apply} = 6.1 \text{ W/cm}^2$.

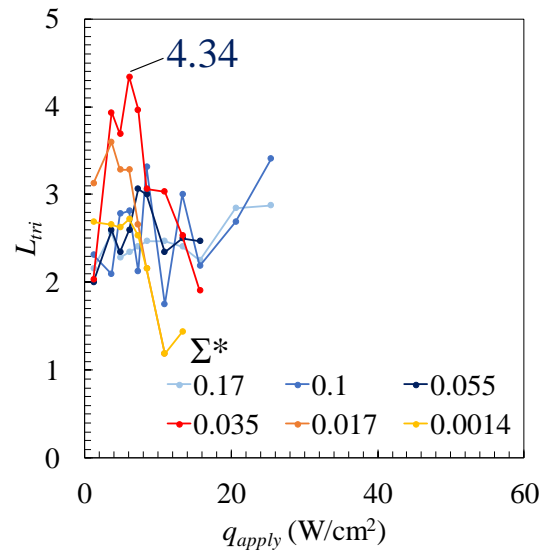


Figure 11. L_{tri} as a function of heat flux on each radius distribution with the PTFE-ammonia evaporator. L_{tri} is normalized by the length of saturated wick.

h_{evap} in this case, so the tendency of L_{tri} to q_{apply} are similar to h_{evap} to q_{apply} in Figure 9. L_{tri} is affected by Σ^* . The longest L_{tri} is 4.34 at $\Sigma^*=0.035$ and $q_{apply}=6.1 \text{ W/cm}^2$. L_{tri} is the longest and h_{evap} is the highest with middle Σ^* in simulation conditions. Therefore, h_{evap} can be optimized with pore size distribution. Note that this finding means that pore size distribution directly affects h_{evap} rather than

indirect influence by permeability changed by pore size distribution.

Figure 12 shows the L–V phase distribution in the PTFE–ammonia evaporator which showed the longest L_{tri} and the highest h_{evap} . It is seen that the phase distribution at the contact surface is complicated, then length of the TPCL is increased.

In the simulation here, typical shape of pore size distribution has been investigated. However, the TPCL length may drastically become longer with complicated micro porous structure controlled by additive manufacturing.

5. Conclusions

To find the design methods of microscopic characteristics of the porous media, two–phase thermal hydraulics in the LHP evaporator were investigated. 3D pore–network simulation demonstrated that the TPCL length at the contact surface between the casing and wick has positive correlation with the evaporator heat–transfer coefficient. The TPCL length and the evaporator heat–transfer coefficient showed the maximum at moderate dispersion of pore size distribution in some cases. It is expected that the TPCL length is optimized by adjusting pore size distribution, then the evaporator heat–transfer coefficient is enhanced.

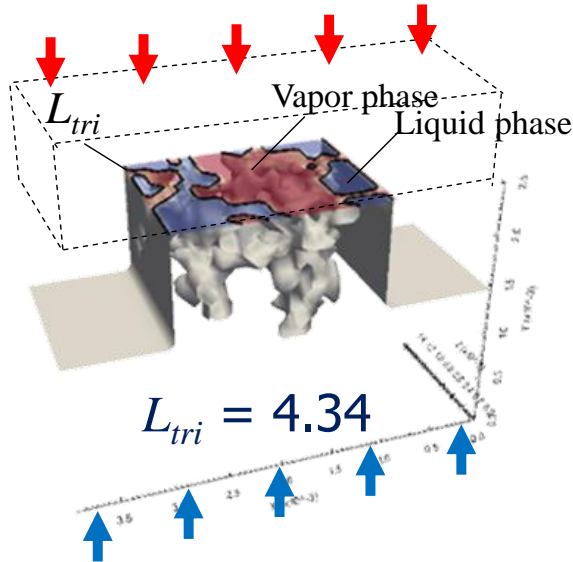


Figure 12. L–V interface shape and phase the distribution at the contact surface between the casing and the wick in the PTFE–ammonia evaporator at $L_{tri} = 4.34$.

Nomenclature

A	area (m ²)
A_{sat}	liquid saturated area (m ²)
c_p	specific heat at constant pressure (J/kg K)
ΔP	pressure difference (Pa)
Δ	mesh size (m)
$g_{i,n}$	flow conductance (m ³)
h_{evap}	evaporator heat–transfer coefficient (W/m ² ·K)
h_{fg}	latent heat (J/kg)
K	permeability (m ²)
k_{case}	thermal conductivity of the casing (W/m·K)
k_{eff}	effective thermal conductivity of the porous media (W/m·K)
L	length (m)
L_{tri}	normalized length of the three–phase contact line (–)
\dot{m}	mass flux vector (kg/m ² ·s)
P	pressure (Pa)
P_{cap}	capillary pressure (Pa)
\dot{Q}	volumetric flow rate (m ³ /s)
r	radius of nucleus bubble (m)
r_{max}	the maximum throat radius (m)
r_{min}	the minimum throat radius (m)
r_{th}	throat radius (m)
S	saturation (–)
T	temperature (°C)
T_{sat}	saturation temperature (°C)
t	thickness (m)
θ	contact angle (deg)
μ	viscosity (Pa·s)
ν	kinetic viscosity (m ² /s)
ρ_v	vapor density (kg/m ³)
σ	surface tension (N/m)
Σ^*	dispersion of pore size distribution (–)

Acknowledgement

The author was financially supported by the foundation of public interest of Tatematsu.

References

- [1] H. Li, Z. C. Liu, B. B. Chen, W. Liu, C. Li, and J. Yang, Development of biporous wicks for flat-plate loop heat pipe. *Exp. Therm. Fluid Sci.*, 2012. 37: p. 91.
- [2] E. Terrado, R. Molina, E. Natividad, M. Castro, P. Erra, D. Mishkinis, A. Torres, and M. T. Martínez, Modifying the heat transfer and capillary pressure of loop heat pipe wicks with carbon nanotubes.

- The Journal of Physical Chemistry C, 2011. 115: p. 9312.
- [3] D. Deng, Y. Tang, G. Huang, L. Lu, and D. Yuan, Characterization of capillary performance of composite wicks for two-phase heat transfer devices. *Int. J. Heat. Mass. Transfer.*, 2013. 56(1–2): p. 283.
- [4] E. A. Silk and D. Myre, Fractal loop heat pipe performance testing with a compressed carbon foam wick structure. *Applied thermal engineering*, 2013. 59(1-2): p. 290.
- [5] B. Wangaskar, S. Khandekar, and K. Balani, Effect of particle morphology on transport parameters of loop heat pipes. in *Joint 19th International Heat Pipe Conference and 13th International Heat Pipe Symposium – IHPC and IHPS*. 2018. Pisa, Italy. No. LHP1_4, 2018.
- [6] M. Nishikawara, T. Sako, H. Yokoyama and H. Yanada, Wicking characteristics of porous media using short copper micro/nanofibers. *International Journal of Heat and Mass Transfer*, 2022. 195: p. 123137.
- [7] B. Richard, D. Pellicone, W. Anderson, Loop heat pipe wick fabrication via additive manufacturing. in the *47th International Conference on Environmental Systems – ICES*. 2017. Charleston, USA. ICES-2017-12.
- [8] A.S. Demidov, E.S. Yatsenko, Investigation of heat and mass transfer in the evaporation zone of a heat pipe operating by the ‘inverted meniscus’ principle. *Int. J. Heat Mass Transfer*, 1994. 37: p. 2155.
- [9] Y. Yamada, M. Nishikawara, H. Yanada, and Y. Ueda, Predicting the performance of a loop heat pipe considering evaporation from the meniscus at the three-phase contact line. *Thermal Science and Engineering Progress*, 2019. 11: p. 125.
- [10] K Odagiri and H Nagano, Characteristics of phase-change heat transfer in a capillary evaporator based on microscale infrared/visible observation. *Int. J. Heat Mass Transfer*, 2019. 130: p. 938.
- [11] The Japan Society of Mechanical Engineers ed., *Heat transfer*, the Japan Society of Mechanical Engineers: p. 131 (2014, in Japanese).
- [12] C. Figus, Y. Le Bray, S. Bories, and M. Prat. Heat and mass transfer with phase change in a porous structure partially heated: continuum model and pore network simulations. *International journal of heat and mass transfer*, 1999. 42(14): p. 2557.
- [13] L. Mottet, T. Coquard, and M. Prat, Three dimensional liquid and vapour distribution in the wick of capillary evaporators. *Int. J. Heat Mass Transf.*, 2015. 83: p. 636.
- [14] E.W. Lemmon, M.L. Huber, and M.O. McLinden, *NIST Standard Reference Database 23: Reference Fluid Thermodynamic and Transport Properties-REFPROP, Version 9.1*, National Institute of Standards and Technology, Standard Reference Data Program, Gaithersburg, 2013.
- [15] M. Nishikawara and H. Nagano, Parametric Experiments on a Miniature Loop Heat Pipe with PTFE Wicks. *International Journal of Thermal Sciences*, 2014. 85: p. 29.
- [16] M. Prat and F. Bouleux, Drying of capillary porous media with a stabilized front in two dimensions. *Phys. Rev. E.*, 1999. 60: p. 647.
- [17] M. Nishikawara, H. Nagano, L. Mottet, and M. Prat, Formation of unsaturated regions in the porous wick of a capillary evaporator, *Int. J. Heat Mass Transf.*, 2015. 89: p. 588.
- [18] M. Nishikawara, Y. Ueda and H. Yanada, Static and dynamic liquid-vapor phase distribution in the capillary evaporator of a loop heat pipe. *Microgravity Science and Technology*, 2019. 31(1): p. 61.

New flat electronics cooling device composed by internal parallel LHPs

Larissa Krambeck^{1*}, Kelvin Guessi Domiciano¹, and Marcia B. H. Mantelli¹

¹Heat Pipe Laboratory, Federal University of Santa Catarina, Florianopolis/SC, Brazil

*Corresponding author email address: larissa.krambeck@labtucal.ufsc.br

Abstract

The thermal performance of a new two-phase device developed for electronics cooling was experimentally investigated in this research. The proposed device is similar to an eight-channel pulsating heat pipe, where two parallel channels, one of them partially filled with a sintered metallic porous medium, are interconnected, forming four parallel loops heat pipes. The wick structure directs the working fluid displacement along the device. Diffusion bonding of machined flat plates was the manufacturing process. A benchmark pulsating heat pipe was also manufactured and experimentally studied, for performance comparison. Distilled water was used as the working fluid. Heat transfer rates from 10 to 160 W were applied to the heat exchangers, at gravity-assisted and horizontal orientations. The experimental results showed that the proposed flat loop heat pipes in parallel arrangement operate successfully in a wide thermal load range at gravity-assisted orientation, being a better alternative than the pulsating heat pipe. Already in the horizontal position, the new heat exchanger worked satisfactorily at low heat loads, while the PHP operated satisfactorily for high power inputs. The major conclusion is that the proposed two-phase loop flat heat pipes in parallel arrangement operate successfully in a specific thermal load range for each orientation, being considered a suitable cooling alternative for flat electronic gadgets.

Keywords: Two-phase loop device; Flat plate; Thermal performance; Electronics cooling;

1 Introduction

Two-phase devices, such as heat pipes, are considered effective solutions for electronics cooling. Their advantages include a wide range of operation temperatures, no requirement of additional energy and the use of the latent heat of a fluid as the major heat transfer mechanism [1].

Usually, the electronic chips to be cooled in CPUs, laptops, video games, tablets and smartphones, have a flat geometry, which leads to the development of flat cooling solutions for easy integration with electronic gadgets. However, the manufacturing process of flat plate devices is still a challenge, jeopardizing their use in actual applications.

Diffusion bonding is a solid-state union process that produces, including the bonding interface, monolithic pieces with the same bulk metal microstructure, as no filler materials are used. Besides the high quality, diffusion bonding allows basically any internal geometry, making this technology a promising solution for flat heat pipe production. This technique requires an appropriate combination of temperature, pressure and time, under an inert atmosphere, for a successful result [2].

Among the diverse types of flat heat pipes, the loop heat pipe (LHP) and pulsating heat pipe (PHP) are interesting devices due to their efficient way of transferring heat.

A flat PHP is composed of a closed loop of parallel small cross-section channels in a serpentine configuration inside a flat plate. Heat is transported by the working fluid displacement along the device

in a pulsating mode, promoted by confined vapor bubbles in the channels. Their oscillating cycles enable the transfer of high and concentrated heat fluxes, at a cost of delayed operation startup, as PHPs usually require higher temperature differences to initiate their working fluid thermodynamic cycle [3].

The LHP is a well-known heat pipe configuration, in which the vapor and liquid flow in separate channels, forming a one-way loop and reducing the dragging forces between the working fluid phases. As a result, this device can carry more heat, being considered a powerful heat transfer device. Their wick structures are responsible for pumping the working fluid along a proper direction within the device [4].

The present research developed a new two-phase flat heat pipe using diffusion bonding technology. The proposed device is similar to an eight-channel pulsating heat pipe in which two adjacent channels are interconnected (instead of all channels), forming four parallel independent loops. One of the channel pairs and part of the evaporator region were recovered by a sintered copper porous medium, aiming to pump the liquid along the device and direct the working fluid displacement in the proper direction. Therefore, these four loops can be considered simplified parallel LHPs.

The thermal performance of the present heat pipe was investigated experimentally and compared with a benchmark PHP, which served as inspiration for testing this new geometry. It should be noted that

these two samples are actually part of a broader research, where the thermal performance of several two-phase gadgets, with the same external flat plate geometry (intended for electronics applications), are compared. For that, these devices are designed, constructed and tested.

2 Fabrication of two-phase devices

The target application of the proposed devices is to remove heat from electronics. Therefore, the external dimensions of 100 x 55 x 2.6 mm³ were selected, as the resulting gadget fits in most tablets, laptops and CPUs. To simplify, from now on, this device, with four loop heat pipes in a parallel arrangement, is denominated as “4-LHP”.

To fabricate the 4-LHP, three copper sheets were diffusion bonded: two full external plates with 0.55 mm thickness and one inner-layer plate of 1.5 mm. The inner plate was machined using a water-cut process to form four independent loop channels (see Figure 1) and piled over one of the external sheets. Their relative positions were fixed by means of spot welding. Copper powder was sintered in specific regions of the channel, to form a porous medium, able to promote the fluid motion in the proper direction. As shown in Figure 1, the sintered capillary structure was divided into two sections: evaporator and liquid line wick. The evaporator wick, with the same height as the channel (1.5 mm), besides pumping the liquid, prevents the just formed vapor to flow back to the liquid line. The wick structure located at the liquid line assists in the liquid return from the condenser to the evaporator region, and has 0.5 mm of thickness, allowing space for the vapor to flow. The used copper powder was Type C, according to the classification proposed by Mera [5], which resulted, after sintering, in a wick with effective porous radius of 21.4 μm, porosity of 53.46% and permeability of 1.99 x 10⁻¹² m².

Figure 2a shows the resulting internal structure of the 4-LHP, after the sintering process. In the sequence, the closing plate was stacked and the set was submitted to the diffusion bonding cycle.

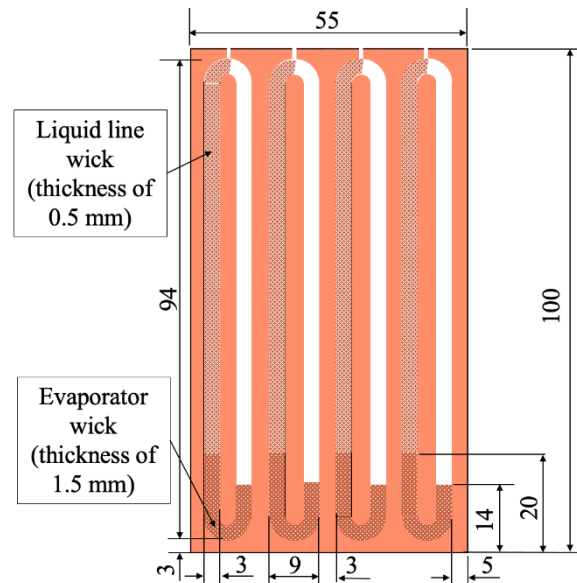
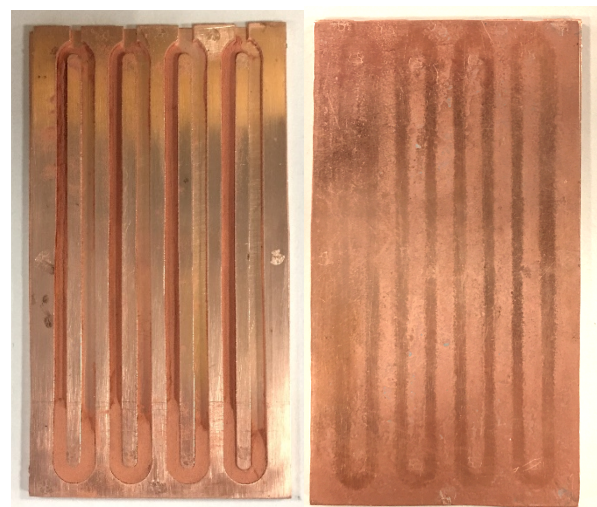


Figure 1. Schematic design of 4-LHP [mm].

The thermal cycle used in both sintering and diffusion bonding processes consisted of maintaining a temperature of 875 °C for one hour in an inert atmosphere of Argon. They were performed in a JungTM furnace at Heat Pipe Laboratory/UFSC. Also, in the diffusion bonding process, a pressure of 6.5 MPa was applied by stainless steel matrixes and screws. Before any thermal cycle, all the pieces were cleaned with acetone and sulfuric acid. Figure 2b shows the resulting heat pipe after the diffusion bonding. It is clear in Figure 2b that the internal geometry designed (four loops) was maintained after the diffusion bonding, without deformations. The channel contours can be seen due to traces of boron nitride on the surface after the first cleaning.



a) Opened device

b) Closed device

Figure 2. The resulting 4-LHP.

The last step of the fabrication was the brazing of the filling tube for the vacuum and charging working fluid procedures. A helium leak detector (Edwards Spectron™ 5000 Helium) was used to check leakages and communication between the loops.

A flat plate PHP, with the same external dimensions, the same mass, and the same cross-section area of the 4-LHP, was made. It consisted of a sandwich of two full plates filled with a jet-water machined plate, with 16 parallel square channels in 8 U-turns fashion, connected in a single closed loop, as shown in Figure 3. The cross-section channel dimensions were 1.5 x 1.5 mm². The manufacturing steps were the same described previously, without the sintering process.

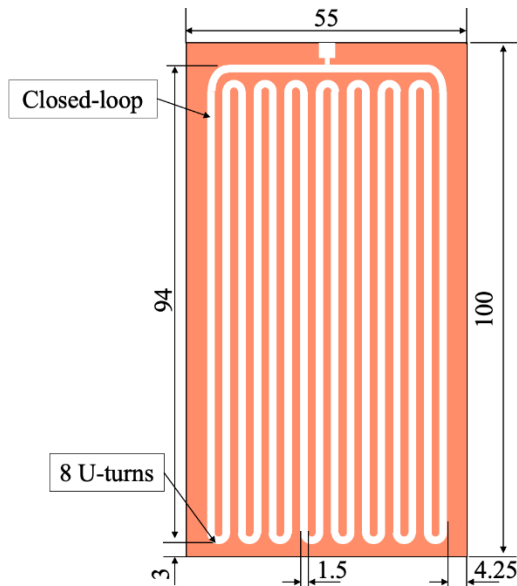


Figure 3. Schematic design of PHP [mm].

Once finished the manufacturing process and after the leakage tests, the devices were ready for charging with the working fluid, which process included the air evacuation, followed by the working fluid filling, with the aid of a Tygon tube and forceps. After being charged, the working fluid inside the device was purged. A vacuum, better than 4×10^{-5} mbar, was provided by a compact turbomolecular pumping station, Edwards™ T-Station 85.

Each of the 4-LHP loops was separately filled with the desired volume of working fluid and purged in the sequence. The purging methodology was the same one proposed by Cisterna et al. (2020).

Degassed distilled water was used as the working fluid in both devices. The best filling ratio study was performed but, in this work, only data for the

volume of working fluid that provided the best thermal performance for each device were analyzed (see Table 1). The volume uncertainty was ± 0.02 ml. Also, the heat pipes with no working fluid were tested to estimate the heat transfer only by conduction.

Table 1. Filling characteristics.

Flat heat pipe	PHP	4-LHP
Working fluid	Distilled water	
Total void volume [ml]	2.85	2.90 A = 0.72 / B = 0.72 C = 0.70 / D = 0.76
Working fluid volume [ml]	1.75	A = 0.20 / B = 0.20 C = 0.20 / D = 0.22

3 Experimental Analysis

Figure 4 schematizes the experimental setup used for thermal tests in both two-phase devices. The heat pipe length was divided into three sections, an evaporator of 15 mm, an adiabatic region of 81 mm and a condenser of 15 mm.

The evaporator's bottom external surface was attached to a heater, composed of a copper block (14 x 55 x 14 mm³), where one cartridge electrical resistor was inserted. A programmable power supply unit (TDK-Lambda™ GEN300-17) fed the electrical resistor. The condenser region was cooled by water provided by a thermostatic bath (Lauda Proline™ RP1845) at a constant temperature of 20 °C, which flew inside a metallic block (15 x 55 x 22 mm³), as shown in Figure 4. The heat source and heat sink resulted in contact areas of 770 and 825 mm², respectively, in which thermal grease was used to reduce the contact resistances. Moreover, an Isoglas™ blanket (30 mm thick) insulated the setup, minimizing the heat loss from the experiment to the environment.

The temperatures of the 4-LHP device were monitored by T-type thermocouples (Omega Engineering™) that measured and recorded the temperature distribution, which worked coupled to a data acquisition system (DAQ-NI™ SCXI-1000), which, in turn, was controlled by the Labview™ software and recorded in a laptop (Dell™). Twelve sensors were fixed at the external surface (see positions in Figure 4) using thermosensitive adhesive strip Kapton™. Also, a thermocouple monitored the room temperature.

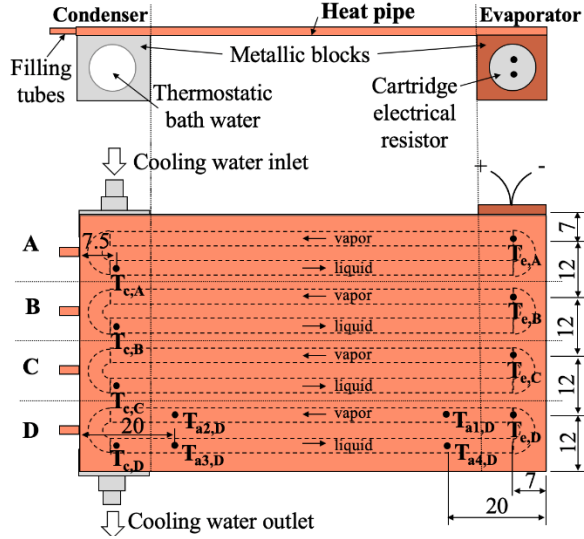


Figure 4. Experimental setup and thermocouple locations in the 4-LHP [mm].

The loops of the 4-LHP were designated as A, B, C and D, according to Figure 4. Thermocouples were denoted by the heat pipe section (“e” for the evaporator, “a” for the adiabatic section and “c” for the condenser) followed by the referenced loop. For example, the $T_{c,A}$ thermocouple corresponds to the temperature sensor in the condenser of the “A” loop heat pipe. Loop D received four more thermocouples, installed in its adiabatic section.

The PHP setup had three temperature sensors in the middle of each region (instead of four), totaling nine thermocouples.

Heating powers from 10 to 160 W (heat fluxes from 1.3 to 20.8 W/cm²), with increasing steps of 10 W, were applied to the heat pipes at gravity-assisted (vertical position, evaporator below the condenser) and horizontal (without gravity assistance) orientations during 600s, to guarantee steady-state operation. The heat flux was expressed by the dissipated thermal load divided by the evaporator contact area. Power steps were applied until the evaporator temperature reached 100 °C, considered the maximum operating temperature for electronics applications. Experimental data were recorded at a rate of 1 acquisition/second.

The temperature distribution was used to analyze the thermal behavior of the novel heat pipe, which was compared with the conventional flat PHP. The overall thermal resistance, R , was used to estimate and compare the thermal performance of the flat heat pipes, defined as:

$$R = \frac{\bar{T}_{evap} - \bar{T}_{cond}}{q} = \frac{\bar{T}_{evap} - \bar{T}_{cond}}{U \times I} \quad (1)$$

where \bar{T}_{evap} and \bar{T}_{cond} are the average temperatures of the evaporator ($T_{e,A}$, $T_{e,B}$, $T_{e,C}$, and $T_{e,D}$) and condenser ($T_{c,A}$, $T_{c,B}$, $T_{c,C}$, and $T_{c,D}$), respectively. The q is the heat load applied by the power supply unit, U is the output voltage and I is the output electric current. The heat loss from the setup to the surroundings was neglected, as the experimental data showed a heat leakage lower than 1% of the power input.

Experimental uncertainties were estimated by the error propagation method [7] considering the thermocouples, data acquisition system and power supply unit uncertainties. Temperature sensors were calibrated in the developed experimental setup, which provided a temperature uncertainty of about ± 0.23 °C. The power supply unit uncertainties were 0.03 V for the voltage and 0.0085 A for the electric current. The maximum uncertainty of the thermal resistance was 0.43 °C/W at 10 W, reducing to less than 0.02 °C/W at 160 W.

4 Results and Discussion

4.1 Temperature distribution of the 4-LHP

Figure 5 shows the temperature readings as a function of time for the 4-LHP at gravity-assisted orientation. As expected, for each thermal load, all the temperatures increased until they reached a steady-state condition. The observed temperature distribution shows that condensate was able to reach the evaporator for 30 W power (heat flux of 3.9 W/cm²), reaching the stable operation typical of LHPs. This behavior was maintained until the maximum dissipated heat load, 160 W (20.8 W/cm²). No dry-out was observed.

Temperature distribution for the 4-LHP at the horizontal position (without gravity assistance) in steps of 10 W is presented in Figure 6. Again, the temperatures raised with the heat load application, achieving steady-state conditions in each power. The 4-LHP was isothermal since the first power input, at 10 W (1.3 W/cm²), showing efficient heat removal. However, at approximately 1300s, a slight curve slope change in the evaporator temperature and a peak in condenser temperature for 30 W (3.9 W/cm²), showed the beginning of evaporator drying. Despite the liquid did not achieve the entire evaporator in the following heat loads, the 4-LHP continued working until it reaches 100 °C. Therefore, the main difference observed between the device operating in vertical and horizontal positions was in the heat transfer operation range.

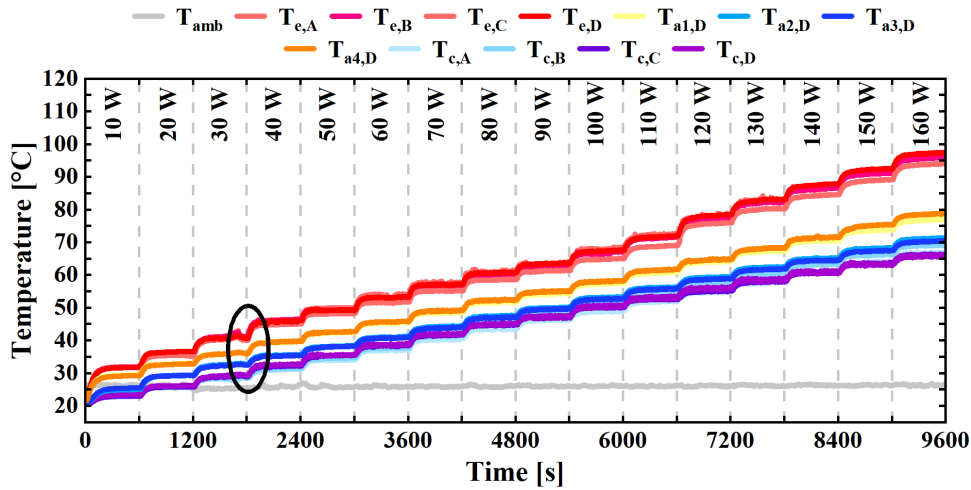
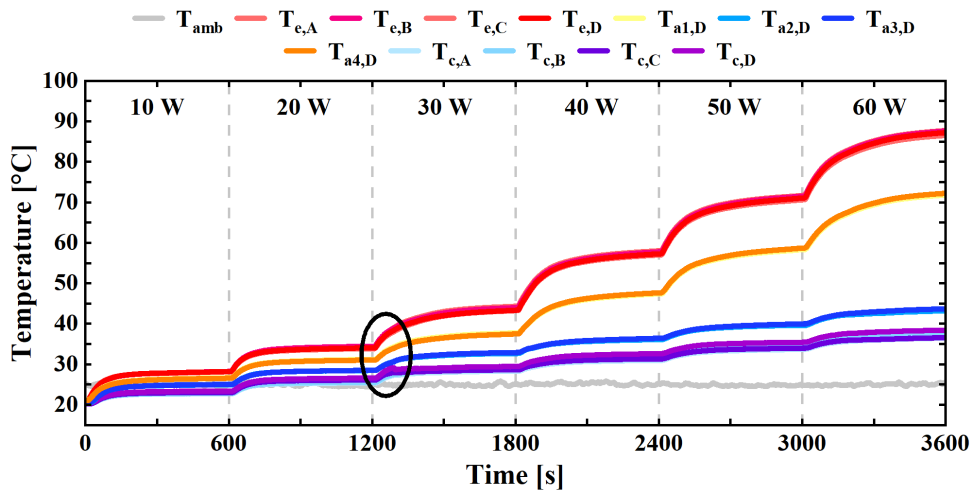
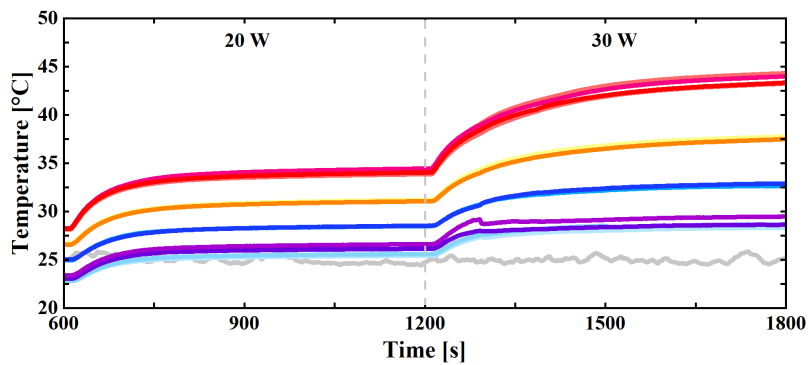


Figure 5. Temperature transient of 4-LHP in the gravity-assisted orientation.



a) Heat loads from 10 to 60 W



b) detailed view from 20 to 30 W

Figure 6. Temperature transient of 4-LHP in the horizontal orientation.

For a better understanding of the 4-LHP behavior in the horizontal position, further tests were carried out with power steps of 2 W, for heating powers from 2 to 30 W (from 0.3 to 3.9 W/cm²). For a sake of conciseness, Figure 7 shows just the temperature distribution of thermocouples fixed on Loop D, which allows for a detailed analysis of working fluid movement.

According to Figure 7, the $T_{c,D}$ (red line), which is located above the heater area over the porous media and liquid, presented the hottest temperature. As expected, the sensor $T_{a1,D}$ (pink line), positioned in the vapor outlet, was the second hottest. Thermocouple $T_{a4,D}$ (light orange line), located in the evaporator inlet, was very similar to the vapor inlet. Although liquid was

presented in this region, the temperature is still high, due to the elevated conduction through the sintered powder and the enclosure. The temperatures of the condenser inlet ($T_{a2,D}$ - light blue line) and outlet ($T_{a3,D}$ - dark blue line) were very close, result of the powerful heat sink used and heat conduction within the region. The coldest thermocouple was in the condenser middle section, $T_{e,D}$ (purple line).

The beginning of the dry-out was characterized by the sudden increase in the evaporator temperature and an abrupt decline in the condenser at 28 W (3.6 W/cm^2). Also, an interesting fact can be observed at this moment. The condenser outlet temperature, $T_{a3,D}$, (dark blue line), surpassed the condenser inlet, $T_{a2,D}$ (light blue line), showing that the heat pipe stopped operating properly and, probably, had vapor in the liquid line.

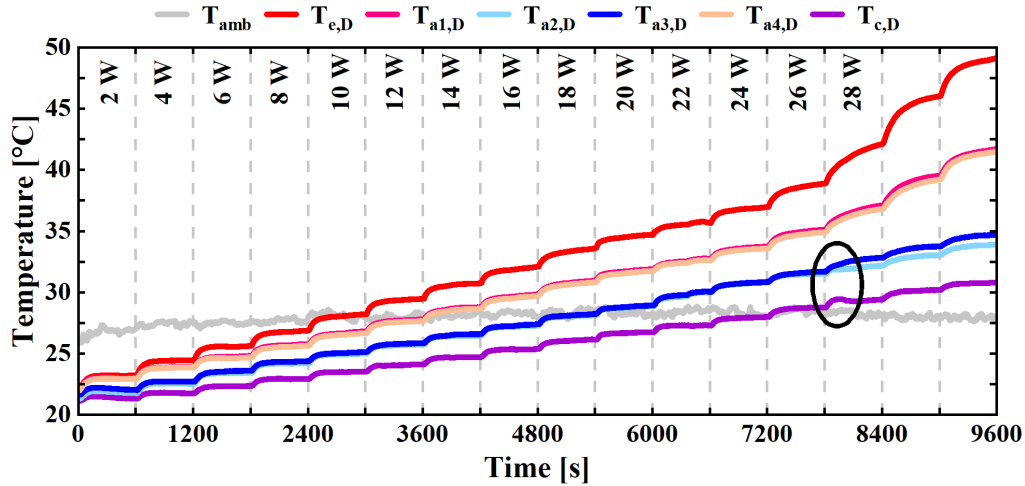


Figure 7. Temperature distribution in loop D of 4-LHP at horizontal orientation.

4.2 Thermal resistance comparison

Figure 8 presents the experimental overall thermal resistance for the PHP and 4-LHP, with its measurement uncertainties (vertical error bars). The thermal resistances of the heat pipes with only conduction heat transfer (empty devices) are also presented. Both empty devices had similar thermal resistance, roughly $1.4 \text{ }^\circ\text{C/W}$.

One can see from this figure that the thermal resistance of the 4-LHP is much smaller than the empty device at both orientations. In the gravity-assisted position, the 4-LHP thermal resistance (light pink line) decreased from 10 to 70 W and remained almost constant after this level at $0.17 \pm 0.02 \text{ }^\circ\text{C/W}$. The 4-LHP thermal resistance at horizontal orientation presents two curves that overlapped: standard test with power increase at 10 W steps (blue line) and detailed test with heat load rise at 2 W steps (light line). The minimum thermal resistance was $0.39 \pm 0.11 \text{ }^\circ\text{C/W}$ at 26 W (3.4 W/cm^2). After that, as noted in the temperature distribution analysis, the evaporator started to dry, increasing the thermal resistance.

On the other hand, the thermal behavior of the PHP was deeply different. The device started to operate properly as a PHP at 30 W, in the gravity-assisted orientation, reducing the thermal

resistance to $0.12 \text{ }^\circ\text{C/W}$ in the highest power level (160 W, which corresponds to 20.8 W/cm^2). At the horizontal orientation, the thermal resistance was the same as the pure conduction resistance (empty PHP) until 60 W (7.8 W/cm^2), when occurred the PHP startup. Then, the thermal resistance declined with every heat load, reaching the lowest value of $0.13 \text{ }^\circ\text{C/W}$ at 160 W (20.8 W/cm^2). The PHP operated well without gravity assistance, for power larger than 110 W (14.3 W/cm^2).

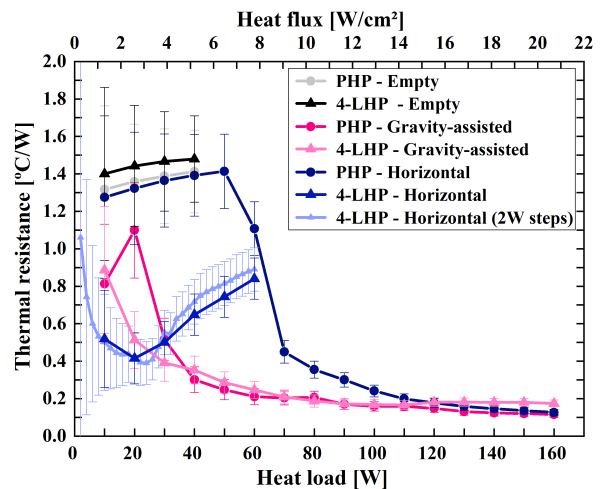


Figure 8. Thermal resistance comparison between the PHP and 4-LHP.

According to the graph in Figure 8, the 4-LHP presented a better thermal performance than that of the PHP at the gravity-assisted orientation, as they showed similar thermal resistances from 40 to 160 W but only the 4-LHP could operate at lower heat loads (10 until 30 W), with the PHP showing a delayed startup. In the horizontal position, each device worked in a different range. The 4 LHP demonstrated a suitable operation for low heat loads (2 to 26 W), while the PHP operated satisfactorily for high power inputs, from 60 to 160 W.

The major conclusion is that the proposed two-phase flat device with LHPs in a parallel arrangement operates successfully in a specific thermal load range for each orientation, being considered a suitable cooling alternative for flat electronic gadgets.

5 Conclusions

The thermal performance of a novel two-phase device, inspired by the flat pulsating heat pipe for electronics cooling, was experimentally investigated in this research. The new design consists of four independent loop heat pipes in a parallel arrangement. A pulsating heat pipe, with the same dimensions, was experimentally analyzed in order to compare the thermal performances of both devices.

The flat loop heat pipes in parallel arrangement showed to be a better alternative for electronics cooling in the horizontal orientation at low heat fluxes (below 26 W, which corresponds to 3.4 W/cm²). On the other hand, the pulsating heat pipes presented better results operating in the horizontal position for high heat flux (above 60 W, which corresponds to 7.8 W/cm²). In the gravity-assisted orientation, both heat transfer devices operated in a wide range of dissipated power; however, the novel worked properly since 2 W (0.3 W/cm²) while the pulsating heat pipe presented a delayed startup.

The major conclusion is that the proposed flat loop heat pipes in parallel arrangement operate successfully in a specific thermal load range for each orientation, being considered a suitable cooling alternative for flat electronic gadgets.

In future work, it is recommended that the volume of the channels of the parallel loop heat pipes should be increased, so that more working fluid can be inserted, increasing the heat exchange capacity of the device, especially in the horizontal position.

Acknowledgements

The authors acknowledge CNPq (grant numbers 149892/2019-5 and 423968/2018-1), FAPESC (grant number 3003/2021), and Graduate Program in Mechanical Engineering of UFSC for providing financial support to the present research and conference participation.

References

- [1] M. B. H. Mantelli, *Thermosyphons and Heat Pipes: Theory and Applications*. Cham: Springer International Publishing, 2021.
- [2] L. Betancur-Arboleda, P. Hulse, I. Melian, and M. H. Mantelli, "Diffusion bonded pulsating heat pipes: fabrication study and new channel proposal," *Journal of Brazilian Society of Mechanical Engineers*, 2020, 42, p. 466.
- [3] S. Khandekar, M. Schneider, P. Schäfer, and R. Kulenovic, "Thermofluid dynamic study of flat plate closed loop pulsating heat pipes," *Microscale Thermophysical Engineering*, 2003, 3954, p. 303.
- [4] H. Tang *et al.*, "Review of applications and developments of ultra-thin micro heat pipes for electronic cooling," *Applied Energy*, 2018, 223, April., p. 383.
- [5] J. P. F. Mera, "Heat and Mass Transfer Analysis of a Copper Loop," Universidade Federal de Santa Catarina, Florianópolis, 2016.
- [6] L. H. R. Cisterna, G. Vitto, M. C. K. Cardoso, E. L. Fronza, M. B. H. Mantelli, and F. H. Milanez, "Charging procedures: effects on high temperature sodium thermosyphon performance," *Journal of the Brazilian Society of Mechanical Sciences and Engineering*, 2020, 42, 8:, p. 1.
- [7] J. P. Holman, *Experimental methods for engineers*, 8th ed. New York, USA, 2011.

THIN LOOP HEAT PIPE WITH STRANDED WIRE AS POROUS MEDIA

Kelvin G. Domiciano^{1*}, Larissa Krambeck¹, and Marcia B. H. Mantelli¹

¹Heat Pipe Laboratory, Federal University of Santa Catarina, Florianopolis/SC, Brazil

*Corresponding author email address: kelvin.guessi@laptucal.ufsc.br

Abstract

A diffusion bonded thin flat loop heat pipe (LHP) with a novel wick structure consisting of an electrical wire strand cable (several twisted copper threads) was developed. The LHP, specially designed to remove heat from electronics, has external dimensions of 76 x 60 mm² and 1.1 mm in thickness. A workbench was fabricated to simulate a typical mobile phone chip processor, in which the heated area (to be cooled) is 1 cm². Water with a filling ratio of 35% was used as the working fluid. The present study experimentally investigated the thermal operation of the LHP with a novel wick structure. The LHP with the new porous media, which present high porosity and permeability, is easier to manufacture, when compared to those with conventional wick structures. The twisted copper threads wick structure proved to be highly effective, supplying necessary capillary pressure for the LHP to work in all positions, even against gravity. The LHP could operate from 2 W/cm² up to 9 W/cm² with a thermal resistance as low as 0.26 °C/W, cooled by natural air convection. The suggested wick structure proved to be very competitive as it is thermally effective, presents low cost and is easier to manufacture, showing to be a good alternative for mass production of thin LHPs, being therefore feasible for the thermal management of smartphones.

Keywords: Loop heat pipe; Thermal performance; Porous media; Twisted copper wire; Electronics

1. Introduction

In the last years, mobile phones have become more sophisticated, consequently demanding more efficient thermal control systems. Two-phase devices are considered interesting temperature control solutions, as they do not demand power consumption, being, therefore, the object of research of several groups [1], [2].

To provide good thermal coupling with the electronic gadgets (heat source), such as in smartphones, the whole device should be thin and the paring surface should to be flat. Besides, it should work without gravity assistance and under natural air convection.

Loop heat pipe (LHP) is a highly effective device that works with the phase change of a working fluid to transfer heat from a heat source to a heat sink. The fluid circulates inside the closed loop due to a capillary driven force generated by a porous wick structure. The wick structure must be well designed, i.e., must provide the capillarity needed for liquid circulation, usually obtained by small porous, which, on the other hand, can cause too high pressure drops, a not desired effect. It also must provide bubble nucleation sites and help in the working fluid evaporation. Sintered metal powder is typical LHPs wicks [3], however, several other types of porous media can be used in LHPs, such as wire, screen, grooves, non-metallic powder materials and others [4].

The use of different types of wick structures, or the design of novel porous media, showed to be an

effective route to improve the thermal performance of LHPs. Shioga et al [1] developed a novel wick structure for flat LHPs, formed by four copper sheets of 0.1 mm in thickness, in which holes of 0.2 mm in diameter, distributed in staggered position, were chemically etched. This way, the authors were able to control the wick pore size, ensuring high heat transportation for the LHP. Kumar et al. [5] studied the effect of oxidation of a sintered copper wick structure in a LHP. The authors concluded that the oxidation reduced the thermal conductivity of pure copper, decreasing the heat leak from the evaporator to the compensation chamber from 18% to 7%. This modification improved the thermal performance of the LHP, increasing the heat transportation capacity from 100 W (pure) to 180 W (oxidized copper). Ling et al [6] investigated a new porous copper fiber sintered wick for the capillary pumping of LHPs. Their main conclusion is that the novel wick resulting capillary pressure was not linear with porosity. They obtained the maximum capillary pumping for wicks with 70% of porosity.

In all recently published studies, the manufacturing processes of LHPs involved two steps, one of them dedicated to the wick structure fabrication. The present work investigates a novel wick structure, never seen in the literature. It is made of twisted thin copper threads of electrical cables, easily found in the market, being suitable to be installed in thin heat transfer devices. This novel wick structure was inserted into a mini LHP 1.1 mm thick, specially designed for removing heat from

compact electronic devices, such as smartphones. The resulting LHP was tested under power transportation conditions similar to those observed in actual operation, in order to evaluate the efficiency of the novel wick structure for real applications.

Therefore, the main objective of this paper is to introduce a novel and efficient wick structure, easy to obtain in the market, that resulted in easy to manufacture LHPs (or other two-phase devices), with just one step fabrication processes.

2. Wick structure and LHP fabrication

Since the main application of the proposed mini LHP is to remove a large amount of heat from chip processors of mobile phones, the external dimensions of the device are set to 76 x 60 mm and 1.1 mm in thickness. Three copper plates were piled and diffusion bonded: two externals, with 0.3 mm in thickness, and one internal, where the main channels were water jet machined, of 0.5 mm thick.

The novel proposed wick structure (see Figure 1), which has high porosity and permeability, is formed by twisting several threads of copper wires of 0.1 mm in diameter from traditional electrical stranded cables. The LHP with this porous media can be easily fabricated by simple steps: the twisted copper wire threads are welded on the surface of one of the external sheets. The twisted copper threads are inserted within the evaporator section and in a fraction of the condenser region. In the evaporator, four braids of around 29 mm in length are installed, leaving space between braids that forms five vapor paths of 1.3 mm width. A wick barrier was manufactured to prevent the return of vapor to the condenser on the reverse path, driving the vapor direction to the vapor tube. It also works as a mechanical support that avoid any deformation of the evaporator section. After the wick is installed, the three plates are piled and the formed stack is diffusion bonded.

Table 1 shows the main characteristics of the proposed LHP. Notice that after the diffusion bonding, the total thickness of the LHP reduced from 1.1 mm to 1.07 mm. More information about diffusion bonding conditions can be seen in [2].



Figure 1. The novel porous media of twisted copper wires inside the LHP.

The tests showed that the filling ratio (FR) of 35% (0.17 ± 0.01 ml) provided the best thermal result. Only results for this filling ration are shown in the present study. Degassed water was used as the working fluid, which is defined as the ratio between the inserted volume of the working fluid and the total internal void volume of the LHP (0.48 ± 0.01 ml).

Table 1. The main characteristics of the thin LHP.

Component	Dimension (Length x Width) [mm]
LHP (L x W x t)	76 x 60 x 1.07
Evaporator	37.5 x 20
Evaporator active area	10 x 10
Evaporator wick	29 x 1.5
Vapor grooves	23.5 x 1.3
Liquid line wick	70.49 x 1
Vapor line channel	79.17 x 3
Liquid line channel	79.17 x 3
Condenser channel	46 x 3
Working fluid	Water

3. Experimental setup

A workbench, to simulate the heat dissipation of a typical chip processor of a mobile phone, was developed. The heat was supplied on the outer surface of the evaporator by means of an electrical resistance inserted inside a copper block. The contact area of 1 cm² was used, which is the usual dimensions of smartphone chips [2]. Polytetrafluoroethylene (PTFE polymer) was used to isolate the evaporator region from the environment. The remained sections were cooled by natural air convection.

Figure 2 shows the experimental setup used for

the thermal evaluation of the LHP. It included a power supply unit, a data acquisition system (DAQ-NI™ SCXI-1000) and a computer. Seven T-type thermocouples (Omega Engineering™) were installed in different positions over the outer surface of the device. Thermocouples T_1 and T_2 were located at the heating area of the evaporator and at the evaporator exit, while T_3 , T_4 and T_5 were positioned at the entry, center and exit of the condenser. T_6 measured the temperature of the evaporator entry and T_{amb} monitored the ambient temperature.

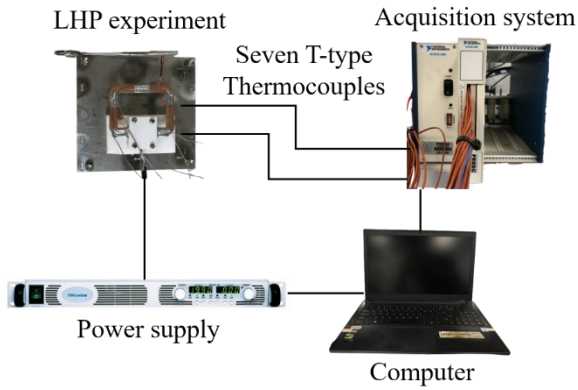


Figure 2. Experimental setup for the thermal evaluation of the LHP

The LHP was evaluated in three different positions to investigate the sensibility and response of the novel wick structure with the gravity action: horizontal (no influence of gravity), gravity-assisted (condenser above the evaporator) and against-gravity orientations (condenser below evaporator).

The applied heat loads increased in steps of 0.5 or 1 W, until the evaporator temperature reached approximately 100 °C, considered the maximum temperature allowed for a safe operation of electronics [7]. The set up was kept at each power input level for 1200 s, ensuring a steady-state operation was reached, which was considered achieved when a maximum temperature variation of 0.1 °C was observed during 1 minute. The environment temperature was maintained at 22 ± 0.7 °C.

The well-known thermal resistance concept was used to evaluate the thermal performance of the LHP, defined as:

$$R = \frac{T_1 - T_4}{q} \quad (1)$$

where q is the applied heat input [W].

The experimental setup was calibrated to reduce the temperature uncertainties, which are related to the thermocouples, data acquisition system and power supply unit. The thermal resistance uncertainty (δR) can be expressed by the following equation [8]:

$$\delta(R) = \left(\left[\frac{\partial R}{\partial T_1} \delta T_1 \right]^2 + \left[\frac{\partial R}{\partial T_4} \delta T_4 \right]^2 + \left[\frac{\partial R}{\partial q} \delta q \right]^2 \right)^{1/2} \quad (2)$$

where δT_1 and δT_4 are the temperature uncertainties of thermocouples T_1 and T_4 . δq is the uncertainty of the heat load, which can be calculated with the voltage input times the current provided to the electrical cartridge by the power supply unit.

4. Results and discussion

Figure 3 shows the transient temperature behavior of the LHP for all applied heat levels in the horizontal orientation. Heat is applied to the outer surface of the evaporator and the temperature increases until it reaches steady-state condition (maximum temperature variation of 0.1 °C in 1 minute).

Increasing the heat input, the steady-state temperature for each power level increased, as expected. The maximum heat flux dissipated by the LHP before reaching the established limit temperature of 100 °C was 9 W. No dry-out condition was observed, indicating that the LHP could probably operate with more power input, however, with a higher temperature.

For low heat loads, less than 2 W, the LHP only transferred heat by conduction through the case material, wick structure and working fluid. At 2 W, an increase in the condenser inlet and center temperatures were indicated by thermocouples T_3 (orange line) and T_4 (blue line), respectively, surpassing the evaporator inlet temperature (T_6 - purple line). This condition means that the LHP started operating transferring heat by two-phase phenomena as the major mechanism.

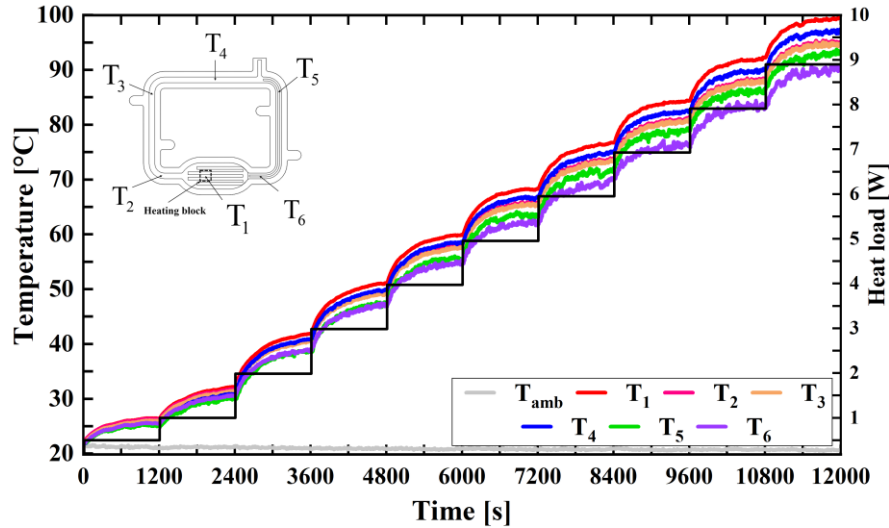


Figure 3. Transient temperature of the LHP operating in the horizontal orientation.

A LHP achieves the startup condition when the working fluid is able to evaporate and vapor leaves the evaporator section to the condenser direction. In the condenser, heat is removed by natural convection and vapor is condensed. The condensate returns to the evaporator pumped by the capillary pressure provided by the wick structure. To guarantee the start-up, a thermodynamic condition must be satisfied: a temperature unbalance should exist between the liquid-vapor interface in the evaporator section and the inlet evaporator region ($T_1 - T_6$), which results in an unbalanced pressure in these regions, that guarantees that the liquid returns to the evaporator [2], [9], [10].

The unbalance temperature between T_1 and T_6 for the LHP operating in the horizontal orientation (see Figure 3), was $3.02\text{ }^\circ\text{C}$. With the increase of the heat load, this temperature difference increased, facilitating the start-up. Above 4 W, the device is already in two-phase operation and so thermocouples T_1 , T_2 , T_3 , and T_4 (evaporator, condenser and vapor line) are nearly equivalent, presumably because most of the condenser length is filled with vapor.

Some temperature fluctuations are observed in the data, which might be related to the two-phase phenomena (bubble formation in the evaporator) or to variations in the natural convection.

Figure 4 gives the average temperature, at the steady-state conditions, of the proposed LHP in the horizontal, gravity-assisted and against-gravity orientations. The horizontal is depicted by

the square dot and solid line, the gravity-assisted is illustrated with a circular dot and dashed line, and the against-gravity orientation is given by the triangle dot and dot line. All thermocouple measurements, except for T_{amb} , are shown in the graph, where the heat load was varied from 0.5 W to 8 W. The power input level of 1 W, 5 W and 6 W are not presented in the graph to improve the quality of viewing.

From Figure 4 it can be noted that the only heat transfer mechanism for loads below 2W was conduction, as all thermocouples measured similar temperatures along the LHP for the three tested positions. At 2 W, there is a temperature difference among the thermocouples T_1 to T_4 , and between T_5 and T_6 . Some temperature differences can be seen in the thermocouples T_1 to T_4 due to the initial condensation phenomenon and measurement uncertainties. As mentioned, this unbalance temperature establishes the perfect condition for the LHP startup. The LHP started up with 2 W, operating in all orientations with an evaporator temperature of around $42\text{ }^\circ\text{C}$ (steady-state condition), i.e., the device proved to be not influenced by the gravity force.

The unbalance temperature between T_1 and T_6 for the horizontal, gravity-assisted and against-gravity orientation were $3.02\text{ }^\circ\text{C}$, $3.63\text{ }^\circ\text{C}$ and $3.40\text{ }^\circ\text{C}$, respectively.

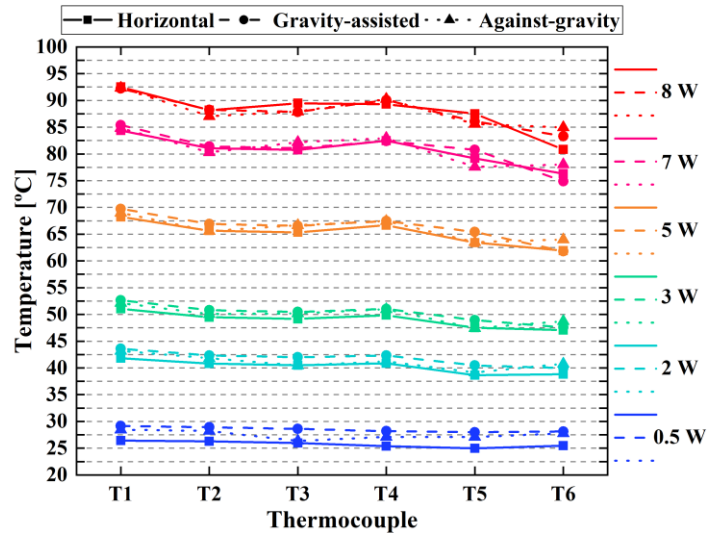


Figure 4. Average temperature at steady-state condition of the LHP operating in the horizontal, gravity-assisted and against-gravity orientation.

It is observed that a larger temperature unbalance between the liquid-vapor interface in the evaporator zone and the inlet temperature of the evaporator is necessary to the LHP to start operating in the gravity-assisted orientation, probably due to the higher pressure drop along the LHP caused by the gravitational force. The larger the heat input, the larger is this unbalance temperature and, presumably, the better the LHP works. Figure 4 highlights that the orientation major effect is felt in the evaporator inlet temperature T_6 , which can be explained analyzing the gravity action over the pressure distribution of the working fluid along the device. In the horizontal orientation, the gravity force does not act in any component of the LHP. In the gravity-assisted position, the gravitational field influences the device by increasing its pressure drop. On the other hand, in the against-gravity orientation, the pressure drop is reduced. For this reason, it is expected that the temperature difference between T_1 and T_6 is lower for the LHP operating in the against-gravity position when compared to the LHP functioning in other orientations.

Figure 5 presents the overall thermal resistance of the proposed LHP with a 35% filling ratio, operating in the three tested positions: horizontal, gravity-assisted and against-gravity. Also, the empty device, i.e., with no working fluid inserted, was tested in the horizontal orientation and is also presented in Figure 5. Without the working fluid, the LHP works only with heat conduction through the case material and the wick structure. In such case, the average thermal resistance of the LHP is 3.49 ± 0.64 °C/W. Obviously, the two-phase operation can happen only in the presence of the

working fluid, decreasing sensibly the device thermal resistance. The LHP is able to transport heat up to 8 W for the gravity-assisted and against-gravity orientation and up to, 9 W for the horizontal mode, before reaching the limit temperature for electronics, of 100 °C. This difference heat transportation difference can be related to the ambient temperature variation during the experimental test (around 22 ± 0.7 °C) and the system uncertainties.

As seen, below 2 W, the LHP still operates but transferring heat only by conduction from the evaporator to the condenser. However, with the wick structure saturated with liquid phase working fluid and no phase change happening, the thermal resistance is lower compared to the empty device, due to the additional heat conduction path (through the working fluid). Another possible explication is a discrepancy caused by system uncertainties, which is higher at low heat loads (see Eq. (2)). Above 2 W, in the horizontal and gravity-assisted orientation, the thermal resistance slope remains almost at a constant level, reaching a minimum thermal resistance of 0.26 ± 0.04 °C/W and 0.41 ± 0.05 °C/W, respectively. The LHP operating in against-gravity mode achieved a constant level of thermal resistance at heat power of 3 W and higher, a little delayed in relation to the other tested conditions. This delay can be associated with the lower unbalance temperature between T_1 and T_6 (against-gravity orientation reduces the pressure drop), which didn't reach the necessary pressure to accomplish the working fluid circulation all along the device. At 3 W, the mass flow rate, which is directly related to the heat load (increasing the power input, the higher the mass flow rate), was

sufficient to fill the most section of the condenser with vapor, especially in the center (T_4), decreasing the thermal resistance of the LHP sharply to a pseudo-stable condition with a minimum value of 0.27 ± 0.04 °C/W.

The thermal performance enhancement, comparing to the empty device with the two-phase LHP, in terms of thermal resistance, was around 93% for the LHP operating in the horizontal and against-gravity orientation. For the gravity-assisted mode, the LHP improved by around 88%.

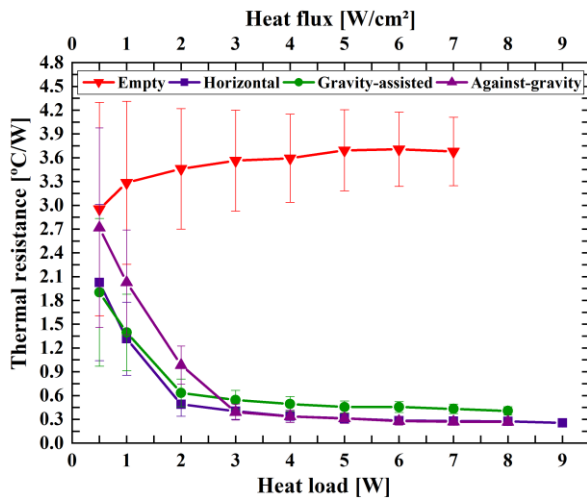


Figure 5. Overall thermal resistance of the proposed LHP operating in the horizontal, gravity-assisted and against-gravity orientation.

Figure 5 shows that the thermal resistance of the LHP operating in the horizontal and gravity-assisted orientation was slightly lower to that of the gravity-assisted condition. According to the startup thermodynamic condition of LHPs explained before, the gravity force adds an additional pressure along the two-phase device, increasing the necessary temperature difference between the working fluid in the evaporator zone (T_1) and the inlet evaporator region (T_6). With this higher unbalance temperature, also higher is heat leakage by conduction from these two regions, which may negatively impact the thermal performance of the LHP, resulting in higher thermal resistances. Another possible explanation is presented by Zhou et al [11]. The author explained that the difference between the thermal resistances of LHP working in the horizontal and gravity-assisted orientations can be related to the larger liquid film thickness in the evaporator, excessively wetting the wick structure.

To sum up, the novel wick structure of twisting

several threads of copper wires proved to be highly effective, not gravity dependent and easy to manufacture, enhancing the thermal performance of LHPs. Lastly, this novel proposed porous media may be able to introduce LHP as a technology that can be produced on an industrial scale.

5. Conclusions

In this study, a new thin loop heat pipe with 1.07 mm of thickness, with a novel wick structure, consisting of twisting several threads of copper wires, was fabricated. Diffusion bonding was used to join the three plates that form the LHP. The proposed LHP was experimentally studied by applying similar smartphone operation conditions (active area of 1 cm²) in order to evaluate the efficiency of the novel wick structure for this application. Three different operation orientations were tested: horizontal, gravity-assisted and against-gravity. Heat was dissipated in the evaporator by means of natural air convection. The working fluid of the LHP was water. The conclusions can be summarized as follows:

- The novel wick structure, the twisted thin copper threads with high porosity and, consequently, high permeability, showed to be extremely easy to manufacture.
- This porous media proved to be highly effective in terms of capillary pumping, supplying the necessary pressure for the working fluid, so that the LHP work could work in all positions, even against the gravity force.
- The proposed heat transfer device with the novel wick structure operated at low heat fluxes, from 2 W/cm² to 9 W/cm² in all orientation modes, with the evaporator temperature, at steady-state conditions, at around 42 °C.
- The loop heat pipe with a filling ratio of 35% of water achieved the minimum thermal resistance of 0.26 ± 0.04 °C/W, 0.27 ± 0.04 °C/W and 0.41 ± 0.05 °C/W for the horizontal, gravity-assisted and against-gravity orientation.

The suggested novel wick structure of twisting several threads of copper wires proved to be very competitive compared to other porous media, being thermally effective, easy to manufacture and with low cost. The LHP with this new porous media can be fabricated at industrial scale, promising to be very effective as a thermal management solution for smartphones.

The authors suggest a further study regarding

the physical properties of the novel wick structure and of its working fluid flow behavior, so that a good comparison with other porous media could be performed.

2016, 109, p. 514.

Acknowledgments

The authors acknowledge FAPESC (Fundação de Amparo à Pesquisa e Inovação do Estado de Santa Catarina) for providing scholarship (grant number 3003/2021) and CNPq (Conselho Nacional de Desenvolvimento Científico e Tecnológico) for their financial support to the present research (grant number 423968/2018-1).

References

- [1] T. Shioga, Y. Mizuno, and H. Nagano, "Operating characteristics of a new ultra-thin loop heat pipe," *International Journal of Heat and Mass Transfer*, 2020, 151
- [2] K. G. Domiciano, L. Krambeck, J. P. M. Floréz, and M. B. H. Mantelli, "Thin diffusion bonded flat loop heat pipes for electronics : Fabrication , modelling and testing," *Energy Conversion and Management*, 2022, 255, November 2021:
- [3] Y. F. Maydanik, M. A. Chernysheva, and V. G. Pastukhov, "Review: Loop heat pipes with flat evaporators," *Applied Thermal Engineering*, 2014, 67, 1–2:, p. 294.
- [4] M. B. H. Mantelli, *Thermosyphons and Heat Pipes: Theory and Applications*. Cham: Springer International Publishing, 2021.
- [5] P. Kumar, M. Gachake, and S. Khandekar, "Effect of wick oxidation on the thermal performance of a copper-acetone loop heat pipe," *Applied Thermal Engineering*, 2022, 200, October 2021:, p. 117627.
- [6] W. Ling, W. Zhou, W. Yu, and X. Chu, "Capillary pumping performance of porous copper fiber sintered wicks for loop heat pipes," *Applied Thermal Engineering*, 2018, 129, p. 1582.
- [7] Y. Maydanik, S. Vershinin, M. Chernysheva, and S. Yushakova, "Investigation of a compact copper-water loop heap pipe with a flat evaporator," *Applied Thermal Engineering*, 2011, 31, 16:, p. 3533.
- [8] J. P. Holman, *Experimental methods for engineers*, 8th ed. New York, USA, 2011.
- [9] Y. F. Maydanik, "Loop heat pipes," 2005, 25, p. 635.
- [10] M. A. Chernysheva, S. V. Vershinin, and Y. F. Maydanik, "Operating temperature and distribution of a working fluid in LHP," *International Journal of Heat and Mass Transfer*, 2007, 50, 13–14:, p. 2704.
- [11] G. Zhou, J. Li, and L. Lv, "An ultra-thin miniature loop heat pipe cooler for mobile electronics," *Applied Thermal Engineering*,

Theoretical and experimental investigation of rotating heat pipes

Wessel W. Wits^{1*}, Henk Rompelman², Yannick Jeggels², Davoud Jafari¹ and Norbert Engelberts²

¹ University of Twente, Enschede, Netherlands

² Optimal Thermal Solutions B.V., Bussum, Netherlands

*Corresponding author email address: w.w.wits@utwente.nl

Abstract

This paper presents the thermal behaviour of heat pipes that rotate in the horizontal plane. Enabling high-performance electronics cooling, working under various operating conditions, necessitates a deep understanding of the system in which heat pipes play a critical role. Depending on the orientation of the heat pipe with respect to the rotating arm, the working fluid experiences acceleration forces that may either promote or hinder working fluid circulation. In this paper, we address the following question: *to what extent does the system design dictate heat pipe performances?* To this goal, (1) we established an analytical model based on conventional heat pipe limits to predict heat pipe performance taking rotational speed and resulting centrifugal forces into account, and (2) we developed an experimental set-up to validate model predictions. Hereto, two heat pipes are mounted on opposite ends of a rotating beam. The radial offset with respect to the rotational axis, rotational speed and the heat pipe's mounting angle with respect to the rotating beam were varied systematically. A commercially available copper-water heat pipe Ø10x250 mm with a sintered wick was examined. Experimental results show consistent results for operation in both static and rotating environments. Moreover, static heat pipe models show good agreement and may be used for rotating heat pipes provided that the gravitational constant is adjusted accordingly. Above 1g of opposing acceleration forces on the liquid flow, heat pipe performance quickly diminishes and evaporator dry out was observed. Acceleration forces supporting the liquid flow show similar results as a correctly functioning heat pipe; however, the capillary limit can be significantly extended.

Keywords: Electronics cooling; Thermal management; Rotating heat pipes; Experimental investigation

1. Introduction

Due to the fourth industrial revolution, systems are getting more digitized and connected. As a consequence, the amount of electronics inside such systems is increasing. As the reliability of electronic components is heavily influenced by temperature, thermal management is becoming progressively more dominant and already important at the system design level. Heat pipes nowadays are an important asset to the (thermal) engineers' toolkit in their quest to improve system performances. By exploiting a fluid's phase-change behaviour high heat transfer performance can be achieved in a small form factor

[1,2]. While originally predominantly used in aerospace applications, due to the miniaturization and performance increase of electronic components, heat pipes have become a well-established solution in electronics cooling. This can also be observed by the number of heat pipe publications annually in Figure 1, showing a sharp increase at the turn of the century, which can be correlated to the criticality of electronics cooling.

In this study, heat pipes that operate in a rotating environment are examined. Rotation results in continuous centrifugal forces that are exerted on the working fluid in addition to the gravitational forces.

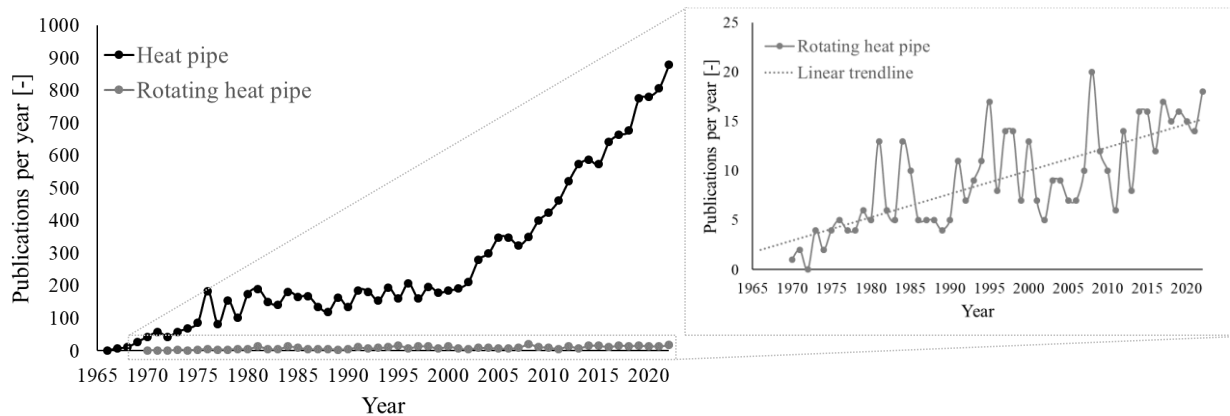


Figure 1. Annual publications concerning heat pipes and specifically rotating heat pipes; source Scopus.com (data retrieved on December 5th, 2022) using keywords: rotating, revolving, whirling, gyrating and spinning to catalogue rotating heat pipes.

First publications on rotating heat pipes appear around 1970 discussing wickless rotating heat pipes. Thereafter, as shown by the inset in Figure 1, a relatively constant growth in annual publications can be observed up to about 15 annual publications in 2022. This shows that 1) compared to heat pipes in general, rotating heat pipes are relatively little researched, 2) research interest in rotating heat pipes did not follow the aforementioned change in trend at the turn of the century, but 3) there is a steadily growing interest. The fact that the sharp increase at the turn of the century is not correlated to publications on rotating heat pipes suggests that rotating heat pipes are not applied abundantly for electronics cooling (yet).

1.1. Background on rotating heat pipes

The first rotating heat pipe was based on a rotating wickless hollow shaft [3]. A hollow shaft conical in shape and rotating along its longitudinal axis may return the working fluid utilizing centrifugal acceleration rather than capillary pressure [4]. In 1973, modelling enabled predicting heat pipe performance “to within plus or minus 20 percent” [5]. The work of Daniels [6,7] between 1975 and 1980 aided a lot in analysing factors affecting the performance of a rotating heat pipe.

For conventional heat pipes used in electronics cooling applications, the capillary limit is often the critical limitation [8]. The advantage of a rotating heat pipe is superior working fluid transport capability due to the centrifugal acceleration [9]. Needless, the intended application needs to facilitate a rotating environment. Reported applications are e.g. in turning [10], drilling [11], grinding [12], abrasive milling [13], continuous annealing [14], and motorized spindles [15]. In these cases, cooling is required due to mechanical (manufacturing) processes.

Similar to the conclusion of Figure 1, the utilization of rotating heat pipes in electronics cooling applications was not found. In fact, to the knowledge of the author team, in the field of electronics cooling, no applications were reported

other than rotating radar systems [16]. However, with the advent of the Internet of Things (IoT), there is a plethora of smart products and related use-cases brought to the market [17]. Typical for IoT devices is that they are physical devices embedded with electronics (e.g. sensors, actuators, network connectivity), which enable these devices to connect and exchange data. As the performance demand, e.g., sensing or computing power, of such products will continue to increase, so will the need for better cooling solutions. Finally, since IoT devices are ideally positioned on non-stationary, e.g. rotating objects, this introduces the timely need for this study. Needless, next to continuous rotation, heat pipes are also finding application in mobile platforms such as train and electric vehicle cooling systems. Thus, there is a need to study the fundamental guiding principles for predicting heat pipe performances under different terrestrial, non-stationary conditions that impact the operation of electronics components and systems.

2. Theoretical modelling

Gravity and rotation introduce acceleration vectors in the radial and axial directions of the heat pipe, which must be accounted for as they affect working fluid circulation [16]. In this study, the heat pipe is revolving in the horizontal plane around a central axis introducing a centrifugal force, as shown in Figure 2. The heat pipe’s radial offset r in combination with the rotational speed N will determine the body forces the working fluid experiences. The mounting angle α determines the centrifugal contribution the heat pipe experiences. For sufficient working fluid circulation, the axial acceleration component is the most important, as this component either promotes or hinders working fluid return from the condenser to the evaporator section. For a mounting angle of 0° , the heat sink (i.e. the condenser section) is oriented towards the central axis and hence working fluid is duly propelled towards the evaporator section. In the opposite case, for a mounting angle of 180° , the heat source (i.e. the evaporator section) is oriented towards the central axis and working fluid must be

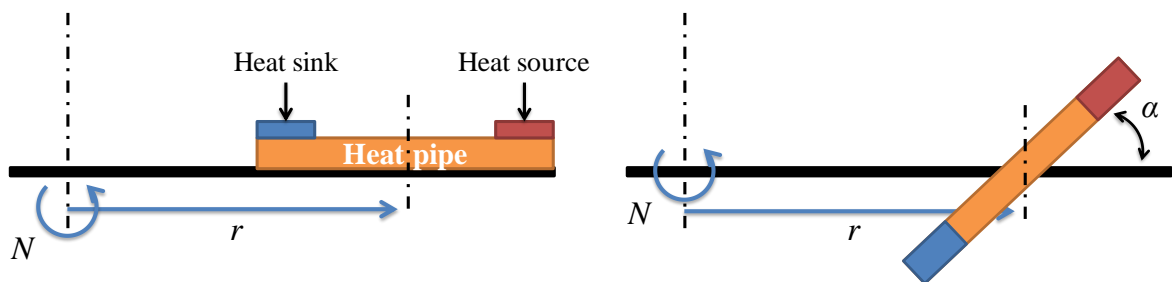


Figure 2. Illustration of the rotating heat pipe set-up: side view (left) and top view (right).

transported against the centrifugal force contribution of the rotating set-up. For a mounting angle of $\pm 90^\circ$, no acceleration vector is present in the axial, working fluid transport direction at the midpoint of the heat pipe. Away from the midpoint the heat pipe does not exactly follow the circle of rotation and hence a minor contribution in axial direction will be present here. In this study however this contribution, which also has an opposite direction on the other side of the midpoint, is neglected.

As the set-up rotates in the horizontal plane, the centrifugal acceleration a_c can be defined as:

$$a_c = \omega^2 \cdot r \rightarrow a_c = \left(\frac{2\pi}{60}\right)^2 \cdot N^2 \cdot r \quad (1)$$

where, N [rpm] is the rotation speed and r [m] is the radial offset from the rotational axis. As aforementioned, this centrifugal acceleration may either hinder or promote working fluid circulation depending on the heat pipe's mounting angle. The axial acceleration a_x can be described as:

$$a_x = a_c \cdot \cos \alpha \rightarrow a_x = \left(\frac{2\pi}{60}\right)^2 \cdot N^2 \cdot r \cdot \cos \alpha \quad (2)$$

where, a positive axial acceleration refers to working fluid being promoted towards the evaporator section. Vice versa, a negative axial acceleration refers to the situation in which the wick structure must overcome the acceleration vector similar to a working fluid ascending against gravity.

For stationary heat pipes in a terrestrial environment, the capillary limit is well described in literature. Here, we adopt the description of Faghri [1], assuming that working fluid and wick properties are constant along the heat pipe length and vapour flow properties may be neglected:

$$\dot{Q}_{cap,max} = \left[\frac{\rho_l \sigma_l h_v}{\mu_l} \right] \left[\frac{KA}{l} \right] \left[\frac{2}{r_c} + \frac{\rho_l g l}{\sigma_l} \cos \varphi \right] \quad (3)$$

where, in the first bracket thermodynamic working fluid properties are given: liquid density ρ_l , surface tension σ_l , latent heat of vaporization h_v and liquid viscosity μ_l . The second bracket describes wick structure properties: permeability K , cross-sectional surface area A and axial length l . Finally, the last bracket describes the driving force generated by the wick's pore radius r_c and gravitation acceleration contribution by the heat pipe's orientation angle φ . In this case, an orientation angle of 0° denotes bottom heating and the promotion of working fluid flow towards the evaporator section by gravity.

Equation (3) describes the axial acceleration due to the orientation in the gravitation field in a similar manner as Equation (2) describes the orientation

with respect to the centrifugal acceleration. In both cases, an angle of 0° denotes a positive contribution by either centrifugal or gravitational acceleration, while an angle of 180° denotes hindering or ascending of the working fluid due to continuous rotation or gravity, respectively.

In the experimental work of this study, the parameters N and r of Equation (1) have been selected such that the centrifugal acceleration equals the gravitational acceleration:

$$\left(\frac{2\pi}{60}\right)^2 \cdot N^2 \cdot r = n \cdot g \quad (4)$$

where, n [-] indicates the number of g -forces. Hence, by adjusting n , stationary heat pipe experiments can be compared to rotational heat pipe experiments, as will be discussed in the Chapter 4.

3. Experimental set-up

In order to study the effects of a rotating environment, a purpose-built experimental set-up was developed according to Figure 3. A central beam was mounted on a rotating platform. In order to balance the set-up, two heat pipes were mounted on opposite ends of the beam. This also allowed for faster collection of experimental data. The motor and motor controller, which control the rotational speed of the system, are shown at the bottom. Input power to generate a heat load is transferred across a rotary joint to the rotating beam and heat pipes. Finally, temperature recordings are stored locally by a data acquisition unit that sits in the middle of the beam. Acquired data was offloaded after a number of experimental runs.

Commercially available copper-water heat pipes were tested. As the working fluid is known (i.e. water), thermodynamic fluid properties of Equation (3) can be found in literature assuming a working fluid temperature. A heat pipe of 250 mm with an outer diameter of $\varnothing 10$ mm was selected as test specimen. The heat pipe's wall thickness and the thickness of the sintered wick were 0.60 mm and 0.83 mm, respectively, as shown in Figure 4. This leaves a vapour flow passage of $\varnothing 7.1$ mm, which (after calculation) satisfies the assumption of Equation (3) that vapour flow properties may be neglected compared to liquid flow through the wick structure. Unknown parameters of Equation (3) are the wick's effective pore radius r_c and permeability K . The former has an influence on the capillary pressure and is an important parameter for operation against an axial acceleration, while the latter is a measure of the liquid flow resistance. In fact, the ratio of the two is often used to evaluate and rank

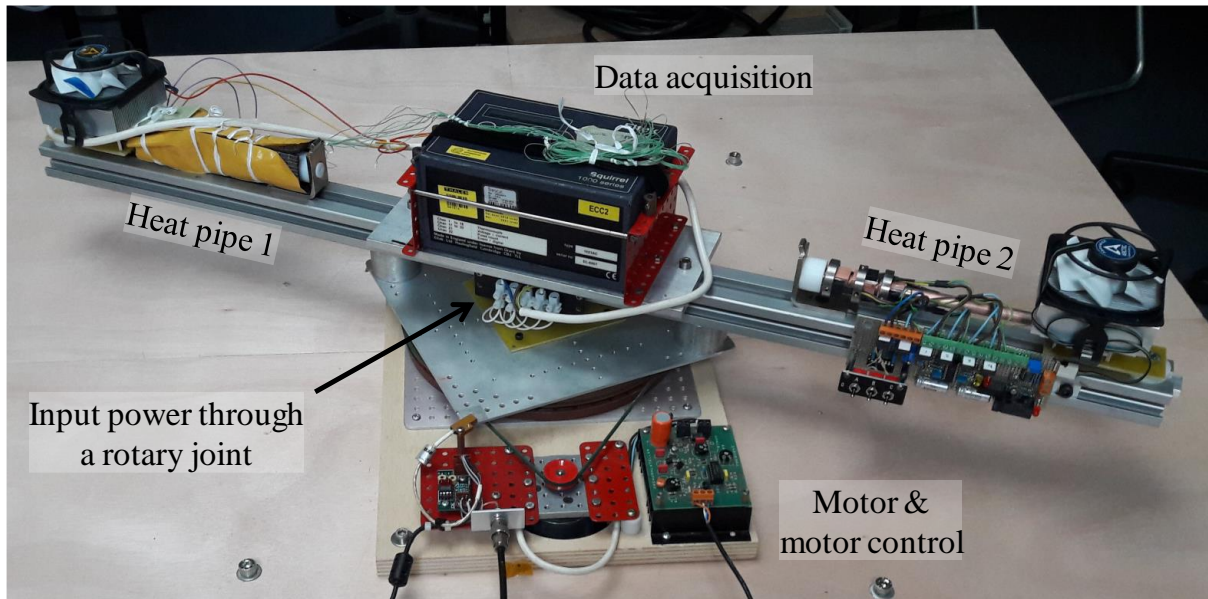


Figure 3. Experimental set-up showing two heat pipes on a beam rotating around a central axis.

capillary structures [18]. In this study, both parameters were determined experimentally.

The heat pipe was mounted on the rotating beam with its midpoint at a radial offset of 348 mm. The platform rotation was varied from 36 rpm to 72 rpm, which would allow for an axial acceleration of 0.5g to 2.0g, according to Equation (4).

At the evaporator end, heat is inserted using three times two power Metal-Oxide-Silicon Field-Effect Transistors (MOSFETs). A set of power MOSFETs was clamped on opposite sides of a copper block, which was soldered to the heat pipe. Voltage and forward current were recorded to measure the input power. At the condenser end, heat is expelled to the environment using a fan-driven heat sink. The heat sink was also clamped on a copper block soldered to the heat pipe. Copper and soldering were applied to have a good conductive connection into and out of the heat pipe. Figure 4 shows the experimental

configuration of both the evaporator and condenser sections. During the experiment, the heat pipe was encapsulated, as Heat pipe 1 in Figure 3, to minimize heat losses to the environment.

Heat pipe performance was determined by measuring the temperature gradient across the axial length, as shown in Figure 5. Eleven Type-K thermocouples were used to measure the temperatures logged by the data acquisition unit sitting at the middle of the rotating beam. The evaporator temperature was measured at six locations: three times on the copper blocks (e_1 , e_3 and e_5) and three times directly on the heat pipe next to the copper block (e_2 , e_4 and e_6). The temperature of the adiabatic section was measured midway the heat pipe (a_1). The condenser temperature was measured at four locations: once directly on the heat pipe just before the copper block (c_1) and at three locations inside the copper block (c_2 , c_3 and c_4).

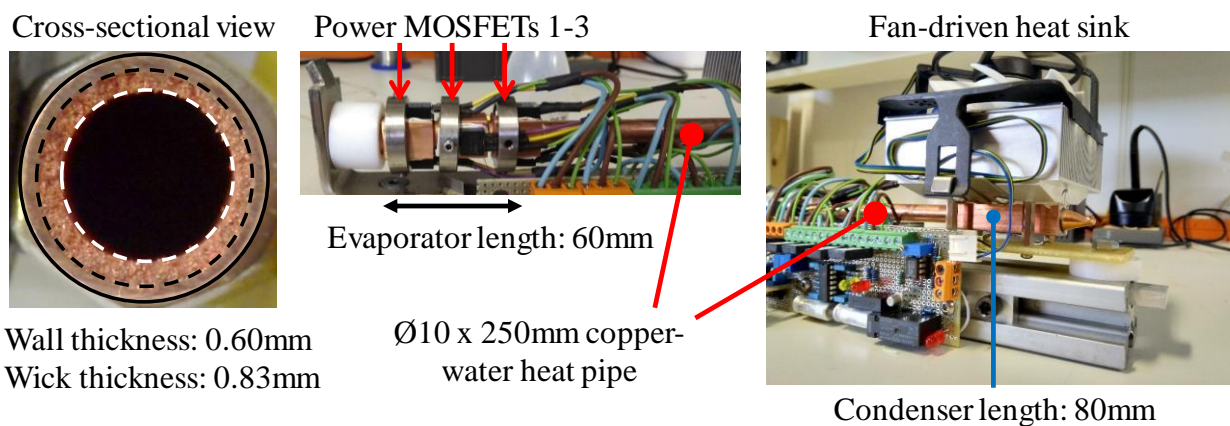


Figure 4. Configuration of evaporator, condenser and cross-sectional geometry of the heat pipe.

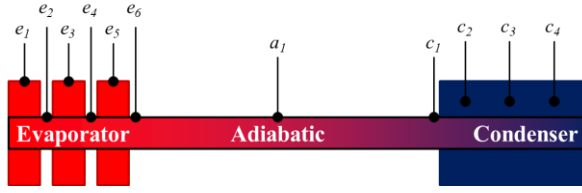


Figure 5. Thermocouple locations along the heat pipe length schematically.

For each measurement sufficient time was taken for the set-up to reach a (new) steady-state situation. Performance was determined by defining the heat pipe's temperature gradient as the difference in average temperatures between the evaporator and condenser sections:

$$\Delta T = \frac{\sum e_i}{6} - \frac{\sum c_i}{4} \quad (5)$$

As dry out first occurs at the outmost copper block also the spread of evaporator temperatures is taken into account. The maximum and minimum temperatures measured at the evaporator section were compared to the average evaporator temperature. This spread is depicted as an error bar in the measurement results. As the spread enlarges, evaporator dry out commences from the outmost heater location.

4. Experimental investigation

4.1. Initial static heat pipe measurement

Initially heat pipes were tested in a conventional manner in a static set-up. Five orientations were considered from evaporator down ($\varphi = 0^\circ$) to evaporator up ($\varphi = 180^\circ$) modes. The former is hereafter defined as $+1g$, while the latter is defined as $-1g$ referring to the direction of the working fluid's liquid phase in relation to the (gravitational) acceleration. Similarly, 45° , 90° and 135° are defined as $+0.7g$, $0g$ and $-0.7g$.

Figure 6 shows the thermal gradient according to Equation (5) in relation to the input power for the five orientations. The markers indicate the measured average, while the error bars indicate the aforementioned spread at the evaporator section. The figure shows that if the evaporator is below the condenser (i.e. $+1.0g$ and $+0.7g$) the heat pipe functions correctly and no dry out was observed. In fact, the thermal performance in both cases is nearly identical. The thermal gradients show a linear trend in relation to the input power and, hence, the quotient, also known as the thermal resistance, is constant at around 0.1 K/W . In horizontal mode dry out occurred at around 100 W . In the case, the evaporator is above the condenser dry out occurs much sooner, as can be expected. At $-1.0g$ and $-0.7g$

dry out commenced at 25 W and 50 W , respectively.

From Figure 6, the unknown parameters describing the wick properties from Equation (3) were determined. The wick's pore radius r_c and permeability K were found by minimizing the input power difference between the three dry-out limits that were found experimentally and the computed capillary limit of Equation (3). The wick's effective pore radius and permeability were found to be $25 \mu\text{m}$ and $4.0 \cdot 10^{-11} \text{ m}^2$, respectively, assuming a working fluid temperature of 70°C . Both numbers are in line with other literature sources; e.g., the review paper of Jafari et al. [18] determines values around $25 \mu\text{m}$ and $1.0 \cdot 10^{-11} \text{ m}^2$ for the effective pore radius and permeability of a sintered wick, respectively, and Mwaba et al. [19] specify $30 \mu\text{m}$ and $1.2 \cdot 10^{-11} \text{ m}^2$, respectively.

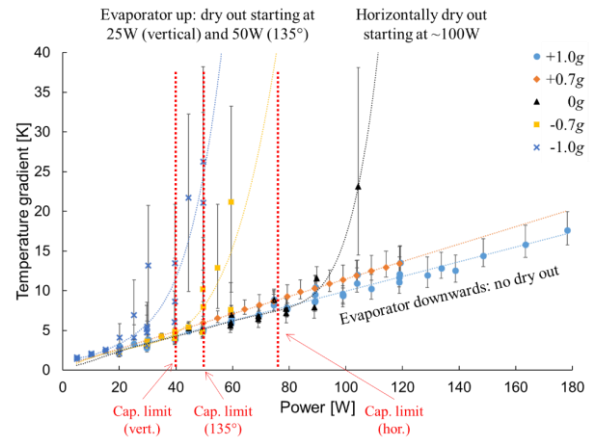


Figure 6. Heat pipe thermal gradient in a static set-up for five orientations.

Using the experimentally determined wick parameters, the capillary limit for the vertical, 135° and horizontal orientations were computed to be 40 W , 50 W and 75 W , respectively. These limits are also depicted in Figure 6 by the three vertical dotted red lines. For the evaporator up modes, the found limit corresponds well. In the horizontal case however dry out was estimated already at 75 W . The offset compared to the experimentally found limit around 100 W may be explained by the fact that the heat pipe with additional peripherals, such as heaters, cooling fan, insulation, etc., could have easily been oriented slightly off the horizontal axis.

4.2. Rotating heat pipe measurements

In the first rotating experiment, the heat pipes were oriented with the evaporator section on the outside (i.e. $\alpha = 0^\circ$); hence, subjecting the working fluid's liquid phase to a positive acceleration. Two rotational speeds were tested (51 rpm and 72 rpm)

giving the working fluid a +1.0g and +2.0g acceleration at the midpoint of the heat pipe. The experimental results are shown in Figure 7. For reference, also the static evaporator down measurement is shown in the figure.

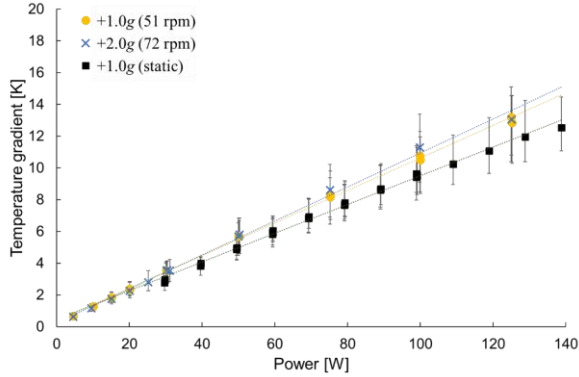


Figure 7. Temperature gradient while rotating with positive acceleration towards the evaporator.

Figure 7 demonstrates that the heat pipe response to a positive 1g axial acceleration due to a centrifugal force is similar to a static gravitational acceleration. The figure also demonstrates that a higher acceleration force does not give better performance: the heat pipe is already working optimally. Minor differences between the rotating results and the stationary results may be explained by the fact that during rotation next to the axial acceleration, there is also a radial acceleration vector, which is not present in the stationary case. Also, the performance of the cooling fan at the condenser section may differ from stationary to rotating. As observed, this results in a slightly poorer performance at higher input powers.

More practically, this result shows that from an engineering perspective axial acceleration towards the evaporator due to rotation may be modelled as a heat pipe operating in an evaporator down mode vertically in the gravitational field. Also the thermal resistance remains similar to the stationary case at around 0.1 K/W.

In the second rotating experiment, the heat pipes were oriented with the evaporator section towards the rotation axis (i.e. $\alpha = 180^\circ$); hence, subjecting the working fluid's liquid phase to a negative acceleration. Four rotational speeds were tested (from 36 rpm to 72 rpm) giving the working fluid a -0.5g to -2.0g acceleration at the midpoint of the heat pipe. The experimental results are shown in Figure 8. Again, for reference, this time the static evaporator up measurement is shown in the figure. The dotted lines indicate a polynomial fit through the data points to illustrate the overall trend.

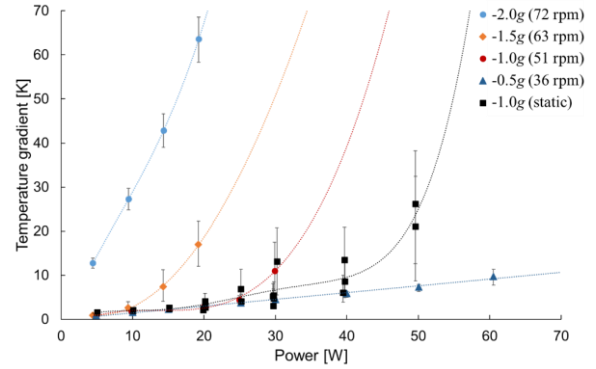


Figure 8. Temperature gradient while rotating with negative acceleration towards the evaporator.

Figure 8 demonstrates that heat pipe responses to a negative axial acceleration due to a centrifugal force of 1.0g and higher are similar to a static gravitational acceleration. The onset of evaporator dry out in a rotating environment at -1.0g is around 30 W almost identical to 25 W for the static -1.0g case. As no steady-state measurements were taken above 30 W for the rotating -1.0g case, the rise (red dotted fit) above 30 W may be considered arbitrary.

At higher axial accelerations of -1.5g and -2.0g, evaporator dry out commences at lower power loads, as can be expected from Equation (3). According to this model, as aforementioned, at -1.0g dry out commences at 40 W. Following this model, at -1.5g and -2.0g dry out should commence at 23 W and 6 W, respectively. This is also reflected in the measurement results of Figure 8. Hence, similar to above, also axial acceleration towards the condenser section due to rotation may be modelled as a heat pipe operating in an evaporator up mode. The actual axial acceleration may be modelled by adjusting the gravitational constant g of Equation (3) using the number of g -forces n of Equation (4).

Finally, at -0.5g the model predicts dry out at 58 W. The heat pipe remained operational successfully until 60 W. Measurements at higher heat loads were not conducted; however, at 60 W the evaporator spread already increased compared to the 50 W measurement. It may therefore be assumed that dry out would have commenced at the next higher heat load setting.

In the third rotating experiment, the platform rotation was set to a constant value of 51 rpm and the mounting angle of heat pipes was adjusted from 90° to 180° between measurements, effectively going from a 0g condition to a -1.0g condition. The experimental results are shown in Figure 9. Note that the results at 180° are identical to the -1.0g results of Figure 8 and for reference the static measurements are shown as well.

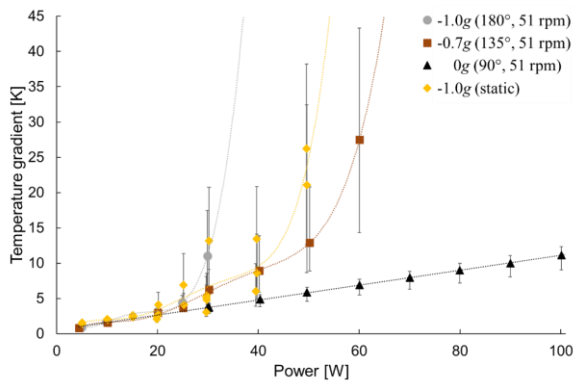


Figure 9. Temperature gradient while rotating with constant speed and adjusting the mounting angle.

In essence, Figure 9 shows similar heat pipe responses as was the case for the aforepresented increasing negative axial acceleration. The onset of evaporator dry out for the $-1.0g$ cases are similar to Figure 8. At $-0.7g$ the model predicts dry out at 51 W, while the measurements show that the onset is earlier around 30 W; however, the exponential rise in temperature occurs above the 50 W measurement. For $-0.7g$, between 20 W and 50 W the figure indicates a linear trend between temperature gradient and input power. The thermal resistance here is about 0.3 K/W, three times higher than the 0.1 K/W of the $0g$ measurement and the positive axial acceleration cases of Figure 7. As the heating elements were positioned on opposite sides of the heat pipe, it is likely that due to the also acting radial acceleration forces at a mounting angle of 135° , the thermal resistance of the evaporator is higher as can also be deduced from the temperature spread.

5. Conclusions and recommendations

Theoretical and experimental work for heat pipes in a rotating environment has been presented. Successful heat pipe operation and experimental performances were determined for a number of application parameters. The influence of centrifugal forces on the axial acceleration of the liquid phase of the working fluid has been discussed. Also the thermal performances of stationary and rotating heat pipes have been compared.

Results have shown that when the rotation promotes axial acceleration towards the evaporator the heat pipe's capillary limit, i.e. Equation (3), for an evaporator down mode vertically in the gravitational field may be used. Vice versa, when the rotation hinders axial acceleration towards the evaporator, the capillary limit may be used as well. In fact, the actual axial acceleration may be mimicked by adjusting the gravitational constant.

When the heat pipe functions correctly, the heat pipe's thermal resistance during rotation is similar to the stationary case at around 0.1 K/W. During dry out the thermal resistance increases exponentially as can be expected. For positive axial acceleration, a higher acceleration force does not increase the heat pipe's thermal performance. For negative axial acceleration, heat pipe performance quickly deteriorates.

In the current set-up, commercially available copper-water heat pipes were tested. This study presented results for a $\text{Ø}10 \times 250$ mm heat pipe with a sintered wick. In future work also other geometries will be considered, as well as different types of wick structures. Moreover, rather than only rotating in the horizontal plane, the platform can also be set at an angle or more interestingly on a 6-DOF movable platform. In the latter case, motion control needs to be coupled to the position and velocity of the heat pipe in space.

References

- [1] A. Faghri, *Heat Pipe Science And Technology* (Global Digital Press, 2016), Second edn.
- [2] D. A. Reay, P. A. Kew, R. McGlen, and P. D. Dunn, *Heat pipes : theory, design, and applications* (Elsevier, 2014).
- [3] V. H. Gray, The rotating heat pipe-A wickless, hollow shaft for transferring high heat fluxes. American Society of Mechanical Engineers (Series), 1969.
- [4] S. H. Chan, Z. Kanai, and W. T. Yang, Theory of a rotating heat pipe. *Journal of Nuclear Energy*, 1971. 25(10): p. 479.
- [5] P. J. Marto, Analytical and experimental investigation of rotating, noncapillary heat pipes. NASA Contractor Reports, 1973.
- [6] T. C. Daniels and F. K. Al-Jumaily, Investigations of the factors affecting the performance of a rotating heat pipe. *International Journal of Heat and Mass Transfer*, 1975. 18(7): p. 961.
- [7] T. C. Daniels and R. J. Williams, The effect of external boundary conditions on condensation heat transfer in rotating heat pipes. *International Journal of Heat and Mass Transfer*, 1979. 22(8): p. 1237.
- [8] W. W. Wits and J. B. W. Kok, Modeling and Validating the Transient Behavior of Flat Miniature Heat Pipes Manufactured in Multilayer Printed Circuit Board Technology. *J Heat Trans-T Asme*, 2011. 133(8).
- [9] S. F. Li and Z. H. Liu, Parametric study of rotating heat pipe performance: A review. *Renewable and Sustainable Energy Reviews*, 2020. 117.
- [10] R. L. Judd, H. S. MacKenzie, and M. A. Elbestawi, An investigation of a heat pipe cooling system for use in turning on a lathe. *The International Journal of Advanced Manufacturing Technology*, 1995. 10(6): p. 357.
- [11] T. C. Jen, Y. M. Chen, and F. Tuchowski. Investigation of heat pipe drilling application. in American Society of Mechanical Engineers, Heat Transfer Division, (Publication) HTD. 2004.
- [12] J. Chen, Y. Fu, Q. He, H. Shen, C. Y. Ching, and D. Ewing, Environmentally friendly machining with a revolving

- heat pipe grinding wheel. *Applied Thermal Engineering*, 2016. 107: p. 719.
- [13] J. Chen, Y. Fu, Z. Gu, H. Shen, and Q. He, Study on heat transfer of a rotating heat pipe cooling system in dry abrasive-milling. *Applied Thermal Engineering*, 2017. 115: p. 736.
- [14] M. Celik, M. Patki, G. Paulussen, W. De Jong, and B. J. Boersma, Dynamic modeling of the heat pipe-assisted annealing line. *Journal of Heat Transfer*, 2019. 141(9).
- [15] F. Liang, J. Gao, F. Li, L. Xu, Z. Wang, and H. Jiang. A central cooling structure for motorized spindles: Principle and application. in *InterSociety Conference on Thermal and Thermomechanical Phenomena in Electronic Systems, ITherm*. 2019.
- [16] W. W. Wits and G. J. Te Riele, Heat pipe array for planar cooling of rotating radar systems. *Journal of Heat Transfer*, 2019. 141(9).
- [17] J. A. Shipman, S. Chigullapalli, J. Mata, and T. A. Martin. Thermal power envelope for IoT modules. in *Thermal Measurement, Modeling & Management Symposium (SEMI-THERM)*, 2017 33rd. 2017. IEEE.
- [18] D. Jafari, W. W. Wits, and B. J. Geurts, Metal 3D-printed wick structures for heat pipe application: Capillary performance analysis. *Applied Thermal Engineering*, 2018. 143: p. 403.
- [19] M. G. Mwaba, X. Huang, and J. Gu, Influence of wick characteristics on heat pipe performance. *International Journal of Energy Research*, 2006. 30(7): p. 489.

Developing of a gravity independent heat pipe with asymmetric compensating element

K. I. Delendik^{1*}, N. V. Kolyago¹, O. G. Penyazkov¹, O. L. Voitik¹

¹ A.V. Luikov Heat and Mass Transfer Institute of the National Academy of Sciences of Belarus, Minsk, Republic of Belarus

*Corresponding author email address: kdelendik@yahoo.com

Abstract

This work is concerned with developing and investigating of gravity independent heat pipe. It was developed by manufacturing of seamless asymmetric metal compensating element by electrotyping method. The design of heat pipe with this element and application of mesh wicks ensure heat pipe operate stably and reliably at various orientations and positions. Thermal resistance is 0.05–0.07 K/W at 50 W. Developed heat pipe is insensitive to deep freezing, possibility of displacement of the heat source and heat receiver by ± 1.5 mm with mechanical reaction [– 1.9; +2.5 N] at distance between fixing and loading points equal 55 mm.

Keywords: Gravity independent heat pipe; Asymmetric central compensating element; Thermal resistances; Mechanical reaction

1. Introduction

Heat pipe (HP) with a central compensating element of mode of deformation can decrease force reaction and compensate mode of deformation caused during transportation, installation and operation of heat pipes. It has the advantage of applicability in multiple possible configurations where the heat sink may be out of plane with the heat source, allowing heat removal from heat sources [1–5].

At low temperatures the liquid crystallization might severely damage the case of HP. Application of asymmetric central compensating element overcomes these technical challenges. HP with asymmetric figurate-shape bellows can pass successfully a test at temperatures below freezing point of water.

The aim of the paper was to develop a gravity independent heat pipe with an asymmetric central compensating element which exhibits a resistance to deep freezing.

2. Development of HP

HP (Figure 1) consists of a sealed copper case having a rigid flat evaporator section, a rigid flat condenser section, obtained by pressing round tubes with an outer diameter 8 mm, and a flexible metal asymmetric figurate-shape bellows adiabatic section located between the evaporator section and the condenser section along a longitudinal length inside the body; a working fluid – water contained inside the HP; a wick structure disposed along the length of the body, wherein the wicking structure comprises a series of parallel meshes. The total length of HP excepting charging tubes is 130 mm,

the length of the central compensating element is 45 mm.

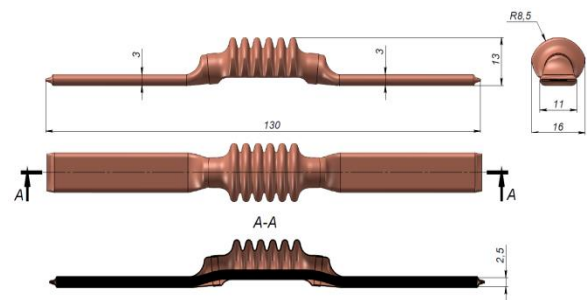


Figure 1. Heat pipe drawing.

Creation of HP consists of next milestones: shaping of edge sections of the case, manufacturing of asymmetric central compensating element, wick manufacturing, heat pipe assembly, charging, testing.

2.1. Shaping of edge sections of the case

Molding press for thin-walled copper tubes was designed and manufactured (Figure 2–Figure 4). The external height of tube is 3.3 mm. Edge sections are presented in Figure 5.

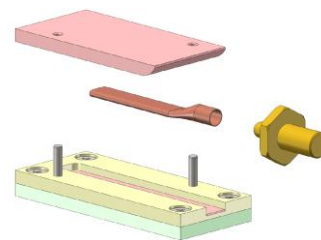


Figure 2. Sketch of set for tube shaping.

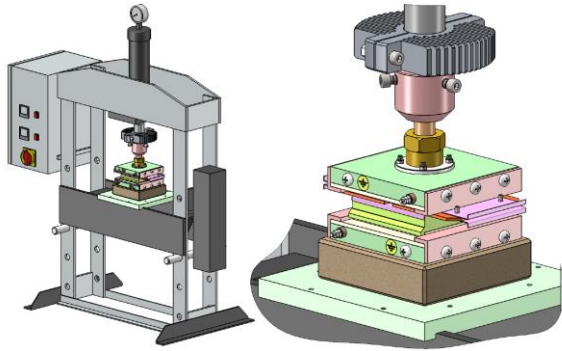


Figure 3. Molding press sketch.



Figure 4. Photo of molding press.



Figure 5. Photo of edge sections.

2.2. Design of asymmetric metal compensating element

Such methods as corrugation (mechanical, hydraulic, elastomeric, etc.), chemical and electrotyping methods are used for metal bellows manufacturing

Mechanical, hydraulic and elastomeric methods are based on the deformation of material in special molds. The process consists of several steps: rolling metal in a tube, welding, fold's forming and their subsequent treatment. Small and medium-sized bellows can be produced by these methods [6,7]. These methods have a number of disadvantages: high cost of equipment and impossibility of making irregular or complicated bellows.

Chemical method consists of metal deposition during metal reduction reactions on a precise mold [8]. Coating thickness depends on reaction time.

Bellows has uniform thickness and small amount of internal tension after the mold separation and thermal treatment. Main disadvantages are necessity of preliminary estimation of reaction velocity and impact of edge boundary effects on forming metal film.

Electrotyping method is similar to chemical method but deposition of metal on the mold occurs due to the electrochemical reaction.

Main advantage of electrotyping method consists in the possibility of manufacturing bellows with any wall thickness and complexity of the detail [9]. Bellows manufactured by electrotyping method require less mechanical treatment because reaction can be conducted in conditions that provide metal coating with high surface quality. Thermal treatment after deposition decreases amount of internal tensions, leading to good durability and deformation properties of a final product. Thus, electrotyping method is the most promising method of metal figurate-shape bellows manufacturing.

Seamless asymmetric metal compensating elements (Figure 6, Figure 7) was developed by electrotyping method (Figure 8). Seamless designs show very tight tolerances with long life-cycle for high-precision applications.

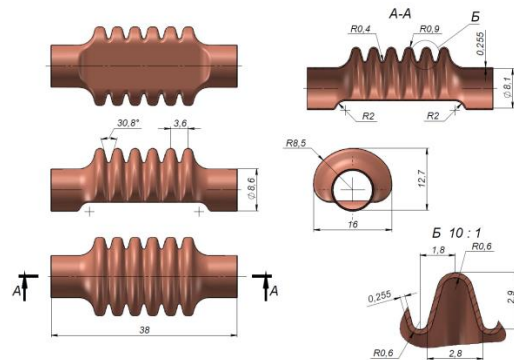


Figure 6. Drawing of asymmetric central compensating element.



Figure 7. Photos of asymmetric central compensating element.

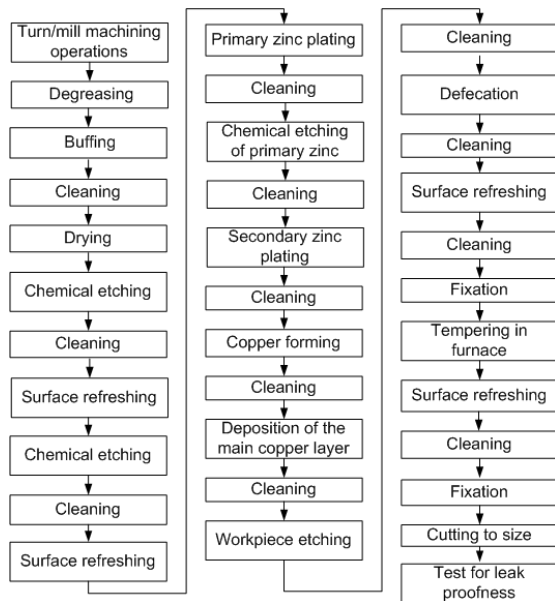


Figure 8. Block schematic diagram of technology process of bellows forming.

2.3. Design of wick

Wick was formed by a set of braided brass #210 mesh (cell size is 0.071 mm, wire diameter is 0.050 mm) [10].

The wick width was 5 mm (Figure 9). In order to avoid creases at the edges using a cutting tool and to obtain an accurate mesh width, a laboratory technology was developed on the base of photolithographic method.



Figure 9. Photo of wick assembly.

Thickness of the wick after crimping by hot molding press is 2.3 mm.

Porosity of wick by weighting $\varepsilon=0.524\pm 0.03$, $RE=5.7\%$ with a confidence level of 0.95. Wick permeability was $K = 90\pm 2.5 \mu\text{m}^2$, $RE=2.8\%$ with a confidence level of 0.95.

2.4. Heat pipe assembly

Compensating element and edge sections were soldered. Wick was pulled through case. Assembly was crimped by hot molding press (350°C) in set to external height of 3 mm (Figure 10). Charging

tube was welded to case.

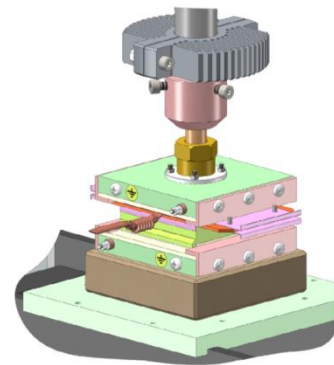


Figure 10. Sketch of molding press with pipe.

2.5. Charging

Charging set (Figure 11) with degassed working fluid was worked out for evacuation to pressure of approximately 10^{-6} bar and accurate filling of 0.05–1.5 ml sized volumes (figure 7). Basic to this procedure is microsyringe charging method [11,12]. Syringe was used to feed the required quantity of fluid into an evacuated HP. Dead volumes in T-joints and other connectors were estimated to predict the actual charged amount.

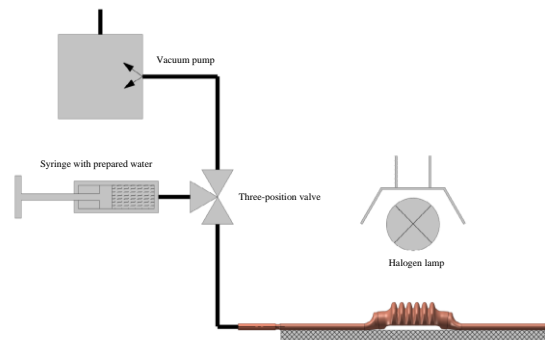


Figure 11. Scheme of charging set.

After charging HP was sealed (Figure 12).

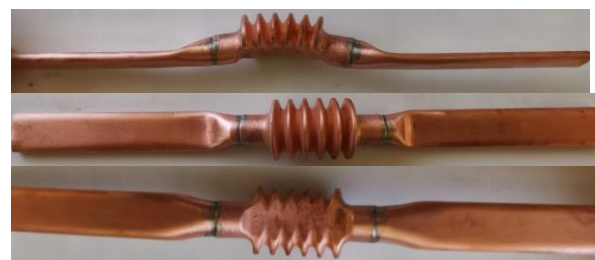


Figure 12. Photos of heat pipe.

3. HP performance

The thermal performance test (Figure 13) was focused on measuring the temperature of HP case during operation of HP with applied power of 50 W. Heater was used to supply the power to HP. Dimensions of the electric heater: length $L(h) = 40$ mm, width $W(h) = 35$ mm. A digital power meter was connected to the variac for the measurement of the input power Q_{in} .

$$Q_{in} = IU \quad (1)$$

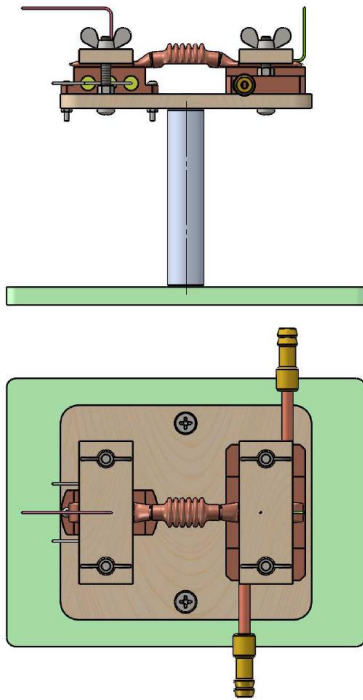


Figure 13. Scheme of experimental set for thermal testing.



Figure 14. Photos of test section with HP.

Water jacket was set on bottom of the condenser surface of HP for heat removal. Dimensions of the cooler: length $L(c) = 40$ mm, width $W(c) = 36$ mm.

A layer of thermal compound Prolimatech PK-3 with the thermal conductivity of 11 W/m K was smeared on the contact surface between heater and HP, and the contact one between water jacket

and HP to reduce the contact thermal resistance. A wood insulating blocks were set under heater and cooler to minimize the heat loss and also hold the entire assembly in a stable position. The blocks have holes for thermocouple mounting.

The electric heater was supplied with an electrical power $Q = 50 \pm 2$ W, and at the same time water was supplied to the cooler. Steady state condition of HP was considered a state at which changes of temperatures T_1 , T_2 and T_0 with rate $\leq 1^\circ\text{C}$ in 5 minutes. Water temperature and flow rate were adjusted in such a way that: the temperature value T_0 at steady state operation of HP do not exceed 70°C . Throughout the testing process, the cooling water was kept at a constant flow rate and constant inlet temperature. All the K-type thermocouple measurements were collected by data acquisition system synchronized to a computer at 1 s intervals.

Thermal resistance of HP R was calculated as

$$R = \frac{T_1 - T_2}{Q} \quad (2)$$

where Q is heat load; T_1 is temperature of evaporator part (thermocouple T_1); T_2 is temperature of the condenser part (thermocouple T_2). Since the whole assembly is wrapped by thermal insulation materials, the heat loss was thought to be negligible, as the experimental results confirm, Q_{in} differs slightly from Q_{out} (Q_{out} was approximately 97% of applied power Q_{in}). Thus in the following calculations Q_{in} was used. Uncertainty of measurements was determined. Source of experimental uncertainty is in all measurements: temperature, voltage, current. Calibration of thermocouples was carried out with an accuracy of 0.1°C . Uncertainty of measurement was estimated by employing error propagation method.

Thermal resistances were 0.068 ± 0.007 K/W at horizontal orientation (Figure 15), 0.061 ± 0.006 K/W at vertical orientation when heat source was above cooler (Figure 16), 0.050 ± 0.005 K/W at vertical orientation when cooler was above heat source (thermosyphon orientation) (Figure 17). Thus developed HP was gravity-independent, adapted to work in various conditions of orientation and localization.

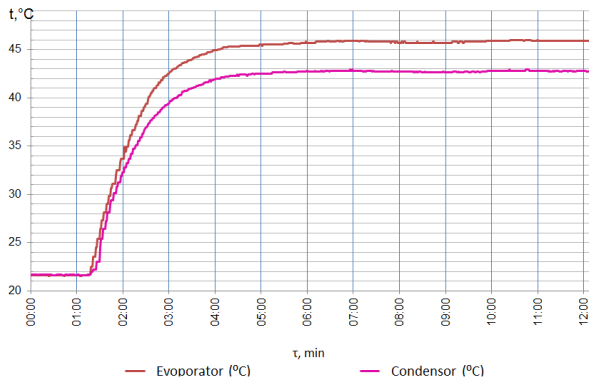


Figure 15. Temperature dependence at horizontal orientation.

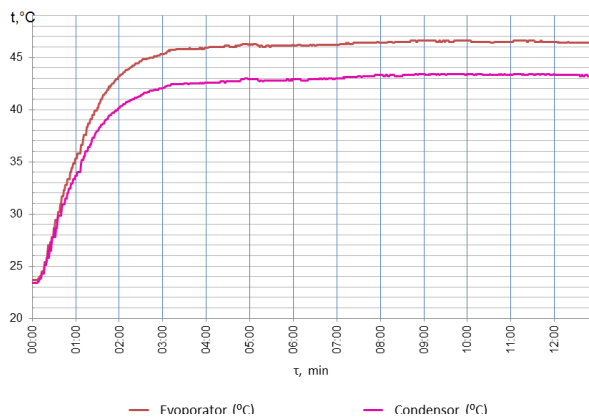


Figure 16. Temperature dependence at vertical orientation.

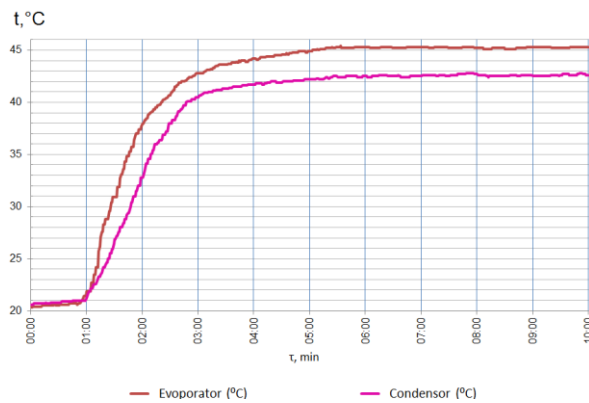


Figure 17. Temperature dependence at thermosyphon orientation.

4. Mechanical characteristics

The mechanical characteristics of HP were tested by measuring the mechanical reaction during 21 cycles of loading, which were carried out using a tensile machine INSTRON 5567 and a tooling (Figure 18, Figure 19).



Figure 18. Photos of tensile machine INSTRON 5567.

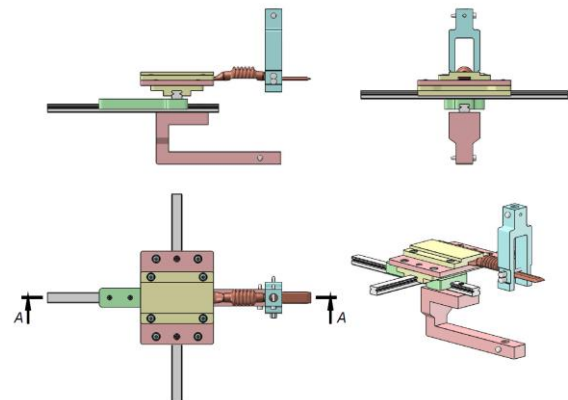


Figure 19. Scheme of experimental set for mechanical testing.

One end of HP was tightly attached to the tooling (Figure 20). At the second end of HP, the grip of the tensile machine was hinged on flat sections at the transition point from flat section to round section. The grip was moved cyclically by ± 1.5 mm 21 times. Velocity of movement of grip was 0.15 mm/s. During the cyclic loading, the reaction force was recorded. The distance between the fixing and loading points of HP is 55 ± 1 mm.

The test results are shown on Figure 21.

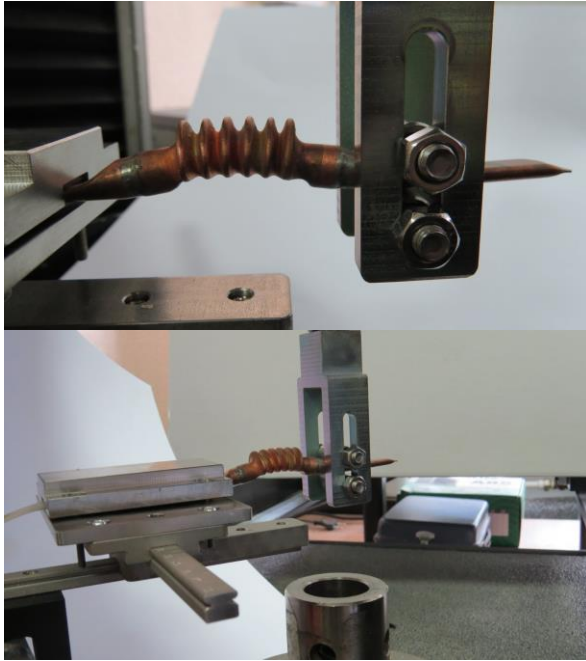


Figure 20. Photos of mechanical testing.

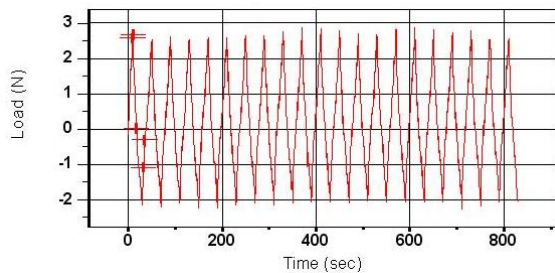


Figure 21. Dependence of the reaction force of HP on time.

Developed heat pipe has resistance to deep freezing, possibility of displacement of the heat source and heat receiver by ± 1.5 mm with mechanical reaction $[- 1.9; +2.5$ N] at distance between fixing and loading points equaled 55 mm.

5. Reliability testing

HP carried out aging test. HP was placed to a climate chamber. Temperature of chamber increased to 130°C and keep constant during 8 h. After that it successfully passed the thermal performance test. Thermal resistances changed within the experimental error $RE < 10\%$.

HP carried out the thermal cycling test. It was placed to a climate chamber, the temperature in the climate chamber changed cyclically 5 times from -40 to 80°C . After that it successfully passed the thermal performance test. Thermal resistances changed within the experimental error $RE < 10\%$.

HP was immersed in liquid nitrogen and kept for 1 hour, then thermal test were repeatedly carried out. HP successfully passed deep freezing tests without breakages and deformations. Thermal resistances changed within the experimental error $RE < 10\%$.

6. Conclusion

Developed heat pipe with the asymmetric central compensating element has high thermal performance characteristics (thermal resistances $0.05\text{--}0.07$ K/W at 50 W), resistance to deep freezing, possibility of displacement of the heat source and heat receiver by ± 1.5 mm with mechanical reaction $F \in [- 1.9; +2.5$ N]. The design of heat pipe with seamless asymmetric metal compensating element and mesh wicks ensure heat pipe operate stably and reliably at various orientations and positions. Developed heat pipe is gravity independent.

References

- [1] M. J. Gibbons, M. Marengo, T. Persoons, A review of heat pipe technology for foldable electronic devices. *Applied Thermal Engineering*, 2021. 194: 117087. doi:10.1016/j.applthermaleng.2021.117087.
- [2] T. Jaipurkar, P. Kant, S. Khandekar, B. Bhattacharya, S. Paralikar, Thermo-mechanical design and characterization of flexible heat pipes. *Applied Thermal Engineering*, 2017. 126: p. 1199–1208.
- [3] C. Yang, C. Chang, C. Song, W. Shang, J. Wu, P. Tao, T. Deng, Fabrication and performance evaluation of flexible heat pipes for potential thermal control of foldable electronics. *Applied Thermal Engineering*, 2016. 95: p. 445–453.
- [4] J. Huang, W. Zhou, J. Xiang, C. Liu, Y. Gao, S. Li, W. Ling, Development of novel flexible heat pipe with multistage design inspired by structure of human spine. *Applied Thermal Engineering*, 2020. 175: 115392. doi:10.1016/j.applthermaleng.2020.115392.
- [5] J. Panyam, M.D. Chavanpatil, US 2011 / 0020457 A1, 2011.
- [6] H. T. Kashi, M. Bahrami, J. S. Karami, G. Faraji, Microstructure and mechanical properties of the ultrafine-grained copper tube produced by severe plastic deformation. *Iranian Journal of Materials Science and Engineering*, 2017. 14: p. 32–40.
- [7] F. Samadpour, G. Faraji, P. Babaie, S.R. Bewsher, M. Mohammadpour, Hydrostatic cyclic expansion extrusion (HCEE) as a novel severe plastic

deformation process for producing long nanostructured metals. *Materials Science and Engineering A*, 2018. 718: p. 412–417.

[8] V.E. Hamren, Method of fabricating miniature bellows by electroless chemical deposition, US 3,040,426, 1962.

[9] M. Deterre, E. Lefeuvre, Y. Zhu, M. Woytasik, A. Bosseboeuf, B. Boutaud, R. Dal Molin, Micromachined piezoelectric spirals and ultra-compliant packaging for blood pressure energy harvesters powering medical implants, in *IEEE International Conference on Micro Electro Mechanical Systems (MEMS)*, 2013: p. 249–252.

[10] K. I. Delendik, N. V. Kolyago, O. G. Penyazkov, O. L. Voitik, Development of heat pipes for cooling thermally stressed electronics elements. *Journal of Engineering Physics and Thermophysics*, 2019. 92: p. 1529–1536.

[11] S. Somasundaram, H. Bin, W. Mengyao, C. S. Tan, E. N. Wang, Charging of miniature flat heat pipes. *Heat and Mass Transfer*, 2018. 54: p. 3131–3136.

[12] K. Delendik, O. Voitik, N. Kolyago, O. Penyazkov, Smartphone still burning ...current trends in smartphone cooling. *The Science and Innovations*, 2020. 206: p. 34 – 43.

Thermal performance of an ultra-thin flexible flat heat pipe with hydrophilic / hydrophobic coupling wick structure

Maofei Yang¹, Jinwang Li^{1,2*}, Jiyuan Li¹

¹College of Astronautics, Nanjing University of Aeronautics and Astronautics, Nanjing, China

²Jiangsu Province Key Laboratory of Aerospace Power System, Nanjing, China

*Corresponding author email address: ljw@nuaa.edu.cn

Abstract

Heat pipe relies on the latent heat of internal working medium phase change to transfer heat efficiently. It is widely used in the heat dissipation of electronic devices. With the development of flexible folding electronic equipment, ultra-thin flexible flat heat pipe with higher heat transfer performance, thinner thickness and repeated bending with the equipment is needed. In this paper, ultra-thin flexible flat plate heat pipes with a thickness of 0.6 mm were designed and fabricated by using copper foil Mylar as the flexible shell and using hydrophilic / hydrophobic modified copper wire mesh as wick. The results show that the ultra-thin flexible flat plate heat pipe could achieve $\pm 90^\circ$ bending. Among the bend angles of 90° , 45° , 0° and -90° , there is a minimum thermal resistance value of 4.96 K/W when the heat pipe is bent at 90° . Compared to the unmodified heat pipe, the modified heat pipe has the better heat transfer performance. When the heating power is 10 W, the effective thermal conductivity of the unmodified heat pipe and the modified heat pipe are 425 W/(m·K) and 458 W/(m·K), respectively.

Keywords: Heat pipe; Flexibility; Ultrathin; Modification

1. Introduction

With the rapid development of the electronic industry, foldable and wearable electronic devices are becoming more and more common in the market. In the face of its complex structure, narrow space, and the need for repeated folding of high-performance heat dissipation, the traditional rigid heat pipe is no longer suitable because of its large thickness and cannot be bent. Although the ultra-thin rigid heat pipe can achieve certain bending through the elastic deformation of the metal shell, its performance will be greatly reduced after repeated bending, which is difficult to be applied to the application scenarios of large bending angle and repeated bending of flexible electronic devices. Therefore, using flexible shell and tube materials to make ultra-thin flexible heat pipes that can be repeatedly bent and deformed has become a new research direction to solve the problem.

The good flexibility of polymer film can realize the bending deformation of the heat pipe, and at the same time has the advantages of light weight, ultra-thin and insulating, which is the ideal packaging material for ultra-thin flexible heat pipe. Polymers were currently selected as ultra-thin flexible heat pipe shell materials, Such as polyethylene terephthalate(PET), liquid crystal, polyimide, FR4, and so on[1-5]. However, due to the limitations of the characteristics of the polymer material itself, this type of flexible heat pipe usually faces the problem of increased thermal resistance and poor air tightness. Oshman et al. [6] reduced the overall thermal resistance by adding thermal vias of the electroplated copper array to the surface of the

liquid crystal polymer. Heish et al. [7] embedded copper sheets on the silicone rubber housing by means of a hot pressing process at the evaporation and condensation ends, enhancing the thermal conductivity of the heat pipe. In the face of polymer heat pipe leakage problems and the generation of non-condensable gases that limit long-term reliability, polymer and metal films are often combined. Oshman et al. [8] used the PAVVF4W material (Mylar) as the shell material. It was a composite material with a multilayer of polymer and aluminum, consisting of a low-density linear CPP of 89 μm internally, and a shielding effect of 9 μm aluminium foil for working medium, 20 μm of polyethylene and PET of 12 μm on the outside. The heat pipe used a three-layer sintered copper wire mesh as the wick, and deionized water as working medium. An ultra-thin flexible flat heat pipe with a thickness of 1.31 mm was made, showing a minimum thermal resistance of 1.2 K/W, which was lower than the 4.6 K/W of copper sample under the same test conditions. Liu et al. [9] used an aluminum composite packaging film with high toughness and good sealing as the shell to produce ultra-thin flexible flat heat pipes with a thickness of 1.47 mm. The evaporation section and the condensation end remove the polyamide layer on the surface of the aluminum foil by laser ablation process, which improves the local thermal conductivity. Three layers of hydrophilic modified copper wire mesh were embedded in the chlorinated polypropylene (CPP) layer on the inner surface of the shell by hot pressing, reducing the contact thermal resistance. The minimum thermal resistance of the heat pipe

was 0.525 K/W, and the thermal conductivity reached 1499 W/m·K.

Another important component of flexible flat heat pipe is the wick. Wire mesh is the first choice for the flexible heat pipe wick due to its good bendability. When it was used as the wick of heat pipe, the surface is modified, and the hydrophilic modification can improve its wettability and capillary force value. Hydrophobic modification promotes condensation efficiency [10]. Hydrophilic property in evaporation section and hydrophobic property in condensation section are coupled to improve the heat transfer performance of heat pipe. The methods of hydrophilic modification of wire mesh include electrochemical deposition [11,12], alkali-assisted oxidation [13-16], etc. The hydrophilic wire mesh chemical treatment is achieved via hydrophobic modification.

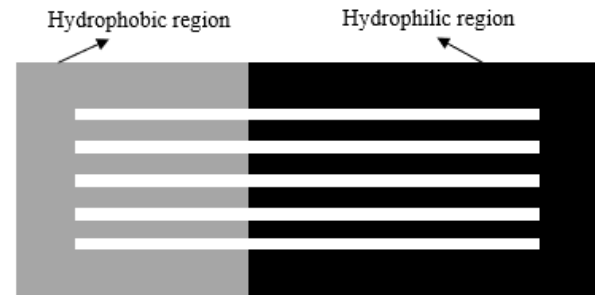
In combination with the above, this paper developed an ultra-thin flexible flat heat pipe with outside size of 120 mm× 60 mm× 0.60 mm. The shell material was copper foil mylar film. Three layers of 200 mesh copper wire mesh was used as the wick, and the working medium was deionized water. Hydrophilic modification of the wick by alkali-assisted oxidation method was used to improve capillary force and wettability of working medium. The chemical treatment of one end of the copper mesh was hydrophilic while the other end was hydrophobic. A strip channel was machined on the surface of the copper wire mesh as a steam flow path to achieve gas-liquid coplane to reduce the thickness of the heat pipe. The performance test platform of flat heat pipe was built, and the influence of hydrophilic modification, heat dissipation method and bending angle on heat transfer performance was studied in order to provide support for the heat dissipation of electronic devices.

2. Experiment

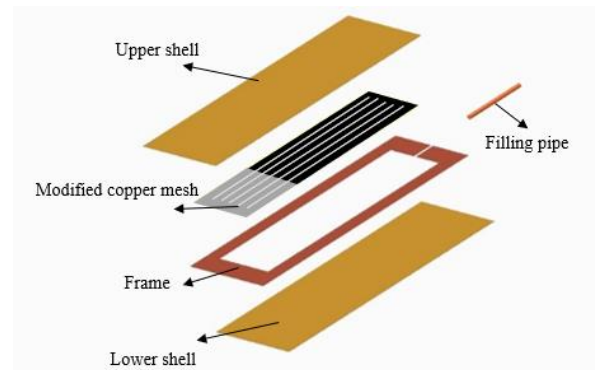
2.1. Design of the ultra-thin flexible flat heat pipe

The ultra-thin flexible flat heat pipe shell adopted 25 μm thick copper foil mylar, which was commercially available and composed of a composite layer of polyethylene terephthalate (PET) on each side with an overall thickness of 0.18 mm. While satisfying the needs for an ultra-thin and flexible heat pipe, the presence of copper foil could reduce thermal resistance and increase thermal conductivity, prevent the penetration of non-condensable gases, and ensure the overall airtightness. It adopted a three-layer structure, with the upper and lower layers as the cover shell,

and the middle was the frame structure where the wick was placed. By mechanically cutting a 2 mm wide steam channel on the copper wire mesh, this gas-liquid coplanar design could reduce the overall thickness of the heat pipe, which was shown in Figure 1.



(a) wick structure



(b) heat pipe composition

Figure 1. Ultra-thin flexible flat heat pipe structure

In the experiment, it was found that the connection between the tube and the shell after hot pressing was not tight enough, and the heat pipe made could not ensure air tightness, so an adhesive was selected as seal. The heat pipe had an internal dimension of 100 mm× 40 mm× 0.30 mm and a 1 mm diameter liquid-filled tube, as shown in Figure 2.



Figure 2. Ultra-thin flexible flat heat pipe

The detailed parameters of the ultra-thin flexible flat heat pipe were listed in Table 1.

Table 1. Characterization of the ultra-thin flexible flat heat pipe

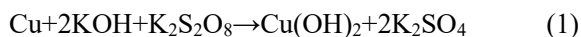
Parameter	Dimension
External dimensions (L×W×H)	120 mm×60 mm×0.60 mm
Internal dimensions (L×W×H)	100 mm×40 mm×0.30 mm
Evaporator area	20×20 mm ²
Condensation area	40×40 mm ²
Wick structure	200 mesh × 3 layers
Wick type and material	copper wire mesh
Work medium	Deionized water

2.2. Wick modification

The copper wire mesh was modified by chemical methods, and the resulting nanostructure changed the infiltration of the surface of the suction core. The hydrophilic wick had a stronger water absorption ability, and the droplet condensation mechanism of the hydrophobic condensing surface promoted the efficiency of the reflux of the condensed liquid. Firstly, the mesh was pretreated before the reaction to remove its impurities and oils on the surface: the mesh was placed in an ultrasonic cleaner with 10wt% H₂SO₄ cleaning liquid and was cleaned for 5 minutes. After that, the mesh was further rinsed with deionized water and dried. Then the mesh was ultrasonically cleaned for 5 minutes using absolute ethanol as the cleaning solution. Finally the sample was re-rinsed with deionized water and dried naturally.

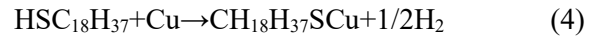
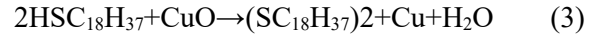
2.2.1. Hydrophilic modification

Set up a 2.5 mol/L of KOH and 0.065 mol/L of K₂S₂O₈ mixed solution in a beaker, place it in a water bath pot with temperature of 70 °C, fully submerge the wire mesh in the mixed solution, and remove it when the reaction has completed. Rinse it with deionized water, then dry for 30 minutes at 180 °C in a tubular furnace[17]. It is possible to create a copper wire mesh containing CuO nanowires when it has naturally cooled at room temperature. The chemical equation of the reaction is as follows[18]:



2.2.2 Hydrophobic modification

In a beaker, make a 0.0025 mol/L n-octadecyl mercaptan ethanol solution, place it in a constant temperature water bath at 70 °C, and immerse the lower end of the previously hydrophilic treated copper mesh for 40mm (the condensation area is 40 mm×40 mm), with a reaction time of 30 minutes. After the reaction, remove the wire mesh and wash it with deionized water before drying it. The chemical principle of the reaction is as follows:



2.3. Construction of the experimental platform

The flexible flat heat pipe heat transfer performance test platform was shown in Figure 3.

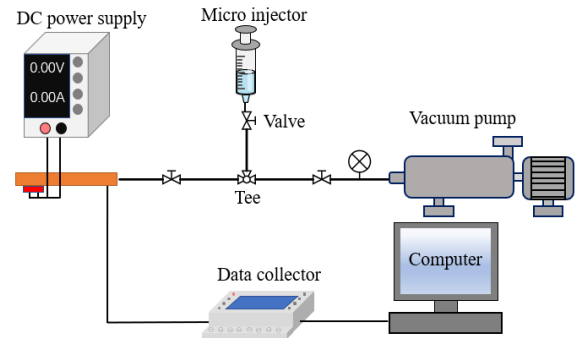


Figure 3. Schematic diagram of the experimental apparatus

The whole test system had a heating module (DC power supply + heating plate), a data acquisition module (K-type thermocouple + data collector + computer), and a vacuum injection (vacuum pump + micro injector + valve + vacuum gauge). High-quality thermal grease was applied between the heater and the heat pipe to lower the thermal contact resistance. After attaching the thermocouple to the surface of the heat pipe, the evaporation section and insulation section were wrapped with thermal insulation cotton. The arrangement points of the thermocouples were as follows:

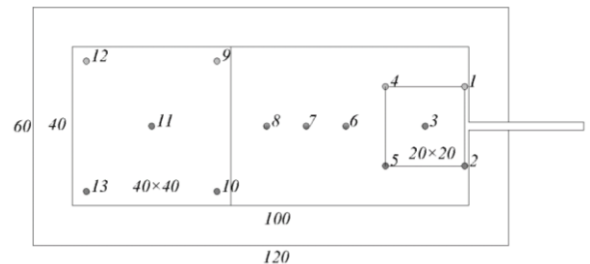


Figure 4. Arrangement of temperature measurement points

Measuring points 1~5 were set in the evaporation section, measuring points 9~13 were in the condensation section, and measuring points 6~8 were set in the insulation section. The thermocouple probe was covered with silicone thermal adhesive to keep it from coming off during the experiment. High-temperature tape was applied for additional reinforcement after curing.

Four placement angles: -90° (evaporation portion horizontal, condensation section vertical down), 0° , 45° and 90° (evaporation section horizontal condensation section straight up) were studied to examine the effects of placement angle on heat pipe thermal performance. The schematic diagram was shown in figure 5:

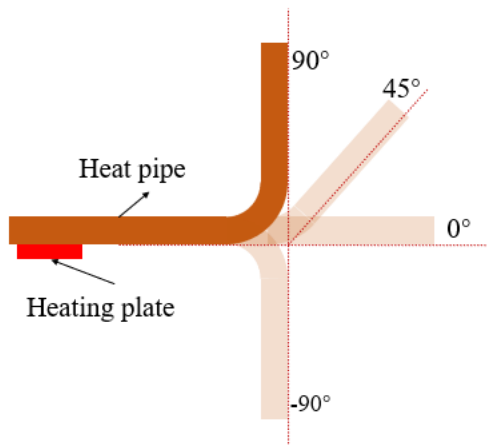


Figure 5. The schematic diagram of placement angles

2.4. Data and error analysis

The previous experimental study found that the heat pipe had the best filling rate when the pores of the wire mesh were filled with 100% of the working medium. This optimal filling rate for the heat pipe was used in this experimental study.

The effective thermal resistance of the heat pipe was determined as followed:

$$R = \frac{T_e - T_c}{Q} \quad (5)$$

Where R is the effective thermal resistance of the heat pipe, $^\circ\text{C}/\text{W}$; T_e is the temperature of evaporation section, $^\circ\text{C}$; T_c is the temperature of condensation section, $^\circ\text{C}$; Q is the heat transfer quantity of the heat pipe, W .

The effective thermal conductivity was calculated as follow:

$$K_{eff} = Q' \cdot \frac{L_{eff}}{\Delta T} \quad (6)$$

$$Q' = Q \cdot \frac{L_{eff}}{L} \quad (7)$$

Where Q' is equivalent power, W ; Q is total input power, W ; ΔT is the temperature difference between evaporation section and condensation section, $^\circ\text{C}$; L_{eff} is the distance between the center of evaporation section and the center of condensation section, m ; L is the total length of the heat pipe, m ; A is cross-sectional area of the heat pipe, m^2 .

Since the experiment's thermal insulation effect of the cotton insulation covered in both evaporation section and the insulation section is good, the inaccuracy brought on by the heat loss is disregarded, and the power meter's reading is the total input power Q . The temperature measurement error of type K thermocouple is 0.1°C . The minimum temperature measured by the experiment is room temperature (20°C), and its relative error is 0.5%; the error of data collector is 0.2%, thus the uncertainty of the temperature measurement is 0.54%. The employed power supply's maximum relative voltage and current errors are 0.17% and 5.81%, respectively. The uncertainty of size is 0.83%. The uncertainty of thermal resistance is 5.84% and the uncertainty of thermal conductivity is 5.89%. All the uncertainty was listed in table 2.

Table 2. Uncertainty of the testing system

Item	Uncertainty/error
K-type Thermocouples	$\pm 0.1^\circ\text{C} / 0.5\%$
Data collector	0.2%
Temperature measurement	0.54%
DC power supplier	0.17% & 5.81%
Dimensional measurements	0.83%
Thermal resistance	5.84%
Thermal conductivity	5.89%

3. Experimental results and analysis

The heat transfer performance of the heat pipe under different conditions were studied. The effects of bending angle, different cooling methods, different copper mesh wicks with different contact angle were investigated.

3.1. Influence of bending angle

The performance of the ultra-thin flexible flat heat pipe under various bending angles was investigated under the conditions of forced water cooling in the condensation section of the heat pipe. The experimental result of thermal resistance of the heat pipe at various bending angles was shown in Figure 6. It was evident that the heat pipe's thermal resistance was decreased as the bending angle was increased from -90° to 90° . It showed that the reverse gravity situation had no obvious effect on the heat transfer of the heat pipe. So the heat pipe may operate in reverse gravity condition. The

thermal resistance of the heat pipe at 0° was marginally smaller than that at -90° . There was a minimum value of 4.96 K/W when the heat pipe was bent at 90° . This was because the gravity-assisted working media reflux effect became stronger as the bending angle raised.

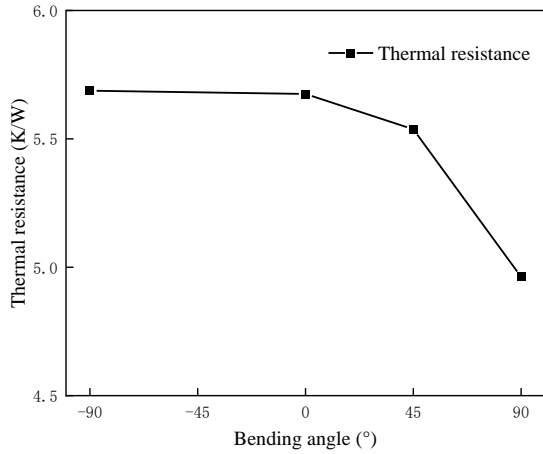
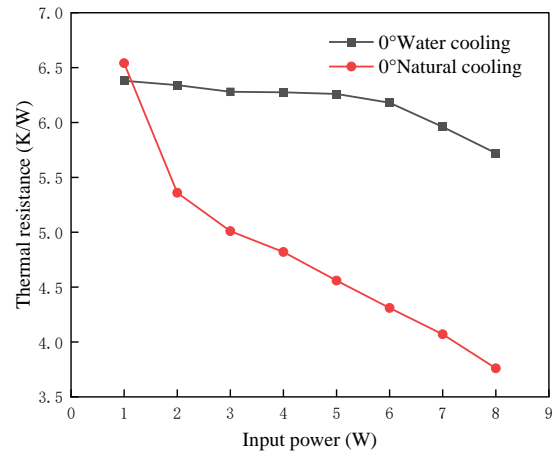


Figure 6. Relationship between thermal resistance and bending angle of heat pipe

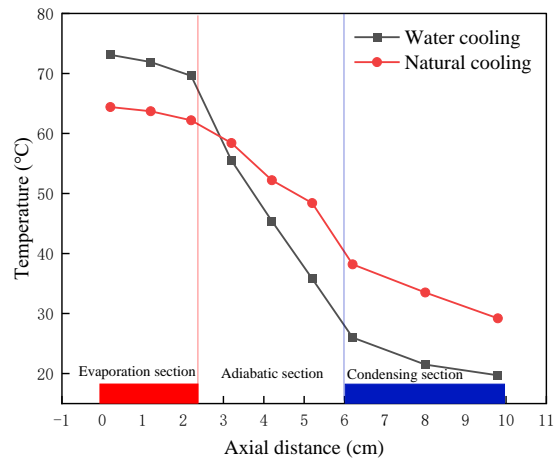
3.2. Influence of heat dissipation mode in the condensation section

Heat pipes were arranged horizontally to compare the effects of forced water cooling and natural cooling on the heat transfer performance of the heat pipe. The results were shown in Figure 7. It can be seen from Figure 7 that with the increase of heating power, the thermal resistance of the heat pipe was decreased. When the heating power was bigger than 1 W, the thermal resistance of the water cooling heat pipe was bigger than that of natural cooling heat pipe. When the heating power was 8 W, the thermal resistance of the heat pipe for the two heat dissipation techniques of water cooling and natural cooling were 5.72 K/W and 3.76 K/W, respectively. The temperature in the condensation section and the adiabatic section was lower when the heat pipe was cooled by water. The cause of this phenomenon was that: the vapor channel was very small in the ultra-thin flexible flat heat pipe, the vapor channel in condensation section had been hydrophobic modification, the temperature of the condensing section of water cooling heat pipe was lower, it was easier blocked in the condensing section after the vapor was condense. As a result, the temperature of evaporation section raised and the working medium in the evaporation section decreased, the thermal resistance of the whole heat pipe increased. When natural cooling was used in the condensation section, the temperature of the condensation section was increased in order to

dissipate the same heat power compared with that of natural cooling.



(a) Relationship between thermal resistance and heating power



(b) Axial distribution of heat pipe temperature at 8 W

Figure 7. The effect of heat dissipation on heat pipes

3.3. Effects of hydrophilic/hydrophobic modification

A tiny syringe was used to inject deionized water droplets into the modified and unmodified copper mesh. While the droplets on the surface of the copper mesh modified for hydrophobic conditions were spherical, those in the hydrophilic region immediately diffused and absorbed into mesh. The results were shown in Figure 8. It can be seen from Figure 8 that there was a distinct separation between the hydrophilic area and the hydrophobic regions, whereas the water drops on the copper mesh that had not been modified were elliptical spherical. The contact angle of the surface of the copper mesh was measured before and after the modification by using a contact angle analyzer. The volume of deionized water droplets

was 5 μL . The hydrophilic copper mesh had a contact angle of 0° , the hydrophobic copper mesh has a contact angle of 146.78° , and the unmodified copper mesh has a contact angle of 125.54° .

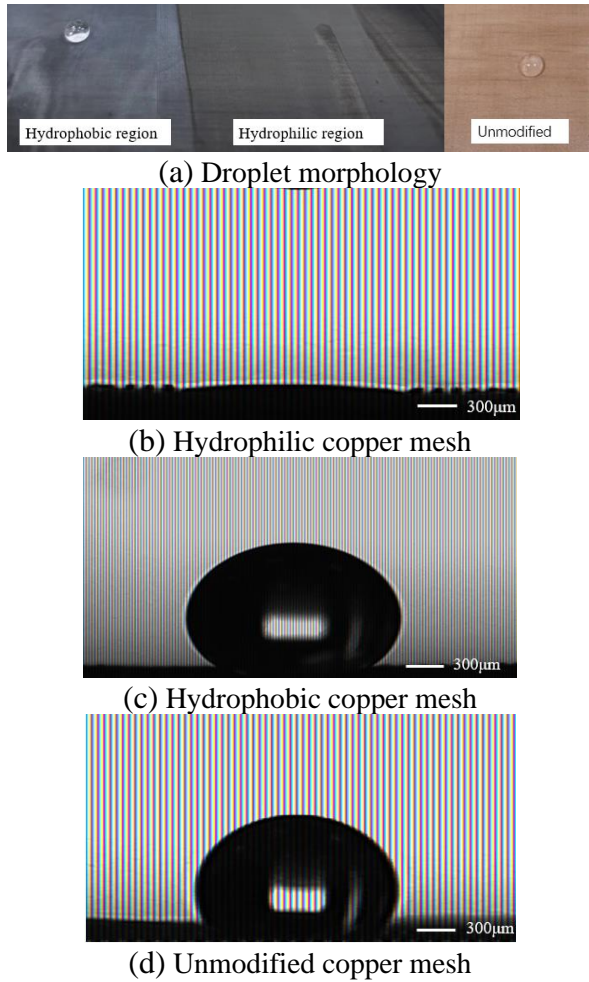


Figure 8. Effects of hydrophilic/hydrophobic modification

The heat transfer performances of heat pipes having different copper mesh wicks with different contact angle were investigated. Natural cooling was used at the condensation section. The heating power was 1 W to 10 W. The temperature of the evaporation section exceeded 75°C after 10 W. The results were shown in Figure 9. It can be seen from Figure 9 that the heat pipe's thermal resistance dropped as the heating power increased. When the heating power was 10 W, the thermal resistance of the unmodified heat pipe was 3.68 K/W, and the thermal resistance of the modified heat pipe was 3.41 K/W. The thermal conductivity of copper was $401\text{ W}/(\text{m}\cdot\text{K})$. The equivalent thermal conductivity of the unmodified heat pipe was $424\text{ W}/(\text{m}\cdot\text{K})$ and the equivalent thermal conductivity of the modified heat pipe was $458\text{ W}/(\text{m}\cdot\text{K})$. When heating power was bigger than 8 W, the modified heat pipe outperformed copper in

terms of heat transfer. When heating power reached 10 W, the unmodified heat pipe also outperformed copper in terms of heat transfer.

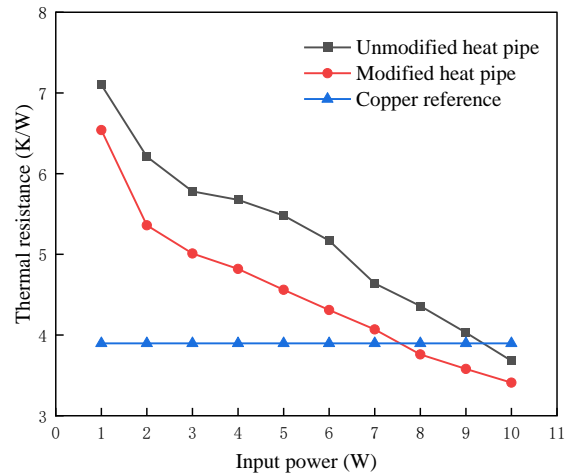


Figure 9. Thermal resistance of the heat pipe before and after modification

4. Conclusion

In order to improve the heat transfer performance of the flexible flat heat pipe, the internal copper mesh wick was modified with hydrophilic/hydrophobic matching. Additionally, the gas channel was processed on the wick to form a gas-liquid coplanar structure in order to decrease the thickness of the heat pipe. The main conclusions are as follow:

(1) The ultra-thin flexible flat heat pipe can bend $\pm 90^\circ$. Among the bend angles of 90° , 45° , 0° and -90° , there is a minimum thermal resistance value of 4.96 K/W when the heat pipe was bent at 90° (evaporation section horizontal condensation section straight up).

(2) The heat transfer efficiency of the heat pipe is more sensitive to different heat dissipation. The natural cooling method has a superior heat dissipation effect than water cooling, and its input power can reach up to 10 W, compared to 8 W for water cooling.

(3) Compared to the unmodified heat pipe, the modified heat pipe has the better heat transfer performance. When the heating power is 10 W, the effective thermal conductivity of the unmodified heat pipe and the modified heat pipe are $425\text{ W}/(\text{m}\cdot\text{K})$ and $458\text{ W}/(\text{m}\cdot\text{K})$, respectively.

Acknowledgments

This study was supported by National Natural Science Foundation of China (No. 11802125) and Jiangsu Province Key Laboratory of Aerospace Power System (China).

References

- [1] J. Li, N. Lu, and Y. Sun, Research Progress and Prospect of Heat Pipe Capillary Wicks. *Frontiers in Heat and Mass Transfer*, 2022. 18:24.
- [2] C. Oshman, B. Shi, C. Li, R. Yang, Y. C. Lee, G. P. Peterson, and V. M. Bright, The Development of Polymer-Based Flat Heat Pipes. *Journal of Microelectromechanical Systems*, 2011. 20(2): p. 410.
- [3] W.-P. Shih, G.-W. Wu, and S.-L. Chen, Lamination and Characterization of a Polyethylene-Terephthalate Flexible Micro Heat Pipe. *Frontiers in Heat Pipes*, 2012. 3(2) : p. 284.
- [4] R. Lewis, L.-A. Liew, S. Xu, Y.-C. Lee, and R. Yang, Microfabricated ultra-thin all-polymer thermal ground planes. *Science Bulletin*, 2015. 60(7): p. 701.
- [5] K.-S. Yang, T.-Y. Yang, C.-W. Tu, C.-T. Yeh, and M.-T. Lee, A novel flat polymer heat pipe with thermal via for cooling electronic devices. *Energy Conversion and Management*, 2015. 100: p. 37.
- [6] C. Oshman, Q. Li, L.-A. Liew, R. Yang, Y. C. Lee, V. M. Bright, D. J. Sharar, N. R. Jankowski, and B. C. Morgan, Thermal performance of a flat polymer heat pipe heat spreader under high acceleration. *Journal of Micromechanics and Microengineering*, 2012. 22(4).
- [7] S.-S. Hsieh and Y.-R. Yang, Design, fabrication and performance tests for a polymer-based flexible flat heat pipe. *Energy Conversion and Management*, 2013. 70: p. 10.
- [8] C. Oshman, Q. Li, L.-A. Liew, R. Yang, V. M. Bright, and Y. C. Lee, Flat flexible polymer heat pipes. *Journal of Micromechanics and Microengineering*, 2013. 23(1) : p. 015001.
- [9] C. Liu, Q. Li, and D. Fan, Fabrication and performance evaluation of flexible flat heat pipes for the thermal control of deployable structure. *International Journal of Heat and Mass Transfer*, 2019. 144(12): p. 118661.1.
- [10] R. Wen, Q. Li, G. Wu, W. Wang, Y. Chen, X. Ma, D. Zhao, and R. Yang. Hydrophobic copper nanowires for enhancing condensation heat transfer. *Nano Energy*, 2017, 33(3): p. 177.
- [11] L. A. Liew, C. Y. Lin, R. Lewis, S. Song, L. Qian, R. Yang, and Y. C. Lee, Flexible Thermal Ground Planes Fabricated with Printed Circuit Board Technology. *J. Electronic Packaging*, 2017. 139(1): p. 011003.1.
- [12] J. LUO, Y. WANG, S. LV, and D. MO. Capillary characteristics of gradient structure modified copper mesh. *Journal of Engineering Thermophysics*, 2021, 42 (6): p. 1531.
- [13] D. Lee and C. Byon, Fabrication and characterization of pure-metal-based submillimeter-thick flexible flat heat pipe with innovative wick structures. *International Journal of Heat and Mass Transfer*, 2018. 122: p. 306.
- [14] C. LIU, J. XU, and X. JI. Heat transfer characteristics of super hydrophilic / super hydrophobic matching ultra-thin heat pipe. *Chemical Industry and Engineering Progress*, 2018, 37(06): p. 2067.
- [15] J. LI, Y. YANG, C. XU, and H. Qiu. Heat transfer characteristics of ultra-thin planar heat pipe with nanostructured wick. *Journal of Engineering Thermophysics*, 2020, 41 (11): p. 2762.
- [16] Y. TANG. Research on heat transfer characteristics of ultra-thin heat pipe based on mesh wick. Doctoral dissertation, South China University of technology, 2020.
- [17] T. Hao, X. Ma, Z. Lan, N. Li, and Y. Zhao, Effects of Superhydrophobic and Superhydrophilic Surfaces on Heat Transfer and Oscillating Motion of an Oscillating Heat Pipe. *Journal of Heat Transfer*, 2014. 136(8): p. 082001.
- [18] Y. Ji, H. H. Chen, Y. J. Kim, Q. Yu, X. Ma, and H. B. Ma, Hydrophobic Surface Effect on Heat Transfer Performance in an Oscillating Heat Pipe. *Journal of Heat Transfer*, 2012. 134(7): p. p.074502.1.

Experimental investigations on a loop heat pipe in the context of BTMS

Milan Vachhani¹, Kalpak R Sagar¹, Durganand Jha¹, Vipul M patel¹, Hemantkumar B Mehta^{1*}

¹ Sardar Vallabhbhai National Institute of Technology, Surat, India

*hbm@med.svnit.ac.in:

Abstract

The heat pipe family has shown its potential in the Battery Thermal Management System (BTMS) in electric vehicles because of its high heat transfer rate. The conventional Loop Heat Pipe (LHP) system makes battery modules more complicated because liquid and vapor lines are separated at the bottom and top or vice versa. In the present work, a novel LHP is constructed with the separation of vapor and a liquid line at the top position of the cylindrical evaporator. The length of both vapor and liquid line of LHP is kept 1.5 m long. The preliminary experimental test setup is developed to investigate its thermal performance. The constructed LHP system is tested with DI water and acetone at different heat sink conditions. The present DI water and acetone-filled LHP system transferred 30W for a maximum evaporator temperature of 60 °C. When compared to acetone-filled LHP, the novel water-filled LHP system showed very little dependence on heat sink temperature.

Keywords: Electric Vehicle; BTMS; Thermal Management; Loop Heat Pipe

1. Introduction

The Electric Vehicles (EVs) and Hybrid Electric Vehicles (HEVs) market demand batteries with high power density, economics, and a longer life span to compete with conventional vehicles [1]. The temperature plays a vital role in the efficient performance of the battery. Higher operating temperature adversely affects the charging capacity, discharging rate (C-rate), electrode life, and vehicle safety. It is observed that the suitable operating temperature range for the Lithium-Ion batteries is 25-45 °C, and it is essential to maintain battery temperature below 60°C to avoid thermal runaway [2]. Battery Thermal Management System (BTMS) is essential for longer battery life, better capacity, and fire prevention. There are several methods available for BTMS, like air cooling, liquid cooling (water/oil/refrigerant), Phase Change Material (PCM) based cooling, thermoelectric cooling, heat pipe-based cooling, or a combination of multiples [3]. Among all, heat pipe has shown its potential in the BTMS because of its high heat transfer rate. The Heat Pipes (HPs) are typically used in groups (arrays) to increase heat transfer and temperature uniformity within the battery module. Heat pipe groups can significantly increase the cost, total size, and weight of a BTMS when dealing with a large amount of energy and a large-size battery pack, as well as long-distance heat transfer. [4].

A Loop heat pipe (LHP) is gaining popularity among the scientific community to address the shortcomings of standard heat pipes [5]. LHP is a high-efficiency phase change heat transfer device that can transmit heat in multi directions over long distances using separate vapor and liquid lines. Various research groups have recently conducted

systematic comprehensive evaluations of BTMS involving various types of heat pipes. According to extensive studies, a considerable study is focused on standard HPs, but little on LHP, even though LHP has various advantages over standard heat pipes, such as long-distance heat transfer potential, and ease to couple with HVAC of EVs [5]. The available conventional design in the literature of Loop Heat Pipes (LHP) seems complicated to implement with battery pack modules because of the separation of liquid and vapor lines at the bottom and top or vice-versa.

In this paper, a novel LHP is constructed with vapor and liquid lines separated at the top of the cylindrical evaporator. The practical potential of a novel LHP is examined for BTMS of Lithium-Ion batteries by simulating battery heat generation with the help of Ni-Cr wire with DC power supply. Our present study focuses on developing and testing a single LHP using DI water and acetone as working fluids. The performance of LHP with both working fluids is discussed with sink temperatures ranging from 20 °C, 25 °C, and 30 °C.

2. Experimental Test Setup

A novel LHP, shown in Fig. 1, is constructed with the separation of vapor and liquid lines at the top of the evaporator. The LHP system is constructed of copper tubing and includes a cylindrical evaporator. The evaporator section is powered by a Gw-Instek Make DC power supply and heated with Ni-Cr wire. The condenser tubing is cooled with water and kept at different temperatures by using a constant temperature water bath. T-type thermocouples are used to measure temperatures at various locations throughout the LHP system, as shown in Fig.1. Temperature signal data is collected using a

National Instruments-based DAQ system equipped with an NI cDAQ-9178 chassis and an NI 9219 temperature module. The vapor line is brazed at the top of the cylindrical evaporator with a capillary pipe 1500 mm long. The cylindrical evaporator is brazed with four liquid lines to distribute working fluid uniformly by drilling holes at 90 degrees on the evaporator's circumference without disturbing the mesh structure. To prevent heat loss the vapor line, liquid lines, and compensation chamber are insulated with a black foam insulation sleeve. Furthermore, to avoid heat loss from evaporator, it is insulated with glass wool. Table.1 shows dimensions of all components of LHP.

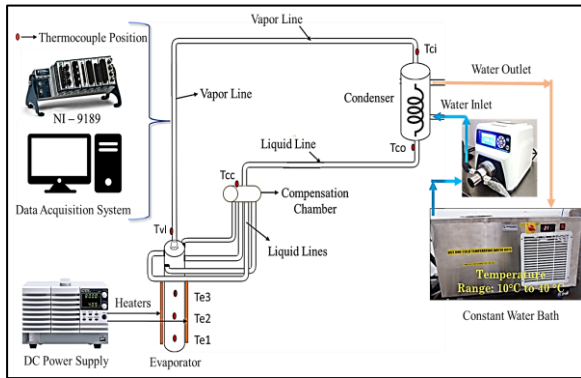


Figure 1. Schematic of LHP experimental test setup.

Table.1. Primary dimensions of LHP

Component	Parameters	Values (mm)
Evaporator	ID/OD	10/12
	Active length	120
Mesh	Two-layer screen copper mesh	N=100
Vapor line	ID/OD	1.3/3.2
	Length	1500
Liquid line	ID/OD	1.3/3.2
	length	1500
Condenser	ID/OD	1.3/3.2
	length	1500
Compensation chamber	ID/OD	16/19
	Length	70

3. Results and Discussion

In the present study, LHP is filled with DI water and acetone in equal amounts of 20 mL, making up for 40% of the total volume of the LHP. The Fig.1 shows the position of seven T-type of thermocouples used in experimental test setup. Three thermocouples are used in evaporator section of LHP. One thermocouple is used at inlet of vapor line and one thermocouple at compensation chambers. The remaining two thermocouples are

used to measure inlet and outlet temperature of the condenser section. Figure 2 shows a typical temperature-time characteristics for DI water with 20 ml filling volume in LHP at 25 °C sink temperature. The operation of LHP in the present work begins with a heat load of 20 W and is gradually increased with steps of 10 W. The fast response and stable state are achieved in a short period of time with each step increase in heat load. The startup process of LHP is represented in Fig. 2. When a heat load is applied to the evaporator, the evaporator wall temperature rapidly rises, while the condenser inlet temperatures stay unchanged. At this point, pool boiling in the evaporator has just begun, and bubbles have formed in the evaporating zone. High pressure inside the evaporator is caused by the gradual accumulation of vapor in the evaporator zone, and this pressure is responsible for forcing the two-phase flow from the evaporator to the condenser. As a result, condenser inlet temperatures rise sharply, indicating that the two-phase flow entered the condenser. At the start of the heat load, the evaporator temperature rose until working fluid entered the condenser section's inlet. The evaporator temperature then dropped suddenly as liquid from the compensation chamber entered the evaporator, and the evaporator temperature began to oscillate around the mean temperature. This indicates that working fluid circulation has been attained, enabling the LHP to start successfully.

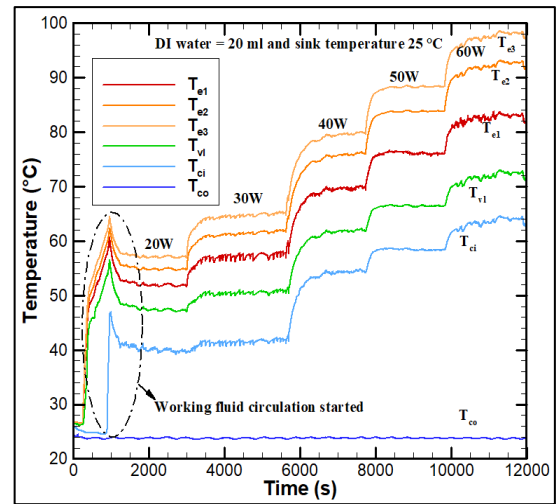


Figure 2. Temperature-time characteristics of LHP for DI water at 25°C sink temperature

Thermal resistance (R_{th}) in the LHP is calculated as the ratio of time averaged temperature difference between evaporator (T_E) and the condenser section (T_C) at each steady state.

$$R_{th} = \frac{T_E - T_C}{Q} \quad (1)$$

$$T_E = \frac{T_{e1} + T_{e2} + T_{e3}}{3} \quad (2)$$

$$T_C = \frac{T_{ci} + T_{co}}{2} \quad (3)$$

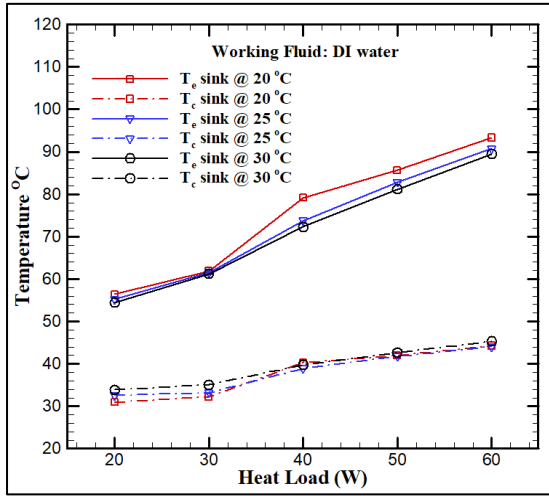


Figure 3. Time average evaporator and condenser temperature at different heat sinks for DI water

The thermal performance of LHP is analyzed for DI-water and acetone working fluids. The sink temperature is varied from 20 °C, 25 °C and 30 °C. Figure 3 shows the time averaged evaporator and condenser temperature at each steady state with heat load for DI water at different heat sinks. The LHP started working from 20 W heat load for DI water. The present LHP system transferred a heat load of 30W for a maximum evaporator temperature of 60 °C. It is observed that as heat load increases, the temperature difference between T_E and T_C increases. The average evaporator temperature is observed more for 20 °C sink temperature and lower for 30 °C. At higher heat load the effect of heat sink temperature is reduced for DI water based LHP.

Figure 4 shows the time averaged evaporator and condenser temperature at each steady state with heat load for acetone as working fluid at different heat sinks. The LHP started working from 10 W heat load for acetone filled LHP. The present LHP system transferred a heat load of 30W for a maximum evaporator temperature of 60 °C. It is observed that as heat load increases, the temperature difference between T_E and T_C increases. The average evaporator temperature is observed more for 20 °C sink temperature and lower for 30 °C. As shown in Fig.4 the influence of heat sink temperature is observed for acetone filled LHP as the temperature difference between T_E and T_C is reduced with increase in heat sink temperature.

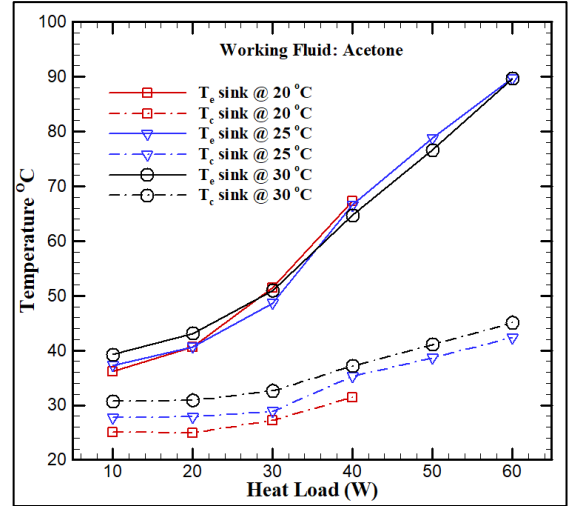


Figure 4. Time average evaporator and condenser temperature at different heat sinks for acetone

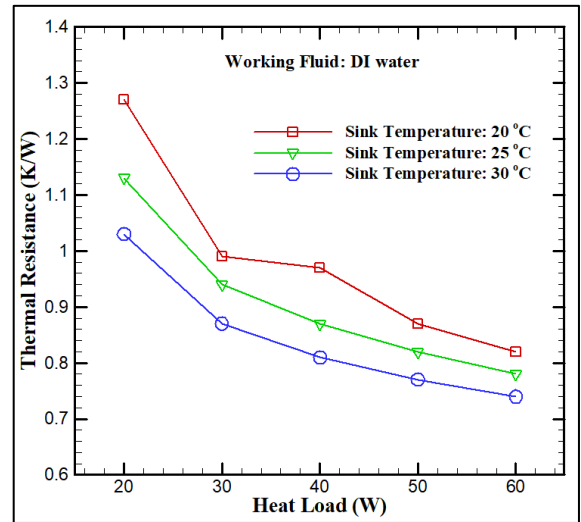


Figure 5. The thermal resistance of water LHP with different heat sinks

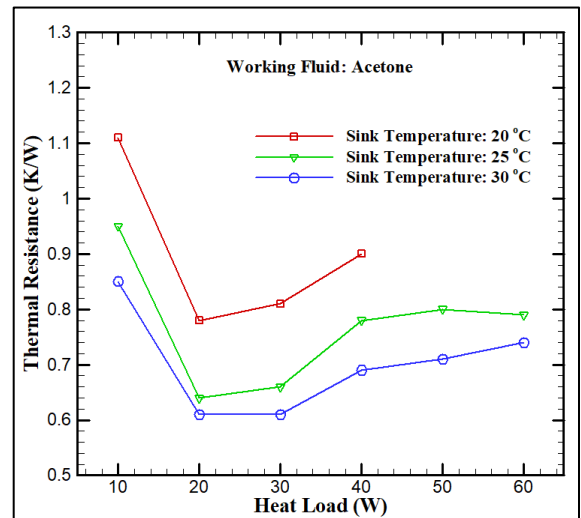


Figure 6. The thermal resistance of acetone LHP with different heat sinks

Figure 5 shows the thermal resistance obtained for DI-water filled LHP. It is observed that as the heat load increases, the thermal resistance of DI-water filled LHP decreases for all heat sink temperatures. At each heat load, thermal resistance is observed lower for 30 °C sink temperature. It is evident from Fig.5, at the low heat load effect of heat sink was observed more compared to the high heat load at the evaporator section. The lowest thermal resistance of 0.75 K/W is observed for DI-filled LHP at 30 °C heat sink temperature.

Figure 6 shows the thermal resistance obtained for acetone filled LHP. It is observed that, for acetone filled LHP thermal resistance first decreases and then increases after particular heat load for all sink temperatures. This phenomena can be attributed to the fact that the screen mesh structure was originally designed for DI-water filled heat pipe. When the same mesh is employed for acetone filled LHP, sufficient capillary force could not be produced and hence fluid is not driven uniformly through the evaporator section. Therefore, at high heat load more increase in evaporator temperature is observed for acetone filled LHP. The lowest thermal resistance of 0.6 K/W is observed for DI-filled LHP at 30 °C heat sink temperature. The novel LHP system with DI-water shows the absence of strong dependency on heat sink temperature compared to acetone-filled LHP.

4. Conclusion

A novel LHP is designed with the separation of vapor and liquid lines at the top position of the evaporator in the context of simple construction BTMS with different battery modules. The practical potential of a LHP system is examined for BTMS of Lithium-Ion batteries by simulating battery heat generation with the help of Ni-Cr wire and DC power supply. The constructed LHP system is tested with DI water and acetone at different heat sink conditions. The present LHP system transferred 30W for a maximum evaporator temperature of 60 °C. The lowest thermal resistance of 0.75 K/W and 0.6 K/W is observed for DI-water and acetone filled LHP at 30 °C heat sink temperature.

5. Acknowledgements

This work is financially supported by the Science and Engineering Research Board (SERB) order No. CRG/2021/008103.

References

- [1] A. Foley and A. G. Olabi, Renewable energy technology developments, trends and policy implications that can underpin the drive for global climate change. *Renewable and Sustainable Energy Reviews*, 2017. 68: p. 1112-1114.
- [2] N. Sofyan, A. Mizan, A. Z. Syahrial, and A. Subhan, Characteristic of LiFe (1-X) VxPO4/C Using Carbon Pyrolyzed from Table Sugar for Lithium-Ion Battery Cathode. In *Materials Science Forum*. 2018. 929: p. 33-41.
- [3] J. Kim, J. Oh, H. Lee, Review on battery thermal management system for electric vehicles. *Applied Thermal Engineering*, 2019. 149: p. 192-212.
- [4] Y. Huang, Y. Tang, W. Yuan, et al., Challenges and recent progress in thermal management with heat pipes for lithium-ion power batteries in electric vehicles. *Sci. China Technol. Sci.* 2021. 64: p. 919-956.
- [5] M. Bernagozzi, A. Georgoulas, N. Miché, C. Rouaud, and M. Marengo, Novel battery thermal management system for electric vehicles with a loop heat pipe and graphite sheet inserts. *Applied Thermal Engineering*. 2021. 194: p. 117061.

Thermal Performance of an Asymmetric Pulsating Heat Pipe with Aqueous Surfactant Solution

Est Dev Patel* and Subrata Kumar

*Indian Institute of Technology, Patna, India
dev.pme17@iitp.ac.in*

Abstract

An asymmetric closed-loop pulsating heat pipe (aCLPHP) has been studied with aqueous surfactant solutions in vertical bottom heat mode. A dual-loop aCLPHP setup was fabricated using copper capillary tubes of 2.4 and 3.4 mm internal diameters. The aqueous surfactant solution with sodium dodecyl sulphate (SDS) at 500–2500 ppm was prepared to have different properties like surface tension and dynamic viscosity than the pure deionized water. The working fluid filling ratios (FR) of 50% and 60% in 0° (horizontal), 30°, 60°, and 90° (vertical) orientations have been investigated by monitoring the temperature and pressure variations under various heat load patterns. The condenser section was kept at 20 °C by a coolant supply with a flow rate of 20 kg/h. The maximum thermal resistance decreased by 73.5%, and the heat load range was enhanced by 16.67% with the aqueous solutions in the vertical orientation compared to pure water. Hence, the heat pipe has shown better startup and thermo-hydrodynamic behavior due to improved wettability and low surface tension.

Keywords: Asymmetric pulsating heat pipe; Thermal management; Surfactant solutions; Two-phase flow start-up

1. Introduction

The miniaturization of electronic devices has led to thermal management problems in domestic as well as industrial applications. The generated heat flux necessarily needs to be dissipated to keep the junction or device temperature below the maximum allowable limit [1]. High temperatures can lead to malfunctioning operations or a complete failure due to thermal stress [2]. Device reliability and performance can be improved by designing a multidisciplinary thermal management system for electronic devices.

The conventional cooling methods, whether natural or forced convection, have low heat transfer coefficients, require power, and are unsuitable for complex devices [3]. There are various two-phase flow systems, such as jet impingement, flow boiling, and spray cooling, that have high heat dissipation potential, but they could be costly and complex for such devices [4]. Therefore, the passive and two-phase flow systems, the heat pipes are sustainable approaches to thermal management. A high heat transfer coefficient is achieved by utilizing the latent heat of evaporation and condensation of the working fluid in a closed system [5-7]. So, heat pipes are widely accepted for electronics, solar, power systems, and avionics applications [3,8].

The pulsating heat pipe is a new member of the heat pipe family, having thermally-driven self-oscillatory two-phase flow behaviour for the working fluid [5]. First in 1990, Akachi introduced pulsating heat pipe [9]. The pulsating heat pipe can be used in a wide variety of applications that depend

on electronics systems as a main component. The most important part of a heat pipe is the mechanism involved in returning the condensate to the evaporator zone. The serpentine closed-loop structure of capillary tubes or machined channels on a flat plate is used in the pulsating heat pipe. The capillary action through wick material or the gravity force completes the recirculation of the working fluid in conventional heat pipes. At the same time, thermally excited oscillatory slug-plug flow behaviour in a capillary-size tube achieves net circulation action of working fluid. Despite so much development in our understanding of the pulsating heat pipe over the past three decades, there is still a requirement for more efforts to make it viable for industrial or domestic applications.

One of the important design parameters for the pulsating heat pipe is the diameter of the capillary tube or channel. The distribution of partially filled working fluid into vapour plugs and liquid slugs along the entire length is required for it to function. This phenomenon is achieved by selecting the cross-section using the Bond number, equation (1) [10]. The ratio of buoyancy force to surface tension force provides a capillary length depending on the working fluid properties. The dominance of surface tension forces helps to form the train of vapour plugs and liquid slugs [11].

$$d_{cr} = Bo \sqrt{\frac{\sigma}{g(\rho_l - \rho_g)}} \quad (1)$$

Where, d_{cr} is critical diameter, σ surface tension, ρ_l density of liquid phase, ρ_g density of vapor

phase, and g gravitational acceleration. The value of the Bond number varies from 0.7 to 1.8 to select the diameter of the channel [12].

The working fluid selection plays a very important role in deciding the thermal performance of a pulsating heat pipe. Thermal performance is influenced by thermo-physical properties such as boiling point, latent heat, specific heat, surface tension, dynamic viscosity, and thermal conductivity [8]. It is observed that working fluids with higher latent heat, lower dynamic viscosity, and lower surface tension can perform better in the pulsating heat pipe. The thermo-physical properties of water are best in this regard, but the delayed startup due to high surface tension and dynamic viscosity cause problems. So, to overcome this issue, water based surfactant solutions have been utilised for better startup, thermo-hydrodynamics, wettability, and bubble nucleation in the pulsating heat pipe [13,14]. The latent heat of the working fluid remains the same, but properties like dynamic viscosity and surface tension are changed with the addition of surfactants to water. We have performed experimental investigations with the working fluids acetone and pure water in the same experimental setup [15]. A visualisation study was also performed to find out the impact of operating conditions on the dual-loop setup [16]. Because the critical diameter was close to the larger diameter tube to form an asymmetric pulsating heat pipe, the thermal performance with working fluid acetone was improved. In an asymmetric single loop pulsating heat pipe, working fluid water at 50 and 60% has better thermal performance [12]. The asymmetric channels increase the pressure differences and the unbalanced driving force [17]. The experiments with the aqueous surfactant solution were planned to improve the thermal performance of the dual loop setup with the working fluid water as well. Kumar et al. [18] reported startup at a lower evaporator temperature using the surfactant solution and a dual-loop pulsating heat pipe. The optimum concentration was 500 PPM at 60% filling ratio in their study.

According to the literature, thermo-physical properties influence the thermal performance behaviour of a pulsating heat pipe. The present article has been focused on improving the thermal performance of the dual-loop asymmetric pulsating heat pipe with aqueous surfactant solutions. The experiments are conducted with various operating conditions to characterise the

pulsating heat pipe, such as inclination angles, filling ratios, and heat load patterns.

2. Experimental details and procedure

The prepared experiment setup specifications are listed in Table 1. The testing facility schematic is shown in Figure 1, along with all the necessary equipment required to run the experiments. The test specimen was installed over a rotatable panel and a bench to set various inclination angles. For these two turns (bend radius: 10 mm), two cartridge heaters were sandwiched between copper plates to function as the evaporator. The detailed description of the evaporator and heat pipe specimen is shown in Figure 2. The condenser section of the setup was kept in an acrylic jacket with an inlet and outlet for the coolant. The coolant supply at a constant flow rate and temperature was maintained while testing the thermal performance using a rotameter (Eureka SSRS-MGS-9) and constant temperature bath (chiller) (Siskin Profichill RHC-250 ST-100).

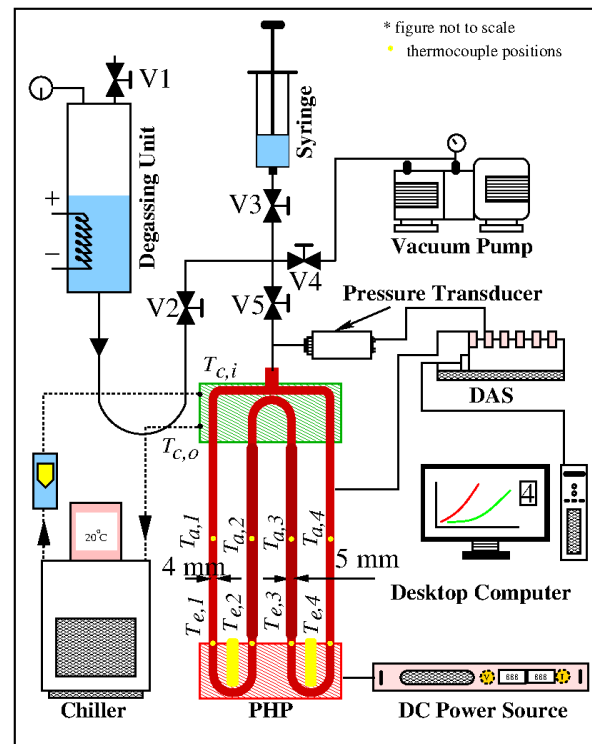


Figure 1. Schematic diagram of the pulsating heat pipe setup

The test specimen was equipped with a pressure transducer (Honeywell make; model AP122, range 0–1293 mmHg) at the condenser end. The tubes wall of adiabatic section have individual thermocouples (Tempsons make; T-type, probe diameter 0.5 mm). The evaporator thermocouples were inserted into the machined evaporator plate.

The condenser section thermocouples were placed at the jacket inlet and outlet ports. The thermal interfaces were filled using thermal paste (Cooler Master; $k \approx 8$ W/mK) for thermocouples and heater surfaces. Teflon insulation plates ($k \approx 0.25$ W/mK) covered the evaporator section. The adiabatic section was covered with a Nitrile foam tape ($k \approx 0.04$ W/mK of 3 mm thick) for insulation. The cartridge heaters in the evaporator section were connected to a DC power source (Keysight LXI N5771A). The signals from all thermocouples and pressure transducer were recorded from a data acquisition system (DAS) (National Instruments cDAQ-9189, 9213, and 9205) at 10 Hz.

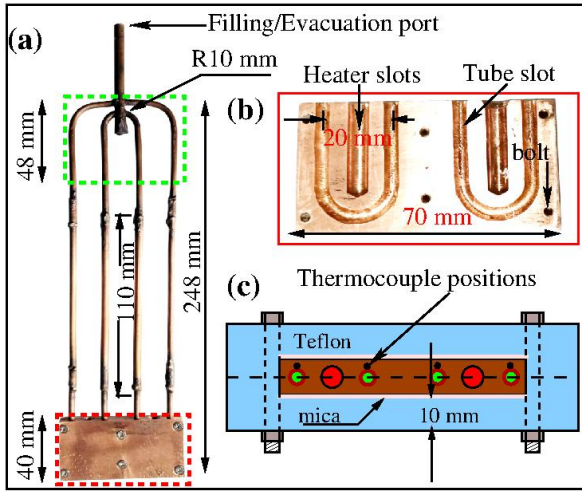


Figure 2. (a) Heat pipe specimen, (b) machined evaporator plate, and (c) schematic of evaporator assembly

The working fluid charging system consisted of stainless steel fittings (Swagelok make; ferrule fittings), a steel tank (degassing facility of 250 ml), and a syringe (Nipro 12 ml). A vacuum pump (Welch CRV Pro2, capacity 0.0002 mmHg) was used to evacuate the empty heat pipe before filling it with the working fluid.

The working fluid was prepared using pure water (Milli-Q, Merck) and sodium dodecyl sulphate (SDS) (CMC \approx 2500 PPM, CAS RN 151-21-3, TCI, C₁₂H₂₅NaO₄S \geq 97%). A cleaned conical flask was used to make the solution with the help of a magnetic stirrer. The aqueous surfactant solution was prepared with concentration values of 500, 1000, 1500, and 2500 PPM by adding SDS solvent to the water by weight. The solution was first degassed using a heating and venting method to remove non-condensable gases. This working fluid was supplied to the evacuated heat pipe with the help

of a syringe at the desired filling ratio. The filling ratio is the ratio of the filled to the empty volume of the heat pipe.

Table 1. The pulsating heat pipe experimental setup details

Tube material	Copper
Internal Diameter	2.4 & 3.4 mm
Number of turns	2
Filling Ratios	50 & 60%
Orientation	0°, 30°, 60° & 90°
Length	248 mm
Maximum heat load	70 W
Evaporator area	70×40 mm ²
Evaporator length	35 mm
Adiabatic length	160 mm
Condenser length	48 mm

3. Thermal performance calculations

The heat input ($Q_{in} = V \times I$) to the evaporator section causes temperature variations. The thermal performance has been estimated based on the average evaporator and condenser temperatures for an individual heat load. For a thermocouple, the average temperature can be written as [19]:

$$T_{e,1} = \sum_{j=1}^n T_{e,1,j} \quad (1)$$

Similarly, for other thermocouples $T_{e,2}$, $T_{e,3}$, $T_{e,4}$, $T_{c,i}$, and $T_{c,o}$. So, the mean evaporator and condenser temperatures can be represented as:

$$T_e = \frac{T_{e,1} + T_{e,2} + T_{e,3} + T_{e,4}}{4} \quad (2)$$

$$T_c = \frac{T_{c,i} + T_{c,o}}{2} \quad (3)$$

In operating condition, the sensible heat transfer to the coolant can be written as: $Q_c = \dot{m}c_p(T_{c,o} - T_{c,i})$ [20]. Where, c_p is the specific heat, \dot{m} mass flow rate of the coolant.

The sensible and the total heat input mean, ($Q = \frac{Q_{in} + Q_c}{2}$) effectively is transferred between the condenser and evaporator sections [20,21]. The heat loss to the ambient from the different sections can be $Q_{loss} = Q_{in} - Q$. After start-up and before dry-out, the maximum heat loss was 5.2% at a 60 W heat load. Before startup, the heat is mainly absorbed by the working fluid, evaporator, and tube walls. On the other hand, at a dry-out condition, the heat is absorbed only by the evaporator section and not the working fluid. The

average thermal resistance can be written as equation (4) [21].

$$R_{th,avg} = \frac{T_e - T_c}{Q} \quad (4)$$

The maximum uncertainty associated with the thermal resistance and heat load estimations in this study was 7.7% and 2.7%, respectively.

4. Results and discussion

4.1. Start-up and transient characteristics

The heat input to the evaporator section of the pulsating heat pipe raises the temperature of the working fluid inside the tube. As the temperature of the wall is higher than the fluid temperature, a single phase flow heat transfer behavior is observed, as shown in Figure 3.

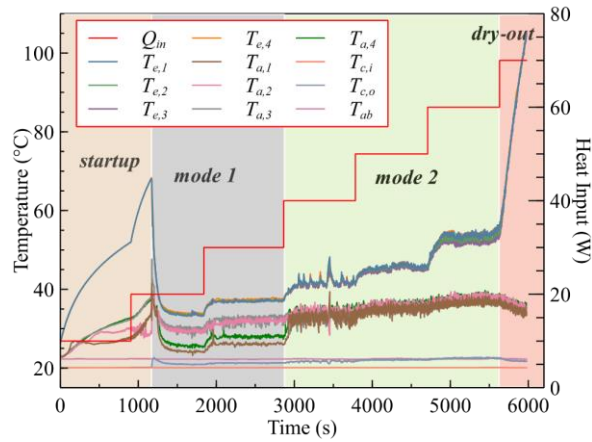


Figure 3. Temporal variations of temperature with surfactant solution (1500 ppm, FR=60%) in vertical orientation

The initial heat load of 10 W was insufficient to activate the heat pipe. However, the adiabatic section temperature fluctuations indicate small-scale movement of the fluid. The startup of the heat pipe occurs when the heat load is 20 W, there is a sudden drop in the evaporator temperature, and the pseudo-steady state operation is achieved. A high transfer coefficient because of the two-phase flow effectively decreases the evaporator temperature. After startup, there is a temperature difference and fluctuations in the adiabatic sections, i.e., *mode 1* operates in circulatory-oscillatory mode. The middle two columns, having a larger cross-section, have a higher temperature than the outer columns. This state was continued up to a 30 W heat load, but at a slightly higher temperature. Further variation in the heat load, i.e., *mode 2*, the temperature difference between the adiabatic sections, indicates the dominance of purely oscillatory motion. The

variations in the heat loads change the thermo-hydrodynamic behavior of the heat pipe. The operation was gradually approaching the *dry-out* of the evaporator at 70 W of heat load.

4.2. Thermal performance under sudden heat loads

In this section, the thermal performance behavior with sudden heat loads will be discussed based on the temperature variations. Figure 4 shows the temperature variation at 50 W of heat load operating in vertical orientation. The sudden or abrupt heat loads were selected from the gradually applied heat loads. As discussed above, the pulsating heat pipe failed to maintain the evaporator temperature at a 70 W heat load, so, 50 and 60 W loads were applied suddenly. The heat pipe established a successful startup at 50 W of heat load and a pseudo-steady state evaporator temperature. The temperature of all the columns was nearly equal and achieved a pseudo-steady state after startup. The same temperature in all columns indicates that the fluid is having the same direction of motion, which can only be possible if there is purely oscillatory motion of the working fluid in the individual columns.

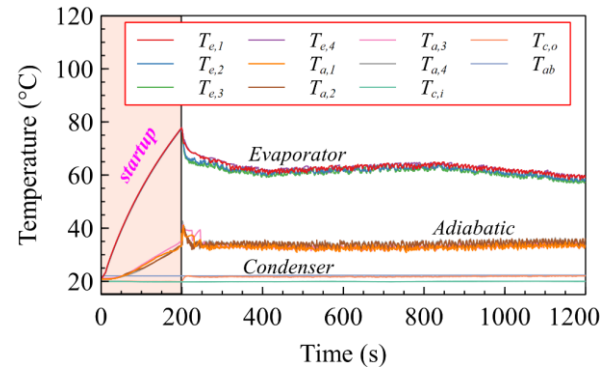


Figure 4. Startup of two-phase flow heat transfer at heat load 50 W SDS 1000 PPM (FR=60%)

4.3. Effects of inclination angles

The average thermal resistance is compared when operating the heat pipe at different inclination angles. In vertical (90°) orientation, the heat pipe has the lowest thermal resistance, as shown in Figure 5. The horizontal orientation operation shows the highest thermal resistance and a significant drop in thermal performance. The change in thermal performance with lowering the inclination angle shows the contribution of buoyancy force to the oscillatory flow of the working fluid. In vertical operation, the perfect cylindrical bubble with hemispherical ends helps to push the adjacent liquid towards the condenser

section more effectively than bubbles with oblate ends [10].

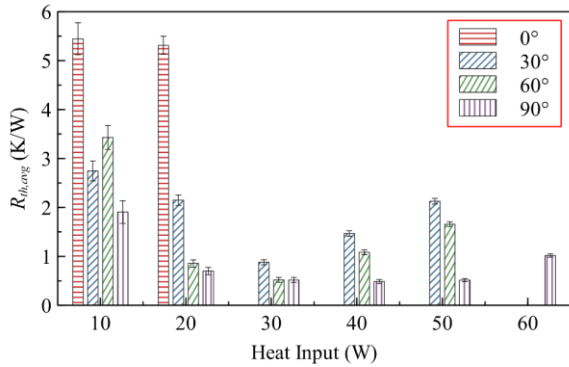


Figure 5. Thermal performance under various inclination angles at 1000 PPM (FR 50%)

The bubbles are pointed towards the upper wall with oblate ends, and working fluid is escaping these bubbles, making the pumping inefficient. An inefficient movement of fluid from the hot region reduces the thermal performance of the heat pipe and increases the operating temperature. Eventually, the horizontal operation of the asymmetric pulsating heat pipe fails in this configuration and operating condition.

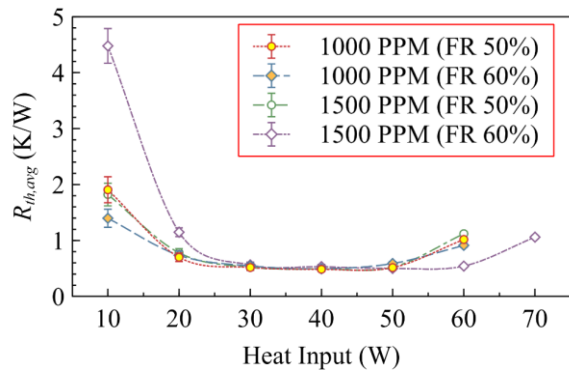


Figure 6. Average thermal resistance at different filling ratios for various surfactant concentrations

4.4. Effects of filling ratios

The effect of the filling ratio on the thermal performance behavior is shown in Figure 7. The optimum range is 50–60% of the filling ratio for the pulsating heat pipes [15,18]. The low filling ratio is liquid-deficient, while the high filling ratio operation becomes vapor deficient. So, both phases are required to have an optimum value of vapor and liquid for the pumping action between the evaporator and the condenser section. The concentration of surfactant at 1500 PPM at a 60% filling ratio shows higher heat transfer capability than a 50% filling ratio. The solutions having 500 and 2500 PPM concentrations were used at a 60%

filling ratio only. At higher filling ratios, the contribution of sensible heat transfer increases, which delays the start-up of two-phase heat transfer [11].

4.5. Effect of surfactant concentration

The concentration impact of the surfactant in the solution over the thermal performance is shown in Figure 7 for the vertical orientation operations. The change in driving force due to the variation in the properties of surface tension and viscosity affects the operating temperature and hence the thermal resistance [8]. The heat load capability was unchanged for the 1500 and 2500 PPM of the pulsating heat pipe. The thermal resistance was changing with concentration variations.

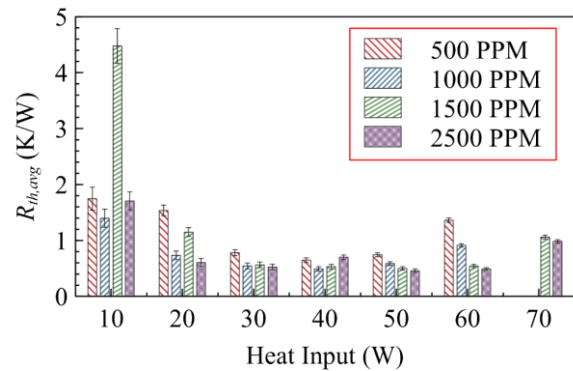


Figure 7. Variation in the thermal performance due to surfactant concentration (FR 60%)

4.6. Thermal performance comparison

Figure 8 shows the comparison of thermal performance among asymmetric (non-uniform) and conventional channel pulsating heat pipes for working fluids such as pure deionized water and aqueous surfactant solutions.

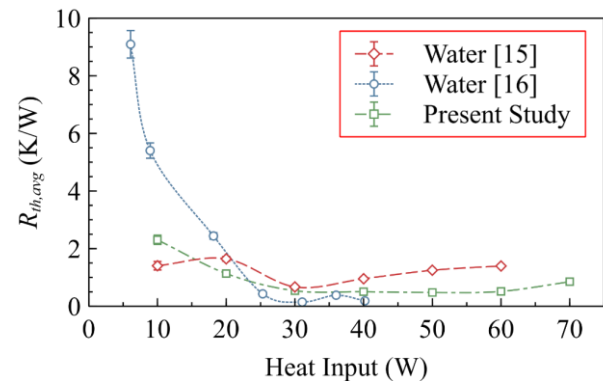


Figure 8. Thermal performance comparison for conventional, asymmetric configuration, and for working fluids

The thermal resistance based on the input power was used to compare different configurations of the heat pipe. The lower surface tension and improved wettability decrease the operating temperature, which improves startup performance and lowers the thermal resistance. The heat load range was almost equivalent to the working fluid, pure water.

5. Conclusions

The present study has focused on improving the startup phenomena and the thermal performance of a dual-loop asymmetric pulsating heat pipe using an aqueous surfactant solution. The operating parameters like inclination angle, filling ratio, and heat load patterns have also affected the thermal performance. The change in physical properties such as surface tension and improved wettability of surface tension and viscosity results in early two-phase flow startup even at low evaporator temperatures.

The surfactant concentration between 1000 and 2500 shows better thermal performance. The minimum thermal resistance of 0.46 K/W was obtained operating in vertical orientation, which is required for many passive thermal management applications. The heat pipe has shown better operating characteristics up to a 30° inclination angle.

By introducing larger diameter tubes in the adiabatic section, this asymmetric pulsating study aimed to improve the circulatory-oscillatory motion of the working fluid. At higher heat loads, the expected unidirectional flow might happen if the larger channels are placed alternately for further enhancement of the thermal performance.

Acknowledgements

This work is partially supported by Ministry of Electronics and Information Technology through Visvesvaraya PhD Scheme with reference number MeitY/PhD/2552.

Nomenclature

d	diameter	mm
V	Voltage	V
T	Temperature	°C
I	Current	A
\dot{m}	Mass flow rate of coolant	kg/h
$R_{th,avg}$	Thermal resistance	W/K
Q	Heat	W

References

- [1] HS Blanks, The temperature dependence of component failure rate*. *Microelectron Reliab.* 1980. 20: p. 297-307.
- [2] R. Perez, Thermal Physics of failure. *SAE Tech Pap.* 1996. 105: p. 74-78.
- [3] I. Mudawar, Assessment of High-Heat-Flux Thermal Management Schemes. *IEEE Trans Components Packag Technol.* 2001. 24(2): p. 122-141.
- [4] Sohel Murshed SM and Nieto de Castro CA, A critical review of traditional and emerging techniques and fluids for electronics cooling. *Renew Sustain Energy Rev.* 2017. 78(May): p. 821-833.
- [5] B. Tong, T. Wong, and K. Ooi, Closed-loop pulsating heat pipe. *Appl Therm Eng.* 2001. 21(18): p. 1845-1862.
- [6] M. Mameli, M. Marengo, and S. Khandekar, Local heat transfer measurement and thermo-fluid characterization of a pulsating heat pipe. *Int J Therm Sci.* 2014. 75: p. 140-152.
- [7] S. Khandekar, AP Gautam, and PK Sharma, Multiple quasi-steady states in a closed loop pulsating heat pipe. *Int J Therm Sci.* 2009. 48(3): p. 535-546.
- [8] Nazari M Alhuyi, MH Ahmadi, R Ghasempour, and MB Shafii, How to improve the thermal performance of pulsating heat pipes: A review on working fluid. *Renew Sustain Energy Rev.* 2018. 91: p. 630-638.
- [9] Hisateru Akachi. Structure of heat pipe. *United State Pat.* 1990. Patent number 4,921,041 (19).
- [10] N Saha, PK Das, and PK Sharma, Influence of process variables on the hydrodynamics and performance of a single loop pulsating heat pipe. *Int J Heat Mass Transf.* 2014. 74: p. 238-250.
- [11] S Khandekar and Groll M, An insight into thermo-hydrodynamic coupling in closed loop pulsating heat pipes. *Int J Therm Sci.* 2004. 43(1): p. 13-20.
- [12] ED Patel and S Kumar, Thermal performance of a single loop pulsating heat pipe with asymmetric adiabatic channel. *Appl Therm Eng.* 2023. 219. doi:10.1016/j.applthermaleng.2022.119541
- [13] K Bao, X Wang, Y Fang, X Ji, X Han, and G Chen. Effects of the surfactant solution on the performance of the pulsating heat pipe. *Appl Therm Eng.* 2020. 178. doi:10.1016/j.applthermaleng.2020.115678
- [14] V Ayel, M Slobodeniuk, R Bertossi, et al. Thermal performances of a flat-plate pulsating heat pipe tested with water, aqueous mixtures and surfactants. *Int J Therm Sci.* 2022. 178. doi:10.1016/j.ijthermalsci.2022.107599
- [15] ED Patel, and S Kumar, A capillary tube pulsating heat pipe with asymmetric adiabatic channels for thermal management. *IEEE Trans*

Components, Packag Manuf Technol.
Published online 2022.

doi:10.1109/TCPMT.2022.3225470

- [16] ED Patel and S Kumar, The Impact of Variation in Filling Ratios, Evacuation Pressure, and Heat Input on Thermal Performance of Pulsating Heat Pipe. IEEE Trans Components, Packag Manuf Technol. 2022. 12(2): p. 259-269.
- [17] DS Jang, JS Lee, JH Ahn, D Kim, and Y Kim, Flow patterns and heat transfer characteristics of flat plate pulsating heat pipes with various asymmetric and aspect ratios of the channels. Appl Therm Eng. 2017. 114: p. 211-220.
- [18] M Kumar, R Kant, AK Das, and PK Das. Effect of Surface Tension Variation of the Working Fluid on the Performance of a Closed Loop Pulsating Heat Pipe. Heat Transf Eng. 2018. 40(7): p. 509-523.
- [19] VM Patel, Gaurav, and HB Mehta, Influence of working fluids on startup mechanism and thermal performance of a closed loop pulsating heat pipe. Appl Therm Eng. 2017. 110: p. 1568-1577.
- [20] CY Tseng, KS Yang, KH Chien, SK Wu, and CC Wang, A novel double pipe pulsating heat pipe design to tackle inverted heat source arrangement. Appl Therm Eng. 2016. 106: p. 697-701.
- [21] B Markal, AC Candere, M Avci, and O Aydin, Effect of double cross sectional ratio on performance characteristics of pulsating heat pipes. Int Commun Heat Mass Transf. 2021. 127.
doi:10.1016/j.icheatmasstransfer.2021.105583

Bionic Two-phase Loops Inspired by Water Transport System of Trees

Hongxing Zhang¹, Yuandong Guo², Boyang Sun², Guoguang Li¹, Jianyin Miao^{1*}, Guiping Lin², Dongsheng Wen²

¹ Beijing Key Lab of Space Thermal Control Technology, China Academy of Space Technology, Beijing, P.R. China

² School of Aeronautic Science and Engineering, Beihang University, Beijing, PR China

*Corresponding author email address: redlincoco@hotmail.com

Abstract

Trees have been evolving on the earth for over 400 million years. Its water transport system, including the powerful and reliable driving method and water transport network, has evolved to be efficient and effective enough to survive even in the extreme weather condition. The fundamental principles of the water transport system of trees are reviewed and analysed. Inspired by the trees, a two-phase loop driven by both osmotic pressure and capillary force is presented to improve the heat transfer ability and operation stability of two-phase heat transfer technology for spacecraft thermal control. An osmotic two-phase loop was set up to validate the feasibility and investigate its performance and characteristics. By using an osmotic membrane of 151.2cm² and NaCl solution of 5mol/L to provide an osmotic pressure of 175kPa, the water loop succeeded to circulate and transfer over 120W heat at an adverse elevation over 200cm.

Keywords: Osmotic pressure; Two-phase loop; Water transport; Tree

1. Introduction

The 156-m eucalyptus amygdalina in Australia is the tallest tree on the earth. The California redwoods are more than 120m tall and have been growing on the earth for thousands of years [1]. Woodward [2] (2004) analyzed how tall could the trees be and what stops them growing any taller. The conclusion is that water supply is the key constraint on height, given that it is essential for the other physiological factors. For the tall trees, great driving force of over 2MPa is required to overcome the gravity when water is transported from roots to leaves. It was estimated that the amount of vaporized water from all the plants on the earth is about 3.2×10⁷ million tons per year [3]. A 45-m redwood needs to transport about 600kg water from roots to leaves each day [2]. However, trees have been evolving for over 400 million years on the earth. The water transport system of trees, including the powerful and reliable driving method and water transport network, has evolved to be efficient and effective enough to survive even in the extreme weather condition.

This paper reviews the fundamental principles of the water transport system of trees and the controversial Cohesion-Tension Theory that was proposed by biologists to explain the water transport principles. Especially, the important roles of the capillary force in leaves and the osmotic pressure in roots for the water transport system of trees are discussed.

Inspired by the water transport system of trees, a two-phase loop driven by both osmotic pressure and capillary force is presented to improve the heat

transfer ability and operation stability of two-phase heat transfer technology for spacecraft thermal control. An osmotic two-phase loop was set up to validate the feasibility and investigate its performance and characteristics.

2. Water Transport System of Trees

Natalya^[4](2008) and Jensen^[5](2016) reviewed the analysis on the long-distance water transport process in plants. As Fig.1 shows, the process includes the water suction from soil by roots, the upward transport of water and dissolved minerals through the xylem from roots to leaves, the water evaporation in leaves, and the downward transport of sugars produced by photosynthesis along the phloem from leaves to the growing organs, such as flowers, fruits and roots.

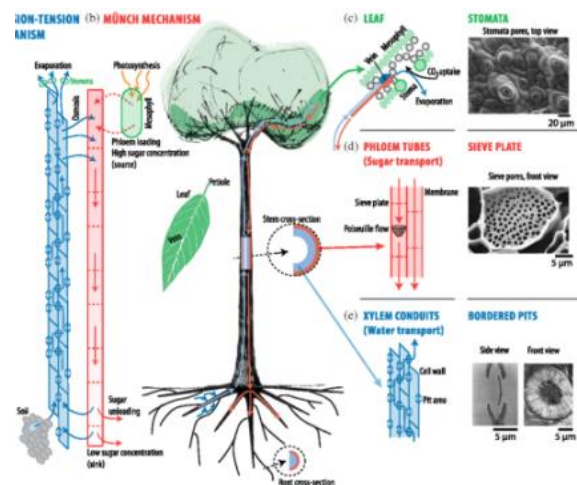


Figure 1. Water transport in Trees [5]

The water and dissolved mineral substances are absorbed from the soil through the large surface of the root hairs due to the high root pressure, which is up to 5MPa and generated by the osmotic pressure in root cells. It is partially responsible for driving the upward flow of liquid in the xylem^[4]. Only 1-2% of the large amount of water transferred to leaves is used for the photosynthesis to produce sugars. Most of the water evaporates in the porous tissue of leaves and generates the capillary force, which is also used for driving the water upstream flow in the xylem^[4,5].

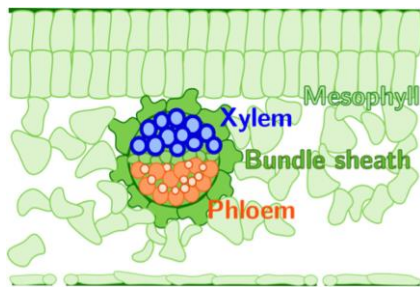
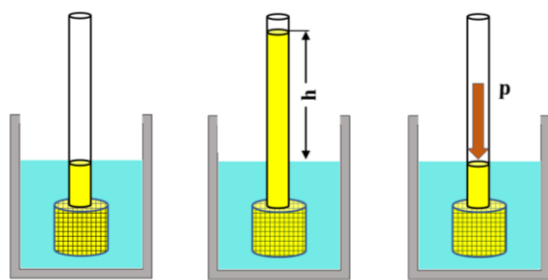


Figure 2. Water and sugar transport in Leaves^[5]

The physical phenomenon of osmosis widely exists, referring to the process that the water flows from low solute concentration side to high solute concentration side through a natural or artificial semi-permeable membrane. Definition of osmotic pressure is the pressure generated by or associated with osmosis and dependent on the molar concentration and absolute temperature. The essence of osmotic pressure is the chemical potential difference of solution. Osmosis can be understood as the process of two solutions with different chemical potentials moving towards the equilibrium state. The osmosis and osmotic pressure are shown in Figure 3.



a) Initial state b) Equilibrium c) Osmotic pressure

Figure 3. Osmosis and osmotic pressure

An important part of applications of osmosis is the membrane technology. Membrane technology developed based on the osmosis achieved a rapid development around 1960 and gradually rose to become an important branch of separation technology. It uses thin film materials with selective permeability properties to separate,

purify and concentrate liquids. Breakthroughs have been made in the theoretical development of membrane technology and various more advanced membrane technologies have also made great progress.

3. Conception of A Bionic Two-phase Loop

Engineers can learn a lot from the water transport system of trees, for example, the efficient and effective water transport network, the reliable driving mode by both the capillary force and the osmotic pressure.

Inspired by the water transport system of trees, a bionic two-phase loop driven by both osmotic pressure and capillary force is proposed to improve the heat transfer ability and operation stability of two-phase heat transfer technology for spacecraft thermal control.

As shown in Fig. 4, the system consists of an evaporator, a condenser, vapor and liquid lines, a control valve, an osmotic membrane, working fluid and high concentration solution.

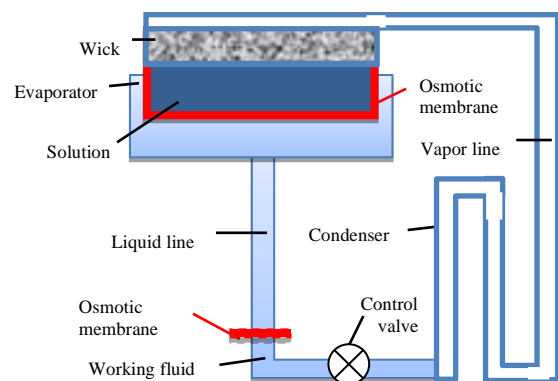


Figure 4. Constitution of the bionic two-phase loop

In the bionic two-phase loop, the driving parts contains the NaCl solutions of different concentrations and permeable membranes. The osmotic pressure difference between solutions of different concentrations will drive the water through the permeable membrane into the side of the high-concentration solution to form a liquid column with a certain height. The working fluid can be transported to the top evaporator against gravity. Heat is taken away by the solvent endothermic phase transition and the solute is left to maintain the solution concentration unchanged. After the solvent is cooled by the condenser, it flows back to the low concentration side and is driven by osmotic pressure again to transport across the membrane, forming a complete closed loop.

In contrast to the traditional mechanical pumped fluid loop or capillary loop (loop heat

pipes and capillary pumped loop), the advantages of this loop are as follows.

(1) The driving forces, including the osmotic pressure and capillary force, are both passive, and do not need power supply.

(2) The osmotic pressure is able to provide a much higher driving force than traditional ways, which can then increase the heat transfer capability and heat transfer distance. For instance, the NaCl solution of 0.5 mol/L can create a driving force of more than 2.5MPa.

(3) The two-driving-force mode can improve the stability of two-phase loops. The osmotic pressure works as a push force while the capillary force is an pull force. This is beneficial to the stable operation of two-phase flow.

(4) This loop can also be designed with multi-evaporators to accumulate multi-heat sources. The osmotic pressure provides the push force while the capillary force can be automatically adjusted according to the individual heat load of the source.

However, this paper only describes the characteristics of a two-phase loop driven by the osmotic pressure. More information about the two-driving-force mode will be published soon.

4. Test Setup

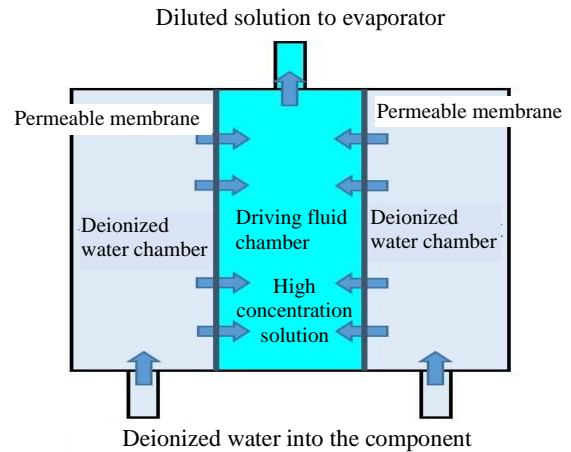
4.1 Osmotic Pressure Drive Component

In order to introduce osmotic pressure to the two-phase loop as a driving force, it is necessary to design an osmotic pressure driving unit which provides driving force to supply working fluid. The necessary condition for the osmosis phenomenon is to choose permeable membranes and solutions with different concentrations.

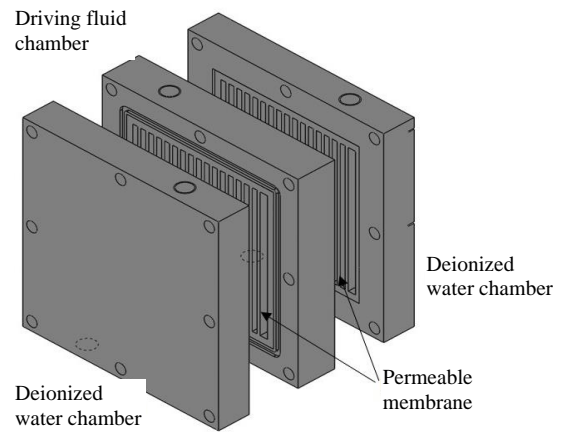
The osmotic pressure driving unit consists of driving fluid chamber for high concentration solution, deionized water chamber, permeable membrane, sealing and structure component. The driving fluid chamber is filled with high concentration sodium chloride solution and separated from the deionized water chamber by permeable membrane, shown in Figure 5.

Considering the requirements of water permeability, environmental adaptability and performance, the loop uses the HTI-CTA FO membrane composed of active layer of cellulose triacetate and support layer of polyester screen, which has an upper temperature limit of 70°C and a maximum water flow rate of 18L/m²h. The working fluid of the bionic loop is the sodium chloride aqueous solution with good solubility, high osmotic pressure and stable chemical properties. The concentration of the sodium

chloride aqueous solution is 5mol/L. Main parameters of this unit are shown in Table 1.



(a) Fluid flow inside



(b) Structure

Figure 5. Working principle and structure of osmotic pressure driving unit

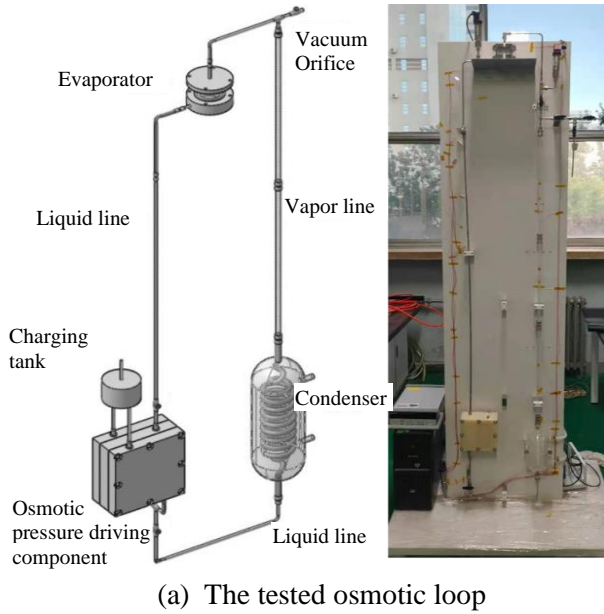
Table. 1 Parameters of osmotic pressure driving unit

Item	Parameters
Driving liquid chamber size	16mm*16mm*2mm
Deionized water chamber size	16mm*16mm*3mm
Osmotic pressure driving unit material	POM
Effective membrane area of permeable membrane	151.2cm ²

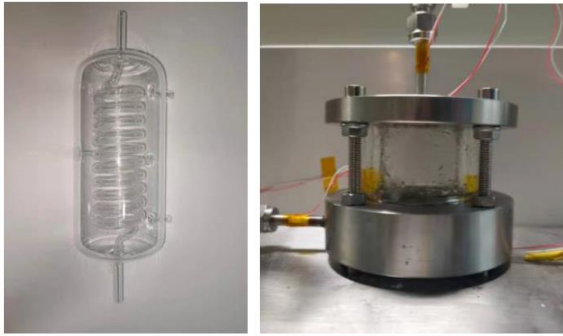
4.2 Osmotic Two-phase Loop

An osmotic two-phase loop was set up to validate the feasibility and investigate its performance and characteristics. By using a 151.2cm² osmotic membrane and 5mol/L NaCl solution to provide osmotic pressure, this loop succeeded to circulate and transfer over 120W heat at an adverse elevation over 200cm.

The loop is composed of osmotic pressure driving unit, evaporator, condenser, liquid and vapor line. The test bench of the bionic two-phase loop is shown in Figure 6.



(a) The tested osmotic loop



(b) Condenser (c) Pool boiling evaporator

Figure 6. Test setup of the osmotic two-phase loop

There is an adverse elevation of 2m between the evaporator and the condenser. A pool boiling evaporator is used in the experiments of the bionic loop. The condenser of the bionic loop is a glass spiral tube condenser. The liquid line is a stainless-steel pipe with an outer diameter of 6mm and the vapor line is a glass pipe with an outer diameter of 10mm. The structure of some parts of the bionic loop is shown in Figure 6. The parameters of evaporators and condenser are shown in Table 2 and Table 3.

Table 2. Pool boiling evaporator

Item	Pool boiling evaporators
Dimensions	Base/top:90mm; thickness:10mm Glass wall: 60mm; height:40mm
Liquid storage space	17.5ml

Table 3. Condenser parameters

Item	Parameters
Glass shell	length 300mm, diameter 100mm
Glass spiral tube	Tube diameter 10mm; Pitch 20mm, Height 200mm
Vapor line inlet/outlet	Outer diameter 10mm; inner diameter 8mm
Cooling water inlet/outlet	Outer diameter 10mm; inner diameter 8mm
Condensation area	180cm ²

The test bench mainly includes the simulated heat source system, the cooling system and the data acquisition system. PTC ceramic heaters are used to simulate the heat load of devices. In the experiment, the heat load of the ceramic heating plate is controlled by adjusting the voltage and current output by the DC power supply. The cooling system uses AC2600D-T cooling water circulation machine to circulate cooling water to the condenser. The cooling water temperature can be adjusted between 0-50°C. The maximum refrigerant flow rate is 2m³/h and the maximum cooling capacity is more than 1kW.

The data acquisition system can collect the temperature and pressure information of the bionic loop experiment platform. It uses the T-type thermocouples to measure the temperatures and the SMP131-TLD pressure sensor to measure the pressures. The DAQ970 data acquisition instrument is used to collect and process the experiment data.

5. Test Results and Discussion

5.1 Osmotic Pressure

As the driving force of the bionic loop, the osmotic pressure affects the heat transfer capability, the anti-gravity performance, heat transfer distance and so on.

To estimate the performance of the osmotic pressure driving unit, the flow rate and the osmotic pressure were measured.

The flow rate refers to the water supply per unit time from the osmotic pressure driving unit to evaporators, which affects the maximum heat load on the bionic loop.

The device, shown in Figure 7, was used to measure the flow rates at adverse elevations of 1m, 1.5m and 2m. The test results are listed in Table 4.

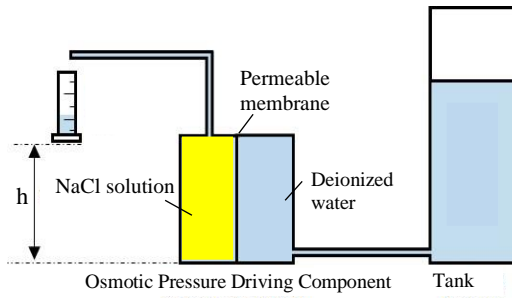


Figure 7. Flow rate testing device

Table 4 Flow rate of the osmotic pressure driving unit

Adverse elevation	Volume flow rate (ml/min)	Flow rate (L/m ² h)
1m	3ml/min	12L/m ² h
1.5m	3ml/min	12L/m ² h
2m	3ml/min	12L/m ² h

Test results show that the adverse elevation between the evaporator and the osmotic pressure driving unit has almost no effect on the water supply. The osmotic pressure driving units can provide stable water supply to the evaporator at various adverse elevation less than 2m. The volume flow rate of the osmotic pressure driving unit to the evaporator is 3ml/min when the anti-gravity height is 1m, 1.5m or 2m. The flow rate is 12L/m²h.

The theoretical maximum heat transfer capability of the bionic loop can be calculated in the case that all the water supply from osmotic pressure driving unit to the evaporator vaporizes to transfer heat to the condenser. The theoretical maximum heat load should be 120W.

Osmotic pressure generated by osmotic pressure driving unit is the main driving force, which affects the anti-gravity performance of the bionic loop. In order to measure the maximum osmotic pressure driving force, the device, shown in Figure 8, was used to test the osmotic pressure by the designed osmotic pressure driving unit. The change curve of the osmotic pressure over time is shown in Figure 9.

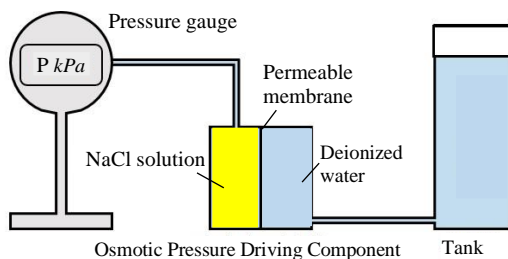


Figure 8. Osmotic pressure testing device

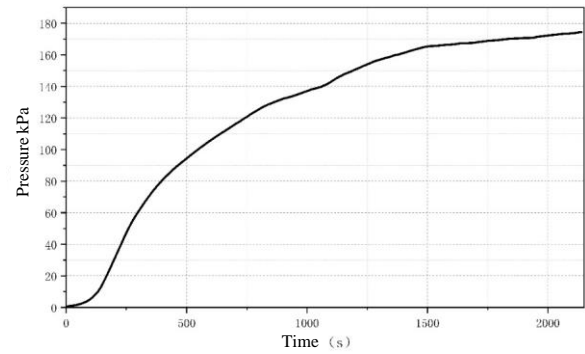


Figure 9. Tested osmotic pressure

Test results show that the osmotic pressure driving unit can generate a driving force of about 175kPa, which is greater than the traditional loop heat pipes. The greater the osmotic pressure driving force can be generated, the greater the gravity resistance and flow resistance the system can be overcome, which means the osmotic pressure of the driving unit determines the anti-gravity performance of the bionic loop.

Note that the theoretic osmotic of 0.5 mol/L NaCl solution should have generated an osmotic pressure of more than 2.5MPa. However, the test result of 5mol/L solution is much less than the calculated value. This should've been caused by the sealing problem of the osmotic pressure driving unit, which should be improved in the future.

5.2 Start-up Characteristics

Tests were conducted to investigate the effects of heat loads on the start-up process and working fluid distribution in the loop, especially in the pool boiling evaporator. Figure 10 shows the temperatures of the loop with pool-boiling evaporator at a heat loads of 100W over time.

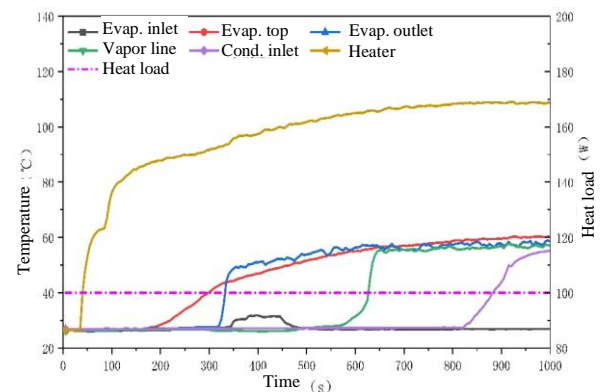


Figure 10. Start-up process of the bionic loop with a pool boiling evaporator

As illustrated in Figure 11, when the heat load is less than 120W, the liquid working fluid in the pool boiling evaporator rises slowly. When the

heat load is more than 120W, the liquid working fluid in the evaporator decreases. The change of liquid working fluid level in the evaporator indicates that the heat transfer capability of the bionic loop is about 120W.

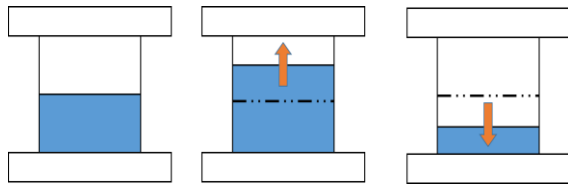


Figure 11. Liquid level change in the pool boiling evaporator at various heat loads

It can be found that the start-up process of the bionic loop can be divided into three stages. In the first stage, the working fluid in the evaporator absorbs heat and vaporizes. At that time, both the temperature and pressure of the vapor line rise rapidly. In the second stage, high-temperature vapor moves forward along the vapor line. The temperatures on the vapor line rise gradually. The beginning of the third stage is marked by the entry of high-temperature vapor into the condenser. The temperature and pressure of the vapor line reaches the maximum value and remain stable thereafter.

5.3 Operation Performance at Adverse Elevations

The anti-gravity performance of the bionic loop is the ability to run stably in different working conditions when there is an adverse elevation between the evaporator and the condenser. In the experiment, the anti-gravity performance is tested at a 2m adverse elevation.

The bionic loop with pool boiling evaporator was applied with 100W to start up. Then, the heat load on pool boiling evaporator was increased from 100W to 160W, and then decreased to 100W. The temperature curves of the bionic loop over time are shown in Figure 12.

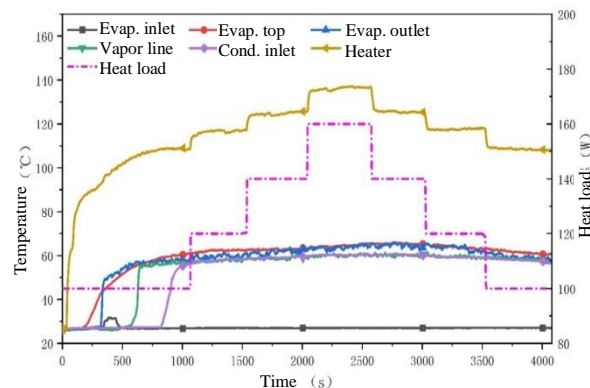


Figure 12. Operating temperatures at various heat loads

It can be found that bionic loop can be started smoothly and operate stably. The heat transfer capability of the bionic loop is about 120W. According to the test of the osmotic pressure driving unit, the theoretical maximum heat load based on the working fluid flow rate is also 120W. The test result is consistent with the theoretical analysis.

6. Conclusions

The principles of the water transport system of trees are analysed. Inspired by the trees, a two-phase loop driven by both osmotic pressure and capillary force is presented.

(1) The bionic two-phase loop driven by both osmotic pressure and capillary force can extraordinarily improve the heat transfer ability and operation stability of two-phase heat transfer technology.

(2) An osmotic two-phase loop was set up to validate the feasibility and investigate its performance and characteristics. By using an osmotic membrane of 151.2cm² and NaCl solution of 5mol/L to provide an osmotic pressure of 175kPa, the water loop succeeded to circulate and transfer over 120W heat at an adverse elevation over 200cm.

(3) More research should be conducted to investigate the bionic two-phase loop driven by both the osmotic pressure and the capillary force, which should have obvious advantages.

References

- [1] George Koch, Stephen Sillett, Gregg Jennings, and Stephen Davis, How Water Climbs to the Top of a 112 Meter-Tall Tree, *Essay 4.3* (2006), 5 pages, in *Plant Physiology Online*, Fifth Edition.
- [2] Ian Woodward, Tall Storeys. *University of Sheffield Nature*, Vol 428, 22 April, 2004
- [3] David J Beerling, and Peter J. Franks, The hidden cost of transpiration, *Nature* 464 (2010), 495-496.
- [4] Natalya N. Kizilova, Long-distance liquid transport in plants, *Proceedings of the Estonian Academy of Sciences*, 2008, 57, 3, 179-203
- [5] K. H. Jensen, et. al., Sap flow and sugar transport in plants, *Reviews of Modern Physics*, Vol 88, July - Sept., 2016.

Experimental Investigation of a Novel Flat-plate Loop Heat Pipe

Guoguang Li, Hongxing Zhang*, Zhichao Jia, Jianyin Miao, Chang Liu, Sixue Liu, Zenong Fang

¹ Beijing Key Lab of Space Thermal Control Technology, China Academy of Space Technology, Beijing, P.R. China

² School of Aeronautic Science and Engineering, Beihang University, Beijing, PR China

*Corresponding author email address: redlincoco@hotmail.com

Abstract:

The new type stainless steel ammonia flat-plate loop heat pipe uses reinforced structure to improve the compressive strength of the shell. A performance test was carried out for the normal temperature zone to investigate the influence of the relative position of the evaporator and the compensator on the working temperature. It is found that when the compensation chamber is located above the evaporator, and the evaporator has a favorable posture for liquid supply, the working temperature will be slightly lowered. The maximum heat transfer power is significantly increased in the gravity attitude, and decreased in the anti-gravity attitude. Through the analysis of heat transfer resistance under the condition of horizontal posture, the thermal resistance of the shell is the main reason for the increase of the thermal resistance of the system was founded. The flat plate evaporator with this structure is more suitable for working in the normal temperature range and has a smaller thermal resistance.

Keywords: Stainless steel; Ammonia; Flat-plate loop heat pipe; Thermal control

1. Introduction

The loop heat pipe is a passive two-phase heat transfer component, which has many advantages such as high reliability, high power cooling capacity, long-distance transmission, anti-gravity operation and high temperature control accuracy. With the miniaturization of electronic equipment, the application advantages of flat-plate loop heat pipe gradually become prominent. In addition to inheriting the advantages of traditional loop heat pipe, the flat-plate loop heat pipe has the characteristics of small size and convenient installation, which have become a research hotspot in recent years^[1-5].

Small loop heat pipes can be divided into disc type and flat type according to the relative positions of the evaporator and the compensation chamber^[2].

In 2000, on the basis of the cylindrical loop heat pipe, considering the effect of removing the thermal resistance caused by the saddle, Yu Maydanik^[3] et al. developed a small discoid ammonia loop heat pipe. The heat pipe, with a diameter of 30mm and a thickness of 12mm, considered the influence of parasitic heat leakage on the operation of the heat pipe, and proved that in the case of high heat flux, the disc structure evaporator with lighter weight is more advantageous than the cylindrical evaporator for the system thermal resistance.

In 2014, Wang D, Liu Z^[4] et al. developed a small discoid ammonia loop heat pipe, with a heating surface of 19cm², a thickness of the capillary core

of 2.8mm, and a maximum heat transfer capacity of 180W. Through different sealing methods and the use of heat insulation core measures to avoid the negative effects of parasitic heat leakage, it was proposed that the structural strength and reservoir volume are the disadvantages of the disc structure.

On the basis of the cylindrical loop heat pipe, the disc structure small loop heat pipe achieved a breakthrough in weight reduction and small system thermal resistance. Through continuous attempts, the problem of parasitic heat leakage caused by the capillary thickness of the disc evaporator has been solved. But in the case of long-distance and large-area heat transfer, the shortcomings of the disc structure were gradually exposed. Through continuous improvement, a flat-plate loop heat pipe was emerged.^[6-10]

In 2011, Yu Maydanik^[5] et al. tested a flat-type loop heat pipe, which can adapt to small space installation and long-distance transmission. In order to reduce the thermal resistance of the system, the copper-water structure was selected. The size of the evaporator was 80(L)×42(W)×7(H). The maximum heat transfer capacity was 1200W. The total thermal resistance of the system was greater than 0.1°C/w under the working condition of 400W. The working temperature was close to 50°C. The low-power start-up verified the heat leakage problem, and proved the working ability of the copper water structure below 100°C.

In 2022, K Xiong, S Wang^[11-13] developed a flat copper-water evaporators. A porous structure was set inside the compensation chamber to supply liquid to the evaporator under unfavorable postures.

The internal ring reinforcement structure was designed to improve the strength of the compensation chamber. The maximum heat transfer capacity was 750w. The effective heat absorption area was 9cm². The system thermal resistance was about 0.1°C/w. In the tests of heat transfer capacity, the evaporator worked with high power and high heat flux under different angles.

At present, compared with the disc-type and flat-type small loop heat pipe structures, the flat-type has better structural advantages, and the design features of the compensation chamber can adapt to long-distance heat transmission, which is more suitable for use in small spaces. Most of the flat-plate loop heat pipe evaporators studied so far are copper-water systems, although they can also achieve greater heat transfer capacity and lower thermal resistance. However, the ammonia working fluid has the best working performance in the normal temperature zone. The higher quality factor makes the system thermal resistance of ammonia working fluid smaller. The ammonia working fluid has a better use effect in the normal temperature zone.^[14-15]

A flat-plate loop heat pipes was designed and tested for the normal temperature zone, which can be used in small spaces, large areas and long distances. The stainless steel-ammonia system was adopted. And the evaporator has a reinforced structure, which can adapt to the high pressure of ammonia working medium during use at room temperature. The capillary structure inside the reservoir can realize the hydraulic link between the evaporator and the working fluid in different postures. The heat transfer performance of this flat-plate loop heat pipe was comprehensively tested.

2. Test Piece and Bench

2.1 Design of Test Piece

The test piece used ammonia working fluid, nickel powder evaporating core, stainless steel shell and pipeline, a 8mm thick evaporator, and a cylindrical compensation chamber with 2cm diameter. The main design parameters are shown in the table below.

Table 1. Loop heat pipe design parameter table

Parameters	Unit	Values
Evaporator length × width × height	mm	55×50×8
Diameter of vapor channel	mm	1
OD/ID ×length of vapor pipeline	mm	3/2 ×500

OD/ID ×length of liquid pipeline	mm	3/2 ×500
Area of condenser	cm ²	800
Pipeline length	mm	3200
compensation chamber	mL	20

In order to improve the ability of the evaporator to withstand internal pressure, stainless steel was used as the shell material for the whole evaporator. A reinforced structure was designed inside the evaporator to improve the pressure resistance of the evaporator, as shown in Figure1; The cylindrical compensation chamber was located on one side of the evaporator. And a strengthening structure was set inside the evaporator. The metal mesh can realize the hydraulic connection between the working medium in the compensation chamber and the capillary.

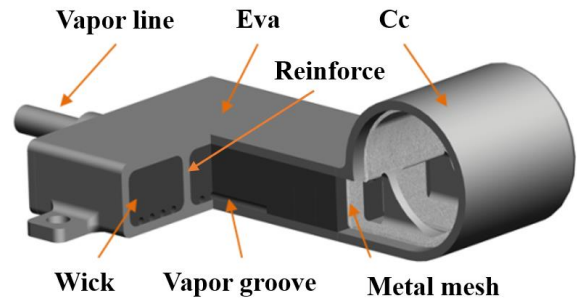


Figure 1. Schematic of the internal structure of the evaporator

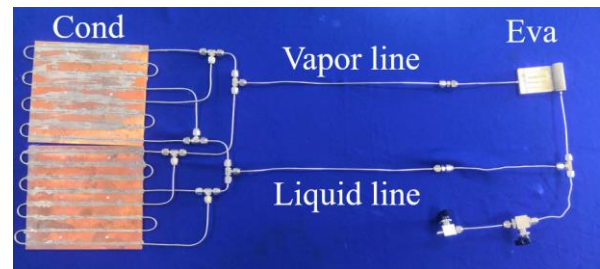
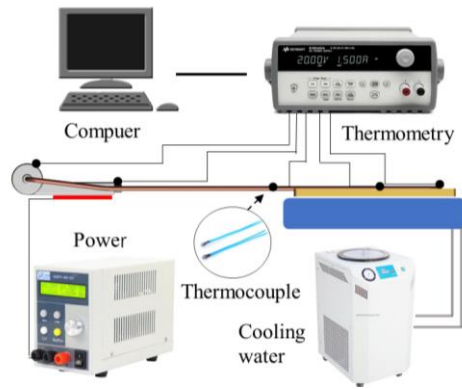


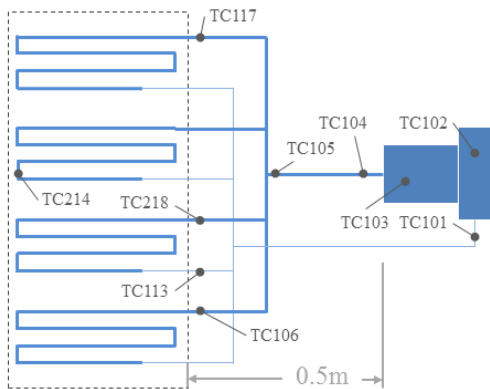
Figure 2. Physical picture of the test piece

2.2 Test Bench

The test setup can be divided into heat source, cold source and test equipment, including test computer, thermometer, thermocouple, refrigerator, cold plate, simulated heat source and power supply, as shown in Figure3(a).



(a) Schematic of the test bench equipment



(b) Thermocouple layout of the test piece

Figure 3. Schematic of test bench and layout of thermocouples

Agilent temperature measurement equipment was used to collect and record the temperature of characteristic points on the flat-plate loop heat pipe. T-type thermocouples were arranged on the test piece shell, as shown in Figure 5b. The main temperature monitoring points included: inlet of the compensation chamber (TC101), compensation chamber (TC102), evaporator (TC103), outlet of the evaporator (TC104), inlet of the condenser (TC105) and pipe in the cold plate. Among them, the temperature measuring point of the compensation chamber was located above the compensation chamber, which was used to monitor the temperature of the two-phase state in the compensation chamber. The layout of the other points is shown in Figure 3. Four-way parallel condenser is simplified as one way. During the test, the temperature value at TC105 at the outlet of the evaporator was taken as the operating temperature of the loop heat pipe.

3. Test Results and Discussion

3.1 Influence of orientation of the evaporator and compensation chamber on heat transfer performance

While the loop heat pipe running, the liquid in the compensation chamber supplies the evaporator to maintain a stable circulating flow of working fluid. Under different orientations of the evaporator and compensation chamber in the gravity field, the gas-liquid interface in the compensation chamber will be different, which affects the heat leakage from the evaporator to the compensation chamber.

In this study for the structure of the flat-plate loop heat pipe, the compensation chamber was used as a storage device for the liquid working fluid. The operation of the loop heat pipe was analyzed through three attitudes. The schematics of the three orientations of the test piece are respectively shown in Figure 4: the evaporator was horizontal to the compensation chamber, the evaporator was higher than the compensation chamber, and the compensation chamber was higher than the evaporator.

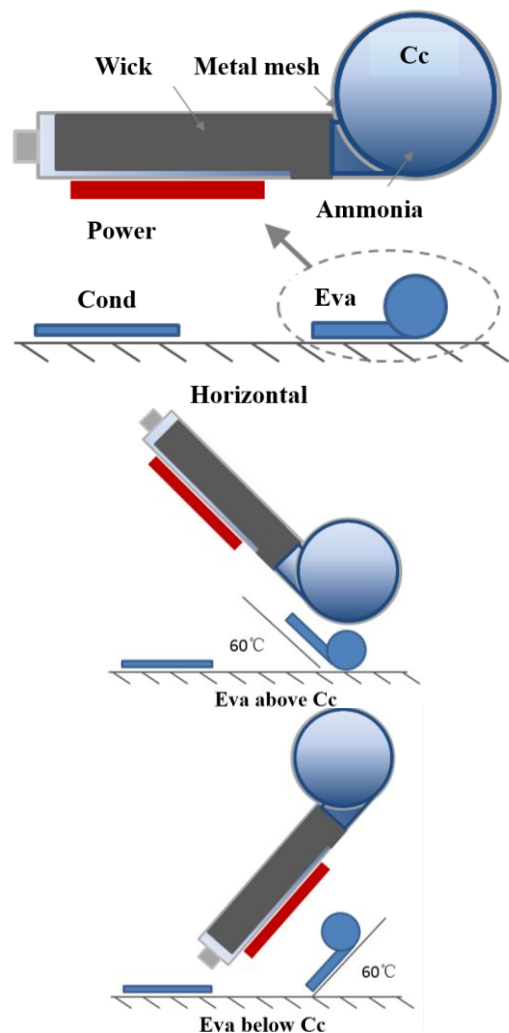


Figure 4. Schematic of the orientation of the compensation chamber and evaporator

In the test, the water circulation refrigerator was set at 25°C. Different heat loads were applied to the evaporator by simulating the heat source to test the working temperature of the loop heat pipe in different attitudes. The experimental temperature curves in three different attitudes are shown in Figure 5-7. Test results show that the flat-plate loop heat pipe can operate normally in three attitudes.

The working curve in the horizontal position is shown in Figure 5. At 200W, the working temperature was relatively stable, and the temperature fluctuation was small. With the increase of power, the system working temperature rised, and the system temperature difference gradually increased. At 460W, the temperature was close to 10°C. Among them, point 104 was the steam outlet point, and No. 105 was the temperature of the steam pipeline. With the increase of power, the temperature of the two gradually increased. If the temperature level of the same saturated steam is the same, it means that superheated steam exists at the outlet of the evaporator under high power, and superheat exists in the liquid phase transition process under high heat flux. The curve of the attitude of the evaporator higher than the compensation chamber is shown in Figure 6. The curve of the attitude of the evaporator lower than the compensation chamber is shown in Figure 7. As shown, the working temperature increased with the increase of power, and a temperature fluctuation phenomenon happened under high power. During the test, point 104 was the outlet point of steam, which was the highest temperature of the system. When the evaporator was higher than the compensation chamber, superheated steam always existed at the evaporator outlet under high power, and the steam superheat was about 2.5°C. When the evaporator was lower than the compensation chamber, there was no phenomenon of superheated steam, indicating that the phenomenon of superheated steam can be reduced under the condition of sufficient liquid supply, which is beneficial to the operation of the evaporator.

The test results also show that the heat transfer limit of the loop heat pipe in the three postures was relatively similar, about 460W. When the load of the simulated heat source was further increased, it dried out. This is because the heat transfer limit of this flat-plate loop heat pipe is

mainly limited by the maximum capillary force of the evaporator.

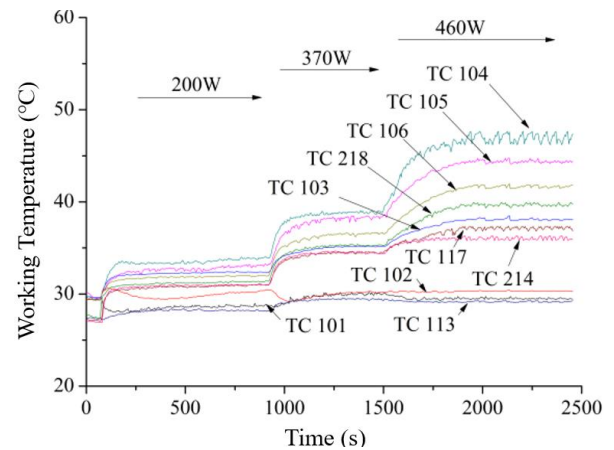


Figure 5. Temperature curve of Eva and Cc at horizontal position

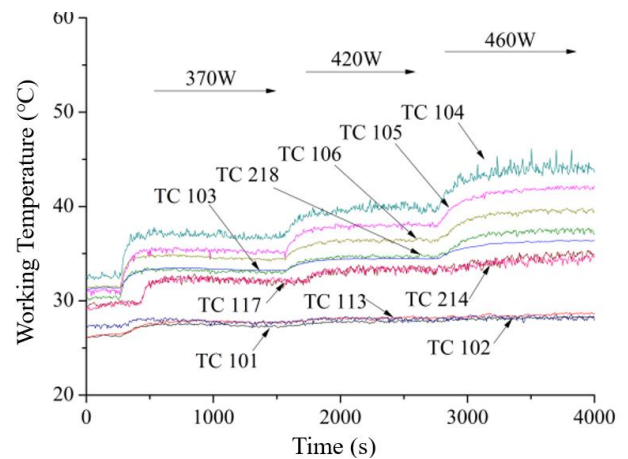


Figure 6. Eva above Cc temperature curve

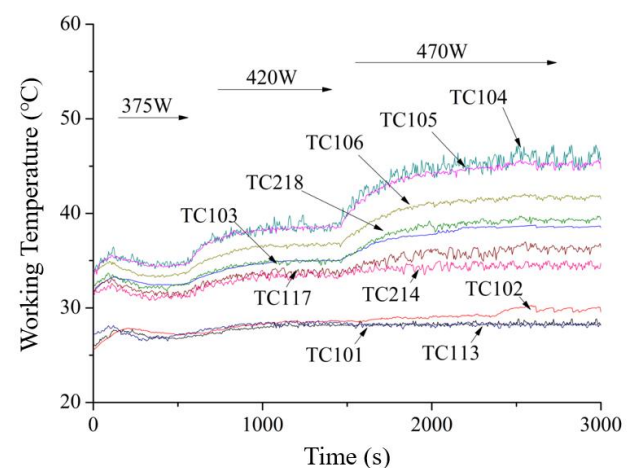


Figure 7. Eva below Cc temperature curve

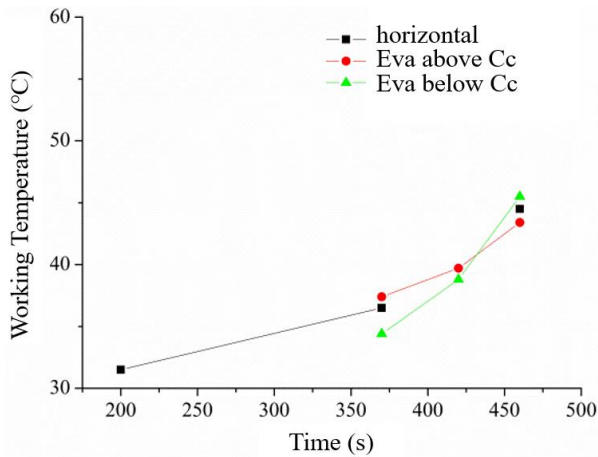


Figure 8. Evaporator operating temperature curves under different postures

3.2 Influence of orientation of evaporator and condenser on heat transfer performance

The relative position of the evaporator and condenser directly affects the circulation flow resistance of the loop heat pipe. When the evaporator is higher than the condenser, the liquid backflow needs to overcome gravity; when the evaporator is lower than the condenser, the liquid can be driven back to the evaporator by gravity. The heat transfer performance and ultimate capacity tests of the flat-plate loop heat pipe were carried out under two kinds of evaporator and condenser attitude, as shown in Figure 9.

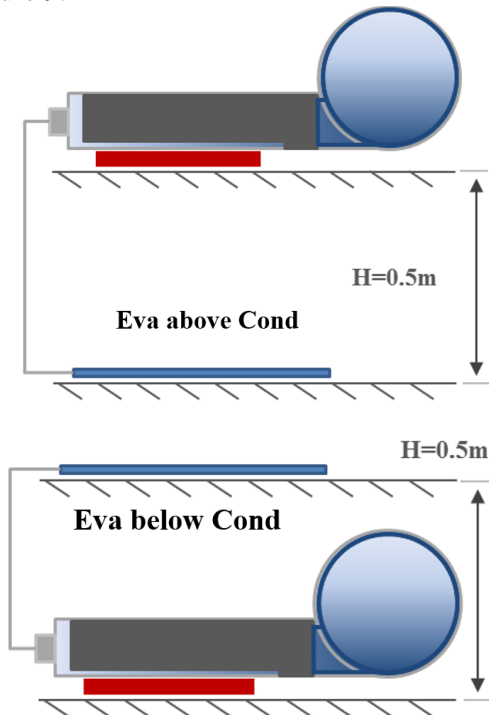


Figure 9. Positional relationship between the evaporator and condenser

The test curves under the direction of 0.5m against gravity and 0.5m along gravity are respectively shown in Figure 10 and Figure 11. The test results show that the limit heat transfer in reverse gravity, horizontal and parallel gravity postures were 420W, 460W and 475W respectively. The limit heat transfer capacity in parallel gravity was largest, and the limit heat transfer capacity in reverse gravity was smallest.

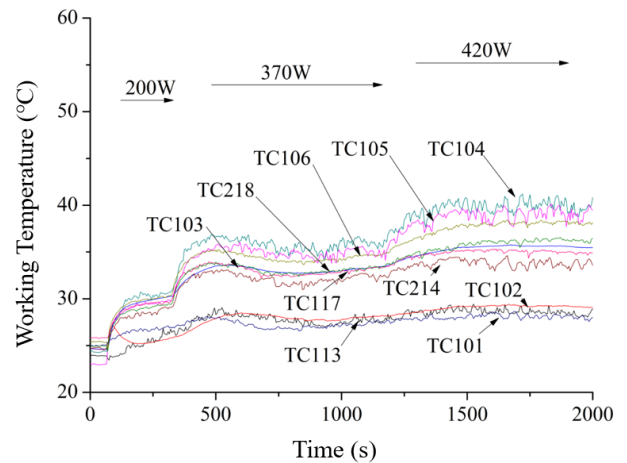


Figure 10. Inverse gravity (0.5m) test curve

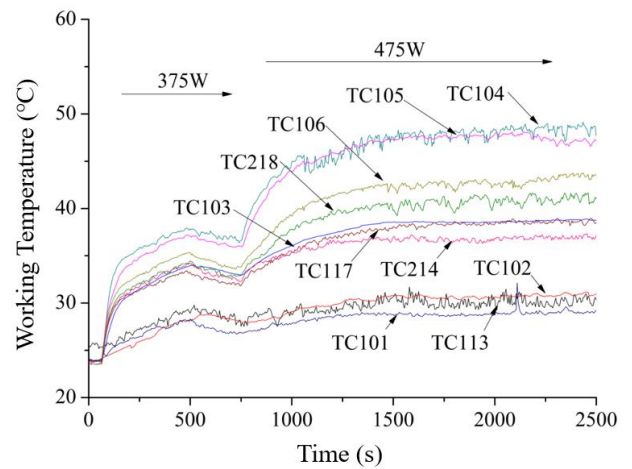


Figure 11. Test curve along gravity (0.5m)

3.3 Analysis of the System Thermal Resistance

The system thermal resistance of the loop heat pipe is also the main parameter to measure the performance of the heat pipe. The thermal resistance of the flat loop heat pipe with this structure was analyzed.

As shown in the Figure 12, R1 is the thermal resistance of the shell, which is the thermal resistance caused by the heat passing through the 1mm stainless steel shell. Since there was no

temperature point set on the bonding surface between the evaporator and the heat source, the heating power and heating area (25cm²) can be used to infer the temperature difference of the shell, corresponding to the temperature difference of the three working conditions under the horizontal working condition.

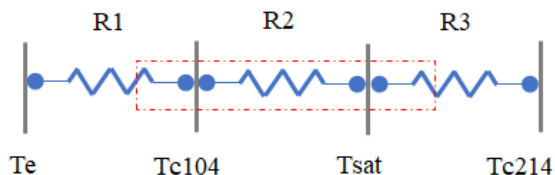
As mentioned above, while the loop heat pipe working, superheat generated, especially under high power. It can be seen that the outlet temperature of Tc104 is relatively high, and the temperature difference between the outlet temperature and the saturation temperature Tsat is the superheat R2.

R3 is the working fluid flowing into the condenser from the steam pipe to condense. The thermal resistance can be understood as the sum of the temperature difference caused by the condensation heat transfer of the working fluid, the temperature difference caused by the stainless steel pipeline, and the temperature difference caused by the pipeline and the condensing plate.

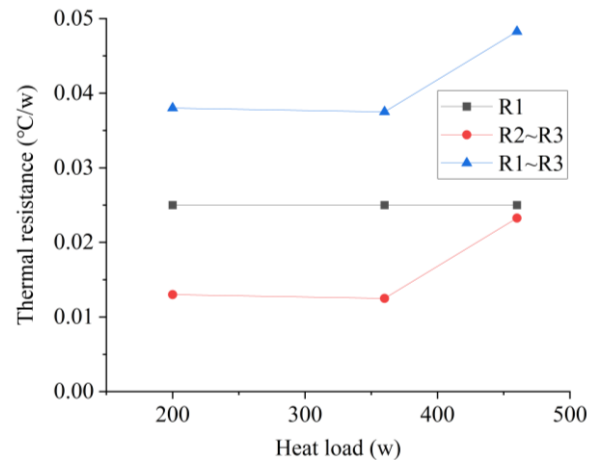
The temperature difference between R2~R3 is the working temperature difference of the loop heat pipe, and the degree of superheat gradually increased with the increase of power. The shell temperature difference accounted for about half of the total temperature difference, as the main component of the system thermal resistance.

In Figure 12(b), it can be seen that the stainless steel shell causes a large system thermal resistance, but by using ammonia as the working fluid, the total temperature difference of the system is still less than 0.05°C/W. In the normal temperature zone, it has certain advantages in use.

Te: Out surface temperature of shell
Tc104: Evaporator outlet temperature
Tsat: Saturated steam temperature
Tc214: Condenser temperature



(a) Schematic of temperature difference distribution



(b) System thermal resistance

Figure 12. Resistance curves under different heat transfer power in horizontal attitude

4. Conclusions

The experimental investigation of the new type of stainless steel-ammonia plate loop heat pipe shows that the plate evaporator is more suitable for small space, high heat flow, and long-distance heat transmission. By improving the structural strength and using ammonia working medium, the demand of high power heat transfer in constant temperature area is met.

Through the tests under the three positional relationships between the evaporator and the compensation chamber and the two positional relationships between the evaporator and the condenser, the influence of the operating posture of the loop heat pipe on the heat transfer capacity was fully analyzed. The tests prove that the flat plate evaporator with this structure can meet the use requirements of different postures.

Contraposed horizontal posture, the temperature difference and thermal resistance of the loop heat pipe were analyzed. Although the stainless steel shell has a relatively large system thermal resistance, the use of ammonia working fluid can still control the system thermal resistance within 0.05°C/w. And the evaporator has a small thermal resistance in use.

References

[1] Zhang Hongxing, Theoretical and Experimental Research on Loop Two Phase Heat Transfer Technology [D], Beijing University of Aeronautics and Astronautics, 2006

[2] Hongxing Zhang, Guoguang Li, Ling Chen, Development of Flat-plate Loop Heat Pipes for Spacecraft Thermal Control, Joint 19th IHPC and 13th

IHPS, Pisa, Italy, June 10-14, 2018

[3] Yu. F. Maidanik, s.v. vershinin, m.a. chernysheva. Development and Tests of Miniature Loop Heat pipe with a flat Evaporator[J]. SAE transactions,2000,109(1):652-656.

[4] Wang, Dongdong; Liu, Zhichun; Shen, Jun; Jiang, Chi; Chen, Binbin; Yang, Jinguo; Tu, Zhengkai; Liu, Wei (2014). Experimental study of the loop heat pipe with a flat disk-shaped evaporator. *Experimental Thermal and Fluid Science*, 57(), 157–164. doi:10.1016/j.expthermflusci.2014.04.017

[5] Yu. Maydanik, S. Vershinin, M. Chernysheva, S. Yushakova , Investigation of a compact copper Water loop heat pipe with a flat evaporator[J] *Applied thermal Engineering*, 31(2011), 3533-3541

[6] Mariya A. Chernysheva*, Vladimir G. Pastukhov 1, Yury F. Maydanik 1, Analysis of heat exchange in the compensation chamber of a loop heat pipe[J]. *Energy*, 2013,55,253-262

[7] Maydanik, Yury; Chernysheva, Mariya; Vershinin, Sergey (2020). High-Capacity Loop Heat Pipe with Flat Evaporator for Efficient Cooling Systems. *Journal of Thermophysics and Heat Transfer*, (), 1–11. doi:10.2514/1.T5845

[8] Liu, Zhichun; Wang, Dongdong; Jiang, Chi; Yang, Jinguo; Liu, Wei (2015). Experimental study on loop heat pipe with two-wick flat evaporator. *International Journal of Thermal Sciences*, 94(), 9–17. doi: 10.1016/j.ijthermalsci.2015.02.007

[9] Zhang, Zikang; Zhang, Hao; Lai, Xiaotian; Liu, Zhichun; Liu, Wei (2020). Numerical study on thermohydraulic behavior in compensation chamber of a loop heat pipe with flat evaporator. *Applied Thermal Engineering*,115073.doi:10.1016/j.applthermaleng.2020.115073

[10] Huan Li, ZhiChun Liu, BinBin Chen, et al. Development of bi-porous wicks for flat-plate loop heat pipe, *Experimental Thermal and Fluid Science* 37 (2012) 91-97.

[11] Zhang, X., Huo, J., Wang, S. Experimental investigation on temperature oscillation in a miniature loop heat pipe with flat evaporator[J]. *Experimental Thermal and Fluid Science: International Journal of Experimental Heat Transfer, Thermodynamics, and Fluid Mechanics*, 2012, 3729-36.

[12] Xiong Kangning, Meng Like,Wang Shuangfeng, et al. Experimental investigation on thermal characteristics of a novel loop heat pipe for cooling high heat flux electronic chips[J]. 2022,187.

[13] Kangning xiong, shuangfeng wang, Experimental

investigation on thermal characteristics of a novel loop heat pipe for cooling high heat flux electronic chips[J] *International Journal of Heat and Mass Transfer*,2022

[14] Singh, R.; Akbarzadeh, A.; Mochizuki, M. (2010). Thermal Potential of Flat Evaporator Miniature Loop Heat Pipes for Notebook Cooling. *IEEE Transactions on Components and Packaging Technologies*, 33(1), 32–45. doi: 10.1109/TCAPT.2009.2031875

[15] Wu T, Wang T, Ma Z, et al. Experimental investigation on the start-up performance of a loop heat pipe with three flat disk evaporators combined[J]. *Applied Thermal Engineering*, 2022, 216: 119128.

The Application of Loop Heat Pipe in Chinese Survey Space Telescope

Zenong Fang¹, Qiang Zhou¹, Zhen Fang², Lu Wang¹, Jinyin Huang¹, Wei Lu¹, Hongxing Zhang¹, Jianyin Miao^{1*}

1 Beijing Key Lab of Space Thermal Control Technology, Beijing Institute of Spacecraft System Engineering, China Academy of Space Technology, Beijing, P.R. China

2 School of Aeronautic Science and Engineering, Beihang University, Beijing, PR China

**Corresponding author email address: fzn501@126.com*

Abstract

Chinese Survey Space Telescope (CSST), Chinese flagship space-based optical observatory, was planned to launch around 2024 to survey and capture a general map of sky. The surveying field of CSST would be 300 times larger than that of Hubble telescope. The survey results were believed to provide the whole mankind with fresh knowledge about distant galaxies, dark matter, dark energy and the past and future evolutions of the universe. CSST was consisted with observing system and spacecraft platform. The thermal load of observing system and spacecraft platform both exceeded 1000W. The feature of high thermal load, low working temperature and long heat-transfer distance of vibration-free observing system and spacecraft platform resulted into significant challenges to CSST thermal control subsystem. Ammonia-LHP developed by Chinese Academy of Space Technology (CAST) was chosen to solve the thermal control problem, owing to its advantage of no vibration, low working temperature and high heat-transfer capability. The heat-transfer limit of single ammonia-LHP exceeded 520 W and heat-transfer-temperature-difference was less than 10 °C in the working temperature of -15 °C. The start-up and shutdown time of ammonia-LHP were measured as 125 s and 350 s. The low-temperature working performance of ammonia-LHP developed by CAST was proved to meet the demand of CSST. The thermal control problems of CSST were solved by ammonia-LHP developed by CAST.

Keywords: Chinese Survey Space Telescope; Loop heat pipe; Heat-transfer capability; Adverse elevation

1. Introduction

Chinese Survey Space Telescope (CSST), Chinese flagship space-based optical observatory, was planned to launch around 2024 to survey and capture a general map of sky. The surveying field of CSST would be 300 times larger than that of Hubble telescope. The survey results were believed to provide the whole mankind with fresh knowledge about distant galaxies, dark matter, dark energy and the past and future evolutions of the universe. The schematic diagram of CSST is shown in Figure 1.

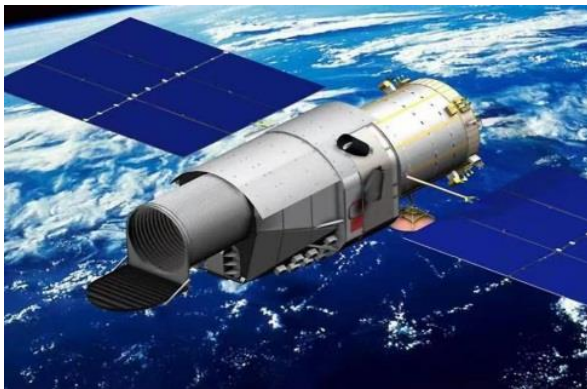


Figure 1. The schematic diagram of CSST.

CSST was consisted with observing system and

spacecraft platform. The high thermal load, low working temperature and long heat-transfer distance of vibration-free observing system and spacecraft platform resulted into significant challenges to CSST thermal control subsystem. The thermal load of observing system and spacecraft platform both exceeded 1000W. For observing system, the higher ratio of signal to noise came with less vibration and lower working temperature. By calculating, the working temperature of heat-transfer device would be in the range of -20 °C to -10 °C. The heat-transfer distance of observing system and spacecraft platform even exceeded 10 m, because of the large diameter of CSST.

The most common heat-transfer devices in the field of spacecraft thermal control were regarded as grooved heat pipe (GHP), loop heat pipe (LHP) and mechanical-pumped fluid loop (MPFL)[1]. For traditional GHP, the thermal load and heat-transfer distance of CSST exceeded GHP's abilities. Though, the heat-transfer capability of MPFL could meet CSST's demand, the inevitable vibration of mechanical-pump would decline observing system's stability enormously and result into poor accuracy of surveying data eventually.

LHP was an effective capillary-pumped two-phase heat-transfer device with no vibration, high heat-transfer capability and long heat-transfer distance[2]. Therefore, the thermal control solution based on LHP was eventually proposed by Chinese Academy of Space Technology (CAST) to control temperature and transfer waste heat for observing system and spacecraft platform. In CAST, the research of LHP started in 1980s. The first Chinese LHP was developed and applied in recoverable satellite by CAST in 2002. After 2002, tens of LHPs developed by CAST was applied in Chinese different spacecraft to solve thermal control problems, such as GF-7, CE-5 and CM-1.

2. The thermal control solution based on ammonia-LHP

The observing system of CSST contained several separated units which worked independently. Each observing unit used 2 to 4 LHPs to transfer working waste heat. The waste heat was radiated to outer space by radiator eventually, as shown in Figure 2. Meanwhile, the precise temperature control of observing system was achieved by LHPs to improve quality of observing data. The spacecraft platform of CSST used 10 LHPs to dissipate waste heat including backup LHPs.

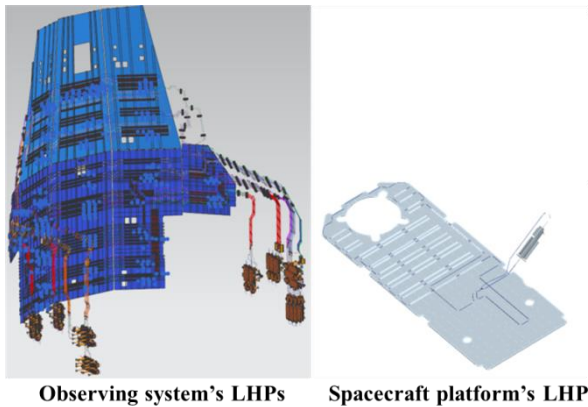


Figure 2. The thermal control solution of observing system and spacecraft platform based on LHPs

According to above thermal control solution, by calculation, the heat-transfer capability of single LHP should be larger than 350W to meet the demand of CSST, especially in the temperature range of -20 °C to -10 °C. Ammonia, as the most common working medium for LHP, had a high Dunbar number which meant the excellent heat-transfer capability for ammonia-LHP. The Dunbar number of ammonia declined rapidly in the low temperature which brought about the reducing heat-transfer capability of ammonia-LHP. The

biggest challenge of ammonia-LHP application in CSST was the relatively low working temperature. The low-temperature working performance of ammonia-LHP in the range of -20 °C to -10 °C was firstly investigated in the research. The low-temperature heat-transfer capability of ammonia-LHP was proved to meet the demand of CSST.

3. Methods

The heat-transfer demand of observing system's LHPs was more rigorous than that of spacecraft platform. Thus, the heat-transfer capability of observing system's LHPs was mainly tested. The design parameters of observing system's LHPs were shown in Table 1.

Table 1. The design parameters of observing system's LHPs.

Items	Design parameter
Working medium	Ammonia
Main wick material	Nickel
Pipe material	Stainless steel
Evaporator material	Stainless steel
Container chamber material	Stainless steel
Inner-diameter of vapor pipe	5 mm
Length of vapor pipe	2.5 m~5 m
Inner-diameter of condensing pipe	5 mm
Length of condensing pipe	5 m~6.7 m
Inner-diameter of liquid pipe	2 mm
Length of liquid pipe	1 m~3.5 m
Adverse elevation	3.5 m

The adverse elevation was defined as vertical height between evaporator and condenser (ΔH), as shown in Figure 3. Owing to the large diameter of CSST, the adverse elevation even reached 3.5 m for observing system's LHPs. On the ground, capillary driving force of main wick should overcome not only the flow resistance of working medium but also gravity if the evaporator was higher than condenser[3]. Thus, adverse elevation would decline LHP's heat-transfer capability on the ground. In the space, owing to zero-gravity, the heat-transfer capability of LHP would not affected by attitude and adverse elevation. In order to verify the correctness of thermal design in thermal balance experiment, LHPs should meet the heat-transfer demand of observing system on the ground which was more rigorous than on orbit.

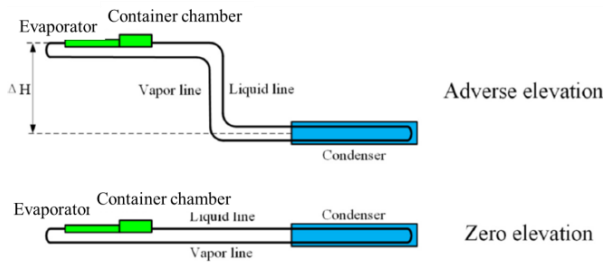


Figure 3. The schematic diagram of LHP's attitude and adverse elevation

Above all, single LHP should transfer waste heat no less than 350W with 3.5 m adverse elevation in the temperature range of -20 °C to -10 °C on the ground.

4. Results and analysis

4.1 Start-up performance of LHP

Normally, LHP's start-up process became more difficult with the decrease of beginning temperature, owing to the volumetric shrinkage of working medium with the declining temperature. Thus, the start-up performance of ammonia-LHP was tested in the low temperature. By analysis, the beginning temperature of evaporator/container chamber and outer loop would not less than -20 °C and -50 °C on orbit, respectively. Thus, the beginning temperature of evaporator/container chamber and outer loop were separately set as around -23 °C and -52 °C. The thermoelectric cooler and start-up-heater was started simultaneously to start up LHP. The start-up-heater was applied on a small zone of evaporator to increase thermal flux.

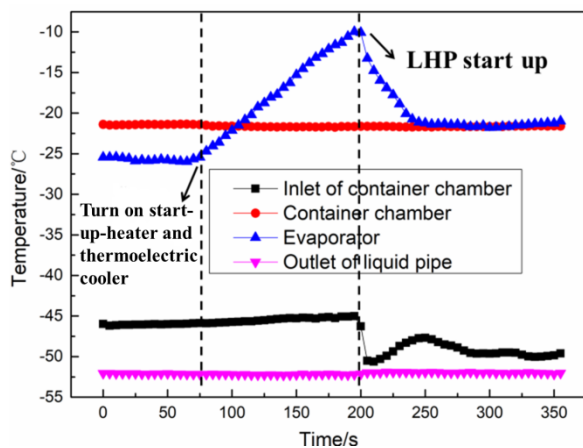


Figure 4. The temperature change of ammonia-LHP in the process of start-up

The temperature change of LHP in the process of start-up was shown in Figure 4. It was shown that the temperature of evaporator rose after start-up-heater was turned on. 125 s later, the

temperature of evaporator reached peak value, and then declined rapidly. At the same time, the temperature of inlet of container chamber also declined rapidly which meant LHP started up successfully. Thus, LHP's start-up time was 125 s which met the demand of CSST.

4.2 Operation performance of LHP

In LHP's operation mode, thermal load of observing system or spacecraft platform was applied on evaporator and thermoelectric cooler kept charged. The temperature change of ammonia-LHP with the increase of thermal load was shown in Figure 5. The working temperature of LHP, namely container chamber's temperature or two-phase temperature, was set as -15 °C in this experiment to test low-temperature heat-transfer capability. With the increase of thermal load, the temperature of evaporator and condensers increased gradually. The working temperature of LHP, namely container chamber's temperature maintained at -15 °C stably. When thermal load was added to 520 W, LHP still worked stably and evaporator's temperature was no more than -5 °C. That was to say, the heat-transfer limit of observing system's LHP exceeded 520 W and heat-transfer-temperature-difference was less than 10 °C in the working temperature of -15 °C, which met the demand of CSST.

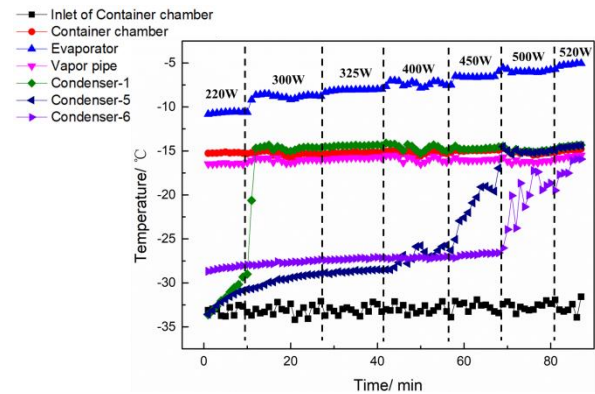


Figure 5. The temperature change of ammonia-LHP in the process of operation

4.3 Shutdown performance of LHP

The temperature change of LHP in the process of shutdown was shown in Figure 6. At 25s, the thermal load of observing system or spacecraft platform was stopped and thermoelectric cooler kept charged. The temperature of evaporator and condensers declined gradually until temperature balance. At 375s, container chamber was heated and thermoelectric cooler was turned off. The temperature of inlet of container chamber rose rapidly which came close to container chamber. It

was conclude that the low-temperature working medium stopped flowing from condenser to container chamber. The shutdown process of LHP was achieved successfully. LHP's shutdown time was 350 s which met the demand of CSST.

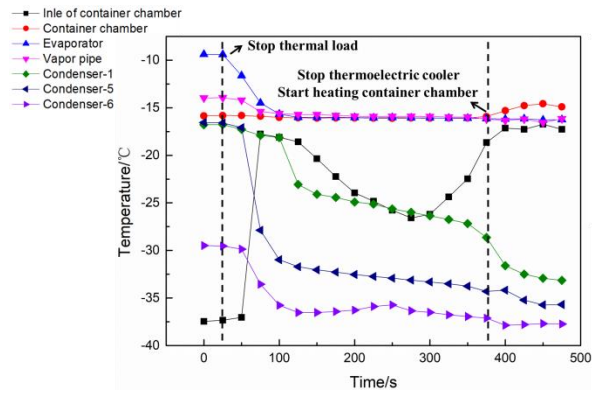


Figure 6. The temperature change of ammonia-LHP in the process of shutdown

Thus, it was the conclusion that thermal control problems of CSST were solved by ammonia-LHP developed by Chinese Academy of Space Technology.

5. Conclusions

CSST was consisted with observing system and spacecraft platform. The feature of high thermal load, low working temperature and long heat-transfer distance of vibration-free observing system and spacecraft platform resulted into significant challenges to CSST thermal control subsystem. Ammonia-LHP developed by CAST possessed the advantage of no vibration, low working temperature and high heat-transfer capability. The heat-transfer limit of single ammonia-LHP exceeded 520 W and heat-transfer-temperature-difference was less than 10 °C in the working temperature of -15 °C. The start-up and shutdown time of LHP were measured as 125 s and 350 s which met the demand of CSST. The thermal control problems of CSST were solved by ammonia-LHP developed by CAST.

References

- [1] Y. F. Maydanik and S. V. Vershinin, Development and tests of ammonia miniature loop heat pipes with cylindrical evaporators. *Applied Thermal Engineering*, 2009. 29(11-12): p. 2297.
- [2] V. G. Pastukhov and Y. F. Maydanik, Experimental investigations of a loop heat pipe with active control of the operating temperature. *International Journal of Thermal Sciences*, 2022. 172: p. 107351.

- [3] H. Wang, G. Lin, X. Shen, L. Bai, R. Yang, and D. Wen, Effect of evaporator/condenser elevations on a loop heat pipe with non-condensable gas. *Applied Thermal Engineering*, 2020. 180: p. 115711.

Theoretical and experimental research on the variable control heat pipe

Huizhi Wang, Sixue Liu, Zhendong Fu, Wei Lv, Jianxin Chen, Jinyin Huang, Jianyin Miao, Hongxing Zhang*

Beijing Key Lab of Space Thermal Control Technology, China Academy of Space Technology, Beijing, P.R. China

**Corresponding author email address: zkydwang@163.com*

Abstract

The variable control heat pipe is composed of an evaporation section, a transition section, a condensation section and a gas storage chamber. When the heat load or condensation conditions change, the temperature of the evaporation section remains constant by adjusting the size of the condensation area. It has passive heat transfer, light weight and high reliability. Based on the plane interface theory, the structural design and performance test verification of the variable control heat pipe are carried out in this paper. The test results show that the variable control heat pipe can achieve full conduction with the evaporation section of 40 °C and the gas storage chamber of 30 °C, and the heat transfer is greater than 50W. The variable control heat pipe can achieve full blocking with the evaporation section of -5 °C and the gas storage chamber of -20 °C, and the heat leakage of the evaporation section is about 3W.

Keywords: Variable control heat pipe; Plane interface; Full conduction; Full blocking

1. Introduction

Near-Earth asteroid sampling and main-belt comet detection missions are faced with complex space high and low temperature environments, which place extremely high requirements on the adaptive adjustment capability of thermal control systems. The detector faces huge challenges in an extremely complex environment. First, the detector faces the problem of heat backflow under strong external heat flow in the near-ground and attached sampling stage. Second, the detector faces the problem of high-power heat dissipation in the electric propulsion working stage. Third, during the transfer of the detector to the main belt comet, the solar light intensity gradually decreased to 1/10 of that near the earth, and the electric power of the whole device near the main belt was greatly limited. The traditional large heat dissipation surface and the whole device compensated heating way are not feasible here. This puts forward stringent requirements for thermal control in complex space environments, and it is necessary to adopt thermal control measures with low power consumption that can independently adjust the heat dissipation capacity of the whole device in a large range.

The variable control heat pipe (VCHP) can keep the temperature of the evaporation section constant by changing the size of the condensation area when the heat load or condensation conditions change, which can ensure a large range of independent control of the heat dissipation capacity of the whole device. It has passive heat transfer, light weight, reliability, and has been successfully applied on the Chang'e-3 and Chang'e-4 probes [1-2]. Therefore, the thermal control subsystem of the asteroid probe chooses VCHP as the main way of heat regulation

of the whole device. The temperature range of Chang'e-3 instruments and equipment is -43 °C to 50 °C, but the temperature range of instruments and equipment on the asteroid probe is only -5°C to 40°C. The narrower operating temperature region has caused many difficulties in the design and verification of the variable heat pipe, such as the requirement for the control gas with higher sensitivity and stricter electrical resource constraints.

Based on the plane interface theory, this paper carried out the design and experimental verification of VCHP, and finally realized the performance prediction of VCHP in the space microgravity state and complex thermal environment, which provides support for near-Earth asteroid sampling and main-belt comet detection missions.

2. Theoretical design of the VCHP

As shown in Figure 1, the VCHP is composed of evaporation section, transition section, condensation section, joint and gas storage chamber, with a certain amount of control gas and heat transfer working medium ammonia. When the VCHP is not working, the control gas and the ammonia steam are evenly mixed and distributed in the steam space of the whole VCHP. After the startup of the VCHP, the control gas is swept to the condensation section by ammonia steam, and the ammonia steam is cooled in the condensation section and returns to the evaporation section along the tube core. At this time, the control gas neon is not cooled and stays at the end of the condensation section and in the gas storage chamber. Finally, all the control gas is gathered in the gas storage chamber and the condensation section to form an air plug.

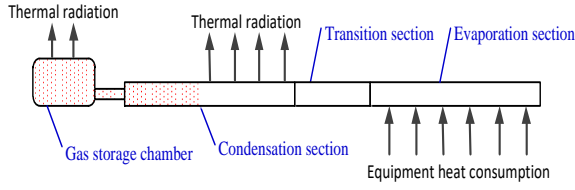


Figure 1. Schematic diagram of VCHP

The design of VCHP can be divided into heat transfer design and variable thermal conductivity design. Based on the plane interface theory, the design calculation and performance analysis of VCHP are carried out in this paper. The basic assumptions of the plane interface theoretical model are as follows [3]:

- (1) The VCHP has been in stable working condition;
- (2) There is an obvious plane interface between steam and gas, which completely separates saturated steam from gas steam mixture in blocking section;
- (3) The total pressure in VCHP is equal along the axial direction, and the axial steam pressure drop is ignored;
- (4) The gas steam mixture in the gas storage chamber and the condensation section obeys the ideal gas law;
- (5) Ignore the axial heat conduction along the pipe wall and core.

2.1. Heat transfer capacity design

The VCHP are named BTP1, BTP4, BTP5 and BTP8 respectively. The heat transfer capacity design is mainly determined by the tube type. The maximum heat transfer of BTP1, BTP4, BTP5 and BTP8 are 56W, 76W, 76W and 56W respectively.

2.2. Variable thermal conductivity design

The design requirements of VCHP are shown in Table 1. The variable thermal conductivity depends on the volume of the gas storage chamber and the filling amount of the control gas.

Table 1. Design requirements for VCHP.

working condition	Evaporation section	condensation section	gas storage chamber
High temperature	40 °C	40 °C	30 °C
Low temperature	-5 °C	-140 °C	-20 °C

Based on the plane interface theory, it can be obtained that the volume ratio of the gas storage chamber and the condensation section.

$$\frac{V_s}{V_c} = \frac{1}{\left(\frac{(P_{E,\max} - P_{S,\max})}{T_{S,\max}} - \frac{(P_{E,\min} - P_{S,\min})}{T_{S,\min}} \right) (P_{E,\min} - P_{C,\min})}$$

Where, V_s refers the volume of gas storage chamber, V_c refers the volume of condensation section, $P_{E,\max}$ refers saturated vapor pressure of ammonia in evaporation section (40 °C), $P_{S,\max}$ refers saturated vapor pressure of ammonia in gas storage chamber (30 °C), $P_{S,\min}$ refers saturated vapor pressure of ammonia in gas storage chamber (-20 °C), $P_{E,\min}$ refers saturated vapor pressure of ammonia in evaporation section (-5 °C), $P_{C,\min}$ refers saturated vapor pressure of ammonia in condensation section (-140 °C).

Therefore, the volume ratio of the gas storage chamber and the condensation section is 4.3. According to the volume ratio of the gas storage chamber and the condensation section, the volume of the gas storage chamber can be obtained as 170.5cm³, and the filling volume of the control gas can be obtained as 2.59×10⁻²mol.

3. Introduction of test device

The test device of VCHP is shown in Figure 2. A film heater is pasted on the outside of the evaporation section of VCHP to simulate the heating of the load. The aluminum plate is used as the simulated heat dissipation surface of VCHP. The simulated heat dissipation surface of the aluminum plate is sprayed with E51-M paint, and the other side is pasted with a film heater to simulate the external heat flow. A film heater is attached to the outside of the gas storage chamber to control temperature and simulate external heat flow.

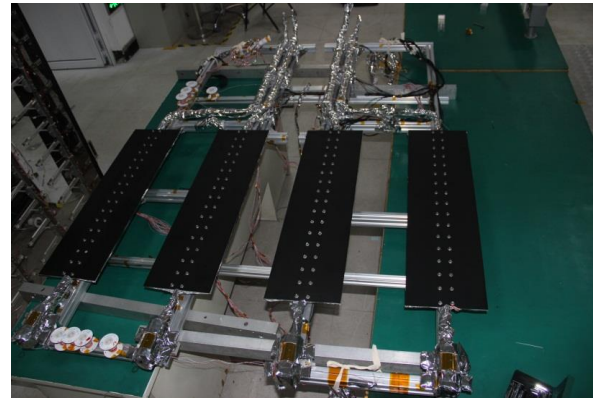


Figure 2. Test device of VCHP

4. Test verification of the VCHP

Figure 3 shows the test results of VCHP under full conduction at high temperature. When the temperature of the evaporation section is about 40 °C, and the temperature of the gas storage chamber is not more than 30 °C, VCHP can realize the full conduction state. For VCHP1, VCHP2,

VCHP3 and VCHP4, the heat transfer is 54.8W, 59.9W, 59.6W and 51.8W respectively, which meet the system index requirement of more than 50 W.

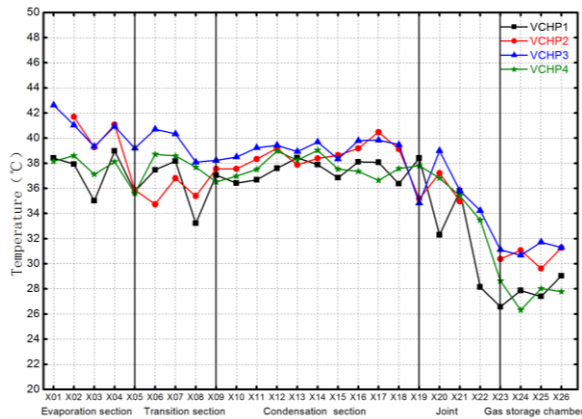


Figure 3. High temperature full conduction condition

Figure 4 shows the test results of VCHP under the low temperature full blocking condition. When the temperature of the evaporation section is about -5°C , and the temperature control of the gas storage chamber is about -20°C , VCHP can be completely blocked. For VCHP1, VCHP2, VCHP3 and VCHP4, the heat leakage of the evaporation section is 3.1W, 3.1W, 3.1W and 2.6W respectively, the control power of the gas storage chamber is 2.2W, 2.0W, 2.0W and 2.1W respectively. Under the condition of full blocking at low temperature, the average heat leakage of the evaporation section of the four VCHP is 2.98W, which meets the system heat leakage index requirement of less than 3W.

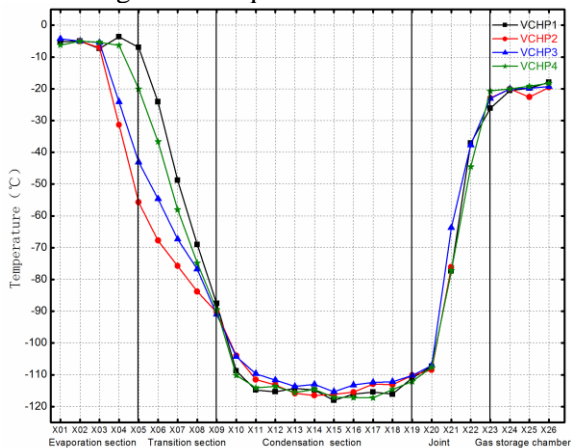


Figure 4. Low temperature full blocking condition

5. Conclusion

In this paper, the theoretical design and experimental verification of VCHP are carried out.

(1) When the temperature of the evaporation section is about 40°C , and the temperature of the gas storage chamber is not more than 30°C , VCHP can realize the full conduction state. When the temperature of the evaporation section is about -

5°C , and the temperature control of the gas storage chamber is about -20°C , VCHP can be completely blocked. Test results verify the accuracy of the calculation model of VCHP.

(2) For the high temperature full conduction state, the maximum heat transfer of VCHP1, VCHP2, VCHP3 and VCHP4 reaches 54.8W, 59.9W, 59.6W and 51.8W respectively, meeting the system index requirement of more than 50W.

(3) For the low temperature full blocking state, the heat leakage of VCHP1, VCHP2, VCHP3 and VCHP4 is 3.1W, 3.1W, 3.1W and 2.6W respectively, and the average heat leakage meets the system index requirement of less than 3W.

References

- [1] Zhang Youwei, Song Xin, Zhang Bingqiang, Liu Zijun, Miao Jianyin, Lv Wei. Application of the variable control heat pipe technology in Chang'e-3 Lander. The 14th China Heat Pipe Conference, 2015, Beijing.
- [2] Zhang Youwei, Song Xin, Si Dongbo, Liu Zijun. Thermal analysis method of the variable control heat pipe. The 12th Symposium on Space Thermophysics, 2015, Beijing.
- [3] Zhang Hongxing, Miao Jianyin, etc. Development and test results of closed two-phase thermosyphons for the Chinese Moon Exploration Spacecraft "CE-3".

Effect of binary mixtures on flat plate pulsating heat pipe operation in ground and reduced gravity environment

Maksym Slobodeniuk^{1*}, Vincent Ayel¹, Remi Bertossi², Cyril Romestant¹ and Yves Bertin¹

¹*Prime Institute CNRS – ENSMA – Université de Poitiers, Chasseneuil, France*

²*DRII, IPSA, Ivry-sur-Seine, France*

**Corresponding author email address: maksym.slobodeniuk@ensma.fr*

Abstract

The present work presents experimental results of a copper flat plate pulsating heat pipe (FPPHP) tested during the ESA 74th Parabolic Flight Campaign (under Lunar, Martian and microgravity conditions) and under normal gravity during preliminary ground tests. The tested FPPHP consists of 16 embedded square shape channels (3×3 mm²) and filled with 16% ethanol and 28% methanol aqueous solutions, and pure water as a reference fluid. Volumetric filling ratio of the working fluid is of 50% at ambient temperature.

No significant temperature oscillations have been founded during ground-based tests for the FPPHP in vertical position (bottom heating mode) and for all fluids. In horizontal orientation, FPPHP filled with both alcohol aqueous solutions showed stable operation for all heat power levels (50 W – 200 W) for a condenser temperature equal to 40 °C and for applied power higher than 100 W at 20 °C (start-up reached). Water-filled FPPHP operated almost in pure conduction mode at 20 °C condenser temperature and 50 W of applied power (following heat load augmentation led to high amplitude temperature oscillations). Stable temperature and pressure oscillations have been reached for all power levels with cooling temperature increasing until 40 °C.

Results found during parabolic flights tests showed evaporator and adiabatic zone temperature profiles very similar for the three fluids: non-significant oscillations for normal gravity phases (device operates in vertical position with bottom heating) and sharp temperatures increases during microgravity phases, lower temperature increases during phases of Martian and Lunar gravities. Regular pressure oscillations and temperature drops during reduced gravity periods have been observed for the three tested fluids almost for all parabolas at 150 W heat load, which means stable oscillatory flow inside FPPHP. Temperature drops absence and pressure oscillations damping during parabolas for 50 W of heat load attests stopover phenomena and evaporator dry-out.

Keywords: Flat plate pulsating heat pipe; Binary mixture; Lunar, Martian and Microgravity; Two-phase heat transfer.

1. Introduction

Specific demands on spacecraft thermal management systems, as well high heat fluxes rejection, limited energy consumption and overall system reliability, lead to a great interest in the passive two-phase cooling solutions. Among high efficient passive thermal management devices for electronic equipment [1], one of the most promising cooling technology is the pulsating heat pipe (PHP). The latter are thermally driven two-phase passive devices based on phase change induced liquid motion and capillary forces: liquid/vapor intermittent slug flow oscillates in a single capillary tube wound between hot and cold sources. Consequently, heat transfer process related to PHP operation consists in both latent and sensible heat transfer, which is considered to increase thermal performances. Simple design without any porous structures, moving parts and sub-systems, coupled with high heat transfer performance, makes PHP a very promising technology for future exploitation onboard space apparatuses.

The PHPs operation behavior and performances are greatly influenced by the working fluid

properties. Some of them are directly affected by fluid flow behavior, whereas others have influence on by thermal performances. However, it is possible to improve the performances of PHPs by mixing different fluids in various volume ratios, according to their thermophysical properties. During the last decade, authors studied PHPs operations with classical binary mixtures in different proportions, as well water-acetone, water-ethanol, ethanol-acetone [2-4], and even immiscible water-HFE7100 mixtures [5] and pentane / heptane / methanol mixtures [6]: the positive influence of the mixtures on the PHP start-up and dry-out prevention have been reported. The dominating importance of the filling ratio, mixing ratio and binary mixture type on the PHP operation have also been observed.

Pachghare and Mahalle [7] have shown a great improvement of the thermal performance of their PHP filled with water-methanol mixture compared to pure methanol and, specifically, pure water. A more detailed information can be found in review works on pulsating heat pipes [8, 9].

The main purpose of the present work is an experimental study on the operation of a flat plate

pulsating heat pipe with square-shaped channels and filled with water, water / methanol and water / ethanol solutions. Influence of the reduced gravity was also studied thanks to an ESA parabolic flight campaign.

2. Experimental apparatus and data treatment

2.1. Test section

Developed for ground and microgravity tests, the flat plate pulsating heat pipe is composed of a copper rectangular plate ($80 \times 200 \times 3.5 \text{ mm}^3$) in which a unique groove with square shape ($3 \times 3 \text{ mm}^2$) is milled. This groove forms a closed loop serpentine with 8 U-turns in the evaporator zone. The plate with milled channels (Fig. 1, right) is covered with a thin copper plate ($80 \times 200 \times 1 \text{ mm}^3$) using solder with silver addition to guarantee perfect sealing at the plate boards, and between adjacent channels relative to one-another. The filling / evacuation and pressure ports are also welded on opposite sides of the FPPHP. Assuming the thickness of the soldering junction as negligible, the depth of the channel remains equal to 3 mm. Evaporator heater is composed of a copper plate ($80 \times 40 \text{ mm}^2$) with milled serpentine channel in which is inserted a heating wire (Thermocoax® Type NcAc15, 1 mm of external diameter), is soldered on the bottom-back side of the FPPHP. The heat load applying to the evaporators is ensured by the ELC ALR3229 power source. Measurements of the output electrical tension and current are provided by the internal means of the power source (DC, 0-30 V, $\pm 0.03\%$; 0-20 A, $\pm 0.05\%$).

The condenser cooling plate (copper, $80 \times 100 \times 10 \text{ mm}^3$) with milled serpentine channel is brazed on the top-back face of the FPPHP plate. Heat rejection is provided by water circulation through the serpentine channel.

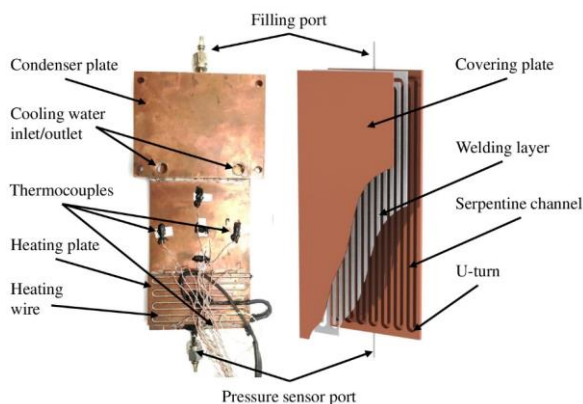


Figure 1. Photo and scheme of the FPPHP.

Temperature measurements in the evaporator zone were provided by 9 T-type thermocouples ($\pm 0.7 \text{ }^\circ\text{C}$) installed in grooves milled on the backside of PHP, on the ribs between adjustment channels (precise positions can be seen in Fig. 2). Also five thermocouples are glued on the device backside in the adiabatic zone. NI-9213 module was used to record measured temperatures.

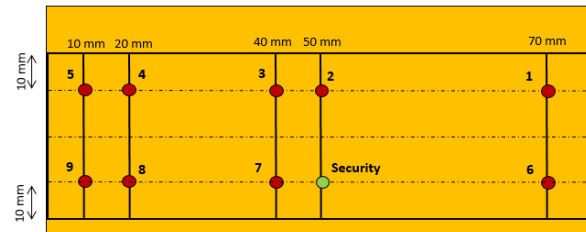


Figure 2. Thermocouple positions on evaporator.

Pressure values inside the FPPHP were acquired thanks to a pressure sensor (GE® PTX5076, $\pm 200 \text{ Pa}$) connected to the port at bottom rib of the device and centered (sensor membrane) relatively to the device to prevent the liquid column pressure influence. Grabbing of the pressure values from the transducers are realized with NI-9215 voltage measurement module.

2.2. Experimental conditions

The operating conditions for the ground experimental campaign are summarized below:

- Working fluids: water, water / 16% ethanol and water / 28% methanol solutions ($FR \approx 50\%$);
- Heat load: from 50 W to 200 W by steps of 50 W;
- Coolant temperatures (T_{cool}): 20 $^\circ\text{C}$ and 40 $^\circ\text{C}$ for ground, and $\sim 25 \text{ }^\circ\text{C}$ for parabolic flight tests;
- Positions: horizontal with gravity vector perpendicular to the FPPHP plate, vertical favorable (evaporator below condenser), vertical favorable with respect to ground reference (aircraft floor for parabolic flights).

For each of these operating conditions, heat power was supplied to evaporator by steps of 50 W starting from 50 W and up to 200 W or less, if the evaporator's dry-out limit was reached and/or if evaporator temperatures exceeded 100 $^\circ\text{C}$. During ground tests, each power step was maintained until the FPPHP reached a relatively steady state mode for both temperatures and pressure signals. For parabolic flight tests, the same procedure has been carried out but heat power has been changed for each sequence of five successive parabolas.

The parabolic flight

Nowadays, the simplest approach to reach microgravity conditions is the parabolic flight, during which an aircraft (Airbus A310 ZERO-G) flies from steady horizontal flight to following maneuvers (Fig. 3 [13]):

- aircraft climbs up to 50° for about 20 s with accelerations levels (perpendicular to the aircraft floor) between 1.8g and 2g;
- power of all aircraft engines are reduced for about 20 to 25 s just for air drag compensation (parabolic free fall, *i.e.* microgravity phase);
- the aircraft dives down to 42° during around 20 s with accelerations levels between 1.6g and 2g;
- back to a steady horizontal flight.

All these maneuvers are combined in sequences of five parabolas with intervals of around one minute between each, for a duration of few minutes.

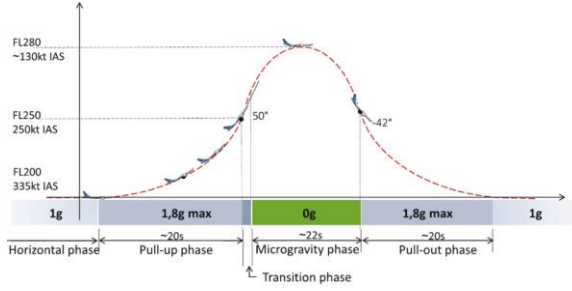


Figure 3. Parabolic flight trajectory.

One day of flight allows reaching thirty parabolas plus one for adjustment in the six sequences of five successive parabolas. The residual accelerations sensed by experimental setups attached to the aircraft floor structure are typically in the order of 0.01g during microgravity phases. Note that, during this particular flight, sequences of five parabolas were alternated between gravity levels equivalent to those reached on the Moon, Mars and microgravity conditions.

2.3. Data processing

Thermal resistance is an important and usually used parameter indicating the device heat transfer performance and will be used here for this specific analysis. Taking into account the time and space averaged temperatures of the evaporator and secondary cooling liquid, divided by the heat power supplied to the evaporator, the thermal resistance can be calculated as follows:

$$R_{th} = \frac{\overline{T_{ev}} - \overline{T_{cool}}}{Q} \quad (1)$$

where $\overline{T_{ev}}$, $\overline{T_{cool}}$ and $Q = U \times I$ are the evaporator and

cooling liquid temperatures, the heat load, and the tension and current measured on the heater ends, respectively.

As experimental measurements conducted with certain accuracy and knowing the absolute error of measurements, the uncertainties for both applied heat power and thermal resistance can be expressed as follows [10]:

$$\frac{\partial Q}{Q} = \sqrt{\left(\frac{\partial U}{U}\right)^2 + \left(\frac{\partial I}{I}\right)^2} \quad (2)$$

$$\frac{\partial R}{R} = \sqrt{\left(\frac{\delta T_{ev}}{\overline{T_{ev}} - \overline{T_{cool}}}\right)^2 + \left(\frac{\delta T_{cool}}{\overline{T_{ev}} - \overline{T_{cool}}}\right)^2 + \left(\frac{\delta Q}{Q}\right)^2} \quad (3)$$

Resulting uncertainties on the heat load vary in the range of 0.08% to 0.15%. The minimum uncertainty for the thermal resistance has been founded for higher heat loads (higher temperature difference between evaporator and cooling water) and is equal to 6.7%. However, low heat loads lead to an error value of 27%.

3. Experimental results

In this part, the results obtained for the FPPHP tested on ground and during parabolic flights are presented in terms of temperature and pressure (and acceleration for PF) temporal histories and thermal resistances. Lines colored in the shades of red corresponds to the evaporator temperatures evolutions, orange line represents temperature evolutions in the center of the adiabatic zone ($T_{ad,m}$), blue one displays condenser cooling liquid average temperature, green, dark grey and gray (dashed) indicate the values of heat load, pressure and acceleration normal to the aircraft floor during the flights, respectively. Note that only four most representative temperatures (T_{ev1} to T_{ev4}) corresponding to the thermocouples N°1, 2, 3 and 5 (fig. 2) are plotted to better readability.

Temperature and pressure evolutions for ground tests are plotted only for FPPHP filled with water to give the general representation of their behavior and to highlight the common phenomena with other fluids. Comparison of the FPPHP performances for different fluids and coolant temperatures are showed thanks to thermal resistances curves.

3.1. Ground tests

Effect of the FPPHP orientation

In vertical position (BHM), fluid motion inside current FPPHP provoked not only by the pressure difference between two ends of the liquid plug, but

also thanks to gravity forces, pushing the liquid from condenser to evaporator.

Temperature and pressure histories for FPPHP filled with water and tested at 20 °C condenser temperature are shown in Fig. 4 and 5 (vertical and horizontal orientations, respectively). Despite significant fluctuations of the evaporator temperatures observed in vertical position (BHM), almost no significant oscillations of adiabatic temperature and pressure have been observed (Fig. 4).

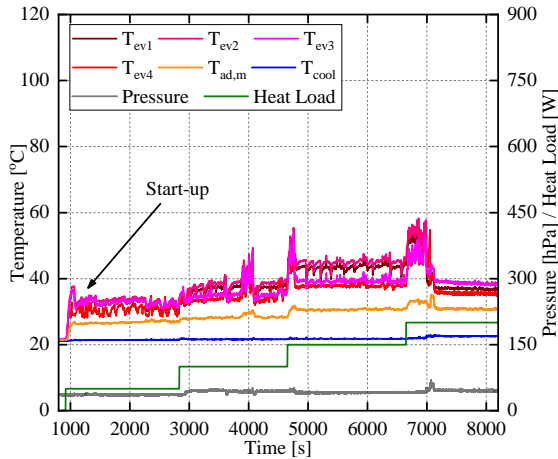


Figure 4. Temperature and pressure responses of the FPPHP at $T_{cool} = 20\text{ °C}$ (water, vertical, BHM).

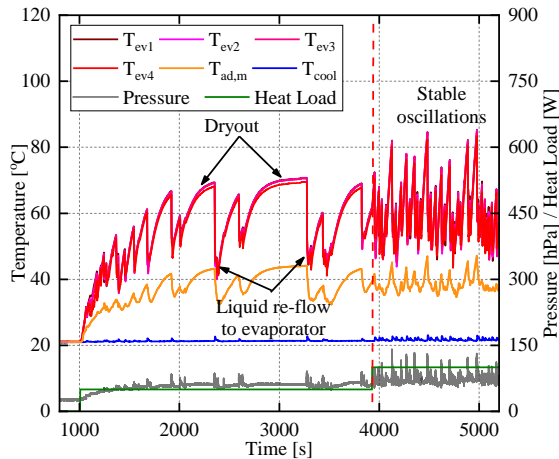


Figure 5. Temperature and pressure responses of the FPPHP at $T_{cool} = 20\text{ °C}$ (water, horizontal).

Fig. 5 shows that the FPPHP tested in horizontal position shows different thermohydraulic behavior than in vertical position. In this position, capillary forces keep the fluid distributed in the slug/plug pattern along the channel. Furthermore, absence of gravity forces makes the vapor plugs pressure difference the main force to drive the fluid back to evaporator.

As shown in Fig. 5, evaporator temperatures for FPPHP tested in horizontal position at 50 W - and 100 W- of applied powers are quite higher than in vertical position. Moreover, the temperature behavior seems to be very different – evaporator and adiabatic temperatures increase (to $\sim 70\text{ °C}$ and $\sim 45\text{ °C}$, respectively) and suddenly drop (accompanied with pressure surge). This temperature rise occurs when the liquid remains collected in the condenser and the device operates in dry mode, which explains smooth parts of curves. In this case, heat transfer occurs mostly by conduction through the copper plate.

Simultaneous temperature and pressure drops with few following oscillations mean the liquid reflow to the evaporator and short period of normal operation. Heat load increase up to 100 W led to regular vigorous oscillations – device normal operation mode. Unfortunately, with following heat load augmentation, values of the temperature peaks exceed allowed temperature range (100 °C, due to security reasons) and experiment for water have consequently to be stopped.

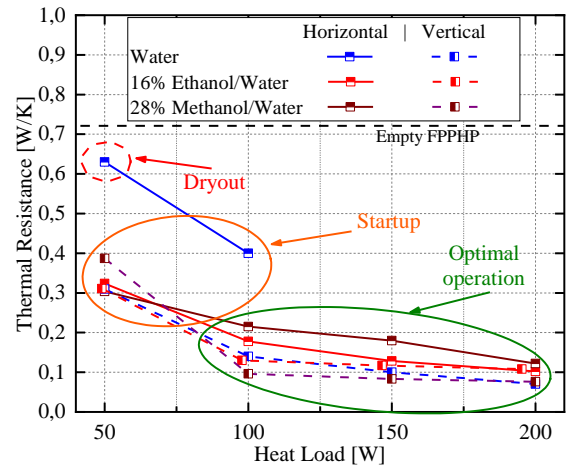


Figure 6. Effect of the FPPHP orientation on device thermal resistance ($T_{cool} = 20\text{ °C}$).

Fig. 6 represents values of the thermal resistance calculated with Eq. (1) for FPPHPs filled with all tested fluids and tested in vertical and horizontal positions at 20 °C of condenser coolant temperature. Based on the temperature and pressure evolutions for the tested cases, the operation of the FPPHP could be classified as follows:

- “dry-out” – liquid collected in the condenser and evaporator dry-out occurs;
- “startup” – fluid flow oscillations are very rare during low heat input levels;

- “optimal operation” – fluid circulates intensively between condenser and evaporator causing higher heat transfer rate.

The device was observed to operate dried only with water and when tested in horizontal position at 20 °C and applied power of 50 W. The thermal resistance for empty device was experimentally characterized and is represented by the black dashed line (0.72 W/K). Most of the thermal resistance values obtained are ranging from 0.31 to 0.33 W/K at 50 W (for both device orientations), except with water in horizontal position (0.64 W/K) and methanol/water mixture in vertical position (0.39 W/K). Following heat load increase up to 100 W led to the significant thermal resistance decrease especially for FPPHP tested in vertical position. The favorable gravitational head (bottom heated mode) enhances device performance (clearly seen for 100 W and 150 W).

Effect of the coolant temperature

Another parameter influencing FPPHP operation is the condenser temperature. As outlined in Fig. 7, which shows the temperature and pressure evolutions for the water-filled device tested in horizontal position with the condenser temperature fixed at 40 °C, startup occurred at lower heat load (50 W) and dry out have not been observed along all heat load applied, as well stable and regular temperature and pressure oscillations.

Input heat power increase led to the temperature and pressure oscillations with higher frequencies, but almost without changes in amplitude (starting from 100 W).

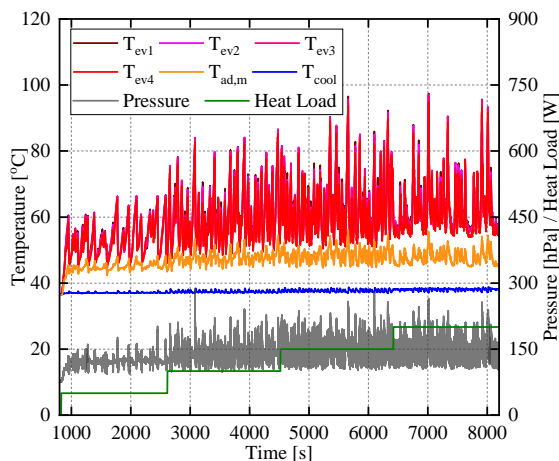


Figure 7. Temperature and pressure responses of the FPPHP at $T_{cool} = 40$ °C (water, horizontal orientation).

From Fig. 8 it can be seen that a higher condenser temperature leads to lower thermal resistances for all tested fluids. This trend have been observed for

all heat loads for the FPPHP in horizontal position. Obviously, the fluids’ thermophysical properties remarkably affect the PHP operation. With overall system temperature increase, fluid viscosity and surface tension decrease, leading to the decrease of viscous and capillary pressure losses, resulting in better PHP performances. It is interesting to note that with water, the gain in thermal performance is higher compared to the cases with alcohol aqueous mixtures. This could be explained by initial higher viscosity and surface tension of water than for other two fluids. Nevertheless, FPPHP filled with alcohol aqueous mixtures operate in optimal mode starting from lower heat load (50 W).

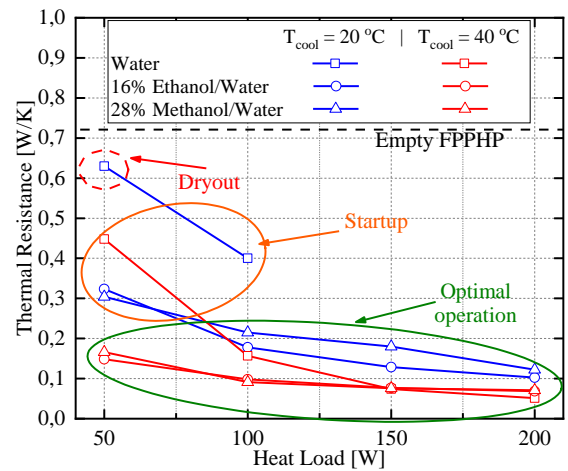


Figure 8. Effect of the coolant temperature on the FPPHP thermal resistance (horizontal).

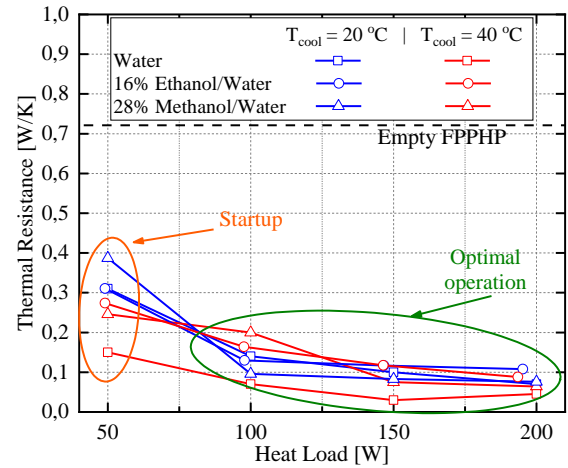


Figure 9. Effect of the coolant temperature on the FPPHP thermal resistance (vertical, BHM).

For the FPPHP tested in vertical orientation (BHM), no significant influence of the condenser temperature has been observed, except with water (Fig. 9). Again, it could be explained by the temperature-induced decrease of surface tension and following liquid menisci break up resulting to the flow regime transition from slug/plug to

annular, in which PHP operates with highest thermal performances.

3.2. Parabolic flight tests

Influence of working fluid

Transient responses of temperatures and pressure signals can be seen in fig. 10, 11 and 12 – for the three fluids – according to the varying gravity acceleration field (dashed grey curve) during a series of five parabolas. The overall trends of the curves are relatively consistent with what was observed previously [11, 12]. During normal gravity periods, FPPHP filled with water and tested at 50 W (Fig. 10) operates stably with temperature fluctuations amplitude lower than those observed in fig. 4 during ground tests (in the range of the measurements uncertainty). The increase in the mean temperature level is correlated with that of the aircraft ambient air temperature.

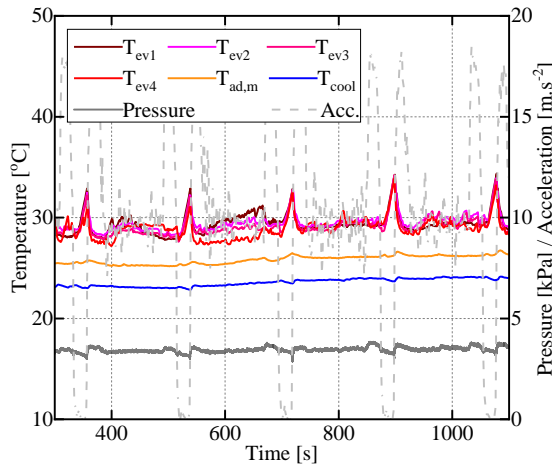


Figure 10. Temperatures, pressure and acceleration responses of the FPPHP during a series of 5 successive parabolas (water, microgravity, 50 W).

That said, on one hand, hypergravity periods are accompanied with small temperature drops and pressure augmentation. On the other hand, no temperature and / or pressure drops have been observed during microgravity phases. This fact indicates that, for the device filled with water and tested at 50 W of applied power, dry-out without any fluid flow reactivation takes place during every periods of 22 s of microgravity. This seems to be corresponding to the results obtained in horizontal position with this fluid (see fig. 6).

From Fig. 11 it can be seen that for water/ethanol mixture, device operating during normal gravity without significant evaporator temperature oscillations. But with microgravity appearance the evaporator temperatures increase due to systematic initial evaporator dry-out (similar to PHP tested in horizontal position), for all parabolas.

Nevertheless, one can observe some evaporator temperatures sudden decrease and fluctuating as well the pressure during the first, third, fourth and fifth parabolas of fig. 11. This was attributed to reactivation phases of the fluid flow inside the device [11]. Same observations could be done for higher heat loads (ex.: Fig. 13 for 150 W of applied power) but with higher temperature peaks and rarer reactivations.

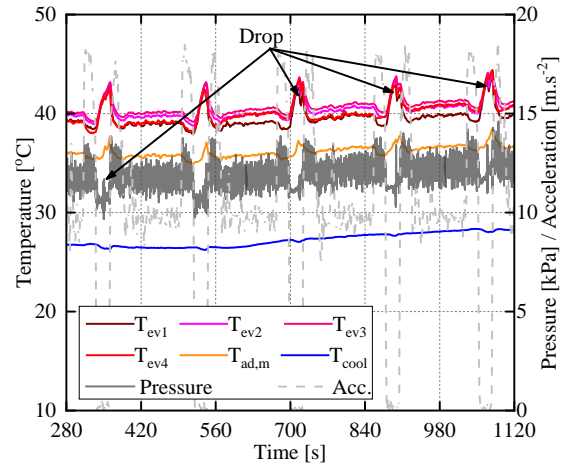


Figure 11. Temperatures, pressure and acceleration responses of the FPPHP during a series of 5 successive parabolas (water - 16% ethanol, microgravity, 50 W).

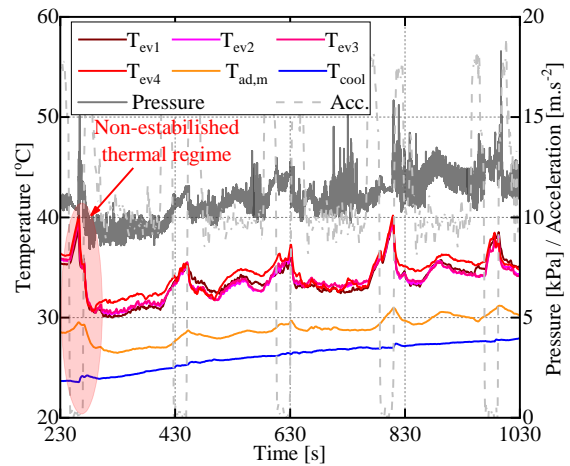


Figure 12. Temperatures, pressure and acceleration responses of the FPPHP during a series of 5 successive parabolas (water - 28% methanol, microgravity, 50 W).

Temperature histories for the device filled with water/methanol mixture are presented in Fig. 12. Because it was the first test during the flight and heat load has been applied just before first parabola, temperature increases up to 35 °C without oscillations, showing that the start-up did not really occurred before. It seems that the temperature level becomes stable just after the first parabola, and the

transition between microgravity and beginning of hypergravity phases (after 250 s) provokes a change in the device operation mode, accompanied with temperature drop and following stabilization with lower temperature level and low oscillation amplitude. Then, microgravity periods are characterized by evaporator temperature augmentation but at this time with more frequent fluctuations, attributed to reactivations phases, than with water case. Probably, for this case, liquid was not accumulated in the condenser zone and dry-out was not reached, but FPPHP operates in the pulsating mode with reduced oscillation frequency. Also, pressure oscillations during microgravity phases seem to confirm these trends.

Influence of gravity level

As mentioned in section 2.2, the peculiarity of this parabolic flight campaign lies in the fact that three levels of reduced gravity have been tested: microgravity, Lunar (0.18g) and Martian gravities (0.38g). Fig. 13, 14 and 15 show the transient responses of temperatures and pressure signals – only for water/ethanol solution – according to the varying gravity acceleration field (dashed grey curve) during a series of five parabolas.

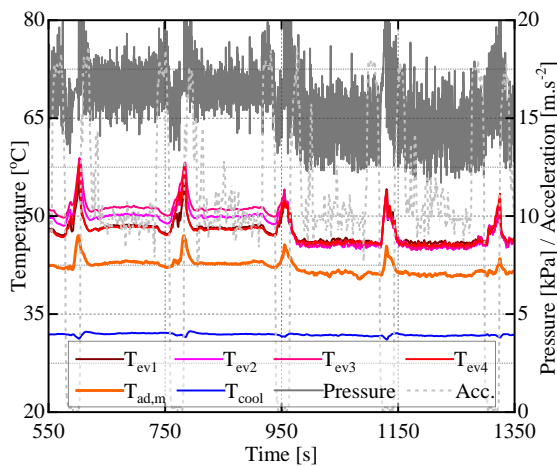


Figure 13. Temperatures, pressure and acceleration responses of the FPPHP during a series of 5 successive parabolas (water - 16% ethanol, microgravity, 150 W).

As shown in Fig. 13, normal gravity conditions for the FPPHP tested during a series of parabolas at 150 W of applied power are characterized by evaporator temperature smooth fluctuations. During microgravity periods, FPPHP mostly operate in “dried” mode, accompanied with high temperature rise, and sometimes short-term reactivations (parabolas 2, 3 and 5). One can observe a temperature decrease and homogenization in the evaporator zone after the

third parabola. This can be attributed to a better slugs/plugs distribution in the device during the microgravity period.

During Lunar gravity periods (Fig. 14), evaporator temperature increases are still observed, but with maximum peak temperature about three times lower than for microgravity periods (~2-3 °C). High and very frequent temperature oscillations, as well pressure oscillations, have been registered during all parabolas.

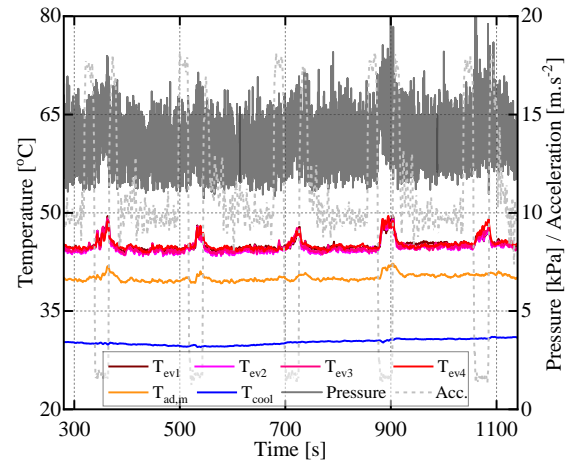


Figure 14. Temperatures, pressure and acceleration responses of the FPPHP during a series of 5 successive parabolas (water - 16% ethanol, Lunar gravity, 150 W).

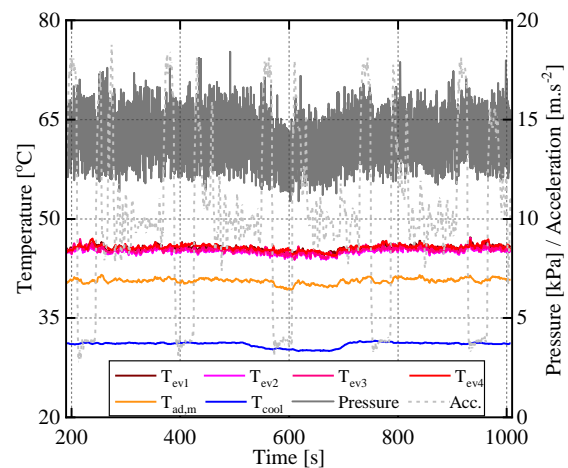


Figure 15. Temperatures, pressure and acceleration responses of the FPPHP during a series of 5 successive parabolas (water - 16% ethanol, Martian gravity, 150 W).

Finally, thermal behavior of the device tested under Martian gravity conditions is presented in Fig. 15. It can be clearly seen that there are not any significant temperature or pressure changes caused by Martian gravity level. It seems that, in vertical BHM, the level of gravity does not influence that much the operation of the FPPHP, at least on a

range of gravity levels from the Martian (0.38 m/s^2) to hyper (1.8 m/s^2) gravity levels. In general, the same conclusions can be done for the two other mixtures, but with slight higher temperature increase in microgravity. Unfortunately, this specific point was not further studied following these observations, but it deserves to be studied in more detail afterwards.

4. Conclusions

A copper closed loop flat plate pulsating heat pipe filled with water and alcohol aqueous solutions has been studied in both horizontal and vertical positions, and under different gravity levels (micro, Lunar and Martian gravity) during parabolic flight campaign.

During ground tests, stable temperature fluctuations were observed for the FPPHP tested in horizontal mode and condenser temperature of $40 \text{ }^\circ\text{C}$ with an applied heat power equal or superior to 50 W for all tested fluids. Thermal resistances of the FPPHP filled with water and tested in horizontal position are significantly higher than with alcohol aqueous mixtures. Condenser temperature augmentation leads to highly improve the thermal efficiency, especially for water-filled device.

Operation of the FPPHP in vertical BHM is characterized by a general decrease of thermal resistances with increasing heat loads for all tested fluids. Furthermore, increase of condenser temperature leads to stable operation of the FPPHP and insignificant decrease of evaporator temperatures, and better thermal performances, particularly in horizontal orientation.

In microgravity, using water-alcohol mixtures leads to more frequent fluid flow reactivations, accompanied with temperature drops during the 22 s of microgravity periods.

The temperature increase during the 22 s of reduced gravity decrease with the gravity level increases: no noticeable temperature and pressure difference has been observed during the Martian series of parabolas, showing that a minimum level of gravity (here lower than 38% of normal gravity) does not affect the thermal and hydraulic behavior of the device in vertical BHM. This points seems crucial and deserves further study.

Acknowledgements

This work was supported by ESA MAP project INWIP and ESA MAP project TOPDESS. The authors appreciate the NOVESPACE team for their assistance.

References

- [1] M. Mochizuki, Th. Nguyen, K. Mashiko, Y. Saito, T. Nguyen and V. Wuttijumnong, A review of heat pipe application including new opportunities. *Frontiers in Heat Pipes*, 2011. 2: p.1.
- [2] Y. Zhu, X. Cui, H. Han and S. Sun, The study on the difference of the start-up and heat-transfer performance of the pulsating heat pipe with water-acetone mixtures. *International Journal of Heat and Mass Transfer*, 2014. 77: p. 834.
- [3] L. Caihang, H. Zhuang, Y. Yongwang and Z. Si, Experimental study on thermal performance of pulsating heat pipe with ethanol-acetone mixtures. *International Journal of Heat Technology*, 2015. 33: p. 185.
- [4] X. Han, X. Wang, H. Zheng, X. Xu and G. Chen, Review of the development of pulsating heat pipe for heat dissipation. *Renewable and Sustainable Energy Reviews*, 2016. 59: p. 692.
- [5] R. Xu, C. Zhang, H. Chen, Q. Wu and R. Wang, Heat transfer performance of pulsating heat pipe with zeotropic immiscible binary mixtures. *International Journal of Heat and Mass Transfer*, 2019. 137: p. 31.
- [6] B. Markal and R. Varol, Investigation of the effects of miscible and immiscible binary fluids on thermal performance of pulsating heat pipes. *Heat Mass Transfer*, 2021. 57: p. 1527.
- [7] P. R. Pachghare and A. M. Mahalle, Effect of pure and binary fluids on closed loop pulsating heat pipe thermal performance. *Procedia Engineering*, 2013. 51: p. 624.
- [8] V. Ayel, M. Slobodeniuk, R. Bertossi, C. Romestant and Y. Bertin, Flat plate pulsating heat pipes: a review on the thermohydraulic principles, thermal performances and open issues. *Applied Thermal Engineering*, 2021. 197:117200.
- [9] D. Bastakoti, H. Zhang, D. Li, W. Cai and F. Li. An overview on the developing trend of pulsating heat pipe and its performance. *Applied Thermal Engineering*, 2018. 141: p. 305.
- [10] S. Kline and F. McClintock, Describing uncertainties in single-sample experiments. *Mechanical Engineering*, 1953. 75: p. 3.
- [11] V. Ayel, L. Araneo, P. Marzorati, C. Romestant, Y. Bertin and M. Marengo, Visualization of Flow Patterns in Closed Loop Flat Plate Pulsating Heat Pipe Acting as Hybrid Thermosyphons under Various Gravity Levels. *Heat Transfer Engineering*, 2018. 40: p.227.
- [12] D. Mangini, M. Mameli, A. Georgoulas, L. Araneo, S. Filipposchi and M. Marengo, A pulsating heat pipe for space applications: Ground and microgravity experiments. *International Journal of Thermal Sciences*, 2015. 95: p. 53.
- [13] V. Pletser, S. Rouquette, U. Friedrich, J.-F. Clervoy, Th. Gharib, F. Gai and Ch. Mora, The First European Parabolic Flight Campaign with the Airbus A310 ZERO-G. *Microgravity Science and Technology*, 2016. 28: p. 587.

Simplified hydraulic and thermal models for inverted two-phase thermosyphons

Ricardo Schneider Calomeno*, Fernando Henrique Milanez, Marcia Barbosa Henriques Mantelli

LABTUCAL – Heat Pipes Laboratory, Federal University of Santa Catarina, Department of Mechanical Engineering, Florianópolis, SC, 88040-900, Brazil

*Corresponding author. E-mail: ricardoschneider@labtucal.ufsc.br

Abstract

One possible manner to perform downward heat transfer using passive technologies is to use of inverted two-phase thermosyphons. This device uses the vapor pressure differences between the hot and cold components of the thermosyphon to pump the working fluid inside a closed loop, even against gravity. The operation is periodic and the mass flow inside the loop is controlled by opening and closing valves. In order to bring such devices to practical applications, many challenges still need to be surpassed. One of the challenges is a theoretical modeling that can be used during design. In the present work, simplified theoretical hydraulic and thermal models are presented in order to predict the performance of an inverted two-phase thermosyphon. The models are then employed to evaluate the performance of the inverted two-phase thermosyphon under study for different operational conditions and geometry, especially the height of liquid elevation. Water was considered as the working fluid. The results indicate that the condensed working fluid could be elevated to heights of 2,0 to 10,0 m, at heat transfer rates from 3 to 15 kW, while still keeping acceptable temperature levels for the components of the inverted two-phase thermosyphon.

Keywords: Inverted two-phase thermosyphon; Downward heat transfer; Theoretical model; Periodic operation.

1. Introduction

Passive control technologies, *e.g.*, heat pipes and two-phase thermosyphons, have been increasingly considered as thermal solutions across the industry. Two-phase thermosyphons have the capacity to transfer heat very efficiently when the heat sink is above the heat source, *i.e.*, in the upward direction. Usually, heat pipes are the two-phase devices able to transfer a limited amount of heat in the downward direction with capillary forces used for liquid transportation. Inverted two-phase thermosyphons (ITPT) represent an alternative technology to transfer heat downwards, *i.e.*, with the heat source above the heat sink. Some applications of ITPT are: solar collectors [1-2], house cooling [3], distillation processes and cooling in offshore systems (*e.g.*, oil and gas rigs).

Although ITPT have been studied during the last 20 years [1] many problems still need to be addressed in order to make them feasible, such as the development of models to be used as design tools.

The ITPT investigated in this work is composed by an evaporator, a condenser (a shell-and-tube heat exchanger) and an accumulator (or reservoir), with all components connected by tubes, as shown of Figure 1. Two valves [1-2, 4] are used to open/close the two lines between evaporator and accumulator. It works in a periodic cycle, mainly divided into two processes: (i) vapor transport and

(ii) drainage.

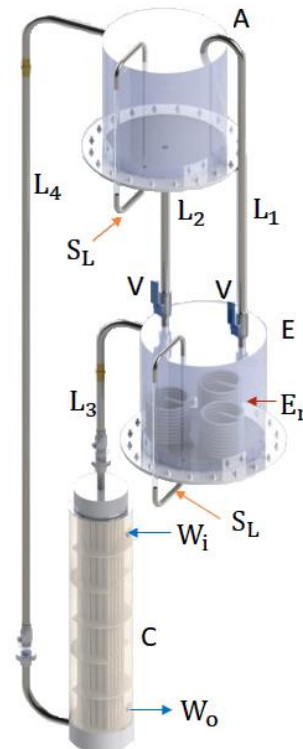


Figure 1. ITPT under study: E – evaporator, C – condenser, A – accumulator, V – valve, E_r – electrical resistances, S_L – external liquid level sensor, W_i and W_o – cooling fluid inlet and outlet, respectively, lines: L_1 – equalization, L_2 – drainage, L_3 – vapor transport (downwards), L_4 – liquid return (upwards).

Referring to Figure 1, in the vapor transport process, both valves V connecting the evaporator to the accumulator are closed. The fluid in the pool inside the evaporator E is heated and vapor flows downwards to the condenser C, through line L_3 , due to the vapor pressure differences.

In the condenser, the vapor condenses and liquid accumulates on the bottom. As the heat is constantly added to the evaporator, the working fluid temperature rises, resulting in a vapor pressure large enough to push the liquid upwards through the liquid return line L_4 to the non-insulated accumulator A, placed above the evaporator. From this instant up the end of the vapor transport process, the system reaches an almost steady state condition, with the pressure difference between the evaporator and accumulator large enough to overcome gravity and flow friction. After working fluid is transferred to the accumulator during the vapor transport process, the drainage process begins with the opening of the two valves. At this instant, there are no pressure differences between evaporator and accumulator (line L_1) and the condensate return by gravity to the evaporator through line L_2 . At the end of the drainage process, both valves are closed again in order for another cycle to start.

Only a few mathematical models have been presented in the literature in order to evaluate the thermal performances of some ITPTs prototypes, with some of them being analytical [3, 5] and others being lumped-element models [2]. However, these models are very specific for each different prototype and cannot be applied easily as a design tool of the ITPT under study here.

The main objective of the present work is to develop theoretical models that can be used as design tools for the ITPT under study and that could also be employed as the basis for modelling other ITPT geometries. As the vapor transport is the major mechanism during the operation of the device and the drainage mainly affecting the total cycle time, only the model concerning the vapor transport is presented here. The simplified model developed here could be easily adaptable to other geometries.

2. Hydraulic and Thermal Models

During the ITPT operation, heat is transferred against gravity by the pressure that the vapor imposes on the liquid in the condenser, that must be large enough to push liquid up to the accumulator. From the thermal point of view,

during this process the system reaches an almost steady condition.

As the objective is to develop a model for the vapor transport only, the model predicts the performance of the condenser of the ITPT of Figure 1 in terms of the pressure variation and heat transfer observed between the evaporator output and the accumulator inlet, which comprises lines L_3 , L_4 and the condenser. Most of the evaporator heat input is transferred to the condenser heat sink, with the condensate leaving the condenser at a temperature which is slightly higher than the heat sink temperature. Therefore, given enough time and fluid inventory in the evaporator, for a fixed value of heat sink temperature and for a fixed heat input, the system can reach an almost steady state. Then, the modelling is based on the following hypothesis: (i) steady-state, (ii) condensation is negligible in line L_3 , (iii) the vapor at the inlet of the condenser is saturated.

At the evaporator output, the vapor is also considered saturated. The vapor condenses along the condenser, leaving it as subcooled liquid. Therefore, inside the condenser, there is a two-phase flow in the beginning, followed by single phase flow at the end. Only liquid flows against gravity from the condenser to the accumulator through line L_4 .

2.1. Pressure difference models

The evaluation of the pressure variation along of the flow is based on the model presented by [6].

The pressure variations for the single-phase flows inside lines L_3 (vapor), L_4 (liquid) and at the bottom of the condenser's tube bank, below the liquid pool level, due to gravity (ΔP_g) and friction (ΔP_f) are predicted, using the following equations [6]:

$$\Delta P_g = \rho g L \sin(\Omega) \quad (1)$$

$$\Delta P_f = f \left(\frac{L}{d} + N_j K_j \right) \frac{\rho u^2}{2} \quad (2)$$

where ρ is density, g is the gravity acceleration, L , Ω and d are, respectively, the tube length, inclination and diameter, N_j is the number of 90° return curves, K_j is the equivalent length for the 90° return curve ($K_j=30$), u is the fluid mean velocity and f is the single-phase friction factor, which is given by [7]:

$$f = \begin{cases} 64Re^{-1} & (Re \leq 2100) \\ 0,316Re^{-1/4} & (2100 < Re < 10^4) \\ 0,184Re^{-1/5} & (Re \geq 10^4) \end{cases} \quad (3)$$

where the Re is the Reynolds number determined by:

$$Re = \frac{4\dot{m}}{\pi d\mu} \quad (4)$$

where \dot{m} is the mass flow rate and μ is the dynamic viscosity.

The two-phase flow pressure variation model for the condenser is based on the separated model [8], with the liquid and the vapor phases flows at different velocities. The expressions for the local pressure gradients due to friction, gravity and flow acceleration (vapor compressibility is neglected), are given, respectively, by [8]:

$$-\left.\frac{dP}{dz}\right|_f = \frac{2\phi_l^2 f_l G^2 (1-x)^2}{\rho_l d_{h,in}} \quad (5)$$

$$-\left.\frac{dP}{dz}\right|_g = [(1-\alpha_v)\rho_l + \alpha_v\rho_v]g\sin(\Omega) \quad (6)$$

$$-\left.\frac{dP}{dz}\right|_x = G^2 \frac{dx}{dz} \left\{ \frac{2x}{\rho_v\alpha_v} - \frac{2(1-x)}{\rho_l(1-\alpha_v)} + \frac{d\alpha_v}{dx} \left[\frac{(1-x)^2}{\rho_l(1-\alpha_v)^2} - \frac{x^2}{\rho_v\alpha_v^2} \right] \right\} \quad (7)$$

where G is the mass flux, x is the vapor quality, ϕ_l is the liquid two-phase multiplier, f_l is the liquid friction factor, $d_{h,in}$ is the internal diameter of the condenser's tube and α_v is the void fraction.

The friction factor of the liquid phase is evaluated by:

$$f_l = 0,0079 \left[\frac{G(1-x)d_{h,in}}{\mu_l} \right]^{-1/4} \quad (8)$$

The two-phase multiplier ϕ_l is calculated as a function of the Martinelli (X) parameter [6] as [9]:

$$\phi_l = \sqrt{1 + C/X + 1/X^2} \quad (9)$$

Constant C in Eq. 9 depends on the fluid flow regime, as presented on Table 1.

Table 1. Constant C value [9].

C	Liquid	Vapor
5	Laminar	Laminar
10	Turbulent	Laminar
12	Laminar	Turbulent
20	Turbulent	Turbulent

The void fraction (α_v) is the ratio between the cross section of vapor and the total flow areas and is also calculated as a function of the Martinelli parameter [9] by:

$$\alpha_v = (1 + 0,28X^{0,71})^{-1} \quad (10)$$

The phase-change section of the condenser is divided into 20 finite volumes, to which the above equations are applied. The finite volume method [10-11] is used to calculate the pressure variation in this section.

2.2. Heat transfer models

From the total heat transferred along the evaporator to the accumulator path, only the heat transferred at the condenser is evaluated here. The condenser is divided in two sections: (i) phase-change (latent heat transfer) and (ii) subcooling region (sensible heat transfer). For each section, the overall thermal conductance (UA) is calculated by:

$$UA = (R_{c,in} + R_{cd} + R_{c,ex})^{-1} \quad (11)$$

where $R_{c,in}$ and $R_{c,ex}$ are convection thermal resistances, respectively, of the condenser tubes internal and external flows, and R_{cd} is the conduction thermal resistance across the condenser tube walls, which is calculated by the following equation:

$$R_{cd} = \frac{\ln\left(\frac{d_{h,ex}}{d_{h,in}}\right)}{2\pi k_t L} \quad (12)$$

where $d_{h,ex}$ is the condenser tube external diameter and k_t is the heat conductivity.

In equation 11, both convection thermal resistances are calculated by:

$$R_{cd} = (\pi d L h)^{-1} \quad (13)$$

where h is the convection heat transfer coefficient.

For the condensation internal flow, in the phase-change section, the following coefficient of heat transfer is used [12]:

$$h_{bi,in} = 25Re_{lv,c}^{0,25} Pr_l^{0,4} (k_l/d_{h,in}) \quad (14)$$

where Pr_l is the liquid Prandtl number, k_l is the liquid heat conductivity and $Re_{lv,c}$ is the Reynolds number, calculated by:

$$Re_{lv,c} = \frac{4\dot{Q}_{lt}}{\pi d_{h,in} L_{bi} h_{lv}} \quad (15)$$

where \dot{Q}_{lt} is the latent heat rate transferred per condenser tube, L_{bi} is the length of the phase-change section and h_{lv} is the vaporization enthalpy.

In the subcooling section, the internal convection heat transfer coefficient is determined from the following expressions, which depends on the Reynolds number [12].

$$Nu_{in} = \begin{cases} 3,66 & (Re_{in} \leq 2300) \\ 0,023Re_{in}^{4/5} Pr^{0,3} & (Re_{in} > 2300) \end{cases} \quad (16)$$

where Nu_{in} is the Nusselt number given by Eq. 17 and Re_{in} is the Reynolds number, calculated by Eq. 18.

$$Nu_{in} = \frac{h_{in}d_{h,in}}{k} \quad (17)$$

$$Re_{in} = \frac{4\dot{m}_1}{\mu\pi d_{h,in}} \quad (18)$$

where \dot{m}_1 is the mass flow rate per condenser tube.

For the tube external flow across the tube bundle in the shell-and-tube heat exchanger, the Bell-Delaware method is applied to predict the heat transfer coefficient in terms of geometry and operation conditions. Further details about this model can be found in [13].

Some additional equations are needed in order to evaluate the thermal behavior of the ITPT. The total mass flow rate in the condenser is calculated by:

$$\dot{m} = \frac{\dot{Q}}{h_{lv} + c_p(T_c - T_a)} \quad (19)$$

where \dot{Q} is the total heat transfer rate at the condenser, c_p is the liquid specific heat, T_c and T_a are the condenser inlet and outlet temperatures, respectively.

The length of the phase-change section per condenser tube is calculated as:

$$L_{bi} = \frac{\dot{m}_1 h_{lv}}{h_{b,i}\pi d_{h,in}(T_c - T_w)} \quad (20)$$

where T_w is the temperature on the internal surface of the tube.

The working fluid temperature at the outlet of the condenser, which is subcooled and equal to the accumulator temperature, is calculated by the following equation [7]:

$$T_a = \bar{T}_{ex} - (\bar{T}_{ex} - T_c) \exp\left\{-\frac{UA_{co}}{\dot{m}_1 c_p}\right\} \quad (21)$$

where \bar{T}_{ex} is the mean temperature of the cooling fluid in the shell-side of the condenser and UA_{co} is the overall thermal conduction of the subcooling section.

The output parameters are the temperatures and pressures at the condenser, the evaporator and the accumulator. Also, the lengths of the phase-changing and subcooling sections are obtained.

The total pressure variation is given by:

$$\Delta P_t = \Delta P_{L3} + \Delta P_c + \Delta P_{L4} \quad (22)$$

where ΔP_{L3} and ΔP_{L4} are the pressure variations at the lines L_3 and L_4 , respectively, each one

calculated from Eqs. 1 and 2. ΔP_c is the pressure variation along the condenser, calculated by the integration of Eqs. 5-7 over the length of the phase-change section and the pressure variation of the subcooled section, calculated with Eqs. 1 and 2.

The total heat transfer at the condenser is:

$$\dot{Q} = N_t(\dot{Q}_{lt} + \dot{Q}_{ss}) \quad (23)$$

where N_t is the number of tubes on the condenser, \dot{Q}_{lt} is the latent heat transfer rate per tube and \dot{Q}_{ss} is the sensible heat transfer rate per tube. These parameters are given, respectively, by:

$$\dot{Q}_{lt} = UA_{bi}(T_c - \bar{T}_{ex}) \quad (24)$$

$$\dot{Q}_{ss} = UA_{co} \frac{(T_a - T_c)}{\ln\left(\frac{\bar{T}_{ex} - T_a}{\bar{T}_{ex} - T_c}\right)} \quad (25)$$

where UA_{bi} is the overall thermal conductance of the phase-changing section.

The pressures at the evaporator (P_e) and the condenser (P_c) are evaluated, respectively, by:

$$P_e = P_c + \Delta P_{L3} \quad (26)$$

$$P_c = P_a + \Delta P_c + \Delta P_{L4} \quad (27)$$

where P_a is the saturation pressure at the accumulator at T_a .

2.3. Algorithm

For the design and simulation of the ITPT, the set of equations described previously were implemented using Python® programming language on Spyder® software. The model solving algorithm is shown in Figure 2.

The input data are the ITPT geometry, the total heat rejected at the condenser (\dot{Q}) and the heat sink characteristics, defined by the temperature (\bar{T}_{ex}) and mass flow rate of the cooling fluid (\dot{m}_{ex}). According to Figure 2, the following procedure is executed.

1. An initial guess for the following parameters are provided: temperature at the evaporator outlet (T_e), temperatures at the condenser inlet (T_c) and outlet (T_a) and the length of the phase-change section (or condensation section) L_{bi} . In the present study the following parameters were guessed: $T_e = T_c = 350$ K, $T_a = 300$ K and $L_{bi} = 30$ cm;

2. The mass flow rate \dot{m} is calculated with Eq. 19;

3. The pressure variation in line L_3 (ΔP_{L3}) is determined using equations 1 and 2. The pressure at the evaporator outlet is given by equation 26. The corresponding saturation temperature is then

used to update T_e . This procedure repeats until the absolute difference between the value of T_e from two consecutive iterations is less than 0,1 K;

4. The conduction and the convection thermal resistances are calculated with Eqs. 12 and 13. UA_{bi} is calculated with Eq. 11. T_w is calculated as the average temperature between the inner and outer surfaces of the condenser tubes. The heat rejection rate per tube in the phase-change section, \dot{Q}_{it} , is calculated with Eq. 24;

5. The length of the condensation section L_{bi} is recalculated with Eq. 20. If the absolute difference between two consecutive iterations is larger than $0,5 \times 10^{-3}$ m, the calculation returns to Step 4;

6. The length of the cooling section L_{co} is calculated as the difference between the condenser total length and L_{bi} . The thermal resistances in the subcooling section are calculated with Eqs. 12 and 13 so the overall thermal conduction of this section, UA_{co} , can be calculated with Eq. 11. T_a is then recalculated with Eq. 21. The heat rejection rate per tube in this section, \dot{Q}_{ss} is calculated with Eq. 25;

7. The following parameters are evaluated: \dot{Q} with Eq. 23, ΔP_{L4} with Eqs. 1 and 2, ΔP_c with the integration along the condensation section with Eqs. 4 to 6 as well as the pressure variation in the subcooling section, given by Eqs. 1 and 2. The total pressure variation between evaporator and accumulator (ΔP_t) is calculated with Eq. 22;

8. The pressure at the condenser (P_c) inlet is recalculated with Eq. 27. T_c is recalculated as the saturation temperature for P_c . If the absolute difference between two consecutive iterations is higher than 0,2 K, then the process returns to Step 2. If convergence is obtained, the algorithm ends.

3. Results and Discussions

The steady state model presented above is employed here to evaluate the performance of the ITPT with the geometry shown in Figure 1.

In the first analysis of this study, the evaporator and the accumulator are kept at the same height, while the condenser height is varied. The internal diameter of lines L_3 and L_4 are both 1,905 cm (3/4 in). The geometry of the condenser can be seen in Table 2. The ITPT working fluid is water. The condenser heat sink cooling fluid is also water at constant temperature of 25°C (298,15 K) and flow rate of 1L/s.

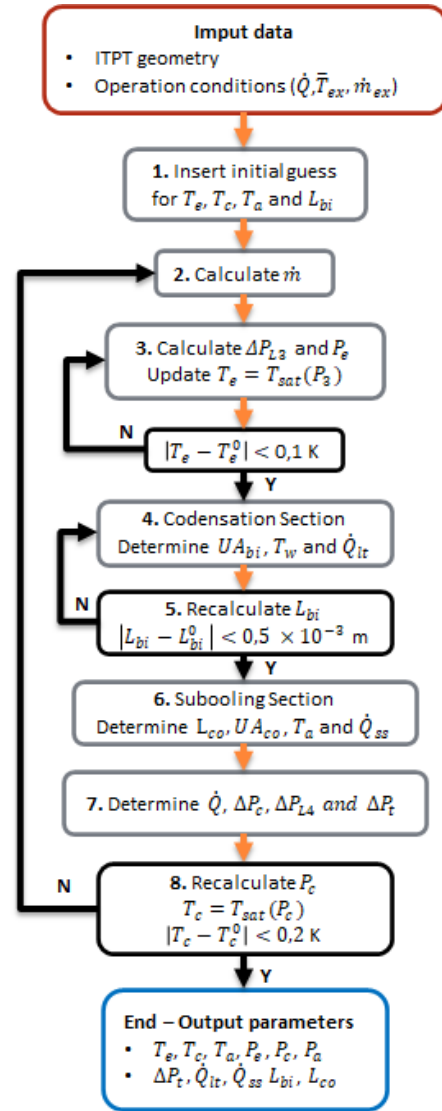


Figure 2. Model solving algorithm.

Table 2. Dimensions of the shell-and-tube heat exchanger used as condenser.

Shell internal diameter	15,0 cm
Number of baffles	5
Baffle cut	18 %
Number of pairs of sealing stripes	1
Number of tubes (N_t)	25
Tube length (L_c)	60,0 cm
Tube internal diameter ($d_{h,in}$)	1,06 cm
Tube external diameter ($d_{h,ex}$)	1,27 cm (1/2 in)

The thermal behavior of the ITPT (Figure 3) was evaluated for five different condenser vertical distances with respect to the evaporator (ΔH_{ec} , length of line L_3), and the accumulator (ΔH_{ca} , length of line L_4) while the condenser is rejecting 10 kW to the heat sink. The estimated temperature of the evaporator, condenser and accumulator for each case are observed in Table 3.

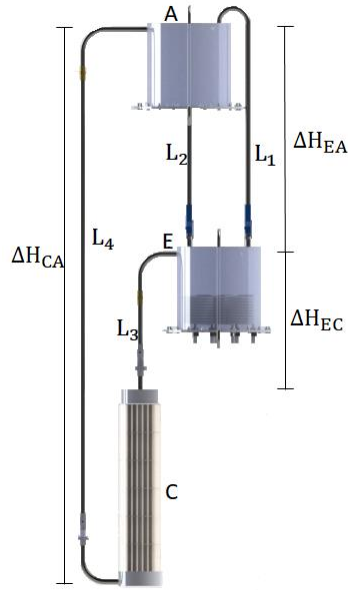


Figure 3. Schematics of the ITPT.

Table 3. Temperatures of evaporator, condenser and accumulator for five different ITPT geometries and a total condenser heat transfer of 10 kW.

ΔH_{ca} [m]	ΔH_{ec} [m]	T_e [K]	T_c [K]	T_a [K]
2,0	0,4	335,2	332,7	301,1
4,0	2,4	350,6	348,0	300,9
6,0	4,4	360,3	358,0	300,8
8,0	6,4	367,6	365,6	300,8
10,0	8,4	373,5	371,8	300,8

As can be observed in Table 3, as the condenser is placed in lower positions, by increasing the height difference between the evaporator and the accumulator, higher are both the evaporator and the condenser temperatures, while the accumulator temperature decreases slightly. That means the lower is the condenser position, the larger is the difference between the saturation pressures at the evaporator and the accumulator in order to overcome the hydrostatic pressure of the liquid in line L_4 . It can be also observed that small increments of the evaporator temperature results in longer vertical distances that the fluid can be transported.

The second parameter analyzed here is the effect of the heat transfer rate at the condenser on the temperatures of the evaporator, the condenser and the accumulator. With the height difference between the condenser and accumulator of $\Delta H_{ca} = 6,0$ m and the height difference between the evaporator and the condenser of $\Delta H_{ec} = 4,4$ m, the heat transfer rate was varied from 3 to 15 kW. The obtained results can be seen on Table 4.

Table 4. Temperatures of the evaporator, the condenser and the accumulator for $\Delta H_{ca} = 6,0$ m, $\Delta H_{ec} = 4,4$ m and for a condenser heat transfer rate from 3 to 15 kW.

Q_c [kW]	T_e [K]	T_c [K]	T_a [K]
3	357,9	357,5	298,8
6	358,8	357,7	299,5
9	359,9	358,0	300,4
12	361,1	358,2	302,0
15	362,6	358,6	304,5

As it can be seen on Table 4, for the same geometry, the evaporator and the condenser temperatures increase with the heat transfer rate at the condenser, which lead to larger pressures difference between evaporator and accumulator. One should observe that, for a considerably large variation in the heat transfer rate from 3 to 15 kW, all the three component temperatures increased by less than 6 K, which is relatively small.

Finally, an analysis of the thermal performance for the five different geometries of ITPT (Table 3) was carried out in terms of the heat rejection rate at the condenser, which was varied from 3 to 15 kW. The pressure differences between the evaporator and accumulator in the vapor transport phase can be seen on Figure 4.

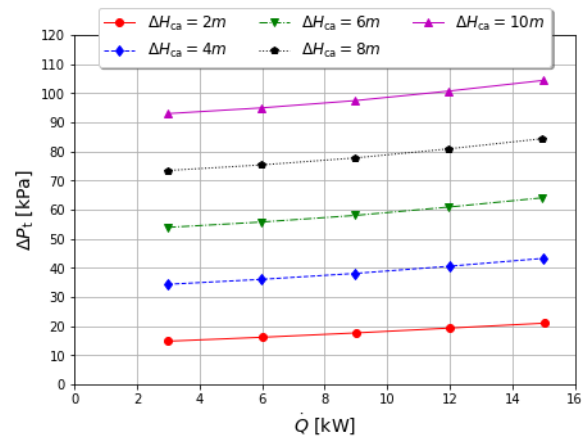


Figure 4. Pressure difference between evaporator and accumulator as a function of the heat transfer at the condenser for five different ITPT geometries.

The main source of pressure variation between evaporator and accumulator is the hydraulic pressure of the condensed liquid column inside line L_4 . As it can be observed in Figure 4 for the same heat transfer rate, the increase in the vertical distance results in a proportional increase on the pressure difference. The inclination of the

pressure variation curve demonstrates only a slight increase in the pressure due friction for larger values of heat transfer rate.

The last parameter under analysis here is the length of the condensation section in terms of the condenser inlet temperature, which can be seen in Figure 5.

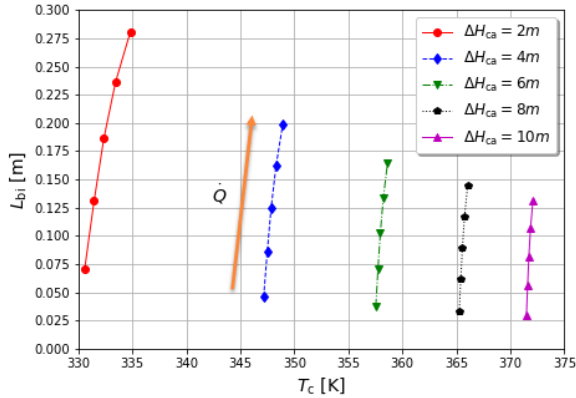


Figure 5. Condensation length per tube as a function of temperature for the five different ITPT geometries.

For the same geometry, the increase of the heat transfer rate requires larger latent heat transfer, which is obtained with a larger condensation length. The growth of the condensation length is practically constant with the increase of the heat transfer rate, while the condenser temperature remains almost constant, as shown on Figure 5. The growth of the condensation length also leads to the increase of the pressure drop during the condensation.

It is interesting to note that, analyzing the condensation length of two different ITPT geometries (ΔH_{CA} values of 4,0 m and 8,0 m) with the same heat transfer rate of 12 kW. It is observed that the condenser inlet temperatures are 348,3 K and 365,8 K while the condensation section length has values of 0,162 m and 0,117 m, respectively. Thus, the rise of the condensation temperature due to longer higher vertical distances results in larger temperature differences between the ITPT working fluid and the heat sink. That leads to the increase of the heat transfer due to condensation. As a result, the system demands a shorter condensation length when the vertical distance is larger, which means a longer length to cool the condensed fluid.

4. Conclusions

In the present work, simplified hydraulic and thermal models were presented in order to predict

the behaviour of the condenser of an inverted two-phase thermosyphon. These models can be easily adapted to several other ITPT geometries. The model inputs are the geometry along with the operational conditions of the condenser, such as heat transfer rate, cooling fluid temperature.

The model was used then to estimate the performance of an ITPT prototype. The results indicate that the device can transport 3 to 15 kW of heat and lift the condensate from 2 to 10 m with temperatures in the range of 332,7 to 375,2 K. The temperatures predicted for the ITPT components with this model are the minimum to guarantee the operation of the device. The pressure variation due to expansion and contraction between the ITPT lines and components were not computed, but they are expected to have a little influence on the final results. Then slightly different temperature values could be expected in real devices.

Currently, an adaptable ITPT prototype is being built and will be tested in the near future. An experimental study will be undertaken in order to evaluate the prototype performance at different operational conditions and vertical distances. The experimental data will be used then to validate the model presented here. This model could then be used as the foundation for the development of a fully transient model.

Acknowledgments

The authors would like to acknowledge the financial support from CNPq in the development of this work.

Nomenclature

A	Area [m^2]
d	Diameter [m]
c_p	Specific heat [$J/(kg \cdot K)$]
f	Friction factor [—]
G	Mass flux [$kg/(m^2 \cdot s)$]
g	Gravity acceleration [m/s^2]
H	High [m]
h	Heat transfer coefficient [$W/(m^2 \cdot K)$]
h_{lv}	Vaporization enthalpy [$J/(kg \cdot K)$]
k	Heat conductivity [$W/(m \cdot K)$]
L	Length [m]
\dot{m}	Mass flow rate [kg/s]
N_t	Number of tubes [—]
Nu	Nusselt number [—]
P	Pressure [Pa]
Pr	Prandtl number [—]
\dot{Q}	Heat transferred [W]
R	Thermal resistance [K/W]
Re	Reynolds number [—]
T	Temperature [K]
\bar{T}_{ex}	Mean temperature of the cooling fluid [K]

UA	Overall thermal conduction [W/K]
u	Mean velocity [m/s]
X	Martinelli parameter [–]
x	Vapor quality [–]

Greek symbols

α_v	Void fraction [–]
Δ	Variation [–]
μ	Dynamic viscosity [$Pa \cdot s$]
ρ	Density [kg/m^3]
ϕ_l	Multiphase multiplier [–]
Ω	Tube inclination [rad]

Subscripts

a	Accumulator	in	Internal
bi	Condensing section	L	Line
c	Condenser	l	Liquid
cd	Conduction	lt	Latent
co	Subcooling section	ss	Sensible
e	Evaporator	v	Vapor
ex	External	w	Wall
h	Heat exchanger	1	Per tube

References

- [1] Y. Dobriansky and R. Wojcik, State of art review if conventional and anti-gravity thermosyphons: Focus on two working fluids. *International Journal of Thermal Sciences*, 2019. 136, p. 491-508.
- [2] S. Filippeschi, On periodic two-phase thermosyphons operating against gravity. *International Journal of Thermal Sciences*, 2006. 45: p. 124-137.
- [3] S. Filippeschi, Y. Su and S. B. Riffat, Feasibility of periodic thermosyphons for environmentally friendly ground source cooling applications. *International Journal of Low-Carbon Technologies*, 2013. 8: p.117-123.
- [4] Y. Dobriansky, A new concept of antigravity thermosyphon. 16th International Heat Pipe Conference – 16th IHPC. 2012, Lyon, France.
- [5] D.A. Neeper, Analytical model of a passive vapor transport heating system. *Solar Energy*, 1988. 41: p. 91-99.
- [6] F.H. Milanez and M. B. H. Mantelli, Heat transfer limit due to pressure drop of a two-phase thermosyphon. *Heat Pipe Science and Technology, An International Journal*, 2010. 1(3): p. 237-250.
- [7] F. P. Incropera and D.P. DeWitt, *Fundamentals of Heat and Mass Transfer: 5th Edition* (John Wiley & Sons, 2001).
- [8] J.G. Collier and J.R. Thome, *Convective boiling and condensation: 3rd Edition* (Claredon, United Kingdom, Oxford, 1994).
- [9] V.P. Carey, *Liquid-vapor phase-change phenomena* (Hemisphere, New York, 1992).
- [10] S.V. Patankar, *Numerical heat transfer and fluid flow* (Hemisphere Publishing Corporation, 1980).
- [11] C.R. Maliska, *Transferência de calor e mecânica dos fluidos computacional: 2nd Edition* (LTC, 2004).
- [12] F. Kaminaga, H. Hashimoto, M.D.C. Feroz, K. Goto and K. Matsumura, Heat Transfer Characteristics of Evaporation and Condensation in Two-Phase Closed Thermosyphons, 8th International Heat Pipe Conference – 8th IHPC. 1992, Beijing, China.
- [13] R.W. Serth, *Process Heat Transfer: Principles and Applications* (Academic Press, 2007) p. 245-275.

Confined Bubble Growth and Heat Transfer Characteristics in the Vapor Grooves of Loop Heat Pipe

Xue Zhou^{1,2}, Yan Lu^{1,2*}

¹ Shanghai Institution of Technology and Physics, Shanghai, China

² University of Chinese Academy of Sciences, Beijing, China

*Corresponding author email address: luyan420@mail.sitp.ac.cn

Abstract

This paper investigated the transient processes of heat and mass transfer in the circumferential grooves of loop heat pipe (LHP) during the device startup. Given that the vapor grooves are filled with liquid, a successful startup of the LHP becomes possible only after formation of the vapor phase in the vapor grooves and their liberation from the liquid. Simulation of confined bubble growth and heat transfer characteristics have been performed for different heat fluxes in the microchannel of loop heat pipe, which contributes to the improvement of the LHP startup performance.

Keywords: Loop heat pipe; startup; vapor grooves; confined bubble growth

1. Introduction

Loop heat pipe (LHP) is a highly effective two-phase heat transfer device, it utilizes the evaporation and condensation of a working fluid to transfer heat, and the capillary forces developed in fine porous wick to drive the circulation of working fluid[1]. Compared with conventional heat pipes, the evaporator and condenser of the LHP are separated and connected by smooth liquid line and vapor line, and the wick is only existing on the evaporator of the LHP. Therefore, it possesses many advantages such as high heat transfer capacity, long distance heat transport and flexible thermal link, as well as strong anti-gravity capability, which has been applied in many space missions successfully^[2].

One of the merits of LHP is that it can startup without external power equipment. The circulation of working fluid in LHP characterizes that it passes into the main, stationary operating mode. However, LHP does not imply a startup or an instant and smooth startup whenever heat loads are applied to the evaporator. It is necessary to exceed the minimum heat load^[3]. The evaporator temperature may rise above the final steady-state operating temperature, and in some cases may even exceed the maximum allowable temperature^[4]. Some of previous investigations pointed out that the value of the minimum heat load and the behaviors of LHP during the startup are determined by the LHP structure, working fluid, environmental conditions, and the initial fluid distribution^[5].

During the startup of LHP, capillary forces formed at the menisci of liquid-vapor interface

in the wick push the liquid vaporized in the evaporator through the vapor line to the condenser, the vapor condenses in the condenser and is pushed back to the evaporator by the capillary forces. It is a comprehensive fluid redistribution process that the locations occupied by liquid and vapor transiently shift to those corresponding to steady state operation through the combined processes of nucleate phase fluid flow through various portions of the loop^[6]. This is concerned with the initial fluid distribution of the working fluid in LHP, which is subject to the history of LHP, the ambient thermal conditions and the working orientation. Maydanik et al.^[7] summarized four startup conditions of LHP according to whether the vapor grooves and evaporator core were filled with liquid before startup. The author indicated that an instant evaporation will occur in the evaporator once the heat load is applied when the interface of liquid and vapor existed in the vapor groove. However, quite a different startup regime is put forward that a nucleate boiling is necessary to form a vapor-liquid interface in the evaporation zone when it is flooded in the vapor grooves. It has a temperature overshoot in this startup condition and the temperature in the steady-state is higher than the situation that vapor filled with liquid, which is observed by some experiment results^[4]. Liu^[8] designed a visualization experimental system based on a transparent quartz glass and monitored bubbles overflowing from the vapor grooves of the evaporator cavity under the boiling startup mode. Kaya et al.^[9] developed a numerical model to simulate the startup performance characteristics of an LHP

for the situation that the vapor grooves are filled with liquid and the compensation chamber is two phase. Chernysheva et al.^[10] divided the startup process into two stages and proposed a relationship eq. (1). between the superheat formed at the first stage of the startup and the origination of viable vapor bubbles of radius r_{cr} according to the nucleation evaporation theory. Tim J et al.^[11] calculated the temperature profile in a cylindrical capillary evaporator subject to a uniform heat flux prior to the initiation of boiling in the same way.

$$\Delta T_{e-cc} \geq \Delta T = \frac{T_{wall} - T_s}{2\sigma T_s} \approx \frac{h_{fg} \rho_v R_b}{h_{fg} \rho_v R_b} \quad (1)$$

The aim of the present investigation is to study the characteristics of the second stage of an LHP startup when the vapor groove is in a fully flooded state. The vapor groove structure adopted in this work is a number of circumferential grooves which are etched on the inner wall of the evaporator shell or the outer surface of the capillary wick, and the vapor is collected through one or two axial channels. Roger et al.^[12] acclaimed that this structure can effectively reduce the conductive resistance, and make the working fluid in the capillary wick evenly distributed. A numerical model of the growth of single bubble in the an LHP circumferential groove has been developed to analyze the thermal characteristics and reveal the main factors that influence the growth of the bubble in the groove.

2. Numerical model

2.1. Governing equations

The volume of fluid (VOF) method can be used to calculate the multiphase flow of immiscible fluid, which has a significant advantage in tracking the gas-liquid interface^[13]. Therefore, it has been widely used in the study of condensation and boiling. In this paper, ANSYS Fluent software is used to build the CFD model of circumferential grooves based on VOF method. Because there are only vapor-liquid two phases in the flow field of circumferential grooves, the sum of volume fractions for the two phases is always equal to unity ($\alpha_l + \alpha_v = 1$). α_l is the volume fraction of liquid and α_v is the volume fraction of vapor. And each cell in the domain is occupied by one phase or a combination of the

two phases, the possible conditions of each phase are as follows:

$\alpha_l = 1$: The cell is filled with liquid phase.

$\alpha_l = 0$: The cell is filled with vapor phase.

$0 < \alpha_l < 1$: The cell is at the interface between the liquid and vapor phases.

The tracking of the vapor-liquid interface is accomplished by solving the volume fraction equations. For the vapor phase, the volume fraction equation is

$$\frac{\partial}{\partial t} (\alpha_l \rho_l) + \nabla \cdot (\alpha_l \rho_l \vec{u}_l) = S_{M-l} \quad (2)$$

In each cell, the physical properties of density ρ , thermal conductivity λ and viscosity μ are determined as volume-fraction weighted average of liquid and vapor phases.

$$\rho = \alpha_l \rho_l + \alpha_v \rho_v \quad (3)$$

$$\lambda = \alpha_l \lambda_l + \alpha_v \lambda_v \quad (4)$$

$$\mu = \alpha_l \mu_l + \alpha_v \mu_v \quad (5)$$

The vapor and liquid phases share a single momentum equation, and share the velocity field. The momentum equation is:

$$\begin{aligned} \frac{\partial}{\partial t} (\rho \vec{u}) + \nabla \cdot (\rho \vec{u} \vec{u}) \\ = -\nabla P + \nabla \cdot [\mu (\nabla \vec{u} + \nabla \vec{u}^T)] \\ + \rho \vec{g} + \vec{F} \end{aligned} \quad (6)$$

where P and g are the pressure field and the gravitational acceleration vector, respectively. \vec{F} is the body force caused by the surface tension at the interface, which is calculated by the continuum surface force (CSF) model proposed by Brackbill et al.^[14]

$$F_{CS} = \sigma_{lv} \frac{\rho C_l \nabla \alpha_l}{\frac{1}{2} (\rho_l + \rho_v)} \quad (7)$$

Where σ_{lv} is the surface tension coefficient and C_l is the surface curvature of liquid phase.

The energy equation is

$$\begin{aligned} \frac{\partial}{\partial t} (\rho E) + \nabla \cdot [\vec{u} (\rho E + P)] \\ = \nabla \cdot (\lambda \nabla T) + S_E \end{aligned} \quad (8)$$

where S_h is the volumetric energy source. E is sensible enthalpy calculated by

$$E = C_p (T - T_{sat}) \quad (9)$$

where T_{sat} is the saturation temperature, and C_p is the specific heat capacity

$$C_p = \frac{\rho_v \alpha_v C_{p,v} + \rho_l \alpha_l C_{p,l}}{\rho_v \alpha_v + \rho_l \alpha_l} \quad (10)$$

where $C_{p,v}$, $C_{p,l}$ are the specific heat capacity for vapor and liquid phases, respectively.

2.2. Phase-change model

The vapor-liquid phase change process plays an important role in the heat transfer process of the circumferential grooves. Therefore, establishing an accurate phase change model is crucial for simulating the heat and mass transfer in circumferential grooves. The Lee model takes saturation temperature as the condition of phase change and it can accurately predict the occurrence of phase change with no limit of position (inside the phases and at the interfaces), the phase change model in this paper is Lee model^[15].

The direction and magnitudes of mass transfer in Lee model can be described based on different temperature regimes as below:

$$S_{M-v} = \begin{cases} C_l \cdot \alpha_l \rho_l (T_l - T_{sat}) / T_{sat}, & T_l > T_{sat} \\ 0, & T_l \leq T_{sat} \end{cases} \quad (11)$$

$$S_{M-l} = \begin{cases} C_v \cdot \alpha_v \rho_v (T_{sat} - T_v) / T_{sat}, & T_v < T_{sat} \\ 0, & T_v \geq T_{sat} \end{cases} \quad (12)$$

C_l and C_v are coefficients and can be interpreted as a relaxation time, which can be represented by:

$$C_l = \frac{6}{D_{Sm}} \sqrt{\frac{M}{2\pi RT_{sat}}} \frac{\rho_v h_{lv}}{\rho_l - \rho_v} \quad (13)$$

$$C_v = \frac{6}{D_{Sm}} \sqrt{\frac{M}{2\pi RT_{sat}}} \frac{\rho_l h_{lv}}{\rho_l - \rho_v} \quad (14)$$

Both C_l and C_v were specified as 0.1 s-1 in this study.

Energy sources S_E in the energy equation are determined by multiplying the calculated mass sources in Eqs. (14) and (15) by the latent heat for the working fluid, and can be expressed as follow:

$$S_{E1} = S_{M-l} \cdot h_{lv} \quad (15)$$

$$S_{E2} = S_{M-v} \cdot h_{lv} \quad (16)$$

where h_{lv} is the latent heat for the working fluid. A single source term for both phases is required in the boiling, Eq. (14) or condensation, Eq. (16) during the heat transfer process.

In order to prevent the interference of other bubbles on the wall during the growth of a single bubble, the mass source term and energy source term are only added to the calculation unit at the vapor liquid interface.

2.3. Computational domain and Solution condition

The computational domain, $0.3 \times 0.12 \text{ mm}$ ($L_x \times L_y$), is shown in Figure 1. It is one cycle of the evaporator periodic structure consisting of the fluid in the circumferential groove. The boundary conditions include constant heat flux surface at the top, pressure outlet on the right whose back-flow temperature was equal to saturation temperature, no-slip conditions at the bottom and symmetry conditions on the left respectively. The working fluid used is water at atmospheric pressure and saturation temperature. The properties of water are obtained from Table 1.

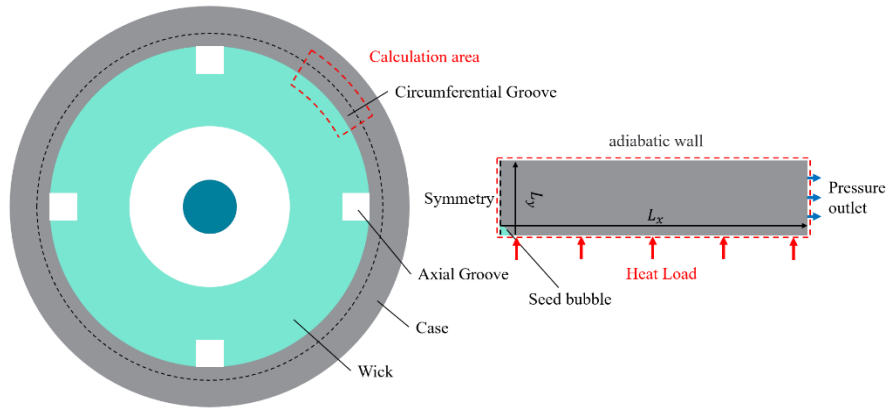
The main assumptions of the model are that (a) The nucleation and growth of bubbles take place in the circumferential groove when the vapor groove is full of liquid, the pressure distribution at the boundary of the computational domain is not affected by the bubble generated in the area outside the computational domain, (b) In nucleate boiling process, the replenishment of the wick is not considered, (c) In the early stage of the startup process, the axial groove is filled with liquid, and the pressure corresponding to the outlet of the circumferential groove are constant as the pressure of saturated liquid in the axial groove.

2.4. Computational settings

The numerical solution was obtained with the pressure-based finite volume scheme using the commercial CFD software, ANSYS FLUENT. A user defined function (UDF) is employed to define the mass and energy transfer at the vapor-liquid interface. The

Table 1 Properties of water at 1 atm

	Water(vapor)	Water(liquid)	Two-phase
Density ρ [kg/m ³]	5.9817×10^{-1}	9.5835×10^3	
Heat capacity c_p [J/(kg·K)]	2.08×10^3	4.2157×10^3	
Thermal conductivity λ [W/(m·K)]	2.457×10^{-2}	6.7721×10^{-1}	
Viscosity μ [kg/(m·s)]	1.2232×10^{-5}	2.8158×10^{-4}	
Surface tension σ_{lv} [N/m]			5.89×10^{-2}
Contact angle [°]			48
Latent heat [J/kg]			2.25677×10^6

**Figure 1** Computational domain

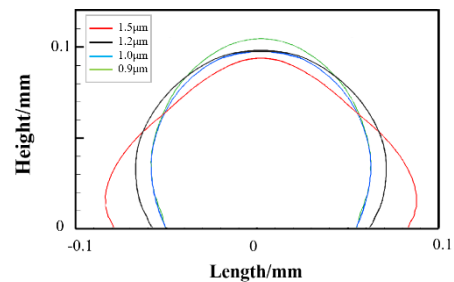
surface tension was computed by the CSF model. In addition, a combination of the SIMPLE algorithm for pressure-velocity, the second order upwind scheme for momentum and energy, and the Geo-Reconstruction scheme for volume fraction and the PRESTO scheme for pressure, are selected. The time step was set as 5×10^{-6} s to make sure that the Courant number was less than 25. At each time step the solution was assumed to converge when the normalized residual of energy equation was lower than 10^{-6} and the normalized residual of all other variables were lower than 10^{-4} .

After applying heat flux density heating, seed bubbles are placed to start the nucleate boiling process when the wall superheat reaches 4K which is calculated by equation (1). Thus,

The following scheme is available for calculating the initial flow field settings.

(1) The right-side boundary of the computational domain is set as the non-slip adiabatic boundary condition, and the heating surface is provided with a constant heat flux, the parameters are consistent with Table 1

(2) Calculate the thermal conduction process of static saturated liquid water in the computational domain until the wall superheat

**Figure 2** bubble contours for different grids at 6 ms

reaches the nucleation condition (4K), and obtain the temperature distribution (thermal boundary layer) and pressure distribution of the computational domain at this time.

(3) Take the flow field obtained in the second step as the initial flow field of nucleate boiling, and first set the seed bubble whose radius is $7.5\mu m$ at the nucleate point, then set the right-side boundary of the flow field in the computational domain as the pressure outlet, and embark on calculating the single bubble nucleate boiling process.

The computational domain includes fluid domain and wall boundary. At the wall boundary, there was an inflation layer located to correctly capture the flow and heat transfer information in this area. Different sizes of grids ($0.9\mu m$, $1.0\mu m$, $1.2\mu m$, $1.5\mu m$) shown as Table 2 have been calculated when a constant heat flux with $10 kW/m^2$ was given to the heating surface, which the width of the groove (L_y) is $0.12mm$. For each element size the shape of bubble contours at the time ($t = 6ms$) and are monitored. The results of bubble shape and evolution of bubble radius are drawn in Figure 2. It is observed from both the Figures that the results of grids C and D are close to each other in terms of shape and diameter. However, grid D has a large number of cells compared to grid C. Due to a large number of cells, the simulations in grid D requires more computational resources and time than grid C. Therefore, to save computational resources and time grid C is selected for further simulations in this case.

Table 2 Computational grids of different sizes

Grid	$\Delta x(\mu m)$	$\Delta y(\mu m)$	Cell amount
A	1.5	1.5	30800
B	1.2	1.2	47000
C	1.0	1.0	66000
D	0.9	0.9	81374

3. Results and discussions

3.1 Growth pattern of single bubble under different heat fluxes

Firstly, the growth pattern under different heat fluxes is presented in this section because

of its significant impact on the nucleate boiling heat transfer.

Figure 3 and Figure 4 illustrate the evolution of the bubble shape and equivalent diameter in the microchannel under different heat fluxes. The length of picture scale corresponds to $0.6mm$ in the following text. It

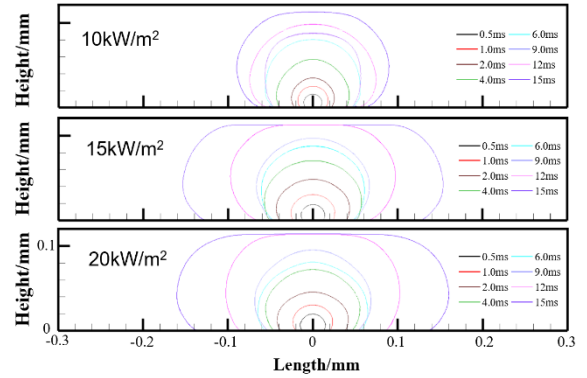


Figure 3 Evolution of the bubble shape under different heat fluxes

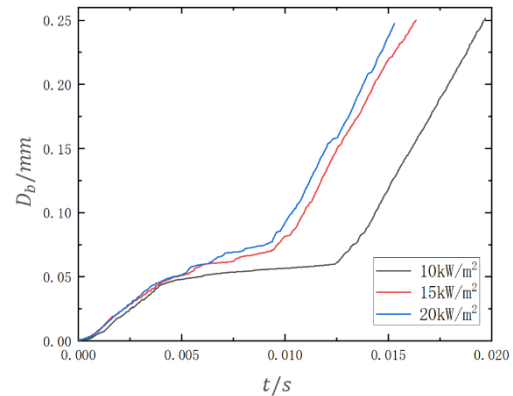


Figure 4 Evolution of bubble equivalent diameter under different heat fluxes

can be observed that the bubble changes from a hemisphere to an ellipsoid and eventually develops into an elongated vapor slug, as observed in slug or annular flows. At the initial stage, the growth of bubble in the groove is the same as that in conventional scale channels. At this time, the shape of bubbles is nearly spherical, mainly affected by surface tension and inertial force. This stage belongs to the free growth stage (0~4ms). The bubble growth basically meets the power function relationship in the conventional channel, i.e. $D_b = kt^n$, k is the coefficient, t is the time of bubble growth, and D_b is the equivalent diameter of the bubble. With the growth of the bubble, the shape of the vapor liquid interface changes from a sphere to a plane, which indicates that the growth of the bubble is restricted by the wall when it does not contact the wall on the other side, and its

growth rate in the height direction starts to slow down. This phenomenon is a unique bubble behavior of nucleate boiling in the microchannel, which is consistent with the experimental observation of Yin et al^[16]. The stage from the beginning of bubble restriction to restricted growth and contacting the wall on the other side is called restricted growth stage (4~8ms). The growth speed of bubbles will change in the restricted growth stage, no longer meeting the power function, but meeting the linear function, i.e. $D_b = kt + n$. When the bubble grows in the height direction and touches the wall on the other side, the bubble elongates in the length direction rapidly. This stage is the elongation stage, which the bubble diameter is exponential with time, i.e. $D_b = a_n t^n$.

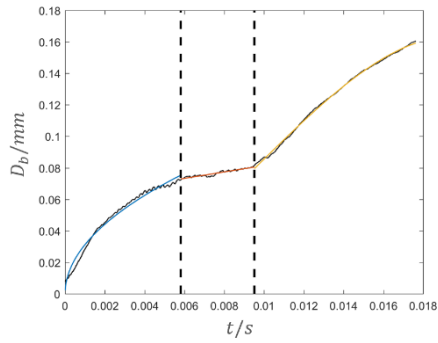


Figure 3 Evolution of bubble equivalent diameter with heat flux of $15kW/m^2$

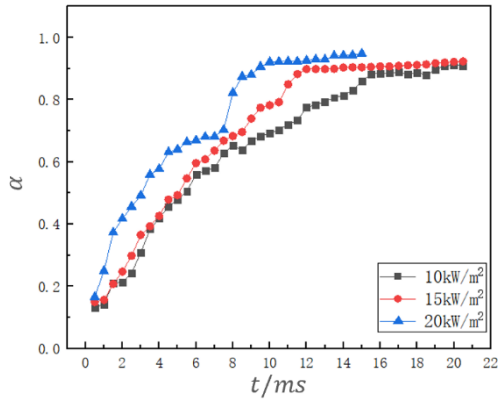


Figure 5 bubble maximal local void fraction under different fluxes

Figure 4 shows the change process of bubble equivalent diameter D_b with a heat flux of $15kW/m^2$. According to the fitting, the power function $D_{b1} = 0.9879t^{1/2}$ is satisfied in the free growth stage of bubble, in which $n = 1/2$ confirms with the heat transfer control stage in the pool boiling at a large space^[17], the linear function $D_{b2} =$

$2.043t + 0.06104$ is satisfied in the restricted growth stage of bubble, and the exponential function $D_b = -4333t^3 + 1277t^2$ is satisfied in the elongation stage of bubble.

Figure 6 shows the bubble maximal local void fraction defined as the ratio of bubble height to channel height^[18], $\alpha = H_b/L_y$ with time. It can be observed that the maximum void fraction begins to stabilize from the restricted growth stage to the elongation stage refer to Figure 5 and Figure 6. With the increase of heat flux, the maximum local void fraction increases faster, and the height of bubble in the elongation stage are 0.114mm, 0.111mm and 0.109mm respectively. This shows that there is a thin liquid film for evaporation in the elongation stage, which can be inferred that there is film evaporation in the vapor grooves at the later stage of startup and the steady-state in LHP. And with the increasing of heat flux, the liquid film gradually thins and finally will retreat into the wick.

3.2 Heat transfer under different heat fluxes

Nucleate boiling dominance is the primary mechanism of heat transfer in a channel. Quantitatively speaking, nucleate boiling dominance is related to bubble dynamics, and HTC depends on heat flux and vapor quality, which is discussed in detail in this section. It is worth stressing that the saturated liquid temperature is set as the reference temperature in the present study.

At each time step, the spatial average heating wall superheat is calculated to obtain its changing trends when different heat fluxes are

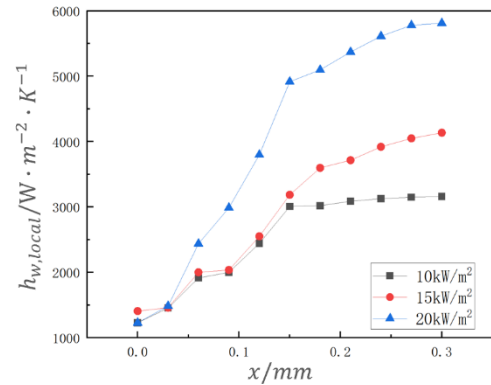


Figure 4 Trends of spatial average heating wall superheats under different heat fluxes.

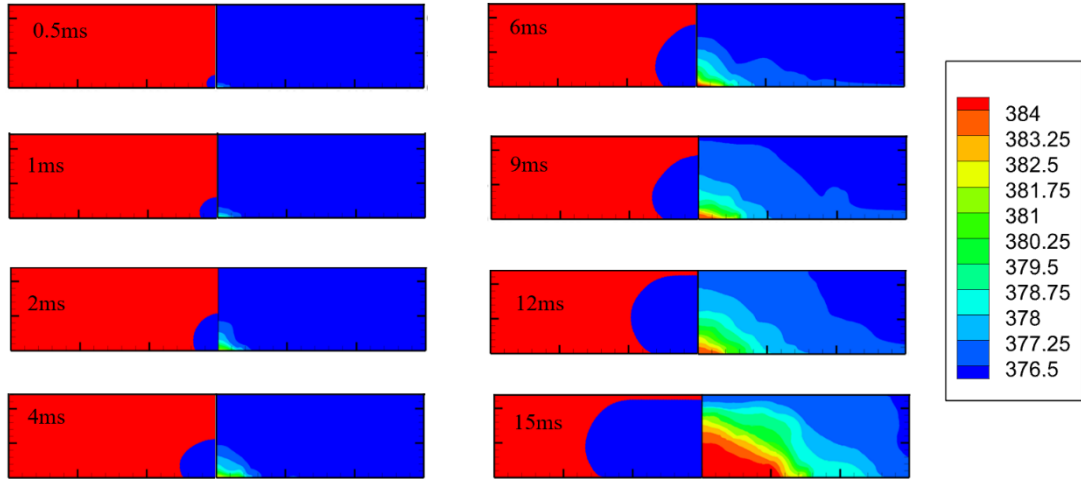


Figure 6 Vapor fraction and temperature distributions with heat flux of $15\text{kW}/\text{m}^2$

applied to the bottom of the groove. As shown in Figure 7 the wall superheats rise slowly at first and then increase quickly later for all cases with different heat fluxes, and the rising amplitude increases with the increasing heat fluxes. The evolution of bubble will greatly decrease the heat transfer and increase the temperature of superheated wall due to the bubble's high thermal resistivity.

The cases with the heat fluxes of $15\text{kW}/\text{m}^2$ is selected to illustrate the details of temperature distributions, contrasting with the bubble shapes in Figure 8. The base of the bubble expands over the heat transfer surface, conduction occurs inside the bubble and the temperature of vapor near the heat transfer surface increases. In addition, evaporation takes place in the region around the interface that decreases the temperature of interface from superheated to the initial mainstream liquid temperature.

Figure 9 depicts the local heat transfer coefficient of the heating surface along x-direction under different heat fluxes. The micro-groove is uniformly divided into 11 subregions along the x-direction. The local heat transfer coefficient is calculated and averaged to explore their relationship. The local heat transfer coefficient here was calculated with the following equation:

$$h_{w,local} = \frac{q''_{w-i}}{T_{w-i} - T_s} \quad (17)$$

where q''_{w-i} indicates the area-weighted average heat flux across the heating surface, the corresponding area-weighted average temperature of the heating surface is denoted

by T_{w-i} , and saturation temperature is represented by T_s . Thus the heat transfer coefficient can be used as an indication to evaluate the energy transportation efficiency from heating to fluid. The bubble starts to grow from the center of the channel ($x = 0$), and no other bubble nucleates and growth to disturb. The vapor fraction gradually decreases along the x-direction, and the thermal resistance gradually increases, so the local heat transfer coefficient along the x-direction gradually rises.

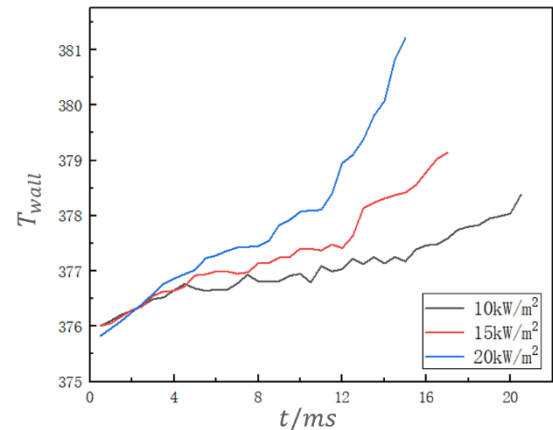


Figure 7 Local heat transfer coefficient along x-direction

4. Conclusions

In this paper, the single bubble growth under the heat flux of $10\text{kW}/\text{m}^2$, $15\text{kW}/\text{m}^2$ and $20\text{kW}/\text{m}^2$ in the microchannel of LHP is simulated with ANSYS FLUENT. The heat transfer mechanisms under different heat fluxes are illustrated by the bubble activities,

distributions of heat transfer coefficient, wall superheat, and vapor fraction. The major conclusions are summarized as follows.

(1) The growth pattern of single bubble is divided into three stages: the free growth stage ($D_b = kt^{1/2}$), the restricted growth stage ($D_b = kt + n$), and the elongation stage ($D_b = a_n t^n$).

(2) At the elongation stage of bubble growth, there is a thin liquid film to evaporate, and with the increasing of heat flux, the liquid film will be thinner and even retreat to the wick of LHP.

(3) Under the same conditions, with the increase of heat flux, the wall superheat and the mass transfer rate from the liquid phase to the vapor phase increases, the growth rate of bubble increases, the restricted growth stage advances, and the local time average heat transfer coefficient increases with the decrease of vapor fraction.

References

- [1] Y. F. J. A. t. e. Maydanik, *2005*, 25, 635-657.
- [2] a) Y. F. Maydanik, M. A. Chernysheva and V. G. Pastukhov, *Applied Thermal Engineering* **2014**, 67, 294-307; b) E. W. Grob, *International Conference on Environmental Systems* **2010**.
- [3] Z. Hongxing, L. Guiping, D. Ting, Y. Wei, S. Xingguo, R. G. Sudakov and Y. F. Maidanik, *Journal of Thermophysics and Heat Transfer* **2005**, 19, 509-518.
- [4] K.-h. Cheung, T. T. Hoang, J. Ku and T. Kaya in *Thermal performance and operational characteristics of loop heat pipe (NRL LHP)*, Vol. SAE Technical Paper, **1998**.
- [5] a) Y. Chen, M. Groll, R. Mertz, Y. F. Maydanik and S. V. Vershinin, *ASME 3rd International Conference on Microchannels and Minichannels* **2005**, pp. 183-189; b) J. I. Rodriguez, M. Pauken and A. Na-Nakornpanom in *Transient Characterization of a Propylene Loop Heat Pipe During Startup and Shut-down*, Vol. SAE International, **2000**; c) J. Ku in *Operating Characteristics of Loop Heat Pipes*, Vol. SAE International, **1999**; d) H. Zhang, G. Lin, T. Ding, X. Shao, R. G. Sudakov and Y. F. Maidanik, *Science in China Series E* **2005**, 48.
- [6] L. Bai, G. Lin and D. Wen, *Applied Thermal Engineering* **2010**, 30, 2778-2787.
- [7] Y. F. Maidanik, N. Solodovnik and Y. G. Fershtater, *IX International Heat Pipe Conference* **1995**, pp. 1-5.
- [8] C. Liu, R. Xie, N. Li, G. Xu and D. J. C. I. E. P. Dong, **2021**, 40, 2401-2415.
- [9] T. Kaya, R. Pérez, C. Gregori and A. Torres, *Applied Thermal Engineering* **2008**, 28, 967-974.
- [10] M. A. Chernysheva, Y. F. Maydanik and J. M. Ochterbeck, *Journal of Thermophysics and Heat Transfer* **2008**, 22, 617-622.
- [11] T. J. LaClair and I. Mudawar, *International Journal of Heat and Mass Transfer* **2000**, 43, 3937-3952.
- [12] V. V. Vlassov and R. R. Riehl, *36th International Conference on Environmental Systems, Norfolk, VA, July 2006*, pp. 17-20.
- [13] C. W. Hirt and B. D. Nichols, *Journal of Computational Physics* **1981**, 39, 201-225.
- [14] J. U. Brackbill, D. B. Kothe and C. J. J. o. c. p. Zemach, **1992**, 100, 335-354.
- [15] W. H. J. I. M. T. F. Lee, REACTOR SAFETY, APPLICATIONS". **1980**, 407-432.
- [16] L. Yin and L. Jia, *Experimental Thermal and Fluid Science* **2016**, 74, 247-256.
- [17] a) H. C. Lee, J. Kim, B. D. Oh and M. H. Kim, *International Journal of Multiphase Flow* **2004**, 30, 697-710; b) X. Frank, N. Dietrich, J. Wu, R. Barraud and H. Z. J. C. E. S. Li, **2007**, 62, 7090-7097.
- [18] L. Yin and L. Jia, *International Journal of Heat and Mass Transfer* **2016**, 98, 114-123.

Thermal performance of the novel loop thermosyphon with annular horizontal evaporator and condenser

Leonard L. Vasiliev*, Alexander S. Zhuravlyov, and Maxim A. Kuzmich

Porous media laboratory, A.V. Luikov Heat and Mass transfer Institute, Minsk, Belarus

* Leonard_Vasiliev@Rambler.ru

Abstract

This paper presents a loop thermosyphon (LTPE) with an annular horizontal evaporator and a copper heterogeneous porous coating used as a wick. It is a new robust passive heat transfer device made of copper tubes filled with R-245fa as a working fluid and with an original vapor chamber. Its ($R = 0.02\text{-}0.03$ °C/W, at $Q = 100\text{-}500$ W and liquid cooling) thermal resistance is insensitive to its inclination to the horizontal when the inclination angle exceeds a certain degrees (8°). The LTPE has a small temperature hysteresis during the increase/decrease of the heat load, and it suppresses temperature pulsations inside the evaporator. The LTPE is suggested as a convenient system for cooling electronic devices, solar receivers, electric and hybrid transport systems. The main goal of this investigation is to improve the heat transfer intensity by increasing the fluid circulation in the annular channel of the evaporator. For thus to achieve it is necessary to know the main LTPE parameters such as the thermal resistance of the evaporator and condenser, total thermal resistance of the thermosyphon, critical heat flux maximum, and the temperature drop along the thermosyphon.

Keywords: Loop thermosyphon; Two-phase heat transfer; Horizontal evaporator, R-245fa working fluid

1. Introduction

Over recent years, various studies have been conducted in various countries on using loop thermosyphons for thermal management of electronic devices, nuclear reactors as well as solar heat recovery, air conditioning, and electric transport cooling systems [1-7]. These thermosyphons can effectively enhance the heat transfer capacity and become the best candidates for choice. Numerous theoretical and experimental studies were carried out to enhance the heat transfer performance of the loop thermosyphons but their capabilities are limited by the dies balance between the driving force and transport resistance. Flow boiling and evaporation in minichannels coated with micro- and nanoparticles is one of the most promising methods for cooling these and similar devices due to the capability of achieving very high heat transfer rates with small variations in the surface temperature for small drops in the temperature across the evaporator [8-11]. Flow boiling in mini- and microchannels can provide a very favorable cooling solution as it can cope more easily with non-uniform heat flux distribution in the substrate to be cooled. A comparative assessment of thermal management systems such as pumped single phase, two-phase and vapor refrigeration systems indicate that the pumped two-phase system provides the most efficient method for cooling high heat flux devices. The operational limits of thermosyphons such as

vapor pressure, sonic limit, viscous and entrainment limit, boiling and capillary limits significantly depend on the heat transfer performance. These operational limits depend on the working fluid used, as well as geometry and inner surface conditions of the thermosyphon. However, several fundamental issues are still not understood and this hinders the transition from laboratory research to commercial applications. It is necessary to concentrate attention on the mode of vapor-liquid plug oscillation in the process of heat transfer, involving the process of the nucleation, growth and collapse of bubbles, liquid film evaporation and condensation, and others. The article focuses the attention on the passive systems. New two-phase loop thermosyphons (LTPEs) are rather simple, robust and at the same time quite efficient heat-transfer devices capable of operating in a wide range of variation of their mode parameters.

2. LTPE design

A new loop thermosyphon is an efficient heat-transfer device capable of operating in a wide range of heat loads and degrees of its inclination to the horizontal. The LTPE consists of a horizontally disposed original cylindrical capillary-coated evaporator, a condenser, a compensation chamber, vapor and liquid pipes between the evaporator and condenser (Figure 1). The main forces responsible for the working fluid circulation inside a thermosyphon are gravity,

capillary, and the surface tension forces. The LTPE has a low thermal and hydraulic resistance in comparison with conventional thermosyphons.

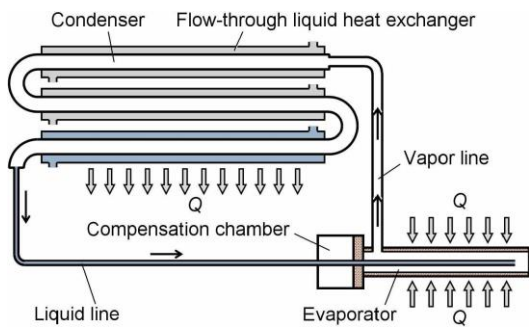


Figure1. Thermosyphon LTPE with horizontally disposed evaporator and condenser.

Experiments show that the LTPE guarantees a shortened start-up time, decreases the evaporator wall temperature, has a small temperature hysteresis during the increase/decrease of the heat load, and suppresses the temperature pulsations inside the evaporator. The principal characteristic feature of the LTPE is the possibility of using a long annular evaporator (up to 1m) with a near uniform temperature field distribution all over the evaporator surface. The evaporator and condenser of LTPE are connected with each other by flexible pipes to transfer liquid and vapor. The liquid line is disposed along the axis of the evaporator. A small annular channel between the porous coating of the evaporator and the liquid line (Figure 2) is used to organize the efficient two-phase heat transfer from the boiling flow up to the developed boiling and evaporation region inside the pores of the wick. The LTPE wick ensures a high liquid surface tension, low contact angle (i.e., good liquid wettability) and has small particles such as an effective pore size. The wick of the LTPE evaporator is manufactured such as to have a pore radius of 60–100 μm , a porosity of 60%, and permeability greater than $1 \cdot 10^{-13} \text{ m}^2$. Two-phase heat transfer (boiling and evaporation), filtration and capillary pumping of the working fluid occur inside the annular minichannel (from the bottom to the top) of the evaporator.

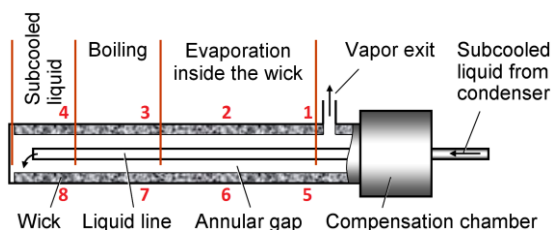


Figure2. Longitudinal cross of the evaporator with coaxial liquid line inside and the liquid compensation chamber; 1–8 are thermocouples on the evaporator surface.

The vapor quality “ x ” undergoes a change along the evaporator on increasing the fraction of vapor phase which influences flow patterns. The pressure drop during the working fluid circulation inside the LTPE is caused by the action of a thin monolayer wick made of sintered copper particles. The evaporator was designed with account for the previously obtained experimental results as experiments on flooded and partially flooded porous surfaces. So as well as in mini channels [2] it has a copper sintered powder porous coating on the internal surface to distribute the liquid phase over the entire surface of the evaporator and to intensify a heat transfer during evaporation. The high porosity of the wick due to the presence of pores of different diameters (mini- and macro) guarantees a high rate of mass flow through the porous structure. The evaporator distributes the liquid along the perimeter of the cross-section, creating conditions for intensive heat transfer during the boiling and evaporation of the liquid over the entire heat exchange surface of the evaporator.

Compensation chamber of the LTPE has a copper porous membrane which separates it from the evaporator volume, Figure 1. The capillary structure (1 mm thick **membrane**) divides the LTPE evaporator into two parts. The smaller part of the evaporator is used as a compensation chamber. The LTPE membrane has large pores ($\sim 100\text{--}150\mu\text{m}$) to ensure a constant contact of liquid with the primary wick of the evaporator. The transport pipes for the liquid and vapor have the smooth walls that significantly reduce the pressure drop during the LTPE operation. A compensation chamber is used to ensure the successful start of the LTPE, supply of the wick with a working fluid by capillary suction, increase the vapor flow quality “ x ” in the vapor pipe and accumulation of non condensable gases inside the chamber, if they are generated in the thermosyphon. Compensation chamber keeps a nearly constant total thermal resistance of the LTPE in a large range of the heat loads.

3. Experimental testing

The scheme of the experimental setup is shown in Figure 3. An electric heater was applied as a source of energy. Heat flow was absorbed by the water cooling system (condenser) includes a

“Julabo” FP-89 thermostat and a flow heat exchanger. The temperature of the cooling liquid (water) was changed from 20 to 80°C at a flow rate of 10 L/min. The precision of the water temperature maintenance in the thermostatic bath was $\pm 0.1^\circ\text{C}$. The temperature of the water was recorded by an Agilent 34980A data acquisition system. The vapor pressure inside the LTPE was measured using a PSA-C01 pressure sensor, and a NI-9203. The precision of the heat flow measurements was $\pm 5\%$.

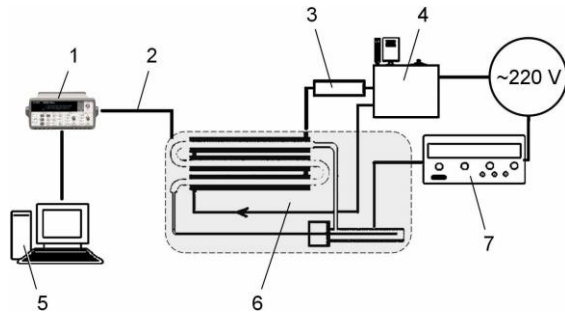


Figure 3. Diagram of the experimental setup for LTPE testing: 1) multifunctional switching and measuring unit Agilent 34980A, 2) connection cable, 3) additional cooling heat exchanger, 4) thermostat, 5) computer, 6) thermosyphon, 7) stabilized constant electric current source.

Working fluid R245fa was used. This hydrofluorocarbon doesn't damage the ozone layer. R245fa properties are presented in Table 1 [8] (with reference to the source [9]).

Table 1. R245fa properties [8].

Physical quantity	Value
Boiling point at 1.01 bar, °C	15.3
Freezing point at 1.01 bar, °C	<-107
Critical temperature, °C	154.05
Critical pressure,	36.4
Liquid density, kg/m ³	1339
Liquid heat capacity, kJ/(kg·K)	1.36
Vapor heat capacity at constant pressure 1.01 bar, kJ/(kg·K)	0.8931
Heat of vaporization at boiling point, kJ/kg	196.7
Liquid thermal conductivity, W/(m·K)	0.081
Vapor thermal conductivity, W/(m·K)	0.0125
Liquid viscosity, mPa s	402.7
Vapor viscosity, mPa s	10.3

During the tests starting from 100W the LTPE heat load increased in 100 W steps up to $Q=600$ W, the decreased back. The LTPE thermal

resistance, temperature field along the evaporator and condenser for different heat loads with uniformly heated evaporator were tested and analyzed. The temperature difference $\Delta T = T_e - T_c$ between the evaporator and condenser is found by subtracting the average condenser temperature from the average evaporator temperature:

$$\Delta T = \sum_n T_{e,i} / n - \sum_k T_{c,j} / k, \quad (1)$$

where n and k are the number of thermocouples on the evaporator and condenser.

The presence of uncertainties in the determination of thermal resistances R_e , R_c , and R_t is less than 6.8%. The heterogeneous wick is a key component affecting the evaporator performance because porous wick provides the intensification of the boiling and evaporation heat transfer. The observed flow reversal and instabilities were attributed by researchers to rapid bubble growth, the presence of a compressible volume ahead of the test section, and nucleation near the channel inlet. The channel surface characteristics, surface wettability, conjugate heat effects and the size of the inlet and outlet manifolds are important parameters that might affect flow instability and reversal. Also, there is a scarcity of experimental heat transfer data on stable and unstable boiling that would allow an understanding of the effect of flow reversal or oscillating flow on heat transfer. The oscillation of bubbles might enhance the heat transfer process in the evaporator. There are a very limited number of experimental studies on flow boiling in small and minichannels at operating conditions relevant to electronic cooling applications, boiling in long or serpentine channels. The presence of uncertainties in the determination of temperatures is less than 6.8%. The uncertainty analysis for experiments was performed in accordance with the methods proposed in [10, 11]. For the stable movement of the vapor and liquid phases along the closed circuit of the LTPE, a balance of forces must be maintained, which ensures sustained circulation of the working fluid. It means the driving forces must prevail over pressure losses: The height of the hydrostatic liquid column was varied by changing the tilt angle of the device by turning it around the longitudinal axis of the evaporator.

3.1. Influence of the working fluid volume on the LTPE total thermal resistance

The LTPE total thermal resistance as a function of heat load Q is shown in Figure 4. The influence of LTPE liquid charging on its total thermal resistance is mostly essential for small heat loads (100-300 W).

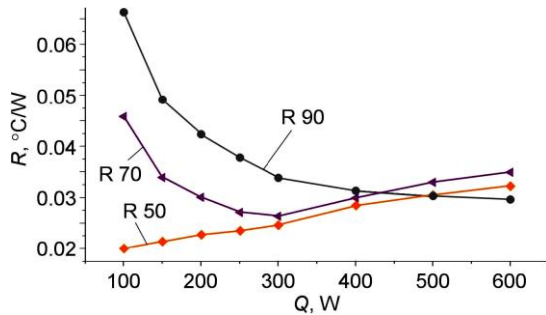


Figure 4. Dependence of LTPE total thermal resistance of the heat load Q for different volumes of R245fa charge. Total lengths of the condenser $L = 600$ mm.

For the small heat loads of the LTPE (100-400 W), the optimal volume of the R245fa is 50ml. Total thermal resistance of LTPE is 0.020-0.027 K/W. For the heat loads range 400-600W, the value of R245fa liquid charging is not so important (50-90 ml), since the LTPE thermal resistance is almost insensitive to it.

3.2. Influence of the condenser three sections length on the LTPE total thermal resistance

During the experiments three different sections of liquid-cooled condenser were used with the length 200 mm, 400 mm, and 600 mm, Figure 5. All three designs of condensers are cooled by forced water convection. The exit of the working fluid flow from the evaporator can be different depending on the heat load value of the LTPE (moist vapor or superheated vapor). The working fluid inside the condenser can be also different depending on the condenser heat exchanger parameters. The LTPE thermal resistance is minimal (0.020-0.025 K/W) for the heat load interval 100-600W when the R245fa volume is 50ml, the total condenser lengths is 600 mm. For such conditions the heat transfer inside the evaporator is a most efficient.

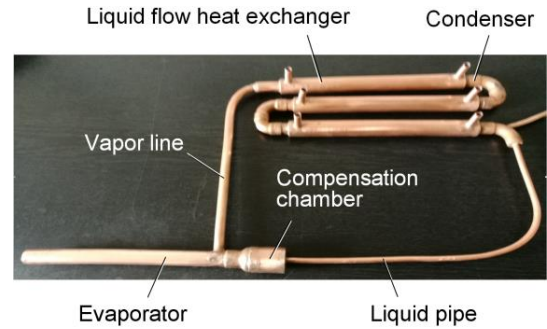


Figure 5. LTPE condenser is cooled by three liquid flow heat exchangers.

Two-phase flow patterns and the condensation process in the horizontal condenser are significantly affected by its cross section and the condenser length. Specifically, as the tube diameter decreases, the flow pattern at the condenser transits from a stratified flow to uniform flow.

Condenser of LTPE is placed above the evaporator, so that the vapor rises due to the buoyancy, and the condensed liquid is drained due to the gravity forces, and goes back to the evaporator of LTPE by the liquid line. The diameter of the vapor line is 10/1 mm and the diameter of the liquid line is 6/1 mm. Inlet for the vapor to the condenser and exit for the liquid from the condenser are positioned on opposite sides of the condenser. The three-part tube condenser of the total length 600 mm has three independent liquid heat exchangers (diameter 15/1 mm) as the coolers, which can be jointed to each other, or used independently. The typical example of the influence of different condenser length on the LTPE thermal resistance is shown in Figure 6. The length of the condenser significantly affects the thermal characteristics of the thermosyphon. Therefore, the correct choice of the condenser geometry provides the optimal solution to the specific problem of thermal control of heat-loaded objects, Figure 6.

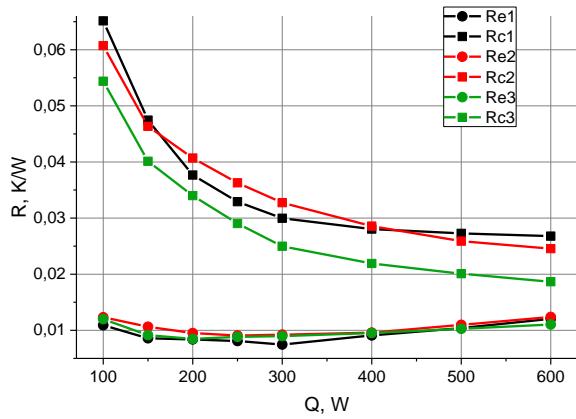


Figure 6. Thermal resistance of the condenser and evaporator (square – condenser, circular – evaporator) as a function of different lengths of condenser heat exchanger ($Re_1=200$ mm, $R_2=400$ mm, $R_3=600$ mm). Volume of R245fa working fluid charging is 90 ml.

3.3. Influence of the thermosyphon inclination to the horizontal

The height of the hydrostatic liquid column was varied by changing the tilt angle of the device by turning it around the longitudinal axis of the evaporator. Figure 7 shows the changes in the temperature values of the evaporator, vapor, liquid, and condenser at different angles of inclination of the thermosyphon to the horizontal under the heat load $Q = 600$ W (the starting load was 100 W). With a change in the angle of inclination, the temperature of the evaporator increased at a practically constant temperature of the condenser, that is, the thermal resistance of the thermosyphon increased, however, the thermosyphon worked well and stably up to an inclination angle of 8° .

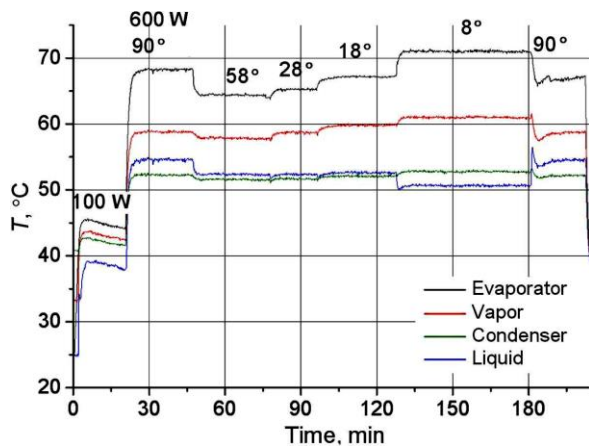


Figure 7. LTPE temperature-time dependence for different tilts of inclination. Heat flow $Q = 600$ W.

Several types of forces act in the LTPE evaporator, including gravity, capillary and surface tension forces, which affect the formation of two-phase flows in the thermosyphon circuit. The ratio between these forces is determined by the dimensionless Bond number (Bo).

$$Bo = \left(\frac{L}{L_c} \right) = \frac{gL^2\Delta\rho}{\sigma}, \quad (2)$$

where

σ - the surface tension coefficient;

g - the free fall acceleration;

$\Delta\rho = \rho_{con} - \rho_{dis}$ in our case, is the difference between the densities of continuous and dispersed media;

$$L_c = \sqrt{\frac{\sigma}{g\Delta\rho}} - \text{the capillary constant;}$$

L - the characteristic length.

For the studied thermosyphon the Bond number is $Bo=14.42$. The Bond number characterizes the size and shape of moving bubbles. In the channels of a thermosyphon with R245fa as a working fluid a liquid flow with small vapor bubbles takes place.

The temperature graphs in Figure 7 show that a LTPE filled with R245fa remains operational with a stepwise deviation of the thermosyphon from the vertical plane to an angle of 8° to the horizon. Of practical interest is the question of whether the inclined LTHPE is able to start working. In order to clarify this issue, an experiment was carried out in which a heat load of 500 W was used. The test results are shown in Figure 8. The system is working well without of any problems.

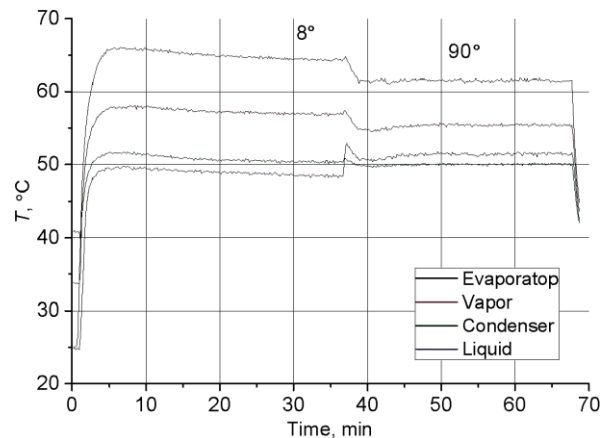


Figure 8. LTPE start up from an inclined position 8° .

As it can be seen from Figure 9, the LTPE is dynamically activated and functions stably. After moving the thermosyphon to a vertical position, the operating conditions of the device are improved, the efficiency of heat transfer increases, and the temperature of the evaporator decreases.

The graphs in Figure 7 show that the optimum angle of inclination for the investigated LTPE is 58°.

The temperature distribution along the thermosyphon in this position is shown in Figure 9. The data obtained testify to the stable and efficient operation of thermosyphon.

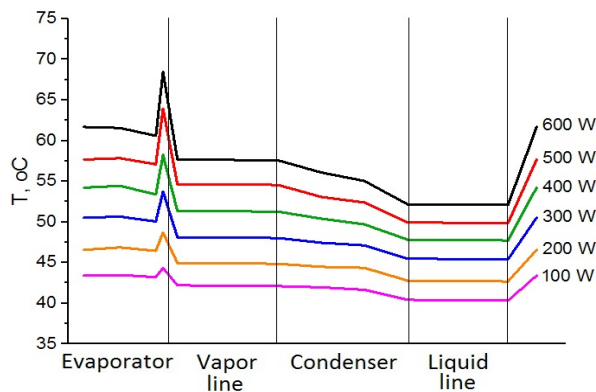


Figure 9. Temperature distribution along the LTPE for different heat loads. Condenser length is 600 mm, R245fa charging 70 ml. Angle of the inclination 58 degree. Cooling water temperature is 40 °C.

4. Conclusion

The loop thermosyphon with a horizontal porous evaporator with R245fa as a working fluid has been studied, its heat transfer characteristics have been determined when the device was located in a vertical plane and at inclinations of up to 8° to the horizontal. It was found that the device worked stably up to an inclination angle of 8°. The tilted LTPE is dynamically activated and functions stably at inclination as its initial position

The geometry and length of the condenser significantly affects the thermal characteristics of the thermosyphon. Therefore, the correct choice of the condenser geometry provides the optimal solution to the specific problem of thermal control of heat-loaded objects.

The thermosyphon with R245fa as a working fluid can be successfully used for cooling

power electronics and other objects with intense heat release.

Nomenclature

P	pressure, bar,
Q	heat flow, W,
R	thermal resistance, K/W, °C/W,
T	temperature, °C

References

- [1] D. Khrustalev. Loop thermosyphons for cooling of electronics. in 18th Semi-Therm. Symp. 2002, San Diego, Calif., USA, 145-150.
- [2] L. L. Vasiliev, L. P. Grakovich, M. I. Rabetsky, L. L. Vassiliev, Jr., and A. S. Zhuravlyov, Thermosyphons with innovative technologies. Applied Thermal Engineering, 2017. 111: p. 1647-1654.
- [3] I. Sviridenko and D. Shevielov, Autonomous thermosyphon system for WWER cooldown. Heat Pipe Scies and Technology – An International Journal, 2011. 2: p. 145-159.
- [4] A. Franco and S. Filippeschi, Experimental analysis of closed loop two phase thermosyphon (CLTPT) for energy systems. Experimental Thermal and Fluid Science, 2013. 51: p. 302-311.
- [5] J. Li, F. Lin, and G. Niu, An insert-type two-phase closed loop thermosyphon for split-type solar water heaters. Applied Thermal Engineering, 2014. 70: p. 441-450.
- [6] L. Han, W. Shi, B. Wang, P. Zhang, and X. Li, Development of an integrated air conditioner with thermosyphon and the application in mobile phone base station. International Journal of Refrigeration, 2013. 36: p. 58-69.
- [7] C. Sarno, C. Tantolin, R. Hodot, Y. Maydanik, and S. Vershinin, Loop thermosyphon thermal management of the avionics of an in-flight entertainment system. Applied Thermal Engineering. 2013. 51: p. 764-769.
- [8] R. Capata and C. Toro, Small-scale ORC energy recovery system for wasted heat: thermodynamic feasibility analysis and preliminary expander design. in: „Whither Energy Conversion? Present Trends, Current Problems and Realistic Future Solutions”, Conference Proceedings Paper – Energies. 2014. 1: p. 1-21.
- [9] E. W. Lemmon, M. L. Huber, and M. O. McLinden, NIST Standard Reference Database 23:

Reference Fluid Thermodynamic and Transport Properties-REFPROP, Version 9.1. 2013.

[10] J. P. Holman, *Experimental Methods for Engineers*, 8th ed. (McGraw-Hill, NY, 2011). 739 p.

[11] Y. Y. Kee, Y. Asako, T. L. Ken, and N. A. C. Sidik, Uncertainty of temperature measured by thermocouple. *Journal Advanced Research in Fluid Mechanics and Thermal Sciences*. 2020. 68 (1): p. 54-62.

Experimental investigation of a coil shaped deployable pulsating heat pipe

Roberta Perna^{1*}, Maksym Slobodeniuk², Luca Pagliarini³, Mauro Mameli¹, Cyril Romestant², Luca Cattani³, Vincent Aysel², Fabio Bozzoli³, Sauro Filippeschi¹

¹ Department of Energy, Systems Land and Construction Engineering, University of Pisa, L. Lazzarino, Pisa, Italy

² Pprime Institute CNRS – ENSMA – Université de Poitiers, UPR 3346, 86961 Futuroscope-Chasseneuil, France

³ Department of Engineering and Architecture, University of Parma, Parco Area delle Scienze 181/A, Parma, Italy

*Corresponding author email address: roberta.perna@phd.unipi.it

Abstract

The development of foldable heat transfer devices is currently a quite intriguing technological challenge in the field of thermal management. Due to its simple structure (i.e. capillary tube without any wick structure inside), the Pulsating Heat Pipe is one of the most promising candidate to be applied to foldable devices. A possible solution is to realize a PHP with the adiabatic section formed as a coil. In this case the adiabatic section is very long and the performance of the PHP can be largely affected. This paper presents the results of the comparison between two twin PHPs built with the same geometry but different adiabatic section shapes (planar and coil).

A full thermal characterization of the planar assessment for different working fluids has been performed: HFE-7000 (filling ratio: 70%) shows the best thermal behavior in horizontal orientation. On the other hand, the coiled PHP has been tested under different orientations and folding configurations (different mutual locations of the evaporator and condenser with respect to gravity) and compared with the planar reference case. The coiled PHP in some configurations seems to present worse thermal performances than the planar one.

Keywords: Pulsating Heat Pipe; Deployable; Long adiabatic section; Pressure drop

1. Introduction

Deployable passive heat transfer devices can be an attractive solution for a wide range of applications (spacecraft electronics thermal control systems [1], moving solar panels for buildings [2] etc.), where the heat source and the heat sink may change their mutual location during the operation.

Since the early 1990s, the Pulsating Heat Pipe (PHP) represents one of the most interesting two-phase passive heat transfer systems because of the high heat transfer performance, a huge versatility and a simple design [3]. Most of the attempts made so far in the scientific literature to obtain a foldable structure, consist of PHPs equipped with an adiabatic polymer section so that the unfolding is allowed by the polymer high degree of elasticity. For instance, a hybrid flexible oscillating heat pipe has been presented by Qu *et al.* [4]. The device is characterized by an adiabatic section made of fluoro-rubber pipes and the heating/cooling sections made of micro-grooved copper tubes. The working fluid is deionized water. Experimental results show that the arrangement of the evaporator with respect to the condenser has a significant influence on the performance of the oscillating heat pipe. Since polymers may be strongly chemically altered by the space environment conditions [5], the polymeric PHP is not recommended. In addition, they are

highly permeable to most environmental gases so the development of a metallic deployable structure is a matter of technical interest but it has been scarcely investigated since now. In 1992, the first patent, published by Cullimore [6], only assessed the basic concept of a metallic tubular PHP as a flexible coil connecting the heat source inside the payload to a deployable radiator. The working fluid is ammonia or water but several important technical details, such as the tube material, are missing. Iwata *et al.* [7] proposed a Pulsating Heat Pipe embedded into the external structural panels of a CubeSat to use the faces as radiators. The pipes between the panels (adiabatic zone) are coiled and this shape allows the device foldability. The working fluid is HFC-134a and the pipe material is stainless steel 304. An improved version was presented in [8] where the same authors propose a new version of the deployable PHP system with lower ID (0.8 mm), lower input power (20 W max.) and a coil diameter of 12 mm, with tubes turned 3 times for each coil junctions.

Perna *et al.* [9] presented a paper describing a PHP built to make itself deployable. The PHP must have the adiabatic section tube turned in a coiled junction. However, the effect of the coil junction on the PHP performances is scarcely investigated. Indeed, a coil junction determines two main effects: first; the length of the adiabatic section is higher

than a straight pipe and, secondly, the shape of the coil could imply unpredictable effects on the fluid-dynamic of working fluid and on the pressure drops. In the literature, the effect of helicoidally turned pipes has been investigated for mass flow rates not typical of PHP.

Furthermore, the influence of a long adiabatic section on the performance of a PHP has been rarely studied in the past works. Arab *et al.* [10] designed, built, and installed an extra-long pulsating heat pipe (ELPHP) applied to a thermosyphon solar water heater. They also tested different PHPs with the same lengths of the condenser and evaporator section (800 mm, and 960 mm, respectively) and different adiabatic sections (from 700 mm to 1800 mm) at different filling ratios (*FR*: 30, 50, and 70%). The results showed that the optimal filling ratio was 70 % and that the instability and the performance were highly degraded as the length of the adiabatic section was increased [10]. A long PHP operating with different filling ratios (25 to 75 %), different adiabatic section lengths (500 to 1000 mm) and different working fluids (acetone, ethanol, and water) was presented by Czajkowski *et al.* [11]. The authors observed that, with a filling ratio of 25%, the dry-out was often reached, even at very low input powers, while the best thermal performances were achieved with a *FR* of 75 % for most working fluids. The PHP were tested in vertical bottom heated mode. The authors show that the adiabatic length does not affect the performances of the device if vertically oriented. In addition, the author noticed that, all operating parameters equal, Acetone has the quickest start-up and the lowest thermal resistance. In conclusion, in order to investigate the double effect of a coiled adiabatic junction on the thermal performances of deployable PHPs, two twin PHPs with same adiabatic section length but different junction shapes (helical and straight tubes) have been built and tested.

This paper compares the thermal performances of two PHPs (planar and deployable) under different experimental conditions. In particular, the planar PHP have been tested with different working fluids FC72 (Perfluorohexane), HFE7000 (Hydrofluoroether), SF33 (hydrofluoroolefin) and N-Pentane. The deployable PHP have been tested with HFE7000 (*FR* = 70 %) and with different deployable angles corresponding to different mutual positions of the condenser and the evaporator with respect to gravity. A comparison between the two PHPs' performances provides a preliminary analysis of the effect of the coiled junction on the oscillation of the fluid inside the device.

2. Test cells

To investigate the effect of a foldable coil-shaped section on the Pulsating Heat Pipe thermal performances, two “twin” devices, with the same overall size but with different shapes of the adiabatic section, have been designed and built: the first one (planar, see Fig. 1) has the following global dimensions of 890 x 420 mm²; the second one (deployable, see Fig. 2) has the same dimensions but with a different assembly. The tube for both is made of aluminum 6063 and is bent into a closed loop serpentine with 11 U-turns at the evaporation section. The inner and outer pipe diameters are respectively 1.6 mm, and 2.6 mm. The adiabatic, evaporator, and condenser lengths are of 720, 10 and 75 mm, respectively (Figure 1). The evaporator zone is sandwiched between two aluminum heat spreaders and equipped with a flat heater (Hotspring®/Maxi - type WRP, 4.8x8.6x500 mm). The condenser section, also, is sandwiched between two aluminum spreaders and thermally connected to a cold plate (20x90x500 mm), cooled by a water flow circulating thanks to a loop, and whose temperature is controlled by a cryostat (Huber® CC240 wl).

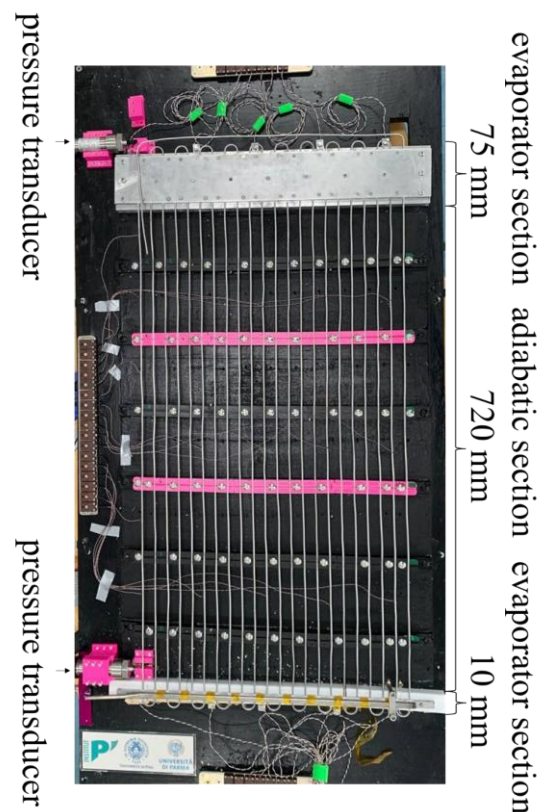


Figure 1. Long planar Pulsating Heat Pipe and main dimensions (photo).

Otherwise, the foldable PHP is shaped as torsional spring in the adiabatic section, with a coil diameter $d = 65$ mm, $N = 3.5$ coils for a total length of $L_{coil} = 715$ mm (90 % L_{tot}) corresponding to the adiabatic length of the planar PHP. The CAD of the deployable Pulsating Heat Pipe and the main components (red for the evaporator section and blue for the condenser section) are shown in Figure 2.

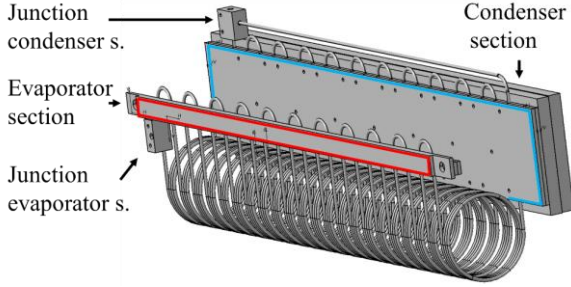


Figure 2. Deployable Pulsating Heat Pipe in folded configuration.

Figure 3 shows the number, the color and the location of thermocouples on the planar Pulsating Heat Pipe: 29 T-type thermocouples are located respectively at the evaporator (25 to 29, red ones), condenser (2 to 6, blue ones), and adiabatic sections (7 to 23). The values reported in the further plots represent therefore the respective average temperatures of evaporator and condenser zones, whereas the other thermocouples represented in Figure 3 are all plotted. Two T-type thermocouples (1 and 24) are located close to the connectors which host the pressure transducers (Keller® PAA-33X, ± 0.5 kPa) and the evacuating/filling ports.

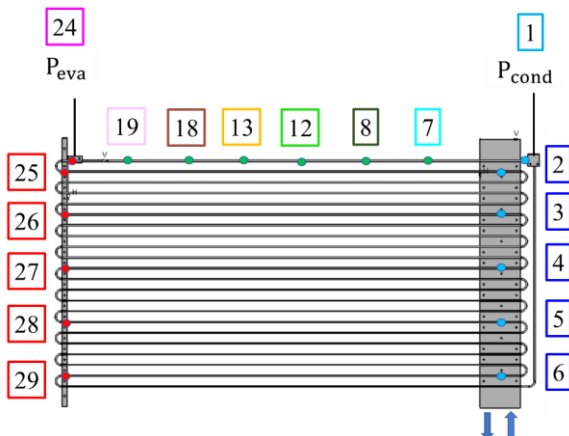


Figure 3. Long planar Pulsating Heat Pipe and location of the thermocouples.

3. Thermal characterization of the twin Pulsating Heat Pipes

The experimental procedure described here for the planar PHP has been mostly followed also for the deployable PHP. Any eventual difference from the two experimental campaigns can be neglected if not specifically mentioned in the paper. To evaluate and compare the thermal performances of both devices, the thermal resistance is calculated as follows:

$$R = \frac{T_{eva} - T_{cond}}{Q} \quad (1)$$

where T_{eva} and T_{cond} are, respectively, the mean temperatures experimentally measured close to the evaporator, and the condenser, sections, respectively, and Q is the heat power supplied. Start-up and pseudo-steady regimes at different power levels are observed. Temperatures and pressures are acquired for each power level, and power is held constant until pressures/temperatures reach a pseudo-stationary regime.

The experimental campaign was divided into three main sets of test: firstly, tests on planar PHP were done to evaluate the effect of the working fluid on its thermal performances and then to assess its thermal resistance; lastly, tests on the deployable PHP were performed under different configurations.

3.1. Effect of the working fluid on the Planar Pulsating Heat Pipe

The start-up and the pseudo steady state regimes were investigated for different working fluids: FC72 (perfluorohexane), HFE7000 (hydrofluoroether), SF33 (hydrofluoroolefin), and N-Pentane. The filling ratio was fixed at 70% for all fluids.

As shown in Table 1, the planar PHP presents stable operation (SO) at 20 W with HFE7000 and N-Pentane as working fluids. Aside, the heat transfer is only due to Pure Conduction or only small amplitude oscillations (SAO) when the PHP is filled with SF33 and FC72. At 40 W, however, for all fluids, the device reaches a stable operation (SO). At 60 W, the evaporator section reached a maximum temperature and the test was stopped for the tests conducted with FC72 and N-Pentane, while the PHP showed stable operation for HFE7000 and SF33. Figures 4 and 5 show the temporal trends of the heat input (Q [W]) and temperatures (T [°C]) at the evaporator, condenser and adiabatic sections for

the PHP filled with HFE7000, and SF33, respectively. As shown in Figure 4, with HFE7000 as working fluid, at 20 W, a start-up is detected from the temperature oscillations which happen after about 15 minutes. From 40 W to 60 W, the evaporator temperature reaches 80 °C, and 130 °C, respectively.

Table 1. Planar PHP: experimental matrix and general behavior (SO: Stable Operation; SAO: Small Amplitude Oscillations; HT: High Temperature > 140 °C).

Working fluid	Heat input [W]		
	20	40	60
FC72	SAO	SO	HT
HFE-7000	SO	SO	SO
SF33	SAO	SO	SO
N-Pentane	SO	SO	HT

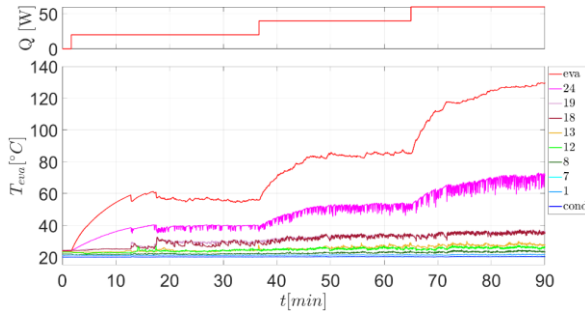


Figure 4. Temperature evolution over time in the planar PHP with HFE7000 ($FR = 70\%$).

In Figure 5, with SF33 as working fluid, at 20 W an initial startup also occurs after 20 minutes but, after 40 minutes the weak oscillations cease, and the device operates in pure conduction or with only small amplitude oscillations. At 40 W, the oscillations regime is stable, and begins less than 20 minutes after the input power step; the quasi-steady regime is achieved when the evaporator temperature is also of around 80 °C. From 40 W to 60 W, the device works properly reaching an evaporator temperature of 120 °C. Comparing Figures 4 and 5, the temperatures at the evaporator section are almost the same during pseudo steady-state regimes, although the oscillations have a greater amplitude for SF33 (Figure 5) compared to HFE-7000 (Figure 5). However, HF7000 shows stable oscillations throughout the heat input range, starting from 20 W heat load applied.

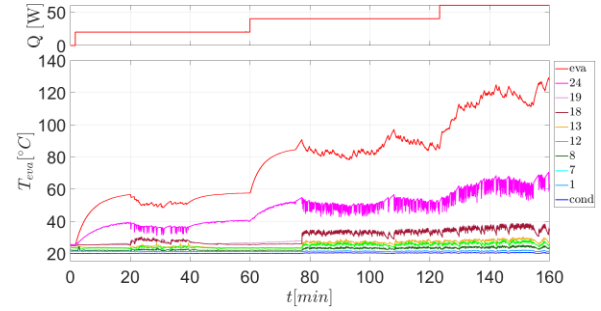


Figure 5. Temperature evolution over time in the planar PHP with SF33 ($FR = 70\%$).

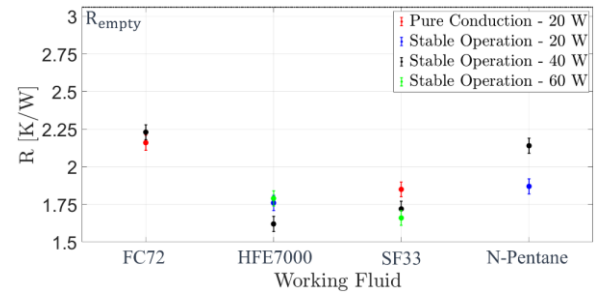


Figure 6. Thermal resistance (R [K/W]) as a function of the working fluid (FC72, HFE7000, SF33 and N-Pentane).

Figure 6 shows the thermal resistances obtained from experiments with different working fluids (HFE7000, SF33, N-Pentane, and FC72) and at different power values: 20 W (red dotted - pure conduction and blue dotted - stable operation), 40 W (black dotted - stable operation) and 60 W (green dotted - stable operation). As shown in Figure 6, the optimal working fluid is HFE7000, as it has the lowest thermal resistance and the most stable operation for all tested heat inputs. Furthermore, as stated by Tsai [12], HFE7000 is not flammable, and it exhibits relatively low toxicity from the results of acute toxicity tests. Therefore, HFE-7000 with a filling ratio of 70% has been adopted for further tests related to the deployable Pulsating Heat Pipe.

3.2. Effect of the Orientation on Deployable Pulsating Heat Pipe

Due to the gravity pressure head and to the effect of the coils, the thermal performances of the deployable Pulsating Heat Pipe shall be affected by the mutual location of the condenser and the evaporator with respect to gravity. If in case of planar PHP horizontally tilted the gravity effect can be neglected, in case of the deployable PHP it cannot be neglected at all. In this paper, three different configurations have been selected in order

to understand the role of gravity in this kind of PHP. The configurations are named according to the deployable angles: $\theta_1 = 0$ deg, $\theta_2 = 90$ deg, and $\theta_3 = 180$ deg, as shown in Figure 7. The θ_3 angle represents the position closest to horizontal for the planar PHP, with only the coils remaining perpendicular to the horizontal plan.

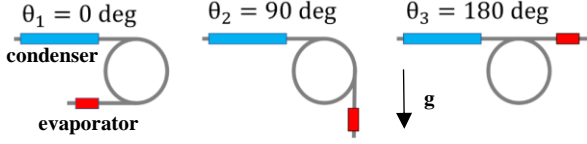


Figure 7. Different configurations of the deployable Pulsating Heat Pipe.

The deployable Pulsating Heat Pipe is filled with HFE-7000 with a filling ratio of 70% and heat input increasing from 20 W to 60 W (by steps of 20 W), as summarized in Table 2.

Table 2. Deployable PHP: experimental matrix and general behavior (see table 1 for acronyms)

θ [deg]	Q [W]	R [K/W]	behavior
0	20	1.85	SO
	40	1.99	SO
	60	-	HT
90	20	0.88	SO
	40	2.14	SAO
	60	-	HT
180	20	2.54	SAO
	40	2.35	SAO
	60	-	HT

As shown in Table 2, at 20 W, the performance deteriorates as the deployable angle increases from 0 to 180 deg. In each configuration, however, at 40 W the device works with stable oscillating operation, while at 60 W the evaporator section reached its maximum temperature and the test was stopped for every angle. Figure 8, 9 and 10 show the heat input (Q [W]) and temperatures (T [°C]) for the three different mutual positions of the evaporator and the condenser (0, 90 and 180 deg, respectively). At 0 deg (Fig. 8), the start-up is detected only 15 minutes after the first power input of 20 W.

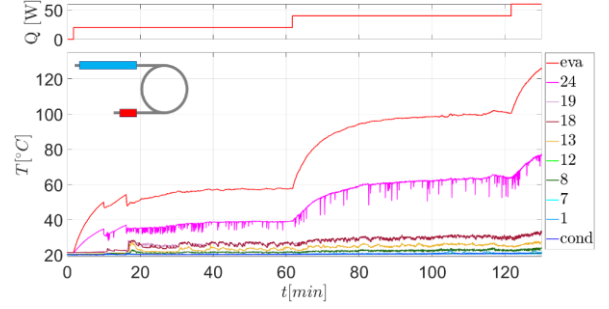


Figure 8. Temperature evolution over time in the deployable PHP with a deployable angle of $\theta_1 = 0$ deg (HFE7000, $FR = 70\%$).

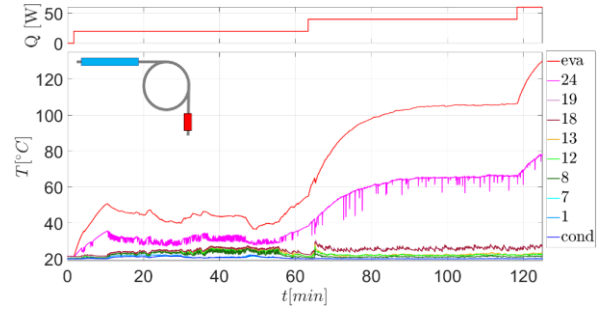


Figure 9. Temperature evolution over time in the deployable PHP with a deployable angle of $\theta_2 = 90$ deg (HFE7000, $FR = 70\%$).

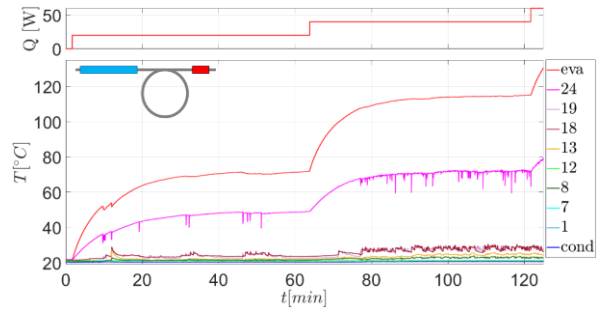


Figure 10. Temperature evolution over time in the deployable PHP with a deployable angle of $\theta_3 = 180$ deg (HFE7000, $FR = 70\%$).

As the PHP is deployed at $\theta_2 = 90$ deg (Fig. 9), although some oscillations start after 10 min from the power input of 20 W, a steady state condition has not been reached. Increasing the heat input from 20 to 40 W, the oscillations reach a stable regime with an average evaporator temperature of around 103 °C. On the other hand, the worst case is observed for $\theta_3 = 180$ deg. As shown in Figure 10, starts and stops are observed for low heat powers (20 W) and a stable operation is reached, but characterized by small amplitude oscillations (40 W).

4. Effect of coil-shaped on the thermal performance

To investigate the influence of the coil-shaped section on the performances of the deployable PHP, the results obtained from the planar PHP in horizontal position will be compared with those of the deployable PHP at $\theta_3 = 180$ deg. In this configuration, both evaporator and condenser are placed at the same quote respect to gravity. The evaporator mean temperature is, for the planar PHP, of 60 °C, 80 °C and 130 °C at 20, 40 and 60 W heat applied, respectively (Figure 4). Whereas in the case of deployable PHP, the thermal behavior is more unstable and, at 20 W, stopovers can be observed (Figure 10), but the evaporator temperatures are of approximately 70 °C (10° higher than the planar PHP). At 40 W, the deployable PHP shows a stable operation but with small oscillations and the evaporator average temperature grows up to 115 °C (35 °C more than the planar PHP). Lastly, at 60 W, the evaporator average temperature grows up to 140 °C and the test was stopped for safety reason.

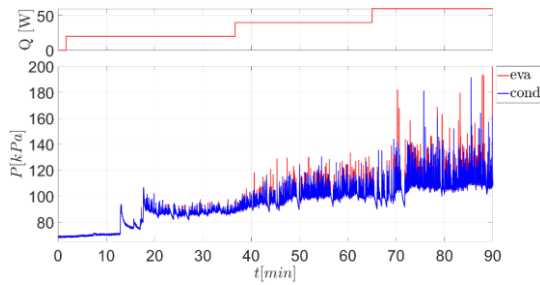


Figure 11. Temporal trends of the power input and the pressure at evaporator and condenser sections (planar PHP, HFE7000, $FR = 70\%$).

Additional information can be observed by comparing the pressures evolutions for both configurations. Figures 11 and 12 show the pressures evolution over time at different heat power steps, for the planar PHP, and the deployable PHP, respectively. In the case of planar PHP, as the heat power increases, the oscillations amplitude also increase, reaching an amplitude of 40 kPa and peaks of 100 kPa at 60 W. In the case of the deployable PHP, as shown in Figure 12, the oscillations are stable but with a lower amplitude of 15 kPa at the same power input (40 W). The portion of the coil of the adiabatic section operates in a sort of antigravity condition and the fluid oscillations are damped.

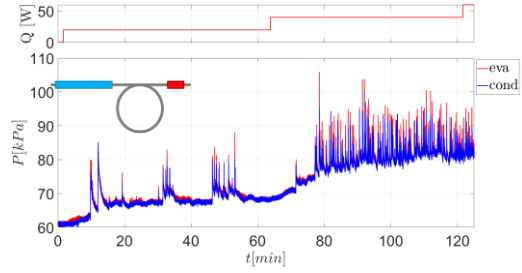


Figure 12. Temporal trends of the power input and the pressure at evaporator and condenser sections (deployable PHP, $\theta_3 = 180$ deg, HFE7000, $FR = 70\%$).

Lastly, Figures 13 and 14 show the pressures difference -between evaporator and condenser- evolution over time, for the planar and the deployable PHP, respectively. In the case of planar PHP the pressures differences between the evaporator and the condenser are of 18 kPa, 55 kPa, and 74 kPa at heat power inputs of 20 W, 40 W, and 60 W, respectively (Figure 13). In the case of deployable PHP, the pressures differences are lower than for the planar PHP, as shown in Figure 14. The pressures differences oscillations amplitudes are of 1-2 kPa for 20 W and of around 10 kPa for 40 W.

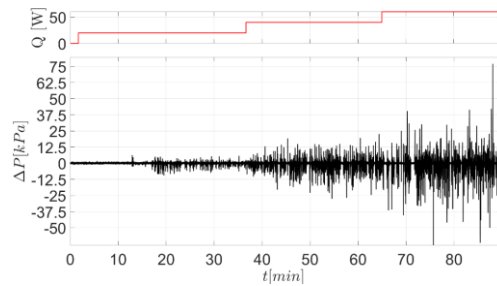


Figure 13. Temporal trends of the power input and pressures difference between evaporator and condenser sections (planar PHP, HFE7000, $FR = 70\%$).

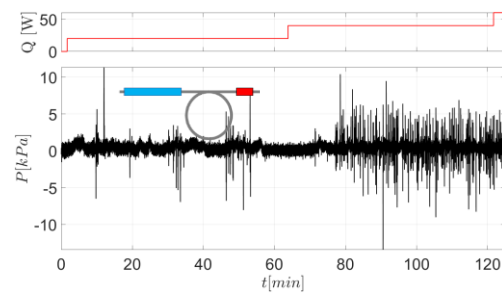


Figure 14. Temporal trends of the power input and pressures difference between evaporator and condenser sections (deployable PHP, $\theta_3 = 180$ deg, HFE7000, $FR = 70\%$).

Therefore, temperatures and pressures curves show that the deployable PHP operates with lower thermal performances than the planar one under identical operating conditions. A next step that would allow us to provide a real comparison of the effect of the deployable coil on the thermo-hydraulic behavior of both devices would be to perform tests under microgravity conditions (like during a parabolic flight campaign in a Zero-gravity plane), in order to avoid the gravity forces that have a huge influence on the pressure instabilities between evaporator and condenser zones.

5. Conclusions

This paper presents an experimental analyze on two twin Pulsating Heat Pipes with the same overall size but different adiabatic section shapes: a planar (with a straight pipe junction) and a deployable with a coiled shaped adiabatic junction. The planar PHP was tested in horizontal position at different heat input levels for different working fluids: FC72 (perfluorohexane), HFE7000 (hydrofluoroether), SF33 (hydrofluoroolefin), and N-Pentane.

On one hand, the best thermal behavior was obtained with HFE7000 as working fluid, showing the more stable oscillating operation with the lowest thermal resistances. On the other hand, the deployable PHP was tested with different deploying angles (0 deg, 90 deg and 180 deg) referring to different mutual positions of condenser and evaporator with respect to gravity orientation. The worst thermal performance was observed for a deployable angle of 180°, i.e. when the condenser and the evaporator are at the same quote and the coiled junction is located at a lower quote in a sort of antigravity orientation. In this case, a more unstable behavior and low amplitude oscillations operation was observed. The thermal resistance of the other two configurations of the deployable PHP are similar than for the planar PHP tested horizontally.

In conclusion, the coil-shaped adiabatic section seems to worsen the thermal performances of the heat transfer device as it increases the thermal resistance and decreases the pressures difference between evaporator and condenser during operation. The coil seems to damp the effect of the gravity force.

Finally, in order to really compare the effect of the coil junction for the devices tested under the same operating conditions, the gravity role should

be eliminated by providing tests in microgravity environment, during a parabolic flight campaign, for example.

Acknowledgments

The present work is carried forward in the framework of the ESA MAP Project entitled Two-phase passive thermal devices for deployable Space Systems (MAP Project number 4000128640). Thanks to the technicians of the University of Pisa, in particular of Energy, Systems, Territory and Construction Engineering, Davide Della Vista, and of the Civil and Industrial Engineering, Emanuele Del Gratta, Roberto Minelli, Dario Mondini, Andrea Di Basco and Gabriele Moretti, for their contribution.

References

- [1] G. Kiper and E. Söylemez, "Deployable space structures," in RAST 2009 - Proceedings of 4th International Conference on Recent Advances Space Technologies, 2009, pp. 131–138. doi: 10.1109/RAST.2009.5158183.
- [2] M. J. Clifford and D. Eastwood, "Design of a novel passive solar tracker," *Solar Energy*, vol. 77, no. 3, pp. 269–280, Sep. 2004, doi: 10.1016/j.solener.2004.06.009.
- [3] M. Mameli, G. Besagni, P. K. Bansal, and C. N. Markides, "Innovations in pulsating heat pipes: From origins to future perspectives," *Appl Therm Eng*, vol. 203, Feb. 2022, doi: 10.1016/j.applthermaleng.2021.117921.
- [4] J. Qu, X. Li, Y. Cui, and Q. Wang, "Design and experimental study on a hybrid flexible oscillating heat pipe," *Int J Heat Mass Transf*, vol. 107, pp. 640–645, 2017, doi: 10.1016/j.ijheatmasstransfer.2016.11.076.
- [5] E. Grossman and I. Gouzman, "Space environment effects on polymers in low earth orbit," in *Nuclear Instruments and Methods in Physics Research, Section B: Beam Interactions with Materials and Atoms*, Aug. 2003, vol. 208, no. 1–4, pp. 48–57. doi: 10.1016/S0168-583X(03)00640-2.
- [6] Brent A. Cullimore. "Heat transfer system having flexible deployable condenser tube". In: United States Patent 5,117,901 (June 1992)
- [7] Naoko Iwata et al. "Innovative Thermal Design Satellite with Networked Variable Conductance Oscillating Heat Pipes". In: *Heat Pipe Science and Technology, An International Journal* 8 (Jan. 2017). doi: 10.1615/HeatPipeSciTech.2017018788.
- [8] Naoko Iwata et al. "Thermal and Structural Performance of a Small Satellite with Networked Oscillating Heat Pipes". In: *Journal of Spacecraft and Rockets* 59.3 (2022), pp. 1016–1028. doi: 10.2514/1.A35242

- [9] Perna R., Mameli M.1, Bucchi F.2, Frendo F.2, Filippeschi S., Preliminary design of a self-deployable Pulsating Heat Pipe by means of a Shape Memory Alloy actuator, Joint 20th IHPC and 14th IHPS, Gelendzhik, Russia, September, 07-10, 2021
- [10] M. Arab, M. Soltanieh, and M. B. Shafii, "Experimental investigation of extra-long pulsating heat pipe application in solar water heaters," *Exp Therm Fluid Sci*, vol. 42, pp. 6–15, Oct. 2012, doi: 10.1016/j.expthermflusci.2012.03.006.
- [11] C. Czajkowski, A. I. Nowak, P. Błasiak, A. Ochman, and S. Pietrowicz, "Experimental study on a large scale pulsating heat pipe operating at high heat loads, different adiabatic lengths and various filling ratios of acetone, ethanol, and water," *Appl Therm Eng*, vol. 165, Jan. 2020, doi: 10.1016/j.applthermaleng.2019.114534.
- [12] W. T. Tsai, "Environmental risk assessment of hydrofluoroethers (HFEs)," *J Hazard Mater*, vol. 119, no. 1–3, pp. 69–78, Mar. 2005, doi: 10.1016/j.jhazmat.2004.12.018.

Heat-mass exchanger with equilibrium transfer of latent energy via heat pipes

Helen Skop^{1*}, Darrell Klammer¹, Dmytro Brega²

¹*Smart Heat Corporation, Skokie, IL, USA*

²*National Aerospace University "KhAI", Kharkiv, Ukraine*

**Corresponding author email address: hskop@yahoo.com*

Abstract

Improving the energy efficiency of industrial processes is seen as one of the key strategies for promoting decarbonization in the United States. One of the most efficient technologies presently employed in heat transfer applications is the heat pipe. However, in low-temperature, moist gas flows, where a significant portion of available energy is stored in the form of latent heat, conventional heat pipe solutions underutilize heat pipe heat transfer capacity. The authors consider the mechanism of energy transfer with a phase change in the presence of a non-condensable component and determine the optimal flow conditions required for stable transfer of latent energy on both sides of the heat pipe. Identifying optimal flow conditions is the key to the development of an efficient latent energy exchanger.

Keywords: Latent energy transfer; Low-temperature exhaust; Moist gas; Heat pipe; Heat and mass exchanger

1. Introduction

Improving the energy efficiency of industrial processes is seen as one of the key strategies for promoting industrial decarbonization across the United States [1]. The improvements will save quads of wasted energy which is released as exhaust gas into the environment by the industrial sector. The most appealing target is low temperature (i.e., <250°C) waste heat, which comprises 80% of total waste heat available for recovery and is characterized as thermally rich, due to the latent energy associated with its large water vapor content [2].

Conventional heat transfer technologies are primarily designed with sensible heat transfer in mind and are unable to effectively and efficiently recover energy from low-temperature moist exhausts. Nevertheless, improving the energy efficiency of industrial processes, for the purpose of decarbonizing the industrial sector, is considered to be of relatively low cost and acceptable complexity [3].

One of the most efficient heat transfer technologies presently employed in industrial applications is the heat pipe. The latent-to-latent energy transfer mechanism facilitated by the heat pipe capitalizes on the high heat transfer efficiency that is under-utilized in conventional latent-to-sensible heat pipe energy transfer systems. The rate of sensible heat transfer exhibits a linear dependence on the temperature of the heat transfer media involved, whereas the rate of latent heat transfer (through both condensation and evaporation) exhibits a non-linear, hyperbolic dependence on the temperature of the medium.

An innovative process, implementing a balanced latent-to-latent energy transfer mechanism facilitated by a heat pipe, could fully capitalize on the heat transfer efficiency potential of the design.

2. Phase change process application

2.1. Processes with wet exhausts

Wet exhausts are generated by a wide range of fired and unfired process applications implemented across the industrial spectrum from food processing (e.g., baking, heating, drying) to multiple manufacturing processes (e.g., ethanol production, chemical and cement manufacturing), exhausting quads of low temperature latent energy to the environment. Depending on the process origin, the mass fraction of water vapor in wet exhausts can range from 12 to 85%. Generally, the presence of water vapor in the exhaust stream is the result of evaporation during the specific industrial processes (e.g., baking or drying) or result of chemical reaction (e.g., hydrocarbon oxidation or fossil fuel combustion).

For many of these processes, wet products require pre-process treatment to promote product moisture stability. This is often achieved through exposure to controlled environmental conditions. One of the most common industrial methods for maintaining a humid pre-processing environment is direct steam injection. The pre-process of direct steam injection requires fuel consumption for the purpose of steam generation in supplement to that already consumed by the primary industrial process.

There are many industrial processes where heat and water in generated exhausts can be converted

into useful input of heat and water for neighbouring processes that otherwise require supplemental fuel and water sources. For example, water vapor in furnace exhaust from a heating, ventilation and air conditioning system could provide humidification to indoor air. In the case of industrial baking, heat and water from oven exhaust could serve as inputs for conditioning dough proofers or be used in sanitation processes.

2.2. Bakery waste heat and water recovery

Wholesale bread baking is one of the major energy consumers across the food processing industry. The total energy required to bake one pound of bread is approximately 530 British thermal units (Btu), consumed throughout oven startup, heating during the baking process, moisture evaporation from the dough, starch gelatinization, pan heating, wall insulation loss, stack gas losses, and baked product.

The adjacent industrial process best suited for reclamation of heat and water vapor recovered from the baking process exhaust is the dough proofer. Conventionally, a wholesale bread bakery would achieve a wet and warm environment (40 °C at 85% relative humidity [RH]) in the proofer by producing steam in a boiler, fired using supplemental fuel, and electrically heating make-up air consuming supplemental electricity.

The idea of using the bakery oven waste heat for dough proofer air preheating has existed for more than two decades. One of the first successful cases was an installation of a heat recovery system at an industrial bread bakery [4] to provide heat to preheat the proofing air. The payback period associated with this application was 3.5 years. The relatively long

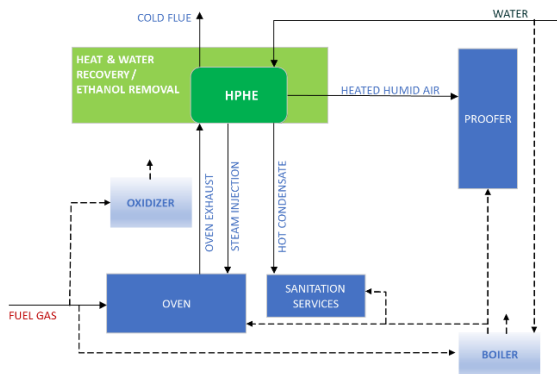


Figure 1. Diagram of a heat and water recovery system for an industrial bakery; flows in the recovery and existing system are depicted by solid and dashed lines, respectively.

payback period was related to the heat transfer mechanism utilized by the system: the exhaust stream was cooled to a level above the dew point temperature, resulting in recovery from the stack gas of only sensible heat. Recovery of sensible heat above the dewpoint temperature meant that less than 20% of available heat was extracted from the stack gas [5].

There is a more efficient way to recover and reuse a larger portion of otherwise exhausted waste heat: condensation of the oven exhaust vapor component, and transfer of the extracted latent heat for humidification and heating of dough proofer air. This process would reduce supplemental fuel consumption by derating or eliminating boiler services and provide a heated and humid environment for dough proofing without generating additional waste heat and pollutant emissions associated with fuel combustion.

In a recovery system like that presented in Figure 1, energy is transferred between similar processes where partial phase changes (condensing and evaporation of the vapor component) occur. These processes are well-balanced by keeping the quality of heat source and heat sink at the same level.

2.3. Latent energy transition: Heat pipes

To balance released and absorbed latent energy, it is necessary to use similar latent energy transfer mechanisms (i.e., phase change). Such mechanisms occur in heat pipes (thermosiphons), which are regarded as the most effective heat transfer elements.

2.1. Latent energy transfer through heat pipes

Heat pipes were used to intensify the process of heat recovery for the bakery in the system mentioned in [4]: the latent heat transfer capacity of heat pipes was used for sensible heat transfer between heat source and sink. In a separate

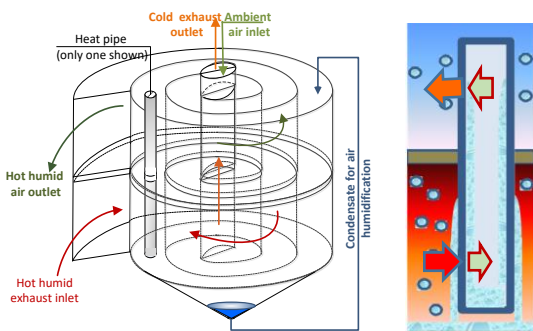


Figure 2. HPHE conceptual design (left) and latent heat transfer diagram for a single heat pipe (right).

industrial application, a power plant condenser utilized heat pipes to transfer the latent heat from steam condensation [6]; however, the heat pipes were again used for sensible heat transfer to air heating, under-utilizing heat pipe heat transfer capacity.

A Heat Pipe Heat Exchanger (HPHE) concept illustrated in Figure 2 assumes the similarity of the phase change processes outside and inside the heat pipes to create optimal conditions for stable balancing of the energy transferred between these processes.

3. Latent energy balance around the heat pipe

The conventional approach for many heat and mass exchange technologies implemented in a range of commercial and industrial applications is based on the established paradigm of kinetic theory, which does not adequately explain the phase-change energy (PCE) conversion balance between exchanging media. Maintaining conversion balance enables maximally efficient and stable heat recovery from wet flows during PCE transfer. Conversion imbalance is the reason that state-of-the-art equipment reaches energy transfer saturation when handling wet flows, resulting in recovery of only a small fraction of the total available heat.

3.1. Latent energy versus temperature

Latent heat (Q_{lat}) content of a saturated air-vapor mixture can be defined by the latent heat of vaporization of water (L_v) and mass flow of vapor (m_v):

$$Q_{lat} = L_v m_v \text{ [J/s]} \quad (1)$$

Based on Ideal Gas Law, the humidity ratio of an air-vapor mixture, where mass flow of dry air is m_d , can be expressed in terms of the ratio of dry air and water vapor gas constant (ε [0.622]), saturation vapor pressure (p_{vs}), and total vapor pressure (p_{tot}):

$$\frac{m_v}{m_d} = \varepsilon \frac{p_{vs}}{(p_{tot} - p_{vs})} \text{ [kg/kg]} \quad (2)$$

According to the equation of Clausius-Clapeyron, the saturation vapor pressure ratio between two cross sections (s1 and s2) along the flow is exponentially proportional to the temperature (T) in those sections, and the ratio of the latent heat of vaporization and the water vapor gas constant (R_v):

$$\frac{p_{vs_{s1}}}{p_{vs_{s2}}} = \exp\left(\left(\frac{L_v}{R_v}\right)\left(\frac{1}{T_{s2}} - \frac{1}{T_{s1}}\right)\right) \text{ [-]} \quad (3)$$

From equations (1) and (2), the latent heat content can be rewritten as follows:

$$Q_{lat} = L_v m_d \varepsilon \frac{p_{vs}}{(p_{tot} - p_{vs})} \text{ [J/s]} \quad (4)$$

Thus, latent energy transfer depends primarily on the change in saturated vapor pressure, which exhibits a hyperbolic relationship with temperature (Figure 3).

3.2. Minimal temperature difference

The hyperbolic dependence of the latent heat contained in a vapor-saturated mixture on temperature is depicted in Figure 3. Figure 3 also shows the processes of the phase transformation of energy occurring around the evaporating and condensing zone of a heat pipe spanning the hot and cold channels of the HPHE. The red curve corresponds to the condensation process in the hot channel and the green curve corresponds to the evaporation process in the cold channel. The shift of the process curves expresses the gap between the released heat of condensations and the absorbed heat of evaporation, and depends on the temperature difference between the hot and cold flows.

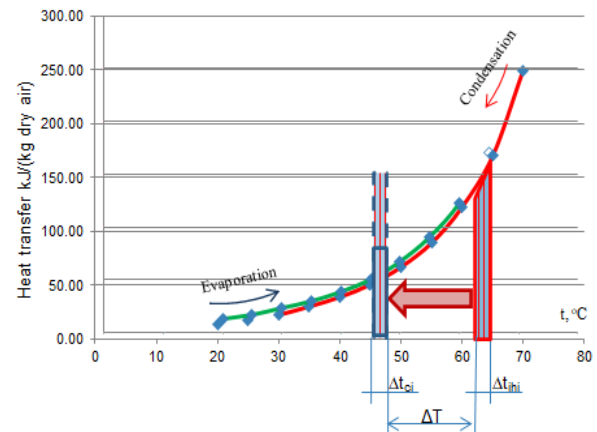


Figure 3. Dependence of latent heat content on the temperature for the saturated air and vapor mixture: latent heat transfer is depicted by the red arrow; condensation and evaporation processes are shown by the red and green curves, respectively; and ΔT represents the temperature difference between the hot and cold flows.

Thus, to ensure that phase transformation processes occur along the heat pipe in both the hot and cold channels, the temperature difference between the flows must be as small as possible so that the latent heat at these flow temperatures differs by no more than the heat transfer losses. Additionally, the temperature difference must be sufficient to ensure heat exchange. To satisfy the conditions for stable provision of saturated conditions, the temperature difference should be minimal and constant along the length of the channels.

Since heat transfer through a heat pipe occurs through phase transformation processes, unlike other heat transfer devices, it can transfer heat intensively at small (e.g., 3 to 5 °C) temperature differences. The use of a heat pipe for transferring heat between phase transformation processes makes it possible to achieve a heat balance with a stable low temperature difference.

To ensure a given temperature difference along the entire length of the channel while allowing for possible changes in incoming flows, the change in the temperature of the flow should be linearly dependent on the length of the channel (see Figure 4). In this case, the dependence of heat transfer rate on temperature is similar to the dependence on length, and the shift of the heat line on length will also be constant along the length of the channel.

3.3. Heat distribution in array of heat pipes

Figure 4 illustrates the computational results of the condensation and evaporation processes for spiral channels in accordance with the HPHE design. The temperature in both channels varies linearly with the channel rotation angle and provides the same temperature difference of 5°C along the entire channel length. With such a stable and small temperature difference, the total (latent and sensible) heat released from the hot stream and

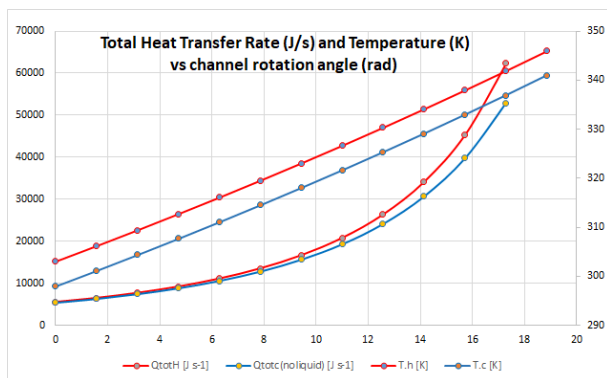


Figure 4. Distribution of temperature and total heat transfer along hot (red line) and cold (blue line) channels of the HPHE.

consumed by the cold stream differs by 5%, which is lost in the heat transfer process. Since the transferred heat decreases along the channel length, the number of pipes and channel width should be reduced proportionally to maintain a uniform distribution of the heat load among the heat pipes along the channel. The HPHE spiral design allows narrowing of the hot flow channel width and a similar widening for the cold flow channel, with the number of heat pipes in both the hot and cold channels increasing or decreasing accordingly. This design compactly and evenly distributes the heat transfer surface throughout the HPHE channels.

3.4. Heat pipe efficiency limits

The efficiency of the developed HPHE mainly depends on the efficiency of the heat pipes. A number of limitations including flow viscosity, acoustic instabilities, capillary forces, surface roughness, and boiling may affect the efficiency of a heat pipe. To estimate the maximum thermal power of pipes employed in the HPHE design concept, the authors used the results [7] where a heat pipe was studied at the similar operating conditions and design parameters: pipe diameter of 0.01 m, height of 2 m, water fill, 90° inclination. Based on the findings of [7], at the rate of possible dew point temperature for the considered application (below 85 °C), heat pipe thermal capacity is mainly regulated by the entrainment limit. Since the model in [7] utilizes less intense air-to air heat transfer, the latent-latent mechanism in the HPHE is expected to achieve a heat pipe capacity of 400-1000 watts (W).

The intense transfer of latent energy through the heat pipe can be limited by thermal resistance of the condensate film formed on the outside of the pipe wall. Researchers are trying to overcome this limit by replacing film condensation with droplet condensation using some hydrophobic materials, which are expensive and lead to further process limitations. More promising technical solution [8] is to use a hydrophobic-hydrophilic ridged surface, which is not technologically matured enough to be cost-effectively and efficiently employed for heat pipe housings.

A more realistic solution for controlling the film resistance can be determined by considering the balance between the film formation rate, which depends on the rate of change in the partial pressure of saturated vapor in the mixture flowing around the heat pipe, and the film flow rate, which mainly depends on the wettability of the pipe material and gravity. A certain balance will allow for

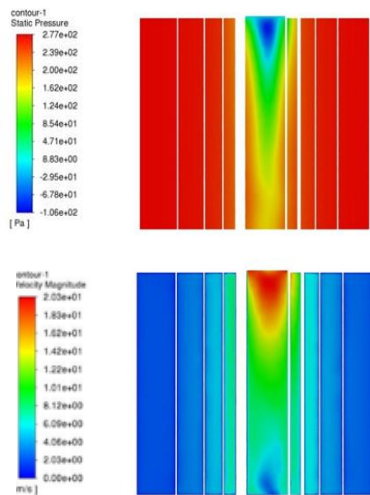


Figure 5. Example of the CFD model of static pressure (Pa) and velocity (m/s) distribution in the hot channel (vertical cross cut).

determination of the maximum allowable height of the pipe (and channel wall) to ensure the allowable film thickness. Uniform distribution of the heat load between the heat pipes in the bundle, does not allow for a thickness greater than the average distribution of condensate in the heat exchanger.

The transfer of heat through a heat pipe in a channel of variable cross section (e.g., that considered for the HPHE) can be affected by changing aerodynamic parameters of the flow (pressure and velocity). To control the influence of these parameters and take them into account in the design of the heat exchanger, an initial CFD model of the process was created. Gradients of pressure and velocity were obtained for a hot flow with a mass of 0.444 kg/s, a mass content of steam of 0.25%, and an inlet temperature of 73 °C (dew point). The resulting distributions of pressure and velocity in the hot channel (Figure 5) showed changes within the limits that do not have a significant effect on heat transfer.

4. Conclusions

In many commercial and industrial processes, low temperature, wet exhausts that would typically be released into the environment can be converted into useful input for neighboring applications and services that would otherwise require additional energy and water sources. For example, the HPHE concept was evaluated for the recovery of heat and water from a bakery oven exhaust: it was determined that the HPHE would be capable of adequately conditioning the hot, humid environment required for dough proofer operation, while derating additional boiler services, and eliminating the additional waste heat and

greenhouse gas and combustion emissions that would be associated with supplemental fuel combustion.

The HPHE concept employs similarity between the phase change processes outside and inside the heat pipes to create optimal conditions for stable balancing of the energy transfer.

To provide a heat transfer balance between PCE processes, the temperature difference between the flows must be as small as possible. To ensure a minimum temperature difference along the entire length of the channel while allowing for possible changes in incoming flows, the change in the temperature of the flow should be linearly dependent on the length of the channel.

Heat transfer surface and channel cross section should be reduced proportionally along the length of the channel to ensure uniform distribution of the heat load.

The condensate film thermal resistance can be controlled by accounting the balance between the film formation rate, which depends on the rate of change in the partial pressure of saturated vapor in the mixture flowing around the heat pipe, and the film flow rate, which mainly depends on the wettability of the pipe material and gravity.

5. Acknowledgement

The authors are grateful to the U.S. National Science Foundation (NSF) for their generous support. This material is based upon work supported by the NSF under Award No. 2124735.

References

- [1] U.S. Department of Energy, U.S. industrial decarbonization roadmap, DOE/EE-2635, United States Government, 2022.
- [2] S. Nimbalkar and A.Thekdi, Industrial waste heat recovery - potential applications. Available Technologies and Crosscutting R&D Opportunities, 2015. doi:10.2172/1185778.
- [3] U.S. Department of Energy, U.S. Department of Energy will fund applied research and development to accelerate decarbonization of American industry, United States Government, 2022.
- [4] E. Masanet, P. Therkelsen, and E. Worrell, Energy efficiency improvement and cost saving opportunities for the baking industry: an Energy Star guide for plant and energy managers, United States Government, 2012. doi:10.2172/1172002.
- [5] H. Skop, J. Pezzuto, and V. Oleynikov-White, Critical aspects of efficient waste heat

recovery from low-temperature wet industrial exhaust. in ASME Summer Heat Transfer Conference. 2013. Minneapolis, United States.

[6] H. Zhang, J. Ranasinghe, D. Wesley Ball Jr, Condenser for a combined cycle power plant, United States patent application US20100024424A1, 2010.

[7] HM. Lee, H-Y. Li, A mathematical model for estimation of the maximum heat transfer capacity of tubular heat pipes. in International Conference on Applied Energy – ICAE. 2017. Cardiff, United Kingdom.

[8] Z. Song, M. Lu, and X. Chen, Investigation of dropwise condensation heat transfer on laser-ablated superhydrophobic/hydrophilic hybrid copper surfaces. American Chemical Society (ACS) Omega, 2020. doi: 10.1021/acsoimega.0c01995.

Heat Loop Pipe for Thermal Management of Powerful LED-based Applications

Donatas Mishkinis^{1*}, Igor Ušakovs¹, Luka Ivanovskis¹ and Ilya A. Galkin²

¹ Allatherm SIA, Riga, Latvia

² Riga Technical University, Riga, Latvia

*Corresponding author email address: Donatas.Mishkinis@allatherm.com

Abstract

Novel concept of Heat Loop Pipe (HLP) is proposed. HLP design combines positive features of classical Heat Pipes: very simple geometrical layout, quick to design & assembly, easy-to-fit into a modern cooling system; and classical Heat Loops (also known as Loop Heat Pipes, Capillary Pumped Loops, Capillary Driven Loops, etc.): proper operation for any orientation in gravity field, long distance heat transfer (up to 10m or even more), capability to manage high powers (kWatts) & high heat flux densities (more than 150W/cm²). Such design is possible due to very efficient thermal insulation (vacuum gap) between vapor (external tube) and liquid (internal tube) lines. It also allows to allocate the transport zone of the HLP in hot environment without a risk of dry out. The use of HLPs can be especially advantageous for thermal management of powerful LED-based lightening devices, such as operation lamps, headlights, searchlights, spotlights, etc. In such applications the concentrated high-power illumination source is very desirable to emit a direct beam of light with lowest distortions and highest energy efficiency. A prototype HLP was manufactured and tested at Allatherm as a cooling system for a new surgical lamp. The HLP was charged by 20g of n-butane and capable efficiently transfer and dissipate more than 60W (corresponding heat flux density on evaporator surface is 15W/cm²), keeping the LEDs inside of specified temperature limits.

Keywords: Heat pipe, Advanced heat transfer, LED thermal management, Heat loop, Heat loop pipe

1. Introduction

Powerful LED-based lightening devices, such as operation surgical lamps, headlights, searchlights, spotlights, etc. require advanced thermal management systems. In such applications the concentrated high-power illumination source is very desirable to emit a direct beam of light with little distortions. Current heat flux densities of power LEDs are very high and can reach up 150-180W/cm² for a single unit, considering recommended solder pads for different configurations [1]. Consequently, it is rather difficult to integrate several LED units in small area/volume due to high heat fluxes issue. Currently, designers are distributing the LEDs over large surfaces and making special systems of multi-lenses and reflectors trying to unite the multiple beams together (Figure 1). Finally, it leads to the problems with optical & energy efficiency and quality of the beam.



Figure 1. Example of modern powerful multi-LED-based spotlight (a) and flashlight (b).

Other important LED technology application is surgical lights which should be designed for optimum light intensity, along with offering diverse color temperatures. Configuration with numerous LEDs of different color with advanced energy control is usually used for this purpose. Modern LED-based operation surgery lights are very advanced and efficient, but they are bulky, occupy large volume of the operating rooms and not easy in maneuvering and positioning [2] (see Figure 2). One of the main reasons is impossibility to allocate and distribute multiple different multi-color LEDs in the best manner due to thermal problem.



Figure 2. Example of a typical modern LED-based lights for operating rooms.

Heat Pipes (HP) and Heat Loops (HL), also known as Loop Heat Pipes, Capillary Pumped Loops, Capillary Driven Loops, etc. are good candidates to manage this LED high heat flux issue. However, classical HP operation is limited by the distance

between a heat sink and source, and they are not efficient at all if the heat source is placed above the heat sink. Heat Loop can have complex external routing of the vapor and liquid transport lines. It often leads to difficulties with allocation and fixation of the HL evaporator to a heat source. Also, a special support structure for the condenser is necessary. Proposed HLP design is particularly effective for a spotlight source when LEDs need to be placed in a limited area around the focus of the lamp.

2. Heat Loop Pipe Concept

To overcome performance limitations of HP technology and design assembly and integration problems associated with HL technology the novel thermal architecture: Heat Loop Pipe (HLP) is proposed.

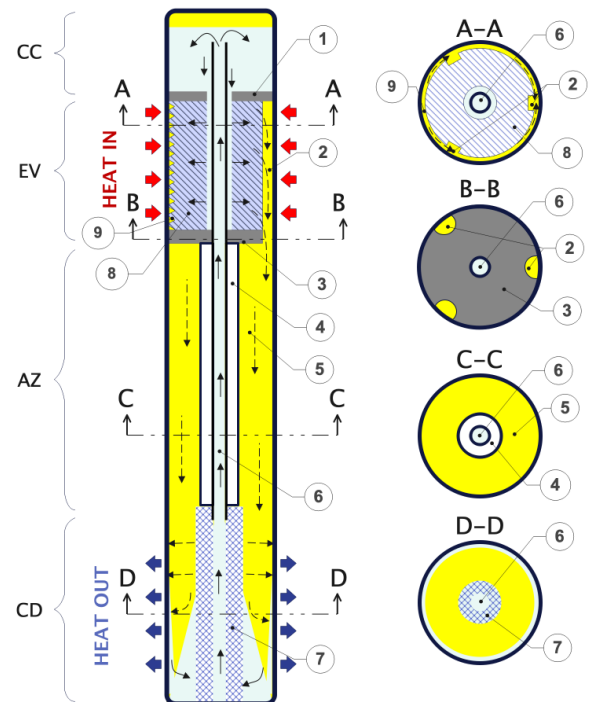


Figure 3. Heat Loop Pipe Conceptual Design. CC – Compensation Chamber; EV – Evaporator; AZ – Adiabatic Transport Zone; CD – Condenser; 1 – Sealing between wick and CC; 2 – Longitudinal vapor removing channels; 3 – Sealing between wick and transport zone; 4 – Thermal insulation layer (vacuum gap); 5 – Vapor transport channel; 6 – Liquid transport channel; 7 – Permeable (screen mesh) central channel in CD; 8 – Capillary wick; 9 – Circumferential vapor collecting channels; A-A, B-B, C-C, D-D – cross-sectional views

HLP combines positive features of classical HP: simple geometrical layout which provides possibility of its easy design, assembly, and integration; and classical HL: good operation against gravity, long distance heat transfer (more than 10m), capability to manage high powers (kilo Watts) & high heat flux densities (more than $150\text{W}/\text{cm}^2$). HLP schematic is shown in Figure 3.

HLP design is possible due to very efficient thermal insulation 4 (vacuum gap) between vapor transport channel 5 (external tube) and liquid transport channel 6 (internal tube). It also allows to allocate the transport zone of the HLP in hot environment without a risk of device dry out.

3. Heat Loop Pipe Prototype

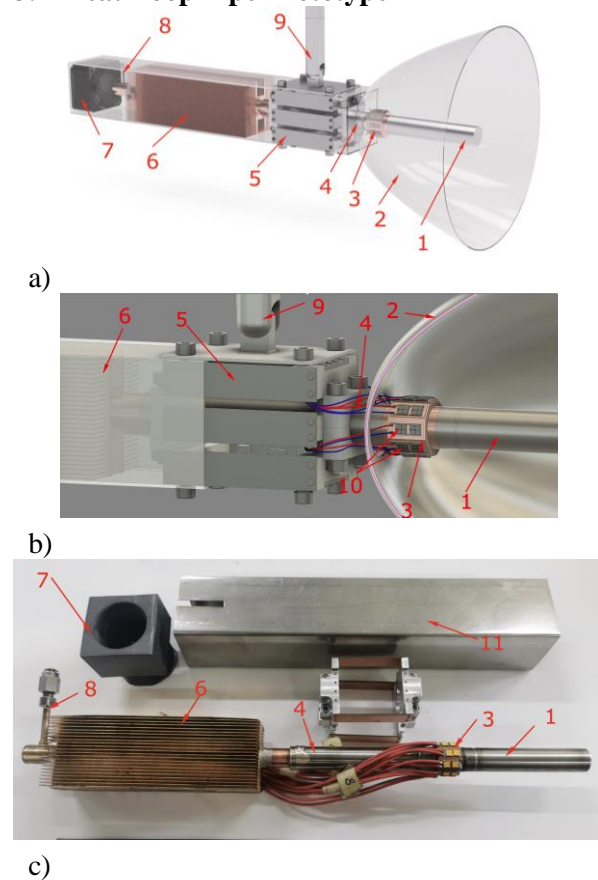


Figure 4. Design of HLP light. a) HLP design; b) Detailed view of EV; c) Photo of manufactured HLP without drivers & Reflector. 1 – CC and Handle for positioning; 2 – Parabolic Reflector; 3 – EV; 4 – Adiabatic Transport Zone; 5 – PCB drivers for LEDs; 6 – Air cooled finned CD; 7 – Fan; 8 – Charging Port; 9 – Support articulating arm 10 – multiple LEDs (18 units in total); 11 – Condenser envelope/ air duct.

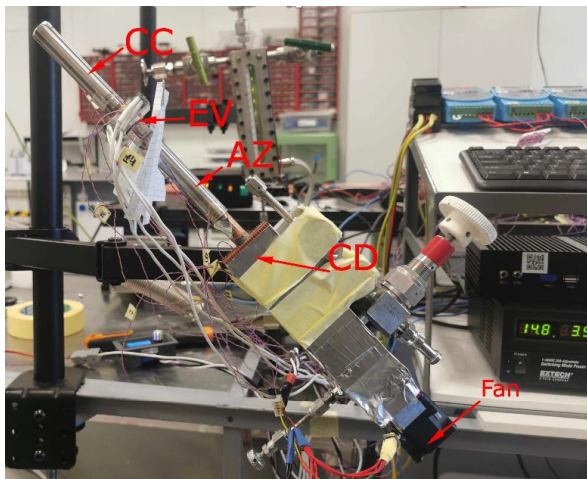
The HLP design was adapted for further use in the advanced surgical lamp. The prototype of HLP was manufactured and tested with an electrical

heater block as a heat source and as a part of the surgical lamp prototype. The HLP prototype has vacuum insulation between transport lines and large stainless steel compensation chamber attached to the copper evaporator. The evaporator external surface was shaped to facilitate mounting of eighteen LEDs (Luxeon LMZ9-QW27). The design of the surgical light prototype with integrated HLP is shown in Figure 4.

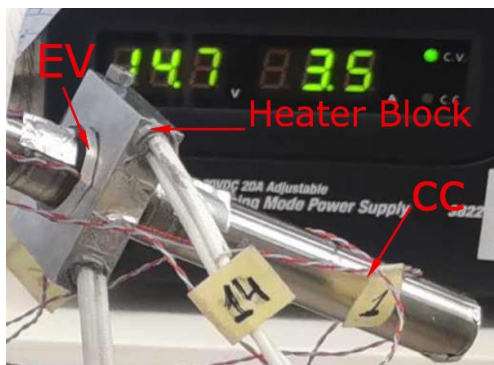
The overall length of the prototype is 350 mm, outer diameter of the main tubing 15 mm, evaporator-condenser shortest distance more than 100 mm. The assembled prototype (with LEDs, fan, copper finned air heat exchanger and reflector) weighs below 1,2 kg.

4. HLP testing

First set of tests was conducted with heater (two 40W 6mm OD cartridges installed in aluminum block) as LED power simulator. Test setup is shown in Figure 5.



a)



b)

Figure 5. Photo of HLP Test setup: general view (a) and EV area with the heater block and thermocouples (b).

Testing was performed for different orientations in gravity field (no significant impact on HLP performance was observed) and for different power steps (see Figure 6.)

The HLP was charged by 20g of n-butane and was found capable to efficiently transfer and dissipate more than 60W (corresponding heat flux density on evaporator surface is $15\text{W}/\text{cm}^2$), keeping (future installed) LEDs within the specified temperature limits (60°C).

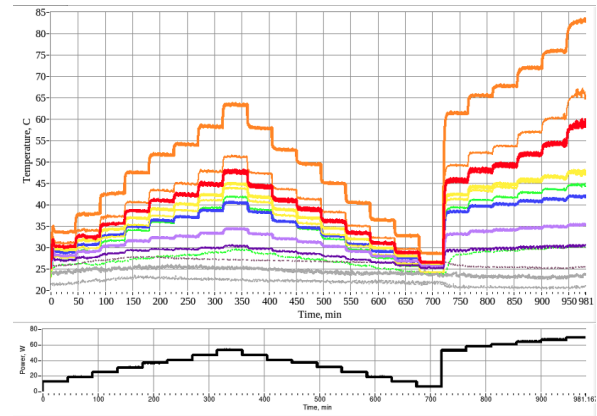


Figure 6. Test results of HLP with heater block: temperature evolution with time for different power steps. Color code for Temperatures on the graph: Orange – Heater block; Red – Evaporator; Yellow – Adiabatic zone (Vapor); Green – Compensation Chamber; Blue – Condenser end, close to charging port (Liquid); Purple – Fins of the Condenser; Grey – Ambient air.

5. Surgical lamp development

The implementation of efficient HLP cooling eliminates the need for distributed light sources and allows the use of spotlights. Considering that for a surgical lamp it is also necessary to ensure the absence of shadows, the necessary functionality and illumination can be realized by an ensemble of only three lamps similar to the one shown in the Figure 4.

It should be mentioned, that HLP thermal architecture allows to take the heat sink completely out of the operation room (with sufficiently long and flexible transport lines), thus reducing the weight and dimensions of the lighting and decreasing demand for operation room ventilation.

The light part of the lamp was implemented as follows. 18 LEDs (9 sets of two) were soldered onto flat faces of HLP evaporator made for this purpose with prismatic shape. Each LED had 560 lm minimal flux at 2800 mA (and 600 lm typical, according to manufacturer data). The thermal interface contact surface was of $4\times 4\text{ mm}^2$ per LED.

A 3D printed reflector covered with an aluminized polyimide tape was installed with a set screw to vary axial position of reflector. At first a simple aluminum tape was used, but its reflectivity fell below expectations both because of low portion of reflected light and rather diffusive reflection. Changing to the highly reflective polyimide tape raised illuminance in the center by at least 1.5 times.

The design of the reflector was driven by requirements for surgical lighting as specified in IEC standard [3], namely:

- central illuminance (at 1 m distance from the device) $40 \text{ klx} \leq E_c \leq 160 \text{ klx}$
- light field diameter d_{10} (where $E > 0.1E_c$) to be no more than twice the d_{50} diameter (where $E > 0.5E_c$)

In other words, the luminaire has to provide a rather high flux density within the light spot and quickly diminish outside of it, to prevent side glares. The following heuristic was used: a parabolic reflector was formed by offsetting the generating parabola off rotation axis, so that its own axis goes through the LEDs annulus. The size and slope of the reflector was chosen to fit the available 3D printing volume and block light from escaping reflector sideways. As an auxiliary tool a piece of ray tracing software was written to visualize beam paths, see Figure 7. The Monte Carlo simulation randomly sampled rays coming from a single LED according to their distribution pattern (as a Lambertian source). The resulting reflector dimensions were $\text{Ø}200 \text{ mm} \times 190 \text{ mm}$ (extra 30 mm cylindrical section provided additional side shielding).

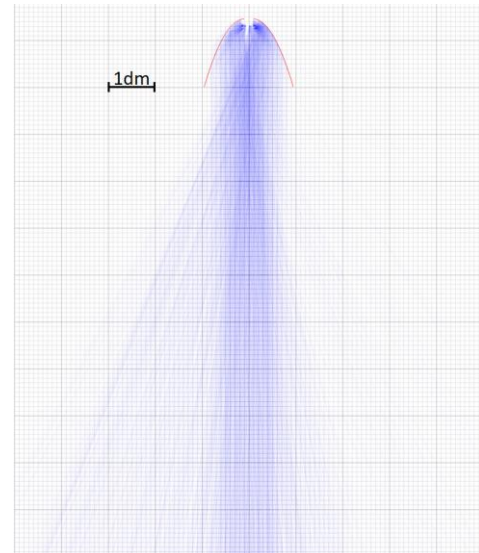


Figure 7. Parabolic reflector in action and ray tracing example (rays falling within $\pm 50 \text{ mm}$ from the section plane are shown). Ray distribution asymmetry is due to uneven LED pattern (9 directions).

Illuminance values were measured in four perpendicular directions at intervals of 0.1 m from the light field center. Light field diameters d_{10} and d_{50} were found by finding luxmeter locations with respective illuminance value (in four respective perpendicular directions, then averaged, like in Figure 8).

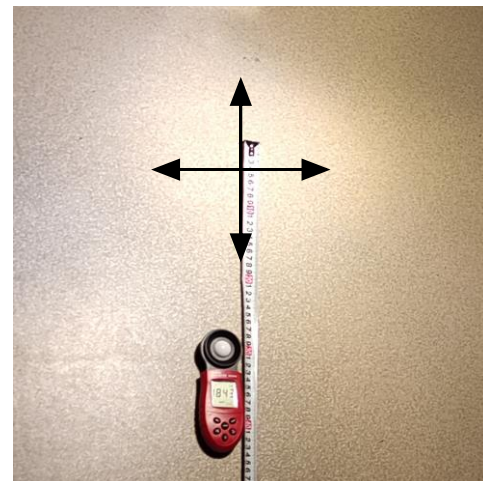


Figure 8. Luxmeter next to measuring tape in the light field, directions of luxmeter displacement indicated.

The LED power was set at 80W (at 1.3A). At this current, the expected total emitted flux $I_{th} = 5000 \text{ lm}$ (manufacturer data), while measured illuminance (see Figure 9), when integrated over illuminated area yields $I_{meas} = 3450 \text{ lm}$. Thus, the efficiency of the optical part of the assembly is close to 70% and there is still room for

improvement. The same is true for illuminance distribution quality: $\frac{d_{50}}{d_{10}} = \frac{0.33\text{m}}{0.80\text{m}} = 0.41$, although in one direction it reached 0.47, which is close to the required 0.5.

As for the central illuminance, $E_c = 18 \text{ klx}$ was reached, so an assembly of three or more light heads (that are necessary for shadow dilution) will be capable to provide the necessary light flux density.

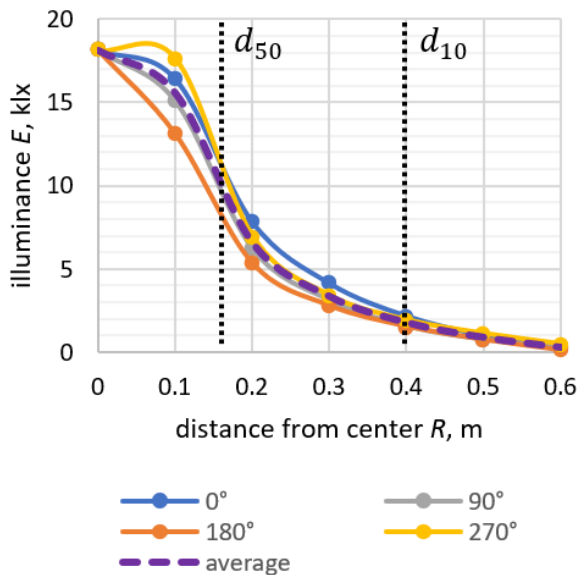


Figure 9. Illuminance distribution w.r.t. light field center (1 m distance from reflector), measured along four perpendicular radii.

6. HLP testing with LEDs

The surgical light prototype (assembly of HLP with LEDs, reflector and finned radiator with Ø38 mm DC fan) was tested at different electric power levels and orientations, see Figure 10 for location of thermocouples.

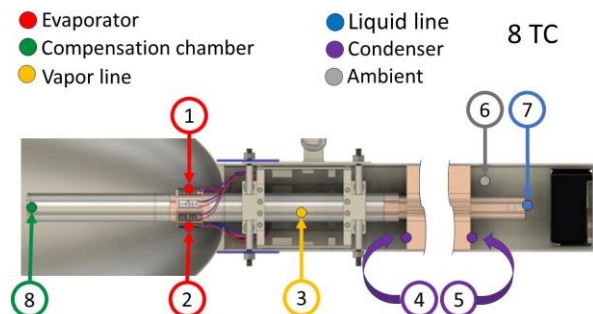


Figure 10. Location of thermocouples on HLP light: 1,2 – evaporator, 3 – vapor line, 4,5 – condenser, 6 – ambient, 7 – liquid line, 8 – compensation chamber.

Power was applied to LEDs in steps from 15W up to 88W with HLP in vertical orientation (EV in the bottom, as in normal operation mode). The measured temperature profiles over time are shown in Figure 11. No hysteresis was observed when power was changed.

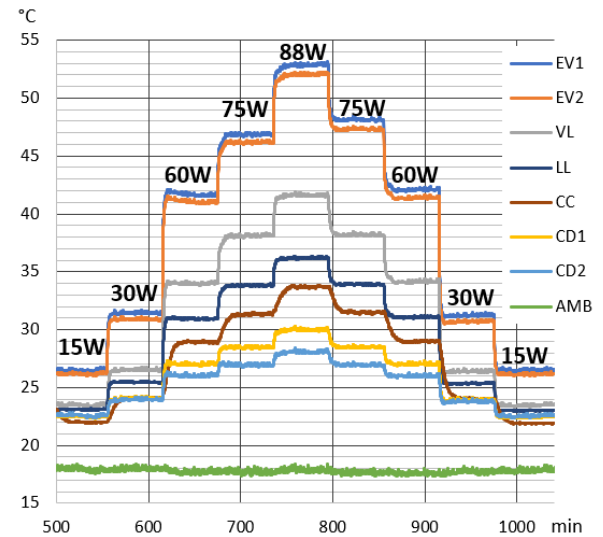


Figure 11. Temperature on HLP elements with LED power ramping up and down in steps. HLP vertical (+90°, EV at the bottom).

In orientation testing, the HLP orientation varied in 45° steps from -90° (EV below CD) to +90° (EV above CD) and back to -90°, see Figure 12.

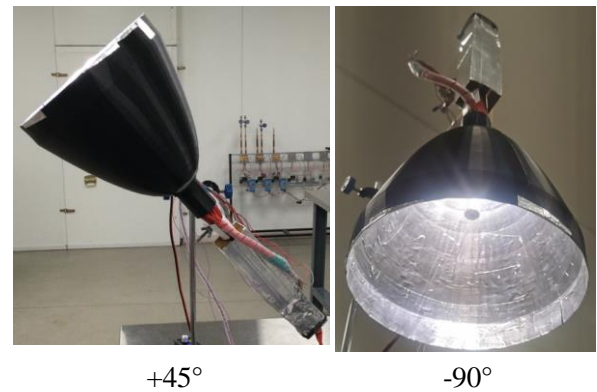


Figure 12. Exemplary HLP orientations, positive angle assumed for EV above the CD.

LED power was set at 75W and 60W, which corresponds to 52W and 43W heat power Q (at 70% heat dissipation ratio). The temperature plot is given in Figure 13.

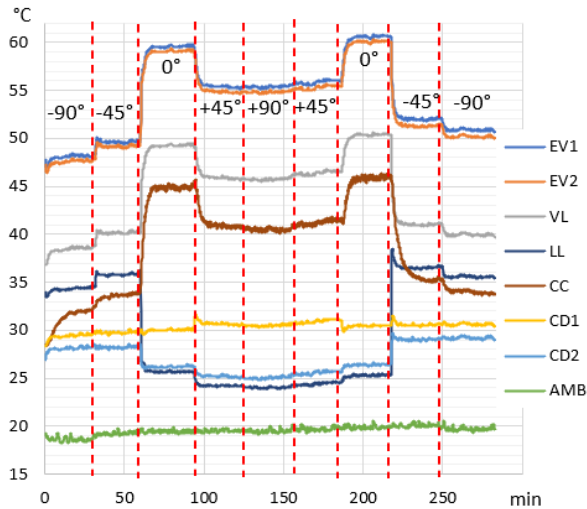


Figure 13. Temperature measurement points and temperature profile at various orientations (75W LED power).

The overall thermal resistance R_o (HLP + air cooled CD) is calculated with respect to the air ambient temperature:

$$R_o = (T_{EV} - T_{AMB})/Q \quad (1)$$

The estimated R_o values are plot in Figure 14. The thermal resistance changes no more than 30%, with worst orientation being the horizontal one. Gravity-positive and gravity-negative orientations differ by no more than 20%.

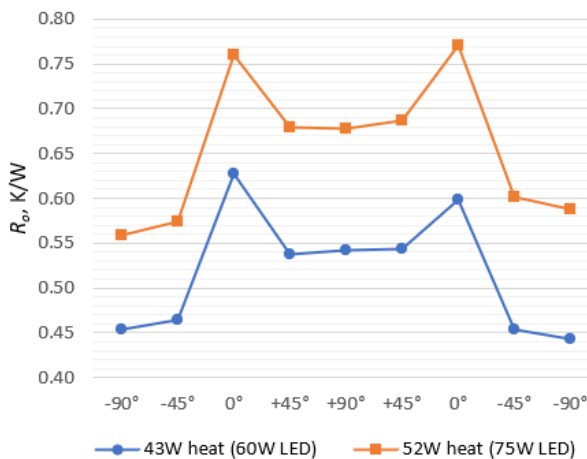


Figure 14. Total (HLP+radiator) thermal resistance dependence on orientation.

7. Conclusions

HLP is a novel capillary pumped heat transfer device which combine the features of HP and HL.

Coaxial location of vapor and liquid lines in HLP inside of the common envelope, on the one hand, provides robustness and compactness of a conventional HP by mimicking its layout. On the other hand, it introduces the elements of a more

effective LHP – separated transport lines and local capillary pump. Vacuum insulation is a technological mean to make such a coaxial arrangement working.

The concept of HLP allows to provide efficient thermal management of a light source placed into the focus of the lamp reflector. It gives possibility to develop simple and efficient (optically and thermally) LED-based high-power lamp.

Special interest is the application of HLP for thermal management for surgical lighting.

The prototype of the light source for surgery lamp with HLP thermal management was successfully designed, manufactured and tested. Test results demonstrate proper and stable HLP LED lamp operation for different powers (from 15 to 88W) and at any orientation in the gravity field.

8. Acknowledgements

This publication/thesis/paper/report is supported by the European Regional Development Fund in the frame of the contract 1.1.1.1/20/A/079 “Research and Development of Two-Phase Thermal Systems Installed in Lighting Equipment for its Functional Improvement” of its Latvian measure 1.1.1.1 “Industry-Driven Research”.

NATIONAL
DEVELOPMENT
PLAN 2020



EUROPEAN UNION
European Regional
Development Fund

INVESTING IN YOUR FUTURE

References

- [1] XLamp® XHP70.3 LEDs Cree- LED Product Family Data Sheet, Web Document (Accessed 25.10.2022) <https://cree-led.com/media/documents/XLamp-XHP70.3.pdf>
- [2] Knulst, A.J., Stassen, L.P.S., Grimbergen, C.A., Dankelman, J. Choosing Surgical Lighting in the LED Era. *Surgical Innovation*. 2009;16(4):317-323. doi:10.1177/1553350609353766
- [3] IEC. International Standard: Medical Electrical Equipment—Part 2-41 Particular Requirements for the Safety of Surgical Luminaires and Luminaires for Diagnosis. Geneva, Switzerland: International Electrotechnical Commission; 2000. 38. IEC Publication No. 60601-2-41 2000.

Numerical simulation of closed-type pulsating heat pipes using Fluent

Hye-Seong Hwang, Duy-Tan Vo, Kwang-Hyun Bang*

Korea Maritime and Ocean University, Pusan, South Korea

Abstract

A three-dimensional numerical simulation of closed-type pulsating heat pipes (PHPs) has been carried out using ANSYS Fluent. The Volume of Fluid (VOF) model was chosen for liquid and vapor two-phase flow and the continuum surface force model was added to the momentum equation. The implementation of variable density and vapor pressure relations for the working fluid was crucial for successful simulation. The pulsating heat pipes for simulations were composed of microchannels engraved on a 1 mm thick copper plate. The channel width was between 0.5 and 1.0 mm of uniform or dual pattern channel width and the number of turns were 7 or 9. The working fluid was degassed FC-72. The comparison of the calculated heat transfer rate to experimental data were reasonable for vertical installation of PHP. For horizontal installation, however, pulsating quickly stopped. In PHPs with dual pattern channel width, which an experiment demonstrated working even in horizontal installation, numerical simulation failed to show oscillatory flow. To solve this shortcoming of the model, implementation of capillary pressure difference is under development.

Keywords: Pulsating heat pipe; Microchannel; Multiphase flow; Numerical simulation; Fluent

1. Introduction

Pulsating heat pipe (PHP) is a loop-type heat pipe which employs two-phase flow of evaporation and condensation inside small-diameter tube without conventional wicks, as first patented by Akachi in 1990[1]. The PHP is simple in construction, low cost, and as long as a temperature difference exists and if it is large enough to maintain evaporation and condensation of working fluid, heat is transferred by pulsating flow without an external pumping power. Such advantages of PHPs have attracted various electronic packaging industries that have demanded an efficient heat dissipation technology.

The past studies on PHPs indicate that the physical parameters that greatly influence the thermal performance of pulsating heat pipes are tube diameter, temperature range, type of working fluid, charging ratio, number of turns, and the arrangement (or inclination against gravity direction) [2]. Along with vast amount of experimental work on PHPs, analytical and numerical studies also have been performed.

Shafii et al. [3] is among the first who have developed a control-volume modeling (one-dimensional) to predict the motion of multiple vapor plugs and liquid slugs inside the PHP channel. Force and energy balance equations were written for individual vapor plug and liquid slug and the equations were solved numerically by finite difference method. Their results showed that the heat transfer is due mainly to the exchange of sensible heat. An addition of in-depth liquid film model for evaporation and condensation to the earlier model [4,5] confirmed again that the major heat transfer mechanism is the exchange of sensible

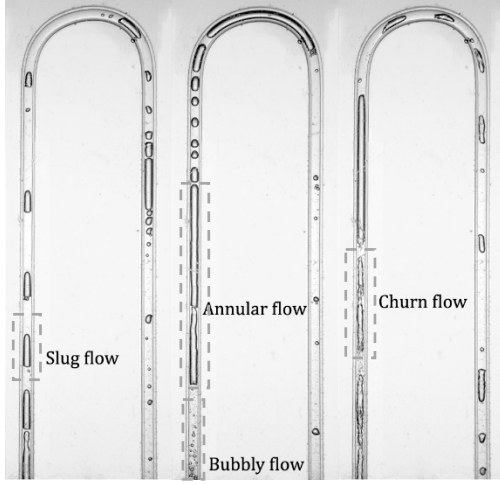
heat. Such mathematical model development revealed various effects of design and operational parameters on the performance of PHP, but did not report any comparative evidence that such characteristics of PHP actually observed quantitatively in experiments.

Bae et al. [6] investigated the effect of film dynamics on fluid motion and thermal performance of PHP and showed a good performance of the model when the results were compared with the experimental data.

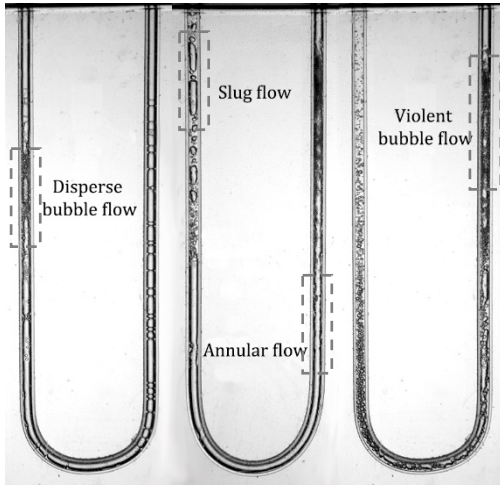
For a PHP to be a versatile device for heat transport, it must work in any orientation. However, the performance of a PHP tends to deteriorate when installed horizontally or heating section is installed on top. To make a horizontally aligned PHP operable, there have been a number of studies in which ideas and techniques have been proposed.

One idea was to increase the number of turns greater than ten based on an analytical solution [6]. Also, asymmetrical arrangement [7], or sometimes called dual-diameter tubes, has been proposed for making horizontal installation operable. Kwon and Kim [8] conducted a systematic experiment in which five-turn PHPs were constructed on silicon wafer with different dual-diameter sizes ranging from 0.2 to 1.8 mm. The thermal performance was tested by varying heat load and an optimum size pair of the dual-diameter was observed. They used ethanol and FC-72 for working fluid but most of the data presented was for ethanol.

For numerical simulation for PHPs, a control-volume approach may have some advantages of implementing detail description of heat transfer and in particular liquid film evaporation modeling.



(Cooling section/Condensation)



(Heating section/Evaporation)

Figure 1. Two-phase flow patterns in heating and cooling sections of PHP (circular tube diameter = 1.8 mm) [9].

However, it has shortcomings on multi-dimensional computation. As shown in Figure 1 of flow visualization of evaporation and condensation in 1.8 mm pyrex tube PHP [9], the flow pattern encompasses not only plug and slug flow, but also bubbly and churn flow. One-dimensional control-volume modeling of PHP flow channel seems good for vapor plug and liquid slug, but it may not be sufficient for bubbly and churn flow. A three-dimensional modeling approach can be suitable for many different and complex geometries of PHPs and also good for resolving various flow patterns.

In computational fluid dynamics approach to the simulation of a PHP, Lin et al. [10] presented a two-dimensional simulation based on volume of fluid (VOF) and mixture model. Their study showed that the mixture model is more suitable for the two-phase flow simulation of PHP. Pouryoussefi et al. [11] also performed a two-

dimensional simulation and reported the chaotic flow behavior in a multi-turn closed PHP. The formation of perfect vapor, liquid plugs, and the liquid film were observed in their study. Liu & Chen [12] simulated a flat-plate oscillating heat pipe (FP-OHP) using a three-dimensional model. They pointed out that the generation and characteristic of vapor slugs and liquid plugs come from the self-growth and coalescence of dispersed bubbles. Daimaru et al. [13] reported a numerical simulation and experiment for an application of PHP to on-orbit systems. Recently, Vo et. al [9] developed a three-dimensional model using Fluent and showed a good performance.

In this paper, a numerical modeling of three-dimensional simulation of microchannel PHPs using Fluent is presented. The width of microchannel PHPs was in the range of 0.6-1.0 mm and the working fluid was FC-72.

2. Mathematical model

Visualization of PHP reveals that the dominant flow pattern of the working fluid is either the slug flow or the annular flow depending on the wall heat flux [9]. Based on this observation, the Volume Of Fluid (VOF) two-phase flow model is thought to be a compatible model to simulate the PHP.

The VOF model is good for surface tracking in fixed Eulerian mesh. The volume fraction of each phase, α_g and α_l , represents the position and the interface in computational cells. If $\alpha_g = 1$, the gas phase only exists in the cell and liquid phase only exists where $\alpha_g = 0$. Naturally, the interface locates in the cell where $0 < \alpha_g < 1$. The sum of volume fractions of all phases is unity,

$$\alpha_g + \alpha_l = 1 \quad (1)$$

For the numerical method, the primary and secondary phases must be designated, and in this study, the coolant liquid was defined as the primary phase to improve solution stability. The continuity equations for vapor and liquid phase are [14],

$$\frac{\partial}{\partial t} (\alpha_g \rho_g) + \nabla (\alpha_g \rho_g \vec{v}_g) = S_g + (\dot{m}_{lg} - \dot{m}_{gl}) \quad (2)$$

$$\frac{\partial}{\partial t} (\alpha_l \rho_l) + \nabla (\alpha_l \rho_l \vec{v}_l) = S_l + (\dot{m}_{gl} - \dot{m}_{lg}) \quad (3)$$

where, \dot{m}_{lg} is the evaporation rate and \dot{m}_{gl} is the condensation rate.

In VOF model, only one velocity field is needed because each computational cell is occupied by either liquid or vapor except the cell that contains

the liquid-vapor interface. The liquid and vapor in the cell that contains the interface are in mechanical equilibrium, i.e, the liquid velocity and vapor velocity are equal. The momentum equation can be written as

$$\frac{\partial}{\partial t}(\rho \vec{v}) + \nabla \cdot (\rho \vec{v} \vec{v}) = -\nabla p + \nabla \cdot [\mu(\nabla \vec{v} + \nabla \vec{v}^T)] + \rho \vec{g} + \vec{F} \quad (4)$$

The continuum surface force (CSF) model proposed by Brackbill et al. [14] was employed for surface tension force, and it is added to the momentum equation as a source term. The general form of surface tension force is

$$F_{vol} = \sigma_{gl} \frac{\rho k_l \nabla \alpha_g}{\frac{1}{2}(\rho_g + \rho_l)} \quad (5)$$

Here, ρ is volume-averaged density. It is noted that the surface tension source term for a cell is proportional to average density in the cell.

The energy equation is as follows.

$$\frac{\partial}{\partial t}(\rho E) + \nabla \cdot (\vec{v}(\rho E + p)) = \nabla \cdot (k_e \nabla T) + S_h \quad (6)$$

In the VOF model, vapor phase and liquid phase co-exist in the interface cell so that energy, E , and temperature, T , must be presented as mass-averaged. For example,

$$E = \frac{\alpha_g \rho_g E_g + \alpha_l \rho_l E_l}{\alpha_g \rho_g + \alpha_l \rho_l} \quad (7)$$

where E for each phase is based on the specific heat of that phase and the common temperature.

Density (ρ) and viscosity (μ) are calculated by volume fraction averaged as Equations (8) and (9). Radiation heat transfer as well as any other volumetric energy source is included as source term, S_h .

$$\rho = \alpha_p \rho_p + (1 - \alpha_p) \rho_q \quad (8)$$

$$\mu = \alpha_p \mu_p + (1 - \alpha_p) \mu_q \quad (9)$$

The geometric reconstruction scheme was used for interfacial tracking, which constructs the interface between fluids using a piecewise-linear approach. The assumption of the model is that the interface has a linear slope within each cell and uses this linear shape for the calculation of advection of the fluid through cell faces. If the flow inside the PHP tube is turbulent, the realizable $k-\epsilon$ turbulent model was used, but in microchannels the

flow was mostly laminar.

The evaporation of working fluid can occur either on the heated wall or at the liquid-vapor interface. An extensive model of boiling on heated wall encompasses three components of boiling heat transfer: latent heat of bubbles that grow and depart, quenching of liquid flowing into the space that departed bubbles occupied, and convective heat transfer by single phase liquid flow that directly contacts the wall. In order to use such a wall boiling model in microchannels, one must build a plausible physical model for each component of the boiling heat transfer, but also check the validity of such model in microchannel. The bubble size may be bigger than the channel width or the liquid film is too thin to allow bubble growth and departure.

In this study, to avoid modeling difficulties and validity of wall boiling model for microchannels, the Lee's model [14] has been employed in which evaporation rate or condensation rate is assumed to be proportional to the difference between the fluid temperature and the saturation temperature.

$$\dot{m}_{lg} = C_{evap} \alpha_l \rho_l \frac{(T_l - T_{sat})}{T_{sat}} \quad (10)$$

$$\dot{m}_{gl} = C_{cond} \alpha_g \rho_g \frac{(T_{sat} - T_g)}{T_{sat}} \quad (11)$$

The coefficients, C_{evap} and C_{cond} are empirical constants in nature so selection of these coefficients must be validated with appropriate experimental data. The ANSYS Fluent code provides 1.0 for these coefficients as the default value, but one must note that in PHP the rate of evaporation and the rate of condensation can be in an equal order because the oscillating or circulating fluid undergoes evaporation and condensation repeatedly as it passes the heating part and cooling part in series. Under this speculation of phase change behavior in PHPs, the following relation between C_{evap} and C_{cond} can be derived.

$$\frac{C_{evap}}{C_{cond}} = \frac{\rho_g}{\rho_l} \quad (12)$$

Based on this relation and validation calculations against 1.85 mm-ID tube PHP test data, Vo et al. [9] proposed the best value of 0.8 for C_{evap} and 80 for C_{cond} . In this study, these values were adopted for the Lee's phase change model.

Under the thermal boundary condition of

constant wall temperature, the heat transfer rate at the wall is calculated by applying the Fourier's law.

$$q = Ak_f \left(\frac{\partial T}{\partial n} \right)_{wall} \quad (13)$$

3. Results and discussions

In the earlier work [15], the thermal performance of micro pulsating heat pipes (MPHP) was investigated experimentally using the MPHP engraved on a 1 mm thick copper plate as shown Figure 2. The working fluid was degassed FC-72. The MPHPs with uniform channel width of 0.8 mm and nine turns worked well when installed vertically with heating section at bottom. However, when it was installed horizontally, the operation seized soon after heat was applied.

Meanwhile, when the PHP was constructed with two different sizes of channel width alternatively between 0.5 and 1.0 mm, it worked good even when it was horizontally installed. The greater the ratio of larger channel width to smaller channel width, the better the thermal performance. The aim of this study was to develop a numerical model to simulate such thermal characteristics of MPHPs.

3.1 Uniform channel width MPHP

Overall dimension of uniform channel width MPHP is shown in Figure 2. It was a closed-type PHP and both the width and the depth of channel were 0.8 mm and engraved on a 1 mm thick copper plate by micro milling machine. The number of turns was nine. At the present simulation, the solid part of copper plate was not modeled and only the fluid volume was included. The meshing details are shown in Figure 3. The total number of meshes was about 200,000. The working fluid was FC-72. The thermal boundary condition was constant wall temperature: the heating surface was at 75°C and cooling surface was at 23°C. These values of boundary temperature were chosen to be compatible with the experimental conditions to simulate.

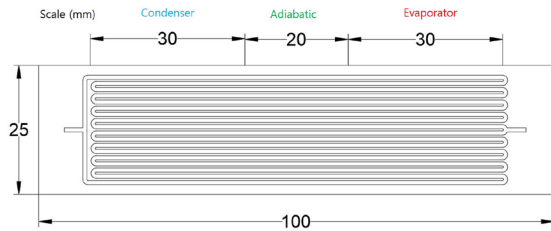


Figure 2. Overall dimension of 9-turn micro pulsating heat pipe, channel width = 0.8 mm.

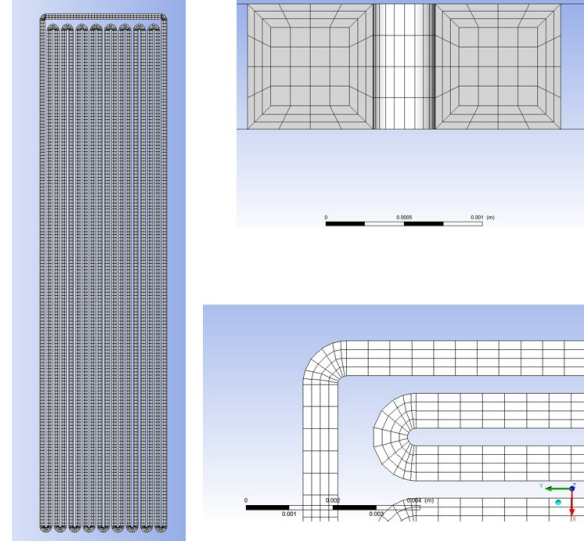


Figure 3. Details of computational mesh.

Table 1. Material properties of FC-72

Property	Liquid	Vapor
Density, kg/m ³	Eq. (15)	Ideal gas
Specific heat, J/kgK	1086.4	864.48
Thermal conductivity, W/mK	0.063241	0.01261
Viscosity, Pa.s	4.655e-4	1.15e-5
Standard state enthalpy	0	86477.2
Molecular weight, kg/kmol	338	338

The material properties of FC-72 are shown in Table 1 at the boiling temperature of 56°C of the atmospheric pressure. Although the assumption of constant property was reasonable for most of properties, it was found from several pre-calculations that the saturation temperature must be given as a function of vapor pressure and liquid density must be a function of temperature. These formulas were built by best-fitting of REFPROP data. For FC-72, these are,

$$T_{sat} = \sum_{k=0}^4 a_k P^k \quad (14)$$

$$a_0 = 267.4, a_1 = 1.42 \times 10^{-3},$$

$$a_2 = 1.53 \times 10^{-8}, a_3 = 1.01 \times 10^{-13},$$

$$a_4 = -2.8 \times 10^{-19}$$

$$\rho_l = \sum_{k=0}^4 b_k T^k \quad (15)$$

$$b_0 = 1266.7, b_1 = 14.12,$$

$$b_2 = -8.82 \times 10^{-2}, b_3 = 2.1 \times 10^{-4},$$

$$b_4 = -1.93 \times 10^{-7}$$

Here the units of T , P , ρ are K, Pa, kg/m^3 , respectively.

The initial conditions of pressure and temperature were 100 kPa and 323.15 K. The uniform initial set of vapor volume fraction corresponding to the fluid charging ratio sometimes caused a convergence problem. To solve such a problem, a realistic initial distribution of vapor and liquid was created by selecting cells randomly that is to be occupied fully by either vapor or liquid and the ratio of the total liquid volume to the total fluid volume (liquid + vapor) is set to be equal to the charging ratio. For Fluent, a journal file was written that contained coordinates of the cells of liquid and was patched after the global initialization. Figure 4 shows an example of initial distribution of vapor volume fraction set by this random distribution method. By this way, the numerical simulation of a PHP starts up from a near-to-real initial distribution of liquid and vapor and this helped a good solution convergence.

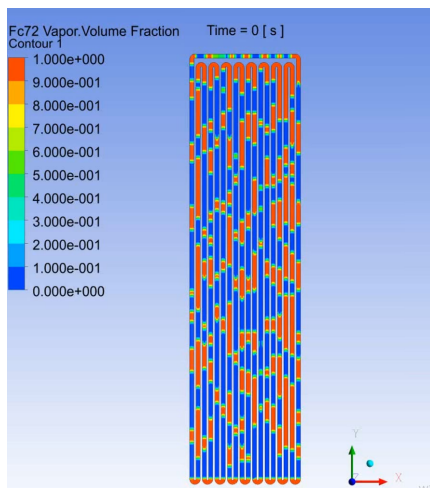


Figure 4. Initial random distribution of vapor (60% charging case).

A set of numerical simulations were performed for three different orientations of MPHP: vertical with the heating at bottom, 10° inclined from horizon, and horizontal installation.

In vertical installation, circulation flow pattern and pulsating flow pattern occurred repeatedly and the heat transfer rate was the highest among the three installation as expected. Figure 5 shows vapor volume fraction distribution at selected times. The animation of transient data of vapor volume fraction showed that the direction of circulation flow was counterclockwise and that the vapor condensed as it passed cooling sections and the liquid evaporated as it passed heating sections.

In horizontal orientation of MPHP, the flow motion started from the random distribution of liquid and vapor and the flow motion stopped in about a few seconds. The vapor volume fraction distribution at selected times is shown in Figure 6. As the flow motion slowed down, the cooling sections were filled with liquid and the heating sections were filled with vapor. The phase change rate became zero.

In the installation of 10° inclined from horizon, the flow motion was almost seized in a few seconds, but there was mild pulsating flow in one or two channels. Figure 7 shows vapor volume fraction distribution at selected times for this case.

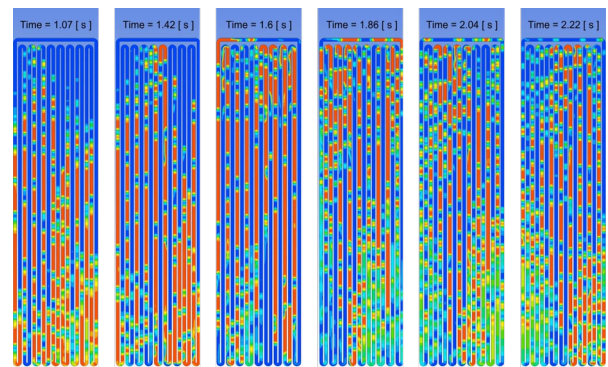


Figure 5. Vapor volume fraction distribution v.s. time (vertical).

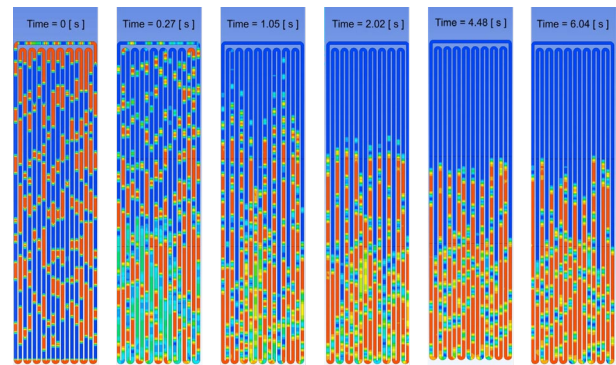


Figure 6. Vapor volume fraction distribution v.s. time (horizontal)

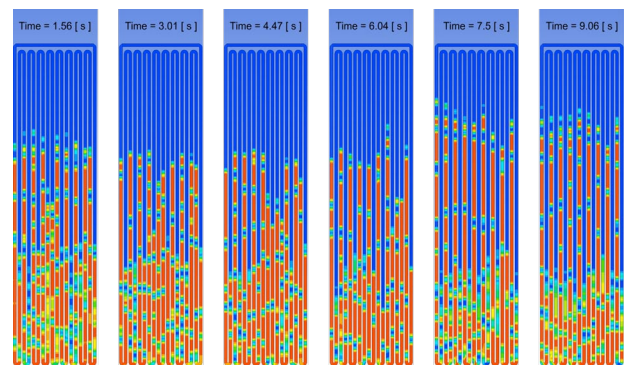


Figure 7. Vapor volume fraction distribution v.s. time (10° from horizon).

The total heat transfer rate was calculated at both sections of heating and cooling separately. The local heat transfer rate at each heating or cooling channel is summed to give the total heat transfer rate. The time variations of heat transfer rate at heating section and cooling section are shown in Figure 8 to 10 for different installation angle.

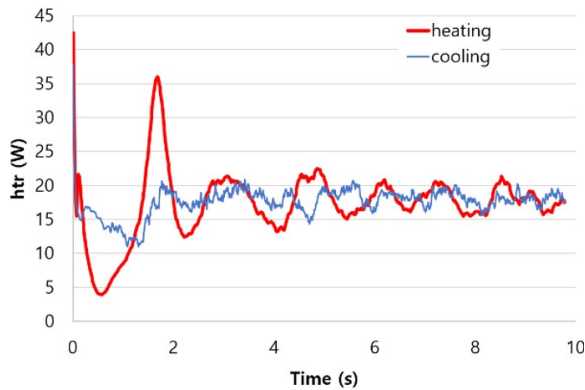


Figure 8. Heat transfer rate at heating and cooling sections (vertical).

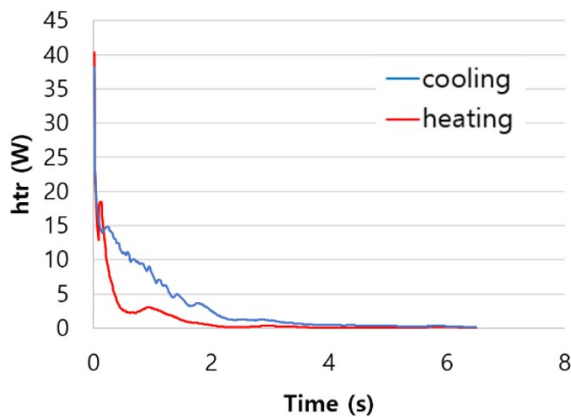


Figure 9. Heat transfer rate at heating and cooling sections (horizontal).

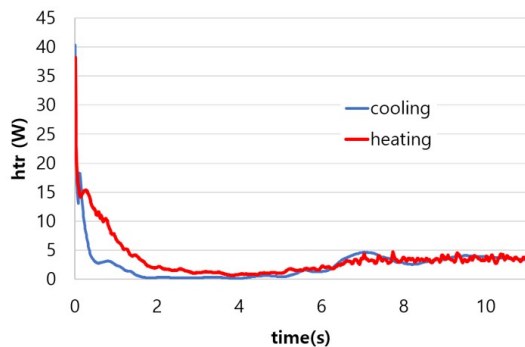


Figure 10. Heat transfer rate at heating and cooling sections (10° from horizon).

At the beginning, the difference between the heating rate and cooling rate was large, but soon the difference became small. The total heat transfer rate oscillated with small amplitude. To compare the heat transfer rate with experimental data, an averaged value over one cycle of oscillation was used.

For comparison of heat transfer rate with experimental data, it is noted that the present simulation did not include the solid part of copper plate, only the fluid volume was included. Therefore, the experimental data was reduced by the amount of heat conduction rate through the copper plate. The conduction-only heat transfer rate was measured with the empty MPHP, i.e. the fluid was not filled. The conduction-only heat transfer rate was 5.4 W. Table 2 shows the comparison of heat transfer rate between the simulation results and the measured data.

Table 2. Comparison of heat transfer rates in different installation angles

Orientation	Calculated (W)	Measured (W)
90°	18.1	14.8
10°	3.24	5.8
0°	0.05	1.41

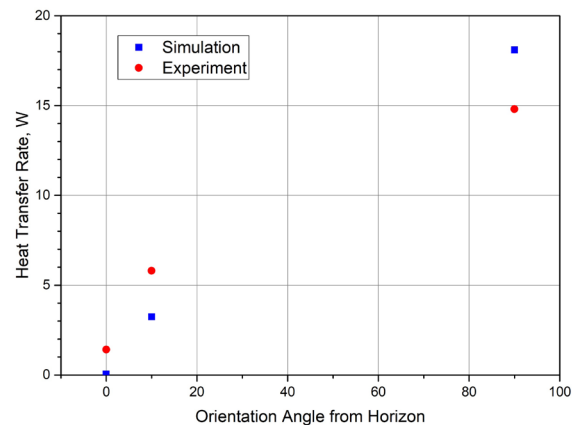


Figure 11. Comparison of heat transfer rate between simulation and experiment (0.8 mm square channel, 9 turns).

3.2 Dual channel width MPHP

An horizontal installation of PHP loses buoyancy force of vapor so that the driving force of vapor pressure difference alone may not be sufficient to drive PHP-style pulsating fluid motion, unless the vapor pressure derivative with respect to temperature is large enough such as that of Freon-123. To make the horizontal installation of PHP operable, an idea of dual-diameter PHP has been

proposed and showed that it actually worked [6]. This idea has been tested also for the present MPHP by constructing dual-size channel width and an optimal ratio of dual channel widths has been sought [15].

There were four different ratios of dual channel widths that had been tested and it was found that the bigger the ratio, the better the heat transfer. In this simulation, two types of MPHP were studied: (1) uniform channel width of 0.8 mm with 0.6 mm depth and (2) dual-pattern channel width of 1.0 mm x 0.6 mm with 0.6 mm depth. These dimensions were chosen to make all MPHPs have same heat transfer area. Table 3 summarizes the dimensions of MPHP that were used in the present numerical study and Figure 12 shows the schematic of dual-pattern type MPHP.

The material property, initial and boundary conditions were same as those of uniform channel simulations as given in the previous section. The comparison of calculated heat transfer rates with experimental data are shown in Table 4 and Figure 13. In vertical orientation, the difference in heat transfer rate between the simulation and the measured value was less than 3%, but in the uniform channel width case, the difference was large, 76%. The measured value of this case (type #2 in Table 3) was 5.94 W, and it seemed too low compared to the case of 0.8 mm depth (type #1 in Table 3), 14.8 W. In these two cases, the difference in heat transfer area was 58% so that the heat transfer rate of type #2 would be approximately 8.8 W. Checking of this measured data should be done in the future.

The working of MPHP with dual channel width in horizontal installation was experimentally demonstrated although the rate of heat transfer was not as high as that of vertical orientation. In simulation, however, the flow motion stopped as was in the case of uniform width case. An additional driving force for fluid motion in dual channel width PHP is believed to be the difference in capillary pressure at the two ends of a long liquid slug with different capillary width at each end. Modeling this pressure difference into Fluent would be a difficult work and a development work is being underway.

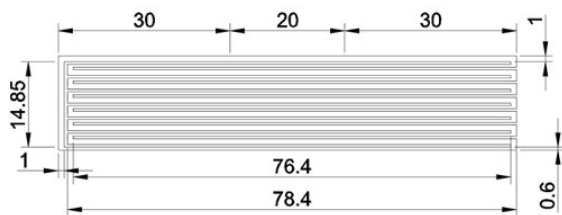


Figure 12. Schematic of dual-pattern channel width MPHP

Table 3. Single and dual-diameter MPHP dimensions [mm].

#	Turn	D	W_1	W_2	W_1/W_2
1	9	0.8	0.8	0.8	1.0
2	7	0.6	0.8	0.8	1.0
3	7	0.6	1.0	0.6	1.7

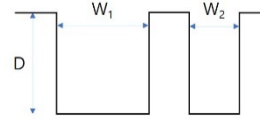


Table 4. Comparison of heat transfer rates in dual-channel width MPHP

Type	Angle	Calculated (W)	Measured (W)
0.8x0.8	90°	10.5	5.94
	0°	0.03	0.61
1.0x0.6	90°	9.6	9.88
	0°	0.03	5.48

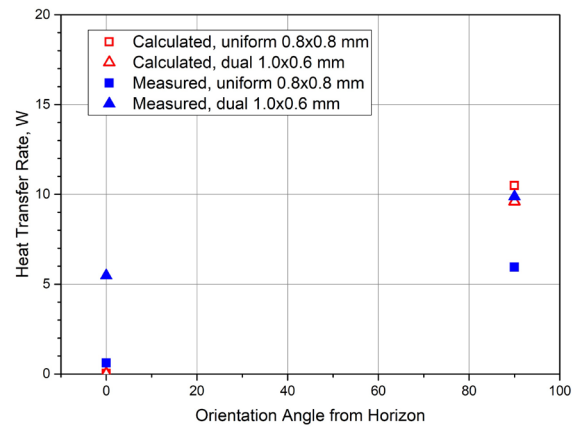


Figure 13. Comparison of heat transfer rate between simulation and experiment (dual channel width)

4. Conclusion

A three-dimensional numerical simulation of closed-type pulsating heat pipes (PHPs) has been carried out using ANSYS Fluent. The Volume of Fluid (VOF) model was chosen for liquid and vapor two-phase flow and the continuum surface force model was added to the momentum equation. The implementation of variable density and vapor pressure relations for the working fluid was crucial for successful simulation. The pulsating heat pipes for simulations were composed of microchannels engraved on a 1 mm thick copper plate. The channel width was between 0.5 and 1.0 mm of uniform or dual pattern channel width and the number of turns were 7 or 9. The working fluid was degassed FC-72.

The comparison of calculated heat transfer rate to

experimental data were reasonable for vertical installation of PHP. For horizontal installation, however, pulsating quickly stopped. In PHPs with dual pattern channel width, which an experiment demonstrated working even in horizontal installation, numerical simulation failed to show oscillatory flow. To solve this shortcoming of the model, implementation of capillary pressure difference is under development.

Acknowledgments

This work has been supported by the National Research Foundation of Korea (Grant No. 2018R1D1A1B07049027).

References

- [1] H. Akachi, Structure of heat pipe, US Patent No. 4921041, 1990.
- [2] S. Khandekar, N. Dollinger, M. Groll, Understanding operational regimes of pulsating heat pipes: an experimental study, *Applied Thermal Engineering*, 2003. 23: p. 707.
- [3] M.B. Shafii, A. Faghri, T. Zhang, Thermal modeling of unlooped and looped pulsating heat pipes, *J. Heat Transfer*, 2001. 123: p. 1159.
- [4] Y. Zhang, A. Faghri, M.B. Shafii, Analysis of liquid–vapor pulsating flow in a U-shaped miniature tube, *Int. J. Heat Mass Transfer*, 2002. 45: p. 2501.
- [5] W. Shao, Y. Zhang, Effect of Film Evaporation and Condensation on Oscillatory Flow and Heat Transfer in an Oscillating Heat Pipe, *J. Heat Transfer*, 2011. 133: p. 042901-1.
- [6] J. Bae, S.Y. Lee, S.J. Kim, Numerical investigation of effect of film dynamics on fluid motion and thermal performance in pulsating heat pipes, *Energy Conversion and Management*, 2017. 151: p. 296.
- [7] C.M. Chiang, K.H. Chien, H.M. Chen, C.C. Wang, Theoretical study of oscillatory phenomena in a horizontal closed-loop pulsating heat pipe with asymmetrical minichannel, *Int. Comm. Heat and Mass Transfer*, 2012. 39: p. 923.
- [8] G.H. Kwon, S.J. Kim, Experimental investigation on the thermal performance of a micro pulsating heat pipe with a dual-diameter channel, *Int. J. Heat Mass Transfer*, 2015. 89: p. 817.
- [9] D.T. Vo, H.T. Kim, J. Ko, K.H. Bang, An experiment and three-dimensional numerical simulation of pulsating heat pipes, *Int. J. Heat Mass Transfer*, 2020. 150: 119317.
- [10] Z. Lin, S. Wang, R. Shirakashi, L.W. Zhang, Simulation of a miniature oscillating heat pipe in bottom heating mode using CFD with unsteady modeling, *Int. J. Heat and Mass Transfer*, 2013. 57: p. 642.
- [11] S.M. Pouryoussefi, Y. Zhang, Analysis of chaotic flow in a 2D multi-turn closed-loop pulsating heat pipe, *Applied Thermal Engineering*, 2017. 126: p. 1069.
- [12] X. Liu, Y. Chen, Fluid flow and heat transfer in flat-plate oscillating heat pipe, *Energy and Buildings*, 2014. 75: p. 29.
- [13] T. Daimaru, H. Nagai, M. Ando, K. Tanaka, A. Okamoto, H. Sugita, Comparison between numerical simulation and on-orbit experiment of oscillating heat pipes, *Int. J. Heat Mass Transfer*, 2017. 109: p. 791.
- [14] *Ansys Fluent Manual*, 2019.
- [15] H.S. Hwang, J. Ko, K.H. Bang, Thermal performance of micro pulsating heat pipes engraved on a thin copper plate, *Joint 20th IHPC and 14th IHPS, Gelendzhik, Russia*, 2021.

The additive microstructures for heat transfer enhancement

Vyacheslav Cheverda*, Anastasia Litvinceva

¹ Institute of Thermophysics SB RAS, Prosp. Lavrentyev 1, 630090, Novosibirsk, Russia

² Novosibirsk State University, Pirogova 1, 630090, Novosibirsk, Russia

*slava.cheverda@gmail.com

Abstract

The idea of this experimental work is to create special microstructures on the heating surface to enhance the heat transfer. The metallic 3D-printer is used to create microstructures. The heat fluxes, which are necessary to initialize bubble formations, have been measured for surface without/with microstructures.

Keywords: Heat transfer enhancement; Boiling; One-phase flow; Critical heat flux.

1. Introduction

One of the most important research topics today is and will long be in demand for the problem of efficient heat transfer [1], [2]. A pulsating heat pipe (PTT) or an oscillating heat pipe was proposed by Akachi (1990) [3]. Since then, the use of pulsating heat pipes has been considered a promising area for use in the fields of solar energy, geothermal energy, in the aerospace industry, and for cooling electronic components due to the special advantages of PTT ([4], [5], [6]): (1) simple structure and low cost: PTTs are made from a long tube that is curved in several places. A characteristic feature of PTT is the lack of a wick, which is present in traditional heat pipes, which are very popular in production. The small diameter of the PTT is also an advantage for saving money on its creation; (2) high heat transfer: according to the results of [7] the equivalent thermal conductivity of PTT can be an order of magnitude higher than the thermal conductivity of copper; (3) the simplicity of miniaturization: the size of the PTT heat transfer device can be very small due to the small internal diameter of the PTT, which is one of the most attractive characteristics of the PTT; and (4) high flexibility: the PTT channel can be integrated into any configuration in accordance with the requirements of the application. Generally speaking, PTT is a proven, simple, reliable, silent and economically viable choice for heat transfer. Due to the uniqueness and simplicity of operation, the PTT has several obvious advantages: with the stable operation of the PTT, the vibrational movements of the liquid plugs and vapor bubbles set in motion a two-phase mixture in the pipe instead of the capillary force created by the wick in conventional heat pipes. Due to the influence of

surface tension, fluid plugs and vapor bubbles form and randomly distribute in the pipe. Evaporation and condensation of the working fluid caused by heat absorption and dissipation are the driving force of vibrations in the pipe, which is counteracted by the flow resistance created by the pipe walls. The following mechanisms are involved in the PTT operation mechanism: evaporation and condensation of a thin liquid film, dynamic contact angle of the working fluid on the tube wall, growth and movement of a Taylor bubble, and coalescence of small bubbles. Therefore, although the structure of the PTT is very simple, the relationship of hydrodynamic and thermodynamic effects during heat and mass transfer to the PTT makes the mechanism of PTT operation very difficult and difficult to fully understand ([8], [9]). The goal of this research is to study the initiation of the boiling process depending on the structure of the heated surface and the flow rate of the liquid inside minichannel.

2. The experimental setup

The setup contains: working liquids supply system, measuring system (sensors) and optical (high-speed camera) systems, working fluids circuits, data acquisition and remote control systems (Figure 1). Two temperature stabilization systems are based on the use of thermo-electrical modules (Peltier elements) and is used to stabilize the liquid and gas temperatures at the inlet to the test cell. All thermo-modules are cooled by water circuit. All temperatures are maintained between 10 and 30 °C. Pure water is used as the working fluid.

Thoroughly degassed water is supplied to the test section by means of the liquid pump from a liquid

container. Liquid flow rate is regulated in the range between 1 ml/min to 50 ml/min. Heat flux from the local heater can be varied up to 300 W/cm². All parameters are controlled remotely by the means of the control and data acquisition system designed on the LabView software platform.

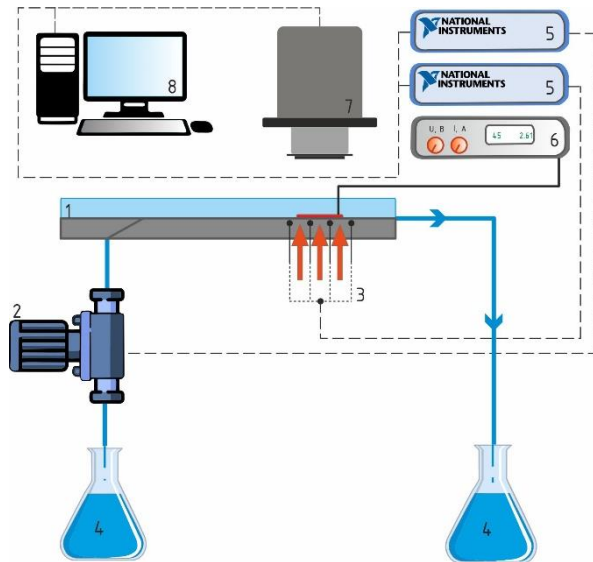


Figure 1. Scheme of the experimental setup: 1 – test section, 2 – liquid pump, 3 – thermocouples, 4 – reservoir with working liquid, 5 – National Instruments, 6 – power supply block, 7 – high-speed camera, 8 – personal computer. [10]

The experimental test section (Figure 2) consists of: textolite base plate; stainless steel substrate with the pressed copper heater; liquid film knife; textolite frame; textolite cover with optical window. The liquid flow is realized in the minichannel equipped with a special liquid nozzle of variable height (100-300 μm).

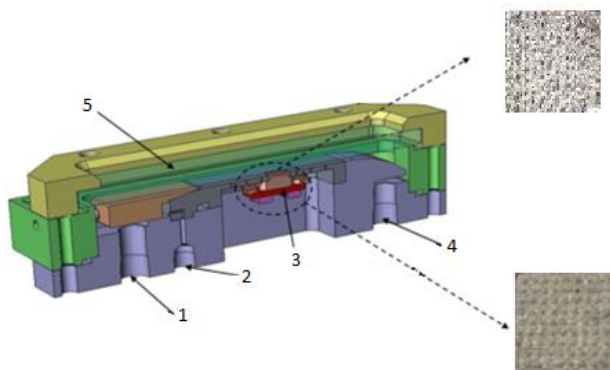


Figure 2. Scheme of the test section. 1 – gas inlet, 2 – liquid inlet, 3 – heater, 4 – gas/liquid outlet, 5 – optical glass.

The basic element of the test section is a flat plate

of stainless steel with a flush heater installed in it 10x10 mm². With help of additive manufacturing the 3D structures are produced on heater surface. Several calibrated thermocouples K-type have been used to manage temperature in several key points. The plate is fixed on the textolite base along with the textolite frame. The frame with the plate is covered by a transparent window forming a rectangular minichannel with dimensions of 59 x 30 x 0.9 mm³ (length, width and depth respectively).

3. The experimental results

The crisis phenomena is studied for two cases: with pillars and for smooth surfaces. For low heat flux on the surface it is possible to observe bubble formations. Later, with heat flux increasing that bubbles are coalescence and after that dry out of the heater surface is observed. For structured surface for low heat fluxes the bubbles are coalescence and evacuated to lateral walls due to capillary forces (Figure 3).



Figure 3. Formation and coalescence of bubbles on heated surface with pillars, $v = 0.006$ m/s, 60 W.

A comparison is made of the critical heat flux for a smooth heater and with pillars (Figure 4). It is demonstrated that the efficiency of heat removal is higher when using a heater with pillars.

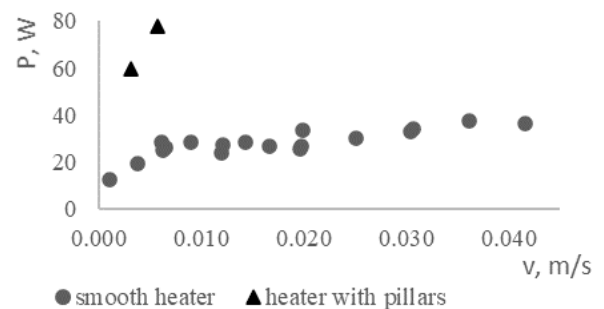


Figure 4. Dependencies critical local heat flux on the liquid superficial velocity.

Acknowledgments

Financial support is received from the Russian Science Foundation (RSF 22-29-01655). Measurement of the wetting angle of the substrate is performed under state contract with IT SB RAS.

References

- [1] Sirmuang W., Amatachaya P. A review of the applications of heat pipe heat exchanger for heat recovery // *Renew Sustain Energy Rev*, 2012. Vol. 16. S. 4303–4315.
- [2] Bin D., Eric H., Mohan K. An experimental platform for heat pipe solar collector testing // *Renew Sustain Energy Rev.*, 2013. Vol. 17. S. 119–125.
- [3] Akachi H. Structure of a heat pipe // Kanagawa. US Patent 4921041. - 1990.
- [4] Khandekar S., Schneider M., Groll M. Mathematical modeling of pulsating heat pipes: state of the art and future challenges // In: *Proceedings of 5th ISHMTASME-joint international conference on heat and mass transfer, India; 2002.*
- [5] Groll M., Khandekar S. Pulsating heat pipes: progress and prospects // In: *Proceedings of international conference on energy and the environment, China; 2003.*
- [6] Khandekar S., Groll M., Charoensawan P., Rittidech S., Terdtoon P. Closed and open loop pulsating heat pipes // In: *Proceedings of the 13th international heat pipe conference, China; 2004.*
- [7] Shang F.M., Liu D.Y., Xian H.Z., Liu J.H. Experimental investigation on enhanced heat transfer of self-exciting mode oscillating-flow heat pipes // *J Eng Thermophys (China)*. 2009. Vol. 30. No. 3. S. 461–464.
- [8] Zhang Y.W., Faghri A. Advances and unsolved issues in pulsating heat pipes // *Heat Transf Eng*. 2008. Vol. 29. No. 1. S. 20–44.
- [9] Khandekar S., Panigrahi P.K., Lefèvre F., Bonjour J. Local hydrodynamics of flow in a pulsating heat pipe: a review // *Front Heat Pipes*. 2010. Vol. 1. No. 1. S. 1–20.
- [10] Eloyan K.S., Ronshin F.V., Cheverda V.V. The influence of additive microstructures on the heat transfer crisis in a two-phase system with a local heating source // *AIP Conference Proceedings* 2135, 2022, Vol. 31, No. 4, pp. 655–663.

3D Printed Oscillating Heat Pipe

Kuan-Lin Chen¹, Kuan-Yu Luo¹, Pratik Prakash Gupta¹ and Shung Wen Kang^{1*}

¹ *Department of Mechanical and Electro-Mechanical Engineering, Tamkang University, New Taipei City 25137, Taiwan*
**Corresponding author email address: swkang@mail.tku.edu.tw; Tel.: +886-2-2621-5656 (ext. 3279)*

Abstract.

In this study, an oscillating heat pipe is made using metal additive manufacturing. The oscillating heat pipe is made using SUS316L metal, which has multiple channels. Each channel has a $2 \times 2 \text{ mm}^2$ cross section, meanwhile the OHP is 51mm wide and 120mm long. The working fluid is methanol. The oscillating characteristics and thermal resistance of the device are studied under different heating loads (20W, 30W, 40W, 60W, and 80W).

The results showed the OHP is completely sealed when the appropriate laser parameters are achieved, but the thickness of the produced device varied when the input parameters are changed which needs to be further investigated. The thermal performance investigation suggested the thermal resistance and the oscillating flow is better reached by the OHP with gaps between channels than the completely packed one.

Keywords: Additive Manufacturing; Pulsating Heat Pipe; Lateral Heat Transfer; Thermal Resistance

1. Introduction

With the development of science and technology, the demand for high-density heat dissipation in many fields, such as aerospace, electronics and sustainable energy are on the rise. The main agenda is to improve the thermal effectiveness of such devices to meet the requirements. Heat pipes are passive heat transfer devices that do not need to be installed with other mechanisms, so they have higher reliability and lower power consumption ratios.

The oscillating heat pipe (OHP) has no capillary structure inside, so the oscillation is achieved by the pressure difference of the working fluid in its vaporization state to start the heat transfer cycle. Generally, for electronic heat dissipation, the heat source with flat heat output surfaces such as CPUs are more common. The oscillating heat pipe is usually made by a bent circular metal pipe which is embedded into a metal block or a vapor chamber for conduction. However, these devices have poor efficiency due to the contact area thermal resistance. For making the flat plate heat dissipation surface, the common practice is to use the traditional process such as milling and lapping. Further the flow channels are made and sealed separately which makes it harder to achieve higher efficiency. At this time, it is necessary to avoid contact loss caused by bonding and sealing processes. This will help to develop a better design and production structure to enhance the heat dissipation capacity.

With the development of additive manufacturing technology, the current interest of many researchers are inclined towards making non conformal shapes and features. This approach made people to apply

additive manufacturing to construct designs that are difficult to achieve with traditional technologies. In order to design an oscillatory heat pipe with excellent performance, it is necessary to do the basic theory research and integrate it to visualize the fluid flow design parameters. The fluid parameters analysis is helpful in the selection and property improvement of working fluid, channel design and adding other components that help to improve performance [1].

As electronic components become thinner and develop higher performance, cooling systems also must extract waste heat from equipment efficiently. In accordance with this trend, researchers have been focused on developing thin and high-performance heat sinks. Compared to other heat transfer devices, the oscillating heat pipe has advantages in its operating characteristics in radiators and can produce various free-form designs with the additive manufacturing technology. This flexibility is very suitable for the heat dissipation of aerospace equipment and components. The development of additive manufacturing can further realize the ideal characteristics of printing with optimal output to be used in aerospace.

Heat pipes as a phase change equipment have always been a good choice for increasing heat transfer efficiency, while the traditional flat heat pipes used in flat heat sources. Also, because the pipes are connected, it will produce obvious lateral heat transfer between different pipes [2]. The temperature difference is reduced due to the lateral heat transfer, which is not helpful for the circulation of the working fluid of the oscillating heat pipe. In recent years, the rapid development of additive manufacturing has brought people to think of its

application for the internal structure of thermal management equipment [3-10]. The surface of the shapes can also be smoothed or transformed to reduce the contact thermal resistance caused by connecting various components. The additive manufacturing process will also improve the integrated molding feature, or reduce the occurrence of poor yield due to process omissions.

Powder-bed fusion (PBF) is one of the additive manufacturing technologies. PBF technology mainly uses a high-density focused energy source (such as laser light or electron beam) to sinter or melt material powder (plastic or Metal) into layer of the desired shape [11]. PBF technology can be divided into three categories: Selected Laser Sintering (SLS), Selective Laser Melting (SLM) and Electron Beam Melting (EBM), SLS and SLM both use a laser beam to print parts, while EBM uses an electron beam. PBF uses high-intensity energy to melt the material, so that the heat energy is very concentrated. Thus, in order to maintain the stability of the upper layer when laying the powder, it is necessary to set up a bottom plate and lock it during printing to provide support. Also, there should be support materials for heat dissipation between the upper layer to bottom plate. The printing volume is also filled with an inert gas to prevent the material from reacting to air during high temperature melting.

Since the printing method of SLS is to sinter the material, the processing temperature is low, and no support structure is required. But the material selection for printing is limited due to the low temperature. SLM uses a high-energy laser to completely melt the material. The working temperature is high, which increases the range of materials available for selection. However, the excessive temperature difference leads to serious stress and strain of the material, which requires certain support assistance structure. However, complete melting with SLM also means possibility of choosing materials, whether it is a single metal (aluminum, copper, etc.) or a multifunctional alloy (Al-Si-10Mg, Ti-6Al-4V, etc.). EBM uses a high-energy beam to locally melt and solidify the material, resulting in less residual stress and less support structure requirement. It is also suitable for printing harder to print metals such as copper, because of the concentrated energy density. However, due to the manufacturing requirement of the preheated powder, the feature size and the powder particle size are large, and the surface produced is relatively rough. Also, the need to maintain vacuum state during manufacturing, increases the manufacturing cost.

Regardless of the process of AM technology, the

processes have a very similar concept. Figure 1 is a workflow diagram where, the blue parts represent preparations such as: part design, software input selection, parameter setting, printing equipment and material selection, etc. During the process, various physical and chemical reactions, interactions, and the results of the printed product are combined to make optimized final processing. Output behaviors are mentioned as red parts such as, printing success and failure, whether the performance of the finished product meeting the standard, and the error with the design are mentioned. Also, because there are a lot of factors that affect AM technology, it takes a lot of resources and manpower to produce.

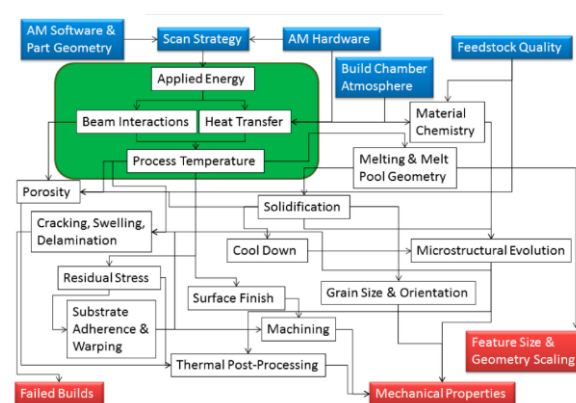


Figure 1 AM technology work flow chart [12]

The manufacturing process of SLM seems to be very simple, which consists of the cycle of laying powder, laser scanning and bottom plate lowering and positioning. But in order to make the manufactured work piece with good quality and complete structure, it is necessary to pay attention to the existence of various influencing factors. Density is the first key property that needs to be paid attention to in additive manufacturing. Too low density will lead to reduced mechanical properties and incomplete airtightness [13]. Excessive energy melts the powder in a fast way and create splash, which will lead to insufficient density of printed parts. In addition, the adjustment of laser parameters and powder quality also seriously affect the result.

Since SLM uses high-intensity energy to completely melt the powder, many common materials today, such as: stainless steel, aluminum, titanium and their alloys, can be printed with a density of more than 99% [14, 15]. Which will produce equipment from the machines of different brands and powders of different manufacturing quality. Under different background conditions the interaction of various factors is also different. It is necessary to test and adjust the conditions of the

machines in use, and it takes a certain amount of effort to establish the best way to use the machine.

PBF is currently the most widely used technology for metal Additive manufacturing, and most of the research on surface properties is based on this technology. Surface quality is often subject to problems in accuracy and roughness due to factors such as insufficient powder density, incomplete powder melting, overheating expansion, and surface spheroidization during the production process. After many experiments and improvements, SLM technology can obtain a surface roughness value (R_a) of 5~10 μm [16], but it still cannot meet the requirement of $R_a < 1\mu\text{m}$.

2. Experimental design

Figure 2 shows the manufacturing process of the oscillating heat pipe, which can be divided into five main processes, which are mentioned in sequence.

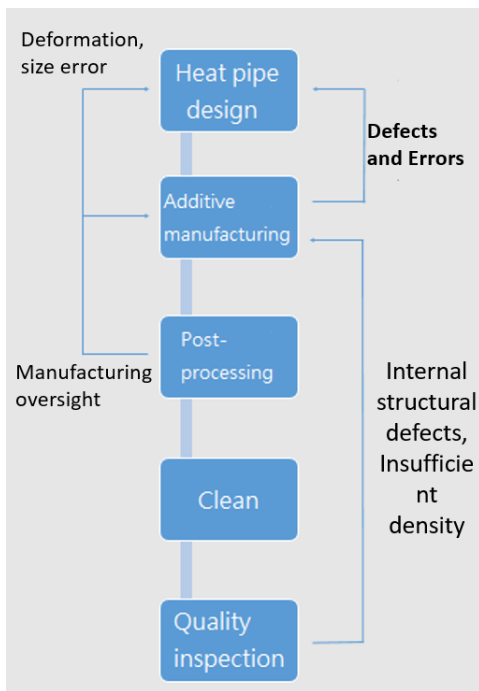


Figure 2 AMOHP manufacturing process

The plate oscillating heat pipe used in this experiment is shown in Figure 3. The length is 120mm (excluding the welded filling tube), the width is 51mm. In which, the evaporation end and the condensation end are each 40mm. The thickness is desired in the design to be at 5.5mm, but the final thickness in product is about 4.2mm. Table 1 is representation of the size setting inputs in printing software. where, the internal flow channel is a square channel with a side length of 2mm, and there

is a 1mm gap between the flow channels. The channels turnover number is 5. For the printing, the material is selected as SUS316L and from that two different PHPs are printed for comparison, one with a gap between the channels and the other without.

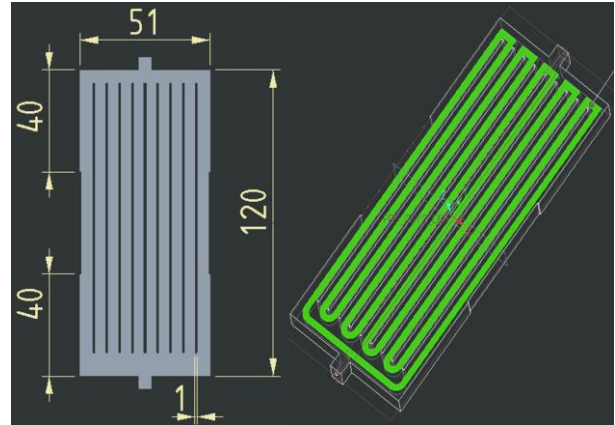


Figure 3 OHP design and schematic diagram

Table 1 OHP size parameters

SUS316L FPOHP				
Length	Width	Thickness (design/real)	Hydraulic diameter	Turn
120mm	51mm	5.5 mm	2mm	5

The equipment used in this experimental additive manufacturing system (Dongtai AMP-160) is shown in Figure 4, which can be divided into subparts such as, nitrogen manufacturing system, powder processing, software and printing control. The left of the picture is the machine body and the right of the picture is the internal working platform, and Table 2 is the working parameters of the AMP-160 machine.

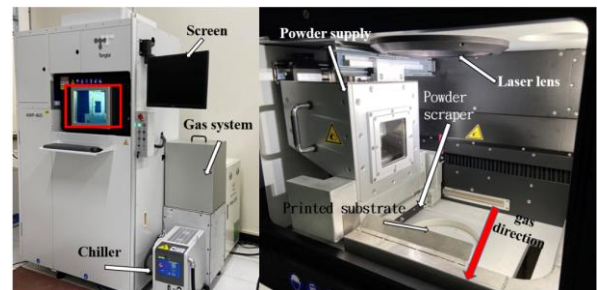


Figure 4 TongtaiAMP-160 AM system

Table 2 AMP-160 Technical data

Laser power	300W
Building volume	$\varnothing 160\text{mm} \times 160\text{mm}$
Focus diameter	50 μm
Building volume	1~10 cm^3/hr
Scanning speed	up to 6600mm/s

layer thickness	20~100 μm
size accuracy	about 100 μm

This study does a theoretical analysis on the manufacturing process of additive manufacturing and laser parameters, such as powder screening, parameter of experiments and post-processing. Among the adjustment of laser input parameters, the most discussed is "Volumetric Energy Density" which is given in equation 1:

$$E_v = \frac{P}{V} \times \frac{1}{H} \times \frac{1}{t} \quad (1)$$

This formula includes parameters such as laser power (P, W), scanning speed (V, mm/s), hatch distance (H, μm) and layer thickness (t, μm). By adjusting the parameters to obtain different volume energy densities, the structure and state of the printed workpiece can be changed. When the energy density is increases, it melts the powder better, which has the effect of improving the density of final product. However, excessive energy density may lead to the printing defects. When the energy density decreases, it has an opposite effect. So different energy densities will change the unit energy received by the powder, thereby affecting the relevant characteristics of the final molded part.

The experiment of printing parameters used equation (1), and fixed the hatch distance and layer thickness to 0.1mm and 0.03mm respectively. Used 16 groups of different laser power and scanning speed to obtain samples with a volumetric energy density of 30~150 J/mm^3 , and calculate the size deviation and density percentage. The size deviation is the difference between the design and the actual size, Density percentage equal to OHP density divides 316L metal density(=7.98 g/cm^3).

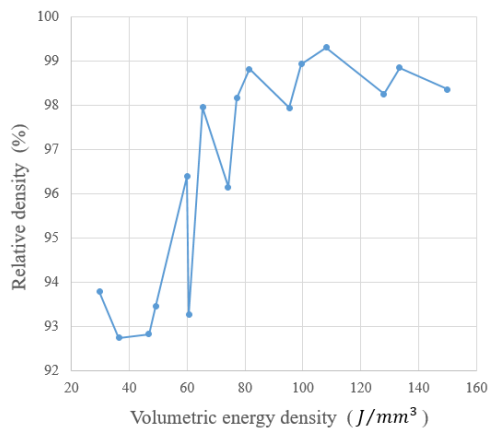


Figure 5 The relationship between E_v & relative density.

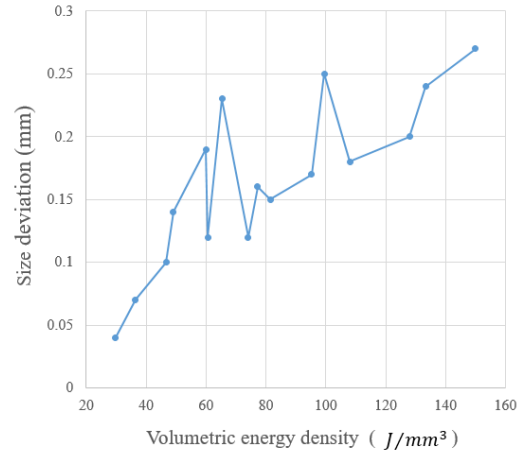


Figure 6 The relationship between E_v & size deviation.

Figure 5 and Figure 6 shows the test results. It can be found from figure that both density percentage and size deviation are positively correlated with E_v , and when $E_v > 80 J/mm^3$, the density percentage can reach more than 98%. Considering the size deviation, the final choice is to use an E_v of about 80 J/mm^3 .

Although setting a high energy density input can be expected to have better density performance, but the powder is easily melted by excessive energy and can encounters poor design and support. In Figure 7(a), it can be clearly observed that the support of the part has peeled off the bottom plate, and the overall shape is distorted. When printing fails, it is necessary to reconfirm whether there is an improper design problem, or parameters adjustment is required, or the support design needs to be replaced. Figure 7(b) is the same parts printed after improvement, and no obvious defects can be found. From consideration and improvements of density, error and defects, the final laser parameters are selected and used, which is shown in Table 3. Figure 8 shows the final additive manufacturing made oscillating heat pipe.

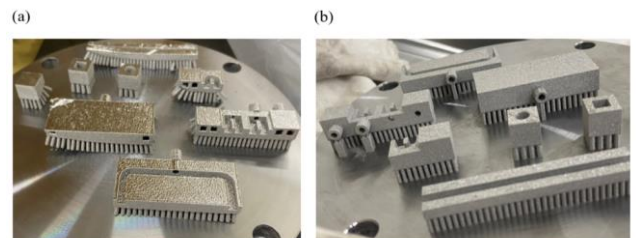


Figure 7 (a) Defects observed with high energy density input, (b) Improved parts after optimized power input.

Table 3 Printing parameters

P	V	t	H	E_p
220W	900mm/s	0.03mm	0.1mm	81.48 J/mm^3

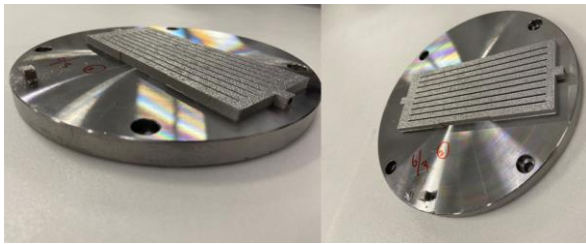


Figure 8 AM OHP

In terms of OHP design, you can refer to Figure 1. Where Figure 9(a) is with separation between the flow channels and Figure 9(b) is with no separation between the flow channels. This is done to see the for experimental comparison between two designs. Figure 9(c) shows the completed OHP for both designs. Both samples are filled with methanol as the working fluid, and the filling rate is set to 55%. The heating power is set to gradually increase from 20W to 80W, and the cold end surface temperature ($T_1 \sim T_5$) and heater surface temperature (T_H) of the heat pipe is measured to observe the oscillation phenomenon.

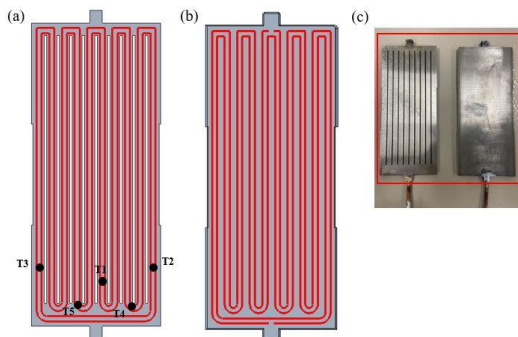


Figure 9 Schematic diagram of the design of the oscillating heat pipe and the actual finished product, (a) There is interval between the channels (b) There is no interval between the channels and (c) Picture of both OHPs.

Pipe wall density is very important for the heat pipe, only a closed cavity can maintain the vacuum and assure the heat pipe to run smoothly. It is necessary to conduct a leak test on the processed heat pipe, the test is divided into positive pressure test and negative pressure test.

a. Positive pressure test:

Fill 5 bar of air into the PHP and put it into water to observe whether there is obvious bubble

formation. In addition to confirming whether there is leakage in the PHP itself and whether the state of the connecting pipeline is stable. If there is a small amount of obvious leakage, we can Use glue to try to seal the leakage, but if there is a lot of leakage (as shown in Figure 10), we need to change the laser parameters and reprint the OHP.

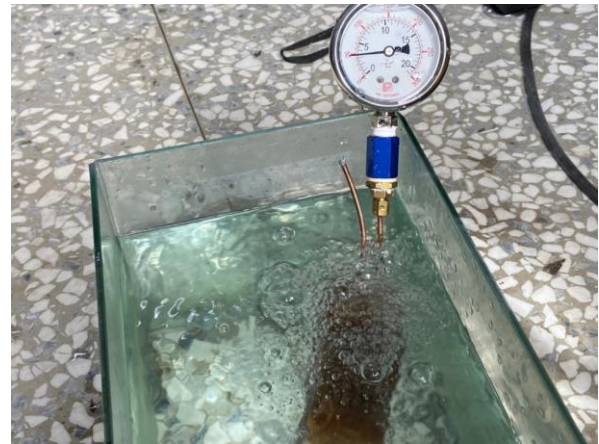


Figure 10 Leak test (with positive pressure)

b. Negative pressure test:

The real working condition of OHP is negative pressure or vacuum. We used a vacuum pump to evacuate air from the experimental pipeline and close the valve. Later we used a pressure gauge to digitize and observe the vacuum. Finally, we observed the pressure that decreases with time, and confirm that the part has the ability to maintain the given pipeline vacuum and is consistent over a long period.

In order to get the true leak status of OHP as much as possible, firstly, the connecting pipelines are tested many times, and the input tube is all sealed with Agilent Torr Seal vacuum glue. First, we used the pump to set a vacuum, then use the hemostatic forceps to close the hose connecting the pump and OHP. After keeping the test subject like this for a period of time, the leakage degree of the pipeline can be obtained. The test results are shown in Table 4.

Table 4 Vacuum line leak testing

Time	Initial vacuum	Final vacuum	Average leak rate
135min	0.235Torr	3.6Torr	0.0248Torr/min
360min	0.235Torr	8.8Torr	0.0239Torr/min
900min	0.235Torr	13.4Torr	0.0145Torr/min
1440min	0.235Torr	20.7Torr	0.0142Torr/min
1750min	0.235Torr	25.0Torr	0.0141Torr/min

It can be known from the test results that the leakage rate will gradually decrease with the increase of the internal vacuum power. so, it is necessary to carry out an appropriate test situation

for the PHP experiment. Finally, after 905 minutes (about 15 hours), the average leakage rate decreased gradually, and finally approached the leakage of 0.014 Torr per minute.

Table 5 shows the leak test records. From the test results, it can be seen that the final average leak rates of the two heat pipes are about 0.016 and 0.017 Torr per minute, respectively. which are slightly higher than the pipeline, and is a reasonable phenomenon. although the two value cannot be subtracted to obtain the degree of leakage of pure OHP, still it can be known that the leakage of the heat pipe itself is not large from the numerical value, which meets the experimental requirements.

Table 5 OHP leak test (including vacuum line)

	Initial vacuum	Final vacuum	Time	Average leak rate
Interval OHP	0.2Torr	23.4Torr	24hr	0.016 Torr/min
No interval OHP	0.2Torr	24.8Torr	24hr	0.017 Torr/min

Figure 11 (a) is the completed OHP, and X-RAY CT is used to photograph the internal structure. From (b), it can be observed that the shape of the internal pipeline is complete, but observing the cross-sectional view (c) will find that due to there is no support design on the upper surface of the rectangular pipe, which is prone to collapse, expansion and other defects. Therefore, the originally designed side length of 3mm was changed to 2mm for improvement.

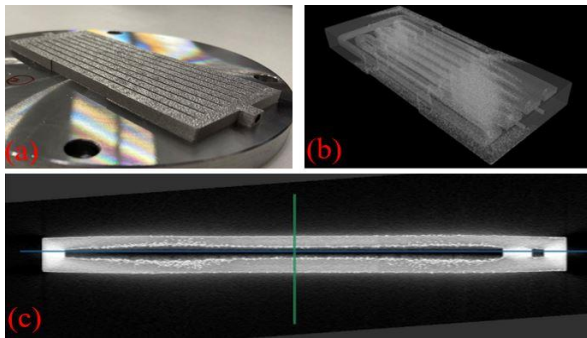


Figure 11 AMOHP and X-RAY CT scan internal structure.

3. Result

The printing, cutting, and post-processing of heat pipes made by additive manufacturing makes the product size relatively difficult to control. In particular, the thickness needs to be processed by wire cutting and grinding, resulting in significant dimensional change errors and will affect the characteristics of the heat pipes. Therefore, it is

necessary to continue to adjust the relevant accuracy and adjustments in the future. Table 6 shows the actual dimensions of the two heat pipes in this experiment.

Table 6 AMOHP size

	Interval OHP		No interval OHP	
	Design	Real	Design	Real
Length	120.0mm	120.1mm	120.0mm	119.8mm
Width	51.0mm	51.1mm	51.0mm	51.1mm
Thickness	4.0mm	4.2mm	4.0mm	3.65mm

The experimental results are shown in Figure 12 and Figure 13. It can be observed that the OHP with has a relatively obvious oscillation range with different intervals. Even when the heating power is 20W and the startup state can be observed. The temperature of the cold end and the temperature of the heater will oscillate up and down. In the state of slow rise, the temperature oscillates to indicate the more violent nature of internal pressure change. This effect causes the bubble and the liquid block to go back and forth between the two ends. This state improves working fluid to evaporate and condense, which increases the overall performance. For non-interval OHP, some oscillations start to occur after 40W and other temperatures start to oscillate at 80W. The main reason is that the temperature between the internal pipes of solid block OHP tends to balance due to lateral heat transfer. The pressure difference is also gradually balanced making it difficult to generate an oscillating flow state.

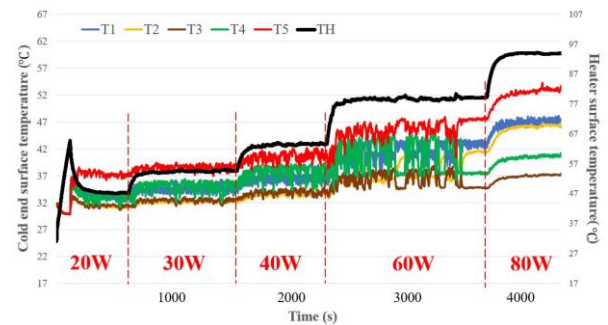


Figure 12 Temperature distributions of OHP with interval channel in relation with input power levels.

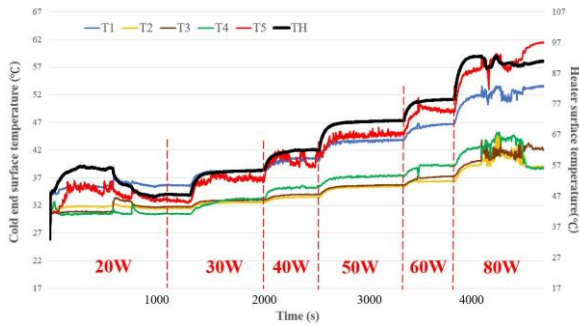


Figure 13 Temperature distributions of OHP with no interval channel in relation with input power levels.

In the Figure 14, we observed that the working fluid oscillates significantly at low power so that the interval channel OHP has better thermal resistance when the input power is low. When we increase the input power, the oscillation effect of no interval channel OHP increases significantly so that the heat transfer efficiency enhances.

We can know from equation (2) that when the conduction area is bigger and the conduction distance is shorter so that the thermal resistance of the heat pipe is lower. The interval channel OHP thermal resistance is slightly greater than the no interval channel OHP thermal resistance because of small contact area and long conduction distance. However, interval channel OHP is better than no interval channel OHP at low power. Therefore, we believe that the design of the interval PHP can improve the heat transfer performance effectively.

$$R = \frac{L}{k \times A} = \frac{1}{h \times A} \quad (2)$$

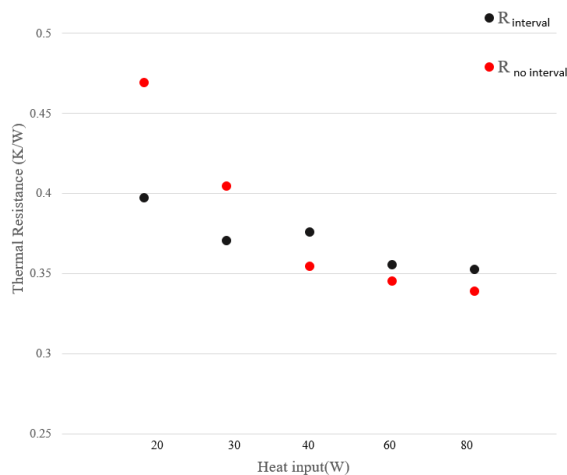


Figure 14 OHP thermal resistance comparison

In the Figure 15, we used effective thermal conductivity to exclude the effect of dimensional errors. In the case of excluding the size factor, it

shows the impact of the oscillating flow on the performance is significant.

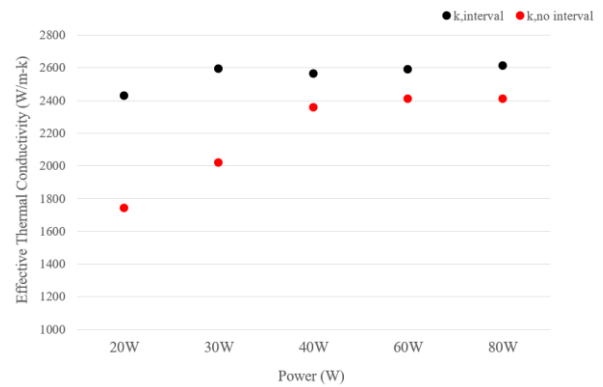


Figure 15 OHP equivalent heat conduction comparison

4. Summary and Recommendations

In this study, additive manufacturing is used to produce a SUS316L oscillatory heat pipe with a length of 120mm, a width of 51mm, and a square flow channel of 2mm. We use methanol as the working fluid to discuss the oscillation characteristics and thermal resistance under the conditions of different input power (20W, 30W, 40W, 60W, 80W). From design to production, additive manufacturing requires complicated experiments and various factors may affect the final state of the finished product. The main conclusions of this study are:

1. Additive manufacturing is suitable for various fields. First of all, in order to improve the quality of production, we must consider the limitations of the equipment and the needs of the application field to adjust.
2. Using the laser energy density as a manufacturing parameter is a simple and fast way. Although this method ignores some of the variables, it produces reliable parts.
3. Compared with the error of length and width, the thickness has a larger error due to the defects of post-processing and the defects of internal structure.
4. When we design the gap between the runners of the heat pipe, the lateral heat transfer is significantly reduced. The increased oscillation phenomenon due to less lateral conduction enables the heat pipe performance to be effectively improved.

Additive manufacturing is a technology with a high degree of freedom. It can accomplish many

complex designs, but users need to consider multiple factors to cope with various constraints.

Oscillating heat pipes are simple and efficient heat transfer devices. We can research the basic theory of the flow channel to optimize the evaporation capacity and pressure distribution. On the other hand, we can also try to print the condenser directly on the OHP to reduce the contact thermal resistance.

Acknowledgement

We would like to Thank National Science and Technology Council (NSTC), Taiwan, Republic of China, for supporting and funding the development of our research with project number 109-2221-E-032 -014 -MY2.

References

- [1] V. Ayel, M. Slobodeniuk, R. Bertossi, C. Romestant, and Y. Bertin, Flat plate pulsating heat pipes: A review on the thermohydraulic principles, thermal performances and open issues, *Applied Thermal Engineering*, 2021, vol. 197.
- [2] H. Y. Noh, A. Yoon, and S. J. Kim, Investigation into the effect of transverse conduction on the thermal performance of a flat-plate pulsating heat pipe, *International Journal of Heat and Mass Transfer*, 2021, vol. 181.
- [3] V. Keriquel, F. Guillemot, I. Arnault, B. Guillotin, S. Miraux, J. Amedee, J. C. Fricain, and S. Catros, "In vivo bioprinting for computer- and robotic-assisted medical intervention: preliminary study in mice," *Biofabrication*, Mar, 2010, vol. 2, no. 1, pp. 014101.
- [4] Z. Zhang, B. Wang, D. Hui, J. Qiu, and S. Wang, "3D bioprinting of soft materials-based regenerative vascular structures and tissues," *Composites Part B: Engineering*, 2017, vol. 123, pp. 279-291.
- [5] B. S. Bucklen, W. A. Wettergreen, E. Yuksel, and M. A. K. Liebschner, "Bone-derived CAD library for assembly of scaffolds in computer-aided tissue engineering," *Virtual and Physical Prototyping*, 2008, vol. 3, no. 1, pp. 13-23.
- [6] X. Wang, S. Xu, S. Zhou, W. Xu, M. Leary, P. Choong, M. Qian, M. Brandt, and Y. M. Xie, "Topological design and additive manufacturing of porous metals for bone scaffolds and orthopaedic implants: A review," *Biomaterials*, Mar, 2016, vol. 83, pp. 127-41.
- [7] N. Labeaga-Martínez, M. Sanjurjo-Rivo, J. Díaz-Álvarez, and J. Martínez-Frías, "Additive manufacturing for a Moon village," *Procedia Manufacturing*, 2017, vol. 13, pp. 794-801.
- [8] B. Graf, A. Gumenyuk, and M. Rethmeier, "Laser Metal Deposition as Repair Technology for Stainless Steel and Titanium Alloys," *Physics Procedia*, 2012, vol. 39, pp. 376-381.
- [9] G. Aviation, "New manufacturing milestone: 30,000 additive fuel nozzles," 2018.
- [10] Y. Cormier, P. Dupuis, B. Jodoin, and A. Corbeil, "Net Shape Fins for Compact Heat Exchanger Produced by Cold Spray," *Journal of Thermal Spray Technology*, 2013, vol. 22, no. 7, pp. 1210-1221.
- [11] W. E. Frazier, "Metal Additive Manufacturing: A Review," *Journal of Materials Engineering and Performance*, 2014, vol. 23, no. 6, pp. 1917-1928.
- [12] W. J. Sames, F. A. List, S. Pannala, R. R. Dehoff & S. S. Babu, "The metallurgy and processing science of metal additive manufacturing," *International Materials Reviews*, 2016, 61:5, 315-360.
- [13] W. Sames, F. Medina, W. Peter, S. Babu, and R. Dehoff, "Effect of process control and powder quality on Inconel 718 produced using electron beam melting," 2014, pp. 409-423.
- [14] T. Vilaro, C. Colin, and J. D. Bartout, "As-Fabricated and Heat-Treated Microstructures of the Ti-6Al-4V Alloy Processed by Selective Laser Melting," *Metallurgical and Materials Transactions A*, 2011, vol. 42, no. 10, pp. 3190-3199.
- [15] A. Majeed, A. Ahmed, A. Salam, and M. Z. Sheikh, "Surface quality improvement by parameters analysis, optimization and heat treatment of AlSi10Mg parts manufactured by SLM additive manufacturing," *International Journal of Lightweight Materials and Manufacture*, 2019, vol. 2, no. 4, pp. 288-295.
- [16] J.-Y. Lee, A. P. Nagalingam, and S. H. Yeo, "A review on the state-of-the-art of surface finishing processes and related ISO/ASTM standards for metal additive manufactured components," *Virtual and Physical Prototyping*, 2020, vol. 16, no. 1, pp. 68-96.

Study of 3D printed capillary structure

Kuan-Yu Luo¹, Pratik Prakash Gupta¹, Kuan-Lin Chen¹ and Shung Wen Kang^{1*}

¹ Department of Mechanical and Electro-Mechanical Engineering, Tamkang University, New Taipei City 25137, Taiwan
*Corresponding author email address: swkang@mail.tku.edu.tw; Tel.: +886-2-2621-5656 (ext. 3279)

Abstract. In this study, a series of metal 3D printed capillary structures were fabricated by selective laser melting (SLM) 3D printed technology. The porosity and capillary force performance of the metal 3D printed test sample and stainless-steel wire mesh was measured to find out whether the porosity and capillary force are related by experiment. The results show that among the lattice structures of metal 3D printed, the lattice structure of OCTET has the lowest porosity among all the metal samples of different structures in this experiment, and has the most outstanding performance in capillary force, with the largest fluid suction capacity within 600 seconds.

Keywords: Additive Manufacturing; Metal 3D Printed; Lattice Structures; Capillary Force Performance.

1. Introduction

The operation principle of the vapor chamber and the heat pipe is the same. They are all in the vacuum chamber. The main difference between the two is the change of the heat transfer path. The heat pipe is a one-dimensional line of conduction, while the vapor chamber is a two-dimensional heat transfer system, and its performance and efficiency are better than that of heat dissipation components with multiple heat pipes arranged together. It is suitable for use in the field of electronic heat dissipation with increasing energy density [1]. Rapidly expand the point heat source into a surface heat source for heat dissipation, reduce the amount of heat transfer per unit area, and eliminate the problem of adverse effects caused by the concentration of hot spots in electronic components. The temperature average effect is obvious, and the maximum temperature difference can be less than 2°C, suitable for industries that require high temperature uniformity. Compared with the heat pipe, the heat spreader has a larger contact area with the heat source, which directly reduces the overall thermal resistance of the system. Figure 1 shows the schematic of a vapor chamber with solid columns and wick columns [2]. When heat was added to the evaporator, the liquid vaporized and moved to the condenser from which the heat was removed. The vapor subsequently condensed back into evaporator through wick structure and wick column, and the cycle was repeated. The wick column is a porous copper wick structure that can easily pump working fluid back to the evaporator. The solid column was made of copper and could support the mechanical strength of the vapor chamber.

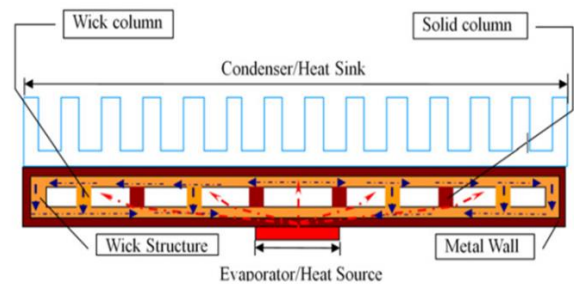


Figure 1. Schematic diagram of the working principle of the vapor chamber.

The capillary structure is a key factor affecting the overall performance of the vapor chamber, the capillary structure of the heat sink evaporator area determines its thermal performance and maximum heat flux, they are used as the capillary wicking medium to drive the circulation of the liquid phase working fluid, and enhance the ability to adsorb gas-phase working fluid in the evaporation zone. The optimal design of the capillary structure is crucial, and in order to operate at higher heat fluxes, many capillary structures have been developed with different fabrication methods, the common ones being grooved, metal woven mesh, metal sintered powder. For the performance of the capillary structure, the capillary pressure it generates and its permeability to the working fluid are the keys to affecting the performance. Ideally, the optimal capillary structure needs to generate high capillary pressure and have high permeability.

In recent years, many studies have been devoted to the development of more advanced composite capillary structures, including composite metal meshes and metal mesh-covered grooves. These structures offer higher capillary pressures than previously possible, but also require

complex fabrication process techniques. As metal 3D printed technology advances, its fabrication of porous capillary structures is likely to be an alternative, offering small feature sizes and 3D arrangements in a variety of possible configurations. In this case, 3D printed offers greater freedom in defining the geometry and properties of the capillary structure. Ramirez et al. [3] used 3D printed technology-EBM to print lattice structures with random openings and meshes. Wong and Leong [4] used 3D printed technology-SLM to print out the lattice structure and tested its heat flux at different temperatures. Jafari et al. [5] investigated the wicking behaviors of a 3D-printed stainless steel porous structure.

Powder Bed Fusion (PBF) is a stack molding of metal powders by sintering, which is further divided into Selective Laser Sintering (SLS) technology and Selective Laser Melting (SLM) [6]. Selective laser sintering (SLS) can be used for various polymer, metal, and alloy powders. In addition to the main metal powder, a certain proportion of binder powder needs to be added. The binder powder is generally a metal powder with a lower melting point or an organic resin. etc., the material powder is irradiated by a laser to melt the special material in it to achieve the effect of a binder, to combine the metal powder to realize metal printing. Since the laser scanning in SLS does not completely melt the powder, it only binds the metal powder through the binder, and cannot completely melt the metal powder to make it completely bonded, so the compactness is not good, resulting in a decrease in the overall mechanical strength and precision, and metal powders with high melting points cannot be sintered. Therefore, a 3D printing technology-SLM, which is suitable for high melting point metal materials, such as aluminum alloy, stainless steel and titanium alloy, and has better mechanical strength after printing, has been developed. After laser scanning in SLM, the powder is completely melted and fused Together, excellent mechanical properties are obtained, and its mechanical strength and forming accuracy are better than SLS [7].

Laser power and scan speed are the main parameters that affect the printing process. Fine high-resolution and high-quality printing are the main advantages of powder bed fusion, making it suitable for printing complex structures. This approach is widely used for advanced applications in various industries, such as tissue engineering, lattices, aerospace, and scaffolding for electronics.

The main advantage of powder bed fusion technology is the use of the powder bed as a support, overcoming the difficulty of removing the support material. The invention of metal 3D printing technology gives us more inspiration and imagination in applications in different fields and solves many bottlenecks that can be realized in theory but cannot be realized due to technological barriers.

Selective laser melting is a metal 3D printing technology. The molding principle is to irradiate metal powder with laser heat to produce local melting (shown in Figure 2); during the manufacturing process of SLM, the metal powder will be heated to complete melting and combined with each other. The seal is built layer by layer, so it is possible to design geometries that cannot be cast or otherwise machined, internal features and channels with machining difficulties. SLM produces strong and durable metal parts that can be used both as functional prototypes and as end-use production parts.

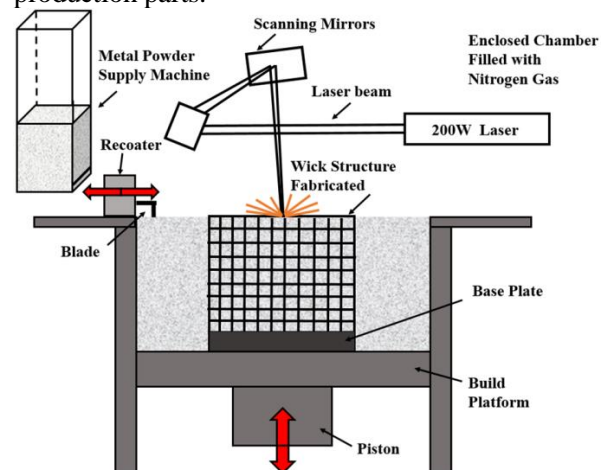


Figure 2. Selective Laser Melting (SLM) Process.

2. Experimental design

According to the literature discussion, in addition to the difference in material selection and fabrication method, the capillary structure mainly affects its capillary performance because of its pore size and porosity.

In the capillary structure of metal 3D printed, it is divided into the capillary structure arranged in a grid and various lattice structures existing in chemical molecules. The reason is that the design and drawing will be done through the software nTopology. After the capillary structure design is completed, the metal 3D printer AMP-160 (as shown in the figure 3) will be used to perform metal 3D printing with selective laser melting technology. Its details are shown in the table 1.



Figure 3. AMP-160 3D printer.

Table 1. 3D printed parameter settings.

SLM machine	AMP-160
Material	316L
Slice Thickness	30 μ m
Laser scan speed	1000mm/s
Laser power	100Watt
Laser diameter	50 μ m
Hatch distance	0.085mm

Capillarity refers to the combination of "adhesion between liquid and object" and "surface tension due to cohesion between liquid molecules" inside a liquid porous object, allowing the liquid to flow to a thin tubular object without applying external force. This phenomenon allows liquids to rise against gravity. This is a liquid interface phenomenon.

In this study, different mesh number of stainless-steel wire mesh (200、300、400 and 500 mesh data shown in Table 2) and 3D printed capillary structure were used for experimental measurement.

In the metal 3D printed capillary structure, it was further divided into the capillary structure arranged in a different line width of grid format shown in Figure 4 and the capillary structure with different lattice patterns shown in Figure 5.

Using the above structure as the unit structure, the sample size is designed as 50mm \times 10mm \times 2mm. The experimental data of porosity and capillary force will be carried out. Porosity is defined as the proportion of void space in the material.

The capillary force was measured by gravimetric method that record the relationship between the weight change of the samples and the time.

Table 2. 316 stainless steel mesh parameter.

Mesh	Wire Diameter (mm)	Pore Size (mm)	Porosity
200	0.05	0.08	0.38
300	0.04	0.045	0.28
400	0.03	0.034	0.28
500	0.025	0.026	0.26

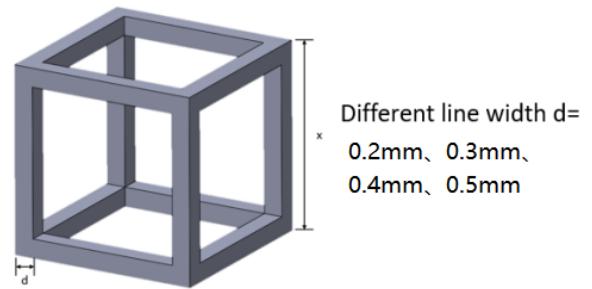
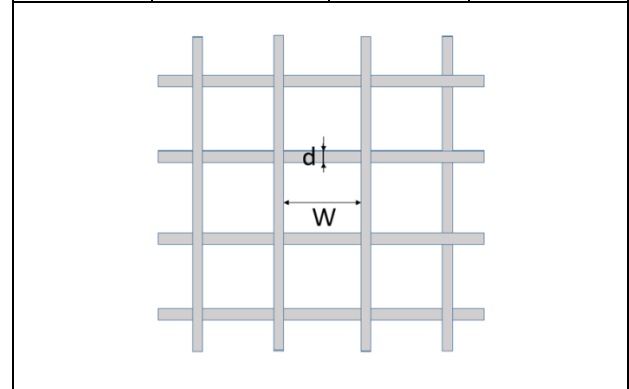


Figure 4. Schematic diagram of the design of grid format structure.

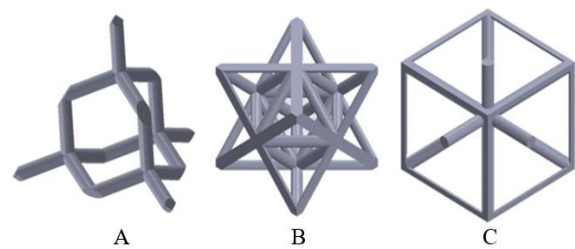


Figure 5. Schematic diagram of the design of the lattice structures (wire diameter 0.2mm) (A) DIAMOND (B) OCTET (C) ISOTRUSS.

3. Result and Discussion

Complete all metal 3D printed samples. The grid format 3D printed samples are shown in figure 6. The lattice format 3D printed samples are shown in figure 7.

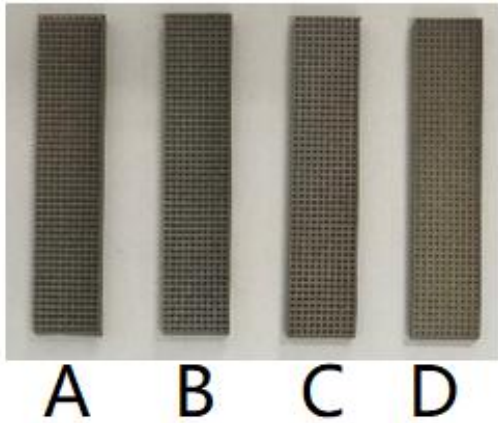


Figure 6. Metal 3D printed sample in grid format with (A) line width 0.2mm, (B) line width 0.3mm, (C) line width 0.4mm and (D) line width 0.5mm.

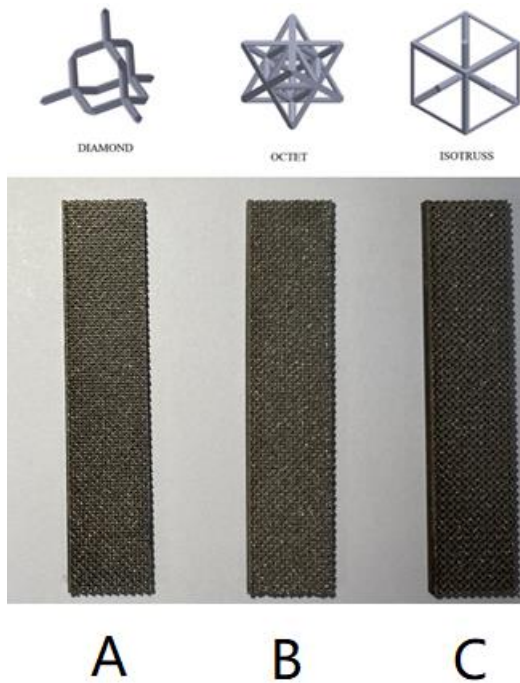


Figure 7. Metal 3D printed sample in lattice format with different base structure as (A) DIAMOND, (B) OCTET and (C) ISOTRUSS.

The porosity of the metal printed sample was measured as shown in Table 3. The capillary force test experiment part is divided into two parts: stainless steel metal mesh and metal 3D printing sample. The metal 3D printing sample is divided into two types: grid arrangement and crystal structure. The weight measurement method is used to obtain each test. The ability of the sheet to wick the working fluid under capillary action. At the beginning of the experiment, put 100g of water in the container below, and mark the measurement position to ensure that the volume of each test piece in

contact with water is the same during the test. Within 300 seconds, the relationship between the weight change of water and time, each test piece will be repeated several times to reduce the experimental error, the experimental equipment is shown in Figure 8.

Table 3. Porosity of metal 3D printed samples.

Types of Samples		Porosity
Grid format	Line width 0.2mm	0.9175
	Line width 0.3 mm	0.8210
	Line width 0.4mm	0.7251
	Line width 0.5 mm	0.6132
Lattice format	DIAMOND	0.82
	OCTET	0.62
	ISOTRUSS	0.69

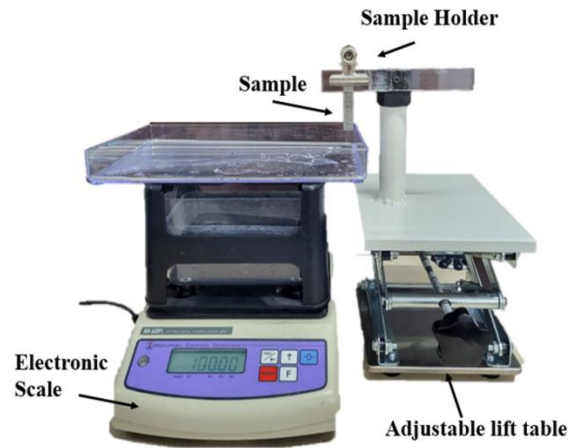


Figure 8. Capillary force test equipment.

It can be seen from Figure 9 that the 500-mesh stainless steel metal mesh has the largest wicking capacity within 300 seconds, because the 500-mesh stainless steel metal mesh has a relatively small pore size, so it has a larger capillary pressure to overcome Gravity attracts. Through the above data, the relationship between the change of fluid weight and time, and the amount of fluid wicked by the sample in each period of time, the wicking rate can be obtained, as shown in Figure 10.

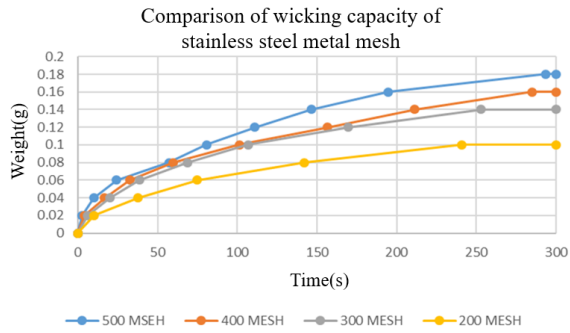


Figure 9. Comparison of wicking capacity of stainless steel metal meshes with different mesh numbers.

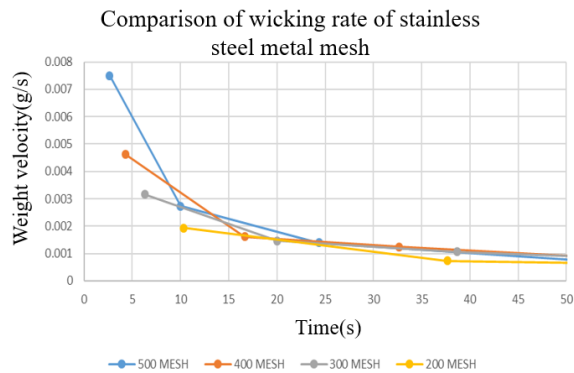


Figure 10. Comparison of wicking rate of stainless-steel metal mesh with different mesh numbers.

By observing Figures 9, it can be found that the wicking speed of fluids with different mesh numbers is more significant in the first few seconds, and as time goes on, the wicking speed gradually decreases until the capillary force on the fluid is equal to Under gravity, the structure is unable to wick more fluid to reach equilibrium. The amount of fluid wicked by stainless steel metal meshes with different mesh numbers within 300 seconds is listed, as shown in Figure 11.

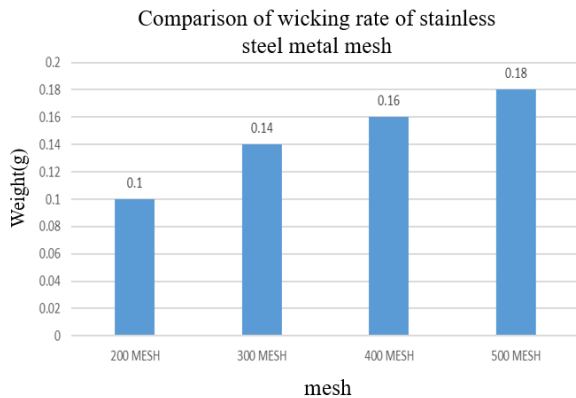


Figure 11. Comparison chart of wicking capacity of stainless steel metal mesh with different mesh numbers

Plot of the experimental data for grid-type metal samples with different line widths shown in Figure 12.

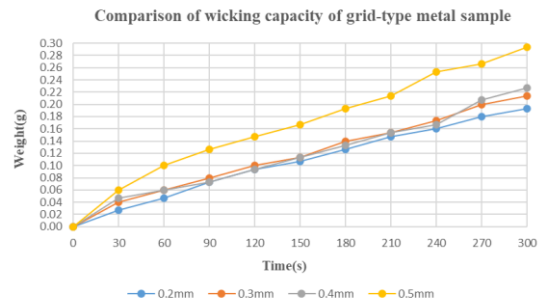


Figure 12. Comparison chart of wicking capacity of grid-type metal samples with different line widths.

It can be seen from Figure 12 that the 0.5mm mesh metal test piece has the largest wicking capacity within 300 seconds, this is because the 0.5mm mesh metal test piece has a relatively small pore size and thus has a larger capillary pore pressure to overcome gravitational attraction.

Through the above data, the relationship between the change of fluid weight and time can be measured and the amount of fluid wicked by the sample in each period of time or the wicking rate can be obtained, as shown in Figure 13.

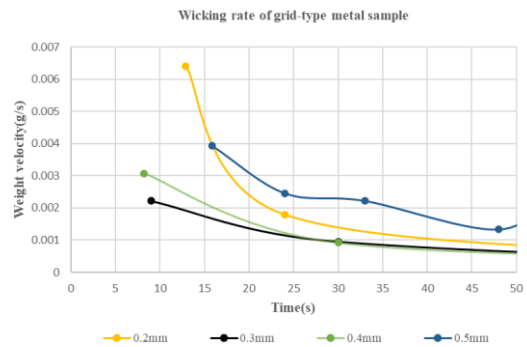


Figure 13. Wicking rate of grid-type metal samples with different line widths.

By observing Figures 13, it can be found that the fluid wicking speed of the test pieces with different line widths is relatively fast in the first few seconds, and the test piece with a line width of 0.35mm is the most significant. The rate of wicking also decreases gradually until the capillary force on the fluid is equal to gravity, and the structure is unable to wick more fluid and reaches equilibrium. The amount of fluid wicked

by the mesh metal test pieces with different line widths within 300 seconds is listed, as shown in Figure 14.

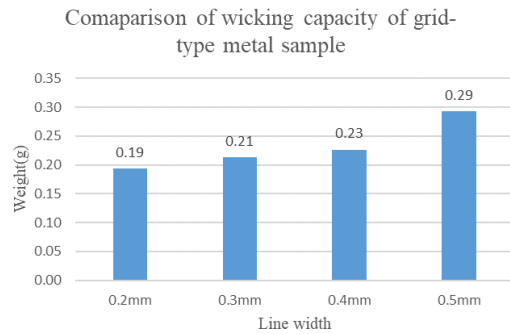


Figure 14. Comparison chart of wicking capacity of grid-type metal samples with different line widths.

Plot of the experimental data of lattice-type metal samples with different lattice structure are shown in Figure 15.

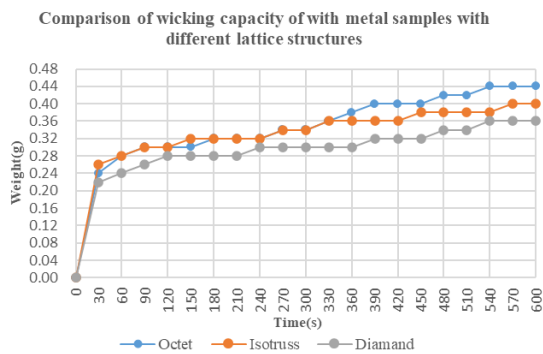


Figure 15. Comparison of wicking capacity of metal samples with different lattice structures.

From Figure 15, it can be seen that the metal test piece with the OCTET lattice structure has the largest wicking capacity within 600 seconds, and the performance of DIAMOND and ISOTRUSS is not much different. From the references and the capillary force measurement experiment of stainless steel metal mesh in the previous chapter, we can know that the biggest factor affecting the performance of capillary force is the size of the pore size of the capillary structure. In terms of unit cell lattice, the lattice structure of OCTET is uniformly distributed in space and has a low porosity. During the 3D printing process, it can print denser pores than other lattice structures, which is conducive to the development of capillary action.

Through the above data, the relationship between the fluid weight change and time, and

the amount of fluid wicked by the metal test piece in each period of time (The wicking rate) can be obtained. Which is shown in Figure 16.

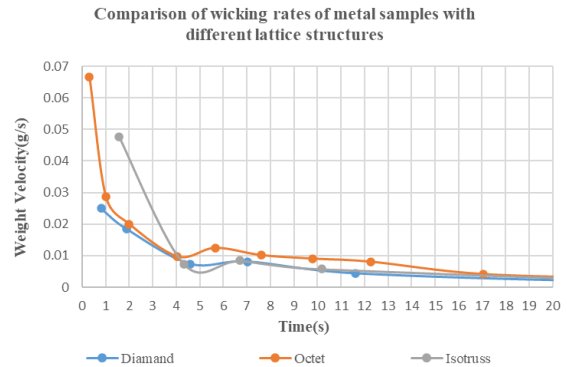


Figure 16. Comparison of wicking rates of metal samples with different lattice structures.

It can be found from Figure 16 that the wicking speed of different lattice structures is significant in the first few seconds. As time goes on, the wicking speed gradually decreases until the capillary force on the fluid is equal to Under gravity and the structure is unable to wick more fluid to reach equilibrium. The amount of fluid wicked by metal test pieces with different lattice structures within 300 seconds is listed in Figure 17.

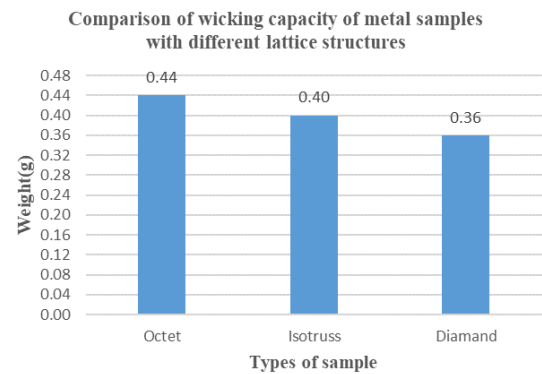


Figure 17. Comparison of wicking capacity of metal samples with different lattice structures.

In the capillary force experiment section, we have chosen the best performing stainless steel wire mesh and grid-type metal sample and compared it with the lattice samples. The experimental results are shown in Figure 18. The amount of fluid wicked in the remaining 5 minutes was compared as shown in Figure 19.

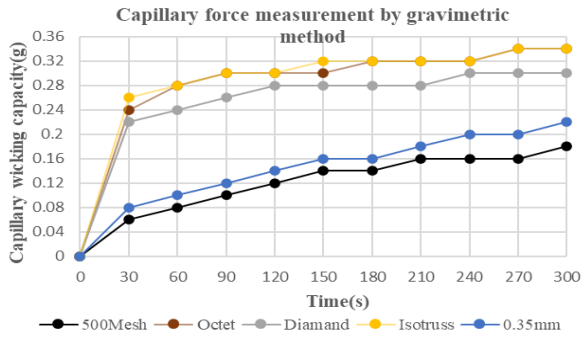


Figure 18. Capillary force measurement by gravimetric method.

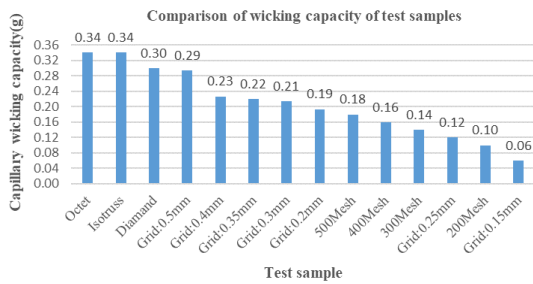


Figure 19. Comparison of wicking capacity of test samples.

In the porosity measurement, the wicking amount of the test pieces with similar porosity is compared, which is shown in Figure 20. Where the DIAMOND lattice structure with a porosity of about 0.82, a mesh structure with a line width of 0.2 mm made by stainless steel is compared to other meshes. Among all four of test pieces of metal mesh, the DIAMOND lattice structure has the best capillary wicking capacity of 0.30 g within 300 seconds.

As shown in Figure 21, between the two capillary structures, one is a mesh with a porosity of about 0.62 and a line width of 0.2 mm and the other is ISOTRUS lattice structure. In this comparison, the ISOTRUS lattice structure has a better capillary wicking amount of 0.34 g within 300 seconds.

As shown in Figure 22, between the two structures where one is the grid-arranged capillary structure with a porosity of about 0.69 and a line width of 0.2 mm, and the other is OCTET lattice structure. In this test, the OCTET lattice structure has a better capillary wicking capacity of 0.33 g in 300 seconds.

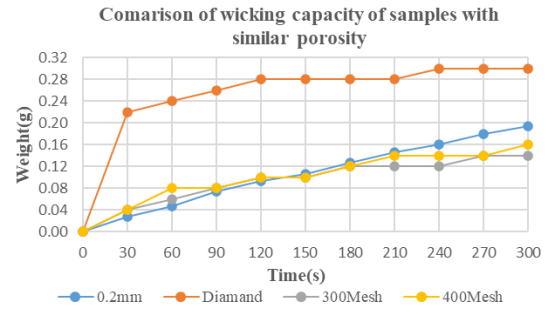


Figure 20. Comparison of wicking capacity of samples with similar porosity of 0.82.

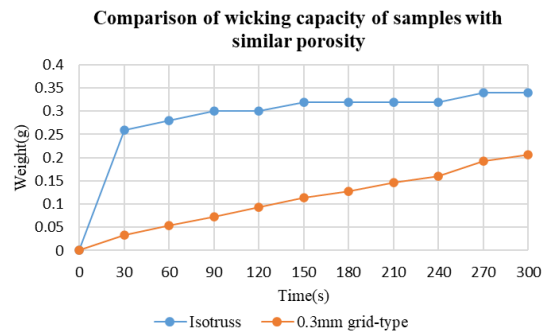


Figure 21. Comparison of wicking capacity of samples with similar porosity of 0.62.

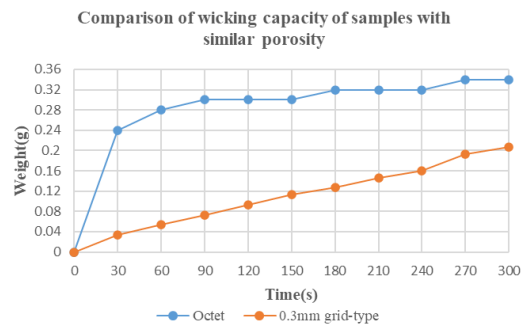


Figure 22. Comparison of wicking capacity of samples with similar porosity of 0.69.

4. Conclusion

In the capillary force experiment section by comparison of test pieces with similar porosity, the lattice structure has better capillary wicking capacity than the metal mesh structures.

Furthermore, the capillary force of the OCTET lattice structure is the most prominent among all the samples. This lattice structure cannot be fabricated by traditional methods, again illustrating the advantages and necessity of using metal 3D printing technology to fabricate the capillary structure of the vapor chamber.

It is expected that these lattice structures can be used in the field of heat pipes in the future as

capillary structures to optimize the performance of heat pipes.

Acknowledgement

We would like to Thank National Science and Technology Council (NSTC), Taiwan, Republic of China for supporting and funding the development of our research with project number 109-2221-E-032 -014 -MY2.

References

- [1] R. Ranjan, J. Y. Murthy, S. V. Garimella, D. H. Altman, and M. T. North, Modeling and design optimization of ultrathin vapor chambers for high heat flux applications, *IEEE Transactions on components, packaging and manufacturing technology*, 2012. 2(9): p. 1465.
- [2] M. C. Tsai, S. W. Kang, and K. V. Paiva, Experimental studies of thermal resistance in a vapor chamber heat spreader, *Applied Thermal Engineering*, 2013. 56: p. 38.
- [3] D.A. Ramirez, L.E. Murr, S.J. Li, Y.X. Tian, E. Martinez, J.L. Martinez, B.I. Machado, S.M. Gaytan, F. Medina, and R.B. Wicker, Open-cellular copper structures fabricated by additive manufacturing using electron beam melting, 2011. 528: p. 5379.
- [4] K. K. Wong and K. C. Leong, Saturated pool boiling enhancement using porous lattice structures produced by selective laser melting, 2018. 121: p. 46.
- [5] D. Jafari, W. W. Wits and B. J. Geurts, Metal 3D-printed wick structures for heat pipe application: Capillary performance analysis, 2018. 143: p. 403.
- [6] T. Wohlers and T. Gornet, History of additive manufacturing, *Wohlers Report*, 2015.
- [7] H. Lee, C. H. J. Lim, M. J. Low, N. Tham, V. M. Murukeshan, and Y. J. Kim, Lasers in additive manufacturing: A review, *International Journal of Precision Engineering and Manufacturing-Green Technology*, 2017. 4(3): p. 307.

Application of additive manufacturing in the development of heat pipe technologies

Pratik Prakash Gupta¹, Kuan-Lin Chen¹, Kuan-Yu Luo¹ and Shung Wen Kang^{1*}

¹ Tamkang University, New Taipei City, Taiwan

*Corresponding author email address: swkang@mail.tku.edu.tw

Abstract

The ever-increasing demand on reliable cooling of devices are increasing with the advancements in technology, while the dependency on such devices is in the incline. Heat pipes are a pillar on extraction of heat from applications ranging from silicon cooling to space shuttle thermal management. The heat transfer devices are also made for specialty cases and should be tested to provide a satisfactory performance. The overall manufacturing and testing of heat pipes and accompanying devices requires multitude of industrial and intellectual resources, which in general also result in mounting cost and time. The efficiency in manufacturing the heat pipes are vastly improved by the advancements in Additive Manufacturing (AM) processes, while presenting the thermal and structural behavior on par or superior to general quality materials. Also the AM processes can be controlled dynamically based on design and use case scenario, which present the opportunity to achieve complicated designs in a continuous process without difficulty. In recent years the trend of using AM to make heat pipes or devices working in conjunction with heat pipes, has increased constantly. This study shows the recent developments and advancement made in the field of heat pipes, with the help of AM processes. The understating of the AM processes in regard to production time, production quality, material used and requirement of thermal performance can significantly improve the selection time in regard to future researches. This study provides a review of the several advances made in past around AM in terms of heat pipe production with a honed in approach towards the comparatives of all the variables.

Keywords: Additive manufacturing, Heat pipe, Different materials, Adversities

1. Introduction

In the recent years, management of heat has become an essential task to improve sustainability and performance of modern industries with the demand growing exponentially. The development of reliable heat transferring devices such as heat pipes (HPs) and heat exchangers (HX) to achieve the requirement for maximum thermal extraction, is in the minds of recent researchers. For past few decades the advancements in heat pipe technologies are in progress which is leading several operations to its full potential. The advancements in heat pipe technologies are due to the multitude of research done for different kinds of heat pipes (ex. LHP, PHP, Micro heat pipes etc.) and different methods of analysis (ex. Numerical analysis and simulation), being in continuous development [1]. The application which requires the utmost utilization of the heat transfer capabilities and flexible design, has to be electronics or silicon cooling specially with the advancements in powerful electronics in last couple of decades [1,2,3,4]. The major components in heat pipes for achieving the optimized working stage is selection of right working fluid and wick. The design of wick plays significant role in the overall performance of a heat pipe [2]. For preferred electronics cooling the size of heat pipes should also be in miniature scale and the wicks

should also be developed to micro scale for best overall cooling performance [3]. Furthermore, the maximizing of cooling the silicon also provides micro scale flat heat pipes which can directly cool the silicon with higher effective surface area. Development and production of ultra-thin heat pipes (UTHPs) for use in electronic devices, specifically CPU cooling has also recently been discussed [4]. From the studies shown before mostly related to silicon and electronic cooling require the dimensions of both the heat pipes and wicks to be minimized with no compromises in actual capability and surface quality. Thus, the alternative of using Additive manufacturing (AM) is a great revelation for production of such niche devices.

Additive manufacturing represents the opportunity to create complex shapes and devices with precise structural properties [5-7]. The research done for creating the OHP using titanium metal alloy, shows the advantages of using SLM with no compromises in performance [5]. The realization of additive manufacturing as an alternative to create small and complex structures i.e., wicks and porous media, has pushed the innovative boundaries in regard to utilizing them in heat transfer devices [6-8]. The performance of heat transferring devices created with the SLM method outperforms from the traditional devices

due to its specialized design for the job [9]. The advantages of SLM over traditional forms of manufacturing (ex. Molding and extrusion), with no compromise in speed and costs of production and larger range of material available shows it as an elusive substitute [9, 10]. Traditional heat pipes and loop heat pipes take advantages from the porous microstructure design created by SLM for the improvements of capillary performance [8]. Even modern applications such as the thermal managements of silicon, also improves from the fact that the heat transferring devices can be directly made in conjunction with them or specially made for them specific to their designs [11].

The application related to AM and specifically SLM have more advantages in special grade devices with thermal capabilities enhanced as well [12-14]. One of the applications of using SLM produced material to make a complex shape, was to make a hollow pipe pitot tube with multiple holes for optimum heat dispersion [12]. The materials used in SLM techniques were tested further to know their physical limitations during heat transfer was also a concern and lead to the analysis [15]. The studies related to discussion of using the AM method to produce designs with thermal and structural integrity was a topic of discussion for few years with various studies [16-19]. The SLM manufacturing system is also can be modified to use with the objective of CNC milling head. The process explained in the study is used as a hybrid system of machining with both SLM manufacturing and CNC milling [13]. The advantages of producing a smaller design with channel like structure to introduce fluid flow heat dissipation and heat transfer is discussed in another study; the devices are completely redesigned by including floe channels to increase thermal dissipation in various areas are a great new initiative [18]. The materials used in SLM are also flexible depending upon the use case [14]. Even devices like heat exchangers can be built with the process without harming the overall performance of the device [14, 19]. The surfaces produced by SLM processes are also comparable or improved from the generally used materials, in terms of roughness and smoothness [19]. The rough surfaces produced from the process can enhance the overall surface area and act like small channels to maximize the heat transfer in passive cooling devices. Even for the general use pipes the internal shape can be optimized to produce better heat transfer without reducing the flow characteristics and internal flow pressure to a problematic degree [20]. The biggest advantages for AM methods for

producing heat transferrable surfaces/devices is the ability to make unachievable designs with similar or better performance even with extra cost is justified for special case and study of any special case requirements [11].

The main agenda of this study is to understand the past progress of studies made in this area, to further improve the understanding for future research. This study made a comparative analysis in terms of different processes, material used and utilization of the same. The selection of material and production speed are very fundamental things to be considered while using AM production, meanwhile the specialty counterparts of AM processes such as surface roughness in relation with the material and process speed are to be considered as well. This study provides a very focused analysis of the possible approaches in the heat pipe production or production of a thermal device in general using AM. While there has been a very few substrata of data available, this papers shines the light on the variables to be considered while starting the research in given field.

2. Material based comparison

The material selection for making a heat pipe arises a question of using copper as the material for it, as it is used for decades to make heat pipes. In terms of industry standards, copper is considered to be one of the best conducting materials with being inexpensive and showing adequate structural properties as well. The application-based usage related to heat transfer arises the question of using copper as the base material to make thermal devices such as heat pipes, using the Additive manufacturing process. Although copper has been applied to be used in few additive manufacturing processes, the difficulties to use it moved the industry into other alternatives such as aluminum or Titanium alloys. One of the first use can be seen in a process related to SLM called direct metal laser re-melting (DMLR) utilized to make different parts and shapes from copper. The method discussed in the process makes a basic structure from putting copper dust and melting it layer by layer. This study found that the specific power or energy density required for copper substrate is much higher than the stainless steel substrate, thus affecting the overall forming of melted particle size. This effect will significantly reduce the overall meting and create structures with lesser structural integrity [21]. Similar test was also conducted to use copper alloy in SLM process to check its workability and built part properties. The research was able to produce a thermally and structurally

stable print using moderate power (800W) and good speed of production (600mm/s). The study said to reach a minimum thickness of 0.05mm with over 96% relative density, which showcase the overall usability in terms of making a heat transfer device. Further the test showed the method for generating better copper and alloy materials, need to compensate with the higher thermal conductivity of copper powder. This shows the copper powder although can be used to make the product, is challenging to deal with it [22]. The material copper is selected because of its thermal and electrical capabilities, which is also changed when it's made by AM. The study of the properties showed the density and conductivity of printed material on par with the demands [23, 24]. The density was also improved with the technique used and speed of production. Although the copper structure making requires a minimum pitch distance with optimization of hatch pitch distance, the product with passable densities can be achieved [24]. The manufacturing of copper is also known to be not fully cooperative with the inputs and it is discussed in another studies. The using of copper resulted in a very porous material with less density than the actual copper. The manufacturing of the specimen also showed the difficulty in optimization and failed strategies for copper material [25]. Another study of the method is done later and found that by increasing the accuracy with lowered powered laser resulted in a material which although suffers from similar porosity problem but shows a great thermal and electrical conductivity with on par resistivity; to be used in electronic components [26]. The results obtained by several studies shows that the copper can be used as a building material in AM, but it has several issues which concern with higher porosity and difficulty to make a suitable end product with reliability. The end product does represent higher thermal conductivity and resistivity, which is usually associated with copper material. In theory and preliminary applications copper can be used to make specialty parts for a specific case but the properties like density, surface roughness and porosity are not as good as the traditional material use like aluminum or titanium alloys [27].

The discussion on the 3D printing of metals in the newer ages are based on the two main alloys used for manufacturing: AlSi10Mg and Ti6Al4V alloy. The debate to use and select which of these frequently used material depends upon many parameters. The structural and thermal abilities of the end product, roughness of the surface, size of end part, speed of production and power required

for the laser, are few of the key points to be considered while selecting the material of AM. The research where the 2 types of material are compared made a couple of joints using them and tested the resulted part. The titanium alloy managed to get parts with better definition and surface roughness. Although there are few more criteria's to be considered like the laser reflectivity, flowability during building and cost of manufacturing, in which the aluminum alloy can be used [28]. Another study was done to check the strength and fatigue of the materials made by AM. Both the titanium and aluminum alloy represented similar ductile yield and ultimate strength and are on par with conventionally made parts. The deciding factor of the built was more dependent upon the structure made, accuracy and porosity rather than the material made itself [29]. A detailed study is also done to check the microstructure and material properties of both the alloys. The titanium alloy presented a better surface roughness than the aluminum model, where the model is needed to sandblast in order to get smoother surface. In terms of strength the titanium alloy made structure needs to be heat treated in order to increase its hardness, whereas the aluminum alloy made structures show very minute change in heat treatment. Another important factor to be considered are porosity produced by AM process and how does it get affected after the process. The study finds that the titanium alloy can produce highly porous material which will reduce after post processing, meanwhile aluminum alloy also has similar properties but the post processing shows the combination of pores. Due to the lower melting point of aluminum alloy it is easier to combine them [30].

All the additive manufacturing processes use different material as base of the manufacturing. The chosen material is a significant factor to consider in getting the desired product with thermal and structural qualities intended of it. There are several different types of material used in the AM process based on the intended purpose.

2.1. Ti-6Al-4V

The titanium alloy is used in AM from the beginning of its trend start to develop in industrial level applications. The Ti-6Al-4V makes a product with high structural and thermal benefits even with high manufacturing power and cost requirements. The use of Ti-6Al-4V alloy in terms of heat pipes or heat transferring device has been shown in the manufacturing of a block Oscillating heat pipe designed for silicon cooling specifically [31]. The design can be achieved

from layer-by-layer manufacturing of a closed loop with only single filling port.

There are also mentions of using titanium alloy in different heat transfer applications other than heat pipes or heat exchangers [32, 33]. There is mention of the titanium alloy being used in different methods of process engineering and its applications [32]. Another review for the additive manufacturing in terms of heat pipe technologies mention the use of Titanium alloy to make a heat pipe and other heat transfer devices [33].

2.2. AlSi10Mg

The use of Additive manufacturing has been in rise due to its uniqueness and ability to get unachievable designs. Another important factor of any AM process is considered from the ease of making the machines to which we can shape the designs. The challenge is mainly to find a material easy to melt with lower powered laser and easily malleable. The choice of latest material for making heat transfer devices is AlSi10Mg, because of its lower melting point and excellent thermal and structural tolerances. One of the first cases of using AlSi10Mg, is to make microstructure of a finned shape to observe nucleate pool Boiling effect from cooling to measure its effectiveness [6].

The use of AlSi10Mg is also in trend with recent publications with using them in thermal applications also increased. The use of AlSi10Mg to make a heat sink to improve the thermal performance in high heat output electronic application was studied with the visible improvements in heat transfer [9].

The mention of the use of aluminum alloy over the conventional metals is shown in the review of thermal energy conversion devices such as heat exchanger or heat sinks [10]. The use of AlSi10Mg to make a flat plate pulsating heat pipe was done with the test for detecting the heat removal capabilities with also consideration of surface roughness [34]. Also for specifically the heat exchanger the use of aluminum alloy is studied briefly and mentioned its benefits [35]. The use of aluminum to make flat plate heat pipes is also studied for the application of cooling LEDs and shown to be effective [36]. By using the additive manufactured part with the heat pipe to dissipate heat is also a consideration. The hollow structure made from Aluminum alloy for a specific case of cooling jet engines also shows the stability and high thermal conductivity of the produced parts [37].

The recent and old reviews also mention the use of material for AM [9, 10, 19, 33].

2.3. Stainless steel

The material which most associated with manufacturing is stainless steel and it has also been in consideration to be used in the Additive manufacturing. The material is cost effective although the surface quality is harder to achieve. For the lower cost applications such as the cooling of Led lights it is a useful material and has been tested. A loop heat pipe was built with the stainless steel by AM and used to cool the LED lights with a much better effectiveness to normal metals [38]. There is also a study to make the wick structure of heat pipe with stainless steel AM. The structure was made to test for capillary effect which can be applied to heat pipes [39]. Another recent study was based on making the stainless-steel wicks with Am for using in loop heat pipes. The study focused on making the LHP to be used in chemical plants and the overall product showed much better efficiency [40].

The trend of using steel in the additive manufacturing is mostly done for wick design in heat transfer devices. Another study has been done for wick structure of flat plate heat pipe. The study shows improvements of the wick structure in terms of phase change characteristics of the FHP with also increased heat transfer [41]. The review papers also mention the use of stainless steel.

2.4. Polycarbonate

The use of polycarbonate which has a very low thermal conductivity is mostly done to make some support structures and insulations. In their use of AM the use is with the heat transfer device to make a complex shape with any other conductor. The use of polymer to make a support structure for the copper heat pipes was tested with the effect of material as mostly insulator [42]. Another recent study used the polycarbonate material to make a flat plate using AM. The study was based on the visualization and flow effect of the PHP with the transparent plate. The material is defiantly useful to see and observe of a process because it is an insulator and doesn't affect the heat transfer in huge way [43].

There are a bunch of studies conducted by Koito et.at. in few years related to heat pipes, while using polymer substances as the base of additive manufacturing. One of the first works started by making an acrylic heat pipe from resins on top of steel structure to realize and

confirm the behaviors of the thermosyphon. The printed structure was directly made on the resin board [44]. The same kind of methodology is used to make a sintered wick inside of the pipe for capillary behavior. The heat pipe with the wick structure put separately was printed also on the board itself [45]. The next application was to print a vapor chamber on the board and it was also build with the same resins with the dimensions of vapor chamber made to cool the electronics [46]. The research led to build the PHP using polymer components in conjunction with metal parts. The design was made to test the performance and behavior of the PHP [47]. The same PHP structure was used to visualize the flow pattern and behavior of the vapor forming and liquid slug flowing in the PHP during operation [48]. All the devices made by the researcher was not meant to break the barriers in performance, although it showed the behavior similar to the working heat transfer devices. Review papers mention polymers to be useful for designing and preliminary testing.

2.5. Other

There is a study based on using a PCB building material to be made layer by layer with the heat pipes or heat extractors in between the layers. The layers were printed and tested with the heat pipes to show a very good method of silicon cooling [49]. There is also a study which uses resin (EpoxyLite EIP4260 resin) to make different complex shapes of heat guides to be used in passively cooling the electronic machines such as wound motors [50].

3. Device based comparison

The devices which are made using AM for the purpose of heat transfer are generally OHP or PHP for cooling a constant heat emitting subject. Even there are very few actual devices made for either investigation and general use, the few case studies show the effects and advantages for AM in terms of producing such devices.

The first study was done to see the effectiveness of AM material in terms of direct contact cooling. The design is based on the thermal management of high heat flux cooling for CPUs or other silicones. The capacity measures from 500 to 1000kW/m². The research for cooling this kind of devices lead to two phase-based coolers and heat pipes. The flat plate heat OHP seemed to be the better option considering the larger surface connection to the heat emitter which in general have a flat surface as well. Also, generally the flat plate OHP have one single loop going from end to end with all the flow pipes in

parallel positions. The study created a design which uses the technology from AM to make the internal loop have both lateral and horizontal turns inside. The design also has only purpose built injection and pressure holes with compact shape, which is shown in figure 1. The compact block shape design makes it easier to cool a constant heat flux due to the loop of flow in an interconnected design, which have larger loop for cooling and heating as well [31].

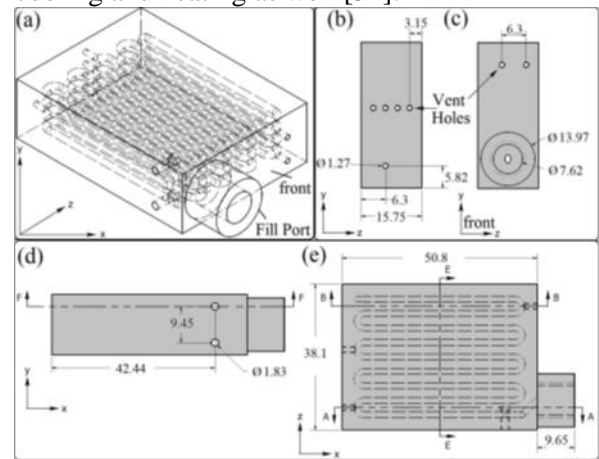


Figure 1. Design and internal pipeline representation of OHP made layer by layer using Ti-6Al-4V [31].

The device when made showed a reliable physical property such as density and surface roughness. The conducted experiments also provide a better insight on the thermal behavior of the built material and the device itself. The device shows a very good thermal ability with a very high thermal conductivity of 110 W/(m K), which is significantly higher than the base material- solid Titanium alloy (Ti-6Al-4V at 6.7 W/(m K)). Even the empty device showed the effective thermal conductivity of 18W/(m K), and shows the superiority of the solid material built by AM.

Another research by Ibrahim et.al.[51] was done with a similar device and using the similar base material (Ti-6Al-4V), in the AM process. It is also a block shaped OHP design with multidirectional interconnected loop inside. This device also has similar compact design and only few ports for filling and venting. The design of the device is shown in figure 2. This device is also made and tested for the intended purpose of cooling CPU or silicon of the flat surface with high heat flux emittance.

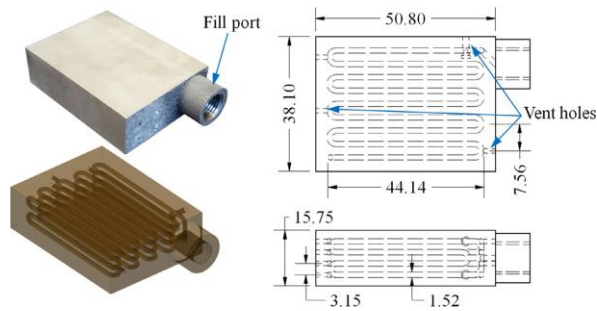


Figure 2. Ti-6Al-4V ML-OHP with fill port and vent holes: (top left) photograph after milling of faces, (bottom left) transparent view of channels in the part and (right) dimensioned drawings (in millimeters) [51].

The device was filled with Novac 7200 and tested for several factors to determine the performance with different orientations. The inside of the loop pipe shows a sintered wick like behavior with the working fluid and can be taken as a factor for reduced start up power. The built material shows no major flaw in the final design which would result in the blockage or reduction of performance. The device is tested with different orientation and with different filling liquids as well. The device which was tested empty showed the maximum thermal resistance and the thermal resistance of other tests are shown in figure 3.

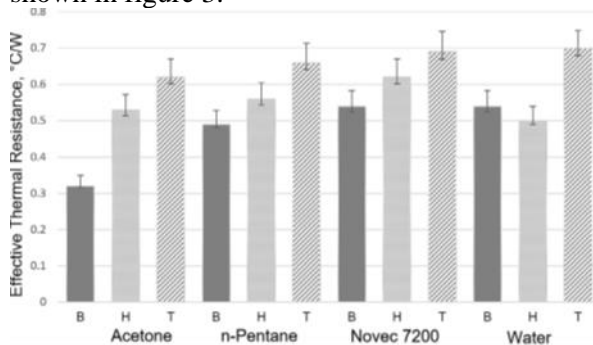


Figure 3.

Another study by Esarte et.al.[38] was focused on creating a loop heat pipe to cool an LED with the power output of 80W. The study focuses on building a wick structure using the AM technology and improving the performance of the loop heat pipe. The tests were done using different testing fluids as water and acetone for knowing the overall performance. The design and method of the wick was made for the best capillary structure and water capillary performance required. The printing process and final product is shown in figure 4.

The final product has the porosity of 17% and shows a great capillary performance evaluated in

the study. The capillary performance of the wick is compared in the figure 5, with different fluids.

The test results of the thermal conductivity and thermal resistance also shows a good increase in performance with different heat load. The effect of fluid charge together with ambient temperature was finally addressed. A higher mass charge is preferable for higher heat loads and vice versa but considering critical restrictions regarding minimum and maximum fluid charge values, according to operative conditions, aiming to avoid excessively high operating temperatures inside the LHP. It was therefore finally charged with 22 g of methanol for our case study as was demonstrated in the previous section. The LHP that has been developed here can effectively control the operating temperature, and the LED junction temperature, under 100 °C for a representative heat load of 80 W, at different ambient temperatures, showing thermal resistance values of under 0.15 °C/W.

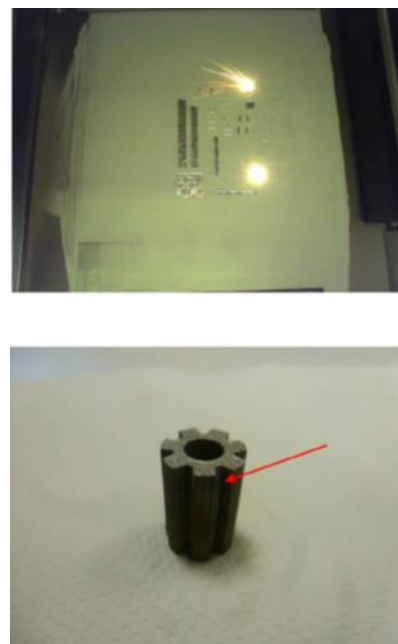


Figure 4. Fabrication of the primary wick, (a) printing procedure highlighting the laser points; (b) final result with a scaffold porosity of 17% [38].

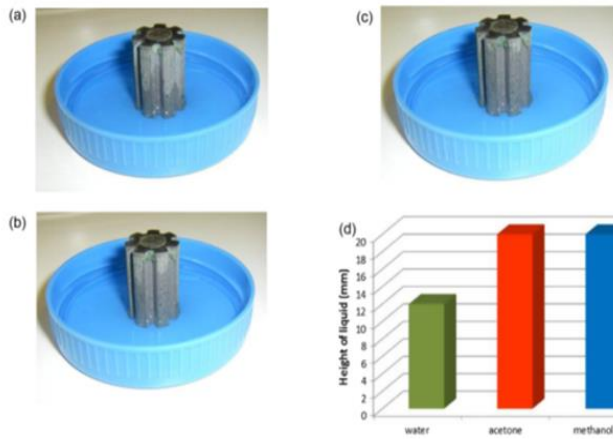


Figure 5. Capillary pumping test, (a) water rising up the primary wick after 5 min; (b) acetone at the top of the primary wick after 1 second; (c) methanol rising up the primary wick after 1 second; (d) comparative heights of the three fluids [38].

The test results of the thermal conductivity and thermal resistance also shows a good increase in performance with different heat load. The effect of fluid charge together with ambient temperature was finally addressed. A higher mass charge is preferable for higher heat loads and vice versa but considering critical restrictions regarding minimum and maximum fluid charge values, according to operative conditions, aiming to avoid excessively high operating temperatures inside the LHP. It was therefore finally charged with 22 g of methanol for our case study as was demonstrated in the previous section. The LHP that has been developed here can effectively control the operating temperature, and the LED junction temperature, under 100 °C for a representative heat load of 80 W, at different ambient temperatures, showing thermal resistance values of under 0.15 °C/W.

The study done by Belfi et.al. [34] was focused on the development of a flat loop heat pipe using the DMLM (direct metal laser melting), by using aluminum alloy as the base material. The design of the LHP is shown in the figure 6.

The tests were done with same heating power of 200W and different cooling temperatures from 0 to -40 °C and two different filling ratios (50%,55%). Also, the test bench was tested horizontally and with 4-degree inclination. The results are based on the thermal resistance ratio (TRR), which should be as low as possible. The inclined setup and higher filling ratio of 55% showed lower TRR than the other equivalents.

Overall, the design of the LHP showed a great promise for heat transfer performance and it can be adapted according to different requirements as well.

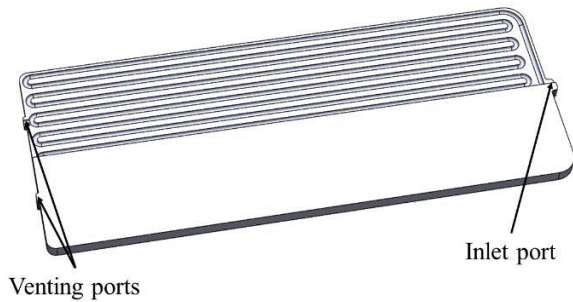


Figure 6. FPPHP CAD model used for the DMLM print job made with aluminum powder and layer resolution of 25 μm and 50 μm [34].

Another study is done on development of wick structure to be used in LHP by Hu et.al.[40] couple years ago, where he studied the effect of 3D printed wick structures with different hole sizes for the mesh. The structures made are very similar to wire mesh, typically used in stacks to produce the structure. The design made by the additive manufacturing is shown in figure 7.

The difference in the hole sizes changes the porosity and the overall heat transfer ability of the wick structure. The study states the heat transfer coefficient is highest and permeability is lowest for the small hole sample and vice versa for the large holes. The samples were put inside of the LHP and tested with same heat loads of varying degrees. The results showed that the sample with median hole size which has permeability and effective thermal conductivity of $2.13 \times 10^{-10} \text{ m}^2$ and $5.38 \text{ W}/(\text{m K})$ respectively, showed the most stable behavior and presented the best heat transfer coefficient and lower thermal resistance even in higher loads. The study showed a way of making the porous structure based on changing the hole size, which is an effective way of making the mesh of LHP with the entire properties depending on the hole size specification. For future studies the structure will be a good baseline to achieve the optimum mesh structure.

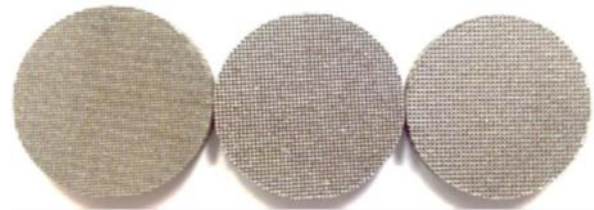


Figure 7. Photo of three 3D printed wicks for the experiment (from left to right Samples A, B and C) [40].

There are couple of studies done by Jafari et.al.[39, 41] in the year 2018 and 2020 on development of a wick structure in general heat pipe applications as well. The first study is based on the testing of the capillary performance of the additively manufactured wick structure. The study also tested with 4 different liquids and checked the rising in the wick structure over time. The properties of 3D printed wick was also tested with various studies where it's showed a better value of the parameters and predicted to be better at heat transfer abilities. The second study was based on the development and testing of a 3D printed wick structure of a flat heat pipe, based on the phase change heat transfer characteristics. The structure of 3D printed mesh is showed in figure 8 with the comparison with conventionally made mesh screens. The figure shows that the design made by 3D printing has similar basic structure with non-smooth outer shapes. The wick made by additive manufacturing showed slightly higher thermal capabilities that the normal screen counterpart.

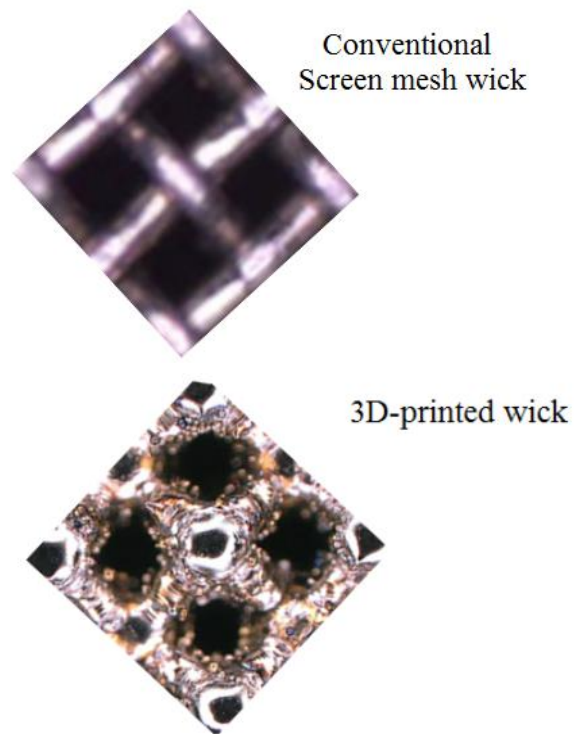


Figure 8. manufactured part pore shape and size compared to conventional screen mesh wicks [41].

Another study on the wick structure is done by Kaur et.al. [19] to be used in heat exchanger. The study is a review of all the lattice structures used in heat exchanger or similar operations, by

Table 1. Structural and Thermal properties of resultant product in terms of the build material during additive manufacturing.

Author	Process	Material	Type of the device	Speed of production	Product roughness	Thermal resistance	Thermal conductivity	Relative thermal conductivity ratio
Thompson et.al.	SLM	Ti-6Al-4V	Flat plate OHP	70µm thickness with 400mm/s scanning rate	40% of stainless steel		110W/mK	16.41
Ibrahim et.al.	PBF	Ti-6Al-4V	Multilayer OHP	40cm/s scanning rate	Variation of 80µm from place to place	0.32-0.7°C/W From different filling liquid	110W/mK	16.41
Esarte et.al.	SLM	Stainless steel	LHP (wick design)	20-75µm thickness with max 10m/s scanning speed	Minimum feature size 150µm	Max. 0.15°C/W	1.48 W/m K	26.9
Belfi et. al.	DMLS	AlSi10Mg	Flat plate PHP	20cm ³ /h max scan speed	25µm layer – 2.053µm 50mm layer – 25.8160µm	Thermal resistance ratio down by 10%		
Hu et.al.	SLM (similar process)	316 stainless steel with other metals	LHP (wick)	20µm thickness with maximum 10m/s scanning speed		Minimum 0.031 for sample B	Sample A- 8.63W/mK Sample B- 5.38W/mK Sample C- 4.06W/mK	172.6 107.6 81.2
Ho et.al.	SLM	AlSi10Mg	1*1cm ² microstructure	550 mm/s	8.5µm		H = 0.7w/cm ²	
Jafari et.al.	SLM	Stainless steel	Wick to use for Heat pipes	Laser scan speed 7m/s	7.8–53.9µm			
Handler et.al.	PBF	AlSi10Mg and Ti-6Al-4V	Heat exchangers		15.68µm		110W/mK	16.41
Jafari et.al.	SLM	Stainless steel	Wick of FHP			Max 0.36°C/W	Max 820W/mK	122.38
Chao et.al.	SLM	aluminum	FHP (Grooves)	300mm/s	Less than 25µm	Max 7°C/W		

considering the process of study and evaluation the different designs used. The different studies showed in the advantages of using additive manufacturing for making the design of the lattices used for their individual studies. The review done let us know that the additively manufactured lattices may result in significantly higher coefficient of heat transfer as compared to conventionally used metal foams. With the freedom of making multiple design adjustments allows different porosities through which higher effectiveness and thermal conductivity of device is to be expected.

The papers are also compared with the results and -abilities of the manufactured parts in Table 1. The analysis in Table 1 can also compare the working range and resultant workability of all the devices as well.

4. Nature of additive manufacturing related to heat pipe manufacturing

The additive manufacturing is the future of making the special grade or special designs in heat pipe. With the advantages of the technology, there are still some challenges and precautions to keep in check if we are making the products. The study of different additive manufacturing technologies gives us the idea about the adversities related to designs and maintaining the criteria to create the final product in which the adversities are minimized. There are few things and procedures which needed to be evaluated during and after the manufacturing process, to create a safe and specified final product. Some of the points which are very important to keep in mind when we are making the heat pipes from additive manufacturing are discussed here.

4.1. Investigation for the abnormalities inside the heat pipe-

There are many possibilities for the imperfections and abnormal structures formation, in terms of additive manufacturing in general. When it comes to the heat transferring devices such as heat pipes where we need to make sure the internal structure is functional as well as in accordance to our required task. The main requirements of a heat pipe come with the vacuum and fluid holding capacity of the final design. The main problem to worry about the final products are to find the trapped powder and

cracks inside of heat pipe. The cracks which can create the gap in the wall of heat pipe and can prevent it from being sealed altogether. The heat pipes with cracks even when they are functional holds a serious threat to the

operational life and conditions of the heat pipe. The crack can loosen and deteriorate the wall slowly in high heating condition which is a main drawback if we are considering the working environment of heat pipes. The determination of where the cracks form and which variables control them is a very important part of the study in achieving a satisfactory final device. There is another main concern about the powder being trapped in the final product due to the additive manufacturing being a layer by layer creation method. The powder inside the product can be removed but sometimes due to the informal deigns on the internal of heat pipes; specially LHPs. The heat pipes made with additive manufacturing should be tested for the powder trapped inside to make sure the powder inside becomes negligible; this will give the working fluid inside the heat pipe chance to be purest and work the best of its abilities. There are few methods which can help us to inspect the cracks and powder trapped inside. The most commonly known method is to use the CT scan machine to check for the imperfections in the product and the test must only be conducted when the level of imperfections doesn't generate a scarcity on the integrity of the product. The main agenda for minimizing the cracks and powder inside the heat pipes are to create a safe product which will not leak due to crack in high heat load. Even though the disadvantages of the powder trapped inside is not proven and needs further research, which can provide an insight to the positive and negative effects of such scenarios. We have done some CT scan with Phoenix Vtomex S240 machine of the model built for a LHP made from additive manufacturing using aluminum alloy as the base. The machine is equipped with a 180 kV/20 W high-power nano focus X-ray tube with best detail detectability of 0.2 micrometer as well as for 3D analysis of higher absorbing objects of up to 10 kg weight and 500 mm in diameter with micro CT. Figure 9 and figure 10 are examples of testing the product with a CT scan machine.

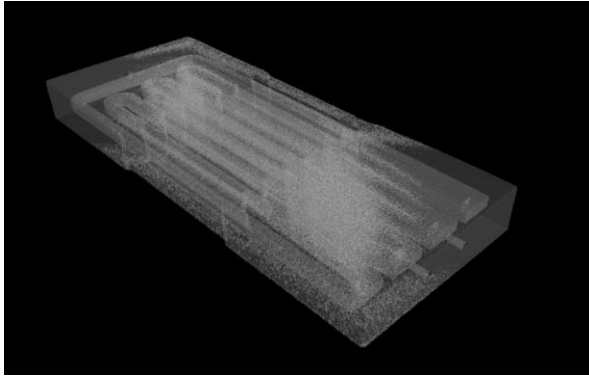


Figure 9. Inspection of Powder stuck inside the LHP using Phoenix Vtomex S240 CT scan machine.

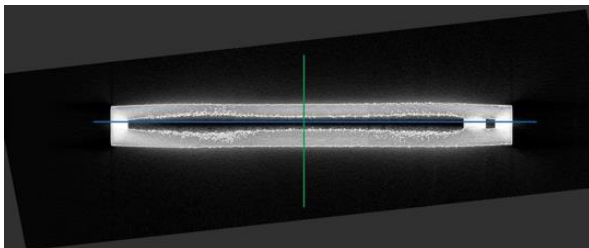


Figure 10. Cross section view of the LHP to show variation in internal surface (Phoenix Vtomex S240 CT scan machine).

Figure 9 shows us the overall design seen the scan machine and can tell us in case of trapped powder and cracks what are the percentages and where exactly to look at for finding such cases. The image shown does not have any serious crack or trapped powder; but in case of the cases happening, it will be visible with the bright spectrums.

Figure 10 is also a very subtle case of observation because of the size of device shown is too small. The device internal passage shows the imperfections and non linear boundaries with the particulate bumps. The crevices and bumps shown in the figure are now so significant but in some cases can create an abnormally behaving heat pipe or heat transfer devices. The boundary should be in the range of deviation from center and should not create a significant peak or valley.

4.2. Laser power and heat management-

Another very important variable is to keep in mind is that in additive manufacturing the overall conditions and input variable plays a significant roles in creating the perfect device. The two main input variables for controlling and determining the power to smoothness of final product surface are; laser input power and printing speed (hatch speed). The general specification of the speed and power of laser is dependent upon the size of device as well the base powder used for

manufacturing. As we can generalize and observe the aluminum alloy requires less laser power than titanium alloy because of the melting points of both the powders. Even though the titanium alloy can produce smoother and cleaner surfaces; the high power from laser produces high heat which can damage or separate the layers of the production. This phenomenon can cause serious damage and render the final product unusable for the cause. Specially for the heat transfer devices the structure which is not strongly bonded can cause fatal accident and cause physical and monitory harm in the working environments. The devices are sometimes also used in special conditions such as space or vacuum; where the dangers of such become even greater. The heat output of the laser power should be minimizing to cause these kinds of harmful effects. The speed of the production should also be optimizing as the faster production speed can cause the product to not form properly and the slower productions peed can cause the product to lose its adhesive capabilities and not tie together.

For additive manufacturing techniques the scanning and hatching speed control depends upon the skin or layer formation of the structure and the size of skin can also be varied depending on the condition. The different kinds of skins or zones are determined during the slicing process at the start of production. Different zones in the slices of a part require different scanning and hatching strategies. This is because the solidified slices can interact with the solidified material in different ways. This is dependent on the thermal stresses inside and in between the slices, the desired material properties (for surface and volume of the parts), and the orientation of the parts on the platform.

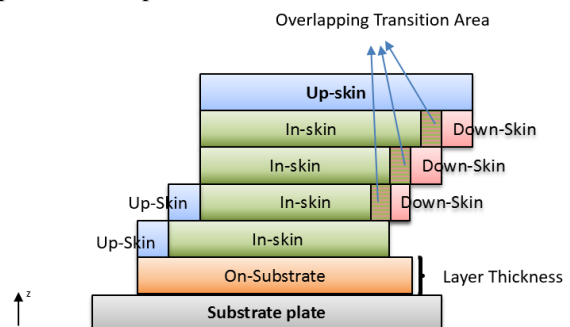


Figure 11. The skin formation shown with illustration, taken from Tongtai User manual Tongtai BP 1.0(For Tongtai AMP 160 3D printer).

In figure 11 the skin formation from the laser is given in detail and conjunction with the lower surfaces. The 'In Skin' is defined as the area

between ‘Up Skin’ and ‘Down Skin’ areas. Defining an overlapping area between Down Skin and In Skin is used to ensure solid lamination of In Skin and Up Skin areas helping to avoid occurrence of tiny regions with untreated material. The Part Border is a contour that surrounds the fill area, e.g. In Skin, Up Skin and/or Down Skin. It defines the outer surface of the part. By controlling these parameters and understanding the power we can create an outer surface similar to that of conformal manufacturing techniques.

Another problem was studied by Yap et.al. [52], who has shown the problem of thermal fluctuations and the how it can form cracks. The study reviewed several other authors and determined the final product can produce crack or notable damages due to this effect. The study also includes the thermal gradient mechanism by Kempen et.al [53], which shows the crack formation and separation of layers in figure 12. More recently, Yasa et al. [54] introduced “sectorial scanning” as a scanning strategy in SLM. This strategy breaks down a layer into small square grids and neighboring grids are scanned perpendicular to one another. It was found that “sectorial scanning” is able to reduce the residual stress significantly. This strategy is now available in processing software, such as Autofab or SLM Build Processor and is known as chessboard strategy.

The problem of crack formation and delamination is especially prevalent in ceramic materials. Ceramics require very high melting temperatures and have very low thermal conductivity, resulting in very high thermal gradient during the process.

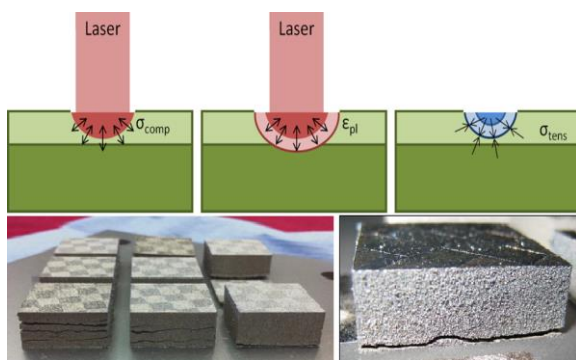


Figure 12. Temperature gradient mechanism (top) leading to crack formation and delamination (bottom). (Reproduced by Yap et.al. [52] with permission from Kempen et.al. [53] at an joint effort.)

4.3. Control of the manufacturing parameters-

There are some parameters which are also important for the final production of heat pipe devices and other structures. The main parameter which should be kept under some specifies condition is density of production. Some cases may require the light weight of the product but in case of heat pipes; the quality of material is significantly more important. The density can make a very big difference when it comes to the vacuum capabilities of the LHP and if it is not up to par ca cause failure of the device. The general case requires the relative density to be higher than 98% to be expected as better quality, but for some cases it should be even higher. For example, the LHP design created by us with different densities, had some difference in terms of packing of the overall structure. The situation is also experienced, where the part is printed using Tongtai AMP 160 3D printer. The LHP is printed with 94-96% density and is showing very high leaks even on the surface where the channels are not exactly beneath. The product develops a structure where, bubbles formed under water when the air is supplied to the LHP, also the pressure measured from the connected gauge also showed the pressure to be dropping over time. Also the surface of the LHP is forming the bubbles even at the points where the channels are not exactly under the holes. This phenomenon also presents the general failure of the packaging of the design. For the application such as LHP the tight packaging is required and the density should be higher. Another device is made by choosing higher density of 98.5%, which showed no leaks under water along with no pressure drop over time of two days in observation. We can say for the application of making heat pipes the density should be chosen at the higher end of spectrum; even it may increase the production time.

5. Conclusion

The study showed the developments and implementations of the AM techniques through different attempts and literature. The overall progress in Heat pipe production with AM has been continuously increasing throughout the years but can only considered to be in preliminary state. This study provides an insight on the way to approach for this topic with the aspects of selecting the right materials, the right methods, and the difficulties in production. By the overall consideration the future studies can be

oriented into a path depending on the requirements of the study. We can deduce some guidelines based on the research done previously

- The constraints of design being a limiting factor on specialized devices, compels the additive manufacturing to be a feasible option. Even with the manufactured parts, the general properties seem on par to be used professionally.
- Various selection of materials to be used on different situations should provide a peace of mind, when using to make or to be used with the heat transfer device.
- There are several devices that can benefit from using additive manufacturing-based parts made from optimization through several refinements. The devices such as LHP, heat exchangers and thermal peripherals.
- There are several factors such as density of the product and quality of production, which impacts the final results and needs to be considered at each level of production. The adversities are also needs to be checked and based on the conditions and factors should be minimized for best output.

Acknowledgement

We would like to Thank National Science and Technology Council (NSTC), Taiwan, Republic of China, for supporting and funding the development of our research with project number 109-2221-E-032 -014 -MY2.

References

- [1] Faghri, A.J.J.o.h.t., Review and advances in heat pipe science and technology. 2012. 134(12).
- [2] Chan, C., et al., Heat utilisation technologies: A critical review of heat pipes. 2015. 50: p. 615-627.
- [3] Chen, X., et al., A review of small heat pipes for electronics. 2016. 96: p. 1-17.
- [4] Tang, H., et al., Review of applications and developments of ultra-thin micro heat pipes for electronic cooling. 2018. 223: p. 383-400.
- [5] Monroe, J., et al. Thermal performance and surface characterization of a selective laser melted flat-plate oscillating heat pipe. in 2015 International Solid Freeform Fabrication Symposium. 2015. University of Texas at Austin.
- [6] Ho, J.Y., et al. Enhanced nucleate pool boiling from microstructured surfaces fabricated by selective laser melting. in International Conference on Micro/Nanoscale Heat Transfer. 2016. American Society of Mechanical Engineers.
- [7] Jafari, D., W.W. Wits, and B.J. Geurts. An investigation of porous structure characteristics of heat pipes made by additive manufacturing. in 2017 23rd International Workshop on Thermal Investigations of ICs and Systems (THERMINIC). 2017. IEEE.
- [8] Esarte, J., et al., Performance assessment of a three-dimensional printed porous media produced by selective laser melting technology for the optimization of loop heat pipe wicks. 2019. 9(14): p. 2905.
- [9] Wrobel, R. and A. Hussein. Design considerations of heat guides fabricated using additive manufacturing for enhanced heat transfer in electrical machines. in 2018 IEEE Energy Conversion Congress and Exposition (ECCE). 2018. IEEE.
- [10] Jafari, D., W.W.J.R. Wits, and S.E. Reviews, The utilization of selective laser melting technology on heat transfer devices for thermal energy conversion applications: A review. 2018. 91: p. 420-442.
- [11] Azizi, A., et al. Additive laser metal deposition onto silicon for enhanced microelectronics cooling. in 2019 IEEE 69th Electronic Components and Technology Conference (ECTC). 2019. IEEE.
- [12] Fasano, M., et al., Passive heat transfer enhancement by 3D printed Pitot tube based heat sink. 2016. 74: p. 36-39.
- [13] Liu, C., et al., Development and experimental validation of a hybrid selective laser melting and CNC milling system. 2020. 36: p. 101550.
- [14] Hein, L., M.J.I.C.i.H. Mortean, and M. Transfer, Theoretical and experimental thermal performance analysis of an additively manufactured polymer compact heat exchanger. 2021. 124: p. 105237.
- [15] Ding, X. and L.J.J.o.M.P. Wang, Heat transfer and fluid flow of molten pool during selective laser melting of AlSi10Mg powder: Simulation and experiment. 2017. 26: p. 280-289.
- [16] Niknam, S.A., M. Mortazavi, and D.J.T.I.J.o.A.M.T. Li, Additively manufactured

- heat exchangers: a review on opportunities and challenges. 2021. 112(3): p. 601-618.
- [17] Nafis, B.M., et al., Additive manufacturing for enhancing thermal dissipation in heat sink implementation: A review. 2021. 42(12): p. 967-984.
- [18] Zhang, C., et al., Additive manufacturing of products with functional fluid channels: A review. 2020. 36: p. 101490.
- [19] Kaur, I., P.J.I.J.o.H. Singh, and M. Transfer, State-of-the-art in heat exchanger additive manufacturing. 2021. 178: p. 121600.
- [20] Moon, H., et al., Heat transfer enhancement of single-phase internal flows using shape optimization and additively manufactured flow structures. 2021. 177: p. 121510.
- [21] Pogson, S., et al., The production of copper parts using DMLR. 2003.
- [22] Zhang, D., Z. Liu, and C. Chua. Investigation on forming process of copper alloys via Selective Laser Melting. in *High Value Manufacturing: Advanced Research in Virtual and Rapid Prototyping: Proceedings of the 6th International Conference on Advanced Research in Virtual and Rapid Prototyping*, Leiria, Portugal. 2013.
- [23] Raab, S.J., et al., Thermal and electrical conductivity of 99.9% pure copper processed via selective electron beam melting. 2016. 18(9): p. 1661-1666.
- [24] Ikeshoji, T.-T., et al., Selective laser melting of pure copper. 2018. 70(3): p. 396-400.
- [25] Silbernagel, C., et al., Electrical resistivity of pure copper processed by medium-powered laser powder bed fusion additive manufacturing for use in electromagnetic applications. 2019. 29: p. 100831.
- [26] Kruth, J.-P., et al., Lasers and materials in selective laser sintering. 2003.
- [27] Calignano, F., et al., Direct fabrication of joints based on direct metal laser sintering in aluminum and titanium alloys. 2014. 21: p. 129-132.
- [28] Nalli, F., L. Cortese, and F.J.E.F.M. Concli, Ductile damage assessment of Ti6Al4V, 17-4PH and AlSi10Mg for additive manufacturing. 2021. 241: p. 107395.
- [29] Ishfaq, K., et al., A state-of-the-art direct metal laser sintering of Ti6Al4V and AlSi10Mg alloys: Surface roughness, tensile strength, fatigue strength and microstructure. 2021. 143: p. 107366.
- [30] Shi, L., et al., Evolution of multi pores in Ti6Al4V/AlSi10Mg alloy during laser post-processing. 2021. 176: p. 111109.
- [31] Thompson, S.M., et al., Additive manufacturing of heat exchangers: A case study on a multi-layered Ti-6Al-4V oscillating heat pipe. 2015. 8: p. 163-174.
- [32] McDonough, J.J.T.S. and E. Progress, A perspective on the current and future roles of additive manufacturing in process engineering, with an emphasis on heat transfer. 2020. 19: p. 100594.
- [33] McGlen, R.J.J.T.S. and E. Progress, An introduction to additive manufactured heat pipe technology and advanced thermal management products. 2021. 25: p. 100941.
- [34] Belfi, F., et al., Space structures with embedded flat plate pulsating heat pipe built by additive manufacturing technology: development, test and performance analysis. 2019. 141(9).
- [35] Handler, E., et al. Design and process considerations for effective additive manufacturing of heat exchangers. in *2017 International Solid Freeform Fabrication Symposium*. 2017. University of Texas at Austin.
- [36] Chang, C., et al., 3D printed aluminum flat heat pipes with micro grooves for efficient thermal management of high power LEDs. 2021. 11(1): p. 1-8.
- [37] Wu, F., A.M. EL-Refaie, and A.J.I.T.o.I.A. Al-Qarni, Additively manufactured hollow conductors integrated with heat pipes: design tradeoffs and hardware demonstration. 2021. 57(4): p. 3632-3642.
- [38] Esarte, J., et al., Optimizing the design of a two-phase cooling system loop heat pipe: Wick manufacturing with the 3D selective laser melting printing technique and prototype testing. 2017. 111: p. 407-419.
- [39] Jafari, D., W.W. Wits, and B.J.J.A.t.e. Geurts, Metal 3D-printed wick structures for heat pipe application: Capillary performance analysis. 2018. 143: p. 403-414.
- [40] Hu, Z., et al., Development of a loop heat pipe with the 3D printed stainless steel wick in the application of thermal management. 2020. 161: p. 120258.
- [41] Jafari, D., W.W. Wits, and B.J.J.A.t.e. Geurts, Phase change heat transfer characteristics of an additively manufactured wick for heat pipe applications. 2020. 168: p. 114890.

- [42] Cage, K., et al. Thermal Design and Testing of a Passive Helmet Heat Exchanger With Additively Manufactured Components. in International Manufacturing Science and Engineering Conference. 2018. American Society of Mechanical Engineers.
- [43] Arai, T. and M.J.A.T.E. Kawaji, Thermal performance and flow characteristics in additive manufactured polycarbonate pulsating heat pipes with Novec 7000. 2021. 197: p. 117273.
- [44] Koito, Y., H. Maehara, and T. Tomimura. Fabrication of Heat Pipes on an Acrylic Resin Board. in International Electronic Packaging Technical Conference and Exhibition. 2013. American Society of Mechanical Engineers.
- [45] Koito, Y., et al. A Capillary-Wick Heat Pipe Fabricated on a Plastic Board (Fundamental Experiments on Heat Transport Characteristics). in International Electronic Packaging Technical Conference and Exhibition. 2015. American Society of Mechanical Engineers.
- [46] Hideyama, F., et al. Fabrication of a Vapor Chamber on a Plastic Board. in International Electronic Packaging Technical Conference and Exhibition. 2015. American Society of Mechanical Engineers.
- [47] Koito, Y. and M. Kawaji. Performance of a pulsating heat pipe fabricated with a 3-D printer. in Heat Transfer Summer Conference. 2017. American Society of Mechanical Engineers.
- [48] Arai, T., M. Kawaji, and Y. Koito. Visualization of Two-Phase Flow in 3D Printed Polycarbonate Pulsating Heat Pipe With Aluminum Substrate. in International Conference on Nanochannels, Microchannels, and Minichannels. 2018. American Society of Mechanical Engineers.
- [49] Muthu, V., et al. Embedded thermal management solution for power electronics PCB using additive manufacturing. in 2017 Asian Conference on Energy, Power and Transportation Electrification (ACEPT). 2017. IEEE.
- [50] Wrobel, R. and A.J.I.T.o.I.A. Hussein, A feasibility study of additively manufactured heat guides for enhanced heat transfer in electrical machines. 2019. 56(1): p. 205-215.
- [51] Ibrahim, O.T., et al., An investigation of a multi-layered oscillating heat pipe additively manufactured from Ti-6Al-4V powder. 2017. 108: p. 1036-1047.
- [52] Yap, C.Y., et al., Review of selective laser melting: Materials and applications. 2015. 2(4): p. 041101.
- [53] Kempen, K., et al., In Solid Freeform Fabrication Symposium Proceedings. 2013.
- [54] Yasa, E., et al. Investigation of sectoral scanning in selective laser melting. in Engineering Systems Design and Analysis. 2010.

Enhanced wicking effect on femtosecond laser treated porous microgroove structured surface

Seunghwan Lee¹, Jaeseon Lee^{1*}

¹ *Innovative Thermal Engineering Laboratory, Ulsan National Institute of Science and Technology
50 UNIST Rd., Ulsan, Republic of Korea*

**Corresponding author email address: jaeseonlee@unist.ac.kr*

Abstract

Wicking ability of the boiling surface can lead to an increase in the critical heat flux (CHF), which is essential for stable thermal management. At nucleate boiling situation, bubble generation and surface rewetting occur repeatedly on surface and boiling heat transfer is maintained stably. However, under CHF condition, film boiling occurs on the boiling surface in which the superheat is rapidly increased and the heat transfer coefficient is reduced critically. Therefore, efficient boiling heat transfer is not achieved. In the present work, a porous microgroove surface structure is suggested to enhance CHF. Porous structure and microgroove structure help the boiling surface to quickly rewet with strong wicking capability, allowing film boiling to be delayed efficiently. The wicking ability of surfaces fabricated under various femtosecond laser processing conditions is evaluated through wicking volume flux measurement. The wicking effect on film boiling is explained through visualization at near CHF situation. Optimized fabrication condition is also determined. The optimized surface structure increases CHF by 186 W/cm^2 compared to the non-treated bare surface.

Keywords: Pool boiling; Critical heat flux; Femtosecond laser; Porous microgroove

1. Introduction

Boiling heat transfer (BHT) is a promising cooling approach due to its advantages, such as increased heat transfer amount, low wall temperature, and excellent heat transfer coefficient (HTC) [1-2]. BHT performance can be generally evaluated by characterizing superheat, HTC, and critical heat flux (CHF). The degree of superheat is defined as the difference between the surface wall and the fluid saturation temperature. It is essential in phase-change cooling when device surface temperature management is important. The magnitude of the HTC reflects the efficiency of the heat transfer method. At nucleate boiling condition, BHT is maintained at an appropriate superheat level through the stable bubble generation. However, local vapor film as heat resistance is formed on the boiling surface at film boiling situation, resulting in a rapid wall temperature rise and decreased HTC. At CHF condition, a vapor film is fully developed on heating surface and no additional phase-change boiling occurs leading to complete reduction of HTC. Evaluating CHF is necessary in boiling heat transfer applications since the transition to film boiling causes thermal management failure. CHF could be affected by various parameters such as capillary force, wettability, and bubble merging. Many research [3-8] attempts have been made to increase CHF or delay the transition to film boiling by surface modification. Li et al. [3] fabricated various nanoscale surface structures including nano-grass and nano-flower by chemical etching. It

explained the relationship between wicking effect and CHF improvement through direct visualization of the liquid- and solid-vapor interfaces. Mo et al. [4] suggested porous honeycomb surface structures by electrochemical deposition for enhancing BHT performance. Ha et al. [5] investigated pool boiling characteristics and critical heat flux mechanisms of microporous surfaces fabricated by sintering. Kim et al. [6] explained interface-induced liquid refreshing by silicon nanowire for extending CHF. Serdyukov et al. [7] demonstrated that the laser texturing of silicon surface can enhance CHF by super-hydrophilicity.

Here, we propose a porous microgroove structured surface for enhancing CHF of boiling surface. Porous structure is ensured through copper powder sintering. The empty space between the sintered powder is a suitable structure for quickly absorbing water into the boiling surface. A periodic microgroove structure is formed on the uppermost layer of surface via femtosecond laser treatment. The periodic microgroove structure itself induces capillary force by the structure morphology. Working fluid can be smoothly supplied to the microgroove channel. Normally periodic micro/nano ripple structures are induced by an ultrashort pulse laser which is slightly shorter than the wavelength of the laser [9]. The interference of the laser beam and a surface plasmon polariton are main factors for forming periodic micro/nano ripple structures [10]. The advantages of femtosecond

laser processing are short process time, accuracy, repeatability, and no thermal denaturation.

The synergy between porous structure and microgroove structure induces strong capillary wicking effect and high wettability, thereby efficiently inhibiting the generation of film boiling. Surface geometry and wettability according to femtosecond laser processing conditions are investigated. CHF for each specimen is evaluated by pool boiling experiment. The relationship between capillary wicking capability and CHF is investigated through bubble visualization and capillary wicking force measurement.

2. Porous microgroove surface structures

2.1. Femtosecond laser processing system

Figure 1 (a) shows a schematic of the femtosecond laser processing setup. This setup consisted of a 1030 nm femtosecond laser (Pharos 15-200-PP) with a pulse duration of 220 fs and a Galvano scanner with an f-theta lens. The laser beam was linearly polarized, and its polarization direction was rotated by using a half waveplate to be aligned parallel with the beam scanning direction. The copper sample was fixed using a porous chuck, and the laser beam was focused on the specimen surface. The focal length of the scanner was 160 mm, and the focused beam diameter was $50 \mu\text{m}$ at the sample surface. The laser beam had a gaussian energy distribution. The laser power was adjusted from the maximum of 11 W by using an attenuator at the maximum pulse repetition rate of 200 kHz. Nitrogen shield gas was supplied at a rate of 50 L/min to prevent oxidation.

2.2. Fabrication method

Figure 1 (b) shows fabrication processing of porous microgroove surface. The first step is sintering copper powder. The copper specimen was fixed with an alumina mold. $30 \mu\text{m}$ copper powder was set on copper specimen and powder was pressed by an alumina jig to form a copper powder layer with a thickness of 0.3 mm . Afterwards, copper powder was sintered under the condition of 500 mTorr argon gas, 850°C , and 1 h to prevent oxidation. The second step is femtosecond laser irradiation. The femtosecond laser was irradiated with a set power and scanning speed at the interval spacing of $50 \mu\text{m}$. The femtosecond laser energy induced melting on the sintered surface in which microgroove structures were formed at the top of a sintered surface. Each sample is named as: Bare,

only laser-processed sample (L1), only copper powder sintered sample (CP), copper powder sintered and laser processed sample (CP@L). Sintering and laser processing conditions for each surface are shown in Table 1.

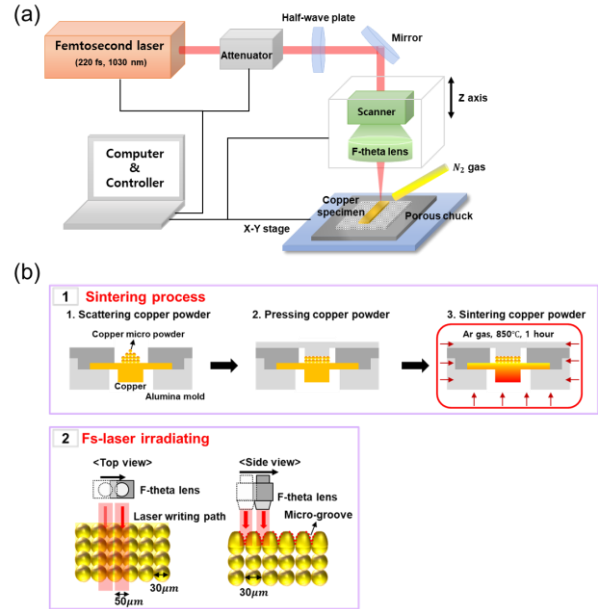


Figure 1. Fabrication system and method, (a) experimental setup of femtosecond laser processing system, (b) fabrication of porous microgroove structured surface.

Table 1. Femtosecond laser processing condition for each sample

Sample	Sintering	Laser power [W]	Scanning speed [mm/s]
Bare	X	0	0
L1	X	11.5	7
CP	O	0	0
CP@L2	O	8.6	14
CP@L3	O	11.5	14

2.3. Characteristics of surface structure

Surface structures of each samples are investigated using scanning electron microscope (SEM) and confocal laser microscope in Figure 2. Since surface roughness is related to wettability and cavity density, pool boiling performance can be affected. Therefore, surface polishing was performed to exclude the influence of the surface

roughness. Fine cracks that come from machining processes are observed on Bare sample (Figure 2 (a1-a2)). The average roughness of the Bare surface is $0.05 \mu\text{m}$, which can be considered a very smooth surface (Figure 2 (a3)). On CP surface which is only sintered, a porous structure is formed because copper micro particles are locally combined with surrounding particles as it melts (Figure 2 (b1-b2)). The diameter of sintered copper powder is about $25\text{-}35 \mu\text{m}$. The micro-sized voids between copper particles induce capillary forces, allowing water to be easily absorbed into inner surface. CP surface has a contact angle of 0° which means that CP surface has super-hydrophilicity.

Only femtosecond laser treated L1 surface structure has periodic microgroove structure (Figure 2 (c1-c2)). The ultrashort wave of the femtosecond laser induces appropriate interference of the laser beam and surface plasmon polariton to form a unique micro/nano ripple structure. The width and height of the microgroove structure are $50\text{-}55 \mu\text{m}$ and $40\text{-}45 \mu\text{m}$ (Figure 2 (c3)), respectively. This microgroove surface generates high surface energy leading to surface wetting with a contact angle of 0° . Grape cluster-shaped cavities are formed in a high density along microgroove ridge. The high wettability and dense nucleation density can be factors that affect pool boiling performance enhancement.

CP@L samples are fabricated by femtosecond laser processing on sintered surface. Periodic micro-groove structures are commonly formed on the top of the sintered layer. CP@L3 surface (Figure 2 (e1-e2)) treated with higher laser intensity has a higher clustered cavity density along the microgroove ridge than CP@L2 (Figure 2 (d1-d2)). The porous microgroove surface structure on CP@L2 has a width of about $50 \mu\text{m}$ and a height of $50 \mu\text{m}$ (Figure 2 (d3)). The surface morphology of CP@L3 consists of a width of about $50 \mu\text{m}$ and a height of $70 \mu\text{m}$ (Figure 2 (e3)). CP@L surfaces also have a contact angle of 0° . Since all of the surface-treated samples have a contact angle of 0° , it is difficult to explain the difference in wicking force between the samples by contact angle. Therefore, the wicking ability must be clarified through comparable parameters such as volume flux.

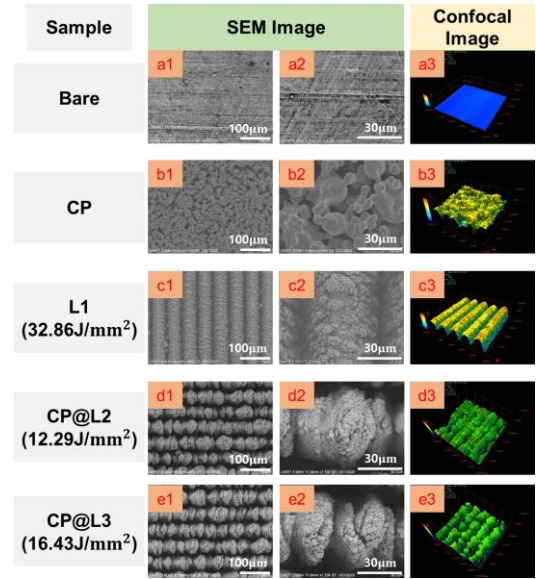


Figure 2. SEM images and confocal laser microscope images of surface samples.

3. EXPERIMENTAL METHOD

3.1. Pool boiling experimental setup

The constructed pool boiling test setup was installed and a comparative evaluation was performed for each test sample. Figure 3 (a) shows the pool boiling experimental setup. Pure deionized water was used as a working fluid which is boiled during 2 hours to degas dissolved air. The lower part of the test setup was composed of a heating block combined with a coil heater. The heating section was insulated by a insulation box filled with glass wool to reduce heat loss. Using the Z-stage, the upper part of the heating block and the lower part of the test sample are in contact. To minimize contact thermal resistance, a thermal grease (Kryonaut, THERMAL GRIZZLY) is applied between the heating block and the test sample. A heat resistant glass wall was used for bubble visualization during boiling. A high-speed camera (MIRO M310, PHANTOM) was used to visualize the bubble motion on the test surface. The pool has a sufficient internal volume of $90 \times 90 \times 195 \text{ mm}^3$ in which the boiling is not affected by the surrounding wall. An immersion heater was submerged in the pool to keep the working fluid at a saturation state. The immersion heater was controlled by a temperature controller (TC200P, TOPS) with the submerged K-type thermocouple (T.C1). The working fluid temperature was maintained at the atmospheric saturation temperature of 100°C . A coil condenser was installed on the top of the setup to recondense the

vapor generated by pool boiling. The coil condenser was supplied with sufficient cooling water flow that a circulating bath supplied 5°C of cooling water at a flow rate of 18 L/min. Figure 3 (b) shows the geometry of the heating block and test sample. A total of three K-type thermocouples were inserted at intervals of 15 mm on the heating block. Through this temperature data, the amount of heat supplied was calculated. The total height of the heating block is 160 mm, and the part of 120 mm was combined with the coil heater. The top column, which conducts heat, has a height of 40 mm and 15 mm in diameter. To calculate the surface temperature of the test sample, a K-type thermocouple was inserted 4 mm away from the bottom of the specimen. The specimen was fixed using a PEEK flange and a PEEK cover. Since the fixing part of samples is very thin as 0.2 mm, thermal resistance is very high. It is judged that the heat loss escaping to the specimen's fixing part is negligible.

Since forming an oxide layer can be an obstacle to obtaining stable experimental results, a 50 nm titanium layer was deposited on all surfaces by plasma sputtering. The thickness of titanium layer on surfaces has a nano-scale with 50 nm much smaller than the scale of surface structures. It does not affect the surface structure and wettability. The supplied heat flux was increased in small steps until CHF point was reached. Reaching the CHF point was identified as a sudden rise in the wall temperature. The heat flux supply was cut off at the CHF point to prevent the system from overheating.

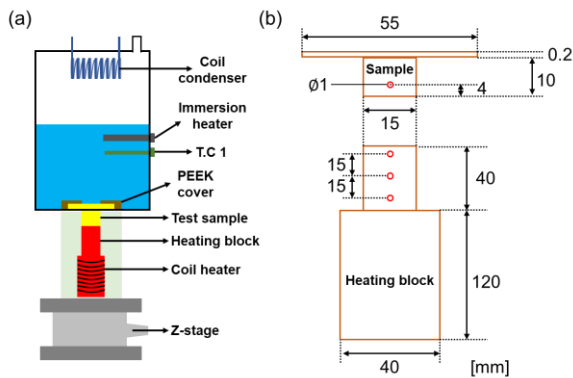


Figure 3. Pool boiling experimental setup, (a) schematic of pool boiling heat transfer test and (b) drawing of heating section.

3.2. Data reduction

The obtained data were reduced to calculate the critical heat flux. The data from the test setup were acquired using the NI-DAQ module. All data were measured in a steady state. Every data point was tested two times to ensure repeatability. During the pool boiling test, the heat flux transferred to the sample surface is calculated based on one-dimensional conduction in the heating block as follows,

$$q'' = k \frac{T_5 - T_3}{X_{tc,5-3}} \quad (1)$$

where q'' is heat flux, k is thermal conductivity of heating block, T_5 is measured temperature by T.C 5, T_3 is obtained temperature by T.C 3, $X_{tc,5-3}$ indicates the distance between T_5 and T_3 .

The surface temperature of test sample is obtained as follows,

$$T_s = T_2 - X_{tc,2-s} \frac{q''}{k} \quad (2)$$

where T_2 is measured temperature by T.C 2, $X_{tc,2-s}$ indicates the distance between T_2 and T_s .

The wall superheat is calculated as follows,

$$\Delta T = T_s - T_1 \quad (3)$$

where T_1 refers the saturation temperature measured by T.C 1.

All thermocouples used are k-type and have a measurement error of ± 1.1 . The error propagation method proposed by Kline and McClintock [11] was used to calculate the uncertainties in experimental parameters. The calculated heat flux uncertainty is ± 2.08 .

4. RESULTS AND DISCUSSION

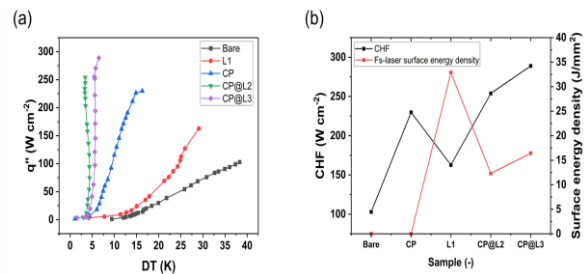


Figure 4. Boiling heat transfer characterization, (a) boiling surface heat flux (q'') as a function of wall superheat (DT) and (b) critical heat flux for each test sample.

Pool boiling experiments on both bare and modified surfaces were conducted. Pool boiling performance was identified by the boiling curve (Figure 4. (a)), defined by the surface heat flux (q'') as a function of the wall superheat (DT). The critical heat flux (CHF) for each sample is specified (Figure 4. (b)). The bare Cu surface has a higher superheat than other structured surfaces at the same heat flux. It is observed that the pool boiling curve is skewed to the right. The CHF on the bare surface is $102.9 \pm 2.08 \text{ W/cm}^2$. The surface rewetting plays an important role in suppressing the formation of the vapor film. However, on the bare surface, there is no surface structure that can allow the surface to be quickly wetted with water. The CHF of L1 surface characterized by the microgroove structure is $162.7 \pm 2.08 \text{ W/cm}^2$. Considering that the CHF of CP surface is $229.7 \pm 2.08 \text{ W/cm}^2$, the porous structure of CP surface is more advantageous for CHF improvement than the microgroove structure of L1. The CHF of CP@L2 and CP@L3, in which the porous structure and the microgroove structure are combined, reaches $253.9 \pm 2.08 \text{ W/cm}^2$ and $278.7 \pm 2.08 \text{ W/cm}^2$, respectively. The CHF of CP@L3 is about 2.7 times higher than that of the bare sample. The CHF improvement varies with the surface morphology. Bubble motion was visualized at near CHF conditions for each test sample to closely analyze the relationship between surface morphology and CHF enhancement.

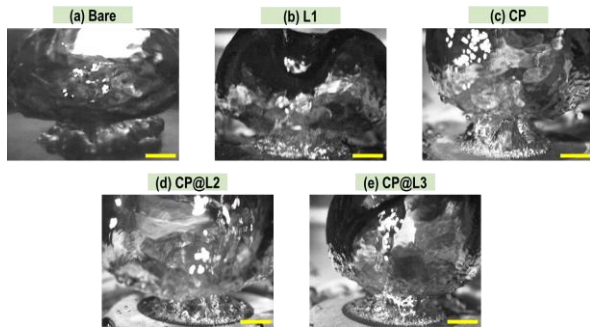


Figure 5. Visualizing bubble motion at near CHF situations, (a) Bare, (b) L1, (c) CP, (d) CP@L2, and (e) CP@L3.

Bubble motion of each sample was visualized at near CHF situations in which supplied heat flux is 90% of CHF. The lower yellow scale bar represents 5 mm. For the bare surface, a very thick and stuck vapor film was observed on the boiling surface (Figure 5 (a)). Since the bare surface does not have a surface structure that induces rewetting, bubbles cannot quickly fall off the boiling surface leading to liquid blanket. Therefore, complete film

boiling occurs at a relatively low heat flux. The L1 surface (Figure 5 (b)) and the CP surface (Figure 5 (c)) inhibited developing vapor film as bubbles with a diameter of $\sim 2 \text{ mm}$ were generated steadily on the boiling surface. The continuous generation of tiny bubbles indicates that the working fluid is continuously supplied to the boiling surface. The rewetting on L1 surface is accelerated by the capillary channel of the microgroove structure. The porous structure on CP surface replenish liquid fast into void space. The CP@L2 (Figure 5 (d)) and CP@L3 (Figure 5 (e)) surface shows distinct bubble dynamics. The microbubble layer of less than 1 mm was formed on the boiling surface and the bubbles were removed at high frequency. The thickness of vapor film is also relatively thin. First, the capillary channel of microgroove structure absorbs working fluid and secondarily the absorbed liquid spreads into the porous space. The superposition of capillary forces in both structures can maximize the rewetting ability on boiling surface. It is verified through visualization that the porous microgroove surface structures are suitable for delaying generation of film boiling. Since all surface-treated samples are super-hydrophilic with a contact angle of 0° , a physical quantity such as volume flux should be considered to evaluate the relative wicking ability.

The test setup and measured wicking capability for each sample are shown in Figure 6. The test setup consists of fluorinated ethylene propylene (FEP) tube, Z-stage, and 3D printing mold (Figure 6 (a)). The FEP tube is filled with water column

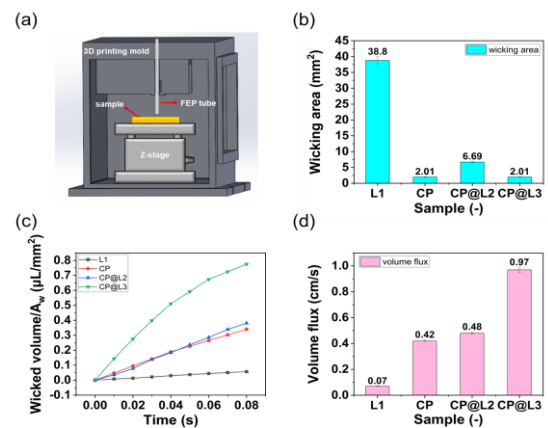


Figure 6. Comparison of wicking ability, (a) test setup for identifying capillary characteristics, (b) wicking area, (c) wicked volume over wicking area, and (d) calculated volume flux for each sample.

which has a height of 2 cm and a test sample is placed on the z-stage. Adjusting z-axis using z-stage, the end of FEP tube contacts with the test sample. At this time, water in tube is absorbed into the test surface by capillary force. The absorbed volume is calculated using the difference in height of the water column over time as follows,

$$V = \Delta h \times A_t \quad (4)$$

where V is absorbed volume into capillary surface, Δh is the difference in height of the water column, A_t is internal cross-sectional area of tube.

The wicking area (A_w) indicates the interface area between capillary water flow and sample surface. The wicking area was measured using ImageJ software. Volume flux is the velocity at which water is soaked into the capillary surface. Volume flux can be calculated by the following equation,

$$\dot{v} = \frac{\partial}{\partial t} \left(\frac{V}{A_w} \right) \quad (5)$$

where \dot{v} is volume flux, t is a variable of time.

Figure 6 (b) shows wicking area for each sample which have various area according to surface structures. Wicking area of L1 surface is 38.8 mm^2 which is a large area compared to other samples. This is because the fluid receives capillary force dominant in the horizontal direction along the microgroove channel of L1 surface. The CP surface shows a wicking area with 2.01 mm^2 in which the porous structure of CP surface induces dominant capillary force in the vertical direction. CP@L2 and CP@L3 have a wicking area of 6.69 and 2.01 mm^2 , respectively. Liquid is absorbed along the microgroove channel and penetrates into the porous empty space. Wicked volume per wicking area is shown in Figure 6 (c). The height variation of the water column is measured with a high-speed camera at 200 frame per second (fps). The wicked volume at the interval of time step 0.01 is calculated by equation 4. The CP@L surfaces, which utilizes the capillary force of the porous structure and the microgroove structure simultaneously, shows the excellent wicked volume. CP@L3 is processed with strong laser intensity to form deeper grooves than CP@L2. The increased hydraulic diameter leads to reducing frictional pressure loss when water is absorbed into the microgroove channel. In Figure 6(d), the volume flux for each sample is expressed. L1 and CP have a volume flux of 0.07 and 0.42 cm/s , respectively. The volume flux of CP@L2 and CP@L3 with porous microgroove structures are 0.48 and 0.97 cm/s , respectively. The volume flux of the porous microgroove

surfaces is greatly improved by the synergistic effect of each two structure compared to the single structures.

5. CONCLUSIONS

Porous microgroove surface structure can be fabricated through sintering and femtosecond laser processing. The porous microgroove surface structure shows improved wicking ability and wettability over the bare surface. This is derived from the collaboration of the porous structure and the microgroove structure, which are advantageous in generating wicking effect. Film boiling can be effectively delayed as working fluid is stably supplied to the boiling surface. It means that the porous microgroove surface structure is able to enhance CHF. It was confirmed through visualization that the increased volume flux of the porous microgroove surface induces the continuous generation of microbubbles at near CHF situation and helps the liquid film to drop off quickly. It is clear that there is a proportional relationship between the volume flux of the sample and the enhancement of CHF. The optimized surface structure increases CHF by 186 W/cm^2 compared to the non-treated bare surface.

Acknowledgment

This material is based upon work supported by the research funding through the National Research Foundation of Korea (NRF), funded by the Ministry of Science and ICT (Grant No. NRF-2020R1A5A8018822), and through the Korea Institute of Energy Technology Evaluation and Planning (KETEP) grant, funded by Ministry of Trade, Industry & Energy (Grant No. 20212020800270) of Republic of Korea.

References

- [1] S. Mori, Y. Utaka. Critical heat flux enhancement by surface modification in a saturated pool boiling: A review. *Int. J. Heat Mass Transfer*, 2017. 108: p. 2534-2557.
- [2] G. Liang, I. Mudawar. Review of pool boiling enhancement with additives and nanofluids. *Int. J. Heat Mass Transfer*, 2018. 124: p. 423-453.
- [3] Li et al. Liquid film-induced critical heat flux enhancement on structured surfaces. *Sci. Adv.*, 2021. 7: eabg4537.
- [4] D.C. Mo, S. Yang, J.L. Luo, Y.Q. Wang, S.S. Lyu, Enhanced pool boiling performance of a porous honeycomb copper surface with radial diameter gradient. *Int. J. Heat Mass Transfer*, 2020. 157: 119867.

[5] M. Ha, S. Graham, Pool boiling characteristics and critical heat flux mechanisms of microporous surfaces and enhancement through structural modification. *Appl. Phys. Lett.*, 2017. 111: 091601.

[6] B.S. Kim, G. Choi, S. Shin, T. Gemming, H.H. Cho, Nano-inspired fluidic interactivity for boiling heat transfer: impact and criteria. *Sci. Rep.*, 2016. 6: 34348.

[7] V. Serdyukov, S. Starinskiy, I. Malakhov, A. Safonov, A. Surtaev, Laser texturing of silicon surface to enhance nucleate pool boiling heat transfer. *Appl. Therm. Eng.*, 2021. 194: 117102.

[8] S.H. Musavi, H. Adibi, S.M. Rezaei, An experimental study on bubble dynamics and pool boiling heat transfer of grinding/laser-structured surface. *Heat. Mass. Trans.*, 2022. <https://doi.org/10.1007/s00231-022-03287-y>.

[9] K. Lee, H. Ki, Enhancing coupling efficiency in laser keyhole welding of copper using femtosecond laser surface modification. *Optics & Laser Technology*, 2021. 139: 106943.

[10] S. Sakabe, M. Hashida, S. Tokita, S. Namba, K. Okamura, Mechanism for self-formation of periodic grating structures on a metal surface by a femtosecond laser pulse. *Phys. Rev. B*, 2009. 79: 033409.

[11] S. Kline, F. McClintock, Describing uncertainties in single-sample experiments. *Mech. Eng.*, 1953. 75: pp. 3-8.

Ceria-Based Robust Superhydrophobic Surfaces for Heat Pipe Applications

Jaehwan Shim¹, Jun Soo Kim¹, Jungchul Lee¹, and Youngsuk Nam^{1*}

¹ Korea Advanced Institute of Science and Technology (KAIST), Daejeon, Republic of Korea

*Corresponding author email address: ysnam1@kaist.ac.kr

Abstract

Superhydrophobic (SHPo) surfaces can provide high condensation heat transfer due to facilitated droplet removal. However, hydrophobic coatings with adequate robustness remain elusive due to the extreme environments within many heat pipe applications, which has limited the application potential of such SHPo surfaces. Here, we propose two types of robust and scalable ceria-based SHPo surfaces, where the superhydrophobicity was induced by not surface coating but hydrocarbon adsorption on the surfaces. The fast recovery of superhydrophobicity was also possible by incorporating hydrocarbon source as a binder to the ceria-based coating. The coating could provide the enhanced durability even after various environmental threats including UV exposure, acidity/salinity exposure, mechanical and frosting damages. Although the coating has the relatively low thermal conductivity and high thickness, the number of small droplets on the surfaces resulted in the improvement of condensation heat transfer performance, which demonstrates that the proposed surfaces are promising technologies to develop robust and scalable SHPo condensers for real-world applications.

Keywords: Ceria; Superhydrophobicity; Durability; Condensation heat transfer performance

1. Introduction

Enhancement of condensation heat transfer performance can provide significant economic and environmental benefits to various energy systems[1]. Prior studies for SHPo condensers with facilitated droplet removal ability have been actively reported, however, issues for long-term stability have also been raised[2]. To overcome the limitations of conventional hydrophobic coatings, rare earth oxides have been suggested as potential materials, but there are still a lot of limitations including the low scalability and the lack of understanding of hydrophobicity mechanisms[3].

In this work, we developed robust and scalable ceria-based SHPo surfaces, where the superhydrophobicity was induced by not surface coating but hydrocarbon adsorption on the surfaces. To shorten the long air exposure time (> 4 days) for hydrophobicity, we incorporated hydrocarbon source as a binder to the coating. Despite the relatively limited thermal conductivity and thickness, the suggested ceria-based surfaces showed the enhanced condensation heat transfer performance, and the improved durability even under various harsh conditions.

2. Sample fabrication process

We introduced two type of ceria coatings. The first type was fabricated using a wet chemical process, named HAC (hydrocarbon-adsorbed ceria). The substrates were dipped into a solution containing $\text{CeCl}_3 \cdot 7\text{H}_2\text{O}$ particles, H_2O_2 solution and DI water for 120 min. Then we exposed the samples to an ambient condition for 4 days to induce

superhydrophobicity.

We also developed another type of ceria coating, named PAC with polydimethylsiloxane (PDMS)-assisted ceria. The substrates were immersed into the solution containing CeO_2 nanoparticles, PDMS and n-hexane for a second, and taken out the samples using a dip coater.

3. Sample characterization

The morphology of the developed surfaces was observed through a scanning electron microscope (SEM) (Figure 1). CeO_2 particles were randomly aggregated to form the hierarchical structures on HAC, and pinecone-like hierarchical structures with CeO_2 particles and PDMS were formed on PAC. The coating thickness of HAC and PAC was $\sim 4 \mu\text{m}$ and $\sim 6 \mu\text{m}$, respectively.

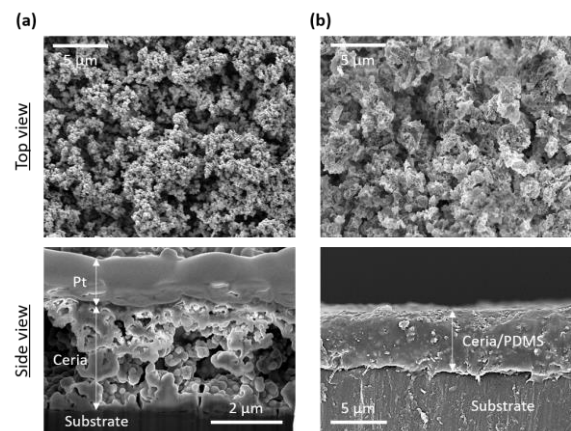


Figure 1. Top-view and side-view SEM images of (a) HAC and (b) PAC surfaces.

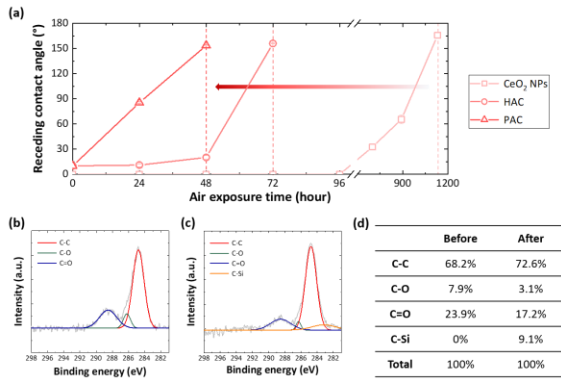


Figure 2. (a) Comparison of receding contact angle along with the exposure to air after Ar plasma treatment. XPS spectra of C 1s of the CeO₂ NPs (b) before and (c) after PDMS-rich environment exposure. (d) The ratio of each chemical bonding obtained by XPS analysis before and after PDMS-rich environment.

To confirm the capability of recovering superhydrophobicity after being damaged, two types of ceria coatings and CeO₂ nanoparticles (NPs) coated-sample were repeatedly exposed to the argon plasma treatment to remove the adsorbed hydrocarbon and an ambient condition until the superhydrophobicity was recovered (Figure 2a). The superhydrophobicity of all coatings was well-recovered, but PAC provides much faster recovery time. To verify this result, CeO₂ NPs were exposed to PDMS-rich environment and observed in X-ray photoelectron spectroscopy (XPS) analysis. Despite the newly formation of C-Si bonding, the ratio of C-C increased and those of C-O and C=O decreased (Figures 2b, 2c and 2d). It is attributed to the volatile hydrocarbon molecules released from PDMS and the facilitated reaction between airborne volatile molecules and ceria[4,5].

4. Durability tests

Heat pipe applications are typically subjected to various malfunctional factors. First, we evaluated the coating durability against the environmental threats including UV and acidity/salinity exposure. To investigate the effects of environmental factors, we exposed the sample to 10 mW/cm² of UV irradiation at 70°C (Figure 3a) and repeatedly exposed to an acidity/salinity solution containing NH₄Cl, NaCl, MgSO₄, KCl, CaCO₃, HNO₃ and DI water (Figure 3b). Then we measured the receding contact angle, which is sensitive to the coating degradation. The results show that no detectable decrease in the receding angle was observed even after 100 days of UV exposure and 15,000 cycles of chemical exposure.

Since the frosting/de-frosting cycles have

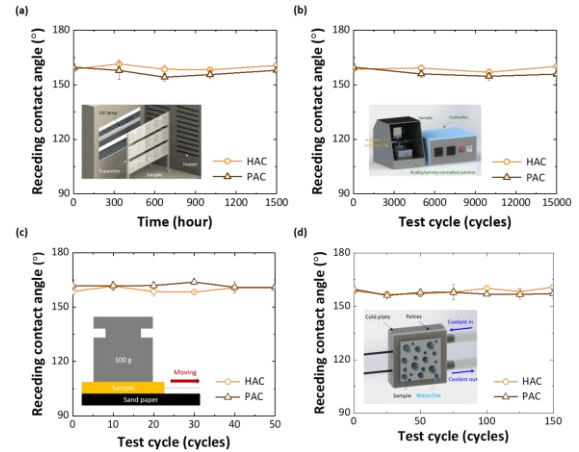


Figure 3. Durability test setups and results for (a) UV resistance, (b) acidity/salinity resistance, (c) mechanical damage and (d) repetition of frosting/de-frosting.

negative effects on the mechanical properties of coating, we conducted the successive frosting/de-frosting cyclic test at the surface temperature -21 °C for frosting and 23 °C for de-frosting (Figure 3c). Additionally, we performed the abrasion test using 600 mesh sandpaper with constant pressure of 2.5 kPa (Figure 3d). The results also demonstrate that both HAC and PAC provided almost consistent receding angle after 50 cycles of abrasion and 150 cycles of frosting/de-frosting, which clarifies the excellent robustness of our coatings.

5. Condensation behavior and the resulting thermal resistance

Typically, conventional SHPo surfaces (Ref) with the relatively small structure/coating thickness and high thermal conductivity are expected to provide higher condensation heat transfer performance. However, the number of relatively small droplets (N_{droplet}) on HAC and PAC was larger compared to Ref (Figures 4a and 4b), which can compensate for penalties of the thickness and thermal conductivity (Figure 4c). Figure 4d shows

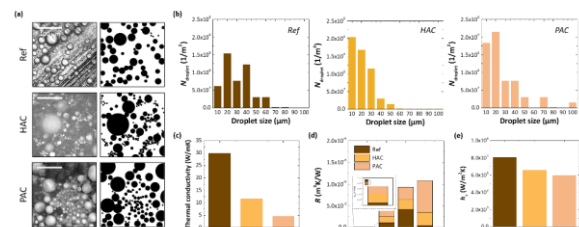


Figure 4. (a) Microscopic and processed images of condensates configuration on each sample. (b) N_{droplet} according to droplet size obtained from the processed images. (c) Thermal conductivity, (d) R and (e) h_c on the investigated samples.

thermal resistances (R) including droplet curvature (R_{cur}), vapor-liquid interface (R_{int}), droplet conduction (R_{drop}) and coating/structure conduction (R_{cs}) calculated using our thermal network model[6]. Based on the result, we calculated condensation heat transfer coefficient (h_c). The difference in h_c between the SHPo samples is not significantly large, and HAC and PAC with high robustness could provide much benefit in terms of long-lasting performance.

6. Condensation behavior without NCGs

To determine the precise condensation heat transfer performance, a controlled condensation chamber was organized to thoroughly eliminate any non-condensable gases (NCGs) (Figure 5). The environmental chamber was evacuated using a vacuum pump until the vacuum pressure of ~ 0.5 Pa was achieved. Degassed water vapor was introduced into the chamber by boiling DI water in a reservoir at 300°C for 60 min, and cold water of 5 L/min was circulated from a thermal bath to control surface temperature. Test sample was attached to a copper block with a thermal paste, and the block was insulated by polycarbonate covers to prevent condensation on any surface other than the test sample. And the condensation behavior was recorded with a CCD camera.

Figure 6 shows the resulting behaviors with increasing supersaturation level (S), the ratio between the vapor pressure and the saturation pressure at the surface temperature. For Bare Cu, which is clean and smooth hydrophilic Cu, vapor condensed and formed a thin liquid film on the entire surface independent of S (Figure 6a). Meanwhile, Figure 6b shows the dropwise condensation behaviors on PAC where discrete spherical condensates were formed and grew to sizes approaching the capillary length (~ 2.7 mm) before being shed off by gravity. Thanks to more efficient droplet removal ability, we expect that the

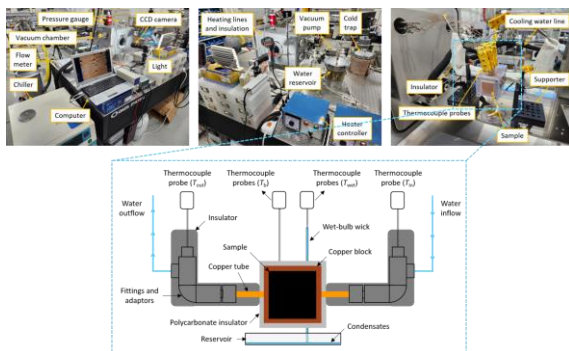


Figure 5. Environmental chamber setup for condensation heat transfer.

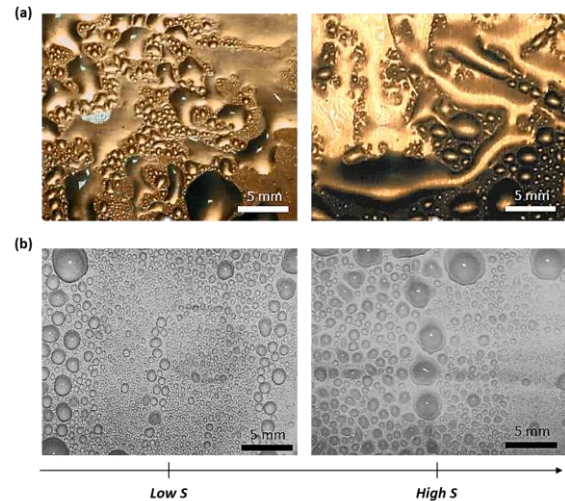


Figure 6. Condensation behaviors according to S on (a) Bare Cu and (b) PAC.

condensation heat transfer performance of PAC would be higher compared to that of Bare Cu.

7. Conclusion

In summary, we introduced robust and scalable SHPo ceria coatings. The faster recovery mechanism of the ceria coating with PDMS was investigated. The outstanding durability of ceria coatings was verified by the exposure to various malfunctional factors. Despite the relatively high thermal resistance related to the coatings, the number of small droplets on the surfaces results in the improvement of condensation heat transfer performance, which is also clarified in the environmental condensation chamber. These findings suggest that the proposed coating can be a promising candidate for real-world applications.

References

- [1] Cho, H. J., Preston, D. J., Zhu, Y. and Wang, E. N., Nanoengineered Materials for Liquid-Vapour Phase-Change Heat Transfer. *Nature Reviews Materials*, 2017. 2.; No. 16092.
- [2] Seo, D., Shim, J., Moon, B., Lee, K., Lee, J., Lee, C. and Nam, Y., Passive Anti-Flooding Superhydrophobic Surfaces. *ACS Applied Materials & Interfaces*, 2020. 12.; p. 4068-4080.
- [3] Fu, S. P., Sahu, R. P., Diaz, E., Robles, J. R., Chen, C., Rui, X., Klie, R. F., Yarin, A. L. and Abiade, J. T., Dynamic Study of Liquid Drop Impact on Supercooled Cerium Dioxide: Anti-Icing Behavior. *Langmuir*, 2016. 32(24): p. 6148-6162.
- [4] Senzai, T. and Fujikawa, Fast Hydrophobicity Recovery of the Surface-Hydrophilic

Poly(dimethylsiloxane) Films Caused by Rechemisorption of Dimethylsiloxane Derivatives. *Langmuir*, 2019. 35:, p. 9747-9752.

[5] Oh, J., Orejon, D., Park, W., Cha, H., Sett, S., Yokoyama, Y., Thoreton, V., Takata, Y., and Miljkovic, N., The Apparent Surface Free Energy of Rare Earth Oxides is Governed by Hydrocarbon Adsorption. *iScience*, 2022. 25:, p. 103691.

[6] Shim, J., Seo, D., Oh, S., Lee, J. and Nam, Y., Condensation Heat-Transfer Performance of Thermally Stable Superhydrophobic Cerium-Oxide Surfaces. *ACS Applied Materials & Interfaces*, 2018. 10:, p. 31765-31776.

Thin and small evaporators of low cost for loop heat pipes

Wei Qu* , Zhihu Xue, and Jijun Yu

China Academy of Aerospace Aerodynamics (CAAA), Beijing, China

*Corresponding author email address: weiqucaa@163.com

Abstract

Evaporators are important for designing loop heat pipes. Four coupling designs are given to evaporators, including capillary wick, vapor-liquid isolating structure, strengthening rib and container. The integration and miniaturization are realized for evaporator, isolator and compensation chamber. The operating theories are analyzed for the overheated degrees of the capillary nuclear center, heat flux and working liquid film. The capillary nuclear centers function together with their imbibition and wetting the working fluid. The equivalent size of the capillary nuclear centers would affect the boundaries of overheated degrees and starting heat fluxes strongly to the evaporators. The optimization of both the working fluid selection and the sizes of the capillary nuclear centers could be coupled to increase the performance. The vapor is easily produced and divorced, the liquid has the smaller resistance to flow back, the vapor and liquid are isolated effectively, these could result in high performance of LHP evaporator. The thinner and smaller LHP evaporator could be realized together with the batch manufacturing and low cost. The design and optimization have wide application and prospect for thermal control of chip field etc..

Keywords: Vapor-liquid isolating; Capillary nuclear center; Boundaries of overheated degrees; The thinner and smaller LHP evaporator

1. Introduction

Loop Heat Pipe (LHP) is an important branch of heat pipe field. Generally, LHP consists of evaporator, isolator, compensation chamber, condenser, vapor line and liquid line. In 1971, the structure of LHP was invented and its principle was successfully tested by experimental results. At that time, the demand of thermal control was smaller. In addition, the invented structure is more complicated, the technology failed to meet the requirements. The next 20 years, the LHP developed slowly. After 1990, with the rapid speed of development of space technology, the demand for thermal control to the elements in spacecraft increased a lot. The advantages of LHP were continually developed and applied. The studies to LHP were correspondingly deepened.

From the beginning of the century, more than 20 years past, with the development of science and technology, the high performance LHPs are needed urgently, especially for the high heat flux evaporator, the long distance transportation, thinner and smaller size. Figure 1 shows several MINI LHP developed by Russian, one evaporator of them has the size of a coin. The design and the processing method are the crux of the matter of thin, small evaporator of high performance.

In space application, long and round evaporator of LHP were reported a lot. This kind of evaporator applied to cylinder surface heat flux. The inner capillary wick was usually cylinder of sintered powder or tube type correspondingly, anti-direction type was in majority.

If the evaporator is designed as the anti-direction type, then the direction of heat flux and the flowing vapor from the capillary wick are opposite. This type is not favor of high heat flux. The main reason is that the heating surface of the evaporator not be made the best. And the structure of this type is also complicated. The starting of the LHP evaporator depends strongly on the liquid distribution in LHP

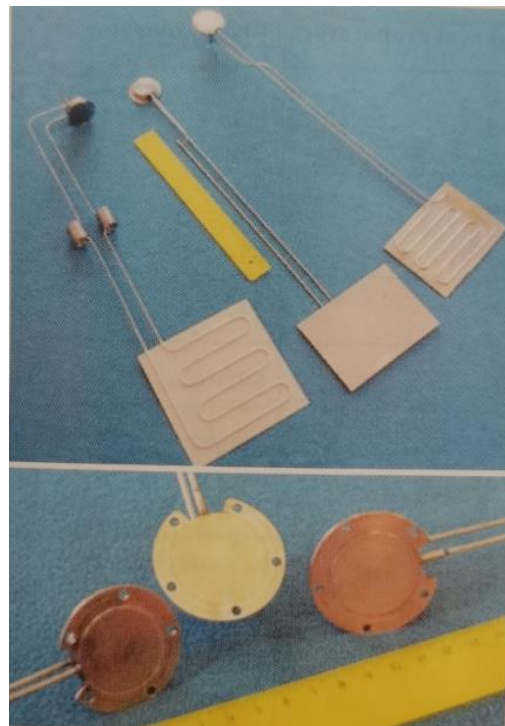


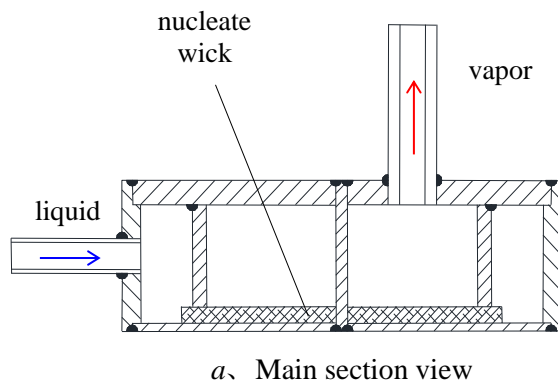
Figure 1. Mini LHP and coin-similar evaporator developed by Russian ^[1]

before operation. Many working conditions need be designed about the startup process. These demands place restrictions on the extended applications.

For some ground applications, the evaporators of LHP are designed as the flat type, there were many theoretical, experimental and test results reported. The inner structures were generally designed as the multi-channels, on the tops of them, the capillary wick sometimes was sintered, or the multi-layer wire mesh was coupled. These composite capillary wick structure could make the smaller liquid returning flow, in the mean time, the capillary pumped force could be bigger.

The tentative directions of designing LHP evaporator are composite capillary wicks as channels plus sintered power wick, channels plus wire meshes, and double-size pores etc..

The capillary structure would affect the performance of LHP evaporator, and the coupling method between the capillary wick and the container also should be paid much more attention. When the capillary wick of the LHP evaporator is fabricated, operating, the capillary wick need



temperature control, the design of LHP is hardly to do as one wishes.

This investigation has two considerations as following.

Firstly, the function of capillary nuclear centers is to be studied mainly. The sizes of capillary nuclear centers will play an important role to starting LHP evaporator. If the capillary force is only considered to affect the evaporator performance, the authors do not believe that is not comprehensive. Secondly, the theoretical analyses to LHP evaporators, especially for using the classic methods, were not reported previously.

Secondly, the classic theoretical analysis on LHP evaporator is expected to be obtained. There were less results reported up to now.

2. Thin and small evaporators of LHP

With the development of electronic technology, the integration degree of related equipment is getting higher and higher with the heat flux increased. However, the space becomes smaller and smaller for heat dissipation. This study faces the applicable field of heat dissipation on chip, hopes to

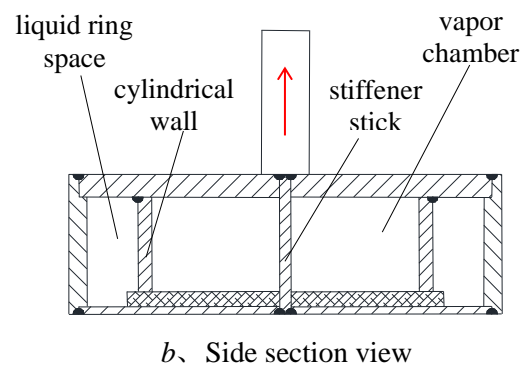


Figure 2. LHP evaporator types of circular plate -circular heating surface, that is, circular-circular combination

contact the container surface tightly, no matter for the types of grooves, of multi-layer wire meshes, of single and double pores sintered, or of other grooves coupling with wire meshes. Otherwise, the contact thermal resistance between the wick and the container would be bigger for heat transfer. There are many technologies of coupling contact as soldering, point soldering, swelling contact, compacting the couple etc.. However, there is also one problem produced, that is the technology is more complicated, and these are not beneficial to the scaling production and low cost.

Relative to the experimental studies, there are less theoretical reports about LHP. In the light of some special situations about the heat transfer and

design LHP evaporator quickly and easily, to realize high performance, miniaturization, and low cost structure.

2.1. high performance evaporator

As shown in figure 2, the evaporator has three functions as evaporating, vapor-liquid isolating and compensation chamber, they are integrated together. The evaporator consists of capillary nuclear centers, isolating ring, stiffener stick and the container. The container is often selected as materials of pure copper or pure aluminium etc., one word is the material of high thermal conductivity. Within the thickness range of permissible strength, the wall to contact the heating source should be as thin as possible, so the thermal

resistance of wall could be smaller.

The vapor-liquid isolating wall is cylindrical. It has the functions of two aspects, one is compressing the capillary wick to the heating wall; the other is that it could separate the outside liquid space from the inside vapor chamber effectively.

As shown in figure 2 and 3, the liquid passage is the annular wick at the bottom of compressing contact, from the peripheral liquid space to the vapor chamber in central section. From here, the liquid flows from the liquid space to the capillary nuclear centers vaporizing. The peripheral perimeter is larger, so the flow resistance is smaller. In the capillary wick structure, the liquid flows inward, the liquid is supplied by infiltration, sometimes the capillary structure is not necessary, the groove structures could meet the requirements.

Further more, the liquid space could be designed to avoid the surface of heating source, the produced vapor would assemble in the vapor chamber and flow to the vapor line. The flow resistance from the capillary nuclear wick to the vapor line is much smaller compared with that of vapor flows to the liquid space. So, the vapor would not flow back or block the liquid supply. The structure could make the liquid and vapor be isolated completely, the evaporator operation is kept to be stable and reliable.

The end section of the isolating ring would compress the capillary wick tightly, the fastening effects to the wick are simple and effective. For all the working conditions of the startup and stable operation for evaporators, the fitness between the capillary wick and the inner heating surface is guaranteed, so the reliability is good. The stiffener stick connected the upper and the lower surfaces of the container, fixed by thread screwing or soldering, it could locate and fix the capillary wick structure effectively. Further, the connection could increase the ability of pressure bearing of the container.

If the working fluid of freon categories is used, their viscosity is generally bigger, the bottom surface of the LHP evaporator could be optimized as multi-grooves fabricated or passages with vertical and horizontal structures, the composite capillary wick is formed plus the single or multi-layers wire meshes, or sintered multi-pore structures.

The high performance of LHP evaporator could be obtained easily by coupling capillary wick structure and working fluid. Before starting the evaporator up, the working fluid distributes in the capillary wick at the bottom of evaporator, and the bottom of the liquid space. While the evaporator works, there is less working fluid in the

evaporator. The thickness of the liquid layer working is enough to be several millimeters, the thermal inertia could be smaller and the performance be higher.

Generally, the designed LHP evaporator is thin and small, the charging working fluid is small, it has high performance, high heat flux, small thermal inertia, high heat transfer capability, stable operation, high reliability, and long working life etc.. The LHP evaporator shown in figure 2 is easy for fabricating technology, the structure and method is simple and reliable, and is easy for mass production.

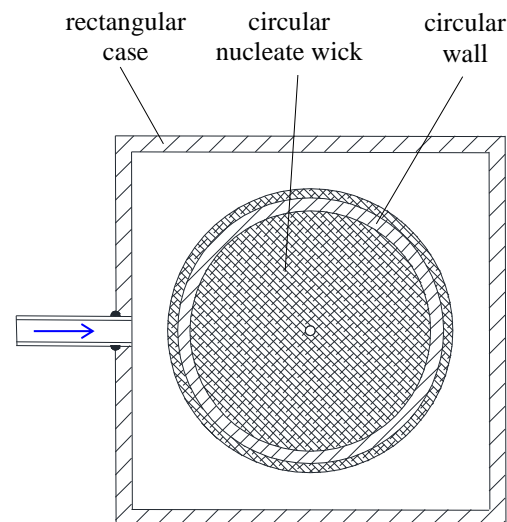
2.2. Four composite designs of thin and small LHP evaporator

Figure 3 shows the vertical views of three combinations of LHP evaporator. There are four combinations of the three plus the one given in figure 2. They each are integrated for evaporator, reservoir and isolator.

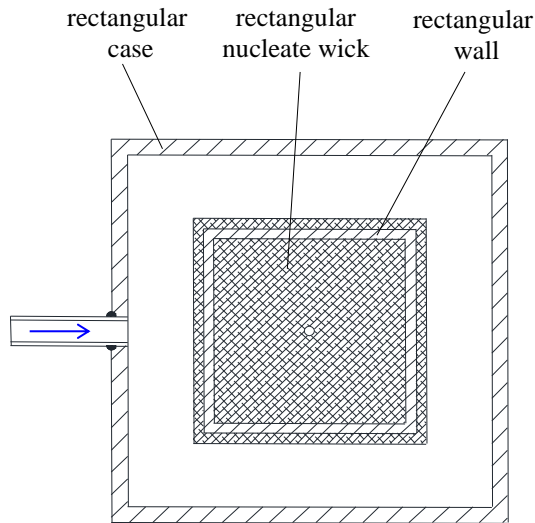
The structure illustrated in figure 3a, is the combination of rectangular plate evaporator and combination. The container is rectangular, the isolating ring is circular, the capillary wick and heating surface are circular surfaces.

The structure illustrated in figure 3b, is the combination of rectangular plate evaporator and rectangular heating surface, that is rectangular-rectangular combination. The container is rectangular, the isolating ring is rectangular, the capillary wick and heating surface are rectangular surfaces.

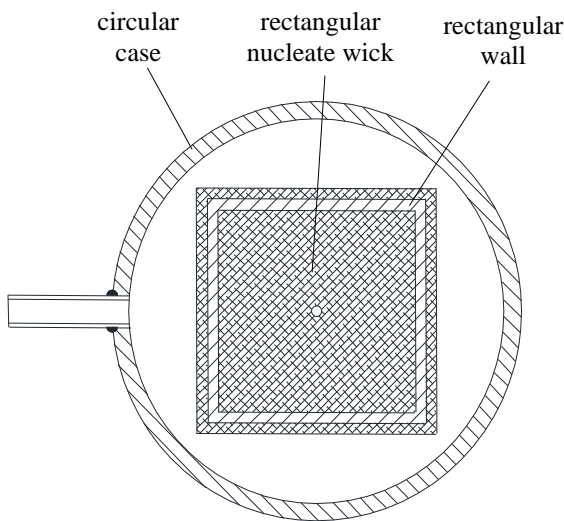
The structure illustrated in figure 3c, is the combination of circular plate evaporator and rectangular heating surface, that is circular-



a. Rectangular plate-circular heating surface, that is, rectangular-circular combination



b 、 Rectangular plate-rectangular heating surface, that is, rectangular-rectangular combination



c、 Circular plate-rectangular heating surface, that is, circular-rectangular combination

Figure 3. Vertical view of three combination designs for LHP evaporator

rectangular combination. The container is circular, the isolating ring is rectangular. The capillary wick and heating surface are rectangular surfaces.

The vapor-liquid isolating ring has rectangular and circular types, which is best to be selected depends on the shape of the heating surface. The size of the isolating ring cross-section designed would adapt the heating surface or slightly larger. During LHP evaporator operating, the surface area circled by the isolating ring is heated, while the outside the isolating ring, which belongs to the liquid space, would not be heated. In the vapor chamber, the produced vapor would escape from the bottom and

flow upward out into the vapor line. The flow resistance upward is much smaller than that is possible to get into the liquid space from the capillary wick between the isolating ring and the heating wall. For starting one LHP and the evaporator or operating stably, the isolating ring could guarantee the vapor and liquid be separated effectively,

The four composite evaporators include the liquid space, and the vapor chamber outside and inside the isolating ring respectively. The center points of top and bottom surfaces could be connected by one stiffener stick according to the vapor pressure and allowable strength. The vapor chamber is one flat cylindrical space like one coin, or flat square space. The vapor tube connects the upper end surface uprightly eccentrically, the stiffener stick is avoided to the tube end place. The liquid space is flat circular ring cylinder like a shim, or flat rectangular ring column, the liquid tube connects the column side surface at normal direction. The tube joints are designed to avoid interference.

The top end of the isolating ring was welded and sealed with upper surface; the bottom end connected the capillary wick. Through the suitable height of the isolating ring, the peripheral capillary wicks were compressed tightly to the heating surface. The capillary wick structure would contact the heating surface tightly by the surrounding isolating ring and the stiffener stick in the middle. The contact thermal resistance is decreased and the performance of the evaporator in increased. If the pressure of the working fluid is smaller, the welding process is not necessary, the assembly process is simple and workable, the mass production is easy to realize.

For some situations, the heating surface of the evaporator and the upper end surface could be punched in the middle, the aperture would coordinate and couple the stiffener stick. The end of the stiffener stick could be welded with the capillary wick, then connect the bottom surface by screw or welding. The stiffener stick could connect and prevent the two surfaces deform due to the pressure difference of inside and outside. The compression ability could increase one order of magnitude at least. If the evaporator is larger, if the allowable strength is exceeded, the number and arrangement could be added to improve.

The circular or rectangular capillary wick inside the evaporator is selected according to the heating source. The capillary wick cake has a hole at the center, the stiffener stick would go through it. It has the function of location to the capillary wick when assembling. The capillary wick cake is equal to or is a little larger than the surrounding circular or rectangular isolating ring. This design would relax

the machining accuracy of the capillary wick, furthermore, it relaxes also the equipment of the manufacturing.

For designing thin and small evaporator, the vapor tube joint and liquid tube joint are perpendicular to each other, and the diameter of the former is larger than the latter. If the space is big enough, the vapor tube joint and liquid tube joint could be set parallel on the top surface. During stable operating of LHP, the flow rates of vapor and liquid are the same. Due to the density difference of the vapor and liquid, the velocity of vapor is much larger than that of liquid, so the tube diameter difference should be considered to decrease flow resistance as low as possible. Then the high performance of LHP could be realized.

3. Theoretical analysis to evaporator of LHP

Capillary wick is the most important structure to be optimized. In this study, the first function of capillary wick is that it provides the vaporization nuclear cores; the second function is that it keeps the heating surface wet and supplies the vaporizing working fluid. There is small amount needed for circulating working fluid, so the charging amount of working fluid need not be too much. That is, the smaller liquid amount is, the smaller thermal resistance is, the small thermal inertia is, the higher performance is. In principle, the evaporating liquid film should be small, as long as the heating surface

is not dried out.

For normal operation of LHP, the liquid returning mass to the evaporator equals to the vapor mass flowing out, the balance is reached. As shown in figure 4, from starting to the stable operating, there would be producing many vapor bubbles, they ceaselessly grow up and escape the liquid layer. When LHP works, the thickness δ_1 is from 1mm to 10mm, the working liquid amount is small.

3.1. The bubble producing, growing up and divorcing in evaporator

The nuclear theory of phase change tells that, if the heat flux to the evaporator wall is increased to a certain extent, the smaller vapor bubbles would produce at the vaporization cores and grow up to the critical divorcing diameter. Then the bubbles flow into the large space, that is vapor chamber.

For globe bubbles, as shown in figure 4(a), the pressure difference between the inner and outer bubbles could be written by Laplace-Young as.

$$P_v - P_l = \frac{2\sigma}{r_n} \quad (1)$$

Where, r_n is equivalent pore radius of the capillary wick of the heating wall.

The capillary wick is considered as the equivalent pores which distribute uniformly. The surface of the capillary wick is immersed by the working fluid liquid. When the heating flux is

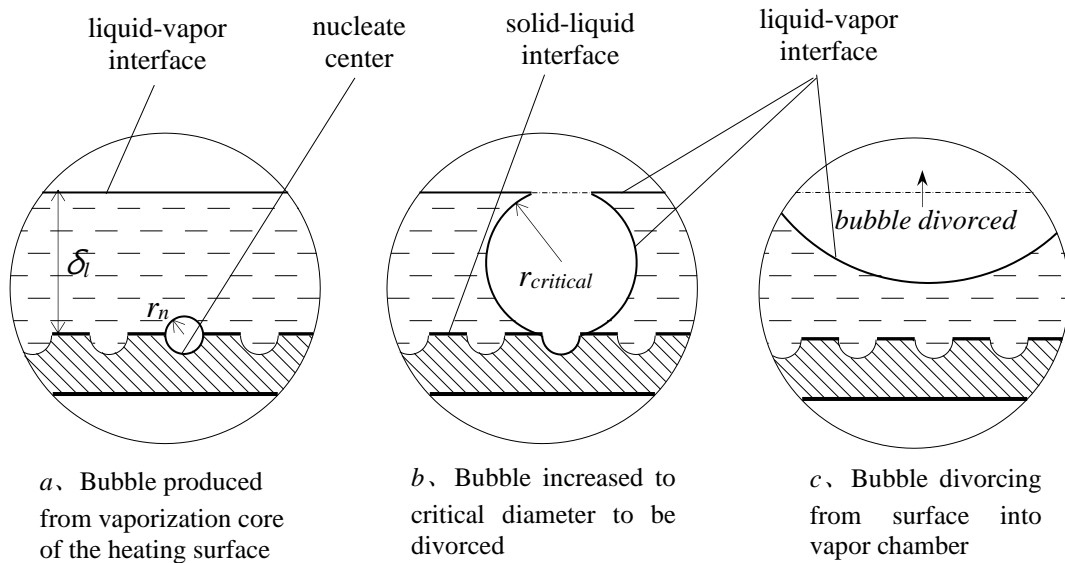


Figure 4. Process of bubble producing, increasing and divorcing from the heating surface of LHP evaporator.

Table 1. Physical properties of four working fluids at 100°C.

Working fluids	Formulae	Pressure, 10 ⁵ Pa	Latent heat of vaporization, kJ/kg	Surface tension, 10 ³ N/m	Thermal conductivity of liquid, W/(m.°C)	Gas constant
Water	H ₂ O	1.01	2257.0	58.91	0.68	461.9
Methanol	CH ₃ OH	3.80	1040.0	15.55	0.18	259.8
Ethanol	C ₂ H ₅ OH	2.26	927.0	15.50	0.17	180.7
Acetone	C ₃ H ₆ O	3.30	472.0	15.00	0.13	143.3

bigger enough, the pores are the bubble source, the phase change from the liquid to bubble vapor corresponds to absorbed heat from heat flux. For the small vapor bubbles at the produced sites, the pressure relation at the interface is written as.

$$\pi r_{globe}^2 (P_n - P_l) = 2\pi r_{globe} \sigma \quad (2)$$

Where, P_n and P_l are the vapor and liquid pressures at the vaporization pores respectively.

Equation (2) is transformed as the type of Laplace-Young equation below.

$$P_n - P_l = \frac{2\sigma}{r_{globe}} \quad (3)$$

From equation (1) and (3), when the bubbles grow up to the size of r_{globe} , however not reach the critical divorcing radius, the pressure difference between the large globe bubble and the new produced bubble is given as.

$$\Delta P_{globe} = P_n - P_v = 2\sigma \left(\frac{1}{r_n} - \frac{1}{r_{globe}} \right) \quad (4)$$

In order to correlate the relative parameters, the equation of Clausius-Claberon is below,

$$\frac{dP_v}{dT_v} = \frac{h_{fg} \rho_v}{T_v} \quad (5)$$

The vapor of bubble is considered as the ideal gas, the state equation is the following.

$$\rho_v = \frac{P_v}{RT_v} \quad (6)$$

Considering equation (5) and (6) simultaneously, there is equation below.

$$\frac{dP_v}{P_v} = \frac{h_{fg}}{R} \frac{dT_v}{T_v^2} \quad (7)$$

Integrate equation (7) from the state (P_n, T_n) to (P_s, T_s) , the following is.

$$\ln \frac{P_n}{P_v} = \frac{h_{fg}}{R} \left(\frac{1}{T_v} - \frac{1}{T_n} \right) \quad (8)$$

Considering equation (4) again, equation (8) becomes below.

$$T_n - T_v = \frac{RT_n T_v}{h_{fg}} \ln \left[1 + \frac{2\sigma}{P_v} \left(\frac{1}{r_n} - \frac{1}{r_{globe}} \right) \right] \quad (9)$$

As shown in figure 4(b), if the globe bubble grows up to the critical state, the bubble would divorce from the wall. This illustrates that the phase change heat transfer reaches the beginning point of the vigorous evaporating. Generally speaking, the critical bubble is much bigger than original produced bubble at the wall. There would be several orders of magnitude larger, possible. So, the following approximate equation is as.

$$\frac{1}{r_n} - \frac{1}{r_{critical}} \approx \frac{1}{r_n} \quad (10)$$

When the bubble is produced at the beginning, the wall is overheated a little extent, the wall temperature is below.

$$T_n = T_v \sqrt[1 - \frac{RT_v}{h_{fg}} \ln \left(1 + \frac{2\sigma}{P_v r_n} \right)] \quad (11)$$

According to equation (11), the degree of superheat is written as.

$$\Delta T = T_n - T_v = T_v \left\{ \sqrt[1 - \frac{RT_v}{h_{fg}} \ln \left(1 + \frac{2\sigma}{P_v r_n} \right)] - 1 \right\} \quad (12)$$

This equation is a classic, conducted from all the classic equations physically, it correlates the degree of superheat, the size or the radius of the capillary wick, the properties of the working fluid, temperature and pressure etc., could be called as the critical degree of superheat.

Again as shown in 4(a), the thickness of the liquid layer is δ_l , to be more accurate, it is the thickness of the vapor and liquid mixture during normal operating of LHP evaporator. If δ_l is smaller,

and the returning liquid is cooler, that is the degree of supercooling is bigger, then the heat flux of the evaporator wall could be written by Fourier law below.

$$q = \lambda_l \frac{T_v}{\delta_l} \left\{ 1 / \left[1 - \frac{RT_v}{h_{fg}} \ln \left(1 + \frac{2\sigma}{P_v r_n} \right) \right] - 1 \right\} \quad (13)$$

3.2. Results and discussion

Four working fluids, they are water, methanol, ethanol and acetone, are used for analysis and calculation. In order for comparing conveniently, the results of 100°C temperature is selected as the baseline. The physical properties of these working fluid are listed in table 1.

The boundaries of superheat degree as a function of the size of vaporization pores are shown in figure 5, for the evaporator heating wall. The results of water and ethanol are illustrated. If the vaporization pores of the capillary wick are designed from 1 micron to 10 microns, the degree of superheat would decrease with the increasing of r_n . For smaller radius of the vaporization pores, the degree of superheat changes severely, the slopes of the absolute value are larger. While for bigger radius of the vaporization pores, the degree of superheat changes gently, the slopes of the absolute value is smaller. Further, for the same radius of the vaporization pores, the degree of superheat of water is much bigger than that of ethanol.

These results enlighten us two aspects. Firstly, the size of vaporization pores need be designed, the equivalent radius should be suitable. The optimization of the capillary wick not only includes the wetting ability, but also the easiness of the phase change heat transfer. The balance point should be found. Secondly, the working fluid of low boiling point is easier to operate than that of high boiling

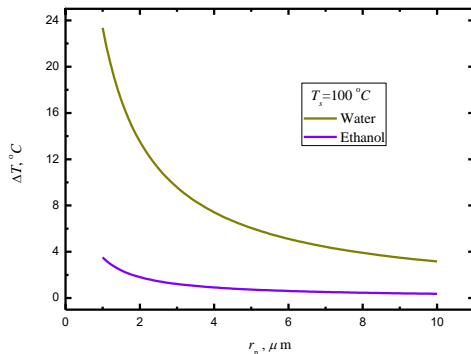


Figure 5. The boundaries of superheat degree versus the size of vaporization core for the heating surface of LHP evaporator.

point. Compared with water, ethanol needs smaller degree of superheat to make LHP evaporator work.

The boundaries of heat fluxes to the evaporator wall versus the size of vaporization pores are shown in figure 6. The results of acetone, methanol and ethanol are illustrated to be compared. If the vaporization pores of the capillary wick are also designed from 1 micron to 10 microns, the heat fluxes would decrease with the increasing of r_n . only the change slopes are different a little. For the three working fluids, the slopes have almost the same trends, the magnitude is in the same order. For all the points in figure 6 which are above the lines of q - r_n curve, the heat fluxes exceed the critical boundaries, the LHP evaporators could work normally. Compared with water, these three working fluids belong to low boiling point, the boundaries of heat flux to start LHP evaporators are lower, are in the order of several tens of watts to one hundred watts per square meters. For small heat fluxes, the thickness of liquid layer is less than 5mm, the evaporators of these three working fluids are easy to be started up.

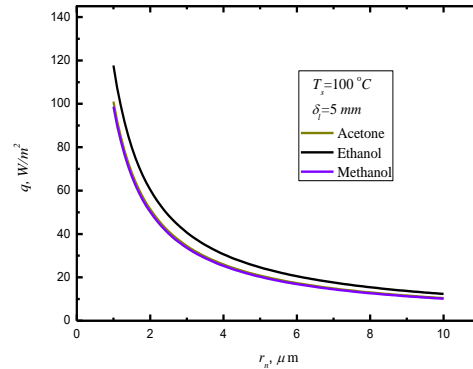


Figure 6. The boundaries of heat flux as a function of the size of vaporization core for the heating surface of LHP evaporator.

The boundaries of heat fluxes to the evaporator wall as a function of the thickness of the working liquid layer are demonstrated in figure 7, when the saturated temperature is 100°C, the vaporization pore radius of capillary wick is 5 microns. The figure shows the results of water and ethanol. The thickness effects of water are remarkable, while for the low boiling points working fluid, as ethanol in the figure, the performance has little impact.

The boundaries of superheat degree are compared in figure 8, for the four working fluids as water, methanol, ethanol and acetone. The boundaries of superheat degree to the evaporator

wall are respectively 13.53°C, 1.38°C, 1.81°C and 1.92°C.

From the view of superheat degree, the methanol evaporator is the easiest to be started up, while the water evaporator is the most difficult to be operated.

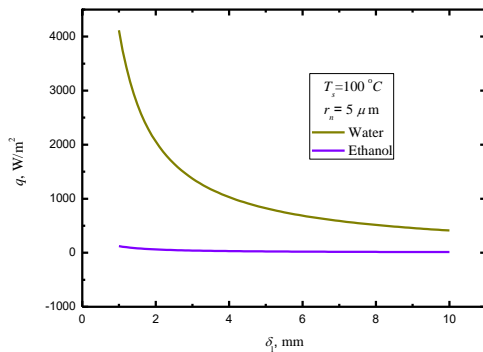


Figure 7. The boundaries of heat flux versus the thickness of working liquid layer for the heating surface of LHP evaporator.

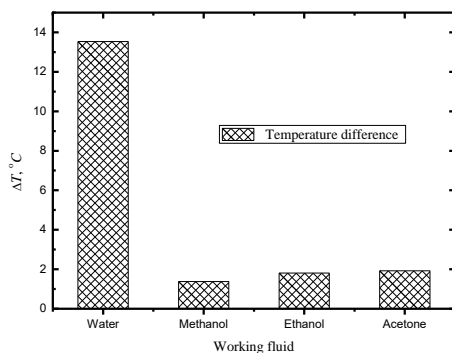


Figure 8. Comparisons of four superheat degree boundaries corresponding to four working fluids of LHP evaporator.

The boundaries of heat fluxes are compared in figure 9, for the evaporators of four working fluids as water, methanol, ethanol and acetone. The boundaries of heat fluxes to operate the LHP evaporator are respectively 1840.82, 50.11, 60.44 and 51.41W/m².

From the view of heat flux, the methanol evaporator is 50.11W/m², which is far less than that of the water, that is 1840.82W/m², the difference is thirty to forty times or so.

4. Summary and conclusions

For LHP optimization, the evaporator, isolator and compensation are integrated together, the high

performance, thin and small evaporators are designed effectively. The size effect of vaporization pores of the capillary wick, the influence of working fluids is analyzed. The thin and small LHP evaporators are designed and optimized. The results are conducive to the application of chip thermal control.

(1) The equivalent size of vaporization pores of capillary wick would affect the boundaries of degree of superheat and heat flux essentially for starting the evaporator. The working fluid should be selected together with the capillary wick pores. The balance could be reached by optimization.

(2) If the working pressure is permitted, the working fluids of low boiling point should be taken precedence, then the boundaries of superheat degree and heat flux could be much lower for evaporator starting up and operations.

(3) If the bubbles are easier to be produced, the returning flow resistance of liquid is small, the vapor and liquid is isolated effectively, the evaporators have the high performance. The thin and small evaporators are also easier to be mass and low-cost production.

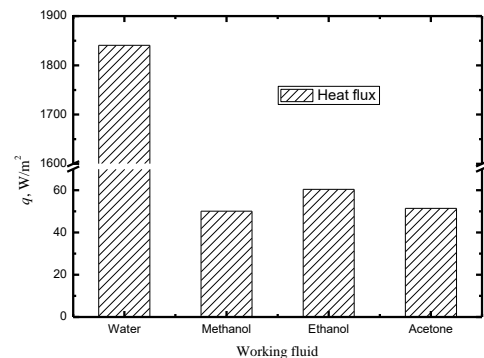


Figure 9. Comparisons of heat flux boundaries corresponding to four working fluids of LHP evaporator.

References

- [1] Y. F. Maydanik, Miniature Loop Heat Pipes, Proc. of the 13th Int. Heat Pipe Conference, Shanghai China, Sept. 21-25, 2004: p. 23-35.
- [2] Y.F. Maydanik, Loop Heat Pipes, Appl. Therm. Eng. 25, 2005: p. 635-657.
- [3] S.Launay et.al., Parametric Analysis of Loop Heat Pipe Operation, a Literature Review, Int. J. Therm.Sci. 46(7), 2007: p. 621-636.
- [4] H. X. Zhang. G. P. Lin etal, Experimental Study on Start-up Characteristics of Loop Heat Pipes, Chinese Science, Series E, 2005, 35(1): p. 1-14.

Development of the flat plate two-phase heat spreader for high heat loads

Hyunmuk Lim¹, Seung M. You², and Jungho Lee^{1*}

¹*Department of Mechanical Engineering, Ajou University, Suwon, Republic of Korea*

²*Mechanical Engineering Department, The University of Texas at Dallas, TX, USA*

**Corresponding author's email address: jungholee@ajou.ac.kr*

Abstract

An advanced two-phase heat spreader offers an attractive methodology for the thermal management of high-power electronics. A new two-phase heat spreader design and experimental thermal performances of the fabricated wickless heat spreader are introduced in this paper. This heat spreader consists of sintered copper particle layers on the top plates, exhibiting boiling heat transfer enhancement and rectangular rib-type supports operating as a working fluid flow path. The new design of a wickless two-phase heat spreader combines a microporous structure to achieve low thermal resistance and high heat flux operations over large heating areas. We experimentally characterize the thermal performance of two-phase heat spreaders in two different heating areas and identify the heating area's orientation effects. The resulting two-phase heat spreader shows good thermal performance without local dry-out at high heat loads > 645 W over the heating areas of 1 in². The thermal resistances were approximately 0.07 K/W at 100 W/cm². These results confirm that boiling heat transfer is an effective thermal management methodology for high heat loads. A prototype wickless heat spreader incorporating boiling-driven working is developed for potential thermal management of high heat loads and high heat flux applications.

Keywords: Two-phase heat spreader; Thermal management; Wickless; Orientation-independent; Boiling-driven;

1. Introduction

Thermal management of high-power electronics has been a major obstacle to achieving reliable and high-performance electronics [1]. Thermal management technologies using phase-change heat transfer can effectively manage heat sources with high heat fluxes that exceed the thermal management level of conventional air cooling or water cooling. However, active two-phase cooling has limitations in application due to high-pressure drop, device complexity, hydrodynamic instability, and requiring additional components. Also, passive two-phase cooling was known to have an operating limit of the heat flux, so it is unsuitable for thermal management of high heat load applications [2]. However, the flat plate two-phase heat spreader proposed in this study is simple and highly reliable. It has the advantage of being able to directly embed into the existing thermal management device of the high heat load applications.

The two-phase heat spreader using the boiling heat transfer (boiling-driven heat spreader) was proposed as a new thermal management device that can be used in high heat flux applications [3]. The boiling-driven heat spreader can maintain low thermal resistance even at high heat fluxes compared to the typical vapor chamber. In addition, it has a rigid structure and is easy to manufacture because of its simple wickless design. However, previous studies of the boiling-driven heat spreader were only interested in the thermal performance

under the high heat flux (~ 200 W/cm²) in a local area (~ 1 cm²).

This paper presents the boiling-driven heat spreader for the thermal management of high heat loads. The boiling-driven heat spreader is designed, fabricated, and tested. The effects of heating power and orientations of the heat spreader on the thermal resistance and the junction temperature are examined. The dimension of the fabricated boiling-driven heat spreader is 100 mm \times 100 mm \times 2 mm-thick, and the heat generation was simulated using a ceramic heater of 1×1 in². The heat transfer rate is varied from 6.45 to 645 W. As a result, there was no local dry-out even at a maximum load of 645 W in a 1 in² heat source, and the thermal resistance is 0.07 K/W.

2. Boiling-driven heat spreader

The schematic diagram of the boiling-driven heat spreader is compared to that of the typical vapor chamber in Figure 1. The boiling-driven heat spreader has a flat plate shape and has no wick structure surrounding the inside of the metal container and the support. This design can implement an operation mechanism completely different from the existing vapor chamber using evaporative heat transfer and capillary flow. The working mechanism of boiling-driven heat spreaders is boiling heat transfer and liquid flow by bubble pumping. To decrease the wall superheat, a microporous structure is coated with the specific

area under the heat source. The microporous structure is fabricated with sintered copper particle layers and can be made 2 to 3 times wider than the heating area. The working fluid circulations could be achieved by the bubble pumping mechanism [4]. The internal supports are designed in a form that can circulate the liquid flow by bubble pumping. This internal shape provides superior rigidity and robustness compared to typical vapor chambers.

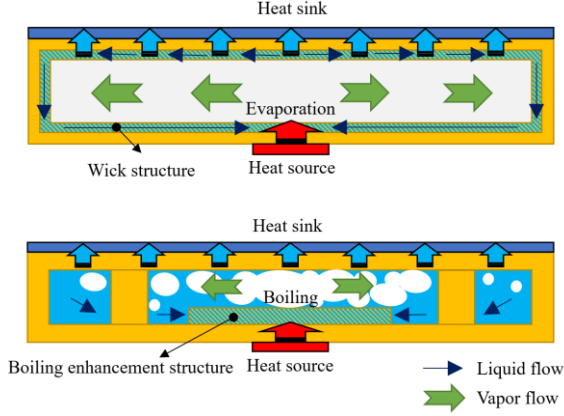


Figure 1. Schematic diagrams of the vapor chamber and boiling-driven heat spreader

3. Methodology

In this study, the boiling-driven heat spreader was fabricated of $100 \times 100 \text{ mm}^2$ and 2 mm thick [5]. The container was made with copper plates, and the microporous structure was fabricated with sintered copper particles on the boiling surface plate. The inner gap of the boiling-driven heat spreader was 0.8 mm, and the microporous structure was sintered with a 300 μm thick. Distilled water was used as the working fluid because of its excellent compatibility with copper. The degassing process was performed to be free from the effects of non-condensable gases. The water degassing was performed with boiling for over 1 hour in the atmosphere. The machined copper container was achieved with a vacuum level below 2 mTorr by the high vacuum turbo pump. After the vacuum process, the container was injected with degassed distilled water. The fabrication process was finished by sealing the injection port after injecting the working fluid. The fabricated boiling-driven heat spreader is shown in Figure 2.

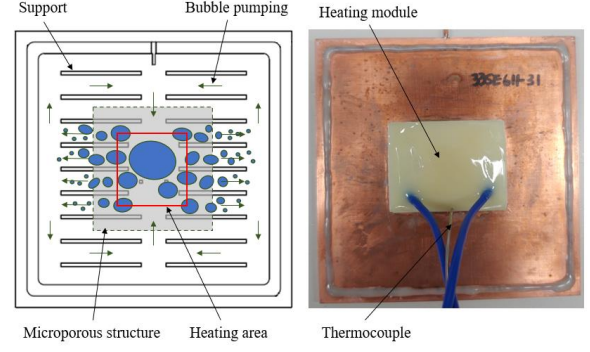


Figure 2. The internal design and a fully fabricated sample of the boiling-driven heat spreader

The thermal performance of the boiling-driven heat spreader was confirmed through an experimental setup using a water-cooled heat sink. As shown in Figure 2, a heating module was insulated with the epoxy on the center of the boiling-driven heat spreader. As shown in Figure 3, to know the temperature of the boiling and condensing surfaces of the boiling-driven heat spreader, metal blocks with the temperature measurement points were placed in the heat source and heat sink regions. The 1 in² ceramic heater was soldered on the copper block, and thermal interface material (Laird Tgrease 1500) was used to minimize the contact thermal resistance between the boiling-driven heat spreader and the water-cooled heat sink. The heat spreader and test rig were clamped together for uniform contact resistance under different orientations. An experiment was carried out by applying a heat flux of up to 100 W/cm². The heating module was powered by the DC power supply (Keysight N8741A). The coolant temperature and flow rates were 40°C and 7 lpm, respectively. T-type thermocouples (OMEGA) were applied to measure the temperatures with the DAQ system (VTI EX1032A).

The thermal resistance of the boiling-driven heat spreader and junction temperature is calculated with a hot side and a cold side temperature as:

$$T_{H.S.} = T_H - \frac{t_{Cu}}{k_{Cu} \times A_{Cu}} \times Q - \frac{t_{solder}}{k_{solder} \times A_{solder}} \times Q$$

$$T_{C.S.} = T_C + \frac{t_{Al}}{k_{Al} \times A_{Al}} \times Q + \frac{t_{grease}}{k_{grease} \times A_{grease}} \times Q$$

$$R_{BDHS} = \frac{T_{H.S.} - T_{C.S.}}{Q}$$

$$T_{junc} = T_H - \frac{t_{Cu}}{k_{Cu} \times A_{Cu}} \times Q$$

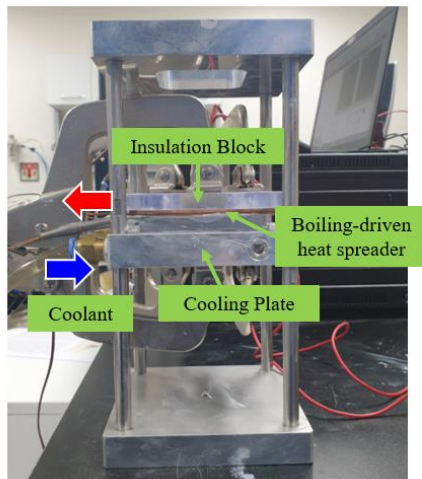
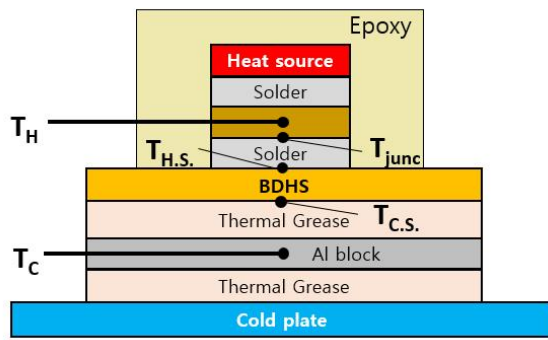


Figure 3. The schematic diagram and photo of the boiling-driven heat spreader test rig

4. Results

The effect of the orientation of the boiling-driven heat spreader with the high power loads is evaluated with the experiment. The boiling-driven heat spreader is tested while facing up (heater is below the heat spreader), facing down (heater is above the heat spreader - depicted in Figure 3), and in the two different vertical orientations (vertical up and vertical right). As shown in Figure 4, the thermal resistance of the boiling-driven heat spreader is maintained at 0.07 K/W in all orientations up to heat fluxes of 100 W/cm². The thermal resistance of 0.07 K/W could include the thermal resistance of the conduction at the copper plate, two-phase heat transfer (boiling and condensation), and convection of the liquid flow. Thermal resistances at low heat flux conditions are relatively high because of the poor heat spreading performances. However, as the power of the heat source increased, the thermal resistance of the boiling-driven heat spreader remained flat regardless of orientation. Suppose it is difficult to dissipate a large amount of heat because

the working fluid supply is insufficient. In that case, the thermal resistance of the boiling-driven heat spreader may increase as the heat flux increases.

Junction temperature should be considered in thermal management due to the limit of the operating temperature of semiconductors. In particular, if the ambient temperature is high, it becomes more challenging to manage the junction temperature. Through the boiling-driven heat spreader, the junction temperature of the heating module could be cooled down to 120°C at 645 W of heat loads (100 W/cm²) when the cold plate is maintained at 40°C. As a result, effective thermal management could be performed with the boiling-driven heat spreader, even if the area of the semiconductor chip is increased to 1 in² and high heat load conditions.

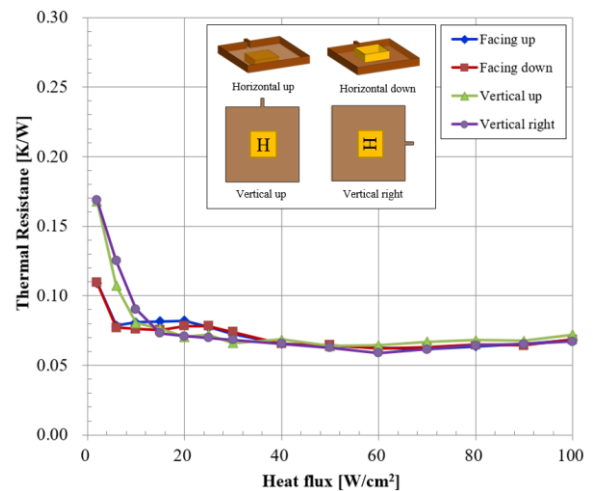


Figure 4. Thermal resistance results from different orientations

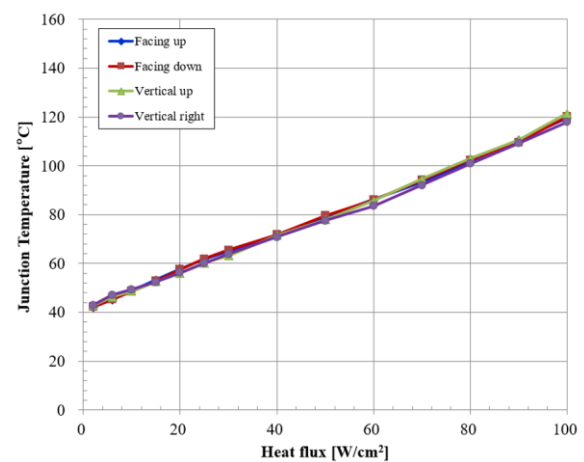


Figure 5. Junction temperature results from different orientations

5. Conclusion

A large and high-power heat source is dissipated externally onto the boiling side of a wickless boiling-driven heat spreader. The performance of the boiling-driven heat spreader is based on boiling heat transfer. The wickless boiling-driven heat spreader is more attractive for highly concentrated and large amounts of waste heat encountered in modern electronic devices. Also, thermal management devices through boiling heat transfer could allow large waste heat to be dissipated at lower temperatures ambient temperature for applications with a large heat source like server-class processors. As a result, the new boiling-driven heat spreaders have the advantage of thermal management for heat sources with high heat flux and enable stable thermal management even at the maximum amount of heat of 645 W. Also, the boiling-driven heat spreader could be performed with orientation-free operation regarding thermal management performance. Therefore, through the development of the boiling-driven heat spreader, excellent heat dissipation performance might be achieved for the thermal management of high-powered electronics.

Acknowledgment

This work was supported by the Civil-Military Technology Cooperation Program of the Institute of Civil-Military Technology Cooperation (ICMTC), with a grant funded by the Defense Acquisition Program Administration and Ministry of Trade, Industry, and Energy (grant no. 18CM5017).

References

- [1] J. Broughton, V. Smet, R. R. Tummala, and Y. K. Joshi, Review of Thermal Packaging Technologies for Automotive Power Electronics for Traction Purposes. *Journal of electric packaging*, 2018. 140: p. 040801.
- [2] H. Lim and J. Lee, Flat plate two-phase heat spreader on the thermal management of high-power electronics: a review. *Journal of Mechanical Science and Technology*, 2021. 35(11): p. 4801-4814.
- [3] J. H. Moon, H. Fadda, D. H. Shin, J. S. Kim, J. Lee, and S. M. You, Boiling-driven, wickless, and orientation-independent thermal ground plane. *International Journal of Heat and Mass Transfer*, 2021. 167: p. 120817.
- [4] X. Wang, J. H. Moon, H. Fadda, D. H. Shin, J. Lee, and S. M. You, Experimental investigation of heat spreading in a wickless and ultrathin thermal ground plane. *Case Studies in Thermal Engineering*, 2022. 31: p. 101799
- [5] H. Lim, S. M. You and J. Lee, New thermal packaging with a boiling-driven heat spreader for thermal management of the power electronics. *Applied Thermal Engineering*, 2022. 219: p. 119515

Investigation of operational limit of oscillating heat pipes by estimating local heat transfer

Naoko Iwata^{1*} and Fabio Bozzoli¹

¹ *University of Parma, Parma, Italy*

**Corresponding author email address: naoko.iwata@unipr.it*

Abstract

So far, several studies proposed mechanisms of Pulsating Heat Pipes' (PHPs') operational limit such as change of flow patterns from slug flow to annular flow, dry-out and occupation of liquid. However, it is not yet clear why there are several different mechanisms and under what conditions these limits are reached. This study aims to provide a more complete picture of the termination mechanism of the self-oscillation of vapor and liquid. Experimental studies on a 10-turn PHP are conducted with charging HFC-134a as the working fluid and changing the filling ratio from 20 % to 80 %. The thermo-fluid behavior in the PHP at the operational limit and transition to it is investigated by temperature distribution measurements with a high-resolution and high-speed infrared camera and estimation of fluid-to-wall heat flux distributions by solving inverse heat conduction problems. The results suggested that the PHP reached to the operational limit in the different mechanism depending on the filling ratio: at high FR (80 %), the liquid volume ratio increased with the increase of the operating temperature, resulting in the compressed liquid phase. At the low FR (20 %), when the large amount of heat was applied, the fluid in the evaporator dried-out and became a superheated vapor. The PHP with the optimum FR (50 %) transferred the maximum heat under the same evaporator temperature, as the fluid in the PHP was able to keep the saturated two-phase state until the evaporator temperature exceeded the critical temperature. The results of this study will deepen our understanding of operational limit, as well as help to improve existing numerical models.

Keywords: Pulsating heat pipe; Operating limit; Local heat flux; Inverse heat conduction problem

1. Introduction

A pulsating heat pipe (PHP) [1, 2] is a promising two-phase passive thermal device that consists of a capillary tube repeatedly bent between an evaporator and a condenser. Heat is transferred from the evaporator to the condenser by the self-excited oscillation of vapors and liquids. Although a number of its potential applications have been proposed [3, 4], PHP has not yet been fully practical due to the lack of the unified modeling for hydrodynamic and heat transport mechanisms, particularly at the operational limit of PHPs. The operating limit of a PHP is the state where the working fluid inside the PHP does not undergo self-oscillation and the heat transfer from the evaporator to the condenser stops. If the heat input to the evaporator continues after the operating limit is reached, the evaporator temperature rises immediately, and the internal pressure of the PHP also increases. In the worst case, this destroys the PHP. In addition, the equipment cooled by the PHP heats up due to the lack of heat transfer, which may cause serious damage to the equipment. Therefore, it is essential to design PHPs so that they do not reach their operating limit during operation. However, critical PHP features including dry-out limit has not been fully understood yet [5]. Mameli et al. [6] also stated, in the recently published review article on PHP studies, that the major challenge for

PHP numerical simulation code is to predict the operational limit.

The amount of heat transfer just before the PHP reaches its operational limit is called the maximum heat transfer rate (Q_{\max}) and has been measured in various studies [7, 8]. However, there is no satisfactory model to predict Q_{\max} because of complicated thermofluidic non-equilibrium phenomena and the large number of complex parameters related to heat transfer in PHPs. Several studies proposed how PHPs reach their operational limit: Yin et al. [8] assumed the change of flow pattern from slug flow to annular flow causes the limit; Kim et al. [9] observed the dry-out phenomenon in a micro-PHP, where all the liquid accumulates in the condenser and is no longer present in the evaporator; Iwata et al. [10] proposed that liquid occupies the entire PHP due to increasing liquid volume as the operating temperature increases. On the other hand, it is not yet clear why there are several different mechanisms that lead PHP to its operating limits and under what conditions these limits are reached. This study aims to provide a more complete picture of the termination mechanism of the self-oscillation of vapor and liquid.

Recently, the authors [11] characterized the thermo-fluid behavior in a micro-PHP by infrared measurement and estimation of fluid-to-wall heat

flux distributions by solving inverse heat conduction problems. In this study, the authors investigate the operational limit of the PHP by extending the methods and conducting experiments on a 10-turn PHP with HFC-134a (1,1,1,2-Tetrafluoroethane) at the filling ratio from 80% to 20%. The final goal is to explain the behaviors of fluid up to the operational limits and how this can vary with the filling ratio, providing a more complete picture of the termination mechanism of the self-oscillation of vapor and liquid.

2. Experimental setup

A stainless-steel tube with inner and outer diameters of 0.88 mm and 1.59 mm, respectively, was bent into 10 turns as sketched in Figure 1. For the working fluid of HFC-134a, in the temperature range from 7 °C (280 K) to 77 °C (350 K), the inner diameter is less than the critical maximum diameter d_{crit} defined by the following equation [12]:

$$d_{crit} = 2 \left[\frac{\sigma}{g(\rho_l - \rho_v)} \right]^{1/2} \quad (1)$$

where σ , g , ρ_l , and ρ_v are the surface tension (N/m), gravitational acceleration (9.81 m/s^2), liquid density (kg/m^3), and vapor density (kg/m^3), respectively. Using the properties of NIST Reference Fluid Thermodynamic and Transport Properties Database mini-REFPROP version 10.0 [13], d_{crit} at 7 °C and 77 °C are calculated to be 1.8 mm and 0.99 mm, respectively. The tubes in the evaporator were attached to a 1.5-mm-thick aluminum spreader by aluminum tapes, while the heat load was provided by a silicone-rubber sheet heater (OMEGA SRFGA-412/10), placed on the back of the spreader.

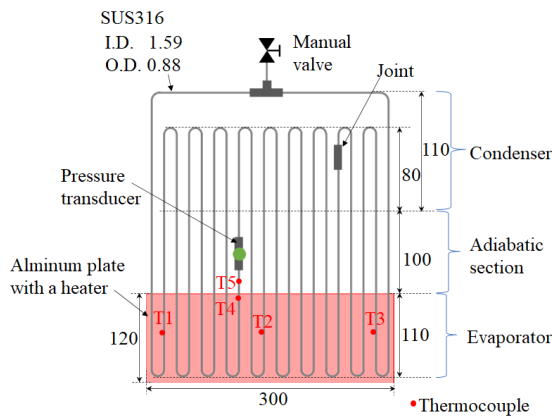


Figure 1. Schematic of PHP (unit: mm).

For charging, first the PHP and the tubes connected to it were vacuumed to below than 30 Pa by vacuum pump (AGILENT DS40M). The pressure was measured by a vacuum gauge (AGILENT 0531TC) and a controller (AGILENT

RGC-150). Then HFC134a ($\text{C}_2\text{H}_2\text{F}_4$, Purity $\geq 98.5\%$) was used as working fluid. The filling ratio was changed to 20 %, 30 %, 50 %, 70 %, and 80 %. The filling ratio was defined as the ratio of the liquid working fluid volume to the total PHP volume at room temperature and was checked by measuring the weight of the PHP with and without the fluid on a precision electronic balance (KERN EG620-3NM) which has a readability of 0.001 g and a verification value of 0.01 g. A fluid mass of 0.01 g corresponds to 0.7 % of the fluid mass in the loop at 100% filling ratio at room temperature.

The PHP was placed at the outlet of a wind tunnel to cool the condenser as shown in Figure 2. A part of the tunnel outlet was covered to prevent the air flowing to the evaporator and the adiabatic section. Atmospheric air was flown to the PHP at the flow velocity of 3.6 m/s near the condenser. The condenser temperature was monitored by an infrared camera (FLIR SC7000, space resolution: 640×512 pixels accuracy: ± 1 K, thermal sensitivity at 303 K: 20 mK). The temperatures of the evaporator and adiabatic section were measured with T-type thermocouples at five locations, as shown in Figure 1. A pressure transducer (Kulite XTEL-190S-1000A) was mounted in the tube of the adiabatic section. During the tests, the PHP operated in vertical bottom heat mode, i.e., with the evaporator at the bottom. A stepwise heat load was provided to the evaporator from 47 W by a DC power supply (Aim-TTi CPX400D) until the PHP reached to the operational limit, i.e., the evaporator temperature rose rapidly, or the evaporator temperatures exceeded the critical temperature of HFC134a, 101 °C. The experimental data were collected, for each power input, when the device reached the pseudo-steady state or the operational limit.

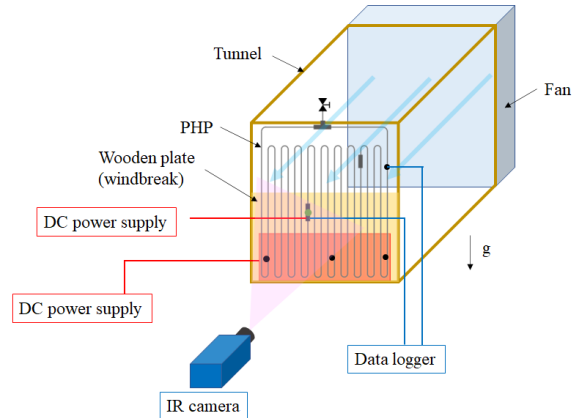


Figure 2. Experimental setup.

3. Heat flux estimation

Using the time-space temperature maps acquired by the infrared camera as input data, the local wall-to-fluid heat flux was evaluated by solving the Inverse Heat Conduction Problem (IHCP) at the tube wall. Specifically, each straight part of the PHP channels belonging to the condenser section was modelled as a 2D-axisymmetric solid domain, outlined in Figure 2. By assuming the thin-wall approximation, the temperature on the external surface was considered equal to that on the internal surface. In addition, due to experimental observations, the temperature gradients along the tube circumference were considered to be negligible.

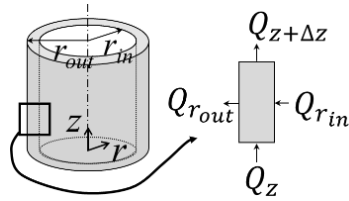


Figure 3. Energy balance at the infinitesimal wall section.

Following the previous assumptions, the energy balance equation becomes:

$$\frac{dU}{dt} = Q_Z - Q_{Z+\Delta Z} + Q_{r_{in}} - Q_{r_{out}} \quad (2)$$

where Q_Z and $Q_{Z+\Delta Z}$ are the conductive terms related to the axial direction z , while $Q_{r_{out}}$ is the power dissipated to the environment by natural convection. The time derivative of internal energy $\frac{dU}{dt}$ is expressed as:

$$\frac{dU}{dt} = \rho c_p \frac{\partial T}{\partial t} \cdot \pi(r_{out}^2 - r_{in}^2) \cdot \Delta Z \quad (3)$$

where ρ and c_p are the stainless-steel density and specific heat, respectively. By expressing the power terms of Equation (2), and combining Equations (2) and (3), the heat flux q , exchanged between the working fluid and the inner wall of the channel, can be finally expressed as:

$$q = \frac{(\rho c_p \frac{\partial T}{\partial t} - k \frac{\partial^2 T}{\partial z^2}) \cdot (r_{out}^2 - r_{in}^2) + \frac{(T - T_{env})}{R_{env}} \cdot 2r_{out}}{2r_{in}} \quad (4)$$

where ρ , c_p , r_{out} , r_{in} , T_{env} , and R_{env} are the stainless-steel density, specific heat, the inner radius of the tube, the outer radius of the tube, the ambient temperature, and the overall heat-transfer coefficient between the channel wall and the surrounding environment, respectively. Due to the noise level of the raw data, a regularization method was applied to the temperature distributions to reliably solve Equation (2).

The environment temperature measured during the experiment was assigned to T_{env} in Equation (4). Due to the noise level of the raw data, a regularization method was applied to the temperature distributions to reliably solve it. The processing target area of the condenser is every straight tube where the distance from the U-shaped apex is from 12 mm to 76 mm, which is equivalent to 160 pixels in the longitudinal direction of the IR camera as shown in figure 4.

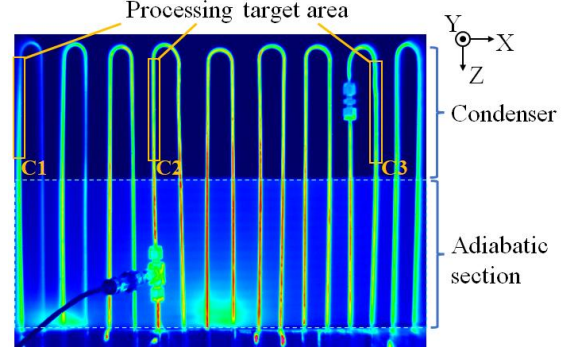


Figure 4. Processing target areas.

4. Results and discussion

4.1. Heat transfer performance

The thermal conductance G was evaluated as the thermal performance of the PHP. It is obtained from the following equation:

$$G = \frac{Q_{net}}{T_e - T_c} \quad (5)$$

where T_e and T_c are the evaporator and condenser temperatures, respectively. The evaporator temperature was evaluated by averaging the temperatures measured with thermocouples for 120 seconds in a pseudo-steady state, as expressed by the following equation:

$$T_e = \frac{T_1 + T_2 + T_3}{3} \quad (6)$$

where T_1 , T_2 , and T_3 correspond to the thermocouples shown in Figure 1. The condenser temperature was derived from the averaging the temperatures of 160 pixels in the areas indicated by C1, C2, and C3 in Figure 4. Since these areas included other than tube surfaces, the maximum temperature was extracted from the transverse temperatures at each Z -directional position and used as the condenser surface temperature. In Equation (5), Q_{net} indicates the net heat input to the evaporator, which is calculated by the following equation:

$$Q_{net} = Q_{ele} - Q_{loss} \quad (7)$$

where Q_{ele} and Q_{loss} are the electrical power input and the heat loss from parts other than the

condenser to the ambient air, respectively. The heat leak was calculated from the averaged surface temperature and surface area of the evaporator or adiabatic section, the averaged ambient air temperature, and the convective heat transfer coefficient obtained by a preliminary test with a sample tube.

Figure 5 shows the correlation between the thermal resistance of the PHP at each filling ratio and the net heat input. The resistance was less than 4 K/W apart from the PHP with FR 20 %. The resistances of the PHP with FR 70 %, 50 %, and 30 % increased when the maximum heat load was applied or even several watts before that. On the other hand, the resistance at FR 80 % monotonically decreased with the increase of the heat input. The resistance at FR 20 % was more than five times higher than that of the other PHPs. Pure thermal conduction, i.e., the thermal resistance of the empty PHP was calculated to be 227 K/W and verified by the experiment, which meant that the FR 20 % PHP was also operating as a PHP or a thermosyphon. The PHP with FR 50 % showed the best performance in terms of the resistance and the maximum heat load, as reported by the previous studies [4].

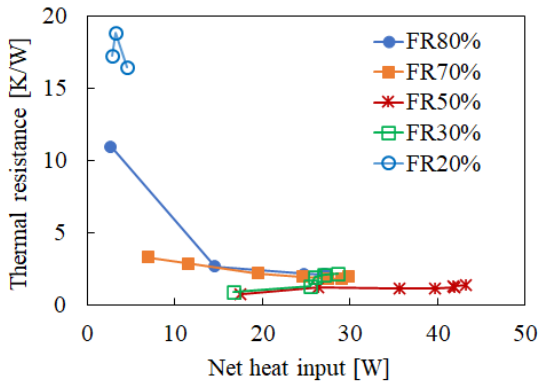


Figure 5. Correlation between net heat input and thermal resistance.

The thermal resistance against the evaporator temperature T_e is plotted in Figure 6. All the PHP was tested until the evaporator temperature exceeded the critical temperature as none of them obviously showed the rapid increase of the evaporator temperature during the test. This was why the maximum evaporator temperature for each FR were in the range of 105 – 115 °C. Comparing Figures 5 and 6, it can be said that the maximum heat load and the correlation between the resistance and the heat input varied depending on the FR, while the correlation between the resistance and the evaporator temperature showed the weaker dependency than that, except for the

PHP with FR 20 %. It is suggested that the PHP reached the operational limit in the different mechanisms depending on the FR, which will be discussed in the following sections.

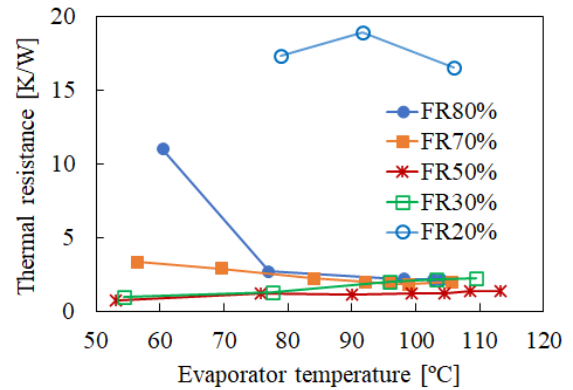


Figure 6. Correlation between evaporator temperature and thermal resistance.

4.2. Operational limit of PHP with high filling ratio

Figure 7 shows the histories of the temperatures, pressure, and the power input of the PHP with FR 80 %. The measured pressure and critical pressure of HFC-134a are expressed as P_{exp} and P_{crit} , respectively, in the legend of Figure 7. At the power input of 98 W, the pressure increased to 4.8 MPa exceeding the critical pressure of 4.059 MPa. On the other hand, the temperatures of the evaporator and the adiabatic section were still lower than the critical temperature of 101 °C. Moreover, when the power input was increased to 105 W, the temperatures increased only 2-3 °C, while the pressure increased 1 MPa. Considering the temperature derivative of pressure at the saturation state (dP/dT_{sat}) of HFC-134a is less than 0.075 MPa/K, the fluid state in the PHP was not the saturated two-phase state. It was estimated to be either supercritical fluid or the compressed liquid shown in Figure 10.

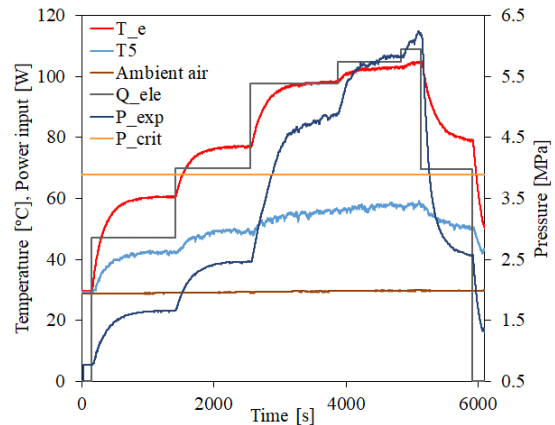


Figure 7. Temperature and pressure histories of PHP with FR 80 %.

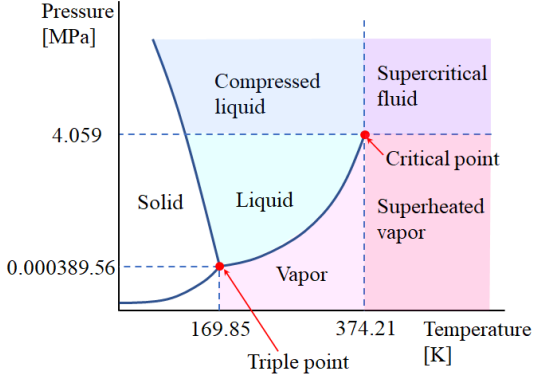


Figure 8. Phase diagram of HFC-134a.

Figure 9 shows a representative IR image of the condenser and adiabatic section of the PHP with FR 80 % at the power input of 105 W, which was the maximum power input kept to the steady state. The temperature distribution of the right-hand tube with temperatures falling from bottom to top and from top to bottom in the left-hand tube, suggested the existence of a unidirectional flow from the right to left in every tube with one U-shaped bend. The condenser temperature distributed from 30 to 70 °C, while that of the adiabatic section was 40 to 85 °C. The fluid coming from the evaporator passed the adiabatic section and was cooled in the condenser, then flew down to the evaporator through the adiabatic tube in the other side.

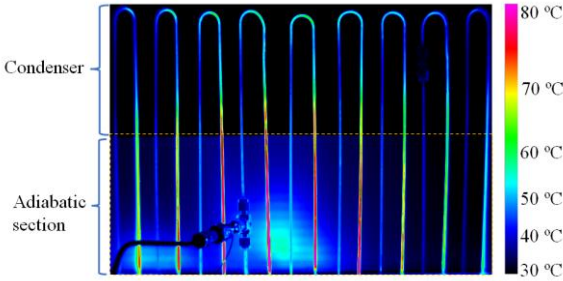


Figure 9. Infrared image of condenser and adiabatic section of PHP with FR 80 % at $Q_{ele} = 105$ W.

Figure 10 shows the filtered temperature and heat flux of the area C2 in Figure 4 of the PHP with FR 80 %. The IR images taken at one-minute-steady state at the heat input of 105 W were processed. The fluctuations in heat flux suggested the active oscillation of the fluid, even though it is not clearly seen by the IR videos and temperature maps. The heat flux varied from 600 W/m² to 10600 W/m², mainly depending on the location. This suggested that a lump of the liquid with relatively low temperature and thus low heat exchange with ambient air, in the middle of the

condenser tube. As previously mentioned in this section, the fluid was hardly supposed to be in the saturated two-phase state in the PHP with FR 80 % at the power input more than 105 W. The flow pattern was therefore not a slug/plug flow, but natural convection alone, with the fluid circulating. Considering the low temperature in the condenser and adiabatic section, the fluid was estimated to be a compressed liquid rather than a supercritical fluid.

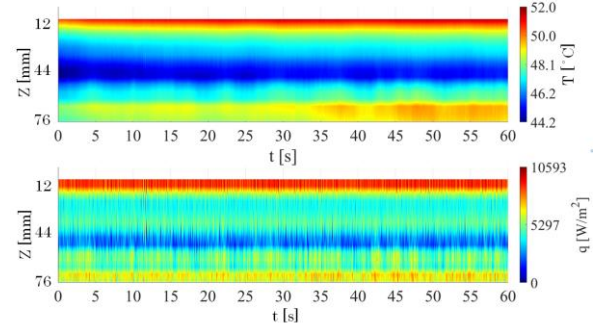


Figure 10. Filtered temperature (top) and heat flux (bottom) of condenser of PHP with FR 80 % at $Q_{ele} = 105$ W.

In terms of pressure changes, this also suggested that the fluid was a single-phase compressed liquid. The pressure change of a liquid was expressed as follows.

$$dP = \frac{\beta}{\kappa} dT \quad (8)$$

where β and κ are the liquid volume expansivity and liquid compression factor, respectively. Assuming β and κ in HFC-134a liquid at 97 °C are 0.055237 K⁻¹ and 0.16701 MPa⁻¹ [13], 1 °C temperature rise in the fluid results in a 0.33 MPa pressure increase. This agrees with the temperature and pressure histories at the heat input of 105 W. termination mechanism of the self-oscillation of vapor and liquid.

The reason for the transition of the two-phase fluid to liquid can be explained by the increase in the ratio of the liquid in the PHP to the total volume of the PHP as the operating temperature increases. The liquid density increases, and vapor density decreases with the increase of the saturation temperature. Assuming the working fluid in the PHP is in a two-phase fluid at a certain saturation temperature T_{sat} , the volume ratio of the liquid η is expressed as the following equation:

$$\eta = \frac{m_f - \rho_v V_{PHP}}{(\rho_v - \rho_l) V_{PHP}} \quad (9)$$

where m_f , V_{OHP} , ρ_l , and ρ_v are the fluid mass, the

internal volume of the PHP, liquid density, and the vapor density at T_{sat} , respectively. Substituting the estimated value of 4.26 cm^3 for V_{OHP} and measured value of 4.20 g for m_f , η for the PHP with FR 80 % with respect to T_{sat} was as shown in Figure 11. The densities, ρ_l and ρ_v , were derived from mini-REFPROP [13]. From Figure 11, it can be seen that η increased as T_{sat} rose and eventually the PHP was fully occupied by the single-phase liquid at T_{sat} of $72 \text{ }^\circ\text{C}$, which was close to the arithmetic mean of the evaporator and condenser temperatures at steady state at Q_{ele} of 105 W , i.e., $74 \text{ }^\circ\text{C}$. Assuming that the fluid was in the saturation two-phase state at a uniform operating temperature which corresponded to the arithmetic mean of the evaporator and condenser temperatures, the above result also suggested that the PHP could reach the operational limit because of the phase change from the two-phase to the single liquid phase. Thanks to the effects of natural convection and inertia of the fluid motion in slug/plug flow, the thermal resistance did not increase radically even after the liquid occupied the inside of the PHP.

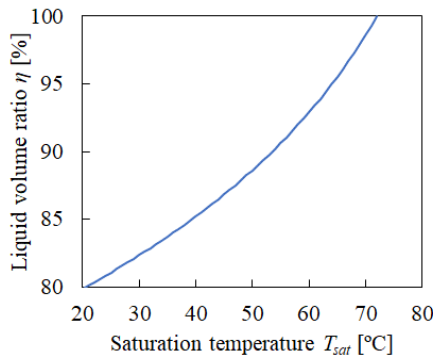


Figure 11. Liquid volume ratio of PHP with FR 80 % with respect to saturation temperature.

4.3. Operational limit of PHP with low filling ratio

Figure 12 shows the histories of the temperatures, pressure, and the power input of the PHP with FR 20 %. Immediately after the heat applied to the evaporator, the pressure and condenser temperature rose rapidly, which indicated the start-up of the PHP. Then, however, they did not increase as high as those of the PHP with FR 80%, though the pressure fluctuated indicating the fluid oscillation. The evaporator temperature increased up to $106 \text{ }^\circ\text{C}$ at the power input of 70 W , exceeding the critical temperature of HFC-134a, but the average pressure remained at 0.91 MPa , which corresponded to the saturation temperature of $35 \text{ }^\circ\text{C}$. This indicated that the PHP reached the

operational limit through a different flow regime than the PHP with FR 80 %.

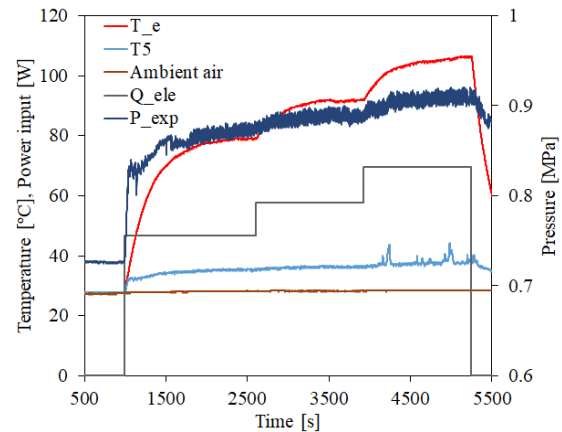


Figure 12. Temperature and pressure histories of PHP with FR 20 %.

A representative IR image of the condenser and adiabatic section of the PHP with FR 20 % at the power input of 70 W is shown in Figure 13. In the adiabatic section, only the right-side tube of each turn had a high temperature up to $50 \text{ }^\circ\text{C}$, while the others were as low as $32\text{--}34 \text{ }^\circ\text{C}$, the same temperature as the condenser tubes. This suggested that the fluid existed in the PHP in the different states depending on the positions. In the evaporator, superheated vapor shown in Figure 8 existed as its temperature exceeded the critical temperature while its pressure was probably below the critical pressure. The superheated vapor rose toward the condenser with being gradually cooled by the exchange with the ambient air. When the vapor was cooled sufficiently in the middle of the adiabatic section or in the condenser, the superheated vapor turned to the two-phase flow. More vapor started condensing in the condenser and flew down to the evaporator through the other side of the tube, i.e., the left-side tube of each turn, which had a lower temperature than the right-side tubes in Figure 11.

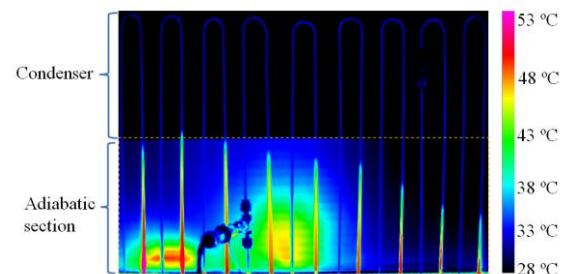


Figure 13. Infrared image of condenser and adiabatic section of PHP with FR 20 % at $Q_{ele} = 70 \text{ W}$.

A question then arose: “what is the flow regime in the condenser?” Considering the heat exchange

with the environment, condensation occurred on the inner wall of the tube. Assuming that the inner walls of all condenser tubes and half of the adiabatic section tube were wetted with a thin liquid film of 100 μm thick, the liquid mass was calculated to be 1.00 g. This corresponded to 96 % of the total fluid mass in the PHP. This suggested that liquid slugs hardly existed in the condenser and the flow regime was unlikely slug/plug flow. This could be explained by another aspect: the driving force was presumably not sufficient to induce and maintain the fluid oscillation.

Figure 14 shows the filtered temperature and heat flux of the area C2 in Figure 4 of the PHP with FR 20 %. The IR images taken at one-minute-steady state at the heat input of 70 W were processed. The temporal and spatial distribution of the temperature was only 1 $^{\circ}\text{C}$. Furthermore, the heat flux also only varied from 400 to 1200 W/m^2 , though the fluctuation was observed. This suggested the thin film condensation on the wall and flowing down to the evaporator by gravity, rather than an oscillating slug/plug flow. In summary, when the FR was small and the amount of the fluid was not enough for keeping the oscillating slug/plug flow, eventually the fluid in the evaporator became superheated vapor. In this experiment, the PHP was placed in the bottom heat orientation, so that even in such a situation, the PHP did not completely lose its function and acted as a kind of thermosyphon.

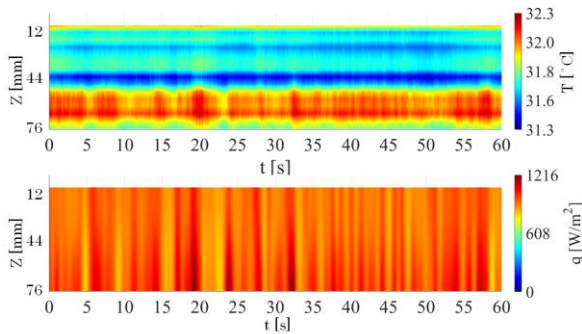


Figure 14. Filtered temperature (top) and heat flux (bottom) of condenser of PHP with FR 20% at $Q_{ele} = 70 \text{ W}$.

4.4. Operational limit of PHP with optimum filling ratio

Figure 15 shows the histories of the temperatures, pressure, and the power input of the PHP with FR 50 %, the optimum FR for this PHP. The temperatures of the evaporator and condenser and the pressure increased with the increase of the power input. Even after the evaporator temperature reached and exceeded the critical temperature of

HFC-134a, the pressure remained below the critical pressure and increased at a rate of increase with respect to temperature (dP/dT) around 0.02 MPa/K. It was therefore unlikely that the fluid is in the compressed liquid phase.

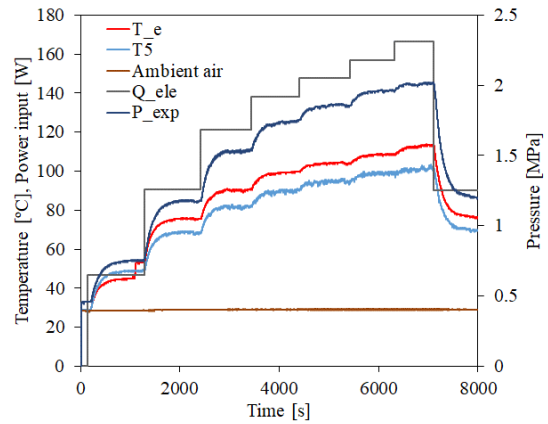


Figure 15. Temperature and pressure histories of PHP with FR 50 %.

Figure 16 shows a representative IR image of the condenser and adiabatic section of the PHP with FR 50 % at the power input of 167 W, the maximum power input for this PHP. Unlike the two previous results of the high and low FRs, the temperature of left-sided tubes was higher than the right-sided tube in each turn, indicating that the fluid circulated from left to right. Furthermore, the condenser temperature was as high as 45 ~ 85 $^{\circ}\text{C}$. From the measured temperature and the pressure, the fluid in the adiabatic section was estimated to be in a two-phase state, close to the critical point in the left tube and around 45 ~ 80 $^{\circ}\text{C}$ at the right tube. There were two possibilities for the fluid state in the evaporator, given that its temperature was above the critical temperature: if the fluid pressure in the evaporator was above the critical pressure, the fluid was supercritical, otherwise it was superheated vapor. Since the evaporator pressure was not measured, it could not be determined.

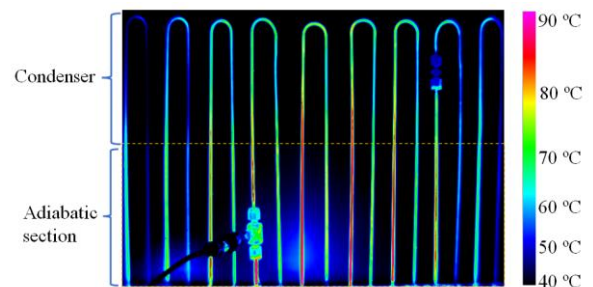


Figure 16. Infrared image of condenser and adiabatic section of PHP with FR 50 % at $Q_{ele} = 167 \text{ W}$.

Figure 17 shows the filtered temperature and heat flux of the area C2 in Figure 4 of the PHP with FR 50 %. The IR images taken at one-minute-steady state at the heat input of 70 W were processed. The heat flux varied from 10000 to 16000 W/m² with the fluctuation. This suggested oscillation or circulation of a two-phase flow, presumably a slug/plug flow or annular flow, but further investigation is required to determine which it is.

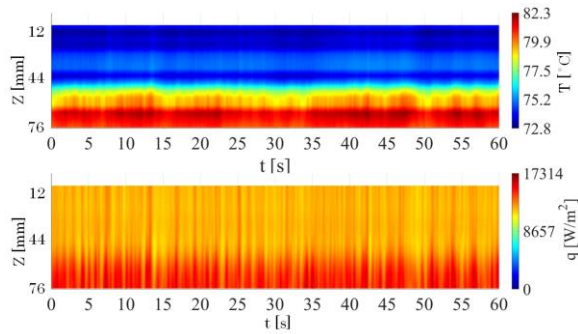


Figure 17. Filtered temperature (top) and heat flux (bottom) of condenser of PHP with FR 50 % at $Q_{ele} = 167$ W.

5. Conclusions

This study aims to provide a more complete picture of the termination mechanism of the self-oscillation of vapor and liquid in a PHP. Experimental studies on a 10-turn PHP are conducted with charging HFC-134a changing the filling ratio from 20 % to 80 %. The thermo-fluid behavior in the PHP at the operational limit and transition to it is investigated by temperature distribution measurements with a high-resolution and high-speed infrared camera and estimation of fluid-to-wall heat flux distributions by solving inverse heat conduction problems. The results suggested that the PHP reached to the operational limit in the different mechanism depending on the filling ratio: at high FR (80 %), the liquid volume ratio increased with the increase of the operating temperature, resulting in the compressed liquid phase. At the low FR (20 %), when the large amount of heat was applied, the fluid in the evaporator dried-out and became a superheated vapor. The PHP with the optimum FR (50 %) transferred the maximum heat under the same evaporator temperature, as the fluid in the PHP was able to keep the saturated two-phase state until the evaporator temperature exceeded the critical temperature.

Acknowledgement

This work has received funding from the European Union's Horizon 2020 research and innovation

programme under the Marie Skłodowska-Curie grant agreement No 894750.

References

- [1] H Akachi, Structure of a heat pipe. United States Patent, 1990. 4921041.
- [2] H. Akachi, Structure of a micro-heat pipe. United States Patent, 1993. 5219020.
- [3] Y. Zhang and A. Faghri, Advances and unsolved issues in pulsating heat pipe. *Heat Transfer Engineering*, 2008. 19(1): p. 20.
- [4] X. Han, X. Wang, H. Zheng, X. Xu and G. Chen, Review of the development of pulsating heat pipe for heat dissipation. *Renewable and Sustainable Energy Reviews*, 2016. 59: p. 692.
- [5] V. S. Nikolayev, Physical principles and state-of-the-art of modeling of the pulsating heat pipe: A review. *Applied Thermal engineering*, 2021. 195: p. 117111.
- [6] M. Mameli, G. Besagni, P. K. Bansal and C. N. Markides, Innovations in pulsating heat pipes: From origins to future perspectives. *Applied Thermal Engineering*, 2022. 203: p. 117921.
- [7] H. Yang, S. Khandekar, and M. Groll, Operational limit of closed loop pulsating heat pipes. *Applied Thermal Engineering*, 2008. 28: p. 49.
- [8] D. Yin, H. Wang, H. B. Ma, and Y. L. Ji, Operation limitation of an oscillating heat pipe. *International Journal of Heat and Mass Transfer*, 2016. 94: p. 366.
- [9] J. Kim and S. J. Kim, Experimental investigation on working fluid selection in a micro pulsating heat pipe. *Energy Conversion and Management*, 2020. 205: pp. 112462.
- [10] N. Iwata, H. Ogawa, and Y. Miyazaki, Maximum heat transfer and operating temperature of oscillating heat pipe. *Journal of Heat Transfer*, 2016. 138(12): P. 122002.
- [11] N. Iwata, F. Bozzoli, L. Pagliarini, L. Cattani, P. Vocale, M. Malavasi, and S. Rainieri, Characterization of thermal behavior of a micro pulsating heat pipe by local heat transfer investigation. *International Journal of Heat and Mass Transfer*, 2022.
- [12] H. Ma, 2015 *Oscillating Heat Pipes* (Springer, New York, 2015).
- [13] mini-REFPROP - Version 10.0, <https://trc.nist.gov/refprop/MINIREF/MINIREF.HTM>, sited at 19 Dec. 2022.

Geyser boiling phenomenon observation in an ethane axial grooved heat pipe working as a two-phase thermosyphon

Francisco Javier Martín-Portugués*, Yago Gómez-Ullate and Francisco Romera

IberEspacio, Torrejón de Ardoz - Madrid, Spain

*Corresponding author email address: fjavier.martinportugues@iberespacio.es

Abstract

Temperature control at cryogenic level is often required by Earth observation, scientific and weather satellites. Often, instruments embarked on these satellites need to operate at temperatures below the operation temperature range of ammonia heat pipes. Heat pipes filled with ethane have been manufactured for applications in which operational temperature varies in the range from -130 °C to the critical point of the ethane (+32 °C). The integration and acceptance of this equipment, either at instrument level or at satellite level, requires in certain cases the operation of the heat pipes in thermosyphon mode. In these cases, where gravity effect cannot be neutralized, it is important to understand the operational scenarios of the heat pipes, which is substantially different from which will occur in flight operation. This is particularly critical at low temperatures, where oscillations associated to geyser boiling phenomenon may occur. This paper presents the test results obtained under different scenarios including variations of applied power, temperature, orientation, evaporator length and filling ratio. The evolution of these oscillations is characterized in terms of amplitude and frequency, together with the global impact in the overall heat pipe conductance.

Keywords: Ethane; Geyser Boiling; Axially Grooved Heat Pipe; Two-Phase Thermosyphon.

1. Introduction

Ethane filled heat pipes have been manufactured for applications whose operational temperature varies in the range from -130 °C to the critical point of the ethane (+32 °C). Integration of this equipment, either at instrument level or at satellite level, requires in certain cases the operation of the heat pipes in thermosyphon mode. In these cases, where gravity effect cannot be neutralized, it is important to understand the operational conditions of the heat pipes, which are substantially different from which will occur in flight operation.

Maximum power that the device can transport, conductance and start-up operation are general parameters that change when a wicked heat pipe works in thermosyphon mode. Depending on the specific operational conditions, additional limitations can apply. This is the case for ethane heat pipes at low temperatures, where oscillations associated to geyser boiling phenomenon have been observed.

This paper presents the test results obtained from ethane heat pipes working in thermosyphon mode under different operational scenarios. These include variations of evaporator length, filling ratio, power, temperature and tilt. The evolution of these oscillations is characterized in terms of amplitude and frequency, together with the global impact in the overall heat pipe conductance.

2. Geyser boiling phenomenon

The main working principle of a two-phase

thermosyphon is simple and well-known. The heat power is supplied through the evaporator, where the liquid contained in the pool inside the device evaporates. Vapor flow moves upward inside the pipe, carrying latent heat from the evaporator to the condenser, where condensation occurs. Then, the generated liquid returns to the evaporator making use the gravity force. However, two-phase thermosyphon are subject to a different number of operating limits, such as viscous, sonic, dry-out, boiling and flooding limitations.

Additionally, another phenomenon called geyser boiling has been observed under specific operational scenarios. This is the case of ethane heat pipes in thermosyphon mode operating at low temperatures, and therefore low pressure. These conditions favour the development of large bubbles at evaporator. These bubbles grow up to reach dimensions in the order of the pipe inner diameter, when abruptly leaves the evaporator to the condenser. Once the liquid is subcooled it flows and returns to the evaporator. The evolution of the phenomenon is schematically presented in Figure 1.

The phenomenon was explained [1-4] for water and ethanol thermosyphons and seems linked to the evaporator conductance degradation and oscillating behaviour found on heat pipes during ground testing of Swift spacecraft [5].

The geyser boiling doesn't prevent thermal operation of a thermosyphon. However, nominal operation on these conditions should be avoided.

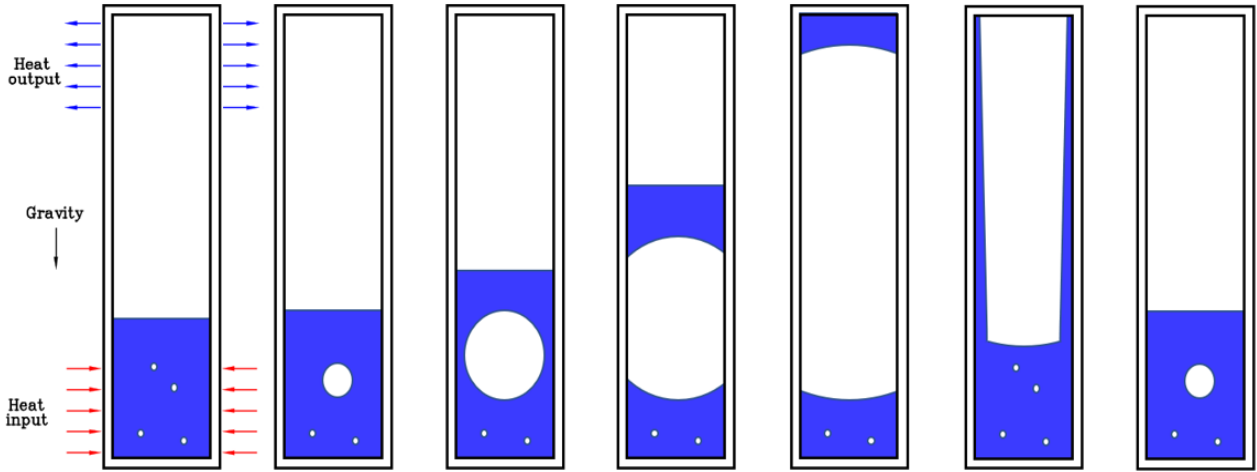


Figure 1. Schematic of geyser boiling phenomenon in a two-phase thermosyphon

The reason for that is to prevent a premature failure due to the structural vibrations associated to the phenomenon, as it can damage the condenser end cap welded joints due to the impacts [6-7].

3. Heat pipe design and test description

Ethane heat pipes have been designed and qualified for a space application [8], aimed to work at a nominal temperature of $-70\text{ }^{\circ}\text{C}$ and to withstand a temperature environment from $-130\text{ }^{\circ}\text{C}$ to $+50\text{ }^{\circ}\text{C}$.

In order to complement the qualification campaign, additional testing including operation in thermosyphon mode has been investigated deeply for heat pipes of same typology. Main features of these units are presented in Table 1.

(184 kg/m^3) has been defined for the operation as a heat pipe in zero-g. Slight variations of this parameter have been included in the study.

Table 1. Test samples description

HP type	Material	Working fluid	\varnothing (mm)	Length (mm)
Axial Grooved	Aluminium	Ethane	12.5	700

The heat pipes have been tested in a vacuum chamber. Tests have been carried out with different inclinations and evaporator lengths. Performance evolution with temperature and power has been studied.

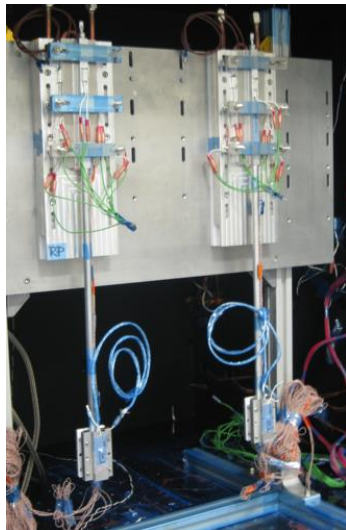


Figure 2. Test specimens during vacuum chamber installation for thermosyphon testing

Based on the specific design needs, including temperature requirements, the nominal filling level

Area	Measurement Point	From beginning (mm)
Evaporator	TE1	8
	TE2	26
	TE3	40
	TE4	52
	TE5	72
Adiabatic	TA1	164
	TA2	290
	TA3	416
	TC7	510
Condenser	TC6	600
	TC5	650
	TC4	675
	TC3	685
	TC2	690
	TC1	695



Figure 3. Test instrumentation

The nominal evaporator length is 80 mm, while the condenser length is 200 mm. Remainder length corresponds to adiabatic area. Heat pipes have been instrumented with thermocouples type T class 1. Detailed measurement plan is presented in Figure 3.

4. Test results

This section presents the results obtained under the different operational scenarios. All tests have been performed inside a vacuum chamber.

The analysis of the results, including the evolution of the phenomenon for the different operational scenarios, is presented in this section.

4.1. Horizontal orientation

A performance test in zero tilt has been carried out in order to have an initial characterization of the heat pipes operation in 0-g equivalent conditions.

For this test, two heat pipes have been installed inside the vacuum chamber. Heat input is located on top of the heat pipe while heat output is on the bottom. Test set up is presented in Figure 4.

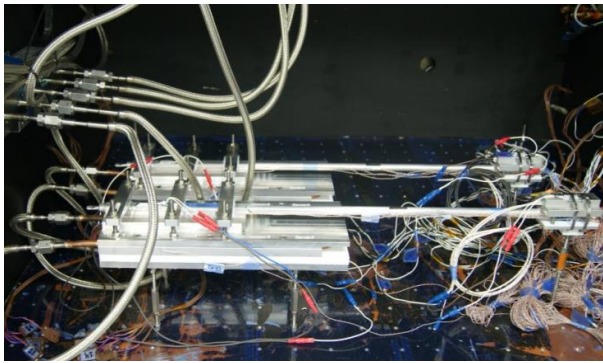


Figure 4. Ethane heat pipes installed inside vacuum chamber for horizontal testing

The test is carried out at -130 °C, -70 °C and -10 °C. The maximum heat transfer power and conductance obtained are reflected in Table 2 and Table 3.

Table 2. Maximum Power (W)

Test Unit \ Temp.	-130 °C	-70 °C	-10 °C
HP1	33	40	25
HP2	36	42	30

Table 3. Conductance (W/K)

Test Unit \ Temp.	-130 °C	-70 °C	-10 °C
HP1	6.17	5.47	3.31
HP2	5.54	6.22	4.08

The results obtained showed values aligned with the expected behaviour and similar to the ones obtained during the heat pipes qualification.

4.2. Thermosyphon in vertical orientation

Reflux mode test is carried out with the heat pipes working in vertical orientation at -90 °C, -50 °C and

-10 °C. This test is performed by applying power at the bottom of the liquid pool and measuring the temperature along the pipe. The liquid pool height for the nominal filling level at -90 °C is 234 mm. Figure 2 presents the test specimens mounted inside the vacuum chamber.

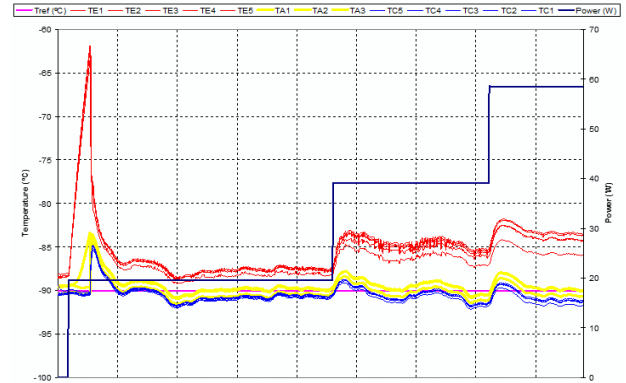


Figure 5. Ethane heat pipes operating in vertical orientation in thermosyphon mode

Reflux mode test has been executed applying power in the range from 5 W to 60 W. Once the heat pipe started up, and steady state conditions are reached, the conductance values obtained are typically much higher than the ones obtained in horizontal and tilt tests, being above 12 W/K. The exception occurs at -90 °C, where conductance between evaporator and condenser decreases down to 5 W/K, specifically for the lower values of the applied power. No sign of dry out has been found in any of the test cases carried out. Figure 5 presents the behaviour obtained for one of the units in vertical orientation and different power levels applied.

Related to the start-up in thermosyphon mode, unlike the horizontal operation, there is a temperature overshoot in the evaporator until the start-up event occurs. This overheat is dependent on the test temperature, being the lower temperature the worst condition to start the operation. Then, while the maximum temperature observed at evaporator is -2 °C during the test at -10 °C, the temperature gradient increases up to almost 30 °C when the test is performed at -90 °C.

Below -90 °C, the performance has been studied with a uniform heat load applied of 5 W, while condenser temperature goes down to -130 °C. Once this temperature is achieved, evolution under different power levels applied has been investigated.

At temperatures around -100 °C, degradation of conductance starts to appear together with the oscillating behaviour associated to the geyser

boiling. Figure 6 presents the temperatures evolution, showing oscillations with a period that decreases when the applied power is increased: from 20 min at 5 W to 1.8 min at 20 W. A temperature variation of 35 °C remains constant independently of power applied for a constant test temperature. Results are equivalent between the two units tested.

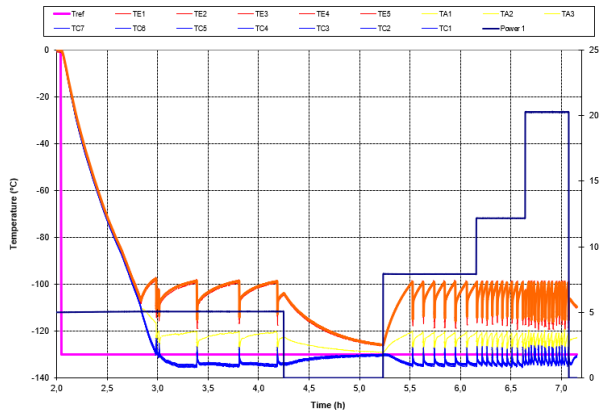


Figure 6. Geyser boiling phenomenon observation under different power

4.3. Thermosyphon in alternative orientation

Modifying the test configuration to a non-vertical orientation allows to investigate the impact of the liquid column, which has an important impact due to the hydraulic pressure in a low saturation pressure environment. Therefore, the test specimens have been tested tilted 3°. This corresponds to a height difference between evaporator and condenser of 36 mm. There are no additional changes in the test configuration.

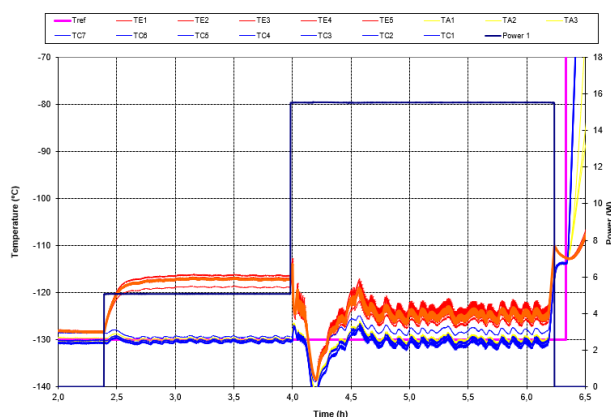


Figure 7. HP2 test results with 36 mm tilt

The test outcome is presented in Figure 7. The results show a degraded operation with no instabilities when power applied is 5 W but which appear once power is increased to 15 W.

Temperature gradients between evaporator and condenser measured are 12 °C and 8 °C, this means more than three times lower than the value obtained for vertical orientation operation.

4.4. Evaporator length impact

Being the phenomenon generated at the evaporator, its physical features, such as dimensions and location, are critical. The impact of the evaporator size has been characterized with two additional configurations, evaporator lengths 30 mm and 40 mm. Considering the heat power applied is 5 W, the results allow to evaluate the performance variations associated to the heating density.

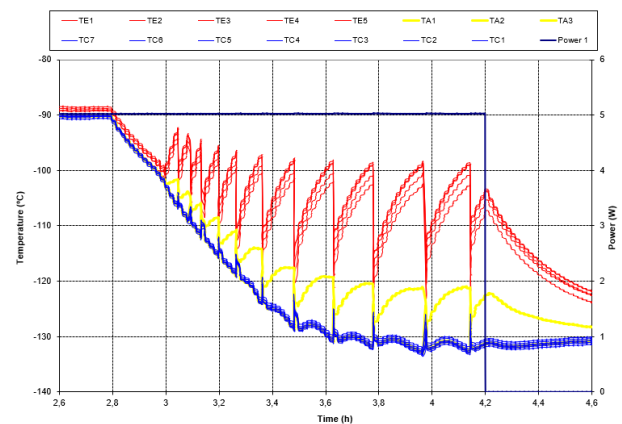


Figure 8. HP1 test results with 40 mm evaporator length

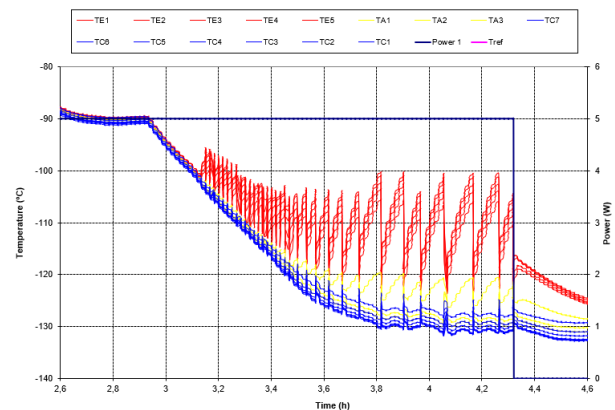


Figure 9. HP2 test results with 30 mm evaporator length

The results obtained are presented in Figure 8 and Figure 9 for evaporator lengths of 40 mm and 30 mm respectively. The outcome of these tests shows no significant differences with respect to nominal test related to the amplitude of the instabilities as variations of 34 °C and 31 °C are obtained. On the contrary, related to the period between the oscillations, it is clearly observed that the shorter the evaporator (larger power density), the higher the

frequency. Period from 20 min with 80 mm evaporator, decreases up to 9.9 min with 40 mm and 5.3 min with 30 mm.

Tests are executed with the evaporator mounted at the bottom of the specimen, being the worst scenario related the liquid column. Locations closer to the liquid–vapor interface, where large bubbles are more complicated to form, are expected to improve the behaviour reducing gradients and instabilities. However, this may be not a direct alternative in case of an assembled heat pipe during instrument or satellite level testing, unless this is considered early during the design phase.

4.5. Working fluid filling level impact

Aimed to study the filling level impact, two additional units identical have been manufactured with different filling ratios:

- 192 kg/m³, 4% over nominal
- 143 kg/m³, 22% under nominal

The liquid pool heights associated to previous filling levels at -90 °C are 245 mm and 182 mm.

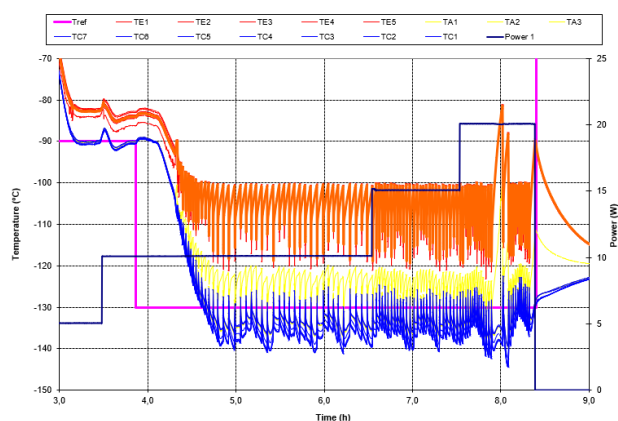


Figure 10. HP3 - Overfilled sample test results

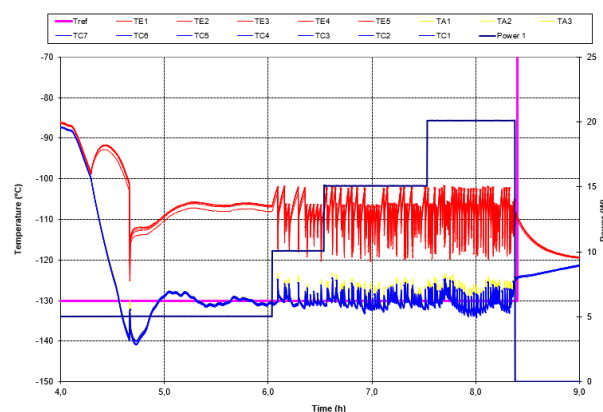


Figure 11. HP4 - Underfilled sample test results

The specimens have been tested in the nominal configuration described in section 3. The results show that larger filling ratios hinder the operation, since the degradation of conductance begins to become noticeable around -90 °C. Oscillations appear around -100 °C with 10 W of power applied. Oscillations amplitude increases to 38 °C.

On the contrary, for the specimen with a smaller filling ratio degradation starts at -100 °C and stabilizes with a temperature gradient of 25 °C, independently of the heating power applied.

4.6. Test results compilation

The test campaign performed allows to deepen our knowledge in the performance of ethane axially grooved heat pipes operating as a two-phase thermosyphon. The results allow to conclude:

- Thermosyphon mode operation of ethane heat pipes show specific limitations associated to gravity impact under low internal pressure conditions. This do not affect the operation under 0-g conditions.
- The phenomenon has been observed at temperatures in the range from -100 °C to -130 °C. Saturation pressure at these temperatures varies from 0.52 bar to 0.052 bar.
- Height of the liquid column has a critical impact on the performance. The larger the height, the bigger the degradation of the operation.
- Oscillations intensity (amplitude) is linked to the operational temperature and is not dependant on the thermal load.
- Frequency of oscillations increases with the thermal load.
- Oscillations period is smaller for shorter evaporators, while there are no relevant amplitude differences.
- For different filling ratios, the smaller the amount of working fluid, the higher the frequency of the instabilities, but with lower amplitude.
- While the phenomenon doesn't prevent the operation, this is degraded compared to the performance at higher temperatures or 0-g conditions. Thermal

conductance values obtained are an order magnitude lower.

5. Conclusions

Heat pipes manufactured for space applications require, in some cases, testing in thermosyphon mode once mounted at instrument or satellite level. In this configuration, the behaviour of the heat pipe is substantially different from which will occur in flight operation. Even while main differences are well known, specific phenomenon may appear under specific operational scenarios.

Geysers boiling phenomenon in axial grooved heat pipes, filled with ethane operating as a two-phase thermosyphon, has been described and observed under different operational scenarios. These include variations of power applied, temperature, orientation, evaporator length and filling ratio.

Temperature oscillations evolution has been studied, resulting in frequency increments with thermal load while its amplitude is constant. Results also show that the amplitude of the temperature fluctuations increases for low temperatures and decreases with shorter liquid columns. Oscillations frequency increases for shorter evaporators, with no relevant amplitude variations.

The phenomenon is directly linked to the low pressure inside the device and the height of the liquid column. Then, being the saturation pressure directly linked to the unit temperature, there are no alternatives to avoid this behaviour at low temperature, apart from reducing the liquid column height.

The behaviour associated to the geysers boiling should be considered at system level in case a heat pipe working as two-phase thermosyphon during ground testing. This approach allows either to develop designs that mitigate the effect, or at least to know the operation in order to understand the implications during ground testing at instrument or satellite level.

References

[1] C. Casarosa, E. Latrofa and A. Shelgii. The Geysers effect in a two phase thermosyphon. *International Journal of Heat Mass Transfer*, 1983. Vol. 26, No. 6, p. 933.

[2] T. F. Lin, W. T. Lin, Y. L. Tsay, J. C. Wu and R. J. Shyu. Experimental investigation of geysers boiling in an annular two-phase closed thermosyphon. *International Journal of Heat Mass Transfer*, 1995. Vol. 38, No. 2, p. 295.

[3] C. Tecchio, J.L.G. Oliveira, K.V. Paiva, M.B.H. Mantelli, R. Galdolfi, L.G.S. Ribeiro. Geysers boiling phenomenon in two-phase closed loop-thermosyphons. *International Journal of Heat and Mass Transfer*, 2017. 111, p 29.

[4] H. Kuncoro, Y. F. Rao, K. Fukuda. An experimental study on the mechanism of geysers in a closed two-phase thermosyphon. *International Journal of Multiphase Flow*, 1995. Vol 21, No. 6 pp 1243-1252.

[5] M. Kobel, J. Ku. Thermal vacuum testing of swift XRT ethane heat Pipes. *American Institute Of Aeronautics And Astronautics*; 21, 6006/6125; (2003) 1089-1096.

[6] D. Jafar, A. Franco, S. Filippeschi, P. Di Marco. Two-phase closed thermosyphons: A review of studies and solar applications. *Renewable and Sustainable Energy Reviews* 53 (2016) 575–593.

[7] N. Y. L. Pabón, J. P. F. Mera, G. S. C. Vieira, M. B. H. Mantelli. Visualization and experimental analysis of Geysers boiling phenomena in two-phase thermosyphons. *International Journal of Heat and Mass Transfer*, 2019. 141 876–890.

[8] F. J. Martín-Portugués, J. Martínez, A. Torres. Ethane Constant Conductance Heat Pipe Qualification according to ECSS for Two-Phase Heat Transport Equipment. *International Heat Pipe Conference – IHPC*. 2018. Pisa, Italy.

Development of a Matlab-based Automatic Lattice 2D Analysis Tool for Heat Pipe Wick Structures

Llywelyn Hughes^{1*}, Daniel Pugh¹, Philip Bowen¹, Richard Marsh¹, Andrew Jones², Tom Halhead²

¹ Cardiff University, United Kingdom

² HiETA Technologies, United Kingdom

*Corresponding author: HughesLR2@cardiff.ac.uk

Abstract

The advancement of additive manufacturing (AM) has been shown to play a vital role in enhancing the development and research surrounding heat pipes. Through improving the manufacturability of novel hybrid and biomimetic-based wick structures, AM has the potential to improve overall heat pipe performance. However, attaining the fine pore sizes and porosity achieved in more traditional heat pipe manufacturing methods may be challenging. Furthermore, validating the constructed geometry and resultant performance characteristics can prove costly and time consuming. Therefore, improving workflow efficiency and effectiveness is essential throughout the research and development of novel wick structures. Here, a Matlab-based 2D Lattice Analysis Tool (LAT), available to download from <https://github.com/llywelynughes/LAT>, and capable of automatic scaled measurements of the planar porosity, diameter, area, perimeter and centroid of each region is presented. Results are shown graphically in the form of a heatmaps and histograms, as well as possibilities for manual measurements and exporting of data and figures for further analysis. The tool has been trialled with results from additively-manufactured lattice structures, heat exchanger channels and contemporary research literature surrounding the deterioration of screen mesh wicked nanofluidic heat pipes. These case studies have shown the value of the effective and efficient automatic image analysis tool, specifically designed for heat pipe wick structures.

Keywords: Heat Pipes; Additive Manufacturing; Lattice; Wick Structures; Matlab.

1. Introduction

Additive Manufacturing (AM), specifically metal Laser Powder Bed Fusion (LPBF), is a rapidly evolving sector and plays a key role in the development of thermal management technologies. Previously, designers and engineers have been limited by the capabilities of conventional manufacturing techniques. The enhanced freedom of AM can result in innovative designs which can aid in improving system performance and efficiency, reducing energy consumption and associated costs, especially in the design of new novel heat pipe wick structures [1].

Since their commercialisation in 1965 [2], heat pipes (HPs) have proven to be suitable thermal management devices for several applications including electronic systems, aerospace, spacecraft and satellites as well as throughout the chemical engineering and nuclear industries. Their passive nature has aided in reducing or eliminating system parasitic losses along with increasing system reliability and maintenance periods. Further benefits of such systems include the possibility for mass and volume reduction through the decreased requirement for additional ancillary equipment such as pumps, valves and control system devices [3]. Their high thermal conductance, often several hundred times greater than that of other heat transfer

devices such as solid copper fins, result in them being considered as thermal superconductors [4,5].

The use of AM technology for heat pipe based systems has many benefits including improved lead times from research and development through to manufacture, and advanced system and component integration. As mentioned, one of the key benefits of AM is the improved manufacturability of novel wick structures that may be tailored to the properties of the working fluid at each section of the HP. This can aid to enhance both capillary pressure and permeability, both of which are limiting factors for the performance of heat pipes [6], leading to improved heat transfer where necessary and reduce pressure loss within the wick. It seems apparent that AM can play an important part in future heat pipe development. Several studies have already been undertaken concerning the benefits and utilisation of AM within the heat pipe industry, while mostly focusing on the design of the wick structure [1,7-10]. As the designs get more complex, so does the analysis of wick geometry and performance. There is therefore a need to ensure that such wick structures are truly characterised and optimised, through ensuring that the final products closely match that of the designed CAD models.

Existing test methods such as micro X-ray Computerised Tomography (μ -XCT) and Scanning

Electron Microscopy (SEM) can be costly processes throughout the initial design stage and often requires subcontracting to external partners [11]. Traditional 2D digital microscopy on the other hand can often be completed inhouse and has much lower costs. However, post-analysis of wick structures may require significant additional time. Improving the workflow efficiency and effectiveness of techniques employed for HP wick structure development is therefore vital for future progression.

This paper describes a newly designed 2D Lattice Analysis Tool (LAT) with the aim of overcoming the challenges faced within HP wick structure analysis.

2. Analysis tool development

This design tool has been developed through Matlab's App Designer feature, and may be run directly through Matlab or as a standalone software [12]. The application includes over 2000 lines of code and enables options for file importing, automatic and manual analysis as well file export and application reset. Figure 1 illustrates the workflow of the analysis tool where the callbacks within each tab, shown in Figure 2, become active and interactable when required.

2.1. File import & Scaling

This tool supports a range of image file formats including BMP, TIFF, PNG and JPEG. which serves well to analyse images from a range of equipment and software. For the analysis, the image must be in greyscale. Through counting the number of colour channels in the original image, the tool can automatically detect this and convert if required.

The image may be analysed with generic pixel count or scaled to appropriate units of choice with a scaling bar or known measurement, as shown in

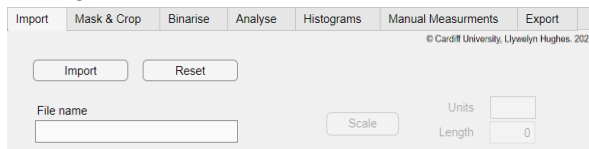


Figure 1. Analysis tool workflow.

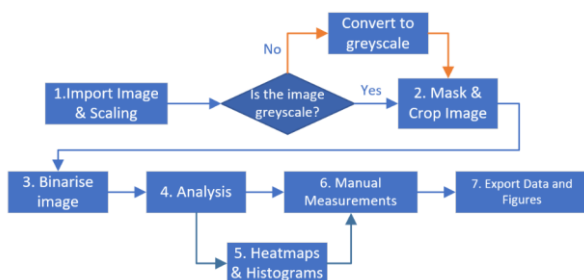


Figure 2. Analysis tool user interface.

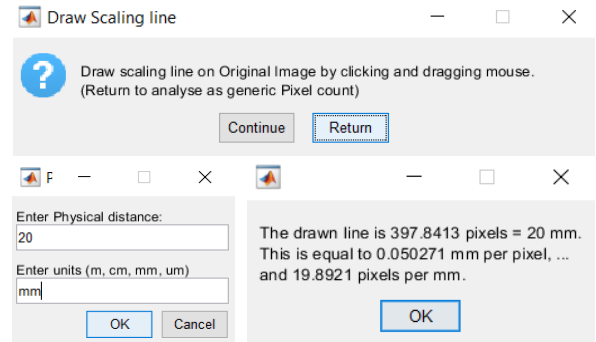


Figure 3. Scaling user interface example. Initial instruction window (Top), user input (Bottom-Left) and scaled results (Bottom-Right).

Figure 3. Scaling is achieved by measuring the pixel length of a drawn line using Pythagoras' theorem with the x and y coordinates of the start and end points of the line, as shown in Equation 1.

$$pix_dist = \sqrt{(x_2 - x_1)^2 + (y_2 - y_1)^2} \quad (1)$$

The user is then prompted to enter physical distance and appropriate units. The tool then calculates the length of each pixel and pixels per unit length. This conversion factor is then used throughout the application for effective scaling of measurements. Protection of any commercially sensitive geometries is also permitted with the ability to analyse generic pixel count.

2.1. Mask & Crop

Once scaled, the image may be cropped with a circle, rectangle, polygon or freehand mask, as shown in Figure 4. Any region which falls outside of the masked area are set to a pixel intensity value of 255 (white) and are discounted from further analysis. Through incorporating a range of masking options, the tool accounts for both simple and complex geometries. It also means imperfections in the image or component can be avoided and enables users to concentrate on specific regions of interest.

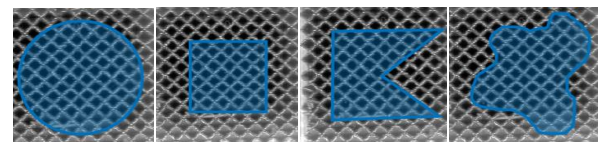


Figure 4. Masking options. From left to right: Circle, rectangle, polygon and freehand.

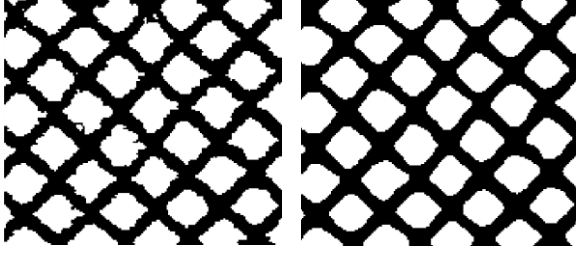


Figure 5. Binarised image with a Gaussian filter standard deviation of 0.01 (Left) and 2 (Right).

2.1. Binarise

Some automatic image processing techniques have been built into the tool. However, to alleviate any further noise or slight imperfections within the image, a 2-D Gaussian smoothing kernel filter with a controllable standard deviation in the range of 0.01 to 2 may be overlaid, as shown in Figure 5.

The tool has been developed to identify and analyse dark or light regions of the image, dependant on the geometry and image being analysed. An adjustable slider is included to control the threshold of the binarised image. The analysis of light regions takes into consideration the pixel intensities greater than the set threshold value, whereas the dark analysis setting considers pixels less than the set threshold value. In the instance shown in Figure 4, the analysis will be undertaken for the dark regions as the interest lies within the porous makeup.

Through displaying the histogram, shown in Figure 6, in conjunction with the output binarised image, the user may effectively control the threshold and smoothing values. Confirmation of acceptable threshold level is achieved through masking the region boundaries onto the greyscale image, as shown in Figure 7. For greater accuracy it should be ensured that the boundary is lined up as closely as possible to the edges of the greyscale image.

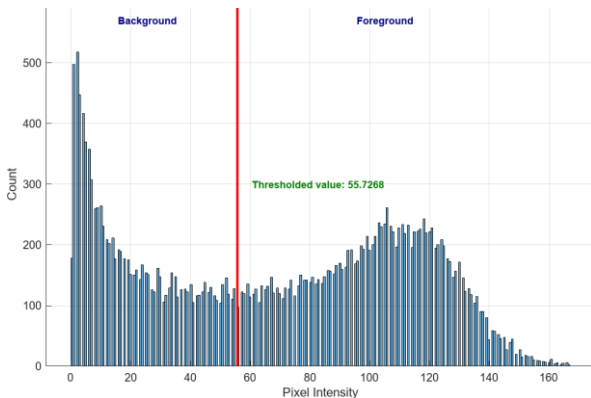


Figure 6. Histogram of greyscale image.

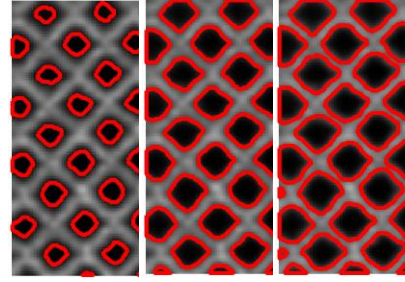


Figure 7. Threshold level: too low (Left), acceptable (Centre), too high (Right) for lattice structure.

A binarising threshold level set too low will reduce the size of the detected porous regions and total planar porosity value, whereas a level set too high will result in greater pore size and porosity value.

2.2. Analysis

The code returns a set of properties for the given regions within the boundaries of a binarised image. As shown in Table 1, the properties are automatically calculated for each region. In this case, the units were generalised in pixel count and each region may be cross-referenced to the displayed image in Figure 8.

Table 1. Example of analysis for a lattice structure pores.

Region	Mean Intensity	Area (pixels*2)	Perimeter (pixels)	Centroid (pixels)	Diameter (pixels)
12	25.2316	300	100.000	32.7700 104.7070	21.3495
13	25.8024	420	76.748	47.281 25.3143	23.1249
14	26.4552	446	79.568	49.4103 64.9126	23.8299
15	26.8256	407	75.913	51.12531 105.9656	22.7642
16	28.9159	416	76.459	52.05048 144.0769	23.0145
17	24.5394	317	67.601	66.6751 7.56467	20.0902
18	25.0142	423	75.632	68.156 44.2057	23.2073
19	26.3771	419	76.012	69.7255 85.6181	23.0973
20	26.6825	378	70.273	71.07407 124.291	21.9382
21	31.3439	378	71.654	72.5873 163.5423	21.9382
22	26.8692	390	72.051	86.941 23.3	22.2837

The diameter is calculated as its equivalent value, which equates to the diameter of a circle with the same area, as shown in Equation 2.

$$D_{eq} = \sqrt{\frac{4A}{\pi}} \quad (2)$$

Where, D = equivalent region diameter and A = region area.

An area threshold slider is also presented to disregard any smaller pores, irregularities or outliers within the image that have not already been automatically filtered out by the software. Further automatic analysis displayed in the tool include calculating the total number of porous regions, total area, average area and diameter as well as the planar porosity of the cropped image. It should be noted that additional information such as standard deviations will also be shown in the exported file.

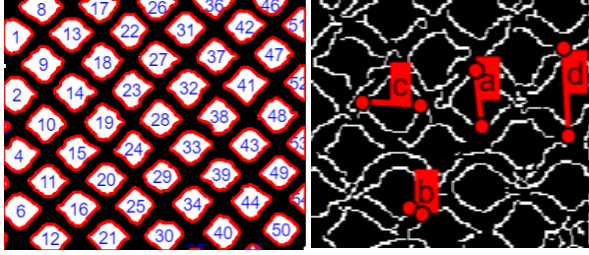


Figure 8. Image showing lattice regions (left) and edge detection (right) with manual measurements.

2.3. Heatmaps & Histograms

To simplify and display the distribution of the variations in area, diameter and perimeter of each region, a separate callback function is created to graphically show the results in the form of histograms and heat maps, as shown in Figure 9. This was achieved by interpolating the data to its nearest neighbour and plotting as a filled contour containing the values of the specified parameters along with the x and y coordinates.

Through utilising this method and sectioning the components at various planes, patterns may be identified. Such patterns include the distribution of pore size at particular sections of the plane, or pore size increasing or decreasing through the z axis. This may be a result of the anisotropic heat dissipation from the component, unoptimised machine parameters, or simply the effect of gravity.

Evidently, the smaller areas identified in the histogram of Figure 9 are a result of the cropping of the original image with partial pores being included in the analysis. Nonetheless, this is required for the porosity calculation of the entire cropped image.

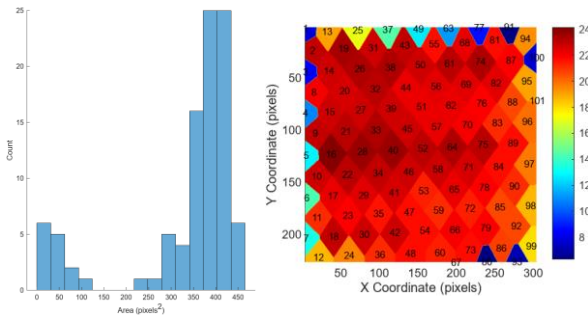


Figure 9. Area histogram (Left) and diameter heatmap (Right).



Figure 10. Canny edge detection example of Heat Exchanger channels with threshold value of 0 (Left) and 0.2 (Right).

2.4. Manual Measurements

The *canny edge detection* method within Matlab offers greater detail for manual measurements than the *regionprops* method previously mentioned. This algorithm detects the edges by looking at the local maxima of the image. Through using both a strong and weak threshold, the canny method is less susceptible to noise, as opposed to other solutions [13]. The threshold level may be easily altered with the use of a variable slider from 0 to 1, to clear any remaining noise, as demonstrated in Figure 10.

Utilising the *drawline* function enables the user to analyse a wide range of measurements within the lattice structure, including strut thickness, cell size, and pore size. The pixel length of the line is calculated (Equation 1) and then converted to the units of choice. As the user has the freedom to undertake any measurements required, no post processing has been built into the tool. The user may perform an analysis of averages, standard deviation or error calculations once the data has been exported. Similarly, the results are tabulated, and shown in a separate figure, as shown in Table 2 and Figure 8 respectively. This function is set within a loop with the table automatically updated with each new measurement iteration.

Table 2. Example of Manual measurements user interface for lattice structure.

Line	Length (pixels)	length (pixels)
a	25.4319	25.4319
b	6.4571	6.4571
c	26.7502	26.7502
d	39.7649	39.7649

2.5. Export and Save

Once the image analysis is complete, the user may export the tables individually as a Comma Separated Variable (.csv) or a .xlsx file. The figures

may also be individually saved to a chosen file path as either .PNG, .JPG, .TIF, .PDF, .EPS or .FIG files. For improved workflow efficiency, the entire analysis and manual measurements data may be automatically saved into a single .xlsx file along with all the figures as individual .PNG images.

3. Practical Examples

The tool presented here may be used and easily modified to suit any applicable case. The following section will exemplify these applications to demonstrate the tool's true capabilities.

3.1 Additively Manufactured Lattice Structure

This section will undertake a deeper analysis of the additively manufactured lattice structure referred to earlier. Due to commercial sensitivity, all analysis for the component will be undertaken as generic pixel count. Analysis was completed on all five visible external faces: x-y, both y-z and both x-z faces.

The number of detected porous regions on each face ranged from 84 to 129, which increases the confidence of the calculated averages, standard deviations and porosity values. The tool's manual measurement feature was used to calculate both the horizontal and vertical cell sizes of each image as well as the strut thicknesses. A total of 10 data points were taken for each parameter and the average values shown in Table 3, along with other automatically calculated parameters.

Table 3. Summary of lattice analysis.

Face	XY	XZ1	XZ2	YZ1	YZ2
Total Pores	98	120	129	84	112
Average Area (px²)	1583.52	1465.62	1453.71	1348.42	1523.97
Average Diameter (px)	44.38	42.77	42.22	39.03	43.55
Porosity (%)	39.73	37.12	37.49	38.14	37.65
Average Horizontal	94.85	93.69	94.77	95.73	94.83
Average Vertical	99.04	98.45	96.83	96.71	96.07
Aspect Ratio (x/y,x/z,y/z)	0.96	0.95	0.98	0.99	0.99
Struts Average (px)	19.49	22.14	24.27	24.33	23.65

This tool has effectively calculated a range of parameters, including pore areas, diameter, porosity, cell and strut sizes as well as aspect ratio. The values are consistent across all faces with an average pore diameter and porosity of 42.39 pixels and 38.03% respectively. As can be seen, the aspect ratio of the unit cells lies very close to unity, as designed. Interestingly, the aspect ratio is below unity for all analysed images. For the XZ and YZ faces, this shows that the unit cells are slightly larger in the z direction. This may be a result of the anisotropic thermal expansion and contraction rates induced within the change of phase of the molten metal during the printing process, or difference in machine resolution of each axis. However, as this deviation is only a maximum of 5% and considered relatively small, this may prove to have little effect on the wick performance. Furthermore, further analysis should be undertaken for a larger dataset to increase confidence in the results. This example has demonstrated a possible method for heat pipe wick structure analysis.

3.2 Heat Exchanger Channel

As the additive manufacturing industry strives towards achieving smaller features for improved heat transfer and flow characteristics, the repeatability of such designs is impacted. This example will analyse the repeatability of seven fine heat exchanger channels shown in Figure 11. Again, the tool will analyse the image in generic pixel count. The exported analysis data is shown in Table 4, with regions identified in Figure 11. Evidently, the area standard deviation accounts for the largest percentage of its average at 18.3%, compared to both perimeter and equivalent diameter indicating values of 4.0% and 8.9% respectively.

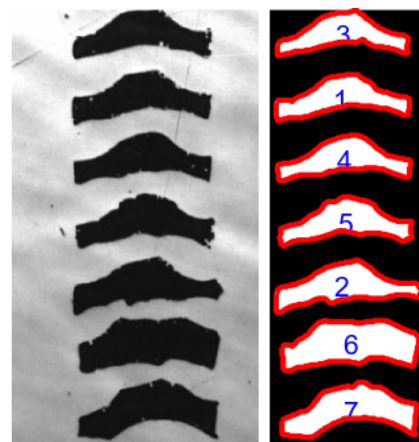


Figure 11. Heat exchanger channels cross-section. Original (Left), region identifier (Right).

Table 4. Tool analysis example data for heat exchange channels

Region	Area (Pix. ²)	Peri. (Pix.)	Dia. (Pix.)
1	2411	271.17	55.41
2	2780	289.28	59.49
3	2249	266.31	53.51
4	2377	267.07	55.01
5	2525	271.05	56.70
6	3666	288.44	68.32
7	3074	289.79	62.56
Average	2726	277.59	58.72
Std. Dev.	499.42	10.99	5.22

Upon inspection of the heatmaps, a trend is present where the areas, perimeters and equivalent diameters tend to increase from the top down, as illustrated in Figure 12. Utilising the manual measurements functions, the width, depth and minimum spacing averages/ standard deviations were measured as 119.92/ 2.78, 35.83/ 3.38 and 17.74/ 4.08 respectively. The largest percentage deviation (23%) was the minimum spacing, which may be attributed from the irregular and inconsistent geometry of the cross-sectional profiles. Further investigation may be required to identify any possible improvements in design, machine parameters or post processing of the structures.

This tool has proven to be effective in analysing microscope images of heat exchanger channel profiles. To obtain results of greater accuracy and confidence, it is recommended to repeat the experiment with larger datasets.

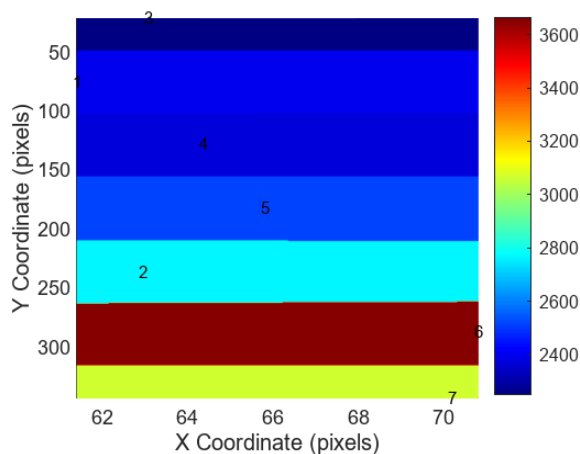


Figure 12. Example area heatmap of heat exchanger channels.

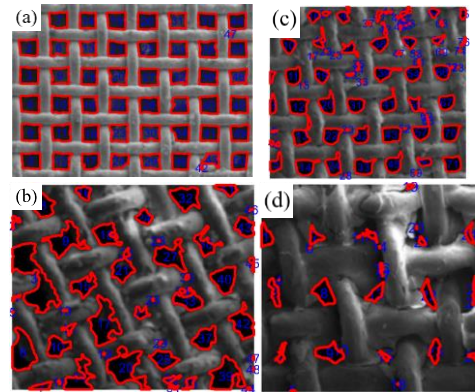


Figure 13. Analysed optical microscope images of mesh wick with $\text{Al}_2\text{O}_3/\text{DI}$ nanofluids as working fluid (a) at 0 months of manufacturing, (b) after 9 months of successive heat input of 72 W, and (c [x100] ,d [x200]) after 9 months of successive heat input of 12 W. Figure adapted from [14].

3.3 Screen Mesh Wick Deterioration

A study conducted by Bhullar et al. [14] investigated the deterioration of screen mesh wick heat pipes due to the use of nanofluids, specifically $\text{Al}_2\text{O}_3/\text{De-ionised water}$, as the working fluid. As stated in their findings, nanofluids are prone to agglomeration and sedimentation over time which can affect the heat pipe's thermal performance. Experiments were conducted at 12, 32 and 72W over a 9 month period. The use of these nanofluids resulted in improved thermal performance due to the nano-coating of Al_2O_3 on the mesh. This resulted in higher localised vapour pressure due to the sporadic flow acceleration, reduced contact angle and boiling limit enhancement. The work identified an increase in capillary action as a result of the deposition of nanoparticles and improved wick wettability, as shown in Figure 13. However, no further analysis into characterising the geometric difference was undertaken. Through utilising the newly designed image analysis tool, porosity as well as areas and equivalent diameters were quickly calculated for evaluation, as shown in Table 5.

As can be seen, the tool has characterised the change in geometry while displaying the key characteristics necessary for heat pipe wick design and development. Further stated in the study was the choking of flow for the 12W (c and d) scenario after the 9 month period. This was a result of low internal vapour pressure allowing for increased agglomeration and sedimentation rates.

Table 5. Analysis of screen mesh wick.

	a	b	c	d
Area_{Av} (μm^2)	4624.27	1949.70	1643.78	515.60
Area_{Tot} (μm^2)	231213.47	93585.66	124927.05	13921.27
Area_{Std. Dev} (μm^2)	1048.64	2284.87	1735.56	629.77
Diameter_{Av} (μm)	75.50	40.47	37.44	20.59
Diameter Reduction (%)	-	46.39	50.41	72.73
Diameter Std. Dev. (μm)	13.85	29.37	26.47	19.93
Porosity (%)	31.68	25.00	15.54	4.86
Porosity Reduction (%)	-	21.09	37.09	84.67

The tool has successfully characterised this phenomenon, especially for case (d) where a reduction of 72.73% and 84.67% was exhibited for the equivalent diameter and porosity respectively. This significantly increased internal pressure drop while considerably reducing permeability. This has shown the value in an effective and efficient analysis tool, specifically designed for heat pipe wick structures. Further experimental work, in conjunction with this tool, could determine the limit at which choking occurs and estimate the life span of such heat pipes at given operating conditions.

In addition to characterising the wick structure, the tool was also able to characterise the Al_2O_3 nanoparticles, as can be seen in Figure 14. However, due to the low quality of the original Transmission Electron Microscope (TEM) image extracted from the paper, additional noise and irregularities were

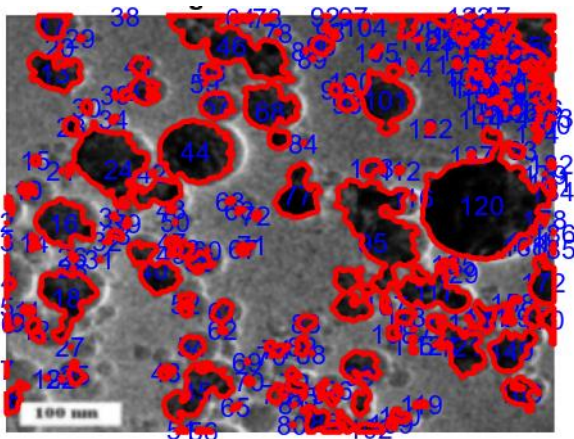


Figure 14. Al_2O_3 nanoparticle analysis regions from Transmission Electron Microscope image.

present during the binarising and region identification process. This has resulted in poor particle separation. Nonetheless, the tool has successfully identified most particles as agglomerations, as opposed to individual particles. However, this may be acceptable for scenarios where total particle area is of interest, as opposed to individual particle count or properties.

4. Conclusion

In conclusion, the proposed 2D analysis tool has been shown to benefit the design and analysis process of additively manufactured wick structures. Effective and efficient key parameter measurements, such as pore area, diameter and perimeter, which lead to wick characterisation and attaining a planar porosity value, further improves the process. This work has proven to further benefit traditional wick manufacturing techniques for improved design and development workflow efficiency, while also characterising the change in wick structure over time. The utilisation of heatmaps and histograms have been shown to be effective methods as visual comparators of the region area, diameter and perimeter. This method has also proven effective in identifying correlations and patterns within the porous makeup of the structure. Furthermore, such a tool can be expanded beyond the application of wick structures for the HP sector and utilised for a wide range of other applications, such as AM powder metrology, surface geometry and component defect characterisation.

Matlab App Designer has proven to be a versatile and a relatively simple platform for the generation of a user-friendly standalone lattice analysis software. Further development of the tool will include an option for automatic thresholding of the binarised image and more in-depth analysis of the regions, through taking into consideration standard deviation of each area to enable any anomalies to be disregarded. The addition of a web-based platform will also be of benefit for a range of applications, with possibilities to run the software on portable devices such as phones and tablets. This work has identified the importance of the image processing techniques used, although additional processing may be required for some images to reduce noise and image imperfections prior to use of the tool. Expanding the tool to analyse a larger number of file formats while also analysing multiple images simultaneously will also be of benefit, especially for future work covering μ -XCT.

Acknowledgments

This work was supported by Cardiff University, the Engineering and Physical Sciences Research Council (EPSRC) [grant number EP/S022996/1] and HiETA Technologies Ltd. The author would also like to take this opportunity to thank B. S. Bhullar, D. Gangacharyulu, and S. K. Das for their permission to use their work as a case study and perform further analysis.

Software Download

The LAT Software is developed under the GNU General Public License v3.0 license and may be freely downloaded from <https://github.com/llywelynhughes/LAT> as an inbuilt Matlab app or a standalone compiled software.

References

- [1] D. Jafari, W. W. Wits, and B. J. Geurts, Metal 3D-printed wick structures for heat pipe application: Capillary performance analysis. *Applied Thermal Engineering*, 2018. 143: p. 403.
- [2] G. M. Grover, T. P. Cotter, and G. F. Erickson, Structures of Very High Thermal Conductance. *Journal of Applied Physics*, 1964. 35(6): p. 1990.
- [3] NASA, State-of-the-Art Small Spacecraft Technology, Report No. NASA/TP—20210021263, 2021.
- [4] R. Savino, D. Paterna, and Y. Abe, Current Developments in Heat Pipes - An Overview. *Recent Patents on Engineering*, 2007. 1(2): p. 153.
- [5] H. Jouhara, A. Chauhan, T. Nannou, S. Almahmoud, B. Delpech, and L. C. Wrobel, Heat pipe based systems - Advances and applications. *Energy*, 2017. 128: p. 729.
- [6] J. R. McDonough, A perspective on the current and future roles of additive manufacturing in process engineering, with an emphasis on heat transfer. *Thermal Science and Engineering Progress*, 2020. 19(100594).
- [7] M. Ameli, B. Agnew, P. S. Leung, B. Ng, C. J. Sutcliffe, J. Singh, and R. McGlen, A novel method for manufacturing sintered aluminium heat pipes (SAHP). *Applied Thermal Engineering*, 2013. 52(2): p. 498.
- [8] Z. Hu, D. Wang, J. Xu, and L. Zhang, Development of a loop heat pipe with the 3D printed stainless steel wick in the application of thermal management. *International Journal of Heat and Mass Transfer*, 2020. 161.
- [9] R. J. McGlenn and C. J. Sutcliffe, Additive Manufactured Titanium-Ammonia Heat Pipes for Thermal Management of Space Electronic Devices, 2020.
- [10] Y. Y. Park and I. C. Bang, 3D printed heat pipe design for space nuclear reactor application. in *Transactions of the Korean Nuclear Society Virtual spring Meeting*. 2021. Jeju, Korea.
- [11] A. Thompson, I. Maskery, and R. K. Leach, X-ray computed tomography for additive manufacturing: a review. *Measurement Science and Technology*, 2016. 27(7).
- [12] Matlab R2022b, The Mathworks, Inc, 2022.
- [13] Edge, (The Mathworks, Inc) <https://uk.mathworks.com/help/images/ref/edge.html> (2022).
- [14] B. S. Bhullar, D. Gangacharyulu, and S. K. Das, Temporal deterioration in thermal performance of screen

mesh wick straight heat pipe using surfactant free aqueous nanofluids. *Heat and Mass Transfer*, 2016. 53(1): p. 241.

All polymer thermal ground plane (TGP) with stable hydrophilized wick

Doriane Ibtsam Hassaine Daoudji^{*1,2, a}, Samaneh Karami^{1,2, a}, Étienne Léveillé^{1,2}, Mahmood Shirazy¹ and Luc G. Fréchette^{1,2}

¹ *Institut Interdisciplinaire d'Innovation Technologique (3IT), Université de Sherbrooke, Québec, Canada.*

² *Laboratoire Nanotechnologies Nanosystèmes (LN2), CNRS-UMI, Université de Sherbrooke, Québec, Canada.*

^a *Contributed equally to this study*

**Corresponding author email address: doriane.ibtsam.hassaine.daoudji@usherbrooke.ca*

Abstract

In this paper, we introduce a stable chemical treatment for hydrophilizing a polymeric wick structure and demonstrated for the first time the fabrication of all-polymer thermal ground planes (TGP). The suggested hydrophilization process is a key step enabling the fabrication of two-phase thermal management components such as vapor chambers, heat pipes and TGP, which can address the thermal challenges of led lamps, Li-ion batteries or in mold electronics. A polymeric TGP is a strong contender for thermal management in these flexible, large surfaces, cost-sensitive and low heat flux emerging technologies. An all-polymer TGP provides on the one hand, the high phase change efficiency and on the other hand, the polymer flexibility, light weight and low manufacturing cost. However, the commonly described polymeric TGP in the literature do not fully benefit from these advantages since the wick and the vapor core mechanical structure are made from metals. The proposed chemical treatment allows to create a super hydrophilic behavior with a contact angle below 20° on high density polyethylene (HDPE) and acrylonitrile butadiene styrene (ABS) surfaces. The all-polymeric TGP was fabricated in a single step with our previously described process where the filling and sealing are done in-situ. Despite being limited by the low material thermal conductivity, this fabricated all-polymer TGP has an effective thermal conductivity of 212 W/m K. Therefore, this all-polymeric TGP conducts heat as well as an aluminum plate of similar thickness. Thus, the present work shows that we can make an all polymeric TGP with a hydrophilic polymer wick in a one-step fabrication process that results in a low-cost thermal management solution.

Keywords: TGPs; polymer; hydrophilization treatment; fabrication, polymeric wick; pillars wick structure.

1. Introduction

Thermal ground planes (TGP) are bi-phasic passive devices with an evaporator section for gathering heat and a condenser section for dissipating it. These heat transport devices are used in different applications including space [1], electronic devices [2] and photovoltaics [3]. TGP transfers heat based on evaporation-condensation of the working fluid in a closed loop. Once the evaporator is in contact with a hot source, the liquid in the porous media evaporates and flows to the condenser. The condensed liquid is then pumped back to the evaporator by the capillary force. This force is generated by a good wettability of the working fluid in the wick structure.

Conventional wick structures are metallic. However, there has recently been a growing demand for flexible electronics and polymers can be a promising candidate since polymers have low Young's modulus [4], which means high flexibility. In addition, polymers are lightweight and low cost compared to metals. Despite these advantages, polymers have some drawbacks that limit their applications in real world. Unsuitable physical and thermodynamic properties of polymers are a critical challenge resulting on a low polymer wick

performance. Indeed, polymers have low wettability, which makes them not very hydrophilic. Therefore, a polymeric wick cannot absorb and transport the working fluid efficiently, which affects the pumping capacity [5]. This results in TGPs with low heat transfer performances [6].

Studies on developing hydrophilic polymer structures have been conducted. However, very few research, focus on creating highly hydrophilic polymer wick for TGPs application [7]. In these studies, the technique of hydrophilization is not applicable on all polymers or if it is versatile, it is not stable over time. One study, for instance, altered poly (-phenylene sulfide) microporous membranes by submerging them in nitric acid (HNO₃) [8]. A significant amount of hydrophilic groups were added to its surface due to the treatment interaction between poly (-phenylene sulfide) and HNO₃. Although this method gave a super hydrophilic surface, it is not a versatile technique and works only on poly (-phenylene sulfide). Moreover, poly (-phenylene sulfide) is an expensive polymer which limits its application compared to the polyethylene family. In a different study, the surface properties of polyethylene terephthalate (PET) were altered using a non-thermal plasma treatment to increase its

hydrophilicity [9]. They treated PET fabrics for 5 minutes and noticed a decrease in the static contact angle from 80° to 25°. However, this method of treatment had two main drawbacks. The treatment did not produce a super hydrophilic surface and it only persisted for a very short time.

There is hardly any research that has been published in the literature on fabricating an all-polymer TGP using a stable hydrophilic polymer wick. The closest concept to an all polymer TGP was the work of Lewis et al. [10], on using ALD (atomic layer deposition) treatment and microfabrication processes. Their approach consists of depositing titanium dioxide (TiO₂) on a microfabricated polymeric wick surface. This thin layer ensures both TGP hermiticity and wick hydrophilicity. However, the microfabrication approach and the ALD treatment significantly increase the TGP cost. Other works have been done on the field of polymeric TGPs [11]–[13] with an 80% composition of metallic parts. In addition to the mandatory metallic layer in the shell to maintain the TGP vacuum and operation, the wick and the mechanical structure in the vapor core of these TGPs were made from metals.

In the view of making all-polymer TGPs, the present study introduces a way to create stable hydrophilic polymeric wicks. To achieve this, a previously presented deposition technique [14] is improved to hydrophilize the surface of high density polyethylene (HDPE) and acrylonitrile butadiene styrene (ABS) sheets. HDPE permits high volume manufacturing processes such as molding. Thus, to fabricate a TGP using these low-cost and high volume industrial techniques, it is necessary to produce a super hydrophilic HDPE wick. In the meanwhile, we used 3D printing processes to fabricate the polymeric wick structure. ABS material is the most common polymers used for this rapid prototyping technology, so it is also of interest.

We start by treating sheets and measuring contact angle to assess the level of hydrophilicity. Through a design of experiments (DoE), the best parameters to treat the polymeric surface for a low contact angle, hence a super hydrophilic surface, are determined. Then, stability of the treated sheets is studied. The treatment versatility was also investigated by applying the best recipe to ABS sheets and confirming its applicability. The treatment was then applied to an 3D printed ABS wicking structure and capillary performance was measured. We finally integrate the wick in our one step-assembly process to make a polymeric TGP, where the filling and

assembly are done in-situ [15]. Thermal performance of the fabricated TGP with the treated wick is measured. Thus, the current study introduces for the first time a fully polymeric TGP with a stabilized hydrophilic polymeric wick. The fabricated all polymer TGP is a promising contender as a thermal management solution for flexible, cost-sensitive, and low heat flux applications.

2. Fabrication methods and process

This section initially presents the chemical treatment to hydrophilize different polymeric materials (HDPE and ABS) and surfaces (sheets and pillars wick structure). Then, the fabrication processes to make a polymeric wick structure and a full polymeric TGP are demonstrated.

2.1. Polymer hydrophilizing treatment

In a TGP, the porous wick structure pumps liquid (water) from the condenser to the evaporator by capillarity. Thus, this porous media must be hydrophilic to absorb the working fluid. Since the contact angle is inversely correlated with the pumping capacity, we must minimize the contact angle as much as possible.

Table 1. DoE for the Hydrophilization treatment

#	Time [h]	DETA/TA [M]	Bicine/NaOH [M]	Temperature [°C]
1	6	3	1	20
2	6	3	5	30
3	6	3	10	40
4	6	5	1	20
5	6	5	5	30
6	6	5	10	40
7	6	10	1	30
8	6	10	5	40
9	6	10	10	20
10	8	3	1	40
11	8	3	5	20
12	8	3	10	30
13	8	5	1	30
14	8	5	5	40
15	8	5	10	20
16	8	10	1	40
17	8	10	5	20
18	8	10	10	30

The present treatment intends to hydrophilize the polymer surface by chemically introducing OH terminations, which decrease the polymer surface contact angle [14]. To prepare the treatment recipe, we start by combining bicine and sodium hydroxide (NaOH) to obtain a bicine buffer solution. Then, tannic acid (TA) and

diethylenetriamine (DETA) were added. TA is used to provide phenol groups and DETA is used to provide amino groups to form covalent bond between them. Polymeric samples were immersed in the heated solution that were continuously mixed. Finally, the samples were taken out of the solutions and were rinsed with deionized water.

The investigated parameters of this hydrophilization treatment include treatment time, reaction temperature and concentration ratios of DETA to TA and bicine to NaOH. To investigate the influence of these parameters, we used the Taguchi DoE with 18 experiments. Taguchi optimization method was used to adopt an orthogonal array, where each parameter has equal weight and it gets the optimum design with few number of runs and therefore low cost [16]. We considered four parameters with three levels for DETA/TA (3, 5, 10), Bicine/NaOH (1, 5, 10), temperature (20°C, 30°C, 40°C) and two levels for time (6h, 8h). Table 1 shows these parameters and their levels for each run.

We used the contact angle measurement as a metric to assess the best ratios, time and temperature combination. This measure was performed on each recipe expressed in Table 1 to examine the sample hydrophilicity. The lower the contact angle, the better the treatment. Results will be presented in section 3.1.

2.2. Wick Design and fabrication

In this study, we made the wick from ABS pillars structure. This porous media is fabricated by stereolithography (Photon Mono X), a 3D printing process for rapid prototyping. This 3D printing process consists of exposing a liquid polymer (ABS plastic like) to a light source through a pattern. The areas where the liquid polymer is exposed to light solidify. This manufacturing method allows features of 50 μm in lateral direction and 100 μm in z direction, normal to the printing plane.

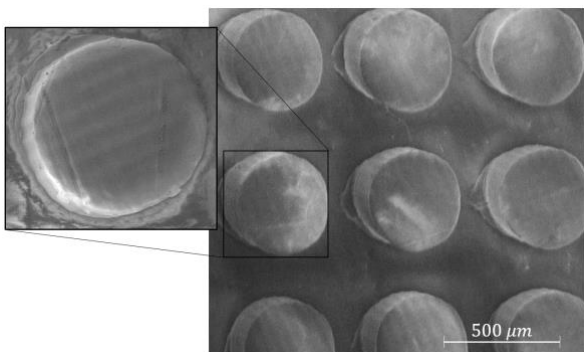


Fig. 1: SEM of the 3D printed pillars structure.

The samples are 2 cm wide, 15 cm long and 600 μm thick. The pillars radius is 200 μm , the high is 400 μm and the spacing is 200 μm . Figure 1 shows a scanning electron microscopy (SEM) picture of the fabricated pillars structure. The pumping capacity of this porous media is function of the pillars spacing and their contact angle with the liquid-vapor-solid interface. Once the porous media is incapable of pumping the liquid back from the condenser to the evaporator a dry-out occurs. Commonly referred to as the capillary limit, this phenomenon depends on the porous media properties, the TGP dimension and test configuration. This limit is estimated for a TGP with dimensions of 15 cm in length, 2 cm in width, and 2.5 mm in thickness. The tested configuration is 7 cm and 4 cm long for the evaporator and condenser respectively.

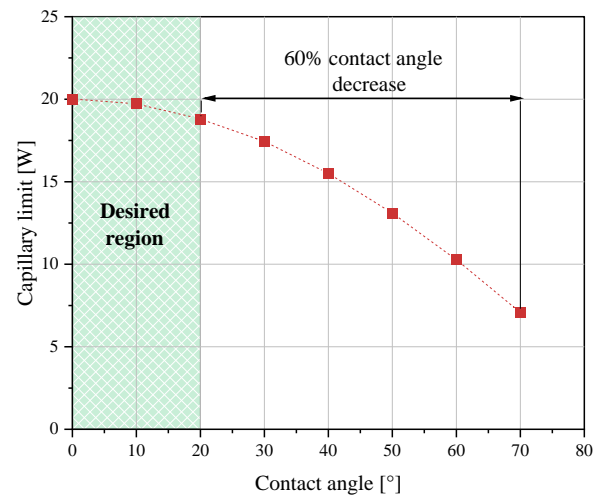


Fig. 2: The impact of the contact angle on the capillary limit demonstrating a 60% decrease for a contact angle variation from 20° to 70°.

According to our model [17], the fabricated TGP pumps up to 20 W before reaching the dry-out at a zero contact angle. Figure 2 shows this limit variation at different contact angles. The pumping capacity decreases with the contact angle increase. Since, the higher the contact angle, the higher the effective pore radius.

We observe that with a contact angle change from 0° to 20°, the capillary limit shows negligible variation, but with a contact angle evolution from 20° to 70°, a 60% capillary limit decrease is reached. Thus, to maintain the TGP pumping capacity, a superhydrophilic wicking structure is required.

2.3. Polymeric TGP fabrication

The material used to fabricate the all polymer TGP is shown in figure 3. We used our previously described one step assembly process to make the

polymeric TGP [15]. The process flow is represented in figure 4. The shell was made of HDPE sheets. This material is well known for its high vapor barrier and thermal conductivity among polymers. The vapor core is filled by a nylon mesh that maintains the vapor core thickness during vacuum. Polymer pillars array is used as a wicking structure to pump the liquid. Water was used as working fluid due to its high surface tension and phase change enthalpy [18].

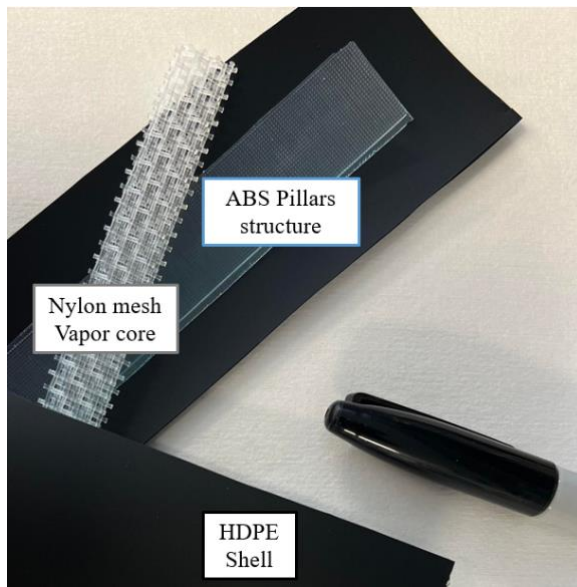


Fig. 3: The shell, vapor core and wick material used to fabricate all polymer TGP.

The first step to fabricate the TGP is preparing the HDPE sheets. They are cut and cleaned with acetone, isopropyl alcohol, then rinsed with deionized water. The second step constitute 3D printing the pillars structure. The third step involves chemically treating the polymeric pillars structure to make it hydrophilic.

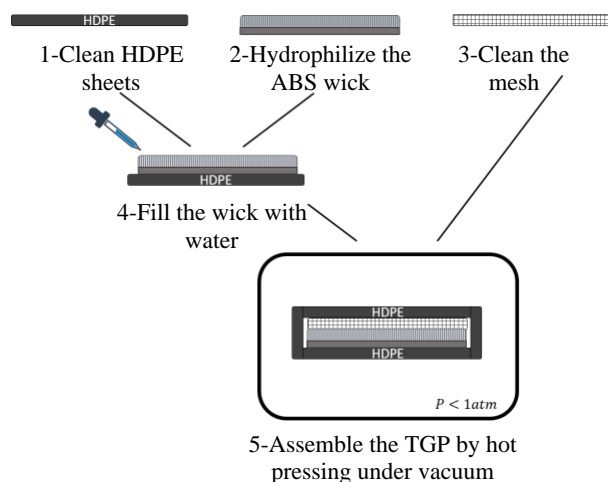


Fig. 4: Polymeric TGP one-step assembly process flow with in-situ filling and bonding.

The last step includes hot pressing the assembled polymeric TGP in a vacuum chamber after injecting the required amount of water into the treated pillars structure.

The recommended method eliminates the use of a filling tube as seen in standard TGPs or vapor chambers. Furthermore, it enables filling, assembling, and sealing to be completed in a single step. As a result, we produce a flexible, efficient and low cost TGP.

3. Characterization

In this section, we first characterize the contact angle provided by the described treatment on HDPE sheets, while varying the recipe time, temperature and concentration ratios. Then, we investigate the treatment longevity in different environments. We also examine the treatment on an ABS sheet, to validate its versatility. Finally, we characterize the thermal properties of the fabricated TGP with the treated ABS pillars structure.

3.1. Contact angle measurement

As a matter of convenience, we first performed the chemical treatment on sheets, to easily observe the contact angle. The presented Taguchi DoE in table 1 delivered 18 recipes by altering the duration, temperature, and concentration. We measured the contact angle on HDPE sheets to extract the hydrophilicity of each recipe. The contact angle measurement on an untreated HDPE sheet is represented in figure 5.

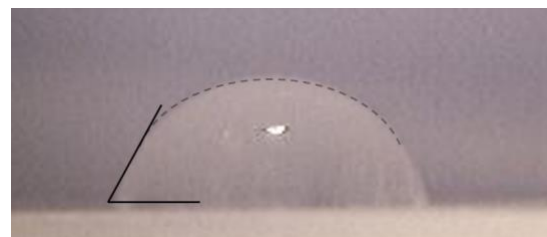


Fig. 5: Contact angle measurement of 70° on HDPE sheet before treatment.

We observe that the initial contact angle is around 70°. The results are displayed in figure 6. The most hydrophilic surface, with a minimal measured contact angle of 15°, was produced by recipe 16. Thus, we kept this recipe for the subsequent work.

The next step was to study the treatment longevity. To monitor the contact angle over time, we kept the treated HDPE sheets in two environments: air and water. These progression over 30 days is shown in Figure 7. The error bars

depict the treatment inhomogeneity across the sheet.

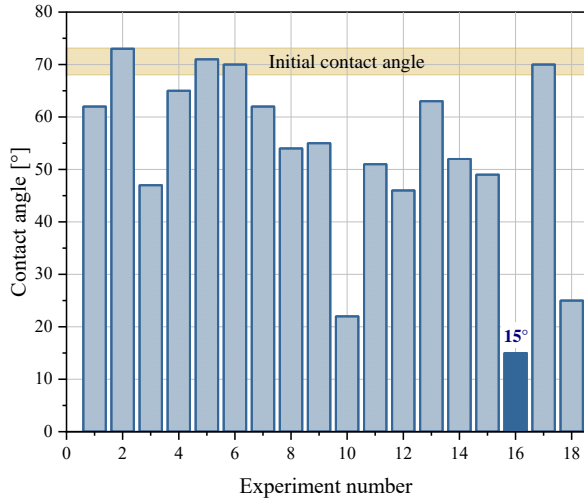


Fig. 6: Contact angle measurement of each DoE recipes on HDPE sheets, with recipe 16 having the smallest contact angle.

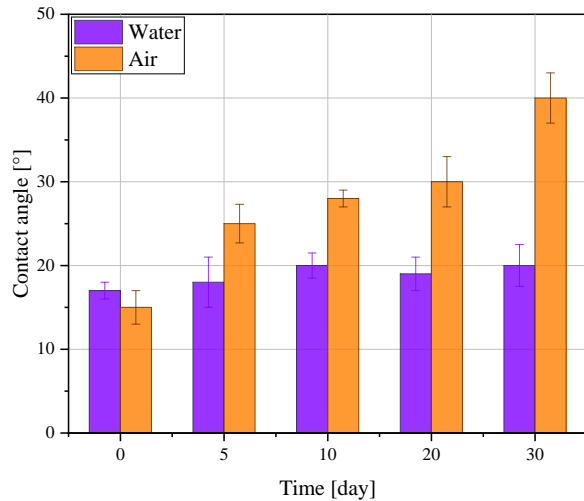


Fig. 7: Contact angle evolution over time illustrating stability in water but degradation in air environment on HDPE sheet surface.

As illustrated, if the samples are immersed in water, the contact angle appears to remain constant over time. On the contrary, if the samples are left in the air, the contact angle increases. The contaminants, such as volatile organic compounds, present in the air rather than in the water environment may be the cause of this decline in hydrophilicity [19]. We conclude that the presented technique is reliable and that polymer TGPs could maintain their hydrophilicity since the pillars are kept in a water environment. Also, keeping the samples in water helps to ensure their hydrophilicity during the fabrication process.

The following step was to confirm that, regardless of the polymer used, we achieve the

hydrophilic behavior. Thus, we also carried out recipe 16 to hydrophilize ABS sheets. The results are displayed in figure 8. We observe that HDPE and ABS samples both have the same contact angle around 15°. We can conclude that the treatment is versatile as with the same recipe, we achieved the same level of hydrophilicity on HDPE and ABS sheets. Future work on characterizing different polymers is required to more broadly study the treatment versatility.

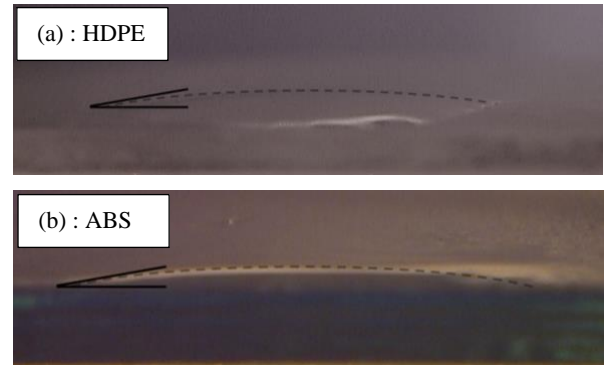


Fig. 8: Contact angle on (a) HDPE, (b) ABS sheet showing super hydrophilicity on different polymers.

3.2. Polymeric TGP characterization

To characterize the fabricated TGP, we used the test bench represented in figure 9. The tested heat rate at the evaporator was fixed at 5 W (0.35 W/cm²), and the cold plate temperature set at 8°C. The top and bottom TGP surfaces were isolated to ensure that the heat is not dissipated through the test bench.

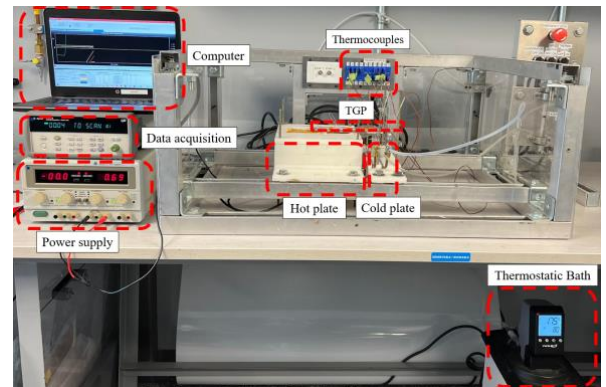


Fig. 9: The TGP characterization test set-up.

Two thermocouples were placed between the TGP bottom surface and the heater and cold plate. These thermocouples are referred to as the TGP evaporator and condenser temperature, T_1 and T_2 respectively. Two additional thermocouples were placed between the TGP top surface and the insulation. These thermocouples are referred to as the vapor temperature. Since the TGP top surface is insulated, we consider that most of the heat

flows through the vapor path. Thus, the upper thermocouples are considered a direct measurement of the vapor temperature. This can be better illustrated by the TGP thermal resistance circuit (Fig. 10) that includes thermal resistance from material conduction (shell and wick), R_{cond} , and Vapor transport, R_{vapor} . The evaporator and condenser vapor temperature are indicated as T_3 and T_4 , respectively.

From these four measurements of temperature, we can extract the TGP total and vapor thermal resistances. The resistance though the material conduction such as the shell and the porous media can then be calculated as the difference between the two.

3.3. Polymeric TGP performance

At a fixed injected heat rate of 5 W, the condenser temperature stabilizes at $T_2=28^\circ\text{C}$, while the evaporator temperature at $T_1=61^\circ\text{C}$. The vapor temperature at the evaporator stabilizes at $T_3=47^\circ\text{C}$ and the condenser at $T_4=44^\circ\text{C}$. The absolute thermocouples error is estimated to be 0.5°C .

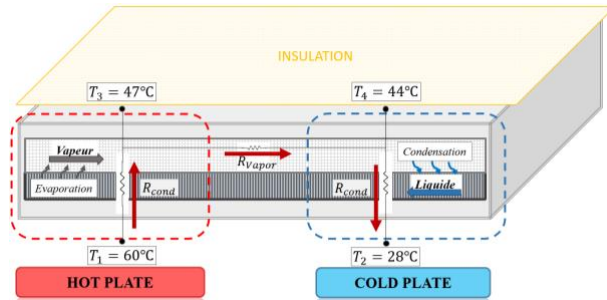


Fig. 10: Thermal resistance circuit for all polymer fabricated TGP.

To account for the test bench heat loss, we used Fourier law to estimate the collected heat from the condenser. This transferred heat rate which is 3.5 ± 0.3 W, represents 70 % of the injected heat in the evaporator. The fabricated TGP has an effective thermal resistance of 9.4 ± 1.0 K/W equivalent to an effective thermal conductivity of 212 ± 28 W/m K. However, the vapor thermal resistance is estimated at 0.8 ± 0.1 K/W. We understand that the major thermal resistance in the fabricated all polymer TGP is from the conduction through the HDPE shell and the ABS pillars structure. This conduction resistance represents 88% of the total thermal resistance. Thus, the material conductivity has to be increased to improve the TGP thermal performances. Therefore, the used resin for the 3D printing should be doped with thermally conductive

additives and the pillars base support must be as thin as possible.

The all polymer TGP performances lasted less than 24 hours due to the polymeric shell poor hermiticity. Consequently, a thin dense layer is mandatory to maintain the vacuum, and the TGP operation. For future work, a laminated polymer-metallic foil is going to be used as a shell material.

4. Conclusion

In this work we introduced an adapted approach to hydrophilize a polymeric wick for TGPs applications. The polymeric wick was hydrophilized by an optimized chemical treatment. It has been proven that this process produces surfaces that are very hydrophilic and stable over time. The versatility of the treatment has also been shown to be effective on HDPE and ABS materials. Thus, an opportunity for high volume manufacturing techniques like HDPE molding is opened to fabricate future TGPs.

We introduced for the first time an all polymer TGP with a treated ABS wick that reached an effective thermal conductivity of 212 W/m K. In comparison, the thermal conductivity range for different polymeric TGPs described in the literature varies from 100 to 1000 W/m K. However, these polymeric TGPs included either unnecessary metallic parts or a pricey hydrophilization treatment like ALD. The TGP operation does not require a metallic wicking or vapor core mechanical structures. Although this material choice improves the TGP thermal conductivity, it increases the cost. The polymeric TGP only requires a metallic layer within its shell to ensure the hermiticity and the long term TGP operation. Thus, the presented primary work shows promising results to introduce a light, low cost, and efficient all polymer TGPs as a thermal management solution.

References

- [1] J. Ku, L. Ottenstein, D. Douglas, M. Pauken, and G. Birur, "Miniature Loop Heat Pipe with Multiple Evaporators for Thermal Control of Small Spacecraft," no. 183, p. 10.
- [2] G. Zhou, J. Li, and L. Lv, "An ultra-thin miniature loop heat pipe cooler for mobile electronics," *Appl. Therm. Eng.*, vol. 109, pp. 514–523, Oct. 2016, doi: 10.1016/j.applthermaleng.2016.08.138.
- [3] M. Yu *et al.*, "Experimental Investigation of a Novel Solar Micro-Channel Loop-Heat-Pipe Photovoltaic/Thermal (MC-LHP-

- PV/T) System for Heat and Power Generation,” *Appl. Energy*, vol. 256, p. 113929, Dec. 2019, doi: 10.1016/j.apenergy.2019.113929.
- [4] C. Jung, J. Lim, and S. J. Kim, “Fabrication and evaluation of a high-performance flexible pulsating heat pipe hermetically sealed with metal,” *Int. J. Heat Mass Transf.*, vol. 149, p. 119180, Mar. 2020, doi: 10.1016/j.ijheatmasstransfer.2019.119180.
- [5] N. Phan, “Flat-evaporator-type loop heat pipe with hydrophilic polytetrafluoroethylene porous membranes,” *Phys. Fluids*, vol. 32, no. 4, p. 047108, Apr. 2020, doi: 10.1063/1.5143561.
- [6] V. Shkolnikov, D. G. Strickland, D. P. Fenning, and J. G. Santiago, “Design and fabrication of porous polymer wick structures,” *Sens. Actuators B Chem.*, vol. 150, no. 2, pp. 556–563, Oct. 2010, doi: 10.1016/j.snb.2010.08.040.
- [7] V. Shkolnikov, D. G. Strickland, D. P. Fenning, and J. G. Santiago, “Design and fabrication of porous polymer wick structures,” *Sens. Actuators B Chem.*, vol. 150, no. 2, pp. 556–563, Oct. 2010, doi: 10.1016/j.snb.2010.08.040.
- [8] Y. Gao, Z. Li, B. Cheng, and K. Su, “Superhydrophilic poly(p-phenylene sulfide) membrane preparation with acid/alkali solution resistance and its usage in oil/water separation,” *Sep. Purif. Technol.*, vol. 192, pp. 262–270, Feb. 2018, doi: 10.1016/j.seppur.2017.09.065.
- [9] M. Azeem *et al.*, “Hydrophilization of Polyester Textiles by Nonthermal Plasma,” *Autex Res. J.*, vol. 21, no. 2, pp. 142–149, Jun. 2021, doi: 10.2478/aut-2019-0059.
- [10] R. Lewis, L.-A. Liew, S. Xu, Y.-C. Lee, and R. Yang, “Microfabricated ultra-thin all-polymer thermal ground planes,” *Sci. Bull.*, vol. 60, no. 7, pp. 701–706, Apr. 2015, doi: 10.1007/s11434-015-0760-9.
- [11] C. Oshman, Q. Li, L.-A. Liew, R. Yang, V. M. Bright, and Y. C. Lee, “Flat flexible polymer heat pipes,” *J. Micromechanics Microengineering*, vol. 23, no. 1, p. 015001, Jan. 2013, doi: 10.1088/0960-1317/23/1/015001.
- [12] S. Xu, R. J. Lewis, L.-A. Liew, Y.-C. Lee, and R. Yang, “Development of Ultra-Thin Thermal Ground Planes by Using Stainless-Steel Mesh as Wicking Structure,” *J. Microelectromechanical Syst.*, vol. 25, no. 5, pp. 842–844, Oct. 2016, doi: 10.1109/JMEMS.2016.2596142.
- [13] S.-S. Hsieh and Y.-R. Yang, “Design, fabrication and performance tests for a polymer-based flexible flat heat pipe,” *Energy Convers. Manag.*, vol. 70, pp. 10–19, Jun. 2013, doi: 10.1016/j.enconman.2013.02.011.
- [14] X. Zhang, P.-F. Ren, H.-C. Yang, L.-S. Wan, and Z.-K. Xu, “Co-deposition of tannic acid and diethylenetriamine for surface hydrophilization of hydrophobic polymer membranes,” *Appl. Surf. Sci.*, vol. 360, pp. 291–297, Jan. 2016, doi: 10.1016/j.apsusc.2015.11.015.
- [15] D. I. H. Daoudji *et al.*, “A Novel One-Step Process to Fabricate Polymeric Thermal Ground Planes,” in *2022 21st IEEE Intersociety Conference on Thermal and Thermomechanical Phenomena in Electronic Systems (iTherm)*, San Diego, CA, USA, May 2022, pp. 1–6. doi: 10.1109/iTherm54085.2022.9899619.
- [16] A. Alafaghani and A. Qattawi, “Investigating the effect of fused deposition modeling processing parameters using Taguchi design of experiment method,” *J. Manuf. Process.*, vol. 36, pp. 164–174, Dec. 2018, doi: 10.1016/j.jmapro.2018.09.025.
- [17] D. I. Hassaine Daoudji, Q. Struss, A. Amnache, É. Léveillé, M. R. Salim Shirazy, and L. G. Fréchette, “Impact of Micropillar Density Distribution on the Capillary Limit of Heat Pipes,” in *ASME 2020 Heat Transfer Summer Conference*, Virtual, Online, Jul. 2020, p. V001T11A002. doi: 10.1115/HT2020-9001.
- [18] A. Faghri, *HEAT PIPE SCIENCE AND TECHNOLOGY*. 6000 Broken Soud Parkway NW, Suite 300: Taylor & Francis Group, 1995.
- [19] M. R. S. Shirazy, S. Blais, and L. G. Fréchette, “Mechanism of wettability transition in copper metal foams: From superhydrophilic to hydrophobic,” *Appl. Surf. Sci.*, vol. 258, no. 17, pp. 6416–6424, Jun. 2012, doi: 10.1016/j.apsusc.2012.03.052.

Theoretical and Experimental Evaluation of Small Diameter Thermosyphons

Gabriel Serafin Couto Vieira^{1*}, Nelson Y. Londoño Pabón¹, and Marcia Barbosa Henriques Mantelli¹

¹ *Department of Mechanical Engineering, Federal University of Santa Catarina, Florianópolis, Brazil*

**Corresponding author email address: gabriel.serafin@labtucal.ufsc.br*

Abstract

The thermal performance of devices based on phase-change phenomena may not respond well to downsizing. The performance of thermosyphons with conventional aspect ratios (ratio between diameter and height) increases with the higher input powers. For ideal conditions (no non-condensable gases and uniform input and output heat fluxes), the condenser and the evaporator tend to have a uniform temperature distributions in steady state operation conditions. In this case, the overall experimental thermal resistance matches classical thermosyphon models. Contrarily, small diameter thermosyphons may not respond the same way to increases in the power input, as an operational limit can be reached. An experimental setup was used to test three thermosyphons of different aspect ratios to verify the accuracy of literature correlations to predict heat transfer of small diameter thermosyphons. The experimental data were compared with results from classical models. The purpose of this work is to verify the thermal performance of long, small-diameter thermosyphons as heat transfer devices and to suggest guidelines for their design.

Keywords: Closed two-phase thermosyphons; Design of thermosyphons; Operation limit; Theoretical thermal resistance

1. Introduction

The miniaturization of components is a trend in many industry branches, such as automobile, medicine, jewelry and electronics. Especially in the latter case, the high reliability of thermosyphons makes them interesting solutions for the thermal control of some electronic devices due to their reliability, weight and independence of the external power sources.

According to Dunn and Reay [1], heat pipe heat sinks proved to be a good solution for electronics temperature control, as they are lighter and more effective than conventional extruded aluminum units. However, the demands of manufacturers for low-cost and compact thermal control systems lead to the development of more efficient and compact heat pipe solutions.

It is noted that the thermal performance of devices based on phase-change phenomena occasionally does not respond well to downsizing. Small-diameter closed two-phase thermosyphons often exhibit unpredicted behaviors. In these cases, the usual mathematical models may not be applicable, since the phase-change phenomena happens in confinement conditions, constraining the vapor bubbles on the evaporator section and causing the drag of liquid droplets into the condenser section.

Jouhara and Robinson [2] performed an experimental investigation of small diameter two-phase closed thermosyphons, with different working fluids: water, FC-84, FC-77 and FC-3283. They found that, while the performance for the water-charged thermosyphon surpassed those of the

other three working fluids, the low saturation point of the tested fluorocarbon liquids granted them a marginal heat transfer improvement at low operating temperatures. It was also stated that the heat transfer correlations used were in good agreement with the experimental data. These authors implemented different heat transfer correlations for both evaporator and condenser sections, which were analyzed separately. The results were compared with data. They concluded that no correlation completely fits thermosyphons.

According to Smith et al. [3], in confined thermosyphons, the smaller the available space in the involucre for upward vapor flow, the more complex the interaction of capillary, buoyancy and inertial forces at the liquid-vapor interface. They suggest that the following parameters influence the performance of closed two-phase thermosyphons: thermophysical properties of the working fluid, filling ratio and tube geometry. Operating conditions, such as: reduced pressure (ratio between the current pressure and the pressure at the critical point) and heat flux are also important in the analysis. In their study, a transparent small diameter thermosyphon with different working fluids (water, ethanol and HFE-7000) was experimentally analyzed. Different fluids yield different levels of confinement, which, in turn, yield different flow regimes. These flow regimes were organized in maps, defined by degree of confinement and rate of vapor production.

The confinement can be analyzed through the dimensionless Co confinement number, which is the ratio of the bubble departure size, given by

$\sqrt{\sigma/(\rho_l - \rho_v)g}$, to the channel diameter d_i :

$$Co = \frac{1}{d_i} \sqrt{\frac{\sigma}{g(\rho_l - \rho_v)}} \quad (1)$$

where σ is the liquid surface tension, g the gravity acceleration and $(\rho_l - \rho_v)$ is the difference between liquid and vapor densities. The closer Co comes to 1, the more confined the flow is. On the other hand, the smaller Co , the larger is the inner diameter in comparison to the vapor bubble size and thus, farther from confinement.

Smith et al. [4] continued the previous studies, explaining the relation between the working fluid flow regimes and its influence over the heat transfer capacity of thermosyphons. They explained how the hydraulic phenomena occurring inside the thermosyphons dictated the heat transfer. Each scenario was analyzed for several combinations of confinement level, imposed heat flux and reduced pressure (ratio between actual vapor pressure and pressure at critical point).

Pabón et al. [5] presented an in-depth study of the Geysier Boiling Phenomenon (GBP) that happened in a glass thermosyphon with a punctual heater. A high-speed camera, a pressure transducer and thermocouples installed inside the thermosyphon allowed the characterization of the GBP. Image analysis and the pressure measurements suggested the existence of different levels of energy storage during the formation of bubbles with a minimum threshold being eventually found. This threshold is represented by the N number, which can differentiate geysering event from other boiling conditions and is given by:

$$N = \frac{P_{max} - P_{min}}{P_{min}} \quad (2)$$

where P_{max} is the peak pressure in the analyzed time interval and P_{min} is the average minimum value.

Cisterna et al. [6] experimentally studied sodium-steel thermosyphons and used the data to elaborate

mathematical models for startup and continuum limits. The startup limit is defined as the minimum heat load required to push the sodium vapor front up to the entrance of the condenser section. The continuum limit is the minimum heat load required to push the vapor front up to the condenser top. Between these two limits, the thermosyphon operates in the “fin regime”, in which heat rejection occurs not only on the active portion of the condenser (filled with vapor), but also on the inactive portion, through heat conduction along the involucre. The enlarged temperature gradient along the condenser actually showed that the vapor may not reach the top of condenser if it is condensed along the condenser length, i.e., the thermosyphon operation also depends on the condenser heat rejection capacity.

The present study aims to provide the groundwork for the design of small-diameter thermosyphons. For this, a series of experiments with different thermosyphons is performed. The experimental and theoretical thermal resistances (obtained from models) are compared. The operational limits of the thermosyphons are also calculated and compared with the actual performance of the devices, which are subject to different heat input levels but the same heat sink temperature, resulting in several different operational regimes. These operational regimes are classified in different categories based on temperature and pressure measurements. The results are summarized as an operation regime map, which combines information regarding confinement, heat flux, thermal resistance and operation regimes.

2. Methodology

2.1. Experimental Setup

Figure 1 depicts the diagram of the workbench. The three studied water-copper thermosyphons were 918mm long with inner diameters of 7.9, 11.1 and 20.2mm. The evaporator, condenser and adiabatic sections were 200, 628 and 90mm long, respectively. The filling ratio was the same for three devices: 66%. The thermosyphon was monitored with Type-T thermocouples (3 for the evaporator section, 3 for the adiabatic section and 8 for the condenser). A pressure transducer was also installed on the topmost position of the condenser.

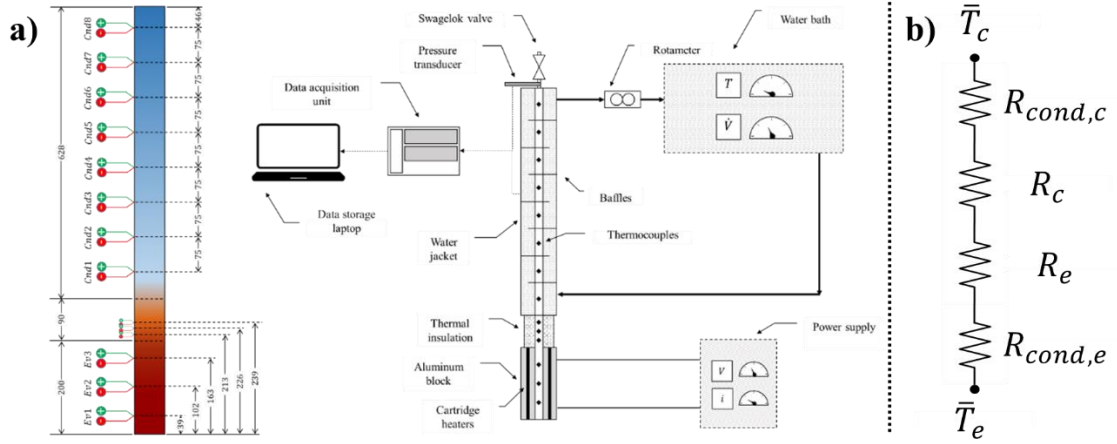


Figure 1. a) Thermocouples distribution and workbench diagram. b) Equivalent electric circuit.

Four cartridge electric resistances were inserted in an aluminum block in close contact with the evaporator, to provide the thermosyphon input power by means of a power supply (MEC 1310). The input power was provided in increasing stepwise fashion, after the steady-state was achieved at each power level. The evaporator and adiabatic sections were thermally insulated from the environment using expanded vermiculite. The heat rejected by the condenser is dissipated to a water jacket. The water jacket is also connected to a rotameter (Omega FL1504A) and a water bath (Lauda RUK-40S). These devices are responsible for keeping a constant cooling fluid mass flow rate of 0.017kg/s and temperature of 20°C.

The data was collected using a National Instruments (NI) data acquisition system, composed by the NI SCXI-1000 module, NI SCXI-1303 terminal and a data acquisition code developed in the LabVIEW software. A data acquisition rate of 1Hz was adopted. The pressure transducer (Omega

PX409-015V5V) is also shown in Figure 1. Additionally, the workbench also counts with three more thermocouples: one installed on the aluminum block and other two on the entry and exit of the water jacket (not shown).

To investigate the effects of decreasing the inner diameter in thermosyphons, the lengths of the evaporator, adiabatic and condenser sections were kept the same for all the devices. This allows the same experimental bench to be used in different thermosyphons.

Thermosyphons with narrower tubes have the characteristics: high aspect ratios, higher vapor pressure losses and higher confinement levels. Besides, the narrower the tube, the larger is the vapor struggle to reach the whole length of the condenser, which might not be used at its full potential.

Table 1 presents ranges of the tested parameters for the studied thermosyphons.

Table 1. Geometrical and thermal aspects of the tested thermosyphons.

d_i [mm]	Aspect ratio (L/d_i)	Vapor temperature range [°C]	Pressure range [kPa]	Heat input [W]	Co
7.9	116	30 – 40.5	4.6 – 7.7	20 – 350	0.34
11.1	83	25 – 44.3	2.1 – 8	20 – 600	0.24
20.2	45	22.5 – 111.5	1.2 – 120.6	20 – 3500	0.15

2.2. Thermal Resistance Modeling

As suggested by Reay and Dunn [1], the heat pipe experimental thermal resistance is defined as the ratio between the differences of the average evaporator and condenser temperatures, \bar{T}_e and \bar{T}_c , divided by the transferred heat (q):

$$R = \frac{\bar{T}_e - \bar{T}_c}{q} \quad (3)$$

However, for small diameter thermosyphons, the experiments showed that models usually under predict the thermal resistances, even when the vapor front is able to reach the whole condenser section.

In steady state conditions, the heat transfer capacity of a thermosyphon can be estimated from its equivalent thermal resistance network. This

overall thermal circuit is formed by following thermal resistances in series: external, wall conduction R_{cond} , evaporator R_e , condenser R_c and phase change. As the wall surface temperatures and heat transfer rate are known, the external thermal resistance do not need to be considered. Furthermore, as the phase-change thermal resistance is generally low, it was also discarded.

The expressions used to estimate the circuit thermal resistances are presented in Table 2 and the Equivalent electric circuit is depicted in Figure 1.b. The evaporator pool thermal resistance $R_{p,e}$ expression was suggested by Imura [7], while the evaporator liquid film $R_{lv,e}$, by Gröll and Rösler [8] and the condenser R_c , by ESDU [9].

Table 2. Theoretical thermal resistance expressions

Symbol	Correlation
$R_{p,e}$	$R_{p,e} = \frac{1}{k_l \pi L_e} \left(0,32 \left(\frac{k_l}{D_i} \right) \left(\frac{\rho_l^{0,65} k_l^{0,3} c_{p,l}^{0,7} g^{0,2}}{\rho_v^{0,25} h_{lv}^{0,4} \mu_l^{0,1}} \right) \left(\frac{p}{p_{atm}} \right)^{0,3} (q_e'')^{0,4} \right)^{-1}$
$R_{lv,e}$	$R_{lv,e} = 0.345 q_e^{\frac{1}{3}} \left[D_i^{\frac{4}{3}} g^{\frac{1}{3}} L_e \left(\frac{h_{lv} k_l^3 \rho_l^2}{\mu_l} \right)^{\frac{1}{3}} \right]^{-1}$
R_c	$R_c = 0.235 q_e^{\frac{1}{3}} \left[D_i^{\frac{4}{3}} g^{\frac{1}{3}} L_c \left(\frac{h_{lv} k_l^3 \rho_l^2}{\mu_l} \right)^{\frac{1}{3}} \right]^{-1}$

The evaporator resistance is divided in two: the pool $R_{p,e}$ and the liquid film $R_{lv,e}$ resistances, which are combined through:

$$R_e = H_p R_{p,e} + (1 - H_p) R_{lv,e} \quad (4)$$

where H_p is the non-dimensional liquid pool height, determined by:

$$H_p = L_p / L_e \quad (5)$$

where L_p is the actual length of the pool and L_e , the evaporator section length. In actual operation conditions, the liquid pool height experiences an increase due to the presence of bubbles within the pool (especially if the evaporator experiences pool boiling). However, it also experiences a decrease

$$q_{max,f} = 0.64 \pi d_i L_e \left(\frac{\rho_l}{\rho_v} \right)^{0,13} \left(\frac{D_i}{4L_e} \right) h_{lv} [\sigma g \rho_v (\rho_l - \rho_v)]^{\frac{1}{4}} \quad (6)$$

The adiabatic section average temperature was used as reference to the working fluid properties in this equation.

On the other hand, as stated by Cisterna et al. [6], the minimum heat load required for the vapor front to reach the end of the condenser section is called continuum limit. If the power input is low, the vapor may have such a small pressure that its flow is not continuum. This minimum heat is:

due to the accumulation of liquid in the condensate films that form along the internal thermosyphon walls. For simplification purposes, two hypothesis are assumed. First, the liquid pool height is undisturbed, so that the liquid film length is $L_f = L_e (1 - H_p)$. Second, due to ebullition, the liquid pool actually occupies the whole length of the condenser, i.e., $H_p = 1$.

2.3. Operational Limits of a Thermosyphon

The thermosyphons used in this research are the same as used by Pabon [10] and by Vieira [11]. Both authors stated that the first operational limit to be reached is the entrainment limit. The maximum heat that the device is able to transport under this condition is calculated by the following expression proposed by Imura et al. [12]:

$$q_{continuum} = \bar{h}_{eq} (T_v - T_\infty) \varphi_{continuum} \pi D l_c \quad (7)$$

where \bar{h}_{eq} is the average equivalent heat transfer coefficient.

It should be noted that the continuum limit proposed by Cisterna et al. [6] was observed for sodium-steel thermosyphons. For the same temperature, the sodium vapor pressure is several orders of magnitude lower than water's and so this limit might not be reached in the present case.

As depicted in the workbench diagram (see Figure 1), the water jacket is divided by baffles. The heat transfer coefficient was calculated for each baffle section, using the Zukauskas correlation. In each section, the cooling fluid temperature was affected by the heat gained from previous sections .

In Eq. 7, the parameter $\varphi_{continuum}$ can be considered a correction to the equivalent convection coefficient (Cisterna et al. [6]) given by:

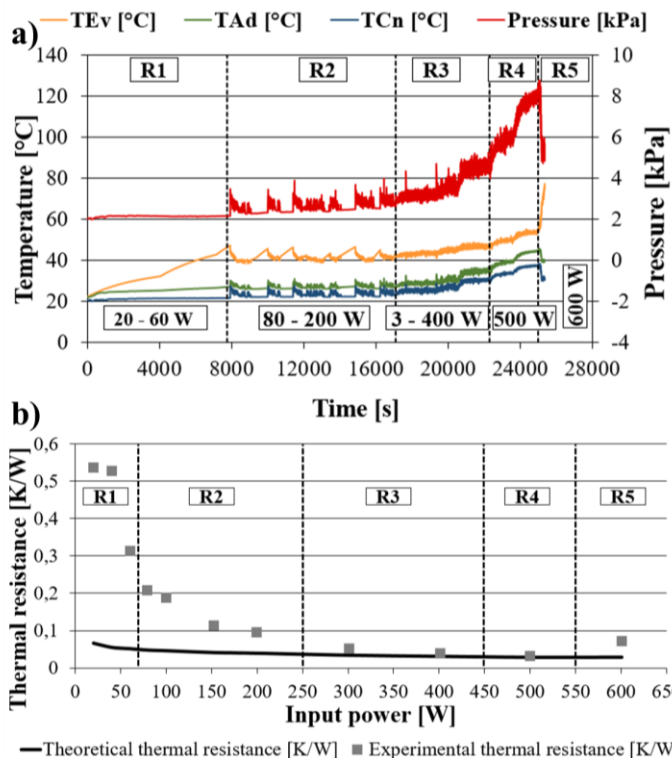
$$\varphi_{continuum} = \left(\frac{0.6 + 2.14L_d}{0.21 + 2.41L_d} \right) \left(\frac{0.1 + 2.14L_d}{0.21 + 2.41L_d} \right) \quad (8)$$

where L_d is the characteristic condenser length:

$$L_d = \frac{L_c}{D} \quad (9)$$

3. Results and discussions

Figure 2 depicts the performance of the $d_i = 11.1mm$ thermosyphon, which is similar to the performance of the other tested thermosyphons. Figure 2.a shows the pressure readings and temperatures of the evaporator T_{Ev} , adiabatic T_{Ad} and condenser T_{Cn} regions, while Figure 2.b shows a comparison between the theoretical and experimental thermal resistances.



— Theoretical thermal resistance [K/W] ■ Experimental thermal resistance [K/W]
Figure 2 - a) Data for the $d_i = 11.1mm$ thermosyphon (divided between the 5 operation regimes) and **b)** Comparison between analytical and experimental thermal resistances.

Usually, thermosyphons increase their heat transfer performance with the increase of the input power. For a device free of non-condensable gases and subjected to uniform input and output heat fluxes, the major characteristic of the fully-developed operation is both the condenser and the evaporator at uniform temperature distributions. Usually, when this fully developed working regime is attained, the experimental thermal resistance presents good agreement with classical thermosyphon modeling. However, for confined thermosyphons, this may not be the case.

In this work, the working regimes of the thermosyphons were classified in five different operational regimes, based on two parameters: i) the distance that the vapor front reached within the condenser and ii) evidence of geyser boiling. The criterion to identify the intermittent ebullition i.e., $N \geq 0.1$, was suggested by Pabón et al. [5] Eq. 2.

The different operational regimes observed are described in following subsections.

3.1. R1 – Operational Regime 1 – Condenser not fully operational

As shown in Figure 1, each thermosyphon is instrumented with 13 thermocouples. As the vapor front advances into the condenser direction, the temperature readings shoot up. At each power step, the averaged readings of each condenser thermocouple are compared with the coolant inlet temperature. The condenser is considered not fully operational if less than half thermocouples present readings above the coolant inlet temperature. In this case, the possibility that heat is conducted through the involucre walls rather than through the vapor front advance is discarded, because the heat transfer coefficient of the water jacket is much higher than the conductance through the tube, keeping the condenser wall at uniform temperature. Furthermore, this behavior is usually observed at low heat loads, when no significant conduction heat transfer is expected.

As seen in Figure 2.a, the operational regime of the device varies with the input power. For 20 to 60 W range, there is an increase in T_{Ev} , however, the hot vapor does not reach the whole condenser, resulting in uneven temperature distribution. This is seen as T_{Cn} remains largely at 20°C, the same temperature of the water-jacket, which justifies its classification in R1 category, where the condenser is not fully operational (more than 50% does not exchange heat with thermal bath). Furthermore, the difference between T_{Ev} and T_{Cn} results in the relatively high thermal resistance values seen in

Figure 2.b.

3.2. R2 – Operational Regime 2 – More than 50% of the condenser operational

Similar to the case presented above, if the vapor front does not reach the thermocouple at the top of the condenser, but stretches over more than half of its extension, the condenser section is considered at operational regime 2, where more than 50% of its length is active.

Figure 2 shows that, from 80 to 200W, boiling is observed (see variations in T_{Ev} , T_{Ad} , and T_{Cn}). Both the temperatures and pressure readings experience cyclical variations, which suggests that, while the input power is enough to activate the condenser region, not enough energy is supplied to make the ebullition on the evaporator a sustainable process. As the vapor does not occupy the whole length of the condenser section, the thermosyphon's thermal resistance is still very high.

Table 3 – Comparison between methods of calculating the experimental thermal resistance.

Imposed heat load [W]	Operational regime	R_{th} according to Eq. 2	R_{th} active portion of the condenser	Theoretical thermal resistance
20	1	0.54	0.39	0.02
40	1	0.53	0.45	0.01
60	2	0.31	0.27	0.01
80	2	0.21	0.18	0.01
100	2	0.19	0.17	0.01

In Table 3, in third column, the whole evaporator was considered active (Eq. 2) for the thermal resistance calculation, while, in the fourth column, only the active portion of the condenser is considered. It can be observed that the thermal resistances by considering only the active portion of the condenser are smaller than that obtained with Eq. 2. This means that the model is not suitable for this condition, as most of the condenser section is inactive for the first two imposed heat loads. In actual applications, a condenser section shorter than 628mm should be advisable for the device operating in these conditions.

3.3. R3 – Operational Regime 3 – Intermittent ebullition

As the input power is increased and if no operational limit is met, the vapor front may reach the whole condenser length. However, having the condenser entirely occupied by the vapor does not imply an ideal working condition. Temperature and pressure oscillations typical of geyser boiling are observed in this region, which increase the overall thermal resistance. A sustained ebullition is only possible for over 300W and 400W, with T_{Ev} , T_{Ad} and T_{Cn} showing that the vapor fills the entire condenser, with T_{Cn} constantly over 20°C (see Figure 2.a). The experimental thermal resistance compares better with the theoretical predictions, as seen in Figure 2.b, with the average error dropping to 37 and 24%, for 300W and 400W, respectively.

3.4. R4 – Operational Regime 4 – Ideal

If all temperatures of the condenser section are higher than the inlet temperature and the previous

criterion is not reached ($N < 0.1$), the thermosyphon is considered fully active, with uniform condenser temperature, free of intermittent ebullition. Due to the smooth temperature oscillations and relatively high heat fluxes, the resulting thermal resistances are the lowest and the best theoretical predictions are reached: for 500W, the error between theoretical and experimental thermal resistance are only 14%.

3.5. R5 – Operational Regime 5 – limit

At higher power inputs, due to the interaction between the various phenomena of mass and heat transfer, operational limits may be reached, as observed by the sudden increase in the evaporator temperature, while the adiabatic and condenser temperatures decrease, resulting in the thermal resistance increase.

3.6. Comparison between thermosyphons

As mentioned before, Figure 2 illustrates the phenomena observed in all the three tested thermosyphons (see input power ranges in Table 2), and so more details of the experimental results for the other tested cases are not shown.

In these other thermosyphons, different power steps were applied, until operational limit were reached (cases $d_i = 7.9$ and 11.1mm) or until the power source reaches its maximum output (case $d_i = 20.2mm$). Each power input led to a different T_{Ad} and to a theoretical operational regime. From one side, the operational limit expressed in Eq. 6 suggests the maximum possible thermosyphon heat load, at the adiabatic section temperature T_{Ad} . On the other hand, a minimum heat input is also

required to fully activate the condenser section. This limit is expressed by Eq. 7. These two equations are used to establish an envelope condition: from one side, Eq. 6 predicts the maximum operational limit and, from the other, Eq. 7 predicts the minimum required power for the thermosyphon to operate with its condenser fully active. These theoretical results are then compared with the actual input power applied.

All of this information is depicted in Figure 4. In the diagrams, the entrainment limit is represented by the short-dashed lines, the continuum limit, by the long dashed lines, areas in light grey shows the heat loads which resulted in the intermittent operational regime (R3) and in dark grey, the ideal regime (R4). The full black line is the imposed heat ($y=x$ axis curve), depicted to facilitate the comparison between the two envelope limit conditions.

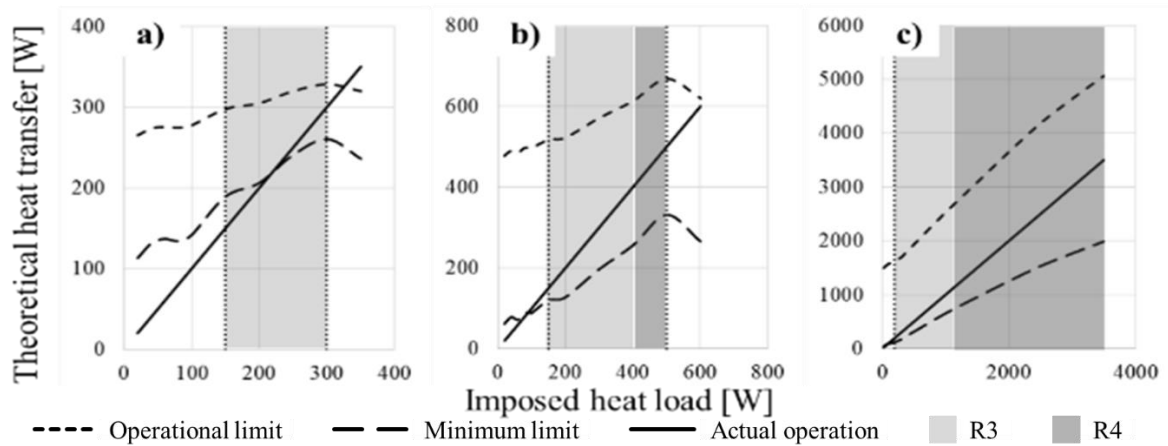


Figure 4. Comparison between experimental and theoretical heat transfer limit for thermosyphon for the same filling ratio a) $d_i = 7.9\text{mm}$ ($Co = 0.34$); b) $d_i = 11.1\text{mm}$ ($Co = 0.24$); and c) $d_i = 20.2\text{mm}$ ($Co = 0.14$).

From Figure 4.a, it is observed that the entrainment limit for $d_i = 7.9\text{mm}$ tube increases at a very small rate with the imposed heat load and that the condenser section is only fully active for a very limited operational range (150 – 300W).

In Figure 4.b, not only the steepness of the entrainment limit over the imposed heat load is more pronounced, but the tube was able to operate at broader power input ranges, with the ideal regime being reached (dark gray area). Actually, in this case, the thermosyphon reached its peak capacity at 500W, when the lowest thermal resistance is attained (See Figure 2).

Finally, in Figure 4.c, the theoretical operational limit increases almost at the same pace of the imposed heat load, which means that, for the tested range, the operational limit would not be reached. Furthermore, the range in which the thermosyphon was able to work without intermittent ebullition (dark gray area) was drastically larger.

For all cases, it was observed that the full lines (actual heat load) crossed the short-dashed lines (operational limit) outside of domain regions in which the thermosyphon was identified as working. This indicates that Eq. 6 predicted well the operational limit, regardless of confinement level.

On the other hand, the continuum transfer limit correlation (Eq. 7) had mixed results. In Figure 4.a,

it was observed that the full line (actual heat load) crossed the long-dashed line (continuum limit) inside of the region identified as fully active condenser. This means that the heat input required to activate the condenser section is actually smaller than the value predicted by the correlation, at least of 150W instead of 190W. In Figure 4.b, the opposite occurred, with full activation of the condenser section occurring only after the expected value, after 150W instead of the predicted 120W. In Figure 4.c, the correlation worked well, with the full activation of the condenser section occurring at 80W, as predicted by the correlation. While the continuum correlations was not developed for the working fluid water (but for sodium) the results showed to be physically coherent. Further studies regarding this correlation could result in a more reliable tool for the design of thermosyphons operating at lower temperature levels.

In Figure 5, the obtained results for the three thermosyphons are condensed in plots of the thermal resistance as a function of the heat flux. Each point contains information regarding operational regime (shape of the symbol) and inner diameter (color of the symbol). Due to the large dispersion, a logarithmic decimal base scale was used on the horizontal axis, to represent the heat flux. The operating regimes were characterized by symbols (R1, square; R2, triangle; R3, filled circle;

R4, hollow circle and R5, the rhombus). The involucre sizes were expressed in different colors. The darker the shade, the larger the inner diameter. Following, individual analyses of the thermosyphons tested are presented.

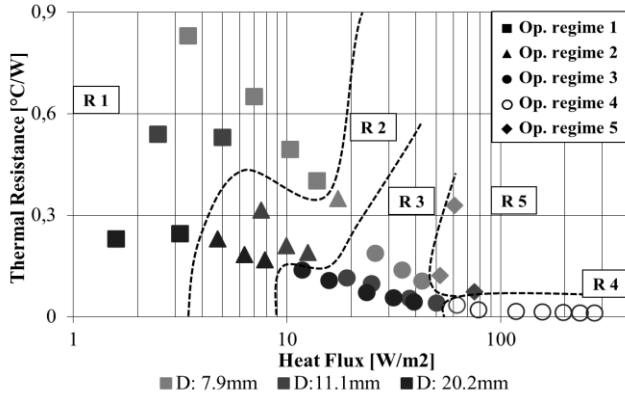


Figure 5. Operation regime map for the tested thermosyphons.

3.6.1 Thermosyphon $d_i=7.9\text{mm}$ and $Co=0.34$

In Figure 5, it is noticed that heat fluxes under $11\text{kW}/\text{m}^2$ are not enough to force the vapor front over the second half of the condenser section. This is seen by the number of times in which R1 and R2 were observed for these heat fluxes. However, considering the aspect ratio of the condenser length and inner diameter, it could be argued that the condenser section is over dimensioned. As the thermal resistance drops over the increasing imposed heat flux, this indicates a gradual activation of the device.

As observed by Smith et al. [4], at low pressures and low heat fluxes, typical geyser boiling is observed. Under these conditions, the extremely high rate of vapor growth is responsible for bursting bubbles, which cause a considerable amount of liquid to be dragged by the released vapor into the condenser section. The accumulated energy is also released as momentum and is responsible for the observed pressure oscillation. In these conditions, heat transfer occurs by sensible and latent heat, as both saturated vapor and liquid are thrown into the condenser section. These mass oscillations are not accounted for in the thermosyphon models, resulting in bad comparisons between data and theoretical results.

The frequency of the temperature oscillations follows the heat flux increase. However, the pressure is reduced at low temperatures, so that the volumes of the vapor bubbles are not reduced and the thermal performance of the device is, therefore, not significantly improved. This is seen from Figure 5, as the thermosyphon with $d_i = 7.9\text{mm}$ never

actually reached R4, going straight to R5.

3.6.2 Thermosyphon $d_i=11.1\text{mm}$ and $Co=0.24$

An interesting performance improvement is observed by comparing the results from thermosyphon with $d_i = 7.9\text{mm}$ to the one with $d_i = 11.1\text{mm}$. While the changes in the geometry of the involucre may seem small, there was a remarkable difference in the thermal performance: not only experimental thermal resistance was significantly smaller, but the this device had actually reached the optimal working conditions, R4. This difference is associated to the lower confinement level, which was enough to allow different flow regimes. As observed by Smith et al. [4], for tubes with larger inner diameter, the liquid plugs above the nucleated bubbles are not sustainable in a column structure, due to the combined effects of the lower surface tension and lower confinement effects. As these plugs are shattered, the dispersed droplets are pushed into the condenser section in a churn-like flow (observable from the temperature readings of operational regimes R2 and R3, in Figure 5).

An increase in the heat flux actually increases the rate of vapor production without altering the confinement level. The flow pattern becomes much more churn-like in the evaporator, as theorized by Smith et al. [4]. Consequently, smaller bubbles are formed and more vigorous vapor production gives rise to churning of the liquid-vapor interface. These bubbles quick break up forces less liquid into the condenser section. In turn, the vapor is then free to condensate on the walls and then return to the evaporator pool. As the condenser section is no longer subjected to heat transfer from a relatively large liquid mass and as the vapor bubbles are more uniformly spread in evaporator section, the heat transfer is augmented.

In the thermosyphon with $d_i = 11.1\text{mm}$, this transition from R3 to R4, which is free of larger temperature and pressure oscillations, resulted in an increase in pressure level. This affects the vapor density, which also increases. In turn, this curbs the rate of vapor growth, leading to smaller, more frequent bubbles and thus to a more stable thermal performance.

3.6.3 Thermosyphon $d_i=20.2\text{mm}$ and $Co=0.15$

The larger inner diameter results in a much lower level of confinement ($Co=0.15$). According to Smith et al. [4], this characterizes the flow as unconfined and may be analyzed considering more conventional convection scenarios. For low heat fluxes, the thermosyphon presented temperature and pressure readings which could be characterized as geysering. However, this does not fit the prescribed

flow regime maps as presented by Smith et al. [3]. In this case, the geysering may have less to do with the confinement and more to do with the formation of large vapor bubbles, caused by the low pressures and low heat fluxes. As seen in previous cases, these conditions favor the nucleation of large bubbles with elevated growth rates.

By further increasing the imposed heat flux, the vapor production on the evaporator becomes closer to a slug-plug flow, eventually landing on a bubbly flow. The unconfinement means that the bubbles do not grow to the size of the tube. In turn, liquid is not tossed into the condenser section. The minimal oscillatory behavior means that the vapor generation is being sustained predominantly by the nucleation of small bubbles.

4. Conclusions

The present study aimed to show experimental data regarding operation of small diameter two-phase closed thermosyphons, as these devices usually have different behaviors when compared to larger diameter conventional devices. Therefore, the effect of confinement in thermosyphons was analyzed. The major conclusions are:

- The thermophysical properties of the working fluids, the inner pressure and the heat loads are parameters that affect the performance of small diameter thermosyphons;

- The behavior of small diameter thermosyphons was classified;

- The obtained results are depicted as an operation regime map, which presents the conditions of confinement, imposed heat fluxes, observed thermal resistances and operational behavior classification;

- The resulting operational behavior map may be used as a design tool, to avoid certain parameter combinations, which are already proven to be fallible;

- The selection of thermal resistance correlations to determine the thermal resistances must be careful. Certain phenomena, not accounted for in the correlations, may drastically deviate the result from the expected results;

- The performances of thermosyphons are very sensitive to the influence of inner diameter. Usual solutions to solve problems like geysers are not applicable to small diameter tubes. An operational limit may be reached before the fully-developed regime is attained;

- The heat load range at which a thermosyphon works is also delimited by its inner diameter. It was

seen that the smaller the inner diameter, narrower is the operation range;

- Small diameter thermosyphons do not require extremely long sections. However, the use of small diameter thermosyphons is feasible.

REFERENCES

- [1] Reay, D.A., Kew, P.A. and McGlen, R.J. Heat Pipe: Theory, Design and Applications. Butterworth-Heinemann, Amsterdam, NED, 2014.
- [2] H. Jouhara, A. Robinson Experimental Investigation of Small Diameter Two-Phase Closed Thermosyphons Charged with Water, FC-84, FC-77 & FC-3283 App. Thermal Eng. 2009. 30. p. 201
- [3] K. Smith, R. Kempers, A. Robinson, Confinement and vapour production rate influences in closed two-phase reflux thermosyphons Part A: Flow regimes Int. J. of Heat and Mass Transfer, 2018. 119: p. 907.
- [4] K. Smith, R. Kempers, A. Robinson, Confinement and vapour production rate influences in closed two-phase reflux thermosyphons Part B: Heat Transfer Int. J. of Heat and Mass Transfer, 2018. 120: p. 1241.
- [5] N. Pabón, J. Mera, G. Vieira, and M. Mantelli, Visualization and Experimental Analysis of Geysers Boiling Phenomena in Two-Phase Thermosyphons. Int. J. of Heat and Mass Transfer, 2019. 141: p. 876.
- [6] L. Cisterna, M. Cardoso, E. Fronza, F. Milanez, M. Mantelli, Operation regimes and heat transfer coefficients in sodium two-phase thermosyphons Int. J. of Heat and Mass Transfer, 2020. 152: p. 876.
- [7] H. Imura, H. Kusuda, J. Ogata, T. Miyazaki, N. Sakamoto, Heat transfer in two-phase closed-type thermosyphons, Engineering, 1979
- [8] M. Gröll, S. Rösler, Operation principles and performance of heat pipes and closed two-phase thermosyphons, J. of Non-Equil. Thermodynamics, 1992. 17, p.91
- [9] ESDU, 81038 - Heat pipes - performance of two-phase closed thermosyphons, 1983
- [10] N. Pabon, Análise teórico-experimental do fenômeno de Geysers Boiling em termossifões bifásicos fechados, Doctoral Dissertation, UFSC, 2019.
- [11] G. Vieira, confinement effects in closed two-phase Thermosyphons, Doctoral Dissertation, UFSC, 2019.
- [12] H. Imura, K. Sasaguchi, H. Kozai, S. Numata, Critical heat flux in a closed two-phase thermosyphon. Int. J. of Heat and Mass Transfer, 1983. 26: p. 1181.

Visual Investigation of Surface Functionalization Effect in Two-Phase Closed Thermosyphons

Gabriel Serafin Couto Vieira^{1*}, and Marcia Henriques Barbosa Mantelli¹

¹Department of Mechanical Engineering, Federal University of Santa Catarina, Florianopolis, Brazil

*Corresponding author email address: gabriel.serafin@labtucal.ufsc.br

Abstract

The thermal performance of thermosyphons is directly associated with the high convection coefficients resulting from the working fluid liquid to vapor phase change, that happens in the evaporator section. A delay in bubble nucleation may lead to unwanted energy accumulation in the evaporator and, eventually, geysering of the working fluid, an undesirable effect in most applications. Actually, boiling can be directly influenced by the inner surface characteristics of the casing. This work aims to investigate strategies to improve the bubble nucleation process inside thermosyphons and to reduce the temperature excess by modifying the evaporator inner surface characteristics. An experimental test bench was designed for the study of bubble dynamics during the phenomenon. Data was gathered with the help of a high-speed camera and thermocouples, installed inside the thermosyphon. The best strategy will be the one that allows the reduction of evaporator wall temperatures and the decrease the oscillations of both temperature and pressure.

Keywords: Thermosyphons; Geysering boiling phenomenon; Surface texturization; Surface Functionalization; Nucleation sites;

1. Introduction

The importance of the surface conditions on nucleated boiling has long been recognized. The relation between the cavity size and the surface-to-liquid bulk temperature difference (temperature excess) required for vapor bubble nucleation can be intricate. Primarily, the smoother a surface, the larger the temperature excess required to initiate nucleated boiling.

In two-phase thermosyphons, phase change phenomena play vital roles. The high thermal conductance of the thermosyphons is directly associated with the high convection coefficients resulting from the working fluid phase change. As thermosyphons rely heavily on these mechanisms, it is expected that the working fluid's behavior can be influenced by the inner surface characteristics of the casing. A delay in bubble nucleation may provoke high accumulation of energy that would, eventually, result in the working fluid geysering. Actually, the intensity of these temperature and pressure surges is related to the level of energy stored in the liquid pool.

The idea of applying texturization techniques inside thermosyphons is not new. Bellani [1] experimented texturizing in copper two-phase loop thermosyphon, where R141b was the working fluid. This author manufactured two evaporator sections: one with inner surface conditions compatible with commercially available copper pipes and the other which was sanded with sandpaper mesh 100 and scratched with a sharpened stainless steel tool. Before the start-up, he noted that the temperature

difference between the involucre wall and vapor line was slightly lower for the sanded-scratched than for the as-received involucre. Also, it was observed that the minimum input power before the start-up was lower for the sanded-scratched involucre than for the as-received one. However, after both devices achieved start-up, there was no more noticeable difference between the two.

Simas [2] also studied experimentally the performance of a copper two-phase loop thermosyphon with different evaporator internal surface finishings. Water was used as the working fluid. A flat evaporator was formed by stacking copper plates, machined in the desired geometry, and by diffusion bonding the resulting pile in an especial furnace. The internal surface finishing was obtained by spot welding a wick (screen mesh) on the evaporator's inner surface. The performance of this device was compared with that of a wickless structure. She concluded that the wicked evaporator provided efficient passive cooling even for concentrated heat sources distant from the liquid pool. The wick capillarity allows the working fluid to reach the heat source region. Furthermore, the thermal measurements suggested that the wick structure also favors nucleated boiling inside the device, which leads to a reduction in wall temperatures.

According to Pabón et al. [3], the intensity of the geysering boiling is related to the level of energy stored in the liquid pool. These authors described an experimental setup consisting of a cylindrical glass

thermosyphon with a 20 mm-wide inner diameter, to which highly concentrated heat was provided. Heat was delivered laterally, in a single small area, adjacent to the liquid pool section, with the objective of creating a punctual nucleation site.

Vieira [4] proposed a test bench capable of reproducing the test conditions experienced by Pabon et al. [3], which would also allow for surface modifications. The rationale was to bring a device as close as possible to geysering and then test which inner surface feature would have the largest impact in avoiding it. Temperature data from Pabón et al. [3] was used to calculate the diameter and depth of the nucleation site, which would lead to the smallest temperature excess.

2. Cavity design

According to Vieira [4], a minimum temperature excess between wall and liquid (ΔT) of 5°C is necessary for the onset of a vapor bubble, for a nucleation site diameter (d_c) of approximately $30\mu\text{m}$ and cavity depth (h_c) deeper than $15\mu\text{m}$.

In the present work, a device was designed to punch cavities with the appropriate size and shape, by pressing a hypodermic needle (Gage number G31) against the studied surface with a certain force. Measurements were performed to identify the resulting cavity diameter and depth. One of these cavities was captured with a white light interferometer (Zygo NewView 7000 Series Scanning White Light Interferometer) and shown in Figure 1.a. The resulting geometry was recorded using in the commercially available software MountainsMap8, as presented in Figure 1.b.

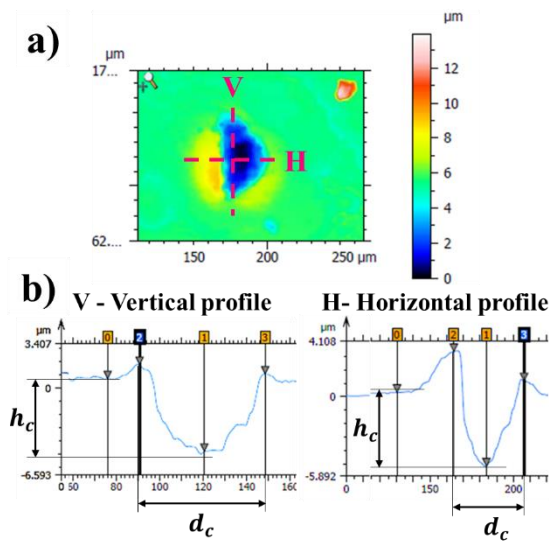


Figure 1. a) Filtered image of a punched cavity. b) Profile analysis of a crater across vertical and horizontal axis. $F_{tool} = 1.83N$.

As seen in Figure 1.a, the indentations do not have radial symmetry. As such, to facilitate the analysis, they are sectioned and have two profile lines (V, for Vertical and H, for Horizontal). The resulting profiles are plotted in the XY graphs shown in Figure 1.b and are examined regarding the horizontal distance between rim borders (d_c) and depth between the surface and lowest point (h_c).

The resulting measurements from Figure 1.b are shown in Table 1, where it is seen that only the d_c in the Horizontal profile line are close to the expected value. On the other hand, it is noticed that none of the h_c values are close to the desired cavity depth.

Table 1. Depth and volume of the punched cavities (G31) (see Figure 1.b).

F_{tool} [N]	Horizontal [μm]		Vertical [μm]	
	h_c	d_c	h_c	d_c
1.53	3.6	34.4	4.1	51.7
1.78	4.6	38.5	4.7	55.3
1.79	4.8	39.2	5.0	57.8
1.82	4.9	39.8	5.2	57.0
1.83	5.8	42.9	6.1	57.7

3. Experimental procedure

2.1. Experimental set up

To investigate the influence of the surface finishing on the liquid-vapor phase change process, a setup that allows for the visualization of bubble formation over a heated textured surface was constructed (details are presented in Vieira [4]).

In the present work, details of a special thermosyphon, made of a half metallic tube, closed with a flat acrylic sheet (for visualization) are presented.

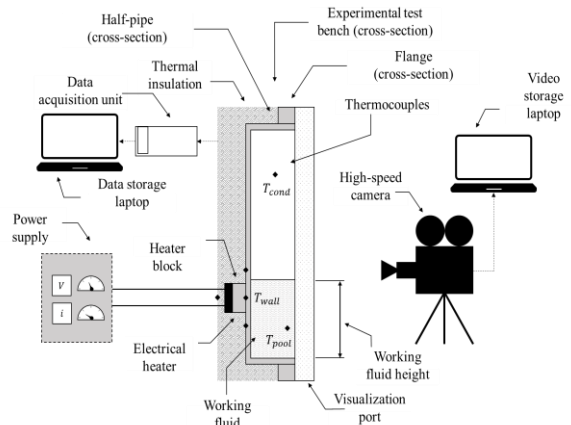


Figure 2. Key components of the experiment.

The device was tested in a specially designed setup, which main elements are shown in the schematic of Figure 2. It consists of three main elements: a visualization port, transparent to visible light (acrylic), a cooper flange, with a groove to accommodate an O-ring for vacuum sealing, and a copper half-pipe soldered on the flange, that receives different surface textures. Water was used as the working fluid. The idea is to study boiling in four major surface conditions: smooth, controlled cavities, sandpaper finished and recovered by a porous medium.

The inner surfaces received the following preparation: they were first smoothed by sanding with several and successive finer sandpaper grades, ranging from mesh numbers 80 to 2000. Afterwards, a slurry made of carbon silicate, water, and penetrating oil was used to polish the surface. This procedure was repeated each time an imperfection was observed in the studied area. The final roughness of the surface is given in the Table 2.

Table 2. Average roughness of the benchmark surface

Roughness parameter	Measurement [μm]
R_z	603.88
R_a	44.704
R_q	75.254

After the surface was prepared, the setup was mounted and tested for leakage using a leak detector. Once hermetic, the device was charged with the working fluid, which was purged to eliminate non-condensable gases.

An electrical heater, composed by a cartridge resistance imbedded in a copper block, is installed on the back of the half-pipe section to provided heat in a very punctual area. The location of the heat source is at 54 mm from the bottom of the evaporator. .

Benchmark boiling tests were performed with the very smooth surface, with different input powers and different working fluid filling volumes, which resulted in the liquid heights of: 54, 64 and 74 mm. The first liquid column is exactly at the same height of the heat source and the other two columns where, respectively, 10 mm and 20 mm above the heater level. After benchmark, the following texturized surfaces were tested: one nucleation site, nine nucleation sites, sanding and recovered by a porous medium (copper wire screen mesh).

The test temperatures were monitored by seven type T-thermocouples at different locations. A data acquisition rate of 2Hz was selected. Besides, a

qualitative analysis was performed with a high-velocity camera Fastcam Mini UX50, manufactured by the company Photron, at a rate of 4000 FPS. The location of the thermocouples are highlighted in Figure 3. T_{wall} is located on the wall between the heater block and the half-pipe section; T_{pool} , on the pool (19 mm above the pool's base) and T_{Cond} , on the region above the working fluid pool (164 mm above the pool's base); T_{Ins} is located at the heater support back surface, and its data is used to calculate heat losses from the heater to the ambient; $T_{Evap,I}$ and $T_{Evap,II}$ are positioned vertically in line with T_{wall} , at different heights (respectively, 10 mm below and above T_{wall}) to monitor the influence of the bubble formation on the adjacent involucre regions and, lastly, the thermocouple T_{Amb} monitors the ambient temperature.

Out of the seven thermocouples, three are of particular interest: T_{wall} , T_{pool} and T_{Cond} .

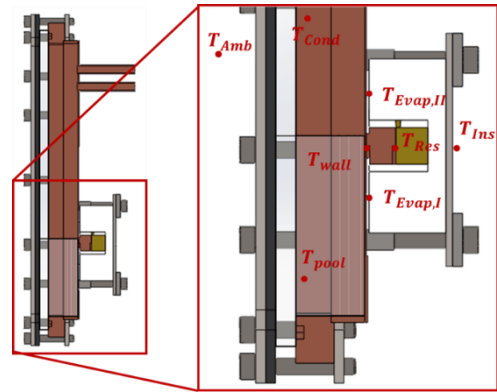


Figure 3. Thermocouples distribution.

2.2. Test bench fine tuning

Geysering happens if the operational conditions promote energy accumulation, which increases when the heat input region is as distant from potential nucleation sites as possible. It is important to note that, in the experimental test bench, the surface at the bottom region is rougher than at the rest of the test section, due to the soldering process.

In the mentioned tested conditions, increasing heat powers were applied until GB was observed at the liquid-vapor interface. The best visual geyser boiling effect was observed for 54 mm working fluid height, as further explained.

As noted by Pabón et al. [3], the higher the liquid column above the heat source, the higher the level of energy accumulation in the liquid pool and more violent if the geysering. In this case, the vapor pressure inside the bubble has to compensate the

hydrostatic forces resulting with the height of the liquid column. This energy accumulation process takes time and higher liquid pool heights decelerates the start up of phase change phenomena. On the other hand, the test bench is limited by the maximum input power that the electrical resistance is able to provide. If the liquid pool is too large, then the available heater may not be sufficient to lead the liquid to the geysering conditions.

The presence of non-condensable gases in the working fluid is another important parameter, as pressure is built up inside the thermosyphon. As observed in the last paragraph, higher pressure may hinder the occurrence of the GB phenomenon. However, as stated by Carey [5], nucleation sites usually host non-condensable gases or small particles that helps in the bubble formation, decreasing the excess temperature for the liquid boiling startup. Therefore, before each loading operation, the working fluid was purged while inside the tube, to avoid contamination with non-condensable gases. Afterward, after the valves communicating the fluid lines to the device were open and the thermosyphon was loaded, the working fluid inside the device would again go through the purging process.

Initially, the purge time, after the loading, was set as 3 minutes (180 seconds). However, this was eventually changed to 5 seconds, as it was acknowledged that a long purging time could completely degas all potential nucleation sites, including the purposely textured ones, increasing, therefore, the accumulation energy necessary for GB to happen, surpassing the heat delivery capacity of the test rig.

These purging conditions, along with different imposed heat inputs were applied to the surface tested in different conditions. Overall, thirty tests were performed. An overview of the test configurations is given in Table 3.

Table 3. Design of Experiments.

Surface condition	Input power [W]	Purge time [s]	Fluid height [mm]
Polished	1.5, 6.5, 11.5	180	54, 64, 74
1 cavity	1.5, 6.5, 11.5	180	54, 64, 74
1 cavity	11.5	5	54, 64, 74
9 cavities	11.5	5	54, 64, 74
Sandpaper	11.5	5	54, 64, 74
Screen mesh	11.5	5	54, 64, 74

2.3. Benchmark tests

It is important to remember that the first surface tested was polished with the objective of eliminating as many potential nucleation sites as possible. The tests conducted under this condition are denominated “benchmark” and its results are compared with those results from other surface conditions.

The combination of a liquid column height of 54 mm, purging time of 180s and 11.5W of power input, for the polished surface, was identified as the condition in which the first occurrence of geysering was observed. As an illustration of the results, Figure 5 depicts the T_{wall} and T_{Cond} data as a function of time for a GB burst and Figure 5 shows a sequence of images taken with a high-speed camera on the precise moment where this phenomenon happened. In both cases, the test conditions is taken as the benchmark.

As seen on Figure 4, T_{wall} decreases almost simultaneously as T_{Cond} increases. This is because just before the bubble burst, a large amount of energy is absorbed in the evaporator to produce the high energy bubble and, after the burst, it is instantaneously released in the condenser in the form of saturated vapor and liquid droplets.

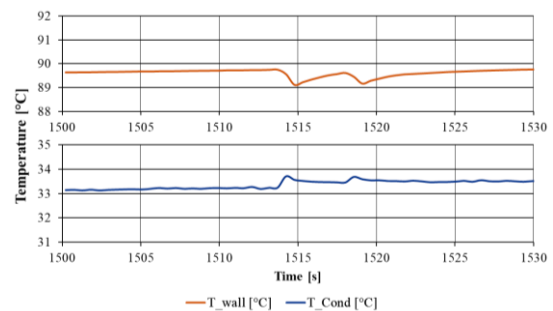


Figure 4. Temperature readings for benchmark test, working fluid height: 54mm; Input power:11.5W.

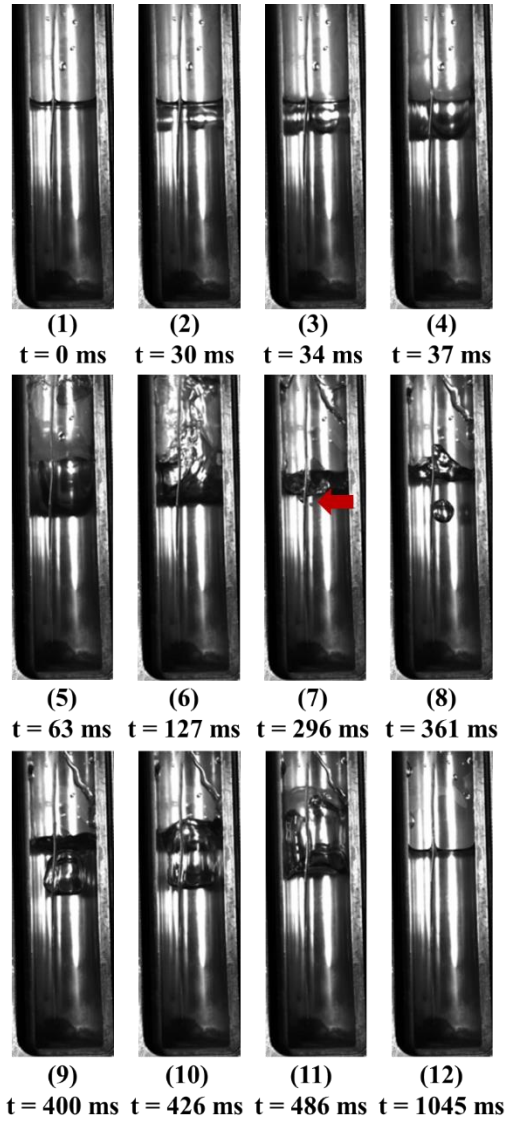


Figure 5. Visualization of ebullition for benchmark test, working fluid height: 54mm; Input power:11.5W.

In Figure 5, these phenomena can be observed in more details. From Figure 5, frames (1) to (3), it is observed the onset and rapid growth of the bubble in a very short period (34 ms). Given the proximity of the bubble to the pool free surface, very little time is needed for the bubble to reach it and burst. Actually, the liquid-vapor interface acts as a membrane, due to the surface tension of the working fluid, which holds the bubble for a while. However, when the bubble reaches the interface and the pressure of the liquid column is released, the bubble breaks suddenly and steam is released at high velocity. The resulting vapor flow drags part of the liquid pool liquid into the condenser region, as seen from Figure 5 (4) to (6). The elapsed time between (6) and (7), is around 169 ms, *i.e.*, the liquid take this time to rise to the condenser and fall back to the

evaporator. The liquid that returns to the evaporator also collects condensed vapor in the condenser region and has significant amount of kinetic energy that disturbs the pool, trapping small vapor bubbles, as seen in frame (7). Depending on the thermodynamic state of the pool, these bubbles can act as "nucleation sites", growing and bursting again, removing even more energy from the pool (as seen in (7) to (11)). In Figure 5 (12), all the accumulated energy is released and the cycle restarts.

The benchmark data presented in Table 4 is used for comparison of other test results, in the observation of the effectiveness of the several surface functionalization / texturization.

Table 4. Average temperature between 25 and 35 minutes for different filling heights and input power of 11.5W (Benchmark).

Filling height [mm]	T_{wall}	T_{pool}	T_{cond}	ΔT	N° of GBP
54	91.3	41.1	35.8	50.2	19
64	86.7	47.7	41.5	39.0	0
74	90.8	51.52	44.4	39.3	7

It should be noted that no nucleated phase change phenomena was visually observed at heat inputs between of 1.5 and 6.5W. This was expected, given the combination of low temperature excess and smooth surfaces. Also obviously, at these testing conditions, all thermocouples registered low temperatures.

Besides, the observation of the T_{pool} for the different filling heights indicates that the closer the heat source is to the free surface of the pool, the larger is the pool temperature distribution, the hotter are the upper liquid layers and the easier is the liquid to evaporate over the liquid-vapor interface, resulting in lower bulk temperature of the pool.

2.4. Other tests

Case: optimal cavity for 180 and 5 seconds purging

The first batch of surface functionalization experiments was conducted with 180s of purge time and with cavities similar to the one described in Figure 1. During the tests, no significant phase change mechanism was detected.

As already observed, it was theorized that the long purge process degassed all the potential nucleation sites. As such, the purge time was

decreased to 5s and only higher power input were applied, avoiding unnecessary tests. However, again, no significant changes were observed.

The main conclusion extracted from these results is that the effect of only one cavity is actually very small, being negligible. Two possibilities were theorized for this phenomenon: either a single punched cavity may not be enough to facilitate the GB trigger or the geometry of the cavity was not adequate to facilitate the bubble nucleation (h_c is too shallow).

Case: multiple cavities

To test the hypothesis that only a single cavity was not enough, a matrix of nine uniformly distant nucleation sites, similar to Figure 1 cavity, is punched on the test bench section, as shown in in Figure 6 (the size of the punched cavities is not in scale to the distances). The horizontal and vertical distances of two cavities is 1.5 mm.

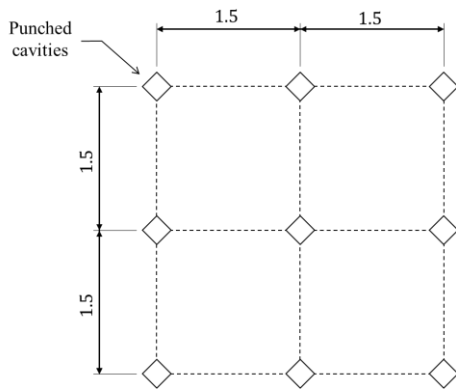


Figure 6. Disposition of the punched cavities.

Again, it was observed that, the texturization was not enough to trigger any sort of bubble nucleation nor significantly change the temperature difference between wall and liquid.

Case: sanding and screen mesh surfaces

To test the hypothesis that the geometry of the cavities were not adequate, other surface functionalization strategies were adopted: sanding the heated surface and covering it with a screen mesh.

A comparison between the temperature results with these new tested strategies is shown in Table 5, together with the temperatures for the other tests (previous sections) and those of the benchmark data, which filling height was 54mm and power input was 11.5W. The reported temperatures are averaged values obtained between the testing time frame from 25 to 35 minutes.

Table 5. Average temperature between 25 and 35 minutes for filling height of 54mm and power input of 11.5W.

Surface condition	T_{wall}	T_{pool}	T_{cond}	ΔT
Polished	91,3	41,1	35,8	50,2
1 cavity (Purge time: 180 s)				
1 cavity (Purge time: 5 s)	95,1	43,7	37,6	51,5
9 cavities	95,2	42,9	38,4	52,3
Sandpaper	88,7	37,3	32,5	51,4
Screen mesh	58,8	42,3	39,7	16,4

As mentioned in the previous sections, none of the surface functionalization strategies presented significant results. The data acquisition system presented some problems during the temperature reading for the case “1 cavity for 180 seconds purging time” and so the measurements are not presented. However, as GB (the most important result) was not observed, this case is mentioned here.

Only when the evaporator surface was covered with a screen mesh, significant results were observed, with the temperature excess dropping by almost a third of the original value. This effect was also observed to the different column fluid heights tested, meaning that the effects of the static pressure over the nucleation sites does affect their ability to nucleate bubbles.

Figure 7 shows all the temperature obtained for all testes cases, illustrating clearly these points. With the screen mesh, T_{wall} dropped from an average value of 90 °C to 58 °C for all filling heights, while T_{pool} and T_{cond} suffer less severe drops, respectively, from around 44 to 43 °C for T_{pool} and from 40 to 38 °C to T_{cond} . Furthermore, the change in phase change mechanism could be visually confirmed. With the addition of the screen mesh, a regime of nucleated boiling was observed, as depicted in Figure 8.

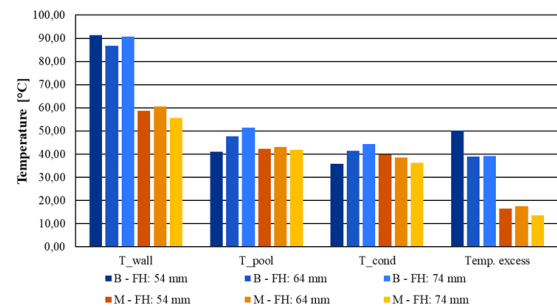


Figure 7. Comparison between average wall, pool and

condenser section temperatures between 25 and 35 minutes for different filling heights – Benchmark (B) versus Screen mesh (M).

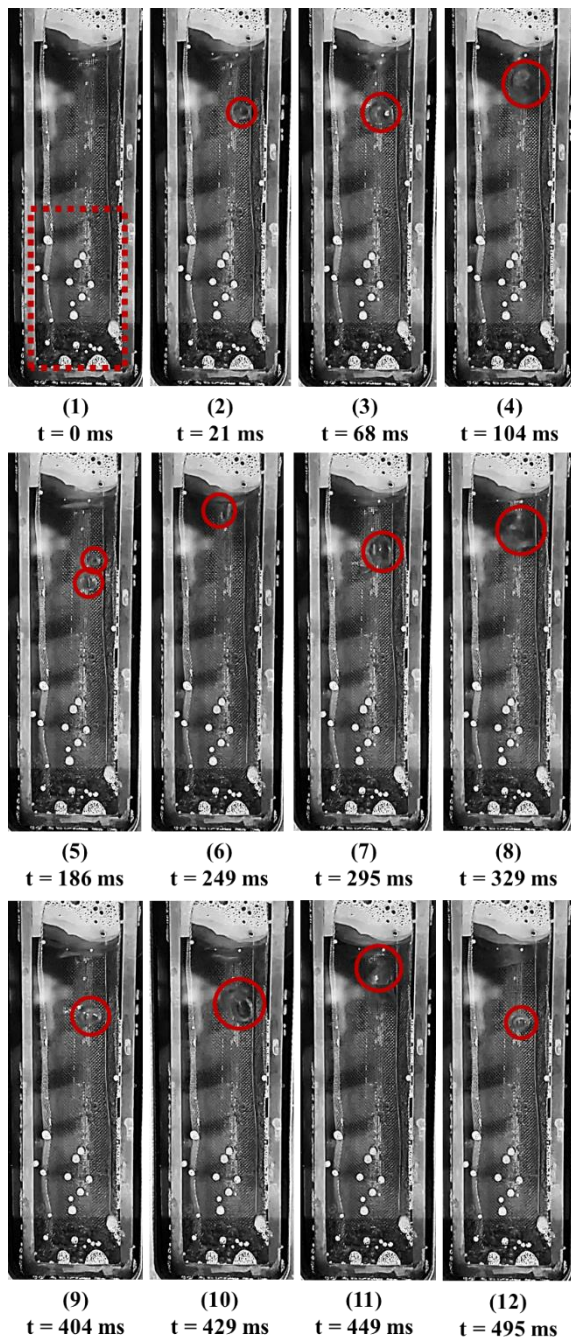


Figure 8. Visualization of ebullition and temperature readings for screen mesh test. Working fluid height: 64mm; input power:11.5W.

Figure 8 pictures were captured from a film made with a cell phone camera (iPhone XR manufactured by Apple, with a frame capture rate of 240 FPS), which has enough resolution to register both the origin and development of bubbles. Four consecutively formed bubbles, on the interval of 495ms, can be seen in these pictures. The first

bubble development is noticeable from frames (1) to (4), the second and third from (5) to (6), the fourth from (7) to (8), while the fifth begins to be formed in frame (9) and coalescences with a sixth bubble, nucleated right after the fifth, as seen in frame (10). This event of two bubbles nucleating within a short period was also observed in Figure 8.5. In frame (11), the combined bubbles reaches the surface and, in frame (12), a seventh bubble appears. As seen in Figure 8, the bubble nucleation rate is around of 14 Hz. In turn, the energy removed by each “secondary” bubble is less intense than for the major ones, when larger amounts of energy are accumulated.

Lastly, as highlighted by the red dotted rectangle in Figure 8 frame (1), there are bubbles entrapped on the surface of the visualization port. However, these bubbles did not interact with the GB experiment, because, as they are quite far from the heat source, no energy was provided to them so that they could be active nucleation sites.

It is believed that the mesh pressed against the involucre created several nucleation sites that activated the bubble nucleation. A diagram in Figure 9 illustrates an idealized screen mesh pressed against the involucre. Due to the woven nature of the mesh, a full contact is not feasible. Rather, the contact points, at the mesh threads knot positions (highlighted in red) worked as grooves. The regions highlighted by the red squares in the Figure 9, which show the gaps formed by the pair thread-wall, might actually form cavities with conditions for bubble nucleation to occur.

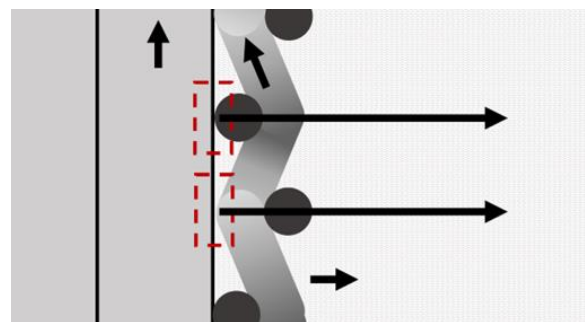


Figure 9. Diagram of the potential nucleation sites formed by the contact between screen mesh and involucre.

4. Conclusions

From the premises that evaporation of the working fluid is the driving phenomenon in thermosyphons, it is expected that an earlier activation of the evaporator section would improve the thermal performance of these devices. The early

activation can be obtained if the evaporator is able to work with smaller heat inputs, which, theoretically, could be obtained by functionalizing the inside surface of the evaporator section.

However, in the present work, this surface was functionalized by several different procedures and it was observed that the thermosyphon performance was virtually the same as observed from the benchmark results, considering the single and multiple cavity strategies used. This indicates that either the number of punched cavities may not be enough to facilitate the phenomenon trigger or the geometry of the cavities is simply not enough to facilitate the bubble nucleation (h_c is too shallow, for instance).

Other more extensive strategies were tested. The first was to sand the evaporator surface with sandpaper mesh 80, in order to create as many possible nucleation sites as possible. Again, this procedure did not result in a significant improvement in the heat transfer process. This means that there is no reason to treat the evaporator inside surfaces of copper tubes bought from the market. This is expected to be true also for other materials.

Only with the addition of a screen mesh layer over the evaporator surface showed important improvements in the performance of the device. This was confirmed through visualization and through temperature measurements. The reason behind this effect is that, by pressing the screen mesh against the inner surface, many nucleation sites were created, enough for the nucleation boiling occur at much smaller temperature excesses.

Thus, in practical terms, the main objective of this work was achieved: to study how to increase the reliability of thermosyphons by enhancing the surface of the evaporator section.

References

[1] P. L. Bellani, Termossifão Bifásico Em Circuito Para Aquecimento Solar Residencial, Master's thesis, Federal University of Santa Catarina, 2017.

[2] G. C. V. Simas, Evaporador Para Termossifão Bifásico Em Circuito Fabricado Por Difusão, Visando Aplicações Veiculares, Master's thesis, Federal University of Santa Catarina, 2017.

[3] N. Pabón, J. Mera, G. Vieira, and M. Mantelli,

Visualization and Experimental Analysis of Geysers Boiling Phenomena in Two-Phase Thermosyphons. *Int. J. of Heat and Mass Transfer*, 2019. 141: p. 876..

[4] G. S. C. Vieira. Surface functionalization in two-phase closed thermosyphons to decrease the severity of Geysers Boiling Phenomenon. Master's thesis, Federal University of Santa Catarina, 2022.

[5] V. P. Carey, *Liquid-Vapor Phase-Change Phenomena* (CRC Press, Boca Raton, FL, 2020).

A data assimilation model of oscillating heat pipe dynamics and performance

Yuxuan Li¹, Jeff D. Eldredge^{1*}, Adrienne S. Lavine¹, Timothy S. Fisher¹, and Bruce L. Drolen²

¹University of California, Los Angeles, Los Angeles, CA, 90095, USA

²Consultant, ThermAvant Technologies, Columbia, MO, 65201, USA

*Corresponding author email address: jdeldre@ucla.edu

Abstract

Oscillating heat pipes (OHPs) have significant advantages for cooling electronics or aerospace systems. Previous modeling of OHPs exhibits a wide range of complexity, particularly in the liquid film modeling, from no film modeling to one dimensional discretization. The model reported here aims to capture essential physics with minimal complexity and treats some parameters typically derived from correlations or experiments (such as the film thickness and film triple point velocity) as functions with tunable constants to be estimated by data assimilation. This model contains two modules. The first module solves the two-dimensional heat equation in the OHP solid structure that contains evaporators and condensers. The second module uses first principles to solve one-dimensional fluid motion and heat transfer equations within the fluid-filled channels, including the phenomena of nucleate boiling and bubble dryout. These two modules are weakly coupled by the immersed boundary method (IBM). The film approach generalizes the commonly-used "film evaporation-condensation" (FEC) model because it allows both varying film thickness and length, enabling the model to capture dryout. After minimal training, the thermal conductance calculated by this model shows good agreement with experiments performed by Drolen et al.

Keywords: Oscillating heat pipe; Immersed boundary method; Data assimilation; Liquid film

1. Introduction

The oscillating heat pipe (OHP) was first introduced as a device for heat transfer enhancement by Akachi [1]. An OHP usually consists of a serpentine capillary channel partially filled with a working fluid, in which multiple liquid slugs and vapor bubbles (sometimes called "plugs") spontaneously form. When a heat load is applied, both evaporation and condensation phase changes will occur, affecting local vapor pressures at the evaporator and condenser. The pressure difference then drives the liquid slug away from the evaporator. Meanwhile, the evaporator region is replenished by liquid and vapor from the condenser. Overall, the liquid slugs act as "pistons" that are pushed by two adjacent vapor "springs". This oscillation process is uniquely different from conventional heat pipes and helps an OHP achieve a low thermal resistance. Moreover, without the wick structures of a conventional heat pipe, an OHP can be much lighter and smaller and easier to manufacture. These features provide the OHP with a significant advantage for cooling electronics or aerospace systems.

OHPs display an attribute, noted by Drolen and Smoot [2], wherein at a given power level, they perform well (i.e., exhibit no dryout) when the heat source is small, but as the heat source area is increased (for the same power), they exhibit dryout at the end of the heated region farthest from

the condenser, undermining the device's performance. For example, in the experimental ASETS-II study (Drolen et al. [3]), the OHP2 configuration, consisting of a condenser at one end, performed well when it was heated with the small heater (0.5 in \times 0.5 in) at all power levels (10-40 W), with no signs of dryout. For the large heater (2 in \times 2 in), the performance was consistently good at 10 W and 20 W, but some of the tests showed signs of partial dryout at 30 W and significantly more of the tests showed partial dryout at 40 W. This behavior is contrary to what would be expected for a conventional constant conductance heat pipe. In that device, one would expect to see good performance when the heat flux is low (large heater) and possibly poor performance as the heat flux is increased (small heater) if the heat flux approaches the boiling limit.

Therefore, a central challenge for physics-based modeling of OHP performance is to capture the transition from nominal (good) to limiting (e.g., dryout) behavior. In the particular case of the ASETS-II studies, our primary objective in this work is to develop a predictive model that can demonstrate good agreement with experimental data at all power levels for OHP1, for both small and large heaters, and for OHP2 with the small heater, with no indications of dryout, and, with the same model except for a change to large heater area, capture the incipient dryout at power levels of 30 W and full dryout at 40 W in OHP2.

Although it is a relatively new member of the heat pipe family, there have been extensive modeling studies of the OHP in the last few decades. A recent comprehensive review is made by Nikolayev [4]. Most models are consistent in their treatments of liquid slug dynamics, bubble nucleation, and slug fusion due to condensation. However, one of their main differences is the treatment of the liquid films along the tube wall adjacent to the vapor bubbles, a critical aspect of dryout. In earlier models, there was either no film [5] or the film was assumed to cover the whole length of the vapor with a pre-determined thickness [6]. Das et al. [7] proposed a "film evaporation-condensation" (FEC) model for a single-branch OHP. This model has a film of constant thickness but time-varying length at each end of the vapor bubble. The FEC model can thus simulate the emergence of a dry spot. Daimaru et al. [8] used the FEC model for multibranch OHPs, with a constant and uniform film thickness set a priori, and showed good agreement with experiments and dry spot temperatures. Rao et al. [9] extended the FEC model to allow both time varying film length and thickness. This extended model requires prior knowledge of the film's triple point velocity, a value that Rao et al. obtained from experiment. This extended version of the FEC model with lumped time-varying film length and thickness is a good trade-off between low complexity and essential physics for the dry spot and film heat transfer. But by prescribing the velocity of the film's triple point, it constrains a degree of freedom with a value that might not be strictly correct. More generally, this velocity is a function of the film curvature, contact angle, and the temperatures along the wall and in the vapor. Nemati et al. [10] introduced an explicit one-dimensional film model by discretizing the film into finite elements. This approach is likely more realistic because it allows multiple dry spots to emerge in one vapor bubble. However, with more degrees of freedom, greater complexity is added to the computations. In the present paper, we will propose a simple but flexible film model that leaves the film's triple point velocity uncertain, but nonetheless conserves mass.

In addition to the uncertainty in the film length dynamics, there is also uncertainty in the film's thickness. As a liquid slug travels, it deposits a film behind it (at the slug's "trailing edge"). Aussillous and Quere [11] showed that in the visco-inertial regime, the film can be at most 50% thicker than Taylor's law for small capillary numbers in the Taylor-Bretherton regime. Thus, there is also an

uncertainty of the relative film thickness compared with Taylor's law.

The triple point physics and the film deposition thickness are among the uncertainties in a model of OHP physics, as is the bubble nucleus size that determines the critical superheat for boiling. The simulation behavior is sensitive to each, so they need to be approximated well. The determination of uncertain parameters from empirical data is the domain of data assimilation (DA), and tools from DA can be used to bridge these uncertainty gaps in OHP modeling. DA is widespread in the atmospheric and oceanic sciences and is gaining popularity in other fields with complex dynamics. Generally, DA fuses two incomplete sources of information, model and observation, to give the optimal estimation of the real state, including the unknown parameters. Among the spectrum of DA tools, the ensemble Kalman filter (EnKF) [12,13] is well-suited for problems with high-dimensional states and complex non-linear physics, such as the present context, in which the state consists of liquid slug and vapor bubble properties, and parameters such as nucleation locations, nucleus size, and film properties can be treated as uncertain distributions.

Thus, in this paper, data assimilation will be used to estimate OHP parameters and estimate the prediction uncertainty. We first propose a model that can capture the two-dimensional conjugate heat transfer problem in a plate with nucleate boiling and can capture vapor bubble dry-out and shows good agreement with the experiments. In order to account for the heat transfer between the capillary tube and the solid plate in which it is embedded, we use an immersed boundary method, [14] which enables simple meshing in the solid plate. The model parameters will initially be determined by manual training from ASETS-II experimental data. Importantly, each parameter is set from limited training data and then left unchanged for further testing. Thus, the model becomes predictive after the training is completed.

2. Model Formulation

In this section, we describe the formulation of the OHP model used in this paper, which is depicted schematically in Figure 1. We first describe the fluid model, which includes the liquid slug, vapor bubble, and liquid film treatments in the OHP capillary tubes. Then we describe the solid model, consisting of the heat transfer within the embedding plate, and the thermal coupling between the solid and fluid models via the immersed boundary method. Several aspects of our model are similar to previous studies. However,

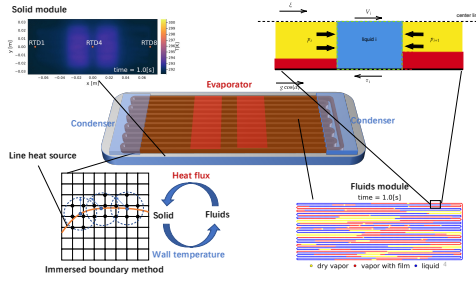


Figure 1. OHP model schematic

Table 1. Fluid model properties table for Butane and the OHP, reference temperature is $T = 291.2\text{K}$

physical meaning	unit	value
liquid density	kg/m^3	5.81e2
dynamic liquid viscosity	J/kgK	1.69e-4
fluid heat conductivity	W/mK	1.08e-1
surface tension	N/m	1.27e-5
latent heat	J/kg	3.68e5
tube hydraulic diameter	m	1e-3
tube perimeter	m	4e-3
tube cross-section area	m^2	1e-6
nucleation site radius	m	3e-5
boiling time interval	s	0.1
film thickness factor w_δ		1.3
nucleation sites number		250

our film treatment and immersed boundary coupling are novel and will be described in detail.

2.1. Fluid Model

The OHP is composed of a series of liquid slugs and vapor bubbles. Liquid films may exist between each vapor bubble and the wall. The fluid model considers mass and energy transfer within and between the vapor bubble, the film, and the liquid slug, as well as the momentum equation for the slug. The fluid model is coupled to a model of conduction in the wall, by taking the wall temperature from the solid model as a boundary condition. It then returns the wall heat flux to the solid model. The coupling with the solid model will be described in the following section; here, we focus only on the fluid model.

2.1.1. Mass Conservation and Kinematics at Liquid-Film Interface

When a liquid slug moves, there will be mass flux into or out of it from two films: one film that is deposited behind it (from the slug's "trailing edge") and another in front of it (at the slug's "leading edge") that it absorbs. Thus, for each liquid slug i (as shown in Figure 2), the two interfaces' velocities $V_{\text{int}}^{(2i)}$ and $V_{\text{int}}^{(2i+1)}$ are not generally equal

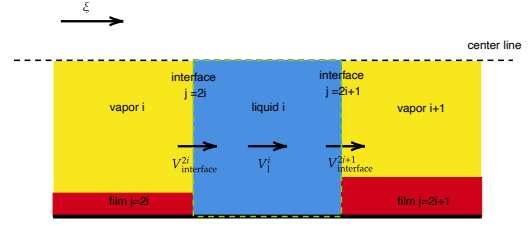


Figure 2. System of labels, indices, and interface kinematics of the OHP slug/vapor/film model.

to each other nor the slug's bulk velocity $V_1^{(i)}$. For simplicity, each interface is considered as a planar surface parallel to the cross-section, and the velocity within the film is assumed to be zero. (Note that all of the velocities are defined relative to the wall.) A control volume analysis of mass conservation for liquid slug i produces a relation between interface and bulk velocity as

$$V_{\text{int}}^{(j)} = V_l^{(i)} + (-1)^{j+1} \frac{\dot{M}_{f \rightarrow l}^{(j)}}{\rho_l A}, \quad (1)$$

where $j = 2i$ or $2i + 1$, and $\dot{M}_{f \rightarrow l}^{(j)}$ is the mass flow rate from film j into the attached liquid slug,

$$\dot{M}_{f \rightarrow l}^{(j)} = (-1)^{j+1} \rho_l V_{\text{int}}^{(j)} A_{f \rightarrow l}^{(j)}, \quad (2)$$

where $A_{f \rightarrow l}^{(j)}$ can be understood as a characteristic film cross-sectional area for a one-dimensional flow of average velocity $V_{\text{int}}^{(j)}$ and density ρ_l . Each $\dot{M}_{f \rightarrow l}^{(j)}$ should have a corresponding $A_{f \rightarrow l}^{(j)}$. Although an accurate $A_{f \rightarrow l}^{(j)}$ for each film j may be determined from experiments, for simplicity, $A_{f \rightarrow l}^{(j)}$ is defined here based on some pre-determined constraints and will be discussed later. In the simulation, Equation 1 is relaxed to $V_{\text{int}}^{(j)} = V_1^{(i)}$.

If the liquid slug moves from left to right in Figure 2, at the leading edge of the liquid slug, the film section closest to the interface is absorbed by the slug. Thus $A_{f \rightarrow l}^{(j)}$ is chosen as the cross-sectional area of the side of the leading film $(2i + 1)$ adjacent to the interface. When $\dot{M}_{f \rightarrow l}^{(j)} = 0$, this means the leading film is dry, and thus $A_{f \rightarrow l}^{(j)} = 0$.

At the trailing edge of the slug, the slug leaves behind a new section of the trailing film $(2i)$ and we expect $\dot{M}_{f \rightarrow l}^{(j)} < 0$. This newly deposited segment of film does not need to have the same cross-sectional area as the film farther to the left.

We derive the thickness δ_l of any new film from the Capillary number correlation [11]:

$$\delta_l = \frac{d}{2} \frac{\text{Ca}^{2/3}}{1 + \text{Ca}^{2/3}} w_\delta, \quad (3)$$

where the Capillary number Ca is defined as

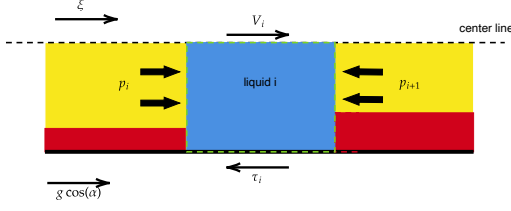


Figure 3. Liquid slug momentum equation graph

$$Ca = \frac{\mu_1 |V|_{\text{avg}}}{\sigma}, \quad (4)$$

where $|V|_{\text{avg}}$ is the average absolute velocity of liquid slugs at each time step, μ_1 is the dynamic viscosity of liquid, σ is the surface tension, and w_δ is the film thickness factor that compensates for the effect of inertia thickening.

In this paper, we idealize all films to have a uniform thickness around the perimeter of the tube, and thus the cross-sectional area of any film $A_{f \rightarrow 1}^{(j)} \approx \delta_1^{(j)} P_w$, where $\delta_1^{(j)}$ is the deposited film's thickness and P_w is the tube's perimeter.

The formulation in this section does not require each film to be of uniform thickness along the tube's axis in each vapor bubble, but the model has been implemented with uniform thickness films. Note, however, that the film thickness can change with time. Based on the above analysis, $A_{f \rightarrow 1}^{(j)}$ can be written as

$$\frac{A_{f \rightarrow 1}^{(j)}}{A} = \begin{cases} \frac{4\delta^{(j)}(d - \delta^{(j)})}{d^2}, & \dot{M}_{f \rightarrow 1}^{(j)} > 0, \\ 0, & \dot{M}_{f \rightarrow 1}^{(j)} = 0, \\ \frac{4\delta_1(d - \delta_1)}{d^2}, & \dot{M}_{f \rightarrow 1}^{(j)} < 0. \end{cases} \quad (5)$$

2.1.2. Liquid Momentum

The momentum equation for the liquid slug can be written as

$$\frac{d(M_1^{(i)} V_1^{(i)})}{dt} = (p_v^{(i)} - p_v^{(i+1)}) A - \rho_1 g \Delta H^{(i)} A - P_w L_1^{(i)} \tau_1^{(i)} \quad (6)$$

where $M_1^{(i)}$ is the mass of liquid slug i , $V_1^{(i)}$ is the cross-sectionally averaged bulk velocity of the liquid slug, $p_v^{(i)}$ is the pressure of vapor i , and $\Delta H^{(i)}$ is the height difference between the two interfaces. For our current simulation for OHPs under microgravity, $g = 0$. $L_1^{(i)}$ is the length of liquid slug i . P_w is the perimeter of the tube. $\tau_1^{(i)}$ is the axial stress in the liquid at the wall. The Churchill friction correlation [15] is used to determine $\tau_1^{(i)}$. In the Churchill equation, the

surface roughness is assumed to be equal to the nucleation site radius.

2.1.3. Liquid Energy

For each liquid slug i , an independent cross-sectionally averaged one-dimensional energy equation is solved:

$$\rho_1 c_{p,1} A \frac{DT_1}{Dt} = k_1 A \frac{\partial^2 T_1}{\partial \xi^2} + P_w q_w'', \quad (7)$$

where ξ is the dimensional coordinate measured along the wall, $c_{p,1}$ is the specific heat of the liquid, k_1 is the thermal conductivity of the liquid, and T_1 is the cross-sectionally averaged liquid temperature. P_w is the tube perimeter and q_w'' is the heat flux going into the liquid at ξ . At any given time, q_w'' can be expressed as

$$q_w''(\xi) = h_1 (T_w(\xi) - T_1(\xi)). \quad (8)$$

where h_1 is the heat transfer coefficient for all liquid slugs,

$$h_1 = Nu_1 \frac{k_1}{d}, \quad (9)$$

and the Nusselt number is $Nu_1 = 3.60$, corresponding to laminar flow in a square duct with a uniform heat-flux boundary condition [16].

2.1.4. Vapor Model

In the model, the vapor is assumed to be saturated. The saturation curve is derived from the CoolProp package [17]. For each vapor bubble, two liquid films are assumed to be located at the two ends, respectively (see Figure 4). The heat transfer in the dry regions (vapor regions not covered by films) are neglected. Each film j has a time varying but spatially uniform thickness $\delta^{(j)}$ and a time varying length predicted by the model, as described below. The two films can meet in the middle of the bubble. Phase change at the bubble-slug interfaces at the two ends is neglected because the bubble-slug (cross-sectional) interface area is small compared to the bubble-film (peripheral) interface area. The heat transfer across the liquid film is assumed to be only by conduction, and the film is assumed thin compared with the tube edge length, thus heat transfer is calculated as if the film were planar:

$$q_f''^{(j)}(\xi) = \frac{k_1}{\delta^{(j)}} (T_w(\xi) - T_v^{(i)}). \quad (10)$$

Here, $q_f''^{(j)}(\xi)$ represents the heat flux at a given location ξ on film j . The total heat transfer rate due to phase change at the film-vapor interface for film j can then be found as

$$q_f^{(j)} = \int_f^{(j)} P_w q_f''^{(j)}(\xi) d\xi, \quad (11)$$

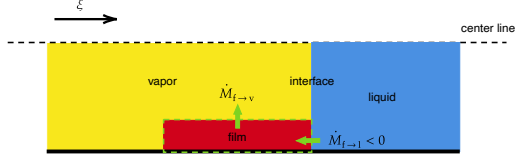


Figure 4. Film mass conservation

where P_w is the perimeter of the cross-section.

The corresponding evaporation (or condensation) mass flow rate for film j can then be expressed as:

$$\dot{M}_{f \rightarrow v}^{(j)} = \frac{q_f^{(j)}}{h_{lv}}, \quad (12)$$

where h_{lv} is the latent heat. As noted previously, phase change at the bubble-slug interface is neglected.

The net mass flow rate into the vapor i from the leading and trailing liquid film can be expressed as

$$\dot{M}_v^{(i)} = \dot{M}_{f \rightarrow v}^{(2i-1)} + \dot{M}_{f \rightarrow v}^{(2i)}. \quad (13)$$

This information is used to keep track of the density within the bubble as a function of time, which then determines the saturation temperature and pressure.

2.1.5. Film Length and Thickness

For simplification, each vapor has two films attached to two interfaces. The film is assumed to have a rectangular shape.

From mass conservation, the mass change of the film comes from the phase change and the interface motion. This relation can be written as

$$\dot{M}_f^{(j)} = -\dot{M}_{f \rightarrow v}^{(j)} - \dot{M}_{f \rightarrow l}^{(j)}, \quad (14)$$

where $\dot{M}_{f \rightarrow v}^{(j)}$ is the phase change mass flow rate and $\dot{M}_{f \rightarrow l}^{(j)}$ is the interface deposition mass flow rate into, or out of, the liquid slug. These terms can be directly derived from the model. Thus $\dot{M}_f^{(j)}$ are determined.

But only knowing the mass change of the film as a whole is not enough. When mass flux enters or exits the film, it will simultaneously change the film's length and thickness. Using the product law for the mass change of the film ($\dot{M}_f^{(j)} = \rho_l L_f^{(j)} \dot{A}_f^{(j)}$), assuming the liquid is incompressible:

$$\dot{M}_f^{(j)} = \rho_l L_f^{(j)} \dot{A}_f^{(j)} + \rho_l A_f^{(j)} \dot{L}_f^{(j)} \quad (15)$$

where $A_f^{(j)}$ is the cross-sectional area of film j .

It is challenging to determine the percentage of mass flow for $\rho_l L_f^{(j)} \dot{A}_f^{(j)}$ and $\rho_l A_f^{(j)} \dot{L}_f^{(j)}$ in these two categories because the actual film shape and the exact heat transfer occurring in the film are not well known. So instead of directly simulating these high-dimensional features, this model focuses on

the final impact of these features: the relative changes of the film's length and thickness. With reference to equations 11, 12, and 14, we propose the following forms for these,

$$\rho_l A_f^{(j)} \dot{L}_f^{(j)} = -\frac{P_w}{h_{lv}} \int_f^{(j)} \eta^{(j)}(\xi) q_f'' d\xi + (-1)^j \rho_l A_f^{(j)} V_{\text{int}}^{(j)} \quad (16)$$

$$\rho_l L_f^{(j)} \dot{A}_f^{(j)} = -\frac{P_w}{h_{lv}} \int_f^{(j)} (1 - \eta^{(j)}(\xi)) q_f'' d\xi - (\dot{M}_{f \rightarrow l}^{(j)} + (-1)^j \rho_l A_f^{(j)} V_{\text{int}}^{(j)}) \quad (17)$$

where $\eta^{(j)}(\xi)$ is a weighting function, defined as

$$\eta^{(j)}(\xi) = H(q_f'') \eta_+ + H(-q_f'') \eta_- \quad (18)$$

where $H()$ is the Heaviside step function. The two predetermined dimensionless numbers, η_+ and η_- , are introduced to represent the effects of the complex phase change: η_+ denotes the percentage of mass flux going to the length change where the film is evaporated ($q_f'' > 0$), and η_- denotes the percentage of mass flux going to length change where the film is condensed ($q_f'' \leq 0$). All films share the same η_+ and η_- in our model. In the current model $\eta_+ = 0.15$ and $\eta_- = 0$. In Equation 16, $\rho_l A_f^{(j)} V_{\text{int}}^{(j)}$ is the portion of $\dot{M}_{f \rightarrow l}^{(j)}$ that goes to $\rho_l A_f^{(j)} \dot{L}_f^{(j)}$. The reason to choose $\rho_l A_f^{(j)} V_{\text{int}}^{(j)}$ is to ensure the tail of the film does not move without phase change. Note that the rate of change of film thickness, $\delta^{(j)}$, can be derived from $\dot{A}_f^{(j)}$ in Equation 17.

2.1.6. Nucleate Boiling and Merging

The model can simulate nucleate boiling by creating a new vapor bubble to break one liquid slug into two at a nucleation site. In the simulation, a finite number of nucleation sites are randomly distributed along the length of the OHP tube. In order to boil, the temperature difference between the wall $T_w(\xi_n)$ and the saturation temperature $T_{\text{sat}}(\xi_n)$ must exceed the superheat threshold $\Delta T_{n, \text{th}}$

To get $T_{\text{sat}}(\xi_n)$ at the liquid slug, first the saturation pressure $p_{\text{sat}}(\xi_n)$ in the liquid slug is derived by linearly interpolating the saturation pressures of the adjacent vapor bubbles. Then the saturation temperature can be derived from the Clausius-Clapeyron equation. The superheat threshold $\Delta T_{n, \text{th}}$ is derived from [18], which depends on the nucleation site radius, gas properties, surface tension, and the Taylor bubble's film thickness. The approach will scan all nucleation sites at uniform time intervals. When superheat exceeds $\Delta T_{n, \text{th}}$, a new vapor bubble of length $4d$ will be created, with the adjacent vapor

bubbles' pressure remaining unchanged.

Similar to the nucleate boiling process that creates new vapor bubbles, the merging function is used to remove a vapor bubble if two liquid slugs collapse (vapor length smaller than $2d$), maintaining the adjacent vapor bubbles' pressure.

2.2. Solid Model

The OHP tube is embedded into a solid plate. The three-dimensional heat equation in the plate $\Omega \subset \mathbb{R}^3$ is

$$\rho_s c_s \frac{\partial T_s}{\partial t} = k_s \left(\frac{\partial^2 T_s}{\partial x^2} + \frac{\partial^2 T_s}{\partial y^2} + \frac{\partial^2 T_s}{\partial z^2} \right) + q_s''', \quad (19)$$

where z represents the thickness direction and q_s''' represents a volumetric heat source whose role we will discuss shortly. In addition to this equation, we have boundary conditions. Along the edges of the plate we set adiabatic boundary conditions. On the top and bottom of the plate we enforce conditions for the adjacent evaporators and condensers. Both of these conditions are modeled via surface heat flux conditions. That is, we set

$$\mp k_s \frac{\partial T_s}{\partial z} = q'', \quad (20)$$

where q'' denotes the heat flux into the plate, and where the $-$ sign is chosen at the bottom surface and $+$ at the top surface of the plate. However, the models for this heat flux differ for evaporators and condensers. Evaporators we will model as prescribed heat fluxes, $q_h'' = W_h/A_h$, where power W_h is delivered over a surface region of area A_h . Condensers, in contrast, are modeled as a reservoir of constant temperature, so that the surface heat flux over the condenser region is given by $q_c'' = h_c(T_c - T_s)$, and heat transfer coefficient h_c is assumed a constant.

If we integrate Equation 19 with respect to z over the thickness d_s of the plate, it becomes

$$\rho_s c_s d_s \frac{\partial \bar{T}_s}{\partial t} = k_s d_s \left(\frac{\partial^2 \bar{T}_s}{\partial x^2} + \frac{\partial^2 \bar{T}_s}{\partial y^2} \right) + q'' + d_s \bar{q}_s''', \quad (21)$$

where \bar{T}_s and \bar{q}_s''' are z -averaged temperature and heat source terms. Furthermore, the integral of the conductive term brings in the heat flux boundary conditions for the evaporators and condensers on the top and the bottom of the plate, represented collectively as q'' . Note that $q'' = 0$ anywhere outside an evaporator or a condenser.

2.3. Fluid-Solid Coupling

Strictly, the wall of the OHP tube is also a surface on which conditions should be specified for the plate. Indeed, the conjugate heat transfer

Table 2. Solid model properties table

physical meaning	unit	value
plate density ρ_s	kg/m ³	2.73e3
plate specific heat c_s	J/kgK	8.93e2
plate thermal conductivity k_s	W/mK	1.93e2
volumetric plate thickness d_s	m	1.5e-3

problems for the solid and OHP fluids are coupled at this wall: e.g., local surface heat flux q_w'' is delivered through the wall from the solid to the fluid, and the local temperature in the solid is equal to the temperature at the wall, $T_w(\xi)$.

To enable these interface conditions in a flexible but accurate manner, we integrate the wall heat flux over the perimeter of the tube at each axial location ξ , resulting in a tube wall heat flux q_w' per unit length of tube. Then, we assume that the diameter of the tube is sufficiently small compared to other dimensions of the plate (e.g., length and width) that, from the perspective of the plate, the heat to/from the OHP tube can be thought of as collecting into or emerging from a line heat source concentrated along the serpentine length of the OHP tube. Thus, we can represent the OHP tube's influence on the plate heat transfer as a volumetric heat source of the following form,

$$q_s''' = - \int_{C_{\text{OHP}}} q_w'(\xi) \delta_{3D}(\underline{x} - \underline{x}(\xi)) d\xi \quad (22)$$

where δ_{3D} is the three-dimensional Dirac delta function and $\underline{x}(\xi)$ describes the curve of the OHP tube centerline. The negative sign ensures the positive sign convention we have used for heat flux into the fluid from the wall. Integrating this term across the plate thickness, as we did to achieve Equation 21), we get

$$\bar{q}_s''' d_s = - \int_{C_{\text{OHP}}} q_w'(\xi) \delta_{2D}(\underline{x} - \underline{x}(\xi)) d\xi \quad (23)$$

where δ_{2D} is the two-dimensional Dirac delta function. In this manner, the OHP tube is immersed in the plate domain [14] and the local heat flux through the tube wall enters the plate heat equation.

Analogously, to obtain the wall temperature T_w for the OHP fluid model, we interpolate the plate temperature $\bar{T}_s(\underline{x})$:

$$T_w(\xi) = \int_{\bar{\Omega}} \bar{T}_s(\underline{x}) \delta_{2D}(\underline{x} - \underline{x}(\xi)) d\underline{x}. \quad (24)$$

The integrals and Dirac delta functions in these equations are represented discretely as sums and discrete Dirac delta functions, respectively. [14]

3. Results

3.1. Thermal conductance

Thermal conductance is defined here as

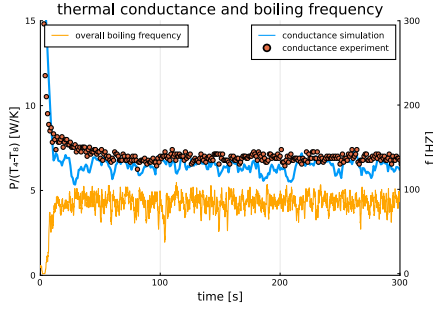


Figure 5. OHP1 40 W curves

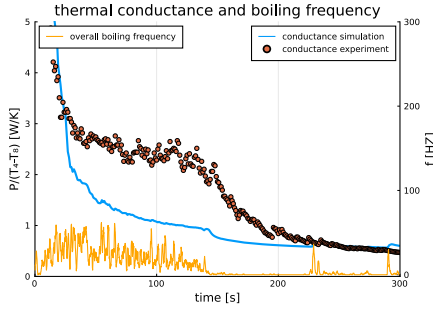


Figure 6. OHP2 40 W curves

$$G = \frac{\text{power}}{T_4 - T_8}, \quad (25)$$

where T_4 and T_8 are the interpolated temperatures from the solid model corresponding to RTD4 and RTD8 results in ASETS-II experiments [3].

Figure 5 shows the thermal conductance curve for the OHP1 40 W case with condensers at both ends. The simulation result (blue curve) agrees well with experiments for both the initial time dependence and the nominally steady-state results. The thermal conductance value fluctuates because of the oscillating nature of OHPs. The orange curve is the moving averaged overall boiling frequency from the numerical simulation. It is hard to validate this value quantitatively because boiling data are not available in the experiments. But the numerical result shows that the boiling is consistent throughout the simulation.

Figure 6 shows the thermal conductance curve for the OHP2 40W case with only one condenser at the right end. This is a more challenging case with the transition from normal operation to runaway dryout. Although the model under-estimated the thermal conductance during the transition, the simulation agrees well with experiments for the initial time constant and successfully predicts the onset of runaway dryout. The boiling frequency curve also shows that this case has a lower boiling frequency at the beginning, and the frequency dramatically decreases when there is onset of runaway dryout around 150 s.

Figure 7 shows the thermal conductance

comparison with ASETS-II experiments for 16 cases. The values are averaged from 200 s to 300 s except for the dryout case. It can be shown that this model can predict small heater cases well using the same parameter set calibrated for large heaters.

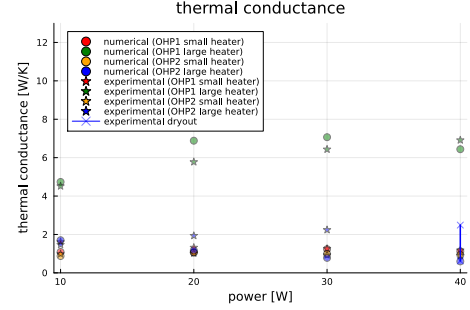


Figure 7. Thermal conductance comparison

3.2. Two dimensional Results

This section shows snapshots of temperature contours and OHP animations. Figure 8 shows the temperature contours of the OHP1 40 W case. The first four snapshots show heat building up in the middle and spreading to the two ends. The last two snapshots show that the temperature field remains nearly unchanged from 100 s to 300 s. Figure 9 shows snapshots of liquid slug and vapor bubble distributions (see figure 1 for context). It also distinguishes vapor bubbles with and without liquid films on the wall. It can be seen that the majority of the vapor bubble length is covered by liquid films throughout the simulation.

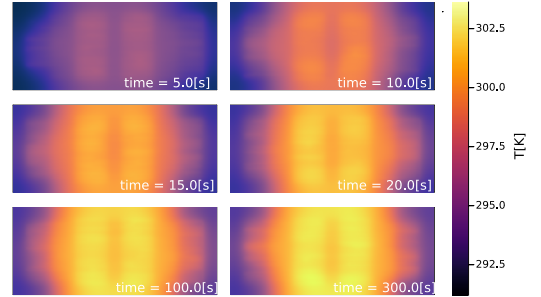


Figure 8. Temperature contours for OHP1 40 W

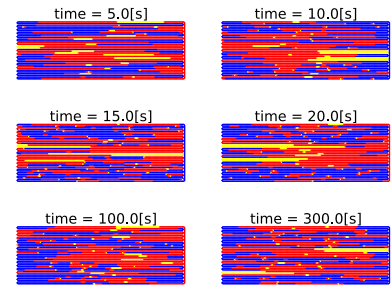


Figure 9. Snapshots for OHP1 40 W. Blue region is liquid, yellow region is dry vapor, and red region is vapor covered by liquid films

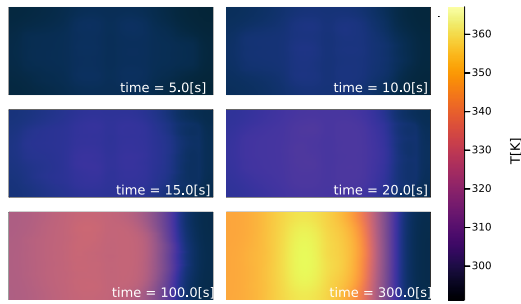


Figure 10. Temperature contours for OHP2 40 W

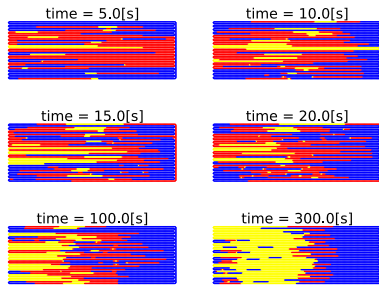


Figure 11. Snapshots for OHP2 40 W, blue region is liquid, yellow region is dry vapor, and red region is vapor covered by liquid films

Figure 10 shows the temperature contours of the OHP2 40 W case. It shows that the peak temperature at 300 s is significantly higher than at 100 s, showing the runaway dryout. The runaway dryout is more evident in Figure 11. The OHP snapshots in Figure 11 show that during start-up, the liquids tend to accumulate to the right end where the only condenser is situated. At 100 s, the result shows the transition to runaway dryout where more dry vapor regions are shown toward the left. The 300 s result shows the liquid and vapor distribution after runaway dryout has occurred and most of the vapor region is dry.

4. Conclusion

A model of oscillating heat pipes has been developed that captures the essential physics, including accounting for liquid films with time-varying length and thickness. The simulation shows good overall agreement with experiments, successfully showing the runaway dryout in the OHP 2 40 W case. This model aims to provide a data-assimilation framework for OHPs. In the future, data-assimilation tools will be used to rigorously infer the uncertain parameters such as the nucleation site size, condenser heat transfer coefficient, and film thickness factor.

Acknowledgments

Support for this work from the CITMAV

consortium is gratefully acknowledged.

References

- [1] H. Akachi, Structure of micro-heat pipe. US Patent 5219020. 1993.
- [2] B. L. Drolen and C. D. Smoot, Performance Limits of Oscillating Heat Pipes: Theory and Validation. *Journal of Thermophysics and Heat Transfer*, 2017. 31(4): p. 920.
- [3] B. L. Drolen, C. A. Wilson, B. S. Taft, J. Allison, and K. W. Irick, Advanced Structurally Embedded Thermal Spreader Oscillating Heat Pipe Micro-Gravity Flight Experiment. *Journal of Thermophysics and Heat Transfer*, 2022. 36(2): p. 314.
- [4] V. S. Nikolayev, Physical principles and state-of-the-art of modeling of the pulsating heat pipe: A review. *Applied Thermal Engineering*, 2021. 195.
- [5] M. B. Shafii, A. Faghri, and Y. Zhang, Thermal Modeling of Unlooped and Looped Pulsating Heat Pipes. *Journal of Heat Transfer*, 2001. 123(6): p. 1159.
- [6] B. Holley and A. Faghri, Analysis of pulsating heat pipe with capillary wick and varying channel diameter. *International Journal of Heat and Mass Transfer*, 2005. 48(13): p. 2635.
- [7] S. P. Das, V. S. Nikolayev, F. Lefevre, B. Pottier, S. Khandekar, and J. Bonjour, Thermally induced two-phase oscillating flow inside a capillary tube. *International Journal of Heat and Mass Transfer*, 2010. 53(19-20): p. 3905.
- [8] T. Daimaru, S. Yoshida, and H. Nagai, Study on thermal cycle in oscillating heat pipes by numerical analysis. *Applied Thermal Engineering*, 2017. 113: p. 1219.
- [9] M. Rao, F. Lefèvre, S. Khandekar, and J. Bonjour, Heat and mass transfer mechanisms of a self-sustained thermally driven oscillating liquid-vapour meniscus. *International Journal of Heat and Mass Transfer*, 2015. 86: p. 519.
- [10] R. Nemati and M. B. Shafii, Advanced heat transfer analysis of a U-shaped pulsating heat pipe considering evaporative liquid film trailing from its liquid slug. *Applied Thermal Engineering*, 2018. 138: p. 475.
- [11] P. Aussillous and D. Quéré, Quick deposition of a fluid on the wall of a tube. *Physics of Fluids*, 2000. 12(10).
- [12] R. E. Kalman, A New Approach to Linear Filtering and Prediction Problems. *Journal of Basic Engineering*, 1960. 82(1): p. 35.
- [13] G. Evensen, Sequential data assimilation with a nonlinear quasi-geostrophic model using Monte Carlo methods to forecast error statistics. *Journal of Geophysical Research: Oceans*, 1994. 99(C5): p. 10143.
- [14] J. D. Eldredge, A method of immersed layers on Cartesian grids, with application to incompressible flows. *Journal of Computational Physics*, 2022. 448: p. 110716.
- [15] S. W. Churchill and M. Bernstein, A Correlating Equation for Forced Convection From Gases and Liquids to a Circular Cylinder in Crossflow. *Journal of Heat Transfer*, 1977. 99(2): p. 300.
- [16] R. K. Shah and A. L. London, *Laminar flow forced convection in ducts: a source book for compact heat exchanger analytical data* (Academic press, 2014).
- [17] I. H. Bell, J. Wronski, S. Quoiloin, and V. Lemort, Pure and pseudo-pure fluid thermophysical property evaluation and the open-source thermophysical property library CoolProp. *Industrial & engineering chemistry research*, 2014. 53(6): p. 2498.
- [18] W. Qu and H. B. Ma, Theoretical analysis of startup of a pulsating heat pipe. *International Journal of Heat and Mass Transfer*, 2007. 50(11-12): p. 2309.

Development of IGBT immersion cooling system for in-wheel motor of electric vehicles

Masataka Mochizuki^{1*}, Hiroshi Shimizu², Yukiko Kato², Hiromichi Kawamura², Masaki Kawaguchi², Hideo Arai², Sadaharu Tamoto², Tooru Ishikawa², Naotake Kumagai³, Yoshio Utaka⁴, Zhihao Chen⁴

¹ The Heat Pipes, Shiohama 1-4-33-1022, Koto-Ku, Tokyo 135-0043, Japan

² e-Gle Co., Ltd. 202C, Bldg- O, Keio University Shin-Kawasaki Town Campus, Shin-Kawasaki 7-1, Saiwai-ku, Kawasaki-city, Kanagawa 212-0032 Japan

³ Keio University, K2 Town Campus, Shin-Kawasaki 7-1, Saiwai-ku, Kawasaki-city, Kanagawa 212-0032, Japan

⁴ Tianjin University, 34 Peiyang Park Campus, Tianjin 300354, China

*Corresponding author email address: mochizuki.masataka@gmail.com:

Abstract

The In-wheel motor which is installed in the wheel of Electric Vehicles (EV) can be ultimate driven system due to no transmission loss and securement in car space. IGBT (Insulated Gate Bipolar Transistor) for motor drive control unit is equipped inside motor has been developed with an immersion cooling system by two phase liquid of electric insulation thermal fluid (Novec-7100), at this time. The air-cooled condenser of multiple smaller sized tubes is established inside the motor, and it is natural circulation system of the Loop thermo-siphon system. In addition to that, the cooling of motor coils is also possible to cool all together, and it can be contributed to 1.81 times enhance the cooling capacity and 1.3 times enhance the drive power of the In-wheel motor as well. There will be advanced of power semiconductor such as Silicon Carbide (SiC) instead of Silicon IGBT. When SiC is applied to motor control, the cooling capacity will be more enhanced to 3.34 times than original air-cooled motor and 1.69 times increased drive power as well.

Keywords: Electric Vehicle, In-wheel motor, IGBT, Immersion cooling, Critical heat flux, Loop thermo-siphon, SiC inverter

1. Introduction ¹⁾

The development of electric vehicles has remarkably progressed, and full-scale practical application is now approaching. The main components of electric vehicle are the motor, inverter, and battery. Since its establishment, e-Gle Co. Ltd. has been conducting research and development of In-wheel motors and other core technologies for electric vehicles. In-wheel motor, an outer rotor drive system in which permanent magnets are placed on the outside and coils are installed on the inner stator, is an ideal driving motor for electric vehicles that has each wheel independent control mechanism that does not use a transmission gear by installing a motor inside the wheels. Furthermore, since there is nothing of energy loss in the transmission, the consumption on the battery can be approx. 10% reduced, so the cruising miles can be extended than On-Board system which is current design. Fig.1 shows an eight-wheeled electric vehicle equipped with In-wheel motor developed by one of the authors, Prof. Hiroshi Shimizu, during his work at Keio University, Japan.



Fig.1 In-wheel motor car (Eliica) by Keio University ²⁾

2. Current EV motor drive and control system (On board system)

On board drive system for EV consists of a motor, gear transmission, IGBTs. A motor rotates approx. 10,000RPM with smaller torque and the power is connected through transmission gear to reduce 10 times smaller speed in order to increase 10 times higher torque then connected to wheels. Fig.2 shows the current On board system for EV.

A large space is necessary for installation and approx. 10% transmission power loss is occurred.

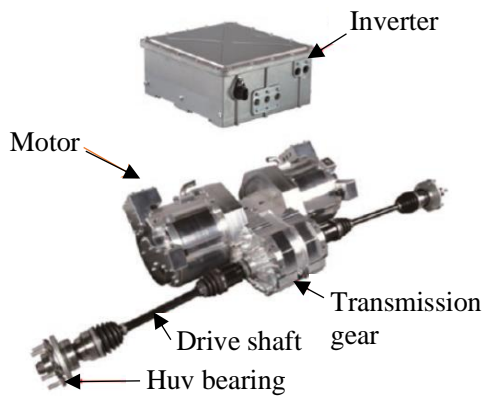


Fig. 2 On-board drive system for EV ³⁾

A motor is cooled by water and Inverter with IGBTs which is separately installed in a car floor is also cooled by water. IGBT is high current switching device to convert from DC to AC for motor drive and control.

3. What is the In-wheel motor? ²⁾



Fig.3 In-wheel motor ²⁾

Fig.3 shows the In-wheel motor developed by e-Gle. The In-wheel motor has a maximum power of 65 kW, a normal power of 25 kW class, high torque 620 Nm,

high efficiency of 95%, small cogging torque, large outer diameter, and thinner thickness, making it easy to mount into the wheels. The in-wheel motor is an outer rotor drive system in which 24 motor coils are placed on the inner stator and 20 permanent magnets are arranged on the outer rotor as achieve 10 times higher torque at 1000RPM. Originally the In-wheel motor is air cooled and IGBTs separately is cooled by water.

4. The immersion cooling system for IGBT and motor cooling system by loop thermo-siphon

The new design concept is indicated that IGBTs should be installed inside of motor which is very hard target due to small space inside of motor. The immersion cooling for IGBT which is to be directly two phased cooled by thermo-dielectric fluid (Novec-7100) and the loop thermo-siphon structure with the air cooled condenser. As a motor generates heat by motor coils and magnets, it should be also cooled using by same thermo-siphon. The air-cooled condenser of multiple

smaller sized tubes without any fins is installed inside the motor, and it is natural circulation system by the loop thermo-siphon structure as shown in Fig.4.

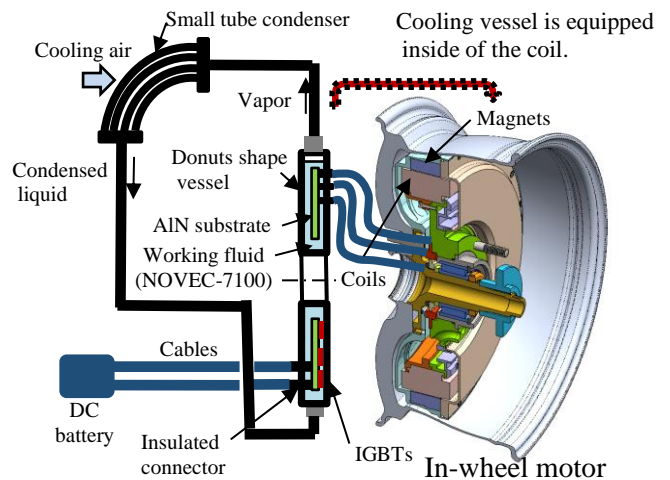


Fig. 4 The immersion cooling system of IGBTs for In-wheel motor ¹⁾

In consideration of the increasing power density of next-generation power semiconductors (SiC, GaN), it has been decided to adopt an immersion cooling system with a higher critical heat flux and a heat transfer coefficient that is one order of magnitude larger than water cooling. The size of IGBT heat source required for drive control of the in-wheel motor is 30 mm square, and 6 pcs. are required. IGBTs are amounted on the Aluminum Nitride (AlN) substrates which is for high temperature and high thermal conductivity.

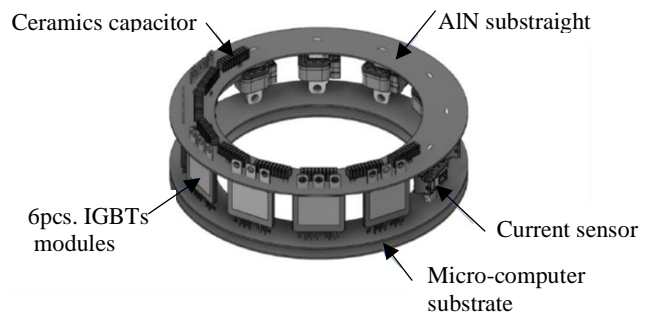


Fig. 5 Donuts shape substrates for IGBTs for In-wheel motor ¹⁾

Fig. 5 shows the AlN substrate with donuts shape and amounted IGBTs and other electronics parts. The motor for EV uses the coil of the plural groups which stood in a row. Therefore, it is divided that plural coils into the group and adopt a method to connect the output of the power device to each coil. There is a power module with a voltage rating of 650 V and a current rating of 400 A, and two built-in IGBTs, which is the outer size of 42 mm× 42 mm,

and 4.7 mm thick. ⁴⁾ A three-phase inverter can be realized using by three of these power modules. The signal to drive the IGBT is supplied by connectors to another annular print circuit board(PCB) equipped with a microcomputer. Furthermore, Fig.5 is used to connect to the DC bus-bar and each coil from the high current terminal of the IGBT. These boards are stacked and installed into a boiling vessel to realize an inverter for in-wheel motor.

5. Evaporation heat transfer coefficient and critical heat flux of IGBT

A IGBT has a dissipation heat of 43.5 W/p at the normal power and 282 W/p at the maximum, and the heat flux of both sides of the IGBT is 2.42 W/cm² and 15.7 W/cm², which is smaller value than Zuber's critical heat flux as shown in equation (1). When the coolant temperature is 160°C(P=1MPa), the critical heat flux shows the maximum value. Practically, it should be used at 120°C or less (P=0.3MPa).

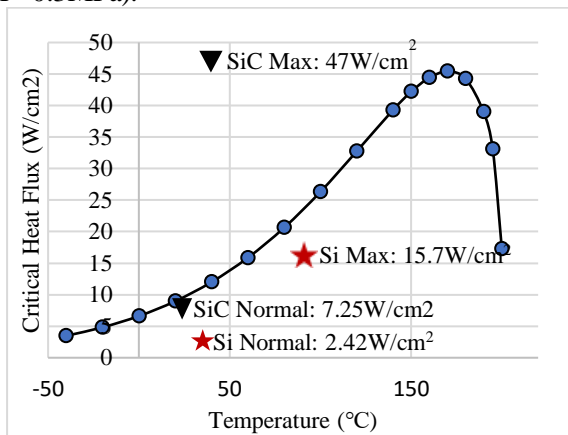


Fig. 6 Critical heat flux of IGBT by Zuber

$$q_{CHF} = 0.131 \rho_v H f g \left[\frac{\sigma g (\rho_l - \rho_v)}{\rho_v^2} \right]^{1/4} \quad (1)$$

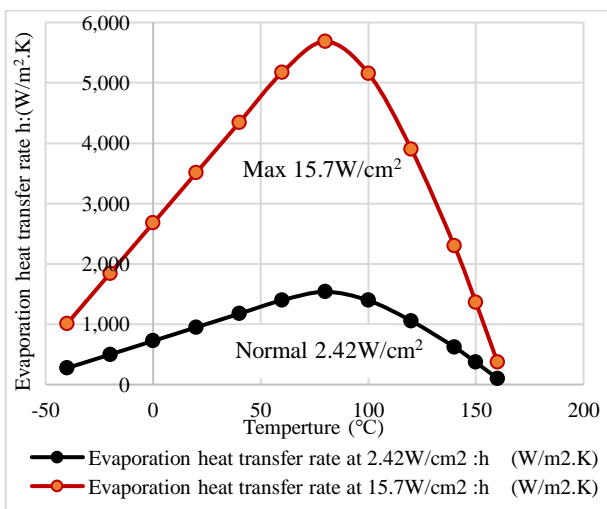


Fig.7 Evaporation heat transfer rate of IGBT

$$\frac{h l_a}{K_l} = 7.0 \times 10^{-4} Pr_l^{0.35} \left(\frac{q l_a}{\rho_v L_{lv} \gamma l} \right)^{0.7} \left(\frac{Pl a}{\sigma} \right)^{0.7} \quad (2)$$

$$l_a = \sqrt{\frac{\sigma}{g(\rho_l - \rho_v)}} \quad (3)$$

Equation (2) (3) show Kutateladze's pool boiling heat transfer coefficient and Fig.7 shows calculation results of heat transfer rates in case of 2.42W/cm² and 15.7 W/cm². At a normal heat flux of 2.42 W/cm², the heat transfer coefficient is obtained 1000-1500 W/m².K, while in the maximum heat flux range, the heat transfer coefficient is as large as 4000-5500 W/m².K. The Kutateladze's formula cannot be estimated properly below 40°C, so that a linear approximation was used in the low temperature range. Fig.8 shows the testing set up to measure critical heat flux using copper heater which is same size of IGBT.

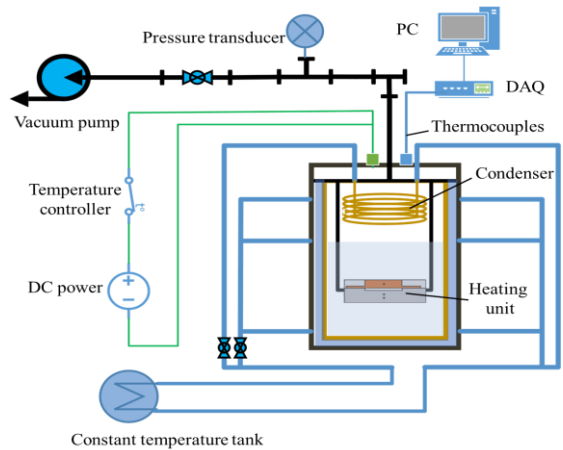


Fig. 8 Test set up for measuring critical heat flux

Fig.9 shows the experimental data of critical heat flux, and the test data predicts approx. 40% higher value than Zuber's model.

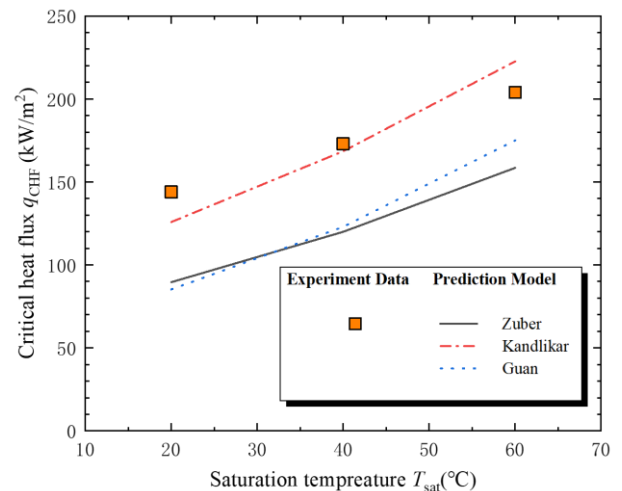


Fig.9 The experimental data of critical heat flux

6. Overall cooling system and air cooled condenser

As shown in Fig.10, the condenser uses a multi-row tube group with an outer diameter of 3 mm and an inner diameter of 2 mm, and has no fins on the air side.

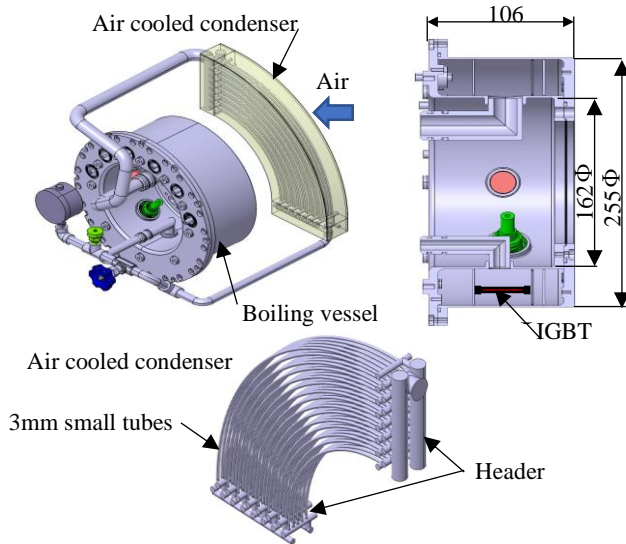


Fig.10 The immersion cooling system with air cooled condenser.

$$h_c = 0.943 \cdot \{\lambda_l^3 \cdot \rho_l^2 \cdot g \cdot H_{fg} / (\mu_l \cdot \Delta T_c \cdot l_c)\}^{1/4} \quad (4)$$

Fig. 11 shows the heat transfer coefficient of film condensation by Nusselt equation (4).

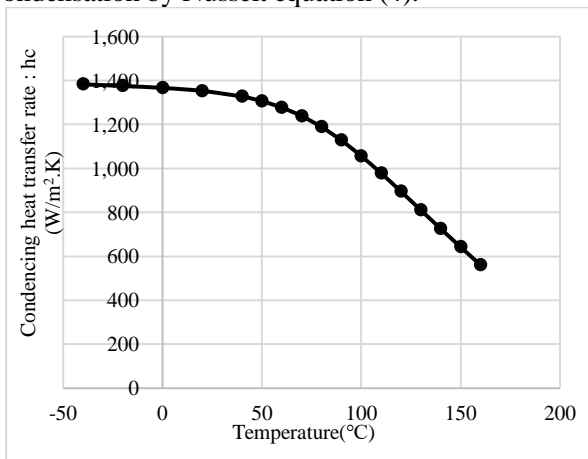


Fig.11 The heat transfer coefficient of Nusselt film condensation

The condensation heat transfer coefficient is calculated to be 1200-1400 W/m².K. by Nusselt's equation of film condensation. The bare tube heat transfer coefficient can be calculated by the Fishenden-Saunders turbulent flow heat transfer equation (5) for staggered circular tubes and calculation results shows in Fig.12.

$$N_u = 0.27 Re^{0.63} Pr_a^{0.36} (Pr_a/Pr_w)^{0.25} \quad (5)$$

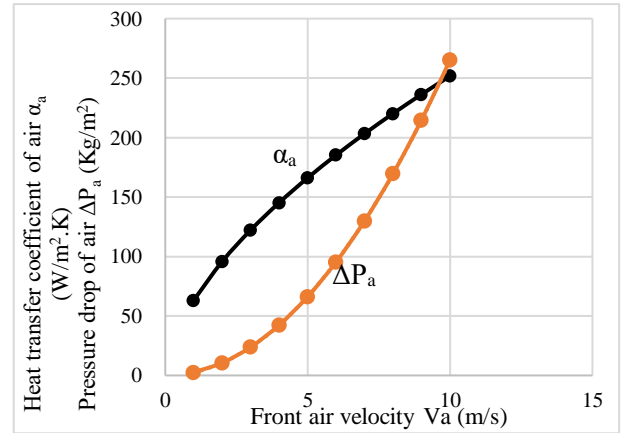


Fig.12 The air heat transfer coefficient of air-cooled condenser

7. Immersion cooling system for IGBT

Fig.13 shows the thermal network of IGBT immersion cooling system in case of P=218W input and 30 deg.C ambient temperature. The temperature of IGBT junction is 56.1 deg.C using kirchhoff's equation. 94% heat is transferred by direct boiling heat transfer and remained 6% heat is passed through 2 pcs. substrates to the coolant.

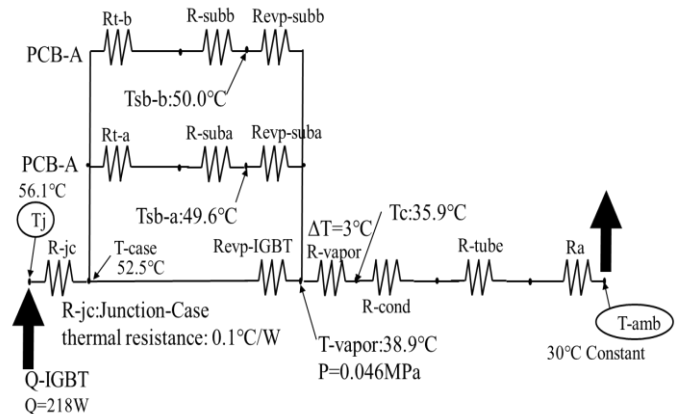


Fig.13 The thermal network of IGBT immersion cooling and temp. distribution in 218W input

8. The air cooling system for In-wheel motor

Fig.14 shows the thermal network and temperature distribution of In-wheel motor without IGBT. The rotational blade inside of outer rotor produces circulation air flow in a motor. The blade can compress air then it is impinged into the 1mm small gap between magnets and coils as shown in Fig.15.(yellow arrow). Main heat is generated from the coils by Joule heat, but iron heat loss could be neglected due to small. Finally, all of heat is removed to outside of motor case. In case of 581W heat loss of motor, the temperature of coils reaches to 180 deg.C which is maximum temperature.

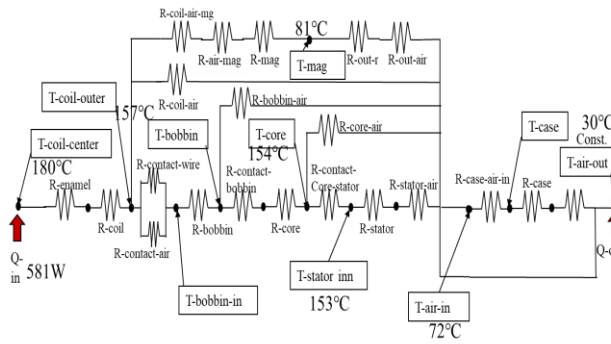


Fig.14 The thermal network of air-cooled In-wheel motor without IGBTs

9. The combined cooling system for In-wheel motor and IGBTs

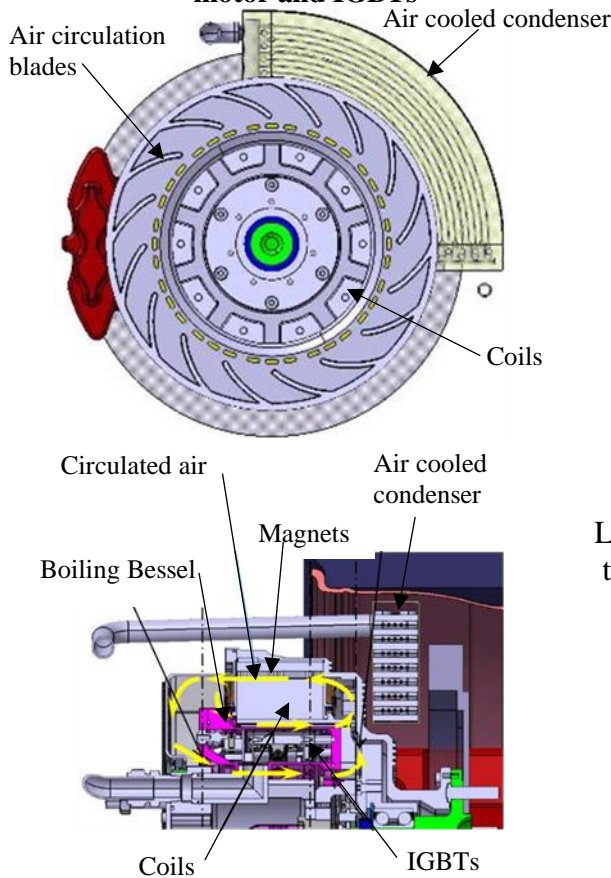


Fig.15 The internal structure of In-wheel motor

The In-wheel motor is basically an air-cooled type with air circulation blade installed in outer rotor. The cooling of IGBT has marginal capacity because of two phase cooling as shown at $T_j=56.1$ deg.C against 120 deg.C at maximum temperature. Fig.15 shows the internal structure of In-wheel motor. Thermally contacting the stator with coils and the evaporation vessel can be transferred the heat from motor to evaporation vessel. Therefore the cooling capacity of motor could be enhanced. Fig.16 shows the cross-sectional view of the in-wheel motor. Due

to 6 pieces IGBTs are installed in the lower space below the center boiling vessel, IGBTs are completely immersed in coolant and kept to be two phase cooled. On the other hand, The motor coils are stated outside of the boiling vessel . The heat of coil is flowed into the boiling vessel passing through motor core and stator. Two pieces of bubble pump structure(yellow and pink color) are set up inner surface of the vessel to lift up the liquid to the higher level using bubble pump effect. Small and many bubbles which are produced on the surface of IGBTs are rising up through 1 mm mini channels with liquid puddles. The vapor tube at the top is connected the air cooled condenser and the condensed liquid is returned back to the vessel by gravity force, which is the exact Loop Thermosiphon.

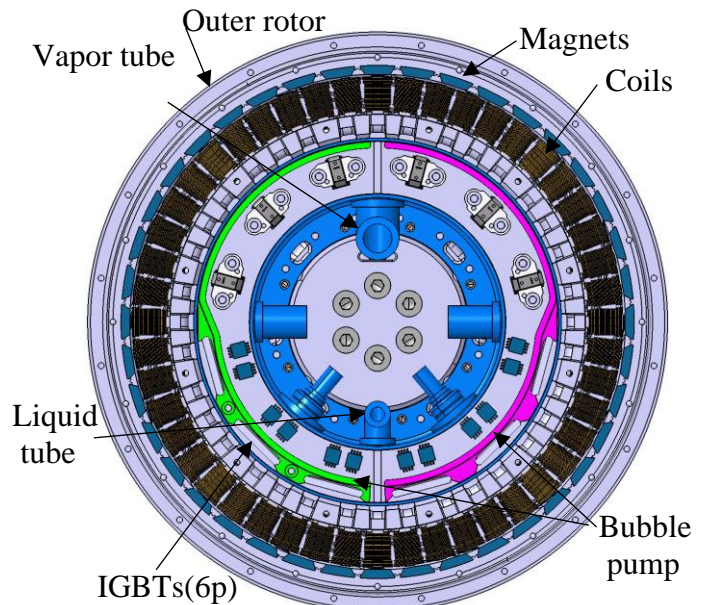


Fig.16 The cross-sectional view of inside of motor

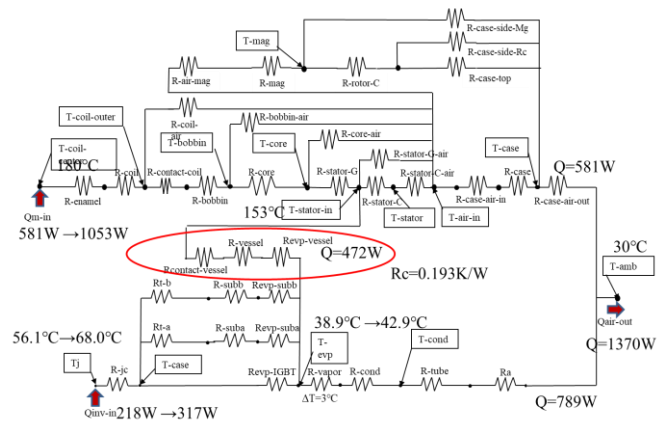


Fig.17 The thermal network of combined cool between Si IGBT immersion cool and motor cool by thermosiphon

Fig.17 shows the combined thermal network using the thermal connector which is 0.193K/W thermal resistance between motor coils and evaporation vessel. Table 1 shows the comparison between individual cool of motor and IGBT, and combined cool together. The motor temperature is much higher than coolant, so that the transferred heat can be controlled by thermal connector. The combined system may help as shown below points.

- 1)The motor cooling capacity can be enhanced 1.81 times than original air cool.
- 2)The motor torque and motor power can be enhanced 1.3 times.
- 3)The junction temperature of IGBT 68 deg.C can be kept less than 120 deg.C of Max.
- 4)The total immersion cooling capacity needs 6.28 Times larger than just cooling IGBTs.
- 5)The transferred heat from motor will be expected 45%.

Table 1 The motor performance improvement using by combined cooling system in case of Si IGBT

Si IGBT Inverter				
		Individual cool	Combined cool	Remark
Motor	Ambient temperature: $T_a(^{\circ}C)$	30	30	
	Heat: $Q_m(W)$	581	1,053	1.81 Times
	Coil temperature: $T_{coil}(^{\circ}C)$	180	180	
	Stator temperature: $T_{stator-in}(^{\circ}C)$	153	153	
	Motor torque: $T_m(N-m)$	381	495	1.3 Times
	Motor Power: $P(Kw)$	56	73	1.3 Times
IGBT	Heat: $Q_{inv}(W)$	218	317	1.45 Times
	IGBT junction temperature: $T_j(^{\circ}C)$	56.1	68	11.9 $^{\circ}C$ up
	Evaporation temp. of NOVEC: $T_e(^{\circ}C)$	38.9	42.9	4 $^{\circ}C$ up
Immersion cool	Thermal resistance of connecting: $R_c(K/W)$	-	0.193	
	Transferred heat from motor: $Q(W)$	0	472	45%
	Immersion cooling capacity: (W)	218	789	3.62 Times
	Total capacity of immersion cooling: (W)	218	1,370	6.28 Times

10. Advantage of SiC inverter for next generation

As next generation of power semiconductor is surely expected to replace from Silicon IGBT to SiC(Silicon Carbide) and GaN(Gallium Nitride) inverter because generated heat can be down 1/3 and the size of semiconductor chip can be shrunk down to 1/3. However the heat flux will be increased 3 times larger. As the heat flux of 7.25 W/cm² at normal and 47W/cm² at Max. are plotted on Fig.6 and it is expected to over than critical heat flux, so that the evaporation area expanding using such as pin fins should be added. Especially it shall be considered in case of low temperature boiling region. Fig.18 shows the heat transfer coefficient of evaporator in case of SiC inverter. Due to higher heat flux in case of SiC, the heat transfer coefficient will be double value than Si

IGBT. Fig.19 shows the combined thermal network using the thermal connector between motor coil and evaporation vessel of 0.0172K/W thermal resistance. Table 2 shows the comparison between individual cool of motor and IGBT, and combined cool together. The combined system may help as shown below points.

- 1)The cooling capacity can be enhanced 3.34 times larger. It is 1053W in Si IGBT but increasing 1940W in SiC inverter.
- 2)The motor torque and motor power can be enhanced 1.69 times larger. 64Kw output motor is possible to practical use.
- 3)The junction temperature of IGBT is 59.1 deg.C in SiC against 68 deg.C in Si IGBT.
- 4) The total immersion cooling capacity increases 1519W.
- 5) The transferred heat from motor will be expected 70%, 1360W.

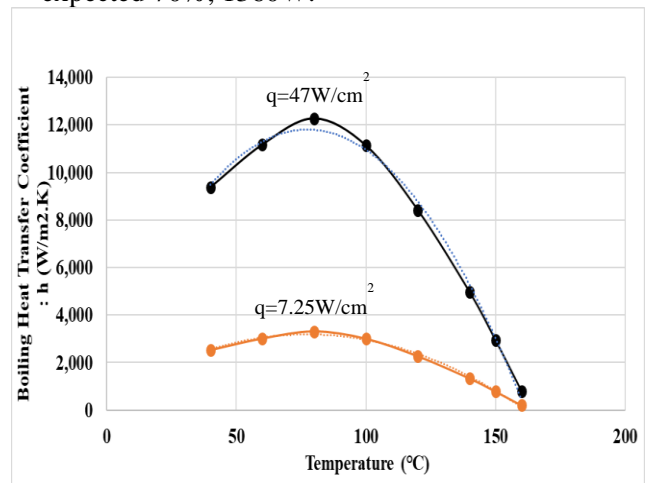


Fig.18 The heat transfer coefficient of evaporator in SiC inverter

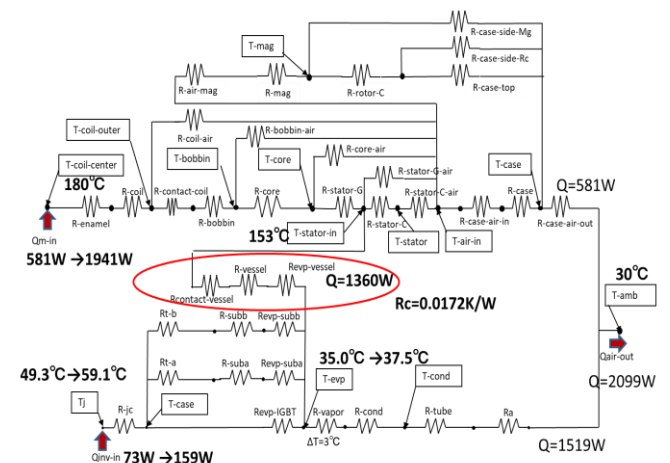


Fig.19 The thermal network of combined cool between SiC inverter immersion cool and motor cool by thermosiphon

Table 2 The motor performance improvement using by combined cooling system in case of SiC inverter

SiC Inverter				
		Individual cool	Combined cool	Remark
Motor	Ambient temperature: Ta(°C)	30	30	
	Heat: Qm(W)	581	1,940	3.34 Times
	Coil temperature: Tcoil(°C)	180	180	
	Stator temperature: Tstator-in(°C)	153	153	
	Motor torque: Tm(N-m)	381	643	1.69 Times
	Motor Power: P(Kw)	56	94	1.69 Times
IGBT	Heat: Qinv(W)	73	159	2.18 Times
	IGBT junction temperature: Tj(°C)	49.3	59.1	9.8 °C up
	Evaporation temp. of NOVEC: Te(°C)	35.0	37.5	2.5 °C up
Immersion cool	Thermal resistance of connecting: Rc(K/W)	-	0.0172	
	Transferred heat from motor: Q(W)	0	1,360	70%
	Immersion cooling capacity: (W)	73	1,519	20.8 Times
	Total capacity of immersion cooling: (W)	654	2,099	3.21 Times

11. Conclusion

Table 3 Overall comparison of cooling effect

	Motor power at 1000RPM(KW)	Motor Torque(N-m)	Heat of motor(W)	Heat of Inverter(W)
Si IGBT Individual cool	62	420	765	261
Si IGBT combined cool	73	495	1053	317
SiC inv. combined cool	94	643	1941	159

Table 3 shows the conclusion remarks which is the overall comparison of cooling effect.

- 1) We have developed a compact and lightweight in-wheel motor for EV with a built-in immersion cooler for cooling IGBT and a condenser inside in-wheel motor.
- 2) The cooling capacity of the air-cooled in-wheel motor can be increased approx. 1.81 times with heat transfer technique from the motor to the boiling vessel by loop thermos-siphon. As a result, the estimated torque and power output can be increased 1.3 times, 495 N-m and 73Kw.
- 3) When replacing from Si IGBT to SiC inverter, the cooling capacity of motor will be able to increase 3.34 times larger. The estimated torque and power output can be increased 1.69 times, 643 N-m and 94Kw.

Acknowledgements

This work was partly supported by the National Key Research and Development Program of China, MOST-JICA International Research Project (2021YFE0192800).

Nomenclature

- 1) q_{CHF} : Critical heat flux (W/m²)
- 2) ρ_v : Vapor density (Kg/m³)
- 3) H_{fg} : Latent heat (J/Kg)
- 4) σ : Surface tension (N/m)
- 5) g : Gravity acceleration (m/s²)
- 6) ρ_l : Liquid density (Kg/m³)
- 7) h : Boiling heat transfer coefficient (W/m².K)
- 8) la : Laplace coefficient (-)
- 9) K_l : Thermal conductivity of liquid(W/m.K)
- 10) Pr_l : Prandtl number of liquid(-)
- 11) q : Heat flux(W/m²)
- 12) L_{lv} : Latent heat (J/Kg)
- 13) γ_l : Dynamic viscosity of liquid(m²/s)
- 14) P : Pressure (Pa)
- 15) h_c : Condensing heat transfer coefficient (w/m².K)
- 16) λ_l : Liquid thermal conductivity (W/m.K)
- 17) μ_l : Liquid viscosity (Pa.s)
- 18) ΔT_c : Temperature difference between vapor temp. and wall temp. at condenser (K)
- 19) l_c : Condenser length (m)
- 20) N_u : Nusselt number (-)
- 21) Re : Reynolds number (-)
- 22) Pr_a : Prandtl number at air temp. (-)
- 23) Pr_w : Prandtl number at tube wall temp.(-)

References

- 1) Mochizuki, etal, #59 the heat transfer symposium in Japan, proceedings, May 2022.
- 2) Internet WEB information, e-Gle Co.Ltd., <https://www.facebook.com/eGleInc>
- 3) R. Yukishima, etal, NTN Technical Review No.83, 2015, pp21
- 4) Infineon Technologies, Double Side Cooled Module Data sheet, FF400R07A01E3_S6 V3.4,(2020)

Thermal characteristics of a 2-m nitrogen cryogenic loop heat pipe with a capillary starter pump

Kimihide Odagiri^{1*}, Xinyu Chang², Hiroki Nagai², and Hiroyuki Ogawa¹

¹ Institute of Space and Astronautical Science (ISAS), Japan Aerospace Exploration Agency (JAXA), Sagamihara, Japan

² Institute of Fluid Science, Tohoku University, Sendai, Japan

*Corresponding author email address: odagiri.kimihide@jaxa.jp

Abstract

A Cryogenic Loop Heat Pipe (CLHP) is a promising heat transport device for the cryogenic thermal design of future space telescopes because of its heat transfer capability and feasibility of various design arrangements. One of the advantages of the CLHP is the heat transfer capability over a long distance. However, there are few numbers of the study on the CLHPs that have heat transfer lengths over 1 m so far. In this study, the 2-m nitrogen CLHP with a capillary starter pump (CSP) is developed. The heat transfer characteristics of the CLHP with various heat load to the CSP is reported in the paper. The designed evaporator and CSP have porous wicks made of stainless steel has a pore radius of 1.0 μm and a permeability of $1.3 \times 10^{-13} \text{ m}^2$. The experiments were conducted with the horizontal condition under the cryogenic thermal vacuum condition. The CLHP started successfully when the heat loads to the evaporator and the CSP were 4 W and 4 W, respectively. The maximum heat transfer capability was 24 W, and the minimum CLHP thermal resistance was 0.064 K/W. The effects of the CSP heat load on the thermal characteristics are discussed.

Keywords: Cryogenic Loop Heat Pipe; Capillary starter pump; 2-m heat transport length; Thermal-vacuum test.

1. Introduction

A Cryogenic Loop Heat Pipe (CLHP) is a promising heat transport device for a cryogenic thermal structure of space telescopes such as JWST [1], Planck [2], and LiteBIRD [3,4] because of its heat transfer capability and feasibility of various design arrangements. In this study, the nitrogen CLHP with an auxiliary loop and a capillary starter pump (CSP) (Figure. 1) is studied. In other studies, the CSP is also called a secondary evaporator and a secondary pump. In this study, the capillary starter pump is used because its main function and purpose is the start-up of the CLHP primary loop.

So far, many researchers have investigated the characteristics of the nitrogen CLHPs with the capillary starter pump as presented in Table 1 [5-10]. T.T. Hoang et al. have developed the nitrogen CLHP with a transport length of 2500 mm. The maximum heat load was 20 W. On the other hand, many researchers have investigated the CLHP with a transport length of less than 1 m. To our best knowledge, the investigation of the long CLHP does not exist except for the reference [5].

One of the advantages of the CLHP is its long-distance heat transfer capability. To enhance the feasibility of utilizing CLHPs in future astronomical space missions, long-distance CLHP is required. Due to few studies regarding long-CLHP, the effects of the CSP heat load on the operating characteristics, the maximum heat transfer capability, and the thermal resistance are not revealed for the CLHP with long heat transfer length.

In this study, a 2-m nitrogen CLHP has been newly developed and tested. The purpose of this study is to investigate its thermal characteristics with various CSP heat load conditions. This paper reports the design of the 2-m nitrogen CLHP, experimental results under the cryogenic thermal vacuum condition, and the thermal resistance of the CLHP.

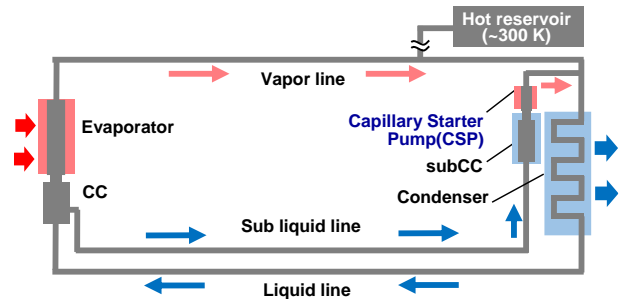


Figure 1. Schematic of the CLHP with an auxiliary loop and a capillary starter pump

Table 1. Previous studies of the nitrogen CLHP

Researcher	Length of the transport lines (V.L./L.L), mm	Maximum heat load, W
T.T. Hoang [5]	2500 / 2500	20
P. Gully [6]	567 / 328	19
Y. Zhao [7]	450 / 660	43
L. Bai [8]	640 / 560	12
Y. Guo [9]	700 / 700	4
H. Cho [10]	680 / 680	12

(V.L. : Vapor Line, L.L: Liquid Line)

2. Experimental setup

2.1. Working principle and specification of the CLHP

Figures 2-3 and Table 1 present the overview and the specification of the CLHP, respectively. The CLHP consists of an evaporator, a compensation chamber (CC), a capillary starter pump (CSP), a sub-CC, a condenser, a vapor line, and a liquid line. The startup mechanism of the CLHP is the same as the one presented in the previous study [10]. At first, the inside of the CLHP is in the supercritical state at room temperature such as 300 K. The condenser and the sub-CC are cooled to liquefy the working fluid. Then, the liquid flows into the CSP. By applying the heat load to the CSP, evaporation occurs and the vapor flows into the condenser. The liquid in the condenser flows into the liquid line and evaporator. The CLHP starts by applying the heat load on the evaporator after the evaporator is sufficiently cooled.

The dimensions of the CLHP were designed based on a one-dimensional steady-state numerical model presented in ref. [11]. To achieve the 2 m heat transfer length, a fine porous wick made of stainless steel [12, 13] was used for the evaporator and the CSP. The wick has a pore radius of $1.0 \mu\text{m}$ and permeability of $1.3 \times 10^{-13} \text{ m}^2$. As shown in Fig. 3, the evaporator and the CSP have the same structure. The length of the vapor line, the condenser, and the liquid line is designed as 2000 mm, 1500 mm, and 2000 mm, respectively. All transfer lines have the same outer/inner diameters of 3.18 mm / 1.75 mm.

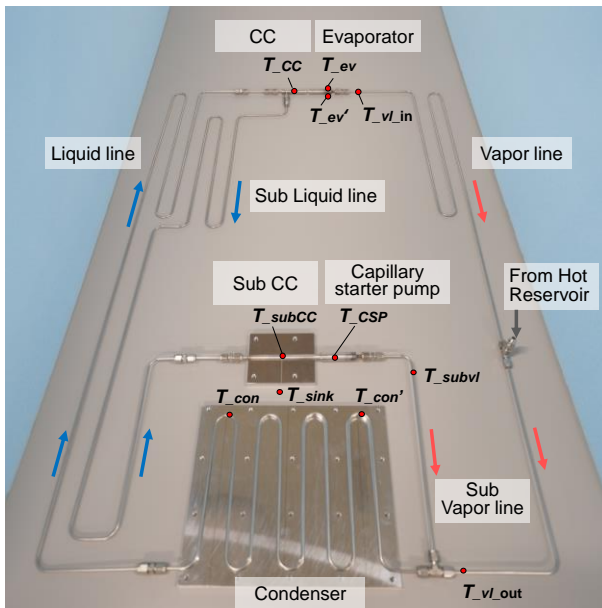


Figure 2. The overview of the cryogenic loop heat pipe with CSP and temperature measurement point.

The hot reservoir has the function of inner pressure reduction when the CLHP temperature is 300 K. The hot reservoir that has a volume of 500 cc is located outside of the thermal vacuum chamber in this experimental setup. The hot reservoir and the CLHP are connected via the hot reservoir line.

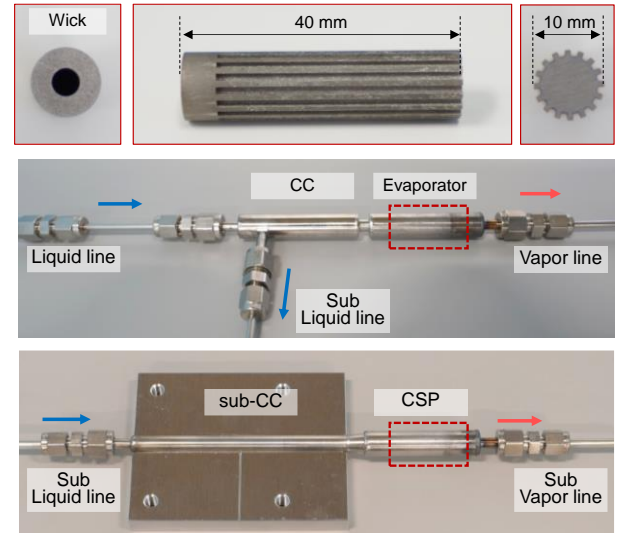


Figure 3. Pictures of the stainless steel wick structure, the evaporator, the CC, the CSP, and the sub-CC.

Table 2. Specification of the CLHP

Evaporator and Capillary starter pump	
O.D. / I.D., mm	12 / 10
Length, mm	54
Porous wick	
Material	Stainless steel
Pore radius, μm	1.0
Permeability, m^2	1.3×10^{-13}
O.D. / I.D., mm	10 / 4
Length, mm	40
Vapor groove width / Length / number, mm	1.0 / 1.0 / 16
Compensation Chamber (CC)	
O.D. / I.D., mm	12 / 10
Length, mm	60
Sub CC (for capillary starter pump)	
O.D. / I.D., mm	8 / 6
Length, mm	100
Vapor line	
O.D. / I.D., mm	3.18 / 1.75
Length, mm	2000
Condenser	
O.D. / I.D., mm	3.18 / 1.75
Length, mm	1500
Liquid line / Sub liquid line	
O.D. / I.D., mm	3.18 / 1.75
Length, mm	2000
Hot reservoir	
Volume, cc	500

2.2. Experimental condition

Figures 4-5 present the schematic diagram of the experimental setup and the picture of the CLHP set in the cryogenic thermal vacuum chamber. In this study, the experiment was conducted in a 70-K thermal vacuum condition. The pressure in the chamber was kept at less than 1.0×10^{-4} Pa so that the effect of convective heat transfer could be neglected. The condenser and sub-CC were cooled by the GM cryocooler. Except for the condenser and the sub-CC, the whole CLHP structure is thermally insulated by multilayer insulation (MLI).

The heat load is applied to the evaporator and CSP by the polyimide surface heaters (Nippon heater co., ltd. PS2550-24/12). Heater power was applied using a DC power supply. Temperatures were measured by 11 T-type thermocouples with an accuracy of ± 1.0 K. The measurement points are shown in Figure. 2. Measurement data was acquired by the data logger (GRAPHTEC co., midi LOGGER GL840). The hot reservoir pressure was measured by the diaphragm pressure gauge (Keyence, GP-M100). The accuracy of the pressure gauge is ± 0.1 MPa.

Nitrogen was used as the working fluid. The filling pressure was determined based on the following method [14]. At first, the required fluid mass necessary for CLHP operation at 80 – 110 K is calculated by Equation (1).

$$M_{REQ} = \rho_{sat,L} V_{Loop,L} + \rho_{sat,V} V_{Loop,V} + \rho_V V_{HR}, \quad (1)$$

where M_{REQ} is the working fluid mass required for CLHP to operate at 80 – 100 K. $\rho_{sat,L}$ and $\rho_{sat,V}$ are the density of liquid and vapor at saturation condition, respectively. $V_{Loop,L}$ and $V_{Loop,V}$ are the volume of liquid and vapor during normal

operation, respectively. ρ_V is the vapor density in a hot reservoir during normal operation. V_{HR} is the volume of the hot reservoir. Then, the fluid mass (M_{CRIT}) is calculated by Equation (2). Specifically, the fluid mass required to fill the CLHP when the loop pressure equals the critical pressure, and the cold volume is at critical temperature (126 K), whereas the remaining volume is at the initial temperature (300 K).

$$M_{CRIT} = \rho_{CRIT} V_{Cold} + \frac{P_{CRIT}}{ZRT_{INIT}} (V_{System} - V_{Cold}), \quad (2)$$

where ρ_{CRIT} is the fluid density at critical condition. V_{Cold} is the volume of the cold part of the loop including the condenser, CSP, and sub-CC. P_{CRIT} is the critical pressure of working fluid. Z is the Van der Waals compressibility factor. R is the specific gas constant. T_{INIT} is the initial temperature. V_{System} is the total system volume including the hot reservoir. When $M_{REQ} < M_{CRIT}$ and the temperatures of the condenser and the sub-CC reach 126 K, the loop pressure becomes subcritical. Then, the charge pressure can be calculated by Equation (3).

$$P_{Charge} = \frac{M_{REQ}}{V_{System}} RT_{room} \quad (3)$$

where P_{Charge} is the charge pressure, T_{room} is the room temperature. In this experiment, the filling pressure was 3.6 MPa.

The heat load to the evaporator (Q_{evap}) was stepped up from 4 W to 24 W by 4 W. Over 24 W, the heat load was stepped up by 2 W. The heat load to the CSP (Q_{CSP}) was variable. Q_{CSP} of 0, 2, and 4 W were used for the experiment. For the startup of

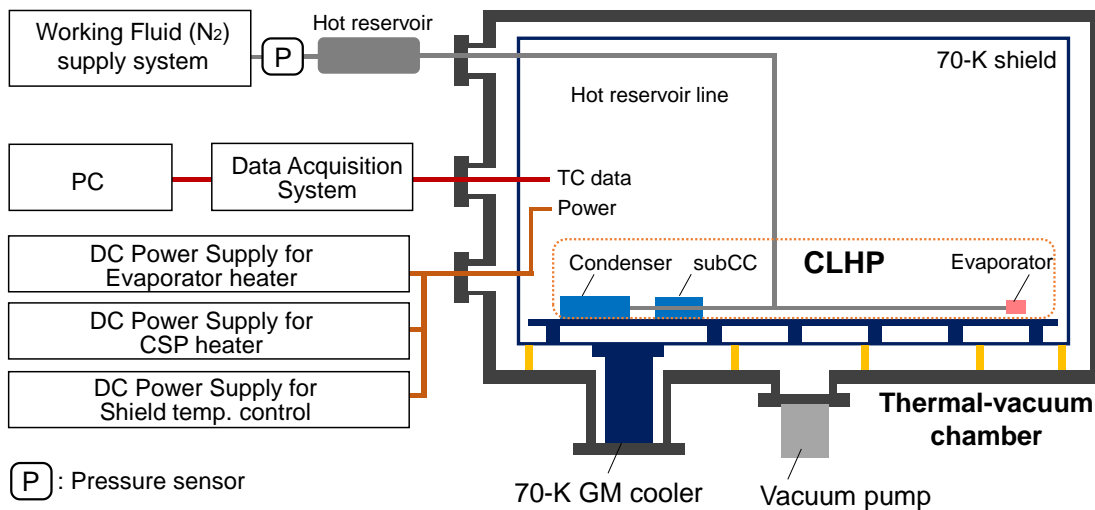


Figure 4. Schematic diagram of the experimental setup

the CLHP at high-temperature condition (i.e., evaporator temperature is over 140 K), Q_{CSP} of 4 W was used. In the case of $Q_{CSP} = 0, 2$ W, the whole CLHP structure was kept at a low temperature (75 – 80 K) as the initial condition. These are different from that for the case of $Q_{CSP} = 4$ W. In addition, it was not possible for the CLHP to start up at $Q_{CSP} = 0$ W. Therefore, after CLHP reached a steady state at $Q_{evap} = 4$ W / $Q_{CSP} = 4$ W, then Q_{CSP} was changed to 0 W and the steady-state temperature data for the case of $Q_{CSP} = 0$ W was obtained.

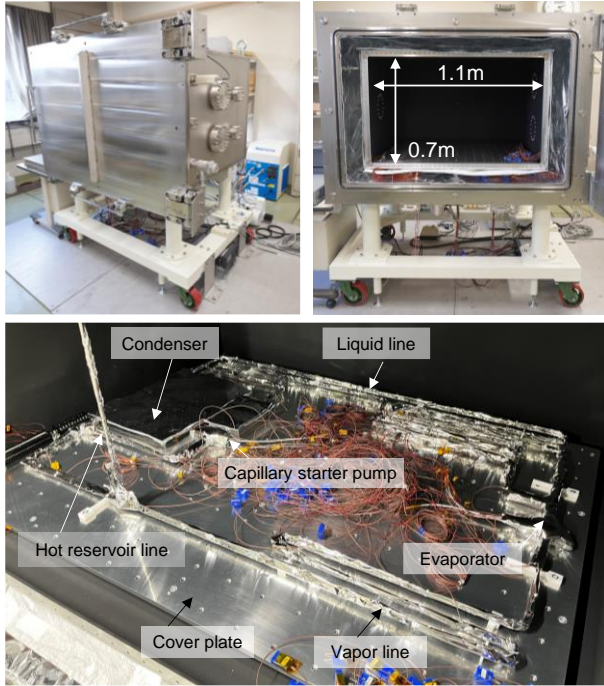


Figure 5. The CLHP in the cryogenic thermal-vacuum chamber.

3. Results and discussion

3.1. Start-up characteristics

Figure 6 presents the temperature profiles of the CLHP startup for the case heat load to the CSP was 4 W. Before the startup, the temperatures of the evaporator, CC, and the vapor line inlet were 144 K, whereas the temperatures of the condenser, CSP, and the sub-CC reached 80 K. At this condition, it is considered that the liquid phase exists in the low-temperature parts. When the heat load is applied to the CSP, evaporation occurs in the CSP. Then, the vapor flows into the sub-vapor line and the outlet of the vapor line. Their temperatures rose to 112 K and became constant. After that, the temperatures of the evaporator, CC, and inlet of the vapor line gradually decreased. This is caused by the low-temperature vapor generated in the CSP gradually flowing into them. As these temperatures became lower, the hot reservoir pressure also decreased. After $t = 13,060$ sec, the overall temperature of the CLHP dropped drastically. This is caused by liquid generated in the condenser reaching the evaporator and the CC. It is considered that the flow in the auxiliary loop, which consists of the CSP, sub-vapor line, condenser, liquid line, CC, sub-liquid line, and the sub-CC reached a steady state, thus the temperature of the CSP and sub-vapor line drastically decreased.

After the evaporator temperature dropped to 79 K, a heat load of 4 W was applied to the evaporator. The evaporator temperature slightly increased, and simultaneously, the vapor line inlet ($T_{vl,in}$) rapidly

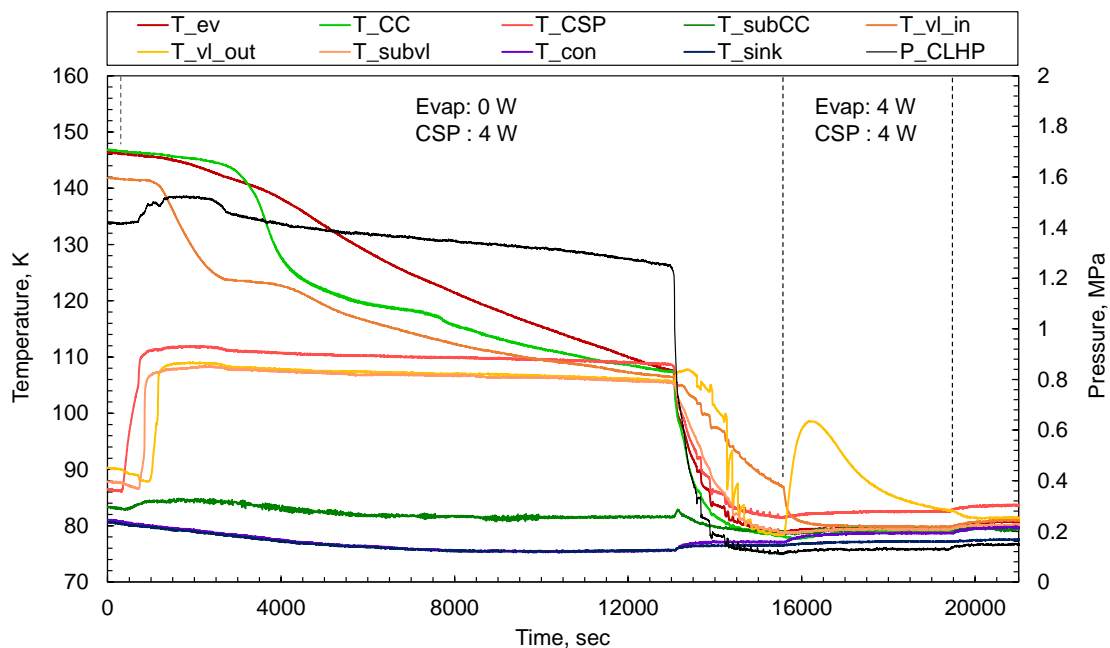


Figure 6. Startup behavior at $Q_{CSP} = 4$ W, $Q_{evap} = 4$ W.

decreased. In addition, an increase in the vapor line outlet temperature (T_{vl_out}) was observed. This is because the low-temperature vapor generated in the evaporator starts to flow into the vapor line. The remained high-temperature vapor in the vapor line is pushed by the vapor from the evaporator and flows into the outlet of the vapor line. Thus, the T_{vl_out} showed a trend that temporarily increased and then decreased. After these behaviors, the temperatures of each element reached a steady state. It was confirmed that the 2-m N_2 CLHP successfully started up.

3.2. Steady-state characteristics

Figures 7 – 9 present the temperature profiles of the step-up evaporator heat load tests at heat loads to the CSP (Q_{CSP}) were 4, 2, and 0 W. Figure 7 shows the continuation of the temperature profiles that are presented in Figure 6.

Based on Figure 7, it is confirmed that the CLHP stably operated with $Q_{evap} = 4 - 24 \text{ W} / Q_{CSP} = 4 \text{ W}$. The dry-out was observed at $Q_{evap} = 26 \text{ W}$. At $Q_{evap} = 24 \text{ W}$, a significant increase in evaporator temperature was observed before reaching the steady state. It is considered that the disappearance of the liquid bridge between the evaporator casing and the wick resulted in the rapid increase of the thermal resistance in the evaporator [11, 13].

Figure 8 shows that the CLHP can operate stably with $Q_{evap} = 4 - 24 \text{ W} / Q_{CSP} = 2 \text{ W}$. As in the case of $Q_{CSP} = 4 \text{ W}$, the CLHP stops to operate at $Q_{evap} = 26 \text{ W}$. In addition, a significant increase in the

evaporator temperature was observed at $Q_{evap} = 24 \text{ W}$.

As shown in Figure 9, the CLHP could operate after Q_{CSP} was switched from 4 W to 0 W. At $Q_{evap} = 4 \text{ W} / Q_{CSP} = 0 \text{ W}$, the temperatures of each part seemed to decrease. It is noted that this trend is not due to the thermo-fluid behavior of the CLHP but to the decrease in the sink temperature. It was clear that the CLHP stably operated at $Q_{evap} = 4 - 24 \text{ W} / Q_{CSP} = 0 \text{ W}$. As in the $Q_{CSP} = 2, 4 \text{ W}$, a significant temperature increase in the evaporator was observed at $Q_{evap} = 24 \text{ W}$, and dry-out was observed at $Q_{evap} = 26 \text{ W}$. In general, the heat load to the CSP is the excess heat input against the heat load to the evaporator because it is considered that the only evaporator removes the heat from the part that needs to be cooled such as detectors and telescope structures. If the heat dissipation from the condenser and the sub-CC is absorbed by the cryo-cooler, the cooling capacity must cover both the removed heat from the detectors and the CSP heat load. Therefore, the CSP heat load is preferred to be as small as possible. This experiment successfully demonstrated that the CLHP could operate at $Q_{CSP} = 0 \text{ W}$ with a heat transfer length of 2 m. This result is important from the viewpoint of the implementation of the CLHP in space telescopes.

3.3. Effect of capillary starter pump heat load on thermal resistance

In this section, the steady-state operating characteristics such as the CLHP thermal resistance,

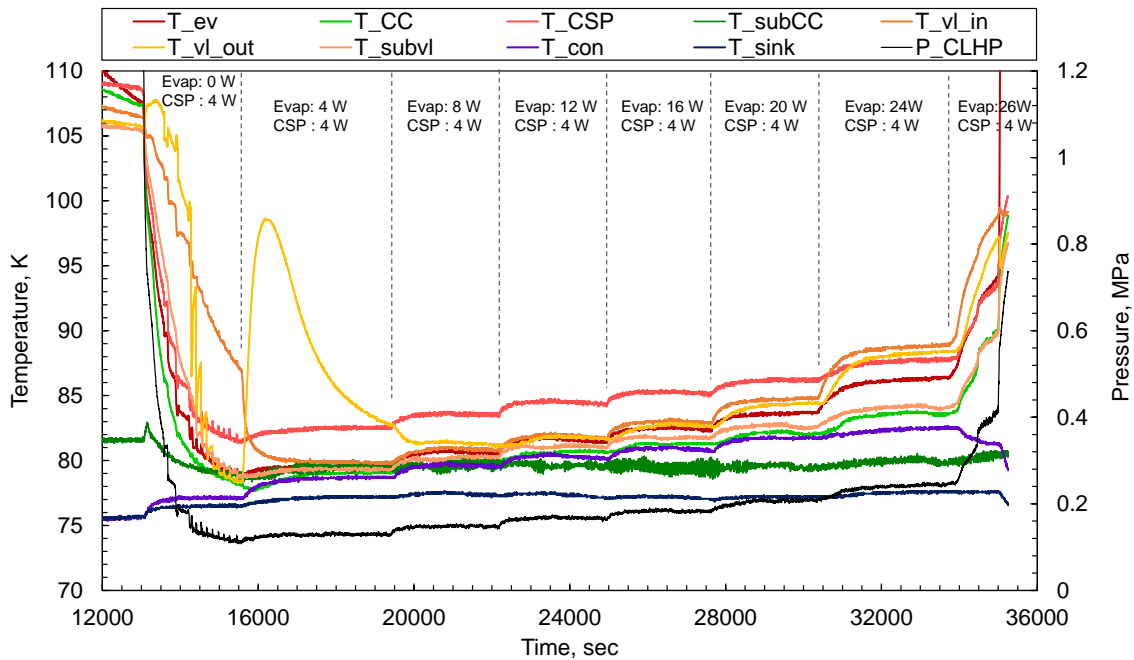


Figure 7. Steady-state operation at $Q_{CSP} = 4 \text{ W}$, $Q_{evap} = 4 - 24 \text{ W}$

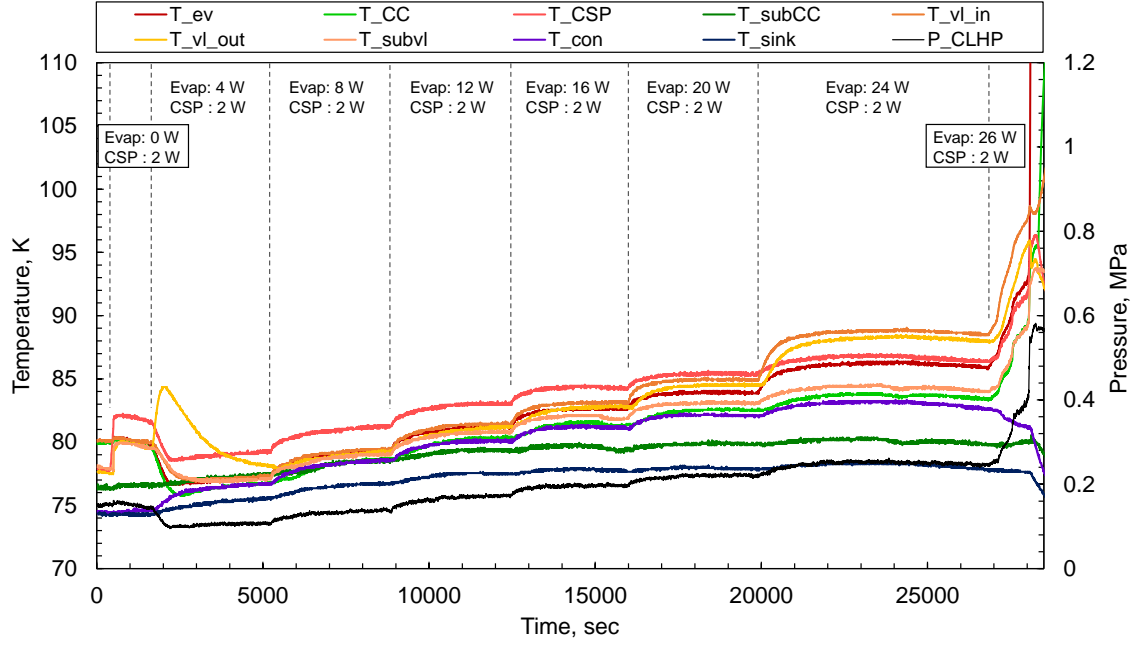


Figure 8. Steady-state operation at $Q_{CSP} = 2 \text{ W}$, $Q_{evap} = 4 - 24 \text{ W}$

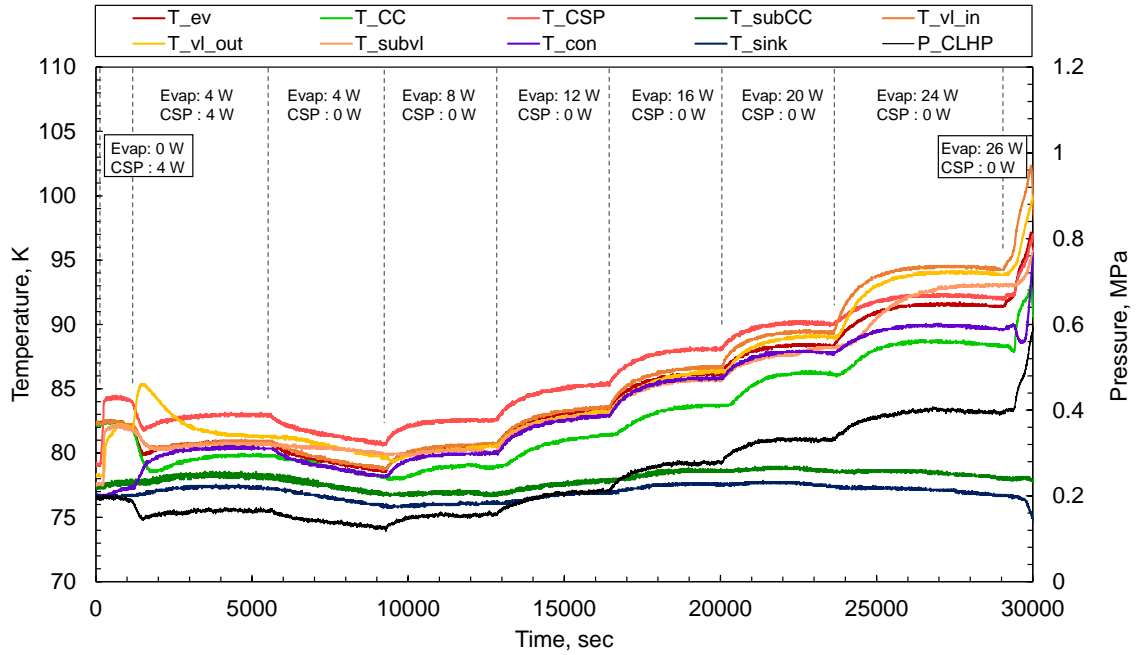


Figure 9. Steady-state operation at $Q_{CSP} = 0 \text{ W}$, $Q_{evap} = 4 - 24 \text{ W}$

the temperature difference between the CC and the sub-CC, and the temperature difference between the CSP and the condenser are discussed. In this experimental setup, it was difficult to precisely control the sink temperature to be constant even if manual temperature control was conducted. The sink temperature fluctuated depending on the heat loads to the CLHP. Therefore, the steady-state operating characteristics are discussed based on thermal resistance and the temperature difference

between the components.

The thermal resistance of the CLHP (R_{LHP}) was calculated by Equation (4).

$$R_{LHP} = \frac{\overline{T_{ev}} - \overline{T_{con}}}{Q_{evap}} \quad (4)$$

$\overline{T_{ev}}$ is the average temperature of T_{ev} and T_{ev}' . $\overline{T_{con}}$ is the average temperature of T_{con} and T_{con}' . Q_{evap} is the heat load to the evaporator which is calculated by the product of applied voltage and

current to the heaters.

Figure 10 presents the effect of the CSP heat load on the thermal resistance of the CLHP. For each condition, the minimum thermal resistance was 0.064 K/W ($Q_{CSP} = 0$ W), 0.13 K/W ($Q_{CSP} = 2$ W), and 0.14 K/W ($Q_{CSP} = 4$ W). The case of $Q_{CSP} = 0$ W showed the lowest value.

For the case of a CLHP with a capillary starter pump and an auxiliary loop, the function of the CSP is different depending on whether the CSP heat load is applied or not. Specifically, when the CSP heat load is applied, the flow from CC to sub-CC and CSP occurs. On the other hand, in case the CSP heat load is not applied, it is considered that vapor flows from the vapor line condensate at the CSP. In other words, the CSP switched its function to the additional condenser at $Q_{CSP} = 0$ W. The case of $Q_{CSP} = 0$ W showed the lowest thermal resistance because the CLHP operates as a single evaporator/multi-condenser LHP.

Figure 11 presents the temperature difference between the CC and the sub-CC ($\Delta T_{CC-subCC} = T_{CC} - T_{subCC}$). For the case of $Q_{evap} = 4$ W / $Q_{CSP} = 2, 4$ W, $\Delta T_{CC-subCC}$ became negative, whereas it became positive for most cases. This means the CC temperature is higher than the sub-CC temperature in most cases. There was a significant difference in $\Delta T_{CC-subCC}$ between the condition of $Q_{CSP} = 0$ W and that of $Q_{CSP} > 0$ W.

$\Delta T_{CC-subCC}$ of $Q_{CSP} = 0$ W became larger than that of $Q_{CSP} > 0$ W. This is because the heat leak from the CSP to the sub-CC is small at $Q_{CSP} = 0$ W. In addition, the temperature of the sub-CC became low because the heat flow from the CC to the sub-CC is considered to be small. Since the pressure in the sub-CC was not measured in this experiment, the internal state of the two-phase liquid-vapor condition is not clear. However, it is considered that the inside of sub-CC was in a liquid single-phase and subcooled because of the following reasons: (1) $\Delta T_{CC-subCC}$ was positive, (2) the CSP worked as the condenser, and (3) the heat leak from CSP to the sub-CC is relatively small.

On the other hand, in the case of $Q_{CSP} > 0$ W, the inside of the sub-CC is assumed to be in the liquid-vapor two-phase condition because of the following reasons: (1) the heat flow from the CC to the sub-CC is large due to the liquid flow occurring from the CC via the sub-liquid line, and (2) the heat leak from the CSP to the sub-CC is large due to the applied heat to the CSP.

Figure 12 presents the temperature difference between the CSP and the condenser ($\Delta T_{CSP-con} = T_{CSP} - T_{Con}$). $\Delta T_{CSP-con}$ were 1.3–1.5 K ($Q_{CSP} = 0$ W) 2.6–4.0 K ($Q_{CSP} = 2$ W), and 4.0–5.4 K

($Q_{CSP} = 4$ W), respectively. The trend $\Delta T_{CSP-con}$

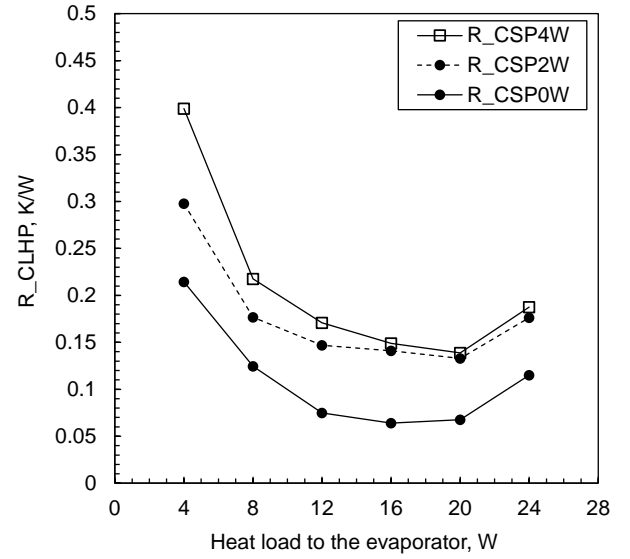


Figure 10. Thermal resistance of the CLHP at $Q_{CSP} = 0, 2, 4$ W

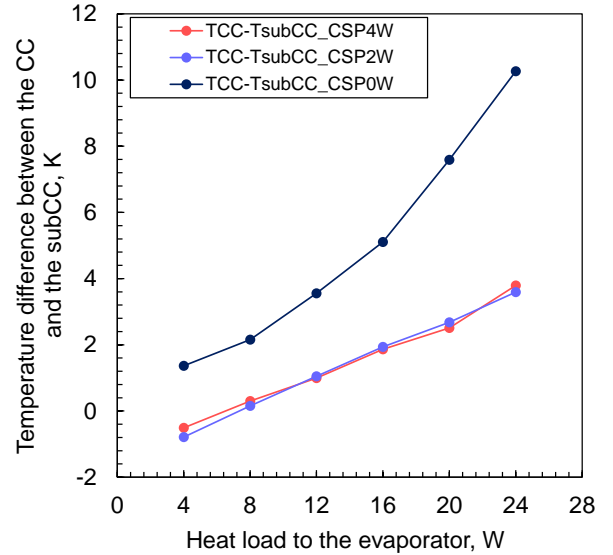


Figure 11. Temperature difference between the CC and the subCC as a function of the heat load to the evaporator at $Q_{CSP} = 0, 2, 4$ W.

increased with the heat load to the CSP was observed. In the case of $Q_{CSP} = 2, 4$ W, $\Delta T_{CSP-con}$ increased with the heat load to the evaporator. This is because the evaporation temperature inside the CSP increased with the temperature of the evaporator and the CC. On the other hand, $\Delta T_{CSP-con}$ is almost constant against the changes in the evaporator heat load at $Q_{CSP} = 0$ W. This is because the CSP worked as the additional condenser. It is considered that $\Delta T_{CSP-con}$ indicates the temperature difference between the two condensers in the $Q_{CSP} = 0$ W. Therefore, the temperature difference and the changes with the

evaporator heat load were slight.

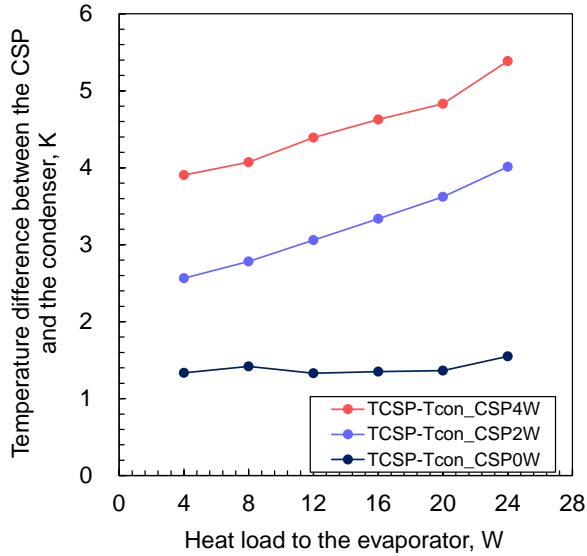


Figure 12. Temperature difference between the CSP and the condenser as a function of the heat load to the evaporator at $Q_{CSP} = 0, 2, 4$ W

4. Conclusion

In this paper, the thermal characteristic of the 2-m nitrogen CLHP with a capillary starter pump (CSP) was studied experimentally. The test was conducted under the cryogenic thermal vacuum condition, and the effect of the heat load to the CSP on the thermal resistance of the CLHP was investigated. The main conclusions are summarized as follows:

- (1) The CLHP successfully demonstrated the start-up at $Q_{CSP} = 4$ W/ $Q_{evap} = 4$ W and stable operation for the $Q_{CSP} = 4$ W/ $Q_{evap} = 4 - 24$ W with the heat transfer length of 2 m. In the case of $Q_{CSP} = 0, 2$ W, the CLHP stably operated at $Q_{evap} = 4 - 24$ W as in the case of $Q_{CSP} = 4$ W.
- (2) The minimum thermal resistances of the CLHP were 0.064 K/W ($Q_{CSP} = 0$ W), 0.13 K/W ($Q_{CSP} = 2$ W), and 0.14 K/W ($Q_{CSP} = 4$ W). The case of $Q_{CSP} = 0$ W showed the lowest value. It is considered that the CSP switched its function to the condenser at $Q_{CSP} = 0$ W. Only in this case, the CLHP operates as a single evaporator/multi-condenser LHP. Thus, it shows the minimum thermal resistance compared with other CSP heat load conditions.

References

[1] R. A. Kimble, L. D. Feinberg, M. F. Voyton, J.A. Lander, et al. James Webb Space Telescope (JWST) optical telescope element and integrated science instrument module (OTIS) cryogenic test program and results. in SPIE Astronomical Telescopes + Instrumentation. 2018. Austin, USA.

[2] PAR Ade, N. Aghanim, M. Arnaud, M. Ashdown, et al., Planck early results. II. The thermal performance of Planck. *Astron Astrophys Suppl Ser.*, 2011, 536, A2.

[3] K. Odagiri, M. Saijo, K. Shinozaki, F. Matsuda, et al., Cryogenic thermal design and analysis for LiteBIRD payload module. in SPIE Astronomical Telescopes + Instrumentation. 2022. Montreal, Canada.

[4] LiteBIRD collaboration, Probing Cosmic Inflation with the LiteBIRD Cosmic Microwave Background Polarization Survey. *Progress of Theoretical and Experimental Physics*. 2022. ptac150.

[5] T. Hoang, T. O'Connell, and D. Khrustalev, Development of a flexible advanced loop heat pipe for across-gimball cryocooling. in SPIE. 2003. 5172

[6] P. Gully, Q. Mo, T. Yan, P. Seyfert, et al. Thermal behavior of a cryogenic loop heat pipe for space application. *Cryogenics*, 2011. 51: 420–428.

[7] Y. Zhao, T. Yan, and J. Liang, Experimental study on a cryogenic loop heat pipe with high heat capacity. *Int. J. Heat Mass Transf.*, 2011. 54: 3304–3308.

[8] L. Bai, G. Lin, H. Zhang, J. Miao, et al., Experimental study of a nitrogen-charged cryogenic loop heat pipe. *Cryogenics*, 2012. 52: 557–563.

[9] Y. Guo, G. Lin, L. Bai, X. Bu, et al., Experimental study on the supercritical startup of cryogenic loop heat pipes with redundancy design. *Energy Convers. Manage.*, 2016. 118: 353–363.

[10] H. Cho, L. Jin, and S. Jeong, Experimental investigation on performances and characteristics of nitrogen-charged cryogenic loop heat pipe with wick-mounted condenser. *Cryogenics*, 2020. 105:

[11] K. Odagiri, H. Nagano, Investigation on liquid-vapor interface behavior in capillary evaporator for high heat flux loop heat pipe. *Int. J. Therm. Sci.*, 2019. 140: 530–538.

[12] K. Odagiri, M. Nishikawara, H. Nagano, Microscale infrared observation of liquid–vapor interface behavior on the surface of porous media for loop heat pipes. *Appl. Therm. Eng.*, 2017. 126: 1083–1090.

[13] K. Odagiri, H. Nagano, Characteristics of phase-change heat transfer in a capillary evaporator based on microscale infrared/visible observation. *Int. J. Heat Mass Transf.*, 2019. 130: 938–945.

[14] T.T. Hoang, T.A. O'Connell, J. Ku, D. Butler, et al., Design Optimization of a Hydrogen Advanced Loop Heat Pipe for Space-Based IR Sensor and Detector Cryocooling. in SPIE, 2003, 5172.

Two-phase wickless unidirectional flow heat transporting device

Vineed Narayanan^{1*}

¹ Mechanical Engineering Department, Motilal Nehru National Institute of Technology Allahabad, Prayagraj, India
*vineed@mnnit.ac.in, vineednarayanan@gmail.com :

Abstract

A wickless unidirectional heat pipe comprises sets of a plurality of capillary tubes and non capillary tubes, with the evaporator and condenser for heat addition and heat rejection, respectively. The device is filled and sealed with two-phase working fluid for heat transportation. The non capillary tubes transport the hot fluid from the evaporator to the condenser, and capillary tubes transport the cooled fluid from the condenser to the evaporator. The driving force is mainly due to the unbalanced force in the evaporator due to heat addition and the capillary force in the capillary tube. Together with negative acceleration pressure drop in the condenser and capillary action in the capillary tubes, the total pressure drop in the system is very less. Therefore, the device can transport heat to a longer distance even with low temperature difference between the evaporator and the condenser.

The flow through the device is unidirectional at all operating conditions; hence the device can be used to transport heat to a longer distance. Since no wick structure is involved, the fabrication and installation of the device are simple.

Keywords: Heat pipe; Wickless heat pipe; Capillary driven; Two phase; Heat transporting device;

1. Introduction

The first heat transportation device was invented by Gaugler [1]. Its importance grew after the 1960s when it found applications in space equipment. The device uses two phase working fluid for the transportation of the heat energy. It absorbs latent heat in the evaporator, and vapour so formed is moved to the condenser, where it rejects the heat of condensation. The liquid so formed is returned to the condenser through the porous wick structure used in the heat pipe due to its capillary action. The quantity of heat transportation is limited to the amount of liquid which can flow through the capillary wick, known as the capillary limit of the heat pipe [2]. The wick may dry out at a higher load due to the unavailability of the working fluid. Another heat pipe known as a loop heat pipe [3] enables the use of a fine pore capillary wick structure, thereby increasing the capillary pumping power. However, the wick structure used in this case is sintered powdered metallic wick with pores of 1 micron [4]. A heat transporting device without the use of a capillary wick structure was invented by Akachi [5], in which a continuous closed tube is used with a unidirectional flow valve. In his later work, he used a smaller tube of capillary dimension to make it operational without using any valve [6]. In this capillary dimension tube, the fluid oscillates while transporting heat energy and is known as a pulsating heat pipe.

This work is about a heat transporting device that does not involve any wick structure and flow of working fluid is unidirectional. Figure 1 shows the

schematic of the device. It consists of the non capillary tube of a diameter greater than the capillary dimension for transporting the hot fluid from the evaporator to the condenser. As shown in Fig. 1, the plurality of capillary tubes is for transporting the cooled fluid from the condenser to the evaporator. The curved tubes of diameter equal to the non capillary tube is used as the evaporator and the condenser. Adding heat causes some vapour formation, and the two-phase mixture enters into the non capillary tube (hot fluid line) due to lower frictional resistance in the non capillary tube. On losing heat in the condenser, the vapour formed in the evaporator is converted into liquid in the condenser and is transported to the evaporator through the set of the plurality of capillary tubes (cold fluid line).

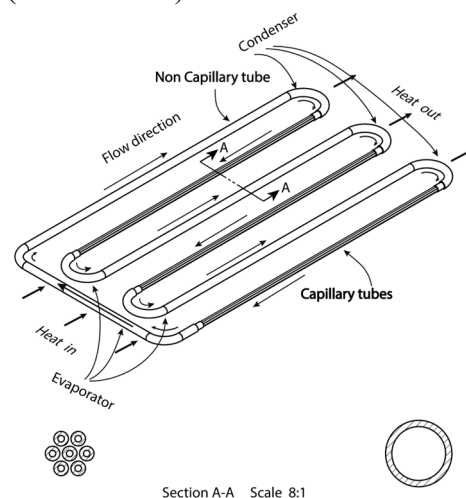


Figure 1. Schematic of the heat pipe used in the current work

For a higher quantity of heat transportation, multiple sets of the plurality of capillary tubes, non capillary tubes, evaporators and condensers are arranged in a serpentine structure, as shown in Fig. 1.

2. Theoretical explanation about the working of the device

To understand the flow of the working fluid in the device, consider an evaporator, as shown in Fig. 1. One end is connected to a plurality of capillary tubes and the other to a noncapillary tube. The flow area for the working fluid through n number of capillary tubes is given by equation (1)

$$A_{capillaries} = n \frac{\pi}{4} d_{i, capillary}^2 \quad (1)$$

And the flow area in the noncapillary tube is given by equation (2)

$$A_{Tube} = \frac{\pi}{4} d_{i, tube}^2 \quad (2)$$

In the evaporator, adding heat increases the working fluid's temperature, and some fraction of the liquid gets converted into vapour. Therefore, the specific volume and pressure increase due to the restriction in expansion or the rigid boundary. Hence, in this process, the pressure and temperature increase. The rise in pressure is the driving potential for the continuous flow in this device.

If the increase in pressure due to heat addition is Δp then forces at the ends of the evaporator are given by

$$\text{At the capillary side} = \Delta p \cdot A_{cap} = \Delta F_{capillary}^h \quad (3)$$

$$\text{At the tube end (non capillary tube)} \\ = \Delta p \cdot A_{Tube} = \Delta F_{Tube}^h \quad (4)$$

$$\text{Since } \Delta F_{Tube}^h > \Delta F_{capillary}^h \quad (5)$$

$$\therefore A_{cap} < A_{Tube} \quad (6)$$

Therefore, fluid is pushed to the tube side, and unidirectional flow is attained.

2.1. The preferred structure of the device

The diameter of the liquid line is preferred to be as minimum as possible to generate the capillary action for pumping the fluid in the device and the unbalanced force generated due to heating and cooling in the evaporator and condenser, respectively. However, if the diameter is too small for the liquid line, the total area for the flow will be very less and the capacity of the device is limited to the area for the liquid to flow. Therefore, in this heat transporting device, it is preferred to use multiple capillary tubes to provide more flow area for the liquid. Using multiple capillary tubes with small diameters increases the flow passage

area for liquid and reduces the liquid hold up in the vapour line. The capillary tubes absorb the liquid in the condenser and transport it to the heat evaporator. Using multiple capillary tubes also makes the system operate like multiple heat transporting devices operating in parallel. Therefore, it can operate over a wide range of operating conditions. At the same time, the flow passage for the hot fluids with higher vapour fraction is preferred to be as maximum as possible for the minimal frictional pressure drop. The vapour line is preferred as a non capillary tube to minimize the surface tension effect on the two phase fluid.

2.2. Theoretical explanation for the working of the device

The processes can be explained in a T-h (Temperature and Enthalpy) plane, similar to the working of a pulsating heat pipe given by Khandeker and Groll [7]. In Fig. 2(a), process 1-2 is a heat addition process. Due to the addition of heat, the vapour is formed; hence specific volume increases. The process is very fast; therefore, the temperature and pressure of the fluid increase. The process is neither a constant pressure process nor a constant volume process. It is a complex process in which pressure, temperature increase, and specific volume increase due to the vapour phase formation.

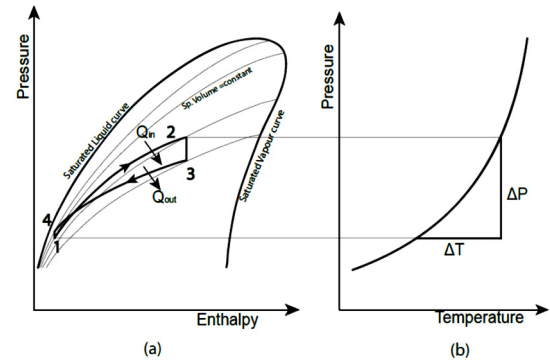


Figure 2 Different processes of the heat transporting device in (a) T-h plane and in (b) PT plane.

Process 2-3 is a flow through the tube after receiving heat in the evaporator, the velocities at the inlet and outlet of the tube are almost equal, and the flow can be assumed as adiabatic. Therefore, from the steady flow energy equation, the process can be considered as isenthalpic. The pressure drop is due to the friction and can be given by the equation (7)

$$\Delta p_f = \frac{4fLG^2}{2\rho D} \quad (7)$$

Where f is the fanning friction factor

G is the mass flux $\frac{\dot{m}}{A}$

\dot{m} is the mass flowrate

A is area for the flow

ρ is the density of the fluid

D is the inner diameter for the flow of fluid

Process 3-4 is the heat rejection process; the process can be assumed as the opposite of heat addition. The vapour condenses, and therefore specific volume decreases. Process 4-5 is a flow through capillary tubes, which also can be considered isenthalpic. The frictional pressure drop for liquid or denser fluid is lesser than for lighter or hot fluid because $\Delta p_f \propto \frac{1}{\rho}$. The acceleration pressure drops in the condenser and evaporator are given by the steady flow energy equation

$$\frac{p_{in}}{\rho_{in}} - \frac{p_{out}}{\rho_{out}} = \dot{Q} + u_{out} - u_{in} + \frac{v_{out}^2}{2} - \frac{v_{in}^2}{2} + g(z_{out} - z_{in}) \quad (8)$$

Where $\dot{Q} + u_{out} - u_{in}$ in the evaporator and in the condenser, the heat interaction and internal energy change cancel each other to a smaller value. However, $\frac{v_{out}^2}{2} - \frac{v_{in}^2}{2}$ is negative, and ρ_{in} is smaller than ρ_{out} for the condenser whereas $\frac{v_{out}^2}{2} - \frac{v_{in}^2}{2}$ is positive, and ρ_{in} is greater than ρ_{out} . Therefore the total pressure drop in the condenser is less than the pressure drop in the evaporator. The driving potential is generated due to the heat addition in the evaporator (See Fig 1).

The pressure developed in the device can be given by equation (9) from the PT curve shown in Fig. 1(b)

$$\left(\frac{\partial p}{\partial T}\right)_{Sat.curve} \cdot \Delta T \quad (9)$$

The pumping pressure induced due to capillary action is given by the Laplace equation as

$$\Delta p_{capillary} = \left(\frac{2\sigma \cos\theta}{r}\right) \quad (10)$$

Where σ is the surface tension

θ is the contact angle

r is the inner radius of the tube

Therefore, the requirement for the device to work is

$$\left(\frac{\partial p}{\partial T}\right)_{Sat.curve} \cdot \Delta T + \Delta p_{capillary} > \Delta p_f^{capillary} + \Delta p_f^{tube} + \Delta p_{gravity}^{tube/capillary} \quad (11)$$

$\left(\frac{\partial p}{\partial T}\right)_{Sat.curve} \cdot \Delta T$ → is the total pressure increase due to temperature difference (see Fig.2 (b))

$\Delta p_f^{capillary}$ is the frictional pressure drop in the capillary tubes or cold fluid line.

Δp_f^{tube} is the frictional pressure drop in the non capillary tubes or hot fluid line.

$\Delta p_{gravity}^{tube/capillary}$ is the head due to the density of the fluid.

3. Performance of the heat transporting device

A specimen was made, as shown in Fig. 3, with copper tubes of an inner diameter of 8 mm and an outer diameter of 9.5 mm for transporting the hot fluid from the evaporator to the condenser. Sets of seven capillary tubes with an inner diameter of 0.79 mm and an outer diameter of 1.79 mm were used as the cold fluid lines for transporting the condensed fluid from the condenser to the evaporator. The evaporator and condenser are tubes of the same diameter as the hot fluid line. Hot and cold baths were used to perform experimental investigation, as shown in Fig. 3. In both hot and cold baths, the water of 10 kg was used. The length of the hot fluid line and cold fluid line (adiabatic section) were fabricated around 30.5 cm. The hot and cold lines were insulated with nitrile rubber to minimize the heat interaction with the surrounding. The hot and cold baths were also insulated to reduce the heat leak to the surrounding. To perform the experiment analysis the hot and cold baths were filled with 10 kg of water in each bath at different temperatures.

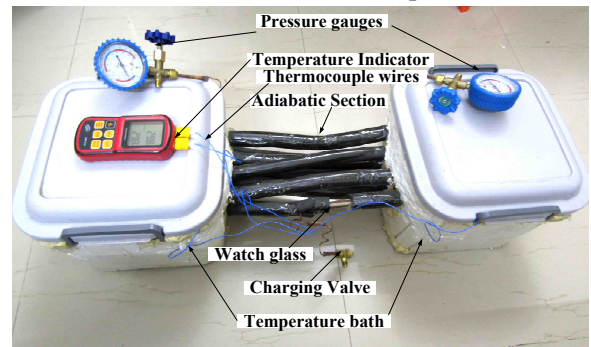


Figure 3. experimental test setup with heat pipe.

4. Results and Discussion

Figure 4 shows the variation of the temperatures of hot and cold bath. The two phase fluid circulation was observed through the sight glass

when there was a sufficient temperature difference between the hot and the cold baths. The circulation was observed till a minimum temperature difference of about 9.6 K between hot and cold baths. The pressure difference between the evaporator and the condenser was observed between 1.6 to 1.3 bar.

From Fig. 4, it can be observed that the temperature of hot fluid drops faster than that of cold fluid. Because due to heat leak from the system. For calculating the heat leak from the system, the hot fluid was filled in the bath, and its temperature drop was tabulated, and its variation is shown in Fig. 5. Knowing the mass of water (10 kg) and assuming the specific heat capacity of water as 4.18 kJ/kg.K. The product of the overall heat transfer coefficient and surface area for the heat interaction (UA) is calculated. The value of UA is obtained as 1.01 W/K. With the UA value, the device's capacity was calculated and found to be around 19.5 W.

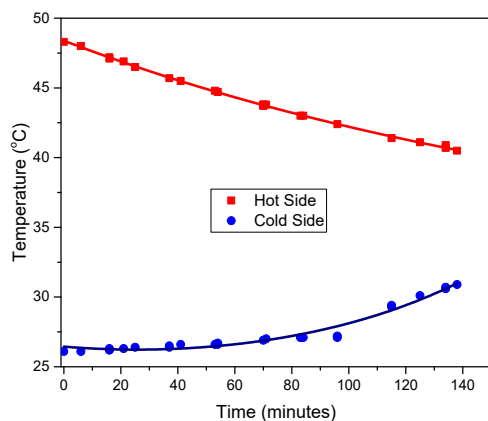


Figure 4. Variation of temperatures of hot and cold baths.

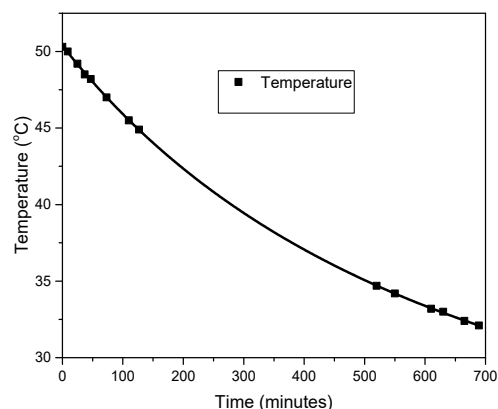


Figure 5. Variation of bath temperature without the action of the heat pipe.

5. Conclusions

A heat pipe with a combination of capillary and non capillary tubes is designed to obtain a

unidirectional flow of working fluid without using any wick structure. A theoretical explanation for the working of the device is attempted. A specimen was fabricated, and experiments were carried out for a heat transportation capacity of 19.5 W. Circulation of the working fluid was observed till the lowest temperature difference of 9.6 K between the hot and the cold baths.

Further studies are required to explain the exact working principles and identify the parameters on which the device's performance depends.

References

- [1] Gaugler RS. Heat transfer device. US 2,350,348, 1944.
- [2] Faghri A, Thomas S. Performance characteristics of a concentric annular heat pipe: Part I-Experimental prediction and analysis of the capillary limit. *Journal of Heat Transfer* 1989;111:844–50. <https://doi.org/10.1115/1.3250795>.
- [3] Dolgirev JE. Heat transfer apparatus. US 4,515,209, 1985.
- [4] Butler D, Ku J, Swanson T. Loop heat pipes and capillary pumped loops-an applications perspective. *AIP Conference Proceedings* 2002;608:49–56. <https://doi.org/10.1063/1.1449707>.
- [5] Akachi. Structure of a heat pipe. US 4,921,041, 1990.
- [6] Akachi. Structure of micro-heat pipe. US 5,319,020, 1993.
- [7] Khandekar S, Groll M. An insight into hermo-hydrodynamic coupling in closed loop pulsating heat pipes 2004;43:13–20. [https://doi.org/10.1016/S1290-0729\(03\)00100-5](https://doi.org/10.1016/S1290-0729(03)00100-5).

Heat Transfer Characteristics for Refrigerant Flow Rate Change in Heat Exchanger using Loop Thermosyphon Technology

Dong-Hyun Cho^{1,*}, Jong-Un Park², Yong-Gyu Chae³, and Soo-Jin Han⁴

^{1,*} Daejin University, Gyeonggi-do, Republic of Korea

² Pukyong National University, Busan, Republic of Korea

^{3,4} Daejin University, Gyeonggi-do, Republic of Korea

*Corresponding author email address: chodh@daejin.ac.kr

Abstract

A heat exchanger using loop thermosyphon technology consists of the evaporators with metal with foams, an insulation unit, and the condensers with internal fins and plate fins. The working fluid inside the evaporator with metal foam is evaporated by the heating of the evaporator in the lower part of the heat exchanger using loop thermosyphon technology and the evaporated steam rises to the condenser with internal fins and plate fins in the upper part to transfer heat in response to the cooling fluid outside the tube. The resultant condensed working fluid flows downward along the inside surface of the tube due to gravity. In the present study, a heat exchanger using loop thermosyphon technology consists of the evaporators which is 480mm wide, 68mm long, and 1,000mm high was used. The heat transfer pipes in the heat exchanger were 15mm in diameter and 1,000mm in length and 98 heat transfer pipes were installed in the heat exchanger. According to the results of the present study, In the evaporating tube with metal foam, the gas begins to be slowly generated from the wall and united on the center and this result was consistent with the gas velocity distribution. As the temperature of the air flowing in the condensers increased, the condensation heat transfer rate of the heat exchanger using loop thermosyphon technology increased. Changes in the temperatures at the outlet of the condensers with insert devices were shown to be a little smaller. Therefore, it can be seen that as the spaces between internal discontinuous pins decreased, the heat transfer performance increased. As the spaces between internal discontinuous pins decreased, the condensers with insert devices pressure drops increased. Strong tendencies for the prediction of the position of gas generation and gas fractions in the evaporating tube appeared according to wall heat flux of the evaporators with metal foam. The oil flows in the vicinity of the evaporating tube with metal foam were considered to be natural convection

Keywords: Loop Thermosyphon; Heat Exchanger, Evaporator, Condenser, Heat Transfer Rater, Heat Transfer Characteristics

1. Introduction

Heat exchanger using loop thermosyphon technology can improve cooling performance because these systems release heat using the latent heat resulting from the boiling and condensation of the working fluid so that high performance systems can be implemented and the prices, sizes, and power consumption of the systems can be reduced^(1,2). As such, cooling systems with high speed rotating shafts using the heat exchanger using loop thermosyphon technology can be made at much lower prices compared to existing cooling systems because they do not required evices such as cooling fluid circulating pumps and chillers. Yosup^(3,4) studied the instability caused by nucleation in static instability in a natural circulation loop installed with two parallel vertical tubes. According to the study results, a new geysering phenomenon occurred as slug bubbles were generated in the channel⁽⁵⁻⁸⁾. Duan et al⁽⁹⁾ constructed an electronic component cooling system using a two-phase loop thermosyphon and conducted experimental and theoretical studies on

refrigerant pressure drops and rises at individual points of the cycle. Song⁽¹⁰⁾ studied the instability caused by nucleation in static instability in a natural circulation loop installed with two parallel vertical tubes. According to the study results, a new geysering phenomenon occurred as slug bubbles were generated in the channel^(11,12). In the present study, experimental studies were conducted on the heat exchanger using loop thermosyphon technology that can discharge the large amounts of heat generated by the high speed rotation of the high speed rotation shafts of high voltage motors, generators, and large lathes, simulations were conducted to evaluate the heat transfer performance, and the results were verified through comparison with experimental results.

2. Experimental facility and method

Figure 1 shows schematic diagram of the experimental facility. The exhaust valves were attached to the condenser so that the working

fluid can be filled and non-condensable gases can be exhausted. As shown in Figure 1, for performance experiments of the 6.5kW grade loop type thermosyphon heat exchanger, the height difference between the evaporator and the condenser was set to 1.75m. The outside diameter of the conveying pipe that connects the evaporator with the condenser is 20mm. To prevent leaks from occurring in the conveying zone that connected the evaporator with the condenser, the conveying zone was checked using high pressure nitrogen and the conveying zone was insulated with 25mm thick glass fibers to reduce heat losses to the outside of pipes occurring when the working fluid flows through the steam and fluid flow pipes. A slidacs was installed to maintain the oil temperature in the oil housing that supplies heat to the evaporator at 20~80°C when the experiment was conducted. The temperatures of the working fluid at the inlet and outlet of the evaporator and the condenser at individual layers were compared.

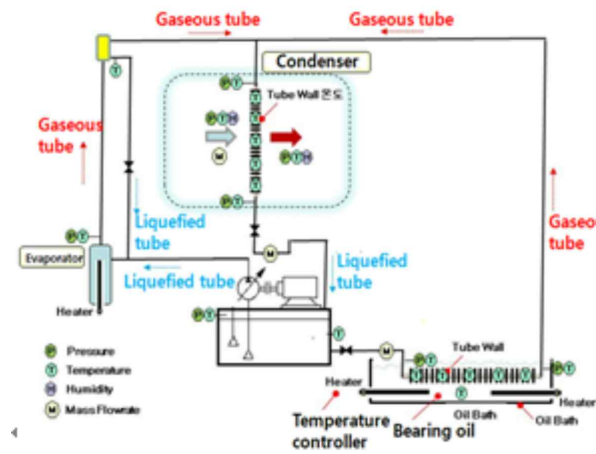


Figure 1. Schematic diagram of heat exchanger using loop thermosyphon technology

Figure 2 shows evaporator with metal foam of loop type two-phase thermosyphon. The evaporator with metal form of the 6.5kW grade loop type thermosyphon heat exchanger made for the present study is 699mm in the outside diameter, 630mm in the inside diameter, and 150mm in the height. In addition, 98 pieces of 12mm diameter copper pipes were installed in the inside of the evaporator with metal form and 100 pieces of 12mm diameter copper pipes were installed on the outside of the evaporator. Furthermore, L type 25mm soft copper pipes were installed on the top and bottom of the evaporator with metal foam

Figure 3 shows evaporating tube with metal foam. The metal foam thickness are 4, 6, 8mm.



Figure 2. Evaporator with metal foam of loop type two-phase thermosyphon

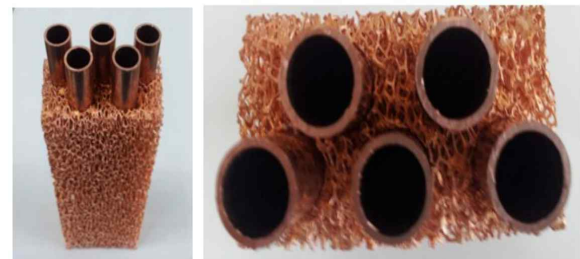


Figure 3. Evaporating tube with metal foam

Figure 4 shows Internal fin types of condenser section. The shape of the condenser heat exchanger plate and the shape of the internal fins inside the condenser are shown. Eighty 12 mm diameter, 1,000mm long copper pipes were installed on the condenser. In addition, exhaust valves were attached to the condenser so that the working fluid can be filled and non-condensable gases can be exhausted

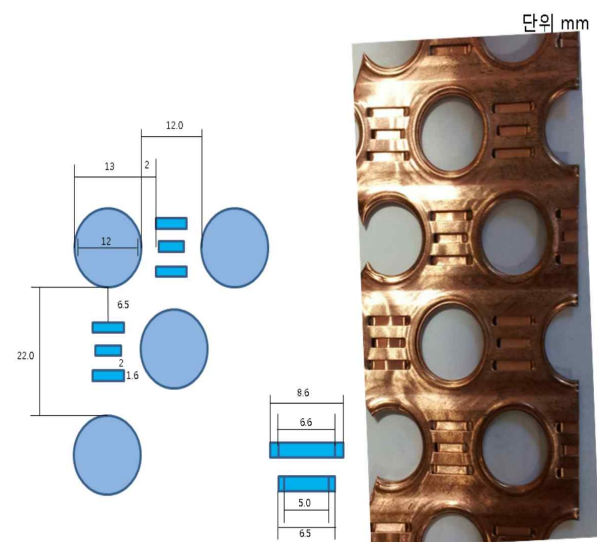


Figure 4. Plate fin of condenser section

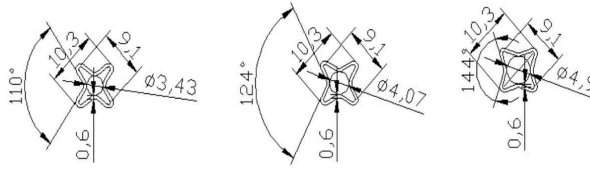


Figure 5. Internal fin types of condenser section

Table 1 shows condenser simulation cases. The simulations were implemented with 0.5mm thick internal pins at angles of 110°, 124°, and 144° under three length conditions; 50mm, 75mm, and 100mm. The condenser is installed with 625 plate pins on its surface. The heat transfer area of one pin is 4.503E-3m² and that of 625 pins is 2.815m². Since the condenser tube area is 0.08m², the entire heat transfer area of the condenser including 625 plate pins is 2.895m².

Table 1 Simulation cases of condenser section

CASE	δ (mm)	Θ (mm)	L(mm)
1	0.5	110	50
2	0.5	110	75
3	0.5	110	100
4	0.5	124	50
5	0.5	124	75
6	0.5	124	100
7	0.5	144	50
8	0.5	144	75
9	0.5	144	100

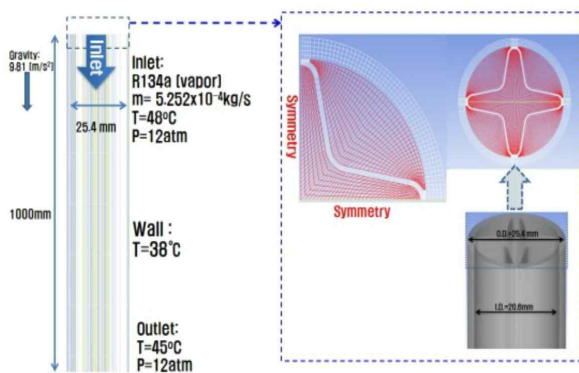


Figure 6. Condenser shape and mesh generation

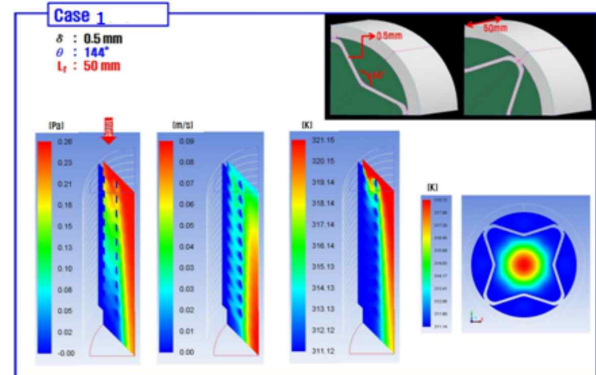
Figure 6 shows the mesh generation of the heat-transfer pipes of the condenser of the loop type two-phase flexible thermosyphon heat exchanger and boundary conditions. ANSYS FLUENT v13.0 was used as a condenser model. Only 1/4 of the circular tube of the condenser was constructed and symmetry conditions were given to the wall to implement heat and flow simulations.

3. Results and discussion

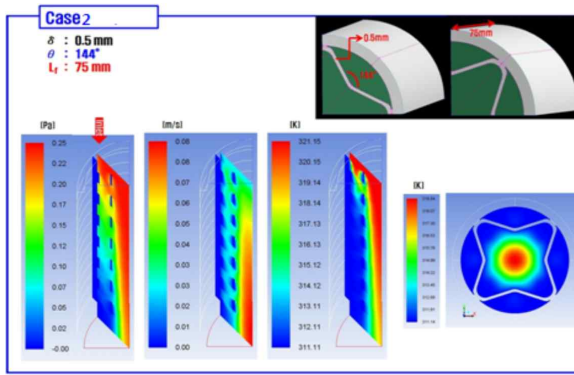
Figure 7 shows the results of simulations in cases 1~3 shown in Table 1. As shown in Figure 7, cases 1~3 show the results of simulations with 0.5mm thick internal pins fixed at an angle of 144° with different spaces between internal discontinuous pins. It can be seen that differences in spaces between internal discontinuous pins have considerable effects on refrigerant flows. As the spaces between internal discontinuous pins decreased, pressure drops increased. Changes in the temperatures at the outlet of the condenser were shown to be a little smaller. Therefore, it can be seen that as the spaces between internal discontinuous pins decreased, the heat transfer performance increased.

Figure 8 shows the results of simulations in cases 4~6 that were implemented with 0.5mm thick internal pins fixed at an angle of 124° with different spaces between internal discontinuous pins.

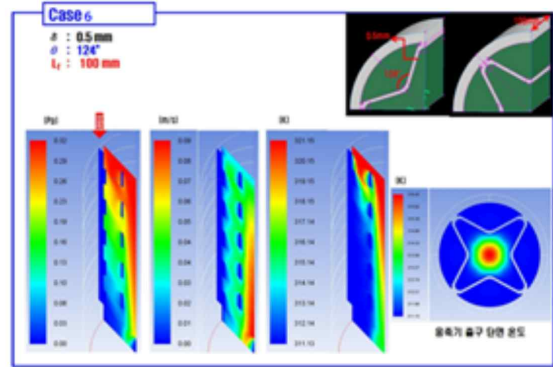
Figure 9 shows the results of simulations in cases 7~9 that were implemented with 0.5mm thick internal pins fixed at an angle of 110° with different spaces between internal discontinuous pins. It can be seen that differences in spaces between internal discontinuous pins have considerable effects on refrigerant flows and that as pin lengths increased, heat transfer performance improved



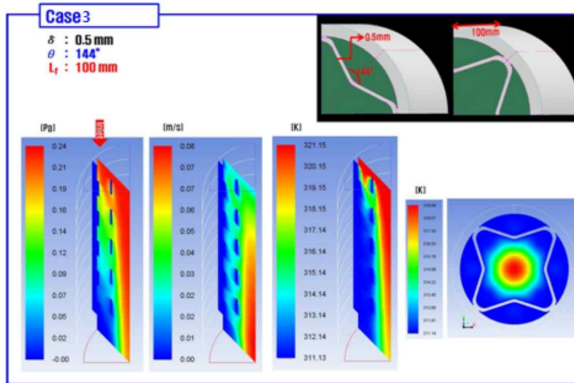
(a) CASE 1



(b) CASE 2

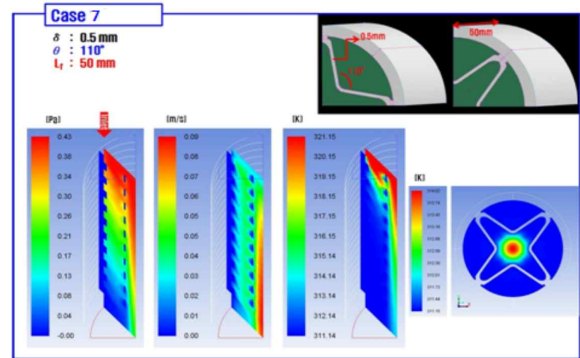


(c) CASE 6



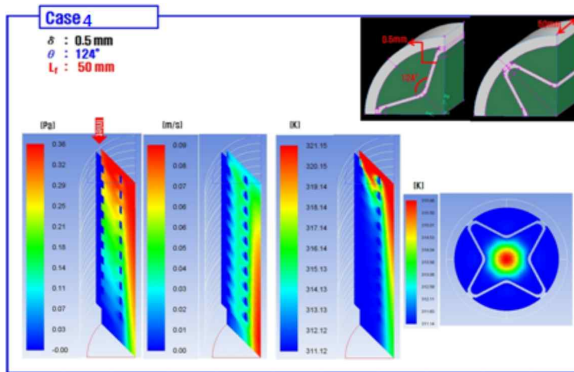
(c) CASE 3

Figure 8. Simulation results of case4~6

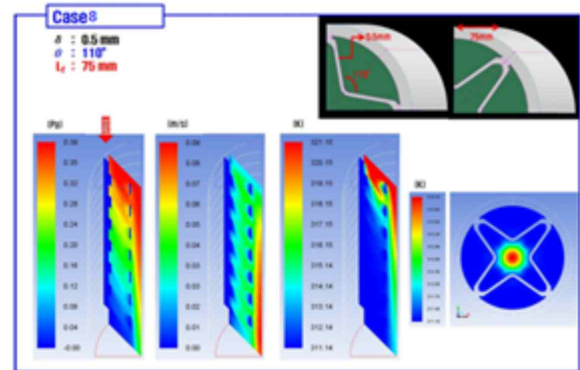


(a) CASE 7

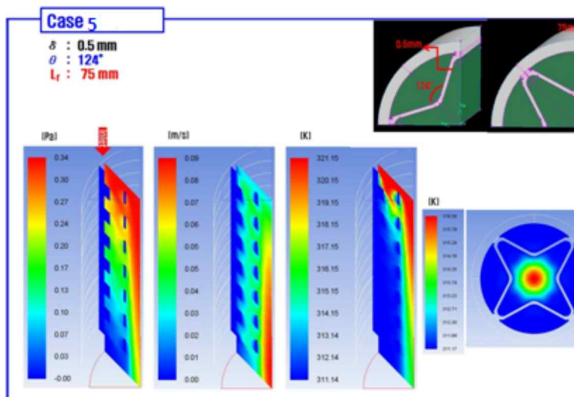
Figure 7. Simulation results of case1~3



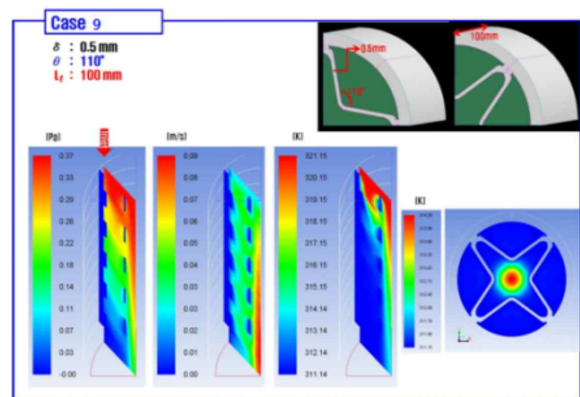
(a) CASE 4



(b) CASE 8



(b) CASE 5



(c) CASE 9

Figure 9. Simulation results of case7~9

Figure 10 and Figure 11 shows analytical model considering evaporator with the metal foam. The thermal resistance measured in parallel by conduction heat transfer and convective heat transfer. Table 1 shows simulation case. Figure 10 and Figure 11 shows the distributions of vapor volume fraction, wall temperatures in the evaporating tube with metal foam. It can be seen that in the evaporating tube with metal foam, the gas begins to be slowly generated from the wall and united on the center and this result was consistent with the gas velocity distribution. In addition, strong tendencies for the prediction of the position of gas generation and gas fractions in evaporating tube with metal foam appeared according to wall heat flux. As porosity had decreased, vapor fraction increased.

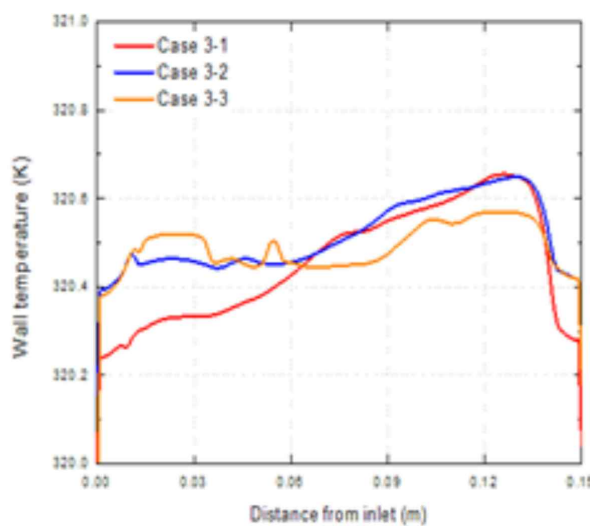


Figure 10. Schematic diagram of heat exchanger using loop thermosyphon technology

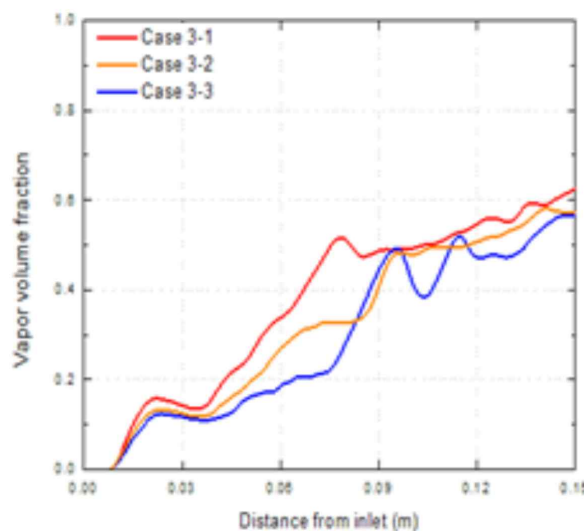


Figure 11. Vapor volume fraction vs. distance from inlet

Figure 12 show the results of condenser temperatures following changes in the temperature of the cooling air flowing in the condenser for heat exchanger using loop thermosyphon technology. The refrigerant used in the experiment is 134a. The experiment was conducted with the quantity of the refrigerant filled in the condenser in a range of 9kg. The air flowing in the condenser was in a range of 0.58kg/s and 1.36kg/s when the experiment was conducted. As the condenser air temperature increased, the condenser refrigerant temperature also increased. Therefore, it can be seen that as the temperature of the air flowing in the condenser increases, the condensation heat transfer rate of the heat exchanger using loop thermosyphon technology increases.

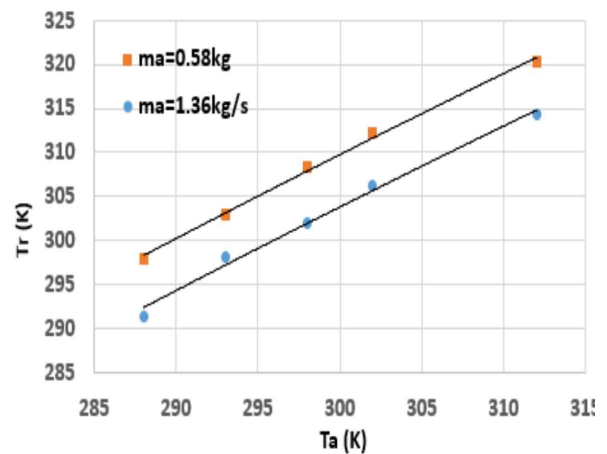


Figure 12. Comparison of refrigerant inlet temperature of Condenser with cooling air temperature of condenser for heat exchanger using loop thermosyphon technology

Fig. 13 shows oil temperature of evaporator with low density and high density metal foam. The refrigerant used in the experiments is 134a. The experiments were conducted at refrigerant charge rates of 6~9kg and the air flow rates in the condenser in a range of 0.58~1.36kg/s. As the oil temperature in the evaporator with metal foam increased, heat flux of evaporator increased. The heat transfer of high density metal foam was higher than that of low density metal foam. Figure 14 shows temperature difference of ambient temperature and oil temperature according to ambient temperature changes. The refrigerant used in the experiments is 134a. Heat transfer performance in accordance with the increased oil temperature increases.

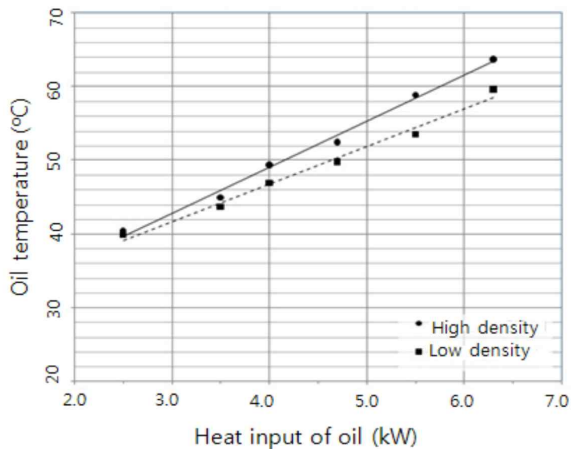


Figure 13. Oil temperature of evaporator with low density and high density metal foam according to heat input of oil

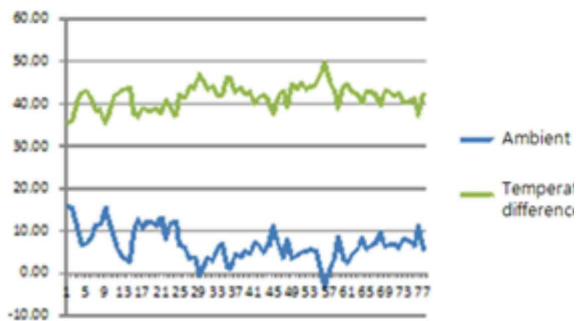


Figure 14. Temperature difference of ambient temperature and oil temperature according to ambient temperature changes

4. Conclusions

The results of a study on the temperature change of cooling air in a heat exchanger using loop thermosyphon technology for heat dissipation of high-speed rotating shafts were summarized as follows

In the evaporating tube with metal foam, the gas begins to be slowly generated from the wall and united on the center and this result was consistent with the gas velocity distribution.

As the temperature of the air flowing in the condensers increased, the condensation heat transfer rate of the heat exchanger using loop thermosyphon technology increased.

Strong tendencies for the prediction of the position of gas generation and gas fractions in the evaporating tube appeared according to wall heat flux of the evaporators with metal foam.

The oil flows in the vicinity of the evaporating tube with metal foam were considered to be natural convection

As the oil temperature in the evaporator with metal foam increased, the boiling steam

generation rate of the loop thermosyphon heat exchanger increased

References

- [1] H. Li, Y. Tang, W. Yuan, R. Zhou, "Numerical analysis on heat transfer of a complete anti-gravity loopshaped heat pipe," *International Journal of Heat and Mass Transfer*, 22017, 109:, p. 824-834.
- [2] J. W. Ye, G. H. Kim and J. S. Lee, Waste heat energy generation system applied by oscillating heat pipe with volumetric effect streaming electrification phenomenon,. 2022 Spring Conference in Thermal Engineering of The Korean Society of Mechanical Engineers, 2022. : p. 247.
- [3] Yosup Seo , In Cheol Bang, JaeYoung Lee, Thermal Hydraulic Characteristics of a Long Heat Pipe and Thermosyphon, *Trans. Korean Soc. Mech. Eng. B*, 2014, p. 1990~1995.
- [4] H. Li, Y. Tang, W. Yuan, R. Zhou, "Numerical analysis on heat transfer of a complete anti-gravity loopshaped heat pipe," *International Journal of Heat and Mass Transfer*, 22017, 109:, p. 824-834.
- [5] M. Nishikawara, H. Nagano, "Optimization of wick shape in a loop heat pipe for high heat transfer," *International Journal of Heat and Mass Transfer*, 2017, 104: p. 1083-1089.
- [6] S. Th. Smith, V. I. Handby and C. Harpham, "A Probabilistic Analysis of the Future Potential of Evaporative Cooling Systems in a Temperate Climate" *Energy Buildings*, 2011, 43 No. 2-3: p. 507-51.
- [7] Ali,999Novel Air Conditioning System Using a Liquid Desiccant, *Applied Thermal Engineering*, 2015, 13:, p. 1213-11223.
- [8] W. Li and S. Wang,"A Multi-Agent based Distributed Approach for Optimal Control of Multi-Zone Ventilation Systems Considering Indoor Air Quality and Energy Use", *Applied Energy*, 2020, 275: p. 115371.
- [9] Duan et al., "Calculation of specific surface area of foam metals using dodecahedron model," *Materials Science and Technology* 2006, 22(11); p.1364-1367.
- [10] J. G. Song., J. H. Lee., I. S. Park., "Enhancement of cooling performance of naval combat management system using heat pipe", *Applid Thermal Engineering* 2021, p.188.
- [11] S. S. Lee, Comparative Analysis of Cooling Performance Through The Implementation Of Heat Pipe Thermal Analysis Mode, *The Korean Society of Mechanical Engineers Annual Meeting*, 2022, p. 1293-1294.
- [12] Yang et al., "Pool boiling heat transfer on copper foam covers with water as working fluid," *International Journal of Thermal Sciences*, 2010, 49(7) p.1227-1237.

Experimental investigation on the thermal performance of a modified geometry thermosyphon heat pipe with surface modification

Sakthi Priya M¹, Sakthivadivel D^{1*}

¹School of Mechanical Engineering, Vellore Institute of Technology, Vellore 632014, Tamil Nadu, India

** Corresponding Author: D. Sakthivadivel (sakthi2energy@gmail.com)*

Abstract

The enhancement of the thermal performance of a thermosyphon heat pipe (THP) has been studied by making an internal surface roughness through a sandblasting (SB) technique. Experiments were conducted at three different geometries of THPs such as uniform geometry plain (UG-Plain), uniform geometry SB (UG-SB), and modified geometry SB (MG-SB), by varying a heat input range of (30-300 W) and the filling ratio of 30% with De-ionized (DI) water as the working fluid. Results showed that the internal wall roughness through sandblasting technique in MG-SB and UG-SB THPs can reduce the evaporator temperature due to the hydrophilic characteristics, resulting in a total thermal resistance reduction of up to 71.39% and 48.27% than UG-plain respectively. Additionally, for the same THPs, the heat transfer coefficient increases at the evaporator while the thermal resistance decreases by around 195.18% and 181.78%, respectively. On the other hand, the condenser thermal performance increases using the surface as hydrophobic characteristics which increase the thermal performance more than the UG-plain.

Keywords: Hydrophilic; Hydrophobic; Sandblasting; Thermosyphon; Wettability.

1. Introduction

In recent years, researchers have been focused on reducing losses and enhancing heat transfer in energy systems in order to address the growing global energy demand resulting from inefficient energy use and conversion in various applications. There are various heat transfer systems with minimal losses and are, therefore, increasingly being used to improve the efficiency of energy systems [1]. One of the promising techniques being practiced in the heat transfer process is heat pipes due to the low thermal resistance (R_{th}), compactness, and minimal usage of the working fluid. Such heat pipes can be categorized into two types namely wick and wickless (thermosyphon) heat pipes [2]. The principle behind them being the same for the vapour travels from evaporator to condenser, the difference between them lies in the fact that, in a wickless heat pipe, vapour condenses and returns to the evaporator due to gravity, whereas in a wick heat pipe, it is due to capillary force. In this study, special attention has been made to thermosyphon heat pipe (THP) due to its ease of use, construction, good thermal performance, and affordability [2,3]. Also, they are widely employed in many technological domains such as solar thermal systems, aerospace, heat exchangers, thermal management in batteries, and electronics cooling. The performance of the

THP system is affected by different factors, such as the inclination angle, filling ratio, the geometrical shape of the heat pipe, dimensions of the THP, working fluid, etc., [4] and it is, therefore, essential to improve its thermal performance to increase the heat transfer, as well as the demand for smaller systems and lower manufacturing costs. Hence, the researchers aim to increase the thermal performance of THP by employing various methods such as placing the wick, surface modification, changing the working fluid, the addition of metal powder in the evaporator section, etc. Among these, surface modification on the inner side of the THP is a successful method to enhance thermal performance.

Some of the researchers Rahimi et al. [5], modified the wettability characteristics of the surfaces, achieving an average thermal performance of 15.3% higher than the non-coated Two-Phase Closed Thermosyphon (TPCT) and its R_{th} decreased by 2.35 times when compared to the conventional TPCT. A similar study was conducted by Zhao et al. [6] on modifying the inner surface of the heat pipe. It is evident that the highest thermal performance was attained while the evaporator surface was hydrophilic by chemical etching treatment and the condenser surface was hydrophobic by dip, droplet, and spray coatings. Similarly, roughening the inner surface of the evaporator section through the use of an Electrostatic Discharge Machine by

Alammar et al. [7] resulted in a 115% decrease in R_{th} and a 68% increase in the heat transfer coefficient (HTC) when the initial pressure was varied from 3 to 30 kPa. Solomon et al. [8] evaluated the thermal performance of anodized and non-anodized THP, they found that the nucleation sites were 2-3 times more numerous in the anodized THP, which improved the heat transfer coefficient HTC of the system. To boost thermal efficiency, Tong et al. [9] made a hydrophobic inner surface of the condenser using Teflon amorphous fluoroplastics by spin coating. When the hydrophobic coating was paired with high acceleration vibration, which resulted in lower R_{th} by up to 21.9%. El-Genk and Ali [10] studied the influence of the microporous surface and its layer thickness on nucleate boiling. This resulted in the enhancement of critical heat flux which is 17 times more than the plain surface. Recent literature stated that the Copper Oxide nanostructured surfaces were coated with HTMS and PTFE to create superhydrophobic surfaces on the condenser. It has been found that the condenser HTC is greater than 380% and 30% more efficient than those of film-wise and dropwise condensation, respectively by Seo et al. [11]. A similar study was conducted by Praveen et al. [12] for silane coating in flat thermosyphon. Compared to the bare heat pipe, a 43.74% reduction in R_{th} was noted in the proposed system when the superhydrophobic condenser was used. This was due to the promotion of dropwise condensation and faster condensate return, as provided by the superhydrophobic condenser.

From the literature findings, it is observed that existing techniques for improving thermal performance rely on surface modification to alter the wettability characteristics of the modified surfaces rather than the adoption of grooves, wick materials, changing the working fluid, etc. This study has demonstrated that the surface modification achieved through sandblasting technique is effective and implemented in the evaporator and the condenser surface is maintained as UG-plain THP. The purpose of this experiment is threefold. Firstly, it seeks to analyze the thermal performance of a conventional design. Secondly, it aims to make the surface of both the conventional and modified THP designs hydrophilic at the evaporator and hydrophobic at the condenser section. Finally, it intends to compare the thermal performance of both THP designs.

2. Design and Fabrication

In this section, the fabricated design of a plain and modified geometry THP is presented. Figure 1 comprises an evaporator, adiabatic, and condenser section having a length of 100 mm, 200 mm and 100 mm respectively with a total length of 400 mm, made up of copper material. Figures 1 (a & b) have a uniform geometry throughout the length, with the only difference being the SB surface provided at the inner side of the evaporator in Figure 1 (b). In Figure (c), modifications are made on both the evaporator and the adiabatic section whose lengths are 100 mm and 190 mm respectively; a variation in diameter at the evaporator section and also a 10 mm long convergent truncated cone (CTC) is connected between the evaporator and the adiabatic section. In addition, SB surfaces are provided at the inner wall of the modified geometry THP as shown in Figure 1 (c).

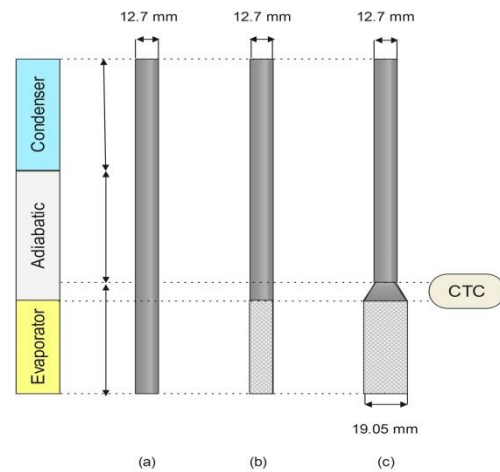


Figure 1. Schematic diagram of THP (a) UG THP, (b) UG-SB THP, (c) MG-SB THP

3. Surface Modification Procedure

To create the desired surface roughness of the inner side of the THP, a sandblasting technique was deliberated. Under 6 bar pressure and 250-300 CFM of sand passing through, five samples were taken as a reference. The first sample was given one pass of sand, the second two passes, the third three passes, and the fourth four passes, with a plain sample being used for comparison, as seen in Figure 2.

The surface roughness of the sample was measured using a MAHR surface rough tester to evaluate two parameters: R_a and R_z . R_a is the average distance between peak and valley points

and the deviation from the mean line over the entire surface and along its length. Other hand, R_z is calculated by measuring the vertical distance between the highest peak and the deepest valley within a given sampling length and then taking the average across five such sampling lengths.



Figure 2. Testing of Different samples S1, S2, S3, S4 and Plain surfaces

To determine the surface roughness, five distinct locations on the sample surface were tested, and the contact angle was also measured and recorded as shown in Table 1. After the inner surfaces of the samples were roughened, they were rigorously scoured with ethanol to remove any grease or other contaminants, followed by a thorough wash with DI water. To measure the wettability of these samples, a Kruss- drop shape analyzer was employed to ascertain their contact angle via the sessile drop technique. Also, Table 1 exhibits the contact angles (CA) measured for both the rough and plain surfaces, while two zoomed images of the above-said surfaces are displayed in Figure 3.

Table 1. Values of R_a , R_z , and contact angle

Item	R_a (μm)	R_z (μm)	CA ($^\circ$)
Plain	0.4028	3.725	116.99
Sample 1	2.944	19.455	81.93
Sample 2	3.045	19.24	70.72
Sample 3	3.17	19.32	66.79
Sample 4	5.25	29.82	89.69

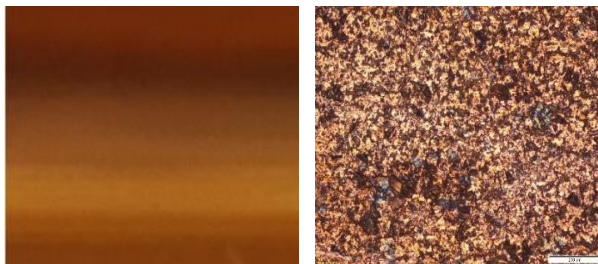


Figure 3. Microstructure images (a) Plain surface, (b) Sandblasted surface

4. Procedure for Testing

The experimental setup of the THP is illustrated in Figure 4 and tested according to the standard procedure. It consists of a Variable Transformer (VARIAC), Thermocouples, Flowmeter, Chilling unit, Data Acquisition system, and PC. To apply the heat flux, the input power (30-300 W) was regulated using the VARIAC. During experiments, T-type thermocouples with accuracy $\pm 0.2^\circ\text{C}$ were attached to twelve positions on the surface of the THPs; four in the evaporator section, four in the adiabatic section, and the remaining four in the condenser section. These thermocouples were used to measure the wall temperature, as indicated by the red line in Figure 4. Once the THP reached a steady state, cooling water was injected out of the storage tank and circulated over the condenser section (test section) through the flow meter. The mass flow rate of the cooling water was adjusted and measured with a flow meter by adjusting the valve. All thermocouples were attached to a Data Acquisition System (Agilent-34972A), which was used to detect and record data on the computer [8].

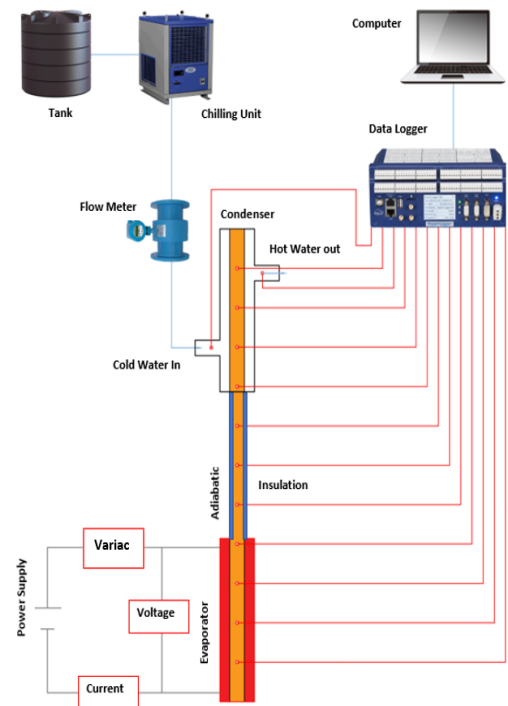


Figure 4. Schematic and Flow Diagram of Experimental setup

5. Performance Evaluation

The performance of the THP can be evaluated by calculating the heat transfer by the THP system, the thermal resistances of the evaporator (R_{evap}), the heat transfer coefficients of both the evaporator (h_{evap}) and condenser (h_{cond}), and condenser (R_{cond}), and the total thermal resistance (R_{total}) of the THP. Heat transfer is expressed using the heat balance equation (1).

$$\dot{Q}_{total} = \dot{m}C_p(T_{out} - T_{in}) \quad (1)$$

The evaporator section and the condenser section thermal resistances are computed using Equations (2) and (3).

$$R_{evap} = \frac{\Delta T_{evap}}{Q_{in}} \quad (2)$$

$$R_{cond} = \frac{\Delta T_{cond}}{Q_{out}} \quad (3)$$

where, $\Delta T_{evap} = T_{evap}^* - T_{vap}^*$ and $\Delta T_{cond} = T_{vap}^* - T_{cond}^*$

Then, the total thermal resistance of the THP system is evaluated using Equation (4) as

$$R_{total} = \frac{\Delta T}{Q_{out}} \quad (4)$$

where $\Delta T = T_{evap}^* - T_{cond}^*$

Equations (5) and (6) are used to compute the heat transfer coefficients for the evaporator and condenser, respectively.

$$h_{evap} = \frac{q_{evap}}{T_{evop,in} - T_{sat}} \quad (5)$$

where, $q_{evap} = \frac{Q_{out}}{\pi d l_{evap}}$

$$h_{cond} = \frac{q_{cond}}{T_{sat} - T_{cond,in}} \quad (6)$$

where, $q_{cond} = \frac{Q_{out}}{\pi d l_{cond}}$

The evaporator and the condenser inner wall temperature is determined by the following Equation (7) and (8) as

$$T_{evap,in} = T_{evop}^* + \frac{qr_{out}}{k} \ln \left[\frac{r_{in}}{r_{out}} \right] \quad (7)$$

$$T_{cond,in} = T_{cond}^* + \frac{qr_{out}}{k} \ln \left[\frac{r_{out}}{r_{in}} \right] \quad (8)$$

6. Results and Discussion

This section deals with the thermal performance of the different THPs. Here, 90° inclination is taken for the discussion throughout the study.

6.1 Temperature Distribution

An inner wall surface roughness of two different geometries THPs were made using the sandblasting technique and was tested and compared to the UG-plain THP to examine the effect of increased heat transfer at varying heat loads. Figure 5 shows the variation of the wall temperature of UG-plain, UG-SB, and MG-SB THPs with varying heat loads. It is observed that a significant reduction in the wall temperature of the MG-SB THP compared with the other two THPs. This is due to the SB surface of the THP wall increasing the nucleation site density, which leads to an increased frequency of bubble generation that effectively removes heat from the THP wall, considerably lowering the wall temperature (Solomon et al.[8] and Alammam et al. [7]). Also, the surface modification made on the inner wall which makes a contact angle of 66.79° i.e., hydrophilic characteristics as per the literature stated [7] causes the surface to be wetted with liquid instead of vapour, resulting in a decrease in the evaporator wall temperature. The SB surface combined with the CTC attached between the evaporator and the condenser of MG-SB helps to rapidly increase the vapor velocity and rewet the evaporator wall.

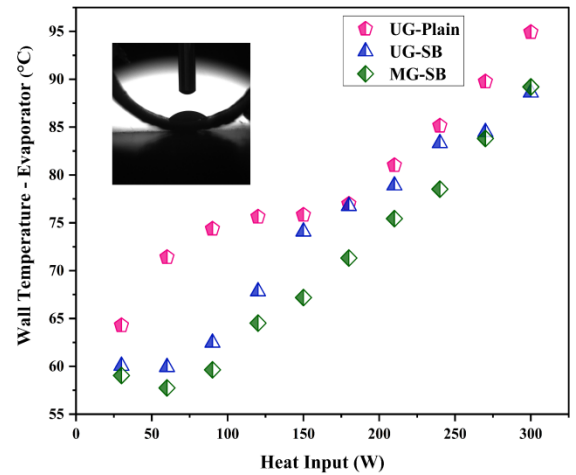


Figure 5. Comparison of evaporator wall temperature between UG-Plain, UG-SB, and MG-SB

However, in the case of the condenser section, the plain surface has been chosen since the sandblasting is not favorable as it makes a contact angle below 90° i.e., hydrophilic characteristics as shown in Table 1. It offers a higher wall temperature of MG-SB than the other two THPs as shown in Figure 5.

The wetting capability of the plain surface has a positive effect on the heat transfer in the condenser. As a result, the formation of liquid film on the condenser surface is decreasing, which helps in reducing the heat transfer resistance, hence it offers a higher wall temperature at the condenser.

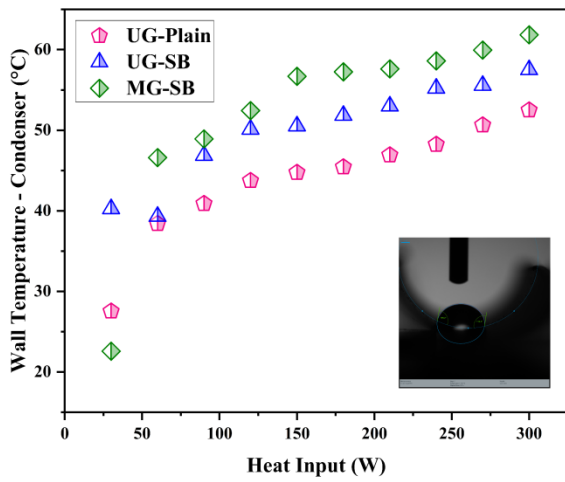


Figure 6. Comparison of condenser wall temperature between UG-Plain, UG-SB, and MG-SB

Figure 6 shows the condenser temperature of all three THPs. Even though all three do not have SB surfaces at the condenser section but it favors MG-SB due to the CTC present in it [13] which helps the vapor to reach the condenser section quickly available for condensation.

6.2 Thermal performance of the THPs

The thermal performance of the THP involves the variation of R_{th} and the HTC. Figure 7 illustrates the variation of total R_{th} over the length of the THPs with varying heat loads. It is seen that a significant decrease in R_{th} for the SB surfaces THPs when compared with the UG-plain THP.

The presence of SB surface on the evaporator wall may reduce the R_{th} due to the increased nucleation sites, which results in the evaporator's

inner surface releasing more heat. Additionally, the SB surface reduces the contact angle, promoting better wettability of the liquid which keeps it in continuous contact with the evaporator wall and removes the vapor away from the wall surface [7]. The average reduction of R_{th} observed in UG-SB THP was 7.05%, which is greater than the reduction seen in UG-Plain THP. Similarly, the CTC effect was also seen between the UG-SB THP and the MG-SB THP, with an average reduction of R_{th} of 22.4%. However, the UG-Plain provides higher R_{th} and it is worsening the heat transfer than the other two THPs. This may be explained by the fact that the plain surface has low surface wettability [8]. Therefore, the formation of liquid film on the inner side of the THP wall. This will prevent the vapour does not directly contact with the inner wall which results in increasing the R_{th} .

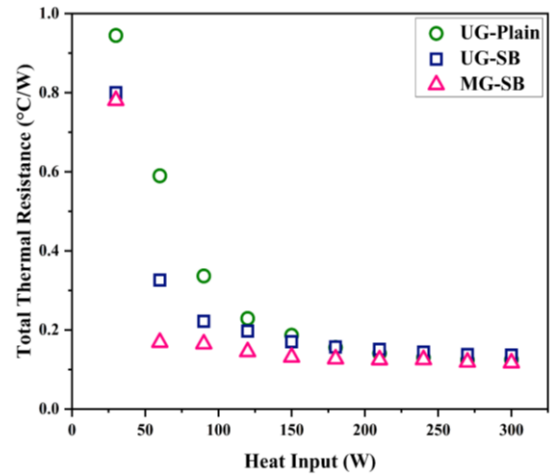


Figure 7. Total thermal resistance between UG-Plain, UG-SB, and MG-SB

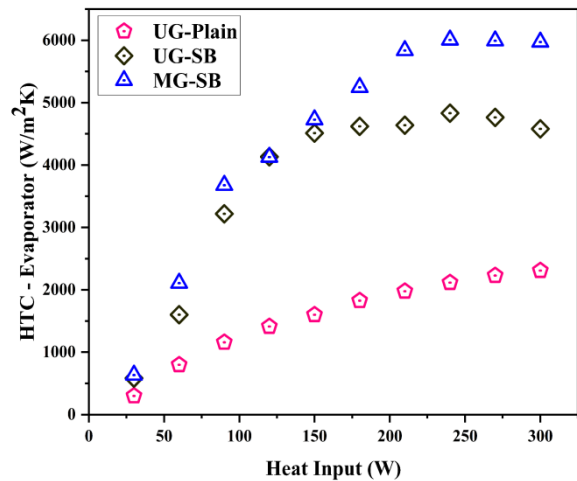


Figure 8. Evaporator HTC between UG-Plain, UG-SB, and MG-SB

Figures 8 and 9, demonstrate a considerable improvement in the HTC of both the evaporator and condenser when THPs are used with SB surfaces. It is shown that the UG-SB has achieved an average HTC of 142.39%, which is higher than that of the UG-plain THP. Concurrently, the MG-SB has attained an HTC that is 18.92% higher than that of the UG-plain THP for the same heat loads.

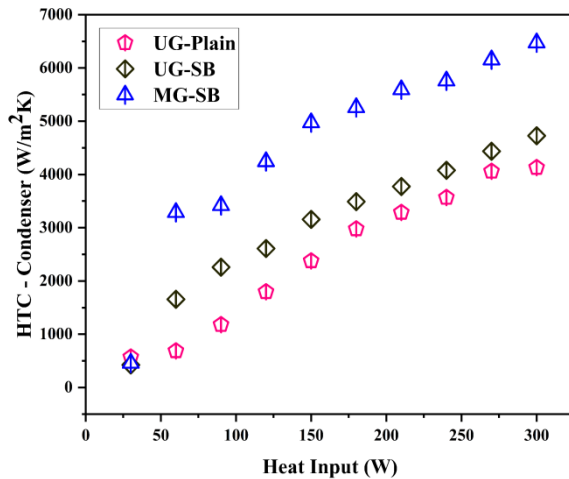


Figure 9. Condenser HTC between UG-Plain, UG-SB, and MG-SB

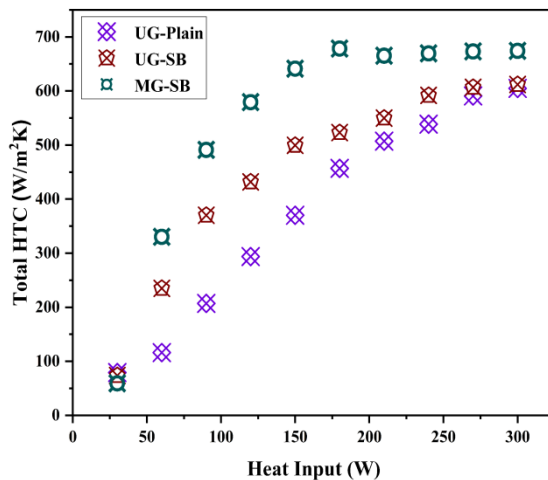


Figure 10. Overall HTC between UG-Plain, UG-SB, and MG-SB

The rate of heat transfer increases as the amount of heat being transferred increases, as demonstrated in Figures 8, 9, and 10. However, the total HTC also achieved for SB surfaces is higher than that of UG plain surfaces. It is observed that the UG-SB has an average HTC of 24.67% more than the UG plain THP. At the same time, MG-SB obtained an average HTC of

22.42% higher than the UG-SB. Thus, the wettability characteristics of the hydrophilic surface of the evaporator section and the hydrophobic surface of the condenser significantly enhance the heat transfer mechanism.

7. Conclusion

Experiments were conducted on three different THPs with different wettability characteristics on the same THP. The thermal performance of the SB surfaces of the THPs can be greatly enhanced by modifying the wettability characteristics of the evaporator and the condenser. It can be concluded that the maximum thermal resistance reduction of MG-SB has 48.27% lower than the UG-SB at the lower inputs of 30-150 W. At the same time for the higher inputs 180-300 W, the same THP performs better reduction in R_{th} which is 19.18% than the UG-SB due to the SB surface in addition to the CTC effect. Thereby enhancing the total HTC of 102.43% higher when compared to the MG-SB with the UG-SB as well as further the total HTC has been observed 28.29% higher when compared to the UG-SB with the UG-plain. The thermal performance of a THP with a roughness created at the inner surface of the evaporator using a sandblasting technique and plain surface at the condenser was evaluated to assess the improvement of its heat transfer properties. The experimental results have been encouraging, motivating further research into THPs with super hydrophilic evaporators and superhydrophobic condensers to further improve the thermal performance. Additionally, research into thermosyphons with superhydrophobic evaporators should focus on various patterns and optimum ratios involving the different passes of sand through sandblasting techniques for further improvement.

Declaration

Ethical Approval:

Not applicable

Competing interest:

Not applicable

Credit authorship contribution statement

Sakthi Priya M: Conceptualization, Methodology, Validation, Formal analysis, Investigation, Writing- original draft;
Sakthivadivel Duraisamy: Conceptualization, Supervision, Project administration, Review & editing.

Acknowledgment

The authors wish to express their sincerest thanks to the School of Mechanical Engineering (SMEC) at the Vellore Institute of Technology, Vellore, India for providing the necessary funds for the Manpower of a Teaching and Research Fellow to conduct this research. The authors express their gratitude to Karunya Institute of Technology, Coimbatore, India for providing assistance with this research.

Availability of data and materials:

Not applicable

Nomenclature

Abbreviations

HTC	Heat Transfer Coefficient
MG	Modified Geometry
SB	Sandblasting
THP	Thermosyphon Heat Pipe
UG	Uniform Geometry
DI	De-ionized
CTC	Convergent Truncated Cone
TPCT	Two-Phase Closed Thermosyphon
W	Watts
CA	Contact Angles
mm	millimetre
m	metre
kW	kilowatt

Symbols and Notations

T_{cond}^*	the average temperature of the condenser ($^{\circ}\text{C}$)
T_{evop}^*	the average temperature of the evaporator ($^{\circ}\text{C}$)
T_{vap}^*	the average temperature of vapour ($^{\circ}\text{C}$)
$T_{cond,in}$	the inside temperature of the condenser ($^{\circ}\text{C}$)
$^{\circ}\text{C}$	degree Celsius
$T_{evop,in}$	the inside temperature of the evaporator ($^{\circ}\text{C}$)

q	heat flux (W/m^2)
Q_{in}	heat input (W)
Q_{out}	heat output (W)
h	heat transfer coefficient ($\text{W}/\text{m}^2\text{K}$)
$^{\circ}$	The angle of inclination (degree)
d	THPs inner diameter (mm)
r_{in}	THPs inside radius (mm)
\dot{m}	mass flow rate (kg/s)
r_{out}	THPs outside radius (mm)
%	percentage
T_{sat}	saturation temperature ($^{\circ}\text{C}$)
c_p	Specific heat capacity (kJ/kgK)
ΔT	Difference in temperature ($^{\circ}\text{C}$)
k	thermal conductivity (W/mK)
R_{evop}	the thermal resistance of the evaporator ($^{\circ}\text{C}/\text{W}$)
R_{cond}	the thermal resistance of the condenser ($^{\circ}\text{C}/\text{W}$)
R_{th}	thermal resistance ($^{\circ}\text{C}/\text{W}$)

Subscripts

atm	atmosphere
evap	evaporator
cond	condenser
in	input
out	output
sat	saturation
th	thermal
vap	vapour

References

- [1] H. Jouhara, A. Chauhan, T. Nannou, S. Almahmoud, B. Delpech, and L. C. Wrobel, "Heat pipe based systems - Advances and applications," *Energy*, vol. 128. Elsevier Ltd, pp. 729–754, 2017. doi:10.1016/j.energy.2017.04.028.
- [2] A. Franco and S. Filippeschi, "Experimental analysis of Closed Loop Two Phase Thermosyphon (CLTPT) for energy systems," *Exp Therm Fluid Sci*, vol. 51, pp. 302–311, Nov. 2013, doi:10.1016/j.expthermflusci.2013.08.013.
- [3] Y. Liu, Z. Li, Y. Li, S. Kim, and Y. Jiang, "Experimental investigation of geyser boiling in a two-phase closed loop thermosyphon with high filling ratios," *Int J Heat Mass Transf*, vol. 127, pp. 857–869, Dec. 2018, doi: 10.1016/j.ijheatmasstransfer.2018.07.018.
- [4] A. Faghri, "Review and advances in heat pipe science and technology," *Journal of Heat Transfer*, vol. 134, no. 12. 2012. doi: 10.1115/1.4007407.

- [5] M. Rahimi, K. Asgary, and S. Jesri, "Thermal characteristics of a resurfaced condenser and evaporator closed two-phase thermosyphon," *International Communications in Heat and Mass Transfer*, vol. 37, no. 6, pp. 703–710, Jul. 2010, doi: 10.1016/j.icheatmasstransfer.2010.02.006.
- [6] Z. Zhao, P. Jiang, Y. Zhou, Y. Zhang, and Y. Zhang, "Heat transfer characteristics of two-phase closed thermosyphons modified with inner surfaces of various wettabilities," *International Communications in Heat and Mass Transfer*, vol. 103, pp. 100–109, Apr. 2019, doi: 10.1016/j.icheatmasstransfer.2019.03.006.
- [7] A. A. Alammar, F. N. Al-Mousawi, R. K. Al-Dadah, S. M. Mahmoud, and R. Hood, "Enhancing thermal performance of a two-phase closed thermosyphon with an internal surface roughness," *J Clean Prod*, vol. 185, pp. 128–136, Jun. 2018, doi: 10.1016/j.jclepro.2018.03.020.
- [8] A. Brusly Solomon, A. Mathew, K. Ramachandran, B. C. Pillai, and V. K. Karthikeyan, "Thermal performance of anodized two phase closed thermosyphon (TPCT)," *Exp Therm Fluid Sci*, vol. 48, pp. 49–57, Jul. 2013, doi: 10.1016/j.expthermflusci.2013.02.007.
- [9] W. L. Tong, M. K. Tan, J. K. Chin, K. S. Ong, and Y. M. Hung, "Coupled effects of hydrophobic layer and vibration on thermal efficiency of two-phase closed thermosyphons," *RSC Adv*, vol. 5, no. 14, pp. 10332–10340, 2015, doi: 10.1039/c4ra14589e.
- [10] M. S. El-Genk and A. F. Ali, "Enhanced nucleate boiling on copper micro-porous surfaces," *International Journal of Multiphase Flow*, vol. 36, no. 10, pp. 780–792, 2010, doi: 10.1016/j.ijmultiphaseflow.2010.06.003.
- [11] D. Seo *et al.*, "Effects and limitations of superhydrophobic surfaces on the heat transfer performance of a two-phase closed thermosyphon," *Int J Heat Mass Transf*, vol. 176, Sep. 2021, doi: 10.1016/j.ijheatmasstransfer.2021.121446.
- [12] P. Dhanalakota, S. Abraham, P. S. Mahapatra, B. Sannakia, and A. Pattamatta, "Thermal performance of a two-phase flat thermosyphon with surface wettability modifications," *Appl Therm Eng*, vol. 204, Mar. 2022, doi: 10.1016/j.applthermaleng.2021.117862.
- [13] M. Sakthi Priya and D. Sakthivadivel, "Experimental investigation on the thermal performance of a novel thermosyphon heat pipe with truncated cone for heat recovery systems," *Energy Convers Manag*, vol. 276, p. 116522, Jan. 2023, doi: 10.1016/j.enconman.2022.116522.



Ground Testable Spacecraft Heat Pipe (GTSHP)

ABSTRACT

The Ground Testable Spacecraft Heat Pipe (GTSHP) system is designed to move heat against gravity through a passive, sealed system. This novel heat pipe is focused on effectively testing heat pipes in the presence of gravity such that the heat pipe being tested is in a favorable orientation. In contrast to the industry standard testing practices which prescribe testing in a neutrally advantageous orientation, this system would allow the full capabilities of heat pipe based thermal control systems to be investigated on the ground.

Trevor Bird

BlueHalo at Air Force Research Labs

Abstract:..... 1
Introduction: 2
Methods of Research: 3
Results..... 5
Future Aspirations..... 6
References 7

Figure 1: Hewitt Robert's Flow Regime Map with Data Overlay 2
Figure 2: GTSHP TC Locations 5
Figure 3: Temperature vs. Time of GTSHP Testing 4

Abstract:

The Ground Testable Spacecraft Heat Pipe (GTSHP) system is designed to move heat against gravity through a passive, sealed system. This novel heat pipe is focused on effectively testing heat pipes in the presence of gravity such that the heat pipe being tested is in a favorable orientation. In contrast to the industry standard testing practices which prescribe testing in a neutrally advantageous orientation, this system would allow the full capabilities of heat pipe based thermal control systems to be investigated on the ground. For the GTSHP to operate, the thermal-fluidic system requires the effective use of a bubble pump and a negligible pressure gradient between its two chambers. In order to facilitate these two requirements, a simulation was designed and implemented to find the required system parameters in which the GTSHP would operate. The final iteration of the simulation gave parameters for a system that allowed for a negligible pressure difference as well as plug-slug flow in the bubble pump. Once these parameters were found, a proof-of-concept system was manufactured and tested. The first iteration of this system has already proven successful at moving heat against gravity, paving the way for future iterations that can facilitate higher heat flux transport. The improved future testing capabilities of heat pipe based thermal management systems will refine our understanding of these systems, ultimately leading to more effective, reliable systems.

Introduction:

The Ground Testable Spacecraft Heat Pipe's passive pump design was based off Sorenson's Bubble Pump. For a bubble pump to operate effectively, two-phase flow must be occurring as plug/slug flow. As bubbles form in a bubble pumps riser tube that span the width of the tube diameter, liquid is able to be lifted on top of this vapor slug. This rise of fluid on top of its vapor counterpart is the pumping action of a bubble pump. The calculations used/derived to shape the design components of the system were heavily based on the Hewitt Roberts flow regime map. Successful solutions to the thermofluidic system parameters supported the design choices which allowed for successful operation of said system. The solutions to pressure variation and power input within the simulated environment were input into two phase momentum flow equations and plotted as the blue line with red dots at 10-watt power increments, overlaid on the Hewitt Robert's Flow Regime Map, seen Figure 1. Once the operational system parameters were found, it was a matter of finding the solutions for the point on the line that bisected the slug flow regime line within the Hewitt Robert's flow regime, shown as the green dot in Figure 1.

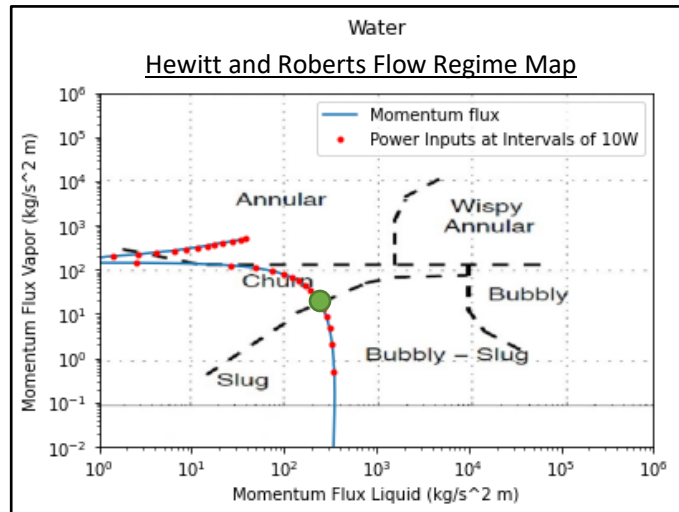


Figure 1: Hewitt Robert's Flow Regime Map with Data Overlay [3]

Once the operational system parameters were found, it was a matter of finding the solutions for the point on the line that bisected the slug flow regime line within the Hewitt Robert's flow regime, shown as the green dot in Figure 1.

The method of solving the thermofluidic system that is the GTSHP is inspired by *Modelling and analysis of Bubble Pump Parameters for Vapor Absorption Refrigeration Systems* by Aman et. Al.[1] The model developed in said paper was a continuation of analysis developed by Delano in 1998 [2], whose research was a continuation of Einstein's refrigeration cycle research. Delano's analysis assumed an ideal system based off the assumptions listed below:

- All supplied heat went into evaporation of water to generate bubbles
- Velocity of bubbles were constant within the bubble pump.
- No heat loss outside of the designed heat rejection zone.
- Constant value slip factor
- Assumption of single-phase flow (avoiding gas fraction)

Because of these assumptions, this analysis had to be changed slightly to bring it closer to a true representation of a physical system that could be manufactured. The main additions to Delano's work came with the introduction of a friction factor and void fraction. The pertinent equations are listed below [1].

$$f = 8 \left[\left(\frac{8}{Re} \right)^{12} + \frac{1}{(A+B)^{1.5}} \right]^{1/12} \quad (1)$$

$$A = \left[2.457 * \ln \left(\frac{1}{\left(\frac{7}{Re} \right)^{0.9} + 0.27 \frac{\epsilon}{D}} \right) \right]^{16} \quad (2)$$

$$B = \left(\frac{37530}{Re} \right)^{16} \quad (3)$$

$$\alpha_d = \frac{\dot{V}'_g}{C_0(\dot{V}'_l + \dot{V}'_g) + v_{b'}} \quad (4)$$

Where f is Darcy's friction factor, ϵ is the pipe roughness in meters, \dot{V}'_g is the unitless Freud number associated with the gaseous volume flux.

Methods of Research:

In order to understand this system in a way that could become analogous to a physical system, the many pertinent equations outlined in the research done by Aman et. Al. were altered in order to be iteratively solved based on the parameters of the system that was inevitably built. In order to solve the system of equations, a multitude of parameters were input into a python script which solved most importantly the pressure equation over 10^6 times per script execution until the outputs aligned with those associated with plug slug flow. This script was used to find which idealized conditions the physical system would become operational under. One of these idealized conditions which allowed the use of water as a working fluid was that of imposing a partial vacuum on the system, thus lowering the boiling point of the water. Other working fluids were input into these calculations and multiple suitable options were found, but due to hazardous waste limitations imposed on the research facility, water was chosen to be used because of its ease of access for use in a controlled environment. This configuration was chosen to allow for safer operation of the initial system at lower overall temperatures.

Once a positive outcome from this script was found, the physical system was designed and manufactured in its simplest form in order to show a proof of concept. The initial system, if successful, would prove validity of this heat pipe system under some of the least favorable conditions. These conditions entailed moving heat against gravity from its highest point of heat acquisition to its lowest point of heat rejection: 2 meters.

The first build did not include all possible data acquisition, only thermocouples placed before and after any components that could lead to temperature change. The reason for minimal data acquisition was to allow for minimal time and monetary input in order to show that the system could achieve startup of the bubble pump. This proof of concept was successful in that the bubble pump did become operational with only power input in the form of heat.

Upon successful proof of concept, the system was upgraded with the following:

- Computer controlled power input
- Analog flow valve in Heat Acquisition Cold Plate (HACP) downcomer
- Analog pressure gauge
- More robust thermal insulation from the environment
 - This included backing heaters on each of the holding tanks as they were the largest uncontrolled surface area.

The installation of the analog flow meter became a hinderance to flow into the heat acquisition cold plate, causing a dry out of the bubble pump. In the end, the removal of the flow meter allowed researchers to observe thermocouple readings that represent this fluidic environment. After this problem was found, the flow meter was removed to continue testing. Future testing will make use of non-intrusive flow metering in the form of an ultrasonic flow meter.

In all testing to date, pressure increase due to leaking at the polycarbonate/aluminum tank interface was a problem that could not be fixed without the removal of the view port. A concession in these preliminary tests was allowed so that researchers could know the status of flow that was accompanied with thermocouple readings. As explained in the results section, these thermal conditions have been associated with their flow type counterpart so that in future iterations of this system, the viewports will not be necessary.

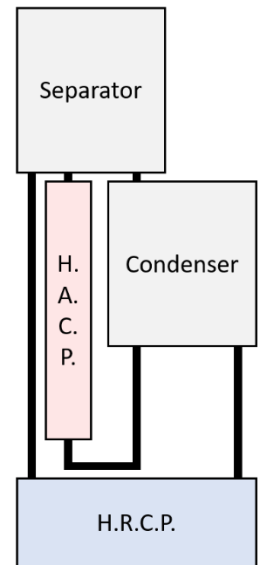


Figure 3: Component Naming Scheme

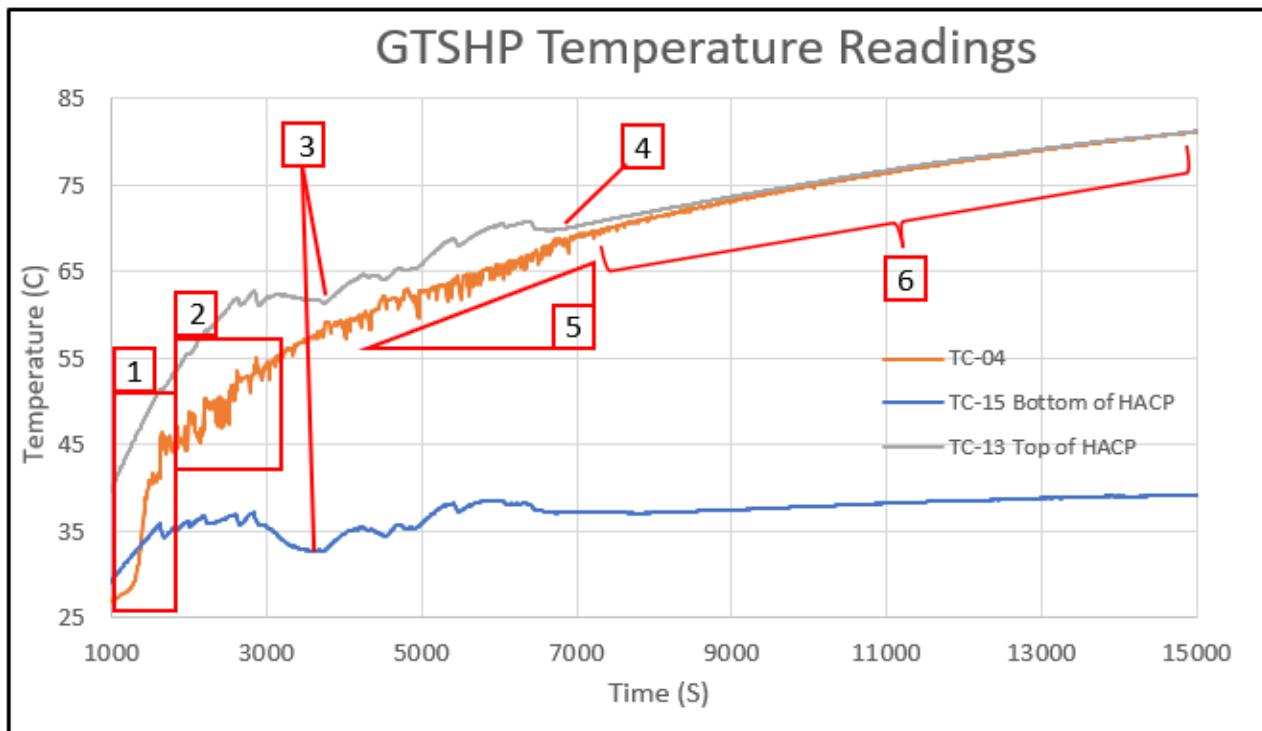


Figure 2: Temperature vs. Time of GTSHP Testing

Results

Through later testing during which the power input could be recorded, a power input value of 60 Watts was imparted onto the HACP. After initial warming of the system, startup of the bubble pump was witnessed along with a rapid increase in temperature for the thermocouple placed ~8cm above the top of the heat acquisition zone of the HACP. This showed the test conductor that indeed the water has enough consistent boiling to raise the water level to that point. This thermocouple became an indicator of the flow characteristics within the bubble pump due to its non-negligible variance in temperature coinciding with flow into the separator. This was followed within 30 seconds by the first burst of liquid out of the top of the HACP into the separator chamber. This initial burst of liquid is termed our point of “Start-up” for the system. As seen in point of interest 1 of Figure 3, this startup consists of a large jump in temperature and a continued oscillation of temperature of TC 04. Researchers concluded that this rapid oscillation of temperature represents plug slug flow. a slug of air passes the point of temperature reading, the temperature drops and for each slug of liquid that passes the temperature increases rapidly.

After 30 minutes of slug-plug flow, researchers witnessed a large amount of rapid fluid movement out of the HACP riser which was accompanied by a noticeable drop in temperature for those thermocouples placed lower on the HACP (shown by point of interest 3 in figure 3). This dip in temperature represents a larger flux of water entering the HACP zone, dropping the average temperature away from its boiling point and stalling the boiling within the HACP riser. This stall is corroborated by a loss of temperature oscillation in TC04 which is used as the boiling indicator. After approximately 15 minutes, the boiling was witnessed to start up again. This stall was not witnessed again through this data set, and it is inferred that this is due to the average temperature of the fluid in the system rising enough to allow for continued boiling without stalling.

Because of the slow leak of vacuum pressure, the boiling temperature of the water in the system slowly increased at a rate matching that of pressure rise. Inevitably, this pressure rise lead to the fluid reaching a boiling temperature that could not be met with a 60-watt power input. Loss of performance is associated with the loss of temperature amplitude over time shown in Figure 3. At the point of amplitude decrease, a slow trickle of water was witnessed to be entering into the separator from the HACP riser. It was inferred that this low amplitude, continual flow represented a bubbly or bubbly slug regime flow. This regime flow was able to be sustained for an extended period, even with a continual rise in pressure. As this was not the intended result, researchers did not continue testing to observe when this flow would also stall out due to increased boiling temperature.

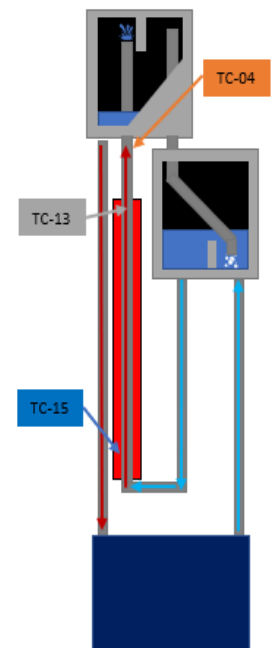


Figure 4: GTSHP TC Locations

Future Work

Upon implementation of a non-intrusive flow meter, researchers hope to calculate the amount of power that is rejected from the system. Power rejected from the system can be calculated using the flow rate and the temperature change across the Heat Rejection Cold Plate (HRCP), from which losses can be calculated. In conjunction with a better understanding of the performance of this system, researchers will further the design of the system to be integrated onto a CCHP as it would be in its intended purpose of testing heat pipe systems on spacecraft during their system level testing. If successful, the only input would be found at the heat acquisition zone of the CCHP, representing the heat produced by onboard systems, the CCHP would move this power to its heat rejection zone, imparting it to the GTSHP. The GTSHP would then transfer this power back into the CCHP at its heat acquisition zone. This feedback would simulate gravity-independent environmental conditions found in flight without the need for active PFL systems to be integrated on the system during testing.

References

- [1] J. Aman, D. S-K Ting, P. Henshaw, Modelling and Analysis of Bubble Pump Parameters for Vapor Absorption Refrigeration Systems. In 2016 ASHRAE Annual Conference. June 25-29, 2016. St. Louis, MO USA.
- [2] A. Delano, Design Analysis of the Einstein Refrigeration Cycle, Ph.D. Thesis, Georgia Institute of Technology.
- [3] Chemical Engineering Division, Studies of Two Phase Flow Patterns by Simultaneous X-Ray and Flash Photography, AERE – M 2159, United Kingdom Atomic Energy Authority, 1969.